長庚科技大學慢性疾病暨健康促進研究中心
成員名單

※ 依中文筆畫順序排列

李江文	Chiang-Wen, Lee
紀妙青	Miao-Ching, Chi
郭星君	Hsing-Chun, Kuo
陳美燕	Mei-Yen, Chen
黃淑倫	Su-Lun, Hwang
劉瑞芳	Jui-Fang, Liu
林資展	Zih-Chan, Lin

長庚科技大學慢性疾病暨健康促進研究中心

論文集

2025.1.1 ~ 2025.12.31

目錄

一、 期刊論文出處及相關訊息..... I

二、 論文全文

序號	論文標題	主要負責教師	頁碼
01	Mir221- and Mir222-enriched adsc-exosomes mitigate PM exposure-exacerbated cardiac ischemia-reperfusion injury through the modulation of the BNIP3-MAP1LC3B-BBC3/PUMA pathway	李江文	1
02	Comparative Evaluation of Dental Clinical Surface Treatments for Polyetheretherketone with Airborne-Particle Abrasion, Hydrofluoric Acid Etching, and Handheld Nonthermal Plasma Activation on Long-Term Bond Performance	李江文	21
03	Dual cell-penetrating peptide-conjugated polymeric nanocarriers for miRNA-205–5p delivery in gene therapy of cutaneous squamous cell carcinoma	林資展	33
04	Effects of ambient fine particulate matter on the exacerbation of psychiatric disorders in southern Taiwan: a case-crossover study	紀妙青	51
05	Peptide from tempeh-like fermented Chenopodium formosanum counters senescence while enhancing antioxidant ability in non-replicative aging	郭星君	64
06	Molecular mechanisms and biomarkers of total parenteral nutrition-induced hepatotoxicity revealed by iTRAQ proteomics analysis	郭星君	75
07	A Novel Erinacine S Derivative from Hericium erinaceus Overcomes Chemoresistance in Colorectal Cancer Cells by Enhancing TRAIL/TNFR1/DR5 Expression through Histone Acetylation	郭星君	93

08	High Prevalence of Cardiometabolic Risks and Health Needs Among Patients With Hepatocellular Carcinoma After Treatment: A Cross-sectional Study	陳美燕	110
09	Inspiratory muscle training and aerobic exercise for respiratory muscle strength in myasthenia gravis post-hospitalization: A randomized controlled trial.	劉瑞芳	117
10	Differential efficacy of olfactory neurospheres from deviated nasal septum and chronic rhinosinusitis patients in regenerating olfactory epithelium.	李江文	127
11	Induction of endogenous IL-10 promotes resolution and tolerance of nitric oxide in microglia	郭星君	148
12	Animal models of psoriasis for novel drug discovery: a literature update.	林資展	159
13	Melatonin attenuates high-fat diet- and particulate matter-induced cardiac injury: involvement of mitochondrial quality and miR-221/222 expression	李江文	176
14	Novel strategies in topical delivery for psoriasis treatment: nanocarriers and energy-driven approaches	林資展	196
15	The relationship between health literacy and medical decision conflict among parents of children newly diagnosed with central precocious puberty	陳美燕	214
16	IPSC-Derived Conditioned Medium Reduces Oxidative Stress and Vascular Remodeling in Rat Models of Pulmonary Arterial Hypertension	紀妙青	222
17	Lutein attenuates rheumatoid arthritis progression by suppressing MAPK/NF-κB signaling and MMP3 and MMP13 expression in fibroblast-like Synoviocytes	李江文	242
18	Protective Effect of Lutein in Cisplatin-Induced Intestinal Barrier Damage by Restoring ZO-1 Expression	李江文	254
19	Targeting c-Src/PKCα/MAPK/NF-κB: Salvianolic Acid A as a Protective Agent against Silica Nanoparticle-Induced Lung Inflammation	李江文	271

20	Mevastatin-Induced HO-1 Expression in Cardiac Fibroblasts: A Strategy to Combat Cardiovascular Inflammation and Fibrosis	李江文	297
21	Inspiratory muscle training facilitates liberation from mechanical ventilation in subacute critically ill patients: A randomized controlled trial	劉瑞芳	314
22	MiR221/222 in the conditioned medium of adipose-derived stem cells attenuates particulate matter and high-fat diet-induced cardiac apoptosis	李江文	323
23	TAS4464, a neddylation inhibitor, mitigates Staphylococcus aureus-induced periprosthetic joint infection by modulating immunosuppressive cell functions	李江文	344
24	Impacts of surface characteristics on biological responses and biofilm formation of 3D-printed denture base resins: An in vitro study	林資展	358

長庚科技大學慢性疾病暨健康促進研究中心

論文集

2025.1.1 ~ 2025.12.31

一、 期刊論文出處及相關訊息

01 Lee, T.L., Shen, W.C., Chen, Y.C., Lai, T.C., Lin, S.R., Lin, S.W., Yu, I.S., Yeh, Y.H., Li, T.K., Lee, I.T., Lee, C.W.*, & Chen, Y.L. (2025). Mir221- and Mir222-enriched adsc-exosomes mitigate PM exposure-exacerbated cardiac ischemia-reperfusion injury through the modulation of the BNIP3-MAP1LC3B-BBC3/PUMA pathway. *Autophagy,* 21(2):374-393. doi: 10.1080/15548627.2024.2395799.

02 Lai, S.Y., Lin, S.I., Chang, C.W., Shen, Y.R., Mine, Y., Lin, Z.C., Fang, M.L., Sung, C.C., Tseng, C.F., Peng, T.Y., & Lee, C.W.* (2025). Comparative Evaluation of Dental Clinical Surface Treatments for Polyetheretherketone with Airborne-Particle Abrasion, Hydrofluoric Acid Etching, and Handheld Nonthermal Plasma Activation on Long-Term Bond Performance. *Polymers,* 17(11):1448. doi: 10.3390/polym17111448.

03 Lin, C.Y., Fang, J.Y., Hsiao, C.Y., Lee, C.W., Alshetaili A., & Lin, Z.C.* (2025). Dual cell-penetrating peptide-conjugated polymeric nanocarriers for miRNA-205–5p delivery in gene therapy of cutaneous squamous cell carcinoma. *Acta Biomaterialia,* 196:332-349. doi: 10.1016/j.actbio.2025.02.056.

04 Hwang, S. L., Lin, Y. C., Lin, C. M., & Chi, M. C.* (2025). Effects of ambient fine particulate matter on the exacerbation of psychiatric disorders in southern Taiwan: a case-crossover study. *International Journal of Environmental Health Research,* 35(11):3210-3221. doi: 10.1080/09603123.2025.2480853.

05 Hsieh, C. C., Lin, H. W., Huang, H. C., Khumsupan, D., Shen, S. Z., Lin, S. P., Hsieh, C. W., Tsai, T. Y., Jantama, S. S. K., Kuo, H. C.*, & Cheng, K. C. (2025). Peptide from tempeh-like fermented Chenopodium formosanum counters senescence while enhancing antioxidant ability in non-replicative aging. *LWT*, 222, 117641. https://doi.org/10.1016/j.lwt.2025.117641.

06 Hsieh, Y. Y., Tsai, J. J., Tung, S. Y., Lee, K. C., Cheng, K. C., Lee, K. F., Hsieh, M. C., Huang, C. Y., Teng, C. C., Shen, C. H., & Kuo, H. C.* (2025). Molecular mechanisms and biomarkers of total parenteral nutrition-induced hepatotoxicity revealed by iTRAQ proteomics analysis. *International Journal of Medical Sciences,* 22(16):4295-4312. doi:

10.7150/ijms.122025.

07 Tung, S. Y., Lee, K. F., Hsieh, Y. Y., Cheng, K. C., Lee, K. C., Lee, L. Y., Chen, W. P., Chen, C. C., Teng, C. C., Hsieh, M. C., Huang, C. Y., & Kuo, H. C.* (2025). A Novel Erinacine S Derivative from Hericium erinaceus Overcomes Chemoresistance in Colorectal Cancer Cells by Enhancing TRAIL/TNFR1/DR5 Expression through Histone Acetylation. *International Journal of Medical Sciences,* 22(16):4278-4294. doi: 10.7150/ijms.119894.

08 Chen, Y.L., Su, C.C., Chang, C.H., James, K., & Chen, M.Y.* (2025). High Prevalence of Cardiometabolic Risks and Health Needs Among Patients With Hepatocellular Carcinoma After Treatment: A Cross-sectional Study. *Cancer Nurs.*, 48(4):327-333. doi: 10.1097/NCC.0000000000001326.

09 Chang, C. L., Fang, T. P., Tsai, H. M., Chen, H. C., Liu, S.F., Lin, H. L.*, & Liu, J. F.* (2025). Inspiratory muscle training and aerobic exercise for respiratory muscle strength in myasthenia gravis post-hospitalization: A randomized controlled trial. *BMC Pulmonary Medicine*, 25, 266.

10 Jiang, R.S.#, Lee, C.W.#, Lin, Y.H., Wang, J.J., Liao, J.B., Peng, K.T., Chiang, Y.C., & Chi, P.L. (2025). Differential efficacy of olfactory neurospheres from deviated nasal septum and chronic rhinosinusitis patients in regenerating olfactory epithelium. *Stem Cell Research & Therapy,* 16(1):166. doi: 10.1186/s13287-025-04270-0.

11 Kuo, H.C., Chen, J.S., Chao, C.N., Lee, K.F., Huang, Y.T., Mao, P.C., Lin, T.C., Chiu, S.C., Huang, Y.L., & Chu, C.H. (2025). Induction of endogenous IL-10 promotes resolution and tolerance of nitric oxide in microglia. *Brain, Behavior, & Immunity - Health,* 49:101094. doi: 10.1016/j.bbih.2025.101094.

12 Lin, Z.C., Yang, S.C., Tran, T.T.P., & Fang, J.Y. (2025). Animal models of psoriasis for novel drug discovery: a literature update. *Expert Opinion on Drug Discovery,* 20(9):1193-1208. doi: 10.1080/17460441.2025.2528959.

13 Chen, Y.C., Lee, M.H., Fu, S.J., Lee, C.W., Shen, W.C., Lai, T.C., Lin, S.R., Lin, S.W., Yu, I.S., Chuang, T.Y., Tsai, J.S., & Chen, Y.L. (2025). Melatonin attenuates high-fat diet- and particulate matter-induced cardiac injury: involvement of mitochondrial quality and miR-221/222 expression. *Biochemical Pharmacology,* 242(Pt 3):117346. doi: 10.1016/j.bcp.2025.117346.

14 Lin C.Y., Lin Z.C., Chang Y.T., Lin T.J., & Fang J.Y. (2025). Novel strategies in topical delivery for psoriasis treatment: nanocarriers and energy-driven approaches. *Expert Opinion on Drug Delivery,* 22(4):565-581. doi: 10.1080/17425247.2025.2472968.

15 Shen, M.Y., Chiu, C.F., Chen, M.Y., Yang, L.Y., Okoli, C.T.C., & Liu, Y.M. (2025). The relationship between health literacy and medical decision conflict among parents of children newly diagnosed with central precocious puberty. *Journal of Pediatric Nursing,* 85:362-369. doi: 10.1016/j.pedn.2025.08.017.

16 Cheng, C. C., Hsu, L. F., Chung, H.H., Lee, C.W., Chiang, C. H., Yang, H. C., Chi, M. C., Lee, M. H., Huang, W. C., & Chi, P.L. (2025). IPSC-Derived Conditioned Medium Reduces Oxidative Stress and Vascular Remodeling in Rat Models of Pulmonary Arterial Hypertension. *Journal of Cellular Physiology,* 240(8):e70085. doi: 10.1002/jcp.70085.

17 Chang, C.J., Chang, T.M., Sun, Y.S., Lin, J.F., Lee, C.W., Fang, M.L., & Liu, J.F. (2025). Lutein attenuates rheumatoid arthritis progression by suppressing MAPK/NF-κB signaling and MMP3 and MMP13 expression in fibroblast-like Synoviocytes. *Immunopharmacology journals,* 164:115360. doi: 10.1016/j.intimp.2025.115360.

18 Chang, C.J., Chang, T.M., Sun, Y.S., Lin, J.F., Lee, C.W., Fang, M.L., & Liu, J.F. (2025). Protective Effect of Lutein in Cisplatin-Induced Intestinal Barrier Damage by Restoring ZO-1 Expression. *Journal of Food Biochemistry,* 9954087.doi: 10.1155/jfbc/9954087.

19 Lin, Y. J., Lee, I. T., Wu, W. B., Yang, C. C., Lee, C. W., Tsai, F. J., Tseng, H. C., Lin, W. N., Hsiao, L. D., & Yang, C. M. (2025). Targeting c-Src/PKCα/MAPK/NF-κB: Salvianolic Acid A as a Protective Agent against Silica Nanoparticle-Induced Lung Inflammation. *Biocell*, 49(7):1265-1290. doi: 10.32604/biocell.2025.066223

20 Lee, I. T., Yang, C. C., Lin, Y. J., Wu, W. B., Lin, W. N., Lee, C. W., Tseng, H. C., Tsai, F. J., Hsiao, L. D., & Yang, C. M. (2025). Mevastatin-Induced HO-1 Expression in Cardiac Fibroblasts: A Strategy to Combat Cardiovascular Inflammation and Fibrosis. *Environmental Toxicology,* 40(2):264-280. doi: 10.1002/tox.24429.

21 Wang, S. J., Fang, T. P., Rowley, D. D., Liu, N. W., Chen, J. O., Liu, J. F., & Lin, H. L. (2025). Inspiratory muscle training facilitates liberation from mechanical ventilation in subacute critically ill patients: A randomized controlled trial. *Frontiers in Medicine,* 11, 1503678. doi: 10.3389/fmed.2024.1503678.

22 Chen, Y. C., Pu, C. M., Lin, S. R., Lin, S. W., Yu, I. S., Shih, H. J., Lee, C. W., Lee, M. H., Kuo, Y. T., & Chen, Y. L. (2025). MiR221/222 in the conditioned medium of adipose-derived stem cells attenuates particulate matter and high-fat diet-induced cardiac apoptosis. *Stem Cell Research & Therapy,* 16, 285. doi: 10.1186/s13287-025-04381-8.

23 Peng, K.T., Chen, J.L., Hsieh, Y.C., Hsiao, C.Y., Yang, C.C., Liu, J.F., Lee, C.W., Chiang, Y.C., & Chang, P.J. (2025). TAS4464, a neddylation inhibitor, mitigates Staphylococcus aureus-induced periprosthetic joint infection by modulating immunosuppressive cell functions. *Biomedicine & Pharmacotherapy*, 192, 118622. doi: 10.1016/j.biopha.2025.118622.

24 Tseng, C.F., Sung, C.C., Yang, Y.T., Chen, F.N., Mine, Y., Chiang, Y.C., Lin, Z.C., Fang, M.L., Chen, H.M., Kok, S.H., & Peng, T.Y. (2025). Impacts of surface characteristics on biological responses and biofilm formation of 3D-printed denture base resins: An in vitro study. *Journal of Dental Sciences*, 20(3):1716-1722. doi: 10.1016/j.jds.2025.03.027.

AUTOPHAGY
2025, VOL. 21, NO. 2, 374–393
https://doi.org/10.1080/15548627.2024.2395799

Taylor & Francis
Taylor & Francis Group

RESEARCH PAPER

OPEN ACCESS Check for updates

Mir221- and *Mir222*-enriched adsc-exosomes mitigate PM exposure-exacerbated cardiac ischemia-reperfusion injury through the modulation of the BNIP3-MAP1LC3B-BBC3/PUMA pathway

Tzu-Lin Lee[a], Wen-Chi Shen[a], Ya-Chun Chen[a], Tsai-Chun Lai[a,b,c], Shu-Rung Lin[d,e], Shu-Wha Lin[f], I-Shing Yu[g], Yen-Hsiu Yeh[h], Tsai-Kun Li[h,i,j], I-Ta Lee[k], Chiang-Wen Lee[l,m,n], and Yuh-Lien Chen [a]

[a]Department of Anatomy and Cell Biology, College of Medicine, National Taiwan University, Taipei, Taiwan; [b]Department of Life Sciences, College of Life Sciences, National Chung Hsing University, Taichung, Taiwan; [c]The iEGG and Animal Biotechnology Center, National Chung Hsing University, Taichung, Taiwan; [d]Department of Bioscience Technology, College of Science, Chung Yuan Christian University, Taoyuan, Taiwan; [e]Center for Nanotechnology, Chung Yuan Christian University, Taoyuan, Taiwan; [f]Department of Clinical Laboratory Sciences and Medical Biotechnology, College of Medicine, National Taiwan University, Taipei, Taiwan; [g]Laboratory Animal Center, College of Medicine, National Taiwan University, Taipei, Taiwan; [h]Department and Graduate Institute of Microbiology, College of Medicine, National Taiwan University, Taipei, Taiwan; [i]Center for Biotechnology, National Taiwan University, Taipei, Taiwan; [j]Centers for Genomic and Precision Medicine, National Taiwan University, Taipei, Taiwan; [k]School of Dentistry, College of Oral Medicine, Taipei Medical University, Taipei, Taiwan; [l]Department of Orthopaedic Surgery, Chang Gung Memorial Hospital, Puzi, Chiayi, Taiwan; [m]Department of Nursing, Division of Basic Medical Sciences, and Chronic Diseases and Health Promotion Research Center Chang Gung University of Science and Technology, Puzi, Chiayi, Taiwan; [n]Research Center for Industry of Human Ecology and Research Center for Chinese Herbal Medicine, Chang Gung University of Science and Technology, Taoyuan, Taiwan

ABSTRACT

Epidemiology has shown a strong relationship between fine particulate matter (PM) exposure and cardiovascular disease. However, it remains unknown whether PM aggravates myocardial ischemia-reperfusion (I/R) injury, and the related mechanisms are unclear. Our previous study has shown that adipose stem cell-derived exosomes (ADSC-Exos) contain high levels of *Mir221* and *Mir222*. The present study investigated the effects of PM exposure on I/R-induced cardiac injury through mitophagy and apoptosis, as well as the potential role of *Mir221* and *Mir222* in ADSC-Exos. Wild-type, *mir221*- and *mir222*-knockout (KO), and *Mir221*- and *Mir222*-overexpressing transgenic (TG) mice were intratracheally injected with PM (10 mg/kg). After 24 h, mice underwent left coronary artery ligation for 30 min, followed by 3 h of reperfusion (I/R). H9c2 cardiomyocytes were cultured under 1% O_2 for 6 h, then reoxygenated for 12 h (hypoxia-reoxygenation [H/R]). PM aggravated I/R (or H/R) cardiac injury by increasing ROS levels and causing mitochondrial dysfunction, which increased the expression of mitochondrial fission-related proteins (DNM1L/Drp1 and MFF) and mitophagy-related proteins (BNIP3 and MAP1LC3B/LC3B) *in vivo* and *in vitro*. Treatment with ADSC-Exos or *Mir221*- and *Mir222*-mimics significantly reduced PM+I/R-induced cardiac injury. Importantly, ADSC-Exos contain *Mir221* and *Mir222*, which directly targets BNIP3, MAP1LC3B/LC3B, and BBC3/PUMA, decreasing their expression and ultimately reducing cardiomyocyte mitophagy and apoptosis. The present data showed that ADSC-Exos treatment regulated mitophagy and apoptosis through the *Mir221* and *Mir222*-BNIP3-MAP1LC3B-BBC3/PUMA pathway and significantly reduced the cardiac damage caused by PM+I/R. The present study revealed the novel therapeutic potential of ADSC-Exos in alleviating PM-induced exacerbation of myocardial I/R injury.

Abbreviation: ADSC-Exos: adipose-derived stem cell exosomes; AL: autolysosome; ATP: adenosine triphosphate; BBC3/PUMA: BCL2 binding component 3; BNIP3: BCL2/adenovirus E1B interacting protein 3; CASP3: caspase 3; CASP9: caspase 9; CDKN1B/p27: cyclin dependent kinase inhibitor 1B; CVD: cardiovascular disease; DCFH-DA: 2',7'-dichlorodihydrofluorescein diacetate; DHE: dihydroethidium; DNM1L/Drp1: dynamin 1-like; EF: ejection fraction; FS: fractional shortening; H/R: hypoxia-reoxygenation; I/R: ischemia-reperfusion; LDH: lactate dehydrogenase; MAP1LC3B/LC3B: microtubule-associated protein 1 light chain 3 beta; MFF: mitochondrial fission factor; miRNA: microRNA; NAC: N-acetylcysteine; OCR: oxygen consumption rate; PIK3C3/Vps34: phosphatidylinositol 3-kinase catalytic subunit type 3; PM: particulate matter; PRKAA1/AMPK: protein kinase AMP-activated catalytic subunit alpha 1; ROS: reactive oxygen species; SQSTM1/p62: sequestosome 1; TEM: transmission electron microscopy; TRP53/p53: transformation related protein 53; TUNEL: terminal deoxynucleotidyl transferase dUTP nick end labeling.

ARTICLE HISTORY
Received 16 January 2024
Revised 19 August 2024
Accepted 20 August 2024

KEYWORDS
ADSC-exosomes; cardiomyocyte; ischemia/reperfusion injury; *Mir221* and *Mir222*; mitophagy; particulate matter

CONTACT Yuh-Lien Chen ylchenv@ntu.edu.tw Department of Anatomy and Cell Biology, College of Medicine, National Taiwan University, Taipei, Taiwan; Chiang-Wen Lee cwlee@mail.cgust.edu.tw Department of Nursing, Division of Basic Medical Sciences, and Chronic Diseases and Health Promotion Research Center, Chang Gung University of Science and Technology, No. 2, Sec. W., Jiapu Rd, Chiayi 61363, Taiwan

Supplemental data for this article can be accessed online at https://doi.org/10.1080/15548627.2024.2395799

© 2024 The Author(s). Published by Informa UK Limited, trading as Taylor & Francis Group.
This is an Open Access article distributed under the terms of the Creative Commons Attribution License (http://creativecommons.org/licenses/by/4.0/), which permits unrestricted use, distribution, and reproduction in any medium, provided the original work is properly cited. The terms on which this article has been published allow the posting of the Accepted Manuscript in a repository by the author(s) or with their consent.

Introduction

Increasing epidemiological evidence suggests that short- and long-term exposure to particulate matter (PM), especially fine particulate matter (PM2.5), can lead to the induction, progression, and worsening of cardiovascular disease (CVD) [1]. Inhalation of PM2.5 causes oxidative stress and inflammatory responses in the lungs, systemic circulation, and related organs/tissues (e.g., heart, vasculature, and adipocytes). Evidence from animal models suggests that atherosclerosis, hypertension, thrombosis, and heart failure associated with cardiovascular disease may be exacerbated by PM2.5 [2,3]. Coronary artery disease is the most common form of CVD. The medical strategy to treat coronary artery disease is timely reperfusion, such as percutaneous coronary intervention/PCI and coronary artery bypass grafting/CABG [4]. However, while reperfusion promotes blood flow recovery in the border zone of myocardial infarction and rescues myocardial cells, it also exacerbates cardiac ischemia-reperfusion (I/R) myocardial injury. The mortality of cardiac I/R injury has increased over the past few decades. Efforts have been made to elucidate the precise cellular and molecular mechanisms of cardiac I/R injury, such as the interaction between autophagy and apoptosis [5]. However, PM-related I/R-induced cardiac injury and its associated mechanisms, especially mitochondrial dysfunction, remain poorly understood.

Several mechanisms, including reactive oxygen species (ROS) overproduction, apoptosis, and imbalanced mitochondrial dynamics, have been proposed to contribute to cardiac I/R injury [6]. A previous study has reported that increased mitochondrial fission and decreased mitochondrial fusion are observed during cardiac I/R injury, resulting in cardiac damage [7]. Mitochondrial fission is regulated by DNM1L/Drp1 (dynamin 1-like) and MFF (mitochondrial fission factor). Furthermore, mitochondria are critical for maintaining normal cellular functions through mitophagy [8]. The role of mitophagy remains controversial. Mitophagy has beneficial and adverse effects on CVD [9]. Autophagy is thought to be cardioprotective during ischemia but detrimental during reperfusion [10,11]. BNIP3 (BCL2/adenovirus E1B interacting protein 3) mediates mitophagy through its cytoplasmic LIR granules, which interact with MAP1LC3B/LC3B (microtubule-associated protein 1 light chain 3 beta)-family proteins [12]. In addition, myocardial I/R injury induces MAPK/JNK activation, increases MFF activity, increases BNIP3 activity, promotes excessive mitochondrial fission, promotes mitophagy, and leads to cell death [13]. BNIP3 is activated upon ischemic stimulation and promotes cardiomyocyte death [14]. Furthermore, PM increases ROS levels and triggers cardiomyocyte apoptosis in AC16 cardiomyocytes [15]. Short-term exposure to PM triggers mitophagy, which leads to mitochondrial dysfunction, partially mediating vascular fibrosis [16]. There are currently no reports elucidating the correlation among myocardial damage, disruption of the fission-fusion process, and mitophagy caused by the exposure of PM combined with I/R or H/R.

Adipose-derived stem cells (ADSCs) secrete paracrine products, including cytokines, growth factors, RNA, and microRNAs, which can be delivered to target organs for repair [17]. As essential transporters of paracrine factors, exosomes play important roles in angiogenesis, immune regulation, and tissue regeneration [18]. Our previous studies have shown that exosomes from ADSCs protect skin flaps and the heart from ischemia/reperfusion injury [19,20]. Evidence suggests that miRNAs are involved in various biological processes, including myocardial mitochondrial ROS, inflammation, and apoptosis [21]. Some evidence suggests that *Mir221* and *Mir222* are key regulators of cardiovascular function and tissue metabolism [22]. In addition, *Mir221* and *Mir222* promotes migration and invasion, as well as inhibits autophagy and apoptosis [23]. *Mir222* has also been shown to be associated with particulate matter exposure alone [24]. In the present study, miRTarBase was used to predict the specific binding sites of *Mir221* and *Mir222* in the 3' untranslated regions of *Bnip3* and *Lc3b*, suggesting that *Mir221* and *Mir222* may mediate mitophagy by regulating the *Bnip3* and *Lc3b* genes. Currently, there is limited knowledge regarding the involvement of *Mir221* and *Mir222* in the induction of cardiomyocyte apoptosis and mitophagy when PM and I/R (or H/R) are combined. The present study demonstrated that PM aggravates cardiac injury caused by I/R or H/R. In addition, *Mir221* and *Mir222* enrichment in ADSC-Exos affects ROS production, mitochondrial dynamics, and mitophagy, thereby reducing cardiac injury through the *Mir221* and *Mir222*-BNIP3-MAP1LC3B/LC3B-BBC3/PUMA pathway.

Results

Changes in ROS production and mitochondrial dynamics in vivo indicate that PM exposure aggravates I/R-induced cardiac injury

Echocardiography was used to assess whether PM affects cardiac function in mice under I/R conditions. Representative echocardiographic images were obtained from control, PM-, I/R-, and PM+I/R-treated mice. Compared to control mice, mice treated with PM or I/R alone had significantly reduced ejection fraction (EF) and fractional shortening (FS) percentages, indicating impaired systolic contractility. Moreover, the EF and FS of the PM+I/R group were even lower than those of the PM and I/R groups (Figure 1A). In addition, the plasma levels of LDH (lactate dehydrogenase) and TNNI (troponin I), which are indicators of cardiac injury, were significantly elevated in the PM+I/R group (Figure 1B). Analysis of the ischemic area using TTC staining revealed that the white infarct area in the PM+I/R group was significantly greater than that in the PM and I/R groups (Figure 1C). The underlying mechanisms affecting the impairment of cardiac function caused by PM exposure in I/R-treated mice were investigated. No obvious histological damage was detected by hematoxylin and eosin staining (Figure S1). To investigate whether the combination of PM exposure and I/R directly leads to cardiomyocyte apoptosis, which causes cardiac dysfunction, TUNEL staining was used to detect the degree of cardiomyocyte apoptosis in mice treated with PM and I/R. The proportion of apoptotic cells was significantly greater in the PM+I/R group than in the PM or I/R alone group according to the TUNEL assay

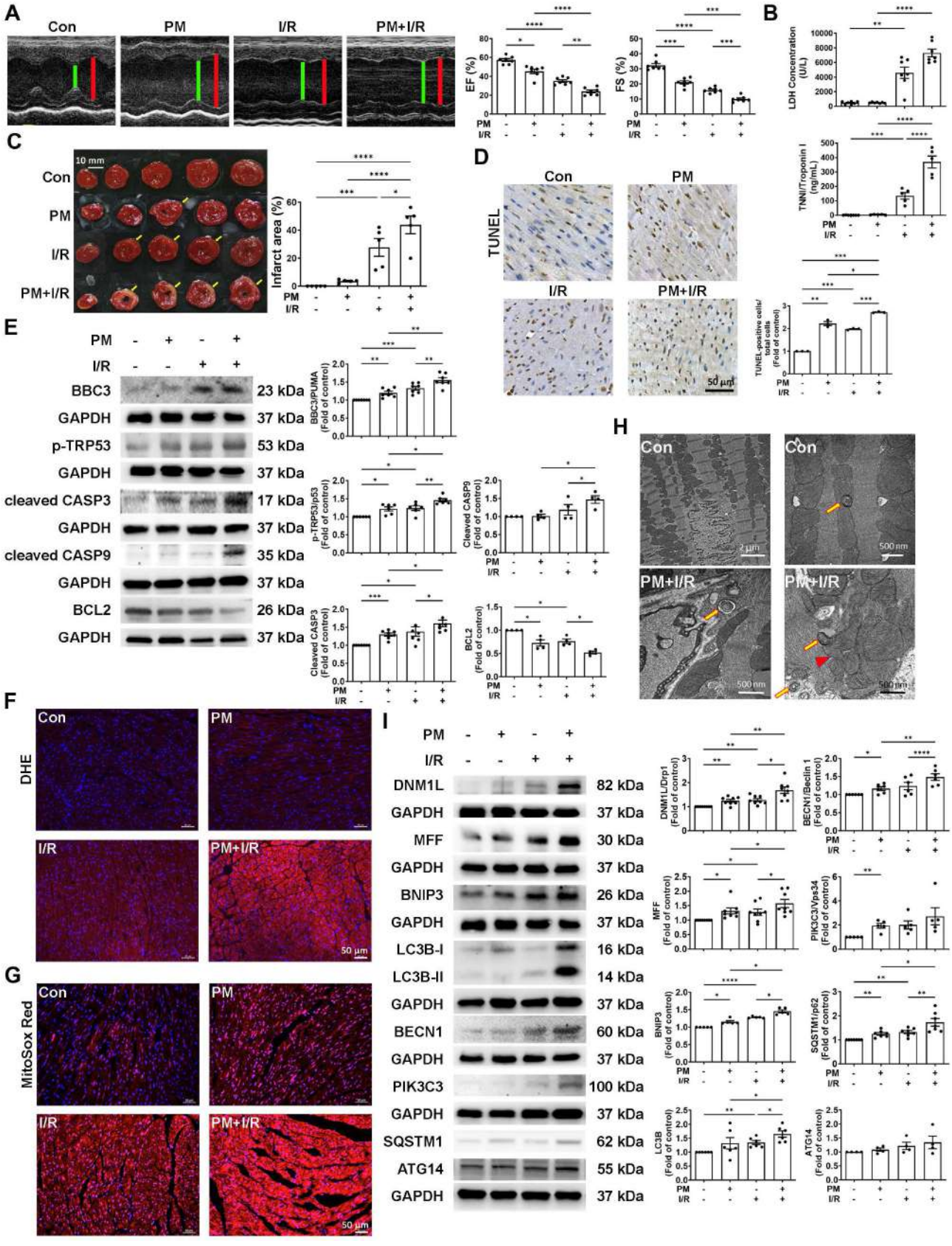


Figure 1. PM significantly impairs cardiac function and increases apoptosis in the hearts of C57BL/6J mice subjected to I/R. C57BL/6J mice were intratracheally injected with PM for 24 h, followed by 30 min of ischemia and 3 h of reperfusion. (A) images of the left ventricular end-systolic diameter (green line) and left ventricular end-diastolic diameter (red line) were obtained by echocardiography. EF and FS percentages were measured in control, PM, I/R, and PM+I/R mice ($n = 7$ mice per group). (B) cardiac injury was assessed by measuring plasma LDH and TNNI levels ($n = 5$-7 mice per group). (C) TTC staining was used to detect the ischemic area. The yellow arrows indicate the ischemic area (scale bar: 10 mm, $n = 5$ mice per group). (D) apoptotic cells were assessed by TUNEL assay (brown). Nuclei were counterstained by hematoxylin staining (blue). Scale bar: 50 μm; $n = 3$ mice per group. (E) Western blot analysis of the expression of apoptosis-related proteins (BBC3/PUMA, p-TRP53/p53, cl-CASP3, cl-CASP9, and BCL2) ($n = 4$-7). (F and G) intracellular and mitochondrial ROS were measured using DHE and MitoSOX red,

(Figure 1D). After PM+I/R treatment, the expression of BBC3/PUMA, p-TRP53/p53, cleaved CASP3 (caspase 3), and cleaved CASP9 (caspase 9) was significantly increased, whereas the expression of the BCL2 antiapoptotic protein was decreased (Figure 1E). I/R-induced cardiac injury is often caused by ROS production [6], and excessive ROS production results in mitochondrial dysfunction. In the present study, dihydroethidium (DHE) and MitoSOX Red were used to measure cellular and mitochondrial ROS, respectively. Cardiomyocytes subjected to I/R exhibited substantial ROS accumulation in cardiac tissue (Figures 1F, 1G, S2A, and S2B). Moreover, TEM analysis of heart tissue revealed mitochondrial ultrastructural changes in the hearts of PM+I/R-treated mice. In the control group, there were many normal mitochondria and myofilaments but few autophagosomes in the cytoplasm of cardiomyocytes. In contrast, the PM+I/R group exhibited many autophagosomes and mitochondrial fission (Figure 1H and S2C). To gain a more comprehensive understanding of mitochondrial dysfunction in PM+I/R hearts, the levels of mitochondrial fission-related proteins (DNM1L/Drp1 and MFF) and mitophagy-related proteins (BNIP3, MAP1LC3B/LC3B, BECN1/Beclin 1, PIK3C3/Vps34, SQSTM1/p62 and ATG14) were evaluated by western blot analysis. The expression levels of DNM1L/Drp1, MFF, BNIP3, MAP1LC3B/LC3B, BECN1/Beclin 1 and SQSTM1/p62 in the PM+I/R group were significantly higher than those in the PM alone and I/R alone treatment groups (Figure 1I). These results revealed that exposure to PM exacerbates I/R-induced cardiac diseases, increases ROS production, accelerates apoptosis, and promotes mitophagy.

PM exacerbates cardiomyocyte apoptosis through ROS generation under H/R conditions

To investigate the detailed mechanism by which PM exacerbates I/R-induced cardiac injury, a cell model was established by treating cells with different PM concentrations for 6 h, followed by 6 h of hypoxia and 12 h of reoxygenation (H/R). In the H/R model, cell viability decreased after 6 h of pretreatment of H9c2 cells with 10 or 50 μg/mL PM (Figure 2A). After treating H9c2 cells with 50 μg/mL PM and subjecting them to H/R (6 h/12 h), apoptosis was evaluated using TUNEL and ANXA5/annexin V-FITC-PI assays. TUNEL analysis revealed that apoptosis was significantly greater in the PM+H/R group than in the PM or H/R group (Figure 2B). The ANXA5/annexin V-FITC-PI assay showed that PM+H/R treatment accelerated apoptosis (Figure 2C). Compared to the PM or H/R group, the BBC3/PUMA, p-TRP53/p53, cleaved CASP3, and cleaved CASP9 expression was significantly increased in the PM+H/R group, whereas the BCL2 expression was significantly decreased in the PM+H/R group (Figure 2D). To study the effect of PM+H/R treatment, mitochondrial ROS was evaluated in H9c2 cells using MitoSOX Red and TO-PRO-3 double staining. Higher levels of mitochondrial ROS were detected in living cells (MitoSox Red-positive and TO-PRO-3-negative cells) under PM+H/R conditions (Figures 2E, 2F, and S2D). As shown by fluorescence microscopy and flow cytometry, PM+H/R treatment significantly increased the amount of cytoplasmic H_2O_2 in living cells (both PI-negative and DCFH-DA-positive cells) (Figures 2G, 2H, and S2E). Similarly, the DHE overlay resulting from fluorescence microscopy and flow cytometry showed that PM+H/R increased the production of cytoplasmic superoxide anions (DHE-positive and $DiOC_6(3)$-positive cells) (Figures 2I, 2J, and S2F). The addition of MitoTEMPO (a mitochondrial antioxidant) and N-acetylcysteine (NAC, an antioxidant) inhibited the PM+H/R-induced increase in mitochondrial ROS observed by fluorescence microscopy and flow cytometry (Figures 2K, 2L, and S2G). Western blot showed that MitoTEMPO or NAC treatment reduced BBC3/PUMA and p-TRP53/p53 expression but increased BCL2 expression (Figure 2M). These results indicated that PM+H/R treatment increased ROS production *in vitro*, leading to apoptosis and cardiac damage.

PM exacerbates apoptosis in H/R-treated cardiomyocytes by worsening mitochondrial function and increasing mitophagy

Previous studies have demonstrated that impaired mitochondrial function or excessive mitochondrial fission can lead to cell death and cardiac injury [25,26]. The ATP concentration, oxygen consumption rate (OCR), and mitochondrial membrane potential (ΔΨm) are critical parameters of mitochondrial function. In the present study, the ATP concentration was significantly lower in the PM or H/R treatment group than in the control group, and the reduction was more significant in the PM+H/R combined treatment group than in the PM or H/R treatment group (Figure 3A). Mitochondrial function was assessed by measuring the OCR using a Seahorse metabolic analyzer. Compared with the control, PM or H/R significantly decreased the OCR (maximum) and ATP levels, which indicated that PM and H/R inhibited oxygen consumption and promoted extracellular acidification (Figure 3B). The effect of PM+H/R on the changes in the ΔΨm was determined using the JC-1 assay. PM+H/R caused a marked difference in the transition of fluorescence emission from red to green, which indicated a decrease in the ΔΨm (Figure 3C and S2H). Furthermore, flow cytometric analysis of JC-1 staining showed that PM+H/R treatment increased the number of cells with a low ΔΨm (JC-1 green positive and red negative) (Figure 3D). MitoTracker was used to examine the effect of PM+H/R on mitochondrial fission. The mitochondrial length in the PM+H/R-treated cells was significantly shorter than that

respectively, and nuclei were stained blue with DAPI. Scale bar: 50 μm. (H) ultrastructural morphology observed via TEM. Autophagosome and mitochondrial fission are indicated by arrowheads and arrows, respectively. Scale bar: 2 μm or 500 nm. (I) Western blot analysis of the expression of mitochondrial fission-related proteins (DNM1L/Drp1 and MFF) and mitophagy-related proteins (BNIP3, MAP1LC3B/LC3B, BECN1/Beclin 1, PIK3C3/Vps34, SQSTM1/p62 and ATG14) ($n = 5$-8). The data are expressed as the mean ± SEM; one-way ANOVA.

Statistical significance was defined as $^*p < 0.05$, $^{**}p < 0.01$, and $^{***}p < 0.001$.

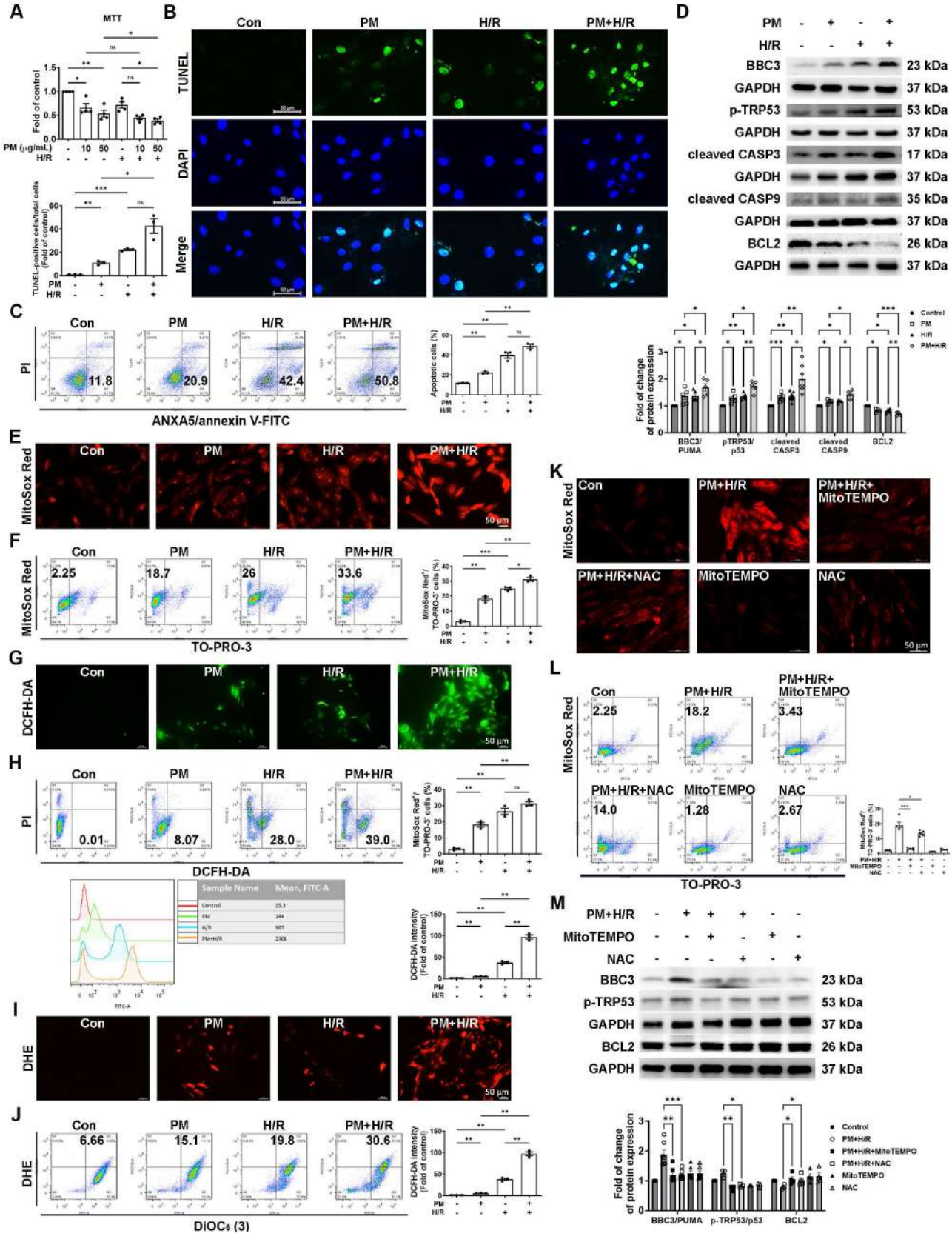


Figure 2. PM significantly exacerbates H/R-induced cardiomyocyte damage. H9c2 cells were pretreated with or without different concentrations of PM (10 or 50 μg/mL) for 6 h, followed by treatment with or without hypoxia for 6 h and reoxygenation for 12 h. (A) cell viability was assessed by MTT assay ($n = 4$). PM (50 μg/mL) was used in the following experiments. (B) a TUNEL assay was used to assess apoptosis. Nuclei were stained with DAPI (blue), and tunel-positive cells were indicated by green fluorescence (scale bar: 50 μm, $n = 3$). (C) flow cytometry was used to measure the number of apoptotic cells via ANXA5/annexin V-FITC-PI staining ($n = 3$). (D) the levels of apoptosis-related proteins were measured by western blot analysis ($n = 4$-7). (E) fluorescence microscopy was used to detect ROS production by MitoSOX red (1 μM) staining (scale bar: 50 μm, $n = 4$). (F) MitoSOX red (1 μM)/TO-PRO-3 (100 nM) staining was used to identify viable cells producing mitochondrial ROS (MitoSOX red-positive/TO-PRO-3-negative) by flow cytometry ($n = 3$). (G) by fluorescence microscopy, DCFH-DA (10 μM) was used to detect cytoplasmic H_2O_2 (scale

in the other treated cells (Figure 3E). To further investigate the mechanism of PM+H/R regulation of mitochondrial fission, the levels of DNM1L/Drp1 and MFF were examined via western blot analysis. The expression of DNM1L/Drp1 and MFF was significantly greater in the PM and H/R groups than in the other treated groups, and PM+H/R treatment significantly enhanced the expression of DNM1L/Drp1 and MFF (Figure 3F). To investigate the mechanism underlying the PM +H/R effects on mitophagy, the expression of BNIP3, MAP1LC3B/LC3B, BECN1/Beclin 1, PIK3C3/Vps34, SQSTM1/p62 and ATG14 was evaluated by western blot analysis. PM+H/R increased the expression of BNIP3, MAP1LC3B/LC3B, BECN1/Beclin 1, SQSTM1/p62, and ATG14 proteins compared to the PM or H/R-alone-treated groups (Figure 3G). The present study investigated whether PM+H/R affects the translocation of *p*- DNM1L/Drp1, DNM1L/Drp1, MFF, BECN1/Beclin 1, BNIP3, and MAP1LC3B/LC3B from the cytoplasm to mitochondria in cardiomyocytes. Compared to PM- or H/R-treated cells, treatment with PM+H/R significantly increased the expression of these proteins in mitochondria (Figure 3H). The effect of PM on mitophagy in H9c2 cells under H/R conditions was verified by acridine orange (AO) staining, which indicated that there was an increase in the number of autolysosomes (AL) in PM+H/R-treated cells (Figure 3I and S2I). PM+H/R-treated cells also showed an increase in mitophagy, as shown by mitochondria-targeted mt-Keima-Red assay (Figure 3I). Fluorescence staining showed that PM treatment increased the localization of BNIP3 and MAP1LC3B/LC3B in the mitochondria of H/R-treated cells (Figure 3J). Normal mitochondria were observed in the cytoplasm of cardiomyocytes in the control group, while several autophagosomes and PM particles were observed in the cytoplasm of cardiomyocytes in the PM+H/R group (Figure 3K and S2J). Moreover, Mdivi-1, a mitochondrial fission inhibitor, reduced PM+H/R-induced mitochondrial dysfunction, as shown by the JC-1 assay (Figures 3L, 3M, and S2K). PM+H/R combined treatment increased ALs, while Mdivi-1 treatment inhibited red fluorescence by AO staining (Figure 3N). The TUNEL assay demonstrated that treatment with Mdivi-1 and bafilomycin A_1 significantly reduced PM+H/R-induced apoptosis (Figure 3O). PM+H/R exposure increased the expression of fission-related proteins (DNM1L/Drp1 and MFF), mitophagy-related proteins (MAP1LC3B/LC3B and BNIP3), and apoptosis-related proteins (BBC3/PUMA and p-TRP53/p53) but decreased the expression of BCL2. However, Mdivi-1 treatment reversed these changes in protein expression (Figure 3P). Similarly, bafilomycin A_1 treatment reversed the effect of PM +H/R on the expression of mitophagy- and apoptosis-related proteins (Figure 3Q). These findings indicated that PM+H/R treatment affects mitochondrial function, mitophagy, and mitochondrial fission, suggesting a potential role for these mechanisms in the cellular response to PM+H/R-induced cardiac injury.

PM+H/R significantly reduces Mir221 and Mir222 expression, while Mir221- and Mir222-enriched ADSC-Exos reduce pm+h/r-induced mitophagy and apoptosis

We have previously demonstrated that an abundance of *Mir221* and *Mir222* in ADSC-Exos reduces injury caused by I/R [20]. To explore whether *Mir221* and *Mir222* regulates PM+H/R-induced mitophagy and apoptosis, the levels of *Mir221* and *Mir222* were assessed by qPCR. Compared to the control group, the expression of *Mir221* and *Mir222* was significantly downregulated in the PM and H/R treatment groups, while treatment with PM+H/R further decreased the levels of *Mir221* and *Mir222* (Figure 4A). However, the addition of ADSC-Exos increased the levels of *Mir221* and *Mir222* in PM+H/R-treated H9c2 cells (Figure 4B). Compared to H9c2 cells and ADSCs, ADSC-Exos contained higher levels of *Mir221* and *Mir222* (Figure S3A). To elucidate the effects of *Mir221* and *Mir222* on mitophagy- and apoptosis-related proteins, target prediction was performed with miRTarBase, which predicted the *Mir221*- and *Mir222*-binding site in the 3'-UTRs of *Bnip3*, *Lc3b*, and *Bbc3/Puma* (Figure 4C). We have previously demonstrated that *Mir221* and *Mir222* target *Bbc3/Puma* and regulate apoptosis [27]. To determine whether *Mir221* and *Mir222* target the 3' UTRs of *Bnip3* and *Lc3b*, the luciferase activity of reporter genes (*Bnip3* and *Lc3b*) was reduced in cells transfected with *Mir221*- and *Mir222*-mimics. Additionally, no significant difference was observed in cells transfected with *Bnip3*- and *Lc3b*-MUT, suggesting that *Mir221* and *Mir222* directly target *Bnip3* and *Lc3b* (Figure 4D). PM+H/R stimulation increased the mRNA and protein levels of *Bnip3* and *Lc3b*, but treatment with ADSC-Exos or *Mir221*- and *Mir222*-mimics decreased the mRNA and protein expression levels of *Bnip3* and *Lc3b* (Figures 4E, F). Compared to the PM+H/R+ADSC-Exo group, the expression of BNIP3 and LC3B was increased in the PM+H/R +ADSC-Exos+*Mir221*- and *Mir222*-inhibitors group (Figure 4G). A Seahorse analyzer was used to examine the efficiency of mitochondrial respiration and mitochondrial function. Treatment with ADSC-Exos and *Mir221*- and *Mir222*-mimics increased the OCR, ATP production, and maximal respiration in PM+H/R-treated cells, which indicated that ADSC-Exos and overexpression of *Mir221* and *Mir222* protect against PM+H/R-induced mitochondrial dysfunction (Figure 4H). Compared to treatment with PM+H/R, MTT assays showed an increase in cell viability after

bar: 50 μm, $n = 3$-5). (H) DCFH-DA/PI staining was used to examine viable cells producing cytoplasmic H_2O_2 (DCFH-DA-positive/PI-negative) by flow cytometry ($n = 3$). (I) DHE (5 μM) was used to detect cellular superoxide anions by fluorescence microscopy (scale bar: 50 μm, $n = 4$). (J) DHE/$DiOC_6(3)$ (90 nM) staining was used to examine viable cells producing cellular superoxide anions (DHE-positive/$DiOC_6(3)$-positive) by flow cytometry ($n = 3$). (K-M) H9c2 cells were pretreated with MitoTEMPO (10 nM) or NAC (5 mM) for 1 h before exposure to PM+H/R. MitoSOX red was used to detect mitochondrial ROS production through fluorescence microscopy and flow cytometry. Western blot was used to detect the levels of cell apoptosis (scale bar: 50 μm, $n = 4$-7). The data are expressed as the mean ± SEM; one-way ANOVA.

Statistical significance was defined as $^*p < 0.05$, $^{**}p < 0.01$, and $^{***}p < 0.001$.

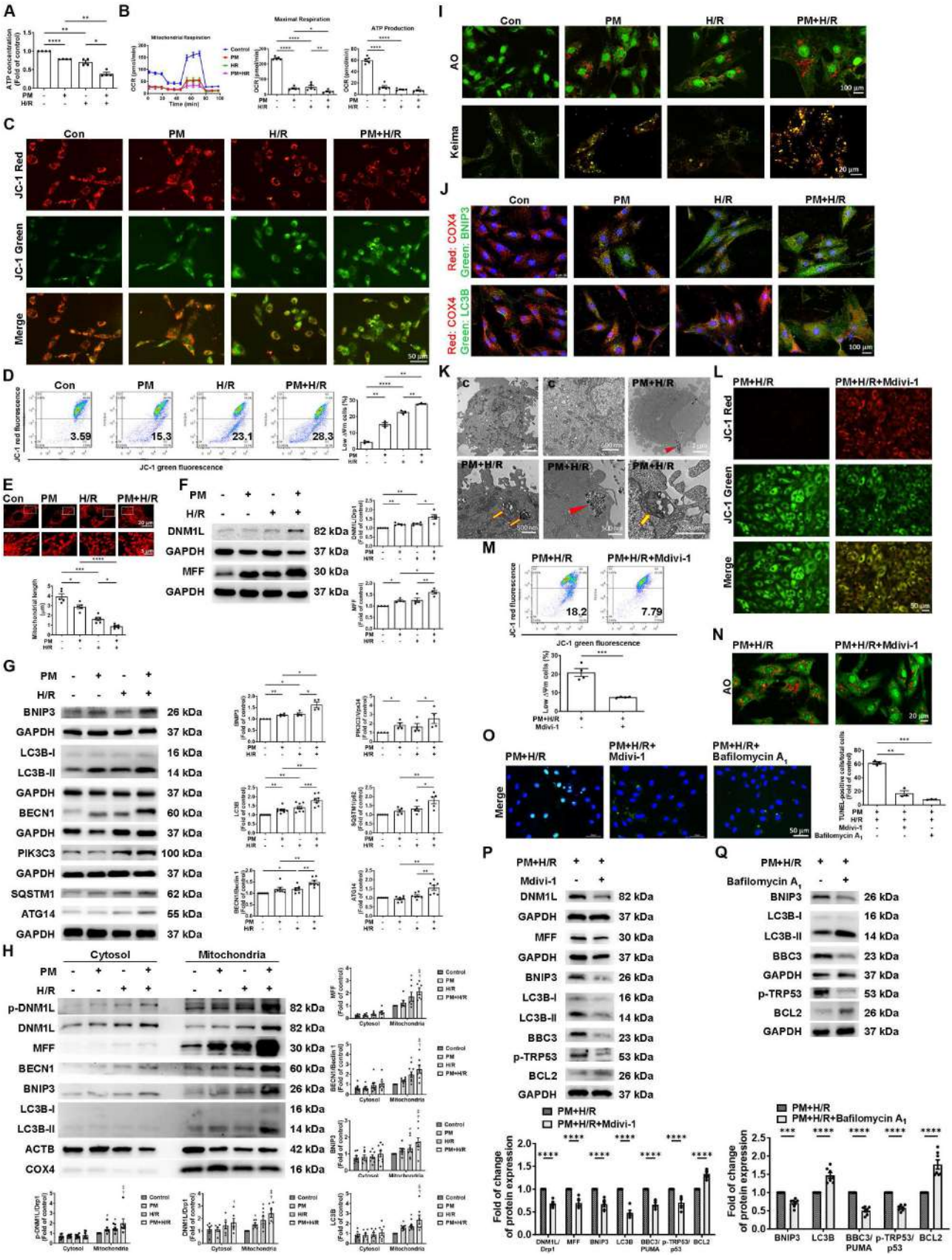


Figure 3. PM exacerbates mitochondrial dysfunction in H/R-treated cardiomyocytes. Cardiomyocytes were pretreated with or without 50 μg/mL PM and then exposed to hypoxia for 6 h, followed by reoxygenation for 12 h. (A) ATP levels were quantified ($n = 4$). (B) the OCR was determined using a seahorse metabolic analyzer. ATP levels and the maximal OCR were quantified ($n = 5$). (C and D) the δψm was determined by JC-1 staining under a fluorescence microscope and flow cytometry. High δψm and low δψm are shown in red and green, respectively (scale bar: 50 μm, $n = 3$). (E) mitochondrial length was measured with MitoTracker staining. The photo shown below is an enlargement of the rectangle above. Scale bar: 20 or 5 μm, as indicated in the panel, $n = 5$). (F) the levels of DNM1L/Drp1 and MFF were detected by western blot analysis ($n = 4$-5). (G) BNIP3, MAP1LC3B/LC3B, BECN1/Beclin 1, PIK3C3/Vps34, SQSTM1/p62 and ATG14 expression levels were

treatment with ADSC-Exos and *Mir221*- and *Mir222*-mimics (Figure 4I). The present study then investigated whether restoring *Mir221* and *Mir222* expression in the presence of PM+H/R alleviates apoptosis. TUNEL assays revealed that ADSC-Exos administration and *Mir221*- and *Mir222*-mimics transfection significantly reduced PM+H/R-induced apoptosis (Figure 4J). In addition, treatment with ADSC-Exos and *Mir221*- and *Mir222*-mimics reduced the effects of PM+H/R-induced upregulation of apoptosis-related proteins (BBC3/PUMA, p-TRP53/p53, and cleaved CASP3) and downregulation of the anti-apoptosis protein BCL2. Conversely, treatment with *Mir221*- and *Mir222*-inhibitors diminished the therapeutic function of ADSC-Exos in reducing apoptosis (Figures 4K,L). To further test the roles of *Bnip3* and *Lc3b* in regulating apoptosis and cell viability, siRNAs targeting *Bnip3* and *Lc3b* were used to knockdown their expression. TUNEL and MTT assays revealed that si*BNIP3* and si*LC3B* reduced cell apoptosis and increased cell viability compared to the PM+H/R group (Figures 5A and 4I). In PM+H/R-treated H9c2 cells, si*BNIP3* and si*LC3B* reduced the expression of BNIP3 and MAP1LC3B/LC3B, respectively, thereby reducing the expression of BBC3/PUMA, p-TRP53/p53 and cleaved CASP3, but increasing the expression of BCL2 (Figures 5B, C). Notably, si*BNIP3* and si*LC3B* effectively reduced the levels of apoptosis-related proteins but had no significant effect on fission-related proteins (DNM1L/Drp1 and MFF) under PM+H/R condition. Moreover, *Bbc3/Puma* knockdown did not affect the levels of BNIP3 and MAP1LC3B/LC3B under PM+H/R condition (Figure 5D). Furthermore, to validate the comprehensive mechanism involving *Mir221* and *Mir222*, we simultaneously overexpressed *Lc3b* and *Bnip3* and transfected *Mir221* and *Mir222*. We then observed the protein levels of BBC3/PUMA, MAP1LC3B/LC3B, and BNIP3 under PM+H/R conditions. western blot analysis demonstrated that *Mir221*- and *Mir222*-transfection reduced PM+H/R-induced BBC3/PUMA levels compared to scramble transfection (Figure 5E). However, simultaneous transfection of *Mir221* and *Mir222* and overexpression of *Bnip3* or *Lc3b* showed no reduction in PM+H/R-induced BBC3/PUMA levels compared to the scramble group.

To investigate whether other signal transduction molecules are involved in PM+I/R-enhanced apoptosis, an AKT pathway phosphorylation array was used to identify specific pathways. PM+H/R treatment induced the upregulation of apoptotic proteins, such as PRKAA1/AMPK, CDKN1B/p27, and p-TRP53/p53 (Figure S4A). Western blot analysis identified significant changes in p-PRKAA1/AMPK and p-CDKN1B/p27 between PM+H/R-treated cells and ADSC-Exos-treated cells (Figure S4B). To elucidate whether ADSC-Exos affect apoptosis in PM+H/R-treated H9c2 cells via the PRKAA1/AMPK-CDKN1B/p27 pathway, H9c2 cells were treated with a CDKN1B/p27 inhibitor (SKPin C1) and an PRKAA1/AMPK inhibitor (compound C). SKPin C1 and compound C reduced the expression of BBC3/PUMA and p-TRP53/p53 but increased the expression of BCL2 in PM+H/R-treated H9c2 cells (Figure S4C). TUNEL assays indicated that SKpin C1 and compound C treatment significantly reduced apoptosis (Figure S4D). These results showed that treatment with ADSC-Exos reduces PM+H/R-induced mitophagy and apoptosis through the BNIP3-MAP1LC3B/LC3B-BBC3/PUMA pathway, and this process is regulated by *Mir221* and *Mir222*. In addition, the PRKAA1/AMPK-CDKN1B/p27 pathway is also involved in PM+H/R-induced apoptosis.

ADSC-Exos attenuate pm+h/r-induced apoptosis by reducing ROS production, mitochondrial fission, and mitophagy

Mitochondrial ROS production was measured under ADSC-Exos treatment, *Mir221*- and *Mir222*-mimics transfection, and MitoTEMPO treatment conditions using MitoSOX Red staining. Fluorescence microscopy and flow cytometry indicated that these treatments reduced the MitoSox Red fluorescence intensity in PM+H/R-treated cardiomyocytes (Figures 6A, 6B, and S2L), which indicated that ADSC-Exos and *Mir221*- and *Mir222*-mimics reduce the mitochondrial ROS levels in PM+H/R-treated H9c2 cells. JC-1 staining assessed by fluorescence microscopy and flow cytometry showed that PM+H/R treatment increased the number of cells with a low ΔΨm. Conversely, treatment with ADSC-Exos, *Mir221*- and *Mir222*-mimics, MitoTEMPO, or Mdivi-1 reversed the decrease in the ΔΨm induced by PM+H/R (Figures 6C, 6D, and S2M). Treatment of H9c2 cells with ADSC-Exos, *Mir221*- and *Mir222*-mimics, MitoTEMPO, and Mdivi-1 significantly increased ATP production in PM+H/R-treated cardiomyocytes (Figure 6E). Moreover, the mitochondrial length was shortened in PM+H/R-treated cardiomyocytes, and it was increased by ADSC-Exos, *Mir221*- and *Mir222*-mimics, MitoTEMPO, and Mdivi-1 (Figure 6F). Western blot analysis revealed that the above treatments also significantly reduced the levels of DNM1L/Drp1 and MFF (Figure 6G). To further confirm the effects of ADSC-Exos and *Mir221*- and *Mir222*-mimics on mitophagy after PM+H/R injury, AO staining, RFP-GFP-LC3B staining, and mitophagy-related proteins

examined by western blot analysis ($n = 4$-8). (H) the levels of p-DNM1L/DRP1, DNM1L/DRP1, MFF, BECN1/Beclin 1, BNIP3, and MAP1LC3B/LC3B in the cytoplasmic and mitochondrial fractions were examined by western blot analysis ($n = 6$-8). (I) ALs were observed via AO staining under a fluorescence microscope (scale bar: 100 μm, $n = 4$-5). Cardiomyocytes were transfected with the mitophagy reporter mitochondria-target Keima (mt-Keima) 48 h before treatment. Control cells showed green fluorescence, while pm+h/r-treated cells showed red fluorescence (scale bar: 20 μm, $n = 6$). (J) the colocalization of BNIP3 (green) or MAP1LC3B/LC3B (green) and COX4/COXIV (mitochondria, red) was observed by immunofluorescence microscopy (scale bar: 100 μm). (K) the ultrastructures of the PM and mitophagosomes were observed using TEM, as indicated in the panel. Scale bar: 2 μm or 500 nm). (L and M) the effect of mdivi-1 (10 μm) on the δψm was examined by the JC-1 assay (scale bar: 50 μm, $n = 4$). (N) the impact of mdivi-1 on ALs was examined by AO staining (scale bar: 20 μm). (O) effect of mdivi-1 and bafilomycin A_1 (10 μm) on apoptosis according to the TUNEL assay (scale bar: 50 μm, $n = 5$). (P and Q) the impact of mdivi-1 and bafilomycin A_1 treatment on the expression of mitochondrial fission-related, mitophagy-related, and apoptosis-related proteins was determined by western blot analysis ($n = 5$-7). The data are expressed as the mean ± SEM; one-way ANOVA.

Statistical significance was defined as $^*p < 0.05$, $^{**}p < 0.01$, and $^{***}p < 0.001$.

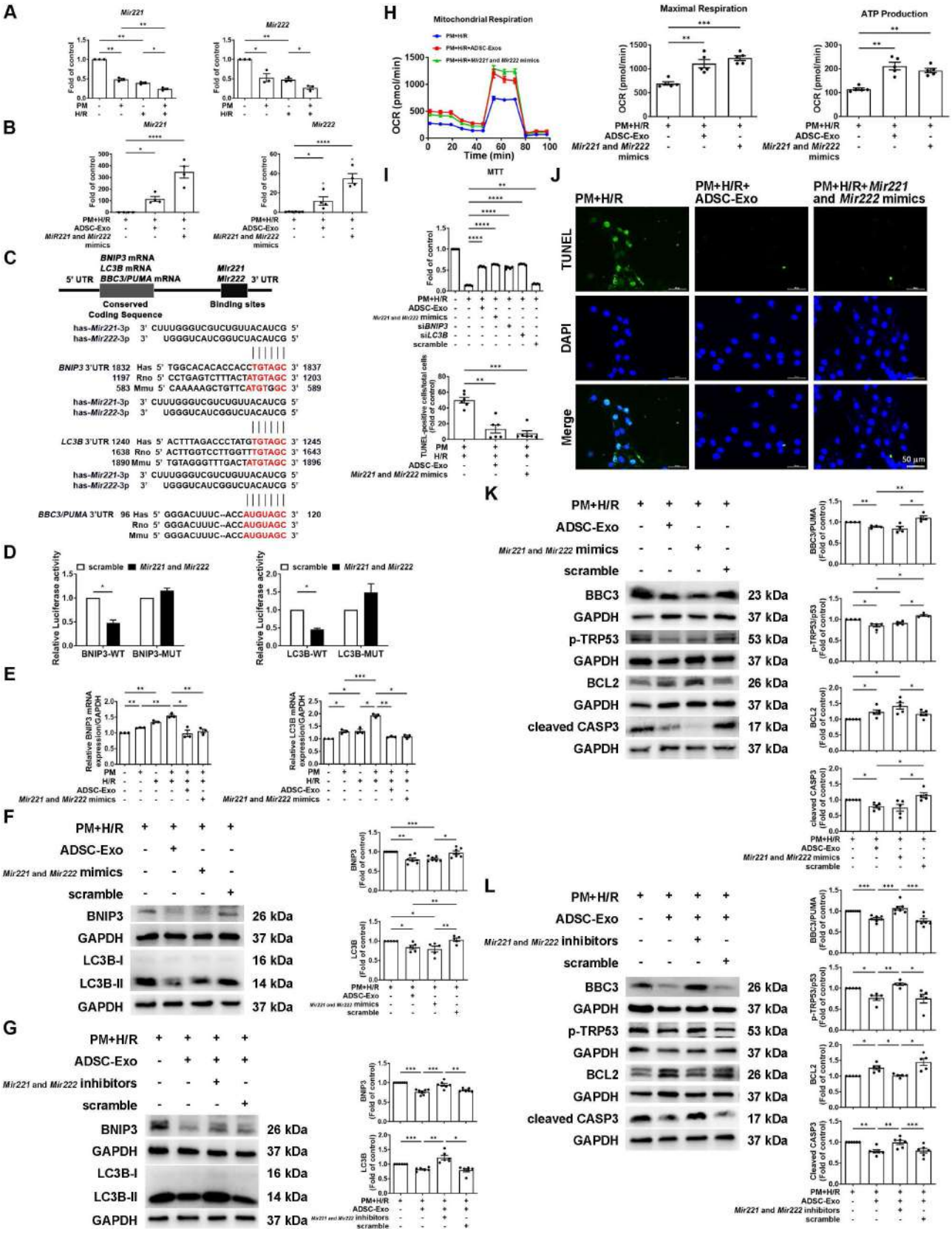


Figure 4. *Mir221* and *Mir222* regulate the expression of *Bnip3* and *Lc3b*, causing PM to aggravate myocardial H/R injury. H9c2 cells were transfected with *Mir221*- and *Mir222*-mimics or inhibitors for 24 h, pretreated with PM for 6 h, and subjected to H/R. (A) *Mir221* and *Mir222* expression in various treatment groups was assessed using qPCR ($n = 3$). (B) the impact of ADSC-Exos or *Mir221*- and *Mir222*-mimics on *Mir221* and *Mir222* expression in pm+h/r-treated cells was assessed by qPCR ($n = 4$). (C) schematic diagram depicting the binding of *Mir221* and *Mir222* to the 3′ UTRs of *Bnip3*, *Lc3b*, and *Bbc3/Puma* target genes. (D) luciferase activities of the *Bnip3* and *Lc3b* reporters in the *Mir221*- and *Mir222*-mimics and scramble groups were measured ($n = 4$). (E) effects of ADSC-Exos or *Mir221*- and *Mir222*-mimics on *Bnip3* and *Lc3b* mRNA expression in pm+h/r-treated cardiomyocytes ($n = 3$). (F and G) the effects of ADSC-Exos, *Mir221*- and *Mir222*-mimics (F), and *Mir221*- and *Mir222*-inhibitors (G) on the expression of mitophagy-related proteins were detected by western blot analysis ($n = 5$-7). (H) effects of ADSC-Exos or *Mir221*- and *Mir222*-mimics on the OCR in cardiomyocytes treated with PM+H/R ($n = 5$). (I) effect of ADSC-Exos, *Mir221*- and *Mir222*-mimics, si*BNIP3*, and si*LC3B* on the viability of pm+h/

expression levels were measured. PM+H/R treatment increased the number of autophagosomes, whereas treatment with ADSC-Exos, *Mir221*- and *Mir222*-mimics, MitoTEMPO, or Mdivi-1 reduced the number of autophagosomes (Figure 6H and S2N). RFP-GFP-LC3B was used to visualize autophagosomes and ALs (yellow dots and red dots, respectively). Treatment with ADSC-Exos and *Mir221*- and *Mir222*-mimics reduced mitophagy (Figure 6I and S2O), as indicated by the reduced number of autophagosomes visualized by RFP-GFP-LC3. In addition, bafilomycin A_1, which functions as a blocker of AL formation, showed an accumulation of autophagosomes under PM+H/R condition. Western blot results showed the addition of bafilomycin A_1 reduced PM +H/R-increased BECN1/Beclin 1, BNIP3 and MAP1LC3B/LC3B levels (Figure 6J). We also treated the cells with MitoTEMPO, Mdivi-1, and bafilomycin A_1 and examine their role in PM+H/R-induced apoptosis. ANXA5/annexin V-FITC-PI assay demonstrated that these treatments significantly decreased the number of apoptotic cells (Figure 6K), and these treatments also reduced the expression of the BBC3/PUMA and p-TRP53/p53 apoptotic proteins but increased the expression of BCL2 (Figure 6L). These results indicated that ROS trigger mitochondrial fission, mitophagy, and apoptosis in PM+H/R-treated cardiomyocytes, while ADSC-Exos inhibit ROS, mitochondrial fission, and mitophagy to attenuate cell apoptosis.

Mir221 and Mir222 attenuate pm+i/r-induced cardiac injury in WT and mir221- and mir222-ko mice and has a similar effect on TG mice

To elucidate whether ADSC-Exos protect mouse hearts from PM+I/R-induced damage through a *Mir221*- and *Mir222*-dependent mechanism, C57BL/6 (WT) and *mir221*- and *mir222*-KO mice were preconditioned with PM for 24 h. After 25 min of occlusion, ADSC-Exos and *Mir221*- and *Mir222*-mimics were intramuscularly injected into the anterior wall, followed by 3 h of reperfusion. LDH and TNNI were significantly increased in the I/R and PM+I/R groups. Treatment with ADSC-Exos or *Mir221*- and *Mir222*-mimics significantly reduced the PM+I/R-induced release of LDH and TNNI (Figure 7A). Treatment of WT and *mir221*- and *mir222*-KO mice with ADSC-Exos or *Mir221*- and *Mir222*-mimics increased *Mir221* and *Mir222* expression in the PM +I/R condition (Figure 7B). Treatment with ADSC-Exos or *Mir221*- and *Mir222*-mimics increased the EF and FS percentages in WT and *mir221*- and *mir222*-KO mice (Figure 7C). In contrast, ADSC-Exos collected from ADSCs transfected with *Mir221*- and *Mir222*-inhibitors failed to improve PM +I/R-induced cardiac dysfunction (Figure S5). The effect of ADSC-Exos on ROS production in cardiac tissue was further assessed. Treatment with ADSC-Exos or *Mir221*- and *Mir222*-mimics significantly reduced cytoplasmic and mitochondrial ROS generation, as detected by DHE and MitoSox Red staining (Figures 7D, 7E, S2P, and S2Q). In addition, PM+I/R increased the expression of BNIP3 and MAP1LC3B/LC3B, while ADSC-Exos and the *Mir221*- and *Mir222*-mimics reduced BNIP3 and MAP1LC3B/LC3B expression, as determined by western blot analysis and immunohistochemistry (Figures 7F, 7G, S2R and S2S). After PM+I/R treatment, BBC3/PUMA and p-TRP53/p53 expression significantly increased, while BCL2 expression decreased in WT as well as *mir221*- and *mir222*-KO mice, while ADSC-Exos or *Mir221*- and *Mir222*-mimics reversed these changes (Figure 7H). Furthermore, the TUNEL assay demonstrated that treatment with ADSC-Exos or *Mir221*- and *Mir222*-mimics reduced cardiac apoptosis (Figure 7I).

Mir221- and *Mir222*-overexpressing TG mice were used to further confirm the critical role of *Mir221* and *Mir222* in PM +I/R-induced cardiac injury. Moreover, myocardial *Mir221* and *Mir222* levels were significantly greater in *Mir221*- and *Mir222*-TG mice subjected to PM+I/R than in WT mice subjected to the same treatment (Figure 7J). Echocardiography showed that the EF and FS were greater in the PM+I/R-treated *Mir221*- and *Mir222*-TG mice than in the PM+I/R-treated normal mice, which was similar to the findings in the ADSC-Exos-treated group (Figure 7K). Compared with those in the PM+I/R-treated WT group, the LDH and TNNI levels in the PM+I/R-treated *Mir221*- and *Mir222*-TG group were significantly lower (Figure 7L). DHE and MitoSox Red staining indicated that *Mir221*- and *Mir222*-TG mice exhibited low ROS levels after PM+I/R treatment, and these results were similar to those obtained for ADSC-Exos-treated WT mice after PM+I/R treatment (Figure 7M, S2T, and S2U). In addition, western blot analysis indicated that *Mir221*- and *Mir222*-TG mice exhibited low expression of BNIP3 and MAP1LC3B/LC3B after PM+I/R treatment, which was similar to ADSC-Exos-treated WT mice after PM+H/R treatment (Figure 7N). Moreover, *Mir221*- and *Mir222*-TG mice also exhibited low expression of p-TRP53/p53 and BBC3/PUMA after PM+I/R treatment, as detected by western blot analysis, and reduced cell apoptosis, as detected by TUNEL assays. These results were consistent with those obtained for ADSC-Exos-treated WT mice after PM+I/R treatment (Figures 7O,P). These findings suggested that ADSC-Exos prevented myocardial PM+I/R injury through *Mir221* and *Mir222 in vivo*. To comprehensively elucidate the regulation of BNIP3, MAP1LC3B/LC3B, and BBC3/PUMA by *Mir221* and *Mir222*, we knockdown *Bnip3* and *Lc3b* in *mir221*- and *mir222*-KO mice. Transfection with

r-treated H9c2 cells ($n = 5$). (J) the impact of ADSC-Exos and *Mir221*- and *Mir222*-mimics on apoptosis in pm+h/r-treated cardiomyocytes was assessed via a TUNEL assay (scale bar: 50 μm, $n = 6$). (K and L) the effects of ADSC-Exos, *Mir221*- and *Mir222*-mimics (K), and *Mir221*- and *Mir222*-inhibitors (L) on the expression of apoptosis-related proteins were assessed by western blot analysis ($n = 4$-7). The data are expressed as the mean ± SEM; one-way ANOVA.

Statistical significance was defined as $^*p < 0.05$, $^{**}p < 0.01$, and $^{***}p < 0.001$.

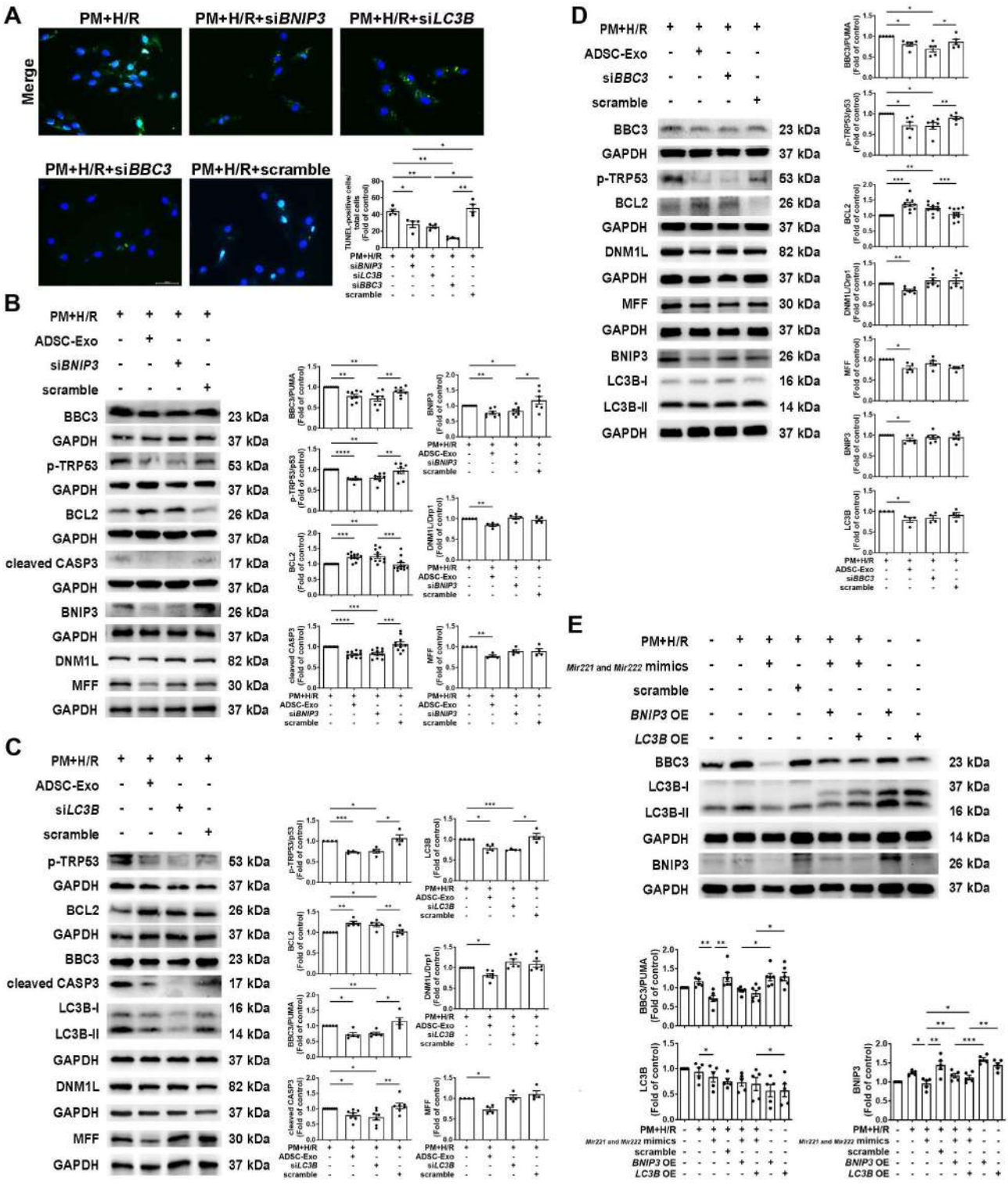


Figure 5. Effects of *Bnip3*, *Lc3b*, and *Bbc3/Puma* downregulation on pm+h/r-induced mitochondrial fission, mitochondrial autophagy, and apoptosis. (A) the effects of the downregulation of *Bnip3*, *Lc3b*, and *Bbc3/Puma* on cell apoptosis in pm+h/r-treated cardiomyocytes were examined by a TUNEL assay (scale bar: 50 μm, $n = 4$). (B and C) the effects of the downregulation of *Bnip3* (B) and *Lc3b* (C) on the expression of mitochondrial fission-related, mitophagy-related, and apoptosis-related proteins in cells exposed to PM+H/R, was determined by western blot analysis ($n = 4$-11). (D) western blot analysis of the effects of *Bbc3/Puma* downregulation on the expression of mitochondrial fission- and mitophagy-related proteins in cells exposed to PM+H/R ($n = 5$-10). (E) H9c2 cells were transfected with *Mir221* and *Mir222* or with *Bnip3* and *Lc3b* overexpression, and then exposed to PM+H/R conditions. The expression levels of BBC3/PUMA, MAP1LC3B/LC3B, and BNIP3 proteins were assessed by western blot. The data are expressed as the mean ± SEM; one-way ANOVA.

Statistical significance was defined as $^{*}p < 0.05$, $^{**}p < 0.01$, and $^{***}p < 0.001$. [Change labels to "si*BBC3*" in panels A and D.]

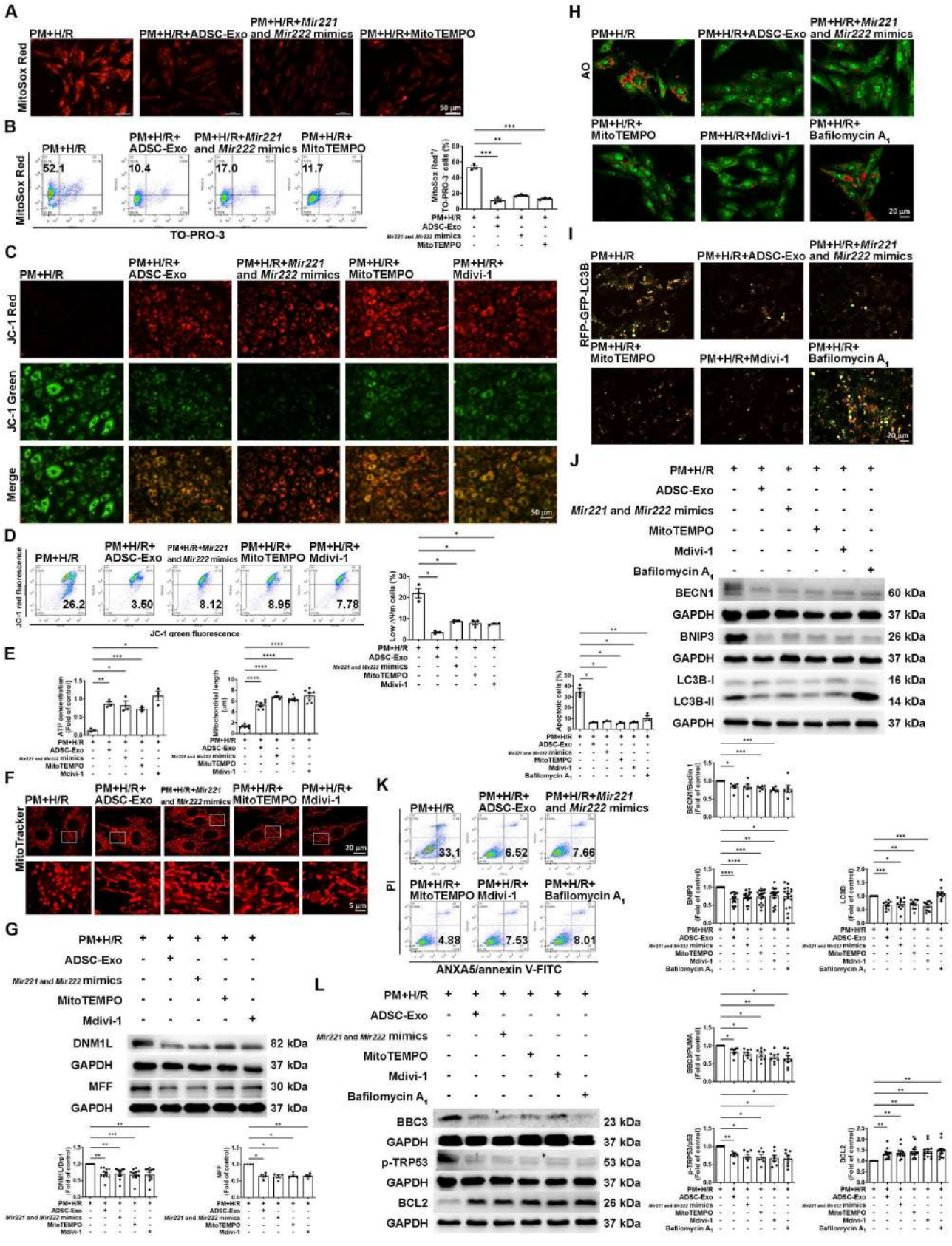


Figure 6. *Mir221* and *Mir222* in ADSC-Exos reduce mitochondrial ROS levels, mitochondrial fission, mitophagy, and apoptosis in cardiomyocytes exposed to PM+H/R. H9c2 cells were treated with ADSC-Exos (2 μg/mL) or transfected with *Mir221*- and *Mir222*-mimics for 24 h, followed by treatment with PM (50 μg/mL) and H/R (6 h/12 h). (A and B) the effects of ADSC-Exos, *Mir221*- and *Mir222*-mimics, and MitoTEMPO treatment on mitochondrial ROS were evaluated via MitoSOX red staining via fluorescence microscopy and flow cytometry (scale bar: 50 μm, $n = 3$). (C and D) the effects of ADSC-Exos, *Mir221*- and *Mir222*-mimics, MitoTEMPO, and mdivi-1 treatment on δψm were assessed by JC-1 staining under fluorescence microscopy and flow cytometry (scale bar: 50 μm, $n = 3$). (E) ATP production was assessed using an ATP assay ($n = 3$). (F) mitochondrial length was assessed by a MitoTracker assay (scale bar: 20 or 5 μm, $n = 7$). (G) the expression of DNM1L/Drp1 and MFF was assessed by western blot analysis ($n = 4$-11). (H) the effects of treatment with ADSC-Exos, *Mir221*- and *Mir222*-mimics, MitoTEMPO, mdivi-1, and bafilomycin A_1 on AL

si*BNIP3* significantly increased EF and FS in *mir221*- and *mir222*-KO mice subjected to PM+I/R treatment, indicating improved cardiac function (Figure 8A). Additionally, western blot showed si*BNIP3* and si*LC3B* significantly reduced BBC3/PUMA expression levels in PM+I/R-treated *mir221*- and *mir222*-KO mice (Figure 8B). Moreover, bafilomycin A_1 treatment significantly reduced BBC3/PUMA expression in PM+I/R-treated WT mice (Figure 8C), showing that inhibition of autophagy contributes to reducing apoptosis in PM+I/R-induced cardiac injury. Taken together, these results indicated that I/R combined with PM exposure leads to increased ROS production, impaired mitochondrial function, maladaptive mitophagy, and increased apoptosis, ultimately leading to cardiac damage.

Discussion

Epidemiological studies have revealed a significant association between short-term exposure to environmental PM and increased daily mortality and hospitalization from cardiovascular diseases [28,29]. In the present study, exposure to PM under I/R conditions exacerbated mitochondrial oxidative stress, leading to mitochondrial fission, mitophagy, and apoptosis. In addition, ADSC-Exos exert their therapeutic effect by effectively alleviating the above effects, thereby mitigating mitochondrial dysfunction and cell apoptosis, ultimately restoring cardiac function. The present results provided evidence that *Mir221*- and *Mir222*-enriched ADSC-Exos reduce mitophagy and apoptosis through the BNIP3-MAP1LC3B /LC3B-BBC3/PUMA pathway and contribute to improving cardiac dysfunction.

Oxidative stress is essential for myocardial damage during acute I/R and chronic remodeling after myocardial infarction [30,31]. PM reduces cell viability and promotes apoptosis by increasing intracellular ROS production and activating the MAPK and NFKB/NF-κB signaling pathways in rat cardiac H9c2 cells [32,33]. The present study showed that PM or I/R treatment alone significantly increased mitochondrial ROS and total ROS production, and PM exacerbated I/R-induced mitochondrial ROS and total ROS. Consistent with the *in vivo* studies, PM exacerbated H/R-induced ROS production and apoptosis in cultured cardiomyocytes. Due to the limitation of the large number of cells required for this study, functionally similar H9c2 cells were used instead of primary cardiomyocytes, but our *in vitro* data are consistent with the *in vivo* findings. Importantly, oxidative stress indicates mitochondrial abnormalities [30]. Mitochondrial quality control includes mitochondrial biogenesis, mitochondrial dynamics (fission/fusion), and mitophagy [34]. In the rat aorta, PM increases SOD2 and mitochondrial fission proteins (DNM1L/Drp1 and FIS1) but reduces the expression of mitochondrial fusion proteins (MFN2 and OPA1) [16]. Previous studies have shown that mitophagy can clear damaged mitochondria after I/R injury, and mitophagy is often viewed as a defensive or adaptive process [35,36]. However, excessive or uncontrolled mitophagy (maladaptive) may leave cells without enough healthy or functioning mitochondria to produce ATP, thus limiting cell viability [37]. Increasing evidence suggests that I/R may cause an imbalance in the autophagy process, leading to additional cytotoxic damage that may induce cell death [10,38]. Moreover, PM activates mitophagy-related proteins, including LC3, SQSTM1/p62, PINK, and PRKN/parkin, in the rat aorta [16]. The present study demonstrated that PM+H/R decreased mitochondrial length and increased the expression of the DNM1L/Drp1 and MFF mitochondrial fission-related proteins. Moreover, the combination of PM and H/R increased the number of ALs and the expression of the BNIP3 and MAP1LC3B/LC3B mitophagy-related proteins. The degree of apoptosis was significantly reduced when mitochondrial ROS production, mitochondrial division, and mitophagy production were inhibited by MitoTEMPO, Mdivi-1, and bafilomycin A_1, respectively. These results suggested that mitochondrial oxidative stress is enhanced after PM+H/R treatment, leading to mitochondrial damage, increased mitochondrial fission, and mitophagy. Thus, the cascade of events driven by oxidative stress ultimately promotes apoptosis.

Mir221 and *Mir222* have been reported to be closely related to inflammation and the pathogenesis of cardiovascular diseases [22,39]. Both miRNAs counteract myocardial fibrosis in pressure overload-induced heart failure [22]. The levels of *Mir221* and *Mir222* in circulating progenitor cells may provide expected pharmacological effects [40]. We have previously reported that the expression of *Mir221* and *Mir222* in cardiac tissue is significantly reduced after I/R injury [20]. In the present study, we found that compared to I/R (H/R) or PM alone, combined treatment with I/R (H/R) and PM significantly reduced the expression of *Mir221* and *Mir222*. We have previously demonstrated that ADSC-derived conditioned media or exosomes containing high levels of *Mir221* and *Mir222* decrease I/R-induced cardiac injury [20,27]. Exosomes derived from various cells are considered a novel drug delivery method. For instance, mesenchymal stem cell (MSC)-derived exosomes containing miRNAs and proteins are considered alternatives to cell therapy and play a promising role in cardiac regeneration and repair [41]. The transfer of *Mir221* and *Mir222* via vascular smooth muscle cells – derived exosomes from diabetes affected vascular inflammation [42]. Few articles have reported the relationships among *Mir221* and *Mir222*, mitophagy, and apoptosis. Elevated levels of *Mir221* and *Mir222* in glioblastoma

accumulation was determined by AO staining (scale bar: 20 μm). (I) cardiomyocytes were transduced with RFP-GFP-LC3 lentivirus for 72 h. The lentivirus allowed the distinction of autophagosomes (GFP+ and RFP+; yellow plots) and ALs (GFP− and RFP+; red plots), as GFP fluorescence was quenched in the acidic ALs. The effects of ADSC-Exos, *Mir221*- and *Mir222*-mimics, MitoTEMPO, mdivi-1, and bafilomycin A_1 on the formation of autophagosomes and ALs assessed by RFP-GFP-LC3 staining (scale bar: 20 μm, $n = 10$). (J) the effects of treatment with ADSC-Exos, *Mir221*- and *Mir222*-mimics, MitoTEMPO, mdivi-1, and bafilomycin A_1 on the expression of mitophagy-related proteins were examined by western blot analysis ($n = 6$-17). (K and L) the effects of ADSC-Exos, *Mir221*- and *Mir222*-mimics, MitoTEMPO, mdivi-1, and bafilomycin A_1 on cell apoptosis were assessed by ANXA5/annexin V-FITC-PI flow cytometry and western blot analysis ($n = 3$-13). The data are expressed as the mean ± SEM; one-way ANOVA.

Statistical significance was defined as $^*p < 0.05$, $^{**}p < 0.01$, and $^{***}p < 0.001$.

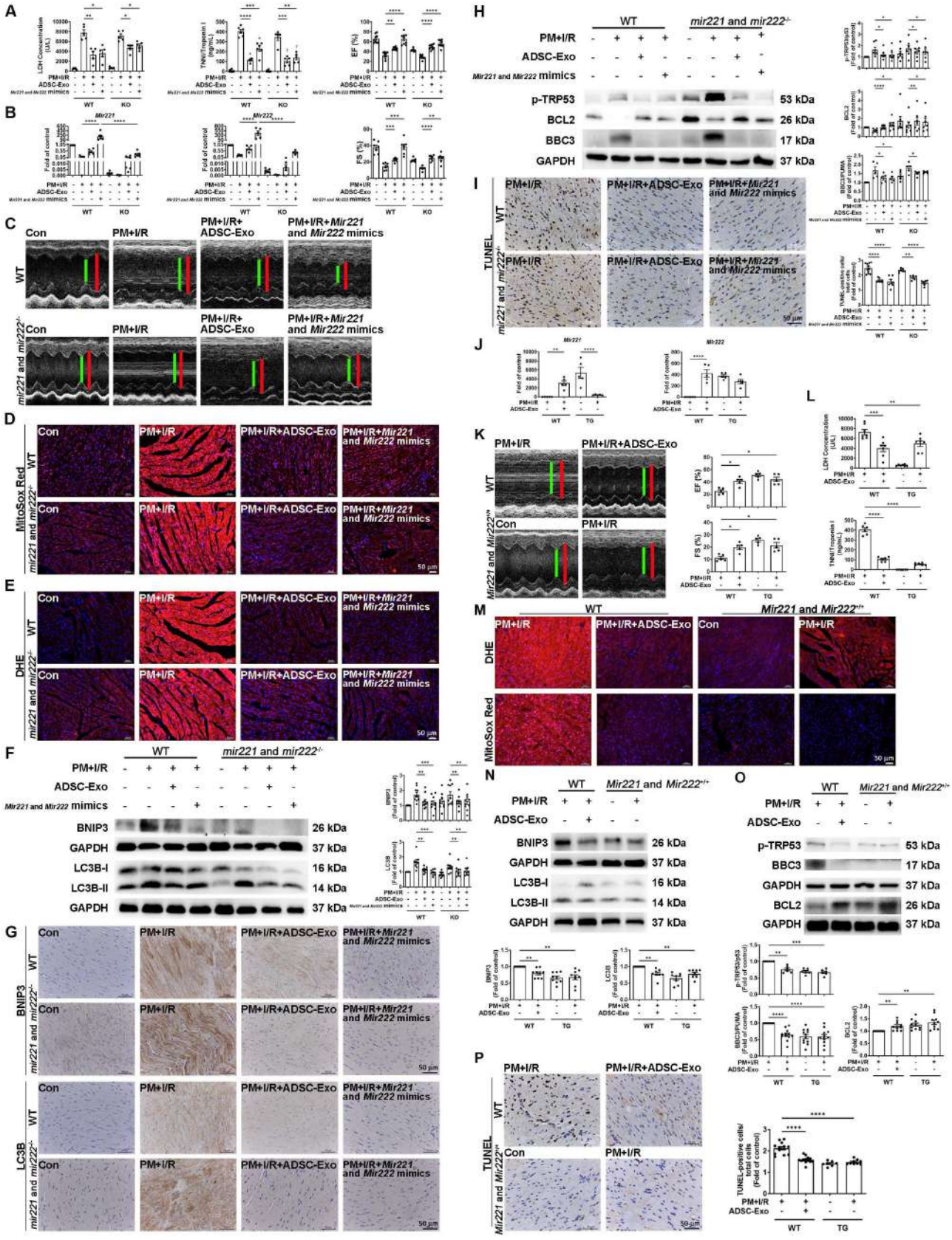


Figure 7. *Mir221* and *Mir222* decrease pm+i/r-induced cardiac damage in WT, *mir221*- and *mir222*-ko, and *Mir221*- and *Mir222*-tg mice. WT or *mir221*- and *mir222*-ko mice were preconditioned with PM for 24 h. Then, 25 min after occlusion, ADSC-Exos (100 µg of protein in 50 µL) or *Mir221*- and *Mir222*-mimics (100 nM) were uniformly intramuscularly injected into the left ventricular marginal zone. The effects of ADSC-Exos and *Mir221*- and *Mir222*-mimics on (A) plasma LDH and TNNI levels ($n = 5$ mice per group), as well as (B) *Mir221* and *Mir222* expression ($n = 4$-7 mice per group), were measured by qPCR. (C) cardiac function was measured via echocardiography ($n = 7$-9 mice per group). (D and E) ROS levels were measured via MitoSOX red staining and DHE staining (scale bar: 50 µm, $n = 3$-7). (F) BNIP3 and MAP1LC3B/LC3B expression was measured via western blot analysis ($n = 9$-10 mice per group). (G) BNIP3 and MAP1LC3B/LC3B expression was measured via immunohistochemistry (scale bar: 50 µm, $n = 3$-8). (H) the expression of apoptosis-related proteins was evaluated by western blot analysis. (I) the number of

promote cell survival, while reducing the levels of these miRNAs leads to increased apoptosis through the upregulation of BBC3/PUMA [43]. Another study has shown that *Mir221* and *Mir222* reduces the expression of the MAP1LC3B/LC3B autophagy protein and inhibits apoptosis in PTC cells [23]. *Mir221* significantly decreases cardiac H/R-induced autophagosome formation and reduces the LC3-II: I ratio [44,45]. Extracellular vesicle-miRNA (hsa- *Mir221*-3p) levels are downregulated after PM exposure, and patients exhibit inflammation during pregnancy [46]. The present study demonstrated that an increase in *Mir221* and *Mir222* significantly reduced the expression of BNIP3, MAP1LC3B/LC3B, and BBC3/PUMA, indicating the regulatory role of *Mir221* and *Mir222* in mitophagy and apoptosis in PM+I/R (H/R)-induced cardiac injury.

This study clarified the regulatory role of *Mir221* and *Mir222* through the BNIP3-MAP1LC3B/LC3B-BBC3/PUMA pathway, but the exact molecular mechanism remains to be further studied. However, it is necessary to verify whether *Mir221* and *Mir222* regulates apoptosis through the PRKAA1/AMPK-CDKN1B/p27 pathway. The present study showed that the PRKAA1/AMPK-CDKN1B/p27 pathway was induced under PM+I/R (or H/R) conditions, whereas treatment with ADSC-Exos or *Mir221* and *Mir222* mimics reversed these changes. Furthermore, PM+I/R (H/R)-induced apoptosis was reversed by treatment with PRKAA1/AMPK and CDKN1B/p27 inhibitors. Previous studies have shown that *Mir221* and *Mir222* inhibits CDKN1B/p27 expression by targeting the 3'UTR [47]. Apo E inhibits smooth muscle cell proliferation by regulating CDKN1B/p27 expression via *Mir221* and *Mir222* [48]. Notably, the present study revealed that in WT and *mir221*- and *mir222*-KO mice subjected to PM+I/R, the administration of ADSC-Exos or *Mir221*- and *Mir222*-mimics significantly reduced p-PRKAA1/AMPK and p-CDKN1B/p27 expression (Figure S4E). Moreover, *Mir221*- and *Mir222*-TG mice also expressed low levels of p-PRKAA1/AMPK and p-CDKN1B/p27, similar to what was observed in PM+I/R+ADSC-Exos-treated WT mice (Figure S4F). These findings suggested that ADSC-Exos may reduce PM+I/R-induced apoptosis by targeting the *Mir221* and *Mir222*-PRKAA1/AMPK-CDKN1B/p27 signaling cascade.

The mechanism of how *Mir221* and *Mir222* regulates ROS production and mitochondrial fission remains to be determined. Previous studies have shown that *Mir221* and *Mir222* directly inhibits the expression of endothelial nitric oxide synthase (eNOS) or SOD2, reducing the production of nitric oxide (NO) and ROS, respectively [39,49]. Additional studies are required to determine whether *Mir221* and *Mir222* regulates ROS production by targeting eNOS and SOD2. Our results demonstrate significant differences in the effects of ADSC-Exos on cardiac function depending on the presence or absence of *Mir221* and *Mir222* within ADSC-Exos (Figure S5).

Overall, the present findings demonstrated that PM aggravates I/R (H/R)-induced cardiac injury. *Mir221*- and *Mir222*-enriched ADSC-Exos reduce PM+I/R-induced mitophagy and apoptosis by downregulating BNIP3, MAP1LC3B/LC3B, and BBC3/PUMA. The present study provides a new treatment for PM+I/R-induced cardiac injury.

Materials and methods

PM preparation for mouse myocardial ischemia-reperfusion (I/R)

SRM 2786 fine particulate matter (<4 microns) is a standard reference material (SRM) that is used according to the US Environmental Protection Agency/EPA national standard for ambient air quality [50]. SRM 2786 was suspended in PBS (Omics Bio, IB3012) at 10 mg/mL concentration and sonicated for 10 min to reduce particle aggregation. All experiments using C57BL/6J mice, *mir221*- and *mir222*-KO mice, and *Mir221*- and *Mir222*-overexpressing transgenic mice were performed in accordance with the Guidelines for the Use of Laboratory Animals of the National Institutes of Health and approved by the Animal Ethics Committee of National Taiwan University (IACUC No. 20180426). Mice were anesthetized by inhalation of 4% isoflurane mixed with 100% oxygen and injected intratracheally with a solution of 200 μg PM in 50 μL PBS. After 24 h, the mice were anesthetized again, and the left coronary artery was ligated with 8–0 nylon suture for 30 min. The occlusion was confirmed by observing the pale myocardium of the left ventricle. The ligation was then removed, and the animals were sacrificed after 3 h of blood flow. All efforts were made to minimize suffering; mice were euthanized through isoflurane overdose, followed by cardiac excision.

Echocardiography

Echocardiography was performed using a small animal high-resolution ultrasound system (Prospect, S-Sharp, Taiwan) equipped with a 40 MHz single-element transducer. M-mode images obtained from the parasternal long axis view (PLAX) were used to assess fractional shortening (FS) and ejection fraction (EF) as parameters for estimating systolic function. The detailed procedures are described in the Supplemental Material.

apoptotic cells was measured by a TUNEL assay (scale bar: 50 μm, $n = 5$-11 mice per group). To investigate the impact of *Mir221* and *Mir222* expression on pm+i/r-induced cardiac damage, *Mir221*- and *Mir222*-overexpression TG mice were preconditioned with PM for 24 h, followed by myocardial I/R. The results were compared to those of PM+I/R WT mice and PM+I/R+ADSC-Exos WT mice. (J) qPCR was performed to measure *Mir221* and *Mir222* expression ($n = 5$ mice per group). (K) echocardiography was used to assess heart function ($n = 5$ mice per group). (L) LDH and TNNI levels in plasma were measured ($n = 6$-7 mice per group). (M) ROS expression was detected using MitoSOX red and DHE staining (scale bar: 50 μm, $n = 3$-7). (N) western blot analysis was used to evaluate the mitochondrial autophagy-related protein levels ($n = 8$-9 mice per group). (O) western blot analysis was used to evaluate the apoptosis-related protein levels ($n = 6$-12 mice per group). (P) a TUNEL assay was used to quantify apoptotic cell numbers (scale bar: 50 μm, $n = 7$-13 mice per group). The data are expressed as the mean ± SEM; one-way ANOVA.

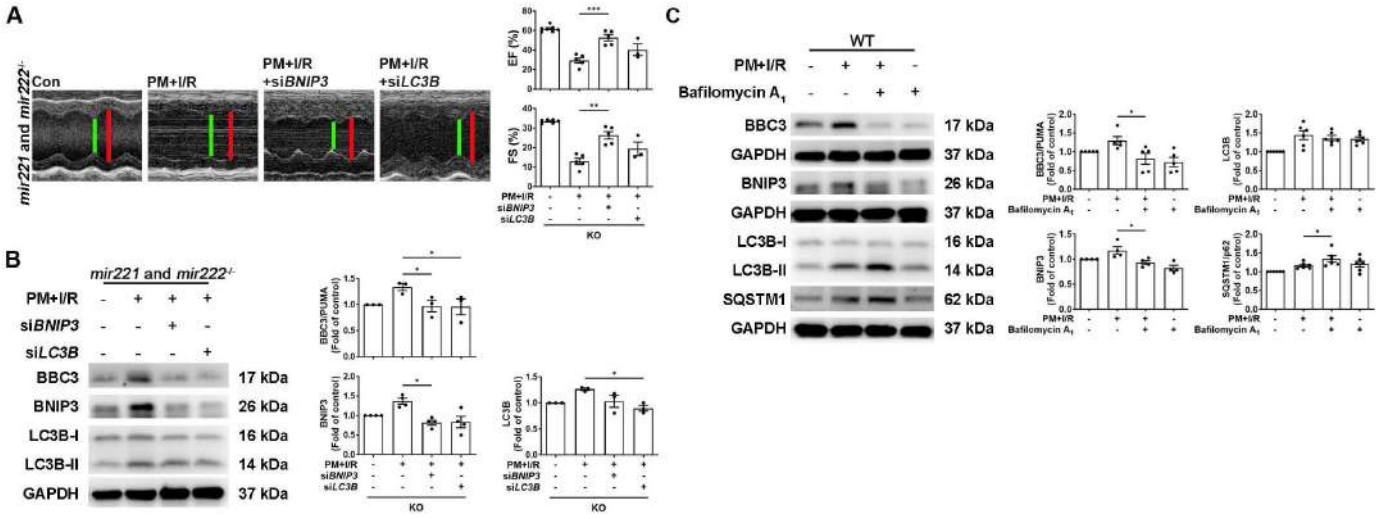


Figure 8. Knockdown of *Bnip3* and *Lc3b* expression improves cardiac function and reduces apoptosis-related proteins. (A and B) *mir221*- and *mir222*-ko mice were preconditioned with PM for 24 h. Then, 25 min after occlusion, si*BNIP3* or si*LC3B* were uniformly intramuscularly injected into the left ventricular marginal zone. EF and FS results were obtained by echocardiography to assess cardiac function ($n = 4$ mice per group). The expression levels of BBC3/PUMA, BNIP3, and MAP1LC3B/LC3B were also examined by western blot ($n = 3$ mice per group). (C) WT mice were intratracheally injected with PM and intraperitoneally injected with bafilomycin A_1 (2.5 mg/kg) for 24 h, followed by 30 min of ischemia and 3 h of reperfusion. The levels of BBC3/PUMA, BNIP3, MAP1LC3B/LC3B, and SQSTM1/p62 were measured by western blot ($n = 4$-5 mice per group).

Statistical significance was defined as $^{*}p < 0.05$, $^{**}p < 0.01$, and $^{***}p < 0.001$.

Cultured cardiomyocytes for hypoxia-reoxygenation (H/R)

Embryonic rat cardiomyocyte-derived H9c2 cardiac myoblasts were obtained from the American Type Culture Collection/ATCC (CRL-1446). The cells were cultured in Dulbecco's modified Eagle's medium (DMEM; Gibco 12,800–017) and exposed to PM at concentrations of 10 μg/mL or 50 μg/mL for 6 h. For hypoxia treatment, the cells were incubated under hypoxic conditions (1% O_2) at 37°C for 6 h, followed by incubation under normoxic reoxygenation conditions for 12 h.

Exosome isolation

Human adipose-derived stem cells (ADSCs, 5×10^5 cells) were seeded into a 10-cm dish. After 24 h of incubation, the conditioned culture medium was collected and centrifuged to remove cells and cell debris. The supernatant (10 mL) was transferred to a sterile vessel, and 2 mL of ExoQuick-TC Exosome Precipitation Solution (System Biosciences, EXOTC50A–1) was added. The mixture was refrigerated overnight and then centrifuged at 10,000 × g for 30 min at 4°C. The resulting pellets were washed with PBS and subsequently suspended in PBS. The morphological characteristics of ADSC-Exos were examined through transmission electron microscopy (TEM). The protein concentration was determined using a BCA protein assay kit (Millipore 71,285-3CN). The isolated ADSC-Exos were stored at −80°C for subsequent use. Examining the characteristics of ADSC-Exos was provided in the supplementary file (Figure S3B to S3D).

MTT assay, TUNEL assay, ANXA5/annexin V-FITC staining, and propidium iodide (PI) staining

The degree of cell viability was determined by a MTT (3-[4,5-dimethylthiazol-2-yl]-2,5-diphenyltetrazolium bromide) assay. The cells were incubated with MTT solution (BIONOVAS, AM0815–0001) at a final concentration of 0.5 mg/mL at 37°C for 1.5 h. Apoptotic cells were detected using terminal deoxynucleotidyl transferase dUTP nick end labeling (TUNEL) staining (*In Situ* Cell Death Detection Kit; Roche Molecular Biochemicals 11,684,817,910) and an ANXA5-FITC-PI staining detection kit (BD Biosciences 640,914). The cells were incubated with TUNEL reagent for 1 h at 37°C in the dark. Slides were counterstained with DAPI to visualize all nuclei and observed under a fluorescence microscope. H9c2 cells were suspended in 100 μL of binding buffer containing 2.5 μL of FITC and 5 μL of PI (100 μg/mL), followed by incubation in the dark at 4°C for 15 min. Cell death was then assessed by flow cytometry.

MitoSOX red, DCFH-DA, and DHE staining

Mitochondrial ROS levels were detected using the MitoSOX Red (Invitrogen, M36008) mitochondrial superoxide indicator. The cells were treated with 1 μM MitoSox Red for 15 min at 37°C. TO-PRO-3 (100 nM; Thermo Fisher Scientific, T3605), a dead cell indicator, was added prior to MitoSox Red analysis using an LSRFortessa flow cytometer (BD Biosciences). Intracellular levels of oxidative radicals and superoxide anions were determined using 2",7"-dichlorodihydrofluorescein diacetate (DCFH-DA; Thermo Fisher Scientific, C369) and dihydroethidium (DHE) (Invitrogen, D11347). Cardiomyocytes were cultured on coverslips, treated with PM+H/R, and then incubated with DCFH-DA (10 μM) for 30 min at 37°C in the dark. The

conversion of DCFH-DA to a fluorescent DCF product was observed using fluorescence microscopy. Five microliters of PI solution (100 μg/mL) was added before flow cytometric analysis of DCFH-DA. PI enters damaged or ruptured cell membranes when the cell dies, providing a method to distinguish between live and dead cells. Cardiomyocytes were incubated in medium containing DHE (5 μM) at 37°C for 15 min. The oxidation of DHE by intracellular superoxide anions produces ethidium, which fluoresces red at 535 nm and is subsequently imaged by fluorescence microscopy. $DiOC_6(3)$ (90 nM; Thermo Fisher Scientific, D273), a lipophilic dye selective for mitochondria in living cells, was added prior to DHE analysis by flow cytometry.

Acridine orange (AO) staining

The cells were briefly washed with PBS and incubated with 1 μg/mL AO hydrochloride solution (Invitrogen, A1301) for 5 min at RT. AO is a fluorophore that accumulates in protonated form within acidic vesicular organelles, including ALs. AO dimerizes at high concentrations, resulting in a metachromatic shift from green to red.

Mitophagy assay using mito-keima

Transfection of mt-Keima red (MBL, AM-V0259) was performed according to the manufacturer's instructions. H9c2 cells were transfected with mt-Keima plasmid (1 μg/mL) in serum-free medium at 37°C for 24 h, then incubated in a hypoxic environment (1% O_2 and 5% CO_2) for 6 h, followed by oxygenation for 12 h. The cells were observed under a fluorescent microscope. Mt-Keima is a pH-sensitive fluorescent protein. When mitochondria are delivered to acidic lysosomes, their excitation spectrum changes from 405 nm to 561 nm and emits in the wavelength range of 570 to 706 nm, showing a color change from green to red.

JC-1 analysis

5,5",6,6"-Tetrachloro-1,1",3,3"-tetraethylbenzimidazolyl-iodocarbocyanine (JC-1, BD biosciences 551,302) was used to analyze changes in the mitochondrial membrane potential. When the mitochondrial membrane potential is low, JC-1 emits green fluorescence as a monomer, and when the mitochondrial membrane potential is high, it aggregates and emits red fluorescence. After various treatments, the cells were incubated with JC-1 (2 μM) for 30 min at 37°C in the dark. Cell fluorescence was monitored using an SP2 microscope (Leica, Wetzlar, Germany) and flow cytometry.

Adenosine triphosphate (ATP) production and seahorse test

Cellular ATP levels were assessed using an ATP assay kit (Invitrogen, A-22066). The cells were lysed and centrifuged (12,000 × g) for 5 min at 4°C. Subsequently, the supernatants were collected and analyzed for ATP levels.

Mitochondrial respiration was assessed with the Seahorse XF Cell Mito Stress Test Kit (Agilent 103,010–100), which directly measures the oxygen consumption rate (OCR) using a Seahorse XFe24 Extracellular Flux Analyzer (Agilent). In brief, cells (1×10^4 cells/well) were seeded into 24-well plates (Agilent). After washing the cells twice with PBS, the medium was changed to XF base medium (pH 7.4 DMEM plus 1 mM pyruvate [Biological Industries, 03–042-1B], 2 mM glutamine [Biological Industries, 03–020-1B], and 10 mM glucose), followed by incubation at 37°C in a non-CO_2 incubator for 1 h. The cells were then injected sequentially through ports in the XF Cell Mito Stress Test Kit (Agilent 103,010–100) with oligomycin (1 μM), FCCP (2 μM), and rotenone (0.5 μM) combined with antimycin (0.5 μM) to assess the ATP-related OCR, maximal OCR and nonmitochondrial OCR.

MitoTracker staining

Mitochondrial length was examined using MitoTracker (Invitrogen, M22425) staining. After the various treatments were completed, the cardiomyocytes were incubated with 400 nM MitoTracker for 1 h at 37°C in the dark. Visualization was performed using total internal reflection fluorescence microscopy (TIRF, Zeiss) and DIC optics, and mitochondrial length was measured using ImageJ software.

Transmission electron microscopy (TEM)

The mitochondrial ultrastructure and mitophagy of cardiac tissue and H9c2 cells were observed by TEM. The samples were fixed in 2% glutaraldehyde and 2% paraformaldehyde in 0.1 M PBS overnight at 4°C. The fixed specimens were dehydrated in ethanol and then embedded in epoxy resin. Ultrathin sections were double-stained with uranyl acetate and lead citrate, followed by examination with a Hitachi H700 electron microscope (Hitachi, Tokyo, JP).

Western blot analysis

The heart was pulverized using liquid nitrogen and subsequently homogenized in RIPA buffer (TOOLS, 1002-W), a commercially available product containing 154 mM NaCl, 1% Nonidet *p*-40 (TOOLS, 9016-45-9), 0.8 mM EDTA, 65.2 mM Tris base, pH 7.8 and 0.25% sodium deoxycholate (TOOLS, 302-95-4) along with a protease inhibitor cocktail (Thermo Fisher Scientific 78,442). The cell lysate was prepared in RIPA buffer containing 1% protease inhibitor cocktail at 4°C for 1 h. The supernatant was retained after centrifuging the lysate at 14,000 × g for 20 min at 4°C. Samples with equal amounts of protein (30 μg) were electrophoresed on SDS-polyacrylamide gels and transferred to PVDF membranes (Millipore, IPVH00010). The membranes were probed overnight at 4°C with the following primary antibodies: DNM1L/Drp1, MFF, BECN1/Beclin 1, BNIP3, MAP1LC3B/LC3B, p-TRP53/p53, CASP3, CASP9, p-PRKAA1/AMPK (1:2000 dilution; Cell Signaling Technology, 8570; 84580; 3495; 3769; 2775; 9284; 9664; 9508; 2535), BCL2 (1:1000 dilution; BD Biosciences

610,539), BBC3/PUMA (1:2000 dilution; Abcam, AB9643), and ACTB/β-actin (1:10000 dilution; Proteintech 66,009–1). The membranes were then incubated with horseradish peroxidase-conjugated goat anti-mouse or anti-rabbit IgG secondary antibodies (Jackson, 111-035-003; 115-035-003). GAPDH (Proteintech 60,004–1) was used as the internal control. The intensity of the bands was quantified using ImageJ software (NIH, MD, USA).

Mitochondrial isolation assay

The Thermo Mitochondrial Isolation Kit (Thermo Fisher Scientific 89,874) was used to isolate mitochondrial and cytoplasmic fractions from H9c2 cell lysates according to the manufacturer's instructions. The mitochondrial and cytoplasmic fractions were stored at −80°C, after which the cellular location and protein expression levels were evaluated by western blot analysis.

Double immunofluorescence staining

Cells on coverslips were washed with PBS, fixed with 4% paraformaldehyde for 15 min at room temperature, and permeabilized for 1 min with 0.1% Triton X-100. The cells were blocked with 1% bovine serum albumin (BSA; Sigma-Aldrich 126,593) in PBS for 1 h at room temperature, followed by were incubation with anti-BNIP3 (Cell Signaling Technology, 3769) or anti-LC3B (Cell Signaling Technology, 2775) primary antibodies (1:200 dilution in PBS containing 1% BSA) overnight at 4°C. After washing with PBS, the cells were incubated with anti-rabbit Alexa Fluor® 488 (Invitrogen, A27034; 1:200 dilution in PBS containing 1% BSA) for 1 h at room temperature. The cells were exposed to COX4/COX IV (Thermo Fisher Scientific, A21348) diluted 1:200 in PBS containing 1% BSA overnight at 4°C. After washing 3 times with PBS, the cells were incubated with anti-mouse Alexa Fluor® 647 (Invitrogen, A20173) for 1 h at room temperature in the dark. The cells were then counterstained with DAPI (1 μg/mL) for 5 min. An SP8 inverted confocal microscope (Leica, Wetzlar, Germany) was used for imaging and analysis.

RNA isolation and quantitative real-time PCR

According to the manufacturer's protocol, total RNA was isolated from cells or frozen mouse ventricular tissues using TRIzol reagent (Thermo Fisher Scientific 78,442). RNA quantification was performed using a NanoDrop™ 2000 spectrophotometer (Thermo Fisher Scientific). The expression levels of *Mir221* and *Mir222* were quantified using commercially available TaqMan MicroRNA assay kits for *Mir221* (000524), *Mir222* (002276), and *RNU6-6P/RNU6B* (001973). For the real-time PCR, TaqMan™ Universal PCR master mix without UNG was used, and the reactions were analyzed by a QuantStudio™ 3 Real-Time PCR System (Applied Biosystems).

Transient transfection

H9c2 cells were seeded into 6-well plates at a density of 2×10^5 cells per well and were grown to 70–80% confluence. The cells were transfected with specific *Mir221*- and *Mir222*-mimics or inhibitors (100 nM/well; Dharmacon) to overexpress or knockdown *Mir221* and *Mir222*, respectively, using Lipofectamine 3000 reagent (Invitrogen, L3000–015) according to the manufacturer's protocol. The cells were then subjected to MAP1LC3B/LC3B and BNIP3 expression analysis.

Dual-luciferase reporter assay

The wild-type (WT) and mutant (MUT) *Bnip3* (or *Lc3b*) 3"-UTR luciferase reporter gene plasmids were produced (Promega 0,000,389,032). Cells were transfected with Mir-NC or *Mir221*- and *Mir222*-mimics along with the WT or MUT *Bnip3* (or *Lc3b*) 3"–UTR reporter plasmids using Lipofectamine 3000 reagent for 48 h.

Statistical analysis

The data were analyzed using SPSS 19.0 statistical software (SPSS, Chicago, IL, USA). The measurement data are presented as the mean ± standard error of the mean (SEM). One-way analysis of variance (ANOVA) was conducted among multiple groups. $p < 0.05$ indicated statistical significance.

Acknowledgements

We thank the technical services provided by the "Transgenic Mouse Models Core Facility of the National Core Facility for Biopharmaceuticals, National Science and Technology Council, Taiwan" and the "Gene Knockout Mouse Core Laboratory of National Taiwan University Center of Genomic and Precision Medicine". In addition, we thank the imaging core and flow cytometric analyzing and sorting core of the first core laboratory, National Taiwan University College of Medicine, for the technical support in image acquisition and analysis.

Disclosure statement

No potential conflict of interest was reported by the author(s).

Funding

This work was supported by research grants from the National Science and Technology Council [MOST 108-2320-B-002-065-MY3; NSTC 111-2320-B-002-022-MY3 to Y.L.C.], Chang Gung University of Science Foundation [grant ZRRPF6N0011 to C.W.L.], and Chang Gung Medical Research Program Foundation [grants CORPF6P0041, CORPF6P0042, CORPF6P0043 to C.W.L.].

Data availability statement

All data are included in the manuscript and supplementary information. Additional materials related to this paper are available upon reasonable request from the corresponding authors.

ORCID

Yuh-Lien Chen http://orcid.org/0000-0002-6498-4008

References

[1] Rajagopalan S, Brauer M, Bhatnagar A, et al. Personal-level protective actions against particulate matter air pollution exposure: a scientific statement from the American heart association. Circulation. 2020;142(23):e411–e431. doi: 10.1161/CIR.0000000000000931

[2] Wang S, Wang F, Yang L, et al. Effects of coal-fired $PM_{2.5}$ on the expression levels of atherosclerosis-related proteins and the phosphorylation level of MAPK in $ApoE^{-/-}$ mice. BMC Pharmacol Toxicol. 2020;21(1):34. doi: 10.1186/s40360-020-00411-8

[3] Holme JA, Brinchmann BC, Refsnes M, et al. Potential role of polycyclic aromatic hydrocarbons as mediators of cardiovascular effects from combustion particles. Environ Health. 2019;18(1):74. doi: 10.1186/s12940-019-0514-2

[4] Yetgin T, Manintveld OC, Boersma E, et al. Remote ischemic conditioning in percutaneous coronary intervention and coronary artery bypass grafting. Circ J. 2012;76(10):2392–2404. doi: 10.1253/circj.CJ-12-0518

[5] Wang A, Zhang H, Liang Z, et al. U0126 attenuates ischemia/reperfusion-induced apoptosis and autophagy in myocardium through MEK/ERK/EGR-1 pathway. Eur J Pharmacol. 2016;788:280–285. doi: 10.1016/j.ejphar.2016.06.038

[6] Xu Y, Tang C, Tan S, et al. Cardioprotective effect of isorhamnetin against myocardial ischemia reperfusion (I/R) injury in isolated rat heart through attenuation of apoptosis. J Cell Mol Med. 2020;24(11):6253–6262. doi: 10.1111/jcmm.15267

[7] Zhou M, Yu Y, Luo X, et al. Myocardial ischemia-reperfusion injury: therapeutics from a mitochondria-centric perspective. Cardiology. 2021;146(6):781–792. doi: 10.1159/000518879

[8] Tong M, Zablocki D, Sadoshima J. The role of Drp1 in mitophagy and cell death in the heart. J Mol Cell Cardiol. 2020;142:138–145. doi: 10.1016/j.yjmcc.2020.04.015

[9] Schiattarella GG, Hill JA. Therapeutic targeting of autophagy in cardiovascular disease. J Mol Cell Cardiol. 2016;95:86–93. doi: 10.1016/j.yjmcc.2015.11.019

[10] Matsui Y, Takagi H, Qu X, et al. Distinct roles of autophagy in the heart during ischemia and reperfusion: roles of amp-activated protein kinase and beclin 1 in mediating autophagy. Circ Res. 2007;100(6):914–922. doi: 10.1161/01.RES.0000261924.76669.36

[11] Gustafsson AB, Gottlieb RA. Autophagy in ischemic heart disease. Circ Res. 2009;104(2):150–158. doi: 10.1161/CIRCRESAHA.108.187427

[12] Rikka S, Quinsay MN, Thomas RL, et al. Bnip3 impairs mitochondrial bioenergetics and stimulates mitochondrial turnover. Cell Death Differ. 2011;18(4):721–731. doi: 10.1038/cdd.2010.146

[13] Jin Q, Li R, Hu N, et al. DUSP1 alleviates cardiac ischemia/reperfusion injury by suppressing the Mff-required mitochondrial fission and Bnip3-related mitophagy via the JNK pathways. Redox Biol. 2018;14:576–587. doi: 10.1016/j.redox.2017.11.004

[14] Huang Z, Han Z, Ye B, et al. Berberine alleviates cardiac ischemia/reperfusion injury by inhibiting excessive autophagy in cardiomyocytes. Eur J Pharmacol. 2015;762:1–10. doi: 10.1016/j.ejphar.2015.05.028

[15] Yang X, Feng L, Zhang Y, et al. Cytotoxicity induced by fine particulate matter ($PM_{2.5}$) via mitochondria-mediated apoptosis pathway in human cardiomyocytes. Ecotoxicol Environ Saf. 2018;161:198–207. doi: 10.1016/j.ecoenv.2018.05.092

[16] Ning R, Shi Y, Jiang J, et al. Mitochondrial dysfunction drives persistent vascular fibrosis in rats after short-term exposure of $PM_{2.5}$. Sci Total Environ. 2020;733:139135. doi: 10.1016/j.scitotenv.2020.139135

[17] Ma T, Sun J, Zhao Z, et al. A brief review: adipose-derived stem cells and their therapeutic potential in cardiovascular diseases. Stem Cell Res Ther. 2017;8(1):124. doi: 10.1186/s13287-017-0585-3

[18] Zou J, Xia H, Jiang Q, et al. Exosomes derived from odontogenic stem cells: its role in the dentin-pulp complex. Regen Ther. 2023;24:135–146. doi: 10.1016/j.reth.2023.05.008

[19] Pu CM, Liu CW, Liang CJ, et al. Adipose-derived stem cells protect skin flaps against ischemia/reperfusion injury via IL-6 expression. J Invest Dermatol. 2017;137(6):1353–1362. doi: 10.1016/j.jid.2016.12.030

[20] Lai TC, Lee TL, Chang YC, et al. MicroRNA-221/222 mediates adsc-exosome-induced cardioprotection against ischemia/reperfusion by targeting PUMA and ETS-1. Front Cell Dev Biol. 2020;8:569150. doi: 10.3389/fcell.2020.569150

[21] Pei YH, Chen J, Wu X, et al. LncRNA PEAMIR inhibits apoptosis and inflammatory response in PM2.5 exposure aggravated myocardial ischemia/reperfusion injury as a competing endogenous RNA of miR-29b-3p. Nanotoxicology. 2020;14(5):638–653. doi: 10.1080/17435390.2020.1731857

[22] Verjans R, Peters T, Beaumont FJ, et al. MicroRNA-221/222 family counteracts myocardial fibrosis in pressure overload-induced heart failure. Hypertension. 2018;71(2):280–288. doi: 10.1161/HYPERTENSIONAHA.117.10094

[23] Shen H, Lin Z, Shi H, et al. MiR-221/222 promote migration and invasion, and inhibit autophagy and apoptosis by modulating ATG10 in aggressive papillary thyroid carcinoma. 3 Biotech. 2020;10(8):339. doi: 10.1007/s13205-020-02326-x

[24] Vriens A, Nawrot TS, Saenen ND, et al. Recent exposure to ultrafine particles in school children alters miR-222 expression in the extracellular fraction of saliva. Environ Health. 2016;15(1):80. doi: 10.1186/s12940-016-0162-8

[25] Sun L, Wang H, Xu D, et al. Lapatinib induces mitochondrial dysfunction to enhance oxidative stress and ferroptosis in doxorubicin-induced cardiomyocytes via inhibition of PI3K/AKT signaling pathway. Bioengineered. 2022;13(1):48–60. doi: 10.1080/21655979.2021.2004980

[26] Xia Y, Chen Z, Chen A, et al. LCZ696 improves cardiac function via alleviating Drp1-mediated mitochondrial dysfunction in mice with doxorubicin-induced dilated cardiomyopathy. J Mol Cell Cardiol. 2017;108:138–148. doi: 10.1016/j.yjmcc.2017.06.003

[27] Lee TL, Lai TC, Lin SR, et al. Conditioned medium from adipose-derived stem cells attenuates ischemia/reperfusion-induced cardiac injury through the microRNA-221/222/PUMA/ETS-1 pathway. Theranostics. 2021;11(7):3131–3149. doi: 10.7150/thno.52677

[28] de Bont J, Jaganathan S, Dahlquist M, et al. Ambient air pollution and cardiovascular diseases: an umbrella review of systematic reviews and meta-analyses. J Intern Med. 2022;291(6):779–800. doi: 10.1111/joim.13467

[29] Nuvolone D, Balzi D, Chini M, et al. Short-term association between ambient air pollution and risk of hospitalization for acute myocardial infarction: results of the cardiovascular risk and air pollution in Tuscany (RISCAT) study. Am J Epidemiol. 2011;174(1):63–71. doi: 10.1093/aje/kwr046

[30] Bugger H, Pfeil K. Mitochondrial ROS in myocardial ischemia reperfusion and remodeling. Biochim Biophys Acta Mol Basis Dis. 2020;1866(7):165768. doi: 10.1016/j.bbadis.2020.165768

[31] Xu Y, Guo W, Zeng D, et al. Inhibiting miR-205 alleviates cardiac ischemia/reperfusion injury by regulating oxidative stress, mitochondrial function, and apoptosis. Oxid Med Cell Longev. 2021;2021(1):9986506. doi: 10.1155/2021/9986506

[32] Cao J, Qin G, Shi R, et al. Overproduction of reactive oxygen species and activation of MAPKs are involved in apoptosis induced by PM2.5 in rat cardiac H9c2 cells. J Appl Toxicol. 2016;36(4):609–617. doi: 10.1002/jat.3249

[33] Luo CM, Feng J, Zhang J, et al. 1,25-vitamin D3 protects against cooking oil fumes-derived PM2.5-induced cell damage through its anti-inflammatory effects in cardiomyocytes. Ecotoxicol Environ Saf. 2019;179:249–256. doi: 10.1016/j.ecoenv.2019.04.064

[34] Ni HM, Williams JA, Ding WX. Mitochondrial dynamics and mitochondrial quality control. Redox Biol. 2015;4:6–13. doi: 10.1016/j.redox.2014.11.006

[35] Zhou H, Zhu P, Wang J, et al. Pathogenesis of cardiac ischemia reperfusion injury is associated with CK2α-disturbed mitochondrial homeostasis via suppression of FUNDC1-related mitophagy.

Cell Death Differ. 2018;25(6):1080–1093. doi: 10.1038/s41418-018-0086-7
[36] Yu W, Xu M, Zhang T, et al. Mst1 promotes cardiac ischemia-reperfusion injury by inhibiting the ERK-CREB pathway and repressing FUNDC1-mediated mitophagy. J Physiol Sci. 2019;69(1):113–127. doi: 10.1007/s12576-018-0627-3
[37] Yang M, Linn BS, Zhang Y, et al. Mitophagy and mitochondrial integrity in cardiac ischemia-reperfusion injury. Biochim Biophys Acta Mol Basis Dis. 2019;1865(9):2293–2302. doi: 10.1016/j.bbadis.2019.05.007
[38] Yang Y, Lin X. Potential relationship between autophagy and ferroptosis in myocardial ischemia/reperfusion injury. Genes Dis. 2023;10(6):2285–2295. doi: 10.1016/j.gendis.2022.02.012
[39] Chistiakov DA, Sobenin IA, Orekhov AN, et al. Human miR-221/222 in physiological and atherosclerotic vascular remodeling. Biomed Res Int. 2015;2015:354517. doi: 10.1155/2015/354517
[40] Mandraffino G, Aragona CO, Cairo V, et al. Circulating progenitor cells in hypertensive subjects: effectiveness of a treatment with olmesartan in improving cell number and miR profile in addition to expected pharmacological effects. PLOS ONE. 2017;12(3):e0173030. doi: 10.1371/journal.pone.0173030
[41] Sun SJ, Wei R, Li F, et al. Mesenchymal stromal cell-derived exosomes in cardiac regeneration and repair. Stem Cell Reports. 2021;16(7):1662–1673. doi: 10.1016/j.stemcr.2021.05.003
[42] Yu H, Douglas HF, Wathieu D, et al. Diabetes is accompanied by secretion of pro-atherosclerotic exosomes from vascular smooth muscle cells. Cardiovasc Diabetol. 2023;22(1):112. doi: 10.1186/s12933-023-01833-4
[43] Zhang C, Zhang J, Zhang A, et al. PUMA is a novel target of miR-221/222 in human epithelial cancers. Int J Oncol. 2010;37(6):1621–1626. doi: 10.3892/ijo_00000816
[44] Chen Q, Zhou Y, Richards AM, et al. Up-regulation of miRNA-221 inhibits hypoxia/reoxygenation-induced autophagy through the DDIT4/mTORC1 and Tp53inp1/p62 pathways. Biochem Biophys Res Commun. 2016;474(1):168–174. doi: 10.1016/j.bbrc.2016.04.090
[45] Zhou Y, Chen Q, Lew KS, et al. Discovery of potential therapeutic miRNA targets in cardiac ischemia-Reperfusion injury. J Cardiovasc Pharmacol Ther. 2016;21(3):296–309. doi: 10.1177/1074248415604463
[46] Ferrari L, Iodice S, Cantone L, et al. Extracellular vesicles and their miRNA contents counterbalance the pro-inflammatory effect of air pollution during physiological pregnancy: a focus on syncytin-1 positive vesicles. Environ Int. 2022;169:107502. doi: 10.1016/j.envint.2022.107502
[47] Fernandez S, Risolino M, Mandia N, et al. miR-340 inhibits tumor cell proliferation and induces apoptosis by targeting multiple negative regulators of p27 in non-small cell lung cancer. Oncogene. 2015;34(25):3240–3250. doi: 10.1038/onc.2014.267
[48] Kothapalli D, Castagnino P, Rader DJ, et al. Apolipoprotein E-mediated cell cycle arrest linked to p27 and the Cox2-dependent repression of miR221/222. Atherosclerosis. 2013;227(1):65–71. doi: 10.1016/j.atherosclerosis.2012.12.003
[49] Togliatto G, Trombetta A, Dentelli P, et al. Unacylated ghrelin promotes skeletal muscle regeneration following hindlimb ischemia via SOD-2-mediated miR-221/222 expression. J Am Heart Assoc. 2013;2(6):e000376. doi: 10.1161/JAHA.113.000376
[50] Schantz MM, Cleveland D, Heckert NA, et al. Development of two fine particulate matter standard reference materials (<4 μm and 10 μm) for the determination of organic and inorganic constituents. Anal Bioanal Chem. 2016;408(16):4257–4266. doi: 10.1007/s00216-016-9519-7

polymers

MDPI

Article

Comparative Evaluation of Dental Clinical Surface Treatments for Polyetheretherketone with Airborne-Particle Abrasion, Hydrofluoric Acid Etching, and Handheld Nonthermal Plasma Activation on Long-Term Bond Performance

Szu-Yu Lai [1,†], Szu-I Lin [1,2,†], Chia-Wei Chang [1,3,†], Yi-Rou Shen [1], Yuichi Mine [4], Zih-Chan Lin [5,6], Mei-Ling Fang [6,7,8], Chia-Chih Sung [2], Chien-Fu Tseng [2,6,9,*], Tzu-Yu Peng [1,*] and Chiang-Wen Lee [5,6,10,11,12,*]

1 School of Dentistry, College of Oral Medicine, Taipei Medical University, Taipei 11031, Taiwan
2 Department of Dentistry, Taoyuan General Hospital, Ministry of Health and Welfare, Taoyuan 33004, Taiwan
3 Division of Family Dentistry, Department of Dentistry, Taipei Medical University Hospital, Taipei 11031, Taiwan
4 Department of Medical Systems Engineering, Hiroshima University Graduate School of Biomedical and Health Sciences, Hiroshima City 734-8553, Japan
5 Department of Nursing, Division of Basic Medical Sciences, and Chronic Diseases and Health Promotion Research Center and Center for Drug Research and Development, Chang Gung University of Science and Technology, Chiayi 613016, Taiwan
6 Research Center for Tooth Bank and Dental Stem Cell Technology, College of Oral Medicine, Taipei Medical University, Taipei 11031, Taiwan
7 Center for Environmental Toxin and Emerging-Contaminant Research, Cheng Shiu University, Kaohsiung 83347, Taiwan
8 Department of Civil Engineering and Geomatics, Cheng Shiu University, Kaohsiung 83347, Taiwan
9 Graduate Institute of Clinical Dentistry, School of Dentistry, College of Medicine, National Taiwan University, Taipei 10048, Taiwan
10 Department of Respiratory Care, Chang Gung University of Science and Technology, Chiayi 613016, Taiwan
11 Department of Orthopaedic Surgery, Chang Gung Memorial Hospital, Chiayi 61363, Taiwan
12 Department of Safety Health and Environmental Engineering, Ming Chi University of Technology, New Taipei City 24301, Taiwan
* Correspondence: d02422002@ntu.edu.tw (C.-F.T.); typeng@tmu.edu.tw (T.-Y.P.); cwlee@mail.cgust.edu.tw (C.-W.L.); Tel.: +886-3-3699721 (ext. 2211) (C.-F.T.); +886-2-27361661 (ext. 5131) (T.-Y.P.); +886-5-3628800 (ext. 2388) (C.-W.L.)
† These authors contributed equally to this work.

check for updates

Academic Editor: Masao Irie

Received: 9 May 2025
Revised: 20 May 2025
Accepted: 21 May 2025
Published: 23 May 2025

Citation: Lai, S.-Y.; Lin, S.-I.; Chang, C.-W.; Shen, Y.-R.; Mine, Y.; Lin, Z.-C.; Fang, M.-L.; Sung, C.-C.; Tseng, C.-F.; Peng, T.-Y.; et al. Comparative Evaluation of Dental Clinical Surface Treatments for Polyetheretherketone with Airborne-Particle Abrasion, Hydrofluoric Acid Etching, and Handheld Nonthermal Plasma Activation on Long-Term Bond Performance. *Polymers* **2025**, *17*, 1448. https://doi.org/10.3390/polym17111448

Copyright: © 2025 by the authors. Licensee MDPI, Basel, Switzerland. This article is an open access article distributed under the terms and conditions of the Creative Commons Attribution (CC BY) license (https://creativecommons.org/licenses/by/4.0/).

Abstract: Polyaryletherketone (PAEK) materials, including polyetheretherketone (PEEK) and polyetherketoneketone (PEKK), possess excellent mechanical properties and biocompatibility; however, their inherently low surface energy limits effective bonding with resin cements. This study investigated the effects of hydrofluoric acid (HF) etching and handheld nonthermal plasma (HNP) treatment on enhancing the adhesive performance of PAEK surfaces. Disk-shaped PEEK (BP) and PEKK (PK) specimens were divided into four groups: APA (airborne-particle abrasion), PLA (nonthermal plasma treatment), LHF (5.0% HF), and HHF (9.5% HF). Surface characterization was performed using a thermal field emission scanning electron microscope (FE-SEM). Surface wettability was evaluated using contact angle goniometry. Cytotoxicity was evaluated using HGF-1 cells exposed to conditioned media and analyzed via PrestoBlue assays. Shear bond strength (SBS) was measured after three aging conditions—NT (no aging), TC (thermocycling), and HA (highly accelerated aging)—using a light-curing resin cement. Failure modes were categorized, and statistical analysis was performed using one-way and two-way ANOVA with Tukey's HSD test ($\alpha = 0.05$). Different surface treatments did not affect surface characterization. PLA treatment significantly improved surface wettability, resulting in the lowest contact angles among all groups, followed by HF etching (HHF > LHF), while APA showed the poorest hydrophilicity. Across all treatments, PK exhibited better wettability than BP. Cytotoxicity results confirmed that all surface treatments were nontoxic to HGF-1 cells, indicating favorable biocompatibility. SBS testing demonstrated that PLA-treated specimens achieved the

highest and most stable bond strength across all aging conditions. Although HF-treated groups exhibited lower bond strength overall, BP samples treated with HF showed relatively less reduction following aging. Failure mode analysis revealed a shift from mixture and cohesive failures in the NT aging condition to predominantly adhesive failures after TC and HA aging conditions. Notably, the PLA-treated groups retained mixture failure patterns even after aging, suggesting improved interfacial durability. Among the tested methods, PLA treatment was the most effective strategy, enhancing surface wettability, bond strength, and aging resistance without compromising biocompatibility. In summary, the PLA demonstrated the greatest clinical potential for improving the adhesive performance of PAEK when used with light-curing resin cements.

Keywords: polyetheretherketone; light-curing cement; shear bond strength; resin bonding; handheld nonthermal plasma treatment; hydrofluoric acid etching; artificial aging

1. Introduction

Polyaryletherketones (PAEKs) are a family of high-performance, semi-crystalline thermoplastic polymers characterized by excellent thermal stability and chemical resistance [1–3]. Their molecular structures are composed of numerous aromatic rings and ether and ketone linkages, forming a resonance-stabilized backbone with delocalized electrons [4,5]. This unique electronic configuration contributes to their superior heat resistance, mechanical strength, and chemical inertness, making PAEKs widely applicable in the aerospace, automotive, and biomedical fields [1,5,6]. Among the PAEK family, the most representative members are polyetheretherketone (PEEK) and polyetherketoneketone (PEKK), both of which exhibit high strength, chemical resistance, and favorable biocompatibility, although they differ slightly in molecular configuration [6,7]. While PEKK may demonstrate superior bonding performance in certain applications, its higher surface polarity and energy can limit its clinical utility [6,8]. In contrast, PEEK has gained widespread adoption in dentistry owing to its excellent toughness, elastic modulus comparable to dentin, and established processability, thereby becoming the most extensively used PAEK material in prosthetic and implant restorative applications [4,6,7,9,10].

PEEK exhibits an elastic modulus of approximately 4–8 GPa, closely matching that of human bone and dentin, allowing it to effectively distribute occlusal forces and reduce stress concentration at the interface between restorations and biological tissues, thereby demonstrating favorable biomechanical compatibility [2,9,11]. Additionally, its lightweight nature, high moldability, and resistance to corrosion have contributed to its increasing use in both fixed and removable dental prostheses [1,2,10]. In removable partial dentures, PEEK serves as a framework material offering a balance of aesthetics, comfort, mechanical stability, and low risk of metal hypersensitivity [10,12]. However, the intrinsic gray-white color of PEEK is not compatible with the natural tooth shade, limiting its use in highly aesthetic anterior restorations [2,6]. Clinically, composite resin veneers or ceramic-based restorations are often applied over PEEK surfaces to enhance aesthetic outcomes [3]. In the field of orthodontics, PEEK has also emerged as a potential alternative to stainless steel in the fabrication of lingual retainers and brackets, offering improved biocompatibility and aesthetic appeal [13,14].

Despite its many advantages, PEEK's inherently low surface energy and chemical inertness hinder the formation of strong, durable bonds with resin-based materials [3,6,8,9]. Achieving stable adhesion is critical for the long-term clinical success of PEEK [15,16]. To address this challenge, ceramic-filled modified materials such as BioHPP (bredent

medical GmbH & Co. KG) have been developed to enhance mechanical strength and confer some degree of bioactivity [1,4,9]. Nevertheless, even modified PEEK (BioHPP) struggles to establish robust chemical bonds with resin cements, necessitating the use of additional surface treatments to improve interfacial reactivity and bond strength [17–20]. Common surface modification strategies include airborne-particle abrasion [21–23], laser ablation [24,25], and etching with concentrated sulfuric acid (98% H_2SO_4) [25–27], all of which increase surface roughness and surface energy to promote mechanical interlocking and enhance the bonding interface. Among these, sulfuric acid etching effectively alters surface topography and introduces reactive functional groups, but its high corrosivity and associated safety concerns limit its clinical applicability [25,28]. Laser ablation, while efficient, may induce surface carbonization or irreversible structural damage, potentially compromising bonding performance [29].

The pursuit of a surface treatment strategy that balances safety and effectiveness forms the basis of this study. The current study investigates two promising surface treatment strategies—hydrofluoric acid (HF) etching, which presents a lower hazard level, and handheld nonthermal plasma (HNP) treatment—to evaluate their effects on the surface characteristics and resin bonding performance of polyetheretherketone. HF reacts with silica (SiO_2) in silicate ceramics to produce highly reactive hexafluorosilicic acid, which induces micro-etching on the material surface, increasing surface roughness and wettability [30,31]. This reaction also promotes the exposure of silanol (–Si–OH) groups, creating active bonding sites that strengthen the chemical interactions between PAEK and resin adhesives, thereby improving overall bond durability [30,31]. Plasma treatment, a non-destructive physical modification method, generates high-energy reactive species from gas excitation and introduces polar functional groups such as carboxyl (–COOH), hydroxyl (–OH), and amide (–$CONH_2$) groups [8,32]. Our previous studies have demonstrated that HNP significantly enhances the surface energy and wettability of PEEK, resulting in improved PEEK–resin adhesion [8,32].

In this study, two clinically relevant HF concentrations (5.0% and 9.5%) and HNP treatment are applied to modify the surface of PAEK specimens, and the results are compared with those obtained from conventional airborne-particle abrasion. Shear bond strength (SBS) tests are performed using light-curing cement, and artificial aging protocols are employed to simulate intraoral conditions and assess the long-term durability of the bonding. Ultimately, this study aims to establish a clinically feasible surface treatment protocol for PAEK-based lingual retainers or brackets, enhancing their adhesion to cement and thus improving their clinical applicability and performance.

2. Materials and Methods

2.1. Sample Preparation and Surface Treatment

Disk-shaped specimens (10 mm in diameter, 2.5 mm in thickness) were designed using 3D modeling software (SOLIDWORKS 2013, Dassault Systèmes SolidWorks Corp., Waltham, MA, USA) and fabricated from PEEK (breCAM BioHPP, bredent medical GmbH & Co. KG, Senden, Germany; BP) and PEKK (Pekkton ivory, Cendres+Métaux SA, Biel, Switzerland; PK) using a dental 5-axis milling unit (Milling Unit M1, Zirkonzahn GmbH, Gais, Italy). All specimens were polished with #600 silicon carbide paper to ensure uniform surfaces, ultrasonically cleaned in isopropanol, and dried in a 37 °C oven under sterile conditions. The specimens were then randomly divided into 4 groups (n = 50 per group) and subjected to different surface treatments, as listed in Table 1.

Table 1. Surface treatment protocols for each experimental group.

Group	Surface Treatment Methods
APA	Airborne-particle abrasion with 110 μm alumina (Cobra, Renfert GmbH, Hilzingen, Germany) at 2 bars for 10 s.
PLA	Handheld nonthermal plasma treatment (PiezoBrush PZ3, Relyon plasma GmbH, Regensburg, Germany) for 10 s.
LHF	5.0% hydrofluoric acid etching (IPS Ceramic Etching Gel, Ivoclar Vivadent, Schaan, Liechtenstein) for 120 s.
HHF	9.5% hydrofluoric acid etching (Porcelain Etchant, Bisco Inc., Schaumburg, IL, USA) for 120 s.

2.2. Surface Characterization

Surface characterization was performed using a thermal field emission scanning electron microscope (FE-SEM; JSM-7800F Prime, JEOL Ltd., Tokyo, Japan). Prior to observation, each sample was sputter-coated with a platinum layer. Imaging was conducted under high-vacuum conditions (9.6×10^{-5} Pa) with an accelerating voltage of 3.0 kV in secondary electron mode. Microstructural details were recorded via the instrument's lower secondary electron detector.

2.3. Wettability

The surface wettability of specimens was evaluated using a contact angle analyzer (Phoenix Mini, Surface Electro Optics Co., Ltd., Gyeonggi-do, Republic of Korea) based on the sessile drop method. A 50 μL droplet of distilled water was gently placed in contact with the specimen surface at room temperature, allowing it to spread naturally. The droplet profile was captured in real time using a charge-coupled device (CCD) camera, and contact angles were calculated using a drop-shape fitting algorithm. Each specimen was measured three times, and a total of ten specimens per group (n = 10) were analyzed. The reported contact angle values represent the mean of ten independent measurements.

2.4. Cytotoxicity Testing

All specimens (n = 5) were sterilized by autoclaving at 121 °C and 1.2 kg/cm^2 for 30 min, then dried under sterile conditions. Human gingival fibroblast-1 (HGF-1) cells (ATCC CRL-2014) were seeded into culture wells at a density of 1×10^5 cells/well and cultured in high-glucose Dulbecco's Modified Eagle Medium (DMEM) supplemented with 10% fetal bovine serum, 100 μg/mL streptomycin, and 100 U/mL penicillin. Cultures were maintained at 37 °C in a humidified atmosphere with 5% CO_2, and the medium was refreshed every three days. Cells at passages 3–7 and full confluence were used for experiments. For cytotoxicity evaluation, specimens were immersed in DMEM at 37 °C for 72 h. HGF-1 cells were seeded into culture wells, and the culture medium was replaced with the conditioned DMEM collected from the specimen immersion. After 48 h of incubation, cell viability was assessed using the PrestoBlue™ cell viability reagent (Invitrogen, Carlsbad, CA, USA) following the manufacturer's instructions. All experiments were performed in triplicate to ensure reproducibility. Optical density (OD) values were normalized against the control group (DMEM only), and the relative growth rate (RGR) was calculated using the formula RGR (%) = $OD_{sample}/OD_{DMEM} \times 100$.

2.5. Bonding Procedure and Shear Bond Strength (SBS) Testing

Before bonding, all specimens were primed with HC primer (SHOFU Inc., Kyoto, Japan) and light-cured for 90 s using a UV curing unit (Phrozen Tech Co., Ltd., Hsinchu City, Taiwan). A bonding ring was positioned on each specimen, and light-curing cement (Transbond XT, 3M ESPE Dental Products, St. Paul, MN, USA) was dispensed into it. A 4.9 N load was applied from above to ensure uniform cement thickness, and excess cement was removed prior to final light-curing using an LED curing unit. Specimens were then

stored in a 37 °C oven to complete polymerization. The bonded specimens were divided into three aging groups (n = 10 each):

(1) NT—stored in distilled water at 37 °C for 24 h;
(2) TC—subjected to 5000 thermocycles (5–55 °C) [33];
(3) HA—subjected to highly accelerated aging (134 °C, 2 bar, 5 h) [34].

SBS testing was conducted using a universal testing machine (JSV-H1000, ALGOL Instrument Co., Ltd., Taoyuan, Taiwan) by applying a shear force at the adhesive interface at a crosshead speed of 1 mm/min until failure. Shear bond strength was calculated for all specimens. Failure modes were examined under a dental magnifier and classified as adhesive, cohesive, or mixture failure.

2.6. Statistical Analyses

The minimum sample size was calculated using power analysis software (GPower v3.1.9.6; Heinrich Heine University, Düsseldorf, Germany) based on previously reported surface characterization, cytotoxicity, and SBS data [8,22,32,35]. Data are expressed as mean ± standard deviation. Normality was assessed using the Shapiro–Wilk test, and parametric tests were applied. One-way analysis of variance (ANOVA) followed by Tukey's honestly significant difference (HSD) post hoc test was used to analyze contact angle, surface energy, and cytotoxicity. SBS values across different surface treatments and aging conditions were analyzed using two-way ANOVA followed by Tukey's HSD test. Statistical analyses were performed using SPSS (v19; IBM Corp., Armonk, NY, USA) and GraphPad Prism (v10; GraphPad Software Inc., San Diego, CA, USA), with the significance level set at $\alpha = 0.05$.

3. Results

3.1. Surface Characterization

The microscopic surface morphologies are presented in Figure 1, revealing no distinct changes across different treatments. APA produced grooves and uneven marks on both BP and PK, with PK showing deeper and more defined patterns. PLA led to moderate roughening with visible linear features, while LHF and HHF caused minor surface irregularities on BP but induced more pronounced erosion and peeling on PK, especially under HHF.

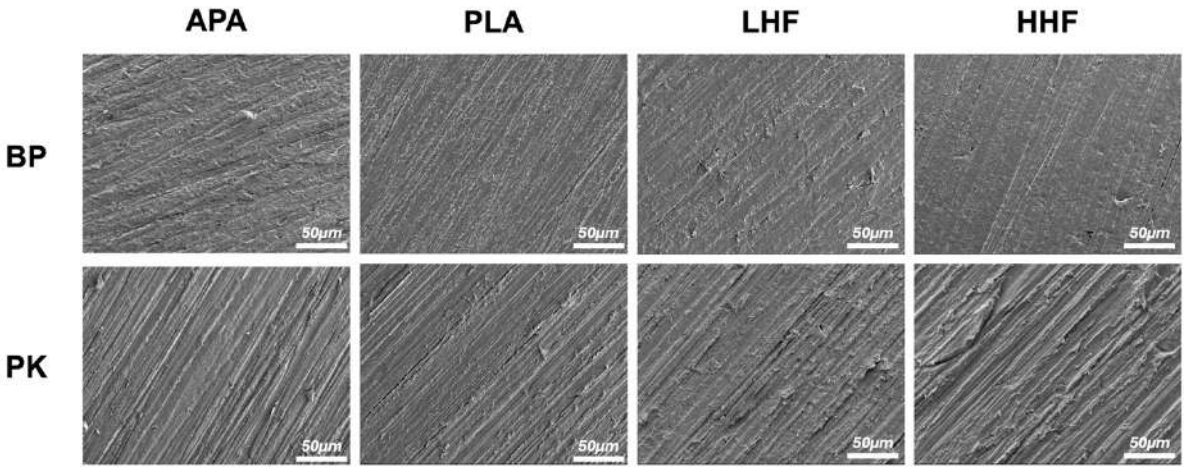


Figure 1. The FE-SEM surface morphologies of PEEK (BP) and PEKK (PK) specimens after different surface treatments. APA: airborne-particle abrasion; PLA: nonthermal plasma treatment; LHF: low-concentration hydrofluoric acid etching; HHF: high-concentration hydrofluoric acid etching.

3.2. Wettability

The results of surface wettability, as shown in Figure 2 and Table 2, indicate that the APA group exhibited the highest contact angles, indicating the poorest wettability. In contrast, the PLA group significantly reduced the contact angle, suggesting a substantial improvement in surface hydrophilicity. HF etching also effectively enhanced wettability, with both the LHF and HHF groups showing lower contact angles than the APA group. Notably, high-concentration HF etching (HHF) resulted in greater hydrophilicity compared with low-concentration HF (LHF). Regarding material differences, PK consistently exhibited lower contact angles than BP under all treatment conditions, indicating higher surface responsiveness and superior wettability. Overall, plasma treatment was the most effective at enhancing surface wettability, followed by HF etching, while airborne-particle abrasion was the least effective.

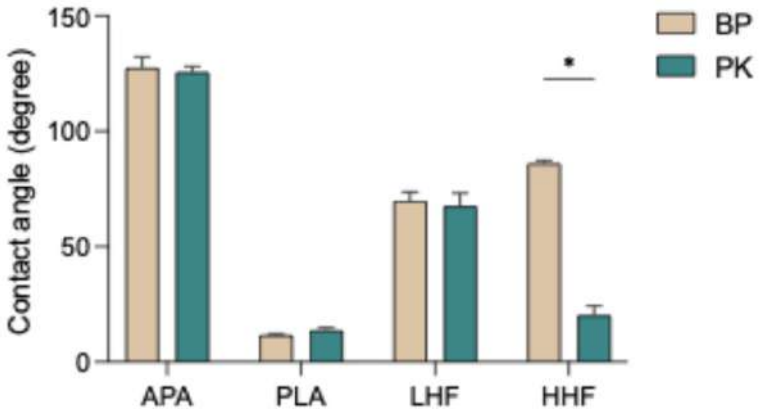


Figure 2. Water contact angles of PEEK (BP) and PEKK (PK) specimens after different surface treatments. APA: airborne-particle abrasion; PLA: nonthermal plasma treatment; LHF: low-concentration hydrofluoric acid etching; HHF: high-concentration hydrofluoric acid etching. The asterisk symbol (*) indicates that there is a significant difference ($p < 0.05$) between the two materials (BP and PK) under the same surface treatment conditions.

Table 2. Results of water contact angles and SBS.

Material	Surface Treatment	Contact Angle (Degrees)		Shear Bond Strength (MPa) NT	TC	HA
BP (PEEK)	APA	127.41 ± 4.72	a	15.18 ± 1.10 ^{a}	11.76 ± 1.04 ^{a}	15.01 ± 2.53 ^{a}
	PLA	11.66 ± 0.52	b	18.06 ± 3.63 ^{b}	12.09 ± 1.18 ^{b}	15.51 ± 2.15 ^{a}
	LHF	69.76 ± 3.88	c	5.51 ± 0.66 ^{c}	4.31 ± 2.60 ^{c}	5.21 ± 1.99 ^{b}
	HHF	86.06 ± 1.26	d	5.17 ± 1.79 ^{c}	4.07 ± 2.30 ^{c}	4.75 ± 0.91 ^{b}
PK (PEKK)	APA	125.66 ± 2.37	A	14.31 ± 2.10 ^{A}	13.01 ± 2.65 ^{A}	13.01 ± 2.65 ^{A}
	PLA	13.79 ± 0.98	B	16.51 ± 1.51 ^{B}	14.53 ± 1.41 ^{B}	16.19 ± 1.94 ^{B}
	LHF	67.55 ± 5.68	C	8.22 ± 2.45 ^{C}	4.81 ± 2.61 ^{C}	5.80 ± 1.95 ^{C}
	HHF	20.30 ± 3.98	D	8.08 ± 2.06 ^{C}	4.64 ± 1.99 ^{C}	4.44 ± 1.79 ^{C}

All the results are presented as average ± standard deviation. Artificial aging condition: NT, stored in distilled water at 37 °C for 24 h; TC, subjected to 5000 thermocycles between 5 °C and 55 °C; HA, subjected to highly accelerated aging at 134 °C and 2 bar for 5 h. Different letters (a, b, c, d for BP and A, B, C, D for PK) in the same column indicate significant differences ($p < 0.05$).

3.3. Cytotoxicity Test

The cytotoxicity results (Figure 3) showed that both BP and PK specimens exhibited comparable cell viability across all surface treatments, with no significant differences between groups ($p > 0.05$), and the results were comparable to the untreated control (DMEM only), indicating no detectable cytotoxic effects.

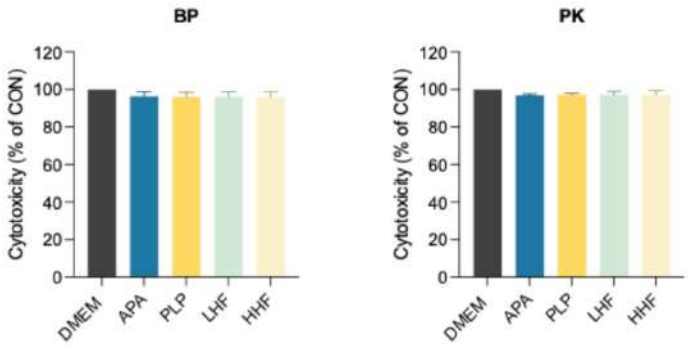


Figure 3. Assessment of cytotoxicity activity by indirect exposure of HGF-1 cells to extracts, consisting of conditioned DMEM collected from the immersion of PEEK (BP) and PEKK (PK) specimens treated with different methods using the PrestoBlue cell viability assay.

3.4. SBS Testing

Figure 4 and Table 2 illustrate the changes in SBS across different surface treatment groups under three artificial aging conditions. Following the TC aging condition, all groups exhibited a significant decrease in SBS ($p < 0.05$), except for the HF-treated groups (LHF and HHF) in the BP. Despite the general reduction, the PLA group maintained a relative advantage ($p < 0.05$). Under the HA aging condition, the decline in SBS was less pronounced than under the TC aging condition, with BP exhibiting a more substantial reduction compared with PK across all surface treatments. Nevertheless, the PLA group consistently exhibited superior performance, with the highest and most stable SBS values across all aging conditions. In contrast, the HF-treated groups (LHF and HHF) showed the lowest SBS values both before and after aging. However, it is noteworthy that the HF-treated BP specimens exhibited only slight decreases in SBS following aging. Furthermore, PK generally exhibited higher SBS values than BP under all conditions.

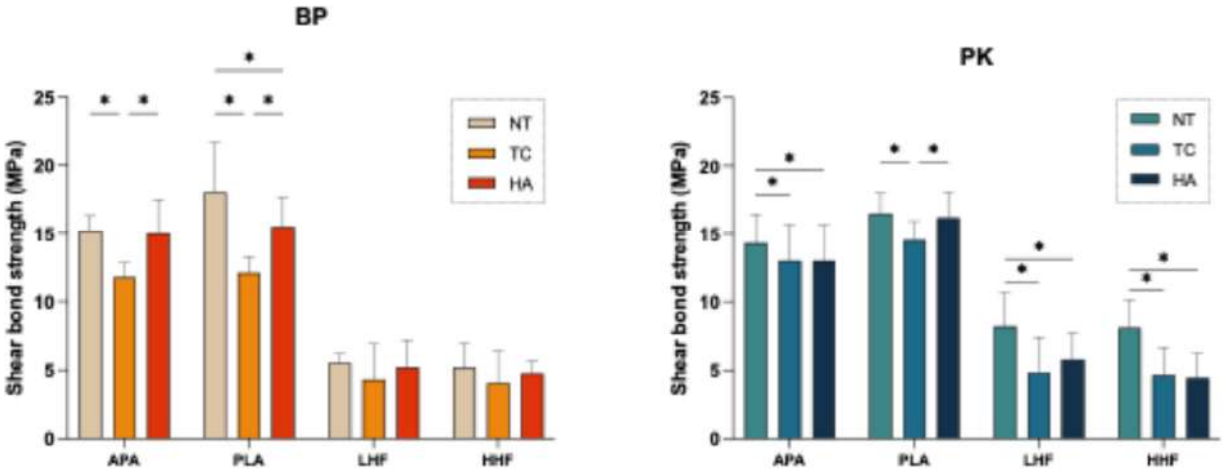


Figure 4. Effects of different surface treatments and aging conditions on the shear bond strength (SBS) of PEEK (BP) and PEKK (PK). NT: stored in distilled water at 37 °C for 24 h; TC: subjected to 5000 thermocycles between 5 °C and 55 °C; HA: subjected to highly accelerated aging at 134 °C and 2 bar for 5 h. The asterisk symbol (*) indicates that there is a significant difference ($p < 0.05$) between the aging conditions (NT, TC, and HA) under the same surface treatment conditions.

3.5. Debonded Interface Analysis

Debonded interface analysis (Figure 5) revealed that, in the NT condition, mixture and cohesive failures were observed in the BP-PLA and BP-HHF groups as well as in the PK-APA and PK-PLA groups. In contrast, adhesive failure predominated in the LHF groups. Following the TC aging condition, the proportion of adhesive failures increased.

Nonetheless, mixture failures were still present in the PK-APA group and in the PLA-treated groups of both materials. Under the HA aging condition, most specimens exhibited adhesive failure, although the PLA-treated groups of both materials retained some instances of mixture failure.



Figure 5. Distribution of failure modes (adhesive, mixture, and cohesive) for PEEK (BP) and PEKK (PK) under various surface treatments and aging conditions (NT, TC, and HA). NT: stored in distilled water at 37 °C for 24 h; TC: subjected to 5000 thermocycles between 5 °C and 55 °C (ISO10477); HA: subjected to highly accelerated aging at 134 °C and 2 bar for 5 h (ISO13356).

4. Discussion

This study evaluated the effects of different surface treatments (Table 1)—airborne-particle abrasion (APA), nonthermal plasma treatment (PLA), and low-concentration (LHF) and high-concentration HF etching (HHF)—on the surface wettability, cytotoxicity, SBS, and bonding durability after artificial aging of PEEK (BP) and PEKK (PK). The results demonstrated that PLA exhibited the best overall performance across all parameters, while PEKK consistently outperformed PEEK, providing important implications for clinical applications.

Although SEM imaging (Figure 1) revealed some surface topographical differences across treatments, the overall morphological variations were relatively subtle, particularly for BP. APA and PLA induced mild surface roughening, while LHF and HHF caused limited morphological changes. The less-pronounced differences suggest that bonding performance may be more influenced by chemical modifications than by surface roughness alone, especially in chemically inert substrates like BP.

The surface wettability results revealed that PLA effectively reduced the water contact angle (Figure 2), significantly enhancing the hydrophilicity of the material surface. This finding aligns with previous studies reporting that plasma treatment introduces hydrophilic functional groups (e.g., hydroxyl, carboxyl) onto polymer surfaces, thereby increasing surface energy [8,17,21,32]. In contrast, APA increased surface roughness only through physical mechanisms without altering the surface chemistry, resulting in higher contact angles (Figure 2 and Table 2) and limited improvement in wettability [22,36]. HF etching also decreased contact angles, with high-concentration etching yielding greater hydrophilicity than low-concentration etching, likely due to the stronger etching effect of high-concentration HF, which exposes more reactive sites on the surface [30]. The modification mechanism of HF etching on PEEK may involve partial fluorination or hydrolysis reactions with the ketone (–C=O) and ether (–O–) groups in the polymer backbone, leading to the formation of hydroxyl (–OH), carboxyl (–COOH), or fluorocarbon (C–F) bonds on the surface, thereby increasing surface polarity and wettability [25,28,30]. In addition, HF etching may induce localized micro-etching, increasing the surface roughness and forming micropores or irregular structures that contribute to mechanical interlocking with resin. However, due to the aromatic structure and high crystallinity of BP, its chemical reactivity is relatively limited, resulting in a restricted increase in surface functional groups after HF etching [30,31]. Across all treatment conditions, PK exhibited lower contact angles than BP (Table 2), indicating superior surface reactivity, which may be attributed to its higher ketone content that enhances sensitivity to surface modification. In addition, the current study found that HHF etching significantly reduced the contact angle on PK surfaces, while an opposite trend was observed for BP containing nano-ceramic fillers (Figure 2). This difference may be attributed to variations in polymer structure and filler composition. PK, with a higher ketone content and rigid backbone, undergoes more pronounced surface erosion under HF treatment, resulting in increased roughness and enhanced hydrophilicity. In contrast, the ceramic fillers in BP are less reactive to HF and may lead to uneven surface degradation, filler exposure, or interfacial instability during etching, ultimately reducing wettability. These findings suggest that the interaction between the polymer matrix and fillers plays a critical role in surface modification outcomes.

Regarding biocompatibility (Figure 3), this study found that all treatment groups exhibited cell viability comparable to the untreated control, with no significant cytotoxic effects, indicating that neither the physical nor chemical treatments left harmful residues on the materials, and their potential impact on soft tissues is relatively safe. This finding corroborates previous reports on the biocompatibility of surface-modified BP and PK, supporting the clinical applicability of these treatment methods [11,28,32].

In terms of bonding performance, PLA achieved the highest initial SBS and maintained stable and superior SBS across all aging conditions (Figure 4), indicating its efficacy in enhancing interfacial bonding strength and durability (Table 2). After the TC aging condition, all groups showed significant decreases in SBS ($p < 0.05$), except for the HF-treated BP groups (LHF, HHF). Nevertheless, the PLA-treated groups retained a relative advantage ($p < 0.05$), demonstrating resistance to thermal cycling stress at the bonding interface. Under the TC aging condition (Figure 4), the reduction in SBS was even greater than under the HA aging condition, with BP showing more pronounced declines; however, PLA still maintained a relative advantage, confirming its superior aging stability. In contrast, the HF-treated groups exhibited the lowest SBS both before and after aging, suggesting limited improvement in bonding performance (Figure 4). Notably, the SBS reduction in the HF-treated groups after aging was not significant, indicating that their aging resistance remained relatively unchanged. This result may be attributed to the introduction of C–F, –OH, and –COOH functional groups by HF etching on the BP surface, which

increased wettability but did not effectively form chemical crosslinks with resin monomers (e.g., MMA, UDMA). Moreover, excessive etching may have weakened the mechanical integrity and introduced interfacial microcracks, thereby limiting the overall bonding performance improvement [19,30,31].

The failure mode analysis (Figure 5) supported the SBS findings. In the NT aging condition, mixture and cohesive failures were observed in the BP-PLA and BP-HHF groups as well as in the PK-APA and PK-PLA groups, indicating sufficient interfacial bonding strength to propagate failure into the resin or substrate. In contrast, adhesive failure predominated in the APA and LHF groups. After the TC aging condition (Figure 5), the proportion of adhesive failures increased overall, suggesting thermal stress weakened the bonding interface; however, the PLA-treated groups still exhibited some mixture failures, reflecting higher resistance to aging. Under the HA aging condition (Figure 4), most specimens exhibited adhesive failure, but the PLA-treated groups of both materials retained some mixture failures, corresponding to the superior SBS results and further supporting the correlation between failure mode and bonding durability.

In summary, PLA demonstrated superior performance in improving the surface wettability, resin bonding, and post-aging bonding stability of both BP and PK while maintaining safety and efficacy, thereby offering a clinically viable surface treatment strategy. Although HF etching increased surface polarity and wettability and introduced microstructural roughness, its contribution to stable chemical bonding was limited, and the potential adverse effects of over-etching on mechanical integrity must be considered. Particularly in BP, despite the detection of C–F, –OH, and –COOH groups after HF treatment, the inert polymer backbone and aromatic ring stability hindered the achievement of functional group density and reactivity comparable to plasma treatment. Furthermore, PK consistently outperformed BP under all treatment and aging conditions, indicating that its higher ketone content and structural characteristics contribute to more stable chemical bonding with resin, making it a more promising candidate for clinical applications requiring long-term bonding stability. While this study independently assessed plasma treatment and HF etching, it did not evaluate their combined application. Future research could explore whether sequential plasma activation followed by HF etching yields synergistic benefits, combining enhanced chemical reactivity and modified surface morphology to further improve interfacial bonding and durability between polymer substrates and resin. This approach may offer a promising surface treatment strategy for high-performance polymers.

5. Conclusions

This study confirmed that surface treatments significantly influenced the surface characteristics, biocompatibility, and resin bonding performance of BP and PK. All treatments were non-cytotoxic. Among them, PLA showed the best overall results, enhancing wettability and achieving the highest and most stable SBS across all aging conditions. While HHF improved wettability, its bond durability was limited. PK outperformed BP in wettability, bonding strength, and aging resistance. Notably, only PLA-treated groups retained mixture failures after aging, indicating better interfacial stability. Overall, PLA is the most effective and clinically feasible surface treatment for improving the adhesive performance of PAEK materials.

Author Contributions: Conceptualization, T.-Y.P.; formal analysis, C.-W.C. and Y.-R.S.; funding acquisition, S.-I.L., C.-F.T. and C.-W.L.; investigation, S.-Y.L. and C.-W.C.; methodology, S.-Y.L. and S.-I.L.; project administration, T.-Y.P. and C.-W.L.; resources, M.-L.F., Z.-C.L. and C.-W.L.; data curation, S.-Y.L. and S.-I.L.; supervision, S.-I.L., Y.M., C.-C.S. and C.-W.L.; validation, M.-L.F., Z.-C.L. and C.-C.S.; writing—original draft, S.-Y.L., S.-I.L. and C.-W.C.; writing—review and editing, Y.M., C.-F.T., C.-W.L. and T.-Y.P. All authors have read and agreed to the published version of the manuscript.

Funding: This research was funded by the National Science and Technology Council of Taiwan (112-2314-B-038-118-MY2), the Division of Research Planning and Development, Department of Research and Development, Taoyuan General Hospital, Ministry of Health and Welfare (PTH114058 and PTH114118), College of Oral Medicine, Taipei Medical University (TMUCOM202501), Chang Gung University of Science and Technology Foundation (ZRRPF6N0011), and Chang Gung Medical Research Program Foundation (CMRPF6P0041, CMRPF6P0042, and CMRPF6P0043).

Institutional Review Board Statement: Not applicable.

Data Availability Statement: The original contributions presented in this study are included in the article. Further inquiries can be directed to the corresponding authors.

Conflicts of Interest: The authors declare no conflicts of interest.

References

1. Gouveia, D.d.N.M.; Razzoog, M.E.; Sierraalta, M.; Alfaro, M.F. Effect of surface treatment and manufacturing process on the shear bond strength of veneering composite resin to polyetherketoneketone (PEKK) and polyetheretherketone (PEEK). *J. Prosthet. Dent.* **2022**, *128*, 1061–1066. [CrossRef] [PubMed]
2. Liu, Y.; Fang, M.; Zhao, R.; Liu, H.; Li, K.; Tian, M.; Niu, L.; Xie, R.; Bai, S. Clinical applications of polyetheretherketone in removable dental prostheses: Accuracy, characteristics, and performance. *Polymers* **2022**, *14*, 4615. [CrossRef]
3. Soares Machado, P.; Cadore Rodrigues, A.C.; Chaves, E.T.; Susin, A.H.; Valandro, L.F.; Pereira, G.K.R.; Rippe, M.P. Surface treatments and adhesives used to increase the bond strength between polyetheretherketone and resin-based dental materials: A scoping review. *J. Adhes. Dent.* **2022**, *24*, 233–245.
4. Henriques, B.; Sampaio, M.; Buciumeanu, M.; Souza, J.C.M.; Gomes, J.R.; Silva, F.; Carvalho, O. Laser surface structuring of Ti6Al4V substrates for adhesion enhancement in Ti6Al4V-PEEK joints. *Mater. Sci. Eng. C* **2017**, *79*, 177–184. [CrossRef]
5. Kadhum, A.S.; Alhuwaizi, A.F. The efficacy of polyether-ether-ketone wire as a retainer following orthodontic treatment. *Clin. Exp. Dent. Res.* **2021**, *7*, 302–312. [CrossRef] [PubMed]
6. Kiliç, M.; Dede, D.Ö.; Küçükekenci, A.S. Comparing the shear bond strength of veneering materials to the PAEKs after surface treatments. *BMC Oral Health* **2023**, *23*, 185. [CrossRef]
7. Peng, T.-Y.; Shimoe, S.; Fuh, L.-J.; Lin, C.-K.; Lin, D.-J.; Kaku, M. Bonding and thermal cycling performances of two (poly)aryl–ether–ketone (PAEKs) materials to an acrylic denture base resin. *Polymers* **2021**, *13*, 543. [CrossRef] [PubMed]
8. Huang, H.-Y.; Lai, S.-Y.; Lee, F.-T.; Wu, Y.-C.; Feng, S.-W.; Nikawa, H.; Peng, T.-Y. Influence of handheld nonthermal plasma on shear bond strength of polyaryletherketone to resin-matrix cement. *J. Dent. Sci.* **2024**, *19*, 2057–2064. [CrossRef]
9. Henriques, B.; Fabris, D.; Mesquita-Guimarães, J.; Sousa, A.C.; Hammes, N.; Souza, J.C.M.; Silva, F.S.; Fredel, M.C. Influence of laser structuring of PEEK, PEEK-GF30 and PEEK-CF30 surfaces on the shear bond strength to a resin cement. *J. Mech. Behav. Biomed. Mater.* **2018**, *84*, 225–234. [CrossRef]
10. Lee, W.-F.; Chen, M.-S.; Peng, T.-Y.; Huang, P.-C.; Nikawa, H.; Peng, P.-W. Comparative analysis of the retention force and deformation of PEEK and PEKK removable partial denture clasps with different thicknesses and undercut depths. *J. Prosthet. Dent.* **2024**, *131*, 291.e1–291.e9. [CrossRef]
11. Najeeb, S.; Bds, Z.K.; Bds, S.Z.; Bds, M.S.Z. Bioactivity and osseointegration of PEEK are inferior to those of titanium: A systematic review. *J. Oral Implantol.* **2016**, *42*, 512–516. [CrossRef] [PubMed]
12. Peng, T.-Y.; Ogawa, Y.; Akebono, H.; Iwaguro, S.; Sugeta, A.; Shimoe, S. Finite-element analysis and optimization of the mechanical properties of polyetheretherketone (PEEK) clasps for removable partial dentures. *J. Prosthodont. Res.* **2020**, *64*, 250–256. [CrossRef] [PubMed]
13. Win, P.P.; Chen, D.D.-S.; Sainbayar, B.; Peng, T.-Y.; Cheng, J.H.-C. Assessment of mechanical characteristics of polyetheretherketone as orthodontic fixed lingual retainers. *J. Dent. Sci.* **2023**, *18*, 1804–1811. [CrossRef]
14. Wu, J.; Wang, X.; Jiang, J.; Bai, Y. Fabrication of a novel aesthetic orthodontic bracket and evaluation of friction properties between PEEK and stainless steel wires. *Technol. Health Care* **2024**, *32*, 269–278. [CrossRef]
15. Gama, L.T.; Duque, T.M.; Özcan, M.; Philippi, A.G.; Mezzomo, L.A.M.; Gonçalves, T.M.S.V. Adhesion to high-performance polymers applied in dentistry: A systematic review. *Dent. Mater.* **2020**, *36*, e93–e108. [CrossRef]
16. Alsadon, O.; Moorehead, R.; Almansour, H.; Bangalore, D.; Alageel, O.; Wood, D. Surface characteristics and adhesion of veneering composite resin to PAEK-based substructure restorative materials. *J. Prosthodont.* **2023**, *32*, 147–153. [CrossRef] [PubMed]
17. Stübinger, S.; Drechsler, A.; Bürki, A.; Klein, K.; Kronen, P.; von Rechenberg, B. Titanium and hydroxyapatite coating of polyetheretherketone and carbon fiber-reinforced polyetheretherketone: A pilot study in sheep. *J. Biomed. Mater. Res. Part B Appl. Biomater.* **2016**, *104*, 1182–1191. [CrossRef]

18. Schönhoff, L.M.; Mayinger, F.; Eichberger, M.; Lösch, A.; Reznikova, E.; Stawarczyk, B. Three-dimensionally printed and milled polyphenylene sulfone materials in dentistry: Tensile bond strength to veneering composite resin and surface properties after different pretreatments. *J. Prosthet. Dent.* **2022**, *128*, 93–99. [CrossRef]
19. Abdelfattah Mohamed, A.M.; El Homossany, M.E.-M.B.; Abdelmoniem, S.M.; Abdelrahman, T.Y. Comparison of tensile bond strength of ball attachments made of different materials to root canal dentin after chewing simulation. *BMC Oral Health* **2022**, *22*, 254. [CrossRef]
20. Yilmaz, B.; Gouveia, D.; Schimmel, M.; Lu, W.-E.; Özcan, M.; Abou-Ayash, S. Effect of adhesive system, resin cement, heat-pressing technique, and thermomechanical aging on the adhesion between titanium base and a high-performance polymer. *J. Prosthet. Dent.* **2024**, *131*, 468–474. [CrossRef]
21. Li, W.; Sang, L.; Jian, X.; Wang, J. Influence of sanding and plasma treatment on shear bond strength of 3D-printed PEI, PEEK and PEEK/CF. *Int. J. Adhes. Adhes.* **2020**, *100*, 102614. [CrossRef]
22. Lee, P.-C.; Peng, T.-Y.; Ma, T.-L.; Chiang, K.-Y.; Mine, Y.; Lee, I.-T.; Yu, C.-C.; Chen, S.-F.; Yu, J.-H. Effect of various airborne particle abrasion conditions on bonding between polyether-ether-ketone (PEEK) and dental resin cement. *Polymers* **2023**, *15*, 2114. [CrossRef]
23. Adali, U.; Sütel, M.; Yassine, J.; Mao, Z.; Müller, W.-D.; Schwitalla, A.D. Influence of sandblasting and bonding on the shear bond strength between differently pigmented polyetheretherketone (PEEK) and veneering composite after artificial aging. *Dent. Mater.* **2024**, *40*, 1123–1127. [CrossRef] [PubMed]
24. Kimura, H.; Tsuka, H.; Morita, K.; Hirata, I.; Nishio, F.; Abekura, H.; Doi, K.; Tsuga, K. Nd:YVO4 laser groove treatment can improve the shear bond strength between dental PEEK and adhesive resin cement with an adhesive system. *Dent. Mater. J.* **2022**, *41*, 382–391. [CrossRef]
25. Peng, T.-Y.; Shimoe, S.; Higo, M.; Kato, M.; Hirata, I.; Iwaguro, S.; Kaku, M. Effect of laser engraving on shear bond strength of polyetheretherketone to indirect composite and denture-base resins. *J. Dent. Sci.* **2024**, *19*, 32–38. [CrossRef]
26. Schmidlin, P.R.; Stawarczyk, B.; Wieland, M.; Attin, T.; Hämmerle, C.H.F.; Fischer, J. Effect of different surface pre-treatments and luting materials on shear bond strength to PEEK. *Dent. Mater.* **2010**, *26*, 553–559. [CrossRef]
27. Silthampitag, P.; Chaijareenont, P.; Tattakorn, K.; Banjongprasert, C.; Takahashi, H.; Arksornnukit, M. Effect of surface pretreatments on resin composite bonding to PEEK. *Dent. Mater. J.* **2016**, *35*, 668–674. [CrossRef] [PubMed]
28. Escobar, M.; Souza, J.C.M.; Barra, G.M.O.; Fredel, M.C.; Özcan, M.; Henriques, B. On the synergistic effect of sulfonic functionalization and acidic adhesive conditioning to enhance the adhesion of PEEK to resin-matrix composites. *Dent. Mater.* **2021**, *37*, 741–754. [CrossRef]
29. Peng, T.-Y.; Ma, T.-L.; Lee, I.T.; Wu, S.-H.; Mine, Y.; Lin, C.-C. Enhancing dental cement bond strength with autofocus-laser-cutter-generated grooves on polyetheretherketone surfaces. *Polymers* **2023**, *15*, 3670. [CrossRef]
30. Ramakrishnaiah, R.; Alkheraif, A.A.; Divakar, D.D.; Matinlinna, J.P.; Vallittu, P.K. The effect of hydrofluoric acid etching duration on the surface micromorphology, roughness, and wettability of dental ceramics. *Int. J. Mol. Sci.* **2016**, *17*, 822. [CrossRef]
31. Lümkemann, N.; Eichberger, M.; Stawarczyk, B. Bonding to Different PEEK Compositions: The Impact of Dental Light Curing Units. *Materials* **2017**, *10*, 67. [CrossRef] [PubMed]
32. Tseng, C.-F.; Lee, I.T.; Wu, S.-H.; Chen, H.-M.; Mine, Y.; Peng, T.-Y.; Kok, S.-H. Effects of handheld nonthermal plasma on the biological responses, mineralization, and inflammatory reactions of polyaryletherketone implant materials. *J. Dent. Sci.* **2024**, *19*, 2018–2026. [CrossRef] [PubMed]
33. *ISO 10477:2020*; Dentistry—Polymer-Based Crown and Veneering Materials. International Organization for Standardization: Geneva, Switzerland, 2020.
34. *ISO 10993:2018*; Biological Evaluation of Medical Devices—Part 1: Evaluation and Testing Within a Risk Management Process. International Organization for Standardization: Geneva, Switzerland, 2018.
35. Peng, T.-Y.; Kang, C.-M.; Feng, S.-W.; Hung, C.-Y.; Iwaguro, S.; Lin, D.-J. Effects of glass-ceramic spray deposition manipulation on the surface characteristics of zirconia dental restorations. *Ceram. Int.* **2022**, *48*, 29873–29881. [CrossRef]
36. Al-Akhali, M.; Al-Dobaei, E.; Wille, S.; Mourshed, B.; Kern, M. Influence of elapsed time between airborne-particle abrasion and bonding to zirconia bond strength. *Dent. Mater.* **2021**, *37*, 516–522. [CrossRef]

Disclaimer/Publisher's Note: The statements, opinions and data contained in all publications are solely those of the individual author(s) and contributor(s) and not of MDPI and/or the editor(s). MDPI and/or the editor(s) disclaim responsibility for any injury to people or property resulting from any ideas, methods, instructions or products referred to in the content.

Acta Biomaterialia 196 (2025) 332–349

Contents lists available at ScienceDirect

Acta Biomaterialia

journal homepage: www.elsevier.com/locate/actbio

Full length article

Dual cell-penetrating peptide-conjugated polymeric nanocarriers for miRNA-205–5p delivery in gene therapy of cutaneous squamous cell carcinoma

Cheng-Yu Lin [a,1], Jia-You Fang [b,c,d,1], Chien-Yu Hsiao [c,e,f], Chiang-Wen Lee [c,g,h,i], Abdullah Alshetaili [j], Zih-Chan Lin [g,*]

[a] Department of Pathology, Duke University School of Medicine, Durham, NC, USA
[b] Pharmaceutics Laboratory, Graduate Institute of Natural Products, Chang Gung University, Kweishan, Taoyuan, Taiwan
[c] Research Center for Food and Cosmetic Safety and Research Center for Chinese Herbal Medicine, Chang Gung University of Science and Technology, Kweishan, Taoyuan, Taiwan
[d] Department of Anesthesiology, Chang Gung Memorial Hospital, Linkou, Taiwan
[e] Department of Nutrition and Health Sciences, Chang Gung University of Science and Technology, Kweishan, Taoyuan, Taiwan
[f] Aesthetic Medical Center, Department of Dermatology, Chang Gung Memorial Hospital, Linkou, Taiwan
[g] Chronic Diseases and Health Promotion Research Center, Chang Gung University of Science and Technology, Puzi, Chiayi, Taiwan
[h] Department of Orthopaedic Surgery, Chang Gung Memorial Hospital, Puzi, Chiayi, Taiwan
[i] Department of Respiratory Care, Chang Gung University of Science and Technology, Puzi, Chiayi, Taiwan
[j] Department of Pharmaceutics, College of Pharmacy, Prince Sattam Bin Abdulaziz University, Al Kharj, Saudi Arabia

ARTICLE INFO

Keywords:
Mir-205–5p
Cell-penetrating peptide
Polymer nanoparticle
Cutaneous squamous cell carcinoma
R9
p28

ABSTRACT

Despite the potential of microRNAs (miRNAs) in suppressing tumorigenesis, the main challenges are achieving tumor-specific selectivity and efficient delivery into cancer cells. In this study, miR-205–5p-loaded polymeric nanoparticles conjugated with dual cell-penetrating peptides (CPPs) were designed for targeting and treating cutaneous squamous cell carcinoma (cSCC). The CPPs, R9, and p28, demonstrated high cell-penetrating/targeting abilities and antitumor activity. The anti-cSCC effect of the nanocarriers was examined using in vitro cellular 2D and 3D models and in vivo spheroid-xenografted murine models. The average size of the dual CPP-conjugated nanocarriers was 193 nm with a zeta potential of 5.7 mV. These nanocarriers were readily internalized by A431 cells, resulting in decreased proliferation compared to naked agomiR and nanoparticles with a single CPP. The nanocarriers induced cell cycle arrest in the G0/G1 stage. By loading the miR-205–5p mimic, the dual CPP-conjugated nanoparticles enhanced cell apoptosis threefold compared to the control, activating caspases and poly(ADP-ribose) polymerase (PARP). The wound healing assay demonstrated that the nanocarriers significantly inhibited the migration and invasion of cSCC cells. Additionally, the CPP-conjugated nanocarriers penetrated cSCC 3D spheroids, reducing spheroidal size and proliferation. In vivo studies demonstrated that the intratumoral CPP-conjugated nanocarriers achieved a 30 % reduction in tumor volume than the PBS control. The number of Ki67-positive cells in the nanocarrier-treated tumor decreased fivefold than the untreated tumors. The nanoparticulate agomiR (1 μM) exhibited no cytotoxicity towards normal keratinocytes. No significant toxicity was observed in the skin and peripheral organs following subcutaneous administration of the nanoparticles in healthy mice. These findings demonstrate that miR-205–5p mimic delivery via dual CPP-conjugated nanocarriers can promote efficient and safe cSCC regression.

Statement of significance: Cutaneous squamous cell carcinoma (cSCC) is a highly invasive skin malignancy with limited treatment options. This study introduces dual cell-penetrating peptide (CPP)-conjugated polymeric nanoparticles for delivering miR-205–5p, a tumor-suppressor microRNA, to cSCC cells. The nanosystem enhances cellular uptake, inhibits cell proliferation, and promotes apoptosis in both 2D and 3D tumor models. In vivo, the nanocarriers demonstrate significant antitumor efficacy with minimal toxicity, highlighting their potential as a

* Corresponding author.
E-mail address: zclin@mail.cgust.edu.tw (Z.-C. Lin).
[1] These author equally contributed to this work.

https://doi.org/10.1016/j.actbio.2025.02.056
Received 13 October 2024; Received in revised form 16 February 2025; Accepted 24 February 2025
Available online 25 February 2025
1742-7061/© 2025 Acta Materialia Inc. Published by Elsevier Inc. All rights are reserved, including those for text and data mining, AI training, and similar technologies.

targeted, non-invasive therapy. This research represents a promising advance in gene therapy for cSCC by combining nanotechnology and CPPs to address challenges in miRNA delivery and tumor targeting.

1. Introduction

Cutaneous squamous cell carcinoma (cSCC) is an epithelial malignancy characterized by the uncontrolled growth and mutation of squamous cells in the skin epidermis. The risk factors include cumulative ultraviolet irradiation, chemical pollutant exposure, age, and systemic immunosuppression [1]. cSCC is the second most common skin malignancy after basal cell carcinoma (BCC) [2]. The risk incidence of this cancer has increased by 50–200 % over the past three decades [3]. It is estimated that the lifetime incidence of cSCC in Caucasians is 7–11 % [4]. Surgical removals, such as excision, cryotherapy, and laser, are the gold standard for early-stage cSCC. However, surgery is inappropriate for patients with multiple or large-area tumors, and it often results in disfiguring damage, thereby reducing the overall quality of life. Additionally, patients with metastatic cSCC require a comprehensive treatment approach. When surgery is not feasible, radiotherapy and chemotherapy serve as alternative treatments. Although both therapies are effective in treating cSCC, the development of resistance and the adverse effects of cytotoxic chemotherapeutic drugs have limited their application [5]. Furthermore, the short-lived responses to chemotherapy often lead to a poor prognosis. It is reported that cSCC recurs most commonly (70–80 %) within two years after diagnosis [1]. Another challenge of the treatments is that the overall survival rate of late-stage cSCC patients has not improved in recent years [6]. Therefore, increasing the effectiveness of treatment and identifying new therapeutic modalities are urgent in reducing cSCC occurrence and metastatic mortality.

Identifying signaling pathways associated with cSCC pathogenesis has led to the discovery of targetable molecules over the last decade [7]. MicroRNAs (miRNAs) are involved in the regulation of post-transcriptional gene expression in cancers. miRNAs are non-coding RNAs of 19–25 nucleotides that regulate the expression of specific messenger RNAs (mRNAs) by hybridizing to the 3′-untranslated region (3′-UTR). This binding involves biological processes, including proliferation, apoptosis, differentiation, and angiogenesis [8]. Many miRNAs have been shown to participate in the development of cSCCs [9]. miRNAs are ideal candidates for targeted therapy because they control gene expression. However, the clinical application of miRNA therapy remains limited due to restricted cellular internalization, insufficient targeted delivery, and finite accumulation at the tumor site [10]. One way to overcome these drawbacks is to use efficient delivery systems to enhance cell permeability. Cell-penetrating peptides (CPPs) are short peptide sequences that can translocate across cellular membranes and aid the cellular uptake of nucleic acids, which are hindered by their large molecular size and negative charge [11]. Both direct translocation and endocytosis are mechanisms for the cellular uptake of CPPs. Evidence supports the capability of CPPs to target anticancer drug delivery to tumors without damaging the membrane and normal tissue [12]. However, CPPs are often susceptible to proteolytic degradation. To stabilize CPPs in vivo, they can be loaded onto nanoparticles to prevent proteolysis and enhance penetration efficiency due to the increased local interface density [13]. The nanocarriers can improve the stability of miRNAs by protecting them from nucleases and enhancing cellular miRNA ingestion [14].

This study aims to develop dual CPP-conjugated nanoparticles for targeted miRNA delivery to cSCC. The nanosystem was constructed with a poly(lactic-*co*-glycolic acid) (PLGA) core decorated with two CPPs, nano-L-arginine (R9) and p28. This nanosystem was hypothesized to efficiently mitigate cSCC invasiveness. R9 has been reported to enhance nucleic acid delivery into cSCC cells [15]. p28, a derivative of azurin from the cupredoxin family of *Pseudomonas aeruginosa,* serves as a CPP and has a distinct affinity with tumor cells, inducing cancer cell apoptosis [16]. p28 has already entered Phase I clinical trials for treating central nervous system cancers and solid tumors [11]. The miR-205–5p mimic was selected as the model miRNA in this study. The dysregulation of miR-205–5p is controversial in various types of cancer cells. It is suppressed in breast, melanoma, renal, and prostate cancers, while it is overexpressed in lung, bladder, ovarian, and head and neck carcinomas [17]. miR-205–5p has been reported to inhibit the proliferation of keratinocytes, the precursors of cSCC cells [18]. One of the targets of miR-205–5p is tumor necrosis factor α-induced protein 8 (TNFAIP8), which was first identified in the SCC cell lines [19]. TNFAIP8 down-regulation can inhibit cancer cell proliferation and increase cell apoptosis [20]. To evaluate the therapeutic efficacy of nanocarriers, an in vitro cell-based experiment using both adherent 2D and spheroid 3D culture systems was conducted to examine the proliferation, apoptosis, and invasion of cSCC. A cell line-derived xenograft nude mouse was used as an in vivo model to assess the antitumor effect of the nanoparticles.

2. Materials and methods

2.1. Fabrication of dual CPP-conjugated nanoparticles

PLGA (50 mg) and miR-205–5p agomiR (sequence: UCCUUCAUUCCACCGGAGUCUG, 50 μl) or fluorescent dye (0.1 mg) in dichloromethane were injected into a solution containing 1,2-distearoyl-*sn*-glycero-3-phosphoethanolamine-N-[maleimide(polyethylene glycol)−2000] (DSPE-PEG-maleimide, 2 mg), 1,2-dioleoyl-3-trimethylammonium-propane (DOTAP, 1 mg), and a polyvinyl alcohol emulsifier. This mixture was immediately and rigorously emulsified using a high-power sonicator, forming PLGA nanoparticles encapsulating miR-205–5p, coumarin 6, or rhodamine 800 (PLGA NPs). The nanoparticles were then incubated with R9 (sequence: RRRRRRRRR, 2.5 mg) and p28 (sequence: LSTAADMQGVVTDGMASGLDKDYLKPDDC, 2.5 mg) (Thermo Fisher Scientific) for four hours at room temperature to fabricate dual peptide-conjugated nanoparticles (DP-PNPs). The proposed structure of DP-PNPs loaded with miR-205–5p mimic is illustrated in Fig. 1. The solvent was removed by evaporation on a magnetic stirrer for 24 h, and miR-205–5p- or fluorescent dye-loaded nanoparticles were purified by ultracentrifugation (12,000 x*g*) for 30 mins, followed by three washes and resuspension in phosphate-buffered saline (PBS). The nanodispersion was centrifuged at 48,000 x*g* and 4 °C for 30 mins to remove the unencapsulated miR-205–5p from the supernatant. The nanoparticle pellet was reconstituted in water to achieve the desired concentration of miR-205–5p. This procedure ensured complete entrapment of miR-205–5p agomiR or fluorescent dye in the nanocarriers for further experiments (Supplementary Figure 1A). Considering the molecular weights of R9 (~1.41 kDa) and P28 (~3.03 kDa), adding equal peptide weights (2.5 mg each) resulted in an approximate 2:1 molar ratio of R9 to P28. This ratio was intentionally designed to enhance R9-mediated intracellular delivery while ensuring sufficient P28 for apoptotic function. This molecular ratio relationship has been explicitly mentioned to clarify our material preparation strategy.

2.2. Nanoparticle size and zeta potential

Dynamic light scattering (DLS) using the Malvern Nano ZS90 was employed to determine the nanoparticle size, polydispersity index (PDI), and zeta potential of the nanocarriers. The z-average, representing the intensity-weighted average size, was calculated from a specific fit to the light scattering correlation function data. The z-average indicated the mean particle size, while PDI specified the width of the particle size

distribution.

2.3. Nanoparticle morphology

The morphology of the nanoparticles was examined using transmission electron microscopy (TEM) and scanning electron microscopy (SEM). A drop of the nanodispersion was placed on a grid to form a thin film without staining. Images were captured at 200 kV using an ultra-high-resolution TEM (Hitachi HT7800). The surface appearance of the nanoparticles was analyzed with field emission SEM (Hitachi SU8220). To minimize the charging effect, the samples were coated with gold using an SPI-Module sputter coater (Eiko 2B-3).

2.4. CPP conjugation efficiency

R9 and p28 were labeled with fluorescein isothiocyanate (FITC) to

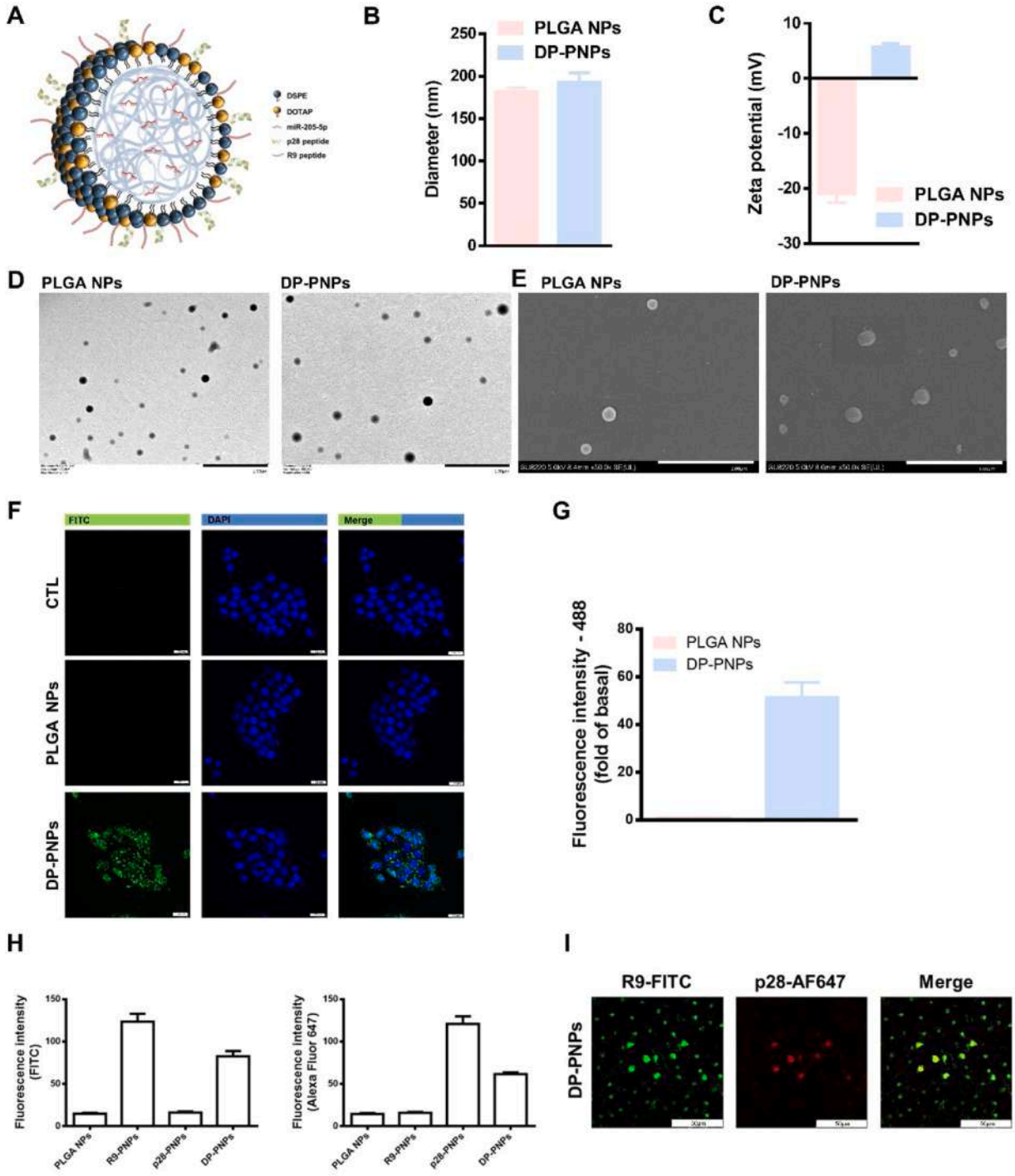


Fig. 1. Preparation and physicochemical characterization of peptide-conjugated nanoparticles: (A) Fabrication process and schematic representation of the nanoparticles. (B) Nanoparticle size distribution. (C) Nanoparticle zeta potential. (D) TEM image of peptide-conjugated nanoparticles. Scale bars, 1 μm. (E) SEM image of peptide-conjugated nanoparticles. (F) Cellular uptake of R9-FITC peptide-conjugated nanoparticles. Scale bars, 1 μm. (G) Fluorescent intensity of R9-FITC peptides on the nanoparticle surface. (H) Fluorescence intensity analysis of R9-FITC (green) and P28-AF647 (red) conjugated on PLGA nanoparticles. (I) Cellular uptake of PLGA nanoparticles conjugated with R9-FITC and P28-AF647 in A431 cells. Scale bars, 50 μm. Data are presented as mean±SEM ($n = 3$).

examine the conjugation efficiency of the nanoparticles. The nanoparticles were resuspended in equal volumes of double-distilled water. To assess peptide binding efficiency, any unbound peptides were removed by ultracentrifugation. The conjugation ratio of the two peptides on the PLGA nanoparticles was quantified using a fluorescence spectrophotometer by measuring the fluorescence intensities of each labeled peptide. Specifically, R9 was conjugated with fluorescein isothiocyanate (FITC) and P28 with Alexa Fluor 647 (AF647). After removing unbound peptides through ultracentrifugation, the fluorescence emission of FITC (excitation/emission: 488/525 nm) and AF647 (excitation/emission: 650/665 nm) was measured separately. The relative fluorescence intensities were used to calculate the ratio of R9 to P28 on the nanoparticle surface, ensuring precise quantification of peptide conjugation, and the fluorescence intensity of the CPPs was quantified using a fluorescence spectrophotometer (Hitachi F2500).

2.5. miR-205–5p encapsulation efficiency

The nanoparticle precipitate was obtained through ultracentrifugation at 12,000 x*g* for 30 mins at 4 °C. The encapsulation of miR-205–5p agomiR in the nanocarriers was determined using agarose gel electrophoresis and NanoDrop spectrophotometer (Thermo Fisher Scientific) at 260 nm.

2.6. 2D cell adherence culture and cell viability assay

The human epidermoid carcinoma cell line (A431) and immortalized human keratinocytes (HaCaT) were cultured in tissue culture flasks with Dulbecco's modified Eagle medium (DMEM) supplemented with 10 % fetal bovine serum (FBS) and 1 % penicillin/streptomycin. To assess the cytotoxicity of the naked miRNA and miRNA-loaded nanoparticles using traditional 2D cell culture, A431 cells were seeded into 96-well plates at a density of 1×10^4 cells/well and maintained in a humidified atmosphere with 5 % CO_2 at 37 °C. The cells were treated with a medium containing various concentrations of naked miR-205–5p, PLGA NPs, R9-PNPs, p28-PNPs, and DP-PNPs. After 48 h or five days of incubation, cell viability was determined using the Cell Counting Kit-8 (CCK-8, Cayman Chemical) according to the manufacturer's instructions. All experiments were conducted in triplicate. Absorbance was measured at 450 nm using a microplate reader (Bio-Rad), with wells lacking cells as blank. Cytotoxicity was determined based on the absorbance reading.

2.7. 3D spheroid culture

A431 cells in 3D spheroids were established using the GEcoll 3D Culture Kit (GEcoll Biomedical). The cells were mixed at a density of 1×10^4 cells/well in a 1-ml mixture of growth medium and A Gel at a 1:1 ratio. The cell suspension mixture (40 μl) was added to each well for five minutes. Once the gel had formed, 1 ml of cold C Buffer was added to cover the dome after 15 mins. After a 15-minute incubation, the C Buffer was replaced with a culture medium. The culture medium was replaced the following day. The cells were then incubated at 37 °C in a CO_2 incubator for 7–14 days to form the spheroids (Supplementary Figure 1B).

2.8. Cellular uptake of the nanoparticles

The fluorescence of cells treated with PLGA NPs, R9-PNPs, p28-PNPs, or DP-PNPs containing coumarin 6 or rhodamine 800 as the dye was analyzed by flow cytometry and confocal microscopy after a 24-hour incubation. The flow cytometry assay detected fluorescence from a gated population of A431 cells labeled with R9-FITC, coumarin 6, or rhodamine 800 on channel FL1 or FL3, with a 488-nm solid-state laser excitation. Data were collected from at least 10,000 cells at a flow rate of 35 μl/min, using a logarithmic scale to estimate both background and cell fluorescence. Nanoparticle internalization in the cells was observed via confocal microscopy (Leica TCS SP8 X AOBS). Following the manufacturer's instruction, the cells were labeled with Hoechst and LysoTracker Green DND-26 (Thermo Fisher Scientific). The images were pseudocolored: blue for Hoechst, green for LysoTracker, FITC, or coumarin 6, and red for rhodamine 800.

2.9. 5-Ethynyl-2′-deoxyuridine (EdU) proliferation staining

The proliferative ability of A431 cells was assessed using EdU staining. Briefly, A431 cells (1×10^4 cells/well) were seeded into a 12-well plate and cultured for 24 h. The cells were then treated with tumor necrosis factor-α (TNF-α, 20 ng/ml), naked or nanoparticulate miRNA (1 μM), and Lipofectamine 2000 (Thermo Fisher Scientific) before being fixed with 4 % paraformaldehyde for 30 mins at room temperature. DMEM containing 20 μM EdU (Abcam) was added to each well, and the cells were incubated at 37 °C for two hours. EdU-positive cells were stained green with iFluor 488, and nuclei were counterstained with 4′,6-diamidino-2-phenylindole (DAPI) at 37 °C for 30 mins. The stained cells were analyzed using a flow cytometer (BD Accuri C6 Plus) and CellQuest software. Confocal microscopy was also used to observe the expression of EdU.

2.10. Cell migration assay

A total of 2×10^5 A431 cells were seeded in a 12-well plate and treated with naked miR-205–5p (1 μM), miRNA-loaded nanoparticles, or lipofectamine 2000 for 24 h. Following the incubation, the cells were detached using trypsin, counted, and centrifuged at 15,000 rpm for three minutes. The resulting cell pellet was resuspended in a medium to achieve a concentration of 8×10^5 cells/ml. The cell suspension was applied to each well of the Ibidi Culture-Insert 2 Well system placed in a 6-well plate. The culture insert was removed the next day. The cells were rinsed with a culture medium, and a fresh growth medium was added. Cell migration was photographed after 48 h. The percentage of the wound healing area was estimated and normalized to the control (0 h) to determine the relative migration rate.

2.11. Flow cytometry analysis of apoptosis and the cell cycle arrest

Apoptotic A431 cells were analyzed after incubation with naked or nanoparticulate miR-205–5p (1 μM) using an Annexin V-FITC/propidium iodide (PI) Apoptosis Detection Kit (BD Biosciences). Briefly, the cells were resuspended in 200 μl of binding buffer and dual-stained with 100 μl each of Annexin V-FITC and PI in the dark for 15 mins at room temperature. The apoptosis rate was evaluated by flow cytometry. For the cell cycle assay, the cells were fixed in 70 % ethanol after seeding and stained using the Apoptosis Detection Kit. The cell cycle analysis was performed using a flow cytometer. All experiments were conducted in triplicate.

2.12. Immunoblotting

A431 cells (1×10^5 cells/well) were seeded into 12-well plates and serum-starved for 24 h. The cells were then treated with TNF-α (20 ng/ml) in the presence or absence of naked miR-205–5p (1 μM) or miRNA-loaded nanoparticles. The cells were collected and centrifuged at 400 x*g* at 4 °C for 5 mins, and the protein amount was determined using Protein Assay Dye Reagent (Bio-Rad). The proteins were analyzed by SDS-PAGE and transferred onto a polyvinylidene difluoride membrane. The membrane was incubated overnight at 4 °C with antibody against TNFAIP8 (ab195810), E2F transcription 1 (E2F1, sc-251), transforming growth factor-α (TGF-α, sc-36), TNF receptor-associated factor 2 (TRAF2, sc-7346), caspase-3 (Cell signaling #9662), caspase-7 (Cell Signaling #12,827), caspase-8 (Cell Signaling #9764), poly(ADP-ribose) polymerase (PARP, Cell Signaling #5625), or glyceraldehyde-3-phosphate dehydrogenase (GAPDH, sc-47,724). A secondary anti-rabbit or anti-

mouse horseradish peroxidase antibody (1:2000, Abcam) was then added and incubated for one hour. The protein bands were visualized using an enhanced chemiluminescence reagent.

2.13. Immunocytochemistry

A431 cells were cultured on coverslips at a density of 1×10^5 cells/well and treated with TNF-α (20 ng/ml), naked or nanoparticulate miR-205–5p (1 μM), and Lipofectamine 2000 for 24 h. The cells were then fixed in 4 % paraformaldehyde for 30 mins. Following fixation, the cells were permeabilized with PBS containing 0.2 Triton X-100 for 15 mins at room temperature and subsequently blocked with 2 % bovine serum albumin for one hour. The coverslips were incubated overnight at 4 °C with a primary antibody against Ki67-Alexa Fluor 488 (1:500 dilution). After incubation, the coverslips were mounted onto a glass slide using Slowfade Gold Antifade Mountant with DAPI. The samples were monitored using confocal microscopy.

2.14. Animals

Male Balb/cAnN.Cg-Foxn1nu/CrlNarl nude mice (6-week-old) were purchased from the National Laboratory Animal Center Taiwan. The animals were maintained in a humidity- and temperature-controlled room (55 % at 25 °C). The animal experiments were approved and conducted per the recommendations outlined in the Guidelines for the Institutional Animal Care and Use Committee of Chang Gung University.

2.15. In vivo safety of the nanoparticles

Naked miR-205–5p agomiR, PLGA NPs, and DP-PNPs (50 μl in PBS) were subcutaneously injected into the backs of the mice ($n = 5$) once a week for two weeks. The concentration of miRNA was 1 μM. A control group received 50 μl of PBS only. The skin was evaluated for gross and microscopic appearances. Histological analysis was conducted using hematoxylin and eosin (H&E) staining. Organ samples were fixed in 10 % buffered formaldehyde for 24 h, embedded in paraffin, sectioned at a 5-μm thickness, and stained with H&E. Hepatic and renal functions were determined by collecting plasma from the tail vein. Levels of glutamic oxaloacetic transaminase (GOT), glutamic pyruvic transaminase (GPT), and blood urea nitrogen (BUN) were measured using ELISA kits (MyBiosource) according to the manufacturer's instructions.

2.16. Hemolysis assay

The hemolysis of erythrocytes was examined to assess the safety of the nanoparticles. Blood samples were obtained from healthy donors via venipuncture and collected into test tubes containing sodium citrate according to the protocol approved by the Institutional Review Board of Chang Gung Memorial Hospital. The erythrocytes were immediately separated via centrifugation at 2000 x*g* for five minutes and washed thrice with 4 vol of normal saline. The erythrocytes collected from 2 ml of blood were resuspended in normal saline (2 ml). Immediately thereafter, 0.25 ml of the nanocarriers were incubated with the erythrocyte suspension. Incubation was performed at 37 °C under magnetic stirring. After one hour, the samples were centrifuged for five minutes at 2000 x*g*. The absorbance of the supernatant was measured at 571 nm to detect the percentage of erythrocyte cells undergoing hemolysis. The hemolysis induced by double-distilled water was taken as 100 %.

2.17. In vivo anti-cSCC activity of the nanoparticles

An A431 cell xenograft animal model was established by subcutaneously injecting 1×10^3 spheroid cells into the backs of mice. The tumors were allowed to grow to about 50 mm^3 (day 14), as measured with an electronic caliper. The mice were then randomly divided into four groups: PBS (control), naked miRNA-205–5p mimic, PLGA NPs, and DP-PNPs. Each mouse received the intratumoral injection of 50 μl of the respective formulation once a week for two weeks. At the end of the experiments, the mice were euthanized. The tumors were collected and measured using an electronic caliper to estimate the tumor volume. The tumor was also weighed. For immunoblotting of TNFAIP8, the tumor extract was transferred to a nitrocellulose membrane and probed overnight at 4 °C with a primary antibody against TNFAIP8 or GAPDH. The membrane was then washed three times and incubated with an anti-mouse horseradish peroxidase antibody (Abcam) for one hour. Using a frozen section, the tumor was harvested and processed for Ki67 immunofluorescent staining.

In the pretreatment experiment, A431 cells (2×10^5 cells) were seeded into a 12-well plate and treated with different agomiR formulations for 24 h. Following this treatment, 1×10^5 cells were subcutaneously administered into the back of mice. Tumor growth was monitored and photographed on Day 21.

2.18. Statistical analysis

All data were analyzed using GraphPad Prism 6 software and are presented as the mean and standard error of the mean (SEM). Comparisons between two groups were performed using the unpaired student's *t*-test, while comparisons among multiple groups were conducted using ANOVA followed by Tukey posttest.

3. Results

3.1. Physicochemical characterization of the nanocarriers

The nanosystem was prepared using PLGA, DOTAP, DSPE-PEG, CPPs, and miR-205–5p through emulsification, nanoprecipitation, and conjugation. DLS measurements indicated that the mean diameter of the PLGA NPs (without CPPs) was 182 nm (Fig. 1B). Incorporation of R9 and p28 (DP-PNPs) increased the size to 193 nm (DP-PNPs). Both nanosystems exhibited a mono-modular size distribution with a narrow range. The surface charge of the PLGA NPs was −21 mV due to negatively charged PLGA (Fig. 1C). The conjugation of CPPs with the nanoparticles resulted in a shift of the zeta potential from negative to positive (5.7 mV), likely due to the cationic nature of R9. Successful development of the nanocarriers was confirmed by TEM, which revealed that the particles were spherical in shape and free from aggregation (Fig. 1D). The average diameters of PLGA NPs and DP-PNPs measured by TEM were 172 and 201 nm, respectively. The SEM imaging also demonstrated a spherical architecture and smooth surface of both the PLGA NPs and DP-PNPs, with average sizes of 169 and 197 nm, respectively (Fig. 1E). These diameters were consistent with the DLS measurements.

Agarose gel electrophoresis and NanoDrop analysis showed that most miR-205–5p molecules were encapsulated in the nanocarriers (Supplementary Figures 2A and 2B). The encapsulation efficiency of the miR-205–5p mimic was determined to be 71 % and 81 % based on agarose gel electrophoresis and NanoDrop analysis, respectively. The PLGA NPs and DP-PNPs were stored at room temperature (25–27 °C) for seven days to evaluate their stability. The size of both nanosystems increased slightly but insignificantly after seven days of storage (Supplementary Figure 2C). No significant change in zeta potential was observed during this period (Supplementary Figure 2D).

3.2. The CPP-conjugated nanoparticles are facilely ingested into the cells

The present study investigated the in vitro anti-cSCC effects of the nanocarriers using the established human squamous carcinoma cell line (A431). Initially, the cellular uptake ability of the polymeric nanoparticles was examined. Fluorescent labeling of CPPs is a commonly used technique to visualize cellular uptake. R9 was labeled with FITC and conjugated with the nanoparticles. The A431 cells were exposed to

PLGA NPs or DP-PNPs for 24 h to monitor cellular internalization using confocal microscopy. PLGA NPs without R9-FITC exhibited no green fluorescence (Fig. 1F). In contrast, cells treated with DP-PNPs showed green fluorescence, indicating preferential entry of CPPs into A431 cells. The merged image demonstrated an intense labeling of CPPs in the cytosol, with CPPs also partially localized to the nuclei and perinuclear regions. Fluorescence spectrometry revealed significant fluorescence from R9-FITC in cells treated with DP-PNPs (Fig. 1G). The fluorescence intensity data obtained from the spectrophotometric analysis clearly indicate the successful conjugation of both R9 (FITC-labeled) and P28 (AF647-labeled) peptides onto the PLGA nanoparticles. The relative fluorescence intensities reflect the respective contributions of the two peptides in the nanoparticle formulation, verifying their simultaneous attachment and presence. The relative fluorescence intensities indicate the ratio of the two peptides, with R9 being slightly more abundant than P28, at approximately 1.3:1. This ratio was determined based on the measured fluorescence intensities after correcting for potential quenching effects. (Fig. 1H). The confocal microscopy images depict the successful cellular uptake of PLGA nanoparticles conjugated with both R9 (FITC-labeled, green) and P28 (AF647-labeled, red) peptides in A431 cells. The fluorescence signals for both peptides are clearly observed, with significant colocalization evident in the merged images, demonstrating that both peptides were simultaneously delivered into the cells by the PLGA nanoparticles (Fig. 1I). To further investigate internalization, nanoparticles labeled with coumarin 6 as a fluorescent dye were incubated with the tumor cells for 24 h and analyzed using flow cytometry. The histogram showed a significant signal shift in fluorescence intensity following treatment with nanoparticles, with CPP-conjugated nanoparticles (R9-PNPs, p28-PNPs, and DP-PNPs) displaying a dramatic increase in signal (Fig. 2A). Flow cytometry data (Fig. 2B) indicated that the conjugation of R9 or p28 alone significantly enhanced cellular uptake. The combination of R9 and p28 resulted in a synergistic effect, with nanoparticle uptake in this group being five times higher than that of PLGA NPs.

Further examination of nanoparticle uptake by A431 cells was conducted using confocal microscopy. The nanoparticles were labeled with rhodamine 800, which emits red fluorescence. A faint red signal was observed in cells treated with free dye and PLGA NPs (Fig. 2C). In contrast, a significant decrease in red fluorescence was detected in cells treated with nanoparticles conjugated with a single CPP (R9-PNPs and p28-PNPs). This result indicates that CPP effectively facilitated the transport of the nanoparticles into the tumor cells. Additionally, dual CPP conjugation further enhanced nanoparticle entry into cSCC cells. The nanoparticles primarily accumulated in the cytosol and perinuclear regions of the cells. Overlay images of LysoTracker (green signal) and the nanoparticles (red signal) demonstrated colocalization within endo-lysosomal compartments.

The uptake of rhodamine 800-loaded nanoparticles was also analyzed by flow cytometry. Similar to the results observed with coumarin-labeled nanoparticles, dual CPP conjugation synergistically increased cellular uptake (Fig. 2D). The ingestion of nanoparticles was further evaluated in cSCC cells grown as spheroids. These spheroids, which are the 3D cell aggregates mimicking in vivo tumor structures, had a diameter of 120−140 μm (Fig. 2E). For PLGA NPs, confocal images showed minimal internalization into spheroids, with most green fluorescence present outside the aggregates, indicating poor penetration. Consistent with the findings from the 2D cell line, conjugation with R9 or p28 alone increased nanoparticle internalization in spheroidal cells. In contrast, the spheroids exposed to DP-PNPs demonstrated substantial penetration. Flow cytometry data further confirmed increased spheroid penetration by R9-PNPs and DP-PNPs (Fig. 2F), with dual CPPs enhancing nanoparticle penetration by five-fold. The lysosome escape behavior of R9 and p28 dual peptides conjugated PLGA nanohybrids. The green fluorescence (LysoTracker 488) marks lysosomes, and the red fluorescence (Rhodamine 800) represents the encapsulated nanohybrids. At early time points, the red and green signals are colocalized, indicating that the nanohybrids are initially confined within lysosomes after cellular uptake. Over time, partial separation of the red signal from the green signal is observed, which confirms the ability of the nanohybrids to escape from the lysosomes. This finding supports the potential intracellular functionality of the nanohybrids following endocytosis (Fig. 2G).

3.3. The CPP-conjugated nanoparticles inhibit cSCC cell proliferation and migration

The cytotoxicity of naked miRNA and miRNA-loaded nanoparticles against keratinocytes, which are normal epidermal cells, was assessed using the CCK-8 analysis. No significant cytotoxic effect was observed in keratinocytes at 24 h post-treatment with naked miR-205–5p at 1 μM and all tested nanoformulations (Fig. 3A). The CCK-8 assay was also employed to evaluate the antiproliferative activity of both naked and nanoparticle-encapsulated miRNA against cSCC cells. Lipofectamine 2000 was used with miR-205–5p mimic as a positive transfection control. Treatment of cSCC cells with TNF-α resulted in a time-dependent increase in cell growth (Fig. 3B). Naked miR-205–5p did not significantly inhibit A431 proliferation, likely due to issues with membrane transport. Lipofectamine 2000 improved the transfection efficiency of naked miRNA, thereby enhancing its ability to suppress proliferation. Nanocarriers containing CPPs significantly reduced the viability of TNF-α-stimulated cSCC cells after two days of incubation, with DP-PNPs demonstrating the greatest inhibitory effect. Cell growth was reduced by 70 % on Day 5 in cells transfected with DP-PNPs compared to the TNF-α control. The EdU assay was also employed to assess the antiproliferative activity of miR-205–5p in various formulations. EdU staining analyzed by flow cytometry yielded results consistent with CCK-8 (Fig. 3C). The quantification of fluorescence intensity from flow cytometry indicated that DP-PNPs exhibited stronger proliferation inhibition than nanoparticles with single CPP (Fig. 3D). DP-PNPs reduced cell proliferation by 41 %. Lipofectamine 2000 did not significantly inhibit A431 cell viability in the EdU assay. EdU immunocytochemistry further investigated cSCC cell proliferation. Confocal microscopic images showed abundant green fluorescence from EdU in control and TNF-α-treated cells (Fig. 3E). This green signal did not significantly decrease after treatment with naked agomiR, PLGA NPs, and Lipofectamine 2000. CPP-conjugated nanocarriers demonstrated lower EdU expression than PLGA NPs and commercial transfection kits. Treatment with R9-PNPs, p28-PNPs, and DP-PNPs reduced EdU fluorescence by 53 %, 54 %, and 73 %, respectively, compared to TNF-α treatment (Fig. 3F).

The motility of A431 cells was assessed using a wound healing assay following treatment with miR-205–5p mimic or its respective nanoparticles. A confluent monolayer of cSCC cells was scratched to create a wound and cultured for 24 h. At the 24-hour mark, near closure was observed in control and TNF-α-activated cells (Fig. 3G). Naked miRNA, PLGA NPs, and Lipofectamine 2000 did not significantly inhibit cell migration. In contrast, CPP-conjugated nanocarriers significantly reduced the invasion capacity of A431 cells. The DP-PNP-treated cells showed a greater reduction in invasion compared to nanocarriers with a single CPP. The migration assay revealed that R9-PNPs, p28-PNPs, and DP-PNPs inhibited wound closure by 37 %, 51 %, and 88 %, respectively, compared to the TNF-α treatment group (Fig. 3H). Suppl. Fig. 4 show the progression of wound closure at different time points, with the dashed lines indicating the initial wound margins. Cells treated with the blank vector exhibit a slower or altered wound closure rate compared to the control or treatment groups, suggesting that the blank vector influences cell invasion and migration. These findings confirm the vector's role in modulating cell behavior and provide additional evidence supporting its effects (Suppl. Fig. 4). Overall, DP-PNPs loaded with miR-205–5p mimic significantly suppressed the proliferative and invasive characteristics of cSCC cells.

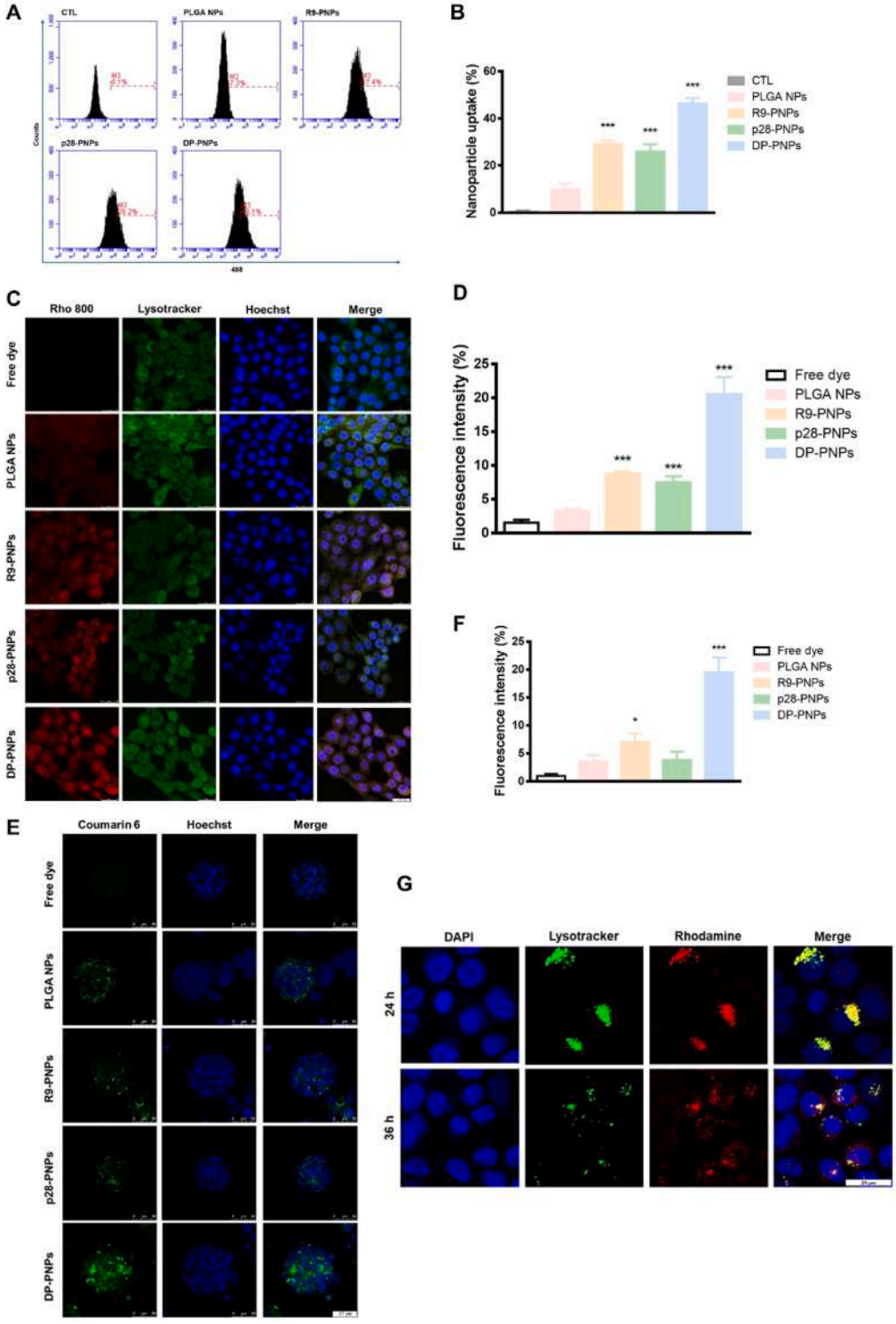


Fig. 2. In vitro targeting efficiency of peptide-conjugated nanohybrids: (A) Flow cytometry histogram representing the uptake of coumarin 6-labeled hybrid nanoparticles by human cutaneous squamous carcinoma (cSCC) cells over 24 h. (B) Percentage of human cSCC cells internalizing coumarin 6-labeled hybrid nanoparticles. (C) Fluorescence microscopy images overlaying Höechst-33,258 (blue), lysotracker (green), and rhodamine 800 (red) showing the uptake of rhodamine 800-labeled DP-PNPs in cSCC cells over 24 h, with free rhodamine 800 as a control. Scale bars, 25 μm. (D) Quantification of fluorescence intensity for rhodamine 800-labeled DP-PNPs. (E) Confocal fluorescence images of A431 spheroids showing different levels of NP internalization, with overlays of Höechst-33,258 (blue) and Coumarin 6 (green). Scale bars, 50 μm. (F) Quantification of fluorescence intensity for Coumarin 6-labeled DP-PNPs. (G) Confocal microscopy images showing lysosomal escape of nanohybrids encapsulating Rhodamine 800 (red) and labeled lysosomes with LysoTracker 488 (green). DAPI (blue) marks the nuclei. At 24 h time points, colocalization of Rhodamine 800 with LysoTracker 488 indicates the localization of nanohybrids within lysosomes. Over a period of 36 h, partial separation of Rhodamine 800 from LysoTracker 488 suggests lysosomal escape. Scale bar: 25 μm. Data are presented as mean±SEM ($n = 4$). *$P < 0.05$ and ***$P < 0.001$, compared to free dye.

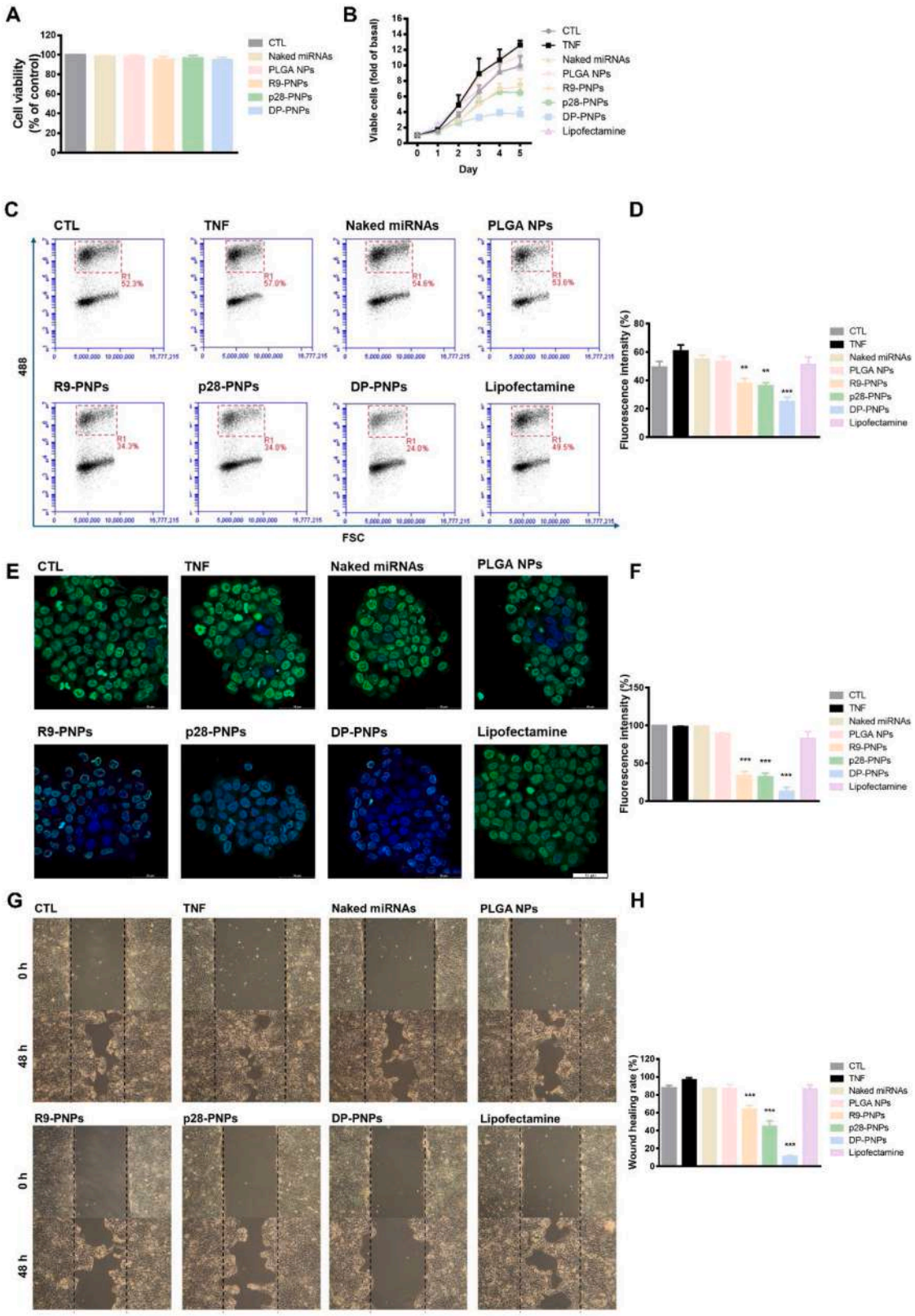


Fig. 3. Peptide-conjugated PNPs enhanced miR-205–5p delivery, inhibiting A431 cancer cell invasion and migration: (A) Cytotoxicity of human keratinocytes (HaCaT) after 24-hour treatment with different PNPs. (B) Growth curve of A431 cells treated with various PNPs over 5 days, measured by CCK-8 assay. (C, D) EdU staining assays comparing proliferation rates across different groups, with images acquired using an Accuri C6 Cytometer. Percentage of gated EdU-positive cells is highlighted. (E) Activities assessed by staining with Alexa Fluor 488-labeled 5-ethynyl-2′-deoxyuridine (EdU-488) and Hoechst 33,342 for DNA (blue), observed under a fluorescence microscope. (F) Quantitative analysis of EdU proliferation ratio using ImageJ. (G) Wound healing assays with representative images at 0 and 48 h. (H) Quantitative analysis of the relative wound healing rate (%). Scale bar = 50 μm. Data are expressed as mean±SEM ($n = 4$). $^{**}P < 0.01$ and $^{***}P < 0.001$, the TNF-α stimulation group.

3.4. The CPP-conjugated nanoparticles arrest the cSCC cell cycle and miR-205–5p-targeted proteins

The A431 cell transwell migration assay demonstrates the effects of the blank vector on cell migration. The bar graph quantifies the number of migrated cells under different conditions, showing a comparison between the control, blank vector, and treatment groups. The data suggest that the blank vector impacts cell migration, as reflected in the migration levels observed. These findings provide further insight into the influence of the vector on cell behavior, enhancing the overall understanding of its role (Fig. 4A). Ki67 protein is commonly used as a marker for active cell proliferation in tumors. A previous study [18] confirmed that miR-205–5p overexpression could downregulate Ki67. This study examined Ki67 expression in cSCC cells using flow cytometry. TNF-α stimulation resulted in Ki67 overexpression in A431 cells. Naked miR-205–5p caused a slight but insignificant reduction in Ki67 overexpression. In contrast, cells treated with CPP-conjugated nanocarriers exhibited a sharp decrease in Ki67 upregulation compared to those treated with naked miRNA (Fig. 4B). Cell cycle progression revealed that naked miRNA agomiR did not alter the cell cycle (Fig. 4C). However, treatment with CPP-conjugated nanosystems led to an accumulation of A431 cells in the G0/G1 phase and a corresponding reduction in the cell population in the G2/M phase. The increase in the G0/G1 population with DP-PNPs (30 %) was greater than that with R9-PNPs (19 %) and p28-PNPs (9 %) (Fig. 4D). These results indicate that CPP-conjugated nanocarriers inhibit cSCC cell growth by inducing cell cycle arrest in the G0/G1 phase.

TNFAIP8 is a potential target of miR-205–5p. TNF-α treatment elevated the protein expression of TNFAIP8 by 2.5-fold compared to the control, as demonstrated by immunoblotting (Fig. 4E). DP-PNPs significantly mitigated this overexpression, whereas other miRNA-loaded formulations did not. Additionally, the level of TNFAIP8-related proteins, including E2F1, TGF-α, and TRAF2, were examined. Consistent with the results for TNFAIP8, only DP-PNPs were effective in downregulating the overexpression of E2F1 and TGF-α in TNF-α-activated cSCC cells (Figs. 4F and 4G). The nanocarriers with dual peptides reduced E2F1 and TGF-α levels to baseline control levels. Densitometric quantification revealed a threefold increase in TRAF2 levels following TNF-α activation (Fig. 4H). Treatment with miR-205–5p in the form of CPP-conjugated nanoparticles and Lipofectamine 2000 reduced this upregulation, with DP-PNPs demonstrating greater suppression compared to the other formulations.

3.5. The CPP-conjugated nanoparticles promote cSCC cell apoptosis

Apoptosis was appraised to define the antitumor mechanisms and further validate the role of the nanoparticles in cSCC. Flow cytometry was performed using Annexin V/PI double-staining. The distribution of viable, early apoptotic, and late apoptotic cells among TNF-α stimulation, naked agomiR, and PLGA NPs was similar (Fig. 5A). In contrast, treatment with CPP-conjugated nanosystems and Lipofectamine 2000 significantly increased the early apoptosis rate. R9-PNPs showed an early apoptosis rate of 18 %, comparable to Lipofectamine 2000 at 21 % (Fig. 5B). p28-PNPs and DP-PNPs significantly increased early apoptosis to 28 % and 31 %, respectively. Further characterization of apoptosis was conducted using the TUNEL assay. Flow cytometry analysis using the Annexin V/PI treatment scheme revealed increased TUNEL-positive cells following treatment with p28-PNPs and DP-PNPs (Fig. 5C), indicating greater apoptotic cell death. The TUNEL-positive population increased by 2- and 2.5-fold after treatment with p28-PNPs and dual peptide-conjugated nanocarriers, respectively (Fig. 5D).

The expression of apoptotic signaling pathway markers, including caspase-3, caspase-7, caspase-8, and PARP, was analyzed by Western blotting. No significant difference in caspase expression was observed after the treatment with naked miR-205–5p and PLGA NPs compared to the TNF-α activation group (Figs. 5E to 5G). In contrast, the protein levels of caspases in cSCC cells treated with CPP-conjugated nanoparticle groups were significantly higher compared to the TNF-α group. Caspase-3 and −8 activities were notably higher in cells treated with DP-PNPs than those treated with single CPP nanocarriers. Lipofectamine 2000 activated the cleaved caspase-7 but did not affect caspase-3 and −8. The activation of PARP was observed in response to CPP-conjugated nanoparticle treatment (Fig. 5H). These data indicate strong activation of proapoptotic caspase, and PARP cascades by DP-PNPs.

3.6. The CPP-conjugated nanoparticles inhibit the growth of cSCC spheroids

The tumor microenvironment can significantly influence the response to anticancer drugs. To evaluate the antiproliferative effects of the nanocarriers in solid tumors, this study utilized a 3D spheroid model. Flow cytometry was employed to count the number of the spheroids, defining cell aggregates >60 μm as spheroids. PLGA NPs significantly reduced spheroid formation from 97 % to 81 % (Fig. 6A), an effect comparable to Lipofectamine 2000 (79 %). CPP incorporation further enhanced spheroid inhibition, with p28-PNPs showing stronger inhibition than R9-PNPs. The dual CPP combination did not provide additional enhancement beyond that achieved with p28-PNPs. Confocal microscopy confirmed the flow cytometry data, revealing that both naked and nanoencapsulated agomiR decreased the spheroid diameter compared to the control (Fig. 6B). Statistically significant reductions in spheroid size were observed only with naked miRNA, p28-PNPs, and DP-PNPs (Fig. 6C), with DP-PNPs demonstrating the most substantial reduction in spheroid size. This study also examined the effect of pretreating A431 cells with nanocarriers before spheroid formation. Pretreatment with CPP-conjugated nanocarriers weakened the ability of cSCC cells to form spheroids (Supplementary Figure 3), with almost no spheroid production observed following the pretreatment with dual peptides. The anti-proliferative effects of the nanoparticles in spheroids were further assessed using EdU and Ki67 assays. TNF-α stimulation increased the EdU signal in spheroids (Fig. 6D). The spheroids treated with CPP-conjugated nanoparticles and Lipofectamine 2000 exhibited lower EdU fluorescence intensity than those treated with TNF-α. R9-PNPs and p28-PNPs similarly reduced EdU levels in spheroids (Fig. 6E), while the combination of R9 and p28 further decreased EdU levels. Consistent with EdU results, the proportion of Ki67-positive cells in spheroids was significantly reduced following the treatment with CPP-conjugated nanocarriers (Figs. 6F and 6G), demonstrating that these nanosystems inhibited A431 cell proliferation in both the 2D and 3D cultures.

3.7. The CPP-conjugated nanocarriers induce negligible toxicity

The mice were given naked agomiR, PLGA NPs, and DP-PNPs via subcutaneous injection for two weeks to assess any potential adverse effects of the nanosystems. All animals survived throughout the experiment. Gross and microscopic observations of the skin surface showed no noticeable changes following administration of any of the miRNA formulations tested, compared to the PBS control (Fig. 7A and 7B). Histopathological analysis of H&E-stained sections from the organs, including heart, liver, spleen, lung, and kidney, revealed comparable structures between PBS control and miRNA formulations in the healthy mice (Figs. 7C to 7G). These findings suggest that the subcutaneously administered nanoparticles might have limited distribution to peripheral organs, with the majority residing in the skin. Biochemical tests of hepatic and renal function (GOT, GPT, and BUN) were within the normal range following treatment with miRNA and nanoparticle (Figs. 7H to 7J). Additionally, in vitro hemolysis tests using human erythrocytes demonstrated complete hemolysis with double-distilled water due to its hypotonic effect (Fig. 7K). However, treatment with free agomiR and nanoparticles did not induce hemolysis in human erythrocytes, indicating that the nanocarriers are safe and maintain isotonic conditions.

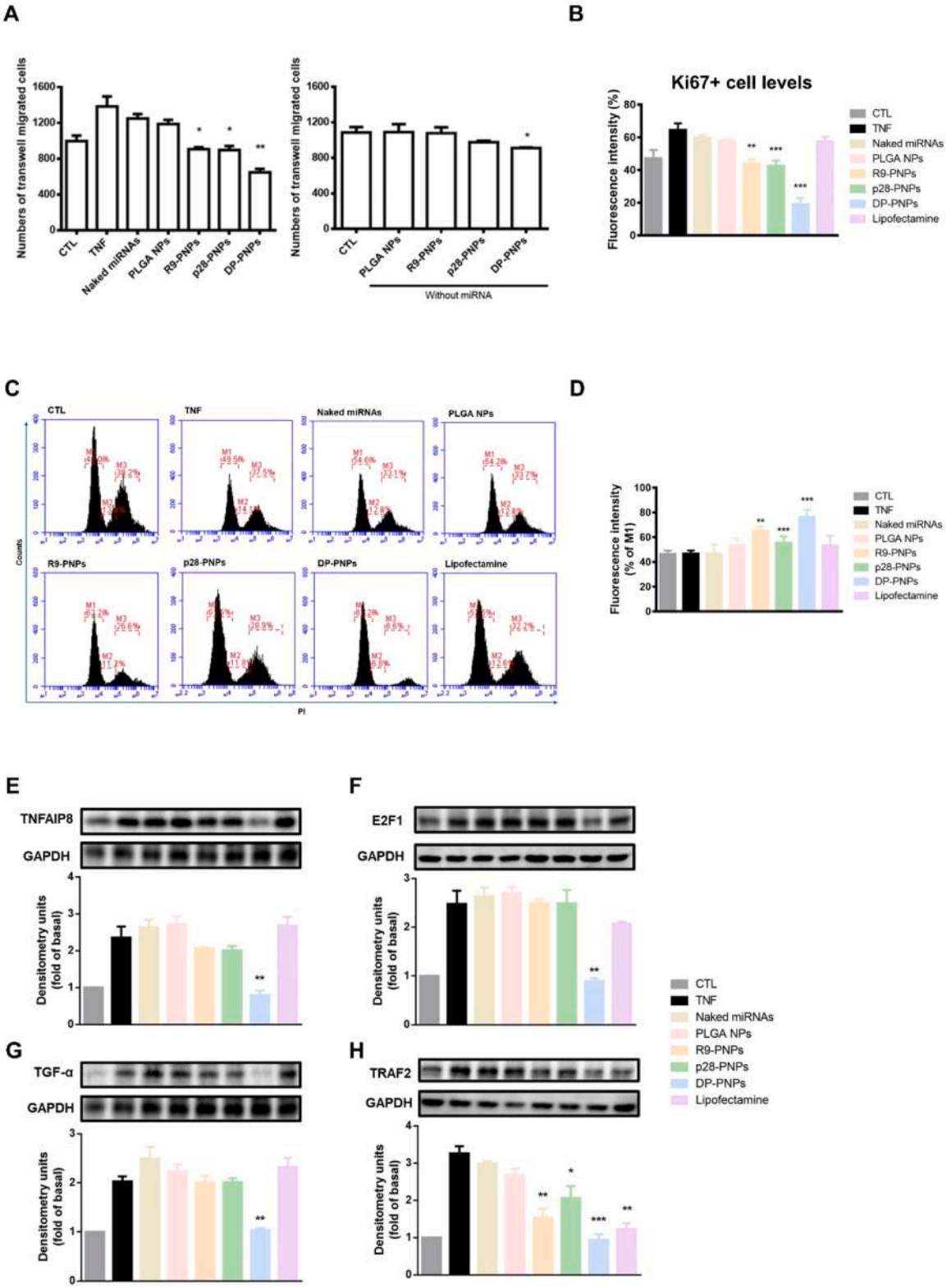
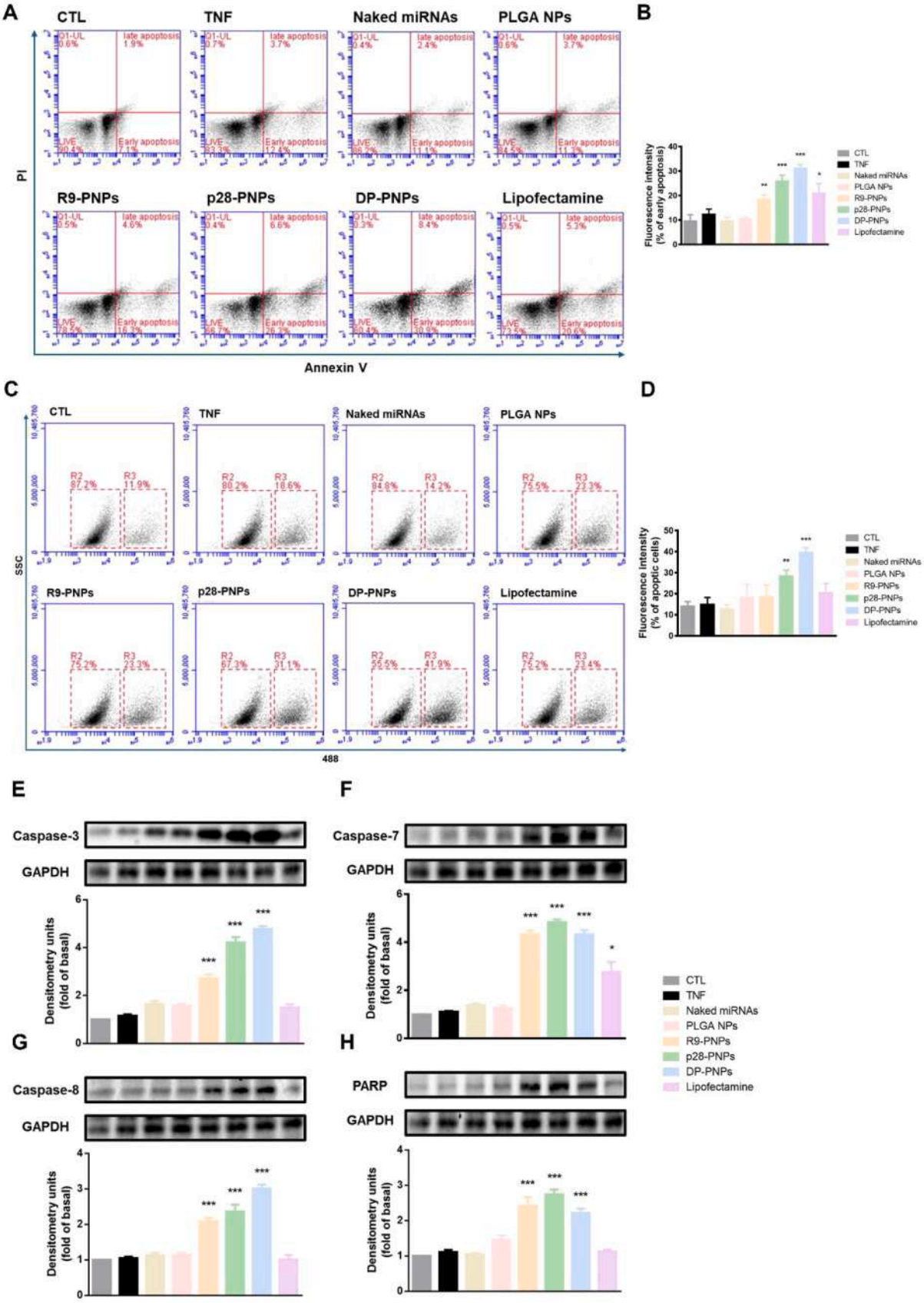


Fig. 4. miR-205–5p encapsulated peptide-conjugated PNPs induce cell cycle arrest by targeting multiple genes essential for cell proliferation: (A) Transwell migration assay of A431 cells under the influence of NPs. (B) Ki67+ cell levels were analyzed by flow cytometry, with histograms showing Ki67 staining in A431 cells compared to the control group. The percentage of Ki67-positive cells is indicated under marker M1. Detection was performed using BD Pharmingen™ Alexa Fluor® 488 Mouse anti-Ki-67 antibody. (C, D) Cell cycle analysis of A431 cells after treatment with different PNPs, harvested after 48 h. Cells were washed twice, then fixed in ice-cold 96 % ethanol before adding PI staining solution and RNAse A in PBS. Analysis was conducted using Accuri C6 flow cytometry. The percentages of cells in sub-G0, G0/G1, S, and G2/M phases were calculated with CellQuest software and are shown on the right side of the histograms. The effect of miR-205–5p on TNFAIP8 signaling was assessed by immunoblot assay on total cell lysates with the indicated antibodies: (E) TNFAIP8, (F) E2F1, (G) TGF-α, (H) TRAF2. Data are presented as mean±SEM ($n = 3$). $^{**}P < 0.01$ and $^{***}P < 0.001$, compared to the TNF-α stimulation group.



(caption on next page)

Fig. 5. Effects of miR-205–5p encapsulated peptide-conjugated PNPs on apoptosis in A431 cells: (A, B) Apoptosis profile assessed using the BD Pharmingen™ FITC Annexin V Apoptosis Detection Kit I, showing an increase in the proportion of total apoptotic cells in A431 cells treated with various PNPs compared to untreated controls. Flow cytometric analysis was conducted 72 h post-treatment. Each plot contains four quadrant markers indicating different cellular states: upper left (necrosis), upper right (late apoptotic/dead cells, positive for both Annexin V and 7-AAD), lower left (live cells), and lower right (early apoptotic cells, positive only for Annexin V). Representative results are shown. (C, D) Apoptotic cells detected using the TUNEL method and flow cytometric analysis, with A431 cells stained for apoptosis with FITC before and after 72 h of treatment. The histogram shows TUNEL-positive cells after PNP treatment within gate R3. Total cell lysates were subjected to immunoblotting with antibodies against (E) Caspase-3, (F) Caspase-7, (G) Caspase-8, and (H) PARP. Data are presented as mean±SEM ($n = 3$). $^{*}P < 0.05$, $^{**}P < 0.01$, and $^{***}P < 0.001$, compared to the TNF-α stimulation group.

The presented in vivo data Fig. 7L shows the biodistribution of dual-peptides PLGA nanoparticles encapsulated with the DiR dye in mice. Using Near-infrared (NIR) fluorescence imaging, the nanoparticles exhibit a strong fluorescence signal predominantly localized in the skin region over time, indicating effective retention and minimal off-target distribution. This confirms the nanoparticles' successful accumulation and localization in the target tissue, supporting their potential for targeted delivery applications (Fig. 7L).

3.8. The CPP-conjugated nanocarriers exert anti-cSCC activity in vivo

To evaluate the anticancer efficacy of miR-205–5p mimic in both free and nanoparticulate forms in vivo, an A431 spheroid xenograft model was established in nude mice. The mice were injected with A431 spheroids on Day 0, and after 14 days of cancer development, PBS or miRNA formulations were intratumorally administered into the tumor. The efficacy of miR-205–5p combined with DP-PNPs was compared to PBS control, free agomiR, and PLGA NPs without CPPs. Visual analysis revealed significant growth of solid tumors from Day 14 to 21 in the PBS control group (Fig. 8A). Tumors in the naked miRNA and PLGA NPs also grew aggressively. By Day 21, tumors in the dual CPP-conjugated nanoparticles group were notably smaller than other treatments. At the end of the experiment, the mice were sacrificed, and xenograft tumors were collected and weighed. The tumors treated with DP-PNPs showed significantly restrained growth relative to naked agomiR and PLGA NPs (Fig. 8B). DP-PNPs reduced tumor weight by 21 % compared to the control on day 21 (Fig. 8C). No significant reduction in tumor weight was observed in the naked agomiR and PLGA NPs compared to the control. Tumor volume reductions followed the same trend as the tumor weight (Fig. 8D), with DP-PNPs reducing volume by 30 % compared to the control.

Ki67, a marker of tumor progression, was assessed by immunofluorescence staining. All treatment groups were positive for Ki67 in the tumor (Fig. 8E). However, fewer Ki67-positive cells were observed in the DP-PNPs group than in others. Fluorescence quantification showed a significant decrease in Ki67 expression in the DP-PNPs group compared to the control (Fig. 8F). Immunoblotting for TNFAIP8 expression indicated that free miR-205–5p mimic did not suppress TNFAIP8 expression compared to the control (Fig. 8G). PLGA NPs showed some inhibition of TNFAIP8, but it was not statistically significant. DP-PNPs exhibited superior suppression of TNFAIP8, reducing its expression by five-fold compared to the PBS control. In vivo data Fig. 8H demonstrates the biodistribution of dual-peptides PLGA nanoparticles encapsulated with DiR dye in an A431 spheroid xenograft model. Near-infrared (NIR) fluorescence imaging shows a strong and localized fluorescence signal in the tumor region, confirming significant nanoparticle accumulation in the tumor site. This result validates the nanoparticles' targeted delivery and retention in tumor tissues, highlighting their potential efficacy in tumor-specific drug delivery applications (Fig. 8H).

A pretreatment study was also conducted where A431 cells were pretreated with naked agomiR or miRNA-loaded nanocarriers for 24 h before subcutaneous injection into mice. After 21 days, tumors in the PBS, naked agomiR, and PLGA NPs groups grew significantly larger (Supplementary Figure 5), while DP-PNPs pretreatment prevented this increase. These results confirm that dual CPP-conjugated nanoparticles significantly inhibit cSCC tumorigenicity in vivo.

4. Discussion

Due to its high incidence and malignant progression, cSCC has become a significant global health concern. cSCC originates from actinic keratosis and progresses to carcinoma in situ, an invasive form, and eventually to a metastatic form. Recently, gene therapy has provided new insights into treating malignant tumors. Among these therapeutic approaches, miRNAs have shown potential as tumor suppressors by inhibiting growth and metastasis. However, miRNAs are typically large and hydrophilic, complicating their penetration through cell membranes. CPPs are membrane transduction peptides with a notable ability to cross cell membranes, a feature that is particularly advantageous for delivering nucleic acids. Nanoparticles are beneficial for loading miRNAs and CPPs, thereby preventing biodegradation and facilitating efficient antitumor activity. This study aims to develop CPP-conjugated miRNA nanoparticles to reduce the malignancy of cSCC. The dual conjugation of R9 and p28 significantly enhances the nanoparticle ingestion into the cSCC cells. Enhanced delivery of miR-205–5p into the cells via CPP-conjugated nanoparticles significantly inhibited cell proliferation, migration, and invasion while promoting apoptosis in vitro. The in vivo result demonstrated that intratumoral DP-PNPs efficiently and safely delivered miR-205–5p agomiR into the cSCC tumor, showing significant anticancer activity.

PLGA was employed as the primary material in the polymeric nanocarriers. PLGA is widely used as a carrier for delivering various biomacromolecules, including proteins, siRNAs, miRNAs, and vaccines [21]. It has been approved by the USFDA and the European Medicines Agency for drug delivery applications due to its biocompatibility and low toxicity. Previous studies [22] reported that PLGA nanoparticles are rapidly internalized by cSCC cell lines compared to melanoma cells and fibroblasts, indicating a selective feature. Thus, PLGA represents an ideal polymer for anti-cSCC nanocarriers. CPPs were conjugated with DSPE-PEG for incorporation into PLGA nanoparticles. These nanocarriers exhibited CPPs on their surfaces, facilitating membrane penetration. The incorporation of PEG protects CPPs from biodegradation and extends their biological half-life [23]. It is reasonable to expect that the conjugation of CPPs with PEG on the nanoparticle surface slightly increased the particle size. The resulting nanoparticles with CPPs had an average diameter of approximately 190 nm, which is suitable for cellular internalization. R9 and p28 are classified as cationic and anionic CPPs, respectively [11,12]. The inclusion of both CPPs altered the negative surface charge of the nanoparticles to 5.7 mV, which may be attributed to the higher concentration of R9 (43.9 μM) compared to p28 (21.5 μM) in the nanoparticles. The positive surface charge of the nanocarriers enhances their interaction with negatively charged cell membranes.

The findings of this study revealed that CPPs facilitate the entry of the nanoparticles into cSCC cells. In addition to the cationic nature of the nanoparticles, R9 and p28 contribute to nanoparticle uptake through various mechanisms. The uptake of the nanoparticles associated with R9 may involve endocytosis and/or direct membrane translocation [24]. Endocytosis is a process by which macromolecules or nanoparticles are transported into cells via vesicles and vacuoles formed from the plasma membrane, whereas direct translocation involves mechanisms such as pore formation, inverted micelle creation, and membrane thinning without requiring energy [25]. A previous study [26] showed that R9 at nM to low μM range primarily enters the cells via endocytosis. In contrast, R9 at concentrations of >10 μM induced a non-endocytic

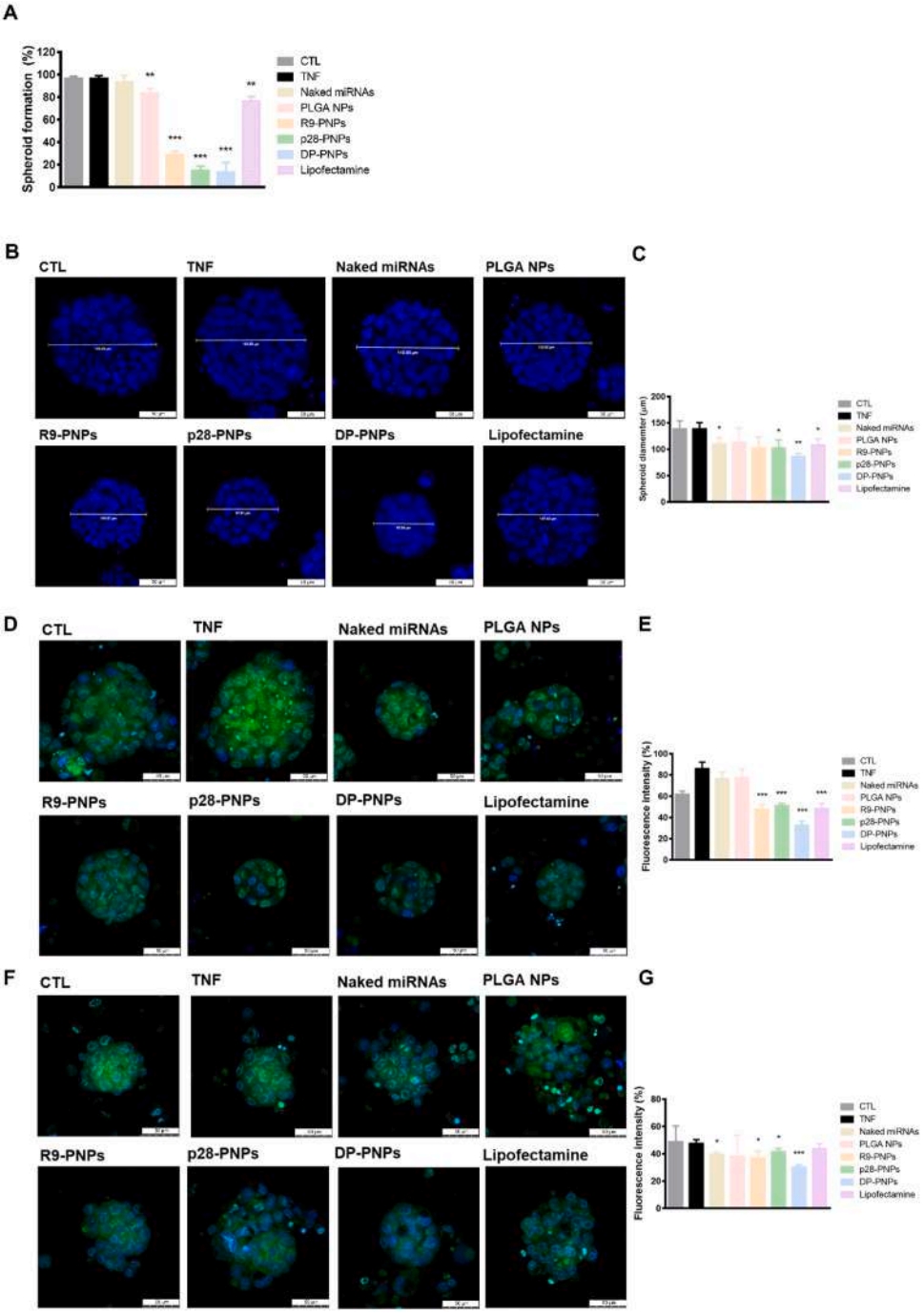
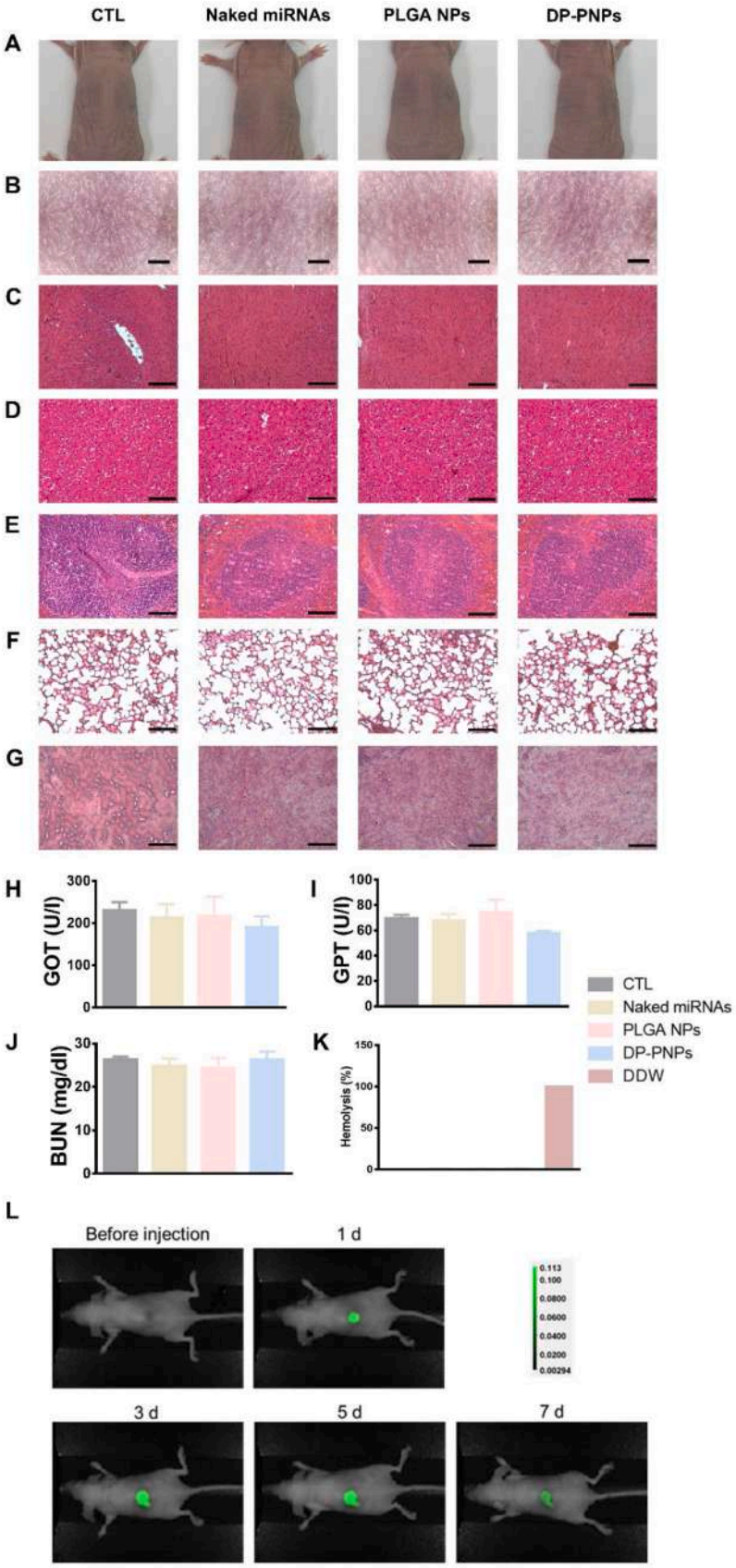


Fig. 6. Effects of miR-205–5p encapsulated peptide-conjugated PNPs on A431 3D spheroid cell proliferation and formation: (A) Spheroid formation by a subpopulation of A431 cells, with 1 × 10^4 cells/well plated under spheroid growth conditions. The number of spheroids was monitored on days 1 and 12, showing a statistically significant increase on day 12 compared to day 1. Data are presented as mean±SEM ($n = 3$). $^{**}P < 0.01$ and $^{***}P < 0.001$, compared to the TNF-α stimulation group. (B, C) Spheroid growth diameter on day 12, with nuclei stained by Hoechst 33,342 (blue). Spheroid diameter was quantitatively analyzed using Leica Application Suite X software. Scale bar = 50 μm (D, E) EdU staining assays comparing proliferation rates among different groups. Cells were stained with Alexa Fluor 488-labeled 5-ethynyl-2′-deoxyuridine (EdU-488) and Hoechst 33,342 (blue), observed under a fluorescence microscope. Scale bar = 50 μm. Quantitative analysis of the EdU proliferation ratio was performed using ImageJ. (F, G) Detection of Ki67+ cell levels using BD Pharminge Alexa Fluor 488 Mouse anti-Ki-67 antibody. Confocal fluorescence images of A431 spheroids showed varying levels of Ki67-positive cells, with overlays of Höechst-33,258 (blue) and Alexa Fluor® 488 (green). Scale bars=50 μm. Quantification of Alexa Fluor® 488 fluorescence intensity. Data are expressed as mean±SEM ($n = 3$). $^{*}P < 0.05$, $^{**}P < 0.01$, and $^{***}P < 0.001$, compared to the TNF-α stimulation group.

pathway involving transient plasma membrane deformation. This membrane disruption is associated with increased intracellular Ca^{2+} due to the R9. The R9 concentration in the nanocarriers was 43.9 μM, suggesting that cellular uptake of CPP-conjugated nanoparticles may involve direct translocation mechanisms. Conversely, the p28-assisted membrane transport does not include membrane disruption [27]. The primary mechanism for p28-mediated membrane permeation is receptor-mediated endocytosis. p28 is a tumor-homing peptide that preferentially enters cancer cells. The membrane receptors that mediate p28 ingestion are typically expressed at higher levels in tumor cells than



(caption on next page)

Fig. 7. Physiological and histological observations for mice receiving different administrations of naked miRNAs, PLGA NPs, and DP-PNPs. Mice ($n = 5$) were intradermally injected in the back once a week for 2 weeks (total of 2 treatments) with 50 μl of naked miRNAs or different PNPs in PBS. Tissue samples from the heart, liver, spleen, lung, kidney, skin, and blood were collected on Day 14: (A) Gross images of mouse back skin on Day 14 captured with a digital camera. (B) Close-up images taken with a hand-held digital microscope. Scale bars=1 mm.Histological images of (C) heart, (D) liver, (E) spleen, (F) lung, and (G) kidney. Scale bars=100 μm. Blood biochemical parameters of (H) GOT, (I) GPT, and (J) BUN. (K) Hemolysis assay on human erythrocytes incubated with different PNPs, with DDW as a positive control. (L) Near-infrared (NIR) fluorescence imaging of DiR-labeled dual-peptides PLGA nanoparticles after direct injection into mice. Fluorescence signals were captured at various time points post-injection using the Pearl Trilogy Imaging System. The images show strong fluorescence intensity in the skin region, confirming the nanoparticles' predominant localization and retention in the skin. The color scale represents the fluorescence intensity. Data are expressed as mean±SEM ($n = 5$).

in normal cells [16]. The amount of p28 in tumor cells is 3–6 times higher than in normal cells [28].

After cellular uptake, the nanoparticles are typically transported to endosomes and lysosomes, which are disassembled to release their cargo molecules into the cytosol [29]. Following internalization, confocal imaging revealed the colocalization of the CPP-conjugated nanocarriers in endosomes/lysosomes. For effective intracellular delivery, it is crucial that CPP-cargo nanocomplexes escape from endocytic organelles and reach the cytoplasm [24]. This step can be a limiting factor in the cellular uptake of CPPs. The valency of R9 increases with a decrease in pH, resulting in greater protonation of R9 in the endosomes (approximately pH 5.5) after ingestion [15]. Due to the specific sequences and conformational properties of p28, this peptide can facilitate its release from endosomes [30]. Consequently, miRNA escape occurs due to endosomal/lysosomal membrane destabilization and leakage. Given the successful pharmacological activity of miR-205–5p-loaded nanoparticles in vitro, effective endosome/lysosome escape is anticipated. A challenge in cancer treatment is the ability of drugs to penetrate the tumor microenvironment and reach the innermost tissues. A 3D spheroid cell culture was established in vitro to mimic the tumor structure for preclinical assay. The PLGA NPs without CPPs were confined to the spheroidal surface, whereas the DP-PNPs were internalized into the spheroids with deep penetration. cSCC exhibits the highest mutational burden among all solid tumors [2]. These mutations drive the proliferation and survival of the cSCC cells, leading to high invasion rates. Ki67 is a biomarker for cell proliferation largely aberrant in cSCC [31]. The mutation of cSCC cells can result in elevated epidermal growth factor receptor (EGFR), with increased EGFR expression correlating directly with elevated Ki67 [32]. The findings showed that naked miR-205–5p mimic did not inhibit Ki67 overexpression in A431 cells, possibly due to difficulties with miRNA penetration across the cellular membrane. In contrast, including miRNA in CPP-conjugated nanocarriers significantly inhibited Ki67 expression. miR-205–5p has been reported as both a positive and negative regulator of proliferation, depending on cell types and conditions [17]. This study confirmed that miR-205–5p acts as a tumor suppressor in cSCC cells. The conjugation of CPPs effectively enhanced the cellular uptake and the subsequent proliferation inhibition of miR-205–5p. While CPPs can sometimes create steric hindrance on the nanoparticle surface that impedes gene delivery [33], this was not observed in our study, as CPPs facilitated agomiR penetration. Elevated Ki67 expression in cSCC patients is often linked to poor clinical outcomes, and the nanosystem in this study may help address this issue.

Ki67 expression in cancers is positively correlated with the expression of TNFAIP8 [34]. TNFAIP8 is an oncogenic protein that regulates tumor growth, survival, invasion, and metastasis. This oncogene targets miR-205–5p in skin, thyroid, breast, and gastric cancers [20,35]. The differential expression gene analysis represents the importance of the TNF signaling pathway in cSCC development [36]. TNF-α binds to TNF receptors type 1 and 2, activating nuclear factor κB (NF-κB) signaling and leading to TNFAIP8 overexpression [19]. The findings of this study showed that TNF-α induces TNFAIP8 upregulation, which enhances cell proliferation. DP-PNPs effectively reduced TNFAIP8 in TNF-α-stimulated cells to baseline control, suggesting that the delivery system efficiently transferred agomiR to cells to modulate target gene expression. Designing effective TNFAIP8 inhibitors could be beneficial in controlling the development of cancers. Another target for miR-205–5p is TGF-α [37]. Cells responding to TNF-α can release TGF-α [38], and high levels of EGFR and its ligand TGF-α are prosurvival factors in many cancers, including cSCC [39].

It has been reported that miR-205–5p targets the 3′-UTR of the transcription factor E2F1 to inhibit the proliferation of melanoma and non-small-cell lung carcinoma cells [40]. E2F1 in keratinocytes plays a role in squamous differentiation, which is crucial for developing cSCC [41]. Therefore, E2F1 represents a viable therapeutic target for cSCC. Similar to the effects observed with TNFAIP8 and TGF-α, DP-PNPs downregulated E2F1 protein levels in A431 cells to baseline control. This effect was not observed with naked miRNA and nanoparticles containing a single peptide, highlighting the importance of dual CPPs for effective proliferation inhibition. Elevated E2F1 levels in cancers are inversely correlated with patient survival [42]. The nanosystem in this study demonstrates potential therapeutic efficacy for cSCC by blocking E2F1 expression. The inhibition of E2F1 can induce cell growth arrest at the G1 checkpoint [41]. Moreover, the ability of DP-PNPs to arrest the G0/G1 stage was confirmed, likely due to E2F1 inhibition. The nanocarriers also inhibited TRAF2 overexpression in TNF-α-stimulated cells. TRAF2 is a key regulator of NF-κB, which can be regulated by miR-205–5p [43]. This study proposes that miR-205–5p-loaded CPP-conjugated nanoparticles inhibit the TNF-α signaling pathway and its downstream molecules by targeting several genes, leading to protein downregulation and proliferation suppression.

Apoptosis is a form of programmable cell death mediated by caspases. TNFAIP8 inhibition is effective in activating the proapoptosis caspase-8 [34,44]. Caspase-8 activates caspase-3 through proteolytic cleavage, which cleaves other caspases. This effect activates PARP, eventually leading to apoptosis [45]. Immunoblotting assays revealed the activation of caspases and PARP in cSCC cells treated with dual CPP-conjugated nanocarriers. Apoptosis induction represents a vital goal in cancer therapy, as apoptosis is generally preferred over necrosis due to the absence of inflammation and minimal damage to adjacent healthy tissues. Beyond the apoptotic effect from miR-205–5p, p28 in the nanocarriers also enhances apoptosis in cSCC cells. p28 induces apoptosis in various cancer cells in a caspase-mediated manner [16,30]. This anticancer CPP preferentially targets cancer cells by interacting with p53, with minimal effect on non-cancerous cells [46]. The findings of this study showed increased apoptosis in A431 cells treated with p28-PNPs than R9-PNPs, suggesting that p28 is more effective in inducing apoptosis.

Surgery remains the primary treatment for low-risk cSCC management. However, high-risk cases, particularly those involving metastasis, resent significant treatment challenges. Adjuvant therapy is crucial alongside surgical resection for these high-risk cases. cSCC is considered more dangerous than BCC and other non-melanoma skin cancers due to its tendency to invade the dermis and its recurrence after resection [47]. The prognosis for metastatic cSCC is poor [1], with a five-year survival rate estimated to be <30 % [2]. miR-205–5p has been shown to suppress the migration of breast cancer cells [48]. This study observed similar effects, demonstrating that miR-205–5p-loaded DP-PNPs reduced A431 invasiveness as indicated by the wound healing assay. The high expression levels of Ki67 and TNFAIP8 are associated with cancer metastasis and recurrence [20,49]. The cell migration inhibition by DP-PNPs may be attributed to the downregulation of Ki67 and TNFAIP8.

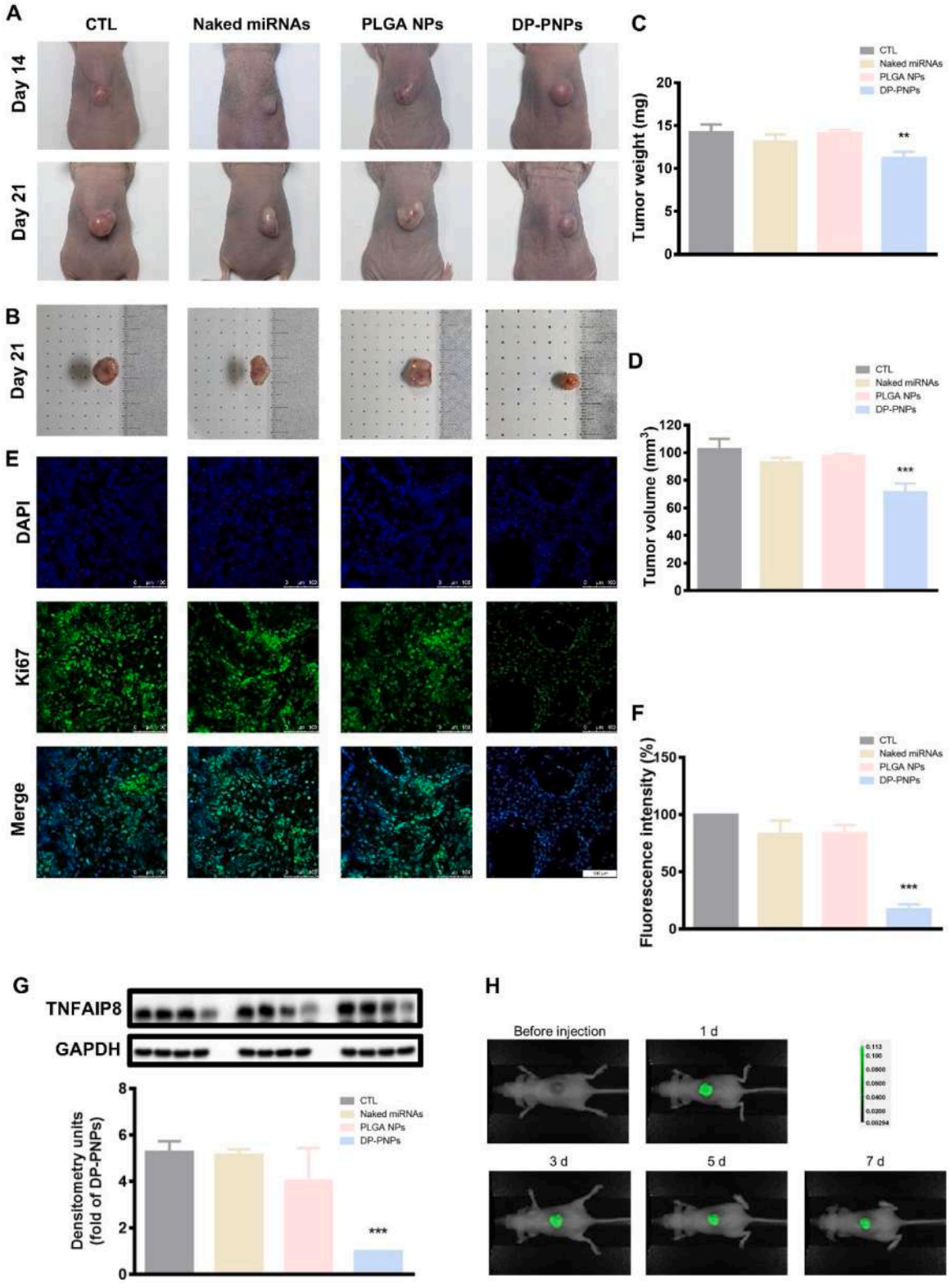


Fig. 8. Effect of miR-205–5p on tumor outgrowth in an A431 cell-induced mouse model: (A) Whole body imaging of A431 xenograft mice following direct injection into the tumor with naked miRNAs, PNPs, or DP-PNPs. (B) Ex vivo imaging of the tumor on day 21. (C) Tumor weight. (D) Tumor volume. (E, F) Immunohistochemical staining of Ki-67 using BD Pharmingen™ Alexa Fluor® 488 Mouse anti-Ki-67 antibody. Confocal fluorescence images of tumor tissue with overlays of DAPI (blue) and Alexa Fluor® 488 (green). Scale bars = 100 μm. Quantification of Alexa Fluor® 488 fluorescence intensity. (G) Western blot analysis of tumor protein extracts to detect changes in TNFAIP8 expression, with GAPDH as a loading control. Relative intensities of TNFAIP8 were determined by densitometry. (H) Near-infrared (NIR) fluorescence imaging of A431 xenograft model mice following the injection of DiR-labeled dual-peptides PLGA nanoparticles. Fluorescence signals were observed at various time points post-injection using the Pearl Trilogy Imaging System. The images show predominant accumulation of the nanoparticles in the tumor region, with minimal signal detected in non-tumor areas, demonstrating effective tumor targeting. The color bar indicates fluorescence intensity. Data are expressed as mean ± SEM ($n = 5$). $^{**}P < 0.01$ and $^{***}P < 0.001$, compared to the control.

Traditional cancer drug testing often relies on 2D cell culture models. However, these models may not accurately reflect drug responses in a clinical setting. The 3D multicellular spheroid model is more advanced for assessing drug efficacy and cSCC cell invasiveness [50,51]. The tumor tissue penetration of free miRNA is typically low, reducing delivery to deeper regions within solid tumors. CPP-conjugated nanocarriers, however, can deliver miRNA effectively into the deeper areas of the spheroid. Consistent with the results from the 2D cultures, CPP-conjugated nanocarriers significantly inhibited cell proliferation in spheroids, leading to a notable reduction in spheroid size. p28, a tumor-targeting peptide, facilitates the targeted delivery of nanoparticles into tumor microenvironment [12].

For the in vivo evaluation of anti-cSCC activity, this study employed intralesional injection as the treatment route to deliver the miR-205–5p mimic. Intralesional therapy, which includes agents such as 5-fluorouracil, methotrexate (Methotrexate), and interferon-α, is utilized for cSCC patients who are not suitable for surgical excision [52]. Intravenous CPPs distribute widely, resulting in low local concentrations and off-target effects [11]. Additionally, CPPs are rapidly cleared from the bloodstream and tissues by peptidases [53] and can be largely degraded by various proteases in the skin [30]. Intralesional delivery offers the advantage of minimizing CPP biodegradation in normal tissues. The findings of this study demonstrated a significant inhibition of cSCC tumor growth following intratumoral DP-PNPs. Tumor progression, as measured by Ki67, was significantly reduced by DP-PNPs. miR-205–5p within this nanosystem significantly decreased the expression of the target protein TNFAIP8. The strong anti-cSCC activity of DP-PNPs is attributed to the effective delivery of miRNA facilitated by the dual CPPs. Given that the peptides are prone to instability, especially in the human body, it is crucial to stabilize them against biodegradation. As highlighted in this study, polymeric nanoparticles effectively protect CPPs. A challenge with cationic CPPs such as R9 is their premature clearance by immune cells. Using neutral or anionic may offer more favorable outcomes. A dual-peptide combination in the nanoparticles is hypothesized to enhance cellular miRNA delivery and prolong its residence in the tumor. An effective tumor-specific delivery system must achieve substantial accumulation in the tumor, successful intracellular uptake upon arrival, and subsequent pharmacological activity within the cells [54]. The dual-CPP-conjugated nanocarriers in this study successfully meet these criteria.

Despite the promising features of nanoparticle delivery systems, toxicity remains a significant concern. Side effects can arise when the nanocarriers impact normal cells. In this study, the effects of the nanoparticles were assessed in normal human keratinocytes. The nanocarriers did not exhibit significant alterations in cell viability. The CPP-conjugated nanoformulations preferentially inhibited cSCC cell growth compared to normal cells, suggesting a selective targeting effect. This selectivity may be attributed to the tumor-specific properties of R9 and p28. R9 has been reported to be non-toxic to non-malignant cells, including epithelial cells, peripheral blood mononuclear cells, and neural crest stem cells [53]. Due to its higher affinity for caveolin receptors in cancer cells, p28 preferentially enters neoplastic cells with reduced toxicities than normal cells [27,28]. Phase I clinical trials of p28 have reported no apparent toxicity and side effects in advanced-stage cancer patients [55].

However, this study has several limitations. Using CPPs such as p28, derived from bacterial sources, may pose potential immunogenicity to neutralize the therapeutic efficacy of the cargo. Immunotoxicity of the nanoparticles was not evaluated in this study; further investigation is needed to address this issue. The xeno-transplantation model in nude mice, while extensively used in preclinical cancer research, may not fully replicate the complexity of human tumors. Consequently, findings from animal studies may not always translate to human applications. Additional evidence from both animal and clinical studies is needed to confirm the applicability of the nanocarriers in this study.

5. Conclusions

This study developed a miRNA delivery system using PLGA nanoparticles conjugated with dual CPPs, R9, and p28, to target cSCC. The nanosystem demonstrated enhanced cellular penetration and tumor targeting due to the CPPs. The prepared nanocarriers reduced proliferation and induced apoptosis in cSCC cells in both 2D and 3D cell cultures. Additionally, the nanosystem inhibited cell migration and invasion, suggesting a potential to impede metastasis. The results indicate that the miR-205–5p-loaded CPP-conjugated nanoparticles act as tumor suppressors in cSCC by inducing tumor shrinkage. These nanoparticles hold promise as a therapeutic candidate for cSCC.

Funding

This work was supported by National Science and Technology Council, Taiwan (MOST-113–2320-B-182–024-MY3 and NSTC 112-2320-B-255-001), Chang Gung Memorial Hospital (CORPD1N0082, COPRD1N0092 and CMRPD1M0542), and Chang Gung University of Science and Technology (ZRRPF6N0011).

Data availability

Data are available on request from the authors.

CRediT authorship contribution statement

Cheng-Yu Lin: Methodology, Investigation, Conceptualization. **Jia-You Fang:** Writing – original draft, Software, Funding acquisition. **Chien-Yu Hsiao:** Methodology, Investigation. **Chiang-Wen Lee:** Writing – review & editing, Resources. **Abdullah Alshetaili:** Writing – review & editing, Methodology. **Zih-Chan Lin:** Supervision, Project administration, Funding acquisition, Conceptualization.

Declaration of competing interest

The authors declare that they have no known competing financial interests or personal relationships that could have appeared to influence the work reported in this paper.

Supplementary materials

Supplementary material associated with this article can be found, in the online version, at doi:10.1016/j.actbio.2025.02.056.

References

[1] A. Wysong, Squamous-cell carcinoma of the skin, N. Engl. J. Med. 388 (2023) 2262–2273.
[2] M.C.G. Winge, L.N. Kellman, K. Guo, J.Y. Tang, S.M. Swetter, S.Z. Aasi, K.Y. Sarin, A.L.S. Chang, P.A. Khavari, Advances in cutaneous squamous cell carcinoma, Nat. Rev. Cancer 23 (2023) 430–449.
[3] J. Caudill, J.E. Thomas, C.G. Burkhart, The risk of metastases from squamous cell carcinoma of the skin, Int. J. Dermatol. 62 (2023) 483–486.
[4] M.S. Chang, M. Azin, S. Demehri, Cutaneous squamous cell carcinoma: the frontier of cancer immunoprevention, Annu. Rev. Pathol. Mech. Dis. 17 (2022) 101–119.
[5] R. Jiang, M. Fritz, S.K.T. Que, Cutaneous squamous cell carcinoma: an updated review, Cancers (Basel) 16 (2024) 1800.
[6] R.L. Siegel, K.D. Miller, H.E. Fuchs, A. Jemal, Cancer statistics, 2021, CA Cancer J. Clin. 71 (2021) 7–33.
[7] R. Corchado-Cobos, N. García-Sancha, R. González-Sarmiento, J. Pérez-Losada, J. Cañueto, Cutaneous squamous cell carcinoma: from biology to therapy, Int. J. Mol. Sci. 21 (2020) 2956.
[8] K. Nemeth, R. Bayraktar, M. Ferracin, G.A. Calin, Non-coding RNAs in diseases: from mechanisms to therapeutics, Nat. Rev. Genet. 25 (2024) 211–232.
[9] N. García-Sancha, R. Corchado-Cobos, J. Pérez-Losada, J. Cañueto, MicroRNA dysregulation in cutaneous squamous cell carcinoma, Int. J. Mol. Sci. 20 (2019) 2181.
[10] H. Tian, L. Cheng, Y. Liang, H. Lei, M. Qin, X. Li, Y. Ren, MicroRNA therapeutic delivery strategies: a review, J. Drug Deliv. Sci. Technol. 93 (2024) 105430.
[11] J. Habault, J.L. Poyet, Recent advances in cell penetrating peptide-based anticancer therapies, Molecules 24 (2019) 927.

[12] M. Zorko, S. Jones, Ü. Langel, Cell-penetrating peptides in protein mimicry and cancer therapeutics, Adv. Drug Deliv. Rev. 180 (2022) 114044.
[13] A. Klimpel, T. Lützenburg, I. Neundorf, Recent advances of anti-cancer therapies including the use of cell-penetrating peptides, Curr. Opin. Pharmacol. 47 (2019) 8–13.
[14] E. Martino, N. D'Onofrio, C. Anastasio, M. Abate, S. Zappavigna, M. Caraglia, M. L. Balestrieri, MicroRNA-nanoparticles against cancer: opportunities and challenges for personalized medicine, Mol. Ther. Nucleic Acids 32 (2023) 371–384.
[15] Y. Ando, H. Nakazawa, D. Miura, M. Otake, M. Umetsu, Enzymatic ligation of an antibody and arginine 9 peptide for efficient and cell-specific siRNA delivery, Sci. Rep. 11 (2021) 21882.
[16] F. Huang, Q. Shu, Z. Qin, J. Tian, Z. Su, Y. Huang, M. Gao, Anticancer actions of azurin and its derived peptide p28, Protein J 39 (2020) 182–189.
[17] Y. Xiao, B. Humphries, C. Yang, Z. Wang, MiR-205 dysregulations in breast cancer: the complexity and opportunities, Noncoding RNA 5 (2019) 53.
[18] Y. Xue, Y. Liu, X. Bian, Y. Zhang, Y. Li, Q. Zhang, M. Yin, miR-205-5p inhibits psoriasis-associated proliferation and angiogenesis: wnt/β-catenin and mitogen-activated protein kinase signaling pathway are involved, J. Dermatol. 47 (2020) 882–892.
[19] S. Niture, X. Dong, E. Arthur, U. Chimeh, S.S. Niture, W. Zheng, D. Kumar, Oncogenic role of tumor necrosis factor α-induced protein 8 (TNFAIP8), Cells 8 (2019) 9.
[20] J. Yang, Y. Huang, B. Dong, Y. Dai, Long noncoding RNA DLEU2 drives the malignant behaviors of thyroid cancer through mediating the miR-205-5p/TNFAIP8 axis, Endocr, Connect 10 (2021) 471–483.
[21] A. Narmani, R. Jahedi, E. Bakhshian-Dehkordi, S. Ganji, M. Nemati, R. Ghahramani-Asl, K. Moloudi, S.M. Hosseini, H. Bagheri, P. Kasharwani, A. Khani, B. Farhood, A. Sahebkar, Biomedical applications of PLGA nanoparticles in nanomedicine: advances in drug delivery systems and cancer therapy, Expert Opin. Drug Deliv. 20 (2023) 1387–1413.
[22] Y. He, S. Wu, M. Rietveld, M. Vermeer, L.J. Cruz, C. Eich, A. El Ghalbzouri, Application of doxorubicin-loaded PLGA nanoparticles targeting both tumor cells and cancer-associated fibroblasts on 3D human skin equivalents mimicking melanoma and cutaneous squamous cell carcinoma, Biomater. Adv. 160 (2024) 213831.
[23] G. Osman, J. Rodriguez, S.Y. Chan, J. Chisholm, G. Duncan, N. Kim, A.L. Tatler, K. M. Shakesheff, J. Hanes, J.S. Suk, J.E. Dixon, PEGylated enhanced cell penetrating peptide nanoparticles for lung gene therapy, J. Control. Release 285 (2018) 35–45.
[24] A. Gori, G. Lodigiani, S.G. Colombarolli, G. Bergamaschi, A. Vitali, Cell penetrating peptides: classification, mechanisms, methods of study, and applications, ChemMedChem 18 (2023) e202300236.
[25] M. Dowaidar, Cell-penetrating peptides with nanoparticles hybrid delivery vectors and their uptake pathways, Mitochondrion 78 (2024) 101906.
[26] K. Melikov, A. Hara, K. Yamoah, E. Zaitsev, L.V. Chernomordik, Efficient entry of cell-penetrating peptide nona-arginine into adherent cells involves a transient increase in intracellular calcium, Biochem. J. 471 (2015) 221–230.
[27] A. Yaghoubi, M. Khazaei, A. Avan, S.M. Hasanian, W.C. Cho, S. Soleimanpour, p28 bacterial peptide, as an anticancer agent, Front. Oncol. 10 (2020) 1303.
[28] B.N. Taylor, R.R. Mehta, T. Yamada, F. Lekmine, K. Christov, A.M. Chakrabarty, A. Green, L. Bratescu, A. Shilkaitis, C.W. Beattie, T.K. Das Gupta, Noncationic peptides obtained from azurin preferentially enter cancer cells, Cancer Res 69 (2009) 537–546.
[29] C.Y. Lin, H.P. Yu, Y.T. Chang, Z.C. Lin, A. Alalaiwe, T.L. Hwang, J.Y. Fang, Targeting anti-inflammatory immunonanocarriers to human and murine neutrophils via the Ly6 antigen for psoriasiform dermatitis alleviation, Biomater. Sci. 11 (2023) 873–893.
[30] S. Reissmann, M.P. Filatova, New generation of cell-penetrating peptides: functionality and potential clinical application, J. Pept. Sci. 27 (2021) e3300.
[31] R.A. Carr, D. Mesiano, C. Heffron, T. Radonic, J. Wiggins, S. Tso, R. Agrawal, E. Cheung, D.N. Slater, L. Nichols, P. Craig, Aberrant p16, p53 and ki-67 immunohistochemistry staining patterns can distinguish solitary keratoacanthoma from cutaneous squamous cell carcinoma, Pathology 55 (2023) 772–784.
[32] J.M. Luís, R. Files, C. Cardoso, J. Pimenta, G. Maia, F. Silva, F.L. Queiroga, J. Prada, I. Pires, Immunohistochemical expression levels of epidermal growth factor receptor, cyclooxygenase-2, and ki-67 in canine cutaneous squamous cell carcinomas, Curr. Issues Mol. Biol. 46 (2024) 4951–4967.
[33] J. Huang, K. Wang, S. Wu, J. Zhang, X. Chen, S. Lei, J. Wu, K. Men, X. Duan, Tumor cell lysate-based multifunctional nanoparticles facilitate enhanced mRNA delivery and immune stimulation for melanoma gene therapy, Mol. Pharm. 21 (2024) 267–282.
[34] L. Zhang, R. Liu, Y.Y. Luan, Y.M. Yao, Tumor necrosis factor-α induced protein 8: pathophysiology, clinical significance, and regulatory mechanism, Int. J. Biol. Sci. 14 (2018) 398–405.
[35] W. Yang, S. Tan, L. Yang, X. Chen, R. Yang, L. Oyang, J. Lin, L. Xia, N. Wu, Y. Han, Y. Tang, M. Su, X. Luo, Y. Yang, L. Huang, Z. Hu, Y. Tao, L. Liu, Y. Jin, H. Wang, Q. Liao, Y. Zhou, Exosomal miR-205-5p enhances angiogenesis and nasopharyngeal carcinoma metastasis by targeting desmocollin-2, Mol. Ther. Oncolytics 24 (2022) 612–623.
[36] D.D. Zou, D. Xu, Y.Y. Deng, W.J. Wu, J. Zhang, L. Huang, L. He, Identification of key genes in cutaneous squamous cell carcinoma: a transcriptome sequencing and bioinformatics profiling study, Ann. Transl. Med. 9 (2021) 1497.
[37] G. Yang, P. Zhang, A. Lv, Y. Liu, G. Wang, MiR-205 functions as a tumor suppressor via targeting TGF-α in osteosarcoma, Exp. Mol. Pathol. 100 (2016) 160–166.
[38] K.A. Janes, S. Gaudet, J.G. Albeck, U.B. Nielsen, D.A. Lauffenburger, P.K. Sorger, The response of human epithelial cells to TNF involves an inducible autocrine cascade, Cell 124 (2006) 1225–1239.
[39] Z. Xiang, M. Wang, C. Miao, D. Jin, H. Wang, Mechanism of calcitrol regulating parathyroid cells in secondary hyperparathyroidism, Front. Pharmacol. 13 (2022) 1020858.
[40] X. Lai, S.K. Gupta, U. Schmitz, S. Marquardt, S. Knoll, A. Spitschak, O. Wolkenhauser, B.M. Pützer, J. Vera, MiR-205-5p and miR-342-3p cooperate in the repression of the E2F1 transcription factor in the content of anticancer chemotherapy resistance, Theranostics 8 (2018) 1106–1120.
[41] L. Endo-Munoz, A. Dahler, N. Teakle, D. Rickwood, M. Hazar-Rethinam, I. Abdul-Jabbar, S. Sommerville, I. Dickinson, P. Kaur, S. Paquet-Fifield, N. Saunders, E2F7 can regulate proliferation, differentiation, and apoptotic responses in human keratinocytes: implications for cutaneous squamous carcinoma formation, Cancer Res 69 (2009) 1800–1808.
[42] Q. Qian, Q. Ma, B. Wang, Q. Qian, C. Zhao, F. Feng, X. Dong, MicroRNA-205-5p targets E2F1 to promote autophagy and inhibit pulmonary fibrosis in silicosis through impairing SKP2-mediated Beclin1 ubiquitination, J. Cell. Mol. Med. 25 (2021) 9214–9227.
[43] M. Tanic, M. Zajac, G. Gómez-López, J. Benítez, B. Martínez-Delgado, Integration of BRCA1-mediated miRNA and mRNA profiles reveals microRNA regulation of TRAF2 and NF-κb pathway, Breast Cancer Res. Treat. 134 (2012) 41–51.
[44] J. Carreras, Y.Y. Kikuti, G. Roncador, M. Miyaoka, S. Hiraiwa, S. Tomita, H. Ikoma, Y. Kondo, A. Ito, S. Shiraiwa, K. Ando, N. Nakamura, R. Hamoudi, High expression of caspase-8 associated with improved survival in diffuse large B-cell lymphoma: machine learning and artificial neutral networks analyses, BioMedInformatics 1 (2021) 18–46.
[45] A. Boice, L. Bouchier-Hayes, Targeting apoptotic caspases in cancer, Biochim. Biophys. Acta-Mol. Cell Res. 1867 (2020) 118688.
[46] T. Yamada, T.K. Das Gupta, C.W. Beattie, p28, an anionic cell-penetrating peptide, increases the activity of wild type and mutated p53 without altering its conformation, Mol. Pharm. 10 (2013) 3375–3383.
[47] E. Kumah, K. Bibee, Modelling cutaneous squamous cell carcinoma for laboratory research, Exp. Dermatol 32 (2023) 117–125.
[48] L. Wang, F.B. Kang, J. Wang, C. Yang, D.W. He, Downregulation of miR-205 contributes to epithelial-mesenchymal transition and invasion in triple-negative breast cancer by targeting HMGB1-RAGE signaling pathway, Anticancer Drugs 30 (2019) 225–232.
[49] Y. Jing, Q. Zhou, H. Zhu, Y. Zhang, Y. Song, X. Zhang, X. Huang, Y. Yang, Y. Ni, Q. Hu, Ki-67 is an independent prognostic marker for the recurrence and relapse of oral squamous cell carcinoma, Oncol. Lett. 17 (2019) 974–980.
[50] A. Kurzyk, A. Szumera-Ciećkiewicz, J. Miłoszewska, M. Chechlińska, 3D modeling of normal skin and cutaneous squamous cell carcinoma. A comparative study in 2D cultures, spheroids, and 3D bioprinted systems, Biofabrication 16 (2024) 025021.
[51] M. Quadri, A. Marconi, S.K. Sandhu, A. Kiss, T. Efimova, E. Palazzo, Investigating cutaneous squamous cell carcinoma in vitro and in vivo: novel 3D tools and animal models, Front. Med. 9 (2022) 875517.
[52] G. Baeza-Hernández, J. Cañueto, Intralesional treatments for invasive cutaneous cell carcinoma, Cancers (Basel) 16 (2024) 158.
[53] S.J. Smith, C.M. Li, R.G. Lingeman, R.J. Hickey, Y. Liu, L.H. Malkas, M. Raoof, Molecular targeting of cancer-associated PCNA interactions in pancreatic ductal adenocarcinoma using a cell-penetrating peptide, Mol. Ther. Oncolytics 17 (2020) 250–256.
[54] D.V. Hingorani, M.F. Camargo, M.A. Quraishi, S.R. Adams, S.J. Advani, Tumor activated cell penetrating peptides to selectively deliver immune modulatory drugs, Pharmaceutics 13 (2021) 365.
[55] S. Mander, S.A. Naffouje, J. Gao, W. Li, K. Christov, A. Green, E.R. Bongarzone, T. K. Das Gupta, T. Yamada, Tumor-targeting cell-penetrating peptide, p28, for glioblastoma imaging and therapy, Front. Oncol. 12 (2022) 940001.



International Journal of Environmental Health Research

ISSN: 0960-3123 (Print) 1369-1619 (Online) Journal homepage: www.tandfonline.com/journals/cije20

Effects of ambient fine particulate matter on the exacerbation of psychiatric disorders in southern Taiwan: a case-crossover study

Su-Lun Hwang, Yu-Ching Lin, Chieh-Mo Lin & Miao-Ching Chi

To cite this article: Su-Lun Hwang, Yu-Ching Lin, Chieh-Mo Lin & Miao-Ching Chi (2025) Effects of ambient fine particulate matter on the exacerbation of psychiatric disorders in southern Taiwan: a case-crossover study, International Journal of Environmental Health Research, 35:11, 3210-3221, DOI: 10.1080/09603123.2025.2480853

To link to this article: https://doi.org/10.1080/09603123.2025.2480853

Published online: 19 Mar 2025.

Submit your article to this journal

Article views: 59

View related articles

View Crossmark data

Full Terms & Conditions of access and use can be found at
https://www.tandfonline.com/action/journalInformation?journalCode=cije20

INTERNATIONAL JOURNAL OF ENVIRONMENTAL HEALTH RESEARCH
2025, VOL. 35, NO. 11, 3210–3221
https://doi.org/10.1080/09603123.2025.2480853

Taylor & Francis
Taylor & Francis Group

RESEARCH ARTICLE

Check for updates

Effects of ambient fine particulate matter on the exacerbation of psychiatric disorders in southern Taiwan: a case-crossover study

Su-Lun Hwang[a,b,c], Yu-Ching Lin[c,d], Chieh-Mo Lin[a,e,f] and Miao-Ching Chi[b,d]

[a]Department of Nursing, Chang Gung University of Science and Technology, Puzi, Taiwan; [b]Chronic Diseases and Health Promotion Research Center, Chang Gung University of Science and Technology, Puzi, Taiwan; [c]Division of Thoracic Oncology, Chang Gung Memorial Hospital Chiayi Branch, Puzi, Taiwan; [d]Department of Respiratory Care, Chang Gung University of Science and Technology, Puzi, Taiwan; [e]Department of Pulmonary and Critical Care Medicine, Chiayi Chang Gung Memorial Hospital, Chang Gung Medical Foundation, Puzi, Chiayi Country, Taiwan; [f]Graduate Institute of Clinical Medical Sciences, College of Medicine, Chang Gung University, Taoyuan, Taiwan

ABSTRACT

This study investigated the impact of short-term exposures to ambient fine particulate matter 2.5 ($PM_{2.5}$) on the exacerbation of psychiatric disorders (PDs) in southern Taiwan between 2014 and 2020. Data on emergency room visits (ERVs) for PDs and air pollutant levels were obtained from the Chang Gung Research Database and the Environmental Protection Administration, respectively. A time-stratified case-crossover design was adopted to estimate the risks of ERVs for PDs. At lag4 days, a 10-μg/m^3 increase in $PM_{2.5}$ was associated with significant increases in ERVs in both single- and multi-pollutant models, with odds ratio (OR) of 1.18 [95% confidence interval (95% CI): 1.00, 1.38] ($PM_{2.5}$), 1.20 (95% CI: 1.00, 1.43) ($PM_{2.5} + SO_2$), 1.23 (95% CI: 1.03, 1.46) ($PM_{2.5} + O_3$), and 1.25 (95% CI: 1.03, 1.52) ($PM_{2.5} + SO_2 + O_3$). For cumulative lags (lag0–6), a 10-μg/m^3 increase in $PM_{2.5}$ was associated with significant increases in ERVs only for multi-pollutant model ($PM_{2.5} + SO_2$), with OR of 1.41 (95% CI: 1.03, 1.93). Among males, significant increases in ERVs were observed at lag4 and lag0–6 days; however, no significant associations were observed in females. In conclusion, short-term exposure to $PM_{2.5}$ increased the risk of PDs exacerbation, exhibiting both delayed and cumulative effects, with male patients found to be more sensitive.

ARTICLE HISTORY
Received 18 November 2024
Accepted 13 March 2025

KEYWORDS
Fine particulate matter; psychiatric disorders; emergency room visits

Introduction

According to the World Health Organization (WHO), mental health conditions are increasing significantly worldwide. Findings from the Global Burden of Disease (GBD) Study in 2019 showed that mental disorders (MDs) are among the top ten leading causes of global health burden. The age-standardized disability-adjusted life-year (DALY) rate for MDs was 1,426.5 per 100,000 population for males and 1,703 per 100,000 population for females worldwide (GBD 2019 Mental Disorders Collaborators 2022). In Taiwan, the one-year prevalence rates (PRs) of MDs rose from 10.8% in 2014 to 12.4% in 2021, and is expected to continue rising (Ministry of Health and Welfare National health expenditure data 2021). Moreover, MDs pose a substantial economic burden on patients in Taiwan. Healthcare costs accounted for 84.25%, 60%, and 29.62% of the one-year total healthcare costs for younger patients diagnosed with schizophrenia, bipolar disorder, and major depressive disorder, respectively (Pan et al. 2019).

CONTACT Su-Lun Hwang slhuang@mail.cgust.edu.tw Department of Nursing, Chang Gung University of Science and Technology, Chiayi Campus, No. 2, W., Jiapu Rd. Puzi, Chiayi 61363, Taiwan (ROC)

© 2025 Informa UK Limited, trading as Taylor & Francis Group

Emerging research by Hu et al. showed that air pollution (AP) accounted for 11.62% of death and 0.84% of DALY worldwide in 2019 (Hu et al. 2023); additionally, the global deaths and disability-adjusted life years (DALYs) attributable to ambient fine particulate matter ($PM_{2.5}$) increased by 102.3% and 67.7%, respectively, from 1990 to 2019, with East Asia and South Asia ranking first and second in $PM_{2.5}$-attributable deaths and DALYs (Sang et al. 2022). Recently, ambient AP has increasingly recognized as a risk factor for MDs. A longitudinal study in the United Kingdom (UK) revealed a rise in poorer mental well-being with long-term exposure to AP (Abed Al Ahad et al. 2022). Growing evidence from epidemiological studies suggests that AP exacerbates MDs (Bernardini et al. 2020), and it has been recognized as an independent risk factor for MDs, including subjective stress and suicidal ideation (Shin et al. 2018), schizophrenia (Antonsen et al. 2020), depression in older populations (Qiu et al. 2023), and psychiatric emergency room visits (ERVs) (Muhsin et al. 2022). A multicity time-series study in China indicated that short-term exposure to ambient air pollutants [$PM_{2.5}$, particulates less than 10 μm in diameter (PM_{10}), and nitrogen dioxide (NO_2)] is associated with an increased risk of daily hospital admission for depression in urban populations (Gu et al. 2020). Also, a case-crossover study in Seoul, South Korea found the risk of emergency departments (ED) visits for psychosis (including schizophrenia and related disorders, and mood disorders with psychotic features) was significantly associated with an interquartile range (IQR) increase (14.9 $\mu g/m^3$) in $PM_{2.5}$ (odds ratio, OR = 1.03) (Lee et al. 2022). A recent meta-analysis revealed an increased risk of depression associated with long-term exposure to $PM_{2.5}$ (relative risk, RR = 1.07) and NO_2 (RR = 1.04), and with short-term exposure to PM_{10}, $PM_{2.5}$, NO_2, sulfur dioxide (SO_2), ozone (O_3), and carbon monoxide (CO) with RRs of 1.01, 1.01, 1.02, 1.02, 1.01 and 1.06, respectively (Borroni et al. 2022). The mechanisms by which air pollutants may trigger acute exacerbation of psychosis include oxidative stress and the formation of inflammatory cytokines that infiltrate the blood–brain barrier, causing neuroinflammation and neurodegeneration (Babadjouni et al. 2017). These processes are thought to lead to depression and psychosis due to dysregulation of neurotransmitters and the hypothalamic-pituitary-adrenal and sympathetic-adrenal-medullary axes (Li et al. 2017).

Prior studies have found that countries in southern Taiwan face a serious $PM_{2.5}$ issue (Hwang et al. 2016, 2017, 2017; Lee et al. 2019; Su et al. 2019; Wang et al. 2021). Research indicates that carcinogenic elements (Cr, Ni, and As) in southwestern Taiwan were attributable to anthropogenic emissions; furthermore, traffic emissions, soil and road dust, coal combustion, and the iron and steel industry are the main contributors to $PM_{2.5}$-bound trace elements in this region (Hwang et al. 2018). Previous studies also report a higher prevalence of depression in southern Taiwan (Lin et al. 2008; Tai et al. 2014), which the prevalence of depression among adolescents in southern Taiwan was 12.3% (Lin et al. 2008). According to statistics from Taiwan's MOHW, the one-year PRs of MDs in Chiayi County, southwestern Taiwan, was 13.3% in 2021, higher than the national average of 12.4% (Ministry of Health and Welfare National health expenditure data 2021). In Taiwan, epidemiological evidence on the relationship between air pollutants exposure and psychiatric disorders (PDs) is sparse, with most studies focusing on depression. Tsai et al. (2021) conducted a case-crossover study in Taipei, Taiwan found that per IQR increase in $PM_{2.5}$ concentrations was associated with a 17% increase in depression admissions on warm days and a 4% increase on cool days. Wang et al. (2022) reported that short-term exposure to air pollutants increased depression risk among community-dwelling older adults. Lo et al. (2021) found that short-term exposure to AP raised the risk of depression in patients with sleep-related breathing disorders. However, few studies have investigated the impact of $PM_{2.5}$ exposure on PDs other than depression, and little is known about the associations between $PM_{2.5}$ and MDs in Taiwan. Therefore, it is essential to explore the effects of $PM_{2.5}$ concentrations on ERVs for MDs in Taiwan. The current study conducted a time-stratified case-crossover study design to investigate the short-term impact of $PM_{2.5}$ exposure on ERVs due to psychotic exacerbations of PDs, using the electronic medical record (EMR) database from the Chang Gung Research Database (CGRD) of Chang Gung Memorial Hospital (CGMH) in Puzi City, located in southern Taiwan, covering the years 2014 to 2020.

Materials and methods

Study area

Puzi City (latitude: 23° 27′40″ N and longitude: 120° 14′31″ E) is a coastal area in Chiayi County, located in southern Taiwan (Figure 1). It has a humid subtropical climate with dry winter, and an annual average temperature of approximately 25.9°C. As of April 2023, the population is 40,865, and the city covers an area of 50 km^2. This study selected Puzi City as the research focus for several reasons. Firstly, Puzi is home to a significant number of petrochemical industries. Secondly, Taiwan's Environmental Protection Administration (TEPA) has established a fixed-site air quality monitoring station (Puzi station) in the city center. Thirdly, $PM_{2.5}$ is the primary air pollutant in Puzi, which faces a severe $PM_{2.5}$ pollution issue (Hwang et al. 2018). According to TEPA reports, during the study period of 2014–2020, the annual average concentration of $PM_{2.5}$ in Puzi City exceeded both TEPA's upper limit of 15 μg/m^3 and the WHO's air quality guideline (10 μg/m^3 in 2005, reduced to 5 μg/m^3 in 2021). From 2014 to 2020, the annual average $PM_{2.5}$ concentrations in Puzi City were 29.6, 24.1, 26.5, 21.9, 22.2, 19.2 and 16.7 μg/m^3, respectively (EPA 2020).

Hospital psychotic emergency room visits data

The Ethics Review Board of Chang Gung Medical Foundation in Taiwan approved this research (IRB number: 201801906B0). This study used data from the CGRD, the largest multi-institutional EMR database collected from CGMH branches across Taiwan. CGMH has seven hospital branches located in Linkou, Taipei, Taoyuan, Keelung, Yunlin, Chiayi, and Kaohsiung (Tsai et al. 2017;

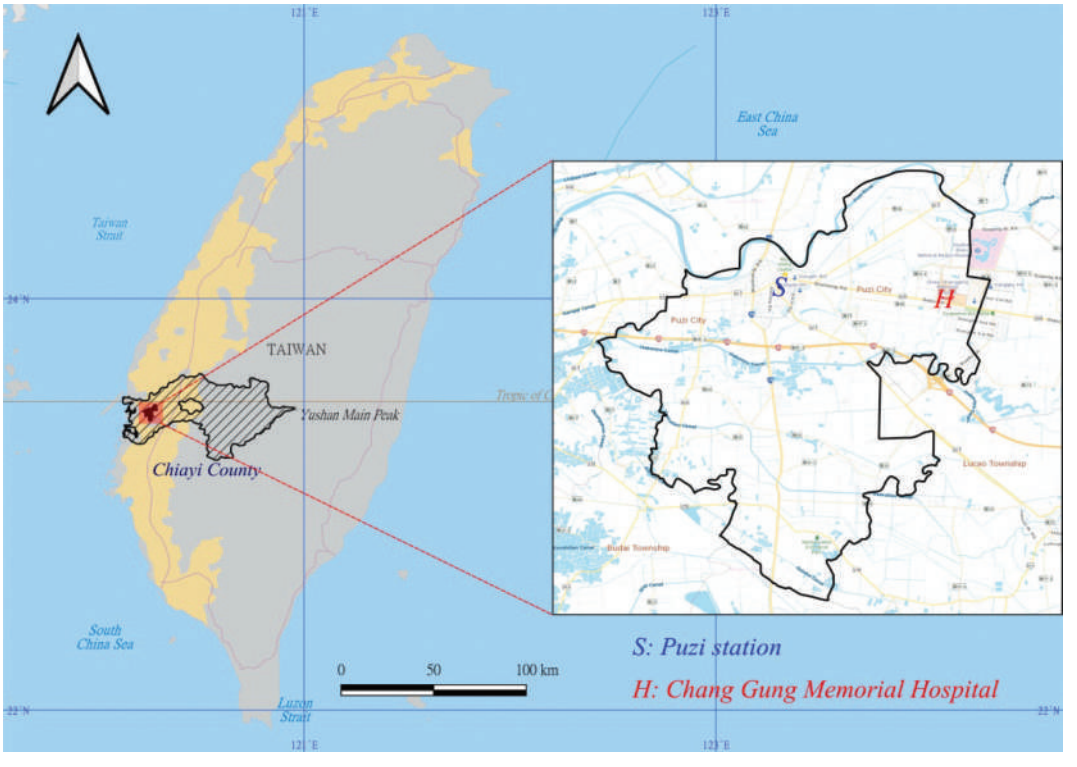


Figure 1. Map of the study area (Puzi City, southern Taiwan) with the locations of the air quality monitoring station (Puzi station, S), and CGMH chiayi branch (CYCGMH, H).

Huang et al. 2022). The Chiayi Branch (CYCGMH) is a regional hospital, located 5 km from the center of Puzi City.

Daily counts of ERVs for PDs at CYCGMH, located in Puzi City, were obtained from the CGRD for the period from 2014 to 2020. In this study, PDs were identified based on primary diagnosis according to the International Classification of Diseases, 10th Revision (ICD-10): PDs with symptoms (F20-F29), including schizoaffective disorders, delusional disorder, and schizotypal disorder; mood disorders with psychotic features (F30.2, F31.2, F31.5, F32.3, F33.3), including bipolar affective disorder and major depressive disorder. A total of 107 hospital ERVs records for PDs were retrieved during the study period.

Ambient air pollutants and meteorological data

The Taiwan Air Quality Monitoring Network (TAQMN), maintained by the TEPA, monitors air pollutants at 77 monitoring stations (Lee et al. 2020; Environmental Protection Administration Taiwan Air Quality Monitoring Network 2021). Among these, a single fixed-site air quality monitoring station (the Puzi station) is located in Puzi City (Figure 1). The Puzi station is situated on the rooftop of a building approximately 3 meters above ground at Chiayi Putzu Primary School (latitude: 23° 27′55″ N and longitude: 120° 14′52″ E), and is surrounded by residential dwellings. During the study period, daily 24-hour average concentration data for $PM_{2.5}$, SO_2, O_3, and meteorological measurements (temperature and relative humidity, RH) were obtained from the Puzi station.

Statistical analysis

This study employed a time-stratified case-crossover design to evaluate the associations between short-term $PM_{2.5}$ exposures and ERVs for psychotic exacerbation in southwestern Taiwan. The case-crossover design, developed to study transient effects on the risk of acute events, was first introduced by Maclure (1991). In this study, a "case day" was defined as the day of an emergency room visit for PDs. "Control days" were selected by matching the day of the week within the same month, with three control days chosen for each case day. Both lagged and cumulative lagged exposures (up to 6 days prior to ERVs) were calculated to explore whether the effects of $PM_{2.5}$ were immediate, delayed, or cumulative. Moreover, subgroup analyses by gender were conducted to investigate possible susceptible subpopulations.

Conditional logistic regression models were used to estimate the OR and 95% confidence interval (CI) between $PM_{2.5}$ concentrations and ERVs for PDs. Two models were applied to estimate the OR of $PM_{2.5}$ on ERVs for PDs: a single-pollutant model, which included only $PM_{2.5}$, and multi-pollutant models, which included up to three pollutants ($PM_{2.5} + SO_2$, $PM_{2.5} + O_3$, and $PM_{2.5} + SO_2 + O_3$). All statistical analyses were conducted using the Statistical Package for the Social Sciences (SPSS) version 22 (IBM Corp., Armonk, NY, USA).

Results

During the study period, a total of 107 hospital ERVs for psychotic exacerbation were recorded in Puzi City (Table 1). The mean age of the patients was 42.1 years (SD = 10.8), with 63.6% male and 36.4% female. The daily mean concentrations of $PM_{2.5}$, SO_2, and O_3 were 25.8 μg/m^3, 2.9 ppb, and 30.8 ppb, respectively, and the mean daily average temperature and RH was 25.5°C and 77.0%, respectively.

Table 2 illustrates the OR and 95% CI of ERVs for psychotic exacerbations in single-day lag models (lag0 to lag6). After adjusting for temperature and RH, the short-term effects of $PM_{2.5}$ exposure on ERVs for psychotic exacerbations were significant at lag4 days for both single- and multiple-pollutant models. At lag4 days, a 10 μg/m^3 increase in $PM_{2.5}$ was associated with a 18%

Table 1. Demographic summary information on ERVs for PDs in Puzi City, Taiwan, 2014–2020.

	ERVs for PDs
	(n = 107)
Age (years) (M ± SD)	
	42.1 ± 10.8
Gender, No (%)	
Male	68 (63.6)
Female	39 (36.4)
Air pollutants concentrations (M ± SD)	
$PM_{2.5}$ (μg/m^3)	25.8 ± 14.4
SO_2 (ppb)	2.9 ± 0.8
O_3 (ppb)	30.8 ± 8.3
Meteorological variable (M ± SD)	
Temperature (℃)	25.5 ± 4.6
RH (%)	77.0 ± 3.4

M: mean; SD: standard deviation.

increase (OR = 1.18, 95% CI: 1.00, 1.38) in the single-pollutant model, and increases of 20% (OR = 1.20, 95% CI: 1.00, 1.43), 23% (OR = 1.23, 95% CI: 1.03, 1.46), and 25% (OR = 1.25, 95% CI: 1.03, 1.52) in the multiple-pollutant models ($PM_{2.5} + SO_2$, $PM_{2.5} + O_3$, and $PM_{2.5} + SO_2 + O_3$, respectively).

For males, the short-term effects of $PM_{2.5}$ exposure on ERVs for psychosis were also significant at lag4 days in both single- and multiple-pollutant models. A 10 μg/m^3 increase in $PM_{2.5}$ was associated with a 21% increase (OR = 1.21, 95% CI: 1.00, 1.48) in the single-pollutant model, and increases of 27% (OR = 1.27, 95% CI: 1.02, 1.58), 24% (OR = 1.24, 95% CI: 1.00, 1.53), and 30% (OR = 1.30, 95% CI: 1.03, 1.63) in the multiple-pollutant models ($PM_{2.5} + SO_2$, $PM_{2.5} + O_3$, and $PM_{2.5} + SO_2 + O_3$, respectively). However, no significant associations were observed between $PM_{2.5}$ and ERVs for psychotic exacerbations in females.

Table 3 illustrates the OR and 95% CI of ERVs for psychotic exacerbations in multiple-day lags (lag0–1 to lag0–6). After adjusting for temperature and RH, significant short-term effects of $PM_{2.5}$ exposure were observed in ERVs for PDs at lag0–6 days for multiple-pollutant model. At a lag of 0–6 days, a 10 μg/m^3 increase in $PM_{2.5}$ was associated with a 41% increase (OR = 1.41, 95% CI: 1.03, 1.93) in the multiple-pollutant model ($PM_{2.5} + SO_2$). For males, significant short-term effects of $PM_{2.5}$ exposure on ERVs for PDs were observed at lag0–6 days in the multiple-pollutant model. A 10 μg/m^3 increase in $PM_{2.5}$ was associated with an increase of 52% (OR = 1.52, 95% CI: 1.03, 2.24) in the multiple-pollutant model ($PM_{2.5} + SO_2$). However, no significant associations were observed between $PM_{2.5}$ exposure and ERVs for PDs in females.

Discussion

In this study, a time-stratified case-crossover analysis was conducted to assess the association between short-term $PM_{2.5}$ exposure and the risk of psychotic exacerbations. The findings revealed a statistically significant association between short-term $PM_{2.5}$ exposure and the risk of acute exacerbations of PDs. Additionally, male patients appeared more vulnerable to $PM_{2.5}$ exposure than female patients, with significantly increased risks observed at a delayed lag (lag4) and cumulative lags (lag0–6). In Taiwan, prior studies exploring the adverse effects of short-term $PM_{2.5}$ exposure on psychosis have been limited, primarily focusing on depression (Lo et al. 2021; Tsai et al. 2021; Wang et al. 2022). The present study broadens this scope by examining the association between short-term $PM_{2.5}$ exposure and ERVs due to psychotic exacerbations from a range of psychiatric disorders in Taiwan. Consistent with previous studies on depression, this study found short-term exposure to $PM_{2.5}$ increased the risk of PDs exacerbation.

Table 2. Odds ratio of ERVs for PDs with every 10 μg/m^3 increase in $PM_{2.5}$, single lag day.

		Lag (days)													
		Lag0		Lag1		Lag2		Lag3		Lag4		Lag5		Lag6	
	Model[a]	OR	95% CI	OR	95% CI	OR	95% CI	OR	95% CI	OR	95% CI	OR	95% CI	OR	95% CI
All	$PM_{2.5}$	1.04	(0.87, 1.24)	1.04	(0.88, 1.24)	1.02	(0.87, 1.20)	1.11	(0.94, 1.31)	1.18*	(1.00, 1.38)	1.10	(0.92, 1.31)	1.06	(0.88, 1.26)
	$PM_{2.5} + SO_2$	1.12	(0.93, 1.36)	1.04	(0.86, 1.26)	1.02	(0.86, 1.22)	1.16	(0.96, 1.39)	1.20*	(1.00, 1.43)	1.13	(0.93, 1.37)	1.14	(0.93, 1.40)
	$PM_{2.5} + O_3$	0.94	(0.77, 1.14)	0.97	(0.81, 1.16)	1.00	(0.84, 1.19)	1.14	(0.96, 1.36)	1.23*	(1.03, 1.46)	1.06	(0.87, 1.29)	0.97	(0.80, 1.18)
	$PM_{2.5} + SO_2 + O_3$	1.01	(0.82, 1.26)	0.97	(0.79, 1.19)	1.00	(0.83, 1.21)	1.20	(0.99, 1.46)	1.25*	(1.03, 1.52)	1.08	(0.87, 1.35)	1.04	(0.83, 1.30)
Male	$PM_{2.5}$	1.04	(0.83, 1.31)	1.06	(0.85, 1.31)	1.05	(0.86, 1.28)	1.21	(0.98, 1.49)	1.21*	(1.00, 1.48)	1.12	(0.89, 1.41)	1.10	(0.88, 1.38)
	$PM_{2.5} + SO_2$	1.15	(0.89, 1.48)	1.03	(0.81, 1.32)	1.08	(0.87, 1.35)	1.23	(0.98, 1.55)	1.27*	(1.02, 1.58)	1.15	(0.90, 1.46)	1.16	(0.90, 1.50)
	$PM_{2.5} + O_3$	0.93	(0.71, 1.22)	0.96	(0.75, 1.22)	1.03	(0.83, 1.27)	1.22	(0.98, 1.51)	1.24*	(1.00, 1.53)	1.05	(0.82, 1.35)	1.02	(0.80, 1.30)
	$PM_{2.5} + SO_2 + O_3$	1.02	(0.76, 1.37)	0.93	(0.71, 1.21)	1.06	(0.84, 1.34)	1.24	(0.97, 1.58)	1.30*	(1.03, 1.63)	1.07	(0.82, 1.40)	1.07	(0.81, 1.40)
Female	$PM_{2.5}$	1.04	(0.79, 1.37)	1.03	(0.78, 1.35)	0.95	(0.71, 1.27)	0.96	(0.73, 1.27)	1.09	(0.83, 1.43)	1.05	(0.78, 1.40)	0.97	(0.72, 1.30)
	$PM_{2.5}$+ SO_2	1.09	(0.80, 1.48)	1.06	(0.78, 1.44)	0.92	(0.67, 1.26)	1.30	(0.75, 1.43)	1.02	(0.74, 1.41)	1.07	(0.77, 1.51)	1.07	(0.75, 1.53)
	$PM_{2.5} + O_3$	0.97	(0.72, 1.31)	0.99	(0.74, 1.32)	0.93	(0.68, 1.27)	1.03	(0.77, 1.37)	1.21	(0.89, 1.66)	1.05	(0.76, 1.45)	0.88	(0.62, 1.24)
	$PM_{2.5} + SO_2 + O_3$	1.03	(0.75, 1.43)	1.03	(0.75, 1.41)	0.89	(0.64, 1.26)	1.12	(0.80, 1.57)	1.15	(0.79, 1.66)	1.08	(0.75, 1.56)	0.98	(0.66, 1.45)

*$p < 0.05$, adjusted odds ratio with 95% confidence intervals (95% CI) were calculated using conditional logistic regression models. [a]: adjusted for temperature and RH.

Table 3. Odds ratio of ERVs for PDs with every 10 μg/m^3 increase in $PM_{2.5}$, cumulative lag day.

Model[a]		Lag (days)											
		Lag0–1		Lag0–2		Lag0–3		Lag0–4		Lag0–5		Lag0–6	
		OR	95% CI	OR	95% CI	OR	95% CI	OR	95% CI	OR	95% CI	OR	95% CI
All	$PM_{2.5}$	1.04	(0.86, 1.27)	1.05	(0.86, 1.28)	1.08	(0.88, 1.34)	1.14	(0.92, 1.42)	1.18	(0.93, 1.48)	1.20	(0.94, 1.54)
	$PM_{2.5} + SO_2$	1.11	(0.89, 1.38)	1.10	(0.87, 1.38)	1.16	(0.91, 1.47)	1.24	(0.95, 1.60)	1.30	(0.98, 1.72)	1.41*	(1.03, 1.93)
	$PM_{2.5} + O_3$	0.91	(0.73, 1.13)	0.93	(0.74, 1.17)	1.00	(0.80, 1.27)	1.09	(0.86, 1.39)	1.11	(0.86, 1.44)	1.11	(0.84, 1.47)
	$PM_{2.5} + SO_2 + O_3$	0.97	(0.76, 1.24)	0.98	(0.76, 1.27)	1.07	(0.82, 1.40)	1.18	(0.89, 1.56)	1.23	(0.90, 1.67)	1.30	(0.92, 1.83)
Male	$PM_{2.5}$	1.06	(0.82, 1.37)	1.08	(0.84, 1.40)	1.15	(0.89, 1.50)	1.11	(0.93, 1.61)	1.26	(0.94, 1.69)	1.30	(0.95, 1.79)
	$PM_{2.5} + SO_2$	1.12	(0.84, 1.50)	1.15	(0.85, 1.55)	1.23	(0.90, 1.68)	1.34	(0.97, 1.85)	1.41	(0.99, 2.00)	1.52*	(1.03, 2.24)
	$PM_{2.5} + O_3$	0.90	(0.67, 1.21)	0.96	(0.71, 1.28)	1.06	(0.79, 1.43)	1.15	(0.85, 1.55)	1.17	(0.85, 1.61)	1.18	(0.83, 1.66)
	$PM_{2.5} + SO_2 + O_3$	0.95	(0.68, 1.33)	1.02	(0.73, 1.43)	1.13	(0.81, 1.59)	1.26	(0.89, 1.79)	1.30	(0.89, 1.91)	1.37	(0.90, 2.09)
Female	$PM_{2.5}$	1.01	(0.74, 1.37)	0.99	(0.71, 1.38)	0.98	(0.69, 1.39)	1.01	(0.70, 1.47)	1.03	(0.70, 1.52)	1.04	(0.68, 1.57)
	$PM_{2.5} + SO_2$	1.08	(0.76, 1.52)	1.02	(0.70, 1.49)	1.04	(0.69, 1.56)	1.06	(0.67, 1.67)	1.10	(0.67, 1.81)	1.18	(0.68, 2.05)
	$PM_{2.5} + O_3$	0.91	(0.64, 1.28)	0.89	(0.61, 1.30)	0.91	(0.61, 1.36)	0.99	(0.65, 1.51)	1.01	(0.65, 1.58)	1.01	(0.62, 1.64)
	$PM_{2.5} + SO_2 + O_3$	0.99	(0.68, 1.43)	0.93	(0.62, 1.41)	0.98	(0.63, 1.52)	1.04	(0.63, 1.70)	1.09	(0.63, 1.86)	1.14	(0.62, 2.10)

*$p < 0.05$, adjusted odds ratio with 95% confidence intervals (95% CI) were calculated using conditional logistic regression models. [a]: adjusted for temperature and RH.

In a related study, Lee et al. (2022) conducted a case-crossover study in Seoul, South Korea, and found that a 10 μg/m^3 increase in the 2-day average concentrations (lag0–1) of $PM_{2.5}$ was associated with a 1.83% increase in ED visits for psychosis. Yoo et al. (2023) reported a 2.78% increase in mental-disorder related ERVs with a 10 μg/m^3 rise in ambient $PM_{2.5}$ concentration on a moving average lag0–3 day in New York City, USA. Similarly, in a case-crossover study of children and adolescents in Ohio, Brokamp et al. (2019) reported that a 10 μg/m^3 increase in $PM_{2.5}$ was associated with a significant increase in psychiatric ED utilization one day (OR = 1.07) and two days later (OR = 1.05). In the current study, a 10 μg/m^3 increase in the 7-day average (lag0–6) and 4 days (lag4) corresponded to increases in ERVs for psychosis of 20% and 18%, respectively. The magnitude of risk estimates for $PM_{2.5}$ on PDs in this study was higher than in previous reports (Brokamp et al. 2019; Lee et al. 2022; Yoo et al. 2023). These discrepancies might be attributed to interregional differences in AP characteristics (e.g. chemical composition and PM concentrations), varying climate conditions and differences in populations at risk (Hwang et al. 2017). Moreover, demographic characteristics, such as socioeconomic factors, social cohesion/support, and healthcare facility availability, may also contribute to the variations in risk estimates (Li et al. 2020).

The delayed effect of short-term $PM_{2.5}$ exposure on ERVs for PDs observed in this study is consistent with previous findings from studies in South Korea (Lee et al. 2022), the USA (Brokamp et al. 2019; Yoo et al. 2023), and Sweden (Muhsin et al. 2022). Oxidative stress plays a crucial role in the neurotoxicity caused by PM exposure and has been implicated in the exacerbations of schizophrenia (Murray et al. 2021). Experimental evidence has shown that PM exposure affects the structure and function of the hippocampus and glutamatergic neurons, with PM-induced oxidative stress aggravating glutamatergic excitotoxicity (Morgan et al. 2011). Furthermore, animal studies suggest that the effects of glutamate on rodent hippocampal neurons can persist for up to 8 days after exposure (Sun et al. 2001), potentially explaining the delayed effects of $PM_{2.5}$ exposure found in the current study.

In terms of sex-specific analysis, this study suggests that male patients exhibit greater vulnerability to $PM_{2.5}$ than female patients. This finding aligns with Lee et al. (2022), who reported a significantly increased risk of psychotic exacerbations in male patients compared to female patients. Similarly, research in subtropical cities in China (Huizhou, Shenzhen, and Zhaoqing) has shown that males are more sensitive to air pollutants than females (Li et al. 2020). This study found that the correlation between $PM_{2.5}$ and ERVs in female PDs patients was weaker than that in males, which may be due to different reasons. One possible explanation is sex-linked biological differences, such as hormonal variations and different physiological responses to AP exposure. In the brain, the enzyme paraoxonase 2 (PON2) exerts anti-inflammatory and anti-oxidant effects, with higher PON2 levels associated with decreased susceptibility to oxidative stress and neuroinflammation (Giordano et al. 2013). An experimental study on mice brain responses (Cole et al. 2016) found males are more susceptible to air pollution-induced neurotoxicity, while female brains express higher levels of PON2 than male brains. Besides biological effects, another explanation is that $PM_{2.5}$ interacts with male-specific factors that are known to be associated with increased risk of mental illness such as lifestyle habits. For instance, in 2020, the smoking rate in Taiwan was 13.1% (men: 23.1%, women: 2.9%) (Lin et al. 2024). The study by Lin et al. (2017) reported that the synergistic interaction of $PM_{2.5}$ and cigarette smoking on depression was significant. Another possibility is the misclassification of real exposure to $PM_{2.5}$. For instance, in Taiwan, women are more willing to take $PM_{2.5}$ preventive behavioral intention than men (Weng et al. 2021), which may lead to the weaker impact of $PM_{2.5}$ on women. Evidence thus suggests that gender may play an important role in modulating susceptibility to AP neurotoxicity; however, the existing literature on sex-specific effects remains inconsistent. A study conducted in Sweden indicated that acute $PM_{2.5}$ exposure could worsen mental health in both males and females (Muhsin et al. 2022). On the other hand, the small number of women in the present study may mean that we were

underpowered to determine the impact of $PM_{2.5}$ on women. Further research is needed to clarify sex-specific influences and the underlying mechanisms.

This study has certain limitations. First, the data were collected from a single hospital, resulting in a small sample size of ERVs for PDs; in the case, the findings of the study should be interpreted with caution. To improve the generalizability of the findings, future studies should include data from multiple hospitals in various cities. Second, this study used data from one fixed-site monitoring station as a proxy for population exposures to $PM_{2.5}$ and other air pollutants; moreover, indoor pollution, daily exposure to other air pollutants, and tobacco use were not considered, which would lead to measurement error or information bias. Nonetheless, we believe that the misclassification could be non-differential and could have resulted in the underestimation of PDs risk. Previous research reported that measurements from the fixed-site monitoring stations may underestimate true ambient $PM_{2.5}$ concentrations (Evangelopoulos et al. 2020). According to a meta-analysis, personal $PM_{2.5}$ exposure is strongly correlated with ambient concentrations ($r = 0.63$) (Chen et al. 2022). Similarly, Sarnat et al. (2006) reported that ambient $PM_{2.5}$ concentrations are strong proxies of corresponding personal exposures. Using ambient concentrations from stationary monitors as proxy exposure estimates for $PM_{2.5}$ introduces measurement error, including classical and Berkson errors, which may bias estimates of health effects; moreover, classical error tends to bias the effect estimate toward the null; whereas Berkson error yields an unbiased effect estimate (Wei et al. 2022). Third, only limited information is available on individual patient characteristics, including specific traits (e.g. pre-existing disease, genetic variations, and behaviors) and socioeconomic status (e.g. education level, employment, and income). Therefore, there was insufficient adjustment for individual features, which might result in residual confounding of the association between $PM_{2.5}$ and health effects. Nonetheless, it is worth noting that the current study used a case-crossover design, which inherently controls for time-invariant covariates, such as individuals characteristics, by comparing individuals to themselves and eliminating time-invariant confounders (Jaakkola 2003). Thus, this limitation did not have a substantial effect on our results.

Conclusion

In conclusion, the results of this study indicate that in southern Taiwan, short-term $PM_{2.5}$ exposure increased the risk of PDs exacerbation and exhibited delayed and cumulative effects. Male patients were found to be relatively more sensitive. These findings contribute to the growing body of literature on $PM_{2.5}$-related exacerbations of psychotic disorders. Further epidemiological and experimental research is needed to clarify the relationship between $PM_{2.5}$ exposure and the severity and progression of psychiatric disorders.

Acknowledgments

The authors wish to thank the Chang Gung Research Database (CGRD) (Number - 17567).

Disclosure statement

No potential conflict of interest was reported by the author(s).

Funding

This study was supported by the Ministry of Science and Technology, Taiwan project number [MOST108-2625-B-255-001] and the Chang Gung Memorial Hospital, Chiayi, Taiwan, R.O.C. grant number [CMRPF6J0101, CMRPF6J0102, CMRPF6L0021 and CMRPF6M0011].

Credit author statement

Su-Lun Hwang: Funding acquisition, Conceptualization, Supervision, Formal analysis, Writing-Original draft, Writing-Reviewing and Editing. **Yu-Ching Lin**: Data curation, Resources. **Chieh-Mo Lin**: Software, Data curation. **Miao-Ching Chi**: Resources.

References

Abed Al Ahad M, Demšar U, Sullivan F, Kulu H. 2022. Air pollution and individuals' mental well-being in the adult po.Pulation in United Kingdom: a spatial-temporal longitudinal study and the moderating effect of ethnicity. PLOS ONE. 17(3):e0264394. doi: 10.1371/journal.pone.0264394.

Antonsen S, Mok PLH, Webb RT, Mortensen PB, McGrath JJ, Agerbo E, Brandt J, Geels C, Christensen JH, Pedersen CB. 2020. Exposure to air pollution during childhood and risk of developing schizophrenia: a national cohort study. Lancet Planet Health. 4(2):e64–e73. doi: 10.1016/S2542-5196(20)30004-8.

Babadjouni RM, Hodis DM, Radwanski R, Durazo R, Patel A, Liu Q, Mack WJ. 2017. Clinical effects of air pollution on the central nervous system; a review. J Clin Neurosci. 43:16–24. doi: 10.1016/j.jocn.2017.04.028.

Bernardini F, Trezzi R, Quartesan R, Attademo L. 2020. Air pollutants and daily hospital admissions for psychiatric care: a review. Psychiatr Serv. 71(12):1270–1276. doi: 10.1176/appi.ps.201800565.

Borroni E, Pesatori AC, Bollati V, Buoli M, Carugno M. 2022. Air pollution exposure and depression: a comprehensive updated systematic review and meta-analysis. Environ Pollut. 292(Pt A):118245. doi: 10.1016/j.envpol.2021.118245.

Brokamp C, Strawn JR, Beck AF, Ryan P. 2019. Pediatric psychiatric emergency department utilization and fine particulate matter: a case-crossover study. Environ Health Perspect. 127(9):97006. doi: 10.1289/EHP4815.

Chen J, Jahn HJ, Sun HZ, Ning Z, Lu W, Ho KF, Ward TJ. 2022. Validity of using ambient concentrations as surrogate exposures at the individual level for fine particle and black carbon: a systematic review and meta-analysis. Environ Pollut. 312:120030. doi: 10.1016/j.envpol.2022.120030.

Cole TB, Coburn J, Dao K, Roqué P, Chang YC, Kalia V, Guilarte TR, Dziedzic J, Costa LG. 2016. Sex and genetic differences in the effects of acute diesel exhaust exposure on inflammation and oxidative stress in mouse brain. Toxicology. 374:1–9. doi: 10.1016/j.tox.2016.11.010.

Environmental Protection Administration Taiwan Air Quality Monitoring Network. 2021. https://airtw.epa.gov.tw/ENG/Information/Standard/AirQualityIndicator.aspx.

EPA. 2020. Air quality annual report of R.O.C. (Taiwan). 2020 (In Chinese). [accessed 2025 Feb 27]. https://www.moenv.gov.tw/page/686030BBD5DFC8DD.

Evangelopoulos D, Katsouyanni K, Keogh RH, Samoli E, Schwartz J, Barratt B, Zhang H, Walton H. 2020. $PM_{2.5}$ and NO_2 exposure errors using proxy measures, including derived personal exposure from outdoor sources: a systematic review and meta-analysis. Environ Int. 137:105500. doi: 10.1016/j.envint.2020.105500.

GBD 2019 Mental Disorders Collaborators. 2022. Global, regional, and national burden of 12 mental disorders in 204 countries and territories, 1990-2019: a systematic analysis for the global burden of disease study 2019. Lancet Psychiatry. 9(2):137–150. doi: 10.1016/S2215-0366(21)00395-3.

Giordano G, Tait L, Furlong CE, Cole TB, Kavanagh TJ, Costa LG. 2013. Gender differences in brain susceptibility to oxidative stress are mediated by levels of paraoxonase-2 expression. Free Radic Biol Med. 58:98–108. doi: 10.1016/j.freeradbiomed.2013.01.019.

Gu X, Guo T, Si Y, Wang J, Zhang W, Deng F, Chen L, Wei C, Lin S, Guo X, et al. 2020. Association between ambient air pollution and daily hospital admissions for depression in 75 Chinese cities. Am J Psychiatry. 177(8):735–743. doi: 10.1176/appi.ajp.2020.19070748.

Hu W, Fang L, Zhang H, Ni R, Pan G. 2023. Changing trends in the air pollution–related disease burden from 1990 to 2019 and its predicted level in 25 years. Environ Sci Pollut Res Int. 30(1):1761–1773. doi: 10.1007/s11356-022-22318-z.

Huang YT, Chen YJ, Chang SH, Kuo CF, Chen MH. 2022. Discharge status validation of the chang gung research database in Taiwan. Biomed J. 45(6):907–913. doi: 10.1016/j.bj.2021.12.006.

Hwang SL, Chi MC, Guo SE, Lin YC, Chou CT, Lin CM. 2018. Seasonal variation and source apportionment of PM2.5-bound trace elements at a coastal area in southwestern Taiwan. Environ Sci Pollut Res Int. 25(9):9101–9113. doi: 10.1007/s11356-017-1144-2.

Hwang SL, Guo SE, Chi MC, Chou CT, Lin YC, Lin CM, Chou YL. 2016. Association between atmospheric fine particulate matter and hospital admissions for chronic obstructive pulmonary disease in Southwestern Taiwan: a population-based study. Int J Environ Res Public Health. 13(4):366. doi: 10.3390/ijerph13040366.

Hwang SL, Lin YC, Guo SE, Chi MC, Chou CT, Lin CM. 2017. Emergency room visits for respiratory diseases associated with ambient fine particulate matter in Taiwan in 2012: a population-based study. Atmos Pollut Res. 8(3):465–473. doi: 10.1016/j.apr.2016.11.008.

Hwang SL, Lin YC, Guo SE, Chou CT, Lin CM, Chi MC. 2017. Fine particulate matter on hospital admissions for acute exacerbation of chronic obstructive pulmonary disease in southwestern Taiwan during 2006-2012. Int J Environ Health Res. 27(2):95–105. doi: 10.1080/09603123.2017.1278748.

Hwang SL, Lin YC, Lin CM, Hsiao KY. 2017. Effects of fine particulate matter and its constituents on emergency room visits for asthma in southern Taiwan during 2008-2010: a population-based study. Environ Sci Pollut Res Int. 24(17):15012–15021. doi: 10.1007/s11356-017-9121-3.

Jaakkola JJ. 2003. Case-crossover design in air pollution epidemiology. Eur Respir J Suppl. 21(40 suppl):81s–85s. doi: 10.1183/09031936.03.00402703.

Lee M, Lin L, Chen CY, Tsao Y, Yao TH, Fei MH, Fang SH 2020. Forecasting air quality in Taiwan by using machine learning. Sci Rep. 10(1):4153. doi: 10.1038/s41598-020-61151-7.

Lee W, Byun S, Jung J, Kim H, Ha TH, Myung W, Lee H. 2022. Short-term air pollution exposure and exacerbation of psychosis: a case-crossover study in the capital city of South Korea. Atmos Environ. 269:118836. doi: 10.1016/j.atmosenv.2021.118836.

Lee YY, Hsieh YK, Chang-Chien GP, Wang W. 2019. Characterization of the air quality index in Southwestern Taiwan. Aerosol Air Qual Res. 19(4):749–785. doi: 10.4209/aaqr.2019.02.0080.

Li H, Cai J, Chen R, Zhao Z, Ying Z, Wang L, Chen J, Hao K, Kinney PL, Chen H, et al. 2017. Particulate matter exposure and stress hormone levels: a randomized, double-blind, crossover trial of air purification. Circulation. 136(7):618–627. doi: 10.1161/CIRCULATIONAHA.116.026796.

Li H, Zhang S, Qian ZM, Xie XH, Luo Y, Han R, Hou J, Wang C, McMillin SE, Wu S, et al. 2020. Short-term effects of air pollution on cause-specific mental disorders in three subtropical Chinese cities. Environ Res. 191:110214. doi: 10.1016/j.envres.2020.110214.

Lin CH, Wang CY, Chen KF, Chiu S-P, Huang W-T, Fan S-Y. 2024. The trajectory of smoking cessation after treatment and its related factors in Taiwan. Sci Rep. 14(1):13270. doi: 10.1038/s41598-024-64311-1.

Lin HC, Tang TC, Yen JY, Ko CH, Huang CF, Liu SC, Yen CF. 2008. Depression and its association with self-esteem, family, peer and school factors in a population of 9586 adolescents in southern Taiwan. Psychiatry Clin Neurosci. 62(4):412–420. doi: 10.1111/j.1440-1819.2008.01820.x.

Lin H, Guo Y, Kowal P, Airhihenbuwa CO, Di Q, Zheng Y, Zhao X, Vaughn MG, Howard S, Schootman M, et al. 2017. Exposure to air pollution and tobacco smoking and their combined effects on depression in six low- and middle-income countries. Br J Psychiatry. 211(3):157–162. doi: 10.1192/bjp.bp.117.202325.

Lo K, Chiang LL, Hsu SM, Tsai CY, Wu D, Chou CJ, Chuang HC, Liu WT. 2021. Association of short-term exposure to air pollution with depression in patients with sleep-related breathing disorders. Sci Total Environ. 786:147291. doi: 10.1016/j.scitotenv.2021.147291.

Maclure M. 1991. The case-crossover design: a method for studying transient effects on the risk of acute events. Am J Epidemiol. 133(2):144–153. doi: 10.1093/oxfordjournals.aje.a115853.

Ministry of Health and Welfare. National health expenditure data. 2021. https://dep.mohw.gov.tw/DOS/lp-5103-113.html.

Morgan TE, Davis DA, Iwata N, Tanner JA, Snyder D, Ning Z, Kam W, Hsu YT, Winkler JW, Chen JC, et al. 2011. Glutamatergic neurons in rodent models respond to nanoscale particulate urban air pollutants in vivo and in vitro. Environ Health Perspect. 119(7):1003–1009. doi: 10.1289/ehp.1002973.

Muhsin HA, Steingrimsson S, Oudin A, Åström DO, Carlsen HK. 2022. Air pollution and increased number of psychiatric emergency room visits: a case-crossover study for identifying susceptible groups. Environ Res. 204(Pt A):112001. doi: 10.1016/j.envres.2021.112001.

Murray AJ, Rogers JC, Katshu MZUH, Liddle PF, Upthegrove R. 2021. Oxidative stress and the pathophysiology and symptom profile of schizophrenia spectrum disorders. Front Psychiatry. 12:703452. doi: 10.3389/fpsyt.2021.703452.

Pan YJ, Kuo KH, Yeh LL. 2019. Healthcare cost, service use and mortality in major psychiatric disorders in Taiwan. J Affect Disord. 246:112–120. doi: 10.1016/j.jad.2018.12.046.

Qiu X, Shi L, Kubzansky LD, Wei Y, Castro E, Li H, Weisskopf MG, Schwartz JD. 2023. Association of long-term exposure to air pollution with late-life depression in older aAdults in the US. JAMA Netw Open. 6(2):e2253668. doi: 10.1001/jamanetworkopen.2022.53668.

Sang S, Chu C, Zhang T, Chen H, Yang X. 2022. The global burden of disease attributable to ambient fine particulate matter in 204 countries and territories, 1990-2019: a systematic analysis of the global burden of disease study 2019. Ecotoxicol Environ Saf. 238:113588. doi: 10.1016/j.ecoenv.2022.113588.

Sarnat SE, Coull BA, Schwartz J, Gold DR, Suh HH. 2006. Factors affecting the association between ambient concentrations and personal exposures to particles and gases. Environ Health Perspect. 114(5):649–654. doi: 10.1289/ehp.8422.

Shin J, Park JY, Choi J. 2018. Long-term exposure to ambient air pollutants and mental health status: a nationwide population-based cross-sectional study. PLOS ONE. 13(4):e0195607. doi: 10.1371/journal.pone.0195607.

Su SY, Liaw YP, Jhuang JR, Hsu SY, Chiang CJ, Yang YW, Lee WC. 2019. Associations between ambient air pollution and cancer incidence in Taiwan: an ecological study of geographical variations. BMC Public Health. 19(1):1496. doi: 10.1186/s12889-019-7849-z.

Sun DA, Sombati S, DeLorenzo RJ. 2001. Glutamate injury-induced epileptogenesis in hippocampal neurons: an in vitro model of stroke-induced "epilepsy". Stroke. 32(10):2344–2350. doi: 10.1161/hs1001.097242.

Tai SY, Ma TC, Wang LC, Yang YH. 2014. A community-based walk-in screening of depression in Taiwan. Sci World J. 2014:184018. doi: 10.1155/2014/184018.

Tsai MS, Lin MH, Lee CP, Yang YH, Chen WC, Chang GH, Tsai YT, Chen PC, Tsai YH. 2017. Chang Gung Research Database: a multi-institutional database consisting of original medical records. Biomed J. 40(5):263–269. doi: 10.1016/j.bj.2017.08.002.

Tsai SS, Chiu YW, Weng YH, Yang CY. 2021. Relationship between fine particulate air pollution and hospital admissions for depression: a case-crossover study in Taipei. J Toxicol Environ Health A. 84(17):702–709. doi: 10.1080/15287394.2021.1932652.

Wang F, Chen T, Chang Q, Kao YW, Li J, Chen M, Li Y, Shia BC. 2021. Respiratory diseases are positively associated with $PM_{2.5}$ concentrations in different areas of Taiwan. PLOS ONE. 16(4):e0249694. doi: 10.1371/journal.pone.0249694.

Wang KC, Lo YC, Liao CC, Jou YY, Huang HB. 2022. Associations between symptoms of depression and air pollutant exposure among older adults: results from the Taiwan longitudinal study on aging (TLSA). Front Public Health. 9:779192. doi: 10.3389/fpubh.2021.779192.

Wei Y, Qiu X, Yazdi MD, Shtein A, Shi L, Yang J, Peralta AA, Coull BA, Schwartz JD. 2022. The impact of exposure measurement error on the estimated concentration-response relationship between long-term exposure to $PM_{2.5}$ and mortality. Environ Health Perspect. 130(7):77006. doi: 10.1289/EHP10389.

Weng YL, Liang CC, Tseng CC, Lee SY, Yeh GL. 2021. A survey of $PM_{2.5}$ preventive behavioral intention and related factors among community elderly in Northern Taiwan. Med (Baltim). 100(29):e26675. doi: 10.1097/MD.0000000000026675.

Yoo EH, Roberts John E, Eum Y, Li X, Chu L, Wang P, Chen K. 2023. Short-term exposure to air pollution and mental disorders: a case-crossover study in New York City. Environ Res: Health. 1(1):015001. doi: 10.1088/2752-5309/ac6439.

LWT - Food Science and Technology 222 (2025) 117641

Contents lists available at ScienceDirect

LWT

journal homepage: www.elsevier.com/locate/lwt

Peptide from tempeh-like fermented *Chenopodium formosanum* counters senescence while enhancing antioxidant ability in non-replicative aging

Chen-Che Hsieh [a,1], Hui-Wen Lin [b,c,1], Hsiao-Chu Huang [d], Darin Khumsupan [e], Szu-Chuan Shen [f], Shin-Ping Lin [g,h,i], Chang-Wei Hsieh [j,k], Tsung-Yu Tsai [l], Sirima Suvarnakuta Jantama [m], Hsing-Chun Kuo [n,o,p,q,*], Kuan-Chen Cheng [d,e,l,r,s,**]

[a] *Department of Seafood Science, National Kaohsiung University of Science and Technology, No. 142, Haijhuan Rd., Nanzih District, Kaohsiung, 81157, Taiwan R.O.C*
[b] *Institute of Medicine, Chun Shan Medical University, Taichung, Taiwan R.O.C*
[c] *Department of Medical Research, Chung Shan Medical University Hospital, Taichung, Taiwan R.O.C*
[d] *Institute of Food Science and Technology, National Taiwan University, No. 1, Sec. 4, Roosevelt Rd., Taipei, Taiwan R.O.C*
[e] *Institute of Biotechnology, National Taiwan University, No. 1, Sec. 4, Roosevelt Rd., Taipei, Taiwan R.O.C*
[f] *Undergraduate and Graduate Programs of Nutrition Science, School of Life Science, National Taiwan Normal University, Taipei, Taiwan R.O.C*
[g] *School of Food Safety, Taipei Medical University, 250 Wu-Hsing Street, Taipei 11042, Taiwan R.O.C*
[h] *Ph.D. Program in Drug Discovery and Development Industry, College of Pharmacy, Taipei Medical University, 250 Wu-Hsing Street, Taipei 11031, Taiwan R.O.C*
[i] *Research Center of Biomedical Device, Taipei Medical University, 250 Wu-Hsing Street, Taipei 11031, Taiwan R.O.C*
[j] *Department of Food Science and Biotechnology, National Chung Hsing University, 145 Xingda Rd, South Dist, Taichung, 40227, Taiwan R.O.C*
[k] *Department of Food Science, National Ilan University, No. 1, Sec. 1, Shennong Rd., Yilan City, Yilan County, 260007, Taiwan R.O.C*
[l] *Department of Food Science, Fu Jen Catholic University, No. 510, Zhongzheng Rd., Xinzhuang Dist., New Taipei City, 242062, Taiwan R.O.C*
[m] *Faculty of Pharmaceutical Sciences, Ubon Ratchathani University, Warinchamrap, Ubon Ratchathani, 34190, Thailand*
[n] *Department of Nursing, Division of Basic Medical Sciences, Chang Gung University of Science and Technology, Chiayi, Taiwan R.O.C*
[o] *Research Fellow, Chang Gung Memorial Hospital, Chiayi, Taiwan R.O.C*
[p] *Chronic Diseases and Health Promotion Research Center, Chang Gung University of Science and Technology, Chiayi, Taiwan R.O.C*
[q] *Research Center for Food and Cosmetic Safety, College of Human Ecology, Chang Gung University of Science and Technology, Taoyuan, Taiwan R.O.C*
[r] *Department of Optometry, Asia University, 500, Lioufeng Rd., Wufeng, Taichung, Taiwan R.O.C*
[s] *Department of Medical Research, China Medical University Hospital, China Medical University, 91, Hsueh-Shih Road, Taichung, Taiwan R.O.C*

ARTICLE INFO

Keywords:
Chenopodium formosanum
Glycine-rich peptides
Non-replicative aging
Nrf2 pathway
Oxidative stress

ABSTRACT

The study assesses the protective effects of glycine-rich peptide (GRP) from tempeh-like fermented *Chenopodium formosanum* against non-replicative aging. By pretreating Hs68 cells with GRP and irradiating them with UVA, a reduction in oxidative stress was observed which positively contributed to cell survival rate. Moreover, transcriptomic analysis demonstrated that pretreatment with GRP prevents the downregulation of oxidative stress responses and an upregulated expression of cell cycle. Additionally, GRP was found to increase the expression of Nrf2 pathway while decreasing the expressions of *p53* and *p21*. These findings were further investigated in *Caenorhabditis elegans*, where GRP treatment could extend lifespans and improve resistance to oxidative stress. Finally, molecular docking studies indicated GRP binds to the KEAP-BTB inhibitory site inhibitory site, potentially inhibiting activity of single O-linked β-N-acetylglucosamine transferase which facilitates activation of Nrf2

Abbreviations: ACE, angiotensin-converting enzyme; ARE, antioxidant response element; CCK-8, cell counting kit-8; BP, biological process; ChIP, chromatin immunoprecipitation; c-Fos, fos proto-oncogene; c-Jun, jun proto-oncogene; DEGs, differential expression genes; DPP4, dipeptidyl peptidase-4; DMSO, dimethyl sulfoxide; FCS, fermented *Chenopodium formosanum* sprouts; FudR, floxuridine; gcs, glutamylcysteine synthetase; GO, gene ontology; GRP, glycine-rich peptide; GSR, glutathione reductase; gst, glutathione S-transferase; HO-1, heme oxygenase-1; IIS pathway, insulin/insulin-like signaling pathway; Keap1-BTB, kelch-like ech-associated protein 1- broad complex, tramtrack, and bric-a-brac; *Mus musculus*, Mouse reference genome; NAC, N-acetylcysteine; NF-kB, Nuclear factor kappa B; NGM agar, nematode growth medium; Nrf2, nuclear factor, erythroid 2; NQO1, NAD(P)H: quinone oxidoreductase 1; OGT, single O-linked β-N-acetylglucosamine transferase; *p53*, cellular tumor antigen; *p21*, cyclin-dependent kinase inhibitor 1; ROS, reactive oxygen species; *Skn-1*, transcription factor skinhead-1; SA-β-Gal, senescence-associated β-galactosidase; SOD, superoxide dismutase 1; UV, ultraviolet.

* Corresponding author. Department of Nursing, Division of Basic Medical Sciences, Chang Gung University of Science and Technology, Chiayi, Taiwan, ROC.
** Corresponding author. Institute of Food Science and Technology, National Taiwan University, No. 1, Sec. 4, Roosevelt Rd., Taipei, Taiwan, ROC.
E-mail address: kccheng@ntu.edu.tw (K.-C. Cheng).

[1] Dr. Chen-Che Hsieh and Dr. Hui-Wen Lin did the same contribution on this research.

https://doi.org/10.1016/j.lwt.2025.117641
Received 23 January 2025; Received in revised form 7 March 2025; Accepted 11 March 2025
Available online 13 March 2025
0023-6438/© 2025 The Authors. Published by Elsevier Ltd. This is an open access article under the CC BY license (http://creativecommons.org/licenses/by/4.0/).

pathway. These results highlight the capability of GRP as a protective agent against oxidative stress and non-replicative aging.

1. Introduction

Chenopodium formosanum is a pseudo-cereal native to Taiwan which is commonly known as Taiwanese quinoa (Huang and Chien, 2020). *C. formosanum* is rich in nutrients and antioxidants, which can potentially serve as an excellent precursor of bioactive peptides (Kuo et al., 2021). As a result, the fermentation of *C. formosanum* can further amplify these bioactive ingredients. Hsieh, Yu, Cheng, et al. (2023) used *R. oligosporus,* which possesses rich proteolytic enzymes, to ferment *C. formosanum* and discovered seven new glycine-rich peptides from the hydrolysate which can act as antioxidants, reducing intracellular oxidative stress (Hsieh, Yu, Cheng, et al., 2023), One glycine-rich peptide (GGGGGKP) obtained from fermented *C. formosanum* can reduce exogenous oxidative stress by regulating the phosphorylation of NF-κB, inducing anti-inflammatory and ROS suppression effects. The preparation method for this glycine-rich peptide involved initially obtaining a low-molecular-weight protein fraction using MWCO. This was followed by desalting and gel filtration through FPLC, using Sephadex G-25 superfine and Superdex 30 Increase SEC column to isolate a single peptide. Subsequently, LC-ESI-Q-TOF-MS/MS analysis was performed, and the peptide sequence composition was confirmed by matching against a database (Hsieh, Yu, Cheng, et al., 2023).

Furthermore, other glycine-rich peptides (GGLGDVLGGLP and GEGW) derived from food or plants such as *C. quinoa* and *Acheta domesticus*, served as promising protectants against free radicals and oxidative stress due to their unique sequence compositions (Mirzaei et al., 2018; Ren et al., 2022; Vilcacundo et al., 2017). This phenomenon is due to *R. oligosporus* utilizing its endogenous enzymes (amylase, β-glucosidase, and proteinase) to cleave covalently bound phenolic compounds from cell walls of the plant substrates, metabolizing them into small hydrophobic peptides and phenolic compounds. Moreover, it was found that these bioactive peptides do not cause bioaccumulation (Guo et al., 2023; Hsieh et al., 2023). Therefore, the tempeh-like fermented *C. formosanum* may potentially possess multiple antioxidants, anti-ACE, and anti-DPP4 agents (Hsieh, Yu, Kuo, et al., 2023).

Many studies have shown that substances extracted from natural fruits and herbs possess antioxidant activity and can modulate relevant signaling pathways to achieve bioactive effects. For instance, myricitrin from Chinese bayberry has been found to prevent peroxynitrite-mediated glutathione depletion in astrocytes. Flavonoids in tartary buckwheat have demonstrated both antioxidant and antidiabetic effects. Additionally, lemon verbena has been shown to exert antioxidative properties that delay damage under glucotoxic conditions in adipocytes. Therefore, it is feasible to use bioactive substances from natural fruits and herbs to regulate diseases induced by oxidative stress (Bao et al., 2016; Chen et al., 2013; Olivares-Vicente et al., 2024).

Recent studies have demonstrated that microbial strains such as *Lactobacillus*, and *Rhizopus* can generate bioactive peptides with antioxidant and anti-aging properties. Hydrolysis using lactic acid bacteria (LAB) has been shown to produce bioactive peptides with improved antioxidant activity and reduced cellular protein production, presenting a promising strategy for developing functional foods with enhanced nutritional benefits (Lee et al., 2023). Bioactive peptides from fermented *C. formosanum* sprouts have shown potential as antioxidant agent (Hsieh, Yu, Cheng, et al., 2023). *C. formosanum* protein releases bioactive peptides during germination, fermentation, and digestion. Enzymatic hydrolysis using microbial fermentation and bioconversion is the primary method for preparing these peptides. The hydrolysate is assessed for biological activities, such as angiotensin I converting enzyme and antioxidant effects (Hsieh, Yu, Kuo, et al., 2023). Atmospheric radiation, a main factor in photoaging, produces ROS, damaging proteins, lipids, nucleic acids, and cell membranes, leading to reduced cellular integrity and mitochondrial dysfunction. Bioactive peptides may use their antioxidant properties to mitigate oxidative stress caused by photoaging (Lu et al., 2023).

Non-replicative aging stems from the free radical theory which posits that excessive free radicals produced during mitochondrial metabolic processes, such as cellular respiration, play a significant role in aging (Nandita et al., 2020). This concept has been validated by numerous *in vitro* and in vivo models that simulate the damages caused by free radicals. For instance, UV radiation-induced ROS in skin cells leads to photoaging (Fu et al., 2014; Huang & Chien, 2020), and the resulting ROS stimulates cellular pathways which ultimately triggers the release of inflammatory cytokines (Salminen et al., 2022). In addition, the production of ROS can be influenced by the insulin/insulin-like signaling (IIS) pathway. One study examined IIS pathway (SKN-1/NRF2) in nematodes and discovered that it could serve as a method to predict life span (Xiong et al., 2021). Consequently, examining gene expression associated with IIS pathways in an animal model may be a practical tool to verify the biological activity of substances extracted from food (Ye et al., 2021).

This study investigates the anti-aging effects of glycine-rich peptide (GRP) from fermented *C. formosanum* sprout. Employing Hs68 cells and *Caenorhabditis elegans* as the models, GRP's abilities to enhance cell viability, reduce oxidative stress, and its impact on aging-related enzymes and genes, mainly through the Nrf2 pathway, are investigated. This study seeks to establish its unique advantages in mitigating oxidative stress and extending lifespan. By addressing the gap in knowledge regarding the role of GRPs in non-replicative aging, this study contributes to the growing field of functional food research and the development of dietary interventions for age-related oxidative stress management.

2. Materials and methods

2.1. Materials

C. formosanum grains were purchased from Quinoa Green Biotech Co., Ltd (Taichung, Taiwan). *Rhizopus microsporus* var. *oligosporus* BCRC 31996 and human foreskin fibroblast (Hs68) cell line were obtained from Bioresource Collection and Research Center (BCRC) (Hsinchu, Taiwan). *Caenorhabditis elegans* and *Escherichia coli* OP50 were obtained from the National Core Facility for Biopharmaceuticals (Taipei, Taiwan). Medium ingredients such as peptone, yeast extract, potato dextrose broth, lysogeny broth, and agar were purchased from BioShop Canada Inc. (Ontario, Canada). EDTA solution, trypsin, and antibiotics (penicillin/streptomycin) were purchased from GE Healthcare Life Science (Logan, Utah, U.S.A). Vivaspin 15R and Vivaspin Turbo 15 were obtained from Sartorius Stedim Biotech GmbH (Goettingen, Germany). Cell culture media (Dulbecco's Modified Eagle Medium, or DMEM, supplemented with high glucose, phenol red, and L-glutamine) and fetal bovine serum were retrieved from GE Healthcare Life Science. Senescence β-Galactosidase Staining Kit (Abbkine, Inc., Wuhan, China) and Radio-Immunoprecipitation Assay (RIPA) Buffer (10X) were obtained from Cell Signaling Technology (Beverly, MA, U.S.A). CCK-8 was purchased from Cyrus Bioscience (Neihu, Taiwan). Nrf2 antibody (GTX103322) was purchased from GeneTex (Hsinchu, Taiwan). All chemicals used in this study were of analytical grade and purchased from Merck (Burlington, MA, U.S.A).

2.2. Preparation of FCS

C. formosanum sprouts, weighing 1.5 kg (wet condition, the moisture content was 63.25 ± 4.15 g/100 g), were subjected to sterilization in a bioreactor (FS-V-SA05P, Major Science, Taoyuan, Taiwan). The sterilization process was carried out for 20 min at 121 °C. Subsequently, 75 mL of *R. oligosporus* spores, with the concentration of 10^6 spores/mL (constituting 5 mL/100 g of the total), were inoculated onto the sterilized sprouts. The methodology employed for the solid-state fermentation process was referred from previous research (Hsieh, Yu, Kuo, et al., 2023), which involved maintaining the temperature of 35 °C, aeration volume of 0.4 vvm (air volume/culture volume/min), and rotation speed at 5 rpm. The fermentation duration was set to four days. After the fermentation, all the fermented products were collected and stored at −20 °C.

2.3. Isolation of GRP from FCS proteins

The glycine-rich peptide was prepared as descripted in previous research (Hsieh, Yu, Cheng, et al., 2023). Briefly, the lyophilized FCS was ground into powder, sieved through a 30-mesh screen, and stored at −20 °C. The FCS was degreased by submerging it in n-hexane (1:3 w/v) at 37 °C for 2 h. After drying the mixture with a rotary vacuum evaporator, the degreased FCS sample was mixed with phosphate-buffered saline (1:10 w/v) until homogenized. The homogenized sample was centrifuged at 15,000×*g* for 30 min at 4 °C, yielding a supernatant. This supernatant was heated to 70 °C to inactivate enzymes. Following a referenced protein extraction method, ammonium sulfate was added to the FCS supernatant to reach 90 % saturation, inducing salting-out. The resultant mixture was again centrifuged under similar conditions to collect protein precipitate. Afterward, GRP from FCS was purified using Superdex 30 Increase SEC column with fast protein liquid chromatography (ÄKTA purifier UPC 10, GE Healthcare Life Science, Utah, USA). The flow rate was set to 0.5 mL/min. Standards including Gly-Tyr, Leu enkephalin, Met enkephalin, and Val-Tyr-Val were used in the detection of glycine-rich peptide. The sequence of glycine-rich peptide is Gly- Gly- Gly- Gly- Gly-Lys-Pro, which was identified by BIOTOOLS Biotechnology Co., Ltd. (Taipei, Taiwan) (Hsieh, Yu, Kuo, et al., 2023).

2.4. Cell culture and UVA irradiation

The cells underwent pretreatment with 50 and 100 μg/mL GRP, which were diluted in serum-free DMEM, for a duration of 24 h. Subsequently, the cells were washed with 100 μL of PBS, followed by 100 μL of phenol red-free DMEM. For UV-A irradiation, the cells in a 96-well plate were positioned directly under the UVP crosslinkers (365 nm, Chingtek Instrument Co., Ltd., New Taipei, Taiwan). The Hs68 cells were positioned 10 cm away from an UVP crosslinkers and were exposed to UVA radiation at a dose of 15 J/cm^2 (λ_{max}, 365 nm) for approximately 75 min (Hsiao et al., 2023; Lu et al., 2023). The irradiation dose was calculated based on Equation (2.1). 1 mmol/L NAC was used as positive control.

$$\text{Dosage}\left(\text{J}/\text{cm}^2\right) = \text{Intensity}\left(\text{mW}/\text{cm}^2\right) * \text{time} \qquad \text{(Equation 2.1)}$$

2.5. Cell viability

In the cell viability assessment, the Cell Counting Kit-8 (CCK-8, Dojindo Molecular Technologies, Inc., Rockville, MD, USA) was employed and the procedure was based on the manufacturer's instructions (Hsiao et al., 2023).

2.6. ROS production

In the study, 5×10^5 cells were seeded in each well of a 96-well plate. These cells were then pretreated with the GRP at a concentration of 50 and 100 μg/mL for 24 h. After GRP was removed, the cells were subjected to UVA exposure at a dose of 15 J/cm^2. Subsequently, H_2DCFDA was added, and the cells were cultured for an additional 30 min. Imaging was performed using a fluorescent microscope. The relative fluorescence intensity of these images was analyzed utilizing ImageJ image analysis software (NIH, Bethesda, MD, USA) (Hseu et al., 2018).

2.7. Detection of senescence-associated β-galactosidase activity

SA-β-Gal activity was carried out based on the modified method described by related researches (Han et al., 2017; Makpol et al., 2011). Cells were stained using the SA-β-Gal staining kit (Abbkine, Inc., Wuhan, China). The staining procedure was adhered to the manufacturer's protocol. Cell images were captured using a microscope at 400x magnification under three bright fields. The cells exhibiting blue-green stains were counted. The percentage of SA-β-Gal positive cells was determined by the ratio of stained cells to the total number of cells which indicates the presence of cellular senescence.

2.8. RNA-sequencing

Following the same cell culture procedure, cells were pre-treated with GRP and then exposed to UVA for 75 min. Afterward, the cells were harvested and RNA was extracted for subsequent experiments. The construction of the cDNA library and the sequencing analysis were carried out by BIOTOOLS Biotechnology Co., Ltd. (Taipei, Taiwan). High-throughput paired-end 150 bp sequencing was performed using the Illumina NovaSeq 6000 system (Illumina, San Diego, CA, U.S.A). The gene expression analysis was referenced from the Mus musculus-GRCm38 gene database and was calculated using feature counts. DEGs between each treatment group were identified using DESeq2, which ensured biological repeatability. The criteria for significant differential expression were set at a log2 fold change ≥2 and an adjusted p-value of ≤0.05. These parameters were applied in the GO analysis, as described by previous research (An et al., 2021; Farrukh et al., 2014).

2.9. Quantitative PCR (qPCR) analysis

RNA samples were reverse transcribed into cDNA by utilizing the GScript First Strand Synthesis Kit (GeneDireX, USA). Subsequently, quantitative PCR analysis was performed to amplify the promoter region of the DNA fragment. Specific primers were employed for the detection, as detailed in Table S1. To standardize the results, the relative abundance of housekeeping genes was exploited as the internal standard. Data regarding fold enrichment and the percentage of specific genes were collected and calculated (Chou and Ting, 2023).

2.10. ChIP analysis

After the treatments, the cells were incubated with 1 % formaldehyde at 37 °C to facilitate DNA–protein cross-linking. Then, glycine (125 mmol/L) was added to the cells and allowed to react for 5 min before transferring to lysis buffer. The cells were incubated overnight at 4 °C with Nrf2 antibodies in the presence of protease inhibitors, followed by washing with elution buffer. The cross-linked immunoprecipitated complexes were then incubated at 65 °C for 2 h. DNA fragments were subsequently purified using the ChIP DNA Clean & Concentrator Kit (Zymo, Tustin, CA, U.S.A), and quantitative PCR analysis was conducted to amplify the promoter regions of the GSR, SOD, and NQO1 genes using specific primers (as listed in Table S2) (Ryu et al., 2019; Tanigawa et al., 2007; Wang, Xu, et al., 2016). Data on the fold enrichment and percentage of specific genes in ChIP were collected and calculated according to the method described by previous researches (Harvey et al., 2009; Marionnet et al., 2010).

2.11. Lifespan assay and pharyngeal pumping

The method was adapted from previous research with modifications (Wang et al., 2020). Briefly, 30–50 L4 stage *C. elegans* N2 (Wild-type) were placed on NGM agar with *E. coli* OP50, 1 mmol/L NAC, and either 50 or 100 μg/mL GRP. The worms were cultured at 20 °C and periodically transferred to fresh agar every two days to maintain adequate food supply. They were monitored until death to determine their life spans. FudR-added NGM agar was used to inhibit reproduction. The procedures to determine pharyngeal pumping rate and the lifespan assay were obtained from previous research with slightly modifications (How et al., 2018). On the seventh day of the assay, a minimum of 20 worms were examined under a microscope to count their pharyngeal contractions per minute (pumps rate/min).

2.12. Stress resistance

The process to determine stress resistance was based on previous research with alterations: L1 stage *C. elegans* N2 (Wild-type) in M9 buffer were treated in a 96-well plate with *E. coli*, 1 mmol/L NAC, and either 50 or 100ug/mL GRP for 48 h. Post-treatment was carried out by adding 50 μL Juglone (250 μmol/L final concentration). Juglone was prepared by diluting a hundred folds of 50 mmol/L DMSO stock with M9 buffer. The survival rates were observed after 6 h (Shi et al., 2012).

2.13. Molecular docking simulation

The crystal structure of Keap1 (BTB domain) was retrieved from the Research Collaboratory for Structural Bioinformatics Protein Databank (Keap1-BTB; PDB entry: 4CXT). Utilizing AutoDockTools, all water molecules were removed from the receptor, and hydrogen atoms and Kollman charges were manually added to the structure, as detailed by previous research (Marionnet et al., 2010). Ligand structures were obtained from the PubChem database. Again, AutoDockTools was used to remove water molecules from the receptor. Hydrogen atoms and Gasteiger charges were then added to the ligands. A grid box with the dimension of 36 Å × 51 Å × 45 Å along the X-, Y-, and Z-axes was created to incorporate the Keap1-BTB protein structure, while the grid spacing was set at 0.375 Å. The grid center for Keap1-BTB was determined to be X = 5.043, Y = −9.302, and Z = −13.046. The docked conformations between Keap1-BTB and various compounds were ranked based on the predicted binding free energy (affinity) values, which are expressed in

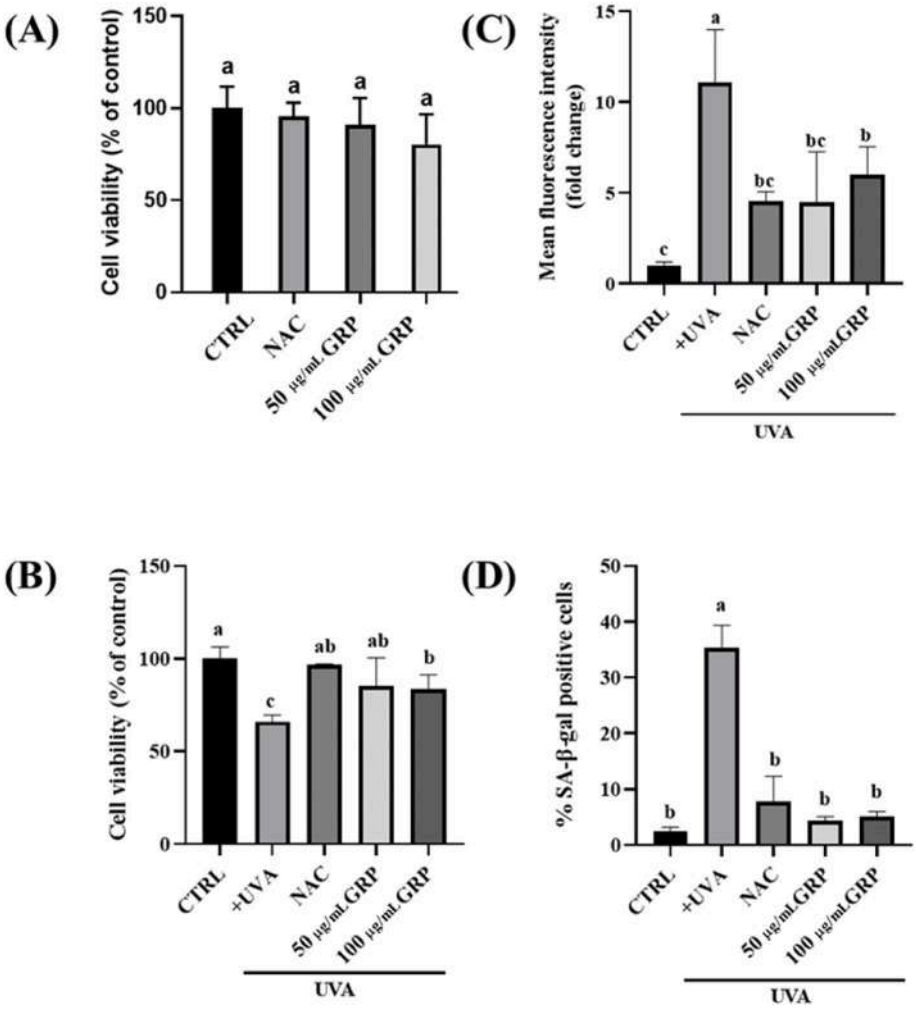


Fig. 1. Effect of GRP on SA-β-gal activity and ROS production in UVA irradiated Hs68 cells. (A) Cell viability at different doses of GRP treatment; (B) Cell viability at different doses of pretreated GRP with UVA irradiation; (C) Mean fluorescence intensity changes according to ImageJ software analysis; (D) Percentage of SA-β-gal positive cells compared to the total Hs68 cell numbers.
The experimental results were repeated three times, and all were expressed in the form of mean ± standard deviation (SD). Different letters indicate significant differences ($p < 0.05$).
CTRL: Without treatment; UVA: Being exposed to 15 kJ/cm^2 UVA; NAC: Pretreated with 1 mmol/L N-acetylcysteine before 15 kJ/cm^2 UVA-irradiation. GRP: Pretreated with 50 or 100ug/mL GRP before 15 kJ/cm^2 UVA-irradiation.

kcal/mol. The docking results for all compounds that interacted with Keap1-BTB were visualized using the Pymol software (Shi et al., 2012).

2.14. Statistical methodology

All experiments were performed in triplicate, and the resulting measurement values are presented as mean ± standard deviation. Statistical analysis were performed using IBM SPSS 20 (International Business Machines Co., New York, USA). The differences between mean values were assessed using analysis of variance, with Duncan's multiple range test for post-hoc comparisons. The p-value of less than 0.05 was deemed statistically significant.

3. Results and discussion

3.1. GRP modulates ROS production and prevents UVA-induced aging

As illustrated in Fig. 1A, different concentrations of GRP and 1 mmol/L NAC demonstrate minimal effects to cell viability, which indicates their biocompatibility. After inducing the cells with 15 J/cm^2 UVA irradiation, it can be observed that cells pretreated with NAC (1 mmol/L) and GRP at 50 μg/mL showed an increase in survival rate (Fig. 1B). Furthermore, 50 μg/mL GRP possesses a relatively similar modulating effect to NAC on the pretreated cells, suggesting that GRP may be able to alleviate oxidative stress induced by UVA. This highlights GRP's ability to attenuate damages from photoaging, as can be seen in Fig. 1C and S1A. Moreover, it can also help eliminate DNA-damaging ROS products such as hydrogen peroxide and lipid peroxides (Hsieh, Yu, Cheng, et al., 2023). In a study conducted by Rom et al. (2022), they found that glycine supplementation could enhance GSH production and reduce oxidative stress, thereby alleviating the pathogenesis of atherosclerosis (Rom et al., 2022). Given that GRP is rich in glycine and showing similar antioxidative effects to NAC, supplementation of GRP is speculated to enhance GSH activity, potentially delaying oxidative stress.

Yin and Jiang et al. (2013) reported that β-galactosidase activity in UVA-irradiated fibroblasts is activated in a dose-dependent manner (Yin & Jiang, 2013). By pretreating Hs68 cells with 1 mmol/L NAC as well as GRP at 50 μg/mL and 100 μg/mL, the senescence-associated (SA)-β-gal staining ratios were significantly reduced ($p < 0.05$) by 7.76 ± 4.61 %, 4.36 ± 0.75 %, and 5.06 ± 0.95 %, respectively (Fig. 1D and Fig. S1B). The reduction of cellular senescence indicator like SA-β-gal activity suggests GRP's ability in delaying photoaging. Similarly, the low molecular weight peptides (458 Da) from *Agaricus blazei* also demonstrate a dose-dependent reduction of SA-β-gal-positive cells in a D-galactose-induced senescence model (Feng et al., 2022). These findings imply GRP's potential in combating against non-replicative aging by reducing oxidative stress, which is comparable to other natural health products derived from food.

3.2. Possible mechanism regulated by GRP according to transcriptomic analysis

UV radiation can damage gene expression patterns, altering differential DEGs. After UVA exposure, 2175 DEGs from Hs68 cells were upregulated while 3257 were downregulated. On the other hand, when the cells were pretreated with 100 μg/mL GRP prior to UVA exposure, 494 genes were upregulated, and 655 genes were downregulated, as can be observed in Fig. S2 A and B. These numbers reveal notable differences of gene expression between the experimental groups. Through the bioinformatics database Gene Ontology (GO), variations between groups and genes involved were examined which focused on biological effects and mechanisms within Hs68 cells during GRP pretreatment and after UVA exposure (Thomas et al., 2019). The DEGs, both upregulated and downregulated, underwent GO analysis for functional categorization. Compared to the non-irradiated control group, the UVA-induced group experiences significant upregulation from oxidative stress (Fig. 2A) and reduction in the negative regulation of the cell cycle (Fig. 2B). Conversely, the group pretreated with GRP before UVA exposure shows noticeable downregulation in response to oxidative stress (Fig. 2C) and elevation in the positive regulation of cell cycle (Fig. 2D). The analysis from QuickGO (https://www.ebi.ac.uk/QuickGO/) reveals that the response to oxidative stress (GO:0006979) and regulation of cell cycle (GO:0051726) are categorized under Biological Process. Moreover, as shown in Fig. S2 C, D, post-GRP treatment leads to further downregulation after subjecting the cells to UVA, in addition to an improvement in the positive regulation of the cell cycle (GO:0045787). Thus, GRP can delay cellular aging.

Exposure to 3 J/cm^2 UVA increases oxidative stress by 4 folds which can induce collagen degradation and phosphorylation of c-Fos, c-Jun, and NF-κB in Hs68 cells [17]. In addition, discovered that exposure to 10 J/cm^2 UV results in *p53* mRNA translation and homo-oligomerization in Hs68 cells, leading to G2/M phase arrest (Farrukh et al., 2014). Hence, even UV radiation at low exposure can instigate responses of many transcription factors to alter gene expression. ROS play a crucial role in cellular senescence by activating stress-induced signaling pathways, including MAPK/ERK and PI3K/Akt, which regulate apoptosis and inflammatory responses (Albanesi et al., 2023; Odawara et al., 2024). In particular, excessive ROS production impairs mitochondrial function, leading to a decline in ATP production and increased oxidative damage to lipids, proteins, and DNA (Lebiedzinska-Arciszewska et al., 2024; Li et al., 2022). These effects collectively contribute to non-replicative aging by disrupting cellular homeostasis and promoting SASP expression (Mahmud et al., 2024). Functional enrichment analysis revealed that GRP treatment at 100 μg/mL significantly reduces ($p < 0.05$) intracellular ROS levels by 33 % while modulating the phosphorylation and nuclear translocation of NF-κB (Hsieh, Yu, Cheng, et al., 2023). Furthermore, previous studies have demonstrated that bioactive peptides from fermented sources can activate the Nrf2/Keap1 signaling pathway, thereby upregulating phase II detoxification enzymes and mitigating oxidative damage, given the role of ROS in perpetuating cellular senescence (Lin et al., 2024). Consequently, the method can provide insights into the biological pathways and offer predictions for overall regulatory mechanisms. According to the gene functional enrichment analysis, it is hypothesized that GRP may regulate oxidative stress pathways, altering cell cycle arrest and thereby providing protection against photoaging.

3.3. Enhancing Nrf2 pathway and reducing oxidative stress in counteracting non-replicative aging

Under an oxidative stress condition, the Nrf2 pathway is activated which facilitates the translocation of Nrf2 into the nucleus to bind with antioxidative genes [25]. The interaction results in the production of enzymes, such as HO-1 and NQO1, to alleviate oxidative stress. This finding is highlighted in Ahmed et al. (2017) as it shows the potential of antioxidants in delaying aging (Ahmed et al., 2017). Meanwhile, this study compared the untreated and 100 μg/mL GRP-pretreated cells under UVA radiation (15 J/cm^2). Based on Fig. 3A and B, the pretreated cells exhibited a significant increase ($p < 0.05$) in the expression levels of *Nrf2* (3.86 times) and *HO-1* (2.32 times). The finding aligns with Chu et al. (2016) as they reported that *C. formosanum* extract can activate the Nrf2/HO-1 pathway in Hs68 cells, protecting cells against UV-induced photoaging by upregulating *Nrf2* and *HO-1* expression (Chu et al., 2016). Furthermore, GRP pretreatment at 100 μg/mL significantly decreased *p53* and *p21* expressions by 2.81 and 0.23 folds, respectively, compared to control (Fig. 3C and D). The results from this research study are similar to those found in Chen et al. (2019) as they employed ChIP assays and reported that 1,25-dihydroxyvitamin D3 in natural substances can inhibit ROS production by upregulating the Nrf2 transcription factor (Chen et al., 2019). The upregulation of Nrf2 reduces DNA damage and suppresses *p53* and *p21* gene expression, contributing to the

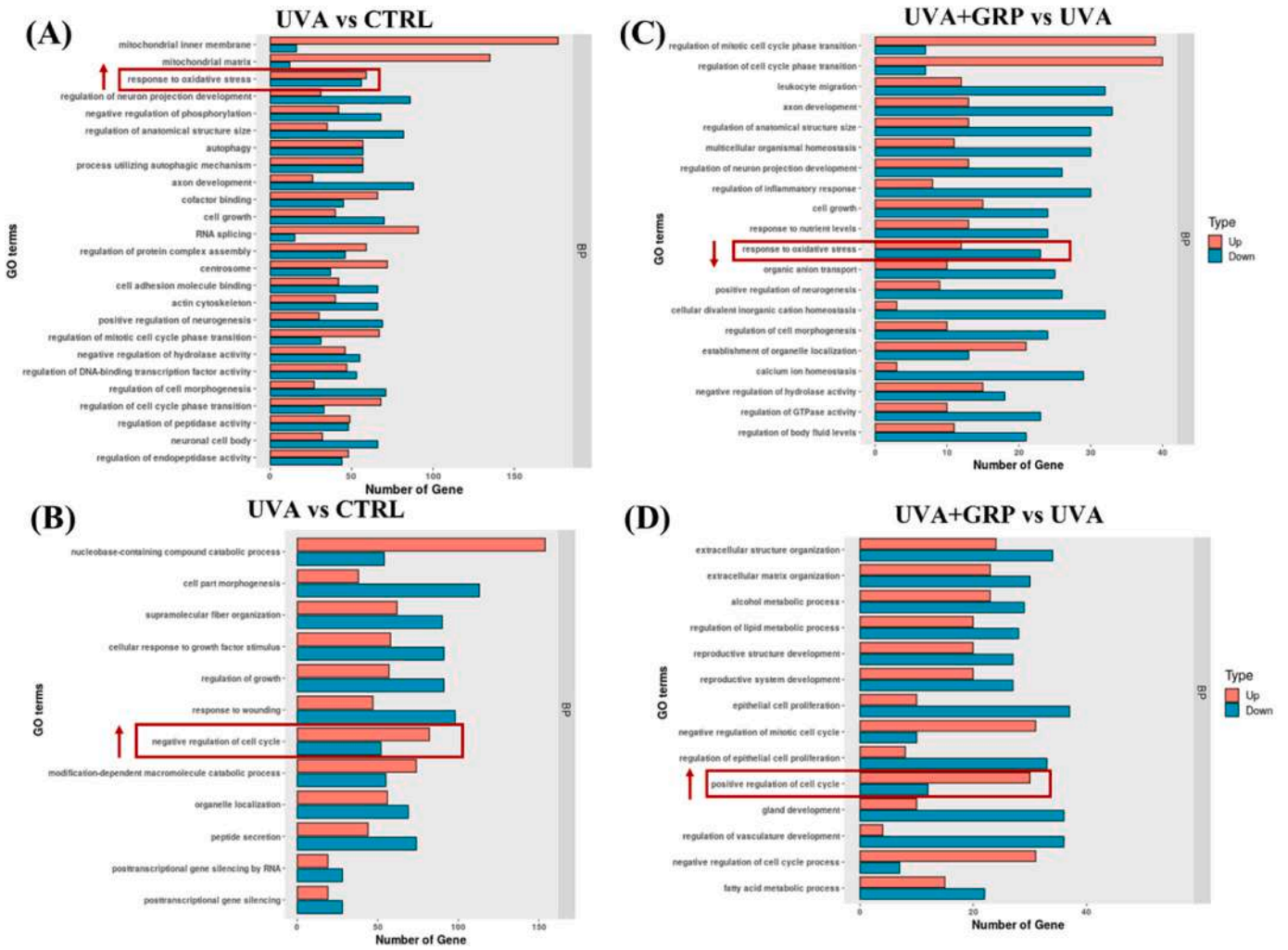


Fig. 2. Gene Ontology (GO) enrichment analysis. (A) UVA vs CTRL groups upregulate responses to oxidative stress; (B) UVA vs CTRL groups modulate the negative cell cycle process; (C) UVA + GRP vs UVA groups downregulate responses to oxidative stress; (D) UVA + GRP vs UVA groups modulate the positive cell cycle process.
BP: Biological process; CTRL: Without treatment; UVA: Being exposed to 15 kJ/cm^2 UVA; NAC: Pretreated with 1 mmol/L N-acetylcysteine before 15 kJ/cm^2 UVA-irradiation. GRP: Pretreated with 50 or 100ug/mL GRP before 15 kJ/cm^2 UVA-irradiation.

delay in cellular aging (Chen et al., 2019). Proteins such as p53 and p21 are identified as inhibitors of cyclin-dependent kinases which can activate senescent cells and arrest them in the G0/G1 phase of cell cycle (Sasaki et al., 2014). These findings emphasize the functions of antioxidants in natural foods for combating cellular aging: They may play a vital role in the enhancement of Nrf2 transcription factor and the activation of ARE.

In addition, Nrf2 activation has been observed to protect cells from oxidative stress by stimulating the expression of key antioxidant enzymes, including SOD, GSR, and NQO1 (Duangjan et al., 2019; Hsieh et al., 2024; Tang et al., 2021). Moreover, Nrf2 plays a crucial role in modulating DNA-protein interactions essential for cellular homeostasis, particularly by regulating gene transcription involved in detoxification and oxidative stress response. This regulatory mechanism is vital for the expression of genes responsible for maintaining redox balance and mitigating oxidative damage. Nrf2 exerts its protective function by binding to antioxidant response elements (AREs) in the promoter regions of target genes, thereby facilitating their transcription and enhancing cellular resilience against oxidative insults (Das et al., 2004; Lopez-Ruiz et al., 2023; Wu et al., 2023). After UVA exposure, the groups pretreated with 50 and 100 μg/mL GRP were observed to have expression upregulation in *GSR* (1.33 and 2.75 times), *SOD* (1.44 and 1.86 times), and *NQO1* (2.27 and 2.49 times) compared to the untreated group with statistically significant differences ($p < 0.05$) (Fig. 3E, F, and G). It can be concluded that GRP reduces oxidative stress induced by UVA through the induction of Nrf2 pathway which suppresses the manifestation of non-replicative aging.

3.4. *Effects of GRP on lifespan extension and stress resistance in C. elegans*

GRP was pretreated on *C. elegans* to determine its role in extending lifespan and improving stress resistance on the organisms. Fig. 4A demonstrates that the survival curves of GRP- and NAC-treated *C. elegans* exhibit a rightward shift. Compared to the control group, the average lifespan increases by 9.7 ± 2.0 % for NAC, 13.4 ± 3.8 % for 50 μg/mL GRP, and 11.0 ± 2.8 % for 100 μg/mL (Table 1). In another study, peptides from sesame at 50 μg/mL were shown to extend the average lifespan of *C. elegans* by 5.2 %, demonstrating the anti-aging potential of peptides found in natural foods (Wang, Ma, et al., 2016). On the other hand, Oh et al. (2015) reported that an addition of NAC to *C. elegans*' diet can extend the average lifespan by 28.1 % (Oh et al., 2015). This may be attributed to the enhanced resistance to oxidative stress, heat stress, and UV radiation.

In addition to the average life span, pharyngeal pumping rate of *C. elegans* may also serve as another biological marker associated with

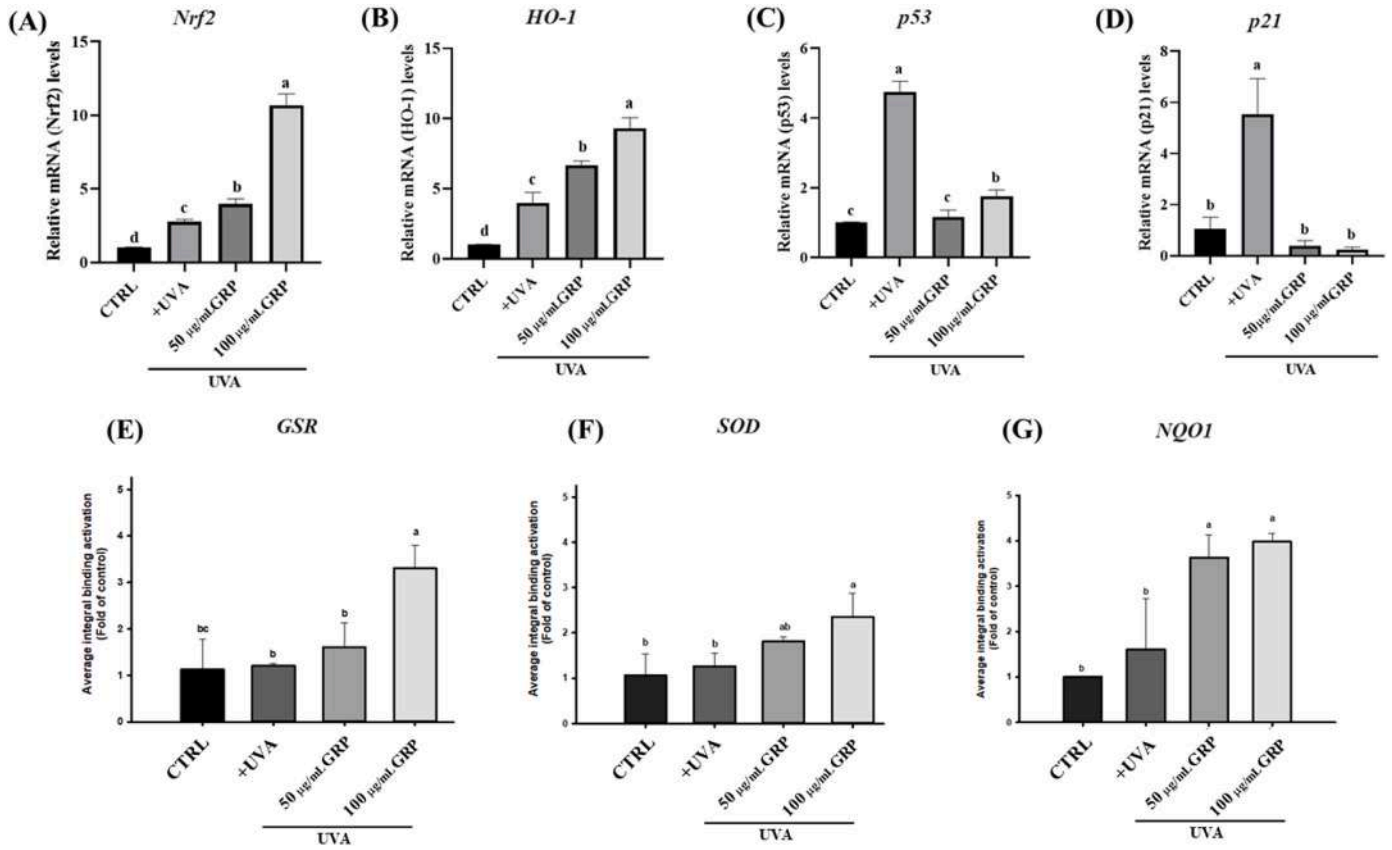


Fig. 3. Effect of GRP on gene expressions (A to D) and ChIP analysis of irradiated cells (E to G). (A) *Nrf2*; (B) *HO-1*; (C) *p53*; (D) *p21*; (E) *GSR*; (F) *SOD*; (G) *NQO1*.

The experimental results were repeated three times, and all were expressed in the form of mean ± standard deviation (SD). Different letters indicate significant differences ($p < 0.05$).

CTRL: Without treatment; UVA: Being exposed to 15 kJ/cm^2 UVA; GRP: Pretreated with 50 or 100ug/mL GRP before 15 kJ/cm^2 UVA-irradiation.

worm aging (Chiu et al., 2018). Pharyngeal pumping rate could be investigated to assess health which is correlated to the remaining lifespan (Bansal et al., 2015). On Day 7, the pharyngeal pumping rates of *C. elegans* after treating with NAC and GRP (at 50 and 100 μg/mL) were 280 ± 4, 223 ± 11, and 276 ± 8 pumps/min, respectively, compared to 203 ± 10 pumps/min in the control group (Fig. 4B). Additionally, juglone was exploited to induce oxidative stress in *C. elegans* (Moliner et al., 2019). It was found that the addition of NAC, 50 μg/mL GRP, and 100 μg/mL GRP can significantly enhance the survival rate of *C. elegans* by 98.5 ± 0.1 %, 80.4 ± 0.1 %, and 80.6 ± 2.4 %, respectively, compared to the control group ($p < 0.05$) (Fig. 4C). This finding indicates the capability of GRP as a worm supplement to enhance resistance to oxidative stress. Further testing under oxidative stress revealed that both 50 and 100 μg/mL treated-GRP promote gene expression of *skn-1* (1.67, 1.70 times), *gcs-1* (2.87, 5.75 times), *gst-4* (1.44, 1.86 times), and *gst-7* (3.01, 3.99 times) compared to the juglone-treated group with statistically significant differences ($p < 0.05$), as illustrated in Fig. 4D, E, F, and G. The transcription factor SKN-1, when exposed to juglone, moves to the nucleus and activates the expression of multiple detoxification genes (Kahn et al., 2007; Wu et al., 2016). SKN-1 induces the expression of phase II detoxification genes, such as gcs-1 and trx-1, which are essential for oxidative stress resistance (Hwang et al., 2022). Activation or overexpression of *skn-1* activate the SKN-1/Nrf2 pathway, leading to upregulation of antioxidant genes, reduced ROS accumulation, and prolonged lifespan in *C. elegans*, while the loss of this transcription factor may have an opposite effect (An et al., 2005; Kell et al., 2007; Tao et al., 2023). This study illustrates that GRP increases gene expression of *skn-1*, which can subsequently be hypothesized that the increased activity of SKN-1 reduces endogenous ROS through nuclear translocation (Fig. 4D). Similarly, high hydrophobic amino acids content peptides similar to GRP that was extracted from *Phalaris canariensis* also triggers an overexpression of *gst-4* gene in *C. elegans*, implying its potential as a natural antioxidant in foods (Urbizo-Reyes et al., 2022). Thus, a mechanism of GRP in increasing lifespan and improving stress resistance in *C. elegans* is speculated.

3.5. Molecular interactions and inhibitory OGT mechanisms of GTP on the Keap-BTB

As mentioned previously, Nrf2 transcription factor regulates gene expression that is responsible in modulating ROS. On top of that, Keap1 protein is a negative regulator Nrf2, whereby BTB domain on Keap1 is the inhibitory site (Chen et al., 2017; Xu et al., 2022). By simulating the molecular interaction of GRP peptide, it is hypothesized that the peptide targets and binds to the Keap1-BTB inhibitory site, creating a docking affinity of −5.22 kcal/mol. Based on Fig. 5, GRP forms four hydrogen bonds with Ser102, Ser103, and Ser166, where their bond lengths are measured to be between 2.98 and 3.21 Å. The first three glycine residues in the GRP peptide predominantly form these hydrogen bonds. Additionally, GRP's glycine residues and Ser104, Pro105, Phe139, Gln163, Ile164, and Asp165 also create covalent bonding. The molecular docking results suggest that the distinctive repetitive glycine structure in GRP confers an inhibitory effect on Keap1-BTB. Furthermore, lysine and proline residues of the GRP peptide are found to covalently bond at the Keap1-BTB inhibitory pocket, specifically at Thr60, Phe64, Ala140, Tyr141, Thr142, and Ala143 (Fig. 5).

Protein glycosylation is one of the most common post-translational modifications in mammals. Within the context of Keap1, its

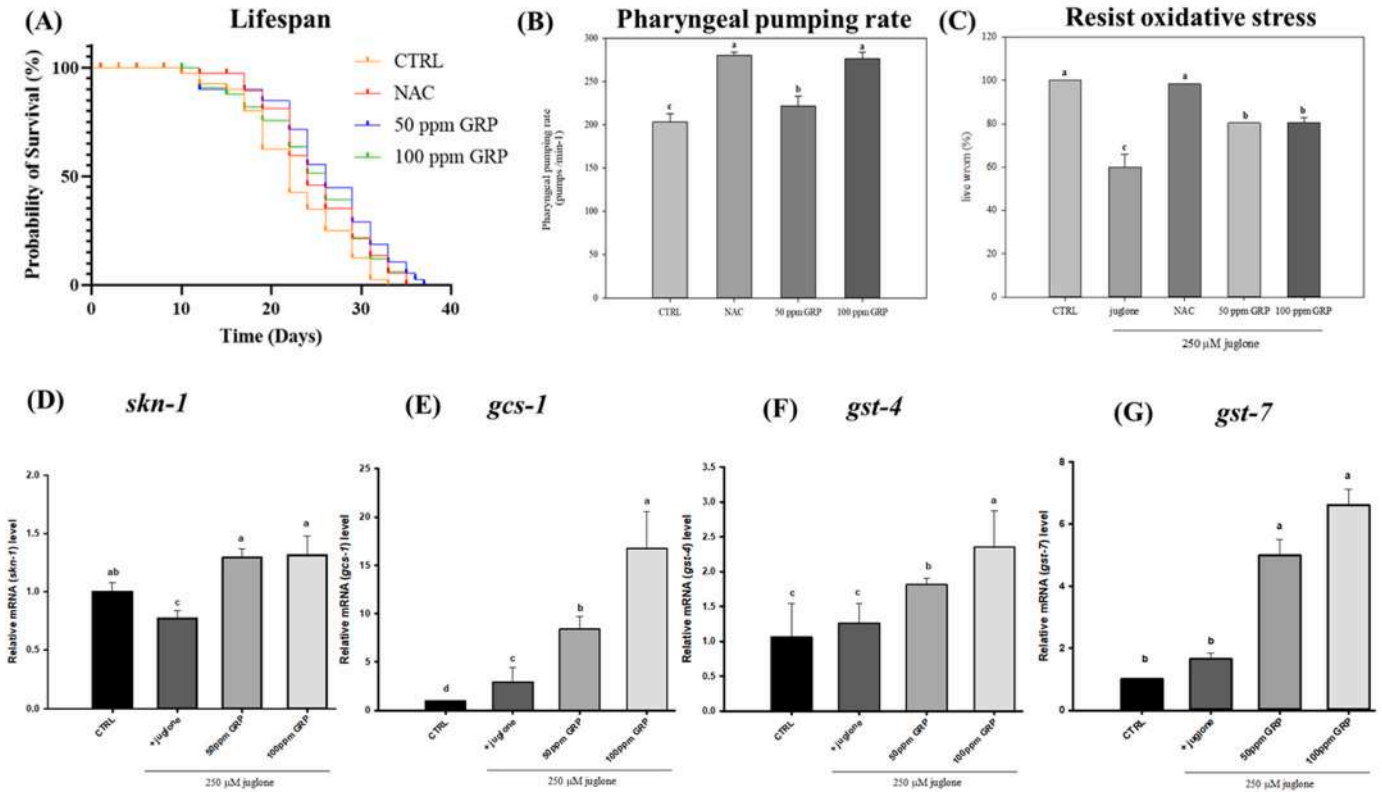


Fig. 4. Effect of different treatments on N2 wild-type *C. elegans*. (A) Lifespan study; (B) Pharyngeal pumping rate; (C) Resistance to oxidative stress; (D) *skn-1* gene expression; (E) *gcs-1* gene expression; (F) *gst-4* gene expression; (G) *gst-7* gene expression.
The experimental results were repeated three times, and all were expressed in the form of mean ± standard deviation (SD). Different letters indicate significant differences ($p < 0.05$).
CTRL: Without treatment; Juglone: Treated with 250 μM Juglone; NAC: Treated with 1 mmol/L N-acetylcysteine supplement; GRP: Treated with 50 or 100 μg/mL of GRP.

Table 1
Effect of GRP on the mean lifespan of N2 wild-type *C. elegans*.

Group	Mean lifespan	% of control
CTRL	22.8 ± 0.58^{b}	100.0 ± 2.54^{b}
1 mmol/L NAC	25.0 ± 0.46^{a}	109.7 ± 2.02^{a}
50 μg/mL GRP	25.82 ± 0.86^{a}	113.4 ± 3.78^{a}
100 μg/mL GRP	25.26 ± 0.63^{a}	111.0 ± 2.77^{a}

The experimental results were repeated three times, and all were expressed in the form of mean ± standard deviation (SD). Different letters indicate significant differences ($p < 0.05$).
CTRL: Without treatment, CTRL: Without treatment; NAC: Treated with 1 mmol/L NAC supplement; GRP: Treated with 50 or 100 μg/mL GRP.

glycosylation depends on the activity of a single OGT (Mehboob and Lang, 2021). Keap1 is found to physically interact with OGT at 11 alternative glycosylation sites which are located in different domains of Keap1. Key sites within the α-helices of the BTB domain, such as Ser104, Ser102, Ser103, and Ser166, are essential for Keap1 homodimerization and its interaction with CUL3 (Chen et al., 2018). When Keap1 is glycosylated by OGT, it triggers an inhibition of Nrf2. Therefore, the inhibition of OGT would effectively reduce the assembly of Keap1 in the Cul3-dependent ubiquitin ligase complex, activating the Nrf2 protein to enter the nucleus and stimulate the transcription of antioxidant response genes (How et al., 2018; Wang et al., 2020).

This interaction then decreases the Nrf2-KEAP complex state which enhances the translocation of Nrf2 into the nucleus. Consequently, Nrf2 could bind with ARE upon entering the nucleus and facilitate antioxidative mechanisms.

4. Conclusions

The comprehensive analysis of glycine-rich peptides from tempeh-like fermented *C. formosanum* reveals their significant role in combating oxidative stress and delaying photoaging. By comparing to NAC, GRP exhibits similar protective effects in enhancing cell survival after UVA irradiation. This is achieved by regulating gene expression of cell cycle and modulating oxidative stress responses. Furthermore, in vivo studies showed that GRP extends the lifespan of *C. elegans* and enhances their resistance to oxidative stress, underscoring its potential as a dietary supplement for health span extension. Additionally, molecular docking investigation identified GRP's potential mechanism as the inhibitor of OGT at the KEAP-BTB inhibitory site, thereby enhancing the Nrf2 pathway. These findings suggest that GRP, with its antioxidative properties, could serve as an effective natural intervention in delaying non-replicative aging and mitigating the effects of environmental stressors.

CRediT authorship contribution statement

Chen-Che Hsieh: Writing – original draft, Conceptualization. **Hui-Wen Lin:** Writing – original draft, Conceptualization. **Hsiao-Chu Huang:** Formal analysis, Data curation. **Darin Khumsupan:** Formal analysis, Data curation. **Szu-Chuan Shen:** Formal analysis, Data curation. **Shin-Ping Lin:** Formal analysis, Data curation. **Chang-Wei Hsieh:** Resources, Formal analysis. **Tsung-Yu Tsai:** Resources, Formal analysis. **Sirima Suvarnakuta Jantama:** Resources, Formal analysis. **Hsing-Chun Kuo:** Writing – review & editing, Supervision, Project administration, Funding acquisition, Conceptualization. **Kuan-Chen Cheng:**

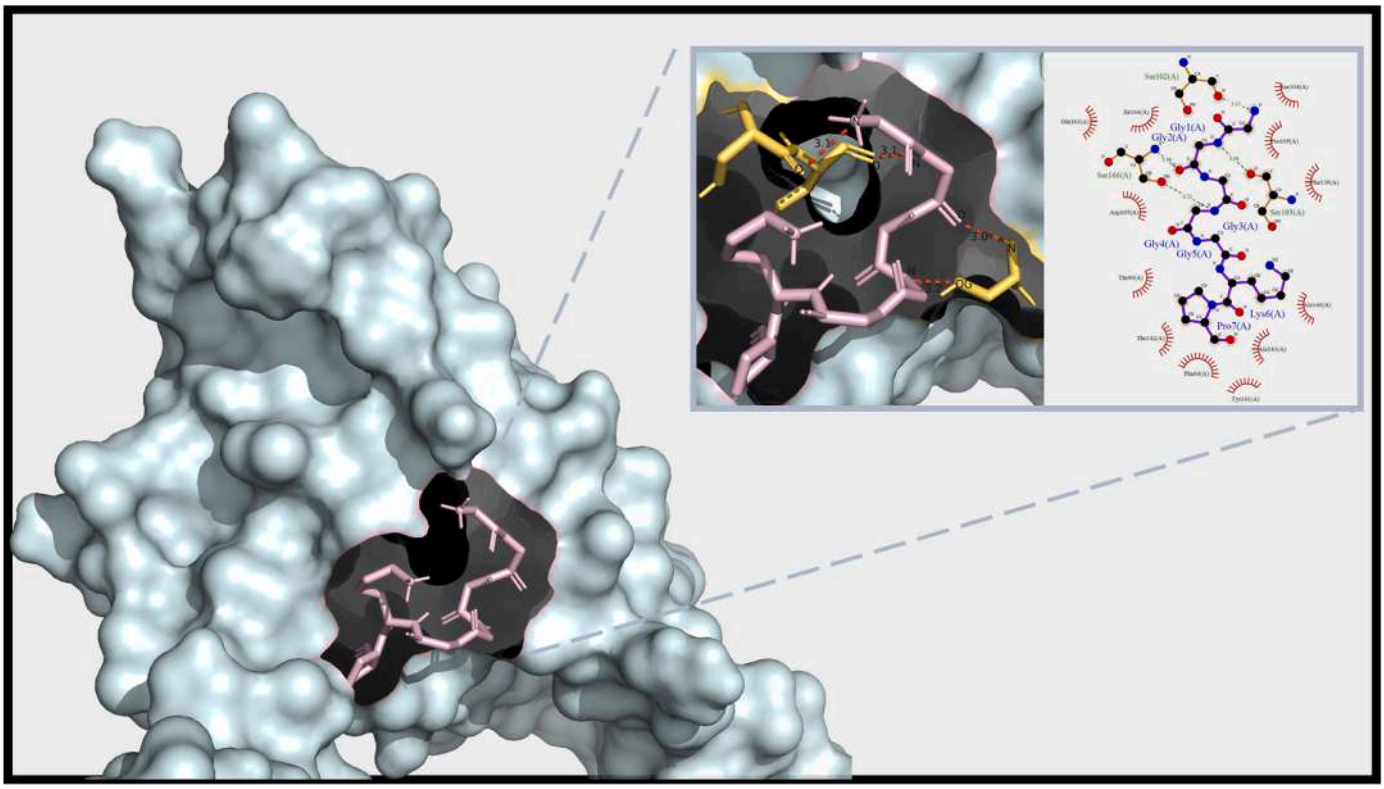


Fig. 5. The inhibition of Keap1-BTB by a glycine-rich peptide (GRP) obtained from tempeh-like fermented *Chenopodium formosanum*.

Writing – review & editing, Supervision, Project administration, Funding acquisition, Conceptualization.

Declaration of competing interest

I have nothing to declare.

Acknowledgments

The Funding for this study was provided in part by research grants from the Chang Gung Memorial Hospital, Chiayi, Taiwan. This study was supported by grants BMRPD42, CMRPF6M0071, CMRPF6M0072, CMRPF6M0073 and ZRRPF6P0011 from Chang Gung Memorial Hospital, Chiayi, Taiwan, and Chang Gung University of Science and Technology, Chiayi Campus, Taiwan. This work was supported by grants NSTC 112-2320-B-002-013-MY3; 112-2221-E-002-040-MY3; 113-2320-B-255-001-; 113-2222-E-992 -009 -MY2 from the National Science and Technology Council (NSTC), R.O.C. National Core Facility for Biopharmaceuticals, NSTC, particularly *C. elegans* Core Facility, for assistance.

Appendix A. Supplementary data

Supplementary data to this article can be found online at https://doi.org/10.1016/j.lwt.2025.117641.

Data availability

Data will be made available on request.

References

Ahmed, A. S. I., Sheng, M. H., Wasnik, S., Baylink, D. J., & Lau, K. H. W. (2017). Effect of aging on stem cells. *World Journal of Experimental Medicine, 7*, 1. https://doi.org/10.5493/wjem.v7.i1.1

Albanesi, C., Mercurio, L., Bailey, J., Glick, A., Dellambra, E., Scarponi, C., & Madonna, S. (2023). RAS-activated PI3K/AKT signaling sustains cellular senescence in experimental models of psoriasis via P53/P21 axis. https://doi.org/10.21203/rs.3.rs-3209194/v1.

An, J. H., Vranas, K., Lucke, M., Inoue, H., Hisamoto, N., Matsumoto, K., & Blackwell, T. K. (2005). Regulation of the *Caenorhabditis elegans* oxidative stress defense protein SKN-1 by glycogen synthase kinase-3. *Proceedings of the National Academy of Sciences, 102*, 16275–16280. https://doi.org/10.1073/pnas.0508105102

An, J., Zhang, S., Xia, X., Dong, Z., Zhou, W., Mai, W., & Jin, D. (2021). Transcriptomics changes and the candidate pathway in human macrophages induced by different PM2.5 extracts. *Environmental Pollution, 289*, Article 117890. https://doi.org/10.1016/j.envpol.2021.117890

Bansal, A., Zhu, L. J., Yen, K., & Tissenbaum, H. A. (2015). Uncoupling lifespan and healthspan in *Caenorhabditis elegans* longevity mutants. *Proceedings of the National Academy of Sciences, 112*, E277–E286. https://doi.org/10.1073/pnas.1412192112

Bao, T., Wang, Y., Li, Y. T., Gowd, V., Niu, X. H., Yang, H. Y., & Chen, W. (2016). Antioxidant and antidiabetic properties of tartary buckwheat rice flavonoids after in vitro digestion. *Journal of Zhejiang University - Science B, 17*, 941. https://doi.org/10.1631/jzus.B1600243

Chen, P. H., Ho, P. C., Tsui, Y. C., Lin, C. H., Chi, J. T., & Boyce, M. (2018). Functional crosstalk among oxidative stress and O-GlcNAc signaling pathways. *Glycobiology, 28*, 556–564. https://doi.org/10.1093/glycob/cwy027

Chen, P. H., Smith, T. J., Wu, J., Siesser, P. F., Bisnett, B. J., Khan, F., Hogue, M., Lin, Z., Mayo, L. D., Jelinek, D. F., Chi, J. T., & Boyce, M. (2017). Glycosylation of KEAP1 links nutrient sensing to redox stress signaling. *The EMBO Journal, 36*, 2233–2250. https://doi.org/10.15252/embj.201696113

Chen, L., Yang, R., Qiao, W., Zhang, W., Chen, J., Mao, L., & Miao, D. (2019). 1,25-Dihydroxyvitamin D exerts an antiaging role by activation of Nrf2-antioxidant signaling and inactivation of p16/p53-senescence signaling. *Aging Cell, 18*, Article e12951. https://doi.org/10.1111/acel.12951

Chen, W., Zhuang, J., Li, Y., Shen, Y., & Zheng, X. (2013). Myricitrin protects against peroxynitrite-mediated DNA damage and cytotoxicity in astrocytes. *Food Chemistry, 141*, 927–933. https://doi.org/10.1016/j.foodchem.2013.04.033

Chiu, H. F., Chen, T. J., Lu, Y. Y., Han, Y. C., Shen, Y. C., Venkatakrishnan, K., Golovinskaia, O., & Wang, C. K. (2018). Efficacy of protein rich pearl powder on antioxidant status in a randomized placebo-controlled trial. *Journal of Food and Drug Analysis, 26*, 309–317. https://doi.org/10.1016/j.jfda.2017.05.010

Chou, Y. J., & Ting, Y. (2023). Plasma-activated water regulated transcriptome gene expression leading to high germination and growth of mung beans. *Chemical and Biological Technologies in Agriculture, 10*, 146. https://doi.org/10.1186/s40538-023-00497-2

Chu, C. C., Chen, S. Y., Chyau, C. C., Fu, Z. H., Liu, C. C., & Duh, P. D. (2016). Protective effect of Djulis (*Chenopodium formosanum*) and its bioactive compounds against carbon tetrachloride-induced liver injury, in vivo. *Journal of Functional Foods, 26*, 585–597. https://doi.org/10.1016/j.jff.2016.08.025

Das, P. M., Ramachandran, K., vanWert, J., & Singal, R. (2004). Chromatin immunoprecipitation assay. *Biotechnology, 37*, 961–969. https://doi.org/10.2144/04376RV01

Duangjan, C., Rangsinth, P., Gu, X., Zhang, S., Wink, M., & Tencomnao, T. (2019). Glochidion zeylanicum leaf extracts exhibit lifespan extending and oxidative stress resistance properties in *Caenorhabditis elegans* via DAF-16/FoxO and SKN-1/Nrf-2 signaling pathways. *Phytomedicine, 64*, Article 153061. https://doi.org/10.1016/j.phymed.2019.153061

Farrukh, M. R., Saeed, M., & Ahmad, I. (2014). Oxidative stress mediated Ca2+ release manifests endoplasmic reticulum stress leading to unfolded protein response in UV-B irradiated human skin cells. *Journal of Dermatological Science, 75*, 24–35. https://doi.org/10.1016/j.jdermsci.2014.03.005

Feng, Q., Lu, X., Yuan, G., Zhang, Q., & An, L. (2022). Effects of Agaricus blazei polypeptide on cell senescence by regulation of Keap1/Nrf2/ARE and TLR4/NF-κB p65 signaling pathways and its mechanism in D-gal-induced NIH/3T3 cells. *Journal of Functional Foods, 72*, Article 104037. https://doi.org/10.1016/j.jff.2020.104037

Fu, P. P., Xia, Q., Hwang, H. M., Ray, P. C., & Yu, H. (2014). Mechanisms of nanotoxicity: Generation of reactive oxygen species. *Journal of Food and Drug Analysis, 22*, 64–75. https://doi.org/10.1016/j.jfda.2014.01.005

Guo, H., Hao, Y., Yang, X., Ren, G., & Richel, A. (2023). Exploration on bioactive properties of quinoa protein hydrolysate and peptides: A review. *Critical Reviews in Food Science and Nutrition, 63*, 2896–2909. https://doi.org/10.1080/10408398.2021.1982860

Han, B. I., Hwang, S. H., & Lee, M. A. (2017). A progressive reduction in autophagic capacity contributes to induction of replicative senescence in Hs68 cells. *The International Journal of Biochemistry & Cell Biology, 92*, 18–25. https://doi.org/10.1016/j.biocel.2017.09.005

Harvey, C. J., Thimmulappa, R. K., Singh, A., Blake, D. J., Ling, G., Wakabayashi, N., Fujii, J., Myers, A., Biswal, S., Sporn, M. B., Liby, K. T., & Kensler, T. W. (2009). Nrf2-regulated glutathione recycling independent of biosynthesis is critical for cell survival during oxidative stress. *Free Radical Biology and Medicine, 46*, 443–453. https://doi.org/10.1016/j.freeradbiomed.2008.10.040

How, C. M., Li, S. W., & Liao, V. H. C. (2018). Chronic exposure to triadimenol at environmentally relevant concentration adversely affects aging biomarkers in *Caenorhabditis elegans* associated with insulin/IGF-1 signaling pathway. *The Science of the Total Environment, 640*, 485–492. https://doi.org/10.1016/j.scitotenv.2018.05.314

Hseu, Y. C., Kumar, K. J. S., Chen, C. S., Chen, S. C., Huang, H. C., Wang, H. M., Lin, C. M., & Lee, H. Z. (2018). Trans-cinnamic acid attenuates UVA-induced photoaging through inhibition of AP-1 activation and induction of Nrf2-mediated antioxidant genes in human skin fibroblasts. *Journal of Dermatological Science, 90*, 123–134. https://doi.org/10.1016/j.jdermsci.2018.01.004

Hsiao, Y. F., Chen, Y. C., Lai, Y. C., Chen, H. Y., & Tsai, P. J. (2023). Physicochemical properties and protective effects on UVA-induced photoaging in Hs68 cells of Pleurotus ostreatus polysaccharides by fractional precipitation. *International Journal of Biological Macromolecules, 228*, 537–547. https://doi.org/10.1016/j.ijbiomac.2022.12.254

Hsieh, C. C., Yu, S. H., Cheng, K. W., Liou, Y. W., Hsu, C. C., Hsieh, C. W., & Cheng, K. C. (2023). Production and analysis of metabolites from solid-state fermentation of *Chenopodium formosanum* (Djulis) sprouts in a bioreactor. *Food Research International, 168*, Article 112707. https://doi.org/10.1016/j.foodres.2023.112707

Hsieh, C. C., Yu, S. H., Kuo, H. C., Cheng, K. W., Hsu, C. C., Lin, Y. P., & Cheng, K. C. (2024). Alleviation of PM2.5-induced alveolar macrophage inflammation using extract of fermented *Chenopodium formosanum* Koidz sprouts via regulation of NF-κB pathway. *Journal of Ethnopharmacology, 318*, Article 116980. https://doi.org/10.1016/j.jep.2023.116980

Hsieh, C. C., Yu, S. H., Kuo, H. C., Khumsupan, D., Huang, H. C., Liou, Y. W., & Cheng, K. C. (2023). Glycine-rich peptides from fermented *Chenopodium formosanum* sprout as an antioxidant to modulate the oxidative stress. *Journal of Food and Drug Analysis, 31*, 5. https://doi.org/10.38212/2224-6614.3476

Huang, A. H., & Chien, A. L. (2020). Photoaging: A review of current literature. *Current Dermatology Reports, 9*, 22–29. https://doi.org/10.1007/s13671-020-00288-0

Hwang, M., Shrestha, C., Kang, S., & Kim, J. (2022). MEKK-3 acts cooperatively with NSY-1 in SKN-1-Dependent manner against oxidative stress and aging in *Caenorhabditis elegans*. *Biology, 11*(10), 1526. https://doi.org/10.3390/biology11101526

Kahn, N. W., Rea, S. L., Moyle, S., Kell, A., & Johnson, T. E. (2007). Proteasomal dysfunction activates the transcription factor SKN-1 and produces a selective oxidative-stress response in *Caenorhabditis elegans*. *Biochemical Journal, 409*, 205–213. https://doi.org/10.1042/BJ20070521

Kell, A., Ventura, N., Kahn, N., & Johnson, T. E. (2007). Activation of SKN-1 by novel kinases in *Caenorhabditis elegans*. *Free Radical Biology and Medicine, 43*, 1560–1566. https://doi.org/10.1016/j.freeradbiomed.2007.08.025

Kuo, H. C., Kwong, H. K., Chen, H. Y., Hsu, H. Y., Yu, S. H., Hsieh, C. W., & Cheng, K. C. (2021). Enhanced antioxidant activity of *Chenopodium formosanum* koidz. By lactic acid bacteria: Optimization of fermentation conditions. *PLoS One, 16*, Article e0249250. https://doi.org/10.1371/journal.pone.0249250

Lebiedzinska-Arciszewska, M., Suski, J., Bonora, M., Pakula, B., Pinton, P., Duszynski, J., & Wieckowski, M. R. (2024). The relation between mitochondrial membrane potential and reactive oxygen species formation. In *In mitochondrial bioenergetics: Methods and protocols* (pp. 133–162). New York, NY: Springer US. https://doi.org/10.1007/978-1-0716-4264-1_8.

Lee, J. Y., Yoo, D. G., Jeon, Y. B., Moon, S. H., Kim, O. H., Lee, D. H., & Kim, C. H. (2023). Functional characteristics of whey protein-derived peptides produced using lactic acid bacteria hydrolysis. *Journal of Dairy Science and Biotechnology, 41*(1), 34–43. https://doi.org/10.22424/jdsb.2023.41.1.34

Li, A., Zheng, N., & Ding, X. (2022). Mitochondrial abnormalities: A hub in metabolic syndrome-related cardiac dysfunction caused by oxidative stress. *Heart Failure Reviews, 27*(4), 1387–1394. https://doi.org/10.1007/s10741-021-10109-6

Lin, H., Zhao, J., Xie, Y., Tang, J., Wang, Q., Zhao, J., & Liu, P. (2024). Identification and molecular mechanisms of novel antioxidant peptides from fermented broad bean paste: A combined in silico and *in vitro* study. *Food Chemistry, 450*, Article 139297. https://doi.org/10.1016/j.foodchem.2024.139297

Lopez-Ruiz, A., Chandrashekar, K., & Juncos, L. A. (2023). Nrf2 activation in the glomeruli and podocytes: Deciphering the renal mechanisms of Nrf2. *Kidney, 4*(10), 1350–1352. https://doi.org/10.34067/KID.0000000000000268

Lu, J. J., Cheng, M. C., Khumsupan, D., Hsieh, C. C., Hsieh, C. W., & Cheng, K. C. (2023). Evaluation of fermented turmeric milk by lactic acid bacteria to prevent UV-induced oxidative stress in human fibroblast cells. *Fermentation, 9*, 230. https://doi.org/10.3390/fermentation9030230

Mahmud, S., Pitcher, L. E., Torbenson, E., Robbins, P. D., Zhang, L., & Dong, X. (2024). Developing transcriptomic signatures as a biomarker of cellular senescence. *Ageing Research Reviews*. , Article 102403. https://doi.org/10.1016/j.arr.2024.102403

Makpol, S., Durani, L. W., Chua, K. H., Mohd Yusof, Y. A., & Wan Ngah, W. Z. (2011). Tocotrienol-rich fraction prevents cell cycle arrest and elongates telomere length in senescent human diploid fibroblasts. *BioMed Research International, 1*, Article 506171. https://doi.org/10.1155/2011/506171

Marionnet, C., Pierrard, C., Lejeune, F., Sok, J., Thomas, M., & Bernerd, F. (2010). Different oxidative stress response in keratinocytes and fibroblasts of reconstructed skin exposed to non-extreme daily-ultraviolet radiation. *PLoS One, 5*, Article e12059. https://doi.org/10.1371/journal.pone.0012059

Mehboob, M. Z., & Lang, M. (2021). Structure, function, and pathology of protein O-glucosyltransferases. *Cell Death & Disease, 12*, 71. https://doi.org/10.1038/s41419-020-03314-y

Mirzaei, M., Mirdamadi, S., Ehsani, M. R., & Aminlari, M. (2018). Production of antioxidant and ACE-inhibitory peptides from *Kluyveromyces marxianus* protein hydrolysates: Purification and molecular docking. *Journal of Food and Drug Analysis, 26*, 696–705. https://doi.org/10.1016/j.jfda.2017.07.008

Moliner, C., Míguez-Mosquera, M., Llorent-Martínez, E. J., Guisantes-Batan, E., Bahrim, G. E., Fernández-de Córdova, M. L., & Ruiz-Medina, A. (2019). Viola cornuta and viola x wittrockiana: Phenolic compounds, antioxidant and neuroprotective activities on *Caenorhabditis elegans*. *Journal of Food and Drug Analysis, 27*, 849–859. https://doi.org/10.1016/j.jfda.2019.05.005

Nandita, H., Manohar, M., & Gowda, D. V. (2020). Recent review on oxidative stress, cellular senescence and age-associated diseases. *International Journal of Pharmaceutical Sciences and Research, 11*, 1331–1342. https://ijrps.com/home/article/view/806.

Odawara, T., Yamauchi, S., & Ichijo, H. (2024). Apoptosis signal-regulating kinase 1 promotes inflammation in senescence and aging. *Communications Biology, 7*(1), 691. https://doi.org/10.1038/s42003-024-06386-0

Oh, S. I., Park, J. K., & Park, S. K. (2015). Lifespan extension and increased resistance to environmental stressors by N-acetyl-L-cysteine in *Caenorhabditis elegans*. *Clinics, 70*, 380–386. https://doi.org/10.6061/clinics/2015(05)13

Olivares-Vicente, M., Sánchez-Marzo, N., Herranz-López, M., & Micol, V. (2024). Analysis of lemon verbena polyphenol metabolome and its correlation with oxidative stress under glucotoxic conditions in adipocyte. *Journal of Agricultural and Food Chemistry, 72*, 9768–9781. https://doi.org/10.1021/acs.jafc.3c06309

Ren, L. K., Yang, Y., Ma, C. M., Fan, J., Bian, X., Liu, B. X., & Zhang, N. (2022). Identification and in silico analysis of novel antioxidant peptides in broken rice protein hydrolysate and its cytoprotective effect against H2O2-induced 2BS cell model. *Food Research International, 162*, Article 112108. https://doi.org/10.1016/j.foodres.2022.112108

Rom, O., Liu, Y., Finney, A. C., Ghrayeb, A., Zhao, Y., Shukha, Y., & Chen, Y. E. (2022). Induction of glutathione biosynthesis by glycine-based treatment mitigates atherosclerosis. *Redox Biology, 52*, Article 102313. https://doi.org/10.1016/j.redox.2022.102313

Ryu, Y. S., Kang, J. I., Han, Y. K., Lim, J. M., Lee, J., & Kim, E. M. (2019). Marine compound 3-bromo-4,5-dihydroxybenzaldehyde protects skin cells against oxidative damage via the Nrf2/HO-1 pathway. *Marine Drugs, 17*, 234. https://doi.org/10.3390/md17040234

Salminen, A., Kaarniranta, K., & Kauppinen, A. (2022). Photoaging: UV radiation-induced inflammation and immunosuppression accelerate the aging process in the skin. *Inflammation Research, 71*, 817–831. https://doi.org/10.1007/s00011-022-01598-8

Sasaki, M., Kajiya, H., Ozeki, S., Okabe, K., & Ikebe, T. (2014). Reactive oxygen species promotes cellular senescence in normal human epidermal keratinocytes through epigenetic regulation of p16INK4a. *Biochemical and Biophysical Research Communications, 452*, 622–628. https://doi.org/10.1016/j.bbrc.2014.08.123

Shi, Y. C., Liao, V. H. C., & Pan, T. M. (2012). Monascin from red mold dioscorea as a novel antidiabetic and antioxidative stress agent in rats and *Caenorhabditis elegans*. *Free Radical Biology and Medicine, 52*, 109–117. https://doi.org/10.1016/j.freeradbiomed.2011.09.034

Tang, Y. C., Chang, H. H., Chen, H. H., Yao, J. Y., Chen, Y. T., Chuang, Y. J., & Kuo, C. C. (2021). A novel NRF2/ARE inhibitor gossypol induces cytotoxicity and sensitizes chemotherapy responses in chemo-refractory cancer cells. *Journal of Food and Drug Analysis, 29*, 638. https://doi.org/10.38212/2224-6614.3376

Tanigawa, S., Fujii, M., & Hou, D. X. (2007). Action of Nrf2 and Keap1 in ARE-mediated NQO1 expression by quercetin. *Free Radical Biology and Medicine, 42*, 1690–1703. https://doi.org/10.1016/j.freeradbiomed.2007.02.017

Tao, M., Li, R., Xu, T., Zhang, Z., Zheng, D., Xia, Z., & Xu, X. (2023). Vitexin and isovitexin delayed ageing and enhanced stress-resistance through the activation of

the SKN-1/Nrf2 signaling pathway. *International Journal of Food Sciences & Nutrition, 74*(6), 685–694. https://doi.org/10.1080/09637486.2023.2243055

Thomas, P. D., Hill, D. P., Mi, H., Osumi-Sutherland, D., Van Auken, K., Carbon, S., & Mungall, C. J. (2019). Gene Ontology Causal Activity Modeling (GO-CAM) moves beyond GO annotations to structured descriptions of biological functions and systems. *Nature Genetics, 51*, 1429–1433. https://doi.org/10.1038/s41588-019-0500-1

Urbizo-Reyes, U., Kim, K. H., Reddivari, L., Anderson, J. M., & Liceaga, A. M. (2022). Oxidative stress protection by canary seed (*Phalaris canariensis* L.) peptides in Caco-2 Cells and *Caenorhabditis elegans*. *Nutrition*. https://doi.org/10.3390/nu14122415.

Vilcacundo, R., Martínez-Villaluenga, C., & Hernández-Ledesma, B. (2017). Release of dipeptidyl peptidase IV, α-amylase and α-glucosidase inhibitory peptides from quinoa (*Chenopodium quinoa* Willd.) during in vitro simulated gastrointestinal digestion. *Journal of Functional Foods, 35*, 531–539. https://doi.org/10.1016/j.jff.2017.06.024

Wang, T., Jian, Z., Baskys, A., Yang, J., Li, J., Guo, H., & Long, Q. (2020). MSC-derived exosomes protect against oxidative stress-induced skin injury via adaptive regulation of the NRF2 defense system. *Biomaterials, 257*, Article 120264. https://doi.org/10.1016/j.biomaterials.2020.120264

Wang, Z., Ma, X., Li, J., & Cui, X. (2016). Peptides from sesame cake extend healthspan of *Caenorhabditis elegans* via upregulation of skn-1 and inhibition of intracellular ROS levels. *Experimental Gerontology, 82*, 139–149. https://doi.org/10.1016/j.exger.2016.07.001

Wang, C. Y., Xu, Y., Wang, X., Wang, Y., Guo, Y., & Zhang, Z. (2016). Dl-3-n-butylphthalide-induced upregulation of antioxidant defense is involved in the enhancement of cross talk between CREB and Nrf2 in an Alzheimer's disease mouse model. *Neurobiology of Aging, 38*, 32–46. https://doi.org/10.1016/j.neurobiolaging.2015.10.024

Wu, C. W., Deonarine, A., Przybysz, A., Strange, K., & Choe, K. P. (2016). The Skp1 homologs SKR-1/2 are required for the *Caenorhabditis elegans* SKN-1 antioxidant/detoxification response independently of p38 MAPK. *PLoS Genetics, 12*(10), Article e1006361. https://doi.org/10.1371/journal.pgen.1006361

Wu, Q., Lu, F., Lei, J., Liu, Y., Zhu, N., Yu, Y., Ning, Z., & She, T. (2023). Nrf2 signaling pathway: Current status and potential therapeutic targetable role in human cancers. *Frontiers in Oncology*. https://doi.org/10.3389/fonc.2023.1184079

Xiong, L., Deng, N., Zheng, B., Li, T., & Liu, R. H. (2021). HSF-1 and SIR-2.1 linked insulin-like signaling is involved in goji berry (*Lycium* spp.) extracts promoting lifespan extension of *Caenorhabditis elegans*. *Food & Function, 12*, 7851–7866. https://doi.org/10.1039/D0FO03300F

Xu, T. H., Du, Y., Sheng, Z., Li, Y., Qiu, X., Tian, B., & Yao, L. (2022). OGT-mediated keap1 glycosylation accelerates Nrf2 degradation leading to high phosphate-induced vascular calcification in chronic kidney disease. *Frontiers in Physiology, 11*, 1092. https://doi.org/10.3389/fphys.2020.01092

Ye, Q., Li, Y., Wang, C., Zheng, J., Qiao, J., Yang, J., & Wan, Q. L. (2021). Sitagliptin extends lifespan of *Caenorhabditis elegans* by inhibiting insulin/insulin-like signaling and activating dietary restriction-like signaling pathways. *Gerontology, 70*, 90–101. https://doi.org/10.1159/000534863

Yin, B., & Jiang, X. (2013). Telomere shortening in cultured human dermal fibroblasts is associated with acute photodamage induced by UVA irradiation. *Advances in Dermatology and Allergology/Postępy Dermatologii i Alergologii, 30*, 13–18. https://doi.org/10.5114/pdia.2013.33374

IVYSPRING INTERNATIONAL PUBLISHER

International Journal of Medical Sciences

2025; 22(16): 4295-4312. doi: 10.7150/ijms.122025

Research Paper

Molecular mechanisms and biomarkers of total parenteral nutrition-induced hepatotoxicity revealed by iTRAQ proteomics analysis

Yung-Yu Hsieh[1,2], Jai-Jen Tsai[3,4,5], Shui-Yi Tung[1,2], Ko-Chao Lee[6,7], Kung-Chuan Cheng[6], Kam-Fai Lee[8], Meng-Chiao Hsieh[9], Cheng-Yi Huang[9], Chih-Chuan Teng[10,11], Chien-Heng Shen[1*✉], Hsing-Chun Kuo[10,11,12,13*✉]

1. Division of Gastroenterology and Hepatology, Department of Internal Medicine, Chang Gung Memorial Hospital, Chiayi 613016, Taiwan.
2. College of Medicine, Chang Gung University, Taoyuan 333323, Taiwan.
3. School of Medicine, National Yang Ming Chiao Tung University, Taipei, Taiwan.
4. Taipei Veterans General Hospital, Yuan-Shan/Su-Ao Branch, Taipei City, Taiwan.
5. Department of Nursing, Cardinal Tien Junior College of Healthcare and Management, New Taipei City, Taiwan.
6. Division of Colorectal Surgery, Department of Surgery, Chang Gung Memorial Hospital-Kaohsiung Medical Center, Kaohsiung, Taiwan.
7. College of Medicine, Chang Gung University, Kaohsiung, Taiwan.
8. Department of Pathology, Chang Gung Memorial Hospital, Chiayi, Taiwan.
9. Division of Colon and Rectal Surgery, Department of Surgery, Chang Gung Memorial Hospital, Chiayi, Taiwan.
10. Department of Nursing, Division of Basic Medical Sciences, Chang Gung University of Science and Technology, Chiayi, Taiwan.
11. Research Fellow, Chang Gung Memorial Hospital, Chiayi, Taiwan.
12. Center for Drug Research and Development, Chang Gung University of Science and Technology, Taoyuan, Taiwan.
13. Chronic Diseases and Health Promotion Research Center, Chang Gung University of Science and Technology, Chiayi, Taiwan.

*Chien-Heng Shen and Hsing-Chun Kuo contributed equally to this article.

✉ Corresponding authors: Chien-Heng Shen: Division of Gastroenterology and Hepatology, Department of Internal Medicine, Chang Gung Memorial Hospital, Chiayi, Taiwan. E-mail: gi2216@cgmh.org.tw. Hsing-Chun Kuo: Department of Nursing, Division of Basic Medical Sciences, Chang Gung University of Science and Technology, Chiayi, Taiwan. E-mail: kuohc@mail.cgust.edu.tw.

© The author(s). This is an open access article distributed under the terms of the Creative Commons Attribution License (https://creativecommons.org/licenses/by/4.0/). See https://ivyspring.com/terms for full terms and conditions.

Received: 2025.07.19; Accepted: 2025.09.15; Published: 2025.10.10

Abstract

Background/Aims: Total parenteral nutrition (TPN) provides medical nutrients intravenously to patients who cannot obtain proper nutrition through normal dietary means or enteral feeding. One significant concern is the risk of liver damage associated with long-term TPN use. In this study, the TPN-associated acute liver injury proteins and the molecular mechanisms underlying TPN oxidative stress were investigated through a quantitative proteomic survey. The proteomic changes between control and TPN infusion rats were analyzed by using the LC-MS/MS iTRAQ technology.

Methods: Rats were randomly assigned to saline infusion (control group) and TPN infusion (infusion rate of 30 mL/kg/h for 3 h). At the end of treatment, total liver samples from rats of control and TPN infusion groups were separated by iTRAQ-based quantitative proteomic identification. The effects of the differentially expressed proteins on the potential mechanism of hepatocytes were examined through flow cytometry. Additionally, siRNA-based assessments were conducted to examine the role of the endoplasmic reticulum stress (ER stress) as well as in vivo apoptosis of TPN-related liver cells.

Results: The effect of TPN on the biochemical markers of acute liver injury in the experimental rats was examined following palmitic acid treatment of live cells. Forty-eight proteins were differentially expressed between untreated control and TPN infusion liver tissues. The abundances of Elovl5 and Ptbp3 proteins were observed in TPN infusion ($P < 0.05$). Palmitic acid treatment of liver cells increased cell cytotoxicity and generated ROS, and increased the level of Elovl5 and Ptbp3, validated in the TPN infusion in vivo. The treatment of hepatocytes resulted in the activation of the caspases 3, caspase 9, accompanied by the expression and release of apoptotic molecules, cytochrome c, Bcl-2, Bcl-XL, p-IRE1α, and TRAF2. Elovl5 and Ptbp3 knockdown significantly regulated palmitic acid-mediated cytotoxicity of liver cells, including inhibition of apoptosis and ROS generation. Palmitic acid-mediated apoptotic induction was accompanied

by histone H3K4 trimethylation of Elovl5 and Ptbp3 promoters, leading to enhanced transcription through the sustained phosphorylation of ASK1/JNK/p38 pathways.

Conclusions: The mechanism of palmitic acid-induced apoptosis cascade and ER stress in hepatocyte cells involves up-regulation of Elovl5 and Ptbp3. This study provides novel regulators underlying the effects of TPN on liver injury.

Keywords: total parenteral nutrition (TPN), endoplasmic reticulum stress (ER stress), elongation of very long chain fatty acids protein 5 (Elovl5), polypyrimidine tract-binding protein 3 (Ptbp3), ASK1/mTOR/JNK/p38

Introduction

Total parenteral nutrition (TPN), alternatively referred to as intravenous or parenteral nutrition, represents a therapeutic modality implemented when a patient's gastrointestinal tract exhibits inadequate nutrient absorption capacity [1]. For individuals, encompassing both pediatric and adult populations, who demonstrate insufficient ability to consume or absorb nutrients through conventional digestive processes, TPN assumes critical importance in sustaining nutritional adequacy [2,3]. Prolonged reliance on TPN may precipitate hepatic injury, a notable complication manifesting as chronic cholestasis, steatosis, and cirrhosis. Additional terminology frequently employed to characterize these substantial complications includes intestinal atrophy, parenteral nutrition-associated liver disease, impaired glucose and lipid metabolism, cirrhosis, and hepatic failure; the absence of enteral feeding, recognized to disrupt normal enterohepatic circulation, potentially contributes to pathological conditions associated with TPN administration [3,4]. The TPN is frequently associated with liver failure, caused by the pathophysiological process such as oxidative/nitrosative stress, characterized by increased hepatocytes apoptosis [5]. The accumulation of reactive oxygen species (ROS) and peroxides in liver cells damages cellular components and causes cell injury, decreases liver oxidative metabolism capacity and enzymatic antioxidant defense [6,7]. The TPN-related pathogenic mechanism and molecular targets for hepatitis are not clearly understood.

Several clinical and experimental studies demonstrate that TPN-induced oxidative stress is frequently associated with liver failure, damaged cellular components, and cell injury through mitochondrial dysfunction, frequently at a greater risk of TPN-mediated oxidative stress because of accumulation of ROS in liver cells [8]. Oxidative stress affects the major cellular components, such as proteins, lipids, and DNA, and is charactrerized by upregulated activity of NADPH oxidase and decreased activity of cytosolic Cu-ZnSOD [9,10]. An excess of oxidative agents contributes to lipid peroxidation and alters their function against peroxides and toxic compounds [11]. Acute exposure to high levels of ROS may also cause serious damage within the body, such as during TPN infusion, which can lead to liver injury [12]. In liver cells, ER stress disrupts lipid metabolism and causes mitochondrial dysfunction due to an excess of ROS, altering calcium homeostasis and protein misfolding, while saturated fatty acids induce ER stress and apoptosis via ASK1/mTOR/JNK/p38 pathways [13,14]. Recent evidence showed that CHOP has a pro-apoptotic role in regulating hepatic metabolic genes during ER stress, activating multiple cellular signaling pathways. Among them, inositol-requiring enzyme type 1 (IRE1α) binds tumor necrosis factor (TNF) receptor-associated factor 2 (TRAF2), apoptosis signal-regulating kinase 1 (ASK1) and further activates Jun N-terminal kinase (JNK) [15], while its mechanisms of TPN-associated liver injury remains unclear.

TPN-associated proteins in the liver for early prognosis are treated as an urgent issue to identify reliable candidate markers [16]. Among the identified TPN-associated proteins in rats, reliable candidate markers are yet to be developed. To examine the different functions related to expression profiles of various proteins associated with TPN involved in cytotoxicity, and ER stress in rats, proteomic analysis was conducted to process and identify differential protein profiles using iTRAQ-based (isobaric tags for relative and absolute quantitation) LC-MS/MS, followed by tissue microarray [17]. In this study of liver injury of an acute TPN rat mode [18–21], we investigated whether experimental manipulation of expression of proteins, such as elongation of very long chain fatty acids protein 5 (Elovl5) and polypyrimidine tract-binding protein 3 (Ptbp3) can affect hepatotoxicity and the ER stress signaling pathway of the hepatocytes. We found intracellular signaling cascades involved in enhanced expression of Elovl5 and Ptbp3, including the production of ROS and ASK1/mTOR/JNK/p38 pathways. Further, these signaling pathways were found to affect a synergistic function in C/EBP Homologous Protein (CHOP) and transcription activation of the Elovl5 and Ptbp3 promoters. Cumulatively, of the roles of Elovl5 and

Ptbp3 proteins as the novel biomarkers and molecular targets of TPN infusion, holds potential for early prognosis and treatment of TPN-related injury to liver cells.

Materials and Methods

Chemicals and reagents

Total parenteral nutrition solution Kabiven™ was acquired from Fresenius Kabi AB (Uppsala, Sweden). All culture materials were procured from Gibco (Grand Island, NY, USA). Primary antibodies targeting Bcl-2, Bcl-XL, cleaved caspase 3, cleaved caspase 9, cytochrome C, Elongation of very long chain fatty acids protein 5 (Elovl5) and Polypyrimidine tract-binding protein 3 (Ptbp3) and nitrotyrosine were obtained from Santa Cruz Biotechnology (Santa Cruz, CA, USA). The antibodies were respectively sourced from Cell Signaling Technology (Beverly, MA, USA) and Abcam Technology (Abcam, USA), including IRE1α (Ser724), TRFA2, JNK (Thr183), p38 (Thr180) and ASK (Thr1165). Protease inhibitor cocktails, antibody against β-actin, reactive oxygen species (ROS) scavenger (N-acetyl cysteine [NAC]), dihydroethidium (DHE), endoplasmic reticulum stress (ERS) inhibitor (TUDCA), p38 inhibitor (SB203580), JNK inhibitor (SP600125), 3-(4,5-dimethylthiazol-2-yl)-2,5-diphenyltetrazolium bromide (MTT), 2,7-dichlorodihydrofluorescein diacetate (H2DCFDA), SDS, NP-40, and sodium deoxycholate were purchased from Sigma (St. Louis, MO, USA). The TdT-mediated dUTP Nick End Labeling (TUNEL) kits were acquired from Roche (Germany).

Animal experiments

Male Sprague-Dawley rats aged 6 weeks with body weights of 200 ± 25 g were acquired from Taiwan's National Laboratory Animal Center. These specific pathogen-free animals were provided unrestricted access to food (Laboratory Rodent Diet 5001, PMI Nutrition International LLC, MO, U.S.A.) and water and maintained under controlled environmental conditions with alternating 12-hour light and dark cycles. All experimental protocols involving these animals received review and approval from the Institutional Animal Care and Use Committee at Chang Gung Memorial Hospital, Chiayi, Animal Ethics Research Board (IACUC approval number: 2019032104). Isoflurane anesthesia was administered to the rats (5% for induction, 0.25-2.5% for maintenance). Each animal underwent catheterization of the left femoral vein to facilitate solution or TPN administration [17].

The experimental subjects (rats) received intravenous TPN infusion administered through the left femoral artery at a controlled flow rate of 30 mL/kg/h maintained for a duration of 3 hours to induce acute hepatic injury. For the control cohort, normal saline solution (0.9% sodium chloride) was employed as the vehicle. The SmofKabiven® formulation utilized provided a total energy content of 1000 kcal [comprising 13% glucose, 788 mL; amino acids with electrolytes, 456 mL; and lipid emulsion, 204 mL]. Each experimental animal received a cumulative infusion volume of 18 mL TPN administered at the specified rate of 30 mL/kg/h over the 3-hour intervention period. A representative rat weighing 200 g received an approximate energy delivery of 12.4 kcal during the procedure.

Male Sprague-Dawley rats (weighing 200-250g) were randomly assigned to either saline infusion (control group) or TPN infusion groups, with six animals per group. TPN was administered to all treatment animals through the left femoral vein for 3 hours at an infusion rate of 30 mL/kg/h. Blood samples were collected immediately through the left femoral vein and stored in heparin-coated capillary tubes for liver enzyme profiling and biochemical analysis. Liver tissue was harvested, washed with normal saline, and either stored at -80°C or fixed in 10% neutral buffered formalin for subsequent histopathological examinations [18].

Histochemistry and immunohistochemistry

Immunohistochemistry stain (IHC) was performed using a biotinylated secondary antibody (Vectastain Universal Elite ABC Kit, Burlingame, CA, USA). Monoclonal rabbit antibodies against phospho-IRE1 alpha (Ser724), and phospho-ASK1 (Thr845) were diluted in a ratio of 1:200. The omission of primary antibodies was used as the negative control. For three slides, cytoplasm stained with brown was scored as positive. The expression of Protein abundances of Elongation of very long chain fatty acids protein 5 (Elovl5) and Polypyrimidine tract-binding protein 3 (Ptbp3) were quantitatively evaluated using Olympus Cx31 microscope with Image-pro Plus medical image analysis system. The digital images were captured using a digital camera (Canon A640). The positive area and optical density (OD) of Elovl5 and Ptbp3 positive cells were determined by measuring three randomly selected microscopic fields (400× magnification) for each slide. The IHC index was defined as average integral optical density (AIOD) (AIOD = positive area × OD/total area) [17–19]. The TUNEL assay, initially designed as a standard histochemical method to detect DNA

fragmentation resulting from apoptosis (TAAP01D, BioTna).

Hepatocyte cell cultures and maintenance

The cell lines FL83B (CRL-2390) and HepG2 (HB-8065) were procured from American Type Culture Collection (ATCC). As delineated in a preceding publication, these cellular populations were maintained in F-12K Medium (Kaighn's Modification of Ham's F-12 Medium) and DMEM medium, respectively, with supplementation of 10% FBS (Gibco, USA) at a temperature of 37°C within an incubation environment containing 5% CO2.

Apoptosis assay and oil red O stain in liver cells

The morphological characteristics of the cells stained with 4′ ,6-diamidino-2-phenylindole (DAPI) were observed under fluorescence microscopy. Firstly, the cells were fixed with 4% paraformaldehyde for 30 min at room temperature and were then permeabilized in 0.2% Triton X-100 in phosphate-buffered saline three times for 15 min. After PBS washing, the cells were incubated with 1 μg/mL of DAPI for 30 min. The percentage of the apoptotic nuclei in the field of the 200–300 cells was observed and scored. According to a previous report, a fluorescent microscope with a 340/380 nm excitation filter was used under 200 × magnification [22].

For Oil red O staining, the cells were fixed with 10% formalin for 30 min at room temperature followed by washing with PBS three times. After PBS was removed, 500 μl of 60% isopropanol was added and rinsed for 5 minutes to remove water. Following that, 1 mL of freshly prepared ORO solutions were added to the wells respectively and incubated for 15–20 minutes at room temperature. ORO solution was pipetted out, cells were washed with 500 μl of ddH_2O for 15–20 seconds to remove excess dye solution, and then washed with PBS for more than 3 times until the liquid is clarified, pictures were captured (200×) under a microscope within 24 h.

Measurement of lipid droplets and reactive oxygen species and mitochondrial membrane potential

The apoptotic cells (V+/PI−) were measured by the fluorescence-activated cell sorter analysis in a FACS analyser.[23] Nile red: a selective fluorescent stain for intracellular lipid droplets and Nile red-stained, lipid droplet-filled cells exhibited greater fluorescence intensity than did nile red- stained control cells, and the cell populations could be analyzed by flow cytofluorometry. The intracellular accumulation of ROS (O2−) was determined using the fluorescent probes of DHE (Dihydroethidium) and the cells were washed prior to FACS analysis. JC-1 staining to examine the changes in mitochondrial membrane potential. The results are presented as a percentage of fluorescence intensity compared with the control sample. FACS analysis (Attune NxT Flow Cytometer, Thermo Fisher Scientific Inc., Waltham, MA USA). The data of the fluorescent intensity and the number of stained cells were quantified and analyzed and were represented as a percentage of the untreated control group in three independent experiments [24].

Transfection with small Interfering RNA (siRNA)

Elovl5 siRNAs (Catalog: sc-62269), Ptbp3 (Catalog: sc-106897) and control siRNA (Catalog: sc-35448) were purchased from Santa Cruz Biotechnology (Santa Cruz, CA, USA). For transfection, cells were first incubated at 37°C overnight, p53 siRNA or control siRNA were transfected using Lipofectamine™ LTX Reagent with PLUS™ Reagent (Invitrogen™, Cat: 15538100), according to the manufacturer's instructions.

Protein extraction, protein digestion, and iTRAQ labelling

Samples underwent rapid freezing in liquid nitrogen and subsequent lysis utilizing Lysis buffer (iNtRON PRO-PREP™). The extracted proteins were subjected to desalting procedures employing Amicon® Ultra-15 devices (Millipore) and subsequently quantified through implementation of the BCA assay (Thermo Fisher, USA). The resultant peptides were labeled with iTRAQ 4-plex reagents and solubilized in 0.5 M TEAB (pH 8.5). Reduction processes were conducted at 60°C for a duration of 30 minutes, followed by alkylation procedures performed at 37°C for an equivalent 30-minute period (utilizing TCEP in conjunction with iodoacetamide). Following concentration via SpeedVac drying, peptides underwent reconstitution and labeling in accordance with the protocol established by Applied Biosystems. Trypsin digestion was executed prior to the labeling process. Control group samples were designated with iTRAQ tags 114/115, whereas TPN group samples received tags 116/117, with each sample represented by two biological replicates [19].

Database search and protein quantification

Raw MS data were analyzed using Mascot (v2.5) and Proteome Discoverer (v2.1) against the Swiss-Prot human protein database. Search parameters were previously described [19,25].

Proteomic bioinformatic analysis

In iTRAQ analysis, differentially expressed proteins are selected based on a fold change >1.5 or <0.5, a P-value <0.05, and an FDR <0.05. Each protein must have at least one independent peptide identified, with a molecular weight >20 kDa and sufficient sequence coverage for reliable results. Protein annotation and pathway classification were performed using Gene Ontology (GO) and KOBAS 3.0 (KEGG). Statistically significant (FDR $p < 0.05$) differentially accumulated proteins were analyzed, with color intensity indicating significance. Protein-protein interaction networks were constructed using the STRING database (https://string-db.org) [19,25].

Preparation of total cell extracts and immunoblot analyses

The cells were lysed with lysis buffer comprising sterile water, cell lysis solution (RIPA Buffer, Thermo Fisher, Waltham, MA, USA), (Sigma), and Protease inhibitor cocktails (Sigma). Proteins were separated on sodium dodecyl sulfate (SDS)–polyacrylamide gel by electrophoresis and transferred to the polyvinylidene fluoride (PVDF) membrane, and protein expression was detected using specific antibodies in the Chemiluminescence image system (Thermo Fisher Scientific, Waltham, MA, USA).

Quantitative analysis of the area of the photo images in the immunoblots for in terms of their numbers of pixels were performed using the ImageGauge 3.46 software (Fujifilm, Inc.) as previously described [26].

Chromatin immunoprecipitation (ChIP) analysis

Cross-linked immunoprecipitated complexes were reversed at 65°C for 2 hours, followed by elution with a buffer containing 50 mM Tris-Cl (pH 7.5), 1 mM EDTA, and 1% SDS. DNA was purified using the ChIP DNA Clean & Concentrator Kit (Zymo Research). PCR was performed to amplify the promoter regions of **Ptbp3** and **Elovl5** under the following conditions: 94°C denaturation, 60°C annealing, and 72°C extension for 40 cycles. Specific primers were:

Ptbp3 (-490 to -275 bp) Forward: 5′-TGCTCTCAGGTCCGGAAAG-3′, Reverse: 5′-CGACTCGCCCTCCTACAAG-3′.

Elovl5 (-483 to -2181 bp) Forward: 5′-TGCTT CAATTTGCGCAACAG-3′, Reverse: 5′-AGTGAA GTTCTGGATGCCCT-3′. The percentage of input for each ChIP sample was calculated as % **Input = 2^(-ΔCt)**. [27,28]

Statistical analysis

Data are represented as mean ± standard deviation with three repeats from more than triplicate independent experiments. Using the SPSS software (version 10.0; SPSS, Chicago, IL, USA), statistically significant differences were evaluated with one-way ANOVA with post-hoc Mann-Whitney U test and Student's paired t-test and established at $p < 0.05$. [17,18,29].

Results

The effect of total parenteral nutrition on rat liver

Several studies have linked ER dysfunction and activation of the unfolded protein response (UPR), including IRE1, which is also positively correlated with the severity of liver disease [30]. Our previous data demonstrated the generation of free radicals and ER stress induced by liver damage due to TPN [17,18]. Based on these studies, we tested the differential protein expressions before and after oxidative liver damage and conducted molecular toxicology study to examine the generation of ER stress and hepatitis. For analyses, male Sprague-Dawley rats (weighing 200 to 250 g) were used. TPN was applied to all animals through the left femoral vein for 3 h at an infusion rate of 30 mL/kg/h [17,18]. The rat livers of the TPN group exhibited obvious inflammatory reactions and hepatocyte death in the portal zone Z1, periportal zone Z2, and terminal hepatic venule Z3. Compared to the control group, there was a significant decline in the number of hepatocytes of the TPN group (Figure 1). The quantitative analysis showed that the number of hepatocytes in the Z1, Z2, and Z3 zones of the control group was 135 ± 8, 140 ± 10, and 145 ± 11 respectively, while that of the TPN group was 68 ± 5, 60 ± 8, and 70 ± 8 ($p<0.05$) respectively. There were no significant differences of livers appearance were observed between the two groups in liver size or weight during tissue collection from the rats. Further, the serological examination showed a significant increase in the liver damage index of rats of the TPN group and the levels of ALT, AST, and ALP were, respectively, 139 ± 5, 84 ± 3 and 641 ± 7, while that of the control group were 40 ± 5, 25 ± 4, and 544 ± 8 ($p<0.05$), respectively (Table 1). These results indicate that the TPN-induced liver injury is accompanied by significant abnormalities in the liver function and histopathological changes. In future research, we will focus on understanding the molecular mechanisms of these pathological changes and explore related protein markers for better understanding of the mechanism of TPN-induced liver injury.

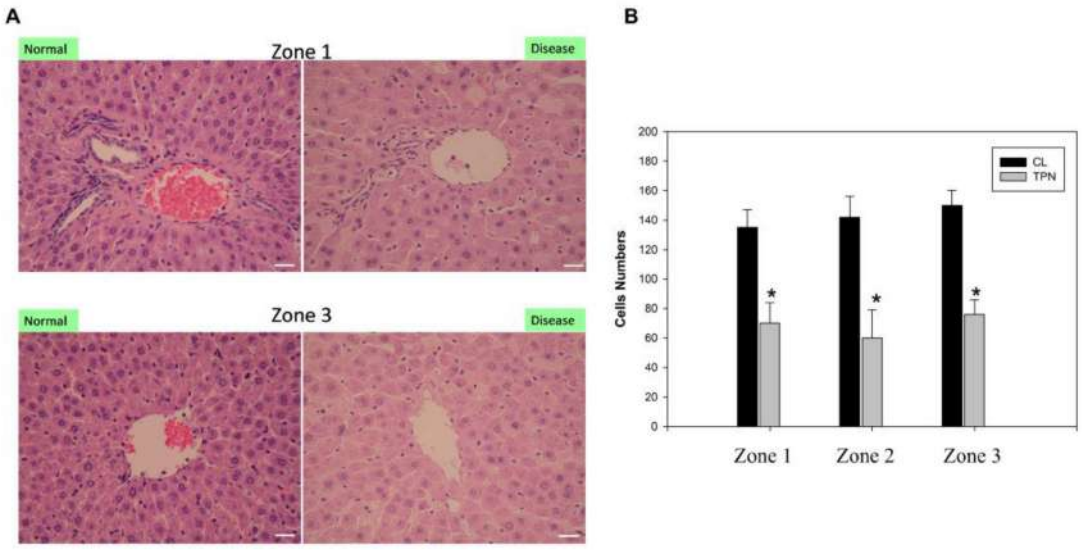


Figure 1. Histological examination of the total parenteralnutrition (TPN) rats. The livers were H&E-stained to examine the portal (Zone 1), mid-zonal (Zone 2) and terminal hepatic venules (Zone 3). (A) Saline infusion control (I); TPN infusion (II); staining of Zone 1 (left column) and Zone 3 (right column) of the liver. Liver pathology in the control group exhibited normal hepatocyte structure and arrangement. The TPN treated group exhibited damaged liver structure, as indicated by monocyte infiltration, steatosis and the presence of necrotic cells. (B) Quantitative evaluation of pathological examinations. Normal hepatocytes were counted from 10 random fields (200× magnification) of each liver sample and the values represent the mean ± SD of six rats.

Table 1. Mean serum liver function in total parenteral nutrition rats

Group	Normal	TPN
GOT (IU/L)	40 ± 5	139 ± 5
GPT (IU/L)	25 ± 4	84 ± 3
ALP (IU/L)	544 ± 8	641 ± 7

Normal: Normal saline; TPN: Kabiven; TPN Flow: 30mL / kg B.W. / hr × 3hr; GOT: Aspartate Aminotransferase; GPT: Alanine Aminotransferase; ALP: Alkaline Phosphatase.

Analysis of differentially expressed proteins in hepatocytes from rats following total parenteral nutrition-induced liver injury by iTRAQ-based quantitative proteomics

An in-depth proteomic analysis of TPN-induced liver injury was conducted, aiming to identify the biomarkers of liver inflammation and explore the associated mechanism. Liver tissues were collected from the animals of various groups, and isotope labeling technique was used to label the proteins in liver tissues to explore TPN-induced liver inflammatory reaction. The iTRAQ chemical calibration method was combined with mass spectrometry to analyze the tissue samples of TPN-induced liver injury, to evaluate the changes in relative protein content (Figure 2). A total of 6,436 proteins were identified in this study, of which quantitative results of 48 proteins were obtained. The analysis further revealed 19 proteins with significantly increased expression (Table 2) and 29 proteins with significantly reduced expression (Table 3) in the control group and TPN group (difference exceeding 1.5 times). Screening and classification of these differentially expressed proteins, Elovl5 and Ptbp3, revealed enhanced expression in the TPN group, and the important role of these proteins in lipid metabolism was shown. These 19 differentially expressed proteins were classified using the PANTHER (Protein Analysis Through Evolutionary Relationships) Classification System (www.pantherdb.org). Further analysis of their molecular and functional characteristics revealed in 6 Kyoto Encyclopedia of Genes and Genomes (KEGG) pathways, 17 biological processes, 5 cellular components, 16 molecular functions, and their network displays were classified (Figure 3). Figure 3 shows a 19-protein network of interactions by using the String database (http://string-db.org), a helpful tool for eliminating protein groups involved in a particular pathway [19,25]. The protein interaction network diagram generated by the String database further revealed the interaction between Elovl5 and Ptbp3 proteins in lipid metabolism. These results showed that the expression levels of Elovl5 and Ptbp3 are closely related to ER stress and lipid metabolism. Further, Elovl5 affects the composition of cellular lipid pools by extending fatty acids [31], while Ptbp3 possibly participates in the ER stress response by regulating the UPR pathway, to reduce the ER stress [32,33]. We also extensively analyzed 29 proteins with reduced expression in the TPN group, and employed the PANTHER system for classification, covering 10 KEGG pathways, 19 biological processes, 20 cellular components, and 20 molecular functions (Figure 4).

The results showed that in TPN-induced liver injury process, the functions and interaction network of these proteins may play an important role in the pathological changes in the liver. Noteworthily, more specific information regarding Elovl5 and Ptbp3 protein abundances and functional characteristics in hepatocytes from rats following TPN-induced liver injury may be determined, particularly in the context of fatty acid metabolism and ER stress, through further experimental studies such as proteomic analyses, gene expression profiling, and functional assays.

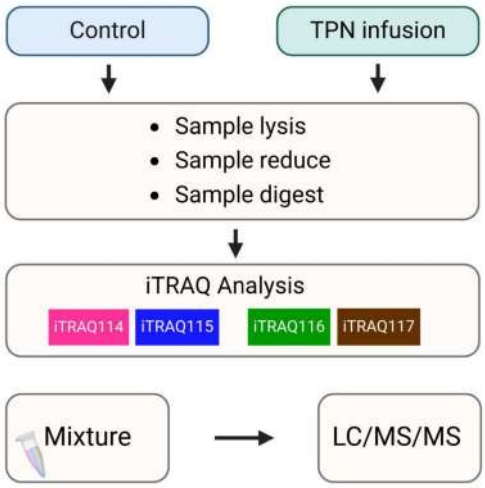


Figure 2. Schematic flowchart of the iTRAQ method by TPN rat model.

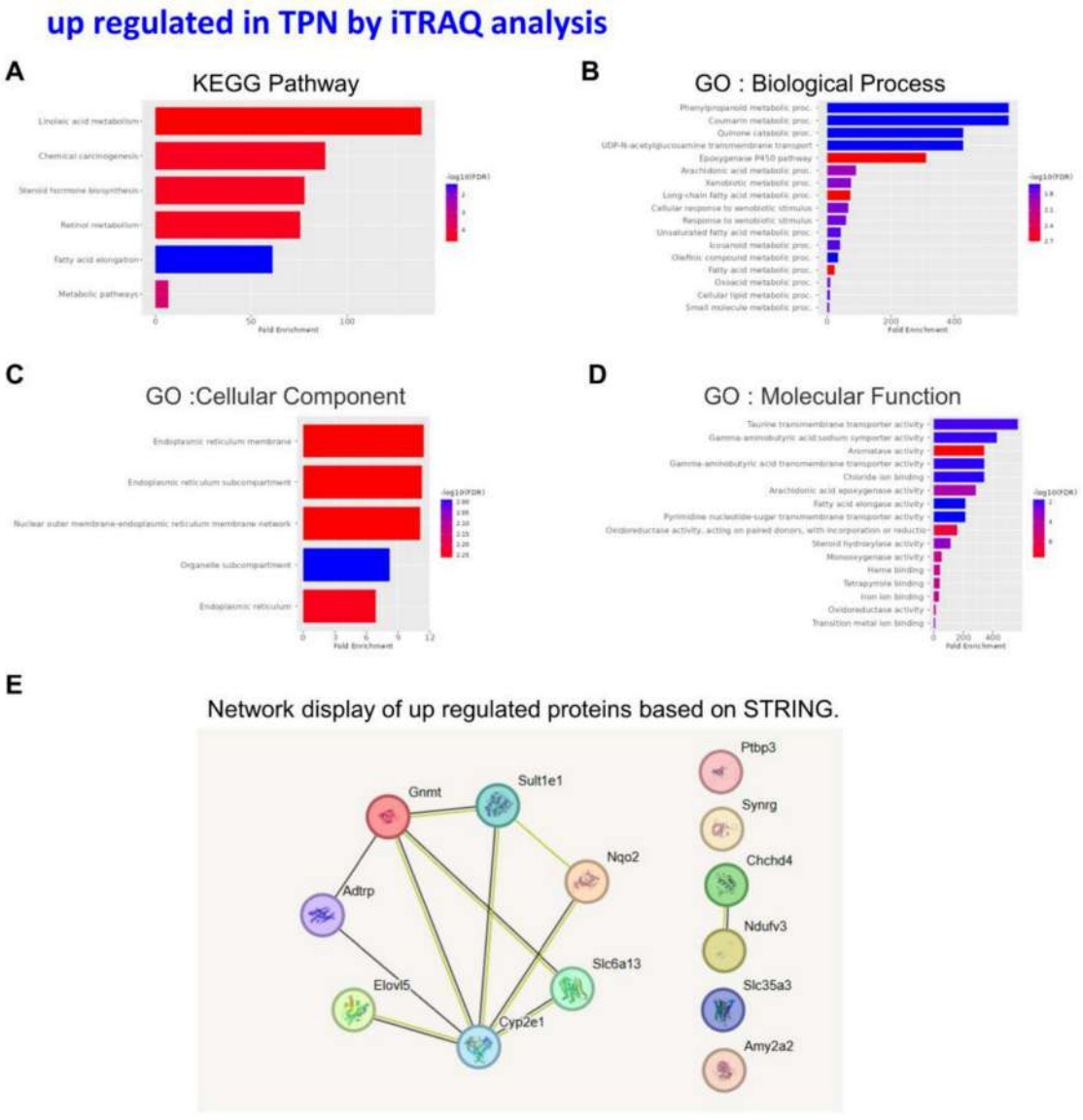


Figure 3. Classification of the identified proteins upregulated from rats following TPN-treatment by the KEGG, GO and STRING database. KEGG pathway (A) Biological process (B) Cellular component (C) Molecular function (D) STRING (E).

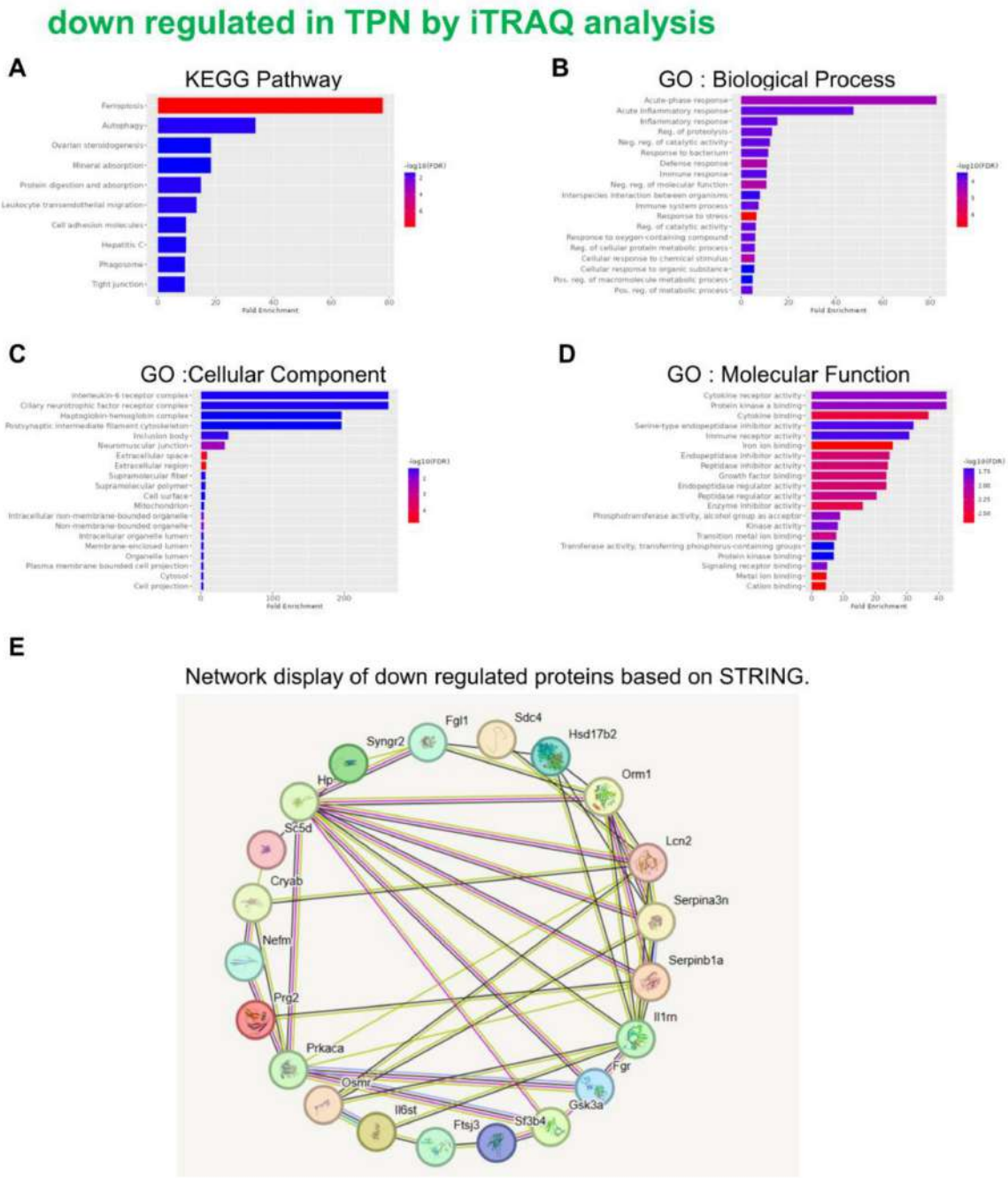


Figure 4. Classification of the identified proteins downregulated from rats following TPN-treatment by the KEGG, GO and STRING database. KEGG pathway (A) Biological process (B) Cellular component (C) Molecular function (D) STRING (E).

Validation of the expression patterns of Elovl5 and Ptbp3 validated *in vivo* in the TPN infusion

An immunostaining analysis system was used to observe the changes in liver tissue through H&E staining and immunohistochemical staining techniques [25]. These analyses included antigen processing, blocking of endogenous catalase, application of the primary antibody and the secondary antibody, and sealing after DAB staining. The expression of specific proteins in the liver was examined. The proteins of special concern included Elovl5, Ptbp3, phospho-IRE1 alpha (Ser724), and phospho-ASK1 (Thr845). Immunostaining analysis revealed that the expression levels of Elovl5 and Ptbp3 were significantly higher, by 2-4 times, in the TPN-induced liver injury group than the control group. In addition, the two ER stress-related proteins, phospho-IRE1 alpha (Ser724) and phospho-ASK1 (Thr845), had significantly increased expression in the TPN group, the difference also being 2-4 times (Figure 5). The death of liver cells in the TPN group was

verified by terminal deoxynucleotidyl transferase dUTP nick end labeling (TUNEL) staining. The death rate of liver cells in the terminal hepatic venule Z3 zone was five times that of the control group (Figure 5). These results further prove the effect of the TPN-induced ER stress on liver injury and emphasize the importance of Elovl5, Ptbp3, and other key proteins in the pathological changes in the liver.

Table 2. Proteins that are up regulated in TPN by iTRAQ analysis

No.	Accession	Gene symbol	Name	MW [kDa]	Ratio: TPN / N	Ratio: TPN / N
1	P05182	Cyp2e1	Cytochrome P450 2E1	56.6	1.75	1.73
2	P00689	Amy2	Pancreatic alpha-amylase	57.1	1.79	1.92
3	Q5M828	Adtrp	Androgen-dependent TFPI-regulating protein	26.9	1.96	1.87
4	Q6AY80	Nqo2	Ribosyldihydronicotinamide dehydrogenase	26.3	2.03	1.71
5	Q6PCU8	Ndufv3	NADH dehydrogenase [ubiquinone] flavoprotein 3, mitochondrial	11.9	2.08	1.69
6	Q920L7	Elovl5	Elongation of very long chain fatty acids protein 5	35.2	2.16	2.00
7	P50169	Rdh3	Retinol dehydrogenase 3	35.6	5.95	6.54
8	Q64581	Cyp3a18	Cytochrome P450 3A18	57.3	1.45	1.47
9	P51590	Cyp2j3	Cytochrome P450 2J3	57.9	1.45	1.55
10	Q9Z118	Ptbp3	Polypyrimidine tract-binding protein 3	56.7	1.47	1.60
11	P05183	Cyp3a2	Cytochrome P450 3A2	57.7	1.48	1.51
12	P11711	Cyp2a1	Cytochrome P450 2A1	56	1.50	1.44
13	P31646	Slc6a13	Sodium- and chloride-dependent GABA transporter 2	68.2	1.51	1.47
14	Q9JKC9	Synrg	Synergin gamma	141.3	1.53	1.45
15	Q5BJN5	Chchd4	Mitochondrial intermembrane space import and assembly protein 40	15.5	1.57	1.44
16	P49889	Ste	Estrogen sulfotransferase, isoform 3	35.4	1.62	3.47
17	P13255	Gnmt	Glycine N-methyltransferase	32.5	1.62	1.49
18	P15149	Cyp2a2	Cytochrome P450 2A2	56.3	1.65	1.43
19	Q6AXR5	Slc35a3	UDP-N-acetylglucosamine transporter	36.1	1.65	1.48

Table 3. Proteins that are down regulated in TPN by iTRAQ analysis

No.	Accession	Gene symbol	Name	MW [kDa]	Ratio: TPN / N	Ratio: TPN / N
1	Q5M8C6	Fgl1	Fibrinogen-like protein 1	36.5	0.40	0.49
2	P02764	Orm1	Alpha-1-acid glycoprotein	23.6	0.41	0.43
3	P11510	Cyp2c12	Cytochrome P450 2C12, female-specific	55.9	0.43	0.41
4	Q4G075	Serpinb1a	Leukocyte elastase inhibitor A	42.7	0.43	0.60
5	P08932		T-kininogen 2	47.7	0.47	0.52
6	Q62730	Hsd17b2	Estradiol 17-beta-dehydrogenase 2	41.9	0.48	0.52
7	P06866	Hp	Haptoglobin	38.5	0.48	0.65
8	P09006	Serpina3n	Serine protease inhibitor A3N	46.6	0.48	0.61
9	P34901	Sdc4	Syndecan-4	21.9	0.48	0.55
10	P40190	Il6st	Interleukin-6 receptor subunit beta	102.4	0.48	0.56
11	Q65Z14	Osmr	Oncostatin-M-specific receptor subunit beta	108.6	0.49	0.51
12	P30152	Lcn2	Neutrophil gelatinase-associated lipocalin	22.5	0.49	0.42
13	Q5QE78	Aox2	Aldehyde oxidase 2	147.8	0.51	0.65
14	O54980	Syngr2	Synaptogyrin-2	24.7	0.51	0.54
15	P25086	Il1rn	Interleukin-1 receptor antagonist protein	20.3	0.52	0.52
16	P12839	Nefm	Neurofilament medium polypeptide	95.7	0.53	0.53
17	O08560	Dgkz	Diacylglycerol kinase zeta	103.9	0.54	0.65
18	Q5RJT2	Ftsj3	pre-rRNA processing protein FTSJ3	94.7	0.54	0.62
19	P36201	Crip2	Cysteine-rich protein 2	22.7	0.59	0.61
20	Q9EQS5	Sc5d	Lathosterol oxidase	35.1	0.61	0.48
21	Q66H85	Ankzf1	Ankyrin repeat and zinc finger domain-containing protein 1	80.5	0.62	0.60
22	P35446	Spon1	Spondin-1	90.7	0.62	0.65
23	Q6P6U0	Fgr	Tyrosine-protein kinase Fgr	58.8	0.64	0.59
24	Q9EPJ0	Nucks1	Nuclear ubiquitous casein and cyclin-dependent kinase substrate 1	27.1	0.64	0.60
25	P18265	Gsk3a	Glycogen synthase kinase-3 alpha	51	0.65	0.64
26	Q6AYL5	Sf3b4	Splicing factor 3B subunit 4	44.3	0.65	0.59
27	Q63189	Prg2	Bone marrow proteoglycan =	25.1	0.66	0.60
28	P27791	Prkaca	cAMP-dependent protein kinase catalytic subunit alpha	40.6	0.66	0.53
29	P23928	Cryab	Alpha-crystallin B chain	20.1	0.67	0.36

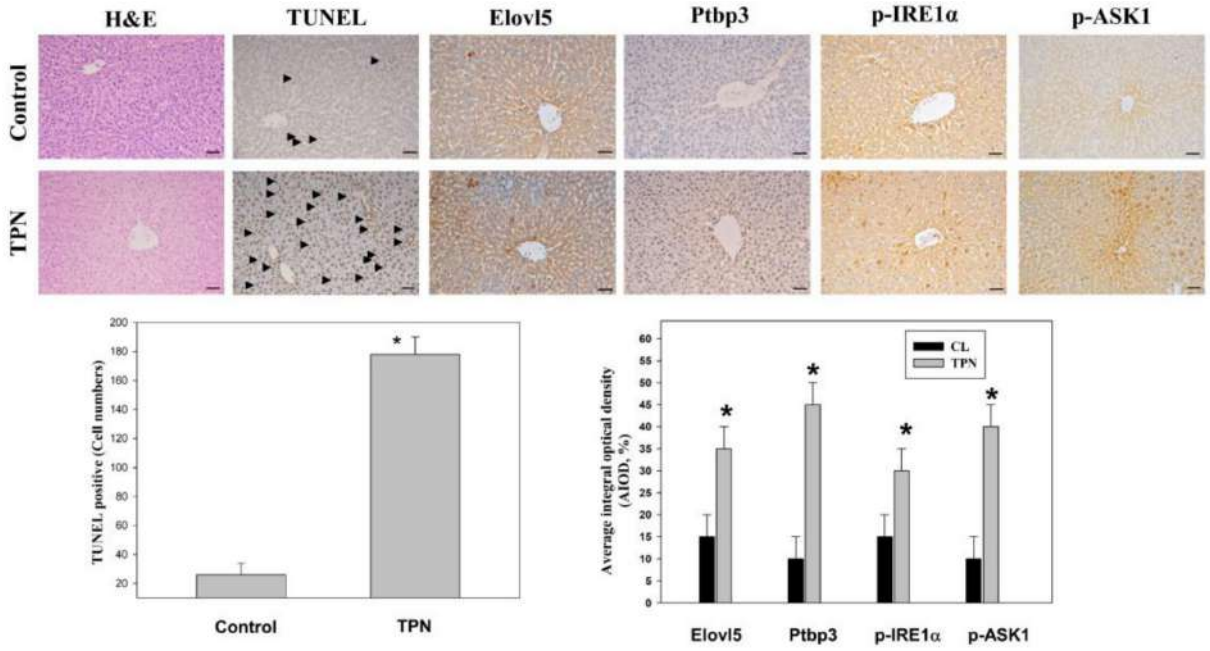


Figure 5. Effects of TPN infusion-induced liver tissue damage in rats' livers from terminal hepatic venules (Zone 3). (A) Rats were randomly administered to saline infusion as control group (Control, n = 6) and TPN infusion (n = 6, an infusion rate of 30 mL/kg/hr for for 3 hours and were determined for liver tissue. Representative liver sections of hematoxylin and eosin (H&E) stained with control group and TPN group animals. Immunohistochemical analysis of these livers from each treatment group was conducted and evaluated in multiple tissue fields. Representative IHC (for TUNEL, ELOVL5, Ptbp3, ASK1 (phospho Thr845) and IRE1α (phospho Ser726) proteins) and H&E staining images in each treatment group are presented. Quantitative immunohistochemical were evaluated with average integrated optical density (AIOD). The positive stained area was evaluated from three randomly selected observation fields of each tissue section. Data are expressed as mean ± S.D. (n = 6 per group). *p < 0.05, compared with the control group, magnification ×200.

Effects of differentially expressed proteins, Elovl5 and Ptbp3 on the lipotoxic effect of palmitate acid on liver cells

Multiple experimental methods were used to observe and analyze the death of cell nuclei, fat vacuole formation, cell viability, lipid oil droplet formation, ROS generation, and mitochondrial membrane potential changes. First, significant changes in the nuclear death of hepatocytes induced by different doses of palmitate acid (0, 100, 300, 500 μM) were observed by DAPI staining and fluorescence microscopy, that revealed significantly increased cytotoxicity with the increase in palmitate concentration (Figure 6A). Next, the Oil-Red-O stain revealed that the palmitate induced the formation of fat vacuoles in hepatocytes, showing a dose-dependent effect of palmitate on lipid accumulation (Figure 6B). The results of Annexin-V FITC/PI fluorescence staining to measure the apoptosis rate of cells showed that the apoptosis rates of hepatocytes were 10%, 20%, and 49%, upon the use of different concentrations of palmitate (0, 100, 300 μM), suggesting a significant apoptosis-inducing effect on hepatocytes (Figure 7). In addition, Nile Red staining was performed and detected through flow cytometry. After 24 h of palmitate treatment, the production of lipid oil droplets in hepatocytes increased significantly, with a significant increase of 1, 2.5, and 4.5 folds, respectively, as the concentration increased (Figure 7). The changes in intracellular ROS production were quantified using DHE staining; with the increase in palmitate concentration (0, 300, 500 μM), the ROS production in the hepatocytes increased significantly, reaching 1, 1.7, and 3.1 fold respectively (Figure 7). In addition, JC-1 staining to examine the changes in mitochondrial membrane potential showed that after 24 h of palmitate treatment, the mitochondrial membrane potential of hepatocytes was significantly reduced, with corresponding rates of 4.7, 0.7, and 0.5, demonstrating a serious damage to the mitochondrial function (Figure 7). These experimental results indicate a significant toxic effect of palmitate acid on hepatocytes, including apoptosis induction, promoting lipid accumulation, increasing ROS generation, and damaging mitochondrial function.

Effects of palmitate acid on protein expression and signaling pathways in hepatocytes

In cell model, palmitate acid induces lipotoxicity, leading to ROS accumulation and subsequent activation of these signaling pathways. The combined activation of JNK, p38, and ASK1 and aggravates ER stress and promotes apoptotic cell death, contributing to the overall lipotoxic effects of palmitate acid [7,8]. The expression of proteins was tested using western blotting. The free radicals are generated through the

ER stress signaling pathway and the process involves two types of proteins: Ire1α/TRAF2. The effects of the ER stress on the differentially expressed proteins Elovl5 and Ptbp3 during hepatitis were further demonstrated. When the palmitate acid concentration was: 0, 100, 300, 500 μM, the treatment of hepatocytes for about 24 h, led to the expression of p-Ire1α/TRAF2, Elovl5, and Ptbp3 (Figure 8A). B-cell lymphoma protein 2 (Bcl-2) is a critical protein in the cell apoptosis. In mitochondria, the Bc1-2 family protein interacts with other apoptins to regulate the stability of mitochondrial structure and function, and acts as the "main switch" for cell apoptosis. The Bcl-2 family includes two kinds of proteins: the anti-apoptotic protein Bcl-2/Bcl-XL, and the pro-apoptotic protein Bcl-2-associated X (Bax). When hepatocytes were treated with palmitate acid at 500 μM for 24 h, there was a decrease in the expression of Bcl-2/Bcl-XL and the release of activated caspase-3/-9 and cytochrome C to the cytoplasmic (Figure 8B). Moreover, this treatment also activated the ROS/ASK/JNK/p38MAPK pathway, especially within the 3-24 h of palmitate acid induction (Figure 8C). Thus, the treatment of hepatocytes led to the induced of the ROS/ASK/JNK/p38MAPK pathway. Therefore, to determine the potential mechanisms of Elovl5- and Ptbp3-mediated cell apoptosis and lipid droplet generation, we transfected siRNAs for Elovl5 and Ptbp3 or scrambled siRNA control particles into hepatocytes and consequently observed downregulated levels of Elovl5 and Ptbp3 proteins (Figure 8D). As shown in Table 5, siRNAs for Elovl5 and Ptbp3 blocked palmitate treatment-induced cell death by 20%, 13%, and 11%, respectively. The siRNA-mediated blockage of Elovl5 and Ptbp3 expression reduced palmitate-induced ROS generation almost by 1.7, 1.2, and 1.3 fold. The elevated levels of Elovl5 and Ptbp3 demonstrate the impact of palmitate-induced ER stress on liver injury and highlight the critical roles of Elovl5, Ptbp3 in the pathological changes observed in liver cells.

Effect of palmitate acid on gene expression of Elovl5/Ptbp3 and its correlation with H3K4me3 histone modifications

The methylation of histones, the H3K4me3 plays an activating effect of the transcriptional activity of genes in the abnormal hepatic lipid metabolism, oxidative stress response, mitochondrial damage and cell apoptosis, particularly in pathogenesis of liver [34,35]. We further continued to explore any possible relation of palmitate acid in regulating the H3K4me3 methylated histone modification to induce the increase in the Elovl5/Ptbp3 protein expression by activating the ER stress ASK1/JNK/p38MAPK pathway. The potential effects of the ASK1/JNK/p38MAPK signaling pathway on the epigenetic regulation of histone modifications was also examined. The histone modifications include methylation and acetylation. The nucleic acid modification occurs at the position where the trimethylated lysine 4 of histone H3 is associated with the chromatin. The role of histone methylation in regulating specific genes was identified through ChIP. The results showed that palmitate acid could induce the Elovl5/Ptbp3 gene expression, and facilitate the crucial phenomenon of histone H3K4me3 modification on the promoter binding site

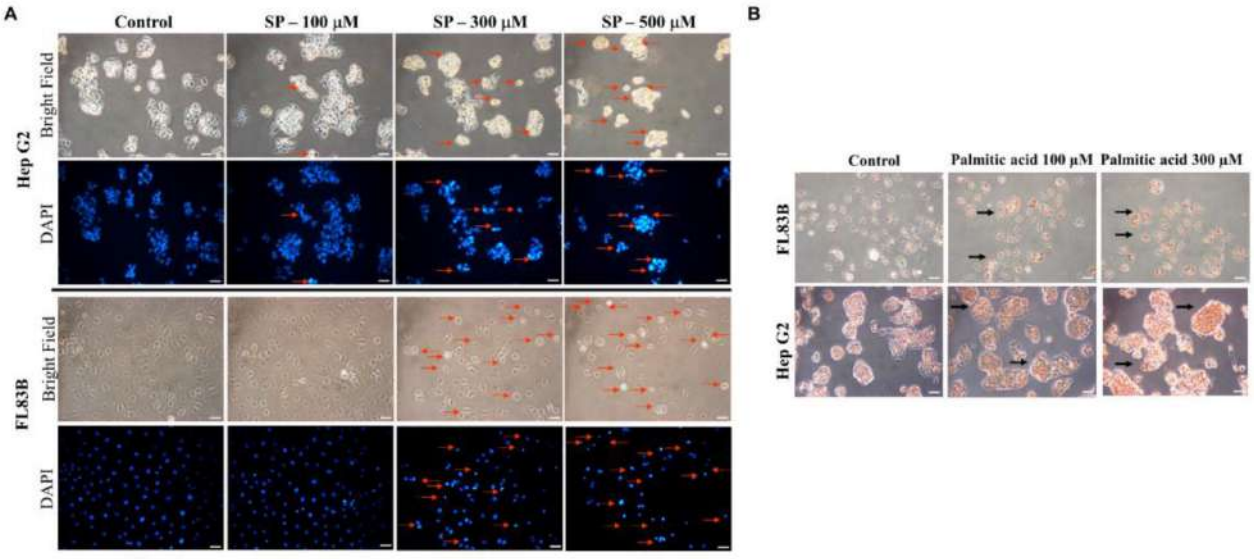
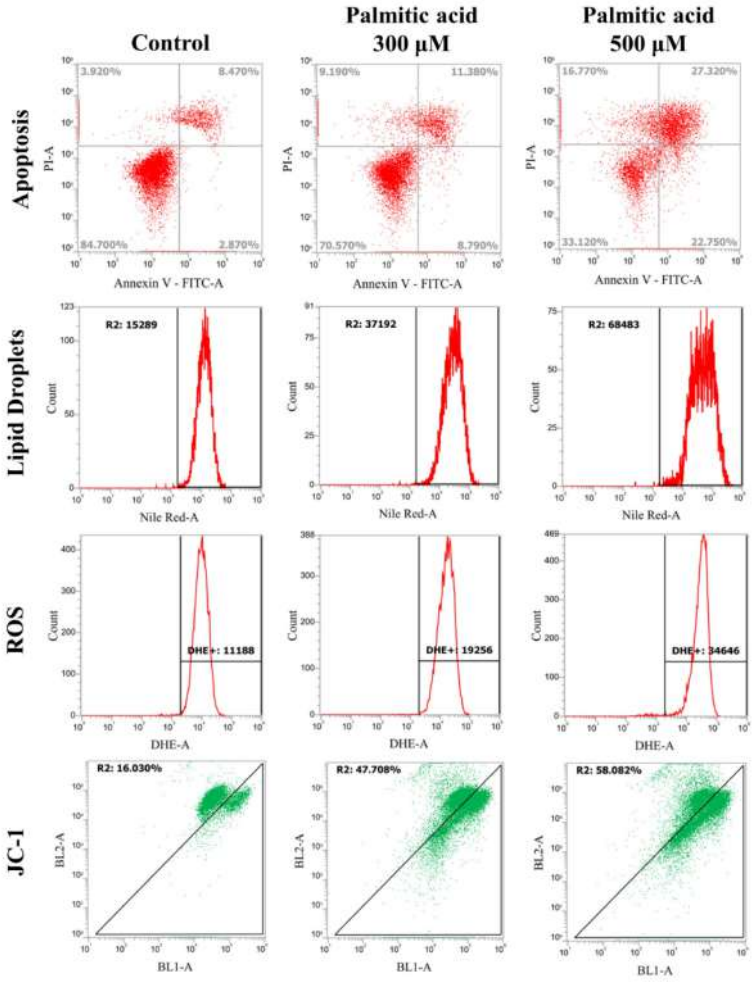


Figure 6. Changes in nuclei by DAPI staining and Oil Red O. Liver cells were treated with Palmitate, and stained with DAPI. (A) Apoptotic cells were measured under fluorescence microscopy as described. Apoptotic cells indicate condensed and damaged nuclei (red arrows). Magnification × 200. (B) Representative bright-field images of Oil Red O stained cells.

(-483~-281/-490~-275) of the genes (Table 4). The effect of the palmitate acid on regulating the H3K4me3 methylated histone modifications was tested using inhibitors. The effects of ER stress-associated proteins ASK1 inhibitor TUDCA (1 mM), JNK inhibitor (50 μM), and p38 inhibitor (20 μM) on Elovl5/Ptbp3 expression and H3K4me3 histone modification varied to different degrees. The ASK1/JNK/p38MAPK pathway affects about 65% respectively. These results showed that palmitate acid can induce the expression of Elovl5/Ptbp3 genes, and increase their expression by regulating the H3K4me3 modification via ASK1/JNK/p38MAPK pathway (Figure 9).



	Control	Palmitic acid 300 μM	Palmitic acid 500 μM
Apoptosis	10 ± 3	20 ± 2	49 ± 2
Lipid Droplets (Fold)	1	2.5 ± 1	4.5 ± 1
ROS (Fold)	1	1.7 ± 0.5	3.1 ± 0.5
JC-1 (monomers/aggregates)	4.7 ± 0.3	0.7 ± 0.2	0.5 ± 0.1

Figure 7. Cells were treated with Palmitate, and induces cell apoptosis, increased lipid accumulation and ROS production and decreasing mitochondria potential in liver cells. After 24 hours of palmitic acid treatment, the hepatocytes were stained with FITC-conjugated Annexin-V and PI for a flow cytometry analysis, as described in the Materials and Methods section. After receiving individual treatment, the percentage of the apoptotic cells is shown in each frame, as indicated. Nile red staining of liver cells and quantitative analysis by FACS. Fluorescence dot plot and relative fluorescence graph. The intracellular ROS of cells treated with palmitic acid for 24 hours was measured by using a FACS analysis, as described in the Materials and Methods section. Representative histograms of typical H2DCFDA/Fluo-3 profiles are shown. The production of ROS was expressed as the fold of the control group. The membrane-permeant JC-1 dye exhibits potential-dependent accumulation in mitochondria, indicated by palmitic acid, which is indicated by a decrease in the green/red fluorescence intensity ratio. Data are presented, based on three independent experiments, as mean ± S.D.

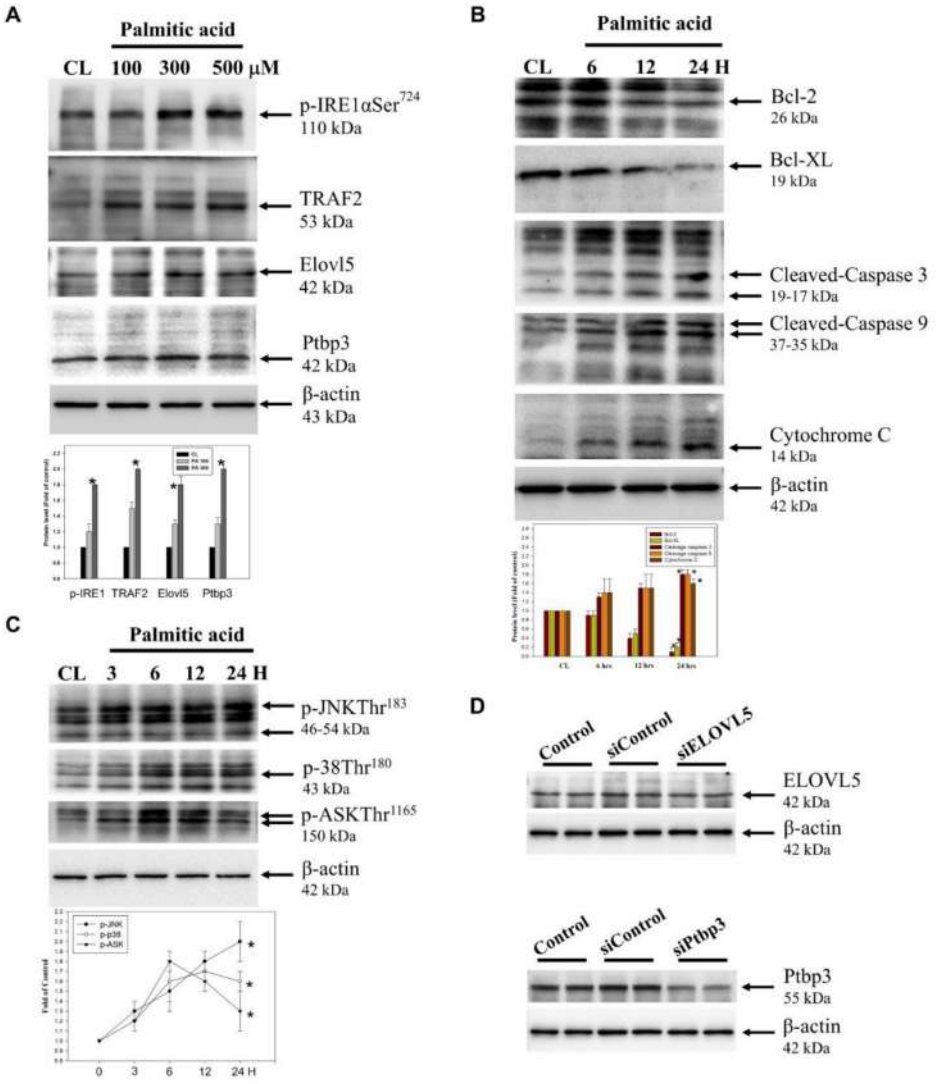


Figure 8. The effect of Palmitate on ER stress-related proteins, hepatocyte injury and and ASK/JNK/p38 MAPK pathways in liver cells. (A, B, C) The protein levels of p-IRE1, TRAF2 and Elovl5 and Ptbp3 ae well as Bcl-2, Bcl-XL, caspase-3, caspase-9, cytoplasmic Cytochrome C, phosphorylation of ASK, JNK, and p38 were determined using Western blotting in sodium palmitate-treated cells. While β-actin served as an internal control, densitometric analysis was used to quantify protein levels with the control at 100%. Data are expressed as the mean ± SD of three independent experiments. * $p < 0.05$, compared with the control group. (D) Protein lysates of the cells from control, siControl, siElovl5, and siPtbp3 clones were subjected to western blot analysis.

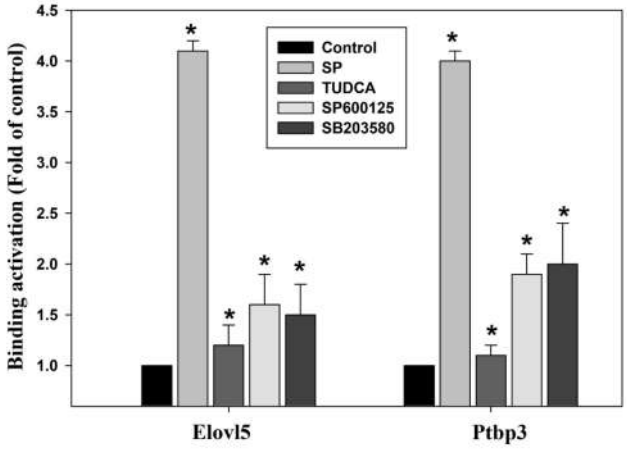


Figure 9. The kinase inhibitors block the binding activities of Elovl5 and Ptbp3 promoter regions, as induced by palmitate treatment. The chromatin immunoprecipitation assay was performed using antibodies against histone Histone H3, trimethylated lysine 4 and Elovl5/Ptbp3 promoters (the -483~-281/-490~-275 target sites, as described in the Materials and Methods) in the precipitated DNA, which was amplified by quantitative real-time polymerase chain reaction using specific primer sets. The liver cells were incubated with or without ER stress inhibitor TUDCA, JNK inhibitor SP600125, or the p38 MAPK inhibitor SB203580 for 24 h at various concentrations. The data are presented as the mean ± SD of three independent experiments. * $p < 0.05$, as compared to the control group.

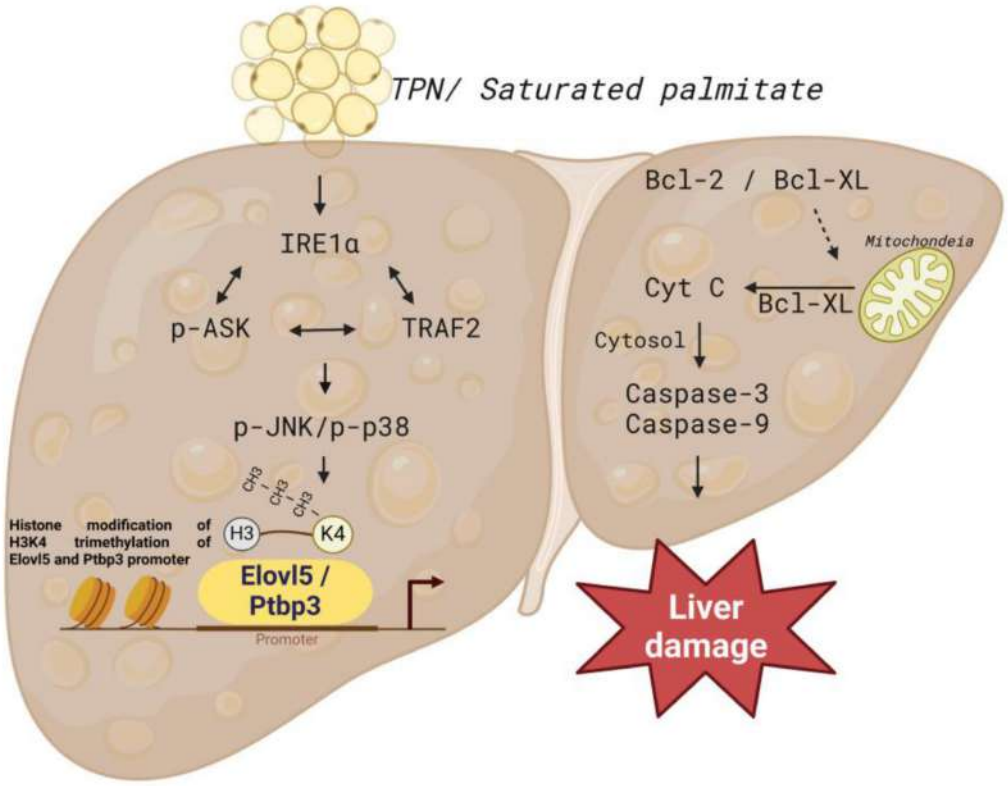


Figure 10. Schematic presentation of the molecular mechanism of palmitate -mediated apoptotic induction and endoplasmic reticulum stress of liver cells. Sodium palmitate treatment increases the expression of Elovl5 and Ptbp3 through ER stress-derived and ASK1/JNK/p38 MAPK-signaling-pathway-mediated histone H3K4me3. Activation of Elovl5 and Ptbp3 by palmitate triggers liver cells death through the inhibition of Bcl-2 and Bcl-XL, activated caspase-3, and -9.

Table 4. The specific primers.

Ptbp3 -490 to -275 bp
Ptbp3 F 5'- TGCTCTCAGGTCCGGAAAG -3'
Ptbp3 R 5'- CGACTCGCCCTCCTACAAG-3'
Elovl5 -483 to -281 bp
Elovl5 F 5'- TGCTTCAATTTGCGCAACAG-3'
Elovl5 R 5'- AGTGAAGTTCTGGATGCCCT-3'

Table 5. The effects of Elongation of very long chain fatty acids protein 5 (Elovl5) and Polypyrimidine tract-binding protein 3 (Ptbp3) inactivation on cell apoptosis and ROS of palmitate treatment in hepatocytes.

	Apoptosis (%)	ROS generation (Fold)
Control	8 ± 2	1
Sodium palmitate	20 ± 3	3.0 ± 0.5
Sodium palmitate + siRNA Elovl5	13 ± 2	1.8 ± 2
Sodium palmitate + siRNA Ptbp3	11 ±2	2.0 ± 2

Discussion

TPN has been widely used in both adult and pediatric patients [1,2]. When the gastrointestinal tract of a patient is not functioning properly due to a disease or dysfunction, normal oral intake or adequate nutrient absorption is hindered. To address this, TPN can be used to provide nutritional therapy [3,7]. Long-term TPN use can lead to hyperglycemia, cholestasis, steatosis, and liver damage. Excessive levels of nutrition can promote the conversion to triglycerides, which are stored in the liver, which can lead to hepatic steatosis and potentially develop into non-alcoholic fatty liver disease (NAFLD). The dysbalanced nutrient delivery and metabolism during TPN can lead to increased production of ROS, causing oxidative stress [14,36,37]. In turn, oxidative stress can contribute to ER stress and cellular damage. To minimize potential complications of TPN, Close monitoring of patients on TPN and individualized nutritional management are essential. Therefore, it is important to seek novel biomarkers for estimating the liver damage of long-term TPN.

This investigation is fundamentally oriented toward establishing an acute liver injury model, rather than investigating the chronic hepatotoxic effects associated with total parenteral nutrition (TPN) [18–21]. Acute injury models are distinguished by their compressed temporal frameworks, and in this particular study, the methodology likely represents a metabolic overload paradigm designed to examine the liver's immediate adaptive responses to rapid nutrient influx. Given that rodents exhibit substantially elevated metabolic rates compared to humans, hepatic responses in rats can develop across

a considerably abbreviated timeframe. Consequently, pathological or biochemical alterations that would typically necessitate extended exposure periods in human subjects may manifest more expeditiously in the rat model. The investigation therefore concentrates on the acute hepatic effects induced by specific TPN components, including lipid emulsions, amino acids, and high-glucose TPN formulations. While this experimental model does not comprehensively replicate the clinical conditions of extended TPN therapy, it yields valuable mechanistic insights regarding early hepatic responses to parenteral nutrient administration and may potentially elucidate the initial pathophysiological processes that precede chronic liver injury. In our study, male rats (200–250 g) received TPN via the left femoral vein for 3 h at 30 mL/kg/h. A significant inflammation and hepatocyte death were noted in the portal (Z1), periportal (Z2), and terminal hepatic venule (Z3) zones in the TPN group, suggesting that TPN-induced liver injury causes significant functional and histopathological changes. Serological tests also demonstrated increased levels of liver damage markers, with ALT, AST, and ALP levels being 139 ± 5, 84 ± 3, and 641 ± 7 in the TPN group, compared with controls ($p<0.05$) (as shown in Figure 1, Table 1). In this study, we first used the iTRAQ proteomic approach and identified differentially expressed proteins in samples from model rats for parenteral nutrition-associated liver disease (Figure 2). A total of 6,436 proteins were identified, with 48 yielding quantitative results. Among them, the expression of 19 proteins was significantly increased, while 29 exhibited decreased expression in the TPN group compared to controls (greater than a 1.5-fold difference). Using the PANTHER classification system, these differentially expressed proteins were categorized into 6 KEGG pathways, 17 biological processes, 5 cellular components, and 16 molecular functions. The String database also revealed the interaction network between these proteins, particularly Elovl5 and Ptbp3, further confirming their involvement in lipid metabolism and ER stress (Figure 3, Table 2). The analysis of the 29 proteins whose expression was downregulated identified their role in 10 KEGG pathways, 19 biological processes, 20 cellular components, and 20 molecular functions (as shown in Figure 4, Table 3). The rats' model of parenteral nutrition-associated liver disease was used to study changes in the ER stress markers, Elovl5 and Ptbp3, and their *in vitro* role was determined. Elovl5 and Ptbp3 were markedly involved in ER stress and the TPN-related injury to liver cells [31–33]. Immunostaining results further showed that the levels of Elovl5 and Ptbp3 were 2-4 folds higher in the TPN-induced liver injury group compared to those in the control group. Similarly, ER stress-related proteins phospho-IRE1 alpha and phospho-ASK1 also showed an increase in expression in the TPN group. These findings further demonstrate the impact of TPN-induced ER stress on injury to liver cells and highlight the critical roles of Elovl5 and Ptbp3 in the pathological changes observed in liver tissue (Figure 5). Further investigations are warranted to determine if stable Elovl5 shRNA and Ptbp3 shRNA may be useful to minimize TPN-induced liver injury.

The network apparently shows that elongation of very long chain fatty acids protein 5 (Elovl5) and polypyrimidine tract-binding protein 3 (Ptbp3) are linked together, whose levels are affected, focusing specifically on its molecular functions to lipid metabolism by modulating the composition of cellular lipid pools through fatty acid elongation [38]. Elovl5 primarily localizes to the ER and plays a role as an enzyme involved in the elongation of fatty acids, particularly as a membrane-bound enzyme involved in lipid metabolism [39]. Elevated Elovl5 levels were also observed in the context of ER stress, highlighting its critical role in lipid metabolism and the pathological changes in liver tissue, including lipid accumulation, inflammation, and fibrosis [40]. Ptbp3 may be associated with the cellular response to ER stress by regulating the splicing of genes encoding proteins in the UPR pathway to restore ER homeostasis [32,33]. Additionally, Ptbp3 can lead to alterations in lipid metabolism, contributing to lipid accumulation in liver cells, a hallmark of NAFLD and non-alcoholic steatohepatitis (NASH), creating a vicious cycle that promotes liver injury. Based on previous reports, our functional studies indicate credible results regarding Elovl5 and Ptbp3. In addition, some novel proteins, which may serve as potential targets for TPN-induced liver injury, were uncovered. In the study, Elovl5 and Ptbp3 expression was knocked-down to evaluate their effects on cell apoptosis and ROS generation (Table 5). Interestingly, Elovl5 and Ptbp3 siRNAs decreased the damage to hepatocytes and the production of ROS potential in hepatocytes. We confirmed these findings *in vitro* by establishing that Elovl5 and Ptbp3 play a role in parenteral nutrition-related liver disease by modulating the ROS generation and cell death. Nonetheless, further study is needed to elaborate the effects of Elovl5 and Ptbp3 in TPN-induced ER stress. The findings will significantly contribute to understanding liver injury through the modulation of key genes involved in the UPR, lipid metabolism, and apoptosis as a potential biomarker or therapeutic target for mitigating liver damage in patients receiving long-term TPN.

TPN has been demonstrated to be involved in ER stress and cell apoptosis, particularly in the liver and intestines, and is associated with factors like nutrient imbalance, lipid overload, and disrupted bile acid metabolism [17,18,41]. Prolonged ER stress has been implicated in induced apoptosis through mechanisms such as CHOP induction, caspase activation, calcium dysregulation, and the binding of IRE1α to TRAF2 and ASK1, as well as JNK/p38 pathways [16,42–44]. In this study, palmitate acid was shown to induce lipotoxicity in HepG2 and FL83B cells, leading to ROS accumulation and activation of signaling pathways, such as JNK, p38, and ASK1 (Figure 6, Figure 7). Western blotting analysis revealed the generation of free radicals through the ER stress pathway, involving increased expression of Ire1α/TRAF2. Furthermore, the expression of Elovl5 and Ptbp3 contributing to the overall lipotoxic effects of palmitate acid was further investigated. Then, treatment of experimental cells with palmitate acid showed decreased expression of Bcl-2/Bcl-XL and the release of activated caspase-3, caspase-9, and cytochrome C into the cytoplasm (Figure 8A, Figure 8B). Palmitate acid treatment also induced the activation of the ASK1/JNK/p38MAPK pathway within 24 h (Figure 8C). Further experimental studies are required for more specific information regarding the abundances and functional characteristics of Elovl5 and Ptbp3 proteins in hepatocytes during TPN infusion, particularly in the context of fatty acid metabolism and ER stress, to determine the regulatory mechanism involved in liver protection and growth with regards to the Elovl5 and Ptbp3 signaling axis.

Trimethylation of histone H3 at lysine 4 (H3K4me3) is a well-known marker of active gene transcription, often found at promoters of actively transcribed genes [34,45]. This modification plays a role in tissue damage and disease progression, particularly in metabolic and liver disorders, by recruiting transcriptional machinery [34]. This trimethylation of histone facilitates the binding of transcription factors, RNA polymerase II, and other components crucial for gene transcription. Aberrant H3K4me3 methylation has a complex role in the regulation of hepatocyte genes, particularly in ER stress conditions [41,46]. H3K4me3 modification influences critical processes like lipid metabolism and activates pathways such as IRE1α, the activation of caspases, calcium dysregulation, and the ASK1, JNK, and p38 pathways, which promote apoptosis of hepatocytes [47,48]. This study examined whether palmitate acid regulates the methylation of histone H3K4, leading to increased expression of Elovl5 and Ptbp3 through the ER stress/JNK/p38MAPK pathway. ChIP analysis revealed that palmitate acid could induce Elovl5 and Ptbp3 expression and modify H3K4me3 at specific DNA binding sites on their promoters. This study additionally demonstrated that palmitate acid modulates Elovl5/Ptbp3 expression and H3K4me3 methylation through the ER stress ASK1/JNK/p38MAPK pathway (Figure 9). Finally, our findings suggest that Elovl5 and Ptbp3 might serve as novel regulators and potential biomarkers or therapeutic targets to improve liver damage in patients on long-term TPN, as their expression is regulated by the ASK1/JNK/p38MAPK pathway and H3K4 methylation.

Conclusions

In this study, the effects of TPN on rat liver cells was comprehensively explored, and the proteomics methods were applied to analyze the profiles of differentially expressed proteins in animal experiments. We particularly focused on the functions of Elovl5 and Ptbp3 proteins in the process of liver injury. The findings revealed that in hepatocytes and animal models treated with TPN, the expression of Elovl5 and Ptbp3 proteins was closely related to the degree of hepatocyte inflammation. These proteins potentially have an important role in the process of liver injury, especially in the mechanism of response to oxidative damage. The palmitate acid can induce liver cell apoptosis and lead to the generation of free radicals; this process is implemented through the ER stress signaling pathway (e.g., p-IRE1α/TRAF2/ASK1/JNK/p38) and the regulation of Elovl5 and Ptbp3 expressions (Figure 10). In addition, the palmitate can induce the expression of genes coding for Elovl5 and Ptbp3, through a process related to the regulation of H3K4me3 histone modification. The activation of Elovl5 and Ptbp3 was demonstrated to further inhibit the expression of anti-apoptotic proteins Bcl-2 and Bcl-XL and activate caspase-3 and caspase-9 expressions, ultimately leading to liver cell apoptosis.

Abbreviations

ASK1, Apoptosis Signal-regulating Kinase 1; CHOP, C/EBP Homologous Protein; Elovl5, Elongation of Very Long Chain Fatty Acids Protein 5; ER stress, Endoplasmic Reticulum Stress; IHC, Immunohistochemistry Stain; IRE1α, Inositol-requiring Enzyme Type 1; iTRAQ, Isobaric Tags for Relative and Absolute Quantitation; JNK, Jun N-terminal Kinase; Ptbp3, Polypyrimidine Tract-binding Protein 3; ROS, Reactive Oxygen Species; TRAF2, Receptor-associated Factor 2; TPN, Total Parenteral Nutrition; TNF, Tumor Necrosis Factor; UPR, Unfolded Protein Response.

Acknowledgments

We thank the Tissue Bank, Chang Gung Memorial Hospital, Chiayi Laboratory Animal Center, Chang Gung Memorial Hospital, Chiayi and Genomics & Proteomics Core Laboratory, Department of Medical Research, Kaohsiung Chang Gung Memorial Hospital for their technical services. Figure 10 was created with BioRender.com.

Funding

Funding for this study was provided in part by research grants BMRPD42, CMRPG6J0151, CMRPG6J0152, CMRPG6J0153, CMRPG6P0221, and ZRRPF6Q0011 from Chang Gung Memorial Hospital, Chiayi, Taiwan, and Chang Gung University of Science and Technology, by the National Science and Technology Council, R.O.C. (NSTC 113-2320-B-255-001- and NSTC 114-2320-B-255-002-).

Ethics approval and consent to participate

Animal care and the standard protocols for animal use were granted approval by the Institutional Animal Care and Use Committee of Chang Gung Memorial Hospital, Chiayi, Animal Ethics Research Board (IACUC approval: 2019032104). All procedures and reporting adhere to the guidelines of the Institutional Animal Care and Use Committee (IACUC).

Competing Interests

The authors have declared that no competing interest exists.

References

1. Lauriti G, Zani A, Aufieri R, Cananzi M, Chiesa PL, Eaton S, et al. Incidence, prevention, and treatment of parenteral nutrition-associated cholestasis and intestinal failure-associated liver disease in infants and children: a systematic review. JPEN J Parenter Enteral Nutr. 2014; 38: 70–85.
2. Javid PJ, Oron AP, Duggan CP, Squires RH, Horslen SP. The extent of intestinal failure-associated liver disease in patients referred for intestinal rehabilitation is associated with increased mortality: an analysis of the Pediatric Intestinal Failure Consortium database. J Pediatr Surg. 2018; 53: 1399–402.
3. Nowak K. Parenteral Nutrition-Associated Liver Disease. Clin Liver Dis (Hoboken). 2020; 15: 59–62.
4. Mullady DK, O'Keefe SJD. Treatment of intestinal failure: home parenteral nutrition. Nat Clin Pract Gastroenterol Hepatol. 2006; 3: 492–504.
5. Zhu L, Baker SS, Gill C, Liu W, Alkhouri R, Baker RD, et al. Characterization of gut microbiomes in nonalcoholic steatohepatitis (NASH) patients: a connection between endogenous alcohol and NASH. Hepatology. 2013; 57: 601–9.
6. Francesca Romana P, Sherrie B, Chiara C, Lorenza P, Licia R, Federica Del C, et al. Hepatocellular Carcinoma Is Associated With Gut Microbiota Profile and Inflammation in Nonalcoholic Fatty Liver Disease. 2019; 69: 107-120.
7. Madnawat H, Welu AL, Gilbert EJ, Taylor DB, Jain S, Manithody C, et al. Mechanisms of Parenteral Nutrition-Associated Liver and Gut Injury. Nutr Clin Pract. 2020; 35: 63–71.
8. Khalaf RT, Sokol RJ. New Insights Into Intestinal Failure-Associated Liver Disease in Children. Hepatology. 2020; 71: 1486–98.
9. Wan S, Maitiabula G, Wang P, Zhang Y, Gao X, Zhang L, et al. Down regulation of NDUFS1 is involved in the progression of parenteral-nutrition-associated liver disease by increasing Oxidative stress. J Nutr Biochem. 2023; 112: 109221.
10. Deleve LD, Kaplowitz N. Importance and regulation of hepatic glutathione. Semin Liver Dis. 1990; 10: 251–66.
11. Negre-Salvayre A, Coatrieux C, Ingueneau C, Salvayre R. Advanced lipid peroxidation end products in oxidative damage to proteins. Potential role in diseases and therapeutic prospects for the inhibitors. Br J Pharmacol. 2008; 153: 6–20.
12. Zhang T, Yan J, Wang N, Dai L, Wang Y, Cai W. Autophagy May Protect Against Parenteral Nutrition-Associated Liver Disease by Suppressing Endoplasmic Reticulum Stress. JPEN J Parenter Enteral Nutr. 2019; 43: 96–106.
13. Malhi H, Bronk SF, Werneburg NW, Gores GJ. Free fatty acids induce JNK-dependent hepatocyte lipoapoptosis. J Biol Chem. 2006; 281: 12093–101.
14. Marí M, Colell A, Morales A, Von Montfort C, Garcia-Ruiz C, Fernández-Checa JC. Redox Control of Liver Function in Health and Disease. Antioxid Redox Signal. 2010; 12: 1295.
15. Dixon BM, Heath SHD, Kim R, Suh JH, Hagen TM. Assessment of endoplasmic reticulum glutathione redox status is confounded by extensive ex vivo oxidation. Antioxid Redox Signal. 2008; 10: 963–72.
16. Maitiabola G, Tian F, Sun H, Zhang L, Gao X, Xue B, et al. Proteome characteristics of liver tissue from patients with parenteral nutrition-associated liver disease. Nutr Metab (Lond). 2020; 17:43.
17. Tsai JJ, Kuo HC, Lee KF, Tsai TH. Proteomic analysis of plasma from rats following total parenteral nutrition-induced liver injury. Proteomics. 2015; 15: 3865–74.
18. Tsai JJ, Kuo HC, Lee KF, Tsai TH. Glycyrrhizin represses total parenteral nutrition-associated acute liver injury in rats by suppressing endoplasmic reticulum stress. Int J Mol Sci. 2013; 14: 12563–80.
19. Lee KC, Chen HH, Cheng KC, Liu TT, Lee KF, Teng CC, et al. Use of iTRAQ-based quantitative proteomic identification of CHGA and UCHL1 correlated with lymph node metastasis in colorectal carcinoma. J Cell Mol Med. 2023; 27: 2004-2020.
20. Shamir R, Zahavi I, Bar-Sever Z, Heckelman B, Marcus H, Dinari G. Total parenteral nutrition-associated cholestasis after selective damage to acinar zone 3 hepatocytes by bromobenzene in the rat. Life Sci. 1993; 52: 371–6.
21. Zahavi I, Rosezki O, Stolkarts Y, Shamir R, Heckelman B, Marcus H, et al. The effect of cisapride on total parenteral nutrition-associated cholestasis in rats. Isr Med Assoc J. 2000; 2: 91-3.
22. Hsieh YY, Lee KC, Cheng KC, Lee KF, Yang YL, Chu HT, et al. Antrodin C Isolated from Antrodia Cinnamomea Induced Apoptosis through ROS/AKT/ERK/P38 Signaling Pathway and Epigenetic Histone Acetylation of TNFα in Colorectal Cancer Cells. Antioxidants (Basel). 2023; 12: 764.
23. Lee KC, Lee KF, Tung SY, Huang WS, Lee LY, Chen WP, et al. Induction Apoptosis of Erinacine A in Human Colorectal Cancer Cells Involving the Expression of TNFR, Fas, and Fas Ligand via the JNK/p300/p50 Signaling Pathway With Histone Acetylation. Front Pharmacol. 2019; 10: 1174.
24. Cheng KC, Kuo HC, Hsieh MC, Huang CY, Teng CC, Tung SY, et al. Identification of Two Novel CIL-102 Upregulations of ERP29 and FUMH to Inhibit the Migration and Invasiveness of Colorectal Cancer Cells by Using the Proteomic Approach. Biomolecules. 2021; 11: 1280.
25. Huang CY, Lee KC, Tung SY, Huang WS, Teng CC, Lee KF, et al. 2D-DIGE-MS Proteomics Approaches for Identification of Gelsolin and Peroxiredoxin 4 with Lymph Node Metastasis in Colorectal Cancer. Cancers (Basel). 2022; 14: 3189.
26. Lee KC, Kuo HC, Shen CH, Lu CC, Huang WS, Hsieh MC, et al. A proteomics approach to identifying novel protein targets involved in erinacine A-mediated inhibition of colorectal cancer cells' aggressiveness. J Cell Mol Med. 2017; 21: 588–99.
27. Teng CC, Tung SY, Lee KC, Lee KF, Huang WS, Shen CH, et al. Novel regulator role of CIL-102 in the epigenetic modification of TNFR1/TRAIL to induce cell apoptosis in human gastric cancer. Food Chem Toxicol. 2021; 147: 111856.
28. Tung SY, Lee KC, Lee KF, Yang YL, Huang WS, Lee LY, et al. Apoptotic mechanisms of gastric cancer cells induced by isolated erinacine S through epigenetic histone H3 methylation of FasL and TRAIL. Food Funct. 2021; 12: 3455–68.
29. Teng CC, Kuo HC, Sze CI. Quantitative proteomic analysis of the inhibitory effects of CIL-102 on viability and invasiveness in human glioma cells. Toxicol Appl Pharmacol. 2013; 272: 579–90.
30. Wang M, Kaufman RJ. Protein misfolding in the endoplasmic reticulum as a conduit to human disease. Nature. 2016; 529: 326–35.
31. Wang X, Yu H, Gao R, Liu M, Xie W. A comprehensive review of the family of very-long-chain fatty acid elongases: structure, function, and implications in physiology and pathology. Eur J Med Res. 2023; 28: 532.
32. Kuwahata M, Yoshimura T, Sawai Y, Amano S, Tomoe Y, Segawa H, et al. Localization of polypyrimidine-tract-binding protein is involved in the regulation of albumin synthesis by branched-chain amino acids in HepG2 cells. J Nutr Biochem. 2008; 19: 438–47.
33. Wu P, Zhang M, Webster NJG. Alternative RNA Splicing in Fatty Liver Disease. Front Endocrinol (Lausanne). 2021; 12: 613213.
34. Kim DH, Kim J, Kwon JS, Sandhu J, Tontonoz P, Lee SK, et al. Critical Roles of the Histone Methyltransferase MLL4/KMT2D in Murine Hepatic Steatosis Directed by ABL1 and PPARγ2. Cell Rep. 2016; 17: 1671–82.
35. Li Y, Reddy MA, Miao F, Shanmugam N, Yee JK, Hawkins D, et al. Role of the histone H3 lysine 4 methyltransferase, SET7/9, in the regulation of NF-kappaB-dependent inflammatory genes. Relevance to diabetes and inflammation. J Biol Chem. 2008; 283: 26771–81.
36. Cui N, Cui M, Li J, Zhu X, Zhu X. Suppression of IRE1 α Attenuated the Fatty Degeneration in Parenteral Nutrition-Related Liver Disease (PNALD) Cell Model. Gastroenterol Res Pract. 2020; 2020: 7517540.

37. Zhu X, Zhang X, Yu L, Xu Y, Feng X, Wang J. Hepatic Overexpression of GRP94 in a Rabbit Model of Parenteral Nutrition-Associated Liver Disease. Gastroenterol Res Pract. 2015; 2015: 269831.
38. Thomas Brenna J, Kothapalli KSD. New understandings of the pathway of long-chain polyunsaturated fatty acid biosynthesis. Curr Opin Clin Nutr Metab Care. 2022; 25: 60–6.
39. Ishihara N, Suzuki S, Tanaka S, Watanabe Y, Nagayama D, Saiki A, et al. Atorvastatin increases Fads1, Fads2 and Elovl5 gene expression via the geranylgeranyl pyrophosphate-dependent Rho kinase pathway in 3T3-L1 cells. Mol Med Rep. 2017; 16: 4756–62.
40. Jakobsson A, Westerberg R, Jacobsson A. Fatty acid elongases in mammals: their regulation and roles in metabolism. Prog Lipid Res. 2006; 45:237–49.
41. Zhang J, Guo J, Yang N, Huang Y, Hu T, Rao C. Endoplasmic reticulum stress-mediated cell death in liver injury. Cell Death Dis. 2022; 13: 1051.
42. Gutiérrez-Uzquiza Á, Arechederra M, Bragado P, Aguirre-Ghiso JA, Porras A. p38α mediates cell survival in response to oxidative stress via induction of antioxidant genes: effect on the p70S6K pathway. J Biol Chem. 2012; 287: 2632–42.
43. Jain AK, Teckman JH. Newly Identified Mechanisms of Total Parenteral Nutrition Related Liver Injury. Adv Hepatol. 2014; 2014: 621380.
44. Zhou H, Liu R. ER stress and hepatic lipid metabolism. Front Genet. 2014; 5:112.
45. Wang H, Helin K. Roles of H3K4 methylation in biology and disease. Trends Cell Biol. 2025; 35: 115-128.
46. Wu X, Xu M, Geng M, Chen S, Little PJ, Xu S, et al. Targeting protein modifications in metabolic diseases: molecular mechanisms and targeted therapies. Signal Transduct Target Ther. 2023; 8: 220.
47. Siwecka N, Rozpędek-Kamińska W, Wawrzynkiewicz A, Pytel D, Diehl JA, Majsterek I. The Structure, Activation and Signaling of IRE1 and Its Role in Determining Cell Fate. Biomedicines. 2021; 9: 156.
48. Liu SY, Rao JX, Deng J, Zhang GJ, Jiang XL, Cheng J, et al. Feedback loop between hepatocyte nuclear factor 1α and endoplasmic reticulum stress mitigates liver injury by downregulating hepatocyte apoptosis. Sci Rep. 2022; 12:11602.

IVYSPRING INTERNATIONAL PUBLISHER

International Journal of Medical Sciences

2025; 22(16): 4278-4294. doi: 10.7150/ijms.119894

Research Paper

A Novel Erinacine S Derivative from *Hericium erinaceus* Overcomes Chemoresistance in Colorectal Cancer Cells by Enhancing TRAIL/TNFR1/DR5 Expression through Histone Acetylation

Shui-Yi Tung[1,2], Kam-Fai Lee[3], Yung-Yu Hsieh[1,2], Kung-Chuan Cheng[4], Ko-Chao Lee[4,5], Li-Ya Lee[6], Wan-Ping Chen[6], Chin-Chu Chen[6], Chih-Chuan Teng[7,8], Meng-Chiao Hsieh[9], Cheng-Yi Huang[9], Hsing-Chun Kuo[7,8,10,11]✉

1. Division of Gastroenterology and Hepatology, Department of Internal Medicine, Chang Gung Memorial Hospital, Chiayi, Taiwan.
2. College of Medicine, Chang Gung University, Taoyuan, Taiwan.
3. Department of Pathology, Chang Gung Memorial Hospital, Chiayi, Taiwan.
4. Division of Colorectal Surgery, Department of Surgery, Chang Gung Memorial Hospital-Kaohsiung Medical Center, Kaohsiung, Taiwan.
5. College of Medicine, Chang Gung University, Kaohsiung, Taiwan.
6. Biotech Research Institute, Grape King Bio Ltd., Taoyuan, Taiwan.
7. Department of Nursing, Division of Basic Medical Sciences, Chang Gung University of Science and Technology, Chiayi, Taiwan.
8. Research Fellow, Chang Gung Memorial Hospital, Chiayi, Taiwan.
9. Division of Colon and Rectal Surgery, Department of Surgery, Chang Gung Memorial Hospital, Chiayi, Taiwan.
10. Center for Drug Research and Development, Chang Gung University of Science and Technology, Taoyuan, Taiwan.
11. Chronic Diseases and Health Promotion Research Center, Chang Gung University of Science and Technology, Chiayi, Taiwan.

✉ Corresponding author: Department of Nursing, Division of Basic Medical Sciences, Chang Gung University of Science and Technology, Chiayi, Taiwan. E-mail: kuohc@mail.cgust.edu.tw.

© The author(s). This is an open access article distributed under the terms of the Creative Commons Attribution License (https://creativecommons.org/licenses/by/4.0/). See https://ivyspring.com/terms for full terms and conditions.

Received: 2025.06.19; Accepted: 2025.09.15; Published: 2025.10.10

Abstract

Hericium erinaceus, renowned for its pharmaceutical potential, is particularly notable for its isolated diterpenoid derivative, erinacine S. Colorectal cancer (CRC) is one of the most prevalent cancers, characterized by CSC that contribute to chemoresistance and sustained tumor growth. While various drugs have been explored, the precise mechanism underlying multifaceted functions of erinacine S in inhibiting chemoresistant human CRC cells remains elusive. By using annexin-V/propidium iodide staining and a Fluo-3 fluorescence staining assay, the cell death and viability in cancer cells and an *in vivo* xenograft mouse model were measured by western blots and an immunohistochemical assay. This study unequivocally demonstrates that erinacine S treatment significantly induces apoptosis and suppresses the aggressiveness of chemoresistant human CRC cells. Erinacine S also exhibits remarkable inhibitory effects on tumor growth in an *in vivo* xenograft mouse model. Immunohistochemical analyses unveiled that erinacine S treatment significantly upregulates the expression of TRAIL, TNFR1, and DR5 proteins while downregulating p-AKT, p-ERK, HIF1α, PCNA, and NFκB levels in the xenograft mouse model of chemoresistant human CRC cells. Erinacine S treatment of HCT-116/FUR cells triggered the activation of extrinsic apoptosis pathways (TRAIL, TNFR1, DR5, and caspase-3) and exerted a time-dependent suppression on the expression of anti-apoptotic molecules like Bcl-2 in intrinsic pathway. The activation of the p-PAK/FAK/p300 pathways was intricately involved in erinacine S-induced transcriptional activation; this was evidenced by histone H3K9K14ac (Acetyl Lys9/Lys14) modifications in the promoters of TRAIL, TNFR1, and DR5. The inactivation of the CXCR4/PI3K/Akt/HIF-1 pathway played a pivotal role in mediating the capacity of erinacine S to inhibit chemoresistant CRC growth while enhancing tumor apoptosis. Thus, erinacine S demonstrates notable inhibitive effects, both *in vitro* and *in vivo*, through the inhibition of invasion, migration, and proliferation in human chemoresistant cell lines, and holds promise as a natural agent for clinical therapy of patients with CRC.

Keywords: Erinacine S; Human chemoresistant human colorectal cancer cells; *Hericium erinaceus* mycelium; H3K9K14ac.

Introduction

Colorectal cancer (CRC) ranks as one of the leading causes of global cancer-related mortality, second only to lung cancer in Western countries [1]. In the United States, approximately 140 thousand individuals are diagnosed with CRC annually, resulting in 50 thousand deaths [2]. A concerning increase in CRC cases has also been observed in Taiwan. The primary cause of mortality in CRC is often attributed to cancer cell metastasis to distant sites. Since CRC is frequently asymptomatic in its early stages, about 35% of patients already have metastatic disease at the time of diagnosis. The post-treatment five-year survival rate for patients with metastatic CRC typically ranges between 10% and 20% [3]. Surgical excision remains the gold standard for curing CRC, and timely intervention is crucial upon diagnosis. High-risk individuals diagnosed with stage 2 CRC are often recommended for adjuvant chemotherapy, typically employing the fluorouracil and oxaliplatin (FOLFOX) regimen [4]. Chemotherapeutic treatment commonly includes 5FU (5-fluorouracil)-based drug combinations. However, the use of partial chemotherapy (FOLFOX) can lead to the development of drug-resistant CRC, promoting tumor invasion and metastasis [5]. One recognized contributor to chemotherapeutic resistance and persistent tumor growth is cancer stem cells (CSCs) [6]. These chemotherapeutic drug-resistant CRC cells stem from the primary CRC cell subgroup, differing in molecular and phenotypic characteristics. They are variously referred to as tumor-initiating cells, tumor-promoting cells, or more commonly, CSCs (7). CSCs exhibit resistance to drugs, which may be attributed to mechanisms such as drug efflux (involving membrane protein P-glycoprotein or P-gp), autocrine signaling pathways (macrophage migration inhibitory factor/ C-X-C chemokine receptor type 4 (MIF-CXCR4 axis), alterations in metabolism (influencing hypoxia-inducible factor 1 or HIF-1α signaling), and transitions in epithelial to mesenchymal transition (EMT) [8]. The current study aims to explore whether novel dietary compounds, such as erinacine S, can induce apoptosis in drug-resistant CRC cells. Additionally, the study investigates the potential effects and associated mechanisms underlying the inhibition of cancer cell invasion and metastasis.

Hericium erinaceus, commonly known as Lion's Mane mushroom, is a medicinally valuable edible fungus with a long history of application in East Asian traditional medicine. This fungus, named after its unique white, furry appearance, was historically regarded as a precious ingredient for both culinary and medicinal purposes [9]. The earliest written records of its use can be traced back to the Sui Dynasty. The Ming Dynasty's The Ben Cao Gang Mu provided detailed documentation of *H. erinaceus*, describing it as mild in nature with a sweet taste, beneficial for supporting the five visceral organs and aiding digestion [10]. According to the Xin Zhong Hua Ben Cao, the whole *H. erinaceus* possesses a sweet taste with neutral properties, capable of supporting the five visceral organs, promoting digestion, nourishing the body, and exhibiting anti-cancer properties [10]. A range of therapeutic properties are associated with this mushroom, including anti-hypoglycemic [11], anti-hypolipidemic [12], anti-inflammatory [13], anti-tumor [14], anti-aging [15], and nerve injury-regulating [16] effects. *H. erinaceus* has also demonstrated potential in countering chronic gastritis, gastrointestinal cancer, and esophagus cancer [17]. Previously, the antioxidative properties of the methanol extract from mushrooms like *H. erinaceus* have been highlighted, identified as key contributors to this trait [18]. Furthermore, *H. erinaceus* extracts are now marketed as food products and dietary supplements in various countries. Examples include "*Hericium erinaceus* Gastric Health Oral Solution" and "Jiangzhong Lion's Mane Sugar-free Crispy Biscuits" in China, "Natural Lion's Mane Mushroom Tincture" in the United Kingdom, and "Real Mushrooms Lion's Mane Mushroom Capsule Supplements" in the United States. These products are recognized for their potential to improve gastrointestinal function and enhance immune system response [19]. However, these investigations primarily utilized extracts from the fruiting body of *H. erinaceus* cultivated via solid-state culture [18]. In contrast, the current study focuses on *H. erinaceus* mycelium produced through liquid-state fermentation, enriched with erinacine compounds (erinacine A–I and erinacine S) [20]. Existing literature has highlighted the potential of *H. erinaceus* extracts from the fruiting body in resisting liver cancer, astrocytoma, gastric cancer, leukemia, and CRC [21,22]. Nevertheless, the specific impact of active constituents extracted using alcohol, particularly erinacine S derived from mycelium produced via liquid fermentation, on drug-resistant CRC cells remains an unexplored field of research.

The loss of control over apoptosis is a pivotal factor that enables cancer cells to evade cell death, thereby promoting their prolonged survival and enhancing invasiveness during tumor progression [23]. Apoptosis can be initiated via two primary pathways: the intrinsic and extrinsic pathways. The intrinsic pathway involves the activation of caspases, particularly within the mitochondria, leading to

apoptosis upon treatment with various natural compounds [24]. B-cell lymphoma 2 (Bcl-2) family members, particularly anti-apoptotic ones like Bcl-2 and Bcl-extra-large (Bcl-XL), are characterized by the presence of at least three BH amino acid sequences. In contrast, the extrinsic pathway involves the interaction of death activators with cell surface receptors, resulting in cell death [25]. Prominent examples include tumor necrosis factor (TNF)-α/Fas ligand, TNF, and FasL (Apo-1L or CD95L) [26,27]. Our study reveals the intricate mechanisms underlying the inhibition of invasive and metastatic capabilities in drug-resistant CRC cells by *H. erinaceus* erinacine S. This inhibition is achieved through the suppression of the macrophage migration inhibitory factor (MIF)/ C-X-C Motif Chemokine Receptor 4 (CXCR4)/ phosphoinositide 3-kinases (PI3K)/ protein kinase B (Akt)/ extracellular signal-regulated kinase (ERK)/ nuclear factor kappa B (NFκB)/ HIF-1α) pathway and the reversal of EMT in HCT-116/5-fluorouracil-resistant (5FUR) cancer cells. Erinacine S induces a programmed cell death process in drug-resistant CRC cells, implicating both intrinsic and extrinsic pathways. Furthermore, erinacine S derived from *H. erinaceus* exhibits the ability to inhibit cell-cycle-related proteins, including CDK2, cyclin D1, and cyclin E, thereby causing cell cycle arrest in the G1 phase. Erinacine S, as an active constituent of *H. erinaceus*, exerts its anti-cancer effects by impeding cancer cell growth, promoting apoptosis, and operating through the p300/ focal adhesion kinase (FAK)/ p21-activated kinase (PAK1) pathway-mediated epigenetic modification of histone H3K9K14ac (acetyl Lys9/Lys14) within the promoters of TNF-related apoptosis-inducing ligand (TRAIL), TNF-receptor 1 (TNFR1), and death receptor 5 (DR5). This epigenetic modulation contributes to the regulation of gene expression in the apoptosis pathway by erinacine S.

Materials and Methods

Information on antibodies and chemical reagents

The antibodies were purchased from Santa Cruz Biotechnology (Santa Cruz, CA, USA), including mouse monoclonal antibodies against CDK2, Cyclin D1, Cyclin E, Bcl-2, Oct-4, SOX-2, H3 histone H3K9K14ac (Acetyl Lys9/Lys14), proliferating cell-nuclear antigen (PCNA) and β-actin. The antibodies were respectively obtained by Abcam Technology (Abcam) and Cell Signalling Technology, including mouse/rabbit polyclonal antibodies against phospho (p)-ERK1/2 Thr202 Tyr204, AKT Thr308, PAK Thr423, FAK Tyr577/579, HIF1α, CBP/p300 and PI3 Kinase p85 (Tyr458), NFκB p105/50, TRAIL, TNFR1, DR5. Mouse/rabbit polyclonal antibodies against CD44 and CD133 (Abcam, Cambridge, UK). All culture materials were obtained from Gibco (Grand Island, NY, USA). Protease inhibitor cocktails, the p300-Binding Protein inhibitor C646, Fluo-3-pentaacetoxymethyl ester (Fluo 3-am), the membrane-permeant JC-1 dye, FAK inhibitor Y15, or the PAK1 inhibitor IPA-3, NP-40, sodium deoxycholate, 2,7-dichlorodihydrofluorescein diacetate (H2DCFDA) and 3-(4,5-dimethylthiazol-2-yl)-2,5-diphenyltetrazolium bromide (MTT) were purchased from Sigma (St. Louis, MO, USA).

Fungus material

H. erinaceus (BCRC 35669) was procured from the Bioresources Collection and Research Center (BCRC) at the Food Industry Research and Development Institute, located in Hsinchu, Taiwan. The fungus name was confirmed by consulting List (https://catalog.bcrc.firdi.org.tw/BcrcContent?bid=35669; accessed Feb 18, 2025).

Hericium erinaceus extracts and analysis of erinacine S

The *H. erinaceus* specimen was initially transferred from an agar slant onto a potato dextrose agar plate, where it was then maintained at a temperature of 26°C for a duration of 15 days, consistent with previously established protocols [28]. Following the extraction of fresh mycelium from *H. erinaceus* using ethanol, the subsequent fermentation process of the *H. erinaceus* mycelia was carried out. These mycelia were subsequently transformed into a powdered form and subjected to fractionation. Using a COSMOSIL 5C18-AR-II column (250 × 4.6 mm; 5 µm particles; Nacalai USA, Inc.), erinacine S showed a retention time of 15.4 min at 1.0 mL min−1 flow with 290 nm UV detection. The compound's yield from H. erinaceus ethanol extraction was confirmed at ~1 g kg−1 via HPLC [28]. Fig. 1 shows erinacine S's chemical structure (PubChem CID: 127047879).

Development of chemoresistance cell lines

The colon cancer cell line, HCT-116, was procured from the Bioresources Collection and Research Center (BCRC) of the Food Industry Research and Development Institute, based in Hsinchu, Taiwan. These cells were meticulously maintained in Dulbecco's Modified Eagle Medium (DMEM), which was augmented with 10% fetal bovine serum (FBS) and 1% penicillin/streptomycin. This maintenance was carried out within a CO_2 incubator, preserving the cells at a temperature of 37°C. To establish the 5FU resistant cell line,

HCT-116/FUR, a previously established protocol 8 was followed. Initially, parental HCT-116 cells were exposed to an initial dose of 0.1 µg/mL of 5FU, and the surviving cells were cultured until they reached a confluence of 80% over the course of three passages (approximately 6 weeks). Subsequently, the cells that endured this initial 5FU treatment were subjected to a concentration of 0.5 µg/mL of 5FU for another three passages (around 6 weeks), and then further escalated to 1.0 µg/mL for an additional three passages (roughly 6 weeks). Ultimately, the 5FU concentration was raised to 2.0 µg/mL for the subsequent 3 weeks (totaling 10 weeks). These cells, now displaying resistance to chemotherapy, were designated as HCT-116/FUR and continued to be cultured in DMEM supplemented with 5FU 2.0 µg/mL, as HCT-116/FUR chemoresistant cells, 10% fetal bovine serum (FBS), along with penicillin-streptomycin [29].

Cell cycle distribution analysis and flow cytometry

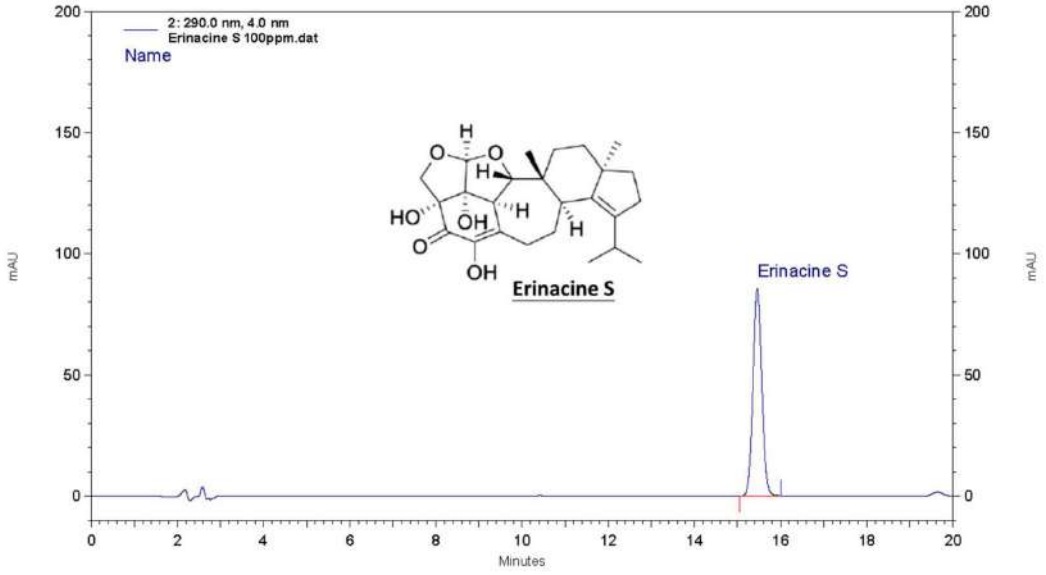
HCT-116/FUR cells were subjected to treatment with either 0.1% DMSO (used as a control) or erinacine S for a duration of 24 hours. Subsequently, only the surviving cell fraction was collected for measurement through cell cycle distribution analysis, as described in a previous publication [30].

Measurement of apoptosis assay

Co-staining with Annexin V–FITC and propidium iodide (Biosource International, USA) was employed for the measurement of cell apoptosis, following established procedures. Subsequent to staining, FACS analysis was conducted using the Attune NxT Flow Cytometer (Attune NxT Flow Cytometer, Thermo Fisher Scientific Inc.), as described in a previous publication [31].

Protein extraction and immunoblot analyses

Cellular lysates were prepared by suspending tumor tissue in lysis buffer. The cellular material was then fragmented through ultrasonic disruption, followed by extraction procedures performed on the generated lysates. The protein content in the supernatant was quantified using a suitable method. For immunoblotting, Immobilon-P membranes (Millipore, Bedford, MA) were employed, along with the appropriate secondary antibodies, following established protocols [32].



Column : Cosmosil 5C18-AR-II, 4.6*250 mm
Flow : 1.0 ml/min
DAD : 290 nm
Oven temp : 40 C
Mobile phase : A-water, B-ACN
Gradient (Time = 20 min) : 0-20 min, 60-65% B

2: 290.0 nm, 4.0 nm
Results

Name	Retention Time	Area	3 Point Purity
Erinacine S	15.460	4898645	0.994139

Figure 1. HPLC analysis of the ethanol *H. erinaceus* mycelium extract. The retention time peak at 15.46 min was demonstrated by a bioreactor (UV detection at 290 nm).

Animal study

The animal care and experimental procedures adhered to in this study were sanctioned by the Institutional Animal Care and Use Committee of Chang Gung Memorial Hospital, Chiayi, Animal Ethics Research Board (IACUC approval: 2020121810). Male BALB/c-nu nude mice, aged 4-6 weeks, with weights ranging from 18 to 20 grams, were procured from the National Laboratory Animal Center in Taiwan. These mice were housed in a specific pathogen-free (SPF) environment and provided with sterilized food and water. For the subcutaneous tumor model, 10^6 cells of both HCT-116 and HCT-116/FUR cell lines were injected into the flanks of 4–6-week-old male athymic BALB/c-nu mice. Post-tumor implantation, mice were distributed randomly into four experimental groups with six animals per group (n = 6). The HCT-116 control group received daily intraperitoneal administration of 0.1 mL DMSO (0.25%). The experimental groups were administered erinacine S intraperitoneally at doses of 1 mg/day and 5 mg/day, respectively, over a 5-day period. Tumor dimensions were systematically recorded every 4 days using caliper measurements. Additionally, weekly body weight assessments were conducted to monitor for potential toxicity effects of the treatment. Upon completion of the 18-day treatment regimen, the animals were ethically sacrificed, followed by collection of tumors and essential organs (liver, lungs, and kidneys) in accordance with previously established protocols [33].

Matrigel Invasion and Scratch Assays

A straight wound line was created in the monolayer of the transfected cells, and images of the wound line were subject to analysis using the Openlab v3.0.2 image analysis software (Improvision, Coventry, UK). Matrigel invasion of tumor cells was assessed using the Boyden chamber, following established procedures with a previously described protocol [34].

Histochemistry and immunohistochemistry analysis

Tumor tissue sections were fixed in 4% formaldehyde and subsequently embedded in paraffin blocks. After hematoxylin and eosin staining, the tissue slides were prepared for microscopic examination. For immunohistochemical analysis, 5-μm-thick sections of each subcutaneous tumor specimen were incubated with monoclonal anti-p-AKT and p-ERK, HIF1α, PCNA, and NFκB p105/50 antibodies (Santa Cruz, CA, USA). Digital images were captured using a digital camera (Canon A640), and the positive area and optical density (OD) of the immunoreactive cells (brown) were analyzed in three randomly selected microscopic fields for each slide. The IHC index was defined as the average integral optical density (AIOD; positive area × OD/total area), following established protocols [35].

Chromatin immunoprecipitation (ChIP) analysis

HCT-116/FUR cells underwent treatment with 1% formaldehyde to establish DNA-protein crosslinks and were subsequently rotated with antibodies specifically targeting histone H3K9K14ac, alongside 2μl of non-immunized rabbit IgG serving as a negative control. Following elution procedures, DNA fragments were isolated and purified utilizing a ChIP DNA Clean & Concentrator Kit (Zymo), after which quantitative PCR analysis was conducted to amplify the promoter regions of TRAIL, TNFR1, and DR5 genes employing specific primer sequences (Table 1). The data were expressed as a percentage relative to a reference gene, as described previously. The reference gene was used to calculate the percent input for each experiment. The results were statistically analyzed using Student's paired t test. A p-value of <0.05 was considered to be statistically significant [28,33,36,37].

Statistical analysis

All data, presented as the mean ± standard deviation, were subjected to group comparisons using either Student's t-test or one-way Analysis of Variance (ANOVA), followed by Tukey's Multiple Comparison Test. A statistically significant difference between values was defined at $p < 0.05$, following the methodology outlined by Lee et al. 2023 [38].

Table 1. The specific primers.

TRAIL -226 to -106 bp	
TRAILf	5'-TGCATGGATCCTGA GGGCAAGG -3'
TRAILr	5'-TTGAACCTGCAACTGTCCCTCCC-3'
DR5 -199 to -75 bp	
DR5f	5'-GCCAGGGCGAAGGTTA-3'
DR5r	5' -GGGCATCGTCGGTGTAT-3'
FAS -2026 to -1849 bp	
FASf	5'-TTGGGTAACTTTGGGTGGTCC-3'
FASr	5'-ATGTGGTTGGTTGTGAAGGGAG-3'
FasL -419 to -282 bp	
FasLf	5' - GGGGGCAGTGTTCAATCTTA-3'
FasLr	5' - TGGAAAGAATCCCAAAGTGC-3'
TNFR -111 to 83 bp	
TNFRf	5' -GAT TGG TGG GTT GGG GGC ACA-3'
TNFRr	5' -ATT AAA GCA GAG AGG AGG GGA GAG A-3'
TNF-α -866 to -651 bp	
TNF-αf	5' -CAA GCA TTA TGA GTC TCC GG-3'
TNF-αr	5' -AAG CTG TGT TGA GTC CTG AG-3'

Results

Establishment of chemoresistant HCT-116/ 5-fluorouracil-resistant cell lines

A small subset of CSCs within cancer cell populations can often elude the effects of chemotherapeutic drugs, subsequently acting as a source of tumor recurrence. Consequently, this study employed a methodology similar to that described by Lee M. Ellis [8,29] to systematically isolate highly drug-resistant CRC cell lines from the initially chemosensitive CRC cell line, HCT-116. Intriguingly, the chemoresistant cell lines exhibited a significantly higher presence of cells expressing CD44 and CD133 compared to their parental counterparts (Fig. 2A). While merely 6% of parental cells demonstrated expression of CD44 and CD133, HCT-116/FUR cells exhibited a notably higher expression of these markers. Moreover, HCT-116/FUR cells displayed a substantially greater expression of Octamer-binding transcription factor 4 (Oct-4) and SRY (sex determining region Y)-box 2 (SOX-2), which are markers associated with putative CSC–like cells [7,8], compared to the parental HCT-116 human CRC cells (Fig. 2B). These findings underscore the presence of CRC cells with enhanced survival capabilities and anti-apoptotic activity, characteristics commonly associated with CRCs [29]. The MTT assay was conducted to compare the cytotoxicity of 5-fluorouracil (5FU) in two cell lines: HCT-116 cells and their resistant variant, HCT-116/FUR cells. The IC_{50} (concentration that inhibits 50% of cell growth) for 5FU was 30 μg/ml in HCT-116 cells and 135 μg/ml in HCT-116/FUR cells. The resistance in HCT-116/FUR cells was induced through continuous culture with an unknown concentration of 5FU (Fig. 2C). And then treatment with 5FU at the IC_{50} concentration induced apoptotic cell death in both HCT-116 and HCT-116/FUR cells, as confirmed by DAPI staining. Specifically, the treatment with 30 μg/ml 5FU resulted in an apoptotic index of 14 for HCT-116 cells compared to 5 for HCT-116/FUR cells (Fig. 2C). Additionally, after treatment with 40 μM ES (IC_{50} in HCT-116/FUR), the cell viability had an index of 20% for HCT-116 cells and 50% for HCT-116/FUR cells (Fig. 2D).

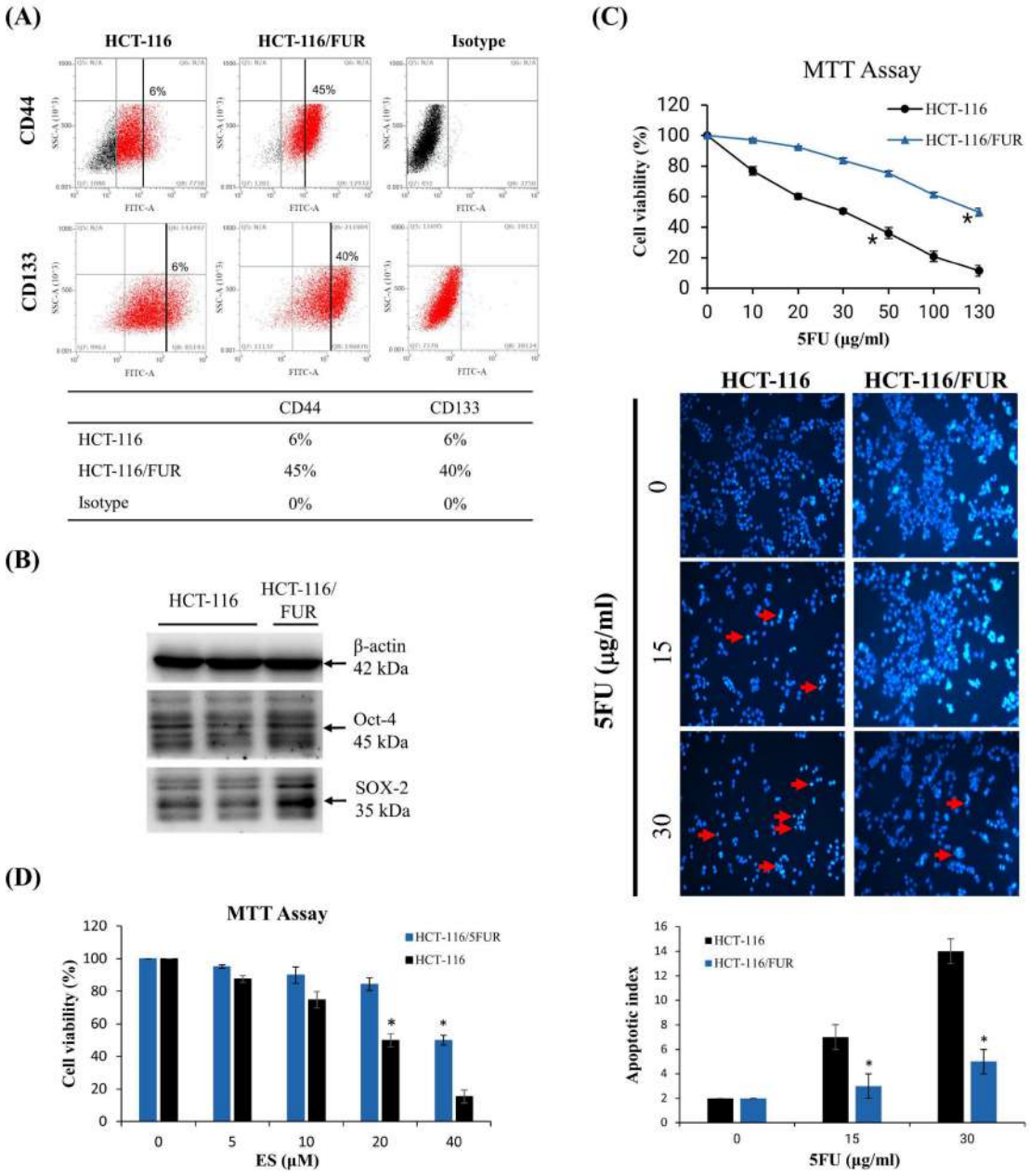
In vitro effect of erinacine S-inhibited migration and invasion as well as tumor growth of chemoresistant HCT-116/FUR cells

For the extraction and purification of erinacine S from fresh mycelium of *H. erinaceus* using ethanol, previously established protocols were followed [28]. To evaluate the inhibitory effect of erinacine S on the growth of chemoresistant HCT-116/FUR cells, various concentrations were administered. First, the scratch-wound assay demonstrated that in comparison to the untreated group (HCT-116/FUR) for 24 h, the HCT-116/FUR cells exhibited enhanced migration more aggressively in response to upregulation due to 5FU treatment (Fig. 3A). However, in the presence of erinacine S, migration was significantly inhibited after 12 and 24 h, and resulted in nearly complete inhibition of cell migration when using 40 μM erinacine S (Fig. 3A, $^{*}p < 0.05$). Furthermore, the Boyden chamber assay revealed more than 23% and 15% reduction in cell invasion when treated with 20 μM and 40 μM erinacine S, respectively, compared to the chemoresistant HCT-116/FUR treated 5FU group ($^{*}p < 0.05$, Fig. 3B). Flow cytometry analysis (Fig. 4) indicated that a higher proportion of HCT-116/FUR cells treated with erinacine S were arrested in the G1 stage of the cell cycle (G1 arrest), compared to the chemoresistant HCT-116/FUR, showed as percentages of 70%, 80%, and 83% (Fig. 4). Apoptosis analysis using Annexin-V and PI staining also revealed a significant dose-dependent increase in apoptotic induction (7%, 33%, and 59%) by erinacine S in HCT-116/FUR cells (Fig. 4). The cells displayed altered spatial dynamics of extracellular $Ca2^{+}$ signaling (1-fold, 1.1-fold, and 1.3-fold) and demonstrated depolarization of mitochondrial potential (ΔΨm), as indicated by the decrease in the ratio of fluorescence intensities of monomers green /aggregates red [3,13,21], compared to the control group without erinacine S treatment, and observed through flow cytometry experiments (Fig. 4).

In vivo growth inhibition of chemoresistant HCT-116/FUR cell xenograft by erinacine S treatment

The *in vitro* findings regarding the anti-chemoresistant effects of erinacine S were corroborated by employing an *in vivo* nude mouse model utilizing chemoresistant HCT-116/FUR cell xenografts. Time-course analysis unveiled a significant reduction in tumor weight of the HCT-116/FUR cell xenografts in nude mice upon erinacine S treatment in a dose-dependent manner at 18 days (Fig. 5). These results indicated the HCT-116/FUR xenograft with 5FU 5mg/kg volumes were increased 63% more than HCT-116/FUR xenograft untreatment group ($^{\#}p < 0.05$), which was shown HCT-116/FUR with 5FU group aggress more better. Under the same HCT-116/FUR xenograft treated with 5FU 5mg/kg, a clear inhibitory effect of erinacine S on the growth of chemoresistant HCT-116/FUR cell tumors, with 46% and 30% reductions compared to the HCT-116/FUR 5FU

treated group (*p < 0.05, Fig. 5). Furthermore, the tumors were examined upon removal and quantified through tissue staining, including hematoxylin and eosin staining, and p-AKT, p-ERK, HIF-1α, proliferating cell nuclear antigen (PCNA), and NFκB p50 staining. The levels of p-AKT (a marker associated with the aggressive status of chemoresistant cells), p-ERK (related to a signaling pathway associated with chemosensitivity), HIF-1α (a key regulator implicated in drug resistance), PCNA (a marker for cell proliferation), and NFκB p50 (a marker for the transduction of proliferative signals) were measured in these experimental animals. The results displayed the HCT-116/FUR xenograft with 5FU 5mg/kg volumes were increased expression of p-AKT, p-ERK, HIF-1α, and NFκB p50 than HCT-116/FUR xenograft untreatment (#p < 0.05, Fig. 6). In addition, erinacine S treatment caused a reduction in the expression of p-AKT, p-ERK, HIF1α, PCNA, and NFκB, compared to the HCT-116/FUR 5FU treated group without erinacine S treatment (*p < 0.05, Fig. 6). The treatment with erinacine S is clearly in accordance with the *in vitro* data.



	CD44	CD133
HCT-116	6%	6%
HCT-116/FUR	45%	40%
Isotype	0%	0%

Figure 2. Chemoresistant cell lines enriched for tumor stem cell markers. (A) Flow cytometric analysis demonstrating enrichment of chemoresistant cell lines HCT-116/FUR for cells expressing CD133 and CD44 compared with the parental HCT-116 human colorectal cancer cell line. Staining controls include cytometric analysis plots using isotype control antibodies. **(B)** Western blotting showing enriched Oct-4 and SOX-2 proteins in the HCT-116/FUR chemoresistant cells compared with parental HCT-116. Data obtained from western blot are derived from a representative study. **(C, D)** The cell viability was measured through MTT Assay experiments. HCT-116 and HCT-116/FUR were treated with different concentrations of 5FU or erinacine S. *p < 0.05, compared with the HCT-116/FUR group for 24 h.

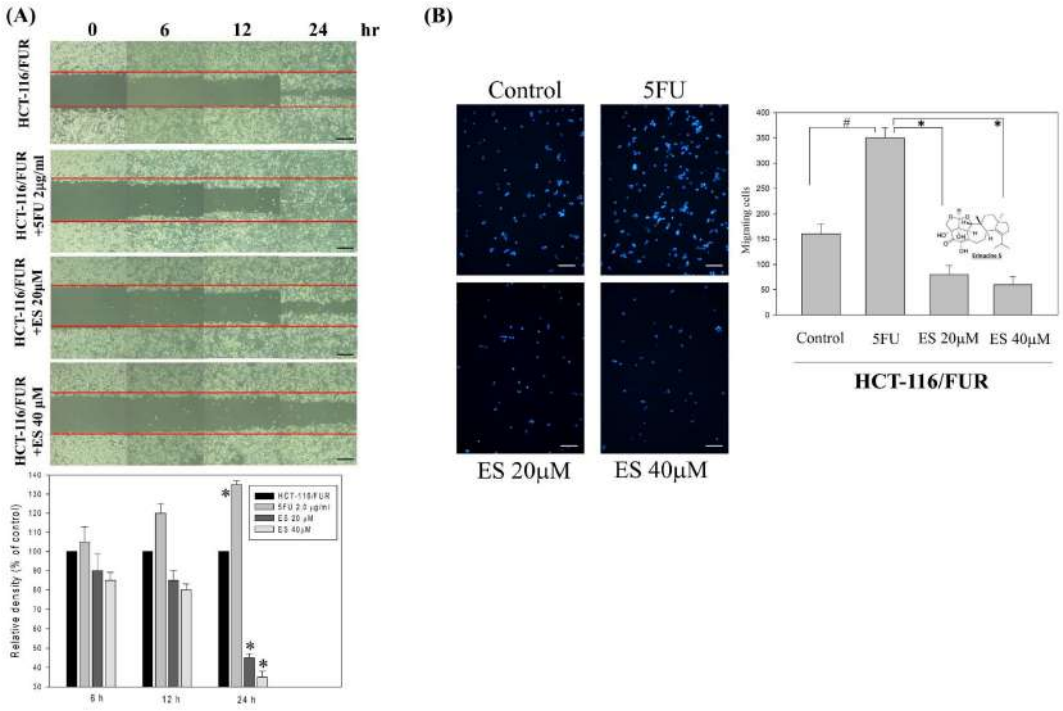
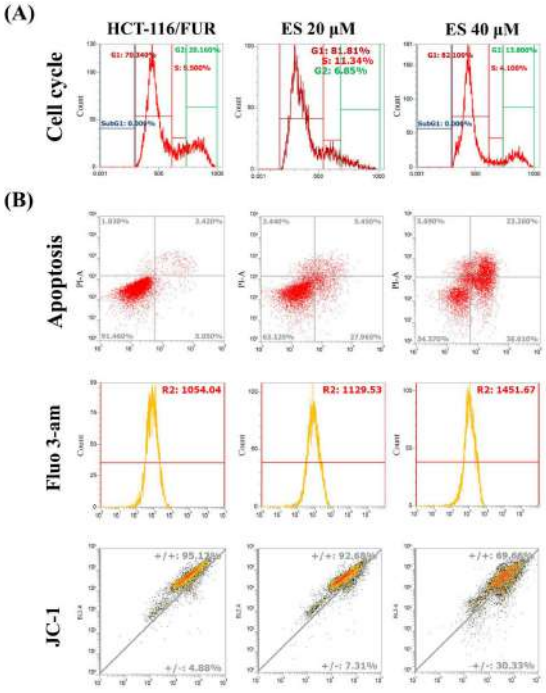


Figure 3. Effects of erinacine S on *in vitro* cell migration and invasiveness of human HCT-116/FUR chemoresistant cells. (A) HCT-116/FUR chemoresistant cells were incubated with erinacines S for 12, 24 and 48 h, and the migration was visualized using the scratch-wound assay as described in the 'Materials and methods section'. The percentage of surface area filled by the HCT-116/FUR cells was subsequently quantified through densitometric analyses relative to the control, set at 100% in the graph. Data are presented as means ± standard deviation (SD) based on three independent experiments. The experiments were performed in triplicate, and data are presented as means ± SD. *$p < 0.05$, compared with the control group for 24 h. **(B)** Effect of erinacine S on the invasive ability of HCT-116/FUR cells. Cells were incubated with various concentrations of erinacine S for 24 h. Invasion through a layer of Matrigel was determined by the Boyden Chamber method as described in 'Materials and methods'. The lower and upper chemotaxis cells were separated by a polycarbonate membrane. Microscopic images detecting cells that migrated into the inner membrane, magnification: 200 ×. The cell migration was quantified by counting the number of cells migrating into the inner membrane. Control cells were untreated. The experiments were performed in triplicate, and data are presented as means SD. The symbol * indicates significantly different means when compared to the control group. *$p < 0.05$, compared with the 5FU treated group for 24 h.



	Control	ES 20 μM	ES 40 μM
G (%)	70 ± 1	80 ± 2	83 ± 1
S (%)	10 ± 1	11 ± 1	5 ± 1
G2 (%)	20 ± 1	9 ± 2	12 ± 2

	Control	ES 20 μM	ES 40 μM
Annexin V-PI Apoptosis (%)	7 ± 1	33 ± 3	59 ± 4
Fluo-3-AM(%)	1	1.1 ± 0.1	1.3 ± 0.1
JC-1 (Monomers/Aggregates)	19 ± 3	12 ± 1	3 ± 1

Figure 4. Effect of erinacine S on cell cycle and apoptosis distribution in HCT-116/FUR chemoresistant cells. (A) After treatment with Erinacine S for 24 h, the HCT-116/FUR cells were fixed and stained with propidium iodide, and the DNA content was analyzed by flow cytometry (FACS). The percentage of cells in each phase (G1, S, and G2/M) of cell cycle was calculated and expressed. **(B)** After the indicated treatment for 24 h, the HCT-116/FUR cells were stained with fluorescence isothiocyanate-conjugated Annexin-V and propidium iodide for flow cytometry analysis as described in 'Materials and methods'. The percentages presented in each frame depict the apoptotic cells.

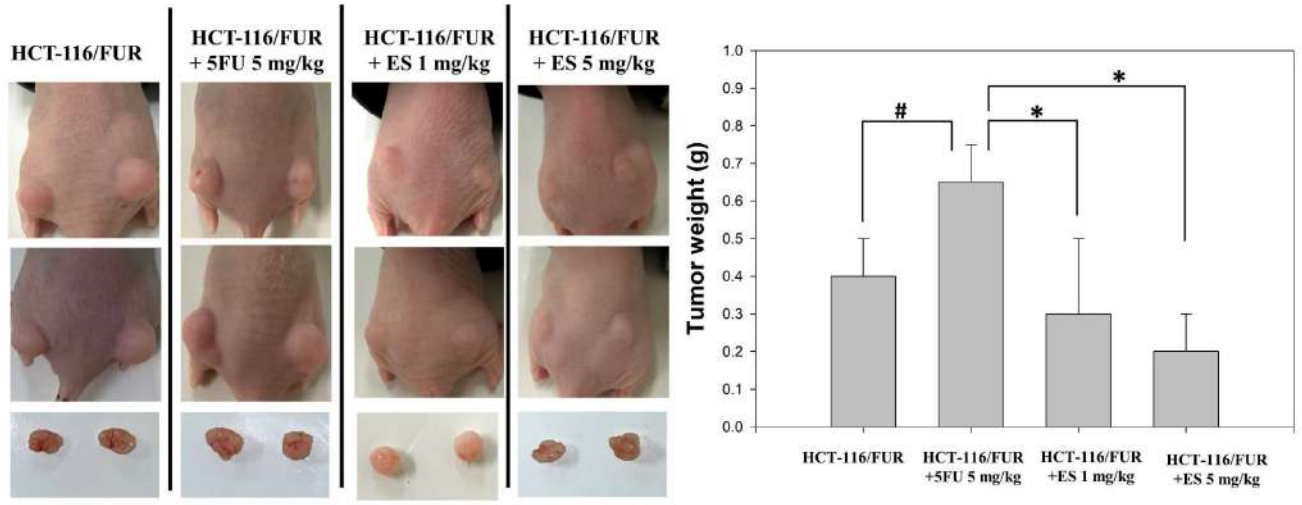


Figure 5. Growth inhibition of HCT-116/FUR chemoresistant cells xenograft due to erinacine S treatment. Nude mice were subcutaneously implanted with HCT-116/FUR into flanks on day 0 and treated with or without (as a control) erinacine S as described in the "Materials and methods." Time course effect of erinacine S on the growth of HCT-116/FUR cells xenograft evaluated in terms of the tumor volume every at 18 days. #$p < 0.05$, as compared to the HCT-116/FUR untreated group; *$p < 0.05$, as compared to the HCT-116/FUR 5FU 5mg/kg treated group.

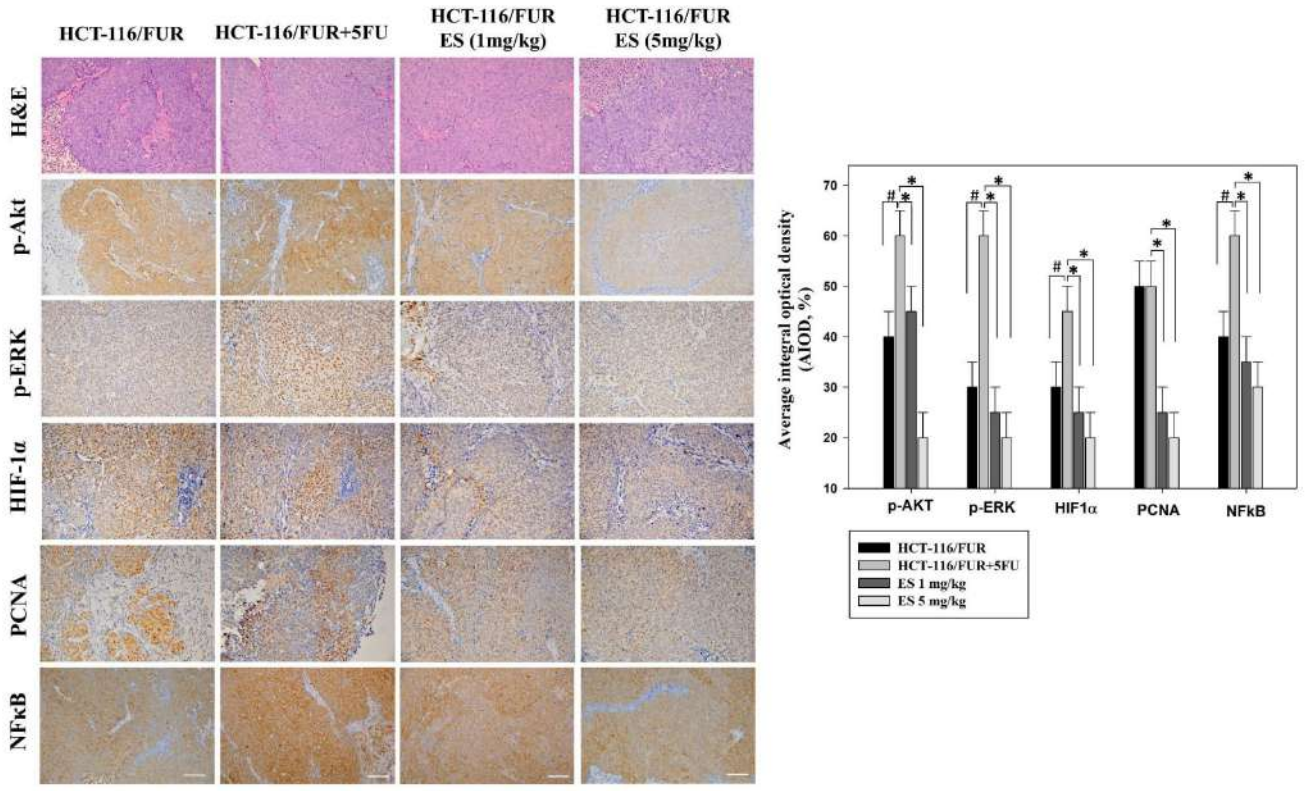


Figure 6. Alteration in the level of proliferative and apoptotic proteins associated with HCT-116/FUR chemoresistant cells in the *in vivo* xenograft mouse model after erinacines S treatment. The tumors of the nude mice, with the indicated treatment, were harvested and prepared for hematoxylin and eosin staining (1st row, upper panel) and the measurement of protein levels of phosphorylated protein kinase B (p-AKT; 2nd row, upper panel), p300 (3rd row, upper panel), hypoxia inducible factor 1a (HIF1α; 4th row, upper panel), proliferating cell nuclear antigen (PCNA; 5th row, upper panel), and nuclear factor kappa B (NF-κB1 p105/p50; 6th row, upper panel), by immunohistochemical analysis. Bottom panel: Quantitative immunohistochemical proteins, p-AKT, p-ERK, HIF1α, PCNA, and NFκB stain, were evaluated by calculating the Average of Integrated Optical Density (AIOD). Per treatment group, multiple tumor fields were evaluated. The positive stained area was examined from three randomly-selected observational fields of each section. The data are expressed as mean ± standard deviation. (n = 6/group). # $p < 0.05$, as compared to the HCT-116/FUR untreated group; *$p < 0.05$, as compared to the HCT-116/FUR 5FU 5mg/kg treated group, at a magnification of ×200.

Erinacine S-mediated activation of the extrinsic cell apoptosis pathway in chemoresistant HCT-116/FUR cells

To further assess the apoptotic mechanisms induced by erinacine S in chemoresistant HCT-116/FUR cells, we examined cell-death and growth-related proteins. Specifically, we measured expressions of CDK2, cyclin D1, cyclin E, cleaved caspase 3, cleaved caspase 9, Bcl-2, TRAIL, TNFR1, and DR5 by western blotting in erinacine S-treated HCT-116/FUR cells. Thus, erinacine S treatment led to an increase in the active forms of caspase-3 and -9, along with enhanced expression of the upstream proteins TRAIL, TNFR1, and DR5 (Fig. 7A and 7B). These proteins are widely recognized as hallmarks of apoptotic cell death. In contrast, following erinacine S treatment, the levels of CDK2, cyclin D1, cyclin E, and the anti-apoptotic protein Bcl-2 decreased in HCT-116/FUR cells (Fig. 7A). Our findings suggest a novel biological property of erinacine S, inducing apoptotic cell death and cell cycle arrest in chemoresistant HCT-116/FUR cells. This effect is achieved through the regulation of a complex protein network involved in extrinsic cell apoptosis and cell cycle pathways.

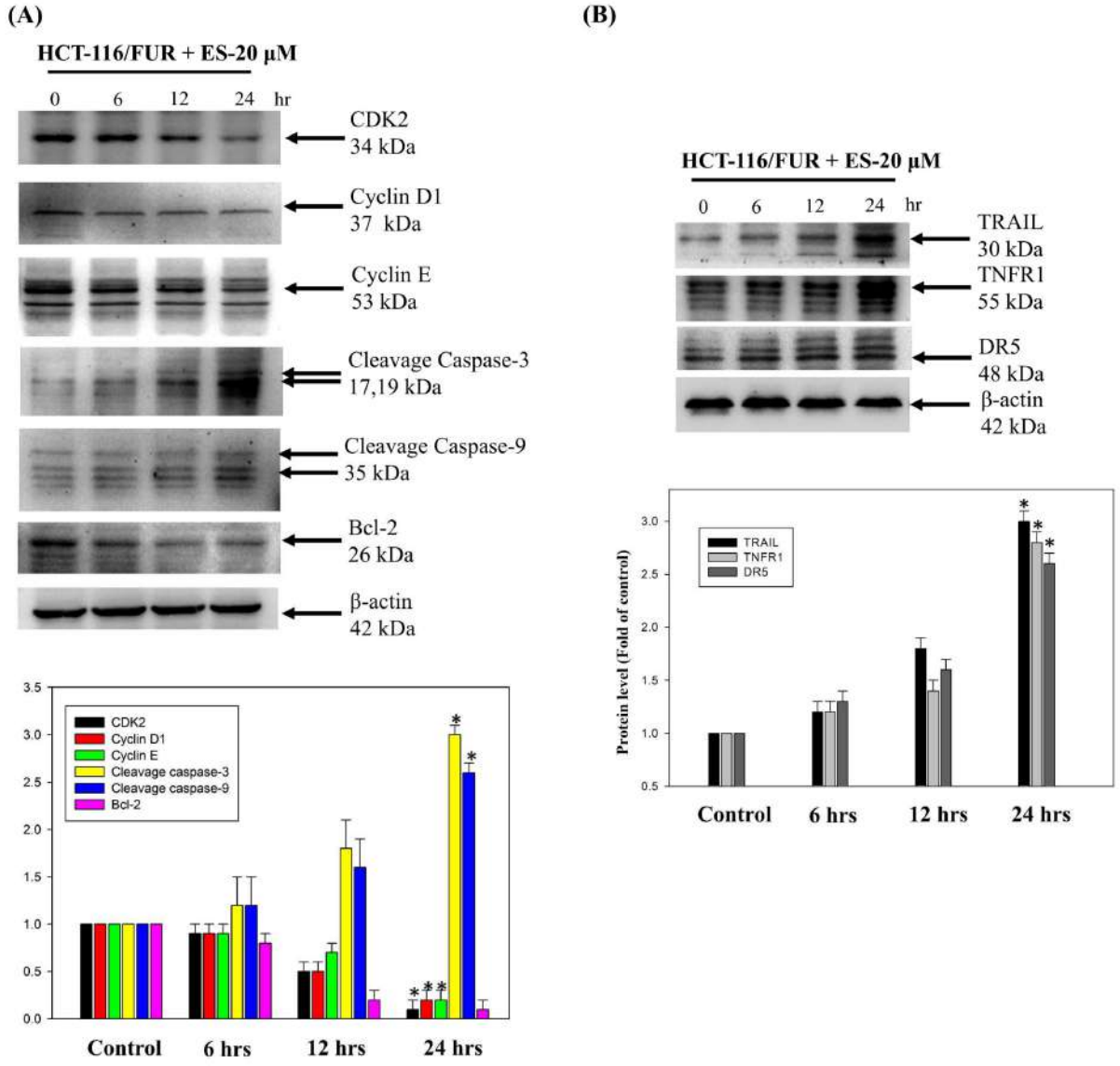


Figure 7. Effect of erinacines S on the protein level of the molecules-related to the cell cycle and cell death in HCT-116/FUR chemoresistant cells. The protein level of proteins (including CDK2, cyclin D1, cyclin E, cleavage caspase 3, cleavage caspase 9, Bcl-2, and TRAIL, TNFR1 and DR5) in erinacines S (ES)-treated HCT-116/FUR cell for 0–24 h were detected by western blotting (B). Here, β-actin served as internal control. *$p < 0.05$, as compared to the HCT-116/FUR untreated group.

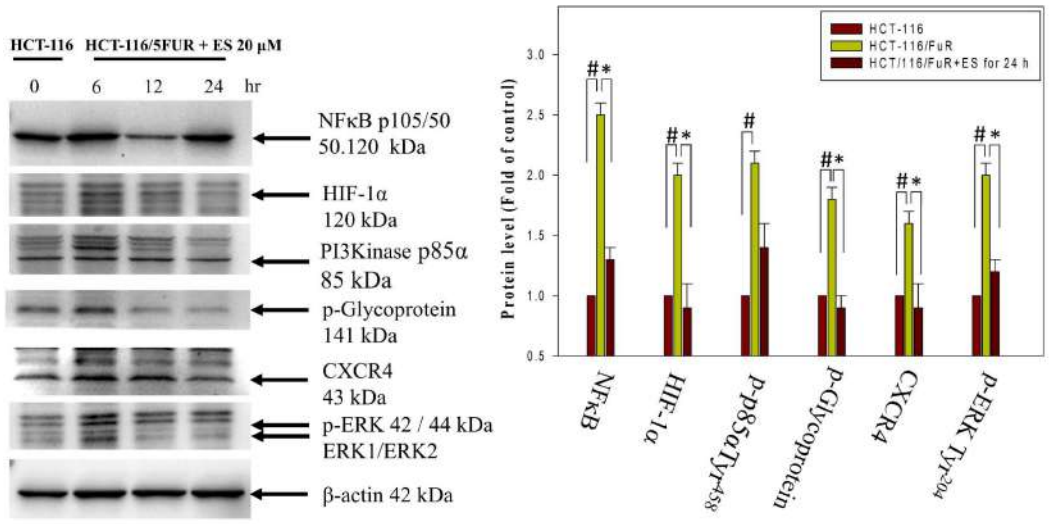


Figure 8. Inactivation of the CXCR4/PI3K/ERK and NFκB/HIF1α/p-GP pathways by erinacine S treatment. Western blotting to determine the protein levels of phosphorylated phosphoinositide 3-kinases (PI3K), extracellular signal-regulated kinase (ERK), and β-actin in the HCT-116/FUR chemoresistant cells treated with or without erinacine S at indicated times. #$p < 0.05$, as compared to the HCT-116 untreated group; *$p < 0.05$, as compared to the HCT-116/FUR untreated group.

Modulation of C-X-C chemokine receptor type 4-related signaling pathway by erinacine S in chemoresistant HCT-116/FUR cells

Chemoresistant cells often develop resistance through various mechanisms, including increased drug efflux (mediated by membrane protein P-gp), activation of autocrine signaling pathways (such as the MIF-CXCR4 axis), metabolic changes (involving HIF-1α), and alterations in the EMT process. These changes contribute to the aggressiveness of chemoresistant cells and are linked to the CXCR4-MIF axis/PI3K/Akt/HIF-1 pathways. We observed a significant increase in CXCR4 and HIF1α expression, as well as the phosphorylation of PI3K and ERK1/2, and NFκB p50 in HCT-116/5FUR cells compared to human parental HCT-116 cells. The latter are often used as a model for studying cell signaling and apoptosis in human CRC cells (Fig. 8). Furthermore, assessment of the effects of erinacine S treatment of HCT-116/FUR cells in terms of the pathways indicated a time-dependent inhibition of the CXCR4/PI3K/Akt/ERK/HIF-1α/NFκBp50 pathways, resulting in reduced cell proliferation and enhanced apoptosis (Fig. 8). Thus, erinacine S may exert its anti-cancer effects by targeting these critical signaling pathways associated with chemoresistance and cell aggressiveness.

Erinacine S increases the expression of TRAIL, TNFR1, and DR5 via PAK/FAK/p300-mediated epigenetic histone acetylation in chemoresistant HCT-116/FUR cells

Our study delved into the mechanisms through which erinacine S enhances the expression of death activators TRAIL, TNFR1, and DR5 in chemoresistant cells through acetylation of histone H3 (H3K9K14ac). This histone modification is known to be associated with the upregulation of these genes [39]. We explored several signaling pathways activated by erinacine S, including ERK1/2, c-Jun kinase (JNKs), protein 38 (P38), and other kinases like PAK (p21-activated kinase), FAK, and p300. Erinacine S treatment led to the phosphorylation of PAK Thr423, activation of FAK Tyr577/579, and sustained expression of p300 in HCT-116/FUR cells with time (Fig. 9). These events are crucial for the induction of cell death activators through signaling pathways and the epigenetic modification of histone H3K9K14ac binding to the promoter regions of TRAIL, TNFR1, and DR5 genes. In our chromatin immunoprecipitation (ChIP) assay, we found that erinacine S treatment increased the H3K9K14ac modification of histone H3 on the promoter regions of TRAIL, TNFR1, and DR5 genes. These modifications were reversed through the inhibition of multiple protein kinases, as the specific PAK1 inhibitor IPA-3, FAK inhibitor Y15, or p300 inhibitor C646 (Fig. 10). These outcomes suggest that erinacine S exerts its effects by modifying histones and promoting gene expression associated with cell death. Therefore, as a novel biological property, erinacine S inhibits growth and apoptosis in chemoresistant HCT-116/FUR cells by epigenetic histone H3K9K14ac (Acetyl Lys9/Lys14) modification of TRAIL, TNFR1, and DR5 genes. Indeed, treatment with erinacine S increased the level of p-PAK, p-FAK, and p300. Assessment of the effects of kinase inhibitors in blocking erinacine S -induced cell death, and determination of apoptosis (%) by flow cytometry analysis for Annexin-V and PI revealed

that PAK1/FAK/p300-specific inhibitors almost blocked erinacine S-induced cell death by 5%, 7%, 5%, respectively (Table 2). Overall, our results reveal a novel biological property of erinacine S, which affects the growth and apoptosis of chemoresistant HCT-116/FUR cells through epigenetic histone modification (H3K9K14ac) of TRAIL, TNFR1, and DR5 genes. This intricate interplay of signaling pathways and histone modifications contributes to the anti-cancer effects of erinacine S.

Table 2. Effects of the kinase inhibitors in blocking erinacine S – induced cell death in HCT-116/FUR human colorectal cancer cells.

	Apoptosis (%)
HCT-116/FUR	4
Erinacine S	28 ± 4
Erinacine S + IPA-3	5 ± 3
Erinacine S + Y15	7 ± 3
Erinacine S + C646	5 ± 3

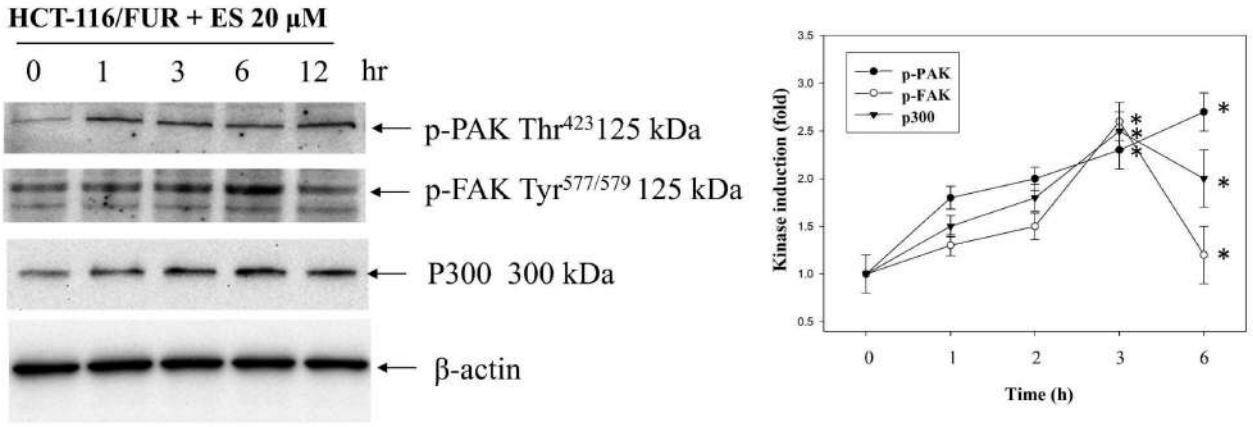


Figure 9. The effect of erinacine S (ES) on PAK/FAK/p300 pathways in HCT-116/FUR cells. The protein levels of phosphorylated p21-activated kinase (PAK), focal adhesion kinase (FAK), and histone acetyltransferase p300 in the HCT-116/FUR cells treated with or without erinacine S were determined at the indicated time by western blotting. The protein levels were quantified by densitometry with the ratio of the untreated control set as 1-fold. The quantitative data are presented as the mean of three repeats from three independent experiments. *p < 0.05, compared with the HCT-116/FUR untreated group.

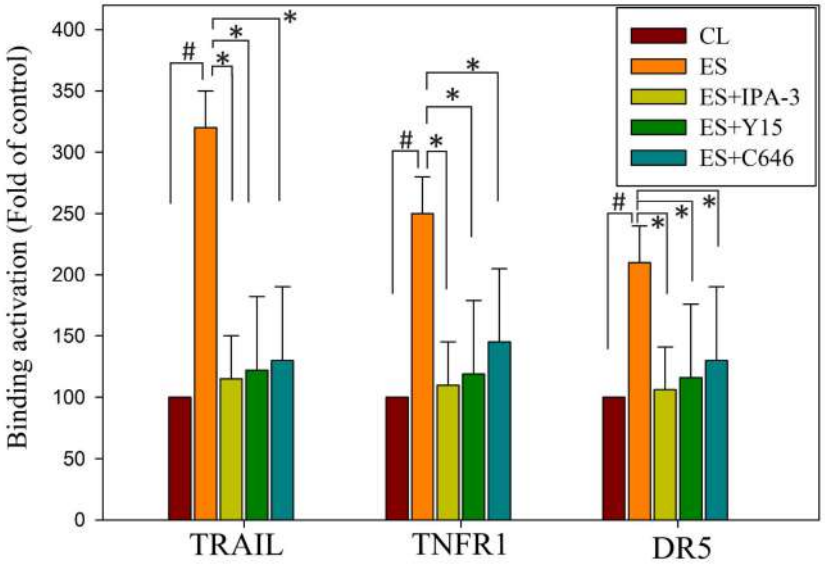


Figure 10. Erinacine S-mediated epigenetic histone H3K9K14ac (Acetyl Lys9/Lys14) of tumor necrosis factor-related apoptosis-inducing ligand (TRAIL), TNFα1, and death receptor 5 (DR5) promoter involves the reactive oxygen species (ROS)-derived and p21-activated kinase (PAK)/focal adhesion kinase (FAK)/P300 signals. In this study, HCT-116/FUR cells were treated with erinacine S with or without specific inhibitors for PAK1 (IPA-3), FAK (Y15), or p300 (C646) for 24 h. Chromatin immunoprecipitation (ChIP) assays were performed using antibodies against histone H3K9K14ac, and the precipitated DNA was quantified by real-time polymerase chain reaction targeting TRAIL, TNFα1, and DR5 promoters. The anti-IgG antibody served as a control, and input DNA was amplified for normalization. Normalized mean CT values were calculated as ΔCT, with ΔΔCt used to determine the effect of erinacine S treatment on specific genes. The results, presented as mean ± standard deviation of three independent experiments with triplicate technical repeats, revealed significant differences. #p < 0.05, compared to that of the HCT-116/FUR untreated control chemoresistant cells; *p < 0.05, as compared to the HCT-116/FUR erinacine S treated group.

Discussion

Erinacines are a group of bioactive compounds predominantly sourced from *H. erinaceus*, commonly referred to as lion's mane mushroom. These compounds have garnered considerable attention due to their health-promoting properties, including their apoptotic-inducing capacity in cancer cells [40]. This apoptotic process, driven by bioactive compounds isolated from *H. erinaceus*, is initiated through the generation of reactive oxygen species (ROS) and subsequent mitochondrial dysfunction, subsequently causing the activation of caspases, and orchestrating a cascade of events that lead to cellular demise [28,32,34,36]. However, there exists a notable gap in our understanding regarding the molecular mechanisms underlying the action of erinacine S, a compound isolated from *H. erinaceus* mycelium, particularly in the context of human chemoresistant CRC. Within this study, we embarked on the exploration of molecular changes that transpire in drug-resistant CRC cells following prolonged exposure to anticancer agents [8,28,41]. These drug-resistant cells, denoted HCT-116/FUR, were meticulously examined to delineate their metastatic capabilities and the mechanisms at play in drug-resistant CRC cells. Our investigations encompassed the characterization of expression profiles in parental HCT-116 human CRC cells and their 5FU-resistant counterparts, employing methodologies such as fluorescence-activated cell sorting and western blot analysis. Strikingly, in contrast to parental HCT-116 cells, HCT-116/FUR cells exhibited significantly augmented expression of CD44 and CD133, putative CSC markers, alongside the stem cell markers OCT4 and SOX2 (Fig. 2). The observed upregulation of the CXCR4/PI3K/Akt/ERK/HIF-1α/NFκB/p50 pathways in drug-resistant CRC cells significantly hindered apoptosis, elucidating a significant role in chemoresistance (Fig. 8). Importantly, our study unveiled a hitherto unreported function of erinacine S, derived from *H. erinaceus* mycelium, namely its potential to suppress the viability of chemoresistant cells both *in vitro* (HCT-116/5FUR cells) and *in vivo* (xenograft mouse model) (Fig 3 and 5). Furthermore, erinacine S induced cell cycle arrest in HCT-116/FUR cells at the G1 stage (Fig. 4 and 5), and triggered apoptosis in a time-dependent manner, as evidenced by indicators like depolarization of mitochondrial potential (DYm) and elevated intracellular Ca^{2+} levels (Fig. 4). Crucially, intraperitoneal administration of erinacine S (at doses of 1 or 5 mg/kg/day) significantly reduced tumor weight within the HCT-116/FUR xenograft model in nude mice compared to the group treated with 5FU (Fig. 5A). Additionally, erinacine S treatment correlated with decreased expressions of p-AKT, p-ERK, HIF1α, PCNA, and NFκB p50 in the tumor region of the HCT-116/FUR xenograft in nude mice (Fig. 6). Our findings further confirmed the activation of caspase 3 and caspase 9 in HCT-116/FUR cells following treatment with erinacine S. Erinacine S treatment also resulted in the inhibition of the proapoptotic protein Bcl-2, and influenced cell-cycle-related proteins, including CDK2, cyclin D1, and cyclin E, leading to cell cycle arrest at the G1 phase (Fig. 7A and 7B).

Lee M. Ellis has illuminated the complex molecular alterations occurring within chemoresistant colorectal cancer cells, specifically concerning intracellular ATP stability regulation and its effects on HIF-1α, a crucial mediator of drug resistance [42,43]. Following Ellis's methodology, we established drug-resistant colorectal cancer cell lines in our investigation of chemoresistance mechanisms, with particular emphasis on HCT-116/FUR chemoresistant colorectal cancer cells [44]. During our exploration of the fundamental molecular mechanisms underlying drug resistance in colorectal cancer cells [29], we examined the sophisticated interactions between various factors. Our findings revealed that drug-resistant colorectal cancer cells demonstrated upregulated expression of multiple components including the MIF-CXCR4 axis, Bcl-2/Bcl-XL proteins, and P-glycoprotein [29]. This upregulation substantially suppressed cellular apoptosis, primarily through the stimulation of the PI3K/Akt/ERK1/2/NFκB signaling cascade. Our study thus provides valuable insights into the mechanisms by which erinacine S induces apoptosis and G1 cell cycle arrest in HCT-116/FUR cells. These effects are intricately associated with the deactivation of the CXCR4/PI3K/AKT/ERK pathway and the NFκB/HIF1α/P-gp pathway. These findings hold promise in the development of innovative strategies to address chemoresistant CRC (Fig. 8). Mani et al. conducted groundbreaking research involving the use of Snail or Twist transcription factors to induce EMT [45]. This process led to the transformation of cancer cells into CSCs with drug-resistant properties, marked by stem cell characteristics and the self-renewal ability [46]. Building upon this research, future studies may explore the impact and underlying mechanisms of *H. erinaceus* erinacine S on curtailing the invasive and metastatic potential of drug-resistant CRC cells, particularly HCT-116/FUR cells.

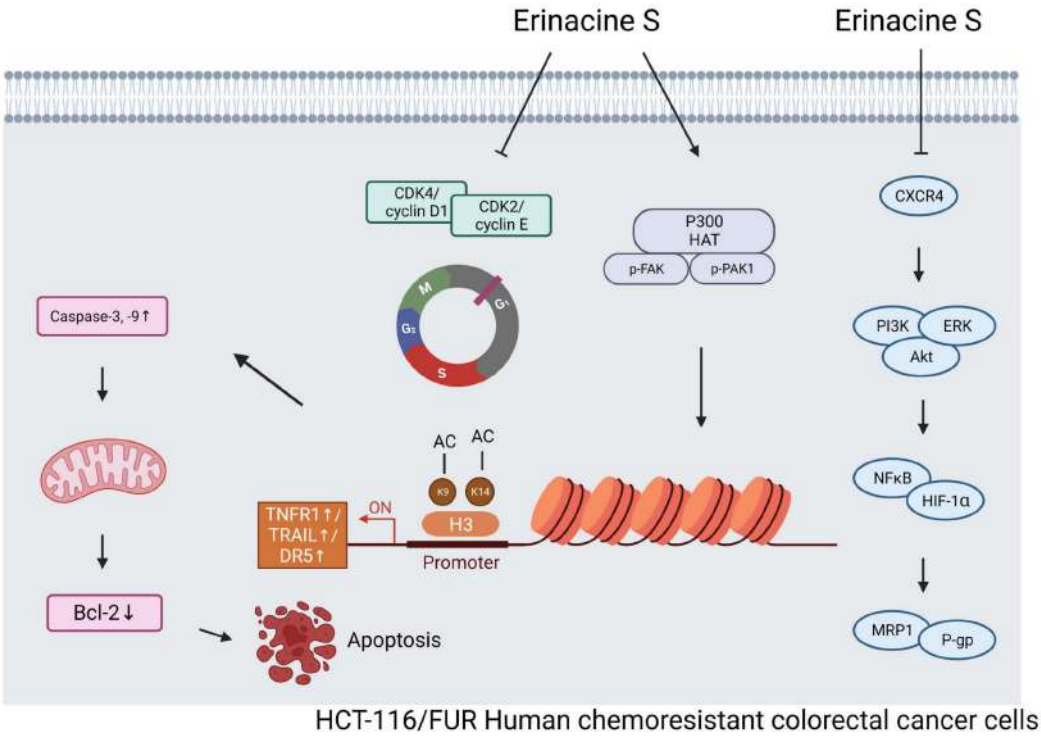


Figure 11. A schematic illustration of the molecular mechanism of erinacine S-mediated inhibition of proliferation, aggressiveness and cell cycle of chemoresistant human colorectal cancer HCT-116/5FUR cells. Erinacine S treatment regulated histone H3K9K14ac of the TRAIL, TNFR1, and DR5 promoters through multiple PAK/FAK/p300 pathways, resulting in the elevation of their protein level. Subsequently, the activation of TNFR1 and TRAIL by erinacine S was critical for an apoptotic pathway to either activate or downregulate caspase-3 and 9, or to inhibit the Bcl-2 protein. On the other hand, the repression of CXCR4/PI3K/AKT/ERK and NFκB/HIF1α/P-gp signaling pathways by the erinacine S treatment may lead to the repression of chemoresistant of HCT-116/5FUR cells.

Numerous dietary phytochemicals have attracted substantial attention due to their potential to modulate the mitogen-activated protein kinase pathway and others, including the AKT/FAK/PAK1 pathways [28,47]. These compounds have demonstrated the capacity to regulate cellular motility and adhesion, inhibit cancer growth, and trigger tumor apoptosis. The impact of these phytochemicals can be contingent upon factors such as concentration, synergistic interactions with other compounds, and the specific chemoresistant cancer type being examined. Notable examples of these phytochemicals, such as resveratrol, curcumin, epigallocatechin gallate, quercetin, genistein, sulforaphane, and berberine, are naturally abundant in food and nutraceuticals [48–50]. They exhibit promising inhibitory effects for both cancer prevention and treatment. In line with our previous investigations, our current research extends to the examination of erinacine A, another compound derived from *H. erinaceus* mycelia. Erinacine A has demonstrated remarkable anticancer properties in human CRC cells. This action is mediated through the ROS-mediated p70S6K/NF-κB/p21 pathway, ultimately resulting in cell cycle arrest and the inhibition of cell proliferation [34]. The upstream signals involved in erinacine A action encompass both the PI3K/mTOR/p70S6K and ROCK1/LIMK2/Cofilin pathways [32]. Erinacine A has been implicated in the remodeling of the actin cytoskeleton through the FAK/AKT/p70S6K/PAK1 signaling pathway and the modulation of 1433S and MTUS2 expression [32,51]. However, whether different bioactive compounds, such as erinacine S share the same anticancer properties against chemoresistant CRC and elicit similar signaling activation patterns, remains uncertain. Specifically, our investigation reveals that the activation of the PAK/FAK/p300 pathways is vital in erinacine S-induced apoptosis and cell cycle arrest in HCT-116/FUR cells (Fig. 9). The PAK/FAK/p300 pathway, within a defined timeframe, is directly implicated in the initiation of oxidative stress induced by phytochemicals (Fig. 9). This highlights the redox-sensitive nature of the pathway, ultimately culminating in apoptosis [52].

Many dietary phytochemicals, commonly found in natural products and herbs, have been extensively examined for their potential to influence the pathways associated with death receptors, thereby facilitating apoptosis in cancer cells. The extrinsic pathway, involving the interaction of death activators with cell surface receptors, serves as a key mechanism for initiating programmed cell death. Notable death receptors in this context include TNF-α/Fas ligand,

TNF, FasL (Apo-1L or CD95L), TNFR-1, Fas, DR4, and DR5, activated through the death region of these receptors [23–25]. Often, promoting the heightened expression of death receptors and the induction of apoptosis are sought-after objectives in cancer therapy. Such efforts can effectively result in the removal of cancer cells from the cell cycle. Recent research has unveiled the involvement of the PAK/FAK/p300 pathways in apoptotic induction in CRC cells [28,33,36,37]. It has become evident that the correlation mechanisms between TRAIL receptors, TNF/TNFR, and DR5, with histone modification, particularly acetylation of H3 Lys K9/K14, represent critical events in apoptosis induction through the upregulation of these death-receptor-related proteins [39,53–55]. Our investigation delved into the molecular underpinnings of how erinacine S elicits apoptosis through the PAK/FAK/p300 pathway, ultimately mediating epigenetic histone H3K9K14ac of TRAIL, TNFR1, and DR5 in chemoresistant CRC cells, specifically HCT-116/FUR (Fig. 10). The emphasis on histone modifications, particularly the epigenetic aspects associated with the aggressive nature of cancer cells, is crucial in understanding how chromatin accessibility and gene expression are regulated. Further studies are imperative to comprehensively elucidate both *in vitro* and *in vivo*, how erinacine S modulates these epigenetic modifications, potentially involving histone methyltransferases (HMTs) or demethylases (HDMs) [23,56].

Conclusions

In summary, this study successfully identified and characterized a drug-resistant CRC cell line, HCT-116/5FUR. It also investigated the effects of the newly extracted compound, *H. erinaceus* erinacine S, on these chemoresistant human CRC cells, highlighting its potential mechanisms of action and epigenetic regulatory properties. Importantly, erinacine S exhibited significant inhibitory effects on tumor growth in an *in vivo* xenograft mouse model. Erinacine S treatment also significantly upregulated the expression of TRAIL, TNFR1, and DR5 proteins, concurrently downregulating the CXCR4/PI3K/AKT/ERK and NFκB/HIF1α/P-gp signaling pathways in chemoresistant human CRC cells. In line with these findings, treatment of HCT-116/FUR cells with erinacine S not only activated extrinsic apoptosis pathways (TRAIL, TNFR1, DR5, and caspase 3, -9) but also suppressed the expression of anti-apoptotic molecules like Bcl-2. This process was intricately associated with the activation of the PAK/FAK/p300 pathways, and implicated the involvement of histone H3K9K14ac (acetyl Lys9/Lys14) on the promoters' regions of TRAIL, TNFR1, and DR5 (Fig. 11).

Abbreviations

5FUR: 5-fluorouracil-resistant
Akt: Protein kinase B
Bcl-2: B-cell lymphoma 2
Bcl-XL: Bcl-extra-large
CXCR4: C-X-C Motif Chemokine Receptor 4
CRC: Colorectal cancer
CSCs: Cancer stem cells
DR5: Death receptor 5
EMT: Epithelial to mesenchymal transition
ERK: extracellular signal-regulated kinase
FAK: Focal adhesion kinase
FOLFOX: Fluorouracil and oxaliplatin
MIF: migration inhibitory factor
PI3K: Phosphoinositide 3-kinases

Acknowledgments

We thank the Tissue Bank, Chang Gung Memorial Hospital, Chiayi and Laboratory Animal Center, Chang Gung Memorial Hospital, Chiayi and Genomics & Proteomics Core Laboratory, Department of Medical Research, Kaohsiung Chang Gung Memorial Hospital for their technical services. Figure 11 was created with BioRender.com.

Funding

Funding for this study was provided in part by research grants BMRPD42, CLRPG8L0063, CMRPG 6L0221, CMRPG6L0222, CMRPG6L0223, CMRP6P0301, ZRRPF6P0011, ZRRPF6Q0011 from Chang Gung Memorial Hospital, Chiayi, Taiwan, Chang Gung University of Science and Technology and by the National Science and Technology Council, R.O.C. Taiwan (MOST 110-2320-B-255-005-MY3, NSTC 113-2320-B-255-001-, NSTC 114-2320-B-255-002-).

Author contributions

SYT: Provision of study material, collection, and assembly of data, histopathological evaluation, and manuscript writing. **KCL**: Design, collection, assembly of data. **KFL** and **YYH**: Conception, collection, and assembly of data. **KCC**: Provision of study material or animals. **CCT**: Provision of study material or animals. **MCH**: Provision of study material, collection, and assembly of data. **CYH**: Administrative support, collection, and assembly of data (flow cytometry). **LYL, CCC**, and **WPC**: Provision of study material or animals. **HCK**: Conception and design, financial support, administrative support, manuscript writing, final approval of the manuscript. All authors read and approved the final manuscript.

Institutional review board statement

Animal care and the standard protocols for animal use were granted approval by the Institutional Animal Care and Use Committee of Chang Gung Memorial Hospital, Chiayi, Animal Ethics Research Board (IACUC approval: 2020121810). All procedures and reporting adhere to the guidelines of the Institutional Animal Care and Use Committee (IACUC).

Data availability statement

All relevant data are within the paper. The raw data supporting the conclusions of this manuscript will be made available by the authors, without undue reservation, to any qualified researcher.

Conflicts of Interest

The authors have stated that there are no competing interests. Authors Li-Ya Lee, Wan-Ping Chen, and Chin-Chu Chen were affiliated with Grape King Biotechnology Inc (Grape King Bio Ltd.). All other authors declare no competing interests. This publication did not receive significant financial support that could have influenced its outcome.

References

1. Siegel RL, Miller KD, Fuchs HE, Jemal A. Cancer Statistics, 2021. CA Cancer J Clin. 2021; 71: 7–33.
2. Center MM, Jemal A, Smith RA, Ward E. Worldwide variations in colorectal cancer. CA Cancer J Clin. 2009; 59: 366–78.
3. Mei ZB, Zhang ZJ, Liu CY, Liu Y, Cui A, Liang ZL, et al. Survival benefits of metformin for colorectal cancer patients with diabetes: a systematic review and meta-analysis. PLoS One. 2014; 9: e91818
4. Douillard JY, Cunningham D, Roth AD, Navarro M, James RD, Karasek P, et al. Irinotecan combined with fluorouracil compared with fluorouracil alone. as first-line treatment for metastatic colorectal cancer: a multicentre randomised trial. Lancet. 2000; 355: 1041–7.
5. Raymond E, Faivre S, Chaney S, Woynarowski J, Cvitkovic E. Cellular and molecular pharmacology of oxaliplatin. Mol Cancer Ther. 2002; 1: 227–35.
6. Paldino E, Tesori V, Casalbore P, Gasbarrini A, Puglisi MA. Tumor initiating cells and chemoresistance: which is the best strategy to target colon cancer stem cells? Biomed Res Int. 2014; 2014: 859871–7.
7. Yang M, Liu P, Huang P. Cancer stem cells, metabolism, and therapeutic significance. Tumour Biol. 2016; 37: 5735–42.
8. Dallas NA, Xia L, Fan F, Gray MJ, Gaur P, Van Buren G, et al. Chemoresistant colorectal cancer cells, the cancer stem cell phenotype, and increased sensitivity to insulin-like growth factor-I receptor inhibition. Cancer Res. 2009; 69: 1951–7.
9. Venturella G, Ferraro V, Cirlincione F, Gargano ML. Medicinal Mushrooms: Bioactive Compounds, Use, and Clinical Trials. Int J Mol Sci. 2021; 22: 1–31.
10. Editorial Committee of Chinese Materia Medica of State Administration of Traditional Chinese Medicine. Xin Zhong Hua Ben Cao. Shanghai: Shanghai Science and Technology Press; 1999. 682 p.
11. Chaldakov GN, Fiore M, Tonchev AB, Dimitrov D, Pancheva R, et al. Homo obesus: a metabotrophin-deficient species. Pharmacology and nutrition insight. Curr Pharm Des. 2007; 13: 2176–9.
12. Mori K, Inatomi S, Ouchi K, Azumi Y, Tuchida T. Improving effects of the mushroom Yamabushitake (Hericium erinaceus) on mild cognitive impairment: a double-blind placebo-controlled clinical trial. Phytother Res. 2009; 23: 367–72.
13. Mori K, Obara Y, Moriya T, Inatomi S, Nakahata N. Effects of Hericium erinaceus on amyloid β(25-35) peptide-induced learning and memory deficits in mice. Biomed Res. 2011; 32: 67–72.
14. Kim SP, Nam SH, Friedman M. Hericium erinaceus (Lion's Mane) mushroom extracts inhibit metastasis of cancer cells to the lung in CT-26 colon cancer-tansplanted mice. J Agric Food Chem. 2013; 61: 4898–904.
15. Ulziijargal E, Yang JH, Lin LY, Chen CP, Mau JL. Quality of bread supplemented with mushroom mycelia. Food Chem. 2013; 138: 70–6.
16. Lee KF, Chen JH, Teng CC, Shen CH, Hsieh MC, Lu CC, et al. Protective effects of Hericium erinaceus mycelium and its isolated erinacine A against ischemia-injury-induced neuronal cell death via the inhibition of iNOS/p38 MAPK and nitrotyrosine. Int J Mol Sci. 2014; 15: 15073–89.
17. Kawagishi H, Ando M, Mizuno T. Hericenone A and B as cytotoxic principles from the mushroom hericium erinaceum. Tetrahedron Lett. 1990; 31: 373–6.
18. Ryu SH, Hong SM, Khan Z, Lee SK, Vishwanath M, Turk A, et al. Neurotrophic isoindolinones from the fruiting bodies of Hericium erinaceus. Bioorg Med Chem Lett. 2021; 31: 127714.
19. Tan YF, Mo JS, Wang YK, Zhang W, Jiang YP, Xu KP, et al. The ethnopharmacology, phytochemistry and pharmacology of the genus Hericium. J Ethnopharmacol. 2024; 319: 117353
20. Wang M, Pan W, Xu Y, Zhang J, Wan J, Jiang H. Microglia-Mediated Neuroinflammation: A Potential Target for the Treatment of Cardiovascular Diseases. J Inflamm Res. 2022; 15: 3083–94.
21. Li G, Yu K, Li F, Xu K, Li J, He S, et al. Anticancer potential of Hericium erinaceus extracts against human gastrointestinal cancers. J Ethnopharmacol. 2014; 153: 521–30.
22. Kim SP, Kang MY, Choi YH, Kim JH, Nam SH, Friedman M. Mechanism of Hericium erinaceus (Yamabushitake) mushroom-induced apoptosis of U937 human monocytic leukemia cells. Food Funct. 2011; 2: 348–56.
23. Neophytou CM, Trougakos IP, Erin N, Papageorgis P. Apoptosis Deregulation and the Development of Cancer Multi-Drug Resistance. Cancers (Basel). 2021; 13: 4363–88.
24. Salvesen GS, Duckett CS. IAP proteins: blocking the road to death's door. Nat Rev Mol Cell Biol. 2002; 3: 401–10.
25. Esposti MD. The roles of Bid. Apoptosis. 2002; 7: 433–40.
26. Lee GT, Kim JH, Kwon SJ, Stein MN, Hong JH, Nagaya N, et al. Dihydrotestosterone Increases Cytotoxic Activity of Macrophages on Prostate Cancer Cells via TRAIL. Endocrinology. 2019; 160: 2049–60.
27. Wajant H. The Fas signaling pathway: more than a paradigm. Science. 2002; 296: 1635–6.
28. Tung SY, Lee KC, Lee KF, Yang YL, Huang WS, Lee LY, et al. Apoptotic mechanisms of gastric cancer cells induced by isolated erinacine S through epigenetic histone H3 methylation of FasL and TRAIL. Food Funct. 2021; 12: 3455–68.
29. Huang WS, Hsieh MC, Huang CY, Kuo YH, Tung SY, Shen CH, et al. The Association of CXC Receptor 4 Mediated Signaling Pathway with Oxaliplatin-Resistant Human Colorectal Cancer Cells. PLoS One. 2016; 11: e0159927–43.
30. Huang CY, Lee KC, Tung SY, Huang WS, Teng CC, Lee KF, et al. 2D-DIGE-MS Proteomics Approaches for Identification of Gelsolin and Peroxiredoxin 4 with Lymph Node Metastasis in Colorectal Cancer. Cancers (Basel). 2022; 14: 3189–208.
31. Lee KF, Tung SY, Teng CC, Shen CH, Hsieh MC, Huang CY, et al. Post-Treatment with Erinacine A, a Derived Diterpenoid of H. erinaceus, Attenuates Neurotoxicity in MPTP Model of Parkinson's Disease. Antioxidants (Basel). 2020; 9: 137–53.
32. Lee KC, Kuo HC, Shen CH, Lu CC, Huang WS, Hsieh MC, et al. A proteomics approach to identifying novel protein targets involved in erinacine A-mediated inhibition of colorectal cancer cells' aggressiveness. J Cell Mol Med. 2017; 21: 588–99.
33. Hsieh YY, Lee KC, Cheng KC, Lee KF, Yang YL, Chu HT, et al. Antrodin C Isolated from Antrodia Cinnamomea Induced Apoptosis through ROS/AKT/ERK/P38 Signaling Pathway and Epigenetic Histone Acetylation of TNFα in Colorectal Cancer Cells. Antioxidants (Basel). 2023; 12: 764–79.
34. Lu CC, Huang WS, Lee KF, Lee KC, Hsieh MC, Huang CY, et al. Inhibitory effect of Erinacines A on the growth of DLD-1 colorectal cancer cells is induced by generation of reactive oxygen species and activation of p70S6K and p21. J Funct Foods. 2016; 21: 474–84.
35. Tsai JJ, Kuo HC, Lee KF, Tsai TH. Proteomic analysis of plasma from rats following total parenteral nutrition-induced liver injury. Proteomics. 2015; 15: 3865–74.
36. Lee KC, Lee KF, Tung SY, Huang WS, Lee LY, Chen WP, et al. Induction Apoptosis of Erinacine A in Human Colorectal Cancer Cells Involving the Expression of TNFR, Fas, and Fas Ligand via the JNK/p300/p50 Signaling Pathway With Histone Acetylation. Front Pharmacol. 2019; 10: 1174.
37. Teng CC, Tung SY, Lee KC, Lee KF, Huang WS, Shen CH, et al. Novel regulator role of CIL-102 in the epigenetic modification of TNFR1/TRAIL to induce cell apoptosis in human gastric cancer. Food Chem Toxicol. 2021;147:111856.
38. Lee KC, Chen HH, Cheng KC, Liu TT, Lee KF, Teng CC, et al. Use of iTRAQ-based quantitative proteomic identification of CHGA and UCHL1 correlated with lymph node metastasis in colorectal carcinoma. J Cell Mol Med. 2023; 27: 2004–20.
39. Oh YT, Sun SY. Regulation of Cancer Metastasis by TRAIL/Death Receptor Signaling. Biomolecules. 2021; 11: 499.
40. Lee SR, Jung K, Noh HJ, Park YJ, Lee HL, Lee KR, et al. A new cerebroside from the fruiting bodies of Hericium erinaceus and its applicability to cancer treatment. Bioorg Med Chem Lett. 2015; 25: 5712–5.
41. Yoshida GJ, Saya H. Therapeutic strategies targeting cancer stem cells. Cancer Sci. 2016;107: 5–11.
42. Zhou Y, Tozzi F, Chen J, Fan F, Xia L, Wang J, et al. Intracellular ATP levels are a pivotal determinant of chemoresistance in colon cancer cells. Cancer Res. 2012; 72: 304–14.

43. Wang R, Bhattacharya R, Ye X, Fan F, Boulbes DR, Xia L, et al. Endothelial cells activate the cancer stem cell-associated NANOGP8 pathway in colorectal cancer cells in a paracrine fashion. Mol Oncol. 2017; 11: 1023–34.
44. Touil Y, Igoudjil W, Corvaisier M, Dessein AF, Vandomme J, Monte D, et al. Colon cancer cells escape 5FU chemotherapy-induced cell death by entering stemness and quiescence associated with the c-Yes/YAP axis. Clin Cancer Res. 2014; 20: 837–46.
45. Assaraf YG, Brozovic A, Gonçalves AC, Jurkovicova D, Linē A, Machuqueiro M, et al. The multi-factorial nature of clinical multidrug resistance in cancer. Drug Resist Updat. 2019; 46: 100645.
46. Ren J, Ding L, Zhang D, Shi G, Xu Q, Shen S, et al. Carcinoma-associated fibroblasts promote the stemness and chemoresistance of colorectal cancer by transferring exosomal lncRNA H19. Theranostics. 2018; 8: 3932–48.
47. Kuo HC, Kuo YR, Lee KF, Hsieh MC, Huang CY, Hsieh YY, et al. A Comparative Proteomic Analysis of Erinacine A's Inhibition of Gastric Cancer Cell Viability and Invasiveness. Cell Physiol Biochem. 2017; 43: 195–208.
48. McCubrey JA, Lertpiriyapong K, Steelman LS, Abrams SL, Yang L V., Murata RM, et al. Effects of resveratrol, curcumin, berberine and other nutraceuticals on aging, cancer development, cancer stem cells and microRNAs. Aging. 2017; 9: 1477–536.
49. Su P, Yang Y, Wang G, Chen X, Ju Y. Curcumin attenuates resistance to irinotecan via induction of apoptosis of cancer stem cells in chemoresistant colon cancer cells. Int J Oncol. 2018; 53: 1343–53.
50. Fontana F, Raimondi M, Marzagalli M, Di Domizio A, Limonta P. Natural Compounds in Prostate Cancer Prevention and Treatment: Mechanisms of Action and Molecular Targets. Cells. 2020; 9: 460.
51. Mamun A Al, Sufian MA, Uddin MS, Sumsuzzman DM, Jeandet P, Islam MS, et al. Exploring the role of senescence inducers and senotherapeutics as targets for anticancer natural products. Eur J Pharmacol. 2022; 928: 174991.
52. Loo G. Redox-sensitive mechanisms of phytochemical-mediated inhibition of cancer cell proliferation. Journal of Nutritional Biochemistry. 2003; 14: 64–73.
53. Elmallah MIY, Micheau O. Epigenetic Regulation of TRAIL Signaling: Implication for Cancer Therapy. Cancers (Basel). 2019; 11: 850.
54. Wang H, Fu C, Du J, Wang H, He R, Yin X, et al. Enhanced histone H3 acetylation of the PD-L1 promoter via the COP1/c-Jun/HDAC3 axis is required for PD-L1 expression in drug-resistant cancer cells. J Exp Clin Cancer Res. 2020; 39: 29.
55. Inoue S, Macfarlane M, Harper N, Wheat LMC, Dyer MJS, Cohen GM. Histone deacetylase inhibitors potentiate TNF-related apoptosis-inducing ligand (TRAIL)-induced apoptosis in lymphoid malignancies. Cell Death Differ. 2004; 11 Suppl 2:S193–206.
56. El Omari N, Bakha M, Imtara H, Guaouguaoua FE, Balahbib A, Zengin G, et al. Anticancer mechanisms of phytochemical compounds: focusing on epigenetic targets. Environ Sci Pollut Res Int. 2021; 28: 47869–903.

High Prevalence of Cardiometabolic Risks and Health Needs Among Patients With Hepatocellular Carcinoma After Treatment

A Cross-sectional Study

Yi-Lin Chen, MSN, RN, Chang-Chao Su, MD, Chia-Hao Chang, PhD, Kathy James, PhD, RN, FAAN, and Mei-Yen Chen, PhD, RN

Background: Many studies have indicated that inadequate health-related behavior is associated with the progression of cancer and cardiometabolic disorders. Because patients with hepatocellular carcinoma may adopt inadequate health behaviors, they are at risk for cancer recurrence, mortality, cardiometabolic disease progression, and worse quality of life.

Objective: To explore the prevalence of cardiometabolic risks and health-promoting behaviors associated with quality of life among patients with hepatocellular carcinoma after treatment.

Methods: A cross-sectional study was conducted from October 2021 to August 2022. Data were collected through face-to-face interviews using a structured questionnaire, and cardiometabolic information was recorded from medical charts.

Results: In total, 115 patients with liver cancer after treatment were enrolled; 73% were male. The mean age was 67.7 years, and high prevalence rates of central obesity (72.2%) and metabolic syndrome (47%) were noted. Inadequate exercise, oral hygiene, and cigarette smoking were common. The health-promoting score was significantly associated with exercise, the number of remaining teeth, and metabolic syndrome, which correlated with quality of life, including positive functional and negative symptoms dimensions.

Conclusions: The findings demonstrated a high prevalence of cardiometabolic risks and inadequate health-related behaviors among patients with liver cancer after treatment. This study highlights the need for healthcare providers to help patients increase health literacy for preventing cardiometabolic risks at outpatient clinics.

Implications for Practice: Findings from this study can be used to advise healthcare providers to educate patients with liver cancer during and after treatment on improving their health-promoting behaviors.

KEY WORDS: Cardiometabolic risks, Health-promoting behavior, Health-related behaviors, Liver cancer, Metabolic syndrome, Quality of life

(*Cancer Nurs* 2025;48:327–333)

Hepatocellular carcinoma (liver cancer, HCC) remains the second leading cause of cancer-related death in Taiwan.[1] It is among the most common malignancies globally, especially in Asia and Africa. Its burden continues to increase worldwide, exerting physical, emotional, and financial strain on individuals, families, communities, and health systems.[2] Most liver cancers are caused by viral hepatitis, such as hepatitis B (HBV) and C virus (HCV) infection.[3] Further, the risk factors for liver cancer include alcoholic hepatitis, obesity, and metabolic disorders.[4] Enhanced by the mass vaccination for HBV at birth approximately 40 years ago, antiviral therapy has effectively eradicated HCV in Taiwan during the last 4 years. However, liver cancer still causes the death of more than 7000 people annually.[1] In addition, HCC has been one of the most common causes of death in Taiwan for over 30 years.

Hepatocellular carcinoma has imposed a significant financial burden on the national health insurance in Taiwan. Cancer and cardiometabolic diseases (eg, hypertension, coronary heart disease, diabetes, stroke) share similar pathological pathways, including chronic inflammation,[5] which, in turn, is correlated with inadequate health-related behaviors, such as cigarette smoking, alcohol drinking, betel-nut chewing, an unhealthy diet (insufficient intake of vegetables and fruits), physical inactivity, and obesity.[6] Because of the inflammatory process, most of these cardiometabolic diseases are associated with preexisting cardiometabolic risk factors,[4] such as elevated systolic/diastolic blood pressure, fasting blood glucose (FBG), and triglycerides; central obesity (waist circumference [WC]); and low serum levels of high-density lipoprotein cholesterol. The presence of 3 or more of these risk factors is categorized as metabolic syndrome (MetS).[7]

Generally, hospitalized patients with HCC should be discharged after treatment with regular outpatient follow-up if complications or pain symptoms are absent. Several studies have indicated that MetS is significantly associated with unhealthy behaviors, such as an unhealthy diet, inadequate exercise, and substance use.[1,7] Patients with HCC may also adopt unhealthy behaviors.[4] Nevertheless, because of the time strain in clinical settings during hospitalization, many healthcare providers, including nurses, are unable to provide detailed health promotion education for patients with HCC after treatment. With a lack of significant guidance and reminders to prevent the risk factors of cardiometabolic diseases, discharged patients would be at risk for liver cancer recurrence, mortality, increased cardiometabolic disease progression, and worse quality of life.[4,6,7] Previous studies addressing the possible mechanism underscoring carcinogenesis and cardiometabolic diseases have focused on reactive oxygen species formation and redox imbalance.[8–10]

Author Affiliations: Departments of Nursing (Ms Chen) and Internal Medicine (Dr Su), Chiayi Christian Hospital; and Department of Nursing, Chang Gung University of Science and Technology (Drs Chang and Chen), Chiayi, Taiwan; Department of Nursing, University of San Diego, California (Dr James); and Department of Cardiology, Chang Gung Memorial Hospital, Chiayi, Taiwan (Dr Chen); School of Nursing, Chang Gung University, Taoyuan, Taiwan (Dr Chen).

Correspondence: Mei-Yen Chen, PhD, RN, Department of Cardiology, Chang Gung Memorial Hospital, No. 2, Chiapu Rd. West Sec., Putz City, Chiayi County 61363, Taiwan, Republic of China (meiyen@mail.cgust.edu.tw).

The authors have no funding or conflicts of interest to disclose.

Accepted for publication December 4, 2023.

Copyright © 2024 Wolters Kluwer Health, Inc. All rights reserved.

DOI: 10.1097/NCC.0000000000001326

Copyright © 2025 Wolters Kluwer Health, Inc. All rights reserved.

Reactive oxygen species are highly reactive derivatives of oxygen metabolism that play a critical role in cellular damage.[11,12] They can activate the proinflammatory pathway and induce endothelial cell dysfunction, leading to the formation of atheromas or an increased risk for cardiometabolic diseases, such as MetS, hypertension, and diabetes mellitus.[11,13] Conversely, adjusting modifiable risk factors, such as sufficient intake of vegetables and fruits, quitting smoking, engaging in regular exercise, and losing weight, could reverse this situation.[14]

In addition, the literature indicates that an unhealthy lifestyle is associated with the progression of cancer and cardiometabolic complications.[2,15] For instance, adopting a healthy diet, maintaining good oral hygiene, and engaging in regular exercise are linked to cardiometabolic disease prevention through inflammation reduction.[16–18] However, few studies have focused on exploring the correlation of cardiometabolic risks and health-related behaviors with the quality of life among patients with HCC after treatment. Because of the advances in liver cancer treatment, such as partial hepatectomy, liver transplantation, radiofrequency ablation, or transarterial chemoembolization, many patients may have a prolonged healthy life expectancy if they adopt health-promoting behaviors. Hence, this study explored the health needs related to the prevalence of cardiometabolic risks and health-promoting behaviors associated with quality of life among patients with HCC after treatment.

Methods

Design and Population

Our study used a cross-sectional, descriptive research design with purposive sampling and was conducted between October 2021 and August 2022. We recruited patients with liver cancer after treatment at a teaching hospital in southern Taiwan. The inclusion criteria were (*a*) age >20 years; (*b*) ability to communicate in Mandarin or Taiwanese; (*c*) being in a stable condition without physical restrictions or cognitive limitations, for instance, the individual should be able to walk independently to the hospital and have clear consciousness; and (*d*) having completed the informed consent form. The exclusion criteria were (*a*) metastasis, (*b*) esophageal variceal bleeding, and (*c*) hepatic encephalopathy. We used the G*Power 3.1.9.7 program (Heinrich-Heine-Universität Düsseldorf, Düsseldorf, Germany) to calculate the number of participants required for multiple linear regression analysis. The parameters were set as effect size: 0.15, α level: .05, power: 0.8, and 15 independent variables. The estimated sample size was 157 to 188.

Procedures and Ethical Considerations

Ethics approval was obtained from the institutional review board of Chiayi Christian Hospital (institutional review board no. 2021090) before conducting the study. Informed consent was obtained from all participants. All patients were informed about the survey by the first author and had the opportunity to decide not to participate in the study at any time. Data were collected through face-to-face interviews using a structured questionnaire, and cardiometabolic information was recorded from medical charts. Before conducting this study, the first author (Y.-L.C.) was trained in data collection by the corresponding author (M.-Y.C.). The first author was a head nurse in the gastrointestinal ward and a student of master of science degree in nursing.

Measurements

Part 1: Demographic Characteristics And Health-Related Behaviors

Part 1 included (*a*) age, sex, educational level, marital status, occupation, living condition (with family/relatives or alone), number of children, health history, viral hepatitis, and major treatment for liver cancer; (*b*) alcohol consumption, betel-nut chewing, cigarette smoking before diagnosis and after treatment (never, quit, current use); (*c*) at least eating 3 servings of vegetables and 2 servings of fruits per day (yes: usually/always; no: never/sometimes); (*d*) adopting at least 3 times per week for 30 minutes per day or 150 minutes per week of exercise (yes: usually/always; no: never/sometimes); (*e*) brush teeth after meals and use dental floss after dinner or before bed (yes: usually/always; no: never/sometimes); and (*f*) the number of remaining teeth and the total number of natural teeth and fixed dentures.

Part 2: Cardiometabolic Risk Factors

According to the national standard,[1] cardiometabolic risk factors were defined as follows: (*a*) WC was used to measure central obesity, with measurements taken in a standing position, at a level midway between the lowest rib margin and the iliac crest (WC in male/female ≥90/80 cm); (*b*) systolic/diastolic blood pressure ≥130/85 mmHg, blood pressure was measured twice after 5 minutes of sitting, and the average value was used; (*c*) FBG ≥100 mg/dL; (*d*) triglycerides ≥150 mg/dL; and (*e*) high-density lipoprotein cholesterol <40/50 mg/dL for male/female subjects. Any patient currently on medications for hypertension, diabetes mellitus, or hyperlipidemia was classified as having elevated cardiometabolic risk.

Part 3: Health-Promoting Behaviors

This study used the Health Promotion Scale (HPs)[19] to investigate the health-promoting behaviors adopted by patients following liver cancer treatment. The HPs included 6 dimensions and 22 items, each with specific items related to health-promoting behaviors: (1) health habits (eg, eating breakfast daily, sleeping enough, wearing fitted shoes), (2) social participation (eg, interacting with friends, participating in community activity programs, religious activities), (3) health responsibility (eg, checking blood pressure, blood sugar, and cholesterol level), (4) nutrition (eg, 1.5-bowl-sized portions of vegetables, 1-bowl-sized portion of fruit, a balanced diet of 5 food groups per day), (5) physical activity (eg, exercising 3 times per week, exercising for 30 minutes per day), and (6) oral hygiene (eg, brushing teeth before bed, brushing teeth 3 times per day).

The Cronbach's α for the total scale was .86. A 4-point response format (1-4) was used to assess the frequency of behaviors (never, sometimes, usually, always), resulting in a total score range of 22 to 88. A higher score indicated a greater adoption of health-promoting behaviors.[19]

© 2024 Wolters Kluwer Health, Inc. All rights reserved.

Copyright © 2025 Wolters Kluwer Health, Inc. All rights reserved.

Part 4: Cancer-Related Quality Of Life

We used the European Organization for Research and Treatment of Cancer Quality-of-Life Questionnaire to assess quality of life. This scale has been validated among patients with cancer in diverse multicultural and clinical research settings.[20] The European Organization for Research and Treatment of Cancer Quality-of-Life Questionnaire has 30 items, which are categorized into 3 dimensions: functionality (16 items covering physical, emotional, cognitive, and social function), symptoms (12 items addressing fatigue, pain, nausea, and vomiting symptoms), and general health status (2 items inquiring about general health and quality of life over the past 7 days). The Cronbach's α for the total scale was .82, and the subscale ranged from .71 to .85. The 4-point response format with rating scores ranging from 1 to 4 (never, sometimes, usually, always) was used to assess the functional and symptoms dimensions. General health status is assessed on a scale ranging from 1 (worse) to 7 (excellent). A higher score in the functional and general health status dimension indicates a higher quality of life. A lower score in the symptoms dimension signifies a higher quality of life. In other words, a higher score in the symptoms dimension correlates with a lower quality of life.

Data Analysis

Data analyses were conducted using SPSS 26 (IBM SPSS Inc, Chicago, Illinois). Descriptive statistics are presented as frequency distributions, percentages, and averages with SDs. We addressed factors associated with a healthy lifestyle using the independent *t* test and analysis of variance. Pearson product-moment correlation was used to explore the correlation between HPs and cancer-related quality of life. We conducted multiple linear regression analyses to investigate the factors determining the total score of HPs. Statistical significance was interpreted as $P < .05$ for all analyses.

Results

Demographic Characteristics and Health-Related Behaviors

Because of the COVID-19 pandemic, only 115 participants enrolled in the study. Although the sample size did not meet the estimated number (n=157–188), we conducted a power analysis using G*Power "*F* test: multiple regression—fixed model, R^2 deviation from zero." The analysis showed that the sample size did not significantly affect the choice of the statistical analyses, and there was a high probability of rejecting the null hypothesis with a 2-sided alternative at a 5% significance level. Table 1 displays data for 115 enrolled participants with liver cancer (73% males). The mean age was 67.7 (SD,11.3) years. Approximately 60% had an education level below senior high school, 60% were unemployed, and 58% had 3 or more children. The major causes of HCC were HBV and HCV infection, accounting for 82.6%. More than 75% of patients received radiofrequency ablation. However, nearly 33% opted for transarterial chemoembolization, and 21.7% underwent partial hepatectomy. The mean follow-up duration after cancer diagnosis was 3.3 (SD,4.2) years.

A significant percentage of participants reported that they did not engage in regular dental check/scaling (91.3%), postmeal toothbrushing (90%), dental floss use after dinner or before bed

TABLE 1. Demographic Characteristics of Participants

Variables	n (%)	Variables	n (%)
Gender		Chronic diseases	
Male	84 (73.0)	No	19 (16.5)
Female	31 (27.0)	Yes	96 (83.5)
Age, y (mean,67.8 [SD,11.3])		Hypertension	57 (49.6)
<65	39 (33.9)	Diabetes	42 (36.5)
≥65	76 (66.1)	Type of viral hepatitis	
Education		HBV	31 (27.0)
≤Junior high school	69 (60.0)	HCV	48 (41.7)
≥ Senior high school	46 (40.0)	HBV and HCV	16 (13.9)
		None/don't know	20 (17.4)
Marital status		Major treatment	
Married	87 (75.7)	RFA (time) 90 (78.3)	
Single/others	28 (24.3)	1	48 (53.3)
Living arrangement		≥2	42 (46.7)
With family/relatives	103 (89.6)	TACE (time)	36 (31.3)
Alone	12 (10.4)	1	22 (61.1)
No. of children (mean,2.8 [SD,1.5])		≥2	14 (38.9)
0	10 (8.7)	Partial hepatectomy (time)	25 (21.7)
1–2	38 (33.0)	1	20 (80.0)
≥3	67 (58.3)	≥2	5 (20.0)
Occupation		Duration of cancer diagnosis (mean,3.3 [SD,4.2])	
None	69 (60.0)	≤2 y	71 (61.7)
Yes (farmers, others)	46 (40.0)	>2 y	44 (38.3)

Abbreviations: HBV, hepatitis B virus; HCV, hepatitis C virus; RFA, radiofrequency ablation; TACE, transarterial chemoembolization.

© 2024 Wolters Kluwer Health, Inc. All rights reserved.

Copyright © 2025 Wolters Kluwer Health, Inc. All rights reserved.

(88.7%), regular exercise (66%), and the consumption of 2 servings of fruit (39%) or 3 servings of vegetables (27.8%) and were current smokers (24.3%). The average number of remaining teeth was 18.8 (SD,5.9), with 55.7% of participants having fewer than 20 teeth. In addition, 72.2%, 62.6%, 53.9%, and 47% of participants had central obesity, elevated FBG, increased blood pressure, and MetS, respectively (Table 2).

Factors Associated With Health-Promoting Behaviors Among Patients With Liver cancer

In Table 3, age 65 years or older ($P<.05$), marital status ($P<.05$), non–substance use ($P<.05$), and regular exercise ($P<.01$) were significantly associated with higher HPs scores. The number of remaining teeth ($P<.05$) and the absence of MetS ($P<.05$) were significantly associated with the nutrition subscale. Multiple linear regression analyses revealed that regular exercise ($P<.001$), the number of remaining teeth ($P<.01$), and the absence of MetS ($P<.05$) were factors significantly associated with the total score of HPs (Table 4).

Correlation Between Health-Promoting Behaviors and Quality of Life

Table 5 shows that the total score of HPs was positively associated with quality of life in the functional dimension ($P<.05$) and general health status ($P<.05$). However, it was negatively associated with the symptoms dimension ($P<.05$). Furthermore, the HPs subscales (healthy habits, healthy diet, and physical activity) showed a significant positive correlation with the functional dimension (all $P<.05$) and a negative association with the symptoms dimension (all $P<.05$). In addition, physical activity was positively associated with general health status ($P<.05$).

Discussion

To our knowledge, this is the first study to demonstrate that the prevalence of cardiometabolic risks and health-promoting behaviors among patients with HCC after treatment may be ignored or neglected as they are not being addressed by healthcare professionals. Adopting more health-promoting behaviors after treatment, combined with the advances in liver cancer treatment, may prolong healthy life expectancy and quality of life in patients with HCC after treatment. Patients with HCC should implement health-promoting behaviors simultaneously to prevent cardiometabolic diseases. Our study findings demonstrated a high prevalence of cardiometabolic diseases, MetS, central obesity, physical inactivity, cigarette smoking, inadequate oral hygiene, and fewer teeth among patients with liver cancer after treatment. These patients need to abstain from alcohol drinking, betel-nut chewing, and cigarette smoking because of their role as potent carcinogens.[2,21] Nicotine in tobacco is

TABLE 2. Health-Related Behaviors and Cardiometabolic Risks Among Patients With Liver Cancer

Variables	n (%)	Variables	n (%)
Vegetables intake (3 servings)		Waist circumference, cm	
Yes	83 (72.2)	M/F<90/80	32 (27.8)
No	32 (27.8)	M/F≥90/80	83 (72.2)
Fruits intake (2 servings)		FBG, mg/dL	
Yes	70 (60.9)	FBG <100	43 (37.4)
No	45 (39.1)	FBG ≥100	72 (62.6)
Alcohol drinking		HDL-C, mg/dL	
Never	50 (47.0)	M/F≥40/50	78 (67.8)
Quit	56 (48.7)	M/F<40/50	37 (32.2)
Current	9 (7.8)	TG, mg/dL	
Betel-nut chewing		<150	107 (93.0)
Never	79 (68.7)	≥150	8 (7.0)
Quit	27 (23.5)	Blood pressure, mmHg	
Current	9 (7.8)	SBP/DBP <130/85	53 (46.1)
Cigarette smoking		SBP/DBP≥130/85	62 (53.9)
Never	54 (47.0)	Metabolic syndrome	
Quit	33 (28.7)	No (<3 components)	61 (53.0)
Current	28 (24.3)	Yes (≥3 components)	54 (47.0)
Regular exercise (30 min/d)		Regular dental check/scaling	
Yes	39 (33.9)	Yes	10 (8.7)
No	76 (66.1)	No	105 (91.3)
Toothbrush after meal		NRT (mean, 18.8 [SD,5.9])	
Yes	11 (9.6)	<20	64 (55.7)
No	104 (90.4)	≥20	51 (44.3)
Dental floss before bed			
Yes	13 (11.3)		
No	102 (88.7)		

Abbreviations: FBG, fasting blood glucose; HDL-C, high density lipoprotein cholesterol; M/F, male/female; NRT, number of remaining teeth; SBP/DBP, systolic blood pressure/diastolic blood pressure; TG, triglyceride.

© 2024 Wolters Kluwer Health, Inc. All rights reserved.

Copyright © 2025 Wolters Kluwer Health, Inc. All rights reserved.

TABLE 3. Association Between Demographics and Health-Promoting Behaviors Among Participants

Variables	n	HH Mean±SD	SP Mean±SD	HR Mean±SD	NU Mean±SD	PA Mean±SD	OH Mean±SD	Total Score Mean±SD
Age, y								
≤64	39	17.3±2.6	12.3±3.6	8.1±3.1	8.7±2.5	3.5±2.4	4.8±1.7	54.7±8.7
≥65	76	18.5±2.4	14.3±4.6	8.9±2.9	8.8±2.5	3.9±2.6	4.8±1.8	59.1±9.3
t		−2.506[a]	−2.302[a]	−1.451	−0.013	−0.758	0.165	−2.397[a]
Sex								
Female	31	17.5±3.3	12.7±3.8	9.1±2.9	8.45±2.6	3.6±2.4	4.7±1.7	55.9±9.3
Male	84	18.3±2.1	13.9±4.5	8.5±2.9	8.9±2.5	3.8±2.6	4.8±1.8	58.2±9.3
t		−1.163	−1.455	0.958	−0.680	−0.486	−0.508	−1.160
Education								
Junior	69	18.3±2.5	13.2±3.8	8.9±2.9	8.5±2.6	3.5±2.4	4.7±1.8	57.1±8.8
High	46	17.7±2.4	14.3±5.0	8.4±2.9	9.2±2.4	4.0±2.7	4.9±1.7	58.4±10.1
t		1.410	−1.248	0.924	−1.564	−1.020	−0.324	−0.710
Marital status								
Married	87	18.1±2.2	14.1±4.6	8.9±2.9	8.9±2.5	3.9±2.6	4.9±1.6	58.8±8.9
Others	28	17.8±3.4	12.3±3.2	7.9±3.2	8.3±2.5	3.3±2.4	4.4±2.1	54.0±9.8
t		0.684	1.929	1.436	1.028	0.997	1.318	2.394[a]
Children								
0 (1)	10	17.1±2.4	12.0±2.8	6.1±3.5	8.4±3.1	3.7±2.8	5.5±1.8	52.8±10.8
1–2 (2)	38	17.2±2.4	13.5±4.2	8.6±2.9	9.2±2.3	3.7±2.5	4.7±1.7	56.9±8.9
≥3 (3)	67	18.7±2.4	13.9±4.6	9.1±2.8	8.6±2.5	3.8±2.6	4.7±1.8	58.7±9.2
F		5.060[b]	.909	4.615[a]	0.766	0.034	0.917	1.959
Post hoc		(3) > (2)		(2), (3) > (1)				
Treatment								
RFA	90	18.0±2.6	13.8±4.2	8.6±2.8	8.6±2.5	3.8±2.5	4.9±1.8	57.7±9.2
Others	25	18.2±2.0	13.0±4.7	8.9±3.4	9.1±2.6	3.6±2.6	4.4±1.6	57.2±9.8
t		−0.243	0.792	−0.416	−0.833	0.307	1.234	0.261
Substance use								
Never/quit	82	18.3±2.4	14.0±4.6	9.0±2.8	8.8±2.5	4.0±2.6	4.9±1.7	58.9±9.0
Current	33	17.5±2.7	12.7±3.6	7.8±3.2	8.7±2.5	3.2±2.3	1.5±1.9	54.3±9.3
t		1.472	1.486	2.031[a]	0.137	1.573	1.155	2.431[a]
No. of remaining teeth								
≥20	51	17.8±2.4	13.6±5.1	8.4±2.8	9.6±2.3	3.4±2.3	5.4±1.9	58.2±9.8
<20	64	18.3±2.5	13.6±3.6	8.9±3.1	8.0±2.5	3.9±2.7	4.3±1.5	57.1±8.9
t		−0.952	0.040	−0.994	3.498[a]	−1.176	3.148[a]	0.620
Regular exercise								
No	76	17.8±2.7	13.1±3.9	8.3±3.0	8.4±2.5	2.0±0.0	4.7±1.8	54.2±8.3
Yes	39	18.5±1.8	14.7±4.9	9.4±2.8	9.5±2.4	7.1±1.3	4.9±1.6	64.2±7.5
t		−1.344	−1.896	−1.897	−2.376[a]	−25.000[b]	−0.838	−6.252[b]
Metabolic syndrome								
No	61	18.3±2.2	14.0±4.6	8.3±3.2	9.4±2.4	3.7±2.6	4.9±1.5	58.6±9.3
Yes	54	17.9±2.7	13.3±4.1	8.9±2.7	8.2±2.5	3.7±2.5	4.7±1.9	56.7±9.3
t		0.917	0.807	−1.075	2.532[a]	−0.013	0.706	1.079

Abbreviations: HH, healthy habits; HR, health responsibility; M, Mean; NU, nutrition; OH, oral hygiene; PA, physical activity; RFA, radiofrequency ablation; SP, social participation.

[a]$P<.05$.

[b]$P<.01$.

highly addictive and a major risk factor for cardiovascular and respiratory diseases, as well as various types of cancer associated with vascular inflammation and endothelial dysfunction.[22] However, in the present study, 24.3% of patients were current smokers.

Previous studies have indicated that having fewer natural teeth and maintaining poor oral hygiene are associated with cardiometabolic diseases.[16,17] The World Health Organization[2] and Centers for Disease Control and Prevention[23] recommend that individuals should have more than 20 teeth remaining by age 80 years. In the present study, 55.7% of patients with HCC had <20 natural teeth, and there were only 18.8 remaining teeth on average. This may have been due to the lack of regular dental check-ups, dental scaling, toothbrushing after meals, and

© 2024 Wolters Kluwer Health, Inc. All rights reserved.

Copyright © 2025 Wolters Kluwer Health, Inc. All rights reserved.

TABLE 4. Factors Associated With Health-Promoting Behaviors Among Participants

Variables	β	SE	t	P	R^2
Constant	28.05	5.86	4.79	<.001	0.391
Age	0.29	0.07	4.27	<.001	
Regular exercise (1=yes)	9.58	1.47	6.54	<.001	
Number of remaining teeth	0.43	0.15	2.87	<.01	
Metabolic syndrome (1=yes)	−3.61	1.43	−2.52	<.05	

Abbreviation: β, standardized coefficient.

Dependent variables: total score of health-promoting behaviors. Predictors: age, number of children, number of remaining teeth, marital status, substance use, regular exercise, and metabolic syndrome.

dental floss use after dinner or before bed. Evidence supports that dental plaques and periodontitis are caused by inadequate oral hygiene, leading to tooth loss and contributing to cardiometabolic diseases through infection and systemic inflammation.[16,17] Despite Taiwan's national health insurance offering free dental check-ups and scaling every 6 months, 91.3% of patients never or rarely used this service. Therefore, healthcare providers should focus on encouraging patients to take advantage of this dental resource in Taiwan.

Experts recommended that sedentary behaviors following a cancer diagnosis are linked to poor prognosis, whereas increased physical activity offered benefits to many cancer survivors.[24,25] The present study showed that more than half of the patients did not adopt regular exercise as part of their daily activities. This may be because the healthcare providers do not include reducing sedentary behaviors for cancer survivorship in their care plan. Therefore, our results highlight the importance of promoting physical activity for patients with liver cancer after treatment.

Because of the COVID-19 pandemic, the government implemented several regulations, including the requirement to wear face masks. In public places, gatherings of too many people were discouraged, and seat arrangements with social distancing were enforced. People were advised to minimize their time in public spaces and to maintain a proper safe distance even with family members at home. These restrictions may have made it unfavorable for some individuals to walk outside during the study period. For instance, in the United States, Himbert et al[25] found that a significant proportion of patients with cancer experienced changes in exercise habits, especially exercising less, during the first 6 months of the COVID-19 pandemic. Furthermore, this may be related to limited social participation, such as reduced interaction with friends or participation in community and religious activities.

In the present study, 72% of patients had central obesity, more than half had elevated blood pressure, and nearly half had MetS. Although most HCC cases were caused by viral hepatitis, 17.4% of cases were due to unknown reasons. Obesity and MetS could induce liver cancer and cardiometabolic diseases through inflammatory mechanisms.[4,8,10] Compared with a recent study of participants without HCC conducted in the same county and who shared similar sociodemographic traits (age and sex distribution), Huang et al[26] found that 59% of participants exhibited central obesity, whereas 39.3% had MetS. Our findings indicate a higher prevalence of cardiometabolic risks among patients with HCC. The results echoed the crucial role of nurses in promoting healthy lifestyles for patients with chronic diseases to empower their self-care ability.[27] Hence, further studies should advocate the importance of the relationship between adopting health-related behaviors and reducing liver cancer recurrence and cardiometabolic risk prevention for patients after treatment.

Furthermore, a beneficial strategy could be implementing personalized healthcare that includes promoting a healthy diet, maintaining oral hygiene, encouraging regular exercise, supporting tobacco cessation, and offering weight loss programs near outpatient clinics. For instance, the health-promoting hospital campaign has been active in Taiwan for several years. We can initiate an interdisciplinary approach in the outpatient nursing department to establish continuity of care and outpatient services.

Limitations

Although this study has some valuable findings, there were a few limitations. First, the cross-sectional study design lacked sequential and long-term observation of the relationship between adopting a healthy lifestyle, cancer-related quality of life, and cardiometabolic diseases. Second, the included patients were not randomized, and the study was conducted at only one teaching hospital in the southern area, which may not be generalizable to other patients with liver cancer. Third, we used self-reports regarding their adoption of healthy lifestyle habits and cancer-related quality of life, which may generate measurement bias and affect the study findings.

Conclusion

This study found a high prevalence of cardiometabolic diseases, MetS, cigarette smoke, physical inactivity, tooth loss, and inadequate oral hygiene among patients with liver cancer after treatment. Healthcare providers should empower patients with liver cancer during or after treatment to engage in health-promoting behaviors. The findings can be used for further evidence of developing individualized health-promoting programs for patients with liver cancer after treatment and connected to the outpatient nursing department to promote continuity of care.

TABLE 5. Correlation Between Health-Promoting Behaviors and Quality of Life

	Quality of Life		
Variables	Functional	Symptoms	General Health Status
Healthy habits	0.221[a]	−0.274[b]	0.143
Social participation	0.061	−0.068	0.154
Health responsibility	0.024	−0.054	−0.025
Healthy diet	0.227[a]	−0.209[a]	0.156
Physical activity	0.195[a]	−0.202[a]	0.193[a]
Oral hygiene	0.043	−0.030	0.046
Health promoting score	0.218[a]	−0.239[a]	0.206[a]

[a]$P<.05$.

[b]$P<.01$.

© 2024 Wolters Kluwer Health, Inc. All rights reserved.

Copyright © 2025 Wolters Kluwer Health, Inc. All rights reserved.

References

1. Health Promotion Administration. Cancer prevention and control. https://www.hpa.gov.tw/EngPages/Detail.aspx?nodeid=3840&pid=10530. Accessed June 10, 2023.
2. World Health Organization. Cancer. https://www.who.int/health-topics/cancer#tab=tab_1. Accessed March 30, 2023.
3. Centers for Disease Control and Prevention. Viral hepatitis. https://www.cdc.gov/hepatitis/. Accessed March 30, 2023.
4. Song M, Liu T, Liu H, et al. Association between metabolic syndrome, C-reactive protein, and the risk of primary liver cancer: a large prospective study. *BMC Cancer*. 2022;22(1):853.
5. Matsumori A. Targeting inflammation in the diagnosis, management, and prevention of cardiovascular diseases. *Glob Heart*. 2022;17(1):80.
6. Zhang YB, Pan XF, Chen J, et al. Combined lifestyle factors, incident cancer, and cancer mortality: a systematic review and meta-analysis of prospective cohort studies. *Br J Cancer*. 2020;122(7):1085–1093.
7. Health Promotion Administration. Metabolic syndrome. https://www.hpa.gov.tw/Pages/List.aspx?nodeid=359. Accessed August 10, 2022.
8. Uchida D, Takaki A, Oyama A, et al. Oxidative stress management in chronic liver diseases and hepatocellular carcinoma. *Nutrients*. 2020;12(6):1576.
9. Li Y, Schoufour J, Wang DD, et al. Healthy lifestyle and life expectancy free of cancer, cardiovascular disease, and type 2 diabetes: prospective cohort study. *BMJ*. 2020;368:l6669.
10. Poznyak A, Grechko A, Poggio P, et al. The diabetes mellitus-atherosclerosis connection: the role of lipid and glucose metabolism and chronic inflammation. *Int J Mol Sci*. 2020;21(5):1835.
11. Yuan T, Yang T, Chen H, et al. New insights into oxidative stress and inflammation during diabetes mellitus–accelerated atherosclerosis. *Redox Biol*. 2019;20:247–260.
12. Jelic MD, Mandic AD, Maricic SM, Srdjenovic BU. Oxidative stress and its role in cancer. *J Cancer Res Ther*. 2021;17(1):22–28.
13. Koelwyn GJ, Aboumsallem JP, Moore KJ, de Boer RA. Reverse cardio-oncology: exploring the effects of cardiovascular disease on cancer pathogenesis. *J Mol Cell Cardiol*. 2022;163:1–8.
14. Lloyd-Jones DM, Allen NB, Anderson CAM, et al. Life's essential 8: updating and enhancing the American Heart Association's construct of cardiovascular health: a presidential advisory from the American Heart Association. *Circulation*. 2022;146(5):e18–e43.
15. His M, Viallon V, Dossus L, et al. Lifestyle correlates of eight breast cancer–related metabolites: a cross-sectional study within the EPIC cohort. *BMC Med*. 2021;19(1):312.
16. Gao S, Tian J, Li Y, et al. Periodontitis and number of teeth in the risk of coronary heart disease: an updated meta-analysis. *Med Sci Monit*. 2021;27:e930112.
17. Hwang SY, Shim JL, Kang D, Choi J. Poor oral health predicts higher 10-year cardiovascular risk: a propensity scores matching analysis. *J Cardiovas Nurs*. 2018;33(5):429–436.
18. Zou L, Zhang M, Fu W, et al. Meta-analysis on the association between the frequency of tooth brushing and hypertension risk. *J Clin Hypertens*. 2022;24(6):689–697.
19. Wang J, Lee CM, Chang CF, Jane SW, Chen MY. The development and psychometric testing of the geriatric health promotion scale. *J Nurs Res*. 2015;23(1):56–64.
20. Aaronson NK, Ahmedzai S, Bergman B, et al. The European Organization for Research and Treatment of Cancer QLQ-C30: a quality-of-life instrument for use in international clinical trials in oncology. *J Natl Cancer Inst*. 1993;85(5):365–376.
21. Barbería-Latasa M, Gea A, Martínez-González MA. Alcohol, drinking pattern, and chronic disease. *Nutrients*. 2022;14(9):1954.
22. Dahdah A, Jaggers RM, Sreejit G, et al. Immunological insights into cigarette smoking–induced cardiovascular disease risk. *Cell*. 2022;11(20):3190.
23. Centers for Disease Control and Prevention. Oral health tips. https://www.cdc.gov/oralhealth/basics/adult-oral-health/tips.html. Accessed December 10, 2022.
24. Belcher BR, Kang DW, Yunker AG, Dieli-Conwright CM. Interventions to reduce sedentary behavior in cancer patients and survivors: a systematic review. *Curr Oncol Rep*. 2022;24(11):1593–1605.
25. Himbert C, Hathaway CA, Daniels B, et al. Factors associated with changes in exercise behaviors during the COVID-19 pandemic. *Cancer Causes Control*. 2022;33(7):939–950.
26. Huang YT, Lin MS, Tsai WH, et al. From self-care behaviors to cardiometabolic risks prevention for the health of farmers: nursing implications. *J Adv Nurs*. 2023;79(8):3025–3034.
27. Riegel B, Westland H, Freedland KE, et al. Operational definition of self-care interventions for adults with chronic illness. *Int J Nurs Stud*. 2022;129:104231.

© 2024 Wolters Kluwer Health, Inc. All rights reserved.

Copyright © 2025 Wolters Kluwer Health, Inc. All rights reserved.

BMC Pulmonary Medicine

RESEARCH

Open Access

Inspiratory muscle training and aerobic exercise for respiratory muscle strength in myasthenia gravis post-hospitalization-a randomized controlled trial

Chia-Ling Chang[1,2], Tien-Pei Fang[3,4], Hsin-Mao Tsai[5], Hui-Chin Chen[3], Shih-Feng Liu[1,2,6], Hui-Ling Lin[3,4,7*†] and Jui-Fang Liu[3,8*†]

Abstract

Background Previous studies have demonstrated the positive effects of long-term inspiratory muscle training (IMT) on inspiratory muscle strength and pulmonary function. However, the benefits of IMT with aerobic exercise (IMT + AE) in patients with myasthenia gravis (MG) remain unclear. This randomized controlled trial aimed to assess the impact of the early, 6-week, moderate-intensity interval IMT + AE on pulmonary function, functional capacity, and respiratory muscle strength in patients with MG post-hospitalization.

Methods Patients with Discharged MG were randomly assigned to either a control group receiving standard medical management or an intervention group undergoing six-week IMT + AE program. Respiratory status was evaluated using the maximum inspiratory/expiratory pressure (MIP/MEP) and pulmonary function tests. Modified Borg dyspnea scores and a six-minute walk test for functional capacity were also employed.

Results Fifty-four participants were assigned to either the control (six$n = 28$) or IMT + AE groups ($n = 26$). At 6 weeks, the IMT + AE group showed significant improvements across all parameters, while the control group only showed notable differences in the modified Borg scale scores and walking distance. MIP improvements were 33.8 ± 36.1 cmH_2O in IMT and 22.1 ± 25.8 cmH_2O in control groups ($P = 0.18$). The IMT + AE group improvements were more substantial in MEP, modified Borg scale, and 6-minute walk distance, in addition to forced vital capacity (FVC) and FVC % of prediction (0.21 ± 0.24 L and 6.17 ± 6.01%, respectively), while the control group showed decreased volumes (-0.06 ± 0.30 L and − 1.79 ± 9.69%, respectively). FVC improvement was significant with IMT + AE (0.21 ± 0.24 L) vs. reduction in the control group (-0.06 ± 0.3 L; $P = 0.001$).

†Hui-Ling Lin and Jui-Fang Liu equally contributed to this work.

*Correspondence:
Hui-Ling Lin
huiling@mail.cgu.edu.tw
Jui-Fang Liu
jfliu01@mail.cgust.edu.tw

Full list of author information is available at the end of the article

© The Author(s) 2025. **Open Access** This article is licensed under a Creative Commons Attribution 4.0 International License, which permits use, sharing, adaptation, distribution and reproduction in any medium or format, as long as you give appropriate credit to the original author(s) and the source, provide a link to the Creative Commons licence, and indicate if changes were made. The images or other third party material in this article are included in the article's Creative Commons licence, unless indicated otherwise in a credit line to the material. If material is not included in the article's Creative Commons licence and your intended use is not permitted by statutory regulation or exceeds the permitted use, you will need to obtain permission directly from the copyright holder. To view a copy of this licence, visit http://creativecommons.org/licenses/by/4.0/.

Conclusions Implementing six-week moderate-intensity interval IMT + AE effectively enhanced respiratory muscle strength, alleviated dyspnea, improved physical capacity, and increased FVC in patients with MG following hospitalization after discharge.

Clinical trial registration The study was registered in The Clinical Trials Clinical Trial (NCT06624345||https://www.clinicaltrials.gov/) on October 12, 2024 (retrospectively registered).

Keywords Myasthenia gravis, Breathing exercises, Muscle strength, Pulmonary function tests, Maximal respiratory pressures, 6-minute walk test

Background

Myasthenia gravis (MG), a chronic autoimmune disorder affecting the neuromuscular system, is characterized by rapid fatigue and weakness in voluntary muscles [1]. This condition occurs when the immune system erroneously targets the neuromuscular junction, attacking acetylcholine receptors. The typical manifestations include ptosis, diplopia, dysphagia, dysarthria, and limb weakness. Symptom intensity can fluctuate, is often exacerbated by physical exertion, and can be ameliorated with rest. Diagnostic procedures include clinical evaluation, serological tests for antibodies, and electromyography [2]. Treatments include pharmacological agents to enhance neuromuscular transmission, immunosuppressive therapies, and sometimes surgical interventions, such as thymectomy [3].

Respiratory impairments, including respiratory muscle weakness, dyspnea, ineffective cough, sleep-disordered breathing, aspiration pneumonia, and respiratory failure, are a significant concern in MG. Patients may experience reduced vital capacity, increased susceptibility to respiratory infections, orthopnea, and paradoxical breathing [4]. Enhancing respiratory muscle strength may reduce the risk of respiratory failure in MG patients [5]. Physical exercise training has been shown to improve functional muscle status. When appropriately designed, exercise programs can enhance muscle strength [6]. A 24-week program combining aerobic and resistance strength training yields significant benefits, including improvements in muscular strength, physical function, lung function, walking speed, and symptom severity [7].

Respiratory muscle training has been proven effective for improving respiratory function [8, 9]. Strengthening inspiratory muscles improves cough function, reduces mucus retention, and enhances exercise capacity [10]. Most rehabilitation programs for patients with MG have been designed with 10-week or longer. Studies have shown the long-term benefits of respiratory muscle training for patients with mild-to-moderate MG, particularly those with hypercapnic respiratory failure [6, 8]. However, the efficacy of short-term approaches remains uncertain.

This combination of interval inspiratory muscle training (IMT) and aerobic exercise has been shown to reduce fatigue risk while enhancing respiratory efficiency and muscle endurance [11–13]. The customizable intensity allows for individual adaptation, potentially reducing respiratory complications, and addressing respiratory and overall physical function. This study aimed to evaluate the efficacy of a six-week early intervention program combining moderate-intensity interval IMT and aerobic exercise (IMT + AE) in improving respiratory function, functional capacity, and dyspnea levels in MG patients.

Methods

Study population

Approved by the Institutional Review Board of Chang Gung Memorial Foundation (Approval number: 201701697A3), this randomized clinical trial was conducted at Kaohsiung Chang Gung Memorial Hospital, Taiwan, from January 2018 to December 2018. This trial was retrospectively registered in The Clinical Trials Registry (NCT06624345). This study adhered to the CONSORT guidelines and the Declaration of Helsinki. With informed consent from all participants, patients with MG were recruited at their initial outpatient visit following discharge due to acute exacerbation.

All enrolled patients were first diagnosed with MG based on clinical features and serial examinations, including serological positivity for acetylcholine receptor antibodies, electromyography, and response to cholinesterase inhibitors. The inclusion criteria were as follows: (A) willingness to participate, (B) age over 18 years, and (C) ability to complete home-based respiratory muscle and exercise training for six weeks. The exclusion criteria were as follows: (A) presence of Myasthenia Gravis Foundation of America (MGFA) classification I or V; (B) diagnosis of heart, kidney, liver, metabolic diseases, or malignant tumors; (C) presence of unstable hemodynamics; (D) diagnosis of New York Heart Association Class III/IV; and (E) presence of pulmonary disease (FEV_1/FVC ratio < 0.7, FEV_1 < 50% predicted), and inability to follow exercise instructions. Patients with MGFA classification I were excluded due to the unlikely involvement of respiratory muscles in disease progression, and those with classification IV were excluded due to the inability to hold the mouthpiece of the IMT device.

Study protocol

Participants were randomly assigned to the IMT or disease control groups using a computer-generated schedule at discharge from the hospital. The assigned codes were sealed in envelopes and randomly selected by a blinded non-researcher for group allocation with an allocation ratio of 1:1. The study aimed for a sample size of 60 patients in order to achieve a significance level (α) of 0.05 and a power of 80% utilizing G Power statistical software, based on the study conducted by Fregonezi et al., using the mean and standard deviation values of maximal inspiratory pressure (MIP) [13].The control group received standard care without additional interventions, while the training group participated in a comprehensive six-week program including inspiratory muscle strength training and aerobic exercise initiation at enrollment. The control group received standard care consisting of acetylcholinesterase inhibitors (pyridostigmine), immunosuppressive therapy (corticosteroids and azathioprine), and additional supportive medications for non-neurological symptoms with bi-weekly clinical follow-up.

Due to the nature of the training procedure, blinding was only applied to the principal investigator during statistical analysis. Patients in the IMT group underwent intervention using a threshold loading device (Dofin Breathing Trainer, Galmed Corp., I-Lan, Taiwan), set within a pressure range of 5–39 cmH_2O. Participants were instructed to place the device in their mouths, inhale deeply against the applied resistance, hold their breath momentarily, and then remove the device for exhalation. Proper use of the device was reinforced through debriefing after the initial session. Patients were guided to perform the exercise in six sets of five breaths, a total of 30 breaths, twice daily.

The interval training protocol began with a warm-up of five breaths, each incorporating a 3-second breath hold followed by a 10-second break between breaths, with a 2-minute rest period. The endurance training protocol involved five breaths with a 3-second breath hold and a 3-second rest between breaths, repeated across four cycles. A cool-down phase was conducted with a final set of five breaths, allowing a 10-second rest between each. The entire training session lasted for approximately 10–15 min, with extended breaks introduced as necessary to minimize hyperventilation symptoms in some patients. The interval IMT protocol is illustrated in Fig. 1 in the Supplement.

The overall goal of the six-week IMT program was to achieve a moderate intensity level of aerobic exercise capacity. The initial loading pressure for the IMT device was set to 30% of the MIP of each participant. Following the principle of sequential progression of IMT, the load pressure was adjusted biweekly at the outpatient clinic. The load progressively increased, reaching 35% of MIP in the second week, 40% in the fourth week, and 45% in the sixth week.

In addition, aerobic exercise training consisted of upper limb exercises (raising arms without resistance), lower limb stepping warm-up, and walking exercises (5-minute slow walking, 2- minute brisk walking, followed by 5-minute slow walking) for 30 min per day. The aerobic exercise intensity was maintained at 50–70% of the participant's maximum heart rate and monitored using a pulse oximeter. Walking speed was measured using a metronome as a guide to ensure consistent pace during home-based training. Furthermore, breathing control training was performed twice daily, including pursed-lip and diaphragmatic breathing, lasting for 10–15 min per session.

To ensure adherence to the exercise protocol, training compliance was monitored through self-reported training diaries, regular phone calls from a research nurse on alternate days, and biweekly reminders during outpatient clinic visits. Training diaries were structured as checklists to track the completion of warm-up exercises, walking sessions, breathing control exercises, and inspiratory muscle training. The participants were also educated on strategies for monitoring progress and managing any potential discomfort or adverse effects.

Outcome measurements

The assessors were blinded to the randomization status of the patients during the outcome evaluation. Measurements were conducted at baseline and week 6 of the study. Demographic data, including age, sex, body height, body weight, body mass index, smoking status, MGFA classification, number of plasmapheresis sessions, and thymectomy history, were collected from both groups at baseline. Patients who underwent thymectomy were documented, irrespective of the timing of the procedure.

The primary outcome was respiratory muscle strength measured using MIP. Secondary outcomes included pulmonary function, dyspnea severity, expiratory muscle strength, and physical capacity on the six-minute walk test. Additionally, to account for the natural recovery of muscle strength following hospitalization, changes in these parameters from baseline to the end of the 6-week study period were calculated and analyzed for comparison. The MIP and maximum expiratory pressure (MEP) were assessed using a pressure manometer (Galemed Inc., Taiwan). The measurements were performed by two respiratory therapists who were randomly assigned to the patients. MIP and MEP were measured by instructing the patient to inhale and exhale with maximum effort against the device, maintaining the pressure for at least 1.5 s. Both measurement procedures were repeated three times with a one-minute rest between each repetition. To minimize fatigue-related effects on outcomes, the respiratory

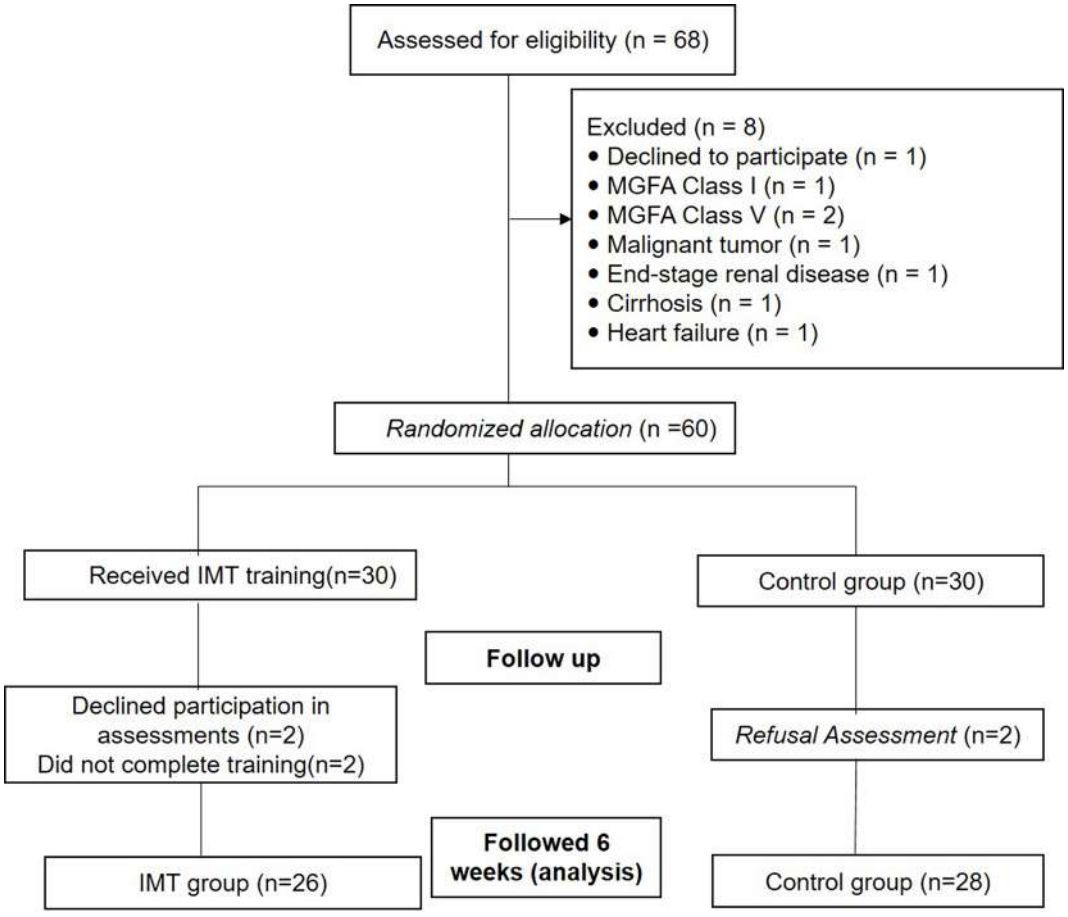


Fig. 1 Study flowchart

therapist continuously monitored patients through objective observations and verbal inquiries. Breaks were provided to maintain the measurement accuracy and reliability if fatigue was observed or reported.

The modified dyspnea Borg scale score was used to evaluate the level of breathing difficulty based on the patient's self-perception of respiratory difficulty. The scores ranged from 0 (no respiratory difficulty) to 10 (extreme respiratory difficulty), with higher scores indicating more severe breathing difficulty. The modified Borg scale was recorded before measuring the MIP at both the baseline and the six-week mark.

The six-minute walk test was used to assess a patient's exercise capacity and endurance according to the American Thoracic Society guidelines [14]. Before the test, patients were instructed to rest for at least 10 min before the test. During the test, patients were asked to walk as quickly as possible. Pulse oxygen saturation levels, heart rates, and modified Borg scale scores were monitored and recorded before, during, and after completion of the test.

Pulmonary function tests in this study strictly adhered to the guidelines of the American Thoracic Society using portable spirometry (Vyaire Spirometer, CareFusion Inc.). Pulmonary function tests for each patient included forced vital capacity (FVC), forced expiratory volume at one second (FEV_1), FEV_1/FVC ratio, and peak expiratory flow . The FVC was obtained by having the patient take a deep breath and then exhale forcefully. The test results are based on three reproducible measurements. Predicted values were calculated based on the patient's age and height.

Statistical analysis

The data were analyzed using SPSS 26.0, and the effect size was determined using the G-Power software. The chi-squared test was used to compare categorical variables between the two groups. Mann-Whitney U tests were used for nonparametric continuous variables. The Wilcoxon rank-sum test was used to assess improvements in each group from baseline to six weeks post-discharge. Statistical significance was set at $p < 0.05$, indicating a significant difference.

Table 1 Baseline characteristics of patients

	IMT group ($n=26$)	Control group ($n=28$)	*P*-value
Age (yr)	54.9 ± 15.2	56.21 ± 13.4	0.74[a]
Body high (cm)	161.1 ± 9.1	157.77 ± 11.56	0.24[a]
Body weight (kg)	64.9 ± 12.7	65.1 ± 16.6	0.97[a]
BMI (kg/m^2)	25.0 ± 3.8	25.6 ± 3.8	0.54[a]
Disease duration (years)	11.5 ± 10.6	11.2 ± 8.7	0.93[a]
Sex			
Woman, n (%)	14 (53.8)	20 (71.41)	0.23[b]
Smoke			
Yes, n (%)	22 (84.6)	24 (85.7)	0.83[b]
MGFA classification			
IIA, n (%)	10 (38.5)	9 (32.1)	0.06[b]
IIB, n (%)	7 (26.9)	3 (10.8)	
IIIA, n (%)	5 (19.2)	8 (28.6)	
IIIB, n (%)	4 (15.3)	8 (28.6)	
Plasmapheresis			
Yes, n (%)	18 (69.2)	14 (50)	0.09[b]
Thymectomy			
Yes, n (%)	10 (38.5)	16 (57.1)	0.14[b]

Notes: Data are expressed as the mean ± standard deviation; [a] statistical analysis was performed using the Mann-Whitney test; [b] statistical analysis was performed using the X^2 test

Abbreviations: IMT, inspiratory muscle training; BMI: Body mass index; MGFA, Myasthenia Gravis Foundation of America

Results

Patient characteristics

A total of 68 patients discharged with MG were initially assessed. Figure 1 illustrates the flow of participant enrollment. Ultimately, 54 patients (26 in the IMT group and 28 in the control group) were included in the final analysis. The trial was concluded after reaching a predetermined sample size. The statistical power was recalculated using MIP along with the final results, and the sample size achieved a power level of 0.78. None of the participants reported experiencing any adverse effects during the intervention.

The baseline patient characteristics are shown in Table 1. At the time of enrollment, there were no significant differences in the physical condition and MG disease status between the two groups. On average, patients had been diagnosed with MG for 11 years, and there was a higher prevalence in women than in men with an elevated incidence of smoking history.

The primary outcomes and other muscle strength measurements are presented in Table 2. The predicted values of MIP, MEP, and 6-minute walk distance were calculated according to the participants' age and height based on a previous study [15]. Given which nature that all participants exhibited enhanced muscle strength and increased walking distance. At the 6-week mark, At the 6-week mark, both groups demonstrated significant improvements in MIP, modified Borg scale scores, and 6-minute walk distance. Notably, only the IMT + AE group showed

Table 2 Comparisons of outcomes between two groups

Variable	Predicted	IMT group ($n=26$)				Control group ($n=28$)				Difference
		Baseline (%predicted)	6 weeks	Change; Δ_1[a]	Change%; Δ_1[a]	Predicted	Baseline (%predicted)	6 weeks	Change; Δ_2	Change%; Δ_2[a]	Δ_1-Δ_2[b] $\Delta_{1\%}$-$\Delta_{2\%}$[b]
MIP (cmH_2O)	73.2 ± 5.1	89.2 ± 49.7 119 ± 64%	123.0 ± 37.8	33.8 ± 36.1 $P<0.001$[§]	57.0 ± 74.2%	73.0 ± 4.8	83.9 ± 43.6 117 ± 59%	108.5 ± 46.7	22.1 ± 25.8 $P<0.001$[§]	46.3 ± 71.3	$P=0.18$ $P=0.57$
MEP (cmH_2O)	98.3 ± 6.6	77.7 ± 22.3 97 ± 35%	98.5 ± 29.9	20.8 ± 20.1 $P<0.001$[§]	15.8 ± 29.3	98.1 ± 6.2	91.4 ± 38.3 94 ± 6%	92.8 ± 37.9	1.4 ± 15.3 $P=0.62$	4.9 ± 25.9	$P<0.001$[§] $P=0.01$[*]
modified Borg scale		1.27 ± 0.82	0.57 ± 0.59	1.50 ± 0.88 $P<0.001$[§]			2.11 ± 0.86	1.29 ± 0.88	0.82 ± 0.83 $P<=0.03$[*]		$P=0.03$[*]
6MWD (meter)	498.2 ± 105.3	374.0 ± 59.4 78 ± 18%	481.9 ± 64.3	107.9 ± 72.1 $P<0.001$[§]	21.7 ± 26.5	481.3 ± 102.9	386.8 ± 96.9 81 ± 22%	412.4 ± 86.4	25.6 ± 46.8 $P=0.03$[*]	13.3 ± 25.9	$P=0.003$[*] $P=0.03$[*]

[a] Δ_1, Δ_2: Changes from the baseline to the 6th week, compared with paired t-test; [b] Δ_1-Δ_2: difference in changes between two groups, compared with Mann-Whitney test; change%: difference in percentage changes, compared with Mann-Whitney test; [*] $P<0.05$; [§] $P<0.001$

Abbreviations: IMT, inspiratory muscle training; MIP, maximum inspiratory pressure; MEP, maximum expiratory pressure; 6 MWD, 6-minute walk distance

Table 3 Comparisons of pulmonary function test

Variable	IMT group ($n=26$)			Control group ($n=28$)			Difference
	Baseline	6 weeks	Change; Δ_1 [a]	Baseline	6 weeks	Change; Δ_2 [a]	Δ_1- Δ_2 [b]
FEV_1 (L)	2.01 ± 0.74	2.21 ± 0.70	0.19 ± 0.34 $P=0.01^*$	1.79 ± 0.71	1.74 ± 0.71	-0.05 ± 0.28 $P=0.41$	$P<0.001^§$
FEV_1 ($\%_{pred}$)	75.01 ± 18.21	78.5 ± 21.2	6.17 ± 1.79 $P=0.01^*$	76.08 ± 14.4	73.12 ± 19.1	-1.79 ± 9.69 $P=0.01$	$P=0.21$.
FVC (L)	2.57 ± 0.85	2.77 ± 0.84	0.21 ± 0.24 $P=0.01^*$	2.45 ± 0.88	2.39 ± 0.94	-0.06 ± 0.30 $P=0.30$	$P<0.001^§$
FVC ($\%_{pred}$)	75.03 ± 18.4	81.2 ± 17.91	6.17 ± 6.01 $P<0.001^§$	76.0 ± 17.9	74.283 ± 18.14	-1.79 ± 9.69 $P=0.01$	$P=0.001^*$
FEV_1/FVC (%)	77.92 ± 9.74	79.22 ± 5.69	1.30 ± 10.38 $P=0.08^*$	72.41 ± 10.72	74.27 ± 9.93	1.86 ± 4.66 $P=0.07$	$P=0.72$
PEF (L/s)	5.04 ± 1.71	5.28 ± 2.21	0.24 ± 1.47 $P=0.41$	4.54 ± 1.96	4.06 ± 1.93	-0.48 ± 1.06 $P=0.02$	$P=0.09$

[a] Δ_1 or Δ_2: Changes from the baseline to the 6th week, compared with paired t-test; [b] Δ_1-Δ_2: the difference of two of changes between two groups, compared with Mann-Whitney test; $^*P<0.05$; $^§P<0.001$

Abbreviations: IMT, inspiratory muscle training; MEP, maximum inspiratory pressure; MEP, maximum expiratory pressure; 6 MWD, 6-minute walk distance

Table 4 Comparative changes in muscle strength and pulmonary function test results after 6 weeks MCID

Outcomes	IMT group ($n=26$)	Control group ($n=28$)	MD (95% CI)	*P* Value	Effect	MCID
MIP (cmH_2O)	33.8 ± 36.1	33.8 ± 36.1	9.96 (-0.06–39.91)	0.05	0.54	26.8
MEP (cmH_2O)	20.8 ± 20.1	20.8 ± 20.1	4.37 (19.21–28.04)	< 0.001 [§]	1.14	25.4
Modified Borg Scale	1.50 ± 0.88	0.82 ± 0.83	-1.05 (-1.51 - -0.59)	< 0.001 [§]	1.46	1.2
6MWD (meter)	0.82 ± 0.83	0.82 ± 0.83	64.12 (25.27–103.02)	0.002 [*]	0.89	52.8
$FEV_{1\ Pred}$	0.82 ± 0.83	-0.05 ± 0.28	7.97 (3.37–12.56)	0.001 [*]	0.95	0.7
$FVC_{\ Pred}$	-0.48 ± 1.06	-0.06 ± 0.30	0.94 (-5.1–6.94)	0.75	0.18	
FEV_1/FVC (%)	-0.05 ± 0.28	1.86 ± 4.66	0.55 (-4.89–3.79)	0.79	0.06	
PEF (L)	1.86 ± 4.66	-0.48 ± 1.06	0.61 (-0.11–1.32)	0.09	0.39	

Abbreviations: IMT, inspiratory muscle training; MIP, maximum inspiratory pressure; MEP, maximum expiratory pressure; 6 MWD, 6-minute walk distance; FEV_1, forced expiratory volume in one second; FVC, forced vital capacity; PEF, peak expiratory flow; MD, mean difference; CI, confidence interval; MDIC, minimal clinically important difference. Comparisons were conducted using the t-test; $^*P<0.05$; $^§P<0.001$

significant improvement in MEP. The improvements in MIP were 33.8 ± 36.1 and 22.1 ± 25.8 cmH_2O in the IMT + AE and control groups, respectively. The differences between the changes in MIP were not significant ($P=0.18$). However, the improvements in the IMT + AE group were more significant in the MEP, modified Borg scale, and 6-minute walk distance.

Table 3 presents the results of the pulmonary function tests. The IMT + AE group reported improvements in FVC and FVC % of prediction (0.21 ± 0.24 L and 6.17 ± 6.01%, respectively), while the control group revealed a declined FVC (-0.06 ± 0.30 L and – 1.79 ± 9.69%, respectively) after 6 weeks of discharge. The difference in the changes between the two groups was significant ($P<0.001$). The improvement of the FEV_1 value was significant with IMT + AE (0.19 ± 0.34) vs. reduction in the control group (-0.05 ± 0.28 L); however, the difference in changes in % of prediction did not reach significance ($P=0.21$). Changes in forced expiratory flow in FEV_1/FVC (%) and peak expiratory flow were insignificant within and between the groups ($P = 0.72$).

Table 4 shows the changes in muscle strength and pulmonary function test results from baseline to 6 weeks between the groups, including the effect size and confidence interval for the comparisons. The IMT + AE group demonstrated significantly greater improvements in MEP ($P<0.001$), modified Borg scale score ($P<0.001$), 6-minute walk distance ($P<0.001$), and FEV_1 as a predicted percentage ($P<0.001$). Additionally, the minimum clinically important difference (MCID) for statistically significant results was calculated using the following equation:

MCID = Cohan's d * standard deviation at baseline.

Discussion

After six weeks of inspiratory muscle and exercise training for patients with MG, significant improvements were observed in expiratory muscle strength, dyspnea severity, exercise capacity, and pulmonary function. This study shows that a six-week pulmonary rehabilitation program employing IMT + AE effectively enhances physical function in individuals with MG.

Improving respiratory muscle strength

Previous studies have shown that IMT strengthens respiratory muscles, counteracts muscle degeneration, and reduces respiratory distress in MG patients [4]. After

six weeks, the IMT group demonstrated a substantial increase in MIP, improving by 33.8 cmH_2O compared with 22.1 cmH_2O in the control group. The positive outcomes align with findings from previous studies that endorse the effectiveness of interval-based IMT [13, 16]. Fregonezi et al. first demonstrated that IMT with 60% workload for 8 weeks improves the MIP and respiratory rate to tidal volume ratio among patients with MG [13]. While most studies reported statistical significance. Del Corral et al. reported minimum clinical differences of 18 cmH_2O in individuals undergoing IMT with long-term post-COVID. The minimal clinically significant difference in IMT in patients with neuromuscular disease is warranted for further study [17]. Our results showed a minimum clinical difference of 26 cmH_2O of MIP in patients with MG.

In contrast, expiratory muscle strength (MEP) exhibited more pronounced improvements in the IMT group, increasing by 20.8 cmH_2O compared to 1.4 cmH_2O in the control group. This finding suggests that IMT + AE effectively engages the expiratory muscles and enhances respiratory efficiency. The active involvement of expiratory muscles during training, particularly the abdominal and internal intercostal muscles, may contribute to their superior adaptability compared with inspiratory muscles. The physiological demands of exercise, especially the hyperventilation response triggered by increased CO_2 levels, further stimulate expiratory muscle activation, facilitate rapid air expulsion, and improve overall respiratory function [18, 19].

When a patient performs IMT training, the process of repeated respiratory loading not only strengthens the inspiratory muscles to increase the strength of the intercostal muscles and diaphragm muscles, but also encourages the expiratory muscles (e.g., rectus abdominis and internal intercostal muscles) and their endurance to participate in active expiration, which further improves the overall respiratory function. This phenomenon can be observed in athletes with enhanced MEP (31%) [20], improved maximal oxygen uptake, and improved anaerobic capacity after 4–12 weeks of IMT [18, 21]. Thus, IMT improves the strength of the intercostal and/or abdominal muscles, generating sustained contraction during exercise, which results in adequate ventilation and improved respiratory muscle efficiency. Reducing the oxygen supply to the intercostal and/or abdominal muscles during skeletal muscle-related exercise can provide greater resistance to fatigue throughout exercise.

Previous studies have reported significant associations between expiratory muscle pressure and functional capacity, and between expiratory muscle pressure and disease severity, indicating that patients with impaired respiratory muscle strength have lower functional capacity and more severe disease [10].

The expiratory muscle strength improvements in our study compared to the control groups are potentially attributable to the incorporation of aerobic exercises, pursed-lip breathing, and diaphragmatic breathing within our intervention. A previous study combining lower-limb endurance exercise with breath control demonstrated significant improvements in expiratory muscle pressure [22]. Therefore, improvements in expiratory muscle training might benefit from breathing maneuvers and aerobic exercises using core muscles.

Enhanced in pulmonary function and fatigue reduction

Pulmonary function assessments revealed significant improvements in FEV_1 and FVC following the IMT + AE intervention. Fernández-Lázaro et al. revealed that a resistance load of ≥ 15% of the MEP applied during IMT improved significantly (54%) within 4 weeks [13]. From week 6, maximal oxygen uptake improved significantly, reaching ≥ 21.5% of the MEP after IMT, proving IMT beneficial for pulmonary function. Given that patients with MG often experience impaired neurotransmission, leading to diminished respiratory muscle strength, these enhancements highlight the potential of IMT in mitigating disease-related pulmonary deficits.

Fatigue is a common symptom in patients with MG that often exacerbates respiratory inefficiency and increases the risk of myasthenic crises. The implementation of IMT improved respiratory muscle endurance, enabling patients to sustain adequate pulmonary ventilation despite a reduced neurological drive. Notably, the modified Borg scale scores showed significant improvement after six weeks of IMT + AE, with a more pronounced reduction in dyspnea severity observed in the intervention group. Hsu et al. reported that a 12-week IMT program significantly delayed muscle fatigue progression and reduced respiratory failure risk in patients with MG [23]. These is consistent with previous studies demonstrating that respiratory muscle training can delay muscle fatigue progression and reduce the risk of respiratory failure.

IMT has been associated with diaphragmatic hypertrophy, increased blood flow to respiratory muscles, decreased dyspnea perception, and optimized neuromotor control, all of which contribute to enhanced respiratory efficiency and endurance. Salazar-Martínez et al. reported IMT's physiological effects of IMT, including diaphragmatic hypertrophy, increased blood flow to exercising muscles, decreased fatigue and dyspnea, increased respiratory efficiency and endurance, changes in muscle fiber composition, and optimized neuromotor control of respiratory muscles [24]. The observed benefits may be attributed to physiological adaptations such as an increased proportion of type IIa muscle fibers, which enhance resistance to fatigue and FRC.

Previous investigations have consistently demonstrated compromised pulmonary function in individuals with MG, particularly in reduced FEV_1 levels [19]. Similarly, Zawadka-Kunikowska et al. reported significantly lower FEV_1 and FVC values in MG patients compared to healthy controls [25]. A related study exploring the efficacy of IMT over 12 weeks noted that improvements in both FEV_1 and FVC alongside reductions in fatigue were appeared among MG patients [26].

This enhancement may be attributed to increased expiratory muscle strength. The IMT program aims to enhance expiratory muscle strength, leading to an increased FEV_1. A previous study demonstrated a correlation between MEP, and six-minute walk distance, and peak expiratory flow in patients with multiple sclerosis [25].

Impact on exercise capacity and dyspnea scores

Disease severity in MG can affect respiratory status, as reflected in patients' dyspnea scores. Generally, patients with mild severity experience dyspnea during exercise or exertional activity, whereas those with a worsening condition have an intense sensation of dyspnea. In severe cases, dyspnea may occur during sleep [25]. The six-minute walk test and dyspnea severity assessments provided further evidence of the efficacy of the intervention. Patients in the IMT + AE group exhibited significant improvements in walking distance, reflecting an enhanced exercise capacity. Dyspnea scores, which serve as important indicators of disease severity, were markedly lower in the intervention group than in the control group. These findings suggest that IMT + AE contributes to meaningful improvements in the functional capacity and respiratory endurance of patients with MG.

Existing studies emphasizing long-term inspiratory muscle strength training have shown positive outcomes, often requiring extended durations to yield noticeable benefits [22, 26]. However, our intervention with a condensed six-week duration exhibit pronounced improvements in the 6-minute walk test and exercise capacity when compared to similar studies [8, 27]. This condensed training regimen may represent a paradigm shift in respiratory rehabilitation for patients with MG, offering a time-efficient alternative to traditional long-term protocols.

Benefits of utilizing intermittent training among MG patients

The intermittent nature of the IMT + AE training program proved advantageous in enhancing respiratory endurance and pulmonary function, while improving adherence to exercise regimens. Incorporating rest intervals allowed patients with MG to sustain higher training intensities without experiencing excessive fatigue, thereby maximizing the benefits of respiratory muscle conditioning.

Clinical observations indicate that many patients with MG exhibit psychological or perceptual reluctance toward physical activity, often resulting in reduced daily activity levels and diminished tolerance for sustained exertion. Continuous exercise protocols may exacerbate muscle fatigue, potentially compromising respiratory performance, and increasing the risk of respiratory failure. Physiologically, prolonged training sessions impose significant metabolic demands on respiratory muscles, leading to cumulative fatigue and impaired endurance. This phenomenon may be linked to the respiratory muscle metabolic reflex, wherein fatigued respiratory muscles signal the central nervous system via type III and type IV sensory nerves, triggering a sympathetic vasoconstrictor response that exacerbates peripheral muscle fatigue and increases perceived exertion [28, 29].

Intermittent IMT addresses these challenges by alternating moderate-intensity exercise with rest periods, effectively mitigating excessive fatigue and optimizing pulmonary ventilation. This structured approach enhanced exercise tolerance, promoted adherence, and reduced the likelihood of training-induced respiratory distress. Given these advantages, intermittent IMT may serve as an effective strategy to improve respiratory function and overall well-being in patients with MG.

Limitations

This study had specific limitations that must be considered when interpreting the results. This single-center nature may affect the generalizability of our findings. Participants were recruited at their initial outpatient clinic visits after discharge. It is possible that the medication regimens were altered to enhance muscle strength. The patient's condition was managed under the same treatment protocol; however, the extent to which these medications influence the outcomes remains unclear. Furthermore, training compliance was monitored using self-reported diaries, phone calls on alternate days, and biweekly reminders during outpatient clinic visits; however, these methods are still subject to bias. MG's progressive nature of MG may also lead to muscle strength fluctuations over time, potentially impacting the long-term sustainability of IMT benefits. Future studies should incorporate objective assessment tools such as fatigue severity scales to enhance the accuracy of evaluating respiratory muscle fatigue and training adherence. In addition, wearable devices can be used to monitor adherence to the training protocol more effectively.

Clinical implications and future suggestions

Based on our findings, we recommend the integration of an individualized IMT training strategy into respiratory

rehabilitation programs for MG patients. A structured approach beginning with low-intensity IMT (30% of MIP) and gradually increasing resistance based on patient fatigue levels may optimize therapeutic outcomes while minimizing the risk of overexertion. Implementing an intermittent IMT strategy consisting of six sets of five breaths (30 breaths total) performed twice daily may further enhance training efficacy by preventing hyperventilation and excessive fatigue.

The use of real-time monitoring tools may provide valuable insights into respiratory fatigue patterns and facilitate personalized training adjustments. Future research should explore the applicability of intermittent IMT + AE in patients with more severe MG, particularly during the recovery phase following myasthenic crisis. Longitudinal studies examining the long-term effects of IMT on hospitalization rates, disease progression, and survival outcomes are warranted to elucidate the clinical utility of respiratory muscle training in MG management.

Conclusion

In conclusion, this study demonstrated that a six-week IMT + AE program significantly improved respiratory muscle pressure, dyspnea severity, exercise capacity, and pulmonary function in patients with MG. The combination of moderate-intensity interval IMT + AE would be an effective strategy for post-hospitalization recovery, potentially enhancing long-term respiratory function and quality of life. Implementing IMT as an early intervention following hospital discharge may benefit patients with MG, reinforcing the need for continued research on objective monitoring and long-term efficacy.

Abbreviations

MG	Myasthenia gravis
IMT + AE	Inspiratory muscle training and aerobic exercise
FVC	Forced vital capacity
FEV_1	Forced expiratory volume at one second
MIP	Maximal inspiratory pressure
MEP	Maximal expiatory pressure

Supplementary Information

The online version contains supplementary material available at https://doi.org/10.1186/s12890-025-03733-7.

Supplementary Material 1: Supplement Figure 1 Interval Inspiratory Muscle Training Protocol. The interval training protocol for inspiratory muscle training consists of a series of breath cycles that incorporate variations in breath-holds and breaks between breaths

Acknowledgements

We would like to express our gratitude to Dr. Hsiu-Lien Chu, Assistant Professor of General Education at the Chang Gung University of Science and Technology, Chiayi Campus, who provided comments on the English version of the manuscript.

Author contributions

J.-F.L. had a role in the study conceptualization, formal analysis, methodology, supervision, writing—original draft, writing, review and editing. C.-L.C. had a role in the study conceptualization, data curation, and methodology. H.-L.L. had a role in the study formal analysis, writing- original draft writing, review and editing. T.-P.F., H.-M.C., H.-C.C., M.-C.C. and S-F.L. had a role in data curation and formal analysis. All authors have read and agreed to the published version of the manuscript.

Funding

Not applicable.

Data availability

The data supporting this research are available from Hui-Ling Lin.

Declarations

Ethics approval and consent to participate

This randomized clinical trial was approved by the Institutional Review Board of the Chang Gung Memorial Foundation (approval number: 201701697A3), and informed consent was obtained from all participants.

Consent for publication

Not applicable.

Competing interests

The authors declare no competing interests.

Author details

[1]Department of Respiratory Therapy, Kaohsiung Municipal Fong Shan Hospital - Under the management of Chang Gung Medical Foundation, Kaohsiung 833, Taiwan
[2]Department of Respiratory Therapy, Kaohsiung Chang Gung Memorial Hospital, Kaohsiung 833, Taiwan
[3]Department of Respiratory Care, Chang Gung University of Science and Technology, Chiayi 613, Taiwan
[4]Department of Respiratory Therapy, Chiayi Chang Gung Memorial Hospital, Chiayi 613, Taiwan
[5]Department of Pharmacy, Chia Nan University of Pharmacy & Science, Tainan 717, Taiwan
[6]Division of Pulmonary and Critical Care Medicine, Department of Internal Medicine, Kaohsiung Chang Gung Memorial Hospital, Chang Gung University College of Medicine, Kaohsiung, Taiwan
[7]Department of Respiratory Therapy, Chang Gung University, Taoyuan 333, Taiwan
[8]Chronic Diseases and Health Promotion Research Center, Chang Gung University of Science and Technology, Chiayi, Taiwan

Received: 15 November 2024 / Accepted: 16 May 2025
Published online: 27 May 2025

References

1. Maggi L, Bernasconi P, D'Amico A, et al. Italian recommendations for diagnosis and management of congenital myasthenic syndromes. Neurol Sci. 2019;40:457–68.
2. Mantegazza R, Cavalcante P. Diagnosis and treatment of myasthenia Gravis. Curr Opin Rheumatol. 2019;31:623–33. https://doi.org/10.1097/bor.0000000000000647.
3. Narayanaswami P, Sanders DB, Wolfe G, et al. International consensus guidance for management of myasthenia Gravis: 2020 update. Neurology. 2021;96:114–22. https://doi.org/10.1212/wnl.0000000000011124.
4. Gilhus NE, Tzartos S, Evoli A, et al. Myasthenia Gravis. Nat Rev Dis Primers. 2019;5:30. https://doi.org/10.1038/s41572-019-0079-y.
5. Corrado B, Giardulli B, Costa M. Evidence-based practice in rehabilitation of myasthenia Gravis. A systematic review of the literature. J Funct Morphol Kinesiol. 2020;5:71.
6. O'Connor L, Westerberg E, Punga AR. Myasthenia Gravis and physical exercise: A novel paradigm. Front Neurol. 2020;11:675. https://doi.org/10.3389/fneur.2020.00675.
7. Chang CC, Chen YK, Chiu HC, et al. Changes in physical fitness and body composition associated with physical exercise in patients with myasthenia

Gravis: a longitudinal prospective study. J Clin Med. 2021;10. https://doi.org/10.3390/jcm10174031.
8. Freitag S, Hallebach S, Baumann I, et al. Effects of long-term respiratory muscle endurance training on respiratory and functional outcomes in patients with myasthenia Gravis. Respir Med. 2018;144:7–15. https://doi.org/10.1016/j.rmed.2018.09.001.
9. Rassler B, Marx G, Hallebach S, et al. Long-term respiratory muscle endurance training in patients with myasthenia Gravis: first results after four months of training. Autoimmun Dis. 2011;2011(808607). https://doi.org/10.4061/2011/808607.
10. Calik-Kutukcu E, Salci Y, Karanfil E, et al. Expiratory muscle strength as a predictor of functional exercise capacity in generalized myasthenia Gravis. Neurosciences (Riyadh Saudi Arabia). 2019;24:95–100. https://doi.org/10.17712/nsj.2019.2.20180024.
11. Ozalp O, Inal-Ince D, Cakmak A, et al. High-intensity inspiratory muscle training in bronchiectasis: A randomized controlled trial. Respirol (Carlton Vic). 2019;24:246–53. https://doi.org/10.1111/resp.13397.
12. Rahbek MA, Mikkelsen EE, Overgaard K, et al. Exercise in myasthenia Gravis: A feasibility study of aerobic and resistance training. Muscle Nerve. 2017;56:700–9. https://doi.org/10.1002/mus.25552.
13. Fregonezi GA, Resqueti VR, Güell R, et al. Effects of 8-week, interval-based inspiratory muscle training and breathing retraining in patients with generalized myasthenia Gravis. Chest. 2005;128:1524–30. https://doi.org/10.1378/chest.128.3.1524.
14. Bodkin C, Pascuzzi RM. Update in the management of myasthenia Gravis and lambert-eaton myasthenic syndrome. Neurol Clin. 2021;39:133–46. ATS Committee on Proficiency Standards for Clinical Pulmonary Function Laboratories. ATS statement: guidelines for the six-minute walk test. Am J Respir Crit Care Med. 2002 Jul 1;166(1):111-7. 10.1164/ajrccm.166.1.at1102. https://doi.org/10.1016/j.ncl.2020.09.007
15. Schoser B, Fong E, Geberhiwot T, et al. Maximum inspiratory pressure as a clinically meaningful trial endpoint for neuromuscular diseases: a comprehensive review of the literature. Orphanet J Rare Dis. 2017;12:52. https://doi.org/10.1186/s13023-017-0598-0.
16. Silva IS, Pedrosa R, Azevedo IG, et al. Respiratory muscle training in children and adults with neuromuscular disease. Cochrane Database Syst Rev. 2019;9(Cd011711). https://doi.org/10.1002/14651858.CD011711.pub2.
17. Del Corral T, Fabero-Garrido R, Plaza-Manzano G, et al. Minimal clinically important differences in inspiratory muscle function variables after a respiratory muscle training programme in individuals with long-term post-COVID-19 symptoms. J Clin Med. 2023;12. https://doi.org/10.3390/jcm12072720.
18. Illi SK, Held U, Frank I, et al. Effect of respiratory muscle training on exercise performance in healthy individuals: a systematic review and meta-analysis. Sports Med (Auckland NZ). 2012;42:707–24. https://doi.org/10.1007/bf03262290.
19. van Kleef ESB, Poddighe D, Caleffi Pereira M et al. Future directions for respiratory muscle training in neuromuscular disorders: A scoping review. Respiration. 2024; 103: 601–621. https://doi.org/10.1159/000539726
20. Griffiths LA, McConnell AK. The influence of inspiratory and expiratory muscle training upon rowing performance. Eur J Appl Physiol. 2007;99:457–66. https://doi.org/10.1007/s00421-006-0367-6. 2006/12/23.
21. Hartz CS, Sindorf MAG, Lopes CR, et al. Effect of inspiratory muscle training on performance of handball athletes. J Hum Kinet. 2018;63:43–51. https://doi.org/10.2478/hukin-2018-0005.
22. Chung AC, Chang CJ, Liu JF, et al. The short- and long-term effects of lower limb endurance training on outpatients with chronic obstructive pulmonary disease. Clin Rehabil. 2024;38:85–97. https://doi.org/10.1177/02692155231192453.
23. Hsu CW, Lin HC, Tsai WC et al. Respiratory muscle training improves functional outcomes and reduces fatigue in patients with myasthenia gravis: a single-center hospital-based prospective study. Biomed Res Int. 2020; 2020: 2923907. https://doi.org/10.1155/2020/2923907
24. Salazar-Martínez E, Gatterer H, Burtscher M, et al. Influence of inspiratory muscle training on ventilatory efficiency and cycling performance in normoxia and hypoxia. Front Physiol. 2017;8:133. https://doi.org/10.3389/fphys.2017.00133.
25. Zawadka-Kunikowska M, Rzepiński Ł, Cieślicka M, et al. Correlation between cardiovascular autonomic and pulmonary ventilation functions in myasthenia Gravis patients. Front Physiol. 2023;91:546–59. https://doi.org/10.3390/arm91060040.
26. Keesey JC. Clinical evaluation and management of myasthenia Gravis. Muscle Nerve. 2004;29:484–505. https://doi.org/10.1002/mus.20030.
27. Graham BL, Steenbruggen I, Miller MR, et al. Standardization of spirometry 2019 update. An official American thoracic society and European respiratory society technical statement. Front Physiol. 2019;200:e70–88. https://doi.org/10.1164/rccm.201908-1590ST.
28. Romer LM, Polkey MI. Exercise-induced respiratory muscle fatigue: implications for performance. Front Physiol. 2008;104:879–88. https://doi.org/10.1152/japplphysiol.01157.2007. 2007/12/22.
29. HajGhanbari B, Yamabayashi C, Buna TR, et al. Effects of respiratory muscle training on performance in athletes: a systematic review with meta-analyses. Strength Cond Res. 2013;27:1643–63. https://doi.org/10.1519/JSC.0b013e318269f73f.

Publisher's note

Springer Nature remains neutral with regard to jurisdictional claims in published maps and institutional affiliations.

Stem Cell Research & Therapy

RESEARCH Open Access

Differential efficacy of olfactory neurospheres from deviated nasal septum and chronic rhinosinusitis patients in regenerating olfactory epithelium

Rong-San Jiang[1,2†], Chiang-Wen Lee[3,4,5†], Yu-Hsuan Lin[6,7,8], Jing-Jie Wang[2], Jia-Bin Liao[9], Kuo-Ti Peng[4,10], Yao-Chang chiang[3] and Pei-Ling Chi[11,12*]

Abstract

Background Olfactory epithelial stem cells hold significant potential for treating olfactory dysfunction by facilitating tissue maintenance and repair. Understanding the inherent qualities of these stem cells is crucial for optimizing their therapeutic efficacy.

Methods Olfactory epithelial samples were collected from patients with deviated nasal septum (DNS) and chronic rhinosinusitis (CRS). These were cultured to form olfactory neurospheres (ONS), which were then analyzed for neural stem cell markers, neurotrophic factor production, and their ability to differentiate into olfactory sensory neurons (OSNs). The regenerative efficacy of these ONS was tested in a methimazole-induced hyposmic mouse model, with the effects on cellular senescence, apoptosis, and proliferation in the olfactory epithelium assessed.

Results Both DNS- and CRS-derived ONS exhibited neural stem cell characteristics. DNS-ONS displayed superior self-renewal capacity and higher neurotrophic factor production compared to CRS-ONS, which showed impaired OSN maturation and lower neurotrophic factor levels. In vivo, DNS-ONS were more effective in restoring olfaction, as evidenced by reduced cellular senescence, decreased apoptosis, and increased cell proliferation in the OE of methimazole-induced hyposmic mice.

Conclusions These findings highlight the importance of selecting the appropriate ONS source for therapeutic applications, with DNS-ONS showing greater promise for olfactory epithelium repair and olfactory function restoration.

Keywords Olfactory neurospheres, Regenerative medicine, Olfactory dysfunction

Introduction

Loss of smell is a common symptom of olfactory disorders, often caused by head trauma, upper respiratory tract infections, or sinonasal inflammation. These conditions degrade olfactory sensory neurons (OSNs) and damage the olfactory bulb [1, 2]. The abnormal replacement of damaged or senescent OSNs leads to neurogenic exhaustion and olfactory dysfunction [3]. The recent association of COVID-19 with impaired olfactory function [4] underscores the challenges in treating olfactory

†Rong-San Jiang and Chiang-Wen Lee contributed equally to this study.

*Correspondence:
Pei-Ling Chi
plchi@vghks.gov.tw
Full list of author information is available at the end of the article

© The Author(s) 2025. **Open Access** This article is licensed under a Creative Commons Attribution 4.0 International License, which permits use, sharing, adaptation, distribution and reproduction in any medium or format, as long as you give appropriate credit to the original author(s) and the source, provide a link to the Creative Commons licence, and indicate if changes were made. The images or other third party material in this article are included in the article's Creative Commons licence, unless indicated otherwise in a credit line to the material. If material is not included in the article's Creative Commons licence and your intended use is not permitted by statutory regulation or exceeds the permitted use, you will need to obtain permission directly from the copyright holder. To view a copy of this licence, visit http://creativecommons.org/licenses/by/4.0/.

impairment, especially due to unclear pathogenic mechanisms. Treatments such as olfactory training therapy, intranasal vitamin A, and corticosteroids (both systemic and intranasal) have been reported to improve olfactory function recovery [5], but their therapeutic efficacy remains controversial.

The olfactory epithelium (OE) is a specialized neuroepithelium that includes horizontal basal cells (HBC) and globose basal cells (GBC), which possess neural stem cell properties essential for regenerating new neurons and the entire OE after injury [6]. Numerous studies have demonstrated the benefits of using OE-derived cells to treat various central nervous system (CNS) diseases in both animal models and clinical applications [7–9]. Human OE-derived stem cells were found to ameliorate ipsiversive rotation in hemiparkinsonian rats [10] and increase neovascularization in ischemic mice [11]. These studies indicate that OE-derived stem cells are a promising source for autologous stem cell therapy for patients with olfactory loss.

Growing evidence suggests that certain disease states can alter stem cell properties, resulting in a reduced stem cell population with age, dysregulated proliferation, and diminished functional capacity [12]. Adipose tissues from obese patients have a diminished reservoir of functionally active stem cells, attributed to a reduction in their stemness properties [13]. Progressive cardiovascular disease has been reported, with endothelial progenitor cells (EPCs) undergoing senescent-like changes that impair their regenerative capacity [14]. The efficacy of autologous cell therapy is influenced by how these diseases impact the regenerative potential of stem cells. While stem cell therapy holds promise for treating diseases that are currently incurable with traditional pharmacological methods, many studies have shown that the efficacy of stem cells can be significantly affected by the physiological state of their source. In olfactory disorders, particularly, understanding these stem cell dynamics is crucial for effective therapy. The therapeutic efficacy of OE derived from patients with a differential diagnosis is largely unknown.

Chronic rhinosinusitis (CRS), characterized by persistent inflammation of the sinonasal mucosa, is a prevalent cause of olfactory dysfunction [15]. Prior studies showed chronic olfactory inflammation switched off the olfactory stem cells regenerative phenotype [16], indicating that the function of OE may be impaired in chronic inflammatory rhinosinusitis and OE derived from patients with CRS may lack efficacy in treating disease. This study presents a robust culture model optimized for expanding olfactory neurospheres (ONS) while maintaining their undifferentiated and self-renewable states in vitro. Our objective is to compare the therapeutic effects and differentiation potential of olfactory epithelial-derived cells from patients with deviated nasal septum (DNS) and chronic rhinosinusitis (CRS). By evaluating the differentiation potential and therapeutic efficacy of these cells, this study aims to identify the optimal source of olfactory neurospheres (ONS) for treating patients with anosmia, potentially improving outcomes for those suffering from olfactory dysfunction.

Materials and methods

Patients and sample collection

Human OE samples were collected with written informed consent under the approval of the Taichung Veterans General Hospital IRB (CF18350A). Tissue specimens were obtained under general anesthesia during routine rhinosurgical procedures. A single 3–4 mm^2 biopsy was taken from either the posterior nasal septum or the medial wall of the superior turbinate (see Table 1 for patient details). After collection, tissue specimens were immediately transferred into Hank's balanced salt solution (HBSS), minced, and digested with collagenase IV for 30 min at 37 °C. The digested tissues were triturated and centrifuged at 300 × g for 5 min. Each piece was then cultured in 6-well plates using ONS medium, consisting of DMEM/F-12, 1% B-27 Supplement (Life Technologies Corp.), 10 ng/ml human recombinant basic fibroblast growth factor (bFGF, R&D Systems, Inc., Minneapolis, MN), and 10 ng/ml human recombinant epidermal growth factor (EGF, R&D Systems, Inc.).

ONS cultures and differentiation into olfcatory sensory neurons

Two weeks after the initial plating, once confluence was achieved, adherent cells were passaged and cultivated in suspension to form olfactory neurospheres (ONS). The culture media were replaced every 2–3 days to maintain optimal growth conditions. To assess the capability of ONS to differentiate into olfactory sensory neurons (OSNs), ONS were enzymatically treated with Accutase (Innovative Cell Technologies #AT104). The resultant single-cell suspensions were subcultured through six passages in this study. For OSN differentiation,

Table 1 Summary of demographics and surgery types in DNS and CRS patient groups

	DNS (n = 29)	CRS (n = 25)	*P* value
Age, years	31.7 ± 10.34	53.6 ± 12.61	< 0.0001
Gender, male	22 (75.9%)	13 (52.0%)	0.0897
Procedure	Septoplasty	Endoscopic sinus surgery	

Data were showed as mean ± SD or the number (%)

DNS Deviated nasal septum, *CRS* Chronic rhinosinusitis

approximately 5×10^5 cells were plated onto Matrigel-coated 6-well plates and cultivated for 4 and 7 days in OSN induction medium, which was supplemented with 300 μM cAMP in ONS medium [17].

Measurement and image analysis of ONS number and size

To evaluate olfactory neurosphere (ONS) formation, 10^3 cells were seeded into ultra-low attachment 24-well plates and cultured in ONS medium. Olfactory epithelium (OE) tissue was isolated from patients, and migrated cells were cultured in 24-well plates at a density of 10^3 cells per well. Non-stem cells adhered to the plates within 1 day, while stem cells formed floating neurospheres. The number of ONS formed was calculated after 1 day, and the diameters of neurospheres were measured after an additional 7 days using phase-contrast photomicrographs. Cell aggregates were classified as neurospheres if they were spherical, optically dense, and had a minimum diameter of 100 μm. Photomicrographs were captured using a Zeiss Axiovert 25 microscope, and sphere diameters were quantified using ImageJ software.

Immunofluorescence

ONS and differentiated ONS after 7 days were seeded onto Matrigel-coated glass coverslips and cultured overnight. The next day, the spheres were fixed with 4% paraformaldehyde for 15 min at room temperature. Fixed cells were rinsed twice with phosphate-buffered saline (PBS) and blocked with a PBS solution containing 5% bovine serum albumin (BSA) and 0.2% Triton X-100 for 1 h at room temperature. Primary antibodies, diluted in a buffer containing 1% BSA, were incubated with the cells overnight at 4 °C. The next day, secondary antibodies were incubated for 1 h at room temperature. Details regarding primary and secondary antibodies used for immunofluorescence staining can be found in Additional file 1: Table S1. Images of stained cells were captured using a laser scanning confocal microscope (Zeiss LSM 710, Germany) and processed with ImageJ software. In ImageJ, the cell area was demarcated by a 25 μm square region of interest (ROI), and five random ROIs were measured to ascertain the positive area within the OE. A minimum of five fields per coverslip were randomly selected, with the counting spanning three coverslips for each group.

Flow cytometry

ONS and 7-day differentiated ONS were dissociated with 200 μl of Accutase at 37 °C for 2 min, followed by gentle pipetting to obtain single-cell suspensions. The single-cell suspensions were fixed and stained using BD Cytofix (BD Biosciences, Franklin Lakes, NJ, USA) as per the manufacturer's instructions. Specific antibodies were used to identify cells in different experimental groups, which were then quantified using an Attune NxT Flow Cytometer (Thermo Fisher Scientific, Waltham, MA, USA).

Quantitative real-time PCR analysis

Total RNA was extracted using TRIzol (Life Technologies), and cDNA synthesis was performed using the High-Capacity cDNA Reverse Transcription Kit (Applied Biosystems) according to the manufacturer's instructions. qRT-PCR was performed using the Fast SYBR Green Master Mix (Applied Biosystems) on a StepOnePlus™ System (Applied Biosystems). Primer sequences specific to ONS- and OSN-associated genes are listed in Table S2. For normalization, gene expression levels were referenced to GAPDH.

Western blot analysis

Cells were lysed using ice-cold RIPA buffer (0.5 M Tris–HCl, 10 mM EDTA, 1.5 M NaCl, 10% NP-40, 2.5% deoxycholic acid, pH 7.4) enriched with a protease inhibitor cocktail (Roche, USA). Protein quantification was conducted using the BCA assay kit (TransGen Biotech, Beijing, China). Equal protein quantities (40 μg) were separated on a 10% SDS-PAGE. Proteins were transferred onto nitrocellulose membranes (PALL, USA) using a transfer buffer (12 mM Tris base, 96 mM glycine, pH 8.3, and 20% methanol). The membranes were blocked for 2 h in TBST buffer containing 5% BSA. Primary antibodies (details in Additional file 1: Table S1) were incubated with the membranes overnight at 4 °C. After three washes with TBST, the membranes were incubated with HRP-conjugated secondary antibodies for 1 h at room temperature. Protein bands were visualized using ECL reagents (Bio-Rad Laboratories, Hercules, CA, USA) and analyzed using ImageLab software (Bio-Rad).

Nuclear fraction isolation from cells

Nuclear fractions from 7-day differentiated ONS were isolated as previously described [18]. Cells were collected and briefly sonicated for 5 s using a Misonix sonicator XL2020 (Misonix, Inc., USA). The samples were then centrifuged at 8000×g for 15 min at 4 °C, and the resulting pellet was collected as the nuclear fraction.

Determination of neurotrophic factors in supernatants

Culture media from ONS and 7-day differentiated ONS were collected and centrifuged at 13,000×g for 15 min to remove cell debris. Neurotrophic factor levels in the supernatants were quantified using Luminex X-MAP technology with the Human Premixed Multi-Analyte kit (R&D Systems, Wiesbaden, Germany).

Mouse model of hyposmia and ONS treatment

Four-week-old male NOD/SCID mice (18–20 g) were obtained from the National Laboratory Animal Center, Taiwan. Male mice were selected to minimize hormonal variability, which could otherwise affect the consistency of the results [19]. Five animals were housed per cage in individually ventilated cages (IVCs). The animal vivarium was a specific pathogen-free (SPF) facility with temperature and humidity control (21 ± 3 °C, 50 ± 10%). Animals were maintained under a reversed light–dark cycle (lights off 09:00 AM–09:00 PM). All experimental procedures complied with European ethical regulations (Directive 2010/63/EU) and were approved by the Institutional Animal Care and Use Committee (IACUC) of Kaohsiung Veterans General Hospital, Taiwan (Ref. 2019-2022-A038). This study was conducted and reported in accordance with the ARRIVE guidelines 2.0 [20].

For cell transplantation, neurospheres were dissociated into single cells at a 1:3 split ratio. Two portions were cryopreserved in liquid nitrogen, each containing the number of cells required for two injections, while one portion was cultured and stored for future use. Prior to injection, cells were thawed, resuspended in PBS, and cell viability was assessed. Approximately 5×10^6 viable cells were injected in 40 µl of PBS. Cell viability and injection details are provided in Table 2.

A schematic of the experimental design is shown in Fig. 5A. Olfactory nerve degeneration was induced by intraperitoneal injection of methimazole (MI) at a dose of 75 mg/kg (#301507, Sigma), administered weekly for 2 weeks, as previously described [21, 22]. After MI treatment, mice were randomly assigned to one of three groups (n = 5 per group): (1) saline (vehicle control), (2) DNS-ONS, or (3) CRS-ONS. Treatments began 2 weeks post-MI injection. DNS-ONS or CRS-ONS was administered intranasally (i.n.) to anesthetized mice (using ketamine, 80 mg/kg, and xylazine, 10 mg/kg). Each mouse received 20 µl of treatment in one nostril, followed by a 3–5 min absorption period before administering 20 µl to the other nostril, once a week for 4 weeks. Following treatment, mice were euthanized via intraperitoneal injection of ketamine (200 mg/kg) and xylazine (20 mg/kg). Olfactory epithelium tissues from all 20 mice were collected for subsequent analysis.

Biodistribution of PKH26-labelled DNS-ONS

PKH26 dye (PKH26GL, Sigma-Aldrich Co.) was diluted to a final concentration of 15 µM in 100 µL of diluent C. Either 5×10^6 cells or PBS (as control) were incubated with the dye at room temperature for 15 min. Following incubation, the cells were washed with PBS and centrifuged at 300 × g for 5 min. The resulting pellet was resuspended in 40 µL of PBS. These PKH26-labelled cells or PKH26-PBS control were administered intranasally to MI-treated mice 24 h before tissue harvesting. Imaging was performed using the IVIS Spectrum (Xenogen, Perkin Elmer) with excitation and emission wavelengths set to 570 nm and 595 nm, respectively. Data analysis was conducted using Living Image Software for IVIS.

Behavioral tests

To assess olfactory function, the food-finding test was employed. Mice were evaluated weekly for 3 weeks prior to MI injection and weekly post-injection until euthanasia. For validation of the hyposmia mouse model, mice were food-deprived for 48 h before being placed in a T-maze. A cheese pellet was hidden beneath sawdust in one of the two arms of the maze, with its location randomized for each trial. The time taken for the mice to locate the food was recorded. Control mice

Table 2 Summary of donor characteristics, injection concentrations, and post-freeze viability for DNS-ONS and CRS-ONS

Donor category	Age (years)	Gender	1st Injection (cells/mice)	2nd Injection (cells/mice)	3rd Injection (cells/mice)	4th Injection (cells/mice)	Cell concentration (pre-freeze, cells/ml)	Cell concentration (post-freeze, cells/ml)	Viability (%)
DNS-ONS	27	F	5.1×10^6	4.8×10^6	4.5×10^6	5.3×10^6	3.0×10^7	1.7×10^7	56
	38	M	4.5×10^6	4.5×10^6	5.7×10^6	5.0×10^6	4.4×10^7	3.6×10^7	82
	29	M	4.8×10^6	5.0×10^6	4.5×10^6	5.8×10^6	4.5×10^7	4.0×10^7	89
	31	F	4.8×10^6	5.1×10^6	5.3×10^6	5.5×10^6	4.1×10^7	4.1×10^7	99
	36	F	5.4×10^6	5.4×10^6	4.6×10^6	5.1×10^6	4.6×10^7	4.0×10^7	87
CRS-ONS	72	M	4.8×10^6	5.0×10^6	4.5×10^6	5.0×10^6	4.2×10^7	4.1×10^7	98
	61	M	4.5×10^6	4.7×10^6	5.6×10^6	5.0×10^6	6.6×10^7	4.8×10^7	73
	55	F	5.0×10^6	5.6×10^6	5.0×10^6	5.6×10^6	6.6×10^7	4.2×10^7	63
	49	M	5.6×10^6	4.6×10^6	5.0×10^6	5.6×10^6	9.6×10^7	5.2×10^7	54
	64	M	5.3×10^6	5.5×10^6	5.6×10^6	4.7×10^6	4.5×10^7	4.3×10^7	90

typically found the cheese within 40 s, whereas MI-treated mice consistently failed to locate it within the 3-min timeframe.

Histological and immunohistochemical examination

After perfusion with saline and 4% paraformaldehyde, the head samples were fixed in 4% paraformaldehyde overnight at 4 °C. The samples were then decalcified using Decalcifier II (Leica Biosystems) for 2 days. Subsequently, the samples were sequentially immersed in 10% sucrose for 1 day and 20% sucrose the following day, before being embedded in paraffin. Sections, 10 μm-thick, were stained with hematoxylin and eosin (H&E) to evaluate the OE thickness. Immunohistochemistry was performed using markers specified in Table S1. Images were captured using a Zeiss fluorescence microscope.

Statistical analysis

Statistical analyses were performed on data from animal studies and cellular experiments, presented as the mean ± standard deviation (SD) from at least four independent trials. Data were analyzed using GraphPad Prism 9 (GraphPad Software, La Jolla, CA, USA). Comparisons involving three or more groups were evaluated using one-way or two-way ANOVA, followed by Tukey's post hoc test. A P value of less than 0.05 was considered statistically significant.

Results

Neurosphere generation from DNS and CRS patient olfactory epithelium

The long-term genetic stability of human OE cell cultures is influenced by factors such as age, sex, donor source, and in vitro manipulation, all of which impact their potential clinical applications [23]. Although protocols for optimizing sphere cultures from OE-derived cells are well-established, successfully generating spheres from all patient biopsies remains challenging. Biopsy specimens were collected from the lateral nasal septum, medial to the superior turbinate, of patients with deviated nasal septum (DNS) and chronic rhinosinusitis (CRS). Table 1 summarizes the details of the 54 specimens, comprising 29 from DNS patients and 25 from CRS patients. OE tissues were isolated, and the migrated cells were cultured on 24-well plates at a seeding density of 103 cells per well. After 1 day, the number of neurospheres formed was comparable between DNS-derived ONS (DNS-ONS) and CRS-derived ONS (CRS-ONS) (Fig. 1B). However, after 7 days in culture, DNS-ONS neurospheres exhibited significantly larger diameters than CRS-ONS neurospheres (Fig. 1C), indicating more robust growth in DNS-ONS. Further analyses revealed that DNS-ONS showed higher BrdU incorporation and Ki67 expression compared to CRS-ONS (Fig. 1D, E), suggesting increased proliferative activity and a greater capacity to enter the S-phase. RNA analysis demonstrated that both DNS-ONS and CRS-ONS expressed neural stemness markers (Nestin, Pax6, SOX1, and SOX2) at significantly higher levels than OE tissue (Fig. 1F). Notably, SOX2 mRNA levels were significantly lower in CRS-ONS than in DNS-ONS. Immunostaining confirmed these findings, highlighting distinct Nestin and PAX6 expression patterns within the ONS (Fig. 1F). Although CRS-ONS exhibited reduced proliferation compared to DNS-ONS, both types could be successfully isolated and expanded, demonstrating similar neural stem cell properties under the applied culture conditions.

OE-derived ONS express HBC and GBC markers

The OE's capacity for neurogenesis is due to HBC and GBC, characterized by self-renewal, multipotency, and quiescence [24]. We investigated HBC and GBC populations in ONS from DNS and CRS patients using immunostaining and real-time PCR. Immunostaining showed that ONS from both patient types were positive for p63 (HBC marker) and ASCL1 (GBC marker) (Fig. 2A). Real-time RT-PCR confirmed the mRNA expression of GBC (ASCL1, Ngn1) and HBC (p63, KRT14) markers in neurospheres compared to OE (Fig. 2B). Consistent with previous findings [25, 26], we observed that OE-derived neurospheres included heterogeneous populations of both HBC and GBC. Western blot analysis confirmed GBC and HBC marker expression in OE-derived neurospheres, while hiPSCs and hiPSC-derived neurospheres did not express these markers (Fig. 2C). SOX2 expression was detected in hiPSCs, hiPSC-NS, and ONS. Flow cytometry revealed higher percentages of p63- and ASCL1-positive cells in DNS-ONS (72.05 ± 5.96% and 59.31 ± 5.76%) compared to CRS-ONS (69.84 ± 8.46% and 60.81 ± 7.26%) (Fig. 2D), with no significant differences in ASCL1 and p63 expression among the groups. These findings suggest that ONS from DNS and CRS patients have the potential to develop into olfactory stem cells, marked by both GBC and HBC populations, which is not observed in hiPSC-NS.

Differentiation of olfactory neurospheres into sensory neurons

To assess the regenerative capacity of ONS in OE neurogenesis, neurospheres were dissociated into single-cell suspensions and incubated with OSN induction medium for 4 and 7 days. The morphology of ONS single cells at 4 and 7 days post-induction is shown in Fig. 3A. MAP2 immunocytochemistry was performed to assess the maturation and functionality of OSNs derived from DNS-ONS and CRS-ONS. As shown in Fig. 3B, cells

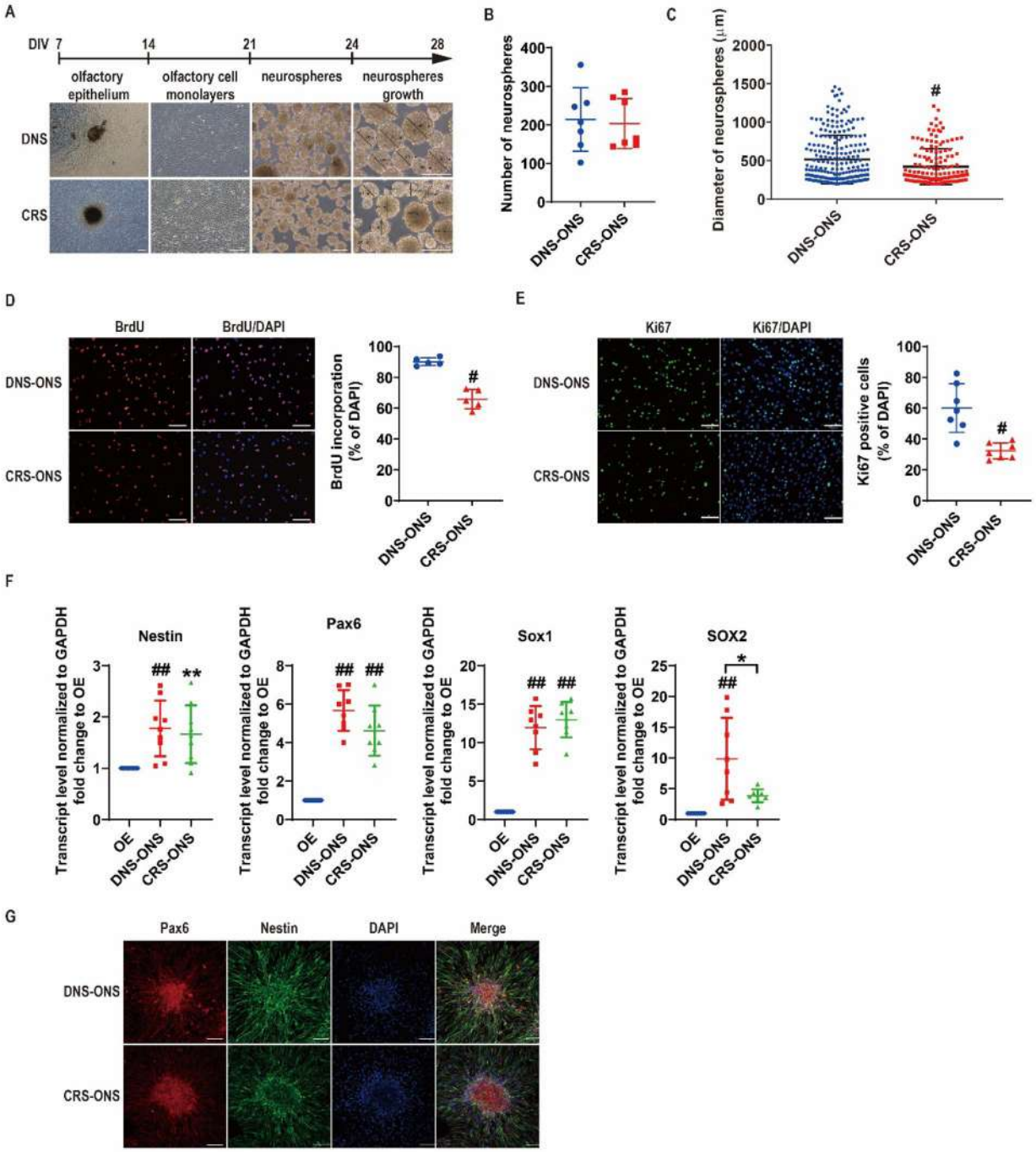


Fig. 1 Generation of olfactory epithelium-derived ONS from patients with DNS and CRS. **A** Phase-contrast images illustrating the generation process of ONS from the olfactory epithelium (OE) of DNS and CRS patients, with a schematic flow diagram. Scale bars, 200 μm. **B** Quantification of neurosphere numbers one day after seeding cells. **C** Comparison of ONS diameters (≥ 250 μm) measured at 28 days post-culture between DNS and CRS patients. **D** Proliferation assessment using BrdU staining. Nuclei were counterstained with DAPI (blue), and dividing cells were labeled with anti-BrdU antibody (red). The percentage of BrdU-positive cells is quantified. Scale bars, 100 μm. **E** Immunostaining of ONS from DNS and CRS patients for the proliferation marker Ki67. Scale bars, 100 μm. Percentage of Ki67-positive cells, calculated by the ratio of green-stained cells to blue DAPI-stained nuclei. **F** Relative gene expression of neural stem cell (NSC) markers Nestin, Pax6, SOX1 and SOX2 in DNS-ONS and CRS-ONS at day 21, compared to OE, measured by RT-PCR. **G** Immunostaining of DNS- and CRS-derived ONS for NSC markers Pax6 and Nestin. Scale bars, 100 μm. Statistical analysis was performed using one-way ANOVA with Tukey's post-hoc test. Data values are represented as mean ± standard deviation. #$P < 0.01$ comparing DNS-ONS to CRS-ONS; **$P < 0.05$, ##$P < 0.01$ comparing OE to ONS (n = 7 per group)

derived from both DNS-ONS and CRS-ONS expressed MAP2, a marker of mature neurons. Differentiated cells from DNS-ONS exhibited a more organized cytoskeletal structure, characterized by microtubules extending along actin filaments, compared to the less organized structure observed in CRS-ONS-derived cells. This suggests that DNS-ONS have a greater capacity for neuronal differentiation and cytoskeletal organization, indicative of enhanced maturation and functionality compared to CRS-ONS-derived neurons. Gene expression of olfactory sensory neuronal proteins in DNS- and CRS-ONS-derived cells was assessed on days 4 and 7 using real-time PCR. The levels of olfactory marker protein (OMP) and adenylyl cyclase 3 (AC3) increased over time during OSN differentiation. Notably, DNS-ONS differentiated cells exhibited higher OMP and AC3 expression than CRS-ONS cells (Fig. 3C). Western blot analysis confirmed that DNS-ONS differentiated cells had higher levels of OMP, Golf, and AC3 than CRS-ONS cells on day 7 post-induction (Fig. 3D). Flow cytometry revealed higher percentages of AC3, OMP, and Golf expression in DNS-ONS differentiated cells (77.17 ± 10.87%, 89.18 ± 2.16%, 43.67 ± 5.32%) compared to CRS-ONS cells (61.61 ± 9.98%, 81.42 ± 5.80%, 31.23 ± 5.67%) (Fig. 3E). These results demonstrate that ONS from DNS and CRS patients can differentiate into OSNs, with DNS-ONS achieving more complete maturation compared to CRS-ONS.

Olfactory neuron maturation deficits in CRS patients

Immature olfactory neurons express growth-associated protein-43 (GAP-43) and TrkB [27, 28]. OMP expression is localized in the nucleus of mature neurons, while immature neurons show reduced OMP levels predominantly in the cytoplasm [27]. We analyzed GAP-43, TrkB, and OMP localization to validate whether CRS-derived ONS exhibit defects in OSN maturation.

CRS-ONS-derived OSNs exhibited higher expressions of GAP-43 and TrkB compared to DNS-ONS-derived OSNs (Fig. 4A). Immunostaining and nuclear fraction analyses showed AC3 and OMP in the nucleus of DNS-OSNs but in the cytosol of CRS-OSNs and undifferentiated cells (Fig. 4B, C). Both BDNF and GDNF, known to be released from the OE, enhance OSN survival [29–31]. Real-time PCR showed a significant increase in BDNF and GDNF levels during DNS-OSN differentiation, with a slight increase in CRS-OSN differentiation. Moreover, on the 7th day following OSN induction, DNS-ONS differentiated cells showed greater levels of BDNF and GDNF compared to CRS-ONS differentiated cells (Fig. 4D). Western blot showed higher BDNF and GDNF levels in DNS-ONS than in CRS-ONS differentiated cells (Fig. 4E, F). BDNF secretion was higher in DNS-ONS than in CRS-ONS differentiated cells. While DNS-ONS showed increased GDNF secretion compared to undifferentiated cells, CRS-ONS did not show a significant difference (Fig. 4G).

Efficacy of DNS and CRS-derived ONS in hyposmic mice

We used a methimazole (MI)-induced NOD/SCID mouse model [21] to investigate the impact of DNS- and CRS-derived olfactory neurospheres (ONS) on olfactory neuroepithelium. Mice received intranasal administrations of DNS- or CRS-ONS for 4 weeks (Fig. 5A). H&E staining revealed that MI-induced mice had atrophied olfactory neurons and disrupted neuronal arrangement. However, after DNS- and CRS-ONS administration, there was a remarkable recovery in the structural integrity of these neurons (Fig. 5B). Immunofluorescence studies showed that OMP expression, compromised in MI-induced mice, was restored in DNS- and CRS-ONS treated mice. AC3-positive cells, scarcely detectable in MI-induced mice, were mainly located in the apical OE regions in DNS- and CRS-ONS treated groups (Fig. 5C). Protein levels of AC3 and OMP were also higher in DNS-ONS treated mice (Fig. 5D). This was mirrored at the protein level for both AC3 and OMP in the OE, especially with DNS-OSC treatment in MI-induced mice (Fig. 5D). Before MI induction, mice found the food pellet in 20 ± 9 s. After a second MI induction, this increased to 168 ± 26 s. Following 8 weeks of DNS- or CRS-ONS treatment, the time decreased to 123 ± 30 and 127 ± 19 s, respectively. By the 9th week, DNS-treated mice found the food in 28 ± 12 s, while CRS-ONS treated mice took 60 ± 19 s (Fig. 5E). Fluorescence imaging confirmed a detectable signal in the brain 24 h after the final intraperitoneal injection of PKH-26-labeled DNS-ONS or PKH-26-labeled PBS (Fig. 5F). Additionally, we performed

(See figure on next page.)

Fig. 2 Markers for HBC and GBC in ONS derived from human OE. **A** Immunostaining images showing ONS derived from DNS and CRS patients, stained for HBC marker p63 and GBC marker ASCL1. Scale bars, 20 µm. **B** Relative gene expression of HBC markers (p63 and KRT14) and GBC markers (ASCL1 and Ngn1) in DNS- and CRS-ONS at day 21, compared to OE, quantified by RT-PCR. **C** Western blot analysis of HBC markers (p63 and ICAM-1) and GBC markers (ASCL1 and SOX-2) in hiPSCs, hiPSC-neurospheres, DNS-ONS, and CRS-ONS. **D** Flow cytometry analysis of intracellular levels of p63 and ASCL1 in DNS- and CRS-ONS. Statistical analyses were performed using two-way ANOVA with Tukey's post-hoc test. Data are presented as mean ± standard deviation. $^{**}P < 0.05$ and $^{\#\#}P < 0.01$ comparing OE to ONS (n = 5 per group)

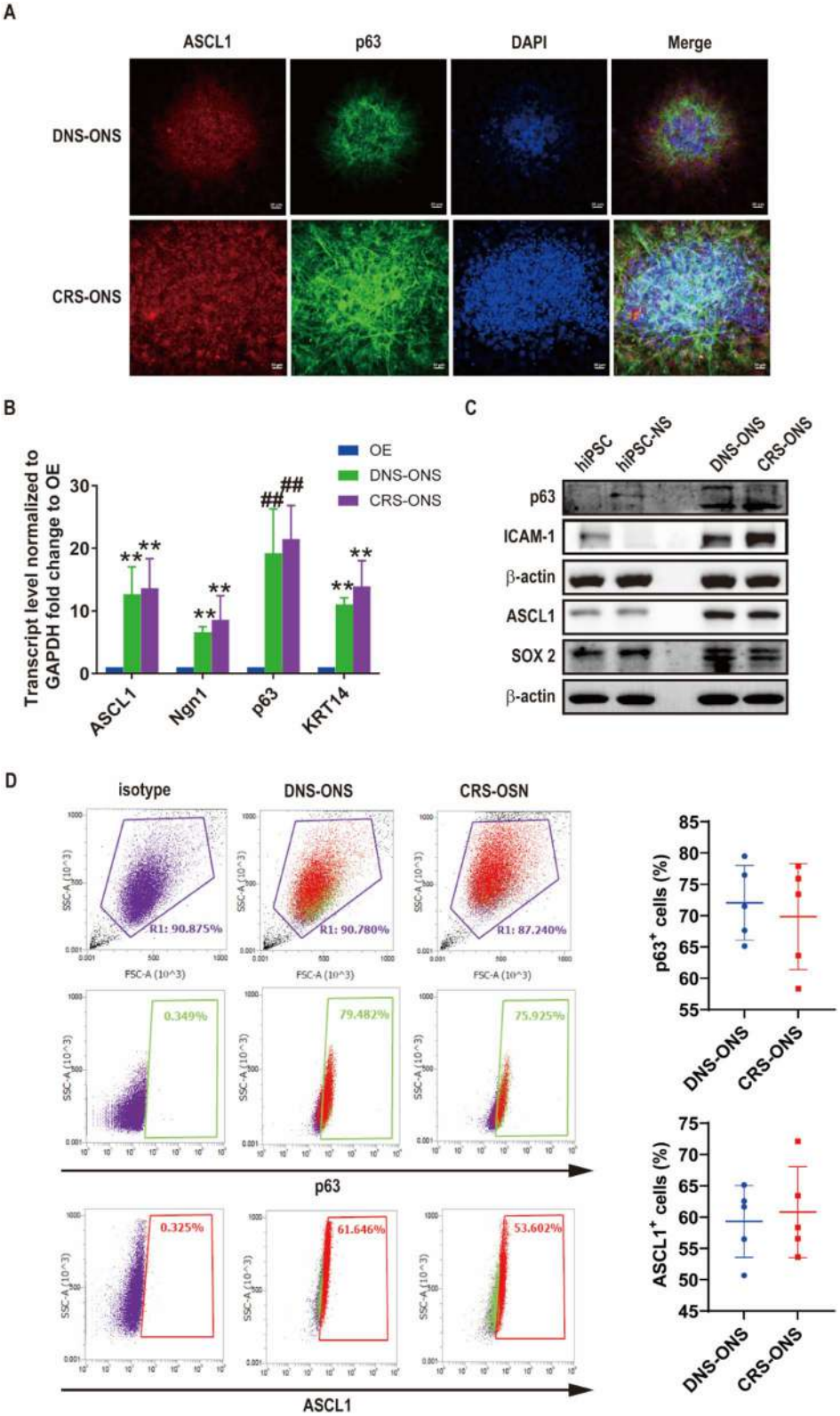


Fig. 2 (See legend on previous page.)

double immunofluorescence staining on sections of the mouse olfactory epithelium using a human-specific mitochondria antibody (hMit) and ADCY3, a marker for olfactory sensory neurons reactive across human, mouse, and rat species. This analysis distinguished endogenous cells from transplanted human cells. As shown in Fig. 5G, hMit-positive cells were identified in the olfactory epithelium, confirming the presence of transplanted human cells. These results demonstrate that the efficacy of ONS in treating hyposmia depends on its source. DNS-derived ONS consistently exhibited superior restorative effects in terms of protein expression, neuronal recovery, and functional outcomes compared to CRS-derived ONS.

DNS-ONS reduces cellular senescence, inhibits apoptosis, and enhances proliferation in MI-induced mice

To investigate the potential of ONS to ameliorate MI-induced olfactory dysfunction by enhancing the regenerative abilities of the OE through decreased inflammation, cellular senescence, and apoptosis while promoting proliferation. Previous studies have shown a link between increased neuroinflammation, cellular senescence, and reduced viability of hippocampal neural stem cells [32]. MI-induced mice showed increased protein levels of senescence markers (γH2AX, p16, p21, HMGB1) and SASP factors (IL-1β, IL-6) in OE tissue lysates. DNS-ONS treatment effectively reduced these levels, while CRS-ONS treatment only reduced γH2AX and IL-6 (Fig. 6A, B). MI-treated mice had elevated HMGB1-positive cells, significantly reduced by DNS-ONS, but only modestly by CRS-ONS (Fig. 6C). MI-induced mice showed increased TUNEL-positive cells (Fig. 6D) and cleaved caspase-3/caspase-3 ratio (Fig. 6E). DNS-ONS treatment reduced these levels significantly, while CRS-ONS had a modest effect. DNS-ONS treatment notably increased Ki67-positive cells, indicating enhanced proliferation, compared to controls and CRS-ONS (Fig. 6F). Ki67 protein levels were also elevated with DNS-ONS treatment (Fig. 6G). Our results suggest that DNS-derived ONS ameliorates olfactory dysfunction by reducing cellular senescence and apoptosis and enhancing cellular proliferation in the OE of MI-induced mice.

Discussion

Olfactory stem cell transplantation has been shown to promote neuronal regeneration in animal models of neurological disorders such as spinal cord injury, stroke, and Parkinson's disease [11, 33, 34]. A recent study demonstrated that treatment with murine adult olfactory stem cells rescues hyposmia in a mouse model [35]. However, a significant gap exists between stem cell research and its clinical application for treating olfactory dysfunction using autologous olfactory stem cells, especially considering patient-specific characteristics that may affect therapeutic efficacy. This study highlights the critical influence of cellular origin on the neurogenic potential of olfactory neurospheres.

In our culture system, ONS derived from the OE of patients contain both GBCs and HBCs, providing a distinct advantage as olfactory-specific stem cells compared to iPSC-derived neurospheres. While both DNS- and CRS-derived ONS exhibit neural stem cell properties (Nestin, SOX2, SOX1, and Pax6) and can be expanded efficiently, DNS-ONS demonstrated superior proliferative potential compared to CRS-ONS. Notably, SOX2 mRNA levels were significantly lower in CRS-ONS than in DNS-ONS. Given SOX2's critical role in neural stem cell self-renewal, proliferation, and differentiation [36], its reduced expression in CRS-ONS likely explains their diminished proliferation rates, differentiation capacity, and neurotrophic factor production.

Differentiated cells from CRS-ONS also showed impaired maturation of olfactory sensory neurons (OSNs) and lower levels of neurotrophic factors such as BDNF and GDNF compared to DNS-ONS. Consequently, DNS-ONS treatment more effectively restored olfactory epithelium (OE) integrity and functionality in methimazole (MI)-induced hyposmic mice compared to CRS-ONS. This can be attributed to DNS-ONS's ability to mitigate cellular senescence, reduce apoptosis, and promote cellular proliferation within the OE.

The OE has the capacity to produce multipotent neurospheres in vitro, which can differentiate into neurons and glia while maintaining the ability to self-renew [33]. In this study, OE-derived neurospheres expressed neural stem cell markers (SOX1, Pax6), GBC markers (ASCL1,

(See figure on next page.)

Fig. 3 ONS differentiation into OSNs. **A** Phase-contrast images depicting the differentiation of OSNs from DNS- and CRS-ONS, supplemented by a schematic flow diagram. Scale bars, 100 µm. **B** Immunostaining images of OSNs from DNS and CRS patients at day 7 post-OSN induction, stained for MAP2 and DAPI. Scale bars, 20 µm. **C** Relative gene expression levels of OSN markers (OMP and AC3) in DNS- and CRS-ONS subjected to OSN induction medium at days 4 and 7, compared to undifferentiated cells, measured using RT-PCR. **D** Western blot analyses showing expression patterns of OSN markers (OMP, Golf, and AC3) in DNS- and CRS-ONS, as well as DNS- and CRS-OSNs at day 7 post-OSN induction. **E** Flow cytometric evaluation of OSN markers—OMP, Golf, and AC3—in DNS- and CRS-derived OSNs. Statistical evaluations were performed using two-way ANOVA for part (**B**), and one-way ANOVA for parts (**D**, **E**), followed by Tukey's post-hoc test. Data are presented as mean ± standard deviation. *$P < 0.05$ and #$P < 0.01$ for differentiating ONS from OSNs groups; **$P < 0.05$ and ##$P < 0.01$ comparing DNS- to CRS-OSNs (n = 5 per group)

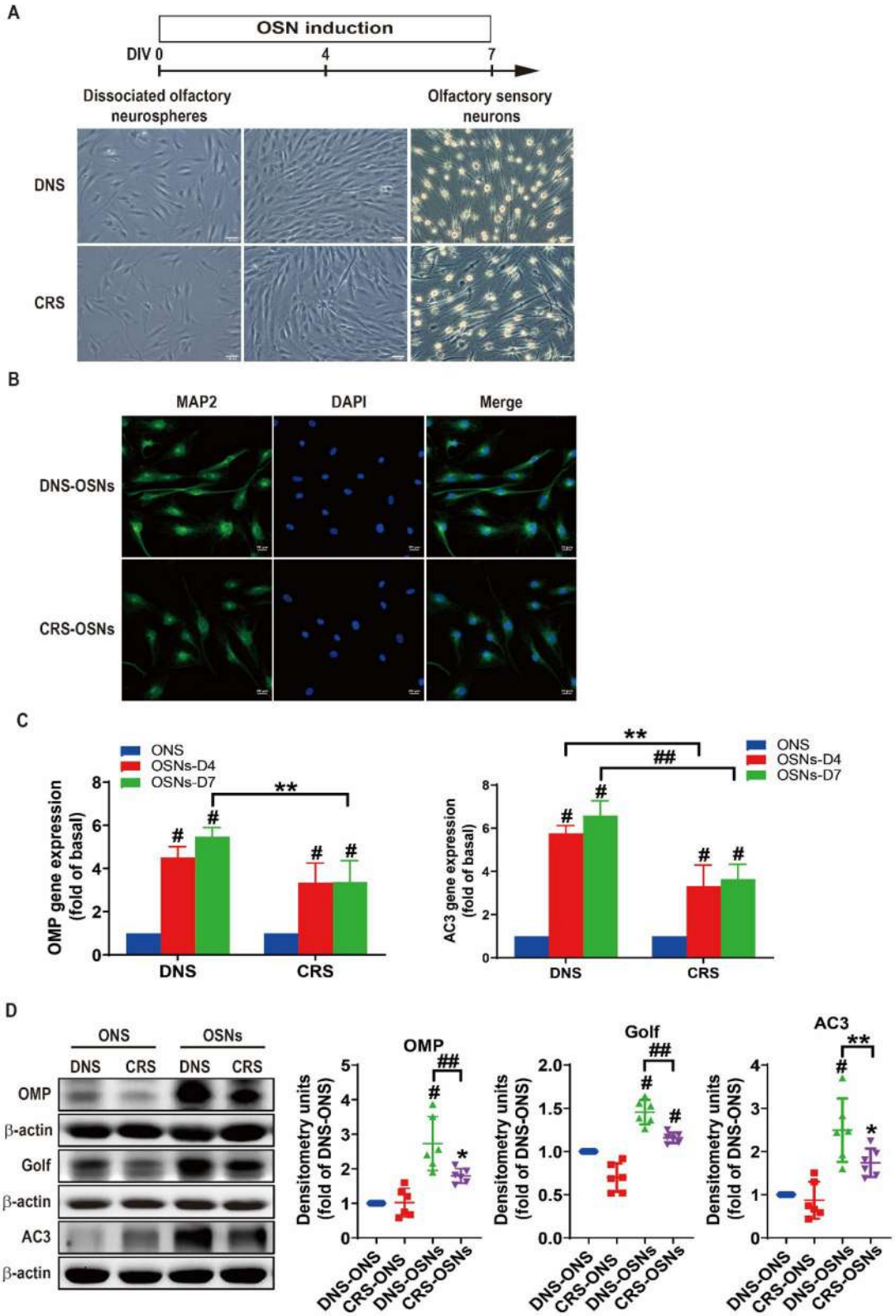


Fig. 3 (See legend on previous page.)

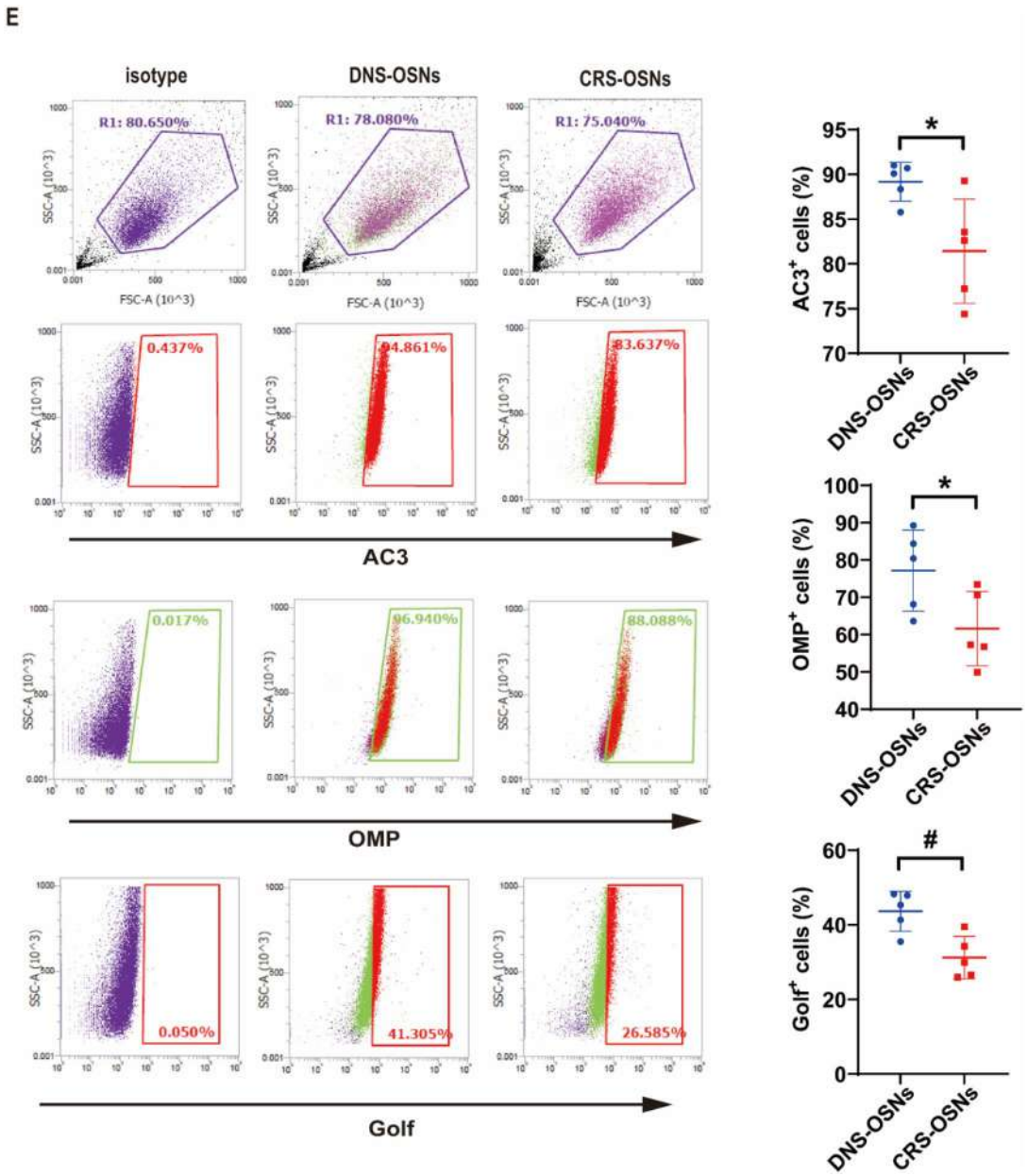


Fig. 3 continued

Ngn1), and HBC markers (p63, KRT14). Notably, iPSC-derived neurospheres lacked ASCL1 and p63 expression, indicating that OE-derived ONS more closely resemble olfactory-specific stem cells. CRS-related impairments in stem cell functionality, as demonstrated by fewer proliferating cells and immature differentiation of OSNs in CRS patients [16], align with our findings of reduced proliferative and regenerative capabilities in CRS-ONS compared to DNS-ONS. Similarly, ONS derived from patients with nasal polyps and Alzheimer's disease demonstrate a restricted capacity for both self-renewal and sphere-formation [37, 38]. Our observations support this, as CRS-ONS compared to DNS-ONS showed reduced proliferative capabilities and promoted immature differentiation of OSNs. This was evident from the decreased expression of Ki67, OMP, AC3, and Golf, and increased expression of GAP43 and TrkB in a differentiation medium.

Olfactory stem cells secrete neurotrophins (e.g., BDNF, GDNF, NGF, NT-3, NT-4, and CNTF) that promote

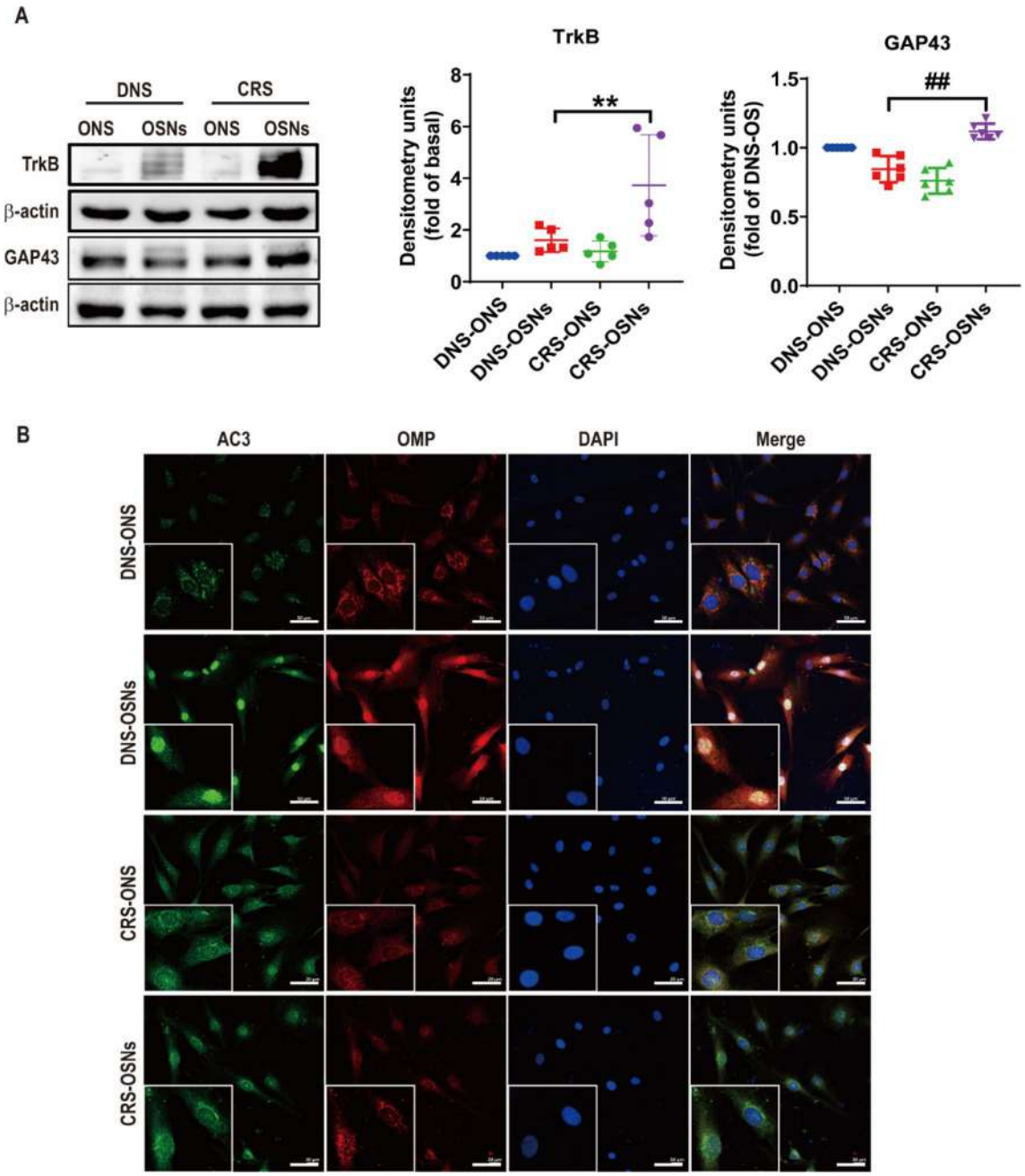


Fig. 4 Impaired differentiation of CRS-ONS into OSNs. **A** Western blot analysis of immature OSN markers TrkB and GAP43 in DNS- and CRS-ONS, and DNS- and CRS-OSNs at day 7 post-OSN induction. **B** Immunostaining images of ONS and OSNs from DNS and CRS patients at day 7, stained for OMP and AC3. Scale bars, 20 µm. **C** Western blot analysis of nuclear fractions from DNS- and CRS-ONS and OSNs collected at day 7 post-induction, with Anti-LaminA as a control. **D** RT-PCR quantification of relative gene expression levels of BDNF and GDNF in DNS- and CRS-ONS exposed to OSN induction medium on days 4 and 7, compared to undifferentiated cells. **E** Western blot analysis of BDNF and GDNF expression in DNS- and CRS-ONS and DNS- and CRS-OSNs at day 7 post-induction. **F** Luminex assays quantifying BDNF and GDNF levels in the culture supernatants of DNS- and CRS-ONS, untreated and after OSN induction medium treatment on day 7 (n = 11 per group). Statistical analyses used one-way ANOVA with Tukey's post-hoc test. Data are presented as mean ± standard deviation. *$P < 0.05$ and #$P < 0.01$ differentiate ONS from OSNs groups; **$P < 0.05$ and ##$P < 0.01$ comparing DNS- to CRS-OSNs (n = 5 per group)

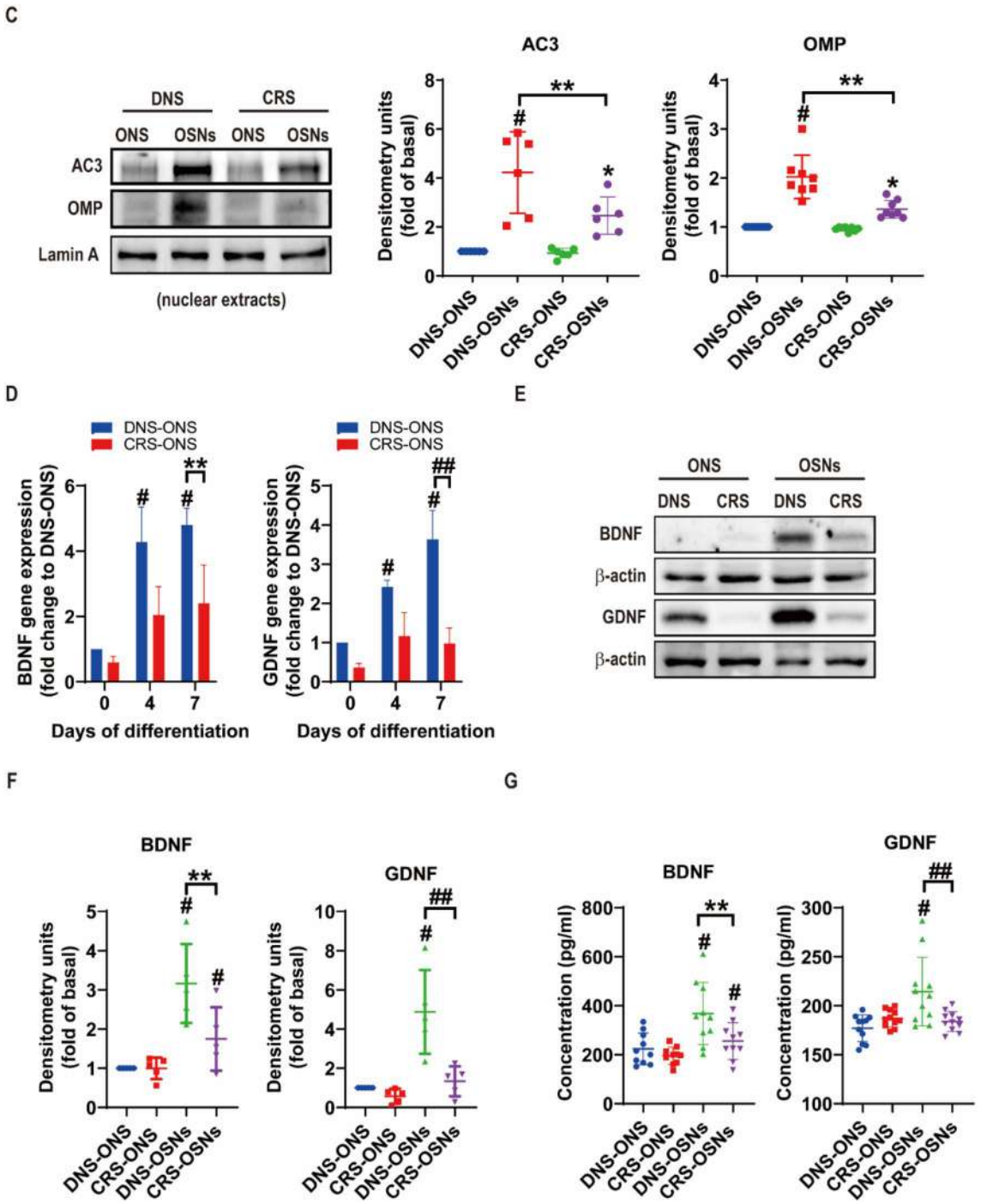


Fig. 4 continued

nerve regeneration [39]. However, persistent inflammation in CRS patients inhibits olfactory stem cells from fully supporting neuron maturation and HBC differentiation [16]. In this study, CRS-ONS secreted significantly lower levels of BDNF and GDNF than DNS-ONS, potentially contributing to their reduced therapeutic efficacy.

Prior attempts have been made to transplant stem cells into the olfactory neuroepithelium. Human cord blood CD133-positive mesenchymal stem cells (MSCs) and adipose tissue-derived MSCs intravenously promote regeneration in the damaged olfactory region [40–42]. Bone marrow-MSCs, introduced

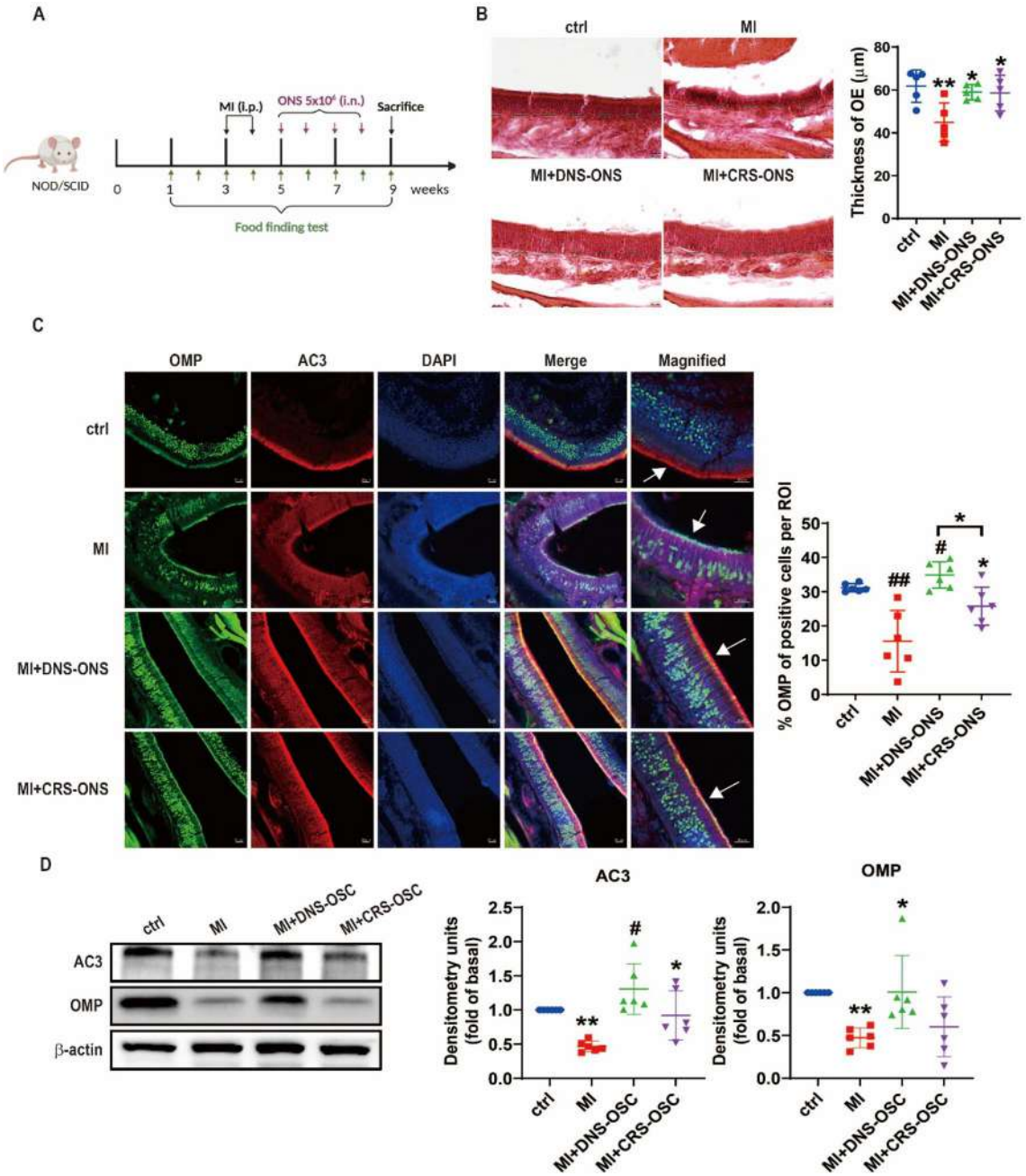


Fig. 5 Impact of DNS- and CRS-ONS on olfactory function recovery in a MI-induced hyposmic mouse model. **A** Timeline and schematic of the MI-induced hyposmic mouse model, illustrating the treatment regimen with DNS- and CRS-ONS. **B** Hematoxylin and eosin-stained sections of the olfactory epithelium (OE) from experimental mice. The OE thickness was measured using ImageJ software. Scale bar, 20 μm. **C** Immunofluorescence images showing the expression of olfactory sensory neuron (OSN) markers OMP and AC3 in OE sections, with DAPI used for nuclear counterstaining. Quantitative analysis of OMP in OE sections was performed with three samples per group, and two images per sample. Scale bars: 20 μm. **D** Western blot analysis of AC3 and OMP protein levels in OE tissues. **E** Quantitative analysis of the time taken by mice to locate food in the food-finding test. **F** Representative IVIS images taken 24 h after intranasal administration of PKH-26-labelled PBS or DNS-ONS to mice. **G** Immunofluorescence images showing the expression of the human-specific mitochondrial antibody (hMit) and AC3 in OE sections, with DAPI used for nuclear counterstaining. Statistical analyses were performed using one-way ANOVA with Tukey's post-hoc test. Data are presented as mean ± standard deviation. *$P < 0.05$ and #$P < 0.01$ for comparisons between MI and either DNS- or CRS-ONS treatment groups; **$P < 0.05$ and ##$P < 0.01$ for comparisons between control and MI groups (n = 5 per group)

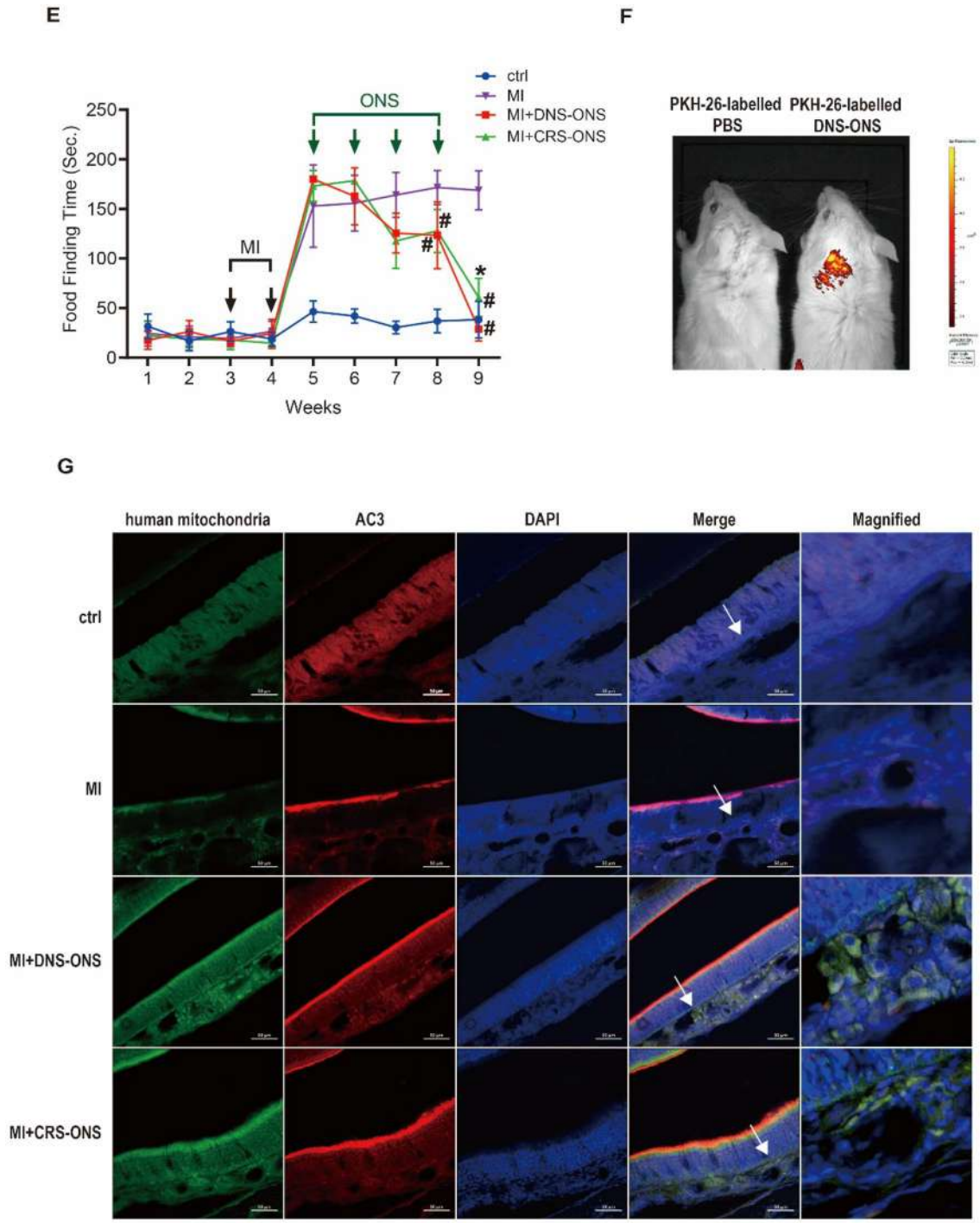


Fig. 5 continued

into irradiated mice, can engraft into the OE, differentiate into olfactory neuronal cells, and restore olfactory functions by expressing NGF and BDNF [43, 44]. Transplantation of neural stem cells (NSCs) into an anosmic mouse model enhanced OMP expression in the OE and recovered olfactory functionality [2].

While MSC and NSC transplantation is promising, procuring MSCs from bone and adipose tissue

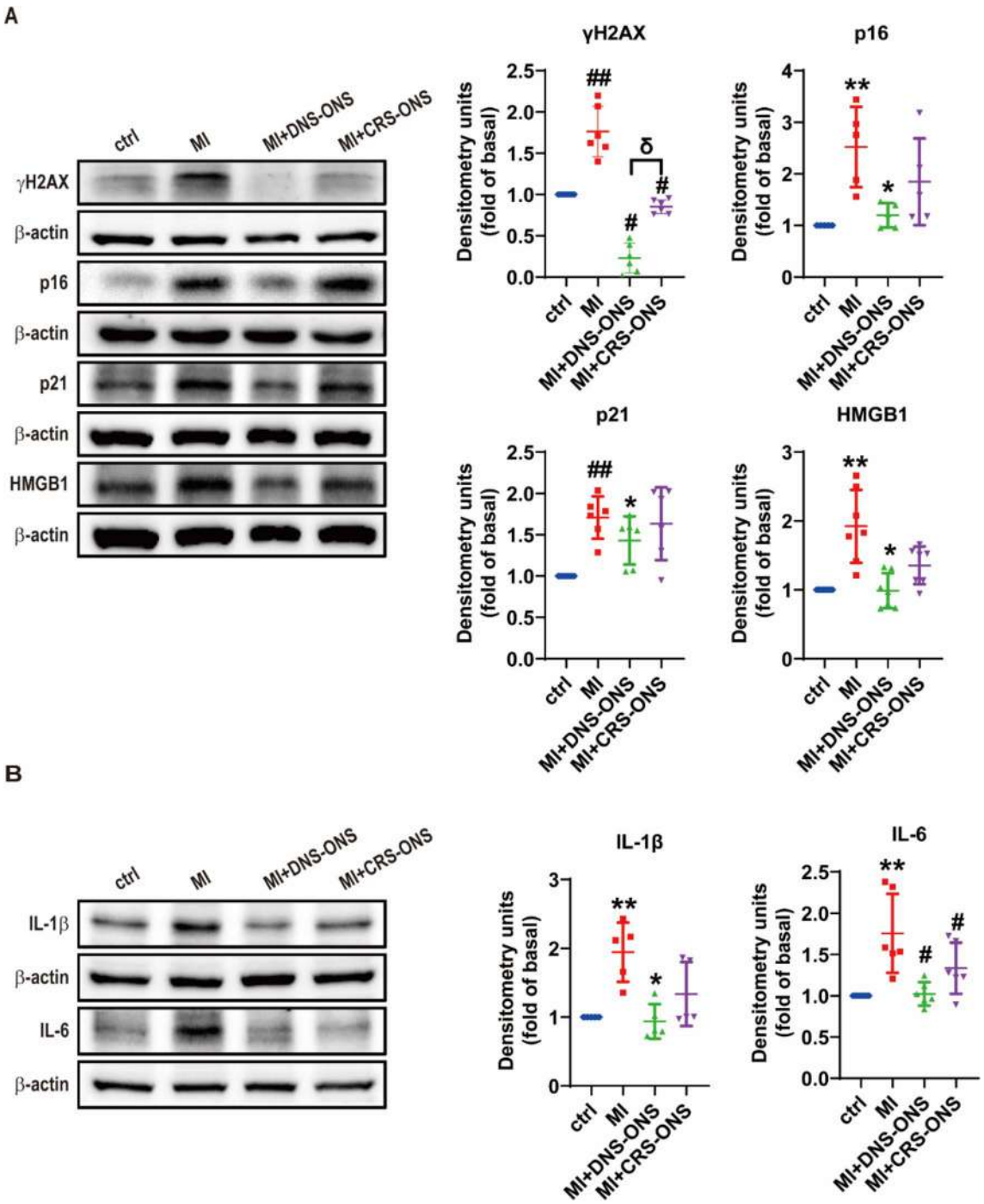


Fig. 6 Impact of DNS- and CRS-ONS on cellular senescence, apoptosis, and proliferation in the OE of MI-Induced Mice. **A** Western blot analysis of cellular senescence markers in OE tissues, including γH2AX, p16, p21, and HMGB1. **B** Western blot analysis of pro-inflammatory cytokines IL-1β and IL-6 in OE tissues. **C** Immunofluorescence images showing HMGB1 and OMP expression in OE sections, with nuclei counterstained using DAPI. Scale bars, 20 μm. **D** Immunofluorescence images of TUNEL-positive cells in OE sections, indicating apoptosis, with nuclei counterstained using DAPI. Quantitative analysis of OMP in OE sections was performed with three samples per group, and two images per sample. Scale bars, 50 μm. **E** Western blot analysis of caspase-3 and cleaved caspase-3 levels in OE tissues. **F** Immunofluorescence images showing Ki67-positive cells in OE sections, indicating cell proliferation, with nuclei counterstained using DAPI. Scale bars, 20 μm. **G** Western blot analysis of Ki67 expression levels in OE tissues. Statistical analyses were performed using one-way ANOVA with Tukey's post-hoc test. Data are presented as mean ± standard deviation. *$P < 0.05$ and #$P < 0.01$ for comparisons between MI and either DNS- or CRS-ONS treatment groups; **$P < 0.05$ and ##$P < 0.01$ for comparisons between control and MI groups (n = 5 per group)

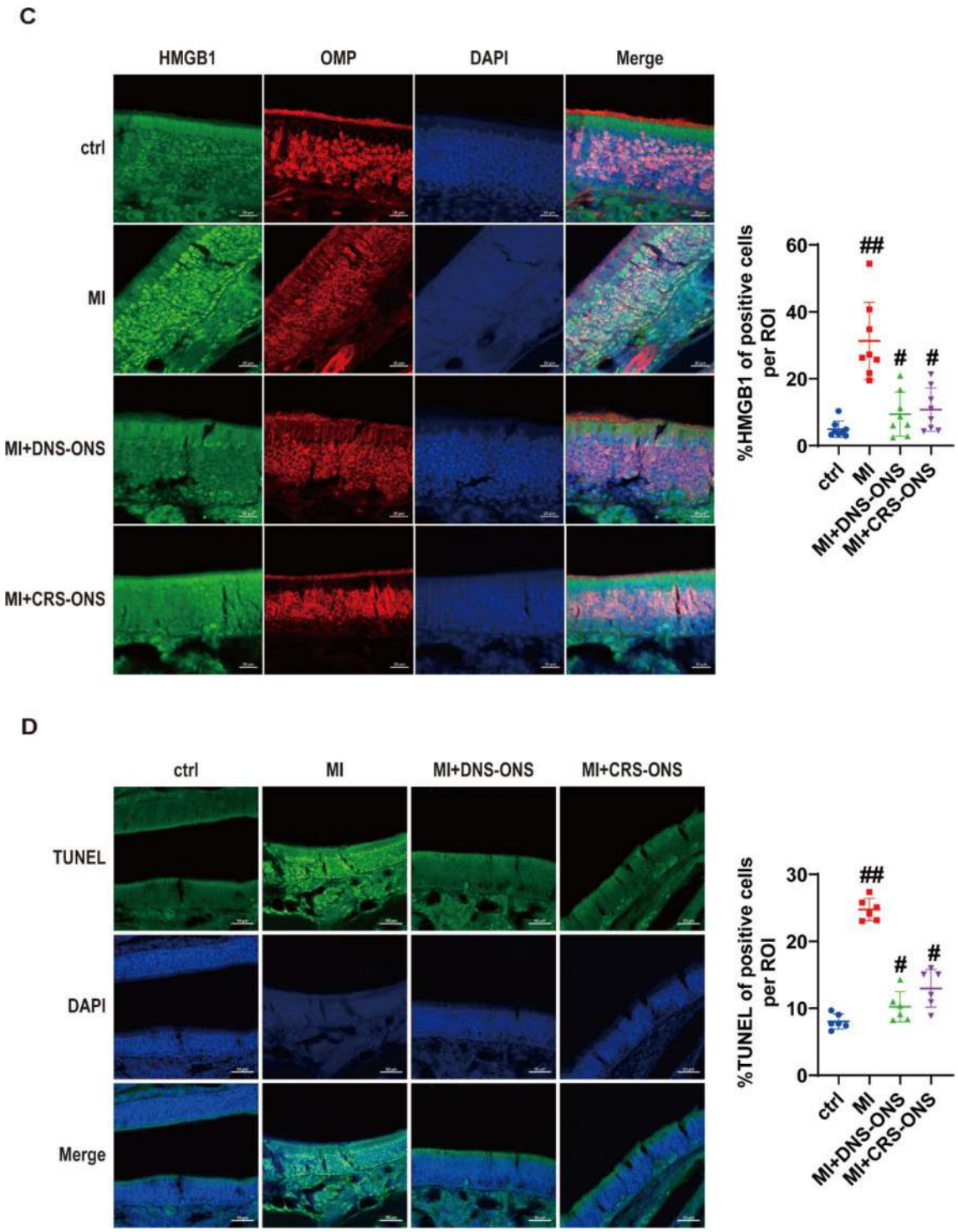


Fig. 6 continued

and NSCs from the brain is invasive. In contrast, OE stem cells can be conveniently harvested from living patients through endoscopically-guided biopsy, making them attractive for cell-based therapies [45]. MSCs originate from mesenchymal embryonic tissue (mesoderm) [46], whereas olfactory epithelial cells arise from the neural crest [47], which can differentiate into neuroectodermal derivatives more effectively than

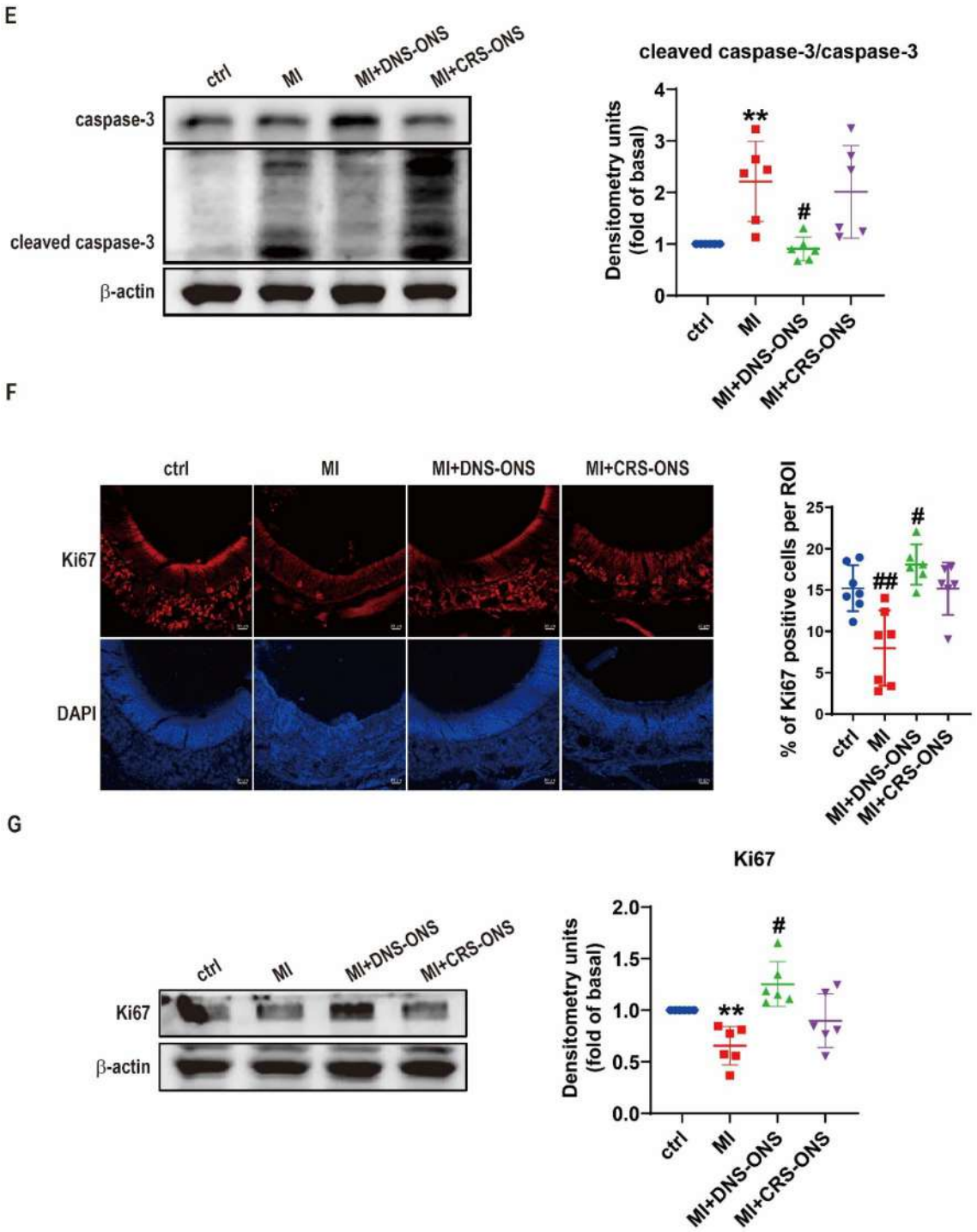


Fig. 6 continued

MSCs. OE-derived stem cells show promise for neurogenesis in conditions like Parkinson's disease [48] and spinal cord injury [49]. A recent study illustrated the therapeutic potential of murine olfactory stem cells in a mouse hyposmia model [35]. Our research demonstrates that human OE-derived ONS can effectively treat a methimazole-induced mouse hyposmia model. This treatment fostered the development of olfactory

neurons, indicated by elevated OMP and AC3 levels in the MI-damaged OE. Additionally, there was an enhancement in olfactory epithelial integrity and thickness, coupled with noticeable recovery at the behavioral level. DNS-derived ONS exhibited superior restorative efficacy compared to CRS-ONS. This aligns with our earlier in vitro study findings, suggesting that CRS-ONS's differentiation into immature OSNs and reduced BDNF and GDNF production might cause its diminished in vivo therapeutic efficacy compared to DNS-ONS.

Cellular senescence, characterized by a pro-inflammatory phenotype, hinders tissue regeneration and has been linked to a diminished structural response in the OE [50]. Mitigating apoptosis in OSNs is crucial for restoring both OE thickness and olfactory function [51]. Our study observed the generation of new cells in MI-damaged OE post-ONS treatment, evidenced by the surge in Ki67-positive cells in MI-induced mice following DNS-ONS treatment. We hypothesized that ONS treatment could combat cellular senescence and apoptosis while fostering cell generation. Supporting this, we detected heightened levels of markers for cell senescence—p16, p21, γH2AX, HMGB1, and pro-inflammatory cytokines IL-1β and IL-6—in the OE of MI-induced mice. These markers were notably diminished post-DNS-ONS treatment. Similarly, the prevalence of TUNEL-positive cells and the expression of caspase-3 were significantly lower in the DNS-ONS-treated groups than in the untreated MI-induced mice. In essence, ONS treatment bolsters the health of the OSNs in MI-damaged OE by mitigating cellular senescence and apoptosis while stimulating new cell generation. It is worth noting that while CRS-ONS treatment led to a reduction in cellular senescence, apoptosis, and proliferation in the MI-damaged OE, its effects were more subdued compared to DNS-ONS.

Our study showed that ONS derived from patients with DNS and CRS have varying abilities in proliferation and differentiation into OSNs in vitro, correlating with their therapeutic efficacy in the hyposmic mouse model. Notably, CRS-ONS demonstrated limited potential for self-renewal and differentiation into mature OSNs, highlighting potential hurdles for therapeutic applications. Understanding the quality of the stem cell source is crucial for its application in regenerative medicine, especially in autologous stem cell transplantation where a patient's disease history must be considered. Future research should identify specific factors within CRS-ONS that hinder proliferation and the differentiation and maturation of OSNs. Addressing these factors could pave the way for tailored therapeutic strategies to enhance olfactory function recovery.

Conclusions

Selecting appropriate stem cell sources is crucial for effectively treating olfactory dysfunctions. Among the sources studied, ONS derived from patients with a DNS demonstrate significantly greater potential in regenerating the olfactory epithelium and restoring olfactory function compared to those derived from CRS. The superior self-renewal capacity, enhanced production of neurotrophic factors, and greater efficacy in reducing cellular senescence and apoptosis position DNS-derived ONS as a more promising candidate for therapeutic applications in olfactory dysfunction.

Abbreviations

CRS	Chronic rhinosinusitis
DNS	Deviated nasal septum
OSNs	Olfactory sensory neurons
ONS	Olfactory neurospheres
OE	Olfactory epithelium
MI	Methimazole
OMP	Olfactory marker protein
ADCY3	Adenylyl cyclase 3

Supplementary Information

The online version contains supplementary material available at https://doi.org/10.1186/s13287-025-04270-0.

Additional file 1.

Additional file 2.

Additional file 3.

Additional file 4.

Acknowledgements

All authors thank the patients who donated their specimens for this study.

Author contributions

Study conception and design: RSJ, and PLC; acquisition of data: CWL,YHL, JJW, and JBL; analysis and interpretation of data: CWL, YHL, JJW, and JBL; drafting and revising of manuscript: RSJ, and PLC. All authors read and approved the fnal manuscript.

Funding

This work was supported by the Kaohsiung Veterans General Hospital (Grant Numbers VGHKS110-143); the Ministry of Science and Technology, Taiwan (Grant Numbers 109-2314-B-075A-002 -MY2, 109-2314-B-075B-009 -MY2); and the Yen Tjing Ling Medical Foundation (Grant Number CI-111-26).

Availability of data and materials

The datasets used during the current study are available from the corresponding authors on reasonable request.

Declarations

Ethics approval and consent to participate

All experimental protocols were conducted in compliance with European ethical regulations (Directive 2010/63/EU) and were approved by the Institutional Animal Care and Use Committee, Kaohsiung Veterans General Hospital, Taiwan, under the approval number 2019-2022-A038, dated 2018-12-24. The title of the approved project is *The Ability of Human Olfactory Stem Cells in Treating Anosmic Mice*. Protocols involving human olfactory epithelium samples were authorized by the Institutional Review Board (IRB) of Taichung Veterans General Hospital, Taiwan, under the approval number CF18350A, dated

2019-01-21. The title of the approved project is *The Ability of Human Olfactory Stem Cells in Treating Anosmic Mice*.

Competing interests
The authors declare that they have no competing interests.

Author details
[1]Department of Otolaryngology, Tungs' Taichung MetroHarbor Hospital, Taichung, Taiwan. [2]Department of Otolaryngology, Taichung Veterans General Hospital, Taichung, Taiwan. [3]Department of Nursing, Division of Basic Medical Sciences, and Chronic Diseases and Health Promotion Research Center, Chang Gung University of Science and Technology, Chiayi, Taiwan. [4]Department of Orthopaedic Surgery, Chang Gung Memorial Hospital, Chiayi, Taiwan. [5]Department of Safety Health and Environmental Engineering, Ming Chi University of Technology, New Taipei City, Taiwan. [6]Department of Otolaryngology, Head and Neck Surgery, Kaohsiung Veterans General Hospital, Kaohsiung, Taiwan. [7]School of Medicine, National Yang Ming Chiao Tung University, Taipei, Taiwan. [8]School of Medicine, Chung Shan Medical University, Taichung, Taiwan. [9]Department of Pathology and Laboratory Medicine, Kaohsiung Veterans General Hospital, Kaohsiung, Taiwan. [10]Graduate Institute of Clinical Medical Sciences, College of Medicine, Chang Gung University, Taoyuan, Taiwan. [11]Department of Medical Education and Research, Kaohsiung Veterans General Hospital, Kaohsiung 81362, Taiwan. [12]Department of Dental Technology, Shu-Zen Junior College of Medicine and Management, Kaohsiung, Taiwan.

Received: 12 August 2024 Accepted: 11 March 2025
Published online: 05 April 2025

References

1. Nordin S, Bramerson A. Complaints of olfactory disorders: epidemiology, assessment and clinical implications. Curr Opin Allergy Clin Immunol. 2008;8:10–5.
2. Lee CH, Jeon SW, Seo BS, Mo JH, Jeon EH, Choi AR, Kim JW. Transplantation of neural stem cells in anosmic mice. Clin Exp Otorhinolaryngol. 2010;3:84–90.
3. Choi R, Goldstein BJ. Olfactory epithelium: cells, clinical disorders, and insights from an adult stem cell niche. Laryngoscope Investig Otolaryngol. 2018;3:35–42.
4. Whitcroft KL, Hummel T. Olfactory dysfunction in COVID-19: diagnosis and management. JAMA. 2020;323:2512–4.
5. Scangas GA, Bleier BS. Anosmia: differential diagnosis, evaluation, and management. Am J Rhinol Allergy. 2017;31:3–7.
6. Peterson J, Lin B, Barrios-Camacho CM, Herrick DB, Holbrook EH, Jang W, et al. Activating a reserve neural stem cell population in vitro enables engraftment and multipotency after transplantation. Stem Cell Rep. 2019;12:680–95.
7. Duan D, Lu M. Olfactory mucosa: a rich source of cell therapy for central nervous system repair. Rev Neurosci. 2015;26:281–93.
8. Feron F, Perry C, Cochrane J, Licina P, Nowitzke A, Urquhart S, et al. Autologous olfactory ensheathing cell transplantation in human spinal cord injury. Brain J Neurol. 2005;128:2951–60.
9. Richter MW, Fletcher PA, Liu J, Tetzlaff W, Roskams AJ. Lamina propria and olfactory bulb ensheathing cells exhibit differential integration and migration and promote differential axon sprouting in the lesioned spinal cord. J Neurosci. 2005;25:10700–11.
10. Murrell W, Wetzig A, Donnellan M, Féron F, Burne T, Meedeniya A, et al. Olfactory mucosa is a potential source for autologous stem cell therapy for Parkinson's disease. Stem Cells (Dayton, Ohio). 2008;26:2183–92.
11. Fan JR, Lee HT, Lee W, Lin CH, Hsu CY, Hsieh CH, Shyu WC. Potential role of CBX7 in regulating pluripotency of adult human pluripotent-like olfactory stem cells in stroke model. Cell Death Dis. 2018;9:502.
12. Oh J, Lee YD, Wagers AJ. Stem cell aging: mechanisms, regulators and therapeutic opportunities. Nat Med. 2014;20:870–80.
13. Pérez LM, Bernal A, de Lucas B, San Martin N, Mastrangelo A, García A, et al. Altered metabolic and stemness capacity of adipose tissue-derived stem cells from obese mouse and human. PLoS ONE. 2015;10:e0123397.
14. Vasa M, Fichtlscherer S, Aicher A, Adler K, Urbich C, Martin H, et al. Number and migratory activity of circulating endothelial progenitor cells inversely correlate with risk factors for coronary artery disease. Circ Res. 2001;89:E1-7.
15. Fokkens WJ, Lund VJ, Mullol J, Bachert C, Alobid I, Baroody F, et al. EPOS 2012: European position paper on rhinosinusitis and nasal polyps 2012. A summary for otorhinolaryngologists. Rhinology. 2012;50:1–12.
16. Chen M, Reed RR, Lane AP. Chronic inflammation directs an olfactory stem cell functional switch from neuroregeneration to immune defense. Cell Stem Cell. 2019;25:501-13.e5.
17. Nakashima N, Nakashima K, Taura A, Takaku-Nakashima A, Ohmori H, Takano M. Olfactory marker protein directly buffers cAMP to avoid depolarization-induced silencing of olfactory receptor neurons. Nat Commun. 2020;11:2188.
18. Chi PL, Luo SF, Hsieh HL, Lee IT, Hsiao LD, Chen YL, Yang CM. Cytosolic phospholipase A2 induction and prostaglandin E2 release by interleukin-1β via the myeloid differentiation factor 88-dependent pathway and cooperation of p300, Akt, and NF-κB activity in human rheumatoid arthritis synovial fibroblasts. Arthritis Rheum. 2011;63:2905–17.
19. Knufinke M, MacArthur MR, Ewald CY, Mitchell SJ. Sex differences in pharmacological interventions and their effects on lifespan and healthspan outcomes: a systematic review. Front Aging. 2023;4:1172789.
20. Percie du Sert N, Hurst V, Ahluwalia A, Alam S, Avey MT, Baker M, et al. The ARRIVE guidelines 2.0: updated guidelines for reporting animal research. PLoS Biol. 2020;18:e3000410.
21. Yamada K, Shiga H, Noda T, Harita M, Ishikura T, Nakamura Y, et al. The impact of ovariectomy on olfactory neuron regeneration in mice. Chem Senses. 2020;45:203–9.
22. Wu Q, Xu X, Miao X, Bao X, Li X, Xiang L, et al. YAP signaling in horizontal basal cells promotes the regeneration of olfactory epithelium after injury. Stem Cell Rep. 2022;17:664–77.
23. Ohnishi Y-I, Iwatsuki K, Ishihara M, Shikina T, Shinzawa K, Moriwaki T, et al. Isolation of human adult olfactory sphere cells as a cell source of neural progenitors. Stem Cell Res. 2015;15:23–9.
24. Schwob JE, Jang W, Holbrook EH, Lin B, Herrick DB, Peterson JN, Hewitt CJ. Stem and progenitor cells of the mammalian olfactory epithelium: Taking poietic license. J Comp Neurol. 2017;525:1034–54.
25. Tanos T, Saibene AM, Pipolo C, Battaglia P, Felisati G, Rubio A. Isolation of putative stem cells present in human adult olfactory mucosa. PLoS One. 2017;12:e0181151.
26. Beites CL, Kawauchi S, Crocker CE, Calof AL. Identification and molecular regulation of neural stem cells in the olfactory epithelium. Exp Cell Res. 2005;306:309–16.
27. Bock P, Rohn K, Beineke A, Baumgärtner W, Wewetzer K. Site-specific population dynamics and variable olfactory marker protein expression in the postnatal canine olfactory epithelium. J Anat. 2009;215:522–35.
28. Verhaagen J, Oestreicher AB, Gispen WH, Margolis FL. The expression of the growth associated protein B50/GAP43 in the olfactory system of neonatal and adult rats. J Neurosci Off J Soc Neurosci. 1989;9:683–91.
29. Woodhall E, West AK, Chuah MI. Cultured olfactory ensheathing cells express nerve growth factor, brain-derived neurotrophic factor, glia cell line-derived neurotrophic factor and their receptors. Brain Res Mol Brain Res. 2001;88:203–13.
30. Marks C, Belluscio L, Ibáñez CF. Critical role of GFRα1 in the development and function of the main olfactory system. J Neurosci Off J Soc Neurosci. 2012;32:17306–20.
31. Feron F, Bianco J, Ferguson I, Mackay-Sim A. Neurotrophin expression in the adult olfactory epithelium. Brain Res. 2008;1196:13–21.
32. Gasperini C, Tuntevski K, Beatini S, Pelizzoli R, Van Lo A, Mangoni D, et al. Piwil2 (Mili) sustains neurogenesis and prevents cellular senescence in the postnatal hippocampus. EMBO Rep. 2023;24:e53801.
33. Murrell W, Wetzig A, Donnellan M, Feron F, Burne T, Meedeniya A, et al. Olfactory mucosa is a potential source for autologous stem cell therapy for Parkinson's disease. Stem Cells (Dayton, Ohio). 2008;26:2183–92.
34. Mariano ED, Teixeira MJ, Marie SK, Lepski G. Adult stem cells in neural repair: current options, limitations and perspectives. World J Stem Cells. 2015;7:477–82.
35. Kurtenbach S, Goss GM, Goncalves S, Choi R, Hare JM, Chaudhari N, Goldstein BJ. Cell-based therapy restores olfactory function in an inducible model of hyposmia. Stem cell reports. 2019;12:1354–65.
36. Bylund M, Andersson E, Novitch BG, Muhr J. Vertebrate neurogenesis is counteracted by Sox1-3 activity. Nat Neurosci. 2003;6:1162–8.

37. Rantanen LM, Bitar M, Lampinen R, Stewart R, Quek H, Oikari LE, et al. An Alzheimer's disease patient-derived olfactory stem cell model identifies gene expression changes associated with cognition. Cells. 2022;11:3258.
38. Yu XM, Li CW, Chao SS, Li YY, Yan Y, Zhao XN, et al. Reduced growth and proliferation dynamics of nasal epithelial stem/progenitor cells in nasal polyps in vitro. Sci Rep. 2014;4:4619.
39. Marshall CT, Lu C, Winstead W, Zhang X, Xiao M, Harding G, et al. The therapeutic potential of human olfactory-derived stem cells. Histol Histopathol. 2006;21:633–43.
40. Franceschini V, Bettini S, Pifferi S, Rosellini A, Menini A, Saccardi R, et al. Human cord blood CD133+ stem cells transplanted to nod-scid mice provide conditions for regeneration of olfactory neuroepithelium after permanent damage induced by dichlobenil. Stem cells (Dayton, Ohio). 2009;27:825–35.
41. Kim YM, Choi YS, Choi JW, Park YH, Koo BS, Roh HJ, Rha KS. Effects of systemic transplantation of adipose tissue-derived stem cells on olfactory epithelium regeneration. Laryngoscope. 2009;119:993–9.
42. Franceschini V, Bettini S, Pifferi S, Menini A, Siciliano G, Ognio E, et al. Transplanted human adipose tissue-derived stem cells engraft and induce regeneration in mice olfactory neuroepithelium in response to dichlobenil subministration. Chem Senses. 2014;39:617–29.
43. Tsujigiwa H, Nishizaki K, Teshima T, Takeda Y, Yoshinobu J, Takeuchi A, et al. The engraftment of transplanted bone marrow-derived cells into the olfactory epithelium. Brain Res. 2005;1052:10–5.
44. Jo H, Jung M, Seo DJ, Park DJ. The effect of rat bone marrow derived mesenchymal stem cells transplantation for restoration of olfactory disorder. Biochem Biophys Res Commun. 2015;467:395–9.
45. Zhang X, Klueber KM, Guo Z, Lu C, Roisen FJ. Adult human olfactory neural progenitors cultured in defined medium. Exp Neurol. 2004;186:112–23.
46. Orbay H, Tobita M, Mizuno H. Mesenchymal stem cells isolated from adipose and other tissues: basic biological properties and clinical applications. Stem Cells Int. 2012;2012:461718.
47. Katoh H, Shibata S, Fukuda K, Sato M, Satoh E, Nagoshi N, et al. The dual origin of the peripheral olfactory system: placode and neural crest. Mol Brain. 2011;4:34.
48. Alizadeh R, Kamrava SK, Bagher Z, Farhadi M, Falah M, Moradi F, et al. Human olfactory stem cells: as a promising source of dopaminergic neuron-like cells for treatment of Parkinson's disease. Neurosci Lett. 2019;696:52–9.
49. Ursavas S, Darici H, Karaoz E. Olfactory ensheathing cells: unique glial cells promising for treatments of spinal cord injury. J Neurosci Res. 2021;99:1579–97.
50. Oleszkiewicz A, Abriat A, Doelz G, Azema E, Hummel T. Beyond olfaction: beneficial effects of olfactory training extend to aging-related cognitive decline. Behav Neurosci. 2021;135:732–40.
51. Li ST, Young TH, Huang TW. Regeneration of olfactory neuroepithelium in 3-methylindole-induced anosmic rats treated with intranasal chitosan. Biomaterials. 2021;271:120738.

Publisher's Note

Springer Nature remains neutral with regard to jurisdictional claims in published maps and institutional affiliations.

Brain, Behavior, & Immunity - Health 49 (2025) 101094

Contents lists available at ScienceDirect

Brain, Behavior, & Immunity - Health

journal homepage: www.editorialmanager.com/bbih/default.aspx

Induction of endogenous IL-10 promotes resolution and tolerance of nitric oxide in microglia

Hsing-Chun Kuo [a,b,c,d], Jia-Shing Chen [e], Chun-Nun Chao [f], Kam-Fai Lee [g], Yi-Te Huang [h], Pin-Cheng Mao [i], Tzu-Chia Lin [j], Shu-Chen Chiu [k], Ya-Ling Huang [l,*], Chun-Hsien Chu [i,j,**]

[a] Department of Nursing, Division of Basic Medical Sciences, Chang Gung University of Science and Technology, Chiayi, Taiwan
[b] Research Fellow, Chang Gung Memorial Hospital, Chiayi, Taiwan
[c] Research Center for Food and Cosmetic Safety, College of Human Ecology, Chang Gung University of Science and Technology, Taoyuan, Taiwan
[d] Chronic Diseases and Health Promotion Research Center, Chang Gung University of Science and Technology, Chiayi, Taiwan
[e] School of Medicine for International Students, I-Shou University, Kaohsiung, 84001, Taiwan
[f] Department of Pediatrics, Ditmanson Medical Foundation Chia-Yi Christian Hospital, Chia-Yi, Taiwan
[g] Department of Pathology, Chang Gung Memorial Hospital, Chiayi, 61363, Taiwan
[h] Department of Geriatrics and Gerontology, National Cheng Kung University Hospital, Tainan, Taiwan
[i] Institute of Basic Medical Sciences, College of Medicine, National Cheng Kung University, Tainan, 701, Taiwan
[j] Institute of Molecular Medicine, College of Medicine, National Cheng Kung University, Tainan, Taiwan
[k] National Laboratory Animal Center (NLAC), NARLabs, Tainan, Taiwan
[l] Department of Laboratory Medicine, E-Da Hospital, Kaohsiung, 824, Taiwan

ARTICLE INFO

Keywords:
IL-10
Nitric oxide
Microglia
Immune resolution
Endotoxin tolerance
Neuroinflammation

ABSTRACT

Endogenous interleukin-10 (IL-10), a potent anti-inflammatory cytokine, is induced in a timely and coordinated manner to dampen microglia-mediated brain inflammation. However, it remains unclear how it alters the inflammatory process to shape the immune polarization of microglia. This study aimed to investigate the anti-inflammatory mechanisms of endogenous IL-10 in activated and tolerized microglia using in vitro multiple-reconstituted primary brain cell cultures and an in vivo IL-10 knockout (IL-10KO) animal model. Upon a single or repeated lipopolysaccharide (LPS) treatment regimen, the expression levels of the inflammatory factors during the neuroinflammatory/tolerance process were measured by quantitative real-time polymerase chain reaction, enzyme-linked immunosorbent assay (ELISA), and Griess reagent assay. ELISA data showed that cell-autonomous induction of endogenous IL-10 occurs in LPS-activated and LPS-tolerized microglia. Furthermore, comparing the LPS-elicited pro-inflammatory factor expressions at different neuroinflammatory stages between the wild-type and IL-10KO groups, our data revealed the failure of negative-feedback suppression of inducible nitric oxide synthesis (iNOS) during immune resolution in the IL-10KO brains. Moreover, LPS-treated IL-10KO microglia increase the supernatant level of nitrite and become overactive during late-stage inflammation, despite no changes in cell number; in contrast, LPS-tolerized IL-10KO microglia fail to program endotoxin tolerance of nitric oxide/inducible nitric oxide synthesis (iNOS). In summary, our data demonstrate that the cell-autonomous induction of endogenous IL-10 in microglia is crucial for mitigating brain immune responses, particularly in the resolution and tolerance of nitric oxide.

1. Introduction

Neuroinflammation has been recognized as a self-defensive approach to remove harmful stimuli and initiate the healing process in the central nervous system (CNS) (Chu et al., 2015; Rodriguez et al., 2022; Rosenblum et al., 2015). In response to potent immune challenges such as lipopolysaccharides (LPS) or neuronal damage, microglia, the primary innate immune cells of the brain, produce various pro-inflammatory and anti-inflammatory mediators in an orchestrated manner along with changing their morphology from a ramified appearance to that of an amoeboid shape (Chu et al., 2015). This LPS-elicited neuroinflammatory process in microglia displays three stereotyping stages: initiation,

* Corresponding author.
** Corresponding author. Institute of Molecular Medicine, College of Medicine, National Cheng Kung University, No. 1 University Road, Tainan, 70101, Taiwan.
E-mail addresses: ed105471@edah.org.tw (Y.-L. Huang), z11108008@email.mcku.edu.tw, chunhsienchu@gmail.com (C.-H. Chu).

https://doi.org/10.1016/j.bbih.2025.101094
Received 30 May 2025; Received in revised form 9 August 2025; Accepted 27 August 2025
Available online 6 September 2025
2666-3546/© 2025 The Authors. Published by Elsevier Inc. This is an open access article under the CC BY-NC-ND license (http://creativecommons.org/licenses/by-nc-nd/4.0/).

propagation, and resolution. During the immune status of initiation and propagation, LPS-activated microglia immediately release pro-inflammatory factors such as superoxide, tumor necrosis factor-alpha (TNF-α), followed by interleukin-1 beta (IL-1β), nitric oxide (NO), prostaglandin E2 (PGE_2), and interleukin-6 (IL-6) in a cascade of rigorous time frame (Chu et al., 2015; Gao et al., 2020). Among them, the generation of NO, which is a versatile mediator, is achieved by the enzyme nitric oxide synthase (NOS) through the conversion of L-arginine (Arg) to L-citrulline. In addition to numerous homeostatic functions of NO at lower physiological concentrations, higher amounts of NO derived from activated glial cells through the transcriptional regulation of the inducible NOS (iNOS) participate in a variety of neurobiological diseases (Saha and Pahan, 2006), including oligodendrocyte degeneration in demyelinating diseases (Mitrovic et al., 1994) and neuronal death during ischemia, trauma, and neurodegenerative diseases (Liu et al., 2002). High levels of iNOS expression in glia, which can lead to oxidative and nitrosative stress in the brain, cause inhibition of neuronal respiration, depolarization, and glutamate release by NO and its toxic metabolite, peroxynitrite ($ONOO^-$), resulting in excitotoxicity and cell death of particularly vulnerable neurons (Brown, 2007; Heales et al., 1999). Therefore, targeting the production of NO/iNOS is a potential therapeutic strategy for inflammation-mediated neurodegenerative diseases (Broom et al., 2011; Tewari et al., 2021). Subsequently, at the immune resolution stage, the anti-inflammatory cytokine, such as interleukin-10 (IL-10), is secreted to eliminate excessive inflammation (Chu et al., 2015; Gao et al., 2020). Consequently, after the precise immune resolution, the activated microglia are reversibly returned to the status of immune homeostasis. However, if this neuroinflammation is uncontrolled and unresolved, active microglia transform into the reactive phenotype and become toxic to neighboring neurons (Block et al., 2007; Burguillos et al., 2011). Tightly regulating and actively terminating the neuroinflammatory response is needed to prevent neural tissue destruction. Thus, understanding the induction of endogenous IL-10 in regulating the neuroinflammatory process may be beneficial for the development of therapeutic strategies in inflammation-mediated neurodegenerative disorders (Dansokho and Heneka, 2018; Swanson et al., 2018; Trovato Salinaro et al., 2018).

Interleukin 10 (IL-10), a potent anti-inflammatory cytokine, holds significant promise in resolving inflammation and maintaining immune homeostasis in both CNS (Gao et al., 2020; Saraiva and O'Garra, 2010; Strle et al., 2001) and peripheral tissues (Kuhn et al., 1993). The main source of endogenous IL-10 production is considered as microglia among brain cells (Chu et al., 2015). However, whether regulation of microglia-derived IL-10 expression profile by other brain cells via a non-cell-autonomous manner is still unclear. In general, the activation of the intracellular signaling cascades and SP1 transcriptional factors by most pro-inflammatory mediators leads to a rapid increase in promoter activity and mRNA expression of IL-10 after the immune challenge (Foey et al., 1998; Saraiva and O'Garra, 2010; Tone et al., 2000). In addition to intracellular signaling cascades, earlier-released TNF-α and PGE_2 from LPS-treated microglia negatively regulate IL-10 induction via the EP2 receptor-mediating G-protein-independent arrestin signaling (Chu et al., 2015). These results imply the complex intracellular and extracellular interactions among different immune factors that regulate endogenous IL-10 induction in the time frame of the neuroinflammatory process. On the other hand, endogenous IL-10 induction plays a crucial role in regulating microglial phagocytosis, repressing the expression and release of pro-inflammatory mediators, and suppressing antigen presentation (Heyen et al., 2000; Kremlev and Palmer, 2005; Qian et al., 2006; Sabat et al., 2010). However, the impacts of endogenous IL-10 on suppressing the expression of pro-inflammatory mediators during the neuroinflammatory process are still controversial due to its later-onset expression pattern. For instance, the induction of endogenous IL-10 by LPS significantly suppresses the production of IL-1β (Gao et al., 2020) but does not affect early-releasing TNF-α (Kuo et al., 2023) in vitro brain cell cultures. Therefore, an in vivo model of neuroinflammation may be needed to depict further the action of endogenous IL-10 in regulating brain immune resolution.

Recently, accumulated evidence demonstrates that microglia are capable of developing innate immune memory to either enhance (trained immunity) or suppress (immune tolerance) subsequent immune responses that are involved in the regulation of neurological disease pathogenesis (Dong et al., 2024; Neher and Cunningham, 2019; Wendeln et al., 2018). For example, two consecutive LPS challenges within a short interval immediately elicit microglial cell endotoxin tolerance (ET), where the production of pro-inflammatory mediators is decreased (Chu et al., 2016). In contrast, that of anti-inflammatory mediators, such as IL-10, is enhanced in LPS-tolerized microglia. In other words, a transient unresponsiveness or reduced sensitivity to subsequent endotoxin challenges in such ET microglial cells is seen. Several studies have demonstrated that ET development in peripheral immune cells, such as macrophages, entails multiple mechanisms, including negative signal transductions, transcriptional networks, and post-translational modifications (Zhang and Cao, 2021; Zhang et al., 2022). Our previous study showed that microglia alone fail to develop ET unless in the presence of neurons and astroglia, unlike macrophages (Chu et al., 2016). The induction of ET in microglia, which display an anti-inflammatory phenotype, prevents excessive toxic damage in the neurons due to reduced secreted cytokine production (Chu et al., 2016; Kuo et al., 2023), such as TNF-α. However, how the LPS-tolerized microglia shape their polarizing phenotype via enhancement of IL-10 production is still unknown. Altogether, this study aimed to determine the impact of endogenous IL-10 induction on regulating immune initiation, propagation, resolution, and tolerance using in vivo animal brain and in vitro brain cell culture models of neuroinflammation.

2. Materials and methods

2.1. Multiple reconstituted primary neuron-glia, mixed-glia, and microglia-enriched cultures and cell treatment

According to the previous reports (Chu et al., 2015, 2016; Liu et al., 2000), the neuron-glia and mixed-glia/microglia-enriched cultures were prepared from the whole brains of E14.5-day embryos and 1-day-old pups, respectively. The culture plates were precoated with poly-D-lysine (20 μg/mL) (P7280; Merck KGaA). Briefly, brain tissue without meninges and blood vessels was dissociated with mild mechanical trituration. For the preparation of neuron-glia cultures, 5×10^5 cells were seeded in each well of 24-well culture plates with culture medium containing MEM, 10 % heat-inactivated fetal bovine serum (FBS), 10 % heat-inactivated horse serum, 1 g/L glucose, 2 mM L-glutamine, 1 mM sodium pyruvate, and 0.1 mM nonessential amino acids for the growth and maintenance at 37 °C in a humidified atmosphere of 5 % CO2/95 % air. The neuron-glia cultures were added with fresh medium (0.5 ml/well) 3 days after cell seeding. Their cellular composition included 11 % microglia, 50 % astrocytes, and 39 % neurons on the 7th day after seeding, which were used for further experiments. For the preparation of mixed-glia cultures, the isolated cells (1.5×10^6 cells) were seeded in 6-well plates in DMEM/F12 medium (#11330032; Thermo Fisher Scientific Inc.), 10 % fetal bovine serum, 2 mM L-glutamine (#25030149; Thermo Fisher Scientific Inc.), 1 mM sodium pyruvate (#11360-070; Thermo Fisher Scientific Inc.), 0.1 mM nonessential amino acids (#11140-035; Thermo Fisher Scientific Inc.), and 50 U/mL penicillin, and 50 μg/mL streptomycin (#10378016; Thermo Fisher Scientific Inc.) and were changed their media four days later. The mixed-glia cultures containing about 80 % astrocytes and 20 % microglia, two weeks after culturing, were used for further experiments. For the preparation of microglia-enriched cultures, the isolated cells (5×10^7 cells) were seeded in 150 cm^2 culture flasks in DMEM/F12 medium (10 % FBS, 2 mM of L-glutamine, 1 mM of sodium pyruvate, 0.1 mM of nonessential amino acids, 50 U/mL of penicillin, and 50 μg/mL of streptomycin) and maintained at 37 °C in a humidified atmosphere of 5

% CO2/95 % air. The medium was changed 4 days later, until reaching confluence. The enriched microglia (99 % pure) were obtained by shaking the flasks for 60 min at 180 rpm after 12–14 days of cell seeding (upon reaching confluence) for further experiments.

Cell Treatment for activated or tolerized microglia is shown in Fig. 1A. Neuron–glial, mixed glial, and microglia-enriched cultures were pre-incubated with or without LPS (*E. coli* O111:B4, Cat# 437627, protein contaminants ≤2.0 %, nucleic acid contaminants ≤2.5 %; 15 ng/mL) from EMD Chemicals, Inc. (Darmstadt, Germany) for 6 h. After replacing the fresh media and waiting an additional 6 h, these cells were re-stimulated with LPS (15 ng/mL). According to previous investigations (Chu et al., 2016; Kuo et al., 2023), immune-activated and immune-tolerant microglia could be induced by once and repeated LPS treatment, respectively. The expressions of supernatant IL-10 were measured at 6 and 24 h in these cells by ELISA.

2.2. Measurement of IL-10 and nitric oxide

The IL-10 level in the supernatant of the neuron-glia, mixed-glia, and microglia-enriched cultures, and animal serum was measured with the commercial ELISA kits from R&D Systems (Minneapolis, MN). The value of IL-10 within the standard curve, along with ~10 % inter- and ~15 % intra-assay coefficients of variation in the single or between different assay runs, is considered acceptable for further calculation. Under physiological conditions, nitric oxide converts to its stable oxidation product, nitrite. The Griess assay is primarily used to quantify nitrite (detection limit: 0.5 μM) to reflect the accumulated supernatant levels of nitric oxide indirectly in biological and chemical research.

2.3. Animal experiments

B10.129P2(B6)-IL-10tm1Cgn/J (IL-10 knockout or IL-10KO) mice and their wild-type (WT) (C57BL/10J) mice were purchased from the Jackson Laboratory (Bar Harbor, ME). According to the previous study (Liu et al., 2008), female mice are more resistant to LPS than male mice. To avoid the gender effect, we only applied male mice in the current study. The male WT (n = 22) and IL-10KO mice (n = 22) in young adulthood (~3 months old) were intraperitoneally injected with saline (10 WT and 10 IL-10KO mice) or LPS (L3012, Merck KGaA) (12 WT and 12 IL-10KO mice; 0.3 mg/kg) to determine the anti-inflammatory effects of endogenous IL-10 on systemic inflammation-mediated neuro-inflammatory cascades in the brains. Several inflammatory factor expression profiles in the brains of these treated animals were measured 1 and 12 h after LPS treatment by real-time PCR, including TNF-α, IL-1β, COX-2, iNOS, and IL-10. In addition, the mortality of these treated animals was measured after LPS treatment to calculate their survival rate. For the animal sacrifice procedure, animals were first anesthetized with 1–3 % isoflurane for anesthesia and then subjected to transcardiac perfusion with saline, followed by 4 % paraformaldehyde for brain tissue dissection and fixation. The WT and IL-10KO mice were group housed on a 12 h/12 h light/dark cycle at a room temperature of 21 °C ± 2 °C and humidity of 55 % ± 5 % and were given free access to water and food. All animal studies received approval from the Institutional Animal Care and Use Committee at Chang Gung University of Science and Technology, aligning with ARRIVE guidelines.

2.4. Reverse transcription quantitative real time-PCR (RT-qPCR)

The whole brain tissues of these animals treated with LPS at 1, 3, 6, and 12 h (Fig. 2 and Fig. S1A and B) and the cell pellet of neuron-glia cultures with a single or repeated LPS treatment (Fig. S2) were collected for further measurement of mRNA expression of inflammatory factors by quantitative RT-PCR as described previously (Chu et al., 2015, 2016). The RNeasy Mini kit (QIAGEN, Valencia, CA) was used to extract

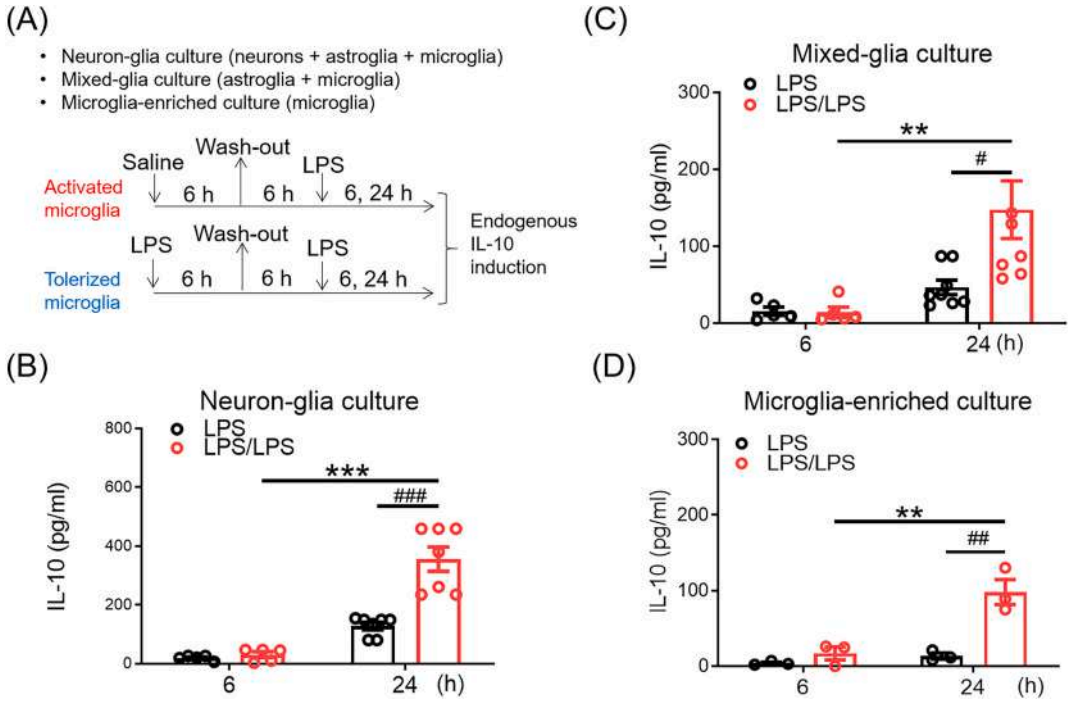


Fig. 1. Cell-autonomous induction of endogenous IL-10 in LPS-activated and LPS-tolerized microglia. (**A**) As an illustrated experimental procedure of endotoxin treatment regimen for the development of the activated and tolerized microglia, the neuron-glia (neurons + astroglia + microglia), mixed-glia (astroglia + microglia), and microglia-enriched cultures were prepared and pre-incubated with a vehicle (activated) or LPS (tolerized) (15 ng/ml) for 6 h. After being replaced with fresh medium for 6 h, LPS (15 ng/ml) was re-added to the cells. (**B-D**). After receiving the endotoxin treatment regimen (activated versus tolerized) as indicated in (A), supernatant levels of IL-10 in neuron-glia (B), mixed-glia (C), and microglia-enriched (D) cultures were detected, respectively, by ELISA assay 6 and 24 h later. Data are expressed as the mean ± SEM from more than three independent experiments (n ≥ 3) in duplicate with two-way ANOVA with Tukey's multiple comparisons test (6-h group versus 24-h group: **p < 0.01, ***p < 0.001; LPS group versus LPS/LPS group: #p < 0.05, ##p < 0.01, ###p < 0.001).

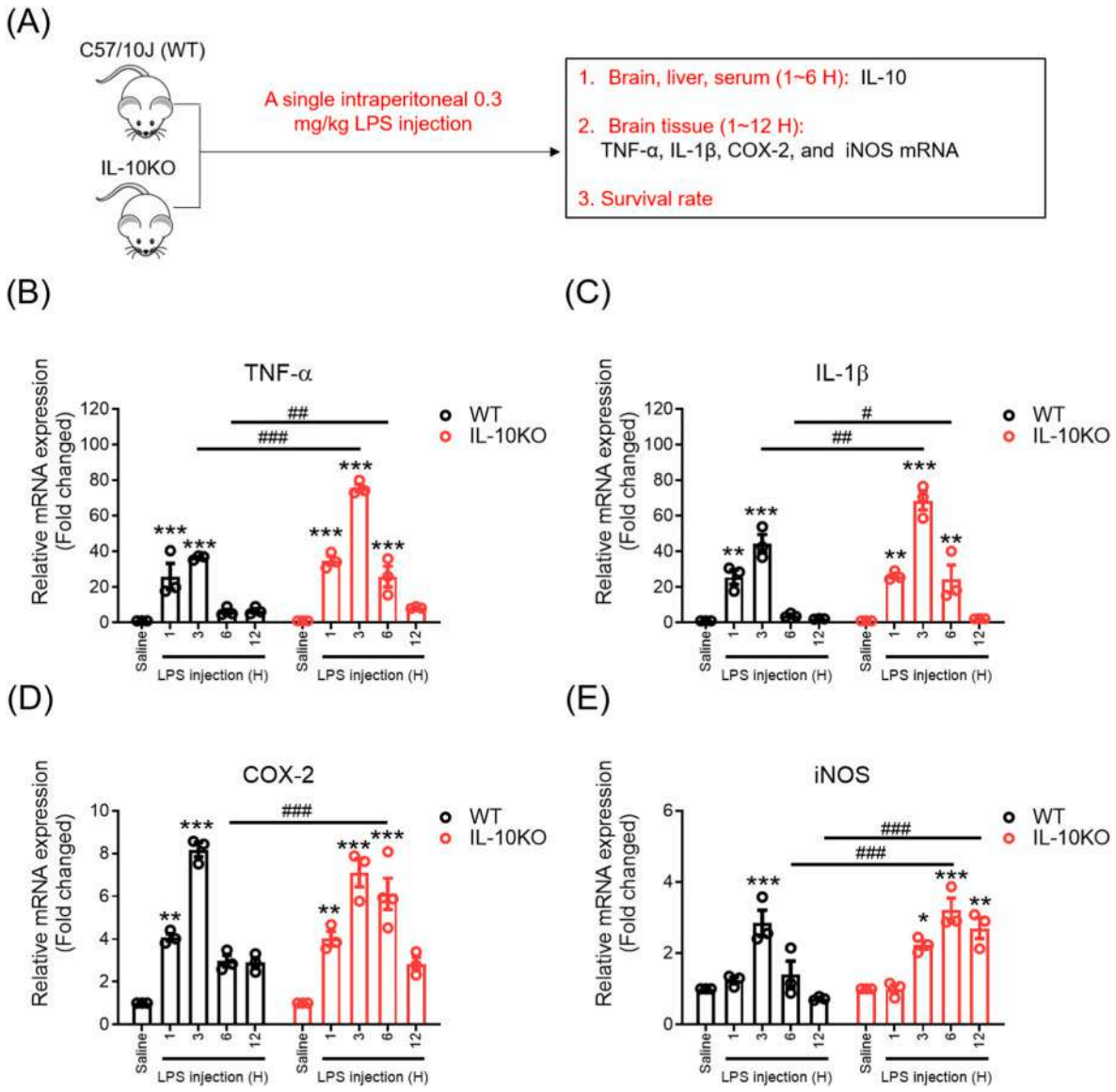


Fig. 2. Deficiency in IL-10 impairs negative-feedback suppression of inducible nitric oxide synthesis in the inflammatory brain. (**A**) Schematic of the experimental design for determining the role of endogenous IL-10 in LPS-induced immune resolution of pro-inflammatory factors. The C57/10J (WT) and IL-10KO mice received intraperitoneal LPS (0.3 mg/kg) and saline treatment, followed by measurement of endogenous IL-10 induction in the brain, liver, and serum, and the inflammatory mRNA expression, including TNF-α, IL-1β, COX-2, and iNOS, using ELISA and real-time PCR at different time points as indicated. Finally, the survival rate of these LPS-treated mice was calculated. (**B-E**) Expression of TNF-α (B), IL-1β (C), COX-2 (D), and iNOS (E) mRNA in the WT and IL-10KO mice's brains after 1, 3, 6, and 12 h of saline (10 WT and 10 IL-10KO) and LPS (12 WT and 12 IL-10KO) treatment was measured by RT-PCR. Data are presented as a fold change relative to the saline-treated control and expressed as the mean ± SEM from three independent experiments performed in triplicate with two-way ANOVA with Tukey's multiple comparisons test (saline group versus LPS group: *p < 0.05, **p < 0.01, ***p < 0.001; WT group versus IL-10KO group: #p < 0.05, ##p < 0.01, ###p < 0.001).

total RNA, according to the manufacturer's instructions. A spectrophotometer measured quantification and qualification (The ratio of absorbance at 260 nm and 280 nm is approximately 2.0) of total RNA. Using MuLV reverse transcriptase (Applied Biosystems, Foster City, CA), first-strand cDNA was synthesized from 2 μg of total RNA. After that, using SYBR-Green Master mix (Applied Biosystems, Foster City, CA), quantitative real-time PCR analysis was performed to amplify cDNA under the conditions as follows: hold at 95 °C for 10 min and perform 40 cycles at 95 °C for 15 s and 60 °C for 1 min. The sequences of the primers designed with Vector NTI software (Invitrogen) were the following: mouse TNF-α forward primer 5′ GAC CCT CAC ACT CAG ATC ATC TTC T 3'; mouse TNF-α reverse primer 5′ CCT CCA CTT GGT GGT TTG CT 3'; mouse COX-2 forward primer 5′ TGA TAT GTC TTC CAG CCC ATT G 3'; mouse COX-2 reverse primer 5′ AAC GGA ACT AAG AGG AGC AGC 3'; mouse iNOS forward primer 5′ GCC ACC AAC AAT GGC AAC A 3'; mouse iNOS reverse primer 5′ CGT ACC GGA TGA GCT GTG AAT T 3'; mouse IL-1β forward primer 5′ CTG GTG TGT GAC GTT CCC ATT A 3′; mouse IL-1β reverse primer 5′ CCG ACA GCA CGA GGC TTT 3'; mouse IL-10 forward primer 5′ CCC TTT GCT ATG GTG TCC TTT C 3'; mouse IL-10 reverse primer 5′ CAA AGG ATC TCC CTG GTT TCT C 3'; mouse GAPDH forward primer 5′ TTC AAC GGC ACA GTC AAG GC 3'; mouse GAPDH reverse primer 5′ GAC TCC ACG ACA TAC TCA GCA CC 3'. Data were normalized to GAPDH expression.

2.5. *Immunocytochemistry staining*

Immunocytochemistry (ICC) staining with anti-ionized calcium binding adaptor molecule 1 (Iba-1; 1:400; 019–19741; FUJIFILM Wako Pure Chemical Corporation, Osaka, Japan) was performed as described in previous studies (Chu et al., 2016, 2023). Briefly, after formaldehyde

fixation and incubation with blocking buffer (0.4 % Triton X-100, 1 % BSA, 4 % normal serum in PBS), the cells were treated with primary anti-Iba-1 antibody diluted in antibody diluent overnight at 4 °C. Following incubation with an appropriate biotinylated secondary antibody, the Vectastain ABC reagents and color development with 3, 3′-diaminobenzidine were used to visualize the bound primary anti-Iba-1 antibody. Then, a CCD camera and the MetaMorph software (Molecular Devices, Sunnyvale, CA, USA) were applied to film Iba-1 images.

The Nikon NIS-Element BR software (Nikon Instruments Inc., Melville, NY, USA) was used to automatically circle and measure the mean intensity value in the areas of Iba-1-positive staining cells under consistent intensity criteria. Protein expression levels of Iba-1 in each staining image are calculated by multiplying the mean intensity by the Iba-1-positive-staining area. The integrated intensity data were obtained from two to six wells per treatment condition in three independent experiments and were expressed as the percentage of the WT saline-treated control (means ± SEM). The microglia number (Iba-1+ cells) in mixed-glia cocultures was manually counted by ~ nine representative areas in each treatment group from three independent experiments performed in triplicate (20X power) and expressed as the percentage of the WT saline-treated control (means ± SEM). 2 to 3 individuals performed cell counting and quantification of immunostaining density.

2.6. Statistical analysis

All data from at least three independent experiments are expressed as the mean ± standard error of mean (SEM) and were compared between groups using the one-way analysis of variance (ANOVA) with Dunnett's multiple comparisons test or two-way ANOVA with Tukey's multiple comparisons test (Prism 10; GraphPad Software, San Diego, CA, USA). In addition, RT-PCR results were normalized to their respective internal loading controls, GAPDH. Standard curves of IL-10 ELISA were plotted, and the data were obtained within the linear range of the curve. A p-value of <0.05 was considered statistically significant. In all cases, a p-value less than 0.05 was considered statistically significant.

3. Results

3.1. Activated and tolerized microglia autonomously produce IL-10

The presence of neurons, astroglia, or other brain cells could change cellular survival (Pesti et al., 2024) and immune properties of microglia via the non-cell-autonomous mechanisms, such as the development of TNF-α (Chu et al., 2016) and PGE_2 (Kuo et al., 2022a) immune tolerance. Using multiple reconstituted primary neuron-glia (neurons, astroglia, and microglia), mixed-glia (astroglia and microglia), and microglia-enriched cultures with once or repeated LPS treatment regimens as described in Fig. 1A, we determined whether activated (LPS-treated group) or tolerized (LPS/LPS-treated group) microglia were capable of producing and enhancing IL-10 production in the presence or absence of neurons or astroglia. Consistent with a previous study (Chu et al., 2016), ELISA data showed that induction of endogenous IL-10 by a single LPS treatment was observed in the supernatants of all neuron-glia, mixed-glia, and microglia-enriched cultures at 24 h (Fig. 1B–D). However, unlike the microglial TNF-α (Chu et al., 2016) and PGE_2 (Kuo et al., 2022b) tolerance, which occurs only in the presence of neurons and/or astroglia, enhancement of LPS-induced IL-10 production in the ET-treated microglia-enriched cultures was similar to that of neuron-glia and mixed-glia cocultures. Our data indicated that activated and tolerized microglia elicited an endogenous IL-10 expression profile in a cell-autonomous manner.

3.2. Deficiency in IL-10 impairs nitrite resolution in the inflammatory brain

To determine the role of endogenous IL-10 induction in regulating brain immune initiation, propagation, and resolution status of the neuroinflammation process in vivo, C57/10J (WT) and IL-10 knockout (IL-10KO) mice in young adulthood were intraperitoneally injected with LPS at 0.3 mg/kg concentration used as a murine neuroinflammation model (Fig. 2A) (Qin et al., 2007). First, the induction of endogenous IL-10 in the brain, liver, and serum by a single intraperitoneal 0.3 mg/kg dose of LPS injection was detected. Real-time PCR analysis showed that compared to the saline-treated mice, the mice with LPS treatment had significantly increased IL-10 mRNA levels of the brain ($p < 0.05$, $F(3, 8) = 13.64$, one-way ANOVA) and liver ($p < 0.05$, $F(3, 8) = 26.59$, one-way ANOVA) by 5 and 50 times, respectively, at 1 h after treatment (Fig. S1A and B). Its expression was sustained at 3 h and slightly reduced at 6 h in the brain of LPS-treated animals, as well as in the liver. Meanwhile, ELISA results revealed that serum level of IL-10 was detected in LPS-treated WT mice at 1 h but not in IL-10KO mice (Fig. S1C, $p < 0.05$, $F(4, 29) = 1043$, two-way ANOVA).

Next, to study how endogenous IL-10 induction affected the neuroinflammatory process in the CNS, we measured the transcripts of the pro-inflammatory factors, including TNF-α (Fig. 2B), IL-1β (Fig. 2C), COX-2 (Fig. 2D), and iNOS (Fig. 2E), in the whole brain tissues of the LPS-treated WT and IL-10KO mice at 1, 3, 6, and 12 h after treatment by real-time PCR. Our data showed that after intraperitoneal LPS injection, the mRNA levels of TNF-α (treated saline vs. one and 3 h LPS treatment in WT mice: $P < 0.001$; $F(4, 20) = 94.42$, two-way ANOVA), IL-1β (treated saline vs. 1 h LPS treatment in WT mice: $P < 0.01$; treated saline vs. 3 h LPS treatment in WT mice: $P < 0.001$; $F(4, 20) = 78.30$, two-way ANOVA), COX-2 (treated saline vs. 1 h LPS treatment in WT mice: $P < 0.01$; treated saline vs. 3 h LPS treatment in WT mice: $P < 0.001$; $F(4, 21) = 62.21$, two-way ANOVA), and iNOS (treated saline vs. 3 h LPS treatment in WT mice: $P < 0.001$; $F(4, 20) = 18.51$, two-way ANOVA) were significantly increased at 1 h, reached the peak at 3 h and then approximately returned to basal level at 12 h in the WT mice's brain. The expression profile of these proinflammatory factors during this time frame reflects three typical immune statuses of an inflammatory process.

Furthermore, LPS-treated IL-10KO group had higher TNF-α (WT vs. IL-10KO mice in three or 6 h LPS treatment: $P < 0.01$, $P < 0.01$; $F(1, 20) = 47.33$, two-way ANOVA), IL-1β (WT vs. IL-10KO mice in three or 6 h LPS treatment: $P < 0.05$, $P < 0.01$; $F(1, 20) = 15.62$, two-way ANOVA), and COX-2 (WT vs. IL-10KO mice in 6 h LPS treatment: $P < 0.001$; $F(1, 21) = 2.049$, two-way ANOVA) expression than that of the WT group at 3 or 6 h, but not 1 h. These data suggested that the induction of endogenous IL-10 had no change in the initiation stage of their neuroinflammatory process but rather suppressed the immune propagation. Moreover, at 12 h of LPS treatment, WT and IL-10KO had similar levels of TNF-α, IL-1β, and COX-2 mRNA, implying that endogenous IL-10 induction did not participate in regulating their immune resolution. Interestingly, compared to the corresponding WT mice, the iNOS transcript in the brain of LPS-treated IL-10KO mice was significantly ~3-fold increased at 6 and 12 h (WT vs. IL-10KO mice in six or 12 h LPS treatment: $P < 0.001$; $F(1, 20) = 16.85$, two-way ANOVA). Our data indicated that, besides the broader impact of IL-10 on the LPS-induced neuroinflammatory process, its endogenous induction may also mainly contribute to the immune resolution of iNOS rather than other proinflammatory factors. Thus, this study further focused on inductive endogenous IL-10-mediated iNOS resolution.

3.3. IL-10KO microglia increase LPS-induced nitrite production in a time- and dose-dependent manner

Since iNOS is an enzyme that converts l-arginine, ultimately leading to microglial nitrite production under brain immune challenges (Liu et al., 2002; Mitrovic et al., 1994; Saha and Pahan, 2006), we

determined whether endogenous IL-10 induction suppressed LPS-induced nitrite production. Mixed-glia cultures containing astroglia and microglia were prepared from postnatal day 1 WT and IL-10KO pups and then treated with LPS (Fig. 3A). During the experimental period, the levels of supernatant nitrite in these cells were measured by Griess reagent assay. Our data showed that LPS treatment induced the production of supernatant nitrite both in WT and IL-10KO mixed-glia cells (Fig. 3B). Supernatant nitrite in the WT cells peaked 72 h after LPS treatment ($P < 0.05$, $F(6, 57) = 21.66$, two-way ANOVA) and began dropping later at 96 h. However, increased supernatant nitrite levels in LPS-treated IL-10KO cells were continually kept extended to 96 h (saline treatment vs. hour 48, hour 72, or hour 96 LPS treatment in IL-10KO mice: $P < 0.001$; $F(6, 57) = 21.66$, two-way ANOVA). At 72 and 96 h, IL-10KO cells produced a ~2-fold amount of supernatant nitrite when treated with LPS compared to the corresponding WT group (WT vs. IL-10KO mice in seventy-two- or 96-h LPS treatment: $P < 0.05$ or $P < 0.01$; $F(1, 57) = 18.38$, two-way ANOVA). Furthermore, under treatment with LPS at 10 and 20 ng/ml (WT vs. IL-10KO mice in 72-h LPS treatment: $P < 0.05$; $F(1, 24) = 39.36$, two-way ANOVA) concentrations, a greater amount of supernatant nitrite in the IL-10KO cells was also observed at 72 h (Fig. 3C). Our data indicated that endogenous IL-10 induction suppressed LPS-induced microglial nitrite production at a late stage in a manner that depended on both time and dose.

3.4. IL-10 deficiency enhances microglia activation at the late-stage inflammation

To determine whether the deficiency in endogenous IL-10 induction affects LPS-induced microglial activation, treatment of WT and IL-10KO mixed-glia cells with or without LPS at different time courses was performed (Fig. 4A) and then subjected to immunocytochemistry staining of Iba-1, which is one of the markers of microglia. Our data showed that the number of IL-10KO microglia (Iba-1-positive cells) was similar to WT microglia at 24, 48, and 72 h (Fig. 4B–E) in vitro incubation but increased at 96 h (Fig. 4B–F) in the absence of LPS ($P < 0.05$; $F(1, 36) = 5.381$, two-way ANOVA). Furthermore, after LPS treatment, WT and IL-10KO microglia had a similar increase in number compared to their corresponding saline-treated control, implying the increased nitrite production in LPS-treated IL-10KO microglia was not due to a change in their cell number. Moreover, both WT and IL-10KO microglia displayed ramified morphology in normal conditions and changed to amoeba-like morphology along with increased cell body size and larger cellular process arms during the LPS-elicited neuroinflammatory process (Fig. 4B). Interestingly, compared to the early stage, intensity of Iba-1expression in the IL-10KO group was increased at 96 h after LPS treatment (Fig. 4G–J) ($P < 0.05$; $F(1, 36) = 16.37$, two-way ANOVA), suggesting IL-10KO microglia became overactive at the late-stage inflammation. On the other hand, the increased Iba-1 intensity of the IL-10KO group was also found at 24 ($P < 0.05$; $F(1, 36) = 11.73$, two-way ANOVA) and 96 h in normal conditions. Together, our data implied that the induction of endogenous IL-10 may play a role in regulating microglia activation at the late stage due to failure of nitrite resolution.

3.5. IL-10KO microglia fail to program endotoxin tolerance of nitrite

Changes in the level of IL-10 and iNOS/nitrite have been well-recognized as the immune hallmark of function-polarized microglia (Orihuela et al., 2016). For example, endotoxin-tolerized microglia exhibit an anti-inflammatory polarization, showing increased IL-10 levels but decreased nitrite expression (Chu et al., 2016). However, the regulatory mechanism of nitrite tolerance in microglia remains unknown. Therefore, we determined whether the enhancement of inductive endogenous IL-10 played a role in nitrite reduction in tolerized microglia. Like the treatments for LPS-tolerized microglia in Fig. 1, neuron-glia cells were pre-treated with a vehicle (the LPS-treated group) or 15 ng/mL of LPS (the LPS/LPS-treated group) for 6 h and then replaced with fresh serum media. LPS (15 ng/mL) was re-added to the neuron-glia cells 6 h later. After LPS treatment, the mRNA level of IL-10 and iNOS of the treated neuron-glia cells was measured by RT-PCR (Fig. S2A). Our data showed that once LPS treatment significantly induced the expression of both iNOS ($P < 0.001$, $F(3, 8) = 410.4$, one-way ANOVA) (Fig. S2B) and IL-10 ($P < 0.001$, $F(3, 8) = 623.9$, one-way ANOVA) (Fig. S2C) at the mRNA level. After receiving the second LPS challenge, LPS-tolerized microglia displayed decreased iNOS

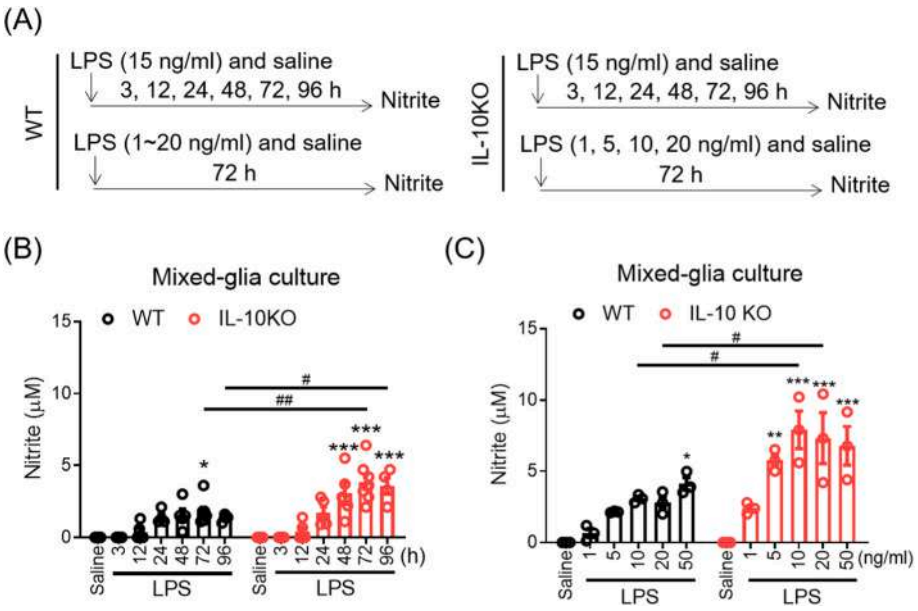


Fig. 3. IL-10KO microglia increase LPS-induced nitrite production in a time- and dose-dependent manner.
(A) Schematic of the experimental design to determine the effects of endogenous IL-10 induction on nitrite production in microglia under LPS challenge. **(B, C)** Measurement of supernatant nitrite in LPS-treated WT and IL-10KO mixed-glia cultures at different time points (B) or concentrations (C) using a Griess reagent. Data are expressed as the mean ± SEM ($n \geq 3$) with two-way ANOVA with Tukey's multiple comparisons test (Saline group versus LPS group: *$p < 0.05$, **$p < 0.01$, ***$p < 0.001$; WT group versus IL-10KO group: #$p < 0.05$, ##$p < 0.01$).

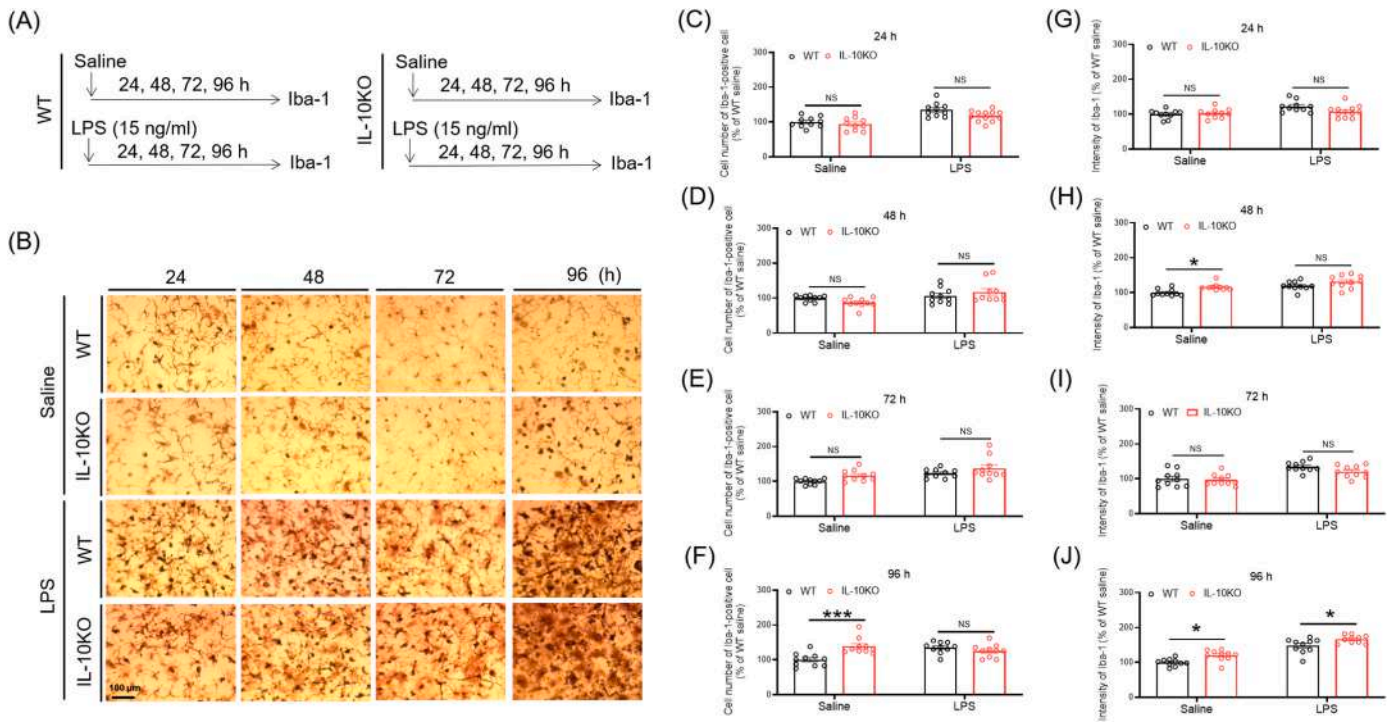


Fig. 4. IL-10 deficiency enhances microglia activation at the late-stage inflammation. (**A**) Schematic of the experimental design for the study of endogenous IL-10 on microglia number and morphology in normal and inflammatory conditions. **(B)** The expression of Iba-1, a marker for microglia, in these mixed-glia cells at 24, 48, 72, and 92 h in the presence and absence of LPS (15 ng/ml) was detected by immunocytochemistry staining. Magnification: 200×; scale bar: 100 μm. (**C-F**) Quantitative data of microglial number (Iba-1-positive cells) in these cells treated with LPS at 24 (C), 48 (D), 72 (E), and 96 (F) hours are shown. Data are expressed as the percentage of the WT saline group (mean ± SEM, each dot represented an individual field from three independent experiments) with two-way ANOVA with Tukey's multiple comparisons test (WT group versus IL-10KO group: ***p < 0.001; NS indicates no significant difference). **(G–J)** The density of Iba-1 immunostaining in these LPS-treated mixed cells at 24 (G), 48 (H), 72 (I), and 96 (J) hours was measured and quantified. Data are shown as integrated intensity and expressed as the percentage of the WT saline group (mean ± SEM, each dot represented an individual field from three independent experiments) with two-way ANOVA with Tukey's multiple comparisons test (WT group versus IL-10KO group: *p < 0.05; NS indicates no significant difference).

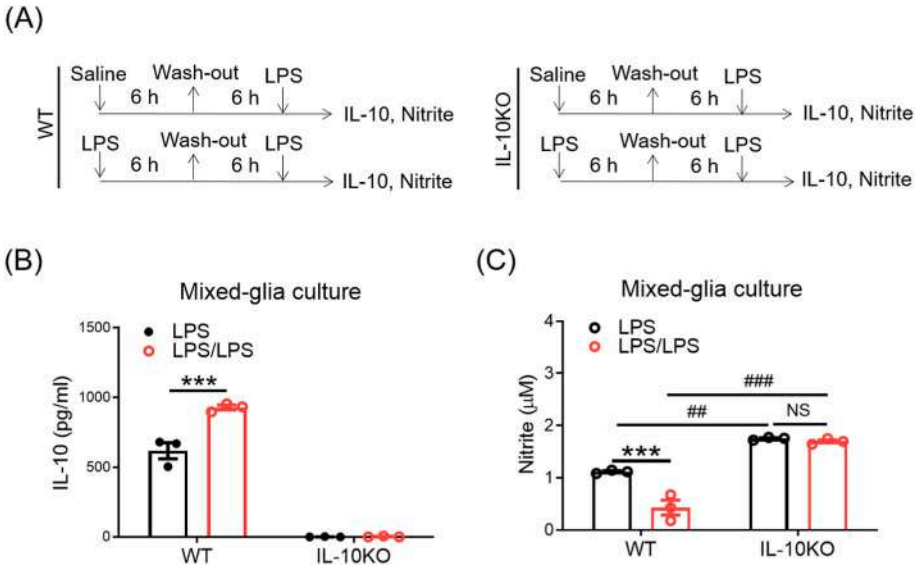


Fig. 5. IL-10KO microglia fail to program endotoxin tolerance of nitrite.
(**A**) Illustration of experimental procedure for studying IL-10's role in nitrite tolerance in LPS-tolerized microglia. WT and IL-10KO mixed-glia cultures were pre-incubated with a vehicle or LPS (15 ng/ml) for 6 h. After 6 h of replacing it with fresh medium, LPS was re-added to the cultures. (**B**) After receiving the ET treatment regimen (LPS versus LPS/LPS) as indicated, supernatant levels of IL-10 in WT and IL-10KO mixed-glia cultures were detected 72 h later by ELISA assay. Data are expressed as the mean ± SEM from three independent experiments in duplicate with two-way ANOVA with Tukey's multiple comparisons test (LPS group versus LPS/LPS group: ***p < 0.001). (**C**) Supernatant levels of nitrite in WT and IL-10KO mixed-glia cultures under an endotoxin treatment regimen were detected 72 h later by a Griess reagent. Data are expressed as the mean ± SEM from three independent experiments in duplicate with two-way ANOVA with Tukey's multiple comparisons test (LPS group versus LPS/LPS group: ***p < 0.001; WT group versus IL-10KO group: ##p < 0.01, ###p < 0.001; NS indicates no significant difference).

expression ($P < 0.001$, $F(3, 8) = 410.4$, one-way ANOVA). Still, they had an increase in IL-10 ($P < 0.001$, $F(3, 8) = 623.9$, one-way ANOVA), showing the anti-inflammatory polarization in tolerized microglia.

According to the results in Fig. 4, IL-10KO microglia had significantly higher nitrite production than WT microglia at 72 h after LPS treatment. Furthermore, the WT and IL-10KO mixed-glia cells were prepared and subjected to the same LPS tolerance treatment regimen. Supernatant levels of IL-10 and nitrite in these cells were measured 72 h after treatment (Fig. 5A). ELISA data showed that the WT mixed-glia cells with the repeated LPS treatment (LPS/LPS group) enhanced IL-10 induction compared to the once LPS-treated cells (LPS group) at 72 h (Fig. 5B, LPS group vs. LPS/LPS group in WT cells: $P < 0.001$; $F(1, 8) = 26.73$, two-way ANOVA). IL-10KO cells had no IL-10 production in the single LPS or repeated LPS treatment. Also, the nitrite level at 72 h after LPS treatment was measured in WT and IL-10KO cells (Fig. 5C). Consistent with Fig. 3, our data revealed that IL-10KO cells produced more nitrite than WT cells at their supernatural level at the late stage of the LPS-induced inflammatory process (WT vs. IL-10KO cells in LPS-treated group: $P < 0.01$; $F(1, 8) = 165.0$, two-way ANOVA), suggesting that endogenous IL-10 induction participated in nitrite resolution. Additionally, in response to this LPS tolerance regimen, the WT cells with the repeated LPS treatment produced lower nitrite than those with the once LPS treatment (LPS group vs. LPS/LPS group in WT cells: $P < 0.001$; $F(1, 8) = 25.13$, two-way ANOVA), indicating that WT cells were capable of developing nitrite tolerance. Importantly, LPS-tolerized IL-10KO cells still produced more amount of supernatant nitrite compared to the corresponding WT cells (WT vs. IL-10KO cells in LPS/LPS group: 0.001; $F(1, 8) = 165.0$, two-way ANOVA) and had similar nitrite levels to those of treated IL-10KO cells with LPS alone, implying that IL-10KO cells failed to develop nitrite tolerance. Our data indicated that the enhancement of endogenous IL-10 induction facilitated the nitrite tolerance, contributing to anti-inflammatory polarization in LPS-tolerized microglia.

4. Discussion

Upon immune stimulation, the induction of individual endogenous cytokines displays a rigid expression profile, leading to a stereotyped neuroinflammatory process consisting of initiation, propagation, and resolution stages. In reality, the interactions among these pro- and anti-inflammatory factors during a neuroinflammatory cascade complexly shape their own expression profiles along with restricted time frames. This study determined how the inductive endogenous IL-10, a potent anti-inflammatory cytokine, regulated the immune status of the neuroinflammatory process and diverse activation of microglia using an in vivo neuroinflammatory model of LPS regimens and in vitro brain cell cultures with once or repeated LPS treatment. Our data revealed the cell-autonomous induction of endogenous IL-10 by LPS-activated and LPS-tolerized microglia. Under a single intraperitoneal 0.3 mg/kg dose of LPS injection, inductive endogenous IL-10 could be detected at the level of serum, liver, and brain tissues in 1 h in WT mice but not IL-10KO mice. Further RT-PCR analysis showed that compared to the WT mice, which had endogenous IL-10 induction, IL-10KO mice had increased the mRNA levels of the LPS-elicited proinflammatory factors (TNF-α, IL-1β, COX-2, and iNOS) in the brains at the stage of immune propagation (3- and 6-h LPS), not initiation (1-h LPS) status. At the immune resolution stage (12-h LPS), the levels of LPS-induced TNF-α, IL-1β, and COX-2 were similarly dropped in both WT and IL-10KO mice's brains. Interestingly, only the LPS-increased iNOS expression was kept high in the IL-10KO group, not the WT group, indicating the deficiency in IL-10 impaired the immune resolution of iNOS, but not TNF-α, IL-1β, and COX-2. Moreover, the Griess reagent assay showed that the production of nitrite, which is generated by a critical enzyme iNOS, is significantly increased at the last stage in LPS-treated IL-10KO microglia in a time and dose-dependent manner. On the other hand, LPS-tolerized IL-10KO microglia failed to program immune tolerance of nitrite, implying that the enhancement of endogenous IL-10 induction participates in developing anti-inflammatory polarization of LPS-tolerized microglia, where nitrite level is reduced, but IL-10 is enhanced. Together, our data demonstrated that microglia-autonomous induction of endogenous IL-10 contributes to immune resolution and tolerance of nitrite.

The LPS injection animal model has been well-documented in determining endotoxemia (Mohammad and Thiemermann, 2020) and inflammatory bowel disease (Williams et al., 2013) and studying neuroinflammation-mediated neurological disorders (da Silva et al., 2024), including depression (Yin et al., 2023) and neurodegenerative diseases (Deng et al., 2020). Depending on administration routes, animal age, sex, endotoxin source, and dose, LPS-induced neuroinflammation models are heterogeneous. In this study, a single IP injection of LPS with a 0.3 mg/kg concentration into young male mice was performed to determine the role of endogenous IL-10 neuroinflammation and the immune tolerance process. Several reports investigated that such a low concentration of LPS IP injection daily for four consecutive days indirectly increased expression levels of glial markers (GFAP and Iba-1) and oxidative stress marker (3-nitrotyrosine) in the olfactory bulb, hippocampus, midbrain, and cerebellum through induced peripheral inflammation-mediated T cells infiltration into the brain. Meanwhile, the knockout TNF-α receptor terminates the peripheral inflammation-mediated microglial activation (Qin et al., 2007). Furthermore, the behavioral tests reveal that mice with this systemically administered LPS display olfactory impairment and anxiety-like behavior as the symptoms of early non-motor Parkinson's disease on days 14–18 post-treatment (Deng et al., 2021). Due to the different ages, the single systemic 0.3 mg/kg LPS dose administration is found to be highly lethal to aged mice (36 % mortality) but not in young and middle mice (Mouton et al., 2012). Our data showed that a single 0.3 mg/kg LPS IP injection could induce a period of short-term, recoverable peripheral and CNS inflammatory events in 12 h, including endogenous IL-10 induction, without any mortality. By contrast, deficiency in IL-10 resulted in the death of all mice within three days after LPS injection (Fig. S1D), emphasizing the crucial role of endogenous IL-10 in safeguarding mice from excessive inflammatory responses. However, the CNS- or microglia-specific IL-10 knockdown animal model is needed to determine further endogenous IL-10's role in the immune resolution and homeostasis of the brain.

As the first defense and inflammatory responder, microglia temporally secrete a broad spectrum and various immunoregulatory factors, including the early-released pro-inflammatory factors and later-on anti-inflammatory IL-10, to protect the neurons against invading pathogens (Hoogland et al., 2015), and terminate the immune initiation and propagation of the neuroinflammatory process for immune resolution and homeostasis (Orihuela et al., 2016). Therefore, elucidating the regulatory mechanism of endogenous IL-10 induction and its impact on glial activation and neuronal survival is crucial for developing anti-inflammatory strategies for neuroinflammation-mediated brain disorders. In addition to well-known intracellular signaling pathways for induction of endogenous IL-10, the early-release proinflammatory TNF-α-PGE2 cascades negatively regulate endogenous IL-10 production through EP2-mediated β-arrestin signaling during an inflammatory process in microglia (Chu et al., 2015). On the other hand, due to its later expression profile, microglia-secreted IL-10 has no effect on the production of LPS-induced TNF-α in the mixed-glia cell model (Kuo et al., 2023). Furthermore, through downregulating NLRP3 inflammasome activation and caspase-1-dependent IL-1β maturation, inductive endogenous IL-10 is capable of preventing IL-1β, chronic neuroinflammation, and dopaminergic neurodegeneration (Gao et al., 2020). Our data revealed that deficiency in IL-10 enhanced the mRNA level of most proinflammatory factors (TNF-α, IL-1β, COX-2, and iNOS) at the immune propagation stage in the mice's brains under LPS IP injection. Interestingly, similar to the WT group, TNF-α, IL-1β, and COX-2 expression in the IL-10KO group went down to basal levels at the immune resolution stage. However, the increased iNOS expression in the

IL-10KO group, not the WT group, still remained at the immune resolution stage as high as at the immune propagation stage. Consistently, the supernatant nitrite level in IL-10KO mixed-glia cells was enhanced at the later time points after LPS treatment. Most recently, a study reports that the early-released IL-10 also plays a role in regulating the appropriate degree of neuroinflammation via the β2-adrenergic signal at the immune initiation stage (Wang et al., 2021). Accordingly, the multi-omics approaches are required for determining the spatial-temporal expression profiles of inductive IL-10 production by the multiple intracellular (Hilliard et al., 2020; Kang et al., 2019; Kwon et al., 2022; Xing et al., 2011) and extracellular (Chu et al., 2015) signaling cascades and its role in immune regulation and innervation at different immune statuses of an inflammatory process in the brain at the levels of mRNA, protein, supernatant, and cell type.

Under repeated LPS stimulations, microglia instigate ("sensitize") the synthesis of anti-inflammatory mediators, such as IL-10 (Chu et al., 2016). In contrast, the production of pro-inflammatory mediators (TNF-α, IL-1β, PGE_2, and nitrite) is decreased ("tolerate"). LPS-tolerized microglia display an anti-inflammatory polarization (Chu et al., 2016) and become refractory to a subsequent endotoxin challenge, a neuroprotective mechanism targeted at preventing excessive toxic damage from cytokine production (Kuo et al., 2023). Our data revealed that increased IL-10 production in the tolerized microglia is critical for their anti-inflammatory polarization by inhibiting nitrite production. In other words, enhanced induction of endogenous IL-10 is required for nitrite tolerance in the tolerized microglia. In addition, a regulatory mechanism study for microglial ET indicates that the intracellular p38 MAPK signaling pathway, rather than the subsequent extracellular IL-10 autocrine cascade, contributes to the tolerance formation to early-released TNF-α (Kuo et al., 2023), suggesting IL-10 induction produced at a later stage does not effectively regulate the production of the earlier inflammatory factors. Noteworthily, the presence of other brain cells, such as neurons and astroglia, regulates the endotoxin tolerance capacity of microglia in the reduction of TNF-α and PGE_2 through M-CSF-mediated ERK signals (Chu et al., 2016) or the cell-cell contacts (Kuo et al., 2022a) to form a self-protective cycle. Whether other brain cells participate in the immune balance of IL-10 (sensitized) and nitrite (desensitized) production in LPS-tolerized microglia is still unclear. Our data showed that microglia alone display a similar expression profile of endogenous IL-10 in both single and repeated LPS treatments compared to microglia with the presence of neurons and astroglia, suggesting a microglia-autonomous induction of endogenous IL-10 in the inflammatory brains. Accordingly, IL-10 and nitrite are mainly produced from the LPS-treated microglia, suggesting microglia develop endotoxin tolerance of nitrite via an IL-10-dependent autocrine mechanism. In addition to immune tolerance, many studies have demonstrated that microglia are capable of developing trained immunity, which is another type of innate immune memory, to enhance subsequent immune responses (Neher and Cunningham, 2019; Wendeln et al., 2018). Interestingly, the trained immunity of microglia enhances the accumulation of AD hallmarks, whereas microglial immune tolerance ameliorates AD pathological hallmarks. Besides the formation of anti-inflammatory polarization in tolerized microglia, it will be interesting to understand the regulatory mechanism of microglia-trained immunity by inductive endogenous IL-10 in neuroinflammation-mediated progressive neurodegenerative diseases.

Although our results are consistent with the role of inductive endogenous IL-10 in nitrite regulation in vivo and in vitro models of LPS-induced neuroinflammation, this study has a few limitations that require awareness. First, due to variability stemming from the effect of female hormones (Liu et al., 2008), only male mice were employed for the LPS immune challenge to increase the sensitivity of the brain neuroinflammation. It would be worthwhile to investigate whether the female counterparts recapture the similar impact of endogenous IL-10 in immune resolution and tolerance. Second, in this study, the preparation of mixed glia cocultures containing 80 % astroglia and 20 % microglia to measure the LPS-induced IL-10 and nitrite production cannot avoid the possible immunoregulatory effects of astroglia or the absence of neurons. However, microglia-enriched cultures do not allow us to measure the levels of IL-10 and nitrite in the inflammatory process in the long term and study the role of IL-10 induction in nitrite tolerance since microglia alone are more susceptible to semi-activated and die one day after cell seeding (Pesti et al., 2024) and fail to develop endotoxin tolerance (Chu et al., 2016). On the other hand, our data revealed that expression patterns of IL-10 induction in LPS once or repeated LPS among neuron-glia, mixed glia, and microglia-enriched cultures were similar, suggesting that neurons and astroglia had no effects on LPS-induced IL-10 production.

The regulatory mechanisms of iNOS expression by IL-10 may include positive transcriptional control of type-2 cationic amino acid transporter (CAT-2) (Huang et al., 2002), suppressor of cytokine signaling 3 (SOCS-3) as a negative feedback regulator (Berlato et al., 2002), and heme oxygenase-1 (HO-1), which is a stress-inducible protein (Lee and Chau, 2002), and activation of STAT3-mediated transcriptional inhibition (Murray, 2005). However, the mechanism by which endogenous IL-10 induction regulates resolution and tolerance of nitric oxide by inhibiting iNOS expression during the inflammatory process in microglia remains to be elucidated. Further study using recombinant IL-10 protein, IL-10 neutralizing antibody, or inhibitors for IL-10 receptor and its downstream signaling molecules, such as STAT3 and SOCS3, is required. Finally, because IL-10 whole-body knockout mice display immediate severe mortality under a single intraperitoneal injection of LPS at such a small amount concentration (0.3 mg/kg), the establishment of brain tissue- or microglia-specific IL-10KO mice is needed to determine further the pathophysiological role of inductive endogenous IL-10 in CNS or microglia at the behavioral, cellular, and molecular levels in a future study.

5. Conclusions

To summarize, using in vitro and in vivo LPS-induced inflammation or immune tolerance models, our research demonstrates that the cell-autonomous induction of endogenous IL-10 in microglial activation is critical for dampening brain immune responses, particularly in nitric oxide resolution and tolerance, contributing to the formation of anti-inflammatory microglia. Targeting the negative feedback loop from inducible endogenous IL-10 to reduce nitrite may be a promising microglia-based therapeutic strategy for inflammation-mediated neurodevelopmental and neurodegenerative disorders.

CRediT authorship contribution statement

Hsing-Chun Kuo: Writing – original draft, Resources, Data curation. **Jia-Shing Chen:** Supervision, Methodology. **Chun-Nun Chao:** Writing – original draft, Resources, Conceptualization. **Kam-Fai Lee:** Methodology, Investigation, Data curation. **Yi-Te Huang:** Formal analysis, Data curation. **Pin-Cheng Mao:** Methodology, Data curation. **Tzu-Chia Lin:** Methodology, Data curation. **Shu-Chen Chiu:** Methodology. **Ya-Ling Huang:** Writing – original draft, Resources, Conceptualization. **Chun-Hsien Chu:** Writing – review & editing, Validation, Supervision, Funding acquisition, Conceptualization.

Ethics approval

The study was conducted according to the guidelines of the Declaration of Helsinki, and approved by the Animal Care and Use Committee of Chang Gung University of Science and Technology.

Availability of data and materials

All data and materials, as well as software application information, are available in the manuscript or are available from the corresponding

author upon reasonable request.

Funding

This work was supported by grants NSTC 111-2320-B-006-018, NSTC 112-2320-B-006-035, and NSTC 113-2320-B-006-037 from the Taiwan National Science and Technology Council. This study was supported by the grants BMRPD42, CMRPF6N0031, CMRPF6N0032, CMRPF6N0033, and ZRRPF6N0011 from Chang Gung Memorial Hospital, Chiayi, Taiwan, and Chang Gung University of Science and Technology, Chia-Yi Campus, Taiwan.

Declaration of competing interest

The authors declare no competing financial interests.

Acknowledgments

We thank Professor Jau-Shyong Hong for supporting this work and National Laboratory Animal Center (NLAC), NARLabs, Taiwan for technical support in contract breeding and testing services.

Appendix A. Supplementary data

Supplementary data to this article can be found online at https://doi.org/10.1016/j.bbih.2025.101094.

Data availability

Data will be made available on request.

References

Berlato, C., Cassatella, M.A., Kinjyo, I., Gatto, L., Yoshimura, A., Bazzoni, F., 2002. Involvement of suppressor of cytokine signaling-3 as a mediator of the inhibitory effects of IL-10 on lipopolysaccharide-induced macrophage activation. J. Immunol. 168, 6404–6411.

Block, M.L., Zecca, L., Hong, J.S., 2007. Microglia-mediated neurotoxicity: uncovering the molecular mechanisms. Nat. Rev. Neurosci. 8, 57–69.

Broom, L., Marinova-Mutafchieva, L., Sadeghian, M., Davis, J.B., Medhurst, A.D., Dexter, D.T., 2011. Neuroprotection by the selective iNOS inhibitor GW274150 in a model of parkinson disease. Free Radic. Biol. Med. 50, 633–640.

Brown, G.C., 2007. Mechanisms of inflammatory neurodegeneration: iNOS and NADPH oxidase. Biochem. Soc. Trans. 35, 1119–1121.

Burguillos, M.A., Deierborg, T., Kavanagh, E., Persson, A., Hajji, N., Garcia-Quintanilla, A., Cano, J., Brundin, P., Englund, E., Venero, J.L., Joseph, B., 2011. Caspase signalling controls microglia activation and neurotoxicity. Nature 472, 319–324.

Chu, C.H., Chen, J.S., Chan, Y.L., Lu, W.J., Huang, Y.T., Mao, P.C., Sze, C.I., Sun, H.S., 2023. TIAM2S-positive microglia enhance inflammation and neurotoxicity through soluble ICAM-1-mediated immune priming. FASEB J. 37, e23242.

Chu, C.H., Chen, S.H., Wang, Q., Langenbach, R., Li, H., Zeldin, D., Chen, S.L., Wang, S., Gao, H., Lu, R.B., Hong, J.S., 2015. PGE2 inhibits IL-10 production via EP2-Mediated beta-arrestin signaling in neuroinflammatory condition. Mol. Neurobiol. 52, 587–600.

Chu, C.H., Wang, S., Li, C.L., Chen, S.H., Hu, C.F., Chung, Y.L., Chen, S.L., Wang, Q., Lu, R.B., Gao, H.M., Hong, J.S., 2016. Neurons and astroglia govern microglial endotoxin tolerance through macrophage colony-stimulating factor receptor-mediated ERK1/2 signals. Brain Behav. Immun. 55, 260–272.

da Silva, A.A.F., Fiadeiro, M.B., Bernardino, L.I., Fonseca, C.S.P., Baltazar, G.M.F., Cristovao, A.C.B., 2024. Lipopolysaccharide-induced animal models for neuroinflammation - an overview. J. Neuroimmunol. 387, 578273.

Dansokho, C., Heneka, M.T., 2018. Neuroinflammatory responses in alzheimer's disease. J. Neural Transm. 125, 771–779.

Deng, I., Corrigan, F., Zhai, G., Zhou, X.F., Bobrovskaya, L., 2020. Lipopolysaccharide animal models of parkinson's disease: recent progress and relevance to clinical disease. Brain Behav Immun Health 4, 100060.

Deng, I., Wiese, M.D., Zhou, X.F., Bobrovskaya, L., 2021. The efficacy of systemic administration of lipopolysaccharide in modelling pre-motor parkinson's disease in C57BL/6 mice. Neurotoxicology 85, 254–264.

Dong, H., Zhang, X., Duan, Y., He, Y., Zhao, J., Wang, Z., Wang, J., Li, Q., Fan, G., Liu, Z., Shen, C., Zhang, Y., Yu, M., Fei, J., Huang, F., 2024. Hypoxia inducible factor-1alpha regulates microglial innate immune memory and the pathology of parkinson's disease. J. Neuroinflammation 21, 80.

Foey, A.D., Parry, S.L., Williams, L.M., Feldmann, M., Foxwell, B.M., Brennan, F.M., 1998. Regulation of monocyte IL-10 synthesis by endogenous IL-1 and TNF-alpha: role of the p38 and p42/44 mitogen-activated protein kinases. J. Immunol. 160, 920–928.

Gao, Y., Tu, D., Yang, R., Chu, C.H., Hong, J.S., Gao, H.M., 2020. Through reducing ROS production, IL-10 suppresses Caspase-1-Dependent IL-1beta maturation, thereby preventing chronic neuroinflammation and neurodegeneration. Int. J. Mol. Sci. 21.

Heales, S.J., Bolanos, J.P., Stewart, V.C., Brookes, P.S., Land, J.M., Clark, J.B., 1999. Nitric oxide, mitochondria and neurological disease. Biochim. Biophys. Acta 1410, 215–228.

Heyen, J.R., Ye, S., Finck, B.N., Johnson, R.W., 2000. Interleukin (IL)-10 inhibits IL-6 production in microglia by preventing activation of NF-kappaB. Brain research. Mol. Brain Res. 77, 138–147.

Hilliard, A., Mendonca, P., Soliman, K.F.A., 2020. Involvement of NFkB and MAPK signaling pathways in the preventive effects of Ganoderma lucidum on the inflammation of BV-2 microglial cells induced by LPS. J. Neuroimmunol. 345, 577269.

Hoogland, I.C., Houbolt, C., van Westerloo, D.J., van Gool, W.A., van de Beek, D., 2015. Systemic inflammation and microglial activation: systematic review of animal experiments. J. Neuroinflammation 12, 114.

Huang, C.J., Stevens, B.R., Nielsen, R.B., Slovin, P.N., Fang, X., Nelson, D.R., Skimming, J.W., 2002. Interleukin-10 inhibition of nitric oxide biosynthesis involves suppression of CAT-2 transcription. Nitric Oxide 6, 79–84.

Kang, J.B., Park, D.J., Shah, M.A., Kim, M.O., Koh, P.O., 2019. Lipopolysaccharide induces neuroglia activation and NF-kappaB activation in cerebral cortex of adult mice. Lab Anim. Res. 35, 19.

Kremlev, S.G., Palmer, C., 2005. Interleukin-10 inhibits endotoxin-induced pro-inflammatory cytokines in microglial cell cultures. J. Neuroimmunol. 162, 71–80.

Kuhn, R., Lohler, J., Rennick, D., Rajewsky, K., Muller, W., 1993. Interleukin-10-deficient mice develop chronic enterocolitis. Cell 75, 263–274.

Kuo, H.C., Chen, S.L., Chiu, S.C., Lee, K.F., Chu, C.H., 2023. Tolerized microglia protect neurons against endotoxin-induced TNF-Alpha production via an LBP-dependent intracellular p38 MAPK signaling pathway. Inflammation 46, 2011–2023.

Kuo, H.C., Lee, K.F., Chen, S.L., Chiu, S.C., Lee, L.Y., Chen, W.P., Chen, C.C., Chu, C.H., 2022a. Neuron-Microglia Contacts Govern the PGE2 Tolerance through TLR4-Mediated de Novo Protein Synthesis. Biomedicines 10.

Kuo, H.C., Lee, K.F., Chen, S.L., Chiu, S.C., Lee, L.Y., Chen, W.P., Chen, C.C., Chu, C.H., 2022b. Neuron-Microglia Contacts Govern the PGE(2) Tolerance through TLR4-Mediated de Novo Protein Synthesis. Biomedicines 10.

Kwon, J., Arsenis, C., Suessmilch, M., McColl, A., Cavanagh, J., Morris, B.J., 2022. Differential effects of toll-like receptor activation and differential mediation by MAP kinases of immune responses in microglial cells. Cell. Mol. Neurobiol. 42, 2655–2671.

Lee, T.S., Chau, L.Y., 2002. Heme oxygenase-1 mediates the anti-inflammatory effect of interleukin-10 in mice. Nat. Med. 8, 240–246.

Liu, B., Du, L., Hong, J.S., 2000. Naloxone protects rat dopaminergic neurons against inflammatory damage through inhibition of microglia activation and superoxide generation. J. Pharmacol. Exp. Therapeut. 293, 607–617.

Liu, B., Gao, H.M., Wang, J.Y., Jeohn, G.H., Cooper, C.L., Hong, J.S., 2002. Role of nitric oxide in inflammation-mediated neurodegeneration. Ann. N. Y. Acad. Sci. 962, 318–331.

Liu, Y., Qin, L., Wilson, B., Wu, X., Qian, L., Granholm, A.C., Crews, F.T., Hong, J.S., 2008. Endotoxin induces a delayed loss of TH-IR neurons in substantia nigra and motor behavioral deficits. Neurotoxicology 29, 864–870.

Mitrovic, B., Ignarro, L.J., Montestruque, S., Smoll, A., Merrill, J.E., 1994. Nitric oxide as a potential pathological mechanism in demyelination: its differential effects on primary glial cells in vitro. Neuroscience 61, 575–585.

Mohammad, S., Thiemermann, C., 2020. Role of metabolic endotoxemia in systemic inflammation and potential interventions. Front. Immunol. 11, 594150.

Mouton, P.R., Kelley-Bell, B., Tweedie, D., Spangler, E.L., Perez, E., Carlson, O.D., Short, R.G., deCabo, R., Chang, J., Ingram, D.K., Li, Y., Greig, N.H., 2012. The effects of age and lipopolysaccharide (LPS)-Mediated peripheral inflammation on numbers of central catecholaminergic neurons. Neurobiol. Aging 33, 423 e427–436.

Murray, P.J., 2005. The primary mechanism of the IL-10-regulated antiinflammatory response is to selectively inhibit transcription. Proc. Natl. Acad. Sci. U. S. A. 102, 8686–8691.

Neher, J.J., Cunningham, C., 2019. Priming microglia for innate immune memory in the brain. Trends Immunol. 40, 358–374.

Orihuela, R., McPherson, C.A., Harry, G.J., 2016. Microglial M1/M2 polarization and metabolic states. Br. J. Pharmacol. 173, 649–665.

Pesti, I., Legradi, A., Farkas, E., 2024. Primary microglia cell cultures in translational research: strengths and limitations. J. Biotechnol. 386, 10–18.

Qian, L., Block, M.L., Wei, S.J., Lin, C.F., Reece, J., Pang, H., Wilson, B., Hong, J.S., Flood, P.M., 2006. Interleukin-10 protects lipopolysaccharide-induced neurotoxicity in primary midbrain cultures by inhibiting the function of NADPH oxidase. J. Pharmacol. Exp. Therapeut. 319, 44–52.

Qin, L., Wu, X., Block, M.L., Liu, Y., Breese, G.R., Hong, J.S., Knapp, D.J., Crews, F.T., 2007. Systemic LPS causes chronic neuroinflammation and progressive neurodegeneration. Glia 55, 453–462.

Rodriguez, A.M., Rodriguez, J., Giambartolomei, G.H., 2022. Microglia at the crossroads of pathogen-induced neuroinflammation. ASN Neuro 14, 17590914221104566.

Rosenblum, M.D., Remedios, K.A., Abbas, A.K., 2015. Mechanisms of human autoimmunity. J. Clin. Investig. 125, 2228–2233.

Sabat, R., Grutz, G., Warszawska, K., Kirsch, S., Witte, E., Wolk, K., Geginat, J., 2010. Biology of interleukin-10. Cytokine Growth Factor Rev. 21, 331–344.

Saha, R.N., Pahan, K., 2006. Regulation of inducible nitric oxide synthase gene in glial cells. Antioxidants Redox Signal. 8, 929–947.

Saraiva, M., O'Garra, A., 2010. The regulation of IL-10 production by immune cells. Nat. Rev. Immunol. 10, 170–181.
Strle, K., Zhou, J.H., Shen, W.H., Broussard, S.R., Johnson, R.W., Freund, G.G., Dantzer, R., Kelley, K.W., 2001. Interleukin-10 in the brain. Crit. Rev. Immunol. 21, 427–449.
Swanson, A., Wolf, T., Sitzmann, A., Willette, A.A., 2018. Neuroinflammation in alzheimer's disease: pleiotropic roles for cytokines and neuronal pentraxins. Behav. Brain Res. 347, 49–56.
Tewari, D., Sah, A.N., Bawari, S., Nabavi, S.F., Dehpour, A.R., Shirooie, S., Braidy, N., Fiebich, B.L., Vacca, R.A., Nabavi, S.M., 2021. Role of nitric oxide in neurodegeneration: function, regulation, and inhibition. Curr. Neuropharmacol. 19, 114–126.
Tone, M., Powell, M.J., Tone, Y., Thompson, S.A., Waldmann, H., 2000. IL-10 gene expression is controlled by the transcription factors Sp1 and Sp3. J. Immunol. 165, 286–291.
Trovato Salinaro, A., Pennisi, M., Di Paola, R., Scuto, M., Crupi, R., Cambria, M.T., Ontario, M.L., Tomasello, M., Uva, M., Maiolino, L., Calabrese, E.J., Cuzzocrea, S., Calabrese, V., 2018. Neuroinflammation and neurohormesis in the pathogenesis of alzheimer's disease and Alzheimer-linked pathologies: modulation by nutritional mushrooms. Immun. Ageing 15, 8.
Wang, Y., Yu, P., Li, Y., Zhao, Z., Wu, X., Zhang, L., Feng, J., Hong, J.S., 2021. Early-released Interleukin-10 significantly inhibits lipopolysaccharide-elicited neuroinflammation in vitro. Cells 10.
Wendeln, A.C., Degenhardt, K., Kaurani, L., Gertig, M., Ulas, T., Jain, G., Wagner, J., Hasler, L.M., Wild, K., Skodras, A., Blank, T., Staszewski, O., Datta, M., Centeno, T. P., Capece, V., Islam, M.R., Kerimoglu, C., Staufenbiel, M., Schultze, J.L., Beyer, M., Prinz, M., Jucker, M., Fischer, A., Neher, J.J., 2018. Innate immune memory in the brain shapes neurological disease hallmarks. Nature 556, 332–338.
Williams, J.M., Duckworth, C.A., Watson, A.J., Frey, M.R., Miguel, J.C., Burkitt, M.D., Sutton, R., Hughes, K.R., Hall, L.J., Caamano, J.H., Campbell, B.J., Pritchard, D.M., 2013. A mouse model of pathological small intestinal epithelial cell apoptosis and shedding induced by systemic administration of lipopolysaccharide. Dis. Model. Mech. 6, 1388–1399.
Xing, B., Bachstetter, A.D., Van Eldik, L.J., 2011. Microglial p38alpha MAPK is critical for LPS-Induced neuron degeneration, through a mechanism involving TNFalpha. Mol. Neurodegener. 6, 84.
Yin, R., Zhang, K., Li, Y., Tang, Z., Zheng, R., Ma, Y., Chen, Z., Lei, N., Xiong, L., Guo, P., Li, G., Xie, Y., 2023. Lipopolysaccharide-induced depression-like model in mice: meta-analysis and systematic evaluation. Front. Immunol. 14, 1181973.
Zhang, Q., Cao, X., 2021. Epigenetic remodeling in innate immunity and inflammation. Annu. Rev. Immunol. 39, 279–311.
Zhang, X., Kracht, L., Lerario, A.M., Dubbelaar, M.L., Brouwer, N., Wesseling, E.M., Boddeke, E., Eggen, B.J.L., Kooistra, S.M., 2022. Epigenetic regulation of innate immune memory in microglia. J. Neuroinflammation 19, 111.

Expert Opinion on Drug Discovery

ISSN: 1746-0441 (Print) 1746-045X (Online) Journal homepage: www.tandfonline.com/journals/iedc20

Animal models of psoriasis for novel drug discovery: a literature update

Zih-Chan Lin, Shih-Chun Yang, Thi Thu Phuong Tran & Jia-You Fang

To cite this article: Zih-Chan Lin, Shih-Chun Yang, Thi Thu Phuong Tran & Jia-You Fang (2025) Animal models of psoriasis for novel drug discovery: a literature update, Expert Opinion on Drug Discovery, 20:9, 1193-1208, DOI: 10.1080/17460441.2025.2528959

To link to this article: https://doi.org/10.1080/17460441.2025.2528959

Published online: 09 Jul 2025.

Submit your article to this journal

Article views: 86

View related articles

View Crossmark data

Full Terms & Conditions of access and use can be found at
https://www.tandfonline.com/action/journalInformation?journalCode=iedc20

EXPERT OPINION ON DRUG DISCOVERY
2025, VOL. 20, NO. 9, 1193–1208
https://doi.org/10.1080/17460441.2025.2528959

Taylor & Francis
Taylor & Francis Group

REVIEW

Check for updates

Animal models of psoriasis for novel drug discovery: a literature update

Zih-Chan Lin[a], Shih-Chun Yang[b], Thi Thu Phuong Tran [c] and Jia-You Fang[d,e,f]

[a]Chronic Diseases and Health Promotion Research Center, Chang Gung University of Science and Technology, Puzi, Taiwan; [b]Department of Microbiology, Soochow University, Taipei, Taiwan; [c]Department of Life Sciences, University of Science and Technology of Hanoi, Hanoi, Vietnam; [d]Pharmaceutics Laboratory, Graduate Institute of Natural Products, Chang Gung University, Taoyuan, Taiwan; [e]Research Center for Food and Cosmetic Safety and Center for Drug Research and Development, Chang Gung University of Science and Technology, Taoyuan, Taiwan; [f]Department of Anesthesiology, Chang Gung Memorial Hospital, Taoyuan, Taiwan

ABSTRACT

Introduction: Psoriasis is a chronic, immune-mediated inflammatory skin disorder with a multifactorial pathogenesis involving keratinocyte proliferation, dysregulated immune responses, and vascular remodeling. The development of effective therapeutics mainly relies on preclinical models that can reproduce disease-relevant mechanisms.

Areas covered: This review outlines current in vivo psoriasis models, including spontaneous mutation models, transgenic and knockout mice, xenotransplantation systems, and cytokine-induced and imiquimod-induced models. Each model is evaluated for its ability to replicate key histological and immunological features of human psoriasis, such as acanthosis, immune cell infiltration, and cytokine network activation. The utility of CRISPR/Cas9 gene editing in generating targeted models is also discussed, thus highlighting its potential use for mechanistic studies. Finally, this review also emphasizes the limitations in translational applicability and the need for multimodel validation strategies regarding psoriasis. This article was based on a comprehensive literature search using PubMed, Scopus, and Google Scholar databases, covering publications from January 2015 to March 2025.

Expert opinion: Despite extensive model development, no single system fully mimics human psoriatic disease. The imiquimod-induced model remains widely used due to its practicality, although it better reflects acute inflammation compared with chronic pathology. The combination of complementary models and the incorporation of human-derived tissues or immune components may improve translational relevance. Advances in genome editing and humanized systems are likely to shape the future of psoriasis research and therapeutic discovery.

ARTICLE HISTORY
Received 10 April 2025
Accepted 30 June 2025

KEYWORDS
Psoriasis; animal model; imiquimod; CRISPR/Cas9; keratinocyte; xenograft

1. Introduction

Psoriasis is a chronic, immune-mediated inflammatory skin disease characterized by the formation of erythematous plaques covered with silvery white scales, and it affects approximately 2–3% of the global population [1]. The disease manifests due to abnormal keratinocyte proliferation, disturbed epidermal differentiation, and intense immune cell infiltration, which primarily involves T helper (Th)1, Th17, and Th22 cells. The pathogenesis of psoriasis is complex and multifactorial, with contributions from genetic, environmental, and immunological factors [2]. Genome-wide association studies (GWASs) have identified multiple susceptibility loci, including genes involved in antigen presentation, cytokine signaling, and immune regulation, thereby underscoring the genetic predisposition to the disease [3]. At the molecular level, psoriasis is driven by hyperactivation of keratinocytes and immune cells, thus leading to a dysregulated cytokine network. The interleukin (IL)-23/IL-17 axis plays a central role in pathogenesis, in which IL-23 produced by dendritic cells (DCs) promotes the expansion of IL-17-producing T cells, which subsequently drive keratinocyte proliferation and inflammatory cytokine production [4]. This cascade perpetuates a cycle of inflammation and epidermal hyperplasia, which eventually leads to the development of the characteristic psoriatic lesions. Despite advances in biologic therapies targeting key cytokines such as tumor necrosis factor (TNF)-α, IL-17, and IL-23, many patients experience incomplete responses, thereby highlighting the need for further research into the underlying mechanisms of psoriasis and the development of novel therapeutic interventions [5].

Preclinical models in psoriasis research play crucial roles in elucidating the complex pathophysiology of psoriasis and facilitating the development of new therapeutic strategies. Since the discovery of psoriasis as an immune-mediated disease, various preclinical models have been developed to mimic distinct aspects of the condition, thereby allowing researchers to investigate molecular mechanisms, evaluate potential drug targets, and predict therapeutic efficacy [6]. However, psoriasis is a unique human disease, and no single animal model can fully replicate its complexity. Therefore, a combination of complementary models is often employed to demonstrate different aspects of disease pathogenesis and treatment responses. Preclinical models of psoriasis can be broadly classified into spontaneous models, genetically engineered models, xenotransplantation models, and induced models.

CONTACT Jia-You Fang fajy@mail.cgu.edu.tw Pharmaceutics Laboratory, Graduate Institute of Natural Products, Chang Gung University, 259 wen-Hwa 1st Road, Taoyuan, Kweishan 333, Taiwan

© 2025 Informa UK Limited, trading as Taylor & Francis Group

Article highlights

- Despite extensive model development, there is yet to be any single system that can fully mimic human psoriatic disease.
- Imiquimod-induced mice model reflects acute psoriatic inflammation.
- K5-Stat3c mice mimic epidermal hyperplasia, cytokine dysregulation.
- Xenograft models use human psoriatic skin in immunodeficient mice.
- Emerging models integrate CRISPR, organoids, and humanized systems
- Advances in genome editing and humanized systems will likely shape the future of psoriasis therapeutic discovery.

Spontaneous models, such as the flaky skin (fsn/fsn) mouse and chronic proliferative dermatitis mouse (cpdm/cpdm), develop psoriasis-like phenotypes due to naturally occurring genetic mutations. These models exhibit features such as epidermal hyperplasia, immune cell infiltration, and increased vascularization, thus providing valuable insights into the genetic and immune components of psoriasis [7]. Genetically engineered models involve the overexpression or deletion of specific genes implicated in psoriasis, such as IL-17, IL-23, and TNF-α, which allows for the elucidation of individual pathways contributing to disease pathogenesis. Transgenic models, including K14-IL-17A and keratin (K)5-signal transducer and activator of transcription (Stat)3c mice, have been instrumental in elucidating the role of cytokines and signaling pathways in psoriasis [8]. Additionally, xenotransplantation models, in which human psoriatic skin is grafted onto immunodeficient mice, provide a unique platform for investigating human-specific immune responses and testing biologic therapies in a controlled environment. These models allow researchers to assess the effects of therapeutic agents on human tissues while preserving the complex cellular architecture and immune interactions of psoriatic lesions [9]. However, challenges such as graft heterogeneity and immune incompatibility limit the widespread application of these models. Induced models, such as the imiquimod-induced psoriasis model and cytokine injection models, have gained prominence due to their reproducibility and ability to simulate key histological and immunological features of psoriasis. Specifically, the imiquimod model mimics the IL-23/IL-17 axis, which makes this model a popular choice for evaluating anti-inflammatory agents [10]. The landscape of psoriasis research has evolved significantly with the advent of novel genetic, cellular, and molecular techniques. Advances in genetic engineering, particularly regarding the application of clustered regularly interspaced short palindromic repeats (CRISPR)/Cas9 technology, have facilitated the development of targeted knockout and knock-in models that more closely mimic human psoriasis [11]. These models have enabled the identification of critical mediators of inflammation and have provided a platform for the testing of potential therapeutic targets. Additionally, xenotransplantation models using human psoriatic skin grafts have allowed researchers to study human-specific immune responses and assess the efficacy of biologic agents.

Despite these advancements, significant challenges remain. Although mouse models are useful for investigating immune responses and cytokine interactions, they often fail to replicate the intricate architecture of human skin, which leads to discrepancies in disease progression and treatment outcomes. Moreover, the immune system of mice differs substantially from that of humans, thus limiting the translational relevance of some findings. Furthermore, although they are more physiologically relevant, xenotransplantation models are labor intensive and costly, with reported variabilities in graft survival and immune responses posing additional challenges.

This review aims to provide a comprehensive and critical analysis of recent advancements in preclinical models of psoriasis, with specific focuses on their strengths, limitations, and translational relevance. The primary objective of this review involves a summary of the evolution of psoriasis models. In this section, we provide an overview of the historical progression of psoriasis models (from the advent of spontaneous and genetically engineered models to more innovative xenotransplantation and induced models). We also evaluate the strengths and limitations of the currently used models. Additionally, this review describes a detailed examination of the translational relevance of each model, with a focus on their ability to replicate key histological, immunological, and molecular features of psoriasis. Another aim of this review is to discuss novel approaches and emerging technologies regarding psoriasis evaluation platforms. These approaches include the exploration of emerging models, including organ-on-a-chip systems and 3D skin models, as well as their potential to complement traditional animal models. Finally, we identify future directions for model development. Suggestions are made to increase animal model validity and improve the predictive accuracy of preclinical studies, with the aim of facilitating the translation of research findings into clinical applications. Moreover, this review synthesizes insights from recent studies and addresses the strengths and weaknesses of existing models. Ultimately, this work aims to accelerate the development of effective therapies that address the unmet needs of patients with psoriasis.

2. Pathophysiology of psoriasis and the need for animal models

2.1. Key molecular and immunological mechanisms of psoriasis

Psoriasis is a chronic inflammatory skin disorder characterized by an intricate interplay between the innate and adaptive immune systems. It primarily involves hyperproliferation of keratinocytes, abnormal differentiation, and inflammation, thus leading to the development of erythematous and scaly plaques. Immunopathogenesis is primarily driven by dysregulated interactions between T cells, DCs, and keratinocytes, which perpetuate a chronic inflammatory loop [12]. A key factor regarding the pathogenesis of psoriasis is the IL-23/IL-17 axis. DCs release proinflammatory cytokines such as IL-12 and IL-23, which polarize naïve T cells into Th1 and Th17 effector cells. Th17 cells secrete IL-17A, IL-17F, and IL-22, which drive keratinocyte proliferation and inflammatory responses [13]. IL-17A induces the expression of chemokine (C-X-C motif) ligand 1 (CXCL1), CXCL2, and CXCL8, thereby attracting neutrophils to the site of inflammation. Additionally, IL-22 promotes acanthosis and epidermal hyperplasia by stimulating keratinocytes. TNF-α and interferon (IFN)-γ further enhance the inflammatory cascade [14]. Additionally,

complex immune interactions are fueled by autoantigens such as cathelicidin (LL-37), which form complexes with nucleic acids and activate plasmacytoid dendritic cells (pDCs) via toll-like receptor (TLR)7 and TLR9. This cascade stimulates pDCs to produce IFN-α, which further activates myeloid DCs; this activation correspondingly increases the production of IL-23 and TNF-α, thereby maintaining the chronic inflammation observed in psoriatic lesions. DC activation is one of several proposed initiating events in psoriasis, which may differ across disease subtypes and patients (Figure 1) [15]. Recent investigations have highlighted a broader role for innate immune cells, particularly macrophages, in psoriasis pathogenesis. Beyond their classical role in phagocytosis, macrophages actively contribute to disease progression by producing pro-inflammatory cytokines such as IL-1β, IL-6, and TNF-α, which amplify the IL-23/IL-17 axis and promote keratinocyte hyperproliferation. Notably, M1-polarized macrophages are enriched in lesional psoriatic skin and have been shown to sustain chronic inflammation via continuous cytokine secretion and interaction with Th17 cellsThe Experimental Animal … . Additionally, pharmacological depletion or modulation of macrophage activity attenuates psoriasiform features in preclinical models, underscoring their therapeutic relevance [16,17]. These findings support a model of psoriasis wherein macrophages act as pivotal amplifiers of inflammation and underscore the necessity of targeting both innate and adaptive immune pathways for effective intervention.

2.2. Challenges in developing effective treatments

Despite significant progress in understanding the immunopathogenesis of psoriasis, the development of curative therapies remains challenging. Current therapies target key cytokines such as IL-17, IL-23, and TNF-α; however, they are often limited by incomplete responses, relapses, and adverse effects. Biologics such as secukinumab (anti-IL-17A), ustekinumab (anti-IL-12/23), and etanercept (anti-TNF-α) have demonstrated efficacy but are not universally effective in all patients. Additionally, a significant subset of patients exhibit partial or no response to treatment due to variations in the immune response or genetic background [18]. Moreover, the heterogeneity of psoriasis, which is characterized by various clinical phenotypes and distinct molecular subtypes, complicates the identification of a universal therapeutic approach. These challenges are further exacerbated by the presence of comorbidities such as psoriatic arthritis, metabolic syndrome, and cardiovascular disease, which require targeted and personalized therapeutic strategies [19].

2.3. The importance of animal models in bridging the gap between in vitro studies and clinical applications

Animal models play an indispensable role in bridging the gap between in vitro studies and clinical applications, as they allow for the investigation of psoriasis pathogenesis in a controlled

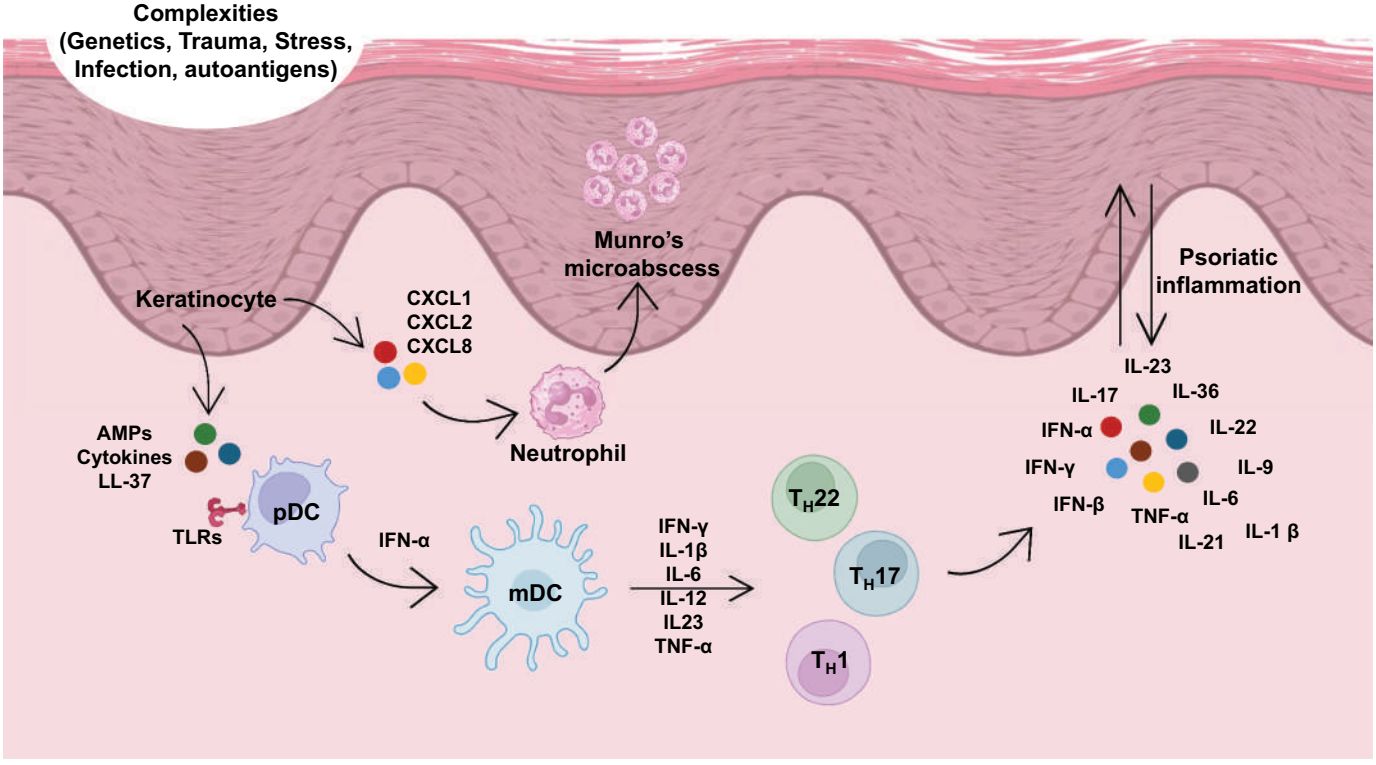


Figure 1. Overview of the core molecular and immune pathways involved in psoriasis. The disease is initiated by the activation of dendritic cells (DCs), which release cytokines such as TNF-α, IL-12, and IL-23. These signals promote the polarization of naïve T cells into Th1 and Th17 subsets. Th1 cells produce IFN-γ, which enhances keratinocyte (KC) activation and inflammation, while Th17 cells release IL-17A/F and IL-22, driving keratinocyte hyperproliferation and impaired differentiation. Activated keratinocytes, in turn, release pro-inflammatory mediators, chemokines, and antimicrobial peptides, which further attract immune cells to the skin. These interconnected signaling events form a chronic inflammatory loop, with the IL-23/IL-17 axis playing a central pathogenic role and serving as a primary therapeutic target. DC activation is one of several proposed initiating events in psoriasis, which may differ across disease subtypes and patients. Created in BioRender. lin, Z. (2025) https://BioRender.com/1fczjra.

environment. Ethical limitations and the difficulty of obtaining human biological samples limit the scope of fundamental and clinical research on human psoriasis, thus making animal models an invaluable tool for understanding disease mechanisms and testing novel therapies [20]. Although psoriasis does not naturally occur in animals, several animal models have been developed to replicate key features of this disease. These models include spontaneous, genetically engineered, xenotransplantation, and directly induced murine models. Among these models, imiquimod-induced dermatitis in mice is one of the most widely used models and mimics the IL-23/IL-17 axis activation and keratinocyte hyperproliferation that are characteristic features of psoriasis [21]. Genetically modified models, such as K5-Stat3C and K14-vascular endothelial growth factor (VEGF) transgenic mice, have been pivotal in elucidating the roles of cytokines, vascularization, and immune cell recruitment in psoriasis-like inflammation [22,23]. However, despite their utility, no single model perfectly reproduces the complex phenotype of human psoriasis. Most models reflect only partial aspects of the disease, such as epidermal hyperplasia, inflammatory infiltration, or microabscess formation. Therefore, careful considerations are necessary when extrapolating data from animal models to human psoriasis [24]. Importantly, the genetic background of mouse strains plays a pivotal role in modulating the psoriasiform phenotype. For example, the CD18 hypomorphic model exhibits marked epidermal hyperplasia, microabscess formation, and immune infiltration only when maintained on the PL/J background, while such features are absent on C57BL/6 or 129S/V strains. Similarly, in the imiquimod-induced model, C57BL/6 mice display more severe erythema, acanthosis, and heightened Th17 responses than BALB/c or DBA/1 mice. These strain-dependent differences impact cytokine expression, neutrophil recruitment, and vascular remodeling, underscoring the necessity of careful strain selection in preclinical psoriasis studies.

2.4. Limitations of animal models and future perspectives

Although animal models have advanced our understanding of psoriasis and facilitated the development of targeted biologics, they possess limitations that must be acknowledged. For example, differences between human and murine immune systems, skin anatomy, and microbiomes often hinder the translation of preclinical findings to clinical applications. Furthermore, most animal models rely on genetic modifications or cytokine overexpression, which may not fully replicate the polygenic and multifactorial nature of human psoriasis [25]. Future research directions should involve improvements in the fidelity of animal models by incorporating humanized skin grafts and advanced technologies such as organ-on-a-chip platforms. These approaches may provide a more accurate reflection of human immune responses and pathophysiology, thereby enhancing the predictive value of preclinical studies. Despite inherent challenges, animal models remain essential for unraveling the complex immunopathogenesis of psoriasis and developing novel therapeutic strategies. Furthermore, the refinement of these models to better reflect human disease remains a priority for advancing psoriasis research and improving clinical outcomes [26,27].

3. Overview of current animal models of psoriasis

3.1. Classification of psoriasis models

Animal models play pivotal roles in understanding psoriasis pathogenesis and exploring potential therapeutic targets. Psoriasis models can be broadly classified into induced models and genetically modified models, with each model exhibiting distinct advantages and limitations.

3.1.1. Induced models

Induced models simulate psoriasiform inflammation via the topical application of irritants, injection of cytokines, or immune cell transfer. These models mimic the acute inflammatory aspects of psoriasis but may not fully reproduce the chronic, multifactorial nature of the disease.

3.1.1.1. Imiquimod-induced Model. This model represents the most widely used induced model and involves the topical application of imiquimod (a TLR7/8 agonist), which leads to acute skin inflammation characterized by erythema, scaling, and epidermal hyperplasia. Imiquimod activates pDCs to produce IFN-α, thereby triggering a cascade of inflammatory responses involving IL-17, IL-23, and TNF-α, which are similar changes that occur in human psoriasis [21].

3.1.1.2. IL-23 injection Model. The intradermal injection of IL-23 induces psoriasis-like skin inflammation by promoting the expansion of Th17 cells and the subsequent production of IL-17A, IL-22, and TNF-α, thereby leading to keratinocyte hyperproliferation and parakeratosis [28].

3.1.1.3. IL-36 dependency in imiquimod Model. Recent studies have demonstrated the importance of IL-36 in mediating skin inflammation in imiquimod-induced models, thus highlighting a potential therapeutic target in IL-36-dependent inflammatory pathways in a preclinical study model [29].

3.1.2. Genetically modified models

Genetically modified models allow for the targeted manipulation of genes implicated in psoriasis pathogenesis, thereby providing valuable insights into immune signaling and keratinocyte biology.

3.1.2.1. Transgenic models. The overexpression of cytokines (such as IL-17A, IL-23, and TNF-α) or growth factors (such as VEGF) in keratinocytes induces psoriasiform skin inflammation. For example, K14-IL-17A transgenic mice can develop acanthosis, parakeratosis, and immune cell infiltration, thus mimicking human psoriasis [30].

3.1.2.2. Knockout models. Mice deficient in negative regulators of inflammation, such as IL-1 receptor antagonist (IL-1RA) and S100A9, exhibit spontaneous psoriasiform inflammation, thereby suggesting their roles in immune homeostasis.

The knockout of caspase recruitment domain family member (CARD)14, which is a key signaling molecule in keratinocytes, attenuates psoriasis-like phenotypes induced by imiquimod and IL-23 [31]. Among knockout models exhibiting spontaneous psoriasiform inflammation, the epidermal-specific deletion of c-jun and junB has provided compelling insights into disease pathogenesis. These double knockout mice (c-jun^Δep/junB^Δep) develop skin lesions that closely resemble human psoriasis, characterized by pronounced acanthosis, parakeratosis, Munro's microabscesses, and dense leukocyte infiltration [32]. Importantly, this model emphasizes the central role of keratinocytes in initiating inflammatory cascades, suggesting that intrinsic dysregulation of epidermal transcription factors can serve as a primary trigger of psoriatic pathology.

3.1.2.3. CRISPR/Cas9 genome Editing. Emerging approaches using CRISPR/Cas9 technology enable the generation of psoriasis models with precise gene alterations, thus enhancing the understanding of psoriasis pathogenesis. For example, in mice with keratinocyte-restricted IL-23A deletions, IL-23 was observed to play a critical role in psoriasiform inflammation [33].

3.1.3. Xenotransplantation models

Xenotransplantation of human psoriatic skin into immunodeficient mice, such as severe combined immunodeficiency (SCID) or nude mice, provides a platform for studying human skin responses in vivo. These models preserve key histopathological features of psoriasis, including hyperplasia, parakeratosis, and immune cell infiltration. However, challenges such as limited graft survival and incomplete immune system interactions limit their widespread application [34,35].

Each psoriasis model exhibits strengths and limitations, which determine each model's suitability for different research applications. A comparative evaluation is essential for selecting appropriate models for investigating specific aspects of psoriasis pathogenesis and drug discovery (Table 1).

3.2. Recent developments and emerging trends

Recent advances in psoriasis modeling have led to the introduction of novel techniques that aim to improve the fidelity and translational relevance of preclinical models.

3.2.1. Humanized mice with immune Reconstitution

Human psoriasis can be replicated by grafting human psoriatic skin and immune cells, thereby preserving lesion phenotypes and facilitating drug evaluation. These types of models bridge the gap between in vitro studies and clinical applications, thus enhancing translational relevance. By incorporating human immune cells into immunodeficient mice with psoriatic skin grafts, a more physiologically relevant environment can be created, thereby enabling a detailed investigation of immune-keratinocyte interactions in psoriasis [36].

3.2.2. Organoid and microfluidic models

The study by Morgner et al. [37] emphasized the application of bilayer skin equivalents as predictive tools in psoriasis research, thus replicating key pathological features and providing a reliable platform for drug screening. These models effectively mimic psoriatic skin by incorporating keratinocytes and fibroblasts in a structured microenvironment, which enables the evaluation of therapeutic interventions. Shaw et al. [38] highlighted the integration of artificial intelligence (AI) with microfluidic platforms, thereby facilitating high-throughput drug screening and real-time monitoring. Three-dimensional skin organoids and microfluidic platforms that integrate keratinocytes, fibroblasts, and immune cells can provide novel avenues for the investigation of complex psoriasis pathophysiology in a controlled microenvironment [37,38].

3.2.3. Single-cell transcriptomics and spatial mapping

Single-cell RNA sequencing and spatial transcriptomics enable high-resolution characterization of immune cell subsets and molecular pathways in psoriasis models, which facilitates the identification of new therapeutic targets [39].

These animal models of psoriasis have significantly advanced our understanding of disease mechanisms and have provided a robust platform for preclinical drug testing. Although no single model is able to fully reproduce the complexity of human psoriasis, the combined use of induced, genetically modified, and xenotransplantation models offers complementary insights. Emerging technologies, such as CRISPR/Cas9 genome editing and humanized mice, are poised to further refine psoriasis modeling, thereby bridging the gap between in vitro and clinical research applications. Careful selection and validation of appropriate models remain critical for translational success in psoriasis research.

Table 1. Comparison of the strengths and limitations of various models.

Model Type	Advantages	Limitations	Ref.
Imiquimod -Induced Model	– Rapid, reproducible, and widely used – Mimics acute inflammation of psoriasis	– Acute, transient inflammation – Limited representation of chronic psoriasis	[21]
IL-23 Injection Model	– Models Th17/IL-23 axis – Suitable for studying cytokine-targeted therapies	– Does not fully replicate the chronic nature of psoriasis	[28]
IL-36 Dependent Models	– Provides insights into IL-36–mediated inflammation – Useful for exploring IL-36 blockade strategies	– Limited to understanding IL-36 pathways	[29]
Transgenic Models	– Allows investigation of specific gene functions – Recapitulates chronic inflammation	– High cost and complex generation – Potential for off-target effects	[30]
Knockout Models	– Evaluates loss-of-function effects – Identifies protective genes and pathways	– Phenotypic variability – Possible compensatory mechanisms	[31]
CRISPR/Cas9-Modified Models	– Precise, targeted gene alterations – Accelerates development of novel models	– Potential off-target effects – Requires sophisticated expertise	[33]
Xenotransplantation Models	– Maintains human skin architecture – Facilitates drug testing on human tissue	– Expensive and labor-intensive – Limited immune system interaction	[34,35]

4. Induced psoriasis models

4.1. Imiquimod-induced model

4.1.1. Mechanism of action

The imiquimod-induced mouse model is the most commonly used model to mimic the pathological hallmarks of psoriasis. Imiquimod, which is a toll-like receptor (TLR) 7/8 agonist, is a small molecule with potent immunostimulatory activity. It was initially developed to treat human papillomavirus-induced skin lesions and certain types of cancers. However, some patients treated with Aldara cream (5% imiquimod) reported the development of psoriatic lesions at both the application site and distant unaffected areas, thereby suggesting a systemic immunomodulatory effect [40]. Imiquimod activates pDCs, which results in the production of proinflammatory cytokines such as IFN-α. This activation subsequently amplifies Th1 and Th17 responses, which are pivotal in the pathogenesis of psoriasis. The IL-23/IL-17 axis plays a critical role in imiquimod-induced psoriatic inflammation [41].

4.1.2. Key findings and drug testing applications

The imiquimod-induced psoriasis model has been widely used in preclinical research to evaluate the efficacy of new therapeutics targeting psoriasis. A significant advantage of this model is its ease of use and reproducibility, thus making it a cost-effective and efficient system for evaluating topical agents. The inflammatory response induced by imiquimod typically peaks after 5–6 days, with significant upregulation of IL-23, IL-17, and related cytokines being observed during this period. Several agents, including small molecules, biologics, and plant extracts, have demonstrated therapeutic efficacy in this model by reducing epidermal thickness, inflammatory cell infiltration, and cytokine production [42]. However, the imiquimod model exhibits certain limitations. For example, this model primarily mimics the acute phase of psoriasis and fails to demonstrate the chronic nature of the disease. Furthermore, prolonged application of imiquimod (more than 2 weeks) can lead to systemic effects, dehydration, and even death in mice, thereby underscoring the need for careful dosing and monitoring [43]. In this review, we summarize a range of therapeutic agents validated through imiquimod-induced murine models. Among these agents, tapinarof and flavone luteolin-7-glucoside were tested in an imiquimod-induced psoriasis model, with the results demonstrating their efficacy in reducing erythema, epidermal thickening, and acanthosis by modulating inflammatory cytokines and blocking the IL-22 signaling pathway. Similarly, the oral administration of acarbose in an imiquimod-induced psoriasis model demonstrated anti-inflammatory effects by decreasing $CD3^+$ T-cell and neutrophil infiltration, in addition to suppressing IL-6, IL-1β, and IL-22. Moreover, cyclosporine was assessed in the asebia mouse model via subcutaneous injections, which led to a decrease in epidermal hyperplasia and a reduction in dermal mast cells. Additionally, delphinidin, which was evaluated in a flaky skin mouse model, reduced epidermal thickness and the infiltration of immune cells, including neutrophils and macrophages, in addition to lowering IL-23, IL-17, and IL-1β levels. These findings underscore the importance of utilizing diverse induced models to assess the therapeutic potential of novel agents in psoriasis treatment (Table 2) [26,44–51].

4.2. Xenograft and humanized models

4.2.1. Transplantation of human psoriatic skin onto immunocompromised mice

Xenograft and humanized models have been developed to overcome the species-specific limitations associated with murine models of psoriasis. For this approach, human psoriatic skin is transplanted onto immunocompromised mice, such as SCID or AGR129 mice. These mice lack functional T and B cells, which prevents immune rejection of the transplanted tissue. Humanized mice are generated by cotransplanting human peripheral blood mononuclear cells, thus enabling the establishment of a functional human immune system within the murine host [52,53]. While xenograft models – such as those involving transplantation of psoriatic lesional skin onto immunodeficient mice (e.g. SCID or AGR129 strains) – are indispensable for studying human-specific immune responses and drug efficacy, they are limited in addressing the initial triggers of disease. This is because the grafted skin already exhibits fully developed psoriatic pathology, including immune activation, keratinocyte hyperproliferation, and vascular changes at the time of transplantation. As such, these models do not permit investigation of the initiating events that lead to psoriasis onset. Therefore, to explore the mechanistic initiation of psoriatic inflammation, complementary models – such as inducible systems or genetically engineered mice – are necessary.

4.2.2. Advantages and disadvantages in mimicking human disease

Xenotransplantation models offer several advantages in psoriasis research. For example, these models allow for the investigation of human-specific immunopathological processes, including interactions between human keratinocytes, fibroblasts, and immune cells. Additionally, these models facilitate the evaluation of targeted biologics and immune modulators with high translational potential [54]. Humanized models have successfully reproduced the characteristic features of psoriasis, including epidermal hyperplasia, parakeratosis, and increased immune cell infiltration [55]. Despite these advantages, xenotransplantation models exhibit significant challenges. For example, they are technically demanding, time-consuming, and costly. Moreover, variabilities in donor skin, graft rejection, and immune heterogeneity can affect the reproducibility of the results. Furthermore, the maintenance of human skin grafts in immunodeficient mice often results in inconsistencies in lesion thickness and inflammatory responses [56].

4.3. Chemical and irritant-induced models

Chemical and irritant-induced models, which involve use of propranolol is employed to induce psoriatic-like lesions via the activation of immune responses and barrier disruption.

Table 2. Drugs approved through direct evaluation using the IMQ-induced psoriasis-like model.

Drug	Murine Model	Route	Mechanism	References
Acarbose	Imiquimod-induced psoriasis	Oral	Reduce CD3+ T cell and neutrophil infiltration while suppressing IL-6, IL-1β, and IL-22 production.	[41]
Apremilast	Imiquimod-induced psoriasis	Oral	Inhibition of PDE4, reduced TNF-α, IL-17, and IL-23, reduced epidermal thickening	[42]
Cyclosporine	Asebia mouse	S.C. injection	Reduce epidermal hyperplasia and lower the number of dermal mast cells.	[24]
Delphinidin	Flaky skin mouse	Topical	Decreased epidermal thickness, along with reduced levels of neutrophils, macrophages, and cytokines IL-23, IL-17, and IL-1β.	[43]
Flavone Luteolin-7-glucoside	Imiquimod-induced psoriasis	Topical	Reduce acanthosis and inhibit the IL-22 signaling pathway.	[44]
Fumaric Acid Esters (Dimethyl Fumarate)	Imiquimod-induced psoriasis	Oral	Modulation of oxidative stress, inhibition of NF-κB, reduced inflammation	[45]
Ruxolitinib	Imiquimod-induced psoriasis	Topical	Potent JAK inhibitor, reduced cytokine-mediated inflammation	[46]
Tapinarof	Imiquimod-induced psoriasis	Topical	Alleviate erythema, diminish epidermal thickening, and decrease tissue cytokine levels.	[47]
Tofacitinib	Imiquimod-induced psoriasis	Oral	JAK-STAT inhibition, reduction in keratinocyte hyperproliferation	[48]

These models are particularly useful for evaluating the efficacy of topical treatments and elucidating the molecular mechanisms underlying skin inflammation. A study by Jin et al. [57] explored the therapeutic effects of IMMH002, which is a novel sphingosine 1-phosphate receptor (S1P)1 modulator, in various animal models of psoriasis, including the propranolol-induced guinea pig model. Propranolol was applied to guinea pig ears for three weeks, and this treatment induced psoriasiform skin lesions characterized by hyperkeratosis, acanthosis, and dermal inflammatory infiltration. The oral administration of IMMH002 at different doses (0.3, 0.6, 1.2, and 2.4 mg/kg) significantly attenuated these pathological changes by reducing epidermal thickening and inflammation. The results of this study demonstrate that IMMH002 effectively decreases proliferating cell nuclear antigen (PCNA) expression in the epidermis, thereby suggesting its potential to alleviate keratinocyte hyperproliferation. Moreover, these findings support the role of IMMH002 as a promising candidate for psoriasis treatment by modulating lymphocyte trafficking and reducing inflammatory responses.

Chemical and irritant-induced models offer advantages in investigating the effectiveness of topical therapies. These models enable the assessments of drug penetration, absorption, and therapeutic efficacy in the context of a disrupted skin barrier. However, variabilities in dosing regimens, application protocols, and species differences often complicate the extrapolation of results to clinical scenarios. Furthermore, chemical-induced models tend to produce acute inflammatory responses, which limits their applicability for studying chronic disease progression [58,59]. Although induced models provide valuable insights into psoriasis pathogenesis and therapeutic responses, it is essential to recognize their limitations. For example, these models primarily reflect acute inflammation rather than chronic psoriasis. Additionally, differences in immune responses between mice and humans can impact the translational relevance of the reported findings. Therefore, a combination of multiple models, including genetically modified and xenotransplantation models, is often recommended to provide a more comprehensive understanding of psoriasis pathophysiology and treatment outcomes [60].

5. Genetically engineered psoriasis models

Genetically engineered models have significantly contributed to elucidating the pathogenesis of psoriasis by providing insights into the molecular mechanisms underlying this complex disease. These models, which are characterized by the targeted overexpression or deletion of key genes implicated in psoriasis pathophysiology, mimic various aspects of the disease, including keratinocyte proliferation, immune dysregulation, and angiogenesis [33]. This section discusses three widely studied genetically engineered psoriasis models: the K5-Stat3c transgenic model, the K14-VEGF model, and cytokine transgenic models of IL-17, IL-23, and TNF-α (Figure 2).

5.1. K5-Stat3c transgenic model

The K5-Stat3c transgenic model demonstrates the crucial role of Stat3 in keratinocyte hyperproliferation and inflammation. Stat3, which is a transcription factor activated by cytokines such as IL-6, IL-22, and IL-23, is upregulated in psoriatic keratinocytes and is associated with epidermal hyperplasia and immune cell infiltration. In this model, constitutively active Stat3 is expressed under the control of the K5 promoter, which is specific to basal keratinocytes [61]. Vats et al. [62] highlighted the importance of the K5-Stat3c transgenic model in elucidating the role of keratinocyte hyperproliferation and immune dysregulation in psoriasis. The K5-Stat3c model overexpresses a constitutively active form of Stat3 in K5-positive basal keratinocytes, thus resulting in spontaneous development of psoriasiform lesions. This model closely mimics the human psoriatic phenotype, which is characterized by epidermal hyperplasia, acanthosis, increased vascularization, and the infiltration of CD4+ T cells and neutrophils. Stat3 activation leads to the upregulation of key cytokines, including IL-23, IL-17, and TNF-α, thereby promoting a Th17-driven inflammatory environment. Moreover, the K5-Stat3c model provides valuable insights into the molecular mechanisms underlying keratinocyte-immune interactions and serves as a robust platform for testing novel antipsoriatic therapies [62]. Upon tape stripping or wounding, K5-Stat3c mice were observed to develop

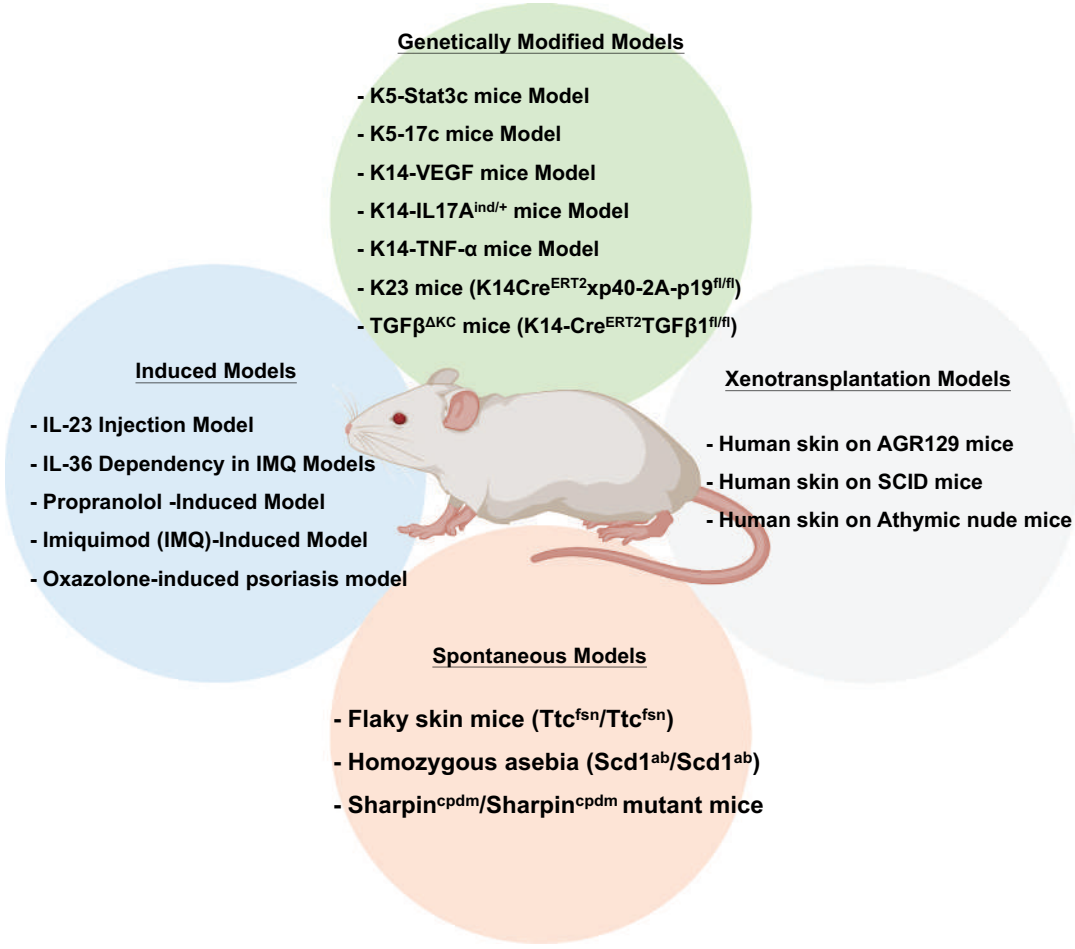


Figure 2. Classification of commonly used animal models in psoriasis research. Experimental models are categorized into four major types based on their method of induction and relevance to human disease. Genetically modified models include mice with transgenic or conditional expression of psoriasis-related genes, such as K5-17c, K14-VEGF, K14-IL17A$^{ind/+}$, K14-TNF-α, K23, and TGFβ^{ΔKC}. Induced models rely on external stimuli such as IL-23 administration, imiquimod (IMQ) application, IL-36 signaling, propranolol treatment, or oxazolone exposure to provoke psoriasiform skin changes. Xenotransplantation models are established by grafting human skin onto immunodeficient mouse strains (AGR129, SCID, or athymic nude mice), enabling the study of human-specific disease mechanisms in vivo. Spontaneous models involve mouse strains with naturally occurring mutations (e.g. Ttc^{fsn}, Scd1^{ab}, and Sharpin^{cpdm}) that lead to skin inflammation resembling psoriasis. These diverse models facilitate the investigation of disease pathogenesis and preclinical evaluation of therapeutic strategies. Created in BioRender. lin, Z. (2025) https://biorender.com/gps6hb5.

spontaneous psoriasiform lesions characterized by acanthosis, parakeratosis, and the infiltration of neutrophils and T cells [63]. The role of Stat3 in psoriatic inflammation was further substantiated by studies demonstrating that the inhibition of Stat3 activity resulted in the resolution of the psoriasiform phenotype. Moreover, K5-Stat3c mice were observed to exhibit elevated levels of proinflammatory cytokines such as IL-17, IL-22, and TNF-α, thereby establishing the Stat3 pathway as a potential therapeutic target in psoriasis [64]. Further evidence for the role of keratinocytes as pathogenic drivers comes from the K5.Stat3C transgenic model, in which constitutively active STAT3 is expressed under the keratin-5 promoter. These mice spontaneously develop psoriasiform skin inflammation with hallmarks of human disease, including epidermal thickening, increased dermal angiogenesis, and a Th17/Th22-skewed cytokine environment. Upon injury or inflammatory challenge, disease severity is exacerbated, highlighting how sustained STAT3 activation in basal keratinocytes can initiate and amplify immune-mediated cutaneous responses.

5.2. K14-VEGF model

The K14-VEGF model is a transgenic mouse model engineered to overexpress VEGF under the control of the K14 promoter, thereby leading to dermal angiogenesis and vascular remodeling. Vascular changes, including increased microvascular density and enhanced endothelial permeability, are hallmarks of psoriatic lesions. VEGF overexpression promotes angiogenesis and leukocyte trafficking, which contribute to the psoriatic phenotype [65,66]. K14-VEGF mice exhibit typical psoriasiform characteristics, including hyperkeratosis, acanthosis, microabscess formation, and increased vascularity. Additionally, inflammatory cell infiltration, which predominantly involves neutrophils and T cells, is prominent in the dermis and epidermis. When treated with imiquimod, K14-VEGF mice exhibit a prolonged psoriasiform phenotype, thus making them a valuable model for long-term studies. Wang et al. [67] investigated the K14-VEGF transgenic model and its role in enhancing the stability and longevity of psoriasis-like inflammation induced by imiquimod. The K14-VEGF model overexpresses

VEGF under the control of the K14 promoter, which leads to increased angiogenesis, hyperproliferation of keratinocytes, and infiltration of inflammatory cells. Compared with wild-type mice, imiquimod-induced K14-VEGF mice exhibited prolonged and stable inflammation, with a maintenance of elevated cytokine levels (including IL-17, IL-23, and TNF-α) and immune cell infiltration beyond 14 days. This model effectively mimics chronic psoriasis features, thereby providing a reliable platform for long-term evaluation of psoriasis pathogenesis and therapeutic interventions [67]. The K14-VEGF model has also been used to assess the efficacy of antiangiogenic therapies, with VEGF inhibitors demonstrating a moderate improvement in psoriatic lesions, thus further emphasizing the contribution of angiogenesis to the pathogenesis of psoriasis [68].

5.3. IL-17, IL-23, and TNF-α transgenic models

IL-17, IL-23, and TNF-α transgenic models have been instrumental in delineating the immune-driven pathology of psoriasis. These cytokines are key mediators of the Th17/IL-23 axis, which orchestrates psoriatic inflammation by promoting keratinocyte proliferation and immune cell recruitment [69].

5.3.1. K14-IL-17Aind/+ model

This model overexpresses IL-17A in keratinocytes, which leads to the accumulation of neutrophils, T cells, and macrophages in the skin. The resulting phenotypes include epidermal hyperplasia, parakeratosis, and microabscess formation, which closely resembles human psoriatic lesions. The K14-IL-17Aind/+ psoriasis model is a genetically engineered mouse model that overexpresses IL-17A under the K14 promoter, thereby closely replicating key features of human psoriasis. This model involves persistent skin inflammation characterized by epidermal hyperkeratosis, parakeratosis, enhanced vascularity, and infiltration of neutrophils and CD3+ T cells. Khmaladze et al. [70] demonstrated that K14-IL-17Aind/+ mice not only develop psoriasiform lesions but also exhibit comorbidities such as arthritis and uveitis, which are commonly associated with psoriasis. This study revealed that, although these mice exhibited a limited response to IL-17A blockade, IL-6 inhibition significantly reduced inflammation, thereby indicating that IL-6 plays a dominant role in maintaining disease severity in this model. Similarly, von Stebut et al. [71] explored the role of IL-17A in driving chronic inflammation and immune dysregulation in K14-IL-17Aind/+ mice. Their findings demonstrated that sustained IL-17A expression induces granulopoiesis and recruits IL-6 R-expressing neutrophils, thus contributing to disease persistence. This study also demonstrated that therapeutic strategies targeting IL-6 effectively ameliorated skin lesions and reduced immune cell infiltration, thereby underscoring the importance of IL-6 as a therapeutic target in IL-17A-driven psoriasis [71]. Notably, the administration of IL-17 inhibitors to these mice attenuated disease severity, thus underscoring the therapeutic potential of the targeting of IL-17A in psoriasis treatment.

5.3.2. K23 and IL-23 transgenic models

IL-23 transgenic models exhibit an exaggerated inflammatory response with an influx of IL-17-producing Th17 cells, macrophages, and dendritic cells. The IL-23/Th17 axis drives sustained keratinocyte proliferation and inflammatory cytokine production, which maintains the chronic nature of psoriatic lesions [72]. This study explored the role of the IL-23 transgenic model in psoriasis by focusing on the contribution of keratinocyte-derived IL-23 to chronic skin inflammation. The findings demonstrated that keratinocyte-produced IL-23 alone is sufficient to induce psoriasis-like skin inflammation characterized by an IL-17 signature. Moreover, this study identified a cell-autonomous mechanism regulated by neural Wiskott-Aldrich syndrome protein (N-WASP), which modulates IL-23 expression in keratinocytes via the degradation of the histone methyltransferases G9a and G9a-like protein (GLP), thereby reducing histone H3 lysine 9 (H3K9) dimethylation at the IL-23 promoter. TNF-α, which is a known IL-23 inducer in psoriasis, triggers this pathway. Moreover, increased IL-23 expression is correlated with decreased H3K9 dimethylation in psoriatic keratinocytes, thus emphasizing the relevance of epigenetic regulation in the pathogenesis of psoriasis [73]. Chen et al. [74] investigated the K23 transgenic model of psoriasis, which conditionally expresses IL-23 in keratinocytes under the control of the K14 promoter. This model involves the development of psoriasis-like lesions characterized by acanthosis, parakeratosis, hyperkeratosis, and dermal inflammatory infiltration. K23 mice not only exhibit hallmark features of psoriasis but also develop psoriatic arthritis (PsA)-like disease, including dactylitis, enthesitis, and bone destruction, with skin inflammation preceding joint pathology. Surprisingly, increased circulating IL-23 levels were not observed, thereby suggesting that IL-23 expression in the skin alone is sufficient to trigger systemic inflammation. Furthermore, K23 mice demonstrated elevated IL-22 levels; moreover, although IL-22 deficiency did not affect psoriasis development, it aggravated PsA-like disease, thus indicating a protective role of IL-22 in joint pathology. The K23 animal model provides valuable insights into the IL-23-driven pathogenesis of psoriasis and PsA, thereby highlighting the contribution of skin-derived cytokines to systemic inflammation.

5.3.3. K14-TNF-α model

The K14-TNF-α transgenic mouse model overexpresses TNF-α, which is a cytokine that plays a pivotal role in psoriatic inflammation by promoting the activation of keratinocytes and immune cells. The phenotype of this model includes epidermal hyperplasia, infiltration of immune cells, and increased cytokine expression in the lesional skin. TNF-α inhibitors, such as infliximab and etanercept, have been shown to mitigate the psoriasiform phenotype in these mice, thus demonstrating the clinical relevance of this model in assessing anti-TNF therapies [75]. The K14-TNF-α transgenic model overexpresses TNF-α under the K14 promoter and induces psoriasiform lesions characterized by epidermal hyperplasia, CD4+/CD8+ T-cell infiltration, and increased IL-6, IL-17, and IFN-γ levels. Additionally, these mice exhibit increased vascular density and expression of

adhesion molecules, thereby promoting leukocyte migration and angiogenesis. Treatment with IBI303 (a humanized anti-TNF-α monoclonal antibody) was observed to significantly reduce inflammation, normalize vascular structures, and inhibit NF-κB activation and VEGF-mediated angiogenesis. The K14-TNF-α model is a robust platform for evaluating TNF-α inhibitors in psoriasis research [76]. Anti-TNF therapies, including etanercept, infliximab, and adalimumab, have been successfully implemented in the treatment of moderate to severe psoriasis. By targeting TNF-α, these biologics effectively reduce inflammation, normalize keratinocyte function, and improve clinical outcomes [77]. However, although genetically engineered psoriasis models have advanced our understanding of psoriasis pathogenesis and have facilitated drug discovery, they exhibit certain limitations. For example, these models often involve the overexpression of a single gene, which may not fully reproduce the multifactorial nature of psoriasis. Moreover, differences in murine and human immune systems and skin architecture may limit the direct translation of findings to clinical settings. Despite these limitations, genetically engineered models remain indispensable tools for investigating the molecular underpinnings of psoriasis and evaluating novel therapeutic strategies [78–80].

6. Emerging and alternative psoriasis models

6.1. 3D skin organoids and ex vivo models

3D skin organoids and ex vivo models provide advanced platforms for studying psoriasis pathophysiology and screening potential therapeutics. These models surpass traditional 2D cultures by replicating the structural complexity and multicellular interactions of human skin. The incorporation of keratinocytes, fibroblasts, and immune cells allows for a more accurate evaluation of inflammatory responses and barrier integrity. Reconstructed human epidermal equivalents (RHEs) and full-thickness skin equivalents (FTSEs), which effectively mimic the epidermal and dermal architectures, are widely used. Recent advances in microfluidic technology and organ-on-a-chip systems have enabled the development of dynamic, perfused environments that closely mimic physiological conditions. These models facilitate high-throughput drug screening, improve disease modeling, and allow for the investigations of skin permeability and host-microbe interactions in psoriasis research [81,82]. Ex vivo models obtained from human or animal skin explants are able to preserve the native skin architecture, including the epidermis and dermis, as well as immune cell diversity. Moreover, these models serve as excellent platforms for assessing drug penetration, inflammation, and immune responses in a more physiologically relevant context. However, challenges such as the limited availability and variability of skin donors, as well as the need for invasive procedures, restrict the widespread applications of these models [56,83]. Despite these limitations, advanced bioengineering technologies (such as 3D bioprinting and organ-on-a-chip systems) demonstrate promise in increasing the complexity and reproducibility of 3D skin models. These systems allow for the coculture of keratinocytes, fibroblasts, and immune cells in a spatially controlled manner, which is critical for replicating psoriasis pathophysiology and drug testing [84].

6.2. Zebrafish models

Zebrafish (*Danio rerio*) have gained recognition as valuable nonmammalian models for studying psoriasis pathogenesis and drug discovery due to their genetic tractability, rapid reproduction, and optical transparency, which facilitate real-time imaging capabilities. Zebrafish possess a stratified epidermis and dermis that closely resemble mammalian skin, although they lack hair follicles and sweat glands. Moreover, zebrafish models have been instrumental in investigating keratinocyte proliferation, immune responses, and inflammatory cytokines associated with psoriasis [85]. Several mutant zebrafish models have been developed to mimic psoriatic conditions. For example, the Hai1 mutant exhibits hyperproliferation of keratinocytes and increased neutrophil infiltration, thus mimicking the inflammatory features observed in human psoriatic lesions. Additionally, the Psoriasis/m14 mutant model demonstrates epidermal overproliferation and keratinocyte differentiation defects, thus making it useful for the investigation of epidermal growth regulation and the impact of potential therapeutic agents [86]. Moreover, gene knockdown models (morphant models) in zebrafish, such as those targeting tnfa and tnfr2, have been used to investigate the role of inflammatory cytokines and neutrophil mobilization. The zebrafish model also facilitates high-throughput screening of anti-inflammatory and immunomodulatory drugs, thereby offering a cost-effective and time-efficient platform for psoriasis research [87]. Despite their advantages in genetic screening and live imaging, zebrafish possess anatomical limitations, including the presence of scales and the absence of a functional water-impermeable epidermal barrier. These differences reduce their relevance for modeling key aspects of human psoriasis, such as stratum corneum integrity and barrier dysfunction associated with transepidermal water loss.

6.3. AI and computational models in drug screening

The integration of AI and computational models in psoriasis research has revolutionized drug discovery by enabling the rapid prediction of therapeutic efficacy and toxicity. In silico models utilize machine learning algorithms to analyze large-scale genomic, proteomic, and metabolomic data; identify novel drug targets; and predict the impact of candidate compounds on psoriasis pathways [88,89]. AI-based models can simulate complex disease mechanisms, thereby providing insights into the interactions among cytokines, immune cells, and keratinocytes. These models also aid in virtual screening, molecular docking, and structure-activity relationship (SAR) analysis, thereby significantly reducing the cost and time associated with traditional drug discovery approaches [90]. The ability of AI models to predict the pharmacokinetics and pharmacodynamics of compounds

further enhances their applications in optimizing drug formulations and dosing strategies [91]. Additionally, organ-on-a-chip platforms integrated with AI algorithms can model skin microenvironments, thus enabling the dynamic evaluation of drug effects on multiple cell types, including keratinocytes, fibroblasts, and immune cells. These platforms offer a high-throughput and personalized approach to drug development, which aligns with the principles of precision medicine [92–94]. Emerging and alternative models, including 3D skin organoids, zebrafish models, and AI-based computational platforms, are transforming psoriasis research by offering more accurate, scalable, and ethically sound alternatives to traditional animal models. Although challenges such as model complexity and validation continue to exist, these innovative platforms demonstrate immense potential for accelerating drug discovery and improving therapeutic outcomes in psoriasis.

7. Application of animal models in novel drug discovery

7.1. Recent advancements in small-molecule drugs, biologics, and natural compounds

The search for effective treatments for psoriasis has led to the development of a range of therapeutic agents, including small-molecule inhibitors, biologics, and natural compounds. Each treatment category offers unique advantages in the targeting of the inflammatory pathways implicated in PsR pathogenesis (Figure 3).

7.1.1. Small-molecule drugs

Small-molecule drugs, particularly Janus kinase (JAK) inhibitors, have demonstrated promise in modulating the inflammatory response in psoriasis. Tofacitinib (a JAK1/3 inhibitor) is approved for the treatment of psoriatic arthritis [95,96], whereas baricitinib (a JAK1/2 inhibitor) is currently being investigated in phase II trials for moderate-to-severe psoriasis [97,98]. Additionally, deucravacitinib, which is a selective tyrosine kinase 2 (TYK2) inhibitor, was approved by the European Union in 2023 for treating moderate-to-severe plaque psoriasis [99,100]. These agents primarily inhibit intracellular signaling molecules involved in cytokine production, thus disrupting the IL-23/Th17 inflammatory axis (a critical pathway in psoriasis development).

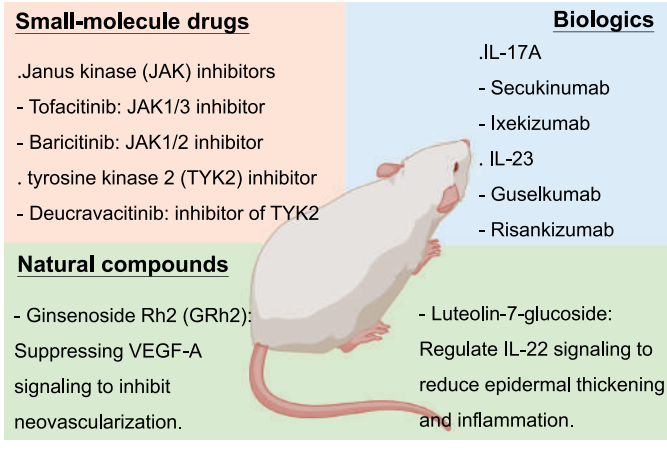


Figure 3. Utilization of psoriasis animal models in the development and evaluation of new therapeutic agents. These models support the preclinical testing of diverse drug classes, including small-molecule inhibitors (e.g. tofacitinib, baricitinib, deucravacitinib) targeting JAK and TYK2 pathways; biologic therapies directed against IL-17A (secukinumab, ixekizumab) and IL-23 (guselkumab, risankizumab); and natural compounds, such as ginsenoside Rh2, which blocks VEGF-A signaling to limit angiogenesis, and luteolin-7-glucoside, which attenuates IL-22 signaling to reduce skin inflammation and thickening. Created in BioRender. lin, Z. (2025) https://BioRender.com/by4i364.

7.1.2. New biologics

Biologic therapies, which include monoclonal antibodies targeting key cytokines, have significantly improved psoriasis management. Agents such as secukinumab and ixekizumab have been shown to inhibit IL-17A [101–103], whereas guselkumab and risankizumab have been observed to block IL-23 [104–106]. These therapies provide superior efficacy compared with traditional systemic therapies and have transformed the management of moderate-to-severe psoriasis.

7.1.3. Natural compounds

Natural compounds, such as polyphenols, flavonoids, and ginsenosides, have gained attention because of their anti-inflammatory, antioxidant, and antiproliferative properties [107,108]. Ginsenoside Rh2 (GRh2), which is a bioactive compound derived from ginseng, has demonstrated antipsoriatic effects by reducing acanthosis, T-cell infiltration, and neovascularization in animal models. The mechanism of action of GRh2 involves the downregulation of VEGF-A signaling, thereby inhibiting neovascularization [109,110]. Additionally, flavonoids such as luteolin-7-glucoside have been shown to modulate the IL-22 signaling pathway and decrease epidermal thickening and inflammation [111,112]. The natural compounds highlighted in this section, such as curcumin and ginsenosides, were selected due to their frequent evaluation in established preclinical psoriasis models and their demonstrated anti-inflammatory or immunomodulatory activity, making them representative of emerging therapeutic strategies under investigation.

7.2. Mechanistic insights and predictive biomarkers from animal models

Animal models provide invaluable mechanistic insights into the pathogenesis of psoriasis, thus enabling the identification of novel therapeutic targets. For example, the Th23/Th17 axis, which was identified via animal studies, has emerged as a pivotal driver of psoriasis, thereby leading to the development of IL-17 and IL-23 inhibitors. Similarly, the role of cytokines such as IL-22 and IL-36 in keratinocyte hyperproliferation and immune cell recruitment has been elucidated via preclinical models [113,114]. Additionally, biomarkers such as Ki-67 (epidermal proliferation) [114], CD3, CD11c, and CD163 (inflammatory infiltration) have been used to assess drug efficacy in animal models [115–118]. Advances in transcriptomic analysis have further identified microRNAs (such as miR-21 and miR-203) that are differentially expressed in psoriatic lesions and serve as potential predictive markers for therapeutic responses [119]. Despite their utility, current animal models

exhibit limitations in fully reproducing the complex genetic, immunological, and histopathological features of human psoriasis. Species-specific variations in cytokine expression, immune cell composition, and skin architecture often limit the translational relevance of preclinical findings. Moreover, differences in skin permeability between mice and humans can lead to discrepancies in drug absorption and efficacy, thus necessitating caution when extrapolating results to clinical settings [120]. To address these limitations, future research should focus on developing hybrid models that integrate multiple systems (such as the combination of in vitro outcomes with in vivo endpoints) and refining xenotransplantation models to increase their predictive accuracy. To enhance translational relevance, future research should pursue hybrid model strategies that integrate complementary systems. For mechanistic elucidation, coupling in vitro 3D organotypic skin models containing keratinocytes, fibroblasts, and immune cells with in vivo cytokine-induced murine models enables direct validation of IL-23/IL-17-driven immune-epidermal interactions. In the context of therapeutic screening, initial evaluation of drug-induced cytokine release in reconstructed human epidermis can be followed by confirmatory testing in xenotransplantation models using lesional psoriatic skin. To assess safety profiles, microfluidic-based skin-on-chip platforms incorporating vascular channels may be linked with in vivo models to capture both local efficacy and systemic immunotoxicity. For studying psoriatic arthritis, dual-compartment models co-implanting psoriatic skin and synovial-like tissue, especially in HLA-transgenic mice reconstituted with patient-derived immune cells, offer promising avenues to simulate both cutaneous and joint inflammation. These hybrid frameworks represent a step forward in refining psoriasis modeling for both mechanistic insight and drug development. Furthermore, advancements in computational modeling and AI-driven drug screening demonstrate promise in complementing traditional animal models, thereby facilitating the identification of safer and more effective therapeutic agents.

8. Conclusions

Psoriasis is a complex immune-mediated disease that is primarily driven by the IL-23/Th17 axis and is characterized by dysregulated interactions between keratinocytes and immune cells. Preclinical models (including imiquimod-induced, xenotransplantation, and transgenic models such as K5-Stat3 and K14-VEGF) have been instrumental in elucidating pathophysiological mechanisms and identifying therapeutic targets. Among these models, imiquimod-induced models are widely used due to their simplicity and reproducibility, although none of the models are able to fully reproduce the human condition. Animal models have significantly contributed to psoriasis drug discovery, particularly regarding the validation of cytokine inhibitors. However, interspecies differences limit their clinical translation. To address this issue, humanized and tissue-engineered models, such as psoriatic skin xenografts and 3D skin equivalents, have been developed to better mimic human disease. Emerging technologies (including organ-on-a-chip, CRISPR/Cas9, and 3D bioprinting) provide more accurate and personalized platforms for modeling disease and testing therapies. The integration of AI and bioinformatics can further enhance high-throughput analysis and therapeutic development. Future research will rely on multidisciplinary approaches that merge humanized, ex vivo, and computational models to drive more effective, patient-specific treatments.

9. Expert opinion

Animal models remain indispensable for elucidating the immunopathogenesis of psoriasis and evaluating novel therapeutics. Despite their utility, current models exhibit significant limitations in fully capturing the heterogeneity and chronicity characteristic of human disease. The widely used imiquimod (IMQ)-induced murine model, for instance, is adept at mimicking acute psoriasiform inflammation via activation of the IL-23/IL-17 axis. However, it lacks key features such as chronicity, sustained immune dysregulation, and the involvement of comorbidities frequently observed in patients, such as psoriatic arthritis and metabolic syndrome. Moreover, the IMQ model predominantly reflects the innate immune component and may underrepresent adaptive immune contributions over extended disease progression. Genetically modified models, such as K5-Stat3c and K14-VEGF mice, offer mechanistic insights into keratinocyte signaling and angiogenesis, respectively. These models have been pivotal in identifying therapeutic targets such as STAT3, VEGF, and downstream inflammatory mediators. Yet, they too are constrained by species-specific discrepancies in immune system architecture and skin physiology. Rodent skin is structurally distinct from human skin in terms of thickness, hair follicle density, and epidermal turnover, which can influence drug absorption and immune cell behavior. This leads to challenges in translating preclinical findings into successful clinical outcomes.

Xenotransplantation models, wherein human psoriatic skin is engrafted onto immunodeficient mice, bridge some of these gaps by preserving the human cellular microenvironment. They allow the study of human-specific immune responses and therapeutic interventions in a semi-in vivo context. However, these models suffer from logistical barriers, including limited availability of human tissue, variability in graft survival, and the need for co-engraftment of immune cells to maintain psoriatic phenotype. Furthermore, such models require specialized facilities and expertise, limiting their scalability and routine use. Emerging strategies in model development are steering the field toward greater physiological and translational fidelity. CRISPR/Cas9-mediated genome editing allows for the generation of precision mouse models bearing human disease-relevant mutations, enabling fine dissection of gene-specific contributions to disease pathology. Similarly, patient-derived organoids and engineered 3D skin equivalents embedded with immune components are gaining traction as high-fidelity platforms for drug screening and mechanistic exploration. These systems recapitulate key aspects of psoriatic epidermal and immune architecture while offering greater control and reproducibility than traditional animal models. Organ-on-a-chip technologies represent another frontier, offering compartmentalized microenvironments with dynamic flow conditions to simulate systemic

interactions. Coupled with human-derived cells, these platforms can model inter-organ crosstalk, including skin-joint and skin-gut axes relevant to psoriasis comorbidities. These approaches support the ongoing paradigm shift toward personalized medicine, where individualized models may inform therapeutic selection based on patient-specific genetic and immunologic signatures. Importantly, the incorporation of comorbidity-representative models is an underexplored yet essential direction. Given the high prevalence of cardiovascular disease, depression, and psoriatic arthritis in affected individuals, preclinical models that emulate these systemic aspects are urgently needed. For example, combining IMQ-induced cutaneous inflammation with models of metabolic syndrome or arthritis could better reflect the clinical complexities of psoriasis and serve as a more holistic platform for testing multi-targeted therapies. Another pressing consideration is the integration of multi-omics platforms – transcriptomics, proteomics, and metabolomics – into preclinical workflows. These datasets, when analyzed using AI-driven bioinformatics pipelines, can reveal predictive biomarkers of therapeutic response and stratify patients for targeted treatments. The synergy of systems biology with innovative model systems may enable early de-risking of drug candidates and improve translational accuracy.

Despite these advances, a standardized framework for model selection, validation, and application remains lacking. Harmonization across research groups concerning endpoint measurements, disease scoring systems, and validation criteria is essential to ensure reproducibility and comparability of findings. Regulatory acceptance of novel platforms, particularly humanized and ex vivo systems, will require rigorous benchmarking against clinical outcomes. Ethical and regulatory pressures are also reshaping preclinical dermatology research. The growing emphasis on the 3Rs (Replacement, Reduction, and Refinement) has prompted increased scrutiny of animal usage and promoted investment in non-animal alternatives. Regulatory agencies, especially in the EU, are increasingly receptive to data from human cell-based models, provided they are robustly validated. This momentum underscores the need for collaborative initiatives between academia, industry, and regulatory bodies to define qualification standards for next-generation preclinical platforms. In conclusion, while conventional animal models have provided invaluable insights into psoriasis pathophysiology and therapy development, their translational limitations necessitate the adoption of complementary, human-relevant platforms. The future of psoriasis research lies in integrative approaches that unify immunological, bioengineering, and computational disciplines. By embracing humanized systems, incorporating AI-guided analytics, developing comorbidity-integrated models, and adhering to standardized protocols, the field can move toward more effective and individualized treatments for this multifaceted disease.

Funding

This work was supported by the National Science and Technology Council, Taiwan [NSTC-113–2314-B-182A-054-MY3], and the Chang Gung University of Science and Technology [ZRRPF6N0011].

Disclosure statement

The authors have no other relevant affiliations or financial involvement with any organization or entity with a financial interest in or financial conflict with the subject matter or materials discussed in the manuscript apart from those disclosed.

Reviewer disclosure

Peer reviewers on this manuscript have no relevant financial or other relationships to disclose.

ORCID

Thi Thu Phuong Tran http://orcid.org/0000-0003-1726-5673

References

Papers of special note have been highlighted as either of interest (•) or of considerable interest (••) to readers.

1. Raharja A, Mahil SK, Barker JN. Psoriasis: a brief overview. Clin Med. 2021;21(3):170–173. doi: 10.7861/clinmed.2021-0257
2. Zhou X, Chen Y, Cui L, et al. Advances in the pathogenesis of psoriasis: from keratinocyte perspective. Cell Death Dis. 2022;13(1):81. doi: 10.1038/s41419-022-04523-3
•• **Updated review article to introduce the pathogenesis of psoriasis.**
3. Demela P, Pirastu N, Soskic B, et al. Cross-disorder genetic analysis of immune diseases reveals distinct gene associations that converge on common pathways. Nat Commun. 2023;14(1):2743. doi: 10.1038/s41467-023-38389-6
4. Li L, Lu J, Liu J, et al. Immune cells in the epithelial immune microenvironment of psoriasis: emerging therapeutic targets. Front Immunol. 2024;14:1340677. doi: 10.3389/fimmu.2023.1340677
5. Lowes MA, Russell CB, Martin DA, et al. The IL-23/T17 pathogenic axis in psoriasis is amplified by keratinocyte responses. Trends Immunol. 2013;34(4):174–181. doi: 10.1016/j.it.2012.11.005
6. Yadav K, Singh D, Singh MR, et al. Preclinical study models of psoriasis: state-of-the-art techniques for testing pharmaceutical products in animal and nonanimal models. Int Immunopharmacol. 2023;117:109945. doi: 10.1016/j.intimp.2023.109945
•• **Review article describing the application of animal models on psoriasis treatment.**
7. Gangwar RS, Gudjonsson JE, Ward NL, et al. Mouse models of psoriasis: a comprehensive review. J Invest Dermatol. 2022;142(3):884–897. doi: 10.1016/j.jid.2021.06.019
8. Hawkes JE, Yan BY, Chan TC, et al. Discovery of the IL-23/IL-17 signaling pathway and the treatment of psoriasis. J Immunol. 2018;201(6):1605–1613. doi: 10.4049/jimmunol.1800013
9. Di Domizio J, Conrad C, Gilliet M, et al. Xenotransplantation model of psoriasis. Inflamm Methods Protoc. 2017;1559:83–90.
10. Hendawy MS, Hashem MM, Zaki AA, et al. Efficacy of *aster chinensis* aerial parts metabolites in BALB/c mice model of imiquimod-induced psoriasis skin inflammation. Inflammopharmacology. 2025;33(4):1973–1996. doi: 10.1007/s10787-025-01652-x
11. Lin ZC, Hung CF, Aljuffali IA, et al. RNA-based antipsoriatic gene therapy: an updated review focusing on evidence from animal models. Drug Des Dev Ther. 2024;Volume 18:1277–1296. doi: 10.2147/DDDT.S447780
12. Guo J, Zhang H, Lin W, et al. Signaling pathways and targeted therapies for psoriasis. Signal Transduct Target Ther. 2023;8(1):437. doi: 10.1038/s41392-023-01655-6
• **The review article introducing the signaling pathways of antipsoriatic drugs.**
13. Bunte K, Beikler T. Th17 cells and the IL-23/IL-17 axis in the pathogenesis of periodontitis and immune-mediated inflammatory diseases. Int J Mol Sci. 2019;20(14):3394. doi: 10.3390/ijms20143394

14. Liu Y, Mei J, Gonzales L, et al. IL-17A and TNF-α exert synergistic effects on expression of CXCL5 by alveolar type II cells in vivo and in vitro. J Immunol. 2011;186(5):3197–3205. doi: 10.4049/jimmunol.1002016
15. Morizane S, Yamasaki K, Mühleisen B, et al. Cathelicidin antimicrobial peptide LL-37 in psoriasis enables keratinocyte reactivity against TLR9 ligands. J Invest Dermatol. 2012;132(1):135–143. doi: 10.1038/jid.2011.259
16. Tan RZ, Zhong X, Han RY, et al. Macrophages mediate psoriasis via mincle-dependent mechanism in mice. Cell Death Discov. 2023;9(1):140. doi: 10.1038/s41420-023-01444-8
17. Ortiz-Lopez LI, Choudhary V, Bollag WB, et al. Updated perspectives on keratinocytes and psoriasis: keratinocytes are more than innocent bystanders. Psoriasis: Targets Ther. 2022;Volume 12:73–87. doi: 10.2147/PTT.S327310
18. Brembilla NC, Boehncke WH. Revisiting the interleukin 17 family of cytokines in psoriasis: pathogenesis and potential targets for innovative therapies. Front Immunol. 2023;14:1186455. doi: 10.3389/fimmu.2023.1186455
19. Yamazaki F. Psoriasis: comorbidities. J Dermatol. 2021;48(6):732–740. doi: 10.1111/1346-8138.15840
20. Kaushik SB, Lebwohl MG. Psoriasis: which therapy for which patient: psoriasis comorbidities and preferred systemic agents. J Am Acad Dermatol. 2019;80(1):27–40. doi: 10.1016/j.jaad.2018.06.057
21. van der Fits L, Mourits S, Voerman JSA, et al. Imiquimod-induced psoriasis-like skin inflammation in mice is mediated via the IL-23/IL-17 axis. J Immunol. 2009;182(9):5836–5845. doi: 10.4049/jimmunol.0802999
22. Sano S, Chan KS, Carbajal S, et al. Stat3 links activated keratinocytes and immunocytes required for development of psoriasis in a novel transgenic mouse model. Nat Med. 2005;11(1):43–49. doi: 10.1038/nm1162
    - **The introduction about the transgenic mouse model for mimicking psoriasis.**
23. Xia YP, Li B, Hylton D, et al. Transgenic delivery of VEGF to mouse skin leads to an inflammatory condition resembling human psoriasis. Blood. 2003;102(1):161–168. doi: 10.1182/blood-2002-12-3793
24. Chau T, Parsi KK, Ogawa T, et al. Psoriasis or not? Review of 51 clinically confirmed cases reveals an expanded histopathologic spectrum of psoriasis. J Cutan Pathol. 2017;44(12):1018–1026. doi: 10.1111/cup.13033
25. Hawkes JE, Adalsteinsson JA, Gudjonsson JE, et al. Research techniques made simple: murine models of human psoriasis. J Invest Dermatol. 2018;138(1):e1–e8. doi: 10.1016/j.jid.2017.10.013
26. Chuang SY, Lin CH, Sung CT, et al. Murine models of psoriasis and their usefulness for drug discovery. Expert Opin Drug Discov. 2018;13(6):551–562. doi: 10.1080/17460441.2018.1463214
27. Sharma A, Sances S, Workman MJ, et al. Multi-lineage human iPSC-derived platforms for disease modeling and drug discovery. Cell Stem Cell. 2020;26(3):309–329. doi: 10.1016/j.stem.2020.02.011
28. Leys L, Wang Y, Paulsboe S, et al. Characterization of psoriasiform dermatitis induced by systemic injection of interleukin-23 minicircles in mice. J Dermatol. 2019;46(6):482–497. doi: 10.1111/1346-8138.14899
29. Sachen KL, Greving CNA, Towne JE, et al. Role of IL-36 cytokines in psoriasis and other inflammatory skin conditions. Cytokine. 2022;156:155897. doi: 10.1016/j.cyto.2022.155897
30. Schüler R, Brand A, Klebow S, et al. Antagonization of IL-17A attenuates skin inflammation and vascular dysfunction in mouse models of psoriasis. J Invest Dermatol. 2019;139(3):638–647. doi: 10.1016/j.jid.2018.09.021
31. Wang M, Zhang S, Zheng G, et al. Gain-of-function mutation of Card14 leads to spontaneous psoriasis-like skin inflammation through enhanced keratinocyte response to IL-17A. Immunity. 2018;49(1):66–79.e5. doi: 10.1016/j.immuni.2018.05.012
32. Zenz R, Eferl R, Kenner L, et al. Psoriasis-like skin disease and arthritis caused by inducible epidermal deletion of Jun proteins. Nature. 2005;437(7057):369–375. doi: 10.1038/nature03963
33. Schön MP, Manzke V, Erpenbeck L, et al. Animal models of psoriasis—highlights and drawbacks. J Allergy Clin Immunol. 2021;147(2):439–455. doi: 10.1016/j.jaci.2020.04.034
34. Sugai J, Iizuka M, Kawakubo Y, et al. Histological and immunocytochemical studies of human psoriatic lesions transplanted onto SCID mice. J Dermatol Sci. 1998;17(2):85–92. doi: 10.1016/S0923-1811(97)00077-7
35. Guerrero-Aspizua S, García M, Murillas R, et al. Development of a bioengineered skin-humanized mouse model for psoriasis: dissecting epidermal-lymphocyte interacting pathways. Am J Pathol. 2010;177(6):3112–3124. doi: 10.2353/ajpath.2010.100078
36. Pouliot-Bérubé C, Zaniolo K, Guérin SL, et al. Tissue-engineered human psoriatic skin supplemented with cytokines as an in vitro model to study plaque psoriasis. Regen Med. 2016;11(6):545–557. doi: 10.2217/rme-2016-0037
37. Morgner B, Werz O, Wiegand C, et al. Bilayered skin equivalent mimicking psoriasis as predictive tool for preclinical treatment studies. Commun Biol. 2024;7(1):1529. doi: 10.1038/s42003-024-07226-x
38. Shaw I, Ali YS, Nie C, et al. Integrating artificial intelligence and microfluidics technology for psoriasis therapy: a comprehensive review for research and clinical applications. Adv Intell Syst. 2024;7(4):2400558. doi: 10.1002/aisy.202400558
39. Cui N, Xu X, Zhou F, et al. Single-cell technologies in psoriasis. Clin Immunol. 2024;264:110242. doi: 10.1016/j.clim.2024.110242
40. Flutter B, Nestle FO. TLRs to cytokines: mechanistic insights from the imiquimod mouse model of psoriasis. Eur J Immunol. 2013;43(12):3138–3146. doi: 10.1002/eji.201343801
41. Zhang JY. Animal models of skin disorders. Animal models for the study of human disease. Elsevier. 2017:357–375.
42. Jabeen M, Boisgard AS, Danoy A, et al. Advanced characterization of imiquimod-induced psoriasis-like mouse model. Pharmaceutics. 2020;12(9):789. doi: 10.3390/pharmaceutics12090789
43. Joseph T, Genkin M, Genkin A, et al. The efficacy of imiquimod-induced psoriasis model on murine cells. Cureus. 2024;16(6):e62914. doi: 10.7759/cureus.62914
44. Chen HH, Chao YH, Chen DY, et al. Oral administration of acarbose ameliorates imiquimod-induced psoriasis-like dermatitis in a mouse model. Int Immunopharmacol. 2016;33:70–82. doi: 10.1016/j.intimp.2016.02.001
45. Silva-Abreu M, Sosa L, Espinoza LC, et al. Efficacy of apremilast gels in mouse model of imiquimod-induced psoriasis skin inflammation. Pharmaceutics. 2023;15(10):2403. doi: 10.3390/pharmaceutics15102403
46. Shahraz A, Kopatz J, Mathy R, et al. Anti-inflammatory activity of low molecular weight polysialic acid on human macrophages. Sci Rep. 2015;5(1):16800. doi: 10.1038/srep16800
47. Palombo R, Savini I, Avigliano L, et al. Luteolin-7-glucoside inhibits IL-22/STAT3 pathway, reducing proliferation, acanthosis, and inflammation in keratinocytes and in mouse psoriatic model. Cell Death Dis. 2016;7(8):e2344. doi: 10.1038/cddis.2016.201
48. Straß S, Geiger J, Cloos N, et al. Immune cell targeted fumaric esters support a role of GPR109A as a primary target of monomethyl fumarate in vivo. Inflammopharmacology. 2023;31(3):1223–1239. doi: 10.1007/s10787-023-01186-0
49. Pandey R, Bakay M, Hakonarson H, et al. SOCS-JAK-STAT inhibitors and SOCS mimetics as treatment options for autoimmune uveitis, psoriasis, lupus, and autoimmune encephalitis. Front Immunol. 2023;14:1271102. doi: 10.3389/fimmu.2023.1271102
50. Smith SH, Jayawickreme C, Rickard DJ, et al. Tapinarof is a natural AhR agonist that resolves skin inflammation in mice and humans. J Invest Dermatol. 2017;137(10):2110–2119. doi: 10.1016/j.jid.2017.05.004
51. Hashimoto T, Sakai K, Sanders KM, et al. Antipruritic effects of Janus kinase inhibitor tofacitinib in a mouse model of psoriasis. Acta Derm Venereol. 2019;99(3):298–303. doi: 10.2340/00015555-3086
52. Salgado G, Ng YZ, Koh LF, et al. Human reconstructed skin xenografts on mice to model skin physiology. Differentiation. 2017;98:14–24. doi: 10.1016/j.diff.2017.09.004
53. Cristóbal L, Asúnsolo Á, Sánchez J, et al. Mouse models for human skin transplantation: a systematic review. Cells Tissues Organs. 2021;210(4):250–259. doi: 10.1159/000516154

54. Mirzoeva S, Yang Y, Klopot A, et al. Early stress-response gene REDD1 controls oxazolone-induced allergic contact dermatitis. J Immunol. 2021;207(7):1747–1754. doi: 10.4049/jimmunol.2100279
55. Bhoir SS, Vishwapathi V, Singh KK. Antipsoriatic potential of *annona squamosa* seed oil: an in vitro and in vivo evaluation. Phytomedicine. 2019;54:265–277. doi: 10.1016/j.phymed.2018.07.003
56. Singh P, Sharma S, Sharma PK, et al. Topical anti-ulcerogenic effect of the beta-adrenergic blockers on diabetic foot ulcers: recent advances and future prospectives. Curr Diabetes Rev. 2024;20(8):23–37. doi: 10.2174/0115733998249061231009093006
57. Jin J, Xue N, Liu Y, et al. A novel S1P1 modulator IMMH002 ameliorates psoriasis in multiple animal models. Acta Pharm Sin B. 2020;10(2):276–288. doi: 10.1016/j.apsb.2019.11.006
58. Suthar D, Raut R, Bajaj A. Advances in skin-mimetic platforms: a comprehensive review of drug permeation models. J Drug Deliv Sci Technol. 2024;98:105887. doi: 10.1016/j.jddst.2024.105887
59. Brito S, Baek M, Bin BH. Skin structure, physiology, and pathology in topical and transdermal drug delivery. Pharmaceutics. 2024;16(11):1403. doi: 10.3390/pharmaceutics16111403
60. Radu A, Tit DM, Endres LM, et al. Naturally derived bioactive compounds as precision modulators of immune and inflammatory mechanisms in psoriatic conditions. Inflammopharmacology. 2025;33(2):527–549. doi: 10.1007/s10787-024-01602-z
61. Nakajima K, Kataoka S, Sato K, et al. Stat3 activation in epidermal keratinocytes induces Langerhans cell activation to form an essential circuit for psoriasis via IL-23 production. J Dermatol Sci. 2019;93(2):82–91. doi: 10.1016/j.jdermsci.2018.11.007
62. Vats K, Tian H, Singh K, et al. Ferroptosis of select skin epithelial cells initiates and maintains chronic systemic immune-mediated psoriatic disease. J Clin Invest. 2025;135(2):e183219. doi: 10.1172/JCI183219
63. Koegel H, von Tobel L, Schäfer M, et al. Loss of serum response factor in keratinocytes results in hyperproliferative skin disease in mice. J Clin Invest. 2009;119(4):899–910. doi: 10.1172/JCI37771
64. Lian P, Li L, Lu R, et al. S1PR3-driven positive feedback loop sustains STAT3 activation and keratinocyte hyperproliferation in psoriasis. Cell Death Dis. 2025;16(1):31. doi: 10.1038/s41419-025-07358-w
65. Canavese M, Altruda F, Silengo L, et al. Clinical, pathological and immunological features of psoriatic-like lesions affecting keratin 14-vascular endothelial growth factor transgenic mice. Histol Histopath. 2011;26:285–296.
66. Canavese M, Altruda F, Ruzicka T, et al. Vascular endothelial growth factor (VEGF) in the pathogenesis of psoriasis—a possible target for novel therapies? J Dermatol Sci. 2010;58(3):171–176. doi: 10.1016/j.jdermsci.2010.03.023
67. Wang X, Sun J, Hu J, et al. IMQ induced K14-VEGF mouse: a stable and long-term mouse model of psoriasis-like inflammation. PLoS One. 2015;10(12):e0145498. doi: 10.1371/journal.pone.0145498
68. Chen Y, Tai Z, Zhu C, et al. Vascular endothelial growth factor a VEGFA inhibition: an effective treatment strategy for psoriasis. Int J Mol Sci. 2023;25(1):59. doi: 10.3390/ijms25010059
69. Liu T, Li S, Yin S, et al. The IL-23/IL-17 pathway in inflammatory skin diseases: from bench to bedside. Front Immunol. 2020;11:594735. doi: 10.3389/fimmu.2020.594735
• **The elucidation of IL-23/IL-17 pathway in psoriatic pathogenesis.**
70. Khmaladze I, Nandakumar KS, Holmdahl R, et al. Reactive oxygen species in psoriasis and psoriasis arthritis: relevance to human disease. Int Arch Allergy Immunol. 2015;166(2):135–149. doi: 10.1159/000375401
71. von Stebut E, Boehncke WH, Ghoreschi K, et al. IL-17A in psoriasis and beyond: cardiovascular and metabolic implications. Front Immunol. 2020;10:3096. doi: 10.3389/fimmu.2019.03096
72. Schinocca C, Rizzo C, Fasano S, et al. Role of the IL-23/IL-17 pathway in rheumatic diseases: an overview. Front Immunol. 2021;12:637829. doi: 10.3389/fimmu.2021.637829
73. Li H, Yao Q, Mariscal AG, et al. Epigenetic control of IL-23 expression in keratinocytes is important for chronic skin inflammation. Nat Commun. 2018;9(1):1420. doi: 10.1038/s41467-018-03704-z
74. Chen L, Deshpande M, Grisotto M, et al. Skin expression of IL-23 drives the development of psoriasis and psoriatic arthritis in mice. Sci Rep. 2020;10(1):8259. doi: 10.1038/s41598-020-65269-6
75. Luo T, Ma Y, Wei W. Murine models of psoriasis and its applications in drug development. J Pharmacol Toxicol Methods. 2020;101:106657. doi: 10.1016/j.vascn.2019.106657
76. Liu Y, Yang G, Zhang J, et al. Anti-TNF-α monoclonal antibody reverses psoriasis through dual inhibition of inflammation and angiogenesis. Int Immunopharmacol. 2015;28(1):731–743. doi: 10.1016/j.intimp.2015.07.036
77. D'Agostino M, Potestio L, Megna M, et al. PsoriasPsoriasIs, pregnancy and lactation: clinical implications and treatments. Expert Rev Clin Immunol. 2025:1–13. doi: 10.1080/1744666X.2025.2514606
78. Ubago-Rodríguez A, Quiñones-Vico MI, Sánchez-Díaz M, et al. Challenges in psoriasis research: a systematic review of preclinical models. Dermatology. 2024;240(4):620–652. doi: 10.1159/000538993
79. Bocheńska K, Smolińska E, Moskot M, et al. Models in the research process of psoriasis. Int J Mol Sci. 2017;18(12):2514. doi: 10.3390/ijms18122514
80. Dand N, Mahil SK, Capon F, et al. Psoriasis and genetics. Acta Derm Venerol. 2020;100(3):55–65. doi: 10.2340/00015555-3384
• **The genetic aspects of psoriasis.**
81. Imran M, Moyle P, Kamato D, et al. Advances in, and prospects of, 3D preclinical models for skin drug discovery. Drug Discov Today. 2024;29(12):104208. doi: 10.1016/j.drudis.2024.104208
82. Moon S, Kim DH, Shin JU. In vitro models mimicking immune response in the skin. Yonsei Med J. 2021;62(11):969–980. doi: 10.3349/ymj.2021.62.11.969
83. Wurbs A, Karner C, Vejzovic D, et al. A human ex vivo skin model breaking boundaries. Sci Rep. 2024;14(1):24054. doi: 10.1038/s41598-024-75291-7
84. Mirshafiei M, Rashedi H, Yazdian F, et al. Advancements in tissue and organ 3D bioprinting: current techniques, applications, and future perspectives. Mater Des. 2024;240:112853. doi: 10.1016/j.matdes.2024.112853
•• **The 3D skin bioprinting of the skin.**
85. Martínez-Navarro FJ, Martínez-Menchón T, Mulero V, et al. Models of human psoriasis: zebrafish the newly appointed player. Dev Comp Immunol. 2019;97:76–87. doi: 10.1016/j.dci.2019.03.018
86. Arjmand B, Alavi-Moghadam S, Kokabi-Hamidpour S, et al. Preparation and validation of zebrafish psoriasis model to investigate the therapeutic effects of stem cells. In: Skin stem cells: methods and protocols. Springer; 2023. p. 227–238.
87. Frantz WT, Ceol CJ. Research techniques made simple: zebrafish models for human dermatologic disease. J Invest Dermatol. 2022;142(3):499–506.e1. doi: 10.1016/j.jid.2021.10.016
• **Zebrafish model for exploring psoriatic pathogenesis.**
88. Gebremeskel E, Biru G, Gemechu H, et al. From diagnosis to treatment: a review of AI applications in psoriasis management. J. Electr. Eng Technol. 2025;20(4):2601–2615. doi: 10.1007/s42835-025-02195-5
• **A recent review for introduction of AI on psoriasis treatment.**
89. Liu Z, Wang X, Ma Y, et al. Artificial intelligence in psoriasis: where we are and where we are going. Exp Dermatol. 2023;32(11):1884–1899. doi: 10.1111/exd.14938
90. Wu Y, Ma L, Li X, et al. The role of artificial intelligence in drug screening, drug design, and clinical trials. Front Pharmacol. 2024;15:1459954. doi: 10.3389/fphar.2024.1459954
91. Chakraborty C, Achar U, Nayek S, et al. CAD-PsorNet: deep transfer learning for computer-assisted diagnosis of skin psoriasis. Sci Rep. 2024;14(1):26557. doi: 10.1038/s41598-024-76852-6
92. Fernandez-Carro E, Angenent M, Gracia-Cazaña T, et al. Modeling an optimal 3D skin-on-chip within microfluidic devices for pharmacological studies. Pharmaceutics. 2022;14(7):1417. doi: 10.3390/pharmaceutics14071417
93. Deng S, Li C, Cao J, et al. Organ-on-a-chip meets artificial intelligence in drug evaluation. Theranostics. 2023;13(13):4526. doi: 10.7150/thno.87266
•• **Organ-on-a-chip technique for drug discovery.**

94. Cho SW, Malick H, Kim SJ, et al. Advances in skin-on-a-chip technologies for dermatological disease modeling. J Invest Dermatol. 2024;144(8):1707–1715. doi: 10.1016/j.jid.2024.01.031
95. Wang T, Wu W, Zhang X, et al. Tofacitinib treatment for plaque psoriasis and psoriatic arthritis: a meta-analysis of randomised controlled trials. Indian J Dermatol Venereol Leprol. 2025;91(2):172–179. doi: 10.25259/IJDVL_14_2024
96. Yadav P, Wairkar S. Tofacitinib in focus: fascinating voyage from conventional formulations to novel delivery systems. Int J Pharm. 2025;671:125253. doi: 10.1016/j.ijpharm.2025.125253
97. Wang J, Ma T, Sun X, et al. Efficacy and safety of Janus kinase inhibitors in the treatment of psoriasis and psoriatic arthritis: an analysis of evidence from 2014 to 2022. Heliyon. 2025;11(3):e42084. doi: 10.1016/j.heliyon.2025.e42084
98. Rosas J, Belzunegui J, Hernández-Cruz B, et al. Real-world evidence for baricitinib in the treatment of rheumatoid arthritis in Spain: a systematic literature review. Adv Ther. 2025;42(5):2403–2428. doi: 10.1007/s12325-025-03161-3
99. Xiong S, Yang J, Yang M, et al. Discovery of a highly potent and selective tyrosine kinase 2 (TYK2) degrader with in vivo therapeutic efficacy in a murine psoriasis model. J Med Chem. 2025;68(7):7560–7578. doi: 10.1021/acs.jmedchem.5c00027
100. Yang H, Li N, Liu Y. Sotyktu (deucravacitinib): the first tyrosine kinase 2 (TYK2) inhibitor approved for the treatment of psoriasis. Drug Discov Stories. 2025:571–586.
101. Daudén E, Ortiz-Salvador JM, Notario J, et al. Secukinumab for treatment of plaque psoriasis in real-world clinical practice in Spain: a literature review. J Clin Med. 2025;14(2):478. doi: 10.3390/jcm14020478
102. Lam J, Cazzaniga S, Seyed Jafari SM, et al. Treatment of psoriasis with Il-17 inhibitors: comparison of long-term effectiveness and drug survival of secukinumab vs ixekizumab in real-world practice. psoriasis-Targets Ther. 2025;15:71–84. doi: 10.2147/PTT.S509495
103. Torii H, Morita A, Yamamoto C, et al. Safety and effectiveness of ixekizumab in Japanese patients with psoriasis vulgaris, psoriatic arthritis, generalized pustular psoriasis, and erythrodermic psoriasis: Post-marketing surveillance. J Dermatol. 2025;52(5):787–801. doi: 10.1111/1346-8138.17695
104. Xiong J, Chen X, Huang K, et al. Successful guselkumab treatment in a patient with comorbid psoriasis and amyotrophic lateral sclerosis: a case study and literature review. Clin Cosmet Invest Dermatol. 2025;18:735–741. doi: 10.2147/CCID.S505143
105. Gerdes S, Hoffmann M, Asadullah K, et al. Effectiveness, safety and quality-of-life effects of guselkumab and ustekinumab in patients with psoriasis: week 104 results from the non-interventional, prospective, German multicentre PERSIST study. J Eur Acad Dermatol Venereol. 2025;39(S1):38–49. doi: 10.1111/jdv.19296
106. Kim J, Lee J, Lee J, et al. Psoriasis harbors multiple pathogenic type 17 T-cell subsets: selective modulation by risankizumab. J Allergy Clin Immunol. 2025;155(6):1898–1912. doi: 10.1016/j.jaci.2025.02.008
107. Patel A, Jain P, Thaker A, et al. Recent review on herbs and medicinal plant-based nanotechnological approach in treating psoriasis. Curr Bioact Compd. 2025;21(3):e300524230528. doi: 10.2174/0115734072312903240523060831
108. Ebrahimi A, Mehrabi M, Miraghaee SS, et al. Flavonoid compounds and their synergistic effects: promising approaches for the prevention and treatment of psoriasis with emphasis on keratinocytes–A systematic and mechanistic review. Int Immunopharmacol. 2024;138:112561. doi: 10.1016/j.intimp.2024.112561
109. Zheng Y, Tan H, Chai J, et al. Ginseng fruit rare saponins (GFRS) improved inflammatory response: In vitro and in vivo assessment. Fitoterapia. 2024;179:106244. doi: 10.1016/j.fitote.2024.106244
110. Lin X, Meng X, Lin J. The role of aryl hydrocarbon receptor in the pathogenesis and treatment of psoriasis. J Cutan Med Surg. 2024;28(3):276–286. doi: 10.1177/12034754241239050
111. Gayibova S, Ivanisova E, Gayibov U, et al. Dietary plant flavone cynaroside and its biological significance. Herbs And spices-New Perspectives In Hum Health And Food Ind: New Perspectives In Hum Health And Food Ind. 2024:211.
112. De Stefano A, Caporali S, Di Daniele N, et al. Anti-inflammatory and proliferative properties of luteolin-7-O-glucoside. Int J Mol Sci. 2021;22(3):1321. doi: 10.3390/ijms22031321
113. Krueger JG, Eyerich K, Kuchroo VK, et al. IL-23 past, present, and future: a roadmap to advancing IL-23 science and therapy. Front Immunol. 2024;15:1331217. doi: 10.3389/fimmu.2024.1331217
114. Nazimek K, Bryniarski K. Macrophage functions in psoriasis: lessons from mouse models. Int J Mol Sci. 2024;25(10):5306. doi: 10.3390/ijms25105306
    - **The role of macrophage on psoriasis.**
115. Borade S, Belgaumkar VA, Chavan RB, et al. Evaluation of IHC ki-67 with clinical correlation in psoriasis. Serb J Dermatol Venereol. 2020;12(2):33–40. doi: 10.2478/sjdv-2020-0006
116. Surcel M, Munteanu AN, Huică RI, et al. Reinforcing involvement of NK cells in psoriasiform dermatitis animal model. Exp Ther Med. 2019;18(6):4956–4966. doi: 10.3892/etm.2019.7967
117. Nakamizo S, Dutertre CA, Khalilnezhad A, et al. Single-cell analysis of human skin identifies CD14+ type 3 dendritic cells co-producing IL1B and IL23A in psoriasis. J Exp Med. 2021;218(9):e20202345. doi: 10.1084/jem.20202345
118. Emmanuel T, Petersen A, Houborg HI, et al. Climatotherapy at the Dead Sea for psoriasis is a highly effective anti-inflammatory treatment in the short term: an immunohistochemical study. Exp Dermatol. 2022;31(8):1136–1144. doi: 10.1111/exd.14549
119. Saleh AA, Tayel SI, Shehata WA, et al. Estimate of circRnas and microRNAs synergies on clinical advance of psoriasis. J Immunoass Immunoch. 2025;46(2):147–168. doi: 10.1080/15321819.2024.2447726
120. Parab S, Doshi G. The experimental animal models in psoriasis research: a comprehensive review. Int Immunopharmacol. 2023;117:109897. doi: 10.1016/j.intimp.2023.109897

Biochemical Pharmacology 242 (2025) 117346

Contents lists available at ScienceDirect

Biochemical Pharmacology

journal homepage: www.elsevier.com/locate/biochempharm

Melatonin attenuates high-fat diet- and particulate matter-induced cardiac injury: involvement of mitochondrial quality and miR-221/222 expression

Ya-Chun Chen [a,1], Ming-Hsueh Lee [b,c,1], Szu-Ju Fu [a], Chiang-Wen Lee [d,e,f], Wen-Chi Shen [a], Tsai-Chun Lai [a,g,h], Shu-Rung Lin [i,j], Shu-Wha Lin [k], I-Shing Yu [l], Tzu-Yi Chuang [m], Jaw-Shiun Tsai [n,o,*,2], Yuh-Lien Chen [a,**,2]

[a] Department of Anatomy and Cell Biology, College of Medicine, National Taiwan University, Taipei, Taiwan
[b] Division of Neurosurgery, Department of Surgery, Chang Gung Memorial Hospital, Chiayi, Taiwan
[c] Department of Respiratory Care, Chang Gung University of Science and Technology, Chiayi, Taiwan
[d] Department of Orthopaedic Surgery, Chang Gung Memorial Hospital, Puzi City, Chiayi County, Taiwan
[e] Department of Nursing, Division of Basic Medical Sciences, and Chronic Diseases and Health Promotion Research Center, Chang Gung University of Science and Technology, Puzi City, Chiayi County, Taiwan
[f] Research Center for Industry of Human Ecology and Research Center for Chinese Herbal Medicine, Chang Gung University of Science and Technology, Guishan District, Taoyuan City, Taiwan
[g] Department of Life Sciences, College of Life Sciences, National Chung Hsing University, Taichung, Taiwan
[h] The iEGG and Animal Biotechnology Center, National Chung Hsing University, Taichung, Taiwan
[i] Department of Bioscience Technology, College of Science, Chung Yuan Christian University, Taoyuan, Taiwan
[j] Center for Nanotechnology, Chung Yuan Christian University, Taoyuan, Taiwan
[k] Department of Clinical Laboratory Sciences and Medical Biotechnology, College of Medicine, National Taiwan University, Taipei, Taiwan
[l] Laboratory Animal Center, College of Medicine, National Taiwan University, Taipei, Taiwan
[m] Department of Pulmonary Medicine, Taoyuan General Hospital, Ministry of Health and Welfare, Taoyuan, Taiwan
[n] Department of Family Medicine, National Taiwan University Hospital, Taipei, Taiwan
[o] Center for Complementary and Integrated Medicine, National Taiwan University Hospital, Taipei, Taiwan

ARTICLE INFO

Keywords:
Particulate matter
High-fat diet
Melatonin
ROS
Mitochondria
miR-221/222

ABSTRACT

Previous studies have shown that exposure to hyperlipidemia or particulate matter (PM) individually affects the progression of cardiovascular disease (CVD), but the combined effects of these factors remain understudied. This study investigated whether combined treatment with a high-fat diet (HFD)/palmitate (PA) and PM exacerbates cardiomyocyte injury and proposed using the antioxidant melatonin. Furthermore, we explored the role of mitochondria and *miR-221/222* in melatonin-mediated reduction of HFD- and PM-exacerbated cardiomyocyte injury. H9c2 cells were treated with or without 50 μM PA, 10 μg/mL PM, and 100 μM melatonin for 24 h. In the *in vivo* experiments, 8–12-week-old wild-type (WT) mice, *miR-221/222* knockout (*miR-221/222*$^{-/-}$) mice, and *miR-221/222* overexpression (*miR-221/222*$^{o/e}$) mice were treated with HFD for 4 weeks. PM was injected intratracheally at the end of the second and third weeks, and melatonin 20 mg/kg was administered orally daily starting at the end of the second week. Combined PA/HFD and PM induced mitochondrial ROS accumulation, subsequent mitochondrial fission, and excessive mitophagy in cardiomyocytes and cardiac tissues. This cascade increases cardiomyocyte apoptosis and fibrosis, leading to cardiac dysfunction. Melatonin treatment reduced mitochondrial ROS accumulation and improved HFD- and PM-induced cardiac dysfunction. Further exploration of the molecular mechanism highlighted that *miR-221/222* upregulation is a downstream effect of melatonin, revealing a novel regulatory pathway for HFD- and PM-induced cardiac injury. This study showed that simultaneous exposure to HFD/PA and PM exacerbated cardiomyocyte apoptosis and fibrosis. These effects could be ameliorated by melatonin-mediated ROS scavenging, maintenance of mitochondrial function, and cardioprotection associated with *miR-221/222*.

* Corresponding author at: Department of Family Medicine, National Taiwan University Hospital, Taipei, Taiwan.
** Corresponding author.
E-mail addresses: jawshiun@ntu.edu.tw (J.-S. Tsai), ylchenv@ntu.edu.tw (Y.-L. Chen).
[1] Ya-Chun Chen and Ming-Hsueh Lee contributed equally to this study.
[2] Yuh-Lien Chen and Jaw-Shiun Tsai contributed equally to this study.

https://doi.org/10.1016/j.bcp.2025.117346
Received 23 June 2025; Received in revised form 20 August 2025; Accepted 17 September 2025
Available online 17 September 2025
0006-2952/© 2025 The Authors. Published by Elsevier Inc. This is an open access article under the CC BY-NC-ND license (http://creativecommons.org/licenses/by-nc-nd/4.0/).

1. Introduction

Abbreviations

AO	acridine orange
Baf	bafilomycin A1
BCL2	B-cell lymphoma 2
CVD	cardiovascular disease
DHE	dihydroethidium
DRP1	dynamin-related protein 1
EF	ejection fraction
FIS1	mitochondrial fission 1
FS	fractional shortening
H&E	hematoxylin-eosin staining
HFD	high-fat diet
KO	*miR-221/222* knockout mice (*miR-221/222*$^{-/-}$)
IF	Immunofluorescence staining
IHC	immunohistochemistry
IVCT	isovolumic contraction time
IVRT	isovolumic relaxation time
LC3B	microtubule-associated proteins 1A/1B light chain 3B
Mdivi-1	mitochondrial division inhibitor-1
MitoQ	mitoquinol
MTT	3-(4,5-dimethylthiazol-2-yl)-2,5-diphenyltetrazolium bromide
OCR	oxygen consumption rate
OE	*miR-221/222* overexpression mice (*miR-221/222*$^{o/e}$)
PA	palmitate acid
PM	particulate matter
PUMA	P53 upregulated modulator of apoptosis
ROS	reactive oxygen species
TUNEL	terminal deoxynucleotidyl transferase (TdT)-mediated dUTP nick end labeling
TEM	transmission electron microscopy
RT-qPCR	quantitative reverse transcription PCR
WT	wild-type mice (C57BL/6)
Δψm	mitochondrial membrane potential

Cardiovascular disease (CVD) has become a leading cause of mortality and morbidity worldwide [1]. Epidemiological and clinical evidence indicate that metabolic factors (such as hyperlipidemia) and environmental factors (such as air pollution) are important risk factors associated with CVD [2,3]. Consumption of a high-fat diet (HFD) for 2 to 4 weeks can induce hyperlipidemia and manifest myocardial damage characterized by fibrosis and inflammation [4]. Consuming an HFD for more than two months can lead to cardiac hypertrophy and fibrosis [5]. Particulate matter (PM) pollution, a significant environmental risk factor affecting CVD, can be inhaled and enter the lung tissue. Specifically, PM2.5 (diameter < 2.5 μm) can easily reach the alveoli and enter the circulatory system through the capillaries, increasing the risk of CVD. PM-induced cardiomyocyte apoptosis is promoted by multiple mechanisms, such as mitochondrial damage [6]. Some studies have highlighted the importance of a single risk factor for CVD, but few have examined the effects of simultaneous exposure to multiple factors. One study showed that PM2.5 exposure increased embryonic lipotoxicity and oxLDL uptake, which may lead to the accumulation of ROS in the presence of concurrent fructose exposure [7]. Another study showed that PM2.5 induced myocardial damage in hyperlipidemic mice via the ROS-pyroptosis signaling pathway [8]. Although some studies have shown that risk factors, especially hyperlipidemia and PM, can cause cardiac tissue damage through ROS accumulation [9,10], the underlying mechanism remains unclear.

Elevated ROS levels in cardiac diseases cause mitochondrial dysfunction and activate mitochondrial fission [11,12]. Dynamin-related protein 1 (Drp1) expression plays a key role in mitochondrial fission, and targeted inhibition of its expression may have protective effects against CVD [11]. Primates exposed to chronic lipid overload showed elevated expression of p-Drp1S616 and Drp1 oligomers, leading to cardiomyocyte death and heart dysfunction [13]. Furthermore, PM exposure enhances mitochondrial fission and inhibits fusion, impairing mitochondrial function and disrupting mitophagy. Fragmented mitochondria undergo mitophagy, where they are transferred to autophagic lysosomes for degradation [14]. The mitophagy-related protein NIX/BNIP3 promotes cardiomyocyte apoptosis or necrosis [15]. Another study reported that HFD-induced cardiac cell apoptosis and fibrosis were caused by mitophagy and could be restored by enhancing autophagy [16]. In addition, PM also induces changes in ROS/PINK1/Parkin-mediated mitophagy in vascular smooth muscle cells, leading to vascular fibrosis [17]. However, whether combined HFD/PA and PM treatment affects mitochondrial dysfunction and mitophagy and leads to myocardial apoptosis and fibrosis remains to be further investigated.

Melatonin is a well-known ROS scavenger with therapeutic potential to alleviate oxidative stress-related diseases [18]. Melatonin protects against myocardial death induced by ischemia/reperfusion (I/R) and cardiac hypertrophy through the reduction of ROS [19]. However, how melatonin exerts its cardioprotective effects remains unclear. Current studies have also highlighted the impact of miRNAs on cardiac dysfunction [20]. Melatonin attenuates cardiac fibrosis by inhibiting *miR-141*-mediated NLRP3 inflammasome in diabetic cardiomyopathy [21]. Melatonin promotes cardiomyocyte proliferation and cardiac repair in mice through *miR-143-3p* [22]. *MiR-221/222* has attracted attention for its role as an essential biomarker and therapeutic target for CVD [23]. A previous study demonstrated that *miR-221/222* has a cardioprotective role in heart failure [24]. In addition, our previous study showed that *miR-221/222* has cardioprotective functions under I/R conditions [25]. Whether melatonin affects the expression of *miR-221/222* and its effect on cardiac function remains to be further studied. This study showed that combined PA/HFD and PM treatment increased ROS production, decreased mitochondrial function, and reduced *miR-221/222* expression, thereby increasing apoptosis and fibrosis, whereas melatonin reversed these effects.

2. Materials and methods

2.1. Establishment of an in vitro model of combined exposure to PA and PM

Rat embryonic ventricular cardiomyocytes H9c2 were purchased from the American Type Culture Collection (ATCC, VA, USA) and cultured in Dulbecco's modified Eagle's medium (DMEM, GIBCO, NY, USA) supplemented with 10 % fetal bovine serum (FBS, Biological Industries, Beit HaEmek, Israel) ~~(Gibco)~~, 1 % L-glutamine (Biological Industries, Beit HaEmek, Israel) and 1 % penicillin/streptomycin/amphotericin (Biological Industries, Beit HaEmek, Israel) at 37℃ in a humidified incubator with 95 % air and 5 % CO_2. Cells were treated with PA/NaCl or PM/DMEM to simulate patient exposure to an HFD and PM.

Sodium palmitate (PA, ≥98.5 %, Sigma, MO, USA) and bovine serum albumin (BSA) (≥96 %, Sigma, MO, USA) were dissolved in 150 mM sodium chloride solution to generate 5 mM PA/NaCl (aq) and 680 mM BSA/NaCl (aq) solutions, respectively. PA/NaCl (2 mM stock solution) was then diluted in culture medium to a final working concentration of 50 or 100 μM [26].

PM from Standard Reference Material 2786 (SRM2786, mean particle size < 4 μm, NIST, USA) was collected in Prague, Czech Republic, in 2005, and the components were characterized by GC/MS [27]. SRM2786 was dissolved in DMEM and sonicated three times for 10 min each to achieve a final 10 mg/mL concentration. The stock solution was stored at −20 °C. The solution was prewarmed, vortexed vigorously at 37 °C for 1 min, and then diluted with DMEM to the optimal concentration. PM (5, 10, or 50 μg/mL) was suspended in 1 mL of DMEM and then added to 10^5 cells seeded onto a 3.8 cm^2 surface. Appropriate concentrations of PA/NaCl, PM/DMEM, or both were added directly to the culture medium for 24 h.

All drug compounds were dissolved individually in DMSO to achieve working concentrations, and the final concentration of DMSO in the culture medium did not exceed 0.1 % (v/v). Cells were pretreated with 1 μM Mitoquinol (MitoQ, ROS inhibitor), 10 μM Mdivi-1 (DRP1 inhibitor), and 10 nM Bafilomycin A1 (Baf, autophagosome-lysosome fusion inhibitor) for 1 h and then PA and PM were added for 24 h [9,17,28]. Appropriate concentrations of melatonin (≥98 %, Sigma, MO, USA) were co-treated directly with PA and PM without pretreatment.

2.2. Establishment of an in vivo model of combined HFD and PM exposure

Male C57BL/6J wild-type (WT) mice, *miR-221/222* knockout (KO, *miR-221/222*$^{-/-}$) mice, and *miR-221/222* overexpression (OE, *miR-221/222*$^{o/e}$) mice, 8–12 weeks old, weighing 20 g, were fed a HFD, 58Y1 (DIO rodent purified diet with 60 % fat blue energy, containing 18.3 % protein, 60.9 % fat, and 20.1 % carbohydrate) (TestDiet, MN, USA) or a regular chow diet for 4 weeks. At the end of the 2nd and 3rd weeks of feeding, some mice were anesthetized by inhalation of 3 % isoflurane and injected intratracheally with 10 mg/mL PM diluted in PBS to simulate an air pollution environment [29]. *MiR221/222* knockout (KO) mice were generated by deleting the X-linked *miR-221/222* gene and backcrossed on a B6 background for 10 generations [30–32]. *MiR221/222* overexpression (OE) mice were generated by pronuclear microinjection of human U6 promoter driven mouse miR-221/222 gene in B6 background [30,31]. For melatonin administration, DMSO-dissolved melatonin diluted 1:49 in PBS was given by oral gavage starting at the end of the second week. Melatonin was injected daily at 100 μL at a 20 mg/kg dose. All animals used in this study were obtained from the Experimental Animal Center, National Taiwan University College of Medicine (Taipei, TW). Animal handling and experimental procedures were performed under the Guide for the Care of Animals approved by the Institutional Animal Care and Use Committee (IACUC) (IACUC Approval Number: 20180426) and the Guide for the Care and Use of Laboratory Animals published by the National Institutes of Health (NIH) Publication number: 86–23, revised 1985).

After a 4-week experimental period, cardiac physiological function was assessed using an ultrasound cardiac examination. Mice were anesthetized with 1.5 % isoflurane inhalation, and echocardiographic analysis was performed using a small animal high-resolution ultrasound system (Prospect, S-Sharp, Taiwan). M−mode images perpendicular to the ventricular septum and posterior wall were obtained to measure left ventricular fractional shortening (FS) and ejection fraction (EF). PW-mode results were determined by Doppler analysis to measure blood flow velocity and evaluate isovolumetric relaxation time (IVRT) and isovolumetric contraction time (IVCT). All echocardiographic measurements were performed by experienced operators blinded to the experimental groups.

After physiological assessment, mice were sacrificed, and heart and blood samples were collected for subsequent experiments. The heart was divided into several parts for the following experiments. Most of the apical tissue was immediately frozen in liquid nitrogen for protein or mRNA extraction, and the remainder was stored in a fixative containing 2 % paraformaldehyde and 2 % glutaraldehyde in preparation for transmission electron microscopy (TEM) examination. Ventricles were isolated and fixed in 4 % paraformaldehyde or 10–30 % sucrose for 3–7 days and then embedded in paraffin or OCT, respectively. For paraffin-embedded sections (5 μm thick), hematoxylin-eosin (H&E) staining, terminal deoxynucleotidyl transferase (TdT)-mediated dUTP nick end labeling (TUNEL) assay, Sirius red staining, or immunohistochemistry (IHC) were used. IHC was used to observe the changes in myocardial morphology. For OCT-embedded sections (7 μm thick), immunofluorescence (IF) staining was performed to verify the extent of fat uptake or ROS accumulation in the myocardium.

2.3. Assessment of cell viability and apoptosis

The viability of cardiomyocytes treated with or without different concentrations of PA (50 or 100 μM), PM (5, 10, and 50 μg/mL), and melatonin (50, 100, and 200 μM) was assessed using a 3-(4, 5-dimethylthiazol-2-yl)-2,5-diphenyltetrazolium bromide (MTT) assay (Sigma, MO, USA). H9c2 cells with various treatments were added with 100 μL of MTT reagent (0.5 mg/mL in sterile PBS) and incubated at 37 °C in the dark for 2 h. Formazan crystals formed by viable cells were dissolved by the addition of 50 μL of DMSO, and the cells were incubated at 37 °C for 15 min. The relative absorbance at 570 nm was measured using an ELISA reader (BioTek, VT, USA) and calculated and normalized to the relative absorbance of the control group.

The TUNEL method was used to detect cardiomyocyte apoptosis. The apoptotic cells were labeled using the In Situ Cell Death Detection Kit (Roche, CA, USA), and then the percentage of TUNEL-positive nuclei to total nuclei was quantified. For *in vitro* labeling, luciferin-dUTP was used to label the 3′OH end, and DAPI to stain the nuclei. For *in vivo* labeling, DAB + POD was used, and the nuclei were stained with hematoxylin. Five randomly selected fields were examined in a blinded manner at 40 × magnification. In each field, the number of TUNEL-positive nuclei was counted and normalized to the total number of nuclei present. Annexin V-FITC and PI apoptosis detection kits (BD Biosciences, CA, USA) were used to determine the degree of cardiomyocyte apoptosis.

2.4. Fibrosis assessment

Paraffin-embedded heart sections, 5 μm thick, were subjected to Sirius red staining and IHC to determine the extent of fibrosis. After incubation with Sirius Red for 1 h, the heart sections were destained, dehydrated, and mounted with a mounting medium. Red represents collagen deposition in heart sections. For IHC, heart sections were deparaffinized and rehydrated, followed by antigen retrieval using 10 mM sodium citrate. Sections were treated with 3 % hydrogen peroxide to eliminate endogenous peroxidase and blocked with normal horse serum. Fibrosis-related primary antibodies, including antibodies against fibronectin (1:200 dilution, Abcam, Cambridge, UK) and ETS-1 (1:100 dilution, Abcam, Cambridge, UK), were incubated with heart sections overnight at 4 °C. Biotin-conjugated secondary antibodies (1:200 dilution) were applied, and avidin–biotin complex (ABC) was added to enhance signal detection sensitivity. Signals were visualized using 3′, 3′-diaminobenzidine (DAB), and sections were counterstained with hematoxylin. In addition, cardiomyocytes were treated and fixed with 4 % paraformaldehyde for 30 min and then permeabilized using 0.1 % Triton X-100. Subsequently, cells were blocked with 1 % BSA (Novagen, Darmstadt, Germany) and incubated with fibrosis-related primary antibodies overnight at 4 °C. After washing three times with PBS, the cells were incubated with a secondary antibody (Alexa Fluor 488 goat anti-rabbit IgG, 1:200 dilution, Invitrogen, MA, USA) for 1 h at room temperature in the dark. Nuclei were stained with DAPI before mounting the

slides using Fluoromount-G (Sigma, MO, USA).

2.5. Protein extraction procedure and Western blot analysis

Cardiomyocytes were lysed with sample buffer and denatured by heating at 100 °C for 10 min. In addition, cardiac tissues obtained from the apex were homogenized and lysed in RIPA buffer (H.M. Biological, Taiwan) supplemented with a protease and phosphatase inhibitor cocktail (Thermo, MA, USA) at 4 °C for 1 h. The protein concentration of each sample was determined using a BCA protein assay kit (Millipore, MA, USA) and adjusted to the same concentration (3 μg/μL).

Equal amounts of protein samples were loaded and separated by SDS-polyacrylamide gel electrophoresis. Then, they were transferred to a polyvinylidene fluoride (PVDF) membrane (Millipore, MA, USA). This was followed by incubation with a blocking solution of 5 % nonfat milk in TBST (10 mM Tris/150 mM NaCl/0.05 % Tween-20, pH 7.5) for 1 h at room temperature and then detected with primary antibodies overnight at 4 °C with the following reagents: Fibronectin (1:4000, ab2413, Abcam, Cambridge, UK), ETS-1 (1:1000, ab186844, Abcam, Cambridge, UK), PUMA (1:1000, ab9643, Abcam, Cambridge, UK), BCL2 (1:1000, BD 610539, BD Biosciences, CA, USA), Caspase 3 (1:1000, #9662, Cell Signaling, MA, USA), p-DRP1 (Ser616) (1:1000, #4494, Cell Signaling, MA, USA), FIS1 (1:1000, 10956–1-AP, Proteintech, IL, USA), p62 (1:1000, #5114, Cell Signaling, MA, USA), BNIP3 (1:1000, #3769, Cell Signaling, MA, USA), LC3B (1:2000, #2775, Cell Signaling, MA, USA), MT1 (1:1000, bs-0027R, Bioss, MA, USA), MT2 (1:1000, ab203346, Abcam, Cambridge, UK), and GAPDH (1:10000, 60004–1-lg, Proteintech, IL, USA).

2.6. Assessment of ROS accumulation in mitochondria or cytoplasm

MitoSOX Red (Invitrogen, MA, USA) and dihydroethidium (DHE, Invitrogen, MA, USA) were used to assess ROS accumulation in the desired mitochondria and cytoplasm. Mitochondrial ROS were detected in cardiomyocytes and cardiac tissue by immersing H9c2 cells or 7-μm-thick OCT-embedded heart sections in 5 μM MitoSOX Red for 20 min in the dark and then observing under a fluorescence microscope. In addition, the red fluorescence intensity of MitoSOX was quantified by flow cytometry and normalized to the *in vitro* control. To detect the accumulation of cytoplasmic ROS, 7-μm-thick OCT-embedded heart sections were incubated with 5 μM DHE in the dark for 20 min and then observed under a fluorescence microscope.

2.7. Assessment of mitochondrial function

Mitochondrial function was assessed by measuring mitochondrial membrane potential (Δψm), oxygen consumption rate (OCR), total ATP content, and *in vitro* mitochondrial dynamics. Δψm was examined using JC-1 staining. Healthy, negatively charged mitochondria allow the lipophilic JC-1 to enter and form aggregated complexes that fluoresce red. In contrast, unhealthy mitochondria fluoresce green as monomers. After H9c2 cells were subjected to different treatments, 1 μg/mL JC-1 (dissolved in DMSO; Cayman, MI, USA) was added to the culture medium, and the cells were incubated at 37 °C in the dark for 30 min. The fluorescence intensity was then observed and measured using a fluorescence microscope and flow cytometer. Further quantification was performed using FlowJo 7.6 software to determine the percentage of cells with low Δψm.

Mitochondrial stress testing was performed using a Seahorse XFe24 instrument and analyzed using Seahorse XFe24 wave software version Wave 2.2 (Seahorse Bioscience, Billerica, MA, USA). OCR was assessed using the Seahorse XF Cell Mitochondrial Stress Test Kit (Agilent, CA, USA) and the Seahorse Biosciences XFe24 Analyzer (Agilent, CA, USA). After different treatments, H9c2 cells (1×10^4 cells/well, seeded in 24-well plates) were washed twice with PBS and incubated in freshly prepared XF basal medium (DMEM, pH 7.3, containing 2 mM L-glutamine). The cells were incubated with 2 % FBS at 37 °C in a CO_2-free incubator for 1 h. In the Mito stress test, a combination of 1 μM oligomycin, 2 μM FCCP, 0.5 μM rotenone, and 0.5 μM antimycin was added sequentially, and the changes in OCR were recorded. Additionally, quantify key parameters of mitochondrial function according to the manufacturer's protocol.

Cellular ATP content was measured using an ATP assay kit (Thermo, MA, USA). Cardiomyocytes were trypsinized and suspended in RIPA buffer on ice, and the supernatant was collected by centrifugation at 14,000 g for 20 min at 4 °C. Luciferin levels were measured using SpectraMax i3x (Molecular Devices, CA, USA), and ATP levels were quantified and expressed as fold changes compared with the control group.

2.8. Assessment of mitophagy

The ultrastructure of mitochondria was examined using TEM to visualize the status of mitophagy. Cardiomyocytes and heart tissues were fixed in 2 % paraformaldehyde and 2 % glutaraldehyde in 0.1 M PBS at 4 °C overnight. The specimens were sequentially dehydrated in ethanol and embedded in epoxy resin. Ultrathin sections were stained with uranyl acetate and lead citrate and then observed under a Hitachi H7000 electron microscope (Hitachi, Tokyo, Japan).

Acridine orange (AO) staining was used to visualize autolysosomes in cardiomyocytes. The cells were incubated with 1 μg/mL AO (dissolved in DMSO) for 5 min at 37 °C in the dark. The fluorescence intensity was then observed and measured using a fluorescence microscope and flow cytometer. The percentage of cells enriched in autolysosomes was further quantified using FlowJo 7.6 software.

2.9. RNA isolation and quantitative reverse transcription PCR (RT-qPCR)

Total RNA was isolated from cardiomyocytes or cardiac tissues using TRIzol reagent (Thermo, MA, USA). Cells or tissues were collected and homogenized with TRIzol, followed by adding chloroform to isolate RNA. The RNA was then precipitated using isopropanol. After RNA was dissolved in DEPC-treated water, the concentration was measured using a NanoDrop™ 2000 spectrophotometer (Thermo, MA, USA).

RNA was reverse-transcribed into cDNA using TaqMan MicroRNA Reverse Transcription Kit (Invitrogen, CA, USA) for miRNA expression analysis. The miRNA template was amplified using specific TaqMan MicroRNA Assay Kit probes. The following probes were used: miR-221 (000524), miR-222 (002276), and U6 (001973). Quantitative PCR was performed using a real-time PCR system (QuantStudio™ 3 Real-Time PCR System, Applied Biosystems, MA, USA). The PCR reaction mixture included an amplified miRNA template, TaqMan MicroRNA Assay Kit probes, and UNG-free TaqMan™ Universal PCR Master Mix (Thermo, MA, USA). PCR cycling conditions were as follows: initial denaturation at 95 °C for 10 min, 40 cycles of denaturation at 95 °C for 15 sec, and annealing/extension at 60 °C for 1 min. The comparative threshold cycle (Ct) method detected the relative miRNA expression levels with U6 as an internal normalization control. The fold change of miRNA expression was calculated using the $2^{-\Delta\Delta Ct}$ formula, where $\Delta Ct =$ Ct (*miR-221* or *miR-222*) – Ct (U6), $\Delta\Delta Ct = \Delta Ct$ (sample) – ΔCt (control). All RT-qPCR experiments were performed in triplicate, and the average value was used for further analysis.

2.10. MiR-221/222 transfection

To investigate the role of *miR-221/222* in the study, miRNA transfection was performed using Lipofectamine 3000 reagent (Invitrogen, CA, USA). H9c2 cells were seeded in 12-well plates at a density of 7.5×10^4 cells per well and transfected with *miR-221/222* mimics (Dharmacon, CO, USA) to overexpress *miR-221/222*. Once cells reached 70–80 %

confluence, they were transfected with *miR-221/222* mimic or scramble (negative control) according to the manufacturer's protocol. Briefly, 1 μg/well of *miR-221/222* mimics or scrambles were mixed with serum-free DMEM medium, P3000, and Lipofectamine 3000 at appropriate ratios. The mixture was incubated for 15 min at 37 °C and transfected overnight. RT-qPCR assessed transfection efficiency.

2.11. Statistical analysis

In vitro and *in vivo* studies included at least three independent biological replicates. Representative results are presented, and data are expressed as mean ± standard error of the mean (SEM). Statistical analysis was performed using Statistical Software for the Social Sciences (SPSS) version 16.0, employing one-way analysis of variance (ANOVA) followed by Tukey's test for multiple comparisons. GraphPad Prism 6.0 was used for data visualization. The significance level was set at $p < 0.05$.

3. Results

3.1. Simultaneous exposure of cardiomyocytes to PA and PM induces apoptosis and fibrosis via increased ROS accumulation, but melatonin attenuates these effects

H9c2 cells were treated with PA and PM to mimic the combined effects of HFD and PM exposure *in vivo*. Treatment with PA (50 and 100 μM) or PM (5, 10, and 50 μg/mL) for 24 h significantly reduced cell viability compared with the control group. Combined treatment with PA (50 and 100 μM) and PM (10 μg/mL) significantly reduced cell viability compared with treatment with PA or PM alone (Fig. 1A, left bar graph). Different melatonin concentrations (50, 100, and 200 μM) did not reduce cell viability and were used to examine the effects of melatonin on PA and PA-induced cardiomyocyte apoptosis. 100 and 200 μM melatonin significantly alleviated the decrease in cell viability induced by PA + PM treatment (Fig. 1A, quantified bar graph on the right). Based on the above results, 50 μM PA, 10 μg/mL PM, or 100 μM melatonin treatment for 24 h were used the subsequent study. The expression levels of melatonin receptor MT1/2 were increased after melatonin treatment in the PA + PM environment (Fig. 1B). The apoptosis of cardiomyocytes was detected by TUNEL and Annexin V-FITC/PI double staining. Fluorescence microscopy showed that the number of TUNEL-positive cells increased significantly after PA + PM combined treatment compared with PM or PA alone. At the same time, melatonin reversed this effect (Fig. 1C, quantitative bar graph on the right). Similarly, flow cytometry revealed that the number of Annexin V/PI-positive cells increased significantly under PA + PM conditions, while melatonin attenuated this induction (Fig. 2A, 2B). In Western blot, apoptosis-related proteins PUMA and caspase 3 expressions were significantly increased. In contrast, the expression of anti-apoptotic protein BCL2 was decreased considerably after PA + PM treatment compared with the PA or PM treatment groups (Fig. 1D). Melatonin reversed these results (Fig. 1D). Previous studies have shown that excessive apoptosis is associated with fibrosis; we next investigated the fibrosis-related proteins, fibronectin and ETS-1 [25]. Immunofluorescence (IF) staining (Fig. 1E) and Western blot (Fig. 1F) showed that fibronectin and ETS-1 expression increased after PA + PM treatment, whereas melatonin significantly attenuated this increase. These results suggest that simultaneous exposure to PA and PM exacerbates cardiomyocyte apoptosis and fibrosis, whereas melatonin significantly attenuates the adverse changes induced by PA + PM co-treatment.

Elevated ROS levels are associated with signaling pathways that drive cellular apoptosis and promote tissue fibrosis [33]. Therefore, we examined ROS levels to determine whether the generation of ROS caused apoptosis and fibrosis induced by the PA + PM combination treatment. MitoSOX Red was used to indicate mitochondrial ROS and measured using fluorescence microscopy and flow cytometry because ROS is primarily produced by mitochondria [34]. Treatment with either PA or PM alone induced mitochondrial ROS production, and combined PA + PM treatment further increased ROS levels in cardiomyocytes (Fig. 1G, top). Melatonin or MitoQ, a ROS inhibitor, significantly attenuated the production of PA- and PM-induced mitochondrial ROS (Fig. 1G, middle and lower). Pretreatment of cardiomyocytes with MitoQ effectively reduced cell viability (Fig. 1H) and reversed PA- and PM-induced apoptosis (Fig. 1I and Fig. 2C). Western blot results showed that MitoQ pretreatment significantly reduced PUMA and caspase 3 levels, induced BCL2, and had an anti-apoptotic effect (Fig. 1K). MitoQ pretreatment significantly attenuated the PA- and PM-induced upregulation of fibronectin and ETS-1 expression, as assessed by IF (Fig. 1J) and Western blot (Fig. 1K). This evidence demonstrated that PA + PM causes cardiac damage and induces mitochondrial ROS production, and melatonin treatment can ameliorate these effects by inhibiting mitochondrial ROS production.

3.2. PA and PM combined treatment significantly induced mitochondrial dysfunction, but melatonin alleviated this effect

Increased mitochondrial ROS production often triggers mitochondrial fission and dysfunction in CVD [11,12]. Therefore, we focused on parameters such as mitochondrial membrane potential (Δψm), mitochondrial stress tolerance, and ATP production to evaluate the effects of combined PA and PM treatment on cardiomyocyte apoptosis and fibrosis via mitochondrial dysfunction. First, we detected Δψm by fluorescence microscopy and flow cytometry using JC-1 staining. PA + PM treatment significantly increased the number of low Δψm cells compared with PA or PM treatment alone (Fig. 3A, top). Melatonin significantly suppressed the increase in low Δψm cells (Fig. 3A, bottom). Mitochondrial stress tolerance was assessed using the hippocampal analyzer. The primary function of mitochondria is to produce ATP through respiration; therefore, we assessed OCR and cellular ATP levels to determine mitochondrial function. The overall OCR of the PA + PM treatment group was lower than that of those treated with PA or PM alone, while melatonin restored the decreased OCR. Furthermore, OCR analysis revealed that mitochondrial ATP production and maximal respiratory rate were restored in the melatonin-treated group (Fig. 3B). PA + PM treatment significantly decreased ATP levels by ATP assay compared with the groups treated with PA or PM alone, whereas melatonin significantly restored the decrease in ATP levels (Fig. 3C). Mitochondrial dynamics is considered a process that maintains mitochondrial quality [35]. Therefore, we assessed mitochondrial length by MitoTracker staining and the expression of key mitochondrial fission-related proteins p-DRP1 and FIS1 by Western blot. Compared with PA or PM alone, PA + PM combined treatment showed significantly reduced mitochondrial length (Fig. 3D) and increased expression of p-DRP1 and FIS1 (Fig. 3E). In contrast, melatonin reversed the PA + PM-induced mitochondrial fission (Fig. 3D, 3E). Cardiomyocytes treated with 10 μM Mdivi-1 (a DRP1 inhibitor) significantly reduced the mitochondrial length and the expression of pDRP1 and FIS1 under PM and PA co-treatment (Fig. 3F, 3G). Furthermore, Mdivi-1 reduced the number of low Δψm cells and increased the overall ATP level under PA + PM combined exposure (Fig. 4A, 4B). To verify the role of mitochondrial fission in PA + PM-induced cardiomyocyte injury, we evaluated cell viability and the extent of apoptosis and fibrosis under Mdivi-1 treatment. Under PA + PM combined treatment conditions, Mdivi-1 restored cell viability (Fig. 2H) and reduced apoptosis (Fig. 3I, 3 J,and Fig. 4C) and fibrosis (Fig. 3K, 3L) levels. MitoQ reduced the treatment of PA and PM-increased ROS production and mitochondrial fission while restoring mitochondrial function (Fig. 5A-5D). These results suggest that melatonin treatment significantly reduced mitochondrial dysfunction and mitochondrial

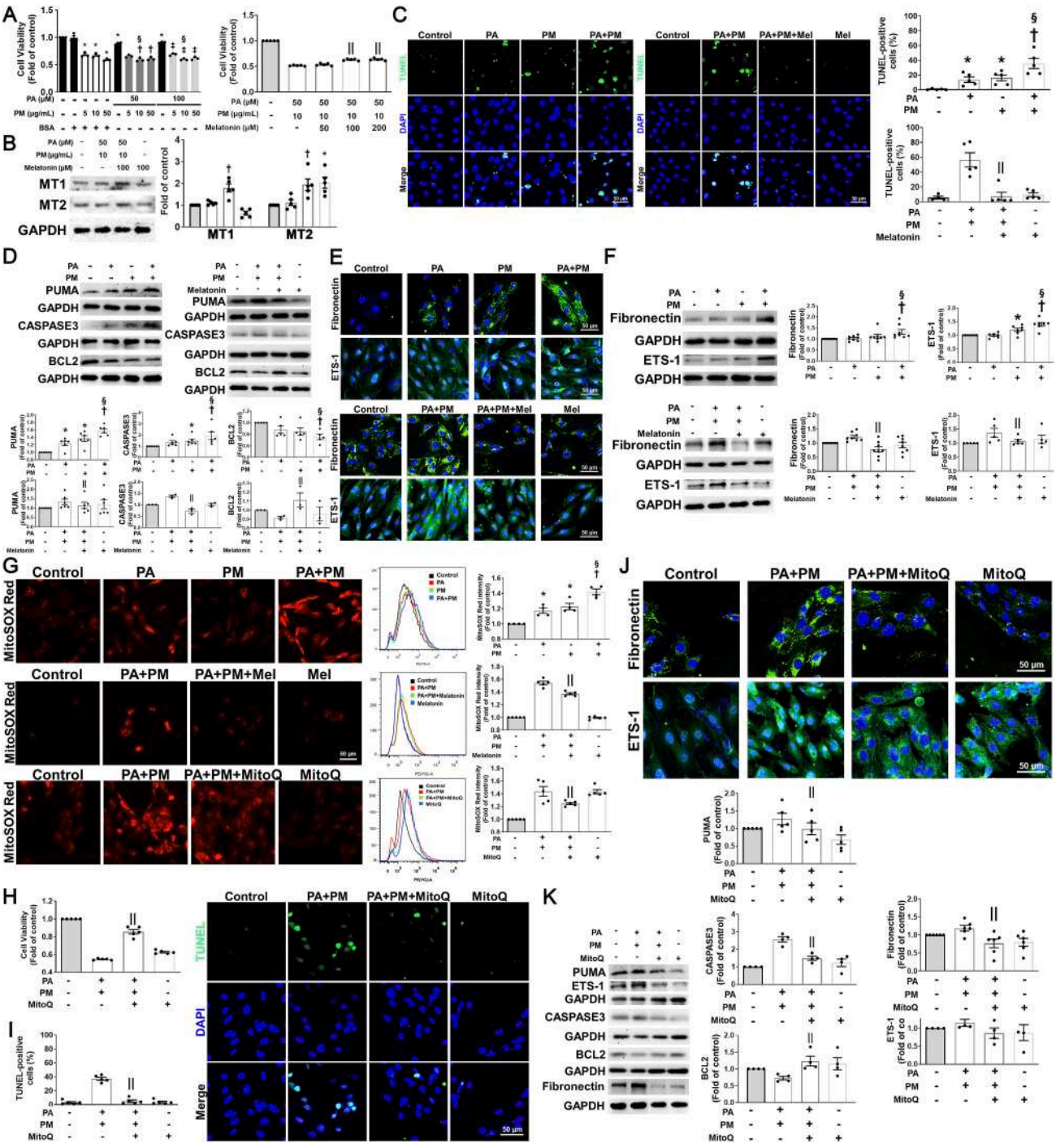


Fig. 1. Combined exposure to PA and PM aggravates cardiomyocyte injury by inducing ROS-dependent apoptosis and fibrosis, whereas melatonin alleviates these effects. (A) Cell viability of cardiomyocytes treated with different concentrations of PA (50 or 100 μM), PM (5, 10, 50 μg/mL), and melatonin (50, 100, and 200 μM) for 24 h was examined by MTT assay. In subsequent experiments, cells were treated with specific concentrations of 100 μM melatonin, 50 μM PA, and 10 μg/mL PM for 24 h. (B) Relative expression levels of melatonin receptor MT1/2. (C) The extent of apoptosis in cells treated with PA (50 μM), PM (10 μg/mL), and melatonin (100 μM) was examined by TUNEL assay (green: TUNEL-positive nuclei; blue: DAPI-stained nuclei; scale bar = 50 μm). Quantitative results are shown in the left panel. (D) The expression levels of apoptosis-related proteins (PUMA, caspase 3, and BCL2) after PA, PM, and melatonin treatment, as well as the quantitative results, were normalized with the internal control. (E) Representative images show fibronectin and ETS-1 expression through IF staining under PA, PM, and melatonin treatment. Green fluorescence indicates the location of fibrosis-related proteins counterstained with DAPI. (F) The expression levels of fibrosis-related proteins were normalized to internal controls by Western blot. (G-K) Cells were pretreated with 1 μM MitoQ for 1 h and then co-treated with PA (50 μM) and PM (10 μg/mL) for 24 h. (G) Mitochondrial ROS levels were assessed using MitoSOX Red staining by fluorescence microscopy and flow cytometry. The bar graph on the right shows the quantitative results of MitoSOX Red fluorescence intensity. (H) Cell viability of MitoQ-treated cells under PA and PM exposure was assessed using an MTT assay. (I) Representative images and TUNEL assay quantification showed that MitoQ treatment reduced apoptosis induced by PA and PM exposure. (J) IF examined the degree of fibrosis under MitoQ treatment. (K) MitoQ treatment under PA and PM exposure affected the expression of apoptosis- and fibrosis-related proteins. All bars represent mean ± SEM (N = 3–8). *p < 0.05 compared with the control group, †p < 0.05 compared with the PA (50 μM) group, ‡p < 0.05 compared with the PA (100 μM) group, §p < 0.05 compared with the PM (10 μg/mL), ||p < 0.05 compared with the PA (50 μM) + PM (10 μg/mL) group. Scale bar = 50 μm.

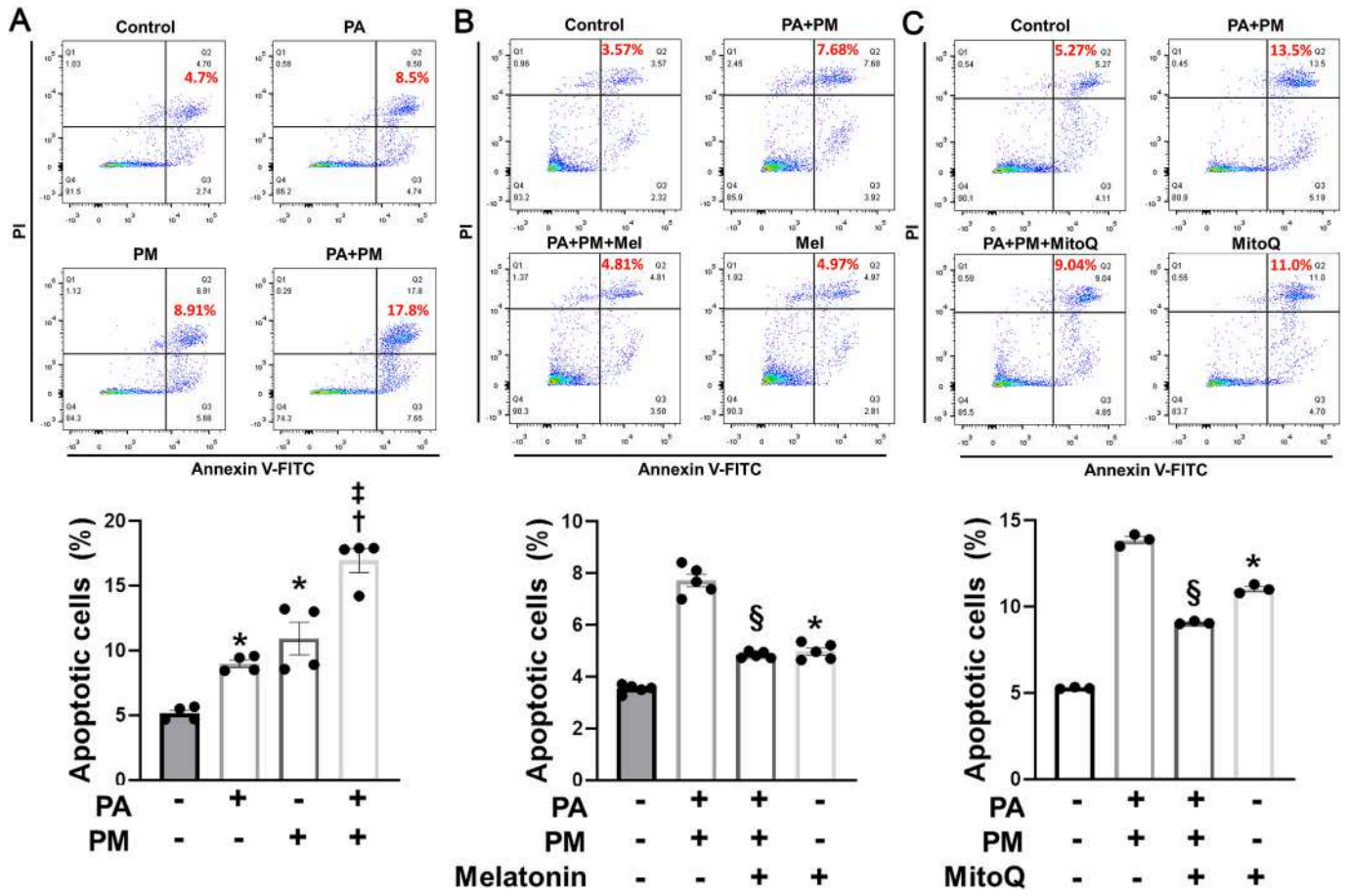


Fig. 2. Apoptosis was detected using Annexin V/PI staining after melatonin or MitoQ administration. Annexin V/PI and PI staining were evaluated by flow cytometry to assess the extent of cell apoptosis. (A) The number of apoptotic cells in the control, PA (50 μM), PM (10 μg/mL), and PA + PM groups indicated that PA + PM significantly induced apoptosis compared with the single treatment group. (B, C) Melatonin (100 μM) or MitoQ (1 μM, a ROS inhibitor) treatment reduced the increased number of apoptotic cells in PA + PM. All bars represent mean ± SEM (N = 3–5). *$p < 0.05$ compared with the control group, †$p < 0.05$ compared with the PA group, ‡$p < 0.05$ compared with the PM group, §$p < 0.05$ compared with the PA + PM group.

fission induced by simultaneous PA and PM exposure, thereby reducing apoptosis and fibrosis.

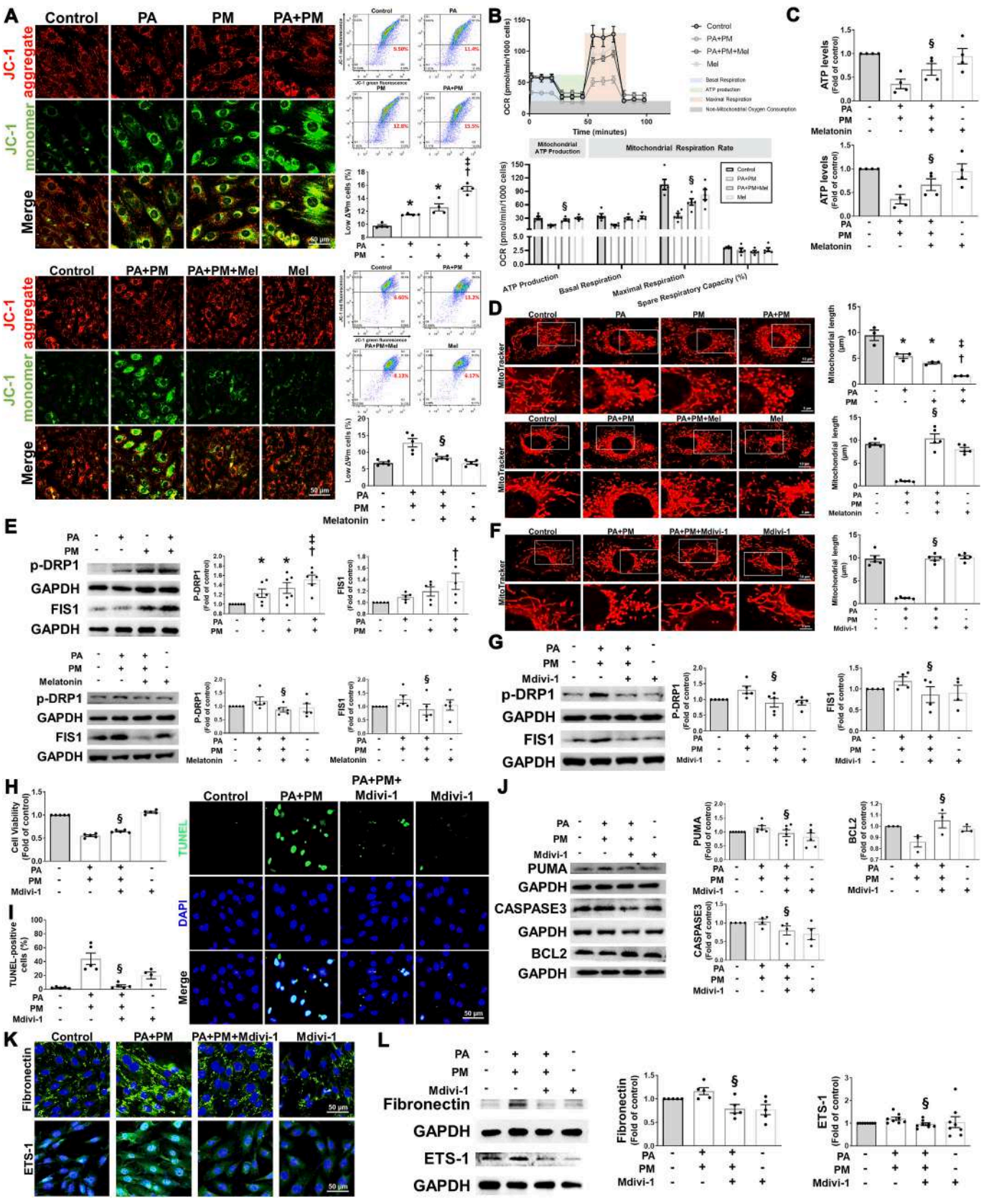
3.3. Combined treatment with PA and PM significantly induced mitophagy, but melatonin administration attenuated this effect

The process of mitophagy is responsible for the clearance of damaged mitochondria. Mitophagy is activated in response to mitochondrial fission [34]. Therefore, we focused on parameters such as autolysosome formation to evaluate the effects of combined PA and PM treatment on apoptosis and fibrosis via mitophagy. First, TEM was used to observe the ultrastructure of cells. The cells and mitochondria in the control group had normal morphology, while the cells in the PA + PM-treated group contained more autophagosomes containing mitochondria (Fig. 6A). PM + PA combined treatment significantly increased autolysomes, whereas melatonin suppressed red fluorescence as detected by AO staining under fluorescence microscopy and flow cytometry (Fig. 6B). In addition, Western blot revealed that the expression of mitophagy-related proteins p62, BNIP3, and LC3BII increased in the PA + PM treatment group, while melatonin decreased the expression of these proteins (Fig. 6C). Furthermore, the ROS inhibitor MitoQ and the DRP-1 inhibitor Mdivi-1 significantly inhibited PA + PM-induced mitophagy by AO staining (Fig. 7A, 7B). BNIP3 and LC3BII levels were increased under PA + PM treatment and inhibited under MitoQ and Mdivi-1 treatment (Fig. 7C, 7D).

To confirm that cardiomyocyte damage was caused by overactivation of mitophagy, we applied the autophagosome-lysosome fusion inhibitor Bafilomycin (Baf). Baf reduced the number of AO-positive cells induced by PA + PM and upregulated the expression of p62, BNIP3, and LC3BII (Fig. 6D, 6E). The decreased cell viability of PA + PM was restored by the addition of Baf (Fig. 6F). In addition, the number of TUNEL-positive cells and Annexin V/PI-positive cells induced by PA + PM was significantly reduced by the addition of Baf (Fig. 6G and Fig. 7E). Furthermore, Western blot results showed that adding Baf reduced the upregulation of apoptosis-related proteins induced by PA + PM (Fig. 3H). Both ICC and Western blot results showed that adding Baf under PA + PM conditions could reduce the expression of fibronectin and ETS-1 (Fig. 3I, 3 J). This evidence suggests that combined exposure to PA and PM triggers cardiomyocyte apoptosis and fibrosis in an enhanced mitophagy-dependent manner.

3.4. Mice fed an HFD and exposed to PM showed increased cardiac dysfunction, apoptosis, fibrosis, ROS generation, mitochondrial fission, and mitophagy, which were alleviated by melatonin

Based on the *in vitro* study results, we established an *in vivo* model to further verify the effects of combined HFD and PM exposure on cardiac function in mice and the therapeutic effects of melatonin treatment. Cardiac function was determined by obtaining EF and FS in M−mode images using echocardiography. The EF of the HFD group alone was lower than that in the control group, and the FS of the HFD + PM group was lower than in the PM group. Melatonin treatment restored the



(caption on next page)

Fig. 3. PA and PM cause mitochondrial dysfunction by triggering fission, whereas melatonin restores mitochondrial function and reduces fission. H9c2 cells were treated with or without 50 μM PA, 10 μg/mL PM, and 100 μM melatonin for 24 h. (A) The results of JC-1 staining were observed through fluorescence microscopy and flow cytometry (scale bar = 50 μm), and the ratio was quantified by flow cytometry. (B) Time-lapse OCR results of the Mito stress test are shown, and quantitative results for individual mitochondrial functions, including ATP production and respiratory rate, are shown in the lower bar graph panels. (C) ATP assay was used to assess cellular ATP levels. (D) Mitochondrial lengths determined by MitoTracker staining were captured and measured by ImageJ (scale bars = 10 and 5 μm). (E) The mitochondrial fission-related proteins p-DRP1 and FIS1 expression levels were determined by Western blot and normalized with internal control. (F-L) Cells were pretreated with 10 μM Mdivi-1 for 1 h and then co-treated with PA (50 μM) and PM (10 μg/mL) for 24 h. (F) The effect of Mdivi-1 on the mitochondrial length was examined using MitoTracker staining (scale bar = 10 and 5 μm). (G) The expression levels of mitochondrial fission-related proteins under Mdivi-1 treatment were analyzed by Western blot. (H) The effects of Mdivi-1 on the cell viability, (I, J) apoptosis, and (K, L) fibrosis under PA and PM co-treatment were examined (scale bar = 50 μm). All bars represent mean ± SEM (N = 4–6). *p < 0.05 compared with the control group, †p < 0.05 compared with the PA (50 μM) group, ‡p < 0.05 compared with the PM (10 μg/mL) group, §p < 0.05 compared with the PA (50 μM) + PM (10 μg/mL) group.

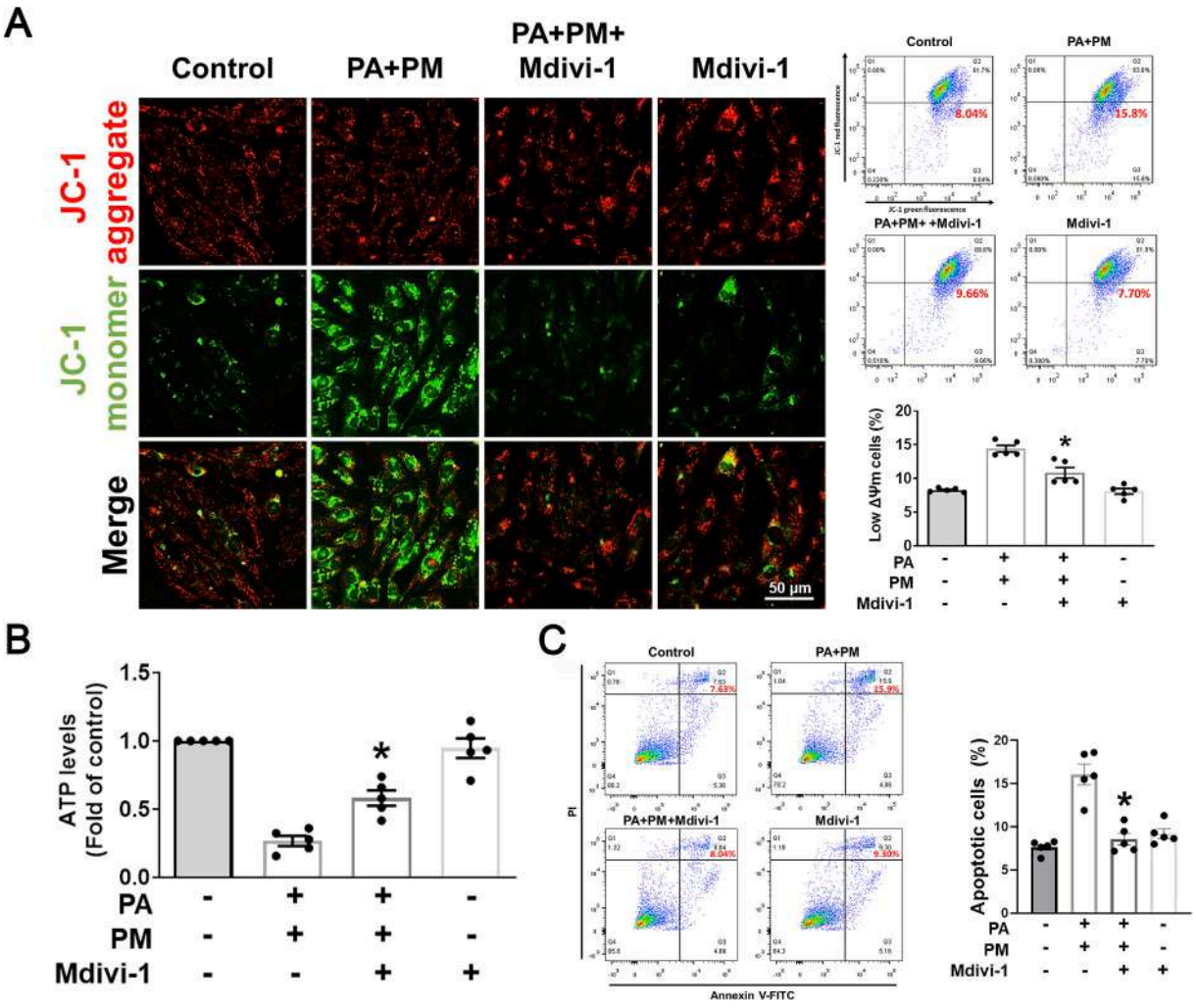


Fig. 4. Co-treatment with PA and PM decreased mitochondrial membrane potential (Δψm) and ATP production and increased apoptosis, while adding Mdivi-1 reduced these effects. H9c2 cells were pretreated with 10 μM Mdivi-1 for 1 h and then exposed to PA (50 μM) and PM (10 μg/mL) for 24 h. (A) JC-1 staining was performed by fluorescence microscopy and flow cytometry to examine the effect of adding Mdivi-1 on the mitochondrial membrane potential of cardiomyocytes under PA + PM treatment. (B) ATP assay was performed to investigate the metabolic function of mitochondria supplemented with Mdivi-1 under PA + PM conditions. (C) Annexin V/PI staining was measured by flow cytometry to examine the effect of Mdivi-1 addition on the extent of cell apoptosis. All bars represent mean ± SEM (N = 5). *p < 0.05 compared with the PA (50 μM) + PM (10 μg/mL) group.

decreasing trends of EF and FS caused by HFD and PM (Fig. 8A). Compared with the HFD or PM treatment groups alone, combined HFD and PM treatment significantly increased IVCT and IVRT from PW mode images, whereas melatonin treatment attenuated these changes (Fig. 8B). The number of TUNEL-positive cells increased in the HFD or PM alone-treated groups. Meanwhile, HFD + PM combined exposure further induced the number of TUNEL-positive cells. Furthermore, melatonin treatment effectively alleviated this increase (Fig. 8C). Similar to the results of TUNEL staining, Western blot analysis showed that the apoptosis-related protein PUMA increased and the anti-apoptotic protein BCL2 decreased in the HFD + PM group. Furthermore, melatonin treatment reversed its manifestation (Fig. 8D). The extent of fibrosis was increased in the HFD + PM group but was reduced after melatonin treatment examined by Sirius red staining and IHC for fibrosis-related proteins, fibronectin, and ETS-1 (Fig. 8E). Furthermore, Western blot results showed that the expressions of fibronectin and ETS-1 were increased in the HFD + PM group but were suppressed during melatonin administration (Fig. 8F). Under fluorescence microscopy of

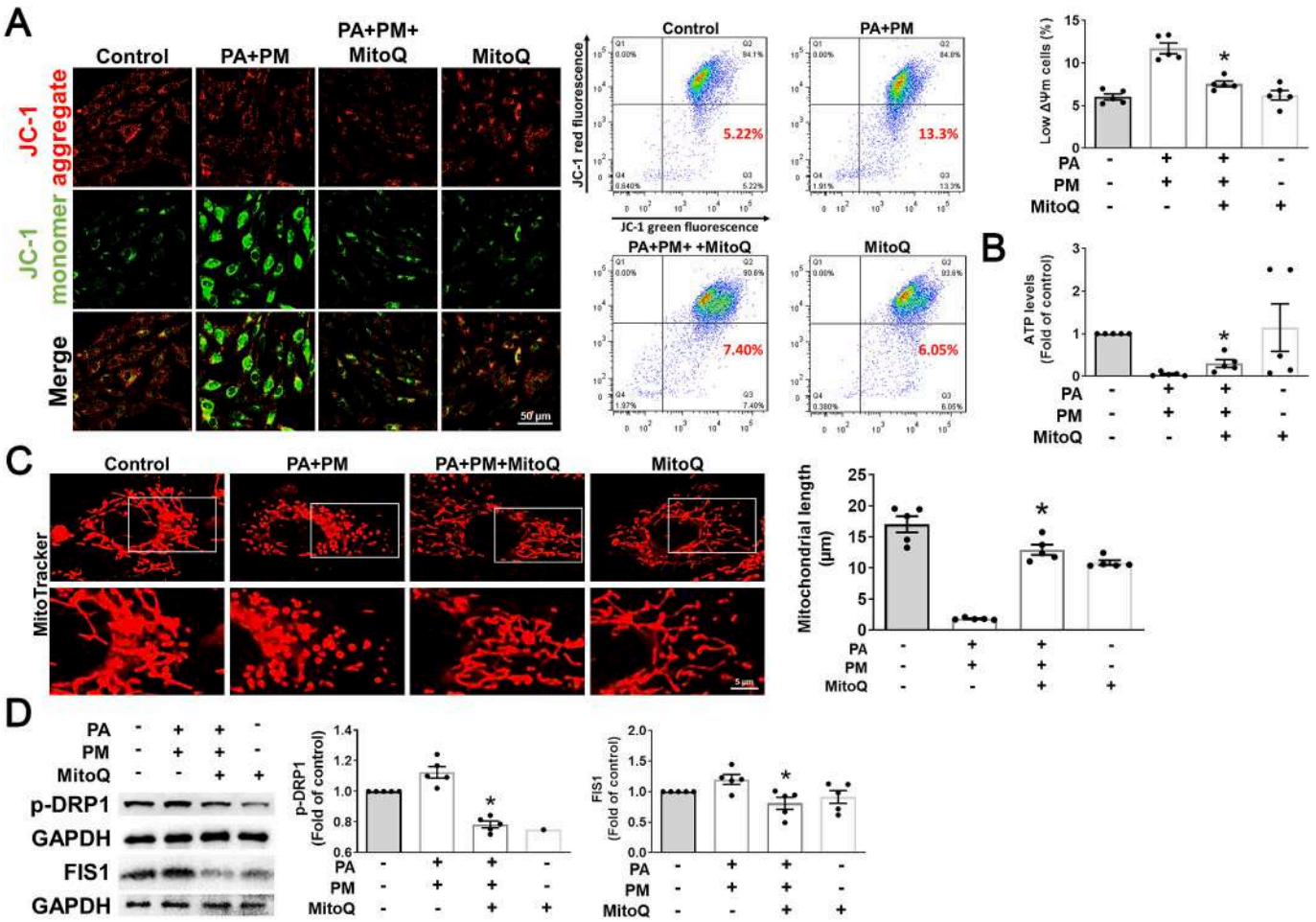


Fig. 5. Combined treatment with PA and PM caused decreased mitochondrial function and increased mitochondrial fission, and the addition of MitoQ, an inhibitor of mitochondrial ROS production, could reduce these effects. H9c2 cells were pretreated with 1 μM MitoQ for 1 h and then exposed to PA (50 μM) and PM (10 μg/mL) for 24 h. (A) Mitochondrial membrane potential (Δψm) was measured by JC-1 staining through fluorescent microscopy and flow cytometry. (B) Assessment of total ATP production by ATP assay. (C, D) Mitochondrial dynamics were measured by MitoTracker staining and the relative expression of mitochondrial fission proteins, p-DRP-1, and FIS1. All bars represent mean ± SEM (N = 5). *p < 0.05 compared with the PA (50 μM) + PM (10 μg/mL) group.

DHE and MitoSOX Red staining, intracellular and mitochondrial ROS production was significantly increased in the HFD, PM alone, and combined treatment groups. Notably, melatonin administration significantly reduced these expression levels (Fig. 8G). In addition, combined HFD and PM treatment induced mitochondrial fission protein markers, p-DRP1 and FIS1, whereas melatonin treatment reduced this increase (Fig. 8H). Furthermore, HFD and PM treatment significantly increased the expression of mitophagy-related proteins p62, BNIP3, and LC3BII. In contrast, melatonin treatment attenuated the excessive mitophagy, further confirming its potential therapeutic effect (Fig. 8I). HFD + PM treatment showed the mitophagosome and mitochondrial cristae disorganization under TEM in the HFD + PM-treated group. The melatonin-treated group showed well-organized cristae and better ultrastructure (Fig. 8J). These data support our *in vitro* findings that exposure to HFD or PM increased cardiac dysfunction, apoptosis, fibrosis, ROS generation, mitochondrial fission, and mitophagy. Furthermore, exposure to HFD and PM exacerbates these consequences. In contrast, taking melatonin significantly reduced these effects.

3.5. *MiR-221/222 plays a role in melatonin ameliorating PA- and PM-induced cardiomyocyte injury*

Previous studies have demonstrated that miRNAs play an essential role in CVD by regulating the expression levels of apoptosis or fibrosis-related proteins [36,37]. Our previous study showed that *miR-221/222* protects against myocardial I/R injury by coordinating anti-apoptotic and fibrotic defense by downregulating the expression of PUMA and ETS-1 [25]. Therefore, the role of *miR-221/222* in PA + PM-induced cardiac injury and its association with melatonin were investigated. The expression of *miR-221/222* in the PA + PM group was significantly reduced compared with the simple treatment group, while melatonin treatment increased the expression of *miR-221/222* (Fig. 9A). In addition, transfection of *miR-221/222* mimics attenuated the decrease in cell viability induced by combined PA and PM exposure, with an effect similar to that achieved by melatonin administration (Fig. 9B). The number of TUNEL-positive cells was significantly decreased after transfection with *miR-221/222* mimics. Annexin V-FITC-positive/PI-positive cells increased after PA and PM treatment, consistent with the decrease in the expression of apoptosis-related proteins and the increase in the expression of anti-apoptotic proteins (Fig. 9C, 9D, and Fig. 10A). In addition, ICC and Western blot results showed that *miR-221/222* mimics significantly reduced the increased expression levels of fibrosis-related proteins induced by combined PA and PM treatment. Notably, the observed efficacy in alleviating fibrosis was comparable to melatonin supplementation (Fig. 9E, 9F).

To further verify whether melatonin alleviates PM + PA-induced

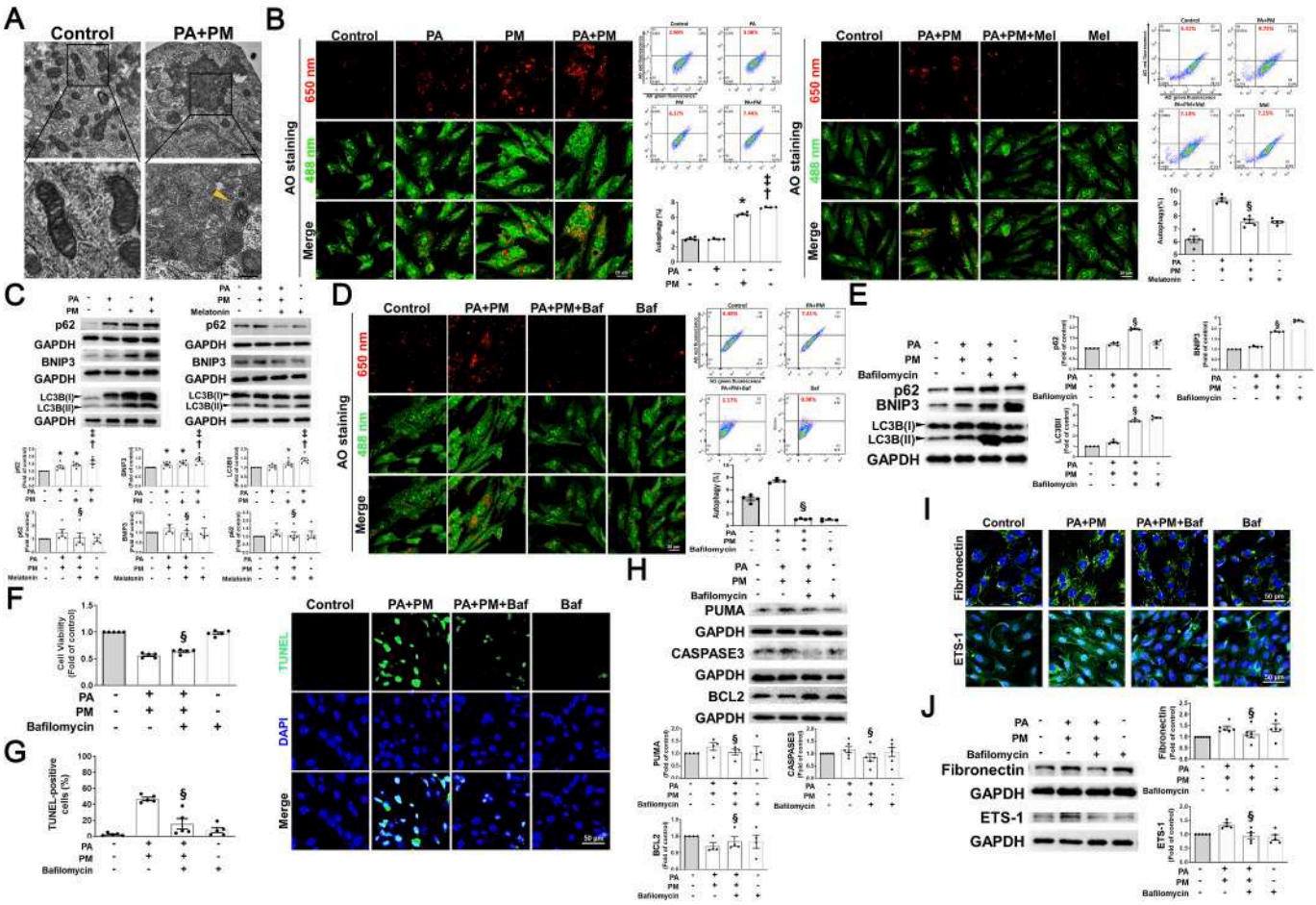


Fig. 6. Combined PA and PM exposure significantly aggravated cardiomyocyte injury by increasing mitophagy, whereas melatonin attenuated the effect. H9c2 cells were treated with or without 50 μM PA, 10 μg/mL PM, and 100 μM melatonin for 24 h. (A) TEM observation of mitochondrial ultrastructure in the control group and the PA + PM group. The yellow arrow indicates an autophagosome engulfing mitochondria (scale bar = 500 and 200 nm). (B) The presence of autophagosomes was examined by acridine orange (AO) staining. Cells expressing high red fluorescence represent cells containing many autophagosomes under fluorescence microscopy (scale bar = 20 μm). The results were quantified by flow cytometry. (C) The expression levels of mitophagy-related proteins p62, BNIP3, and LC3BII were determined by Western blot, and the quantitative results were normalized to the internal control. (D-J) Cells were pretreated with 10 nM Baf for 1 h and co-treated with PA, PM, and Baf for 24 h. The effect of Baf on the extent of mitophagy (D, E), cell viability (F), apoptosis (G, H), and fibrosis (I, J) under PA and PM treatment was examined (scale bar = 50 μm). All bars represent mean ± SEM (N = 4–6). *$p < 0.05$ compared with the control group, †$p < 0.05$ compared with the PA (50 μM) group, ‡$p < 0.05$ compared with the PM (10 μg/mL) group, §$p < 0.05$ compared with the PA (50 μM) + PM (10 μg/mL) group.

cardiomyocyte injury by regulating *miR-221/222* expression, we explored the effects of *miR-221/222* mimics on mitochondrial ROS production and mitochondrial function. MitoSOX Red staining showed that transfection of *miR-221/222* mimics reduced PA- and PM-induced mitochondrial ROS production (Fig. 9G). Transfection of *miR-221/222* mimics restored the decrease in Δψm by combined PA and PM treatment (Fig. 9H). Furthermore, total ATP levels and mitochondrial ATP production were reduced after combined therapy with PA and PM but were reversed after transfection with *miR-221/222* mimics (Fig. 9I, 9 J). MitoTracker staining and Western blot results showed that cells transfected with *miR-221/222* mimics also increased mitochondrial length and decreased the expression of mitochondrial fission-related proteins under combined treatment of PA and PM (Fig. 9K, 9L). Transfection of *miR-221/222* mimics also significantly reduced the number of AO-positive cells and the expression of LC3BII and BNIP3 (Fig. 9M, 9 N). Cells pretreated with Mdivi-1 (mitochondrial fission inhibitor) and Baf (mitophagy inhibitor) increased the expression levels of *miR-221/222* under PA + PM conditions (Fig. 10B). The above results indicate that *miR-221/222* is involved in regulating the pathway by which PA and PM aggravate cardiomyocyte apoptosis and fibrosis, and is also the pathway by which melatonin alleviates the cardiac damage caused by PA and PM.

3.6. The key role of miR-221/222 in the cardiac responses induced by combined HFD and PM exposure and melatonin treatment was verified using wild-type, miR-221/222$^{-/-}$, and miR-221/222$^{o/e}$ mouse models

Wild-type (B6), *miR-221/222*$^{-/-}$ (KO), and *miR-221/222*$^{o/e}$ (OE) mouse models were used to examine the role of *miR-221/222* in HFD- and PM-induced cardiac apoptosis and fibrosis. In wild-type mice, the levels of *miR-221/222* in the HFD and PM alone treatment groups were significantly lower than those in normal mice. In addition, *miR-221/222* levels in the HFD + PM treatment group were significantly lower than in the single treatment group. In contrast, melatonin administration significantly increased the expression of *miR-221/222* compared with the HFD + PM group. The levels of *miR-221/222* in KO mice were relatively lower than those in normal control mice. However, treatment with HFD + PM or HFD + PM + melatonin did not induce changes in *miR-221/222* levels in KO mice (Fig. 11A). Furthermore, KO mice with or without HFD + PM treatment had decreased EF and FS levels compared with normal mice, whereas melatonin treatment slightly improved IVCT and IVRT (Fig. 11B). In KO mice, HFD + PM treatment produced more TUNEL-positive cells than B6 mice receiving the same treatment. Although melatonin administration decreased the percentage of these apoptotic cells in KO mice, it was still higher than in B6 mice

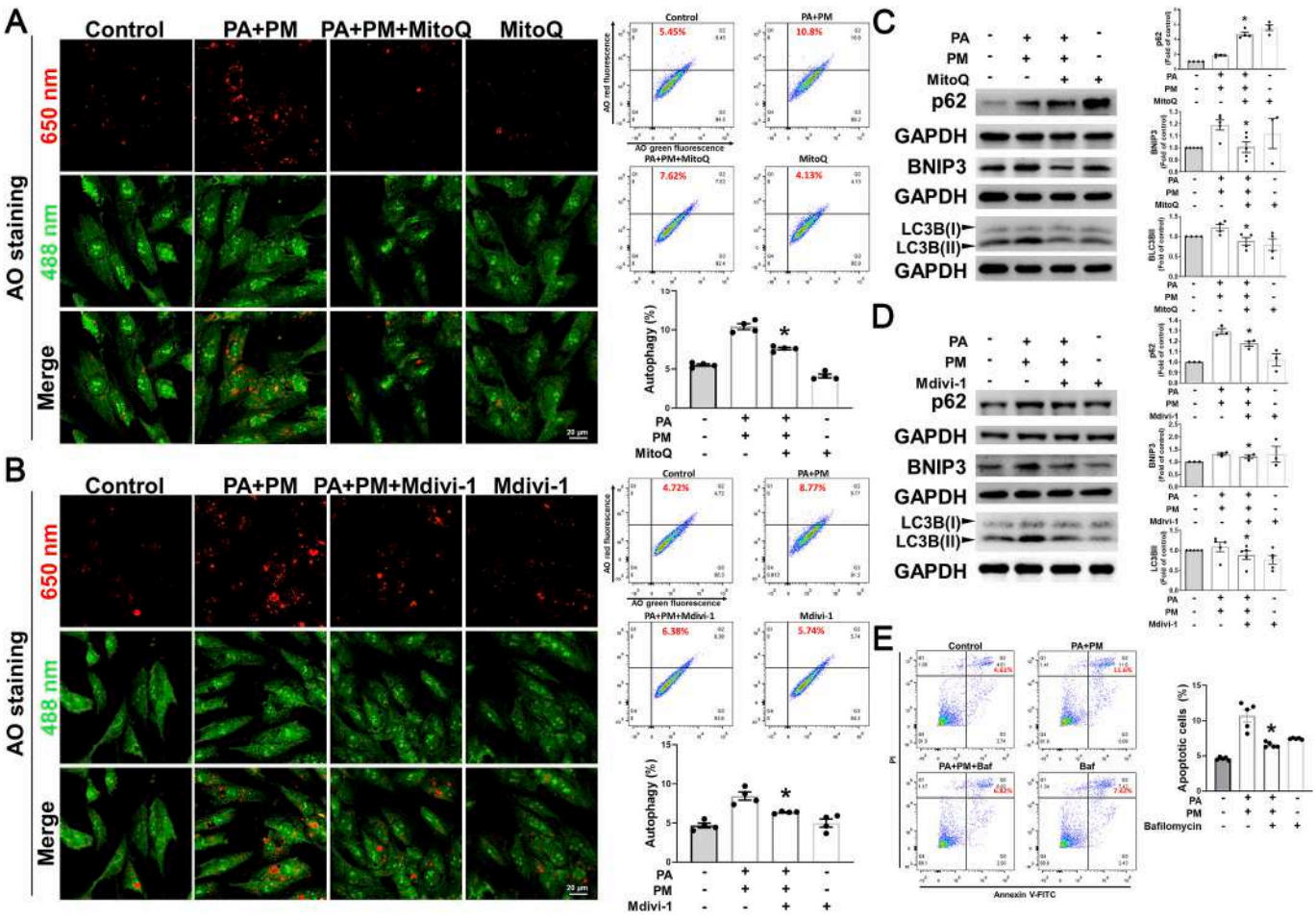
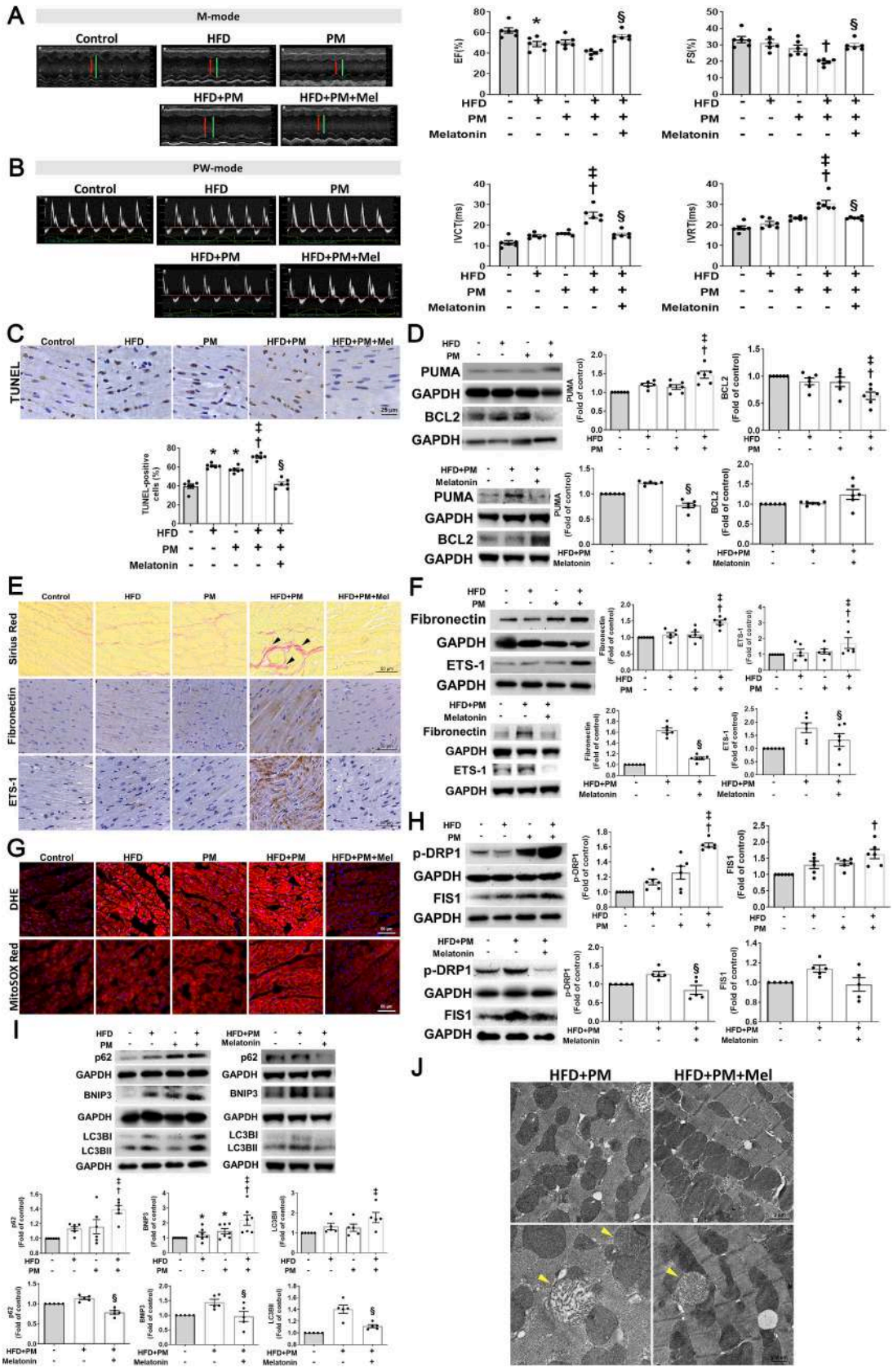


Fig. 7. Adding MitoQ (an inhibitor of mitochondrial ROS production), Mdivi-1 (an inhibitor of mitochondrial fission), and Baf (mitophagy inhibitor) reduced PA + PM-induced mitochondrial autophagy. H9c2 cells were pretreated with MitoQ (1 μM), Mdivi-1 (10 μM) or Baf (10 nM) for 1 h and then exposed to PA (50 μM) and PM (10 μg/mL) for 24 h. (A, B) AO staining showed that MitoQ or Mdivi-1 treatment significantly inhibited PA + PM-induced mitophagy. Representative images were observed by fluorescence microscopy and quantified by flow cytometry. (C, D) Western blot analysis showed that MitoQ and Mdivi-1 treatment inhibited the increased BNIP3 and LC3BII levels under PA and PM co-treatment. However, MitoQ treatment increased p62 expression, but Mdivi-1 decreased p62 expression under PA and PM co-treatment. (E) Annexin V/PI staining was measured by flow cytometry to examine the effect of Baf addition on the extent of cell apoptosis. All bars represent mean ± SEM (N = 3–5). *p < 0.05 compared with the PA (50 μM) + PM (10 μg/mL) group. Bar = 20 μm.

(Fig. 11C). Sirius red staining and IHC assays showed that compared with the B6 HFD + PM group, the collagen deposition and fibrosis-related protein expression in the KO mice receiving the same treatment were relatively higher. In the KO mouse group, HFD + PM treatment exhibited the most apparent fibrosis, whereas melatonin administration slightly alleviated this fibrosis (Fig. 11D). Intracellular and mitochondrial ROS accumulation was significantly increased in KO mice regardless of HFD + PM treatment, whereas melatonin treatment reduced ROS accumulation (Fig. 11E). According to Western blot, PUMA, ETS-1, FIS1, and BNIP3 levels were higher in HFD + PM-treated KO mice than in HFD + PM-treated B6 mice. Nevertheless, melatonin treatment reduced the induction of fibronectin, ETS-1, p-DRP1, FIS1, and BNIP3 and reversed the reduction of BCL2 compared with HFD + PM-treated KO mice (Fig. 11F). We extended the same set of experiments to OE mice. Compared with B6 mice, OE mice showed relatively high expression of *miR-221/222*. However, HFD + PM did not cause significant changes in *miR-221/222* compared with the control group (Fig. 11G). Furthermore, cardiac function was significantly restored in OE mice treated with HFD + PM compared with that in B6 mice treated with HFD + PM, as evidenced by the improvements in EF, FS, IVCT, and IVRT (Fig. 11*H*). Consistent with the assessment of cardiac function, OE mice under HFD + PM had significantly fewer TUNEL-positive cells than B6 mice receiving the same treatment (Fig. 11I). OE mice treated with HFD + PM had less fibrosis and decreased ROS than identically treated B6-treated mice (Fig. 11J, 11 K). Western blot results showed that compared with B6 mice treated with HFD + PM, OE mice receiving the same treatment had lower expressions of fibronectin, ETS-1, and p-DRP1, while higher levels of BCL2 (Fig. 11*L*). These results support the view that simultaneous exposure to HFD and PM may cause myocardial injury by regulating *miR-221/222* levels, while melatonin reduces cardiac injury through *miR-221/222*-mediated reduction. These results support the view that simultaneous exposure to HFD and PM cause myocardial injury by downregulating *miR-221/222* levels, while melatonin reduces cardiac injury through *miR-221/222*-mediated-upregulation.

4. Discussion

The effects of metabolic (hyperlipidemia) and environmental (air pollution) factors on CVD have been extensively studied. However, research elucidating the effects of simultaneous exposure to these two factors remains limited. This study focused on the combined effects of HFD/PA and PM on CVD and explored the damage mechanisms and how the antioxidant melatonin could alleviate the damage. The results showed that cardiomyocyte injury caused by the combined application of HFD/PA + PM was associated with increased mitochondrial ROS,



(caption on next page)

Fig. 8. Mice fed an HFD and exposed to PM exhibited increased cardiac dysfunction, apoptosis, fibrosis, ROS generation, mitochondrial fission, and mitophagy, which were alleviated by melatonin. Eight-week-old male C57BL/6 (B6) mice (N = 6 per group) were used in the following experiments. (A) Representative M−mode echocardiograms of the control, HFD, PM, HFD + PM, and HFD + PM + Mel groups are shown. The green line is diastolic LVID (left ventricular interior dimension); the red line is systolic LVID. The quantification results of EF and FS are shown on the right. (B) Representative PW-mode echocardiograms of the control, HFD, PM, HFD + PM, and HFD + PM + Mel groups are displayed, and the quantitative results of IVCT and IVRT are shown on the right. (C) Cardiomyocyte apoptosis was assessed by TUNEL assay and hematoxylin counterstaining (TUNEL-positive cells: brown; nuclei: blue; scale bar = 25 μm). The right panel shows the quantification of TUNEL assay results. (D) The expression levels of apoptosis-related proteins, including PUMA and BCL2, were determined by Western blot and normalized by internal control. (E) Sirius red staining and IHC examined the extent of fibrosis. Sirius red staining showed the presence of collagen deposition (red: collagen deposition; black arrow: areas of severe collagen deposition). The location of fibrosis-related proteins (fibronectin and ETS-1) was visualized by IHC and counterstained with hematoxylin (scale bar = 50 μm). (F) The levels of fibronectin and ETS-1 expression were measured by Western blot, and the quantification results were normalized to the internal control. (G) Intracellular ROS and mitochondrial ROS accumulation were determined by staining with DHE and MitoSOX Red, respectively, and counterstained with DAPI (ROS expression: red; nucleus: blue; scale bar = 50 μm). (H, I) The expression levels of p-DRP1, FIS1, p62, BNIP3, and LC3BII were measured by Western blot, and the quantitative results were normalized with the internal control. (J) Representative images of mitochondrial ultrastructure and distribution in the HFD + PM and the HFD + PM + Mel groups were obtained through TEM (scale bar = 1 μm and 500 nm). The magnified image shows the presence of mitophagosomes in cardiomyocytes. All bars represent mean ± SEM. *$p < 0.05$ compared with the control group, †$p < 0.05$ compared with the HFD group, ‡$p < 0.05$ compared with the PM group, §$p < 0.05$ compared with the HFD + PM group.

mitochondrial fission, and mitophagy, leading to cardiomyocyte injury, including apoptosis and fibrosis. Studies have also found that melatonin can reduce this damage through these mechanisms. Furthermore, the *miR-221/222*/PUMA axis and *miR-221/222*/ETS-1 axis regulated this cardiac injury, while melatonin alleviated this injury. These results serve as new strategies for the treatment of CVD.

Previous studies have shown that HFD or PM treatment alone can lead to cardiac dysfunction. HFD causes cardiac hypertrophy and impaired cardiac function through Sirtuin3 regulation [38]. HFD increases cardiac apoptosis and fibrosis in rats [39]. PM2.5 exposure induces cardiac fibrosis through oxidative stress, systemic inflammation, and subsequent TGFβ/NOX4/ROS/P38 MAPK pathway [40]. Long-term exposure to PM increases the expression of Col1a1, Col3a1, NOX-4, and TGFβ, produces more ROS, and promotes cardiac fibrosis in juvenile and older female mice [41]. Existing studies have focused on the CVD-causing effects of HFD or PM alone, but few have investigated the additive effects of combined exposures on the cardiomyocytes. Combined exposure to PM and HFD alters intracellular ROS accumulation and activates mice's TGF-β1/Smad3 pathway, aggravating cardiac fibrosis [42]. Simultaneous exposure to PM2.5 and HFD increases ROS generation in smooth muscle cells, leading to vascular remodeling [43]. Our study demonstrated that apoptosis-related protein PUMA and caspase 3 expressions significantly increased after PA + PM treatment compared with the PA or PM treatment groups. In contrast, the expression of anti-apoptotic protein BCL2 was decreased considerably. We also demonstrated that fibrosis-related proteins, fibronectin, and ETS-1 expression significantly increased after PA + PM treatment by immunofluorescence staining and Western blot. Our study showed that simultaneous exposure to HFD/PA and PM exacerbated cardiomyocyte apoptosis and fibrosis both *in vivo* and *in vitro*. Furthermore, co-exposure to HFD/PA and PM induced mitochondrial ROS production, and this response could be reversed by treatment of HFD/PA + PM with the ROS inhibitor MitoQ. In addition, many studies showed that melatonin has beneficial effects in preventing and improving cardiovascular risk factors, including diabetes, hypertension, hyperlipidemia, obesity, myocardial ischemia–reperfusion injury, pulmonary hypertension, and atherosclerosis [44]. This inexpensive and well-tolerated drug is highly recommended for treating different CVDs. Melatonin is a pleiotropic molecule that acts as a free radical scavenger, antioxidant, and circadian rhythm regulator [45]. Melatonin attenuated myocardial oxidative stress and apoptosis induced by obesity in mice fed an HFD [46]. Melatonin pretreatment enhances cell survival after cardiac ischemia/reperfusion (I/R) injury by reducing cellular oxidation and/or endoplasmic reticulum stress and apoptosis [47]. Melatonin has also been shown to minimize cardiomyocyte apoptosis, thereby maintaining cell viability under conditions such as hyperglycemia or ischemia [48]. In addition, melatonin can regulate inflammatory responses and help protect against acute myocardial infarction [49]. However, no studies have investigated the effects of melatonin on HFD/PA and PM-induced apoptosis and fibrosis. This study showed that melatonin significantly reduced HFD/PA + PM-induced cardiac apoptosis and fibrosis, and these effects were achieved by reducing mROS.

Excessive accumulation of ROS is closely associated with mitochondrial dysfunction and mitochondrial dynamics in the pathogenesis of CVD [50]. Mitochondrial dysfunction, including an imbalance of mitochondrial fission and mitochondrial fusion, plays a crucial role in cardiomyocyte apoptosis [51]. Previous studies reported that individual exposure to HFD or PM has been associated with impaired mitochondrial function in cardiac tissues. Abnormal mitochondrial morphology and dysregulated gene expression related to mitochondrial dynamics were observed in myocardial tissues of HFD-treated rats [52]. PM exposure in HL-1 mouse cardiomyocyte cell lines induced mitochondrial depolarization, ROS generation, and impaired mitochondrial function [29]. $PM_{2.5}$ upregulated the protein expression levels of mitochondrial fission-related proteins (Drp1 and Fis1) while downregulated the protein expression levels of mitochondrial fusion-related proteins (Mfn2 and OPA1) [53]. Our recent study showed that mitochondrial fission was enhanced in PM-treated myocardial ischemia–reperfusion injury and may be a potential therapeutic target for cardiomyocytes [31]. Therefore, it is worth exploring whether HFD/PA + PM causes myocardial injury by disturbing mitochondrial dynamics. The present study demonstrated that HFD/PA + PM induced mitochondrial dysfunction, including increased mitochondrial ROS production, decreased mitochondrial membrane potential, OCR, and ATP, and increased mitochondrial fission caused by Drp1 and Fis1 expression. PA and PM co-treatment significantly altered the mitochondrial morphology from their commonly elongated tubular structures to shorter and spherical particles by MitoSox Red staining. These results indicated that PA + PM led to abnormal mitochondrial dynamics during PA + PM-induced myocardial injury.We also demonstrated that Mdivi-1 (Drp1 inhibitor) reduced mitochondrial dysfunction and subsequent apoptosis and fibrosis in cardiomyocytes under an HFD/PA + PM environment. In our study, mitochondrial dysfunction induced by co-exposure with HFD/PA + PM was reduced after MitoQ, and it was shown that the reduced ROS levels decreased mitochondrial fission and cardiomyocyte damage. These results supported that abnormal mitochondrial fission contributes to mitochondrial dysfunction during PA and PM-induced myocardial injury, consistent with previous studies that pointed to excessive mitochondrial fission as the primary cause of cardiac pathologies [54]. Furthermore, melatonin has been demonstrated to prevent Drp-1-mediated mitochondrial fission in diabetic or post-traumatic hearts [54,55]. The present study showed that melatonin effectively prevented Drp1-mediated mitochondrial fission and alleviated mitochondrial dysfunction, which contributes to reducing myocardial injury and improving cardiac function. To the best of our knowledge, our study is the first to demonstrate that melatonin has a cardioprotective effect against HFD/PA and PM-induced cardiac dysfunction via improving mitochondrial function.

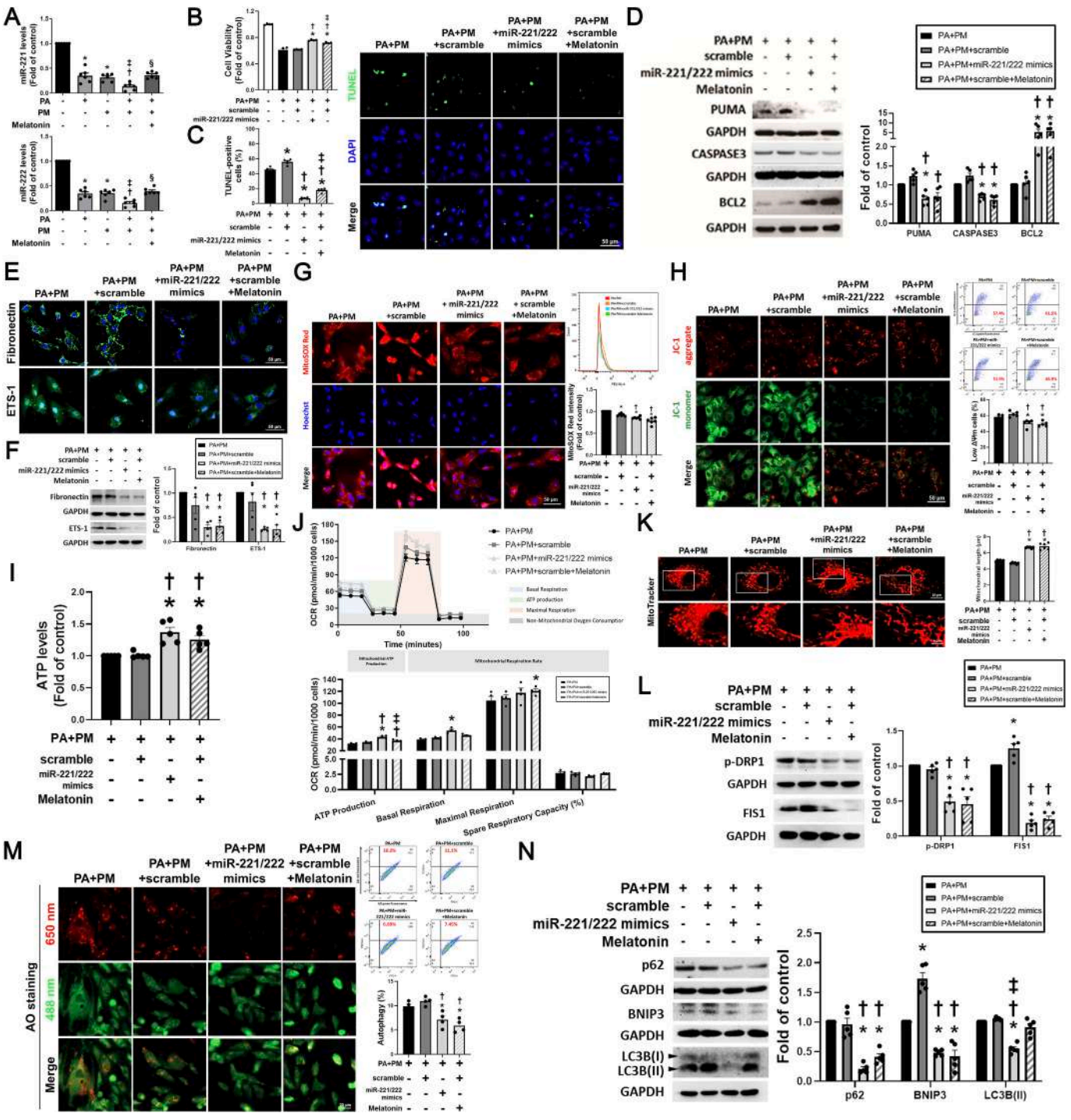


Fig. 9. Combined treatment with PA and PM exacerbated cardiomyocyte injury, while melatonin reduced the effect, both of which were associated with *miR-221/222* expression. (A) H9c2 cells were treated with or without 50 μM PA, 10 μg/mL PM, and 100 μM melatonin for 24 h, and the expression of *miR-221/222* was examined by qPCR. The quantitative results were normalized to U6 and compared with the control group. The bars represent mean ± SEM (N = 6). *p < 0.05 compared with the control group, †p < 0.05 compared with the PA group, ‡p < 0.05 compared with the PM group, §p < 0.05 compared with the PA + PM group. (B-N) H9c2 cells were transfected with scramble for 24 h and then treated with PA, PM, and with or without melatonin for 24 h. In addition, H9c2 cells were transfected with *miR-221/222* mimics for 24 h and then treated with PA and PM for 24 h. The effects of *miR-221/222* mimics transfection on cell viability (B), apoptosis (C, D), fibrosis (E, F), mitochondrial ROS levels (G), mitochondrial function (H, I, J), mitochondrial fission (K, L), and mitophagy (M, N) were examined under PA and PM treatment conditions. All bars represent mean ± SEM (N = 4–5). *p < 0.05 compared with the PA + PM group, †p < 0.05 compared with the PA + PM + scramble group, ‡p < 0.05 compared with the PA + PM + *miR-221/222* mimics group.

Dysregulation of autophagy and mitophagy (a selective autophagy of mitochondria) can contribute to the pathogenesis of CVD [56]. Due to energy shortage, the dysregulated mitophagy leads to reduced cellular resistance to myocardial ischemia/reperfusion injury. Excessive mitophagy and autophagy during the reperfusion period could give rise to irreparable damage to cardiomyocytes and, ultimately, death [57]. The present study demonstrated that combined treatment with PM and PA/HFD induced excessive autophagy and mitophagy in

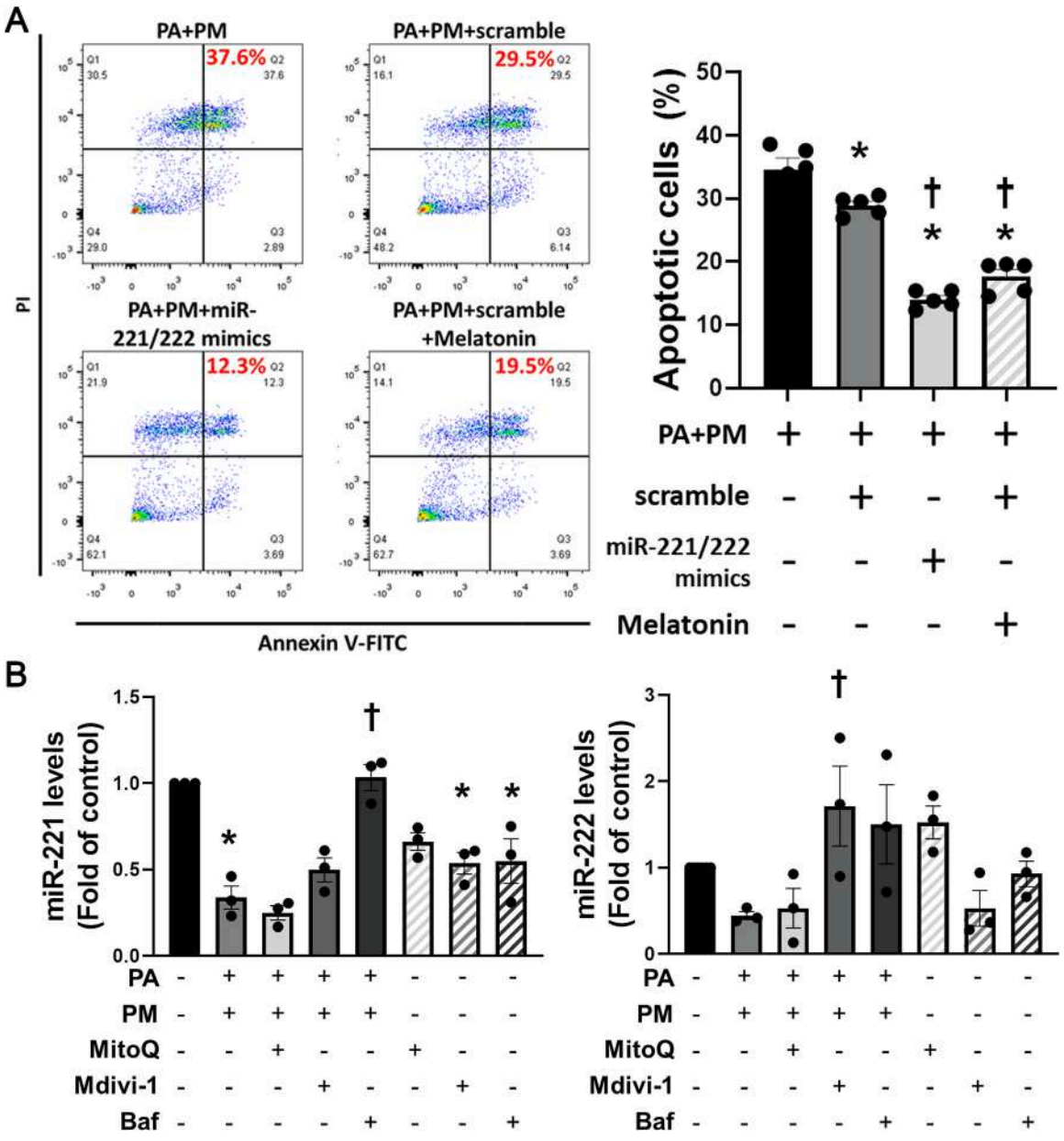
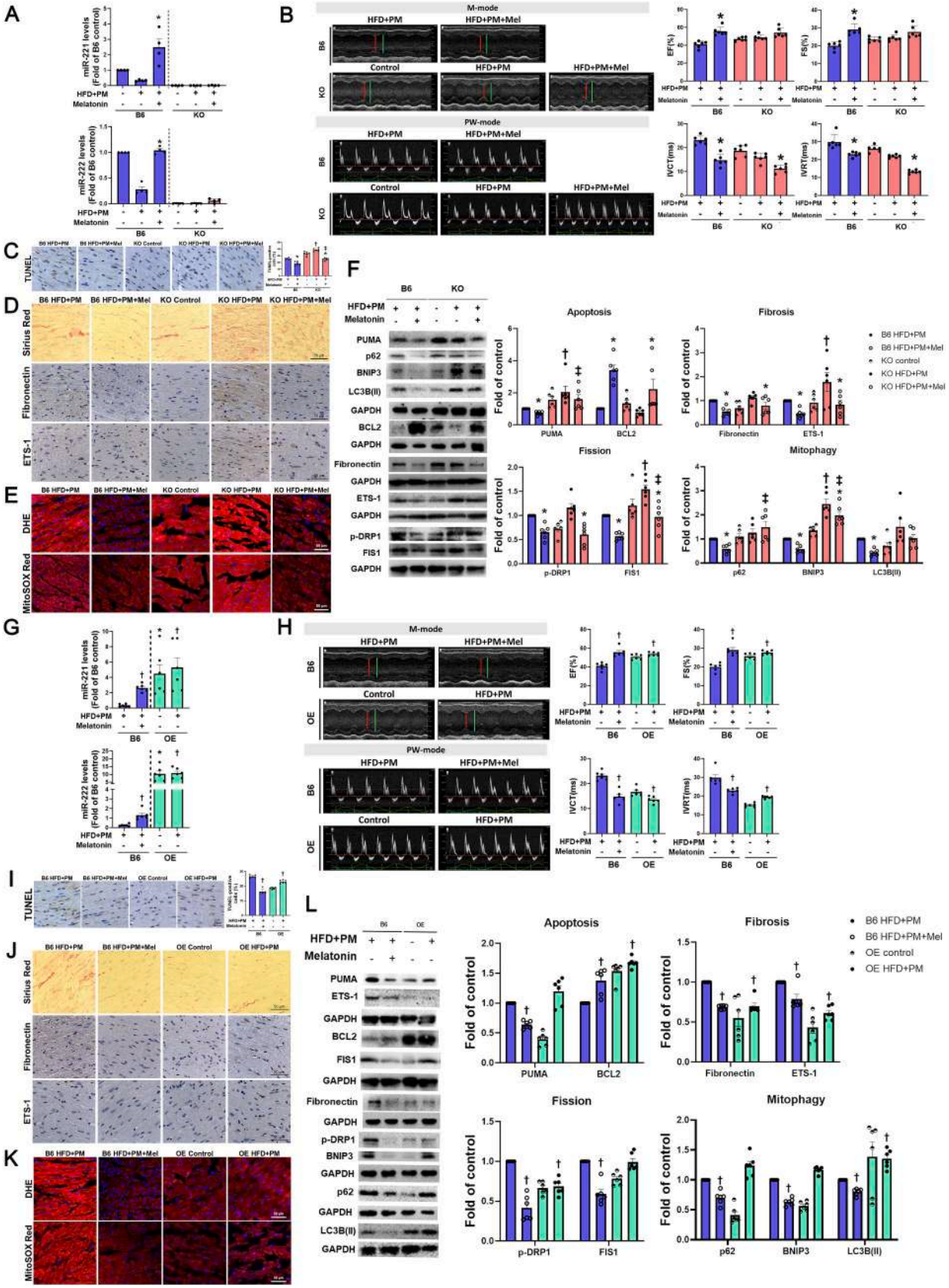


Fig. 10. Transfection of miR-221/222 mimics attenuated PA + PM-induced apoptosis (A) H9c2 cells were transfected with miR-221/222 mimics or scramble controls for 24 h and then treated with PA, PM, and melatonin for 24 h. Annexin V-FITC/PI staining was evaluated by flow cytometry to assess the degree of apoptosis. Cells expressing both Annexin V-FITC and PI were defined as apoptotic cells. The percentage of apoptotic cells was shown on the right. (B) H9c2 cells were pretreated with MitoQ, Mdivi-1, and Baf for 1 h and then exposed to PA + PM for 24 h. The expression of *miR-221/222* was measured by qPCR and normalized to the control group. Baf pretreatment increased *miR-221* levels, which decreased by PA + PM, whereas Mdivi-1 showed increased *miR-222* levels. All bars represent mean ± SEM (N = 5). *$p < 0.05$ compared with the PA (50 μM) + PM (10 μg/mL) group, †$p < 0.05$ compared with the PA + PM + scramble group.

cardiomyocytes by increasing the expression of p62, BNIP3, as well as the LC3II/LC3I ratio, the number of AO-positive cells, and TEM observation. Baf, an autophagy inhibitor, reduced PA and PM-induced apoptosis and fibrosis. Therefore, it is conceivable that the modulation of autophagy and mitophagy may benefit cardiomyocytes and develop a strategy for cardiac injury. According to recent studies, melatonin has been shown to play a dual role by either enhancing or inhibiting autophagy during CVD in different established models [39,57]. The exact mechanism by which melatonin affects autophagy and mitophagy is still an enigma. Melatonin supplementation alleviated cardiac ischemia/reperfusion injury by activating OPA1-related mitochondrial fusion and mitophagy via the AMPK signaling pathway [58]. In contrast, melatonin protects cardiac microvasculature against ischemia/reperfusion injury by inhibiting the voltage-dependent anion channel 1/hexokinase 2/mitophagy axis [59]. Melatonin inhibits ROS-mediated mitophagy and inflammation by activating Nrf2, thereby alleviating PM-induced liver fibrosis [60]. Oral melatonin supplementation in ob/ob mice restored mitochondrial cristae, enhanced mitofusin2 expression, reduced 4-hydroxynonena produced by lipid peroxidation, and decreased p62, a marker of abnormal autophagic flux [61]. Our results showed that melatonin significantly inhibited autophagy and mitophagy by reducing the expression of p62, BNIP3, and the LC3II/LC3I ratio. Combined treatment of HFD/PA and PM showed the presence of mitophagosome and mitochondrial cristae disorganization under TEM. Melatonin treatment showed well-organized cristae and better ultrastructure. These actions of melatonin confer its cardioprotective properties against PM and HFD/PA co-treatment, resulting in the improvement of cardiac apoptosis and fibrosis.



(caption on next page)

Fig. 11. Effects of combined HFD and PM exposure on cardiac injury in C57BL/6 (B6), *miR-221/222*$^{-/-}$ (KO), and *miR-221/222*$^{o/e}$ (OE) are regulated by *miR-221/222* expression. (A) The relative levels of *miR-221* and *miR-222* expression were examined in B6 and KO mice by qPCR. The quantitative results of each group were normalized with U6 and compared with the control group to obtain the relative fold change (N = 4). (B) Representative M−mode and PW-mode echocardiograms of the control, HFD + PM, and HFD + PM + Mel groups of B6 and KO mice are shown. The right panels show comparative and statistical EF, FS, IVCT, and IVRT results in B6 and KO mice (N = 6). (C) TUNEL analysis was performed to determine cardiomyocyte apoptosis in B6 and KO mice (TUNEL-positive cells: brown; nuclei: blue; scale bar = 25 μm). The right panel shows the quantification results of the percentage of TUNEL-positive cells in B6 and KO mice (N = 6). (D) The degree of fibrosis in cardiac tissues of B6 and KO mice was assessed using Sirius red staining and IHC (fibronectin and ETS-1) (scale bar = 50 μm; N = 6). (E) Intracellular and mitochondrial ROS accumulation in B6 and KO mice was detected by DHE and MitoSOX red staining, respectively (ROS expression: red; nucleus: blue; scale bar = 50 μm; N = 6). (F) The expression levels of apoptosis-related proteins (PUMA and BCL2), fibrosis-related proteins (fibronectin and ETS-1), mitochondrial fission-related proteins (p-DRP1 and FIS1), and mitophagy-related proteins (p62, BNIP3, and LC3BII) were examined in B6 and KO mice by Western blot (N = 6). All bars of B6 and KO mice represent mean ± SEM. *p < 0.05 compared with the HFD + PM group, †p < 0.05 compared with the B6 HFD + PM group, ‡p < 0.05 compared with the B6 HFD + PM + Mel group. (G-L) Effects of combined HFD and PM treatment on the expression levels of *miR-221* and *miR-222* by qPCR in B6 and OE mice (G), cardiac function by echocardiography (H), apoptosis by TUNEL assay (I), fibrosis by Sirius Red staining and IHC (J), cellular and mitochondrial ROS accumulation by DHE and MitoSOX Red staining (K), and the expression levels of apoptosis, fibrosis, fission, and mitophagy-related proteins by Western blot (L). All bars represent mean ± SEM for B6 and OE mice. *p < 0.05 compared with the B6 control group, †p < 0.05 compared with the B6 HFD + PM group.

Previous studies have demonstrated that miRNAs play an essential role in CVD by modulating the expression levels of apoptosis or fibrosis-related proteins [36,37]. More importantly, targeted therapy based on miRNAs in cardiomyocytes allows one to treat CVD. Notably, melatonin improves cardiomyocyte proliferation and cardiac regeneration by mediating *miR-143-3p* expression, thereby preventing myocardial infarction [22]. Melatonin attenuates inflammation and cardiac dysfunction in myocardial infarction by regulating the *miRNA-200b-3p*/high mobility group box chromosomal protein 1 axis [62]. This evidence raises the question of whether there is a potential link between the protective effects of melatonin on PA/HFD and PM-induced cardiac damage and miRNA activation. Melatonin was shown to prevent apoptosis or fibrosis by regulating the expression levels of miRNAs. How melatonin downregulates PUMA and ETS-1 expression in PA/HFD- and PM-treated cardiomyocytes was then investigated. This study focused on *miR-221/222* because the 3′UTR of PUMA/ETS-1 is a direct target of *miR221/222* in various cells, including cardiomyocytes [25,31]. Our results showed that PA/HFD and PM reduced the *miR-221/222* expression levels, while melatonin reversed it. In addition, *miR-221/222* mimics significantly reduced the apoptosis and fibrosis in H9c2 cells exposed to PA + PM. Transfection of *miR-221/222* mimics reduced PA- and PM-induced mitochondrial ROS production, Δψm, ATP levels, mitochondrial fission, and mitophagy, thus reducing cardiomyocyte injury. The above results indicate that *miR-221/222* is involved in regulating the pathway by which PA and PM aggravate cardiomyocyte apoptosis and fibrosis, and is also the pathway by which melatonin alleviates the cardiac damage caused by PA and PM. This will help to understand the protective effects of melatonin on cardiomyocytes and provide new therapeutic strategies for PA/HFD + PM-induced cardiac injury. It is demonstrated that the protective effects of melatonin against heart I/R injury were mainly attributed to MT2 activation [63]. In the current study, we found that melatonin significantly increased the expression of MT2. Whether MT2 mediates melatonin-increased *miR-221/222* in our research by regulating the activity of its transcriptional factor will be further investigated.

In conclusion, this study showed that HFD/PA and PM co-exposure led to worsening cardiac function. This effect is mediated through the *miR-221/222*/ROS/mitochondrial fission/mitophagy/apoptosis and fibrosis signaling pathway (Fig. 12). Melatonin can protect cardiomyocytes by regulating the axis. Our study provides new insights into the protective effects of melatonin against myocardial injury induced by HFD/PA and PM co-exposure.

Author contributions

Ya-Chun Chen and Ming-Hsueh Lee participated in the research design, conducted experiments, interpreted the results, and wrote the manuscript. Yuh-Lien Chen and Jaw-Shiun Tsai had full access to all data in the study. They took responsibility for the data's integrity and the accuracy of the data analysis. Szu-Ju Fu also participated in the study design, conducting experiments, and interpreting results. Chiang-Wen Lee, Wen-Chi Shen, Tsai-Chun Lai, Shu-Rung Lin, Shu-Wha Lin, I-Shing Yu, and Tzu-Yi Chuang participated in the discussion of the results.

Fundings

This work was supported by research grants from the National Science and Technology Council (MOST 108–2320-B-002–065-MY3; NSTC 111—2320-B-002–022-MY3 to Y.L.C.), National Taiwan University Hospital (112-S0182; 113-S0186 to J.S.T), Chang Gung University of Science Foundation (grant ZRRPF6N0011 to C.W.L.), and Chang Gung Medical Research Program Foundation (grants CORPF6P0041, CORPF6P0042, CORPF6P0043 to C.W.L.).

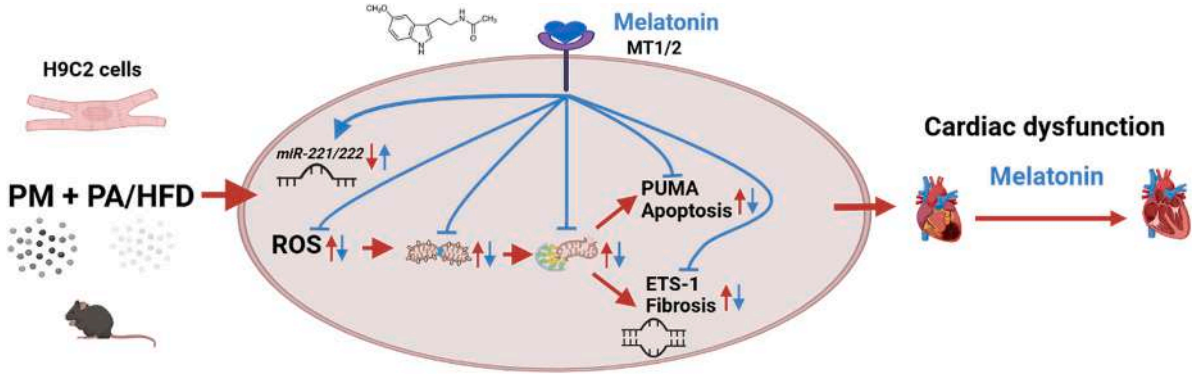


Fig. 12. A graphical abstract summarizing the study findings. This schematic illustration summarizes the effects of HFD/PA and PM co-exposure on cardiomyocyte apoptosis and fibrosis and the potential protective role of melatonin. The effect was mediated through *miR-221/222*/ ROS/ mitochondrial fission/ mitophagy/ apoptosis/fibrosis signaling pathway. Melatonin can protect cardiomyocytes by regulating the axis.

CRediT authorship contribution statement

Ya-Chun Chen: Investigation, Formal analysis, Data curation, Conceptualization. **Ming-Hsueh Lee:** Investigation, Formal analysis, Data curation, Conceptualization. **Szu-Ju Fu:** Investigation, Formal analysis, Data curation. **Chiang-Wen Lee:** Funding acquisition, Formal analysis, Data curation. **Wen-Chi Shen:** Formal analysis, Data curation. **Tsai-Chun Lai:** Data curation, Conceptualization. **Shu-Rung Lin:** Resources, Conceptualization. **Shu-Wha Lin:** Resources, Conceptualization. **I-Shing Yu:** Resources, Conceptualization. **Tzu-Yi Chuang:** Resources, Conceptualization. **Jaw-Shiun Tsai:** Writing – review & editing, Writing – original draft, Funding acquisition, Conceptualization. **Yuh-Lien Chen:** Writing – review & editing, Writing – original draft, Funding acquisition, Conceptualization.

Ethics approval and consent to participate

Animal handling and experimental procedures were performed under the Guide for the Care of Animals approved by the Institutional Animal Care and Use Committee (IACUC) (IACUC Approval Number: 20180426) and the Guide for the Care and Use of Laboratory Animals published by the National Institutes of Health (NIH) publication number: 86–23, revised 1985).

Declaration of competing interest

The authors declare that they have no known competing financial interests or personal relationships that could have appeared to influence the work reported in this paper.

Acknowledgments

We appreciate the Transgenic Mouse Models Core Facility of the National Core Facility for Biopharmaceuticals, NSTC, and the Gene Knockout Mouse Core Laboratory of the NTU Center of Genomic and Precision Medicine for their service. Additionally, we thank the Immune Research Core of the Department of Medical Research at NTU Hospital, the Flow Cytometric Analyzing and Sorting Core, and the Image Core of the First Core Laboratory at NTU College of Medicine for their technical support.

Data availability

Data will be made available on request.

References

[1] K. Mc Namara, H. Alzubaidi, J.K. Jackson, Cardiovascular disease as a leading cause of death: how are pharmacists getting involved? Integr. Pharm. Res. Pract. 8 (2019) 1–11.
[2] Y. Du, X. Xu, M. Chu, Y. Guo, J. Wang, Air particulate matter and cardiovascular disease: the epidemiological, biomedical and clinical evidence, J. Thorac. Dis. 8 (2016) E8–e19.
[3] M. Vaduganathan, G.A. Mensah, J.V. Turco, V. Fuster, G.A. Roth, The global burden of cardiovascular diseases and risk: a compass for future health, J. Am. Coll. Cardiol. 80 (25) (2022) 2361–2371.
[4] Q. Han, S.C. Yeung, M.S.M. Ip, J.C.W. Mak, Dysregulation of cardiac lipid parameters in high-fat high-cholesterol diet-induced rat model, Lipids Health Dis. 17 (1) (2018) 255.
[5] Z. Wang, L. Li, H. Zhao, S. Peng, Z. Zuo, Chronic high fat diet induces cardiac hypertrophy and fibrosis in mice, Metabolism 64 (8) (2015) 917–925.
[6] X. Yang, L. Feng, Y. Zhang, H. Hu, Y. Shi, S. Liang, T. Zhao, Y. Fu, J. Duan, Z. Sun, Cytotoxicity induced by fine particulate matter (PM2.5) via mitochondria-mediated apoptosis pathway in human cardiomyocytes, Ecotoxicol. Environ. Saf. 161 (2018) 198–207.
[7] J.Y. Kim, E.Y. Lee, I. Choi, J. Kim, K.H. Cho, Effects of the particulate Matter$_{2.5}$ ($PM_{2.5}$) on lipoprotein metabolism, uptake and degradation, and embryo toxicity, Mol. Cells 38 (12) (2015) 1096–1104.
[8] R. Jia, M. Wei, J. Lei, X. Meng, R. Du, R. Yang, X. Lu, Y. Jiang, R. Cao, L. Wang, L. Song, $PM_{2.5}$ induce myocardial injury in hyperlipidemic mice through ROS-pyroptosis signaling pathway, Ecotoxicol. Environ. Saf. 254 (2023) 114699.
[9] X. Rao, J. Zhong, R.D. Brook, S. Rajagopalan, Effect of particulate matter air pollution on cardiovascular oxidative stress pathways, Antioxid. Redox Signal. 28 (9) (2018) 797–818.
[10] Z. Zhang, H. Wu, T. Wang, Y. Liu, C. Meng, Mechanisms of myocardial damage due to hyperlipidemia: a review of recent studies, Med. Sci. Monit. 28 (2022) e937051.
[11] J.Y. Jin, X.X. Wei, X.H. Wang, D. Meng, Drp1-dependent mitochondrial fission in cardiovascular disease, Acta Pharmacol. Sin. 42 (2021) 655–664.
[12] J.N. Peoples, A. Saraf, N. Ghazal, T.T. Pham, J.Q. Kwong, Mitochondrial dysfunction and oxidative stress in heart disease, Exp. Mol. Med. 51 (12) (2019) 1–13.
[13] Q. Hu, H. Zhang, N. Gutiérrez Cortés, D. Wu, P. Wang, J. Zhang, J.A. Mattison, E. Smith, L.F. Bettcher, M. Wang, E.G. Lakatta, S.S. Sheu, W. Wang, Increased Drp1 acetylation by lipid overload induces cardiomyocyte death and heart dysfunction, Circ. Res. 126 (4) (2020) 456–470.
[14] S. Pickles, P. Vigié, R.J. Youle, Mitophagy and quality control mechanisms in mitochondrial maintenance, Curr. Biol. 28 (4) (2018). R170–R185.
[15] Y. Chen, W. Lewis, A. Diwan, E.H. Cheng, S.J. Matkovich, G.W. Dorn 2nd, Dual autonomous mitochondrial cell death pathways are activated by Nix/BNip3L and induce cardiomyopathy, Proc. Natl. Acad. Sci. 107 (20) (2010) 9035–9042.
[16] I. Rabinovich-Nikitin, R. Dhingra, L.A. Kirshenbaum, Activation of mitophagy in high-fat diet–induced diabetic cardiomyopathy, Circ. Res. 124 (9) (2019) 1288–1290.
[17] R. Ning, Y. Li, Z. Du, T. Li, Q. Sun, L. Lin, Q. Xu, J. Duan, Z. Sun, The mitochondria-targeted antioxidant MitoQ attenuated PM2.5-induced vascular fibrosis via regulating mitophagy, Redox Biol. 46 (2021) 102113.
[18] R.J. Reiter, J.C. Mayo, D.X. Tan, R.M. Sainz, M. Alatorre-Jimenez, L. Qin, Melatonin as an antioxidant: under promises but over delivers, J. Pineal Res. 61 (2016) 253–278.
[19] M. Tobeiha, A. Jafari, S. Fadaei, S.M.A. Mirazimi, F. Dashti, A. Amiri, H. Khan, Z. Asemi, R.J. Reiter, M.R. Hamblin, H. Mirzaei, Evidence for the benefits of melatonin in cardiovascular disease, Front. Cardiovasc. Med. 9 (2022) 888319.
[20] J. Hanna, G.S. Hossain, J. Kocerha, The potential for microRNA therapeutics and clinical research, Front. Genet. 10 (2019) 478.
[21] H. Che, Y. Wang, H. Li, Y. Li, A. Sahil, J. Lv, Y. Liu, Z. Yang, R. Dong, H. Xue, L. Wang, Melatonin alleviates cardiac fibrosis via inhibiting lncRNA MALAT1/miR-141-mediated NLRP3 inflammasome and TGF-β1/Smads signaling in diabetic cardiomyopathy, FASEB J. 34 (4) (2020) 5282–5298.
[22] W.Y. Ma, R.J. Song, B.B. Xu, Y. Xu, X.X. Wang, H.Y. Sun, S.N. Li, S.Z. Liu, M.X. Yu, F. Yang, D.Y. Ye, R. Gong, Z.B. Han, Y. Yu, D. Bamba, N. Wang, Z.W. Pan, B.Z. Cai, Melatonin promotes cardiomyocyte proliferation and heart repair in mice with myocardial infarction via miR-143-3p/Yap/Ctnnd1 signaling pathway, Acta Pharmacol. Sin. 42 (6) (2021) 921–931.
[23] M.T. Di Martino, M. Arbitrio, D. Caracciolo, A. Cordua, O. Cuomo, K. Grillone, C. Riillo, G. Caridà, F. Scionti, C. Labanca, C. Romeo, M.A. Siciliano, M. D'Apolito, C. Napoli, M. Montesano, V. Farenza, V. Uppolo, M. Tafuni, F. Falcone, G. D'Aquino, N.D. Calandruccio, F. Luciano, L. Pensabene, P. Tagliaferri, P. Tassone, miR-221/222 as biomarkers and targets for therapeutic intervention on cancer and other diseases: a systematic review, Mol. Ther. Nucleic Acids (2022) 1191–1224, 272022.
[24] R. Verjans, T. Peters, F.J. Beaumont, R. van Leeuwen, T. van Herwaarden, W. Verhesen, C. Munts, M. Bijnen, M. Henkens, J. Diez, L.J. de Windt, F.A. van Nieuwenhoven, M. van Bilsen, M.J. Goumans, S. Heymans, A. González, B. Schroen, MicroRNA-221/222 family counteracts myocardial fibrosis in pressure overload–induced heart failure, Hypertension 71 (2) (2018) 280–288.
[25] T.C. Lai, T.L. Lee, Y.C. Chang, Y.C. Chen, S.R. Lin, S.W. Lin, C.M. Pu, J.S. Tsai, Y. L. Chen, MicroRNA-221/222 mediates ADSC-Exosome-induced cardioprotection against ischemia/reperfusion by targeting PUMA and ETS-1, Front. Cell Dev. Biol. 8 (2020) 569150.
[26] D. Wang, M.F. Green, E. McDonnell, M.D. Hirschey, Oxygen flux analysis to understand the biological function of sirtuins, Methods Mol. Biol. 1077 (2013) 241–258.
[27] M.M. Schantz, D. Cleveland, N.A. Heckert, J.R. Kucklick, S.D. Leigh, S.E. Long, J. M. Lynch, K.E. Murphy, R. Olfaz, A.L. Pintar, B.J. Porter, S.A. Rabb, S.S. Vander Pol, S.A. Wise, R. Zeisler, Development of two fine particulate matter standard reference materials (<4 μm and <10 μm) for the determination of organic and inorganic constituents, Anal. Bioanal. Chem. 408 (16) (2016) 4257–4266.
[28] S.B. Ong, S. Subrayan, S.Y. Lim, D.M. Yellon, S.M. Davidson, D.J. Hausenloy, Inhibiting mitochondrial fission protects the heart against ischemia/reperfusion injury, Circulation 121 (18) (2010) 2012–2022.
[29] T.H. Shin, S.G. Kim, M. Ji, D.H. Kwon, J.S. Hwang, N.P. George, D.S. Ergando, C. B. Park, M.J. Paik, G. Lee, Diesel-derived PM2.5 induces impairment of cardiac movement followed by mitochondria dysfunction in cardiomyocytes, Front. Endocrinol. (Lausanne). 13 (2022) 999475.
[30] Y.C. Chen, C.M. Pu, S.R. Lin, S.W. Lin, I.S. Yu, H.J. Shih, C.W. Lee, M.H. Lee, Y. T. Kuo, Y.L. Chen, MiR221/222 in the conditioned medium of adipose-derived stem cells attenuates particulate matter and high-fat diet-induced cardiac apoptosis, Stem. Cell Res. Ther. 16 (1) (2025) 285.
[31] T.L. Lee, W.C. Shen, Y.C. Chen, T.C. Lai, S.R. Lin, S.W. Lin, I.S. Yu, Y.H. Yeh, T. K. Li, I.T. Lee, C.W. Lee, Y.L. Chen, Mir221- and Mir222-enriched adsc-exosomes mitigate PM exposure-exacerbated cardiac ischemia-reperfusion injury through the modulation of the BNIP3-MAP1LC3B-BBC3/PUMA pathway, Autophagy 21 (2) (2025) 374–393.
[32] C.W. Liu, H.C. Sung, S.R. Lin, C.W. Wu, C.W. Lee, I.T. Lee, Y.F. Yang, I.S. Yu, S. W. Lin, M.H. Chiang, C.J. Liang, Y.L. Chen, Resveratrol attenuates ICAM-1 expression and monocyte adhesiveness to TNF-α-treated endothelial cells: evidence

for an anti-inflammatory cascade mediated by the miR-221/222/AMPK/p38/NF-κB pathway, Sci. Rep. 7 (2017) 44689.
[33] S. Yang, G. Lian, ROS and diseases: role in metabolism and energy supply, Mol. Cell Biochem. 467 (1-2) (2020) 13.
[34] S. Kobayashi, F. Zhao, Z. Zhang, T. Kobayashi, Y. Huang, B. Shi, W. Wu, Q. Liang, Mitochondrial fission and mitophagy coordinately restrict high glucose toxicity in cardiomyocytes, Front. Physiol. 11 (2020) 604069.
[35] H.M. Ni, J.A. Williams, W.X. Ding, Mitochondrial dynamics and mitochondrial quality control, Redox Biol. 4 (2015) 6–13.
[36] N.I. Sayed-Pathan, P. Kumar, K.M. Paknikar, V. Gajbhiye, MicroRNAs: a neoteric approach to understand pathogenesis, diagnose, and treat myocardial infarction, J. Cardiovasc. Pharmacol. 78 (6) (2021) 773–781.
[37] T. Sun, Y.H. Dong, W. Du, C.Y. Shi, K. Wang, M.A. Tariq, J.X. Wang, P.F. Li, The role of microRNAs in myocardial infarction: from molecular mechanism to clinical application, Int. J. Mol. Sci. 18 (4) (2017) 745.
[38] H. Zeng, V.R. Vaka, X. He, G.W. Booz, J.X. Chen, High-fat diet induces cardiac remodelling and dysfunction: assessment of the role played by SIRT3 loss, J. Cell Mol. Med. 19 (8) (2015) 1847–1856.
[39] A. Feriani, M. Bizzarri, M. Tir, N. Aldawood, H. Alobaid, M.S. Allagui, W. Dahmash, N. Tlili, K. Mnafgui, S. Alwasel, A.H. Harrath, High-fat diet-induced aggravation of cardiovascular impairment in permethrin-treated Wistar rats, Ecotoxicol. Environ. Saf. 222 (2021) 112461.
[40] J. Wu, Y. Yang, Y. Gao, Z. Wang, J. Ma, Melatonin attenuates Anoxia/Reoxygenation injury by inhibiting excessive mitophagy through the MT2/SIRT3/FoxO3a signaling pathway in H9c2 cells, Drug Des. Devel. Ther. 14 (2020) 2047–2060.
[41] G. Qin, J. Xia, Y. Zhang, L. Guo, R. Chen, N. Sang, Ambient fine particulate matter exposure induces reversible cardiac dysfunction and fibrosis in juvenile and older female mice, Part. Fibre Toxicol. 15 (1) (2018) 27.
[42] J. Jiang, Y. Li, S. Liang, B. Sun, Y. Shi, Q. Xu, J. Zhang, H. Shen, J. Duan, Z. Sun, Combined exposure of fine particulate matter and high-fat diet aggravate the cardiac fibrosis in C57BL/6J mice, J. Hazard. Mater. 391 (2020) 122203.
[43] J. Duan, Q. Sun, S. Liu, L. Lin, X. Ren, T. Li, Q. Xu, Z. Sun, Co-exposure of PM2.5 and high-fat diet induce lipid metabolism reprogramming and vascular remodeling, Environ. Pollut. 315 (2022) 120437.
[44] M. Imenshahidi, G. Karimi, H. Hosseinzadeh, Effects of melatonin on cardiovascular risk factors and metabolic syndrome: a comprehensive review, Naunyn. Schmiedebergs Arch. Pharmacol. 393 (4) (2020) 521–536.
[45] D.X. Tan, L.C. Manchester, E. Esteban-Zubero, Z. Zhou, R.J. Reiter, Melatonin as a potent and inducible endogenous antioxidant: synthesis and metabolism, Molecules 20 (10) (2015) 18886–18906.
[46] Y. Liu, L.N. Li, S. Guo, X.Y. Zhao, Y.Z. Liu, C. Liang, S. Tu, D. Wang, L. Li, J.Z. Dong, L. Gao, H.B. Yang, Melatonin improves cardiac function in a mouse model of heart failure with preserved ejection fraction, Redox Biol. 18 (2018) 211–221.
[47] K. Singhanat, N. Apaijai, S.C. Chattipakorn, N. Chattipakorn, Roles of melatonin and its receptors in cardiac ischemia-reperfusion injury, Cell. Mol. Life Sci. 75 (22) (2018) 4125–4149.
[48] J. Zheng, L. Zhao, Y. Zhang, W. He, X. Guo, J. Wang, Melatonin alleviates high glucose-induced cardiomyocyte injury through suppressing mitochondrial FUNDC1-DRP1 axis, J. Pharm. Pharmacol. 76 (11) (2024) 1431–1448.
[49] Z. Fu, Y. Jiao, J. Wang, Y. Zhang, M. Shen, R.J. Reiter, Q. Xi, Y. Chen, Cardioprotective role of melatonin in acute myocardial infarction, Front. Physiol. 11 (2020) 366.
[50] S.J. Forrester, D.S. Kikuchi, M.S. Hernandes, Q. Xu, K.K. Griendling, Reactive oxygen species in metabolic and inflammatory signaling, Circ. Res. 122 (6) (2018) 877–902.
[51] C. Vásquez-Trincado, I. García-Carvajal, C. Pennanen, V. Parra, J.A. Hill, B. A. Rothermel, S. Lavandero, Mitochondrial dynamics, mitophagy and cardiovascular disease, J. Physiol. 594 (3) (2016) 509–525.
[52] D. Chen, X. Li, L. Zhang, M. Zhu, L. Gao, A high-fat diet impairs mitochondrial biogenesis, mitochondrial dynamics, and the respiratory chain complex in rat myocardial tissues, J. Cell. Biochem. 119 (11) (2018) 9602.
[53] R. Ning, Y. Shi, J. Jiang, S. Liang, Q. Xu, J. Duan, Z. Sun, Mitochondrial dysfunction drives persistent vascular fibrosis in rats after short-term exposure of PM2.5, Sci. Total Environ. 733 (2020) 139135.
[54] M. Ding, J. Ning, N. Feng, Z. Li, Z. Liu, Y. Wang, Y. Wang, X. Li, C. Huo, X. Jia, R. Xu, F. Fu, X. Wang, J. Pei, Dynamin-related protein 1-mediated mitochondrial fission contributes to post-traumatic cardiac dysfunction in rats and the protective effect of melatonin, J. Pineal Res. 64 (1) (2017).
[55] M. Ding, N. Feng, D. Tang, J. Feng, Z. Li, M. Jia, Z. Liu, X. Gu, Y. Wang, F. Fu, J. Pei, Melatonin prevents Drp1-mediated mitochondrial fission in diabetic hearts through SIRT1-PGC1α pathway, J. Pineal Res. 65 (2) (2018) e12491.
[56] S. Ikeda, D. Zablocki, J. Sadoshima, The role of autophagy in death of cardiomyocytes, J. Mol. Cell. Cardiol. 165 (2022) 1–8.
[57] N. Mu, T. Zhang, Y. Zhu, B. Lu, Q. Zheng, J. Duan, The mechanism by which miR-494-3p regulates PGC1-α-mediated inhibition of mitophagy in cardiomyocytes and alleviation of myocardial ischemia-reperfusion injury, BMC Cardiovasc. Disord. 23 (1) (2023) 204.
[58] Y. Zhang, Y. Wang, J. Xu, F. Tian, S. Hu, Y. Chen, Z. Fu, Melatonin attenuates myocardial ischemia-reperfusion injury via improving mitochondrial fusion/mitophagy and activating the AMPK-OPA1 signaling pathways, J. Pineal Res. 66 (2) (2019) e12542.
[59] H. Zhou, Y. Zhang, S. Hu, C. Shi, P. Zhu, Q. Ma, Q. Jin, F. Cao, F. Tian, Y. Chen, Melatonin protects cardiac microvasculature against ischemia/reperfusion injury via suppression of mitochondrial fission-VDAC1-HK2-mPTP-mitophagy axis, J. Pineal Res. 63 (1) (2017) e12413.
[60] L. Zhu, Q. Zhang, C. Hua, X. Ci, Melatonin alleviates particulate matter-induced liver fibrosis by inhibiting ROS-mediated mitophagy and inflammation via Nrf2 activation, Ecotoxicol. Environ. Saf. 268 (2023) 115717.
[61] A. Stacchiotti, G. Favero, L. Giugno, I. Golic, A. Korac, R. Rezzani, Melatonin efficacy in obese leptin-deficient mice heart, Nutrients 9 (12) (2017) 1323.
[62] Z.H. Liu, F. Wu, K. Ren, J.L. Huo, Melatonin attenuates inflammation and cardiac dysfunction in myocardial infarction by regulating the miRNA-200b-3p/high mobility group box chromosomal protein 1 axis, J. Physiol. Pharmacol. 74 (4) (2023).
[63] R. Chen, M. Yang, Melatonin inhibits OGD/R-induced H9c2 cardiomyocyte pyroptosis via regulation of MT2/miR-155/FOXO3a/ARC axis, Int. Heart J. 63 (2) (2022) 327–337.

Expert Opinion on Drug Delivery

ISSN: (Print) (Online) Journal homepage: www.tandfonline.com/journals/iedd20

Novel strategies in topical delivery for psoriasis treatment: nanocarriers and energy-driven approaches

Cheng-Yu Lin, Zih-Chan Lin, Yen-Tzu Chang, Tsai-Jie Lin & Jia-You Fang

To cite this article: Cheng-Yu Lin, Zih-Chan Lin, Yen-Tzu Chang, Tsai-Jie Lin & Jia-You Fang (02 Mar 2025): Novel strategies in topical delivery for psoriasis treatment: nanocarriers and energy-driven approaches, Expert Opinion on Drug Delivery, DOI: 10.1080/17425247.2025.2472968

To link to this article: https://doi.org/10.1080/17425247.2025.2472968

Published online: 02 Mar 2025.

Submit your article to this journal

Article views: 9

View related articles

View Crossmark data

Full Terms & Conditions of access and use can be found at
https://www.tandfonline.com/action/journalInformation?journalCode=iedd20

EXPERT OPINION ON DRUG DELIVERY
https://doi.org/10.1080/17425247.2025.2472968

Taylor & Francis
Taylor & Francis Group

REVIEW

Check for updates

Novel strategies in topical delivery for psoriasis treatment: nanocarriers and energy-driven approaches

Cheng-Yu Lin[a], Zih-Chan Lin[b], Yen-Tzu Chang[c], Tsai-Jie Lin[d] and Jia-You Fang[e,f,g]

[a]Department of Pathology, Duke University School of Medicine, Durham, NC, USA; [b]Chronic Diseases and Health Promotion Research Center, Chang Gung University of Science and Technology, Puzi, Chiayi, Taiwan; [c]Department of Molecular and Cellular Oncology, The University of Texas MD Anderson Cancer Center, Houston, TX, USA; [d]Department of Food Sciences, National Chiayi University, Chiayi, Taiwan; [e]Pharmaceutics Laboratory, Graduate Institute of Natural Products, Chang Gung University, Kweishan, Taoyuan, Taiwan; [f]Research Center for Food and Cosmetic Safety and Center for Drug Research and Development, Chang Gung University of Science and Technology, Taoyuan, Taiwan; [g]Department of Anesthesiology, Chang Gung Memorial Hospital, Linkou, Taiwan

ABSTRACT

Introduction: Psoriasis is characterized by abnormal differentiation and hyperproliferation of epidermal keratinocytes. This condition presents significant challenges for effective drug delivery. In addition to overcoming the thickness of the skin, topical treatments must navigate the complex hydrophobic and hydrophilic properties of the skin barrier. Recent advancements in nanocarrier technologies, including energy-driven methods and microneedles that penetrate the stratum corneum, present promising strategies for enhancing drug permeation through tailored physicochemical properties. A literature search was performed using the databases of Google Scholar, PubMed, and ScienceDirect.

Areas covered: This review highlights recent studies on novel topical delivery methods for psoriasis treatment, addressing current therapeutic options and their limitations. We provide a comprehensive overview of chemical nanoformulations and explore physical strategies to improve delivery rates. Furthermore, we discuss the advantages of various formulations that can carry different types of payloads, offering patients diverse strategies for symptom management. The review covers conventional treatments, emphasizing advancements in nanoparticle design and novel macromolecular drugs. This includes Ribonucleic acid (RNA)-based therapies that protect macromolecular drugs from rapid clearance in the body.

Expert opinion: We argue that intelligent design approaches can enhance efficacy across delivery applications while allowing for precision in treatment strategies, ultimately improving patient outcomes.

ARTICLE HISTORY
Received 11 October 2024
Accepted 24 February 2025

KEYWORDS
Psoriasis; skin; nanocarrier; RNA therapy; microneedle

1. Introduction

Psoriasis, a complex immune-mediated inflammatory skin disorder, is characterized by excessive keratinocyte proliferation, pronounced inflammation, and redness from dilated dermal blood vessels (Figure 1). The traditional treatment options include oral medications and injections, but these approaches come with limitations [1,2]. Oral drugs often suffer from the liver first-pass effect, which significantly diminishes their bioavailability and therapeutic impact. Additionally, the pharmacokinetic nonlinearity of these drugs complicates the achievement of consistent and effective treatment outcomes. The challenge is further compounded by the intricate structure of the skin. The viable epidermis, which lies just beneath the stratum corneum (SC) and ranges from 0.06 to 0.8 mm in thickness, consists of 4–5 layers of dermal fibroblasts and keratinocytes. This layer serves as the primary barrier that drugs must navigate. Effective skin permeation is hindered, as the drug must traverse various skin layers, encountering both lipophilic and hydrophilic environments, which complicates penetration and absorption [3]. In psoriasis, the skin's barrier function is compromised. This condition leads to abnormal thickening of the stratum corneum due to hyperproliferation of keratinocytes, which significantly impedes drug penetration [4,5] (Figure 1). These issues include symptoms such as dry skin and irritation, which further degrade the skin's barrier. Patients experience increased transepidermal water loss (TEWL), diminished hydration of the stratum corneum, and reduced levels of natural moisturizing factor (NMF), free fatty acids (FFAs), and sebum – all factors that exacerbate compromised barrier functions and challenge effective drug delivery [6].

Traditional topical treatments, such as emollients, coal tar, and dithranol, although generally considered safer, often fall short in efficacy and cosmetic acceptability. These treatments primarily target keratinocyte proliferation, hyperkeratosis, immune cell activity, and inflammation but struggle with inadequate skin permeation [7]. This limitation necessitates frequent application and can lead to skin irritation and other side effects. In response to these challenges, researchers are turning to advanced drug delivery systems, such as

CONTACT Jia-You Fang fajy@mail.cgu.edu.tw Pharmaceutics Laboratory, Graduate Institute of Natural Products, Chang Gung University, 259 Wen-Hwa 1st Road, Kweishan, Taoyuan 333, Taiwan

© 2025 Informa UK Limited, trading as Taylor & Francis Group

Article highlights

- Psoriasis necessitates innovative approaches to penetrate the drugs its hydrophobic and hydrophilic layers for effective treatment.
- Polymeric, lipid-based, and inorganic nanoparticles are highlighted as transformative solutions, enhancing drug stability, targeted delivery, and reducing side effects.
- Technologies like iontophoresis, sonophoresis, and thermal ablation utilize energy to enhance skin permeability, improving the skin delivery of drugs and macromolecules.
- RNA-based treatments show potential for addressing psoriasis at the molecular level with improved delivery.
- Integrating nanocarriers with energy-driven methods or microneedles can synergistically overcome delivery challenges.

nanoparticles, to increase treatment efficacy. These cutting-edge systems are designed to improve drug penetration through the thickened and damaged skin barrier typical of psoriasis. By targeting the affected layers more effectively, nanoparticle-based delivery systems could enhance therapeutic outcomes and reduce the need for frequent application [8]. Systemic therapies such as methotrexate and cyclosporin A (CSA), while effective for many patients, carry significant risks, including potential liver and kidney damage and alterations in blood cell counts. Although effective, phototherapy is often prohibitively expensive and time-consuming, limiting its use to a minority of patients [9]. Therefore, the quest for more effective psoriasis treatments drives the development of innovative topical delivery systems. These advancements aim to overcome the inherent barriers posed by the disease, offering new hope for improved therapeutic efficacy and patient outcomes.

2. Nanoparticles

Nanoparticles have emerged as a transformative force in drug delivery systems, effectively addressing many limitations associated with conventional therapeutics. These advanced materials are engineered to traverse a range of biological barriers – systemic, microenvironmental, and cellular – that are often heterogeneous across different patient populations and diseases (Figure 2). By overcoming these barriers, nanoparticles offer significant advantages in improving disease diagnosis and enhancing the specificity of treatments. As the field of nanotechnology evolves, novel solutions that could revolutionize the approach to drug delivery and precision medicine continue to be promising [10]. The application of nanotechnology in drug delivery has captured the interest of researchers across multiple disciplines, driven by the technology's ability to surpass the constraints of traditional systems. Nanotechnology provides a suite of benefits over conventional drug delivery methods, such as improving the solubility of hydrophobic drugs, achieving controlled or sustained release, enhancing the stability of drugs, and targeting therapies more precisely to their intended site of action. These capabilities not only increase therapeutic efficacy but also reduce unwanted side effects, thus representing substantial

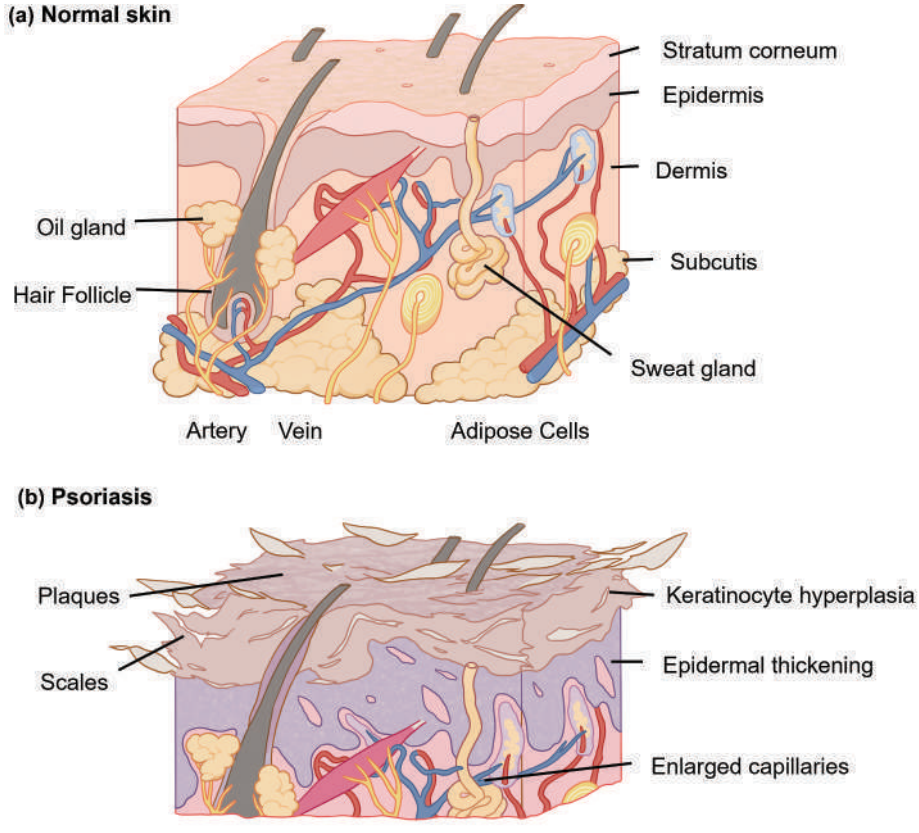


Figure 1. A simplified diagram depicting the structural changes in human skin due to psoriasis. It compares normal skin structure (A) with psoriatic skin (B), highlighting the development of scaly and raised red plaques.

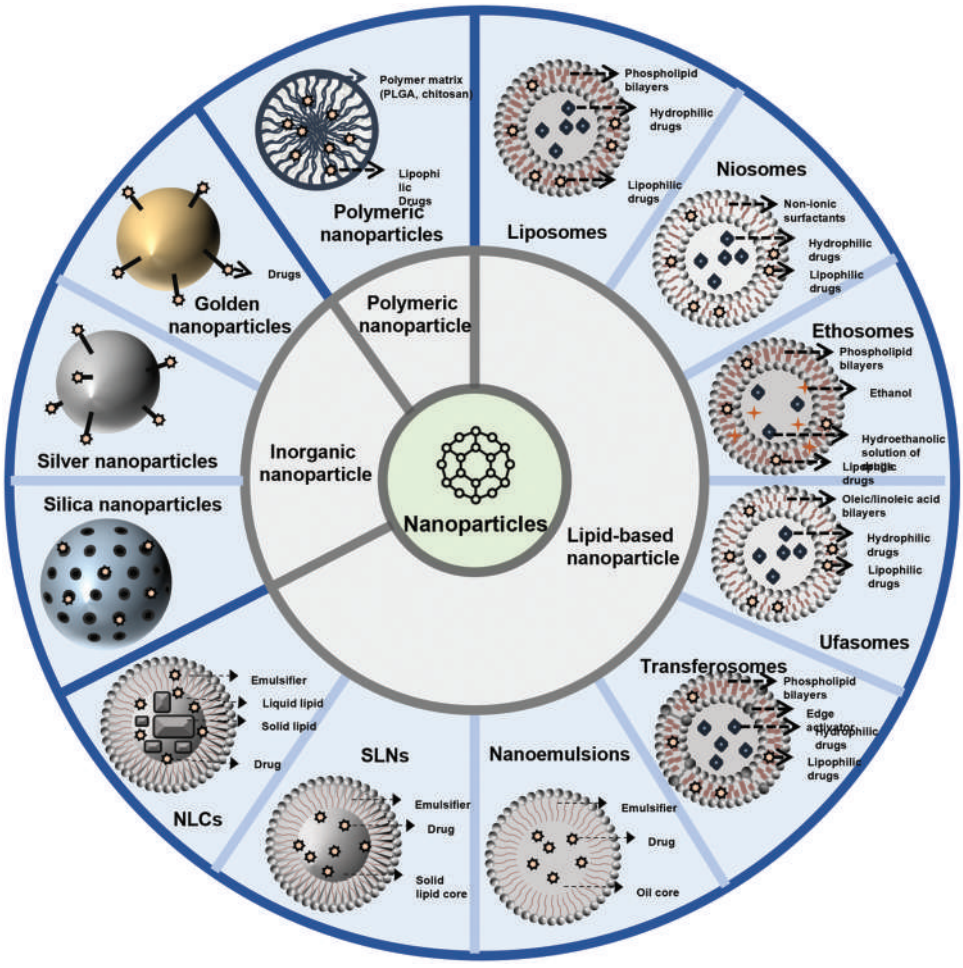


Figure 2. Various types of nanocarriers employed for topical drug delivery in psoriasis.

advancements in the quest for more effective and safer treatments [11].

2.1. Polymeric nanoparticles

One of the prominent categories of nanoparticles employed in drug delivery is polymeric nanoparticles. These particles are crafted from biodegradable polymers such as poly (lactic–coglycolic acid) (PLGA) and chitosan, each offering distinct advantages (Figure 2). Polymeric nanoparticles can be engineered to have well-defined sizes and surface properties, making them highly adaptable to various therapeutic targets. For example, polymeric micelles, which consist of amphiphilic block copolymers, self-assemble into nanoscale structures that can solubilize hydrophobic drugs, thus increasing their bioavailability. Additionally, dendrimers – hyperbranched polymers with precisely controlled structures – allow for the controlled loading and release of both hydrophilic and hydrophobic drugs. Recent innovations have even explored nanohydrogels, which encapsulate therapeutic agents using hydrophobic polysaccharides to further refine drug delivery [12].

Chitosan nanoparticles, in particular, have garnered considerable attention for their use in topical drug delivery. These nanoparticles have been found to significantly enhance the diffusion of drugs through the skin. For example, chitosan nanoparticles loaded with methotrexate (MTX) have been demonstrated to target psoriasis cells more effectively, leading to improved drug accumulation in the epidermis [13,14]. This targeted approach contrasts sharply with traditional methods, such as tacrolimus ointment, in which tacrolimus-loaded chitosan nanoparticles have shown superior efficacy in treating plaque psoriasis. The encapsulation of drugs within chitosan polymers not only facilitates excellent entrapment but also supports controlled release, as evidenced by the Higuchi model of drug release [15]. Combining gallic acid and rutin within chitosan nanoparticles has yielded enhanced therapeutic outcomes, including reduced keratinocyte hyperproliferation and increased antioxidant, anti-inflammatory, and antimicrobial activities, compared with those of nanoparticles containing these agents individually [16].

Similarly, PLGA nanoparticles have proven to be instrumental in enhancing drug delivery for topical applications. These nanoparticles exhibit a strong affinity for skin barriers and are particularly effective at loading lipophilic drugs. PLGA nanoparticles have been shown to significantly improve drug dispersion and therapeutic efficacy in psoriasis-like models by enabling sustained drug release and enhancing skin penetration. For example, PLGA nanoparticles encapsulating lipophilic curcumin have demonstrated increased potential for

penetrating psoriatic skin, with smaller particles (approximately 50 nm) being particularly effective [17]. As a biodegradable copolymer approved by the US Food and Drug Administration (FDA), PLGA forms a reservoir within the skin that enhances drug permeability, prolongs drug action, and improves drug stability; this has been exemplified by shikosin-loaded PLGA nanoparticle hydrogels, which have been used to deliver drugs to the epidermis of psoriatic mice, demonstrating efficacy in inhibiting cell multiplication and improving drug uptake [18,19]. In cases in which drugs are characterized by complex properties, such as cyclosporin A – known for its high lipophilicity and large molecular weight – PLGA-PEG-PLGA nanoparticles have emerged as a promising solution. These nanoparticles are capable of delivering the drug to the dermal layer, the target site for psoriasis treatment. Observations following treatment with PLGA-PEG-PLGA nanoparticles revealed a restoration of excessively proliferated keratinocytes to a nearly normal state, underscoring the potential of these nanoparticles for effective topical drug delivery [20]. PLGA contains carboxylic acid (–COOH) or hydroxyl (–OH) end groups, which can be used for conjugation with ligands, targeting moieties (antibodies, peptides), or polymers like polyethylene glycol (PEG). Researchers employ NIMP-R14 antibody-conjugated nanoparticles targeting neutrophils via Ly6 antigens, enhancing specificity without off-target effects or cytotoxicity, while focusing on functionalized surface chemistry for biocompatibility [21]. The other team utilizes phospholipid-coated PLGA nanohybrids conjugated with anti-desmoglein 3 antibodies for keratinocyte targeting, offering enhanced cellular uptake and degradation with minimal toxicity due to PLGA's biodegradable properties [22]. Unlike first study, which relies on antibody functionalization alone, second study incorporates PLGA and phospholipids, mimicking biological membranes for stability and compatibility. Both strategies aim for precise drug delivery, with second study emphasizing polymeric and lipid coatings for enhanced safety and efficacy against psoriasiform inflammation. Additionally, synthetic biodegradable polymers such as poly-ε-caprolactone (PCL) have been extensively studied for their applications in nanoparticle formulations. The low glass transition temperature and melting point of PCL, combined with its biocompatibility and adjustable properties, make it a versatile material for novel drug delivery systems and tissue engineering applications. Despite its slower degradation rate than other polyesters, PCL can be modified to meet specific clinical needs. Its semicrystalline structure allows for controlled erosion rates, making it an adaptable choice for various therapeutic applications [20]. Micellar nanocarriers offer promising solutions to challenges in drug delivery. Research has shown that MTX, despite its high water solubility, is difficult to encapsulate. However, the introduction of telodendrimer (TD) nanocarriers effectively addressed this issue. By incorporating riboflavin and positively charged groups into TD nanocarriers, researchers have developed a system that can form multivalent hydrogen bonds, π–π stacking, and electrostatic interactions with MTX. Compared with free MTX, this innovative formulation has shown enhanced targeting for psoriasis and demonstrated superior, long-lasting efficacy in reducing skin inflammation [23].

In conclusion, polymer nanoparticles represent a significant advancement in drug delivery systems, addressing the limitations of traditional methods and offering adaptability for various drugs and patient-specific needs. While the potential benefits are substantial, safety concerns remain, particularly regarding cytotoxicity. For example, chitosan nanoparticles have shown that factors such as concentration, exposure duration, and pH can affect toxicity, with smaller nanoparticles generally exhibiting higher toxicity in cells compared to larger ones, as observed in zebrafish models [24]. Poly(lactic-co-glycolic acid) (PLGA), a biodegradable polymer, also shows promise as a nanocarrier but can be toxic to the skin. PLGA nanoparticles coated with dioleoylphosphatidic acid (DOPA), which encapsulate cisplatin and rapamycin, exhibit strong cytotoxic effects due to the synergistic actions of these drugs on human melanoma cells. The DOPA coating enhances compatibility between PLGA and the dual drugs, while PLGA nanoparticles conjugated with anisamide, a targeting ligand that binds to sigma receptors overexpressed in melanoma cells, demonstrate a potent anti-proliferative effect. This underscores the potential of polymer nanoparticles to enhance drug delivery and therapeutic outcomes, particularly in the treatment of skin cancer [25].

2.2. Lipid-based nanocarriers

Lipid-based nanocarriers have revolutionized drug delivery systems through their diverse formulations and unique properties, which enhance the administration and efficacy of therapeutic agents. These nanocarriers include a variety of vesicular systems, such as liposomes, niosomes, ethosomes, ufasomes, and transferosomes, as well as nanostructures, such as nanoemulsions, solid lipid nanoparticles (SLNs), and nanostructured lipid carriers (NLCs) (Figure 2). The fundamental property that makes lipid-based nanocarriers effective is the amphipathic nature of lipids, which possess both hydrophilic (polar) head groups and hydrophobic (nonpolar) tail groups. This dual nature allows lipids to self-assemble in aqueous environments, forming structures such as micelles when the concentration of surfactants exceeds the critical micelle concentration (CMC). Micelles, characterized by their spherical arrangement with hydrophobic tails inward and hydrophilic heads outward, serve as crucial carriers for hydrophobic drugs, improving their solubility and stability while navigating biological barriers more efficiently [26,27].

Nanoemulsions, with particle sizes ranging from 10 to 1,000 nm, are colloidal dispersions that consist of an oil phase, a water phase, and an emulsifier. These systems are stabilized by surfactants that reduce interfacial tension, enhancing drug solubility and penetration through biological membranes [28] (Figure 2). For example, hydrogel-thickened nanoemulsions (HTNs) have shown improved stability and permeability for treating psoriasis. In a study evaluating drug delivery efficiency, a modified nanoemulsion demonstrated a 4.4-fold increase in ibuprofen permeability compared with the initial nanoemulsion [29]. Nanoemulsions enhance the cutaneous delivery of various drugs; for example, compared with marketed gels, hydrogel-thickened nanoemulsions (HTNs) were developed for betamethasone dipropionate,

which have improved stability and drug flux [30]. Natural oils, such as oleoresin from *P. emarginatus* fruits (SO), contain bioactive terpenoids but face challenges in terms of skin penetration due to their low water solubility. Nanoemulsions can enhance the topical effectiveness of these compounds. A study using SO-containing nanoemulsion (SO-NE) for the treatment of cutaneous leishmaniasis (CL) demonstrated a significant reduction in lesion size and parasitic load in mice when SO-NE was combined with intraperitoneal meglumine antimoniate. These results indicate that SO-NE could be a promising option for topical CL treatment [31,32]. They provide comparable stability and drug permeability, making them suitable for drug delivery and gene transfer applications.

Liposomes are versatile vesicular systems composed of one or more concentric lipid bilayers that are capable of encapsulating both hydrophilic and lipophilic drugs (Figure 2). Their compatibility with skin lipids enhances hydration, making them effective for topical drug delivery and improving drug stability and bioavailability. Niosomes are promising structures for drug delivery and gene transfer and are comparable to liposomes made from phosphatidylcholine, phosphatidylethanolamine, and cholesterol. They exhibit similar stability and permeability for drug-sized molecules, making them a cost-effective alternative for delivery applications. Niosomes are formed by mixing nonionic surfactants, cholesterol, and charge-inducing agents, followed by hydration in an aqueous medium. In contrast, liposomes consist of concentric lipid bilayers enclosing aqueous compartments. For topical drug delivery, liposomes are generally considered superior to conventional preparations due to their ability to integrate with skin lipids, enhancing hydration and drug penetration into skin layers [33,34].

Chemical penetration enhancers facilitate drug permeation through the skin by improving drug partitioning into the stratum corneum barrier. These enhancers work by increasing the fluidity of lipid bilayers, interacting with intercellular proteins, disrupting intercellular lipids, enhancing the thermodynamic activity of the drug, and improving stratum corneum hydration. Recent advancements have led to new semisolid formulations, such as proniosomes and microemulsion gels, which further enhance skin penetration. Surfactant vesicles such as niosomes can promote drug delivery through several mechanisms: they can release drug molecules, act as penetration enhancers, adsorb or fuse with the stratum corneum, penetrate through intact skin, or access hair follicles and pilosebaceous units [35,36]. Quercetin (QT), a flavonoid known for its anti-inflammatory properties, faces challenges in topical applications due to its poor water solubility and instability in semisolid forms, where it tends to recrystallize. A novel liposome-in-gel formulation has been developed to increase the stability and effectiveness of quercetin for psoriasis treatment; this formulation uses hydroxypropyl-β-cyclodextrin (HPCD) to stabilize quercetin-loaded liposomes by forming a protective coating through hydrogen bonding with phospholipids [37]. Additionally, a study evaluated the antipsoriatic effects of cannabidiol (CBD) *via* lipid-stabilized nanoparticles (LSNs) in an imiquimod-induced psoriasis mouse model. CBD-loaded LSNs, stabilized with lipids such as cetyl alcohol and lauric acid, were tested *in vitro* on rat skin and *in vivo*. LSNs with coumarin-6 penetrated approximately 100 µm into the skin. Although no significant differences in skin permeation were noted among the LSNs, SALA-stabilized nanoparticles demonstrated greater CBD release in earlier studies and were selected for further testing. The LSN formulations, which were thickened with fumed silica, were applied to excised skin in controlled volumes, indicating that although the applied volume was greater than that typically used in the clinic, it suggested a potentially greater availability of LSNs in practice [38]. Overall, these formulations present exciting opportunities for enhancing the efficacy of topical treatments.

Ethosomes are an innovative type of vesicular nanocarrier made with high concentrations of ethanol (20–45%) and phospholipids. The presence of ethanol enhances the flexibility and deformability of ethosomes, allowing them to penetrate deeper into the skin and deliver drugs more effectively (Figure 2). These carriers have shown promise in treating various skin conditions, including psoriasis and acne, owing to their improved drug encapsulation efficiency and therapeutic outcomes. Other lipid-based nanocarriers, such as ufasomes and transferosomes, have contributed to this field. Ufasomes, which incorporate unsaturated fatty acids, provide increased stability and biocompatibility, whereas transferosomes are highly deformable, facilitating effective skin penetration [39]. The clinical efficacy and safety of ethosomal gels were evaluated in patients with psoriasis (ClinicalTrials.gov identifier: NCT03348462). Safety was assessed through the recording of adverse events. The drug encapsulation efficiency of the ethosomes was greater than 97.2%, and the particle sizes ranged from 146 to 381 nm. Fourier transform infrared (FT-IR) spectroscopy and differential scanning calorimetry (DSC) studies revealed no interaction between anthralin and the components of the nanocarrier. The gel bases tested exhibited excellent drug release sustainability. At baseline, the patients had a median psoriatic area and severity index (PASI) of 3.6 for ethosomes, and after treatment, the mean PASI score was reduced by 81.84%. Notably, no adverse effects were reported. These findings suggest that anthralin-loaded ethosomes could be a promising treatment option for psoriasis [40]. In addition to their medical uses, lipid-based nanocarriers hold potential in cosmetics and skincare. Ethosomes, for example, offer a versatile method for delivering active cosmetic ingredients used in hair loss treatments, skin whitening, and antiaging; their ability to increase the stability and penetration of these ingredients can lead to more effective cosmetic products.

In addition to vesicular systems, nanostructured lipid carriers (NLCs) and solid lipid nanoparticles (SLNs) represent significant advancements in lipid-based nanocarriers [41]. SLNs, which are composed of solid lipids, offer controlled drug release and protection from environmental factors, such as light and oxygen. SLNs have demonstrated their potential in enhancing the stability and bioavailability of drugs, as evidenced by formulations encapsulating noscapine, which presented higher skin levels than traditional formulations. SLNs and NLCs have emerged as innovative drug delivery systems, gaining attention owing to their natural components and scalable synthesis processes. Both systems are suitable for

large-scale production, especially high-pressure homogenization, which minimizes solvent usage.

SLNs are solid lipid vesicles with diameters ranging from 10 nm to 10 µm, enabling the formulation of both hydrophobic and hydrophilic drugs (Figure 2). They facilitate controlled drug release to the skin and increase the stability of compounds against light and oxygen. For example, SLN-encapsulated noscapine (SLN-NOS) was created via response surface methodology and modified high-shear homogenization combined with ultrasound. The results from Franz diffusion cell studies revealed that SLN formulations delivered 46.88% of noscapine to the skin compared with only 13.5% of cream formulations [42]. Compared with commercial gels, SLN gels demonstrated nearly double the degree of skin permeation and over 4.5 times greater skin retention [43]. Furthermore, these nanocarriers provided excellent photostability and enhanced protection for the encapsulated drug. In vitro studies confirmed significant accumulation of ferulic acid (FA) in the epidermis when it was delivered via SLNs, in contrast to the minimal presence of plain FA suspensions. This targeted delivery could mitigate adverse systemic effects, positioning FA-loaded SLNs as a promising approach for psoriasis treatment, although further studies in clinically relevant models are needed [44]. Saini et al. [45,46] also prepared tetrahydrocurcumin-loaded SLN gel, developed via microemulsification, enhances skin penetration, hydration, and topical bioavailability, outperforming free tetrahydrocurcumin and marketed ointments.

NLCs represent a next-generation alternative to SLNs, incorporating a blend of liquid and solid lipids to create a more disordered matrix that enhances drug accommodation [47] (Figure 2). This composition, typically comprising 0.1–30% w/w solid lipids and a liquid:lipid ratio ranging from 70:30 to 99.9:0.1, along with surfactants, improves stability and drug solubility. NLCs increase the therapeutic concentrations of lipophilic drugs in targeted tissues while limiting systemic escape [22]; their ability to increase drug solubility and create a depot effect in the intercellular space of the stratum corneum allows for sustained release into deeper epidermal layers, which is particularly advantageous for conditions such as psoriasis, in which skin permeability is often increased [48]. Research indicates that drug-loaded NLCs demonstrate significantly greater antipsoriatic efficacy in BALB/c mice than do SLNs and the marketed formulation [49]. SLNs offer several advantages, including excellent colloidal stability, small particle size, easy preparation and large-scale production, making them promising candidates for topical drug delivery due to their strong affinity for the stratum corneum and high drug retention in skin layers. Studies have shown that bioadhesive hydrogels based on SLNs exhibit enhanced rheological properties, photostability, skin permeation, and antipsoriatic effects when tested on porcine skin and mouse models [50].

Lipid-based nanocarriers, which encompass vesicular systems such as liposomes, niosomes, ethosomes, and ufasomes, as well as nanostructured systems like nanoemulsions, solid lipid nanoparticles (SLNs), and nanostructured lipid carriers (NLCs), offer numerous advantages for drug delivery. Their unique properties, such as enhanced solubility, stability, and improved penetration, make them valuable tools in both medical and cosmetic applications. However, these systems face several challenges that hinder their clinical utility, including issues with encapsulation efficiency, leakage of water-soluble drugs in the presence of blood components, aggregation, poor storage stability, reproducibility concerns, and difficulties in scaling up for clinical evaluation. Additionally, toxicity remains a significant concern, often arising from the composition, particle size, or charge of the nanocarriers. To minimize potential adverse effects, it is essential to carefully select the lipid composition, formulation, and charge of the nanocarriers. For instance, cationic liposomes can interact with serum proteins, lipoproteins, and the extracellular matrix, potentially causing aggregation or premature release of the loaded agents before reaching the target cells, which can result in systemic toxicity. The chemical nature of the constituents in cationic liposomes also plays a crucial role in determining toxicity, as they can act as surfactants and lead to membrane solubilization, poration, and lysis [51].

2.3. Inorganic nanoparticles

Gold nanoparticles (AuNPs), silver nanoparticles (AgNPs), and silica nanoparticles represent advanced and promising strategies for the treatment of psoriasis, leveraging their unique physicochemical properties to enhance drug delivery, therapeutic efficacy, and safety profiles [52] (Figure 2). Owing to their small size, general nontoxicity, ease of functionalization, and high surface-to-volume ratio, gold nanoparticles are particularly effective for topical drug delivery. AuNPs, with a diameter of approximately 15 nm and a gold core of 3 nm, can penetrate the stratum corneum and target keratinocytes, which is crucial for treating psoriasis, a chronic inflammatory skin condition. When used in conjunction with imiquimod, a topical immunomodulator, AuNPs have demonstrated the ability to prevent psoriasis by downregulating genes involved in the interleukin-17 (IL-17) signaling pathway – a key driver of epidermal hyperproliferation and inflammation [53]. To increase their efficacy and stability, AuNPs are often functionalized with hydrophilic stabilizers. For example, gold nanoparticles functionalized with sodium 3-mercapto-1-propansulfonate (Au-3MPS) and loaded with MTX have shown impressive results. With a loading efficiency ranging between 70% and 80% and a rapid release profile (95% within 24 hours), this formulation not only stabilizes MTX but also enhances its therapeutic activity, proving to be more effective than MTX alone [54]. This combination offers a safe, nontoxic, and effective topical treatment option for psoriasis. Furthermore, AuNPs functionalized with polyphenol-rich extracts (*Cornus mas)*, such as those from *Cornus mas*, have demonstrated significant anti-inflammatory properties. When applied to psoriatic plaques, these nanoparticles reduce the levels of IL-12 and TNF-α, which are critical inflammatory mediators, and improve plaque recovery to a lesser extent. Compared with hydrocortisone ointment, these metallic nanoparticles exhibited superior efficacy in suppressing macrophage activation, with no reported side effects [55].

Silver nanoparticles (AgNPs), while initially studied for their antimicrobial properties, have also shown promise in psoriasis treatment (Figure 2). AgNPs, particularly when combined with

extracts from blackberry fruits, exhibit anti-inflammatory and antioxidant activities at low concentrations [56]. These properties are essential for managing the inflammation associated with psoriasis. In clinical studies, AgNPs have been incorporated into a cream base containing petrolatum, Vaseline oil, cetyl alcohol, and a hydrophilic surfactant. This formulation has demonstrated effective delivery and accumulation in inflamed skin. The results from trials involving AgNP creams revealed greater anti-inflammatory effects than did 1% hydrocortisone cream, including significant reductions in skin thickness. Moreover, AgNPs stabilized with polygalacturonic acid (PGA), a natural polymer, enhance anti-inflammatory activity by reducing free radicals and inflammatory cells in the skin. The biocompatibility and antimicrobial properties of AgNPs, along with their superior clinical performance, highlight their potential as a viable treatment for psoriasis [50].

Silica nanoparticles provide an additional approach for psoriasis treatment through their interaction with various cellular processes, such as oxidative stress, autophagy, and apoptosis (Figure 2). Hollow mesoporous silica nanoparticles loaded with MTX and chlorine e6 (Ce6) represent an innovative chemo-photodynamic therapy. These nanoparticles generate reactive oxygen species (ROS) upon light exposure, which helps in the release of MTX and enhances the permeability of the nanomaterials. The combination of MTX chemotherapy with Ce6 phototherapy has shown powerful therapeutic efficacy against psoriasis-like skin inflammation without noticeable toxic effects [57]. In addition, erianin-loaded dendritic mesoporous silica nanospheres (E/DMSNs) have been developed to address issues related to water solubility, antiproliferation activity, and skin delivery. With pore sizes of 3.5 nm and 4.6 nm, E/DMSNs exhibit significantly stronger antiproliferative and pro-apoptotic effects than free erianin on human keratinocyte cells (HaCaT). This enhanced cellular uptake and skin delivery capability make the use of DMSNs a promising strategy for improving the efficacy of erianin in treating psoriasis [58].

Gold, silver, and silica nanoparticles each offer unique advantages in the treatment of psoriasis, and their combined use holds great promise for advancing therapeutic strategies. These nanoparticle-based approaches can target both the inflammatory and proliferative aspects of the disease with enhanced precision and efficacy. Gold nanoparticles (NPs) have been shown to interact with cellular proteins, potentially inducing free radical-induced cell death or altering protein structures, which may lead to autoimmune-related toxicity [59]. Previous studies have tested several gold NPs with different capping agents for cytotoxicity against leukemia cell lines, with findings suggesting that the toxicity of gold NPs varies depending on factors such as dose, stabilizer type, and the specific cell line used. Additionally, the toxicity of gold NPs is influenced by the type of toxicity assay and their physical and chemical properties. In contrast, silver nanoparticles are known to target mitochondria, induce reactive oxygen species (ROS) production, and deplete glutathione in liver cells, with their toxicity often linked to the release of silver ions. Given these considerations, the use of silver nanoparticles for drug delivery in humans should be approached with caution [60].

3. Energy-driven methods for enhanced drug delivery

In the evolving field of cutaneous drug delivery, energy-driven techniques play a crucial role in overcoming the inherent barriers to improving drug absorption in the skin. These methods, including iontophoresis, electroporation, sonophoresis, and thermal ablation, utilize various forms of energy to facilitate the transport of therapeutic agents through the skin. Each approach offers unique advantages and applications, contributing significantly to the advancement of topical drug delivery technologies.

3.1. Iontophoresis

Iontophoresis is a technique that employs small electrical currents to enhance drug delivery through the skin. This method operates on two primary mechanisms: electrophoresis and electroosmosis. Electrophoresis involves the movement of charged drug molecules in response to an electric field. In this process, anions migrate toward the anode, and cations migrate toward the cathode. Moreover, electroosmosis facilitates the transport of neutral or uncharged molecules by inducing fluid flow through the skin. The effectiveness of iontophoresis is largely influenced by trans-appendageal pathways, which include sweat glands and hair follicles. These natural conduits offer less resistance to ionic flow than the stratum corneum, which is otherwise impermeable to ions (Figure 3). Consequently, iontophoresis is particularly useful for targeting follicular conditions such as acne and androgenetic alopecia [61].

Iontophoretic skin patches operate at low, physiologically acceptable currents, typically ranging from 0.1 to 1 mA cm^2, and have been developed for various applications [62]. For example, iontophoresis has been utilized for delivering drugs such as lidocaine, epinephrine, and fentanyl. More recently, the Zecuity patch, designed specifically for migraine relief, employs iontophoresis to administer sumatriptan over a four-hour period. This device features a microprocessor that continuously monitors skin resistance and adjusts the current to ensure precise drug delivery [63]. While iontophoresis offers controlled and adjustable drug delivery, it may be less suitable for the delivery of large molecules or drugs requiring prolonged application periods.

3.2. Electroporation

Electroporation is a well-established method designed to enhance drug delivery by creating temporary pores in the lipid layers of the skin (Figure 3). A 1998 study emphasized its potential for delivering cyclosporin A (CSA) to treat psoriasis, although its effectiveness is often limited by the barrier properties of the stratum corneum and the physicochemical characteristics of CSA. Initial attempts to use iontophoresis with a 40% ethanol (EtOH) solution in phosphate-buffered saline (PBS) did not result in a significant improvement over passive delivery. However, electroporation pulses were found to significantly increase CSA delivery, yielding a three- to four-fold enhancement compared with that of passive methods,

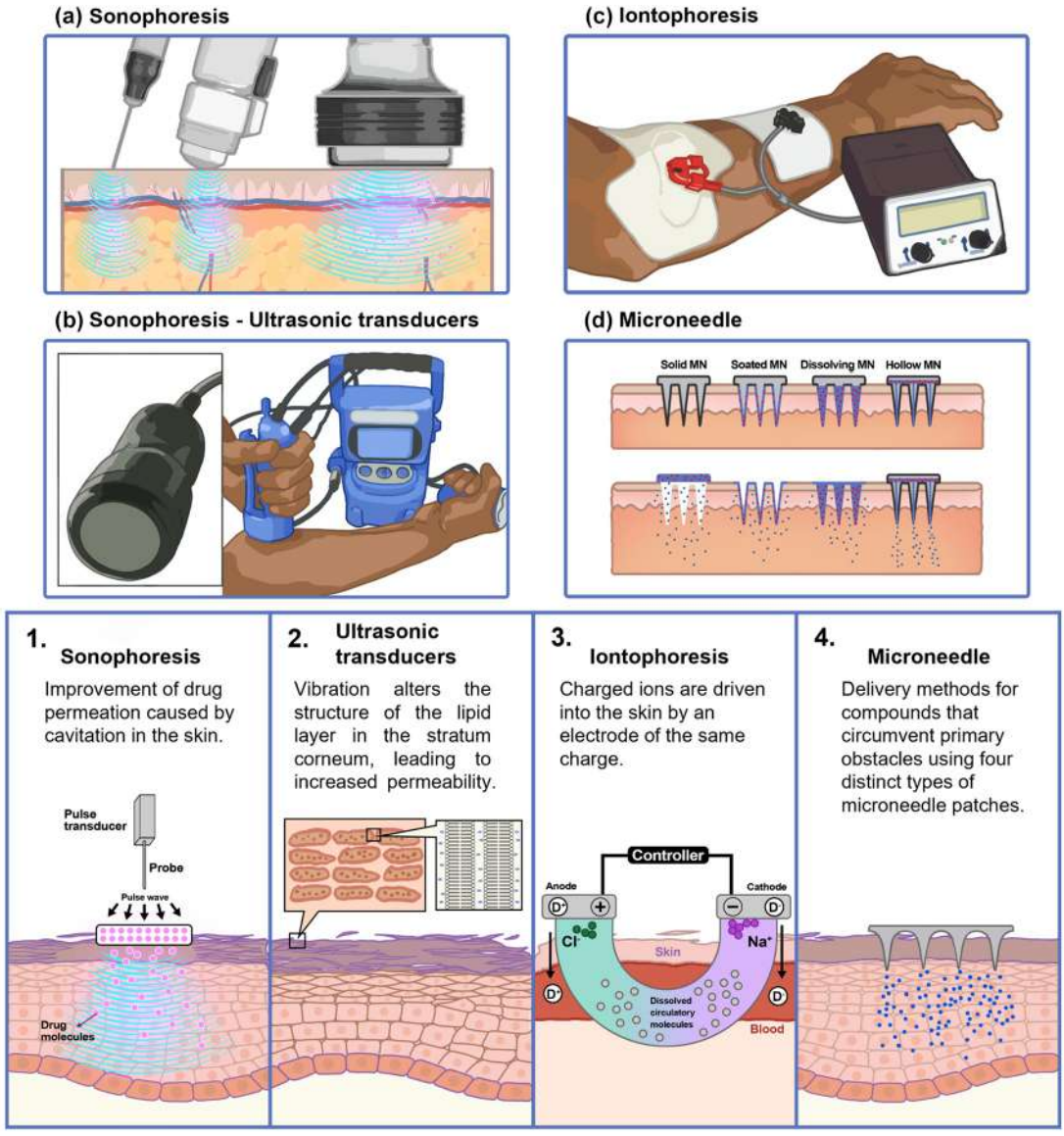


Figure 3. Schematic representation of transdermal drug delivery by different means and mechanisms such as (a) (1) sonophoresis delivery system (b) (2) ultrasonic transducers delivery system (c) (3) iontophoresis delivery system (d) (4) different type of microneedle.

although this increase was not directly proportional to the applied voltage [64].

In a different strategy, researchers explored combining the tight junction-opening peptide AT1002 with iontophoresis (IP) to address the challenges associated with thickened psoriatic skin. This combination takes advantage of the synergistic effects of electrical stimulation, which can disrupt intercellular junctions, and AT1002's ability to open tight junctions. When the AT1002 analog was administered before the IP of fluorescence-labeled oligodeoxynucleotides, it improved the delivery of these molecules into psoriatic skin, whereas IP alone was ineffective. Importantly, the use of NF-κB decoy oligodeoxynucleotides in conjunction with the AT1002 analog significantly reduced the expression of inflammatory cytokine mRNAs in psoriasis, leading to decreased epidermal hyperplasia. These results indicate that this combination can effectively enhance the intradermal delivery of therapeutic agents for psoriasis treatment [65].

While electroporation shows promise for delivering both small and larger molecules into the skin, it faces challenges such as inconsistent delivery rates and the potential for cellular damage, which may affect drug efficacy. Currently, this technique is primarily used in research and is mainly applied to deliver chemotherapeutic agents to superficial skin tumors via surface or penetrating electrodes.

3.3. Sonophoresis

Sonophoresis uses ultrasound waves to facilitate drug delivery through the skin. Ultrasound waves propagate as longitudinal waves and can be categorized based on their frequency into low-frequency (20–200 kHz), intermediate-frequency (0.7–3 MHz), and high-frequency (1–20 MHz) ranges. Low-frequency ultrasound is particularly advantageous for drug delivery due to its superior tissue penetration ability and minimal thermal effects [66] (Figure 3). This technique is effective in

transporting hydrophilic drugs, macromolecules, and gene delivery systems.

Sonophoresis is often used in conjunction with carrier systems such as micelles, liposomes, and dendrimers to enhance drug delivery. The technique has synergistic effects when combined with other permeation enhancers, such as chemical enhancers, iontophoresis, and electroporation. For example, a study involving patients with localized psoriasis revealed that combining sonophoresis with calcipotriol and betamethasone dipropionate gel significantly improved treatment outcomes compared with gel alone [67]. Further research indicated that sonophoresis, when combined with iontophoresis, results in a notable increase in drug permeability. For example, when applied to methotrexate, sonophoresis achieved significantly greater drug penetration into the skin layers than iontophoresis alone. This combined approach is beneficial for enhancing both transdermal and intradermal drug delivery [68].

3.4. Thermal ablation

Thermal ablation represents a promising method for increasing skin permeability by selectively removing the stratum corneum while preserving deeper tissues. This technique involves rapidly heating a small volume of water on the surface of the skin to generate superheated steam, which removes the outermost skin layer. Finite element modeling suggests that brief, microsecond thermal pulses are effective for this purpose without causing significant damage to deeper tissues.

Thermal ablation creates microchannels or pores that are typically 50–100 µm in diameter, significantly increasing skin permeability. This method has been shown to increase the permeability of substances such as sulforhodamine B and bovine serum albumin by up to 1000-fold *in vitro* [69]. The precise control of ablation depth with microsecond pulses makes this approach a promising alternative to other methods that may cause pain or irritation. Lasers and radiofrequency devices also utilize thermal energy for skin ablation. Laser-based techniques offer precise control over the depth of ablation by adjusting the pulse duration and wavelength. Radiofrequency ablation uses high-frequency alternating currents to create microchannels or induce ionic vibration within the tissue, thereby enhancing drug transport. This approach can be tailored to different frequencies to achieve the desired therapeutic effect [70].

Collectively, these energy-driven methods – iontophoresis, electroporation, sonophoresis, and thermal ablation – represent advanced strategies for overcoming the skin barrier and improving the efficacy of topical drug delivery. Each method offers unique advantages and applications, making them valuable tools in the development of more effective and targeted therapeutic interventions. Iontophoresis excels in providing controlled drug delivery through natural skin pathways, whereas electroporation enhances the permeability of smaller molecules despite its challenges. Sonophoresis improves drug penetration with the assistance of ultrasound waves and carrier systems, and thermal ablation provides a precise method for increasing skin permeability by selectively removing the outer skin layer. When used individually or in combination, these techniques offer significant potential for advancing skin delivery and improving patient outcomes across a range of medical conditions.

3.5. Microneedles

Microneedles (MNs) represent a significant leap forward in skin delivery, addressing many of the limitations associated with traditional systems. Originally introduced in 1976, microneedles were developed to overcome the challenges faced by conventional transdermal delivery methods (TDDs). The evolution of microfabrication technologies since the 1990s has resulted in a diverse range of microneedles, which typically vary in length from 25 µm to 2000 µm. Unlike traditional hypodermic needles, microneedles have much sharper tips, allowing them to penetrate the stratum corneum (SC) and create microscale channels for drug delivery while avoiding contact with nerve fibers and blood vessels located deeper in the skin [71]. This innovative approach dramatically enhances drug delivery efficiency and expands the types of drugs that can be effectively delivered through the skin in a minimally invasive, painless manner.

Microneedles address a major challenge in skin delivery: the need to bypass the stratum corneum of the skin, which historically limited the range of drugs that could be effectively delivered. By creating microchannels through this outermost layer, microneedles facilitate the passage of a wider variety of drug molecules into the skin without causing pain or bleeding. This advancement not only broadens the potential market for cutaneous drug delivery but also eliminates the reliance on the physicochemical properties of the drugs. Consequently, microneedle arrays have been successfully employed to deliver a range of substances *in vivo*, including oligonucleotides, desmopressin, DNA, vaccines, insulin, and human growth hormone [72]. The role of the skin as an absorptive organ makes it a key target for topical drug delivery systems. Microneedle patches, which are composed of numerous micron-sized needles, represent an efficient and effective method for drug delivery. These patches include various types, including solid microneedles (SMNs), hollow microneedles (HMNs), dissolving microneedles (DMNs), and coated microneedles (CMNs), each offering unique benefits based on their design and application (Figure 3). The microneedle approach is superior to traditional topical delivery methods due to its minimal invasiveness, painlessness, convenience, and improved patient compliance [73].

HMNs play a critical role in drug delivery but face challenges related to their manufacturing. Most HMNs are produced via silicon microfabrication techniques such as lithography and etching. While effective, these methods are often costly and less adaptable for large-scale production or customization, particularly for flexible substrates. Recent advancements, including dual-molding processes, have shown potential in making HMNs more cost-effective and scalable. Research has demonstrated that HMNs can deliver drugs effectively with reduced dosages and fewer side effects. For example, in the treatment of psoriasis in mouse models, HMNs achieved therapeutic outcomes similar to those of oral doses while minimizing drug toxicity and associated side

effects [74]. As microneedle technology continues to evolve, it promises to significantly enhance the management of chronic conditions such as psoriasis, in which traditional treatments are varied but often limited. Ongoing research and development in this field are expected to further improve the efficacy and applicability of microneedles, potentially transforming topical drug delivery and patient care.

4. Topical small-molecule drugs

Although systemic therapies such as biologics and oral medications have shown effectiveness, topical small-molecule drugs remain a cornerstone in treating mild to moderate psoriasis. These topical therapies minimize systemic side effects and improve patient compliance [75]. This section covers the topical small-molecule agents that are now FDA-approved, including topical corticosteroids, vitamin D analogs, tazarotene, aryl hydrocarbon receptor (AhR) modulators, phosphodiesterase type-4 inhibitors, and their combinatorial therapies. The mechanism of action is first introduced, and the details of these drugs are described.

4.1. Corticosteroids

Corticosteroids are the first-line topical drugs for treating psoriasis due to their anti-inflammatory and antiproliferative effects. These drugs work by binding to glucocorticoid receptors in keratinocytes and fibroblasts and inhibiting the release of proinflammatory cytokines such as TNF, IL-1, and IL-2 (Figure 4). Corticosteroids also downregulate the expression of adhesion molecules on endothelial cells, e.g. endothelial-leukocyte adhesion molecule-1 (ELAM-1) and intracellular

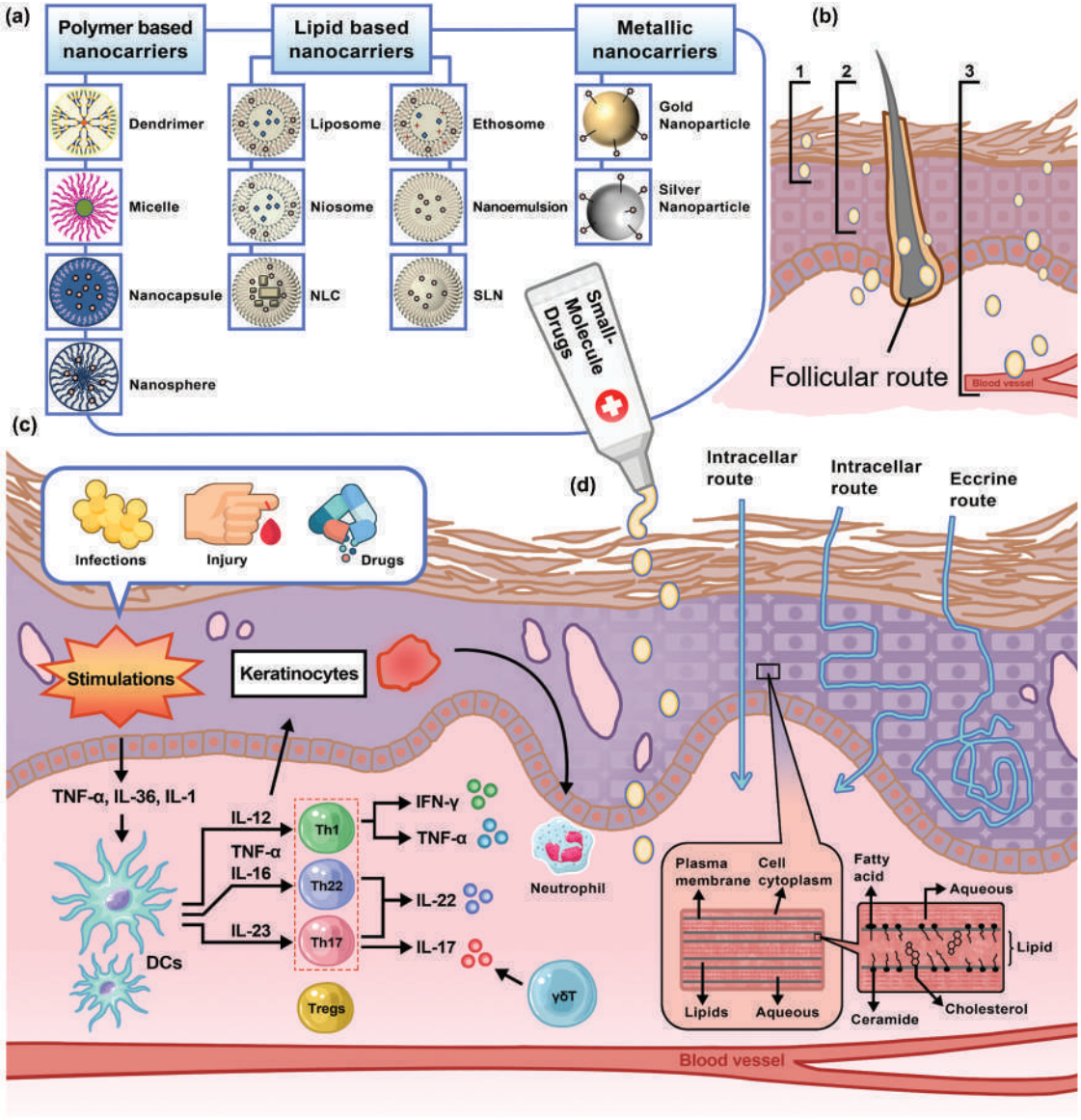


Figure 4. (a) categorize nanoparticles into different types used for topical drug delivery in psoriasis. (b) Possible mechanisms of action for surfactant vesicles in dermal and transdermal applications include (1) the release of drug molecules from nanoparticles, with nanoparticle components serving as penetration enhancers. (2) additionally, nanoparticles can adsorb and/or fuse with the stratum corneum, (3) allowing intact nanoparticles to penetrate unbroken skin. Furthermore, nanoparticles can also penetrate through hair follicles and/or pilosebaceous units, enhancing their delivery efficacy. (c) Inflammatory pathways in the pathogenesis of psoriasis. (d) Possible drug penetration routes across human skin and the structure of the intercellular space.

adhesion molecule-1 (ICAM-1), reducing leukocyte infiltration into the skin [76]. In addition to their anti-inflammatory effects, corticosteroids are known for their antiproliferative effects. They can inhibit fibroblast growth and suppress the synthesis of specific cellular components, such as collagen and mucopolysaccharides, leading to effective protection against the thickening of the stratum corneum and the cellular proliferation characteristic of psoriasis [77]. Owing to their strong anti-inflammatory and antiproliferative effects, the use of Classes 1–7 topical corticosteroids for up to 4 weeks is strongly recommended for treating plaque and scalp psoriasis. Topical corticosteroids are classified into seven levels based on their skin vasoconstrictive activity, ranging from the most potent (Class 1) to the least potent (Classes 6 and 7) [78]. Low-potency corticosteroids are appropriate for use on vulnerable skin compartments, such as the face, and are flexible [79]. Moderate- to high-potency corticosteroids are generally applied as initial treatments.

Currently, two ongoing FDA-approved drugs utilize topical corticosteroids as a combinatorial component. A dual-action aerosol foam containing 0.064% betamethasone dipropionate and 0.005% calcipotriene, approved in 2006. It is indicated for the topical treatment of plaque psoriasis in patients aged 12 and older. In a Phase III clinical trial, the dual-action aerosol significantly lowered the modified Psoriatic Area and Severity Index (mPASI) score and provided greater itch relief compared to the nontreatment group after four weeks [80]. In addition, combination therapy with betamethasone and calcipotriene resulted in a more noticeable improvement in the mPASI score than either treatment alone [81]. The other is a lotion containing 0.01% halobetasol propionate and 0.045% tazarotene, which was first approved in 2019. The results were consistent with those of Enstilar. According to Phase III randomized controlled trials, this lotion significantly reduced psoriasis symptoms, including erythema, plaque elevation, and scaling, particularly in patients with severe baseline symptoms. These findings indicate that the lotion is an effective treatment option for patients with severe localized plaque psoriasis [82].

4.2. Vitamin D analogs

Vitamin D analogs, including calcipotriene and calcitriol, have emerged for the management of psoriasis due to their ability to normalize keratinocyte hyperproliferation and modulate immune responses [83]. The active form of vitamin D regulates epidermal proliferation and differentiation by binding to the VDR in keratinocytes, driving the expression of essential proteins such as keratin 1, involucrin, and filaggrin. This process strengthens the skin barrier by facilitating cornified envelope formation and working with calcium signaling via the calcium-sensing receptor (CaSR). Moreover, vitamin D analogs increase the innate immunity of the skin by promoting the expression of Toll-like receptors, such as TLR2 and CD14, in keratinocytes. This increases the production of antimicrobial peptides such as cathelicidin, reinforcing the skin's defense against pathogens and supporting barrier function [84]. In addition to the induction of innate immunity, vitamin D analogs promote anti-inflammatory pathways and inhibit proinflammatory cytokines. They enhance regulatory T-cell activity, suppress Th1 and Th17 cytokines, and regulate inflammatory gene expression through the NF-κB pathway. These actions are valuable in psoriasis, a condition characterized by aberrant immune activation and rapid keratinocyte turnover, leading to the formation of thick, scaly plaques [85] (Figure 4).

Despite their clinical utility, vitamin D analogs have limitations. One of the most common adverse effects is local irritation, which manifests as erythema and dryness, particularly in sensitive areas such as the face and flexural regions. This irritation can be mitigated by reducing the application frequency or combining treatment with corticosteroids. The synergistic effect of this combination allows for a reduced corticosteroid dosage, minimizing long-term side effects such as skin atrophy while maintaining strong anti-inflammatory and antiproliferative effects [86].

4.3. Retinoids

A topical retinoid, tazarotene, is another commonly used small molecule in psoriasis treatment. It binds to retinoic acid receptors, modulating keratinocyte differentiation, proliferation, and inflammation. Tazarotene downregulates hyperproliferative markers such as keratins K6 and K16 and inflammatory markers such as MRP-8 and ICAM-1. It also promotes the expression of tazarotene-induced genes (TIGs), contributing to its antiproliferative and anti-inflammatory effects [87]. Tazarotene is particularly effective when combined with corticosteroids, as the combination allows lower corticosteroid doses and reduces the incidence of local adverse events such as irritation and erythema. Previous studies have indicated that tazarotene and a topical corticosteroid could improve the local tolerability of tazarotene treatment while improving therapeutic efficacy [88].

4.4. Aryl hydrocarbon receptor (AhR) modulators

AhR, a transcription factor activated by ligands, regulates gene expression in immune and epithelial cells. AhR signaling supports skin homeostasis not only by modulating the differentiation of immune cells and keratinocytes but also by downregulating psoriasis-related proinflammatory cytokines (e.g. IL-17 and IL-22) and upregulating the expression of barrier proteins, including filaggrin. This mechanism rescues aberrant keratinocyte differentiation and hyperproliferation and mitigates psoriasiform skin inflammation [89] (Figure 4). Tapinarof is a secondary metabolite of *Photorhabdus luminescens*, a gram-negative bacillus that acts as an aryl hydrocarbon receptor (AhR) agonist. AhR signaling regulates inflammation and oxidative stress, reduces the production of proinflammatory cytokines such as IL-17, and enhances the expression of crucial skin barrier proteins such as filaggrin and loricrin [90].

One FDA-approved AhR agonist is cream, which contains 1% tapinarof. Since it was approved in 2022, VTAMA has been indicated for the topical treatment of plaque psoriasis in adults, as it has a unique mechanism of action. The results of a Phase III trial revealed that tapinarof can reduce plaque psoriasis severity after 12 weeks and achieve satisfactory efficacy and application ease, indicating that tapinarof is a promising novel treatment [91,92].

4.5. Phosphodiesterase type-4 inhibitors

PDE4 inhibitors are believed to increase the intracellular cyclic adenosine monophosphate (cAMP) concentration, activating protein kinase A (PKA). They subsequently inhibit the activation of the downstream nuclear factor kappa B (NF-κB) pathway in most immune cells. Owing to its notable anti-inflammatory effects, roflumilast was first approved for COPD and then used to treat psoriasis [93]. ZORYVE® cream is a phosphodiesterase four inhibitor consisting of 0.3% roflumilast; it is indicated for the topical treatment of plaque psoriasis, including in intertriginous areas, in adult and pediatric patients six years and older. In the previous randomized clinical trials, DERMIS-1 and DERMIS-2, roflumilast exhibited substantial investigator global assessment (IGA) success and a 75% reduction in the psoriatic area and severity index (PASI) score [94]. The IGA scales rely mainly on the width of the plaque elevation, whereas the PASI scores depend on different body regions and the intensity of redness (erythema), thickness (induration), and scaling [95,96]. The outstanding clinical results illustrate the efficacy of topical roflumilast administration.

Although topical small-molecule drugs are commonly used in clinical settings, they still face serious challenges that need to be overcome. One of the most prominent barriers to effective drug delivery is the compromised stratum corneum of psoriatic skin, which becomes thickened and hyperkeratotic; this altered skin barrier substantially impairs the penetration and bioavailability of topical agents. Therefore, scientists are continually working to develop innovative drug delivery methods to overcome this challenge.

5. Skin delivery for macromolecule drug therapy

The discovery of RNA interference (RNAi) by Mello and Fire has sparked significant interest in posttranscriptional gene silencing, which was initially observed in *Caenorhabditis elegans* with the introduction of exogenous double-stranded RNA (dsRNA), leading to systemic gene suppression. However, naked small interfering RNAs (siRNAs) face challenges such as instability in the bloodstream, poor cell membrane permeability, and potential immunogenicity, necessitating effective delivery systems to harness their therapeutic potential [97]. While siRNAs have been explored for various skin conditions, low skin permeability remains a significant hurdle due to factors such as their negative charge, high polarity, susceptibility to nucleases, and difficulty penetrating the skin barrier. Recent innovations in delivery vehicles – such as liposomes, dendrimers, cell-penetrating peptides, and nanoparticles – aim to increase siRNA delivery efficiency while ensuring high biocompatibility and low immunogenicity [98]. Nevertheless, traditional liposome-based systems struggle with aggregation during permeation processes and phospholipid oxidation, limiting their application in skin research [99]. Enhancing siRNA efficacy also involves facilitating its escape from endosomes, with photosensitive agents potentially rupturing vesicles to release siRNA into the cytoplasm [100]. A notable target for therapeutic intervention is NFKBIZ, which encodes the atypical IκB protein IκBζ and plays a critical role in regulating NF-κB complexes, particularly in inflammatory conditions such as psoriasis. Topically silencing NFKBIZ represents a noninvasive treatment option with minimal side effects, potentially benefiting a wider patient population than single antibody therapies. Recently, ionic liquids (ILs) have emerged as promising materials for enhancing the topical delivery of siRNA due to their tunable properties and excellent safety profile. An IL-based siRNA delivery approach that stabilizes siRNA and enhances its skin penetration demonstrated efficacy in silencing NFKBIZ in an imiquimod-induced psoriasis mouse model [101].

Furthermore, spherical nucleic acid nanoparticle conjugates (SNA-NCs) – gold cores surrounded by covalently bound siRNA – have shown a remarkable ability to penetrate keratinocytes *in vitro* and in human skin within hours, delivering siRNA without requiring barrier disruption or transfection agents. Compared with traditional lipid-based systems, SNA-NCs, which target the epidermal growth factor receptor (EGFR), exhibited over 100-fold greater potency and longer-lasting effects, leading to significant reductions in EGFR expression and related cellular activities in psoriasis models without inducing toxicity [102,103]. Additionally, we developed a novel fusogenic nucleic acid lipid particle (F-NALP) system that combines anti-STAT3 and anti-TNF-α siRNA, demonstrating superior delivery and therapeutic efficacy in reducing relevant mRNA and protein levels in psoriatic plaques [104]. Laser-assisted delivery has also proven effective, creating microchannels in psoriatic skin that facilitate siRNA penetration and significantly reduce inflammatory cytokine levels [105]. Overall, metabolomics research has underscored the importance of ceramides and sphingolipids as biomarkers for cardiometabolic complications, offering new insights into disease pathogenesis and potential therapeutic targets.

RNAi has sparked interest in gene silencing for skin conditions, but challenges such as siRNA instability and low skin permeability limit its effectiveness. Recent advancements in delivery systems have improved siRNA stability and skin penetration. These innovations enhance the therapeutic efficacy of siRNA targeting, especially for conditions such as psoriasis, and highlight the potential for noninvasive gene therapies.

6. Conclusions

This review highlights significant advancements in therapeutic delivery methods specifically designed to address the skin barriers associated with psoriasis (Figures 3 and 4). A considerable body of work has demonstrated the effectiveness of topical treatments in alleviating inflammation caused by psoriasis. Drug delivery platforms, particularly those utilizing nanoparticles, offer a range of customizable features – such as size, shape, charge, and surface properties – that can be optimized for targeted applications. Nanocarriers can synergistically enhance traditional therapies, allowing for improved patient stratification and broader access to effective treatments. By optimizing nanoparticle characteristics, including the type of materials used (e.g. metallic versus lipid-based nanoparticles), we can tailor delivery systems to suit specific skin disorders and therapeutic needs. This versatility enables the simultaneous delivery of multiple drugs in a single dose,

effectively downregulating inflammatory cytokines and improving clinical outcomes, as evidenced by reductions in PASI scores. Many of these nanocarriers have received FDA approval, underscoring their safety as delivery vehicles. Physical methods such as iontophoresis, electroporation, sonophoresis, and thermal ablation utilize various forms of energy to enhance drug transport through the stratum corneum, a key barrier in psoriasis. These energy-driven methods have shown promise in clinical applications, often increasing penetration rates by 3–4 times with minimal side effects. Sonophoresis, which relies on cavitation mechanisms, along with electroporation and thermal ablation, has been particularly studied for its ability to increase drug permeability through the skin. When combined with other delivery techniques, these methods facilitate the transport of hydrophilic drugs, macromolecules, and even gene therapies, providing alternatives to oral delivery for less bioavailable compounds.

Recent advancements in gene therapy have paved the way for potential treatments for psoriasis. Among these innovations, mRNA and siRNA therapies have emerged as particularly promising, with clinical trials showing favorable outcomes. The effective delivery of RNA molecules is critical to ensure that they are not recognized as foreign by the host and can effectively traverse both the extracellular and the intracellular barriers. For gene editing, accessing the nucleus remains a challenge, necessitating the development of targeted delivery systems capable of either passing through nuclear pore complexes or utilizing specific functionalities after endosomal escape. Ultimately, the successful and efficient delivery of siRNA and other RNA-based therapies will require a diverse set of optimized systems, each tailored to meet the unique challenges of delivering these agents to various tissues, thereby unlocking their full therapeutic potential.

7. Expert opinion

Topical medication delivery is one of the most convenient methods for managing skin disorders like psoriasis, an autoimmune condition marked by localized inflammation and systemic complications. Psoriasis leads to immune dysregulation, affecting keratinocytes and resulting in visible lesions. While conventional treatments can alleviate local inflammation, addressing the systemic aspects of psoriasis remains challenging. Recent innovations in treatment options provide a broader range of possibilities for symptom relief. The skin, as the body's first defense, is naturally impermeable, with multiple layers that vary in their hydrophilic properties. This complexity complicates the effective penetration of medications. However, two main strategies have emerged to overcome this barrier: chemical and physical methods, which can be combined to tailor treatments for different forms of psoriasis.

Nanotechnology plays a crucial role in delivering drugs and RNA through protective delivery systems, allowing for prolonged retention and sustained release in the skin. This technology helps maintain local therapeutic concentrations and may also reduce systemic inflammation. Additionally, energy-driven penetration techniques and microneedling can facilitate direct delivery of nanocarriers or medications through the thicker skin typical of psoriasis, increasing the likelihood of effectively targeting the affected areas.

Clinical studies have shown that cyclosporine liposomal gel outperforms cyclosporine in conventional cream formulations at equal drug concentrations. This improvement is attributed to liposomal carriers, which enhance cyclosporine interaction at the cellular level and form cutaneous drug depots at early application stages. These microreservoirs act as slow-release systems in psoriatic areas, leading to higher drug accumulation locally. Pharmacokinetic studies and safety evaluations confirm the tolerability of topical cyclosporine liposomal gel, with consistent reduction in plaque elevation and no development of hot spots [97].

Current treatments for psoriasis include biologics that target inflammatory cytokines such as TNF-α, IL-17, and IL-23. However, cytokine inhibitors can be costly and may increase patients' vulnerability to infections. Newer therapies utilizing siRNA and mRNA offer a more targeted approach with potentially fewer side effects.

However, comprehensive and well-conducted studies are still needed to assess the risks associated with various drug delivery methods, particularly nanoparticle delivery, in terms of skin penetration and potential toxicity. While in vivo studies in psoriasis models have shown enhanced skin permeability with minimal irritation or inflammation, concerns about safety persist. Nanotechnology and alternative delivery methods hold great promise for innovative treatments, but challenges in their practical application remain. Despite progress in understanding psoriasis pathogenesis and exploring new treatments, the disease's complexity requires ongoing updates to therapeutic strategies. To gain a clearer understanding of nanocarriers' impact, transitioning from preclinical studies to clinical trials is necessary. While nanocarriers have shown therapeutic benefits, broader clinical adoption is hindered by the need for further research. Identifying the most effective drug delivery methods for different psoriasis types could significantly improve treatment outcomes, but continued investigation and clinical validation are essential.

Future research in psoriasis treatment may focus on developing innovative delivery systems and nanoparticle formulations for the co-delivery of siRNA targeting IL-17A and corticosteroids, such as clobetasol propionate. This combination approach would address multiple pathogenic mechanisms in psoriasis, enhancing therapeutic efficacy through a broader range of actions. By targeting both molecular and inflammatory pathways, this strategy could significantly optimize treatment outcomes.

Further advancements could emerge from exploring new immunological targets and materials in the field of chemistry. The development of more efficient, safer delivery methods, potentially integrating different delivery techniques and combining molecular drugs with biological agents, may lead to significant progress. These approaches could help reduce inflammation, control systemic immune responses, and promote the healing of skin lesions, improving the management of psoriasis. Future studies are also likely to investigate the synergistic effects of siRNA therapies alongside other molecular targets, with clinical trials aimed at translating promising preclinical

results into effective, real-world treatment options. The future of psoriasis treatment looks promising, with the potential for more personalized, cost-effective, and convenient therapeutic options that can greatly enhance patients' quality of life.

Funding

This paper was funded by Chang Gung Memorial Hospital, Linkou (CMRPD1M0101–3) and the Ministry of Science and Technology, Taiwan (MOST-113-2320-B-182-024-MY3).

Declarations of interest

The authors have no relevant affiliations or financial involvement with any organization or entity with a financial interest in or financial conflict with the subject matter or materials discussed in the manuscript. This includes employment, consultancies, honoraria, stock ownership or options, expert testimony, grants or patents received or pending, or royalties.

Reviewer disclosures

Peer reviewers on this manuscript have no relevant financial or other relationships to disclose.

References

Papers of special note have been highlighted as either of interest (•) or of considerable interest (••) to readers.

1. Liu S, He M, Jiang J, et al. Triggers for the onset and recurrence of psoriasis: a review and update. Cell Commun Signal. 2024;22(1):108. doi: 10.1186/s12964-023-01381-0
   •• **Updated review article to introduce the pathogenesis of psoriasis.**
2. Kocsis D, Horváth S, Kemény Á, et al. Drug delivery through the psoriatic epidermal barrier—A "skin-on-A-Chip" permeability study and ex vivo optical imaging. Int J Mol Sci. 2022;23(8):4237. doi: 10.3390/ijms23084237
3. Goyal R, Macri LK, Kaplan HM, et al. Nanoparticles and nanofibers for topical drug delivery. J Control Release. 2016;240:77–92. doi: 10.1016/j.jconrel.2015.10.049
4. Rapalli VK, Singhvi G, Dubey SK, et al. Emerging landscape in psoriasis management: from topical application to targeting biomolecules. Biomed Pharmacother. 2018;106:707–713. doi: 10.1016/j.biopha.2018.06.136
5. Zhang M, Hong S, Sun X, et al. Exploration of and insights into advanced topical nanocarrier systems for the treatment of psoriasis. Front Med. 2022;15(9):1017126. doi: 10.3389/fmed.2022.1017126
6. Takahashi H, Tsuji H, Minami-Hori M, et al. Defective barrier function accompanied by structural changes of psoriatic stratum corneum. J Dermatol. 2014;41(2):144–148. doi: 10.1111/1346-8138.12393
7. Julian Dinshaw IJ, Ahmad N, Salim N, et al. Nanoemulsions: a review on the conceptualization of treatment for psoriasis using a 'green' surfactant with low-energy emulsification method. Pharmaceutics. 2021;13(7):1024. doi: 10.3390/pharmaceutics13071024
8. Varsha K, Sunil K, Komal S, et al. Dithranol: an insight into its novel delivery cargos for psoriasis management. Curr Drug Res Rev. 2020;12(2):82–96. doi: 10.2174/2589977512666200525154954
9. Agrawal YO, Mahajan UB, Mahajan HS, et al. Methotrexate-loaded nanostructured lipid carrier gel alleviates imiquimod-induced psoriasis by moderating inflammation: formulation, optimization, characterization, in-vitro and in-vivo studies. Int J Nanomed. 2020;15:4763–4778. doi: 10.2147/IJN.S247007
10. Mitchell MJ, Billingsley MM, Haley RM, et al. Engineering precision nanoparticles for drug delivery. Nat Rev Drug Discov. 2021;20(2):101–124. doi: 10.1038/s41573-020-0090-8
    • **Review article describing the application of nanocarriers on drug delivery.**
11. Fereig SA, El-Zaafarany GM, Arafa MG, et al. Tackling the various classes of nano-therapeutics employed in topical therapy of psoriasis. Drug Deliv. 2020;27(1):662–680. doi: 10.1080/10717544.2020.1754527
12. Bodnár K, Fehér P, Ujhelyi Z, et al. Recent approaches for the topical treatment of psoriasis using nanoparticles. Pharmaceutics. 2024;16(4):449. doi: 10.3390/pharmaceutics16040449
13. Mikušová V, Mikuš P. Advances in chitosan-based nanoparticles for drug delivery. Int J Mol Sci. 2021;22(17):9652. doi: 10.3390/ijms22179652
14. Sheikh A, Hazari SA, Molugulu N, et al. Hyaluronic acid engineered gallic acid embedded chitosan nanoparticle as an effective delivery system for treatment of psoriasis. Environ Res. 2023;238(Pt 1):117086. doi: 10.1016/j.envres.2023.117086
15. Fereig SA, El-Zaafarany GM, Arafa MG, et al. Tacrolimus-loaded chitosan nanoparticles for enhanced skin deposition and management of plaque psoriasis. Carbohydr Polym. 2021;268:118238. doi: 10.1016/j.carbpol.2021.118238
16. Shandil A, Yadav M, Sharma N, et al. Targeting keratinocyte hyperproliferation, inflammation, oxidative species and microbial infection by biological macromolecule-based chitosan nanoparticle-mediated gallic acid–rutin combination for the treatment of psoriasis. Polym Bull. 2020;77(343):4713–4738. doi: 10.1007/s00289-019-02984-9
17. Sun L, Liu Z, Wang L, et al. Enhanced topical penetration, system exposure and anti-psoriasis activity of two particle-sized, curcumin-loaded PLGA nanoparticles in hydrogel. J Control Release. 2017;254:44–54. doi: 10.1016/j.jconrel.2017.03.385
18. Shakya AK, Al-Sulaibi M, Naik RR, et al. Review on PLGA polymer based nanoparticles with antimicrobial properties and their application in various medical conditions or infections. Polymers. 2023;15(17):3597. doi: 10.3390/polym15173597
19. Fu J, You L, Sun D, et al. Shikonin-loaded PLGA nanoparticles: a promising strategy for psoriasis treatment. Heliyon. 2024;10(11):e31909. doi: 10.1016/j.heliyon.2024.e31909
20. Kagawa A, Sato A, Makino K, et al. Therapeutic effects of 30 nm cyclosporin A-loaded nanoparticles using PLGA-PEG-PLGA triblock copolymer for transdermal delivery in mouse models of psoriasis. Appl Sci. 2024;14(9):3791. doi: 10.3390/app14093791
21. Lin CY, Yu HP, Chang YT, et al. Targeting anti-inflammatory immunonanocarriers to human and murine neutrophils via the Ly6 antigen for psoriasiform dermatitis alleviation. Biomater Sci. 2023;11(3):873–893. doi: 10.1039/D2BM01521H
22. Lin ZC, Hwang TL, Huang TH, et al. Monovalent antibody-conjugated lipid-polymer nanohybrids for active targeting to desmoglein 3 of keratinocytes to attenuate psoriasiform inflammation. Theranostics. 2021;11(10):4567. doi: 10.7150/thno.56995
23. Dash TK, Konkimalla VB. Poly-ϵ-caprolactone based formulations for drug delivery and tissue engineering: a review. J Control Release. 2012;158(1):15–33. doi: 10.1016/j.jconrel.2011.09.064
24. Guo D, Shi C, Wang L, et al. Rationally designed micellar nanocarrier for the delivery of hydrophilic methotrexate in psoriasis treatment. ACS Appl Bio Mater. 2020;3(8):4832–4846. doi: 10.1021/acsabm.0c00342
25. Liaw HZ, Sheba RD, Rajan R. Chitosan nanoparticle toxicity: a comprehensive literature review of in vivo and in vitro assessments for medical applications. Toxicol Rep. 2023;11:83–106. doi: 10.1016/j.toxrep.2023.06.012
26. Hock IC, Nozlena AS, Fang L, et al. Cytotoxicity of targeted PLGA nanoparticles: a systematic review. RSC Adv. 2021;11(16):9433–9449. doi: 10.1039/D1RA00074H
27. Patil TS, Gujarathi NA, Aher AA, et al. Recent advancements in topical anti-psoriatic nanostructured lipid carrier-based drug delivery. Int J Mol Sci. 2023;24(3):2978. doi: 10.3390/ijms24032978

•• **The review article introducing the topical delivery of anti-psoriatic lipid nanocarriers.**

28. Chauhan I, Yasir M, Verma M, et al. Nanostructured lipid carriers: aa groundbreaking approach for transdermal drug delivery. Adv Pharm Bull. 2020;10(2):150–165. doi: 10.34172/apb.2020.021
29. Halagali P, Angolkar M, Arjun HR, et al. Nanoemulsion for the treatment of psoriasis. Bull Env Pharmacol Life Sci. 2023;12 (5):308–317.
30. Salim N, Basri M, Rahman MB, et al. Modification of palm kernel oil esters nanoemulsions with hydrocolloid gum for enhanced topical delivery of ibuprofen. Int J Nanomed. 2012;7:4739–4747. doi: 10.2147/IJN.S34700
31. Salim N, Ahmad N, Musa SH, et al. Nanoemulsion as a topical delivery system of antipsoriatic drugs. RSC Adv. 2016;6(8):6234–6250. doi: 10.1039/C5RA14946K
32. Kawakami MYM, Zamora LO, Araújo RS, et al. Efficacy of nanoemulsion with *pterodon emarginatus* Vogel oleoresin for topical treatment of cutaneous leishmaniasis. Biomed Pharmacother. 2021;134:111109. doi: 10.1016/j.biopha.2020.111109
33. Babaei V, Ashtarinezhad A, Torshabi M, et al. High inflammatory cytokines gene expression can be detected in workers with prolonged exposure to silver and silica nanoparticles in industries. Sci Rep. 2024;14(1):5667. doi: 10.1038/s41598-024-56027-z
34. Bartelds R, Nematollahi MH, Pols T, et al. Niosomes, an alternative for liposomal delivery. PLoS One. 2018;13(4):e0194179. doi: 10.1371/journal.pone.0194179
35. Suresh PK, Singh P, Saraf S, et al. Novel topical drug carriers as a tool for treatment of psoriasis: progress and advances. Afr J Pharm Pharmacol. 2013;7(5):138–147. doi: 10.5897/AJPPX12.001
36. Alkilani AZ, McCrudden MTC, Donnelly RF. Transdermal drug delivery: innovative pharmaceutical developments based on disruption of the barrier properties of the stratum corneum. Pharmaceutics. 2015;7(4):438–470. doi: 10.3390/pharmaceutics7040438
37. Marianecci C, Di Marzio L, Rinaldi F, et al. Niosomes from 80s to present: the state of the art. Adv Colloid Interface Sci. 2014;205:187–206. doi: 10.1016/j.cis.2013.11.018
38. Zhang Y, Gong S, Liu L, et al. Cyclodextrin-coordinated liposome-in-gel for transcutaneous quercetin delivery for psoriasis treatment. ACS Appl Bio Mater. 2023;15(34):40228–40240. doi: 10.1021/acsami.3c07582
39. Zamansky M, Yariv D, Feinshtein V, et al. Cannabidiol-loaded lipid-stabilized nanoparticles alleviate psoriasis severity in mice: a new approach for improved topical drug delivery. Molecules. 2023;28(19):6907. doi: 10.3390/molecules28196907
40. Abu-Huwaij R, Zidan AN. Unlocking the potential of cosmetic dermal delivery with ethosomes: a comprehensive review. J Cosmet Dermatol. 2024;23(1):17–26. doi: 10.1111/jocd.15895
41. Fathalla D, Youssef EMK, Soliman GM. Liposomal and ethosomal gels for the topical delivery of anthralin: preparation, comparative evaluation and clinical assessment in psoriatic patients. Pharmaceutics. 2020;12(5):446. doi: 10.3390/pharmaceutics12050446
42. Puri A, Loomis K, Smith B, et al. Lipid-based nanoparticles as pharmaceutical drug carriers: from concepts to clinic. Crit Rev Ther Drug Carrier Syst. 2009;26(6):523–580. doi: 10.1615/CritRevTherDrugCarrierSyst.v26.i6.10
43. Rahmanian-Devina P, Askarib VR, Sanei-Far Z, et al. Preparation and characterization of solid lipid nanoparticles encapsulated noscapine and evaluation of its protective effects against imiquimod-induced psoriasis-like skin lesions. Biomed Pharmacother. 2023;168:115823. doi: 10.1016/j.biopha.2023.115823
44. Alam M, Rizwanullah M, Mir SR, et al. Promising prospects of lipid-based topical nanocarriers for the treatment of psoriasis. OpenNano. 2023;10:100123. doi: 10.1016/j.onano.2023.100123
45. Pradhan M, Singh D, Singh MR. Development characterization and skin permeating potential of lipid based novel delivery system for topical treatment of psoriasis. Chem Phys Lipids. 2015;186:9–16. doi: 10.1016/j.chemphyslip.2014.11.004
46. Saini K, Modgill N, Singh KK, et al. Tetrahydrocurcumin lipid nanoparticle based gel promotes penetration into deeper skin layers and alleviates atopic dermatitis in 2, 4-dinitrochlorobenzene (DNCB) mouse model. Nanomaterials. 2022;12(4):636. doi: 10.3390/nano12040636
47. Saini K, Verma S, Kakkar V. Anti-psoriatic effects of tetrahydrocurcumin lipidic nanoparticles in IMQ induced psoriatic plaque: a research report. J Drug Deliv Sci Technol. 2022;71:103301. doi: 10.1016/j.jddst.2022.103301
48. Jijie R, Szunerits S, Barras A, et al. Nanomaterials for transdermal drug delivery: beyond the state of the art of liposomal structures. J Mater Chem B. 2017;5(44):8653–8675. doi: 10.1039/C7TB02529G
49. Kilfoyle BE, Sheihet L, Zhang Z, et al. Development of paclitaxel-TyroSpheres for topical skin treatment. J Control Release. 2012;163(1):18–24. doi: 10.1016/j.jconrel.2012.06.021
50. Arora R, Katiyar SS, Kushwah V, et al. Solid lipid nanoparticles and nanostructured lipid carrier-based nanotherapeutics in treatment of psoriasis: a comparative study. Expert Opin Drug Deliv. 2017;14 (2):165–177. doi: 10.1080/17425247.2017.1264386
51. Raza K, Singh B, Lohan S, et al. Nano-lipoidal carriers of tretinoin with enhanced percutaneous absorption, photostability, biocompatibility and anti-psoriatic activity. Int J Pharm. 2013;456(1):65–72. doi: 10.1016/j.ijpharm.2013.08.019
52. Mascarenhas-Melo F, Carvalho A, Gonçalves MBS, et al. Nanocarriers for the topical treatment of psoriasis - pathophysiology, conventional treatments, nanotechnology, regulatory and toxicology. Eur J Pharm Biopharm. 2022;176:95–107. doi: 10.1016/j.ejpb.2022.05.012
53. Han R, Ho LWC, Bai Q, et al. Alkyl-terminated gold nanoparticles as a self-therapeutic treatment for psoriasis. Nano Lett. 2021;21 (20):8723–8733. doi: 10.1021/acs.nanolett.1c02899
54. Bessar H, Venditti I, Benassi L, et al. Functionalized gold nanoparticles for topical delivery of methotrexate for the possible treatment of psoriasis. Colloids Surf B Biointerfaces. 2016;141:141–147. doi: 10.1016/j.colsurfb.2016.01.021
55. Crisan D, Scharffetter-Kochanek K, Crisan M, et al. Topical silver and gold nanoparticles complexed with Cornus *mas* suppress inflammation in human psoriasis plaques by inhibiting nf-κB activity. Exp Dermatol. 2018;27(10):1166–1169. doi: 10.1111/exd.13707
56. Carvalho-Silva JM, Dos Reis AC. Anti-inflammatory action of silver nanoparticles *in vivo*: systematic review and meta-analysis. Heliyon. 2024;10(14):e34564. doi: 10.1016/j.heliyon.2024.e34564
57. Fan Z, Zhao G, Gan Y, et al. Synergistic chemo-photodynamic therapy based on hollow mesoporous organosilica nanoparticles for reducing psoriasis-like inflammation. J Chem Eng. 2024;490:151613. doi: 10.1016/j.cej.2024.151613
58. Mo C, Lu K, Liu D, et al. Development of erianin-loaded dendritic mesoporous silica nanospheres with pro-apoptotic effects and enhanced topical delivery. J Nanobiotechnol. 2020;18(1):55. doi: 10.1186/s12951-020-00608-3
59. Arati S, Subba RVM, Gavin PR, et al. Toxicological considerations when creating nanoparticle-based drugs and drug delivery systems. Expert Opin Drug Metab Toxicol. 2012;8(1):47–69. doi: 10.1517/17425255.2012.637916

• **The toxicological concern about the nanoencapsulated drugs.**

60. Bakshi P, Vora D, Hemmady K, et al. Iontophoretic skin delivery systems: success and failures. Int J Pharm. 2020;586:119584. doi: 10.1016/j.ijpharm.2020.119584
61. Hasan M, Khatun A, Kogure K. Iontophoresis of biological macromolecular drugs. Pharmaceutics. 2022;14(3):525. doi: 10.3390/pharmaceutics14030525
62. Vikelis M, Spingos KC, Rapoport AM. The iontophoretic transdermal system formulation of sumatriptan as a new option in the acute treatment of migraine: a perspective. Ther Adv Neurol Disord. 2015;8(4):160–165. doi: 10.1177/1756285615585918
63. Gehl J. Electroporation: theory and methods, perspectives for drug delivery, gene therapy and research. Acta Physiol Scand. 2003;177 (4):437–447. doi: 10.1046/j.1365-201X.2003.01093.x
64. Fukuta T, Tanaka D, Inoue S, et al. Overcoming thickened pathological skin in psoriasis via iontophoresis combined with tight junction-opening peptide AT1002 for intradermal delivery of nf-κB

decoy oligodeoxynucleotide. Int J Pharm. 2021;602:120601. doi: 10.1016/j.ijpharm.2021.120601
65. Marathe D, Bhuvanashree VS, Hasmukh Mehta CH, et al. Low-frequency sonophoresis: a promising strategy for enhanced transdermal delivery. Adv Pharmacol Pharm Sci. 2024;2024(1):1247450. doi: 10.1155/2024/1247450
66. Wahba ES. Effect of calcipotriol plus betamethasone dipropionate gel phonophoresis on psoriasis: a single-blind randomized controlled trial. Bull Fac Phys Ther. 2019;24(2):57–65. doi: 10.4103/bfpt.bfpt_23_18
67. Nguyen HX, Banga AK. Electrically and ultrasonically enhanced transdermal delivery of methotrexate. Pharmaceutics. 2018;10(3):117. doi: 10.3390/pharmaceutics10030117
68. Lee LW, Gadiraju P, Park JH, et al. Microsecond thermal ablation of skin for transdermal drug delivery. J Control Release. 2011;154(1):58–68. doi: 10.1016/j.jconrel.2011.05.003
69. Azagury A, Khoury L, Enden G, et al. Ultrasound mediated transdermal drug delivery. Adv Drug Deliv Rev. 2014;72:127–143. doi: 10.1016/j.addr.2014.01.007
70. Ma G, Wu C. Microneedle, bio-microneedle and bio-inspired microneedle: a review. J Control Release. 2017;251:11–23. doi: 10.1016/j.jconrel.2017.02.011
71. Donnelly R, Douroumis D. Microneedles for drug and vaccine delivery and patient monitoring. Drug Deliv Transl Res. 2015;5(4):311–312. doi: 10.1007/s13346-015-0250-2
72. Zhao Z, Chen Y, Shi Y. Microneedles: a potential strategy in transdermal delivery and application in the management of psoriasis. RSC Adv. 2020;10:14040. doi: 10.1039/D0RA00735H
73. Ren Y, Li J, Chen Y, et al. Customized flexible hollow microneedles for psoriasis treatment with reduced-dose drug. Bioeng Transl Med. 2023;8(4):e10530. doi: 10.1002/btm2.10530
74. Elmets CA, Korman NJ, Prater EF, et al. Joint AAD–NPF guidelines of care for the management and treatment of psoriasis with topical therapy and alternative medicine modalities for psoriasis severity measures. J Am Acad Dermatol. 2021;84(2):432–470. doi: 10.1016/j.jaad.2020.07.087
75. Kwatra G, Mukhopadhyay S. Topical corticosteroids: pharmacology. A treatise on topical corticosteroids in dermatology. Springer Nat Singapore. 2018;2:11–22.
76. Pratt WB. The mechanism of glucocorticoid effects in fibroblasts. J Invest Dermatol. 1978;71(1):24–35. doi: 10.1111/1523-1747.ep12543774
77. Cornell RC, Stoughton RB. Correlation of the vasoconstriction assay and clinical activity in psoriasis. Arch Dermatol Res. 1985;121:63–67. doi: 10.1001/archderm.1985.01660010067020
78. van de Kerkhof PCM, Murphy GM, Austad J, et al. Psoriasis of the face and flexures. J Dermatol Treat. 2007;18(6):351–360. doi: 10.1080/09546630701341949
79. Leonardi C, Bagel J, Yamauchi P, et al. Efficacy and safety of calcipotriene plus betamethasone dipropionate aerosol foam in patients with psoriasis vulgaris-A randomized phase III study (PSO-FAST). J Drugs Dermatol. 2015;14(12):1468–1477.
80. Lebwohl M, Tyring S, Bukhalo M, et al. Fixed combination aerosol foam calcipotriene 0.005% (cal) plus betamethasone dipropionate 0.064% (BD) is more efficacious than cal or BD aerosol foam alone for psoriasis vulgaris: a randomized, double-blind, multicenter, three-arm, phase 2 study. J Clin Aesthet Dermatol. 2016;9(2):34–41.
81. Lebwohl MG, Sugarman JL, Gold LS, et al. Efficacy, safety, and tolerability of a halobetasol 0.01%/tazarotene 0.045% fixed combination in the treatment of severe localized plaque psoriasis: post hoc analysis of two phase III randomized controlled trials. J Drugs Dermatol. 2019;3(10):1012–1018. doi: 10.25251/skin.3.supp.29
82. Kim GK. The rationale behind topical vitamin D analogs in the treatment of psoriasis: where does topical calcitriol fit in? J Clin Aesthet Dermatol. 2010;3(8):46–53.
83. Bikle D, Christakos S. New aspects of vitamin D metabolism and action — addressing the skin as source and target. Nat Rev Endocrinol. 2020;16(4):234–252. doi: 10.1038/s41574-019-0312-5
84. Brożyna AA, Slominski RM, Nedoszytko B, et al. Vitamin D signaling in psoriasis: pathogenesis and therapy. Int J Mol Sci. 2022;23(15):8575. doi: 10.3390/ijms23158575
85. Lehmann B. Role of the vitamin D $_3$ pathway in healthy and diseased skin – facts, contradictions and hypotheses. Exp Dermatol. 2009;18(2):97–108. doi: 10.1111/j.1600-0625.2008.00810.x
86. Duvic M, Nagpal S, Asano AT. Molecular mechanisms of tazarotene action in psoriasis. J Am Acad Dermatol. 1997;37(2):S18–S24. doi: 10.1016/S0190-9622(97)80396-9
87. Lebwohl MG, Breneman DL, Goffe BS, et al. Tazarotene 0.1% gel plus corticosteroid cream in the treatment of plaque psoriasis. J Am Acad Dermatol. 1998;39(4):590–596. doi: 10.1016/S0190-9622(98)70008-8
88. Esser C, Rannug A. The aryl hydrocarbon receptor in barrier organ physiology, immunology, and toxicology. Pharmacol Rev. 2015;67(2):259–279. doi: 10.1124/pr.114.009001
89. Bissonnette R, Gold LS, Rubenstein DS, et al. Tapinarof in the treatment of psoriasis: a review of the unique mechanism of action of a novel therapeutic aryl hydrocarbon receptor–modulating agent. J Am Acad Dermatol. 2021;84(4):1059–1067. doi: 10.1016/j.jaad.2020.10.085
90. Lebwohl MG, Gold LS, Strober B, et al. Phase 3 trials of tapinarof cream for plaque psoriasis. N Engl J Med. 2021;385(24):2219–2229. doi: 10.1056/NEJMoa2103629
91. Bagel J, Gold LS, Del Rosso J, et al. Tapinarof cream 1% once daily for the treatment of plaque psoriasis: patient-reported outcomes from the PSOARING 3 trial. J Am Acad Dermatol. 2023;89(5):936–944. doi: 10.1016/j.jaad.2023.04.061
92. Spina D. PDE4 inhibitors: current status. Br J Pharmacol. 2008;155(3):308–315. doi: 10.1038/bjp.2008.307
93. Lebwohl MG, Kircik LH, Moore AY, et al. Effect of roflumilast cream vs vehicle cream on chronic plaque psoriasis: the DERMIS-1 and DERMIS-2 randomized clinical trials. JAMA. 2022;328(11):1073–1084. doi: 10.1001/jama.2022.15632
94. Langley RGB, Feldman SR, Nyirady J, et al. The 5-point Investigator's global assessment (IGA) scale: a modified tool for evaluating plaque psoriasis severity in clinical trials. J Dermato Treat. 2015;26(1):23–31. doi: 10.3109/09546634.2013.865009
95. Manchanda Y, De A, Das S, et al. Disease assessment in psoriasis. Indian J Dermatol. 2023;68(3):278–281. doi: 10.4103/ijd.ijd_420_23
96. Tatiparti K, Sau S, Kashaw SK, et al. siRNA delivery strategies: a comprehensive review of recent developments. Nanomaterials. 2017;7(4):77. doi: 10.3390/nano7040077
•• **The review summarizing the detailed mechanisms of siRNA delivery.**
97. Sufianov A, Beilerli A, Kudriashov V, et al. Advances in transdermal siRNAs delivery: a review of current research progress. Noncoding RNA Res. 2023;8(3):392–400. doi: 10.1016/j.ncrna.2023.05.008
98. Geusens B, Strobbe T, Bracke S, et al. Lipid-mediated gene delivery to the skin. Eur J Pharm Sci. 2011;43(4):199–211. doi: 10.1016/j.ejps.2011.04.003
99. Zaidi SSA, Fatima F, Zaidi SAA, et al. Engineering siRNA therapeutics: challenges and strategies. J Nanobiotechnol. 2023;21(1):381. doi: 10.1186/s12951-023-02147-z
100. Mandal A, Kumbhojkar N, Reilly C, et al. Treatment of psoriasis with NFKBIZ siRNA using topical ionic liquid formulations. Sci Adv. 2020;6(30):eabb6049. doi: 10.1126/sciadv.abb6049
101. Zheng D, Giljohann DA, Chen DL, et al. Topical delivery of siRNA-based spherical nucleic acid nanoparticle conjugates for gene regulation. Proc Natl Acad Sci USA. 2012;109(30):11975–11980. doi: 10.1073/pnas.1118425109
102. Nemati H, Ghahramani MH, Faridi-Majidi R, et al. Using siRNA-based spherical nucleic acid nanoparticle conjugates for gene regulation in psoriasis. J Control Release. 2017;268:259–268. doi: 10.1016/j.jconrel.2017.10.034
• **The use of nanocarriers for siRNA delivery to treat psoriasis.**

103. Marepally S, Boakye CHA, Patel AR, et al. Topical administration of dual siRNAs using fusogenic lipid nanoparticles for treating psoriatic-like plaque. Nanomedicine. 2014;9(14):2157–2174. doi: 10.2217/nnm.13.202
104. Lee WR, Lin YK, Alalaiwe A, et al. Fractional laser-mediated siRNA delivery for mitigating psoriasis-like lesions via IL-6 silencing. Mol Ther Nucleic Acids. 2020;19:240–251. doi: 10.1016/j.omtn.2019.11.013
105. Rajiv K, Sunil D, Basant A. Efficacy of novel topical liposomal formulation of cyclosporine in mild to moderate stable plaque psoriasis: a randomized clinical trial. JAMA Dermatol. 2016;152(7):807–815. doi: 10.1001/jamadermatol.2016.0859

Journal of Pediatric Nursing 85 (2025) 362–369

Contents lists available at ScienceDirect

Journal of Pediatric Nursing

journal homepage: www.pediatricnursing.org

The relationship between health literacy and medical decision conflict among parents of children newly diagnosed with central precocious puberty

Ming-Yi Shen [a,b], Chiao-Fan Chiu [c,d,e], Mei-Yen Chen [f,g], Lan-Yan Yang [h,1], Chizimuzo T.C. Okoli [i], Ying-Mei Liu [c,j,*]

[a] Graduate Institute of Nursing, Chang Gung University of Science and Technology, Taoyuan, Taiwan
[b] Department of Nursing, Linkou Chang Gung Memorial Hospital, Taoyuan, Taiwan
[c] Department of Pediatrics, Linkou Chang Gung Memorial Hospital, Taoyuan, Taiwan
[d] School of Medicine, Chang Gung University, Taoyuan, Taiwan
[e] Graduate Institute of Clinical Medical Sciences, College of Medicine, Chang Gung University, Taoyuan, Taiwan
[f] Department of Nursing, Chang Gung University of Science and Technology, Chiayi, Taiwan
[g] Department of Cardiology, Chiayi Chang Gung Memorial Hospital, Chiayi, Taiwan
[h] Division of Clinical Trial, Department of Medical Research, Taichung Veterans General Hospital, Taichung, Taiwan
[i] College of Nursing, University of Kentucky, Lexington, KY, USA
[j] Department of Nursing, Chang Gung University of Science and Technology, Taoyuan, Taiwan

ARTICLE INFO

Article history:
Received 6 July 2025
Revised 25 August 2025
Accepted 25 August 2025

Keywords:
Central precocious puberty
Children
Health literacy
Medical decision conflict
Parents

ABSTRACT

Purpose: Parents of children newly diagnosed with central precocious puberty often face emotional stress and time-sensitive treatment decisions, highlighting the importance of family-centered care. This cross-sectional study examined the relationship between parental health literacy and medical decision conflict.
Methods: A total of 65 parents of children newly diagnosed with central precocious puberty were recruited. Participants completed questionnaires measuring health literacy and medical decision conflict. Predictors were examined using multiple linear regression.
Results: More than half of the participants had limited health literacy. Parental health literacy significantly predicted medical decision conflict in the simple linear regression analysis ($\beta = -0.45$, $T = -4.03$, $p < .001$), indicating that higher overall health literacy was associated with lower decisional conflict. Specifically, a one-point increase in total health literacy score corresponded to a 0.68-point reduction in conflict. Furthermore, correlation analyses revealed that parental literacy in the communication and interaction domains was particularly associated with lower levels of decision conflict, suggesting that these domains may play a critical role in supporting effective parental decision-making.
Conclusions: Limited parental health literacy is common among families with children newly diagnosed with central precocious puberty. Notably, deficiencies in communication and interaction skills are associated with increased medical decision conflict.
Clinical implications: The results emphasise the need for healthcare professionals to actively assess and support parents' communicative and interpersonal health literacy skills. Equipping clinicians with tools for identifying literacy-related barriers and tailoring information accordingly can facilitate shared decision-making and promote confident, informed parental participation in care decisions.
© 2025 Elsevier Inc. All rights are reserved, including those for text and data mining, AI training, and similar technologies.

Introduction

Precocious puberty is defined as the onset of secondary sexual characteristics before the age of 8 years in girls and 9 years in boys (Banerjee, Kashikar, Rao, & Surve, 2025). Central precocious puberty (CPP), the more common form of precocious puberty, results from the early activation of the hypothalamic-pituitary-gonadal axis (Banerjee, Kashikar, Rao, & Surve, 2025). CPP poses medical and psychosocial challenges for affected children and their families (Mason & Daskas, 2024). A new diagnosis often initiates a time-sensitive and emotionally charged decision-making process, during which parents must rapidly evaluate complex information related to diagnostic procedures and therapeutic options, such as gonadotropin-releasing hormone analogue therapy

* Corresponding author at: No. 261, Wen-Hwa 1st Road, Guishan District, Taoyuan, Taiwan.
E-mail address: ymliu@mail.cgust.edu.tw (Y.-M. Liu).
[1] The fourth author, Dr. Yang, is a statistician and contributed to the statistical analysis in this study.

https://doi.org/10.1016/j.pedn.2025.08.017
0882-5963/© 2025 Elsevier Inc. All rights are reserved, including those for text and data mining, AI training, and similar technologies.

(Breidbart et al., 2024; Ni et al., 2025). These decisions are further complicated by uncertainties regarding long-term outcomes and the need to align choices with family values and the child's best interests.

Parental health literacy, defined as the capacity to access, understand, evaluate, and apply health information, has emerged as a pivotal factor influencing decision quality (Lindly et al., 2022; Ma et al., 2024). A review article reported that one-fourth of parents had low health literacy (Morrison et al., 2019). Limited health literacy can hinder parents' ability to comprehend medical advice, weigh treatment alternatives, and anticipate future consequences, potentially heightening medical decision conflict and post-decision regret (Matchanova et al., 2021). Although health literacy is increasingly acknowledged as a foundation for effective shared decision-making (SDM), its specific role in the early management of paediatric endocrine conditions such as CPP remains insufficiently studied. Importantly, many paediatricians and nurses do not receive formal training in health literacy, which may limit their ability to recognise and address the informational needs of families (Friedman et al., 2025; Ronan et al., 2023).

To address this gap, the current study examined the relationship between parental health literacy and medical decision conflict following a new diagnosis of CPP. By elucidating how informational competencies influence parental decision-making during this critical period, this study aimed to inform the development of targeted communication strategies and decision aids that empower families and improve paediatric endocrine care outcomes. In addition, this study sought to raise awareness among healthcare professionals about the importance of health literacy sensitivity, an often-overlooked yet essential component of effective family-centred practice.

Background

The incidence of CPP has shown a significant global increase and is estimated to have risen 4–10 times over the past two decades, which is attributed to multifactorial influences such as rising childhood obesity rates, nutritional factors, and environmental exposures (Aruna & Giridhar, 2025; Bräuner et al., 2020; Huttunen et al., 2024). Epidemiological studies have consistently reported that girls and children with elevated body mass index (BMI) are at an increased risk of early pubertal onset (Dong et al., 2023; Liu et al., 2021; Wang et al., 2025). CPP is associated with adverse long-term health outcomes, including metabolic disorders (e.g., obesity and type 2 diabetes), cardiovascular diseases (e.g., hypertension and dyslipidaemia), and an elevated risk of hormone-related cancers (Brito et al., 2023). It may also lead to psychosocial challenges, such as compromised adult height, early menarche, and increased emotional distress stemming from premature physical development (Aruna & Giridhar, 2025).

Given these risks, early diagnosis and timely intervention are essential to mitigate long-term physical and psychological consequences. However, initiating treatment, particularly hormone-based therapies, requires a nuanced clinical judgment and active parental involvement in decision-making. This process becomes more complex when the evidence of long-term outcomes is inconclusive or when treatment recommendations vary depending on the child's presentation and family context (Knific et al., 2022). Parents are often required to make important treatment decisions shortly after diagnosis and are frequently under emotional strain and time pressure. The ability to understand and apply medical advice is critical in this setting. However, studies suggest that many parents struggle with complex health information, particularly when it involves medical terminology or probabilistic outcomes (Jacobs et al., 2023). These challenges are more pronounced among individuals with limited health literacy, a construct that encompasses the cognitive and social skills needed to access, comprehend, and apply basic health information (Nutbeam, 2000).

Low health literacy is associated with increased decisional conflict, a psychological state marked by uncertainty and stress when choosing medical options (Roggero et al., 2024). In paediatric endocrinology, where early intervention decisions may affect a child's developmental trajectory for years, high decisional conflict may compromise decision quality, delay treatment, or contribute to future regret and non-adherence (Jonas et al., 2022; Zaidman et al., 2023).

Despite its relevance, limited empirical research has directly examined the impact of parental health literacy on medical decision conflict during early CPP management. Understanding this relationship is critical for identifying at-risk families and designing communication strategies and support systems that enable informed and confident decision-making in paediatric endocrine care.

This study aimed to examine the association between parental health literacy and medical decision conflict in the early management of CPP. Specifically, this study sought to determine whether lower health literacy levels are associated with greater decisional conflict among parents of children newly diagnosed with CPP. We hypothesised that lower parental health literacy would be associated with increased medical decision conflict.

Methods

Design

This cross-sectional correlational study examined the relationship between health literacy and medical decision conflict among parents of children newly diagnosed with CPP. Additionally, this study investigated the predictive power of health literacy for medical decision conflict. This study was conducted according to the Strengthening the Reporting of Observational Studies in Epidemiology (STROBE) guidelines for cross-sectional studies (von Elm et al., 2014).

Study setting and sampling

This study was conducted at the Paediatric Endocrinology Department of a major medical centre in northern Taiwan, which is recognised as one of the largest paediatric hospitals in the country. The participants were parents of children who made their first visit to the study hospital for the evaluation of precocious puberty between January and December 2024. Diagnosis of the condition, defined as the early development of secondary sexual characteristics before age 8 in girls and age 9 in boys, was confirmed through national medical records within six months prior to recruitment, regardless of whether the diagnosis was made at this hospital or another institution. The diagnosis was based on the International Classification of Diseases, Tenth Revision, Clinical Modification (ICD-10-CM) code E30.1 (World Health Organization, 2019).

Eligible participants were those who served as primary medical decision makers (either the mother or father) for the child receiving care. In cases where decisions were made jointly, the parents were asked to agree on which one would participate. Purposive sampling was used to recruit caregivers who met the inclusion criteria. After the attending physician explained the child's medical condition, the first author approached eligible parents, explained the purpose and procedures of the study, and obtained their consent to participate in the study in accordance with the institutional review board (IRB) guidelines. Parents who agreed to participate were asked to complete the questionnaire in a quiet space in the Paediatric Endocrinology Department.

A priori power analysis was conducted using G*Power 3.1 to determine the required sample size for a simple linear regression analysis with one predictor variable (health literacy). Assuming a medium effect size ($f^2 = 0.15$), an alpha level of 0.05, and a statistical power of 0.85, the minimum required sample size was 62 participants.

Inclusion and exclusion criteria

The inclusion criteria were as follows: (1) participants had to be at least 20 years old; (2) fully conscious and oriented; (3) able to

communicate and complete questionnaires in Mandarin; and (4) without any diagnosed intellectual or cognitive impairments.

Exclusion criteria included having a child whose precocious puberty was caused by pathological conditions, such as central nervous system abnormalities, functional ovarian cysts, congenital adrenal hyperplasia, adrenal tumours, or germ cell tumours.

Instrument with validity and reliability

This study utilised four instruments

Parental and Family Demographic Questionnaire. The researcher-developed questionnaire included items on parental age, family socioeconomic status (SES), and the source from which parents obtained information about their children's precocious puberty. SES was assessed based on the index developed by Lin (2007), adapted from Hollingshead's Two-Factor Index of Social Position, which combines educational attainment and occupation. The resulting score classified SES into five levels: low SES (level I), lower-middle SES (level II), middle SES (level III), upper-middle SES (level IV), and high SES (level V), with higher scores indicating higher socioeconomic status. The questionnaire also included items related to symptom recognition and care-seeking behaviours. These items captured data on the first observed symptoms of the child's precocious puberty, the person who initially noticed these signs (e.g., mother, father, or child), and the time interval between symptom recognition and the first medical consultation.

Child clinical data form. A researcher-developed questionnaire was designed based on a comprehensive review of the CPP-related literature. Clinical data were extracted from medical records by the research team and included the children's age, sex, and BMI. BMI was classified according to age- and sex-specific categories established by the Ministry of Health and Welfare, Taiwan (2013): obese, overweight, normal weight, and underweight. Additional variables included bone age, discrepancy between bone age and chronological age, and Tanner stage of secondary sexual characteristics. Bone age was assessed using standard hand and wrist X-rays (Cavallo et al., 2021), interpreted by paediatric endocrinologists according to clinical guidelines. The discrepancy between bone age and chronological age was calculated by subtracting chronological age—defined as the age in years between birth and evaluation—from bone age. In children with CPP, bone age and chronological age often differ, and distinguishing between them is crucial for clinical assessment (Cavallo et al., 2021). Tanner stage was assessed by paediatric endocrinologists based on clinical examination of breast or genital development and other physical markers of puberty, following standard criteria (Emmanuel & Bokor, 2022).

Mandarin Multidimensional Health Literacy Questionnaire (MMHLQ). In this study, the MMHLQ was used to assess the health literacy of parents whose children were newly diagnosed with CPP. This questionnaire, developed by Wei et al. (2017), is a 20-item instrument that assesses five dimensions of health literacy: accessing health information, understanding health information, appraising health information, applying health information, and communication and interaction. Responses were rated on a 4-point Likert scale (1 = very difficult, 4 = very easy), yielding total scores ranging from 20 to 80, with higher scores indicating better health literacy. Health literacy levels were categorised as follows: 0–25, inadequate; 25–33, limited; 33–42, sufficient; and 42–50, excellent. In this study, the internal consistency reliability of the MMHLQ was high, with a Cronbach's α of 0.947.

Question-Format Decisional Conflict Scale (DCS). In this study, the DCS was used to assess the medical decision conflict of parents whose children were newly diagnosed with CPP. The DCS, developed by O'Connor, 1995, consists of 16 items that assess uncertainty and decisional conflict in medical decision-making. The scale comprises five subscales: (1) Informed, which assesses whether participants feel certain about the best choice and understand the benefits and risks of each option; (2) Values Clarity, which evaluates whether participants are unclear about the importance of potential outcomes; (3) Support, which examines whether participants feel supported in decision-making and free from external pressure; (4) Uncertainty, which measures the degree to which participants feel uncertain due to insufficient advice or information; and (5) Effective Decision, which assesses confidence, commitment, and satisfaction with the chosen option. Responses were rated on a 5-point scale (0 = strongly agree, 4 = strongly disagree). The total raw scores (0–64) were converted to a 0–100 scale, with higher scores indicating greater decisional conflict. Scores of <25, 25–37.5, and > 37.5 suggest low, moderate, and high decisional conflict, respectively. This study used a validated Chinese version of this scale (Lu et al., 2019). In the current study, the scale demonstrated excellent internal consistency (Cronbach's α = 0.942).

Data analysis

Data were analysed using IBM SPSS Statistics version 28.0. Descriptive statistics, including frequencies, percentages, means, and standard deviations, were calculated for the participants' demographic characteristics and their children's clinical data. The assumption of normality was tested using the Kolmogorov–Smirnov test before conducting the parametric analyses.

Group comparisons (e.g., sex, educational level, and other demographic variables related to health literacy and medical decision conflict) were conducted using independent samples *t*-tests and one-way ANOVAs, as appropriate.

Pearson's correlation analysis was conducted to examine the associations between parents' demographic characteristics, children's clinical data, health literacy, and medical decision conflict. Additionally, simple linear regression analysis was performed to assess the predictive power of health literacy on medical decision conflict. Statistical significance was set at $p < .05$, and all tests were two-tailed.

Results

Characteristics of the participants

A total of 67 parents of children who were newly diagnosed with CPP met the inclusion criteria. Two parents declined to participate, resulting in a refusal rate of 2.9 %. The primary reason for refusal was a lack of time to complete the questionnaire. As a result, 65 parents completed the study.

Most participants were mothers (n = 54, 83.1 %), while fathers accounted for 11 participants (16.9 %). The mean age of the parents was 40.36 years (range: 31–51 years; standard deviation [SD] = 3.95). Most of the participants had attained university degrees (n = 36, 55.4 %). Regarding SES, the largest proportion of families was classified as upper-middle SES (level IV), with 29 families (44.6 %). Notably, 84.6 % of parents reported that their source of information about their child's precocious puberty was online (Table 1).

Among the children, 61 (93.8 %) were female, with a mean chronological age of 7.79 years (range: 5.1–11.6 years, SD = 1.24) at the time of participation. The average bone age was 8.97 years (range: 4.5–14.0 years, SD = 2.18). The average difference between bone age and chronological age was +1.18 years (range: −2–4 years, SD = 1.50). The average interval between the initial observation of symptoms and the first medical visit was 3.44 months (range: 0–50 months, SD = 7.76). Regarding BMI, 42 children (64.6 %) were classified as being within the normal range, whereas 16 children (24.6 %) were classified as overweight or obese. The initial discovery of precocious puberty symptoms was predominantly reported by the mothers (n = 56, 86.2 %). Among the girls, breast development was the most commonly

Table 1
Demographic Characteristics of Participants ($N = 65$).

Variables	Mean	SD
Age (year)	40.36	3.95
	Number	%
Parenting role		
Mother	54	83.1
Father	11	16.9
Educational level		
High school or below	7	10.8
Junior college	13	20.0
College	36	55.4
Graduate degree or above	9	13.8
SES		
Upper-middle (level IV)	29	44.6
Middle (level III)	25	38.5
Lower-middle (level II)	8	12.3
Low (level I)	3	4.6
Information sources[§]		
Newspapers and magazines	40	61.5
Online information	55	84.6
Family and friends	26	40
Others	6	9.2

Note: SD = standard deviation; SES = socioeconomic status.
[§] Multiple responses allowed.

Table 2
Demographic and Clinical Characteristics of Children with Central Precocious Puberty ($N = 65$).

Variables	Mean	SD	Range
Age (year)	7.79	1.24	5.1–11.6
Bone age (year)	8.97	2.18	4.5–14
BA–CA difference (year)	1.18	1.50	−2 to 4
Time from initial symptom to first visit (month)	3.44	7.76	0–50
	Number	%	
Sex			
Female	61	93.8	
Male	4	6.2	
BMI			
Underweight	7	10.8	
Normal	42	64.6	
Overweight	4	6.1	
Obese	12	18.5	
Initial observer of precocious puberty symptoms			
Mother	56	86.2	
Father	3	4.6	
Other family member	3	4.6	
Self (the child)	2	3.1	
Physician	1	1.5	
First observed sign of precocious puberty			
Female children ($n = 61$)			
Breast development	57	93.4	
Menarche	2	3.3	
Growth spurt	2	3.3	
Male children ($n = 4$)			
Oily skin and acne	1	25	
Voice deepening	1	25	
Pubic or axillary hair growth	1	25	
Growth spurt	1	25	
Tanner stage			
Female children ($n = 61$)			
I	3	4.9	
II	43	70.5	
III	10	16.4	
IV	4	6.6	
V	1	1.6	
Male children ($n = 4$)			
II	1	25	
III	1	25	
IV	2	50	

Note: SD = standard deviation; BA–CA difference refers to the difference between bone age (BA) and chronological age (CA). A positive value indicates advanced bone age relative to the chronological age.

observed sign ($n = 57$, 93.4 %). At the first visit, most children ($n = 44$, 67.7 %) were in Tanner stage 2 (Table 2).

Correlation of parental and child variables with health literacy and medical decision conflict

The Kolmogorov–Smirnov test indicated that the scores on both the health literacy and medical decision conflict scales were normally distributed ($p = .20$), supporting the appropriateness of the parametric analyses. Additionally, Levene's test for the equality of variances revealed no significant violation of the homogeneity-of-variance assumption across groups ($p > .05$), justifying the use of an independent sample t-test or one-way ANOVA for group comparisons.

No significant differences were found in parental health literacy or medical decision conflict scores across parental and child demographic or clinical variables (Table 3). An exception was observed in the comparison by children's sex; parents of male children had significantly higher health literacy scores than those of female children ($t = -2.33$, 95 % CI [−13.75, −1.07], $p = .023$, Cohen's $d = -1.20$), indicating a large effect size.

Association between parental health literacy and medical decision conflict

The average total MMHLQ score was 36.01 (SD = 6.30). The mean subscale scores, ranked from the highest to lowest, were as follows: understanding health information (mean = 36.83, SD = 7.46), accessing health information (mean = 36.68, SD = 7.50), applying health information (mean = 36.68, SD = 7.50), communicating and interacting (mean = 36.68, SD = 7.50), and appraising health information (mean = 32.77, SD = 8.30). According to the total MMHLQ score classification, 35 participants (53.8 %) had "limited" health literacy, 19 (29.3 %) had "adequate" literacy, and 11 (16.9 %) were classified as having "excellent" literacy.

The average total DCS score was 17.64 (SD = 14.87). The mean scores of the five subscales, ranked from highest to lowest, were as follows: value clarity (mean = 26.41, SD = 20.56), uncertainty (mean = 21.58, SD = 19.07), support (mean = 21.58, SD = 19.07), informed decision making (mean = 17.64, SD = 14.87), and effective decision making (mean = 17.64, SD = 14.87). Based on the classification of medical decision conflict levels, most parents of children newly diagnosed with CPP experienced low decision conflict levels ($n = 54$, 83.1 %). Additionally, 10 participants (15.4 %) reported moderate decisional conflict, and only one participant (1.5 %) reported high decisional conflict.

Pearson's correlation analysis was conducted to examine the relationship between parental health literacy and decisional conflicts regarding the medical care of children with CPP. The results showed that the total health literacy (MMHLQ) was significantly negatively correlated with the total score of medical decision conflict and all five DCS subscales (Table 4), indicating that higher health literacy levels were associated with lower medical decision conflict levels ($r = -0.45$, 95 % CI [−0.62, −0.24], $p < .001$).

In particular, the "communication and interaction" subscale of the MMHLQ also demonstrated negative correlations with the DCS total score and each of its subscales, further supporting the association between strong health communication skills and reduced medical decision conflict (Table 4). The "Accessing Health Information" subscale of the MMHLQ was not significantly correlated with the total medical decision conflict score or any of the five DCS subscales.

Predictors of parental medical decision conflict among parents of children newly diagnosed with CPP

A simple linear regression was conducted to examine the predictive effect of parental health literacy on medical decisional conflict among parents of children newly diagnosed with CPP. The simple linear

Table 3
Correlation of Parental and Child Variables with Health Literacy and Medical Decision Conflict ($N = 65$).

Variables	Healthy literacy			Decision conflict		
	Mean (SD)	r / t	p	Mean (SD)	r / t	p
Parent						
Age		0.026	0.836		−0.01	0.959
Sex		−1.72	0.091		0.21	0.838
Female ($n = 54$)	35.44 (5.91)			14.30 (9.36)		
Male ($n = 11$)	39 (7.89)			13.64 (11.27)		
Education		0.13	0.898	0.34		0.734
≤High school ($n = 20$)	36.20 (6.50)			14.80 (9.10)		
≥College ($n = 45$)	35.98 (6.37)			13.91 (9.93)		
SES		0.16	0.850		1.11	0.337
≤Lower-middle ($n = 11$)	35.55 (5.24)			10.45 (10.08)		
Middle ($n = 25$)	35.68 (6.74)			15.60 (9.06)		
Upper-middle ($n = 29$)	36.55 (6.58)			14.38 (9.87)		
Child						
Age		0.06	0.644		−0.02	0.898
Time from initial symptom to first visit		−0.12	0.334			
Sex		−2.33	0.023		0.36	0.721
Female children ($n = 61$)	35.59 (6.20)			14.30 (9.68)		
Male children ($n = 4$)	43.0 (4.97)			12.50 (9.75)		
BMI		0.57	0.568		−0.99	0.326
≤Normal ($n = 49$)	36.31 (6.21)			13.51 (9.26)		
≥Overweight ($n = 16$)	35.25 (6.94)			16.25 (10.69)		
Tanner stage		0.86	0.392		−0.28	0.783
≤II ($n = 47$)	36.47 (6.53)			13.98 (9.74)		
≥III ($n = 18$)	34.94 (5.92)			14.72 (9.54)		

Note: SD = standard deviation.

regression model was statistically significant ($F = 16.20$, $p < .001$), explaining 20.5 % of the variance in medical decision conflict ($R^2 = 0.205$). This corresponds to a medium-to-large effect size ($f^2 = 0.26$), according to Cohen's (2013) guidelines. Parental health literacy was a significant negative predictor of medical decision conflict ($\beta = -0.45$, $T = -4.03$, $p < .001$), indicating that higher health literacy levels were associated with lower medical decision conflict. Specifically, a one-point increase in health literacy was associated with a 0.68-point decrease in medical decision conflict (Table 5).

Discussion

This study examined the association between parental health literacy and medical decision conflict following a new diagnosis of CPP. Our findings support the hypothesis that parents with lower health literacy report significantly higher levels of medical decision conflict when making treatment decisions for their children. Health literacy, particularly in the domains of communication and interaction, appears to be a key factor influencing medical decision conflict among parents of children newly diagnosed with CPP.

Although most sociodemographic variables showed no significant differences in health literacy or medical decision conflict scores, one notable exception was the child's sex. Parents of male children demonstrated significantly higher health literacy than those of female children. This unexpected finding may reflect greater parental concern or engagement when precocious puberty occurs in boys, which is typically perceived as less common and potentially more clinically significant (Cheuiche et al., 2021). Supporting this interpretation, our data showed that 75 % of boys in the sample had Tanner stage greater than 2 compared to only 26.2 % of girls, suggesting that boys may present with more advanced pubertal signs at diagnosis. Tanner stage 2 in boys is characterised by testicular enlargement, which may not be easily recognised by parents, potentially leading to delayed symptom recognition and heightened concern when signs become apparent. Clinical severity and perceived atypicality may prompt parents to seek more information and become more actively involved in decision-making. Future qualitative research is warranted to explore how parental perceptions of urgency, seriousness, and gender norms influence health information-seeking behaviours and health literacy levels.

More than half of the participants were classified as having limited health literacy, underscoring the need for targeted interventions to support parental understanding and engagement in treatment decisions. Prior research has shown that parents with limited health literacy tend to have less active attitudes toward SDM and are more likely to follow low-value treatment plans without further questioning or seeking clarification (Muscat et al., 2024). Although most parents in our study experienced low levels of decisional conflict, approximately 17 % reported moderate-to-high conflict. These findings suggest that a subset

Table 4
Pearson's Correlation Analysis Between Parental Health Literacy and Medical Decision Conflict ($N = 65$).

	DCS											
	Total score		Informed		Values Clarity		Support		Uncertainty		Effective decision	
	r	p	r	p	r	p	r	p	r	p	r	p
MMHLQ												
Total score	−0.45	<0.001	−0.40	0.001	−0.40	0.001	−0.44	<0.001	−0.40	0.001	−0.26	0.035
Accessing health information	−0.22	0.082	−0.24	0.058	−0.17	0.171	−0.19	0.125	−0.18	0.140	−0.07	0.561
Understanding health information	−0.32	0.010	−0.33	0.007	−0.22	0.073	−0.36	0.003	−0.27	0.027	−0.14	0.248
Appraising health information	−0.38	0.002	−0.29	0.017	−0.40	0.001	−0.27	0.030	−0.35	0.004	−0.21	0.089
Applying health information	−0.36	0.003	−0.26	0.037	−0.31	0.013	−0.42	0.001	−0.34	0.005	−0.24	0.056
Communication and interaction	−0.44	<0.001	−0.36	0.003	−0.38	0.002	−0.45	<0.001	−0.42	0.001	−0.34	0.005

Note: MMHLQ = Mandarin Multidimensional Health Literacy Questionnaire; DCS = Question-Format Decisional Conflict Scale.

Table 5
Simple Linear Regression Analysis Predicting Parental Medical Decision Conflict.

Predictor	B	SE	β	*p*	95 % CI for B
	38.84	6.22		<0.001	26.41–51.26
Parental health literacy	−0.68	−0.17	−0.45	<0.001	−1.02 to −0.34

Note: SE = standard error; CI = confidence interval.

of families, particularly those with limited health literacy, may benefit from enhanced decision support during the early stages of diagnosis and treatment planning. Tailored communication strategies and structured SDM tools could be especially beneficial in empowering parents and ensuring informed, value-congruent medical choices.

Nearly 90 % of CPP cases in this study were first identified by mothers, underscoring their pivotal role in recognising early pubertal changes. This finding aligns with previous research suggesting that mothers are often more attuned to subtle physical and behavioural changes in their children due to their primary caregiving roles (Moon & Hoffman, 2008). Supporting this, a recent study found that mothers are more likely than fathers to assume sole responsibility for parent–child communication about sensitive developmental issues, such as sexual maturation, particularly when the parent is less involved (Astle & Brasileiro, 2024). However, this maternal predominance in symptom recognition raises important concerns for children in single-father households who may be at risk of delayed detection and intervention. Fathers may be less familiar with early pubertal signs because of social, cultural, and educational factors. Given the role of fathers in CPP risk (Pham et al., 2022; Yogman & Eppel, 2022), targeted health education and awareness strategies for fathers, especially single fathers, are crucial to ensure the timely identification and appropriate medical consultation for CPP. Future research should explore the decision-making experiences and knowledge levels of fathers in managing pubertal development to inform inclusive family-centred health interventions.

Notably, 84.6 % of parents reported that their primary source of information about their children's precocious puberty was online. Although online sources, including websites, social media, and digital forums, are easily accessible and widely used, the accuracy and reliability of such information are often uncertain. Consistent with this, our findings showed that, among the five domains of parental health literacy, the ability to appraise health information scored the lowest, indicating that many parents face challenges in critically evaluating the quality and trustworthiness of the information they encounter. Conversely, the 'Accessing Health Information' subscale of the MMHLQ was not significantly associated with decisional conflict. This suggests that the ability to retrieve health information is insufficient to reduce conflict unless it is accompanied by higher-order skills such as the ability to interpret, appraise, and communicate that information effectively. Parents relying on unverified or anecdotal online content may receive misleading or incomplete information, which can negatively affect their understanding of the condition and contribute to conflicts in medical decisions. These findings support a more nuanced understanding of health literacy as a multidimensional construct in which appraisal and communication skills may have a more direct impact on decision-related outcomes than functional skills alone (Muscat et al., 2021). While our study did not assess healthcare professionals' health literacy, previous studies have shown that less than half of healthcare professionals are familiar with the concept of health literacy, which may limit their ability to recognise and address parental needs (Friedman et al., 2025; Ronan et al., 2023). Based on this and prior literature, it may be beneficial for paediatric healthcare providers to receive training on health literacy principles, effective communication strategies, tailoring information to parents' comprehension levels, and offering targeted support (Atkinson & Berthelot, 2024; Morrison et al., 2019; Zdunek et al., 2021). Integrating health literacy-informed approaches into SDM processes may not only improve care experiences but also foster more efficient, equitable, and person-centred paediatric endocrine care.

Strengths and limitations

This study is the first to investigate the association between parental health literacy and medical decision conflict in families of children newly diagnosed with CPP, thereby addressing an important yet underexplored area in paediatric endocrine care. A notable strength is the use of validated instruments—the MMHLQ and the DCS—which demonstrated high reliability and allow for meaningful comparisons with international research. However, several limitations should be acknowledged. First, the study was conducted at a single medical centre, which may have limited the generalisability of the findings. Parental experiences, access to information, and decision-making processes vary across institutions, regions, and healthcare systems. Therefore, caution should be exercised when applying these results to a broader population. Second, the use of a cross-sectional design to assess decisional conflict provides only a snapshot of the participants' experiences at one point in time. This approach precludes the examination of changes in parental decision-making processes as a child's diagnosis and treatment progress. Longitudinal studies are recommended to understand the dynamics and temporal patterns of decision-making conflicts in this population.

Implications for practice

The findings suggest that paediatric healthcare providers may benefit from incorporating health literacy–sensitive strategies into the care of families managing CPP. Attention to parents' communication and appraisal skills appears particularly relevant, as limitations in these domains in our study were associated with greater decisional conflict. Practical approaches could involve the use of structured decision aids, the provision of evidence-based informational resources, and targeted educational initiatives that address both mothers and fathers. Integrating such measures into routine paediatric endocrine practice has the potential to support shared decision-making processes and provide more balanced engagement across diverse family contexts.

Conclusion

This study identified parental health literacy as a significant predictor of medical decision conflict among parents of children newly diagnosed with CPP. More than half of the participants demonstrated limited health literacy levels, underscoring critical vulnerability in the context of a condition that is inherently complex and often difficult for families to comprehend. These findings highlight the importance of recognising and addressing health literacy not as a peripheral issue but as a central component in the SDM process. Given that CPP often involves time-sensitive decisions with long-term developmental implications, clinicians must be equipped to assess parental comprehension and tailor their communication. Integrating health literacy screening tools and adopting culturally appropriate educational strategies may enhance parental engagement, reduce decisional conflict, and ultimately lead to better health outcomes. Future clinical protocols should routinely incorporate health literacy assessments as part of patient-centred care, ensuring that all families, regardless of their literacy levels, can actively and confidently participate in decisions affecting their child's health trajectory.

CRediT authorship contribution statement

Ming-Yi Shen: Writing – review & editing, Validation, Software, Resources, Project administration, Methodology, Investigation, Formal analysis, Data curation, Conceptualization. **Chiao-Fan Chiu:** Writing – review & editing, Validation, Supervision, Resources, Methodology. **Mei-Yen Chen:** Writing – review & editing, Validation, Supervision, Methodology. **Lan-Yan Yang:** Validation, Formal analysis, Data curation. **Chizimuzo T.C. Okoli:** Writing – review & editing, Validation,

Methodology. **Ying-Mei Liu:** Writing – original draft, Validation, Supervision, Software, Resources, Methodology, Formal analysis, Data curation, Conceptualization.

Ethical considerations

This study was reviewed and approved by the Institutional Review Board (IRB) of the Chang Gung Medical Foundation (approval no. 202301648A3). Participation in the study was voluntary. To protect participants' privacy and avoid collecting personally identifiable information, the requirement for written informed consent was waived by the IRB. Instead, the participants were provided with a detailed written explanation of the study, and those who agreed to participate provided their consent by reading and accepting the research information sheet before completing the questionnaire. All participants were assured of the confidentiality and anonymity of their responses and informed of their right to withdraw from the study at any time without consequence.

Funding source

This research did not receive any specific grant from funding agencies in the public, commercial, or not-for-profit sectors.

Declaration of competing interest

The authors declare that they have no known competing financial interests or personal relationships that could have appeared to influence the work reported in this paper.

References

Aruna, C., & Giridhar, A. (2025). A precocious puberty. *International Journal of Pharmaceuticals and Health Care Research*, *13*(1), 27–36. https://doi.org/10.61096/ijphr.v13.iss1.2025.27-36.

Astle, S., & Brasileiro, J. (2024). Whose job is it anyway? Parents' perspectives of responsibilities for educating their children about sex. *Sexuality Research and Social Policy*, *21*(2), 759–773. https://doi.org/10.1007/s13178-023-00898-w.

Atkinson, P., & Berthelot, S. (2024). Building health literacy to help direct pediatric care choices effectively. *Canadian Journal of Emergency Medicine*, *26*(12), 840–841. https://doi.org/10.1007/s43678-024-00824-y.

Banerjee, A.A., Kashikar, S., Rao, S., & Surve, S.V. (2025). Precocious puberty: Pathophysiology, contemporary issues and way forward. National Academy Science Letters. https://doi.org/10.1007/s40009-025-01654-x. The cited article does not yet have volume and page numbers. It is currently available as advance online publication. Please keep the DOI citation.

Bräuner, E. V., Busch, A. S., Eckert-Lind, C., Koch, T., Hickey, M., & Juul, A. (2020). Trends in the incidence of central precocious puberty and normal variant puberty among children in Denmark, 1998 to 2017. *JAMA Network Open*, *3*(10), e2015665. https://doi.org/10.1001/jamanetworkopen.2020.15665.

Breidbart, E., Ilkowitz, J., Regelmann, M.O., Ashraf, A.P., Gourgari, E., Kamboj, M.K., … Miller, R. (2024). Precocious puberty and GnRH analogs: Current treatment practices and perspectives amongst US pediatric endocrinologists. Hormone Research in Pædiatrics. https://doi.org/10.1159/000539011. The cited article does not yet have volume and page numbers. It is currently available as advance online publication. Please keep the DOI citation.

Brito, V. N., Canton, A. P., Seraphim, C. E., Abreu, A. P., Macedo, D. B., Mendonca, B. B., ... Latronico, A. C. (2023). The congenital and acquired mechanisms implicated in the etiology of central precocious puberty. *Endocrine Reviews*, *44*(2), 193–221. https://doi.org/10.1210/endrev/bnac020.

Cavallo, F., Mohn, A., Chiarelli, F., & Giannini, C. (2021). Evaluation of bone age in children: A mini-review. *Frontiers in Pediatrics*, *9*, Article 580314. https://doi.org/10.3389/fped.2021.580314.

Cheuiche, A. V., da Silveira Leticia, G., de Paula Leila Cristina, P., Lucena Iara Regina, S., & Silveiro Sandra, P. (2021). Diagnosis and management of precocious sexual maturation: An updated review. *European Journal of Pediatrics*, *180*(10), 3073–3087. https://doi.org/10.1007/s00431-021-04022-1.

Cohen, J. (2013). *Statistical power analysis for the behavioral sciences.* Routledge.

Dong, Y., Dai, L., Dong, Y., Wang, N., Zhang, J., Liu, C., Li, Z., Chu, L., & Chen, S. (2023). Analysis of risk factors of precocious puberty in children. *BMC Pediatrics*, *23*(1), 456. https://doi.org/10.1186/s12887-023-04265-x.

von Elm, E., Altman, D. G., Egger, M., Pocock, S. J., Gøtzsche, P. C., Vandenbroucke, J. P., & Initiative, S. (2014). The strengthening the reporting of observational studies in epidemiology (STROBE) statement: Guidelines for reporting observational studies. *International Journal of Surgery*, *12*(12), 1495–1499. https://doi.org/10.1016/j.ijsu.2014.07.013.

Emmanuel, M., & Bokor, B. R. (2022). *Tanner stages.* Treasure Island (FL): StatPearls Publishing. https://www.ncbi.nlm.nih.gov/books/NBK470280/.

Friedman, S., Morrison, A., Costich, M., Gupta, A., Moore, B., Abrams, M. A., ... Solano, J. (2025). Health literacy curricula in pediatric residency programs: A national survey. *Health Literacy Research and Practice*, *9*(1), e3–e7. https://doi.org/10.3928/24748307-20240813-01.

Huttunen, H., Kärkinen, J., Varimo, T., Miettinen, P. J., Raivio, T., & Hero, M. (2024). Central precocious puberty in boys: Secular trend and clinical features. *European Journal of Endocrinology*, *190*(3), 211–219. https://doi.org/10.1093/ejendo/lvae021.

Jacobs, S., Davies, N., Butterick, K. L., Oswell, J. L., Siapka, K., & Smith, C. H. (2023). Shared decision-making for children with medical complexity in community health services: A scoping review. *BMJ Paediatrics Open*, *7*(1). https://doi.org/10.1136/bmjpo-2023-001866.

Jonas, D., Scanlon, C., & Bogetz, J. F. (2022). Parental decision-making for children with medical complexity: An integrated literature review. *Journal of Pain and Symptom Management*, *63*(1), e111–e123. https://doi.org/10.1016/j.jpainsymman.2021.07.029.

Knific, T., Lazarevič, M., Žibert, J., Obolnar, N., Aleksovska, N., Šuput Omladič, J., Battelino, T., & Avbelj Stefanija, M. (2022). Final adult height in children with central precocious puberty–a retrospective study. *Frontiers in Endocrinology*, *13*, 1008474. https://doi.org/10.3389/fendo.2022.1008474.

Lin, S. C. (2007). *Educational psychology.* Taiwan: Wu-Nan Book Inc.

Lindly, O. J., Cabral, J., Mohammed, R., Garber, I., Mistry, K. B., & Kuhlthau, K. A. (2022). "I don't do much without researching things myself": A mixed methods study exploring the role of parent health literacy in autism services use for young children. *Journal of Autism and Developmental Disorders*, *52*(8), 3598–3611. https://doi.org/10.1007/s10803-021-05240-0.

Liu, Y., Yu, T., Li, X., Pan, D., Lai, X., Chen, Y., Wang, X., Yu, X., Fu, S., & Huang, S. (2021). Prevalence of precocious puberty among Chinese children: A school population-based study. *Endocrine*, *72*, 573–581. https://doi.org/10.1007/s12020-021-02630-3.

Lu, C., Mu, W., Jin, Y. -H., Shi, Y. -X., Li, G., Li, Y., ... Xia, T. (2019). Cross-cultural adaptation and psychometric assessment of the statement format decisional conflict scale for mandarin version. *BMC Health Services Research*, *19*, 1–9. https://doi.org/10.1186/s12913-019-4717-6.

Ma, Y., Gao, J., & Zhang, C. (2024). The mediating effect of perceived social support and health literacy on the relationship between decisional dilemma and participation in shared decision-making among chinese parents of premature infants. *Western Journal of Nursing Research*, *46*(11), 878–889. https://doi.org/10.1177/01939459241285697.

Mason, L., & Daskas, N. (2024). Central precocious puberty: Assessment, diagnosis and decisions about treatment. *Nursing Children and Young People*, *36*(4), 36–42. https://doi.org/10.7748/ncyp.2024.e1492.

Matchanova, A., Babicz, M., Medina, L. D., Fazeli, P. L., Vance, D. E., & Woods, S. P. (2021). Latent structure of health literacy and its association with health-related management and decision-making in HIV. *Psychology & Health*, *36*(8), 985–1002. https://doi.org/10.1080/08870446.2020.1817453.

Ministry of Health and Welfare, Taiwan (2013). Recommended BMI values for children and adolescents. https://www.hpa.gov.tw/Pages/Detail.aspx?nodeid=542&pid=9547.

Moon, M., & Hoffman, C. D. (2008). Mothers' and fathers' differential expectancies and behaviors: Parent x child gender effects. *The Journal of Genetic Psychology*, *169*(3), 261–280. https://doi.org/10.3200/GNTP.169.3.261-280.

Morrison, A. K., Glick, A., & Yin, H. S. (2019). Health literacy: Implications for child health. *Pediatrics in Review*, *40*(6), 263–277. https://doi.org/10.1542/pir.2018-0027.

Muscat, D. M., Cvejic, E., Smith, J., Thompson, R., Chang, E., Tracy, M., ... McCaffery, K. (2024). Equity in choosing wisely and beyond: The effect of health literacy on healthcare decision-making and methods to support conversations about overuse. *BMJ Quality & Safety, 34(4), 213-222*. https://doi.org/10.1136/bmjqs-2024-017411.

Muscat, D. M., Shepherd, H. L., Nutbeam, D., Trevena, L., & McCaffery, K. J. (2021). Health literacy and shared decision-making: Exploring the relationship to enable meaningful patient engagement in healthcare. *Journal of General Internal Medicine*, *36*, 521–524. https://doi.org/10.1007/s11606-020-05912-0.

Ni, M. M., Yang, S. T., Sun, J. Y., Wu, W. W., Li, M., Gu, W., & Ji, X. (2025). Efficacy of first-year GnRHa therapy in girls with idiopathic central precocious puberty diagnosed after age 8: A retrospective study. *Gynecological Endocrinolgy*, *41*(1), 2500481. https://doi.org/10.1080/09513590.2025.2500481.

Nutbeam, D. (2000). Health literacy as a public health goal: A challenge for contemporary health education and communication strategies into the 21st century. *Health Promotion International*, *15*(3), 259–267. https://doi.org/10.1093/heapro/15.3.259.

O'Connor, A. M. (1995). Validation of a decisional conflict scale. *Medical Decision Making*, *15*(1), 25–30.

Pham, H. T., DiLalla, L. F., Corley, R. P., Dorn, L. D., & Berenbaum, S. A. (2022). Family environmental antecedents of pubertal timing in girls and boys: A review and open questions. *Hormones and Behavior*, *138*, Article 105101. https://doi.org/10.1016/j.yhbeh.2021.105101.

Roggero, P., Grima, A. M., Crespo-Escobar, P., Tapsas, D., & Yahav, J. (2024). Conflict between parents, physicians, and healthcare professionals in medical decision-making: How to address it—A systematic review from the ESPGHAN ethics committee. *Journal of Pediatric Gastroenterology and Nutrition*, *79*(5), 1071–1080. https://doi.org/10.1002/jpn3.12365.

Ronan, M., Eagleson, K., Fielden, P., Sutton, N., Gilchrist, S., Schilling, S., Scaini, L., & Ullman, A. (2023). Health literacy in paediatric healthcare: A cross-sectional survey of nurses. *Journal of Children and Young People's Health*, *4*(2), 5–11. https://doi.org/10.33235/jcyph.4.2.5-11.

Wang, Y., Gou, H., & Guo, J. (2025). Risk factors for precocious puberty: A systematic review and meta-analysis. *Psychoneuroendocrinology*, *176*, Article 107427. https://doi.org/10.1016/j.psyneuen.2025.107427.

Wei, M., Wang, Y., Chang, M., & Hsieh, J. (2017). Development of mandarin multidimensional health literacy questionnaire (MMHLQ). *Taiwan Journal of Public Health*, *36*(6), 556–570. https://doi.org/10.6288/TJPH201736106061.

World Health Organization (2019). ICD-10. https://icd.who.int/browse10/2019/en.

Yogman, M. W., & Eppel, A. M. (2022). The role of fathers in child and family health. In M. Grau Grau, & M. las Heras Maestro, Riley Bowles, H. (Eds.), *Engaged fatherhood for men, families and gender equality* (pp. 15–30). Springer Nature.

Zaidman, E. A., Scott, K. M., Hahn, D., Bennett, P., & Caldwell, P. H. (2023). Impact of parental health literacy on the health outcomes of children with chronic disease globally: A systematic review. *Journal of Paediatrics and Child Health*, *59*(1), 12–31. https://doi.org/10.1111/jpc.16297.

Zdunek, K., Schröder-Bäck, P., Alexander, D., Vlasblom, E., Kocken, P., Rigby, M., & Blair, M. (2021). Tailored communication methods as key to implementation of evidence-based solutions in primary child health care. *European Journal of Public Health*, *31*(1), 92–99. https://doi.org/10.1093/eurpub/ckaa234.

Check for updates

Journal of Cellular Physiology

WILEY

Journal of Cellular Physiology

RESEARCH ARTICLE

IPSC-Derived Conditioned Medium Reduces Oxidative Stress and Vascular Remodeling in Rat Models of Pulmonary Arterial Hypertension

Chin-Chang Cheng[1,2,3] | Lee-Fen Hsu[4,5,6] | Hsien-Hui Chung[7,8,9] | Chiang-Wen Lee[10,11,12] | Cheng-Hung Chiang[13] | Hung-Chou Yang[13] | Miao-Ching Chi[4,5] | Ming-Hsueh Lee[6] | Wei-Chun Huang[2,14] | Pei-Ling Chi[15,16]

[1]Division of Cardiology, Department of Internal Medicine, Pingtung Veterans General Hospital, Pingtung, Taiwan | [2]Department of Medicine, School of Medicine, National Yang Ming Chiao Tung University, Taipei, Taiwan | [3]Department of Physical Therapy, Fooyin University, Kaohsiung, Taiwan | [4]Department of Respiratory Care, Chang Gung University of Science and Technology, Chiayi, Taiwan | [5]Chronic Disease and Health Promotion Research Center, Chang Gung University of Science and Technology, Chiayi, Taiwan | [6]Division of Neurosurgery, Department of Surgery, Chang Gung Memorial Hospital, Chiayi, Taiwan | [7]Department of Pharmacy & Clinical Trial Pharmacy, Kaohsiung Veterans General Hospital, Kaohsiung, Taiwan | [8]Preventive Medicine Program, Center for General Education, Chung Yuan Christian University, Taoyuan, Taiwan | [9]Department of Pharmacy and Master Program, College of Pharmacy and Health Care, Tajen University, Pingtung, Taiwan | [10]Department of Nursing, Division of Basic Medical Sciences, and Chronic Diseases and Health Promotion Research Center, Chang Gung University of Science and Technology, Chiayi, Taiwan | [11]Department of Orthopaedic Surgery, Chang Gung Memorial Hospital, Chiayi, Taiwan | [12]Department of Safety Health and Environmental Engineering, Ming Chi University of Technology, New Taipei City, Taiwan | [13]Department of Critical Care Medicine, Kaohsiung Veterans General Hospital, Kaohsiung, Taiwan | [14]Department of Cardiology, Pingtung Christian Hospital, Pingtung, Taiwan | [15]Department of Medical Education and Research, Kaohsiung Veterans General Hospital, Kaohsiung, Taiwan | [16]Shu-Zen Junior College of Medicine and Management, Kaohsiung, Taiwan

Correspondence: Pei-Ling Chi (chi542738@gmail.com)

Received: 6 March 2025 | **Revised:** 24 June 2025 | **Accepted:** 7 August 2025

Keywords: iPSC-derived conditioned medium (iPSC-CM) | oxidative stress | pulmonary arterial hypertension (PAH) | vascular remodeling

ABSTRACT

Pulmonary arterial hypertension (PAH) is a progressive vascular disease characterized by elevated pulmonary vascular resistance, leading to right ventricular (RV) hypertrophy and eventual heart failure. Although current therapies provide symptomatic relief, they offer limited efficacy in reversing the underlying vascular remodeling. In this preclinical study, we investigated the therapeutic potential of induced pluripotent stem cell-derived conditioned medium (iPSC-CM) in a monocrotaline (MCT)-induced rat model of PAH, employing both prophylactic and therapeutic administration strategies. iPSC-CM treatment significantly reduced right ventricular systolic pressure (RVSP) and mitigated RV hypertrophy compared to MCT-only controls. Histological analyses revealed attenuated pulmonary arterial wall thickening and muscularization. At the molecular level, iPSC-CM downregulated the expression of hypoxia-inducible factor 1-alpha (HIF-1α) and platelet-derived growth factor-BB (PDGF-BB) in lung tissues, and modulated oxidative stress by decreasing NADPH oxidase 1 (Nox1) and increasing superoxide dismutase 1 (SOD1) levels. In vitro, iPSC-CM suppressed the proliferation and migration of pulmonary artery smooth muscle cells (PASMCs) under hypoxic and PDGF-BB-stimulated conditions. These findings suggest that iPSC-CM targets key pathogenic pathways involved in vascular remodeling and redox imbalance in PAH. Together, these findings support iPSC-CM as a promising acellular approach for targeting vascular remodeling and oxidative stress in PAH, warranting further investigation toward clinical translation.

Chin-Chang Cheng, Lee-Fen Hsu, Wei-Chun Huang and Pei-Ling Chi contributed equally to this study.

© 2025 Wiley Periodicals LLC.

1 | Introduction

Pulmonary arterial hypertension (PAH) is a progressive disease associated with increased pulmonary vascular resistance, elevated pulmonary arterial pressure and right heart failure (Naeije and Manes 2014). The histopathology of PAH is characterized by medial and adventitial hypertrophy of the pulmonary vasculature, endothelial cell (EC) dysfunction, and excessive proliferation of pulmonary arterial smooth muscle cells (PASMCs) leading to vaso-occlusive and plexiform lesions (Humbert et al. 2019). Despite significant progress in understanding the pathogenesis of PAH, current therapies primarily address vasoconstriction abnormalities and fail to target obliterative vascular remodeling (Dunmore et al. 2021; Sommer et al. 2021). This oversight limits their efficacy, rendering them non-curative and non-preventive.

Endothelial progenitor cells (EPCs) and mesenchymal stromal cells (MSCs) have shown their capability to migrate to sites of vascular injury in various in vivo animal disease models (Granton et al. 2015; Takahashi et al. 1999). These cells secrete paracrine factors effective in reducing pulmonary pressures, regenerating lost microvascular areas, and ameliorating pulmonary vascular and right ventricular remodeling. However, EPCs and MSCs have limitations in their proliferative capacity and can exhibit significant variability in quality due to their diverse donor sources (Chong et al. 2016; van Rhijn-Brouwer et al. 2018). These limitations ultimately impact therapeutic efficacy. Compared to these stem cell therapies, induced pluripotent stem cells (iPSCs) have a more stable molecular signature, proliferative capacity, and tissue repair capacity (Fernandez-Rebollo et al. 2020). Recent studies focusing on paracrine mediators derived from iPSCs have demonstrated a low risk of tumorigenicity upon use. Intravenous injection (IV)-administrated iPSC-derived conditioned medium (iPSC-CM), containing antiangiogenic factors such as TIMP-1, IL-6, and MCP-1, reduces endotoxin-induced acute lung injury by attenuating endothelial cell leakage and reducing the activity of FAK/Snail pathway (Su et al. 2019). Compared to umbilical cord MSCs, conditioned medium from iPSC-derived MSCs is more effective in promoting angiogenesis and supporting cutaneous wound healing (Liang et al. 2021). Although these results point to a paracrine protective effect of iPSC-CM, its therapeutic efficacy for PAH is still under investigation.

Hypoxia-inducible factor (HIF) and platelet-derived growth factor (PDGF) are essential in regulating cell proliferation, differentiation, and migration (Barst 2005; Wu et al. 2023). Elevated levels of HIF-1α and PDGF-BB have been observed in PASMCs from both patients with PAH and animal models of the disease (Cheng et al. 2019; Kurosawa et al. 2019; Perros et al. 2008). Inhibition of the PDGF receptor and HIF-1 in the pulmonary vasculature has proven to be therapeutic in animal models of experimental PAH (Pullamsetti et al. 2020; Wu et al. 2020). In our previous study (Cheng et al. 2019), we demonstrated that hypoxia and PDGF-BB induce proliferation and migration of rat PASMCs, suggesting a significant role of PDGF and HIF-1α signaling in vascular remodeling. This study further examines the effect of iPSC-CM treatment on a PAH model and investigates its mechanism in regulating vascular remodeling under conditions of hypoxia and PDGF-BB-induced stimulation in PASMCs.

2 | Materials and Methods

2.1 | Culture of Murine iPSCs

Murine iPSCs were maintained following the previously described methods (Huang et al. 2016). Briefly, the iPSCs were grown on feeder layers of mouse embryonic fibroblasts (MEFs) in Dulbecco's Modified Eagle Medium (DMEM) (GIBCO, NY, USA) supplemented with 20% fetal bovine serum (FBS) (HyClone Laboratories, UT, USA), 100 U/mL penicillin, 100 μg/mL streptomycin, 2 mM GlutaMAX, 1X non-essential amino acids (NEAA), 12 mM 4-(2-hydroxyethyl)-1-piperazineethanesulfonic acid (HEPES), 1.2 mM sodium pyruvate, and 0.0004% β-mercaptoethanol. The iPSCs were passaged every 4–6 days using collagenase IV and replated onto mitomycin C-treated MEFs. To obtain iPSC-conditioned medium (iPSC-CM) for the treatment of monocrotaline (MCT)-induced PAH rats, the $1\text{-}1.5 \times 10^6$ cells on a dish were cultured with DMEM supplemented with 10 mM NEAA and 0.3% leukemia inhibitory factor (LIF) for 48 h before collection.

2.2 | Rat Model of PAH and Hemodynamic Measurements

All experimental protocols were conducted in accordance with European ethical regulations (Directive 2010/63/EU) and were approved by the Institutional Animal Care and Use Committee at Kaohsiung Veterans General Hospital, Taiwan (Ref. IACUC-2301-2512-22028). Male Sprague-Dawley rats, weighing between 220 and 280 g, were acquired from BioLASCO (Yilan, Taiwan). A schematic representation of the experimental design is provided in Figure 5A. The MCT model was induced through a single subcutaneous injection of MCT (60 mg/kg), as previously described (Chi et al. 2022). Subsequently, the MCT-treated groups of rats were randomized into three groups: (1) saline (as vehicle treatment); (2) iPSC-CM (1 mL) as an early treatment initiated immediately after the MCT injection (prophylaxis, PPx); and (3) iPSC-CM therapy initiated 2 weeks post-MCT injection (treatment, Tx). During the treatment period, the rats received daily intraperitoneal (ip) injections of iPSC-CM. The animals were killed on Day 28 and PAH pathology was assessed following the previously described methods (Chi et al. 2022). For anesthesia, animals received an injection (ip) of 20 mg/kg Zoletil, combined with 1.5%–2.0% isoflurane, and were ventilated through tracheal intubation connected to a rodent ventilator (R145 VentStar, RWD Life Science, China). Right ventricular systolic pressure (RVSP) was directly measured by inserting a catheter (polyethylene-50 tubing with a 24-gauge needle) into the right ventricle (RV) via thoracotomy, connected to a pressure transducer (PowerLab/8SP; AD Instruments Ltd., Dunedin, New Zealand). Following the final hemodynamic assessment, rats were euthanized by exsanguination (under isoflurane anesthesia), and the heart and lungs were harvested. The weight ratio of the RV divided by the

10974652, 2025, 8, Downloaded from https://onlinelibrary.wiley.com/doi/10.1002/jcp.70085 by Chang Gung University Of, Wiley Online Library on [04/05/2026]. See the Terms and Conditions (https://onlinelibrary.wiley.com/terms-and-conditions) on Wiley Online Library for rules of use; OA articles are governed by the applicable Creative Commons License

sum of the left ventricle (LV) plus septum (S) (RV/[LV + S]) was calculated as an index of right ventricular hypertrophy (Chi et al. 2022).

2.3 | Isolation and Culture of Rat PASMC

PASMCs were isolated from the branches of the main pulmonary artery of rat lungs as previously described (Chi et al. 2022). PASMCs were cultured in Medium 231 (M231, Thermo Fisher, Waltham, MA, USA) supplemented with Smooth Muscle Growth Supplement (SMGS, Thermo Fisher, Waltham, MA, USA). Experiments were conducted using cells at passages 3–8. Hypoxia (3% O_2) was induced in an incubator by introducing nitrogen gas, and the oxygen concentration was continuously monitored using an oxygen sensor (Huang et al. 2016). For coculture experiments, iPSCs were placed in a transwell system with a 8-μm pore size insert (Costar Corning Incorporated, Baar, Switzerland), allowing for interaction with PASMCs.

2.4 | Histology and Immunohistochemical Analysis of Pulmonary Arteries

Each lung tissue sample was fixed in 10% formalin and subsequently embedded in paraffin blocks. Tissue sections, 4 μm thick, were stained using the Elastica van Gieson (EVG) method or subjected to immunohistochemistry using anti-α-SMA (1:100, #19245, Cell Signaling Technology, Danvers, MA, USA), anti-HIF-1α (1:100, NB100-105, Novus Biological, Littleton, CO, USA), and anti-PDGF-B (1:100, A1195, ABclonal, China) antibody, followed by anti-rabbit HRP secondary antibody (Santa Cruz Biotechnology, Santa Cruz, CA). For immunofluorescence, lung sections were stained using rabbit anti-HIF-1α, or rabbit anti-PDGF-B, and mouse anti-α-SMA for 1 h, followed by incubation with Alexa 568-labeled anti-mouse, or Alexa488-labeled anti-rabbit, or (Thermo Fisher, Waltham, MA, USA) for 1 h. Lung sections were mounted with the anti-fade reagent in the presence of 4′,6-diamidino-2-phenylindole (DAPI) (Invitrogen, Waltham, MA, USA). Images were acquired using Zeiss fluorescence microscope and quantified with ImageJ analysis software (NIH, Bethesda, MD, USA).

2.5 | Immunohistochemical Detection of 8-OHdG and DCFH-DA

Lung tissue was sectioned into 4-μm frozen slices. After washing with phosphate-buffered saline (PBS) three times, the sections were incubated with 3% bovine serum albumin in PBS for 30 min at room temperature (RT) to block nonspecific binding. The sections were then treated with either 2,7-dichlorofluorescein diacetate (DCFH-DA), a fluorogenic dye from Thermo Fisher Scientific, or 8-Oxo-7,8-dihydro-2′-deoxyguanosine (8-oxodG), a well-established marker of oxidative DNA damage (Guo et al. 2017), for 2 h at RT. Following treatment, the slides were counterstained with DAPI, incubated with anti-fade solution, and immunofluorescence images were captured using a Zeiss fluorescence microscope.

2.6 | Western Blot

PASMCs were lysed using RIPA lysis buffer supplemented with a protease inhibitor cocktail (Sigma Aldrich), and the protein concentration was determined using the Pierce BCA Protein Assay Kit (Thermo Fisher Scientific, Waltham, MA, USA). A total of 30 μg of protein per sample was separated by SDS-PAGE and transferred onto PVDF membranes. The membranes were then incubated with primary antibodies at a dilution of 1:1000: PCNA (ab2426), cyclin D1 (#2978), MMP-1 (10371-2-AP, Proteintech Group, Chicago, IL, USA), MMP-9 (ab38898), HIF-1α (NB100-105), PDGF-B (A1195), PAK1 (#2602), AKT (#9272), and phospho-AKT (#9271). This was followed by incubation with appropriate HRP-conjugated secondary antibodies and detection using ECL reagents (Bio-Rad Laboratories, Hercules, CA, USA). β-actin (1:2000, ab8227, Abcam, Cambridge, MA, USA) served as the internal control.

2.7 | BrdU Incorporation Assay

PASMCs were seeded on coverslips in M231 medium supplemented with 1% Smooth Muscle Growth Supplement (SMGS) and cultured for 24 h. Subsequently, the cells were incubated with a BrdU solution (Roche, Indianapolis, IN, USA) for 2 h. BrdU incorporation was detected using a FITC-conjugated BrdU antibody and analyzed using a fluorescence microscope. The quantification of BrdU-positive cells was normalized to the total number of DAPI-stained cells. Experiments were carried out in triplicate.

2.8 | Alamar Blue Viability Assay

PASMCs were seeded into a 24-well plate in M231 medium and serum-starved for 24 h to synchronize the cell cycle. Before stimulation, cells were either pretreated with iPSC-conditioned medium (iPSC-CM) or cocultured with iPSCs for 2 h, followed by treatment with PDGF-BB (40 ng/mL) or exposure to hypoxic conditions. After the treatment period, the medium was replaced with 300 μL of M231 containing 10% (v/v) Alamar Blue (Biozol, Eching, Germany). Following a 4-h incubation, the fluorescence emission intensity of the reagent was measured using a microplate reader (FilterMax F5, Molecular Devices, Sunnyvale, CA) at an excitation wavelength of 560 nm and an emission wavelength of 590 nm. The results were compared with the fluorescence emission from wells containing untreated cells.

2.9 | Scratch Wound Healing Assay

Cells were seeded on 6-well plates and cells were allowed to grow to complete confluence. Cells were washed with PBS and then treated with 10 μg/mL mitomycin C for 2 h before wounding. Immediately following scratch wounding (0 h) and after incubation of cells for 6, or 24 h, phase-contrast images of the wound healing process were photographed digitally with an inverted microscope. Cell migration was determined by the rate of cells moving towards the scratched area. ImageJ software

10974652, 2025, 8, Downloaded from https://onlinelibrary.wiley.com/doi/10.1002/jcp.70085 by Chang Gung University Of, Wiley Online Library on [04/05/2026]. See the Terms and Conditions (https://onlinelibrary.wiley.com/terms-and-conditions) on Wiley Online Library for rules of use; OA articles are governed by the applicable Creative Commons License

(NIH, Bethesda, MD, USA) was used to quantify the scratched area. All experiments were plated in triplicate wells and were carried out at least three times.

2.10 | Quantitative Real-Time Polymerase Chain Reaction

RNA was extracted using TRIzol (Life Technologies), and complementary DNA (cDNA) synthesis was performed using a High-Capacity cDNA Reverse Transcription Kit (Applied Biosystems) according to the manufacturer's instructions. qRT-PCR was performed with Fast SYBR Green Master Mix (Applied Biosystems) on a StepOnePlusTM System (Applied Biosystems). The following primer sets were used: rat HIF-1α forward, 5′-TCC ATT ATG AGG CTG ACC ATC -3′ and reverse, 5′-CCA TCC TCA GAA AGC ACC ATA-3′; PDGF-B forward, 5′-TGG AGT CGA GTC GGA AAG CT-3′ and reverse, 5′-GAA GTT GGC ATT GGT GCG AT-3′; β-actin forward, 5′-ACA GGA TGCAGA AGG AGA TTA C-3′ and reverse, 5′-ACA GTG AGG CCA GGATAG A-3′; PTEN forward, 5′-GGA AAG GAC GGA CTG GTG TA-3′ and reverse, 5′-TGC CAC TGG TCT GTA ATC CA-3′; TP53 forward, 5′-CCT ATC CGG TCA GTT GTT GGA -3′ and reverse, 5′-TTG CAG AGT GGA GGA AAT GG -3′; KRAS forward, 5′-AGA GTG CCT TGA CGA TAC AGC-3′ and reverse, 5′-TCC CTC ATT GCA CTG TAC TCC -3′; c-Myc forward, 5′-CCT AGT GCT GCA TGA AGA GAC AC-3′ and reverse, 5′-TCC ACA GAC ACC ACA TCA ATT TCT T-3′.

2.11 | Transient Transfection

PASMCs were transfected with 100 nM siRNA duplexes targeting HIF-1α, PAK-1, or scramble control (Sigma-Aldrich) using GenMute siRNA Transfection Reagent (SignaGen Laboratories, MD, USA), according to the manufacturer's instructions.

2.12 | ROS Production Analysis

Intracellular reactive oxygen species (ROS) were detected using DCFH-DA from Thermo Fisher Scientific. Briefly, cells from different treatment groups were isolated and incubated with DCFH-DA (5 μM) for 30 min at 37°C in the dark. Subsequently, the samples were analyzed and quantified by flow cytometry utilizing the Attune NxT Flow Cytometer (Thermo Fisher Scientific). Each measurement was based on the mean fluorescence intensity of 20,000 events.

2.13 | Protein Angiogenesis Array

Angiogenesis-associated proteins in conditioned medium (CM) derived iPSCs and MEFs were analyzed using the Proteome Profiler Mouse Angiogenesis Array Kit (ARY015, R&D Systems, MN, USA). Equal amounts of total protein (100 μg) from each CM sample were incubated with the array membranes at 4°C overnight (16 h). After washing, membranes were incubated with a cocktail of biotinylated detection antibodies and visualized according to the manufacturer's instructions. Spot intensities on the membranes were quantified using ImageJ software (NIH). Background signals were subtracted using the intensity from negative control spots. Each protein spot intensity was then normalized to internal reference spots, and the average signal intensity for each analyte was calculated from duplicate spots.

2.14 | Statistical Analysis

Animal studies are reported as the mean ± standard deviation (SD) from five rats per experimental group. For cellular experiments, data are derived from at least three independent experiments, each performed in triplicate. Comparisons among three or more groups were performed using GraphPad Prism 7 (GraphPad Software, La Jolla, CA, USA), and statistical significance was determined using a one-way analysis of variance (ANOVA) followed by Tukey's multiple comparison test. Statistical significance was set at $p < 0.05$.

3 | Results

3.1 | iPSC-CM Suppresses PDGF-BB and Hypoxia-Induced Proliferation in PASMCs

iPSC-derived cardiac myocytes secrete proangiogenic factors such as VEGF, G-CSF, PIGF1, and IL-8, which promote myocardial repair (Tachibana et al. 2017). Pathological proliferation and migration of pulmonary artery smooth muscle cells (PASMCs) contribute to pulmonary vascular remodeling (Runo and Loyd 2003). This study examined whether iPSC-CM could counteract the proliferative effects of PDGF-BB or hypoxia (3% O_2) on PASMCs. PASMCs were cultured with iPSC-CM or iPSCs in a transwell system to avoid direct contact and then exposed to PDGF-BB or hypoxia for 24 h. The Alamar blue assay showed that iPSC-CM significantly reduced PDGF-BB- and hypoxia-induced PASMC viability, while coculture with iPSCs had no significant effect (Figure 1A,B). Furthermore, hypoxia or PDGF-BB increased PASMC proliferation, as shown by bromodeoxyuridine (BrdU) incorporation. In contrast, iPSC-CM or coculturing with iPSCs inhibited this proliferation (Figure 1C,D). Notably, iPSC-CM exhibited a stronger protective effect against PDGF-BB- and hypoxia-induced proliferation compared to iPSC coculture. Mechanistic analysis revealed that both PDGF-BB and hypoxia upregulated the mRNA and protein levels of proliferating cell nuclear antigen (PCNA) and cyclin D1 in PASMCs (Figure 1E,F). Treatment with iPSC-CM or iPSC coculture significantly downregulated these markers, indicating the mechanism by which iPSC-CM exerts its protective effect.

3.2 | iPSC-CM Suppresses PDGF-BB and Hypoxia-Induced Migration in PASMCs

We investigated the effects of iPSC-CM on PASMC migration using a scratch wound healing assay. This assay measures the capacity for wound closure at 6 and 24 h. The gap created

10974652, 2025, 8, Downloaded from https://onlinelibrary.wiley.com/doi/10.1002/jcp.70085 by Chang Gung University Of, Wiley Online Library on [04/05/2026]. See the Terms and Conditions (https://onlinelibrary.wiley.com/terms-and-conditions) on Wiley Online Library for rules of use; OA articles are governed by the applicable Creative Commons License

by the scratch was observed to close more slowly in PASMCs treated with iPSC-CM or cocultured with iPSCs as compared to those exposed to PDGF-BB alone for 24 h, indicating inhibited migration. Furthermore, iPSC-CM treatment significantly reduced hypoxia-induced wound closure compared to untreated controls. However, no significant effect was observed when PASMCs were cocultured with iPSCs (Figure 2A,B). The observed high expression levels of matrix metalloproteinases (MMPs), specifically MMP-1 and MMP-9, are known to mediate migration and invasion in various cell types (Chi et al. 2022; Cho and Reidy 2002), prompting further investigation into their role in this context. Our results show that PDGF-BB and hypoxia treatment upregulated the expression of MMP-1 and MMP-9. In contrast, PASMCs treated with iPSC-CM or in coculture with iPSCs exhibited a significant reduction in the expression of MMP-1 and MMP-9 (Figure 2C), indicating a potential mechanism for the observed anti-migratory effects of iPSC-CM in vitro.

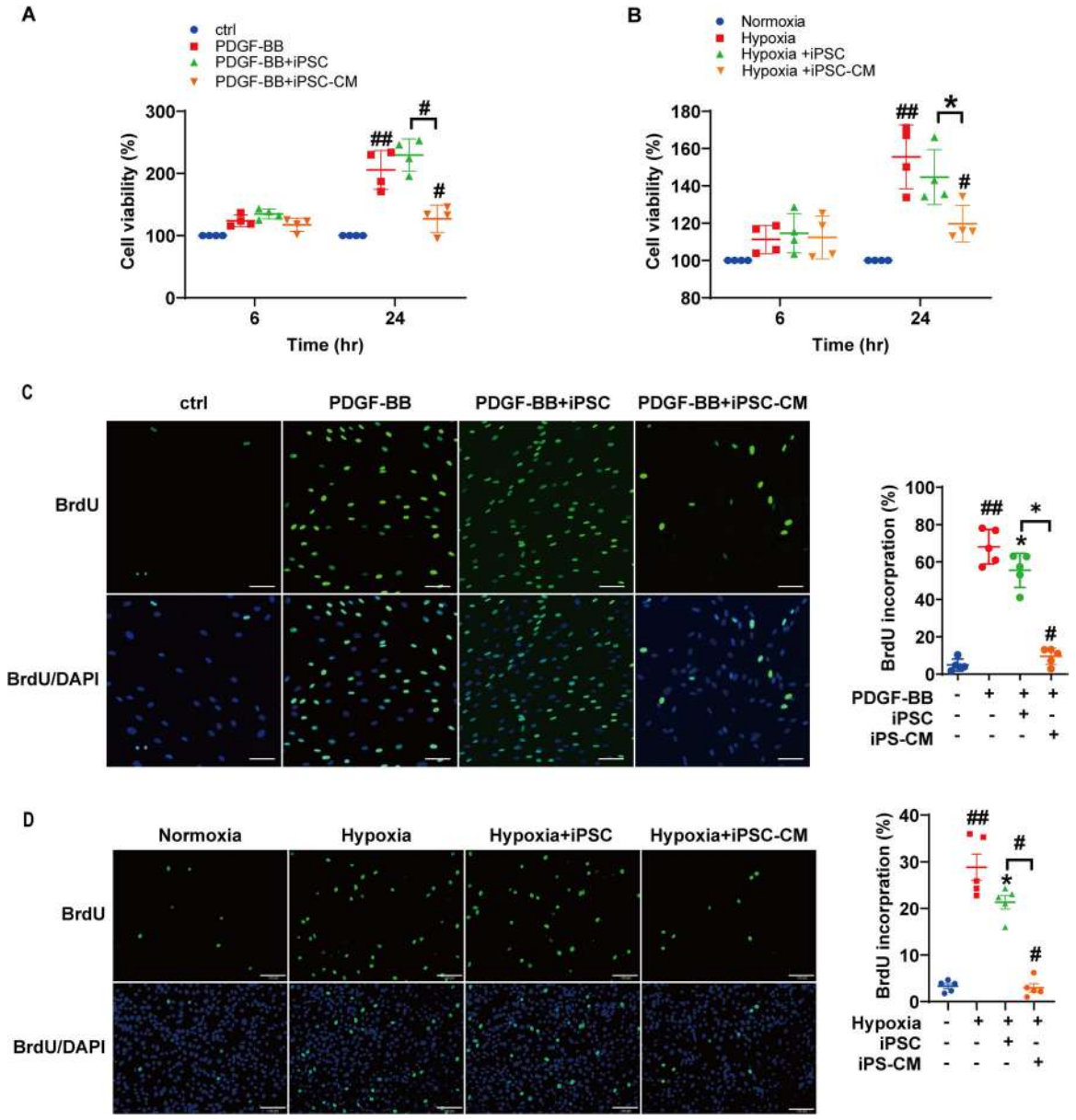


FIGURE 1 | iPSC-CM reduces the proliferation of PASMCs in response to PDGF-BB and hypoxia. (A and B) PASMCs were pretreated with iPSC-CM or cocultured with iPSCs for 2 h, or left untreated, then cultured for 6 and 24 h under normoxia (20% O_2), hypoxia (3% O_2), or with PDGF-BB treatment. Cell viability was assessed using the Alamar Blue assay. (C and D) PASMCs were pretreated with or without iPSC-CM or cocultured with iPSCs for 2 h, then cultured for 24 h under normoxia, hypoxia, or with PDGF-BB. Proliferation was assessed by BrdU staining. Nuclei were stained with DAPI (blue), and proliferating cells were stained with anti-BrdU antibody (green). The percentage of BrdU-positive cells is shown. Scale bars: 100 μm. (E) mRNA levels of PCNA and cyclin D1 were determined using real-time PCR. (F) Protein expression of PCNA and cyclin D1 was assessed using Western blot analysis. Group comparisons were analyzed using one-way analysis of variance (ANOVA) with Tukey's multiple comparison test. Data are presented as mean ± SD. $^{**}p < 0.05$, $^{\#\#}p < 0.01$, comparing control to PDGF-BB- or hypoxia-treated groups. $^{*}p < 0.05$, $^{\#}p < 0.01$, comparing PDGF-BB or hypoxia treatments to groups treated with iPSC coculture or iPSC-CM ($n = 4$–5 per group).

10974652, 2025, 8, Downloaded from https://onlinelibrary.wiley.com/doi/10.1002/jcp.70085 by Chang Gung University Of, Wiley Online Library on [04/05/2026]. See the Terms and Conditions (https://onlinelibrary.wiley.com/terms-and-conditions) on Wiley Online Library for rules of use; OA articles are governed by the applicable Creative Commons License

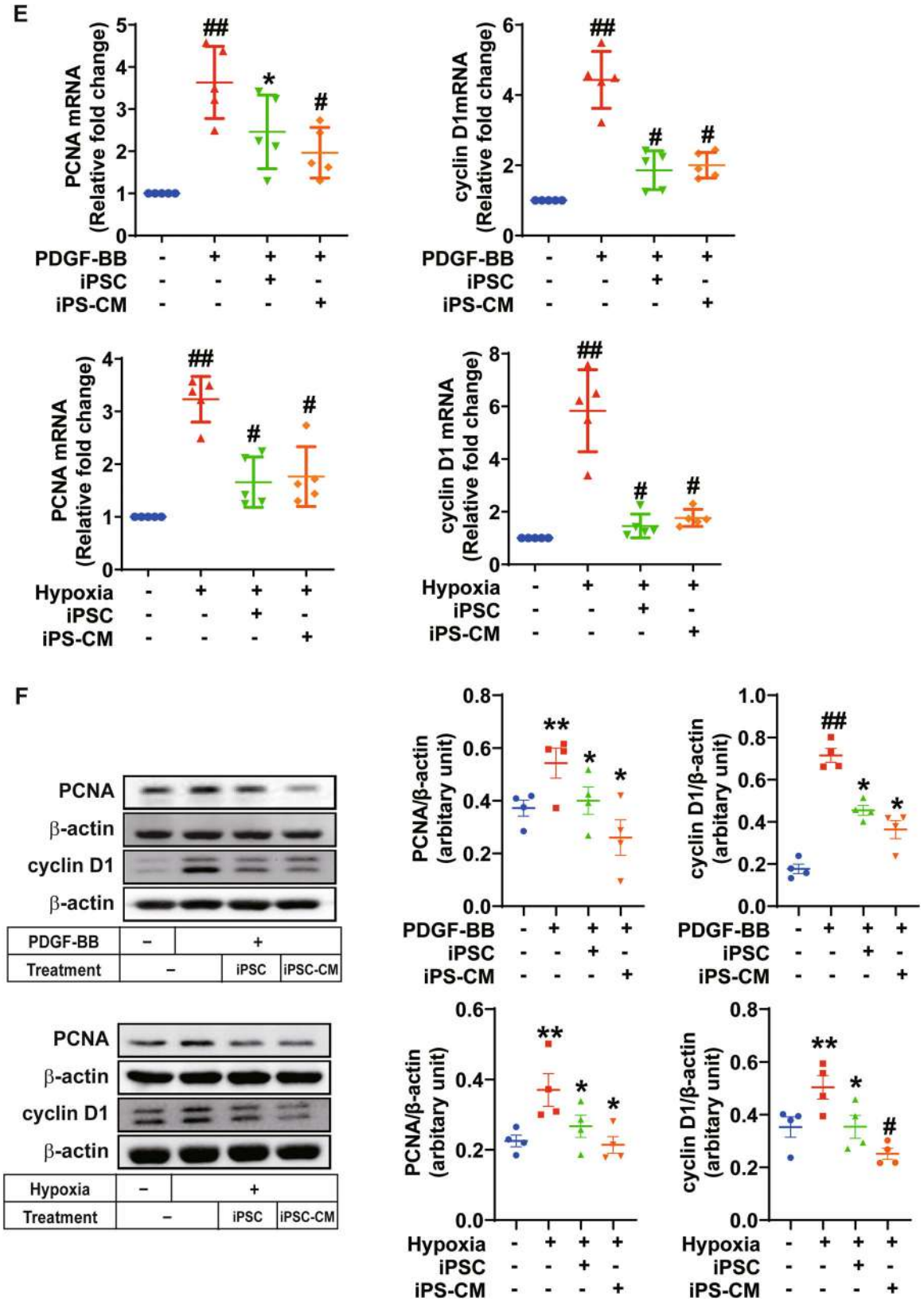


FIGURE 1 | (Continued)

10974652, 2025, 8, Downloaded from https://onlinelibrary.wiley.com/doi/10.1002/jcp.70085 by Chang Gung University Of, Wiley Online Library on [04/05/2026]. See the Terms and Conditions (https://onlinelibrary.wiley.com/terms-and-conditions) on Wiley Online Library for rules of use; OA articles are governed by the applicable Creative Commons License

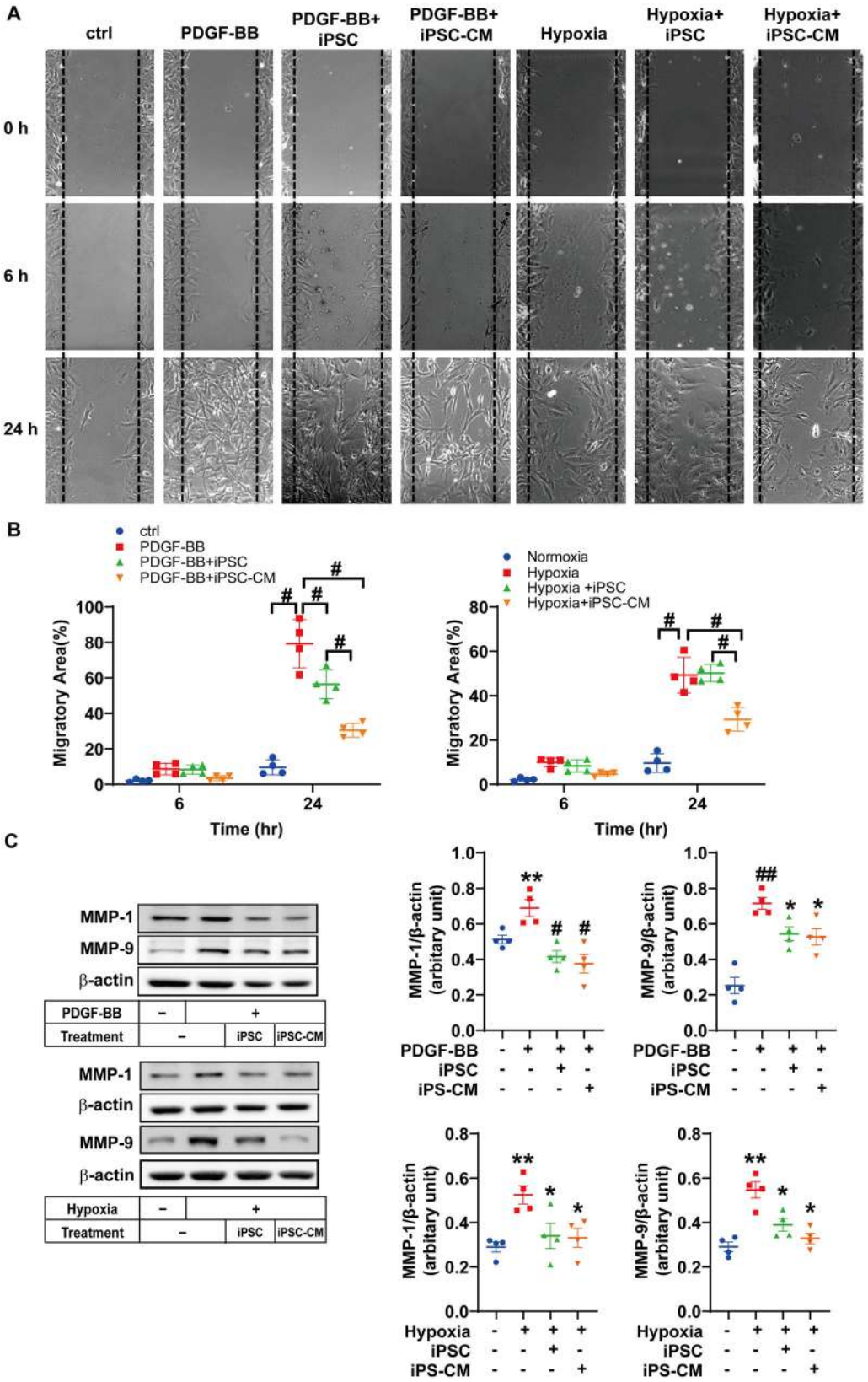


FIGURE 2 | iPSC-CM reduces the migration of PASMCs in response to PDGF-BB and hypoxia. (A and B) PASMCs were pretreated with iPSC-CM or cocultured with iPSCs for 2 h, or left untreated, then cultured for 6 and 24 h under normoxia, hypoxia, or with PDGF-BB. Migration was assessed by a wound-healing assay. Representative bright-field images show wound closure, quantified as the percentage of the area covered by cells. (C) Protein expression levels of MMP-1 and MMP-9 were determined using Western blot analysis. Group comparisons were analyzed using one-way ANOVA with Tukey's multiple comparison test. Data are presented as mean ± SD. $^{**}p < 0.05$, $^{\#\#}p < 0.01$, comparing control to PDGF-BB- or hypoxia-treated groups. $^{*}p < 0.05$, $^{\#}p < 0.01$, comparing PDGF-BB or hypoxia treatments to groups treated with iPSC coculture or iPSC-CM ($n = 4$ per group).

10974652, 2025, 8, Downloaded from https://onlinelibrary.wiley.com/doi/10.1002/jcp.70085 by Chang Gung University Of, Wiley Online Library on [04/05/2026]. See the Terms and Conditions (https://onlinelibrary.wiley.com/terms-and-conditions) on Wiley Online Library for rules of use; OA articles are governed by the applicable Creative Commons License

3.3 | iPSC-CM Attenuates the Proliferation and Migration of PASMC by Targeting the PAK-1/Akt-Dependent HIF-1α Pathway

HIF-1α is implicated in the proliferation of vascular smooth muscle cells across various cardiovascular conditions (Knutson et al. 2021). Our previous study demonstrated that both hypoxia and PDGF-BB elevate HIF-1α expression, contributing to increased proliferation and apoptosis resistance in PASMCs (Cheng et al. 2019). Given that iPSC-CM mitigates PASMC proliferation and migration under hypoxic conditions and PDGF-BB stimuli, we delved into the potential mechanisms through which iPSC-CM regulates HIF-1α. The p21-activated kinase-1 (PAK-1) and Akt, known regulators of cell growth, migration, and HIF-1 activity, are implicated in pulmonary vascular remodeling (Bu et al. 2021; Diebold et al. 2010). We explored the roles of PAK1 and HIF-1α in hypoxia and PDGF-BB-mediated proliferation and migration of PASMCs. PASMCs were transfected with PAK1 or HIF-1α siRNA. As depicted in Figure 3A, PDGF-BB and hypoxia augmented the expression of PAK1, HIF-1α, and AKT phosphorylation in PASMCs. However, PAK1 knockdown led to reduced HIF-1α expression and phosphorylation of AKT. Additionally, silencing either PAK1 or HIF-1α downregulated the expression of PCNA, cyclin D1,

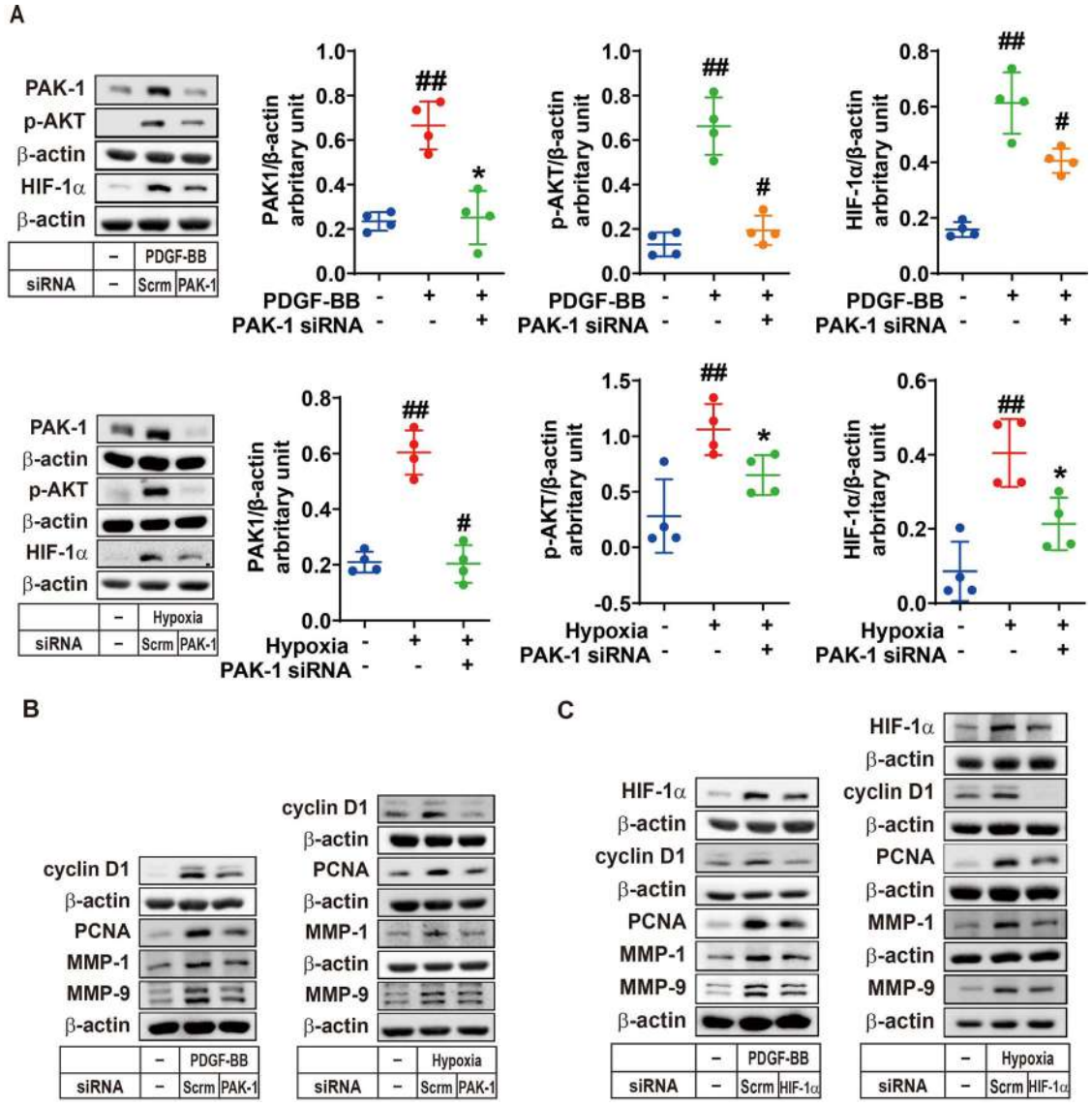


FIGURE 3 | iPSC-CM modulates proteins linked to proliferation and migration in PASMC through a PAK-1/Akt-mediated HIF-1α pathway. (A) PASMCs were transfected with scrambled siRNA or PAK-1-targeting siRNA, followed by PDGF-BB treatment or hypoxia exposure for 6 h. (B and C) PASMCs were transfected with scrambled, PAK-1, or HIF-1α-targeting siRNA, followed by PDGF-BB treatment or hypoxia exposure for 24 h. (D) PASMCs were pretreated with or without iPSC-CM or cocultured with iPSCs for 2 h, then cultured for 6 h under normoxia, hypoxia, or with PDGF-BB. mRNA levels of HIF-1α were determined using real-time PCR. (E–G) Protein expression of HIF-1α, PAK-1, phospho-AKT, and AKT in PASMCs was determined using Western blot analysis. Group comparisons were analyzed using one-way ANOVA with Tukey's multiple comparison test. Data are presented as mean ± SD. $^{**}p < 0.05$, $^{\#\#}p < 0.01$, comparing control to PDGF-BB- or hypoxia-treated groups. $^{*}p < 0.05$, $^{\#}p < 0.01$, comparing PDGF-BB or hypoxia treatments to groups treated with iPSC coculture or iPSC-CM ($n = 4$ per group).

10974652, 2025, 8, Downloaded from https://onlinelibrary.wiley.com/doi/10.1002/jcp.70085 by Chang Gung University Of, Wiley Online Library on [04/05/2026]. See the Terms and Conditions (https://onlinelibrary.wiley.com/terms-and-conditions) on Wiley Online Library for rules of use; OA articles are governed by the applicable Creative Commons License

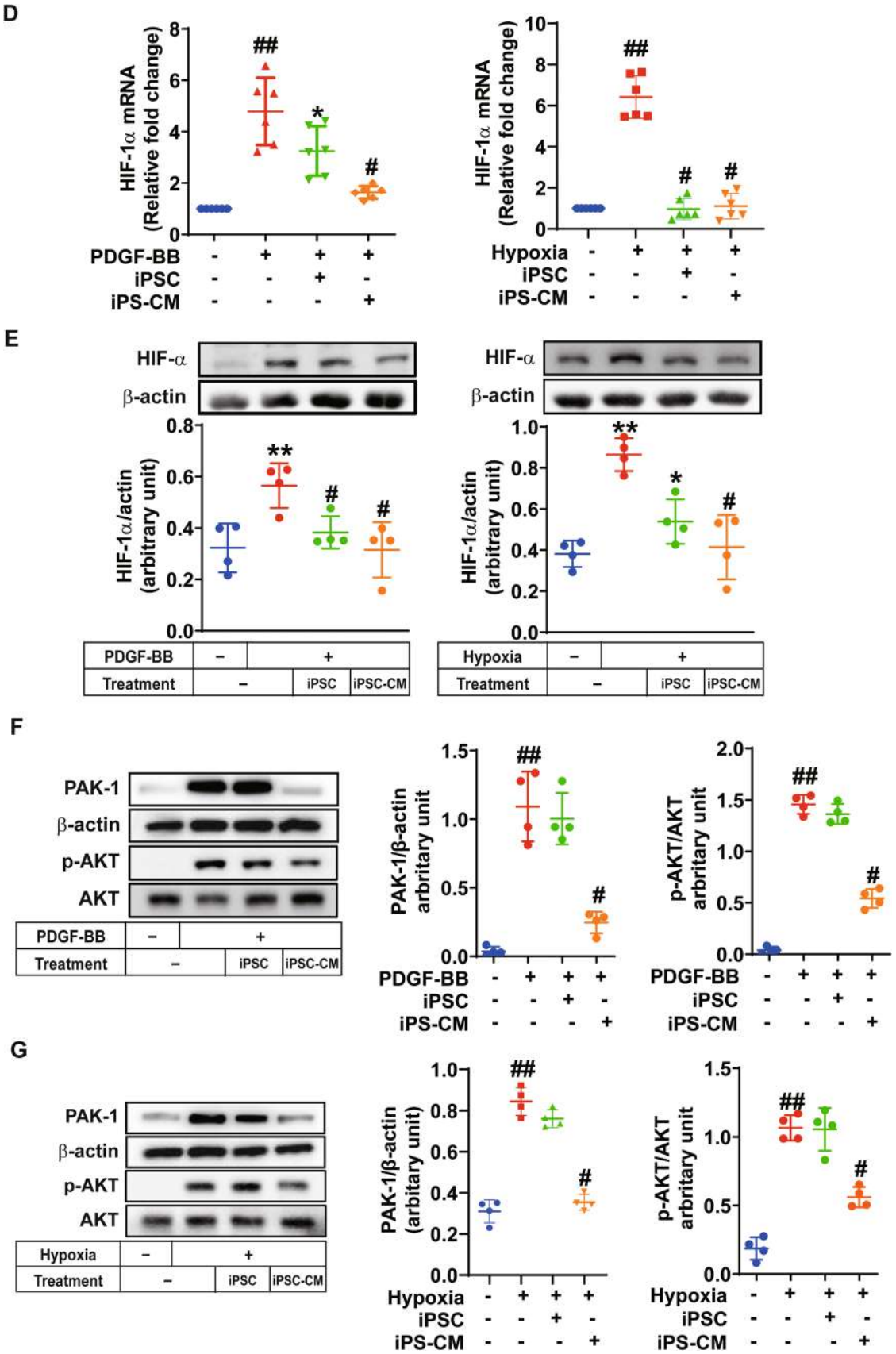


FIGURE 3 | (Continued)

10974652, 2025, 8, Downloaded from https://onlinelibrary.wiley.com/doi/10.1002/jcp.70085 by Chang Gung University Of, Wiley Online Library on [04/05/2026]. See the Terms and Conditions (https://onlinelibrary.wiley.com/terms-and-conditions) on Wiley Online Library for rules of use; OA articles are governed by the applicable Creative Commons License

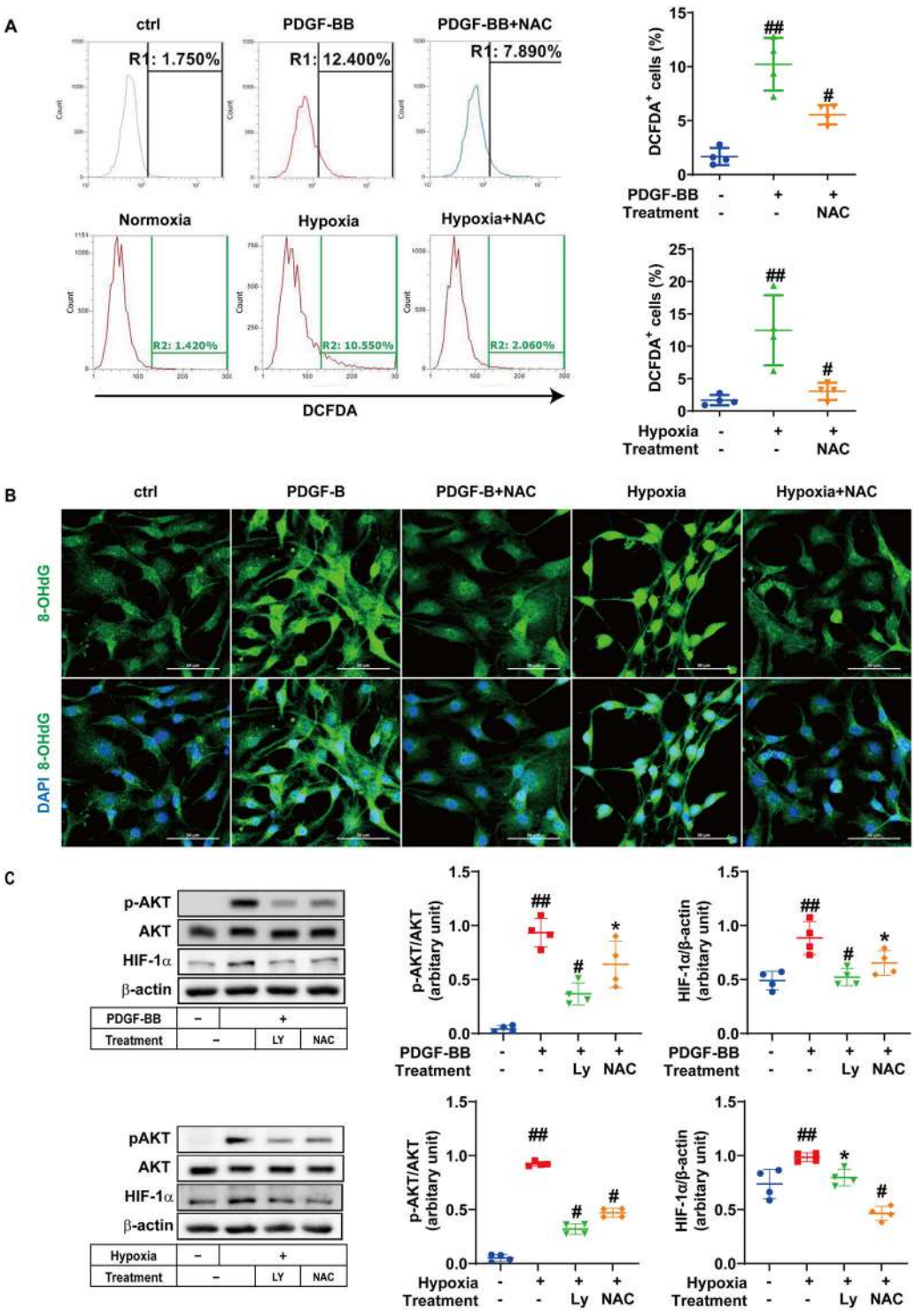


FIGURE 4 | iPSC-CM regulates proliferative and migratory protein in PASMC via a ROS-mediated Akt pathway. (A and B) ROS production in PASMCs under different treatments. Cells were pretreated with NAC (10 mM) for 2 h, then treated with PDGF-BB or exposed to hypoxia for 4 h. ROS was measured using DCFH-DA and flow cytometry and quantified relative to basal levels. Immunofluorescence of 8-oxodG in relative conditionally treated PASMCs. (C and D) PASMCs were pretreated with Ly294002 (10 μM) or NAC (10 mM) for 2 h, then treated with PDGF-BB or exposed to hypoxia for 6 h or 24 h. Protein levels were quantified by Western blot. (E and F) PASMCs were pretreated with or without iPSC-CM or cocultured with iPSCs for 2 h, then cultured for 4 h under normoxia, hypoxia, or with PDGF-BB. ROS generation was assessed using flow cytometry. Immunofluorescence of 8-oxodG in relative conditioned PASMCs. (G) PASMCs were pretreated with Ly294002 (10 μM) or NAC (10 mM) for 2 h, then treated with PDGF-BB or exposed to hypoxia for 4 h. Protein levels were quantified by Western blot. (H) PASMCs were pretreated with Ly294002 or NAC for 2 h, then treated with PDGF-BB or exposed to hypoxia for 24 h. Viability was assessed using the Alamar Blue assay. (I) PASMC migration was assessed at 24 h using a wound-healing assay. Group comparisons were analyzed using one-way ANOVA with Tukey's multiple comparison test. Data are presented as mean ± SD. $^{**}p < 0.05$, $^{\#\#}p < 0.01$, comparing control to PDGF-BB- or hypoxia-treated groups. $^{*}p < 0.05$, $^{\#}p < 0.01$, comparing PDGF-BB or hypoxia treatments to Ly294002 or NAC-treated groups ($n = 4$ per group).

10974652, 2025, 8, Downloaded from https://onlinelibrary.wiley.com/doi/10.1002/jcp.70085 by Chang Gung University Of, Wiley Online Library on [04/05/2026]. See the Terms and Conditions (https://onlinelibrary.wiley.com/terms-and-conditions) on Wiley Online Library for rules of use; OA articles are governed by the applicable Creative Commons License

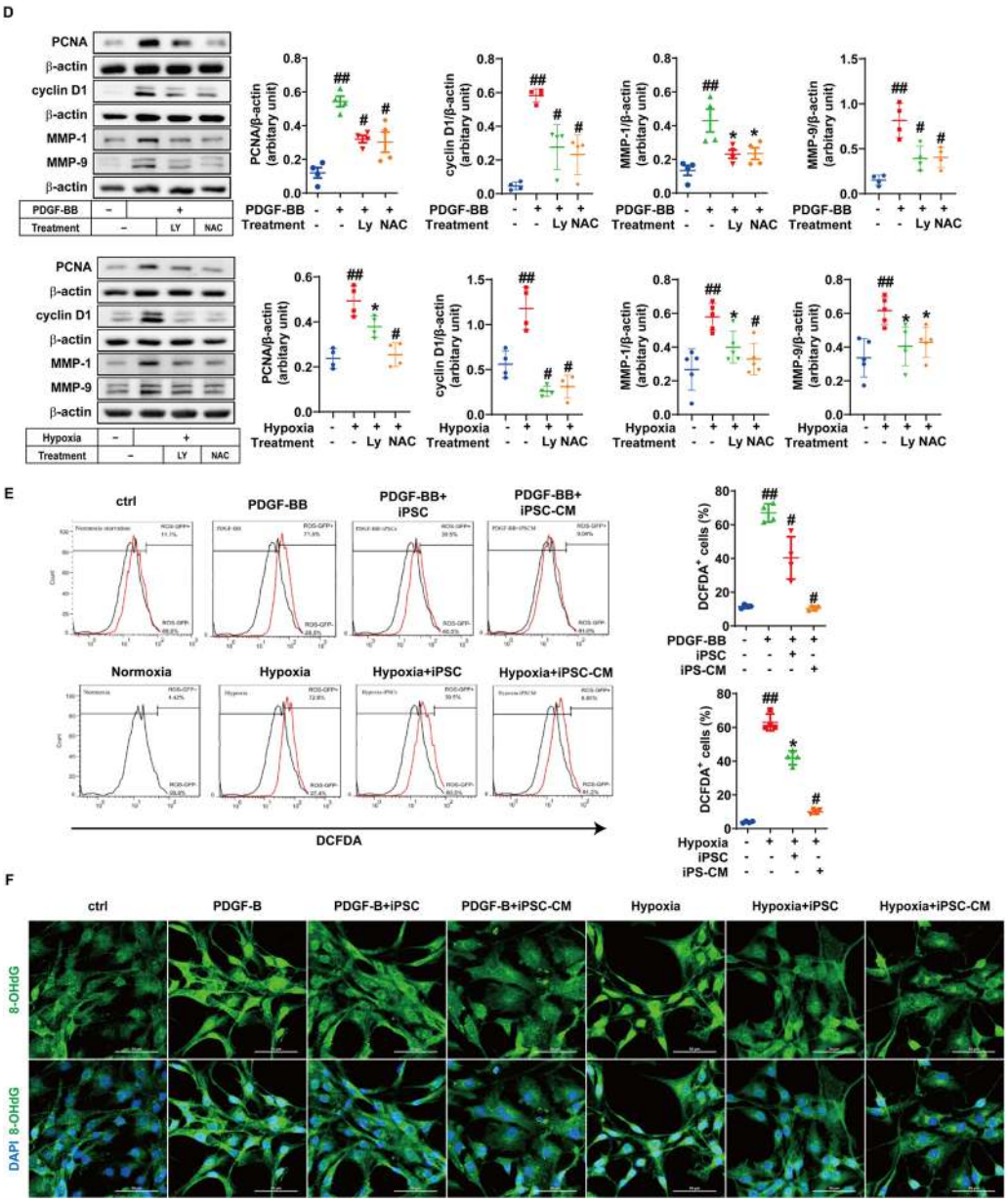


FIGURE 4 | (Continued)

MMP-1, and MMP-9 in PASMCs under PDGF-BB or hypoxia treatment (Figure 3B,C). We then assessed if the observed decrease in PASMC proliferation and migration upon iPSC-CM treatment was mediated through the PAK1 and HIF-1α pathways. iPSC-CM treatment or coculture with iPSCs notably inhibited both PDGF-BB and hypoxia-induced HIF-1α protein and mRNA expression (Figure 3D,E). Moreover, iPSC-CM reduced PAK1 expression and AKT phosphorylation in PASMCs induced by hypoxia and PDGF-BB (Figure 3F,G). Interestingly, while coculturing with iPSCs in PDGF-BB- and hypoxic induced PASMCs did not alter PAK1 expression and AKT phosphorylation. These findings suggest that iPSC-CM treatment attenuates hypoxia and PDGF-BB-induced proliferation and migration by targeting HIF-1α and is mediated through the inactivation of the PAK-1/AKT pathway in PASMCs.

3.4 | iPSC-CM Inhibits ROS Production in Hypoxic and PDGF-BB-Induced PASMC

Numerous studies have demonstrated increased levels of ROS in both human and experimental models of PAH (Bonnet and Boucherat 2018; Fulton et al. 2017). ROS has been shown to stabilize HIF-1α by preventing its degradation (Jin et al. 2020). To explore the molecular mechanisms behind iPSC-CM's ability to reduce HIF-1α expression through ROS inhibition, PASMCs were treated with the ROS scavenger *N*-acetyl cysteine (NAC) before ROS measurement. Both PDGF-BB and hypoxia exposure led to increased ROS production, which was significantly suppressed after NAC pretreatment (Figure 4A). Further investigation of ROS-induced DNA damage was performed by measuring levels of 8-oxo-7,8-dihydro-2′-deoxyguanosine

10974652, 2025, 8, Downloaded from https://onlinelibrary.wiley.com/doi/10.1002/jcp.70085 by Chang Gung University Of, Wiley Online Library on [04/05/2026]. See the Terms and Conditions (https://onlinelibrary.wiley.com/terms-and-conditions) on Wiley Online Library for rules of use; OA articles are governed by the applicable Creative Commons License

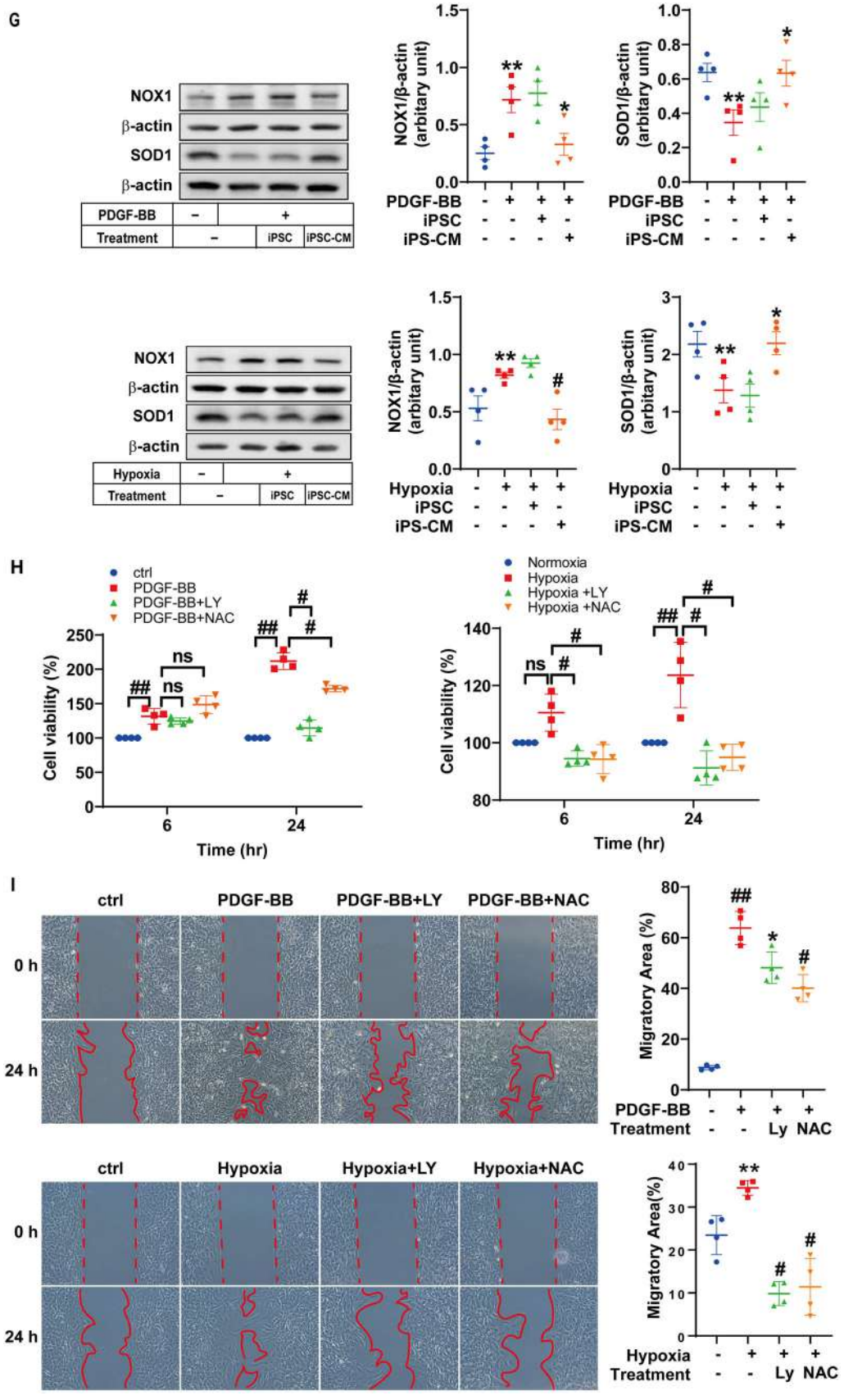


FIGURE 4 | (Continued)

10974652, 2025, 8, Downloaded from https://onlinelibrary.wiley.com/doi/10.1002/jcp.70085 by Chang Gung University Of, Wiley Online Library on [04/05/2026]. See the Terms and Conditions (https://onlinelibrary.wiley.com/terms-and-conditions) on Wiley Online Library for rules of use; OA articles are governed by the applicable Creative Commons License

(8-oxodG), a well-established marker of oxidative DNA damage (Guo et al. 2017). Immunostaining revealed that PDGF-BB and hypoxia increased accumulation of 8-oxodG in nuclear DNA in PASMCs, but this increase was significantly reduced by NAC treatment (Figure 4B). In addition, PDGF-BB and hypoxia-induced HIF-1α expression and AKT phosphorylation were inhibited by pretreatment with the PI3K/AKT inhibitor LY294002 and NAC (Figure 4C). Consistently, LY294002 and NAC also downregulated the expression of cyclin D1, PCNA, MMP-1, and MMP-9 in PASMCs exposed to PDGF-BB or hypoxia (Figure 4D). Moreover, coculture with iPSCs and iPSC-CM effectively reversed the ROS production and 8-oxodG levels in PASMCs induced by PDGF-BB and hypoxia (Figure 4E,F).

NADPH oxidases, particularly Nox1 and Nox4, are major sources of ROS in PASMCs and contribute to PAH pathogenesis (Veit et al. 2013). Our study showed that Nox1 expression was significantly elevated in PDGF-BB-induced and hypoxic PASMCs. Treatment with iPSC-CM notably reduced Nox1 expression (Figure 4G), suggesting that iPSC-CM may lower ROS levels by modulating NADPH oxidase activity. Superoxide dismutase (SOD), an antioxidant enzyme that regulates superoxide levels, plays a crucial role in PAH. Reduced SOD1 expression worsens oxidative stress and accelerates disease progression (Ramiro-Diaz et al. 2013). In our experiments, iPSC-CM upregulated SOD1 expression in both PDGF-BB-induced and hypoxic PASMCs, thereby strengthening the antioxidant defense system. Finally, the effects of various treatments on PASMC proliferation and migration under hypoxic or PDGF-BB conditions were assessed. Both NAC and LY294002 significantly inhibited PASMC proliferation and migration, compared to untreated controls (Figure 4H,I). These results suggest that iPSC-CM reduces ROS production, which in turn inhibits the PAK-1/AKT/HIF-1α pathway. This inhibition leads to the suppression of proteins involved in PASMC proliferation and migration. In addition to the reduction of ROS, the results further support the hypothesis that iPSC-CM treatment can downregulate Nox1 and upregulate SOD1, thus enhancing the antioxidant response.

3.5 | iPSC-CM Alleviates Pulmonary Hypertension and RV Hypertrophy in MCT-Treated Rats

To evaluate the therapeutic potential of iPSC-CM in PAH, we implemented both prophylactic and therapeutic treatment strategies using a well-established MCT-induced rat model. MCT is metabolized into monocrotaline pyrrole, which selectively injures pulmonary arterial endothelial cells and induces smooth muscle cell proliferation, ultimately leading to vascular remodeling and neointimal formation—hallmarks of human PAH pathology (Dai et al. 2018; Nogueira-Ferreira et al. 2015). The experimental design is illustrated in Figure 5A. For the prophylactic group (PPx), rats received iPSC-CM before MCT administration, while the therapeutic group (Tx) received iPSC-CM 2 weeks after MCT injection.

Both treatment regimens significantly attenuated MCT-induced elevations in right ventricular systolic pressure (RVSP) (Figure 5B). No significant changes in left ventricular systolic pressure (LVSP) were observed among MCT-treated rats compared with PBS controls (Figure 5C), confirming that the hypertensive effect was confined to the pulmonary circulation. iPSC-CM also markedly reduced right ventricular (RV) hypertrophy, as evidenced by a decreased right ventricle-to-(left ventricle + septum) weight ratio (Figure 5D). Although MCT treatment led to weight loss at 4 weeks, animals receiving iPSC-CM exhibited significantly less body weight reduction compared to untreated MCT controls (Figure 5E).

To further assess the therapeutic impact of iPSC-CM, we evaluated pulmonary vascular remodeling through histological and immunohistochemical analyses. Elastic Van Gieson (EvG) staining and α-smooth muscle actin (α-SMA) immunostaining demonstrated increased muscularization and luminal occlusion in pulmonary arteries of MCT-treated rats compared to controls (Figure 5F). The medial wall-to-lumen ratio was significantly elevated in MCT rats, whereas both prophylactic and therapeutic iPSC-CM treatments significantly reduced vessel wall thickening and α-SMA expression (Figure 5G,H), indicating effective inhibition of pathological vascular remodeling.

To address the oncogenic safety profile of iPSC-CM, we examined the expression of two oncogenes (c-Myc and KRAS) and two tumor suppressor genes (TP53 and PTEN) in lung tissues from each group. Each group initially included five animals; however, some samples had expression levels below the qPCR detection limit and were marked as “undetermined”. As shown in Supporting Figure 1, c-Myc expression did not differ significantly among the MCT-only, MCT+iPSC, and MCT+iPSC-CM groups. Interestingly, the MCT-only group showed slightly higher c-Myc levels than the treatment groups. KRAS expression was significantly reduced in MCT-treated rats relative to PBS controls but was partially restored following iPSC or iPSC-CM treatment, though levels remained below PBS controls. These data indicate that iPSC-CM does not induce KRAS overexpression beyond physiological norms, suggesting a low risk of oncogenic activation. For tumor suppressor genes, TP53 and PTEN expression levels were preserved or modestly elevated in the iPSC- and iPSC-CM-treated groups compared to MCT-only controls.

Collectively, these results suggest that iPSC-CM infusion neither upregulates oncogenes nor suppresses tumor suppressor gene expression, further supporting the safety of iPSC-CM therapy. In summary, iPSC-CM exhibits both preventive and therapeutic effects in the MCT-induced PAH model by reducing pulmonary pressure, RV hypertrophy, and vascular remodeling without eliciting oncogenic responses in vivo.

3.6 | iPSC-CM Inhibits the Expression of HIF-1α, PDGF-BB, and Proteins Associated With Proliferation and Migration in MCT-Induced Rats

PDGF and HIF-1α are critical drivers of pulmonary vascular remodeling, as demonstrated in various animal models (Balasubramaniam et al. 2003; Pullamsetti et al. 2020). To understand the protective mechanisms of iPSC-CM against MCT-induced PAH, we analyzed the expression of these proteins in lung tissues from MCT-treated rats, both in the

10974652, 2025, 8, Downloaded from https://onlinelibrary.wiley.com/doi/10.1002/jcp.70085 by Chang Gung University Of, Wiley Online Library on [04/05/2026]. See the Terms and Conditions (https://onlinelibrary.wiley.com/terms-and-conditions) on Wiley Online Library for rules of use; OA articles are governed by the applicable Creative Commons License

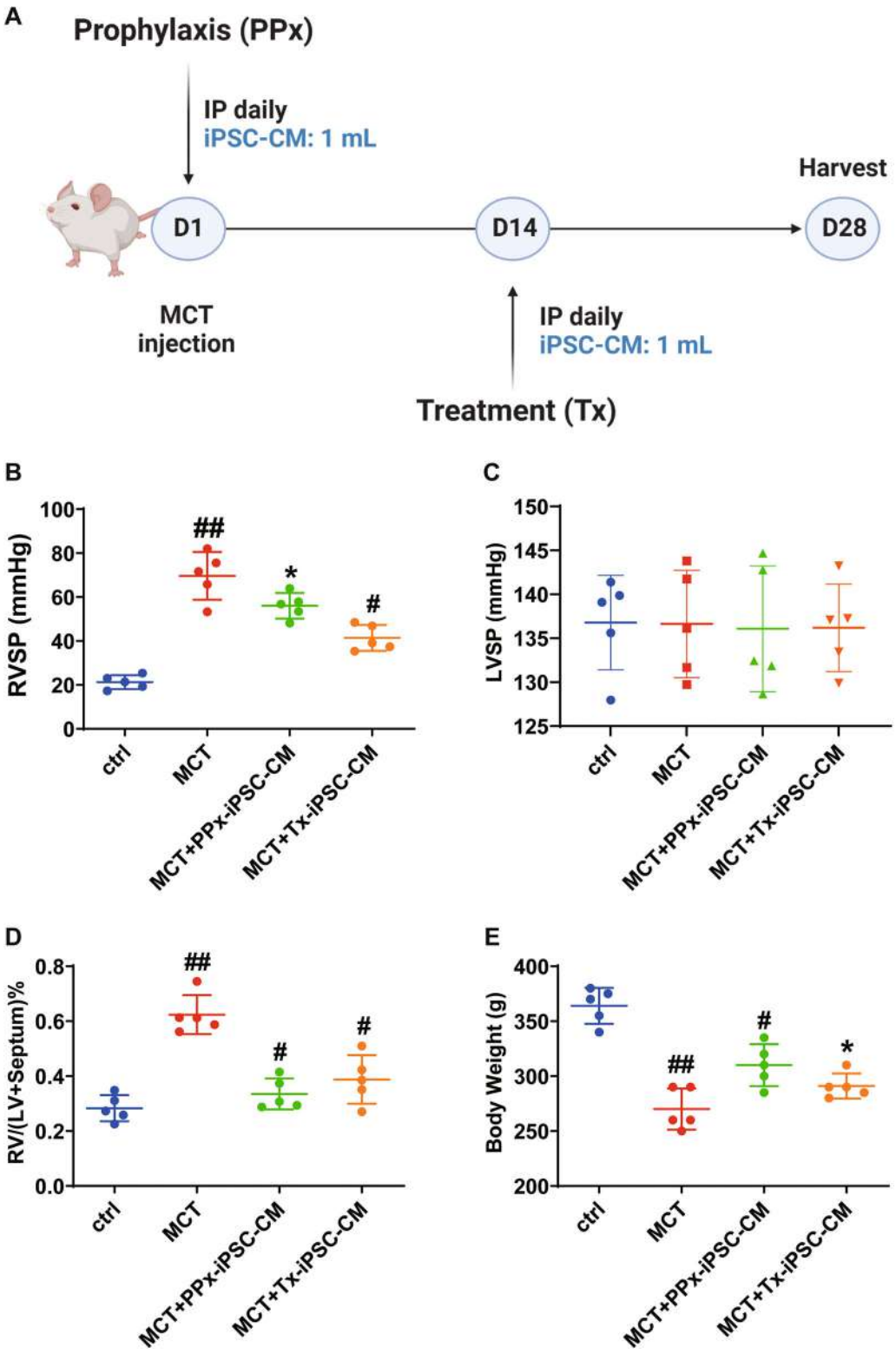


FIGURE 5 | iPSC-CM mitigates MCT-induced PAH in rats. (A) Schematic of the MCT-induced PAH rat model and iPSC-CM treatment regimen: early treatment (PPx) following MCT injection, and treatment initiated two weeks post-MCT injection (Tx). (B) right ventricular systolic pressure (RVSP), (C) left ventricular systolic pressure (LVSP), (D) evaluation of right ventricular hypertrophy, and (E) body weight changes in rats. (F) Elastica van Gieson (EvG) staining and α-smooth muscle actin (α-SMA) immunohistochemistry of lung tissue sections. Scale bars: 50 μm. (G) Medial thickness to lumen diameter ratio calculated using ImageJ software. (H) Quantification of α-SMA protein levels in lung tissue sections. Group comparisons were analysed using one-way ANOVA with Tukey's multiple comparison test. Data are represented as mean ± SD. $^{\#\#}p < 0.01$, comparing control to MCT-treated group. $^{*}p < 0.05$, $^{\#}p < 0.01$, comparing the MCT group to the iPSC-CM-treated groups ($n = 5$ per group).

10974652, 2025, 8, Downloaded from https://onlinelibrary.wiley.com/doi/10.1002/jcp.70085 by Chang Gung University Of, Wiley Online Library on [04/05/2026]. See the Terms and Conditions (https://onlinelibrary.wiley.com/terms-and-conditions) on Wiley Online Library for rules of use; OA articles are governed by the applicable Creative Commons License

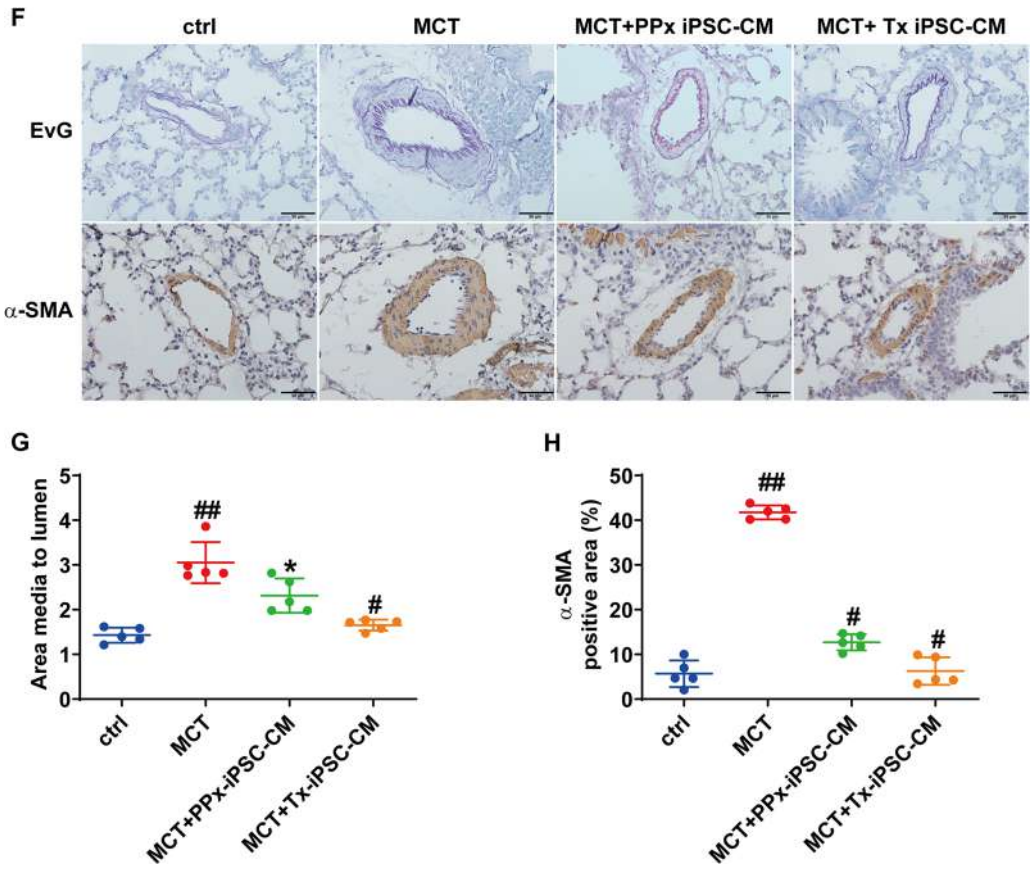


FIGURE 5 | (Continued)

presence and absence of iPSC-CM treatment. Immunohistochemistry revealed elevated levels of HIF-1α and PDGF-B in the pulmonary arterial media of MCT-induced rats, while both prophylactic and therapeutic iPSC-CM treatments significantly reduced these levels (Figure 6A,B). This reduction was further supported by immunofluorescent staining with α-SMA, HIF-1α, and PDGF-B (Figure 6C). Real-time RT-PCR analysis showed significant upregulation of HIF-1α and PDGF-B mRNA in MCT-treated rats compared to controls, which was downregulated by iPSC-CM treatment (Figure 6D).

Similarly, protein levels of HIF-1α and PDGF-B were elevated in the lungs of MCT-treated rats and reduced following iPSC-CM intervention (Figure 6E). Furthermore, the expression of proliferation and migration-associated proteins, such as PCNA, cyclin D1, MMP-1, and MMP-9, was significantly reduced in iPSC-CM-treated rats (Figure 6F). These findings suggest that iPSC-CM mitigates vascular remodeling in PAH by modulating the expression of HIF-1α and PDGF.

3.7 | iPSC-CM Attenuated Oxidative Stress in MCT-Induced Rats

To assess the role of ROS in vivo, we performed DCFH-DA staining on lung tissue sections from MCT-treated rats and control groups. Our results indicated a significant increase in oxidative stress in the MCT group compared with controls, which was significantly reduced in both the prophylactic and therapeutic iPSC-CM treatment groups (Figure 7A). Furthermore, the MCT group exhibited higher levels of 8-oxodG in lung tissue, which were effectively lowered after iPSC-CM treatment (Figure 7B). Additionally, MCT-treated rats showed an imbalance in oxidative stress-related enzymes, with increased Nox1 and decreased SOD1 expression. iPSC-CM treatment restored the balance by reducing Nox1 expression and enhancing SOD1 expression (Figure 7C). These results suggest that iPSC-CM not only reduces oxidative stress but also plays a protective role in mitigating the associated DNA damage, contributing to improved pulmonary vascular remodeling.

4 | Discussion

The present study demonstrates that iPSC-CM directly inhibits hypoxia- and PDGF-BB-induced proliferation and migration of PASMCs, two fundamental pathological mechanisms underlying pulmonary vascular remodeling in PAH. These findings extend previous observations that soluble factors secreted by iPSCs can regulate pulmonary endothelial dysfunction and attenuate aberrant PASMC activation through modulation of the vascular microenvironment (Su et al. 2019; Yi et al. 2021). Our results provide mechanistic insights into how iPSC-CM achieves these therapeutic effects through coordinated suppression of proliferation markers, matrix metalloproteinases, and key signaling pathways, while simultaneously restoring redox homeostasis.

The molecular mechanisms underlying iPSC-CM-mediated PASMC inhibition appear multifaceted. At the cellular level,

10974652, 2025, 8, Downloaded from https://onlinelibrary.wiley.com/doi/10.1002/jcp.70085 by Chang Gung University Of, Wiley Online Library on [04/05/2026]. See the Terms and Conditions (https://onlinelibrary.wiley.com/terms-and-conditions) on Wiley Online Library for rules of use; OA articles are governed by the applicable Creative Commons License

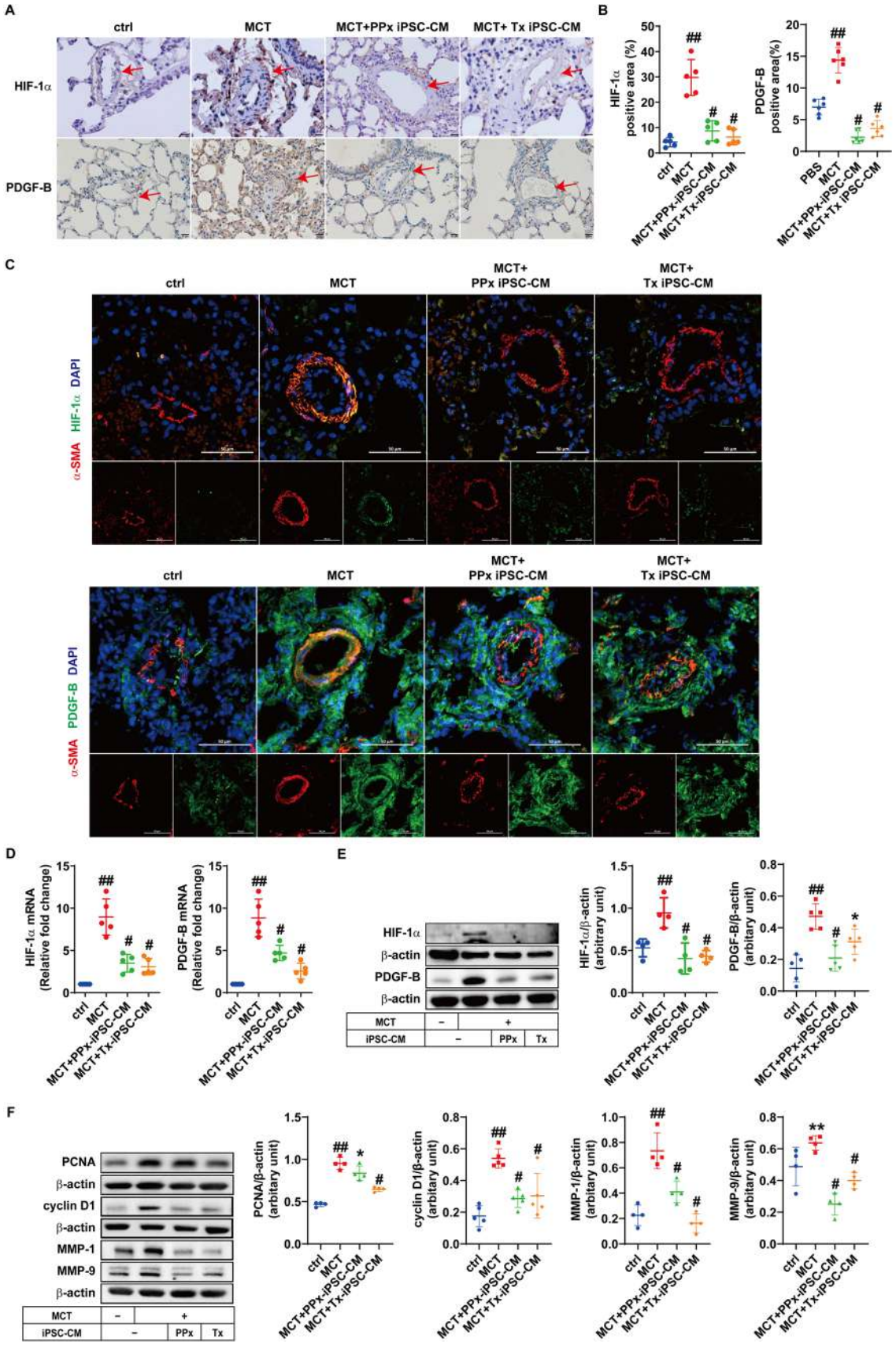


FIGURE 6 | Legend on next page.

10974652, 2025, 8, Downloaded from https://onlinelibrary.wiley.com/doi/10.1002/jcp.70085 by Chang Gung University Of, Wiley Online Library on [04/05/2026]. See the Terms and Conditions (https://onlinelibrary.wiley.com/terms-and-conditions) on Wiley Online Library for rules of use; OA articles are governed by the applicable Creative Commons License

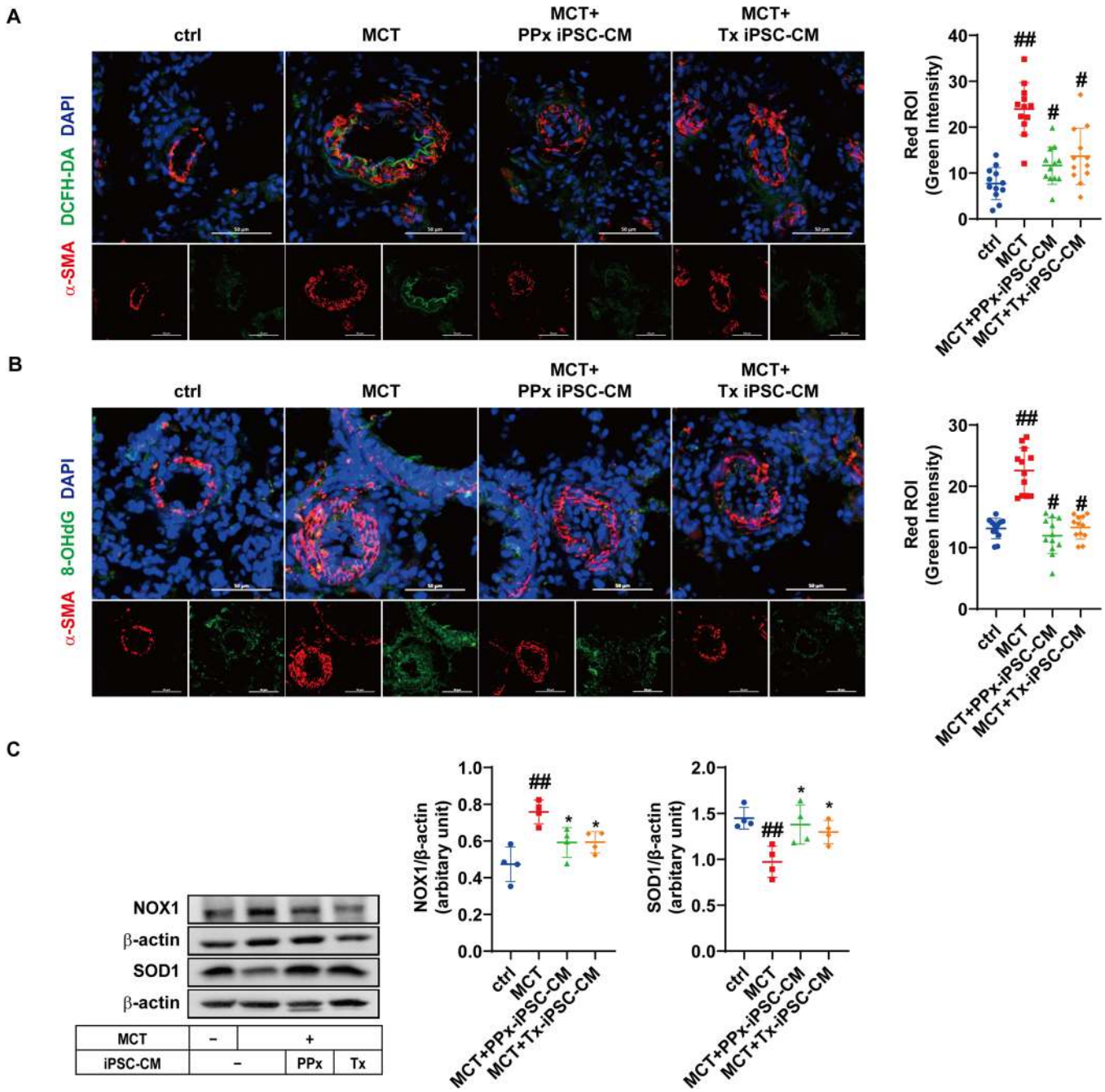


FIGURE 7 | iPSC-CM reduced oxidative stress in a MCT-induced rat model. (A, B) Immunofluorescence staining of DCFH-DA, 8-oxodG, and DAPI (for nuclei) in lung sections. The quantitative analysis shows the integrated density of the green signal (DCFH-DA or 8-oxodG) within the red ROI (α-SMA channel) on the Y-axis. Scale bars represent 50 μm. (C) Protein levels of NOX1 and SOD1 in lung tissue quantified using Western blot analysis. Group comparisons were analysed using one-way ANOVA with Tukey's multiple comparison test. Data are represented as mean ± SD. $^{\#\#}p < 0.01$, comparing control to MCT-treated group. $^{*}p < 0.05$, $^{\#}p < 0.01$, comparing the MCT group to the iPSC-CM-treated groups ($n = 4$ per group).

FIGURE 6 | iPSC-CM mediates the downregulation of HIF-1α, PDGF-BB, and proliferation- and migration-associated proteins in a MCT-induced rat model. (A) Immunohistochemical staining of HIF-1α and PDGF-B in the pulmonary arteries (red arrows). Scale bars: 20 μm. (B) Quantitative analysis of HIF-1α and PDGF-B proteins in lung tissue sections from control, MCT, and iPSC-CM-treated groups. (C) Immunofluorescence of α-SMA, HIF-1α, and PDGF-B and nuclei with DAPI in lung sections. Scale bars: 50 μm. (D) mRNA levels of HIF-1α and PDGF-B in lung tissues determined by real-time PCR. (E and F) Protein levels in lung tissues were quantified using Western blot. Group comparisons were analysed using one-way ANOVA with Tukey's multiple comparison test. Data are represented as mean ± SD. $^{\#\#}p < 0.01$, comparing control to MCT-treated group. $^{*}p < 0.05$, $^{\#}p < 0.01$, comparing the MCT group to the iPSC-CM-treated groups ($n = 4$–5 per group).

10974652, 2025, 8, Downloaded from https://onlinelibrary.wiley.com/doi/10.1002/jcp.70085 by Chang Gung University Of, Wiley Online Library on [04/05/2026]. See the Terms and Conditions (https://onlinelibrary.wiley.com/terms-and-conditions) on Wiley Online Library for rules of use; OA articles are governed by the applicable Creative Commons License

iPSC-CM treatment reduced expression of proliferation markers (cyclin D1 and PCNA) and migration-associated matrix metalloproteinases (MMP-1 and MMP-9), effects mediated through suppression of ROS generation and inhibition of the PAK-1/Akt/HIF-1α signaling axis. The clinical relevance of these pathways is well-established, as PDGF signaling drives PASMC proliferation and migration in PAH pathogenesis (Humbert et al. 2004), with elevated PDGF-A and PDGF-B expression documented in idiopathic PAH patients (Perros et al. 2008). Our observation of reduced PDGF-BB expression in MCT-treated lungs following iPSC-CM administration suggests that attenuation of this pathway represents a key therapeutic mechanism.

Importantly, the antiproliferative effects of iPSC-CM may operate through both direct and indirect mechanisms. While our data demonstrate direct suppression of PASMC responses to hypoxia and PDGF-BB stimulation, iPSC-CM may also indirectly modulate PDGF signaling by reducing inflammatory cell recruitment, as activated immune cells are significant sources of PDGF (van Suylen et al. 1998), and iPSC-CM has been shown to reduce macrophage infiltration (Huang et al. 2016). Additionally, the presence of TIMP-1 in iPSC-CM likely contributes to migration inhibition by counteracting MMP activity and stabilizing endothelial junctions (Su et al. 2019).

Our findings regarding oxidative stress modulation reveal a particularly compelling therapeutic mechanism. Oxidative stress is a well-recognized driver of PAH pathogenesis (Cracowski et al. 2001; Preston et al. 2005; Wong et al. 2013), and our data demonstrate that iPSC-CM treatment partially reversed hypoxia- and PDGF-BB-induced ROS production in PASMCs. Mechanistically, this occurred through dual complementary pathways: downregulation of the pro-oxidant enzyme Nox1 and restoration of the antioxidant enzyme SOD1. This dual approach to redox balance restoration is clinically relevant, as reduced SOD activity has been observed in PAH patients (Archer et al. 2010; Zhang et al. 2020) and SOD3 deficiency exacerbates experimental PAH severity (Tseng et al. 2020; Xu et al. 2011).

The angiogenesis array analysis revealed that iPSC-CM contains elevated levels of multiple factors that can directly influence PASMC behavior, including FGF2, IGFBP-2, MCP-1, MMP-3, OPN, PAI-1, TSP-2, and TIMP-1 compared to MEF-CM (Supporting Information S1: Figure 2). Among the key regulatory factors identified, several demonstrate direct antiproliferative potential. While FGF2 is predominantly recognized as a pro-proliferative factor for VSMCs, it also exhibits the capacity to activate antiproliferative pathways under specific conditions (Hamdin et al. 2023; Relav and Price 2021). Complementing this, IGFBP-2 can modulate smooth muscle cell responses to growth factors (Ta et al. 2018), potentially explaining the reduced sensitivity to PDGF-BB stimulation observed in iPSC-CM-treated PASMCs.

Regarding migration control, the secretome contains potent anti-migratory mediators. TIMP-1 directly counteracts MMP activity, which correlates with the suppressed PASMC migration observed in our functional assays. Similarly, TSP-2 has been shown to counteract the effects of pro-migratory signals, supporting its role as an important mediator in maintaining vascular integrity and preventing excessive remodeling (Kassem et al. 2019).

Interestingly, some factors such as MCP-1 and MMP-3 might initially appear pro-pathogenic; however, within the context of the complete secretome, these mediators may facilitate tissue repair and resolution of pathological remodeling rather than exacerbate disease progression. This complex factor profile indicates that iPSC-CM promotes vascular homeostasis in smooth muscle cells rather than driving uncontrolled proliferation and migration. While individual factor validation studies are needed to establish direct causal relationships, this secretome profile supports a multifactorial paracrine mechanism underlying the observed therapeutic effects, consistent with the emerging paradigm that stem cell-based therapies achieve efficacy through coordinated action of multiple bioactive mediators rather than single-factor mechanisms. This multifactorial strategy may contribute to the sustained modulation of vascular remodeling processes, offering a mechanistic rationale for the observed in vivo efficacy.

An important consideration for any stem cell-derived therapy is the potential risk of oncogenic transformation. We evaluated the oncogenic safety profile of iPSC-CM by quantifying expression levels of key oncogenes (c-Myc and KRAS) and tumor suppressor genes (TP53 and PTEN) in lung tissues. Our analysis revealed no significant upregulation of oncogenes or suppression of tumor suppressor genes following iPSC-CM administration (Supporting Information S1: Figure 1), reinforcing the safety profile of this acellular therapeutic approach.

5 | Conclusion

In conclusion, iPSC-CM treatment significantly improved hemodynamic parameters, reduced right ventricular hypertrophy, and attenuated vascular remodeling in the MCT-induced PAH model through multifactorial mechanisms involving suppression of PASMC proliferation and migration, modulation of the PAK-1/Akt/HIF-1α signaling axis, and restoration of redox homeostasis. The secretome-mediated therapeutic effects demonstrate the potential of acellular stem cell therapies to address multiple pathogenic pathways simultaneously, offering advantages over current single-target approaches. While the MCT model provides valuable mechanistic insights, validation in additional preclinical models and comprehensive safety studies will be essential for clinical translation. These findings support iPSC-derived conditioned medium as a promising therapeutic strategy for PAH, warranting further investigation in translational studies and clinical trials. Future studies should also evaluate scalability, manufacturing stability, and delivery strategies to facilitate clinical application.

Author Contributions

Chin-Chang Cheng, Lee-Fen Hsu, Wei-Chun Huang, and Pei-Ling Chi initiated and guided the study. Chiang-Wen Lee, Cheng-Hung Chiang, Hung-Chou Yang, Miao-Ching Chi, and Ming-Hsueh Lee conducted the in vitro and in vivo studies. Chin-Chang Cheng, Lee-Fen Hsu, Wei-Chun Huang, and Pei-Ling Chi performed the analyses, wrote the paper, and designed the figures.

10974652, 2025, 8, Downloaded from https://onlinelibrary.wiley.com/doi/10.1002/jcp.70085 by Chang Gung University Of, Wiley Online Library on [04/05/2026]. See the Terms and Conditions (https://onlinelibrary.wiley.com/terms-and-conditions) on Wiley Online Library for rules of use; OA articles are governed by the applicable Creative Commons License

Acknowledgments

The authors would like to express their gratitude to the Institutional Animal Care and Use Committee at Kaohsiung Veterans General Hospital, Taiwan, for their invaluable support. We also extend our appreciation to the National RNAi Core Facility at Academia Sinica in Taiwan for providing shRNA reagents and related services, which were essential for our research. This study was supported by the Pingtung Veterans General Hospital (PTVGH112-010), Kaohsiung Veterans General Hospital (KSVGH112-148), Chang Gung University of Science Foundation grants (ZRRPF6N0011), Chang Gung Medical Research Program Foundation Grants (CMRPF6H0121, CMRPF6H0122, CMRPF6H0123), and the Ministry of Science and Technology, Taiwan (MOST 111-2314-B-075B-001 -MY3).

Conflicts of Interest

The authors declare no conflicts of interest.

Data Availability Statement

The data that support the findings of this study are available in the supplementary material of this article.

References

Archer, S. L., G. Marsboom, G. H. Kim, et al. 2010. "Epigenetic Attenuation of Mitochondrial Superoxide Dismutase 2 in Pulmonary Arterial Hypertension: A Basis for Excessive Cell Proliferation and a New Therapeutic Target." *Circulation* 121: 2661–2671.

Balasubramaniam, V., T. D. Le Cras, D. D. Ivy, T. R. Grover, J. P. Kinsella, and S. H. Abman. 2003. "Role of Platelet-Derived Growth Factor in Vascular Remodeling During Pulmonary Hypertension in the Ovine Fetus." *American Journal of Physiology-Lung Cellular and Molecular Physiology* 284: L826–L833.

Barst, R. J. 2005. "PDGF Signaling in Pulmonary Arterial Hypertension." *Journal of Clinical Investigation* 115: 2691–2694.

Bonnet, S., and O. Boucherat. 2018. "The ROS Controversy in Hypoxic Pulmonary Hypertension Revisited." *European Respiratory Journal* 51: 1800276.

Bu, H., S. Tan, B. Yuan, et al. 2021. "Therapeutic Potential of IBP as an Autophagy Inducer for Treating Lung Cancer via Blocking PAK1/Akt/mTOR Signaling." *Molecular Therapy—Oncolytics* 20: 82–93.

Cheng, C. C., P. L. Chi, M. C. Shen, et al. 2019. "Caffeic Acid Phenethyl Ester Rescues Pulmonary Arterial Hypertension Through the Inhibition of AKT/ERK-Dependent PDGF/HIF-1α In Vitro and In Vivo." *International Journal of Molecular Sciences* 20: 1468.

Chi, P. L., C. C. Cheng, C. C. Hung, et al. 2022. "MMP-10 From M1 Macrophages Promotes Pulmonary Vascular Remodeling and Pulmonary Arterial Hypertension." *International Journal of Biological Sciences* 18: 331–348.

Cho, A., and M. A. Reidy. 2002. "Matrix Metalloproteinase-9 Is Necessary for the Regulation of Smooth Muscle Cell Replication and Migration After Arterial Injury." *Circulation Research* 91: 845–851.

Chong, M. S. K., W. K. Ng, and J. K. Y. Chan. 2016. "Concise Review: Endothelial Progenitor Cells in Regenerative Medicine: Applications and Challenges." *Stem Cells Translational Medicine* 5: 530–538.

Cracowski, J. L., C. Cracowski, G. Bessard, et al. 2001. "Increased Lipid Peroxidation in Patients With Pulmonary Hypertension." *American Journal of Respiratory and Critical Care Medicine* 164: 1038–1042.

Dai, J., Q. Zhou, J. Chen, M. L. Rexius-Hall, J. Rehman, and G. Zhou. 2018. "Alpha-Enolase Regulates the Malignant Phenotype of Pulmonary Artery Smooth Muscle Cells via the AMPK-Akt Pathway." *Nature Communications* 9: 3850.

Diebold, I., A. Petry, T. Djordjevic, et al. 2010. "Reciprocal Regulation of Rac1 and PAK-1 by HIF-1Alpha: A Positive-Feedback Loop Promoting Pulmonary Vascular Remodeling." *Antioxidants & Redox Signaling* 13: 399–412.

Dunmore, B. J., R. J. Jones, M. R. Toshner, P. D. Upton, and N. W. Morrell. 2021. "Approaches to Treat Pulmonary Arterial Hypertension by Targeting BMPR2: From Cell Membrane to Nucleus." *Cardiovascular Research* 117: 2309–2325.

Fernandez-Rebollo, E., J. Franzen, R. Goetzke, et al. 2020. "Senescence-Associated Metabolomic Phenotype in Primary and iPSC-Derived Mesenchymal Stromal Cells." *Stem Cell Reports* 14: 201–209.

Fulton, D. J. R., X. Li, Z. Bordan, et al. 2017. "Reactive Oxygen and Nitrogen Species in the Development of Pulmonary Hypertension." *Antioxidants (Basel, Switzerland)* 6, no. 3.

Granton, J., D. Langleben, M. B. Kutryk, et al. 2015. "Endothelial NO-Synthase Gene-Enhanced Progenitor Cell Therapy for Pulmonary Arterial Hypertension: The PHACeT Trial." *Circulation Research* 117: 645–654.

Guo, C., P. Ding, C. Xie, et al. 2017. "Potential Application of the Oxidative Nucleic Acid Damage Biomarkers in Detection of Diseases." *Oncotarget* 8: 75767–75777.

Hamdin, C. D., M. L. Wu, C. M. Chen, et al. 2023. "Dual-Specificity Phosphatase 6 Deficiency Attenuates Arterial-Injury-Induced Intimal Hyperplasia in Mice." *International Journal of Molecular Sciences* 24: 17136.

Huang, W. C., M. W. Ke, C. C. Cheng, et al. 2016. "Therapeutic Benefits of Induced Pluripotent Stem Cells in Monocrotaline-Induced Pulmonary Arterial Hypertension." *PLoS One* 11: e0142476.

Humbert, M., C. Guignabert, S. Bonnet, et al. 2019. "Pathology and Pathobiology of Pulmonary Hypertension: State of the Art and Research Perspectives." *European Respiratory Journal* 53: 1801887.

Humbert, M., N. W. Morrell, S. L. Archer, et al. 2004. "Cellular and Molecular Pathobiology of Pulmonary Arterial Hypertension." *Journal of the American College of Cardiology* 43: S13–S24.

Jin, X., L. Dai, Y. Ma, J. Wang, and Z. Liu. 2020. "Implications of HIF-1α in the Tumorigenesis and Progression of Pancreatic Cancer." *Cancer Cell International* 20: 273.

Kassem, M. M., A. Helkin, K. G. Maier, and V. Gahtan. 2019. "Thrombospondins Differentially Regulate Proteins Involved in Arterial Remodeling." *Physiological Research* 68: 893–900.

Knutson, A., A. L. Williams, W. A. Boisvert, and R. V. Shohet. 2021. "HIF in the Heart: Development, Metabolism, Ischemia, and Atherosclerosis." *Journal of Clinical Investigation* 131, no. 17: e137557. https://doi.org/10.1172/JCI137557.

Kurosawa, R., K. Satoh, N. Kikuchi, et al. 2019. "Identification of Celastramycin as a Novel Therapeutic Agent for Pulmonary Arterial Hypertension." *Circulation Research* 125: 309–327.

Liang, X., F. Lin, Y. Ding, et al. 2021. "Conditioned Medium From Induced Pluripotent Stem Cell-Derived Mesenchymal Stem Cells Accelerates Cutaneous Wound Healing Through Enhanced Angiogenesis." *Stem Cell Research & Therapy* 12: 295.

Naeije, R., and A. Manes. 2014. "The Right Ventricle in Pulmonary Arterial Hypertension." *European Respiratory Review* 23: 476–487.

Nogueira-Ferreira, R., R. Vitorino, R. Ferreira, and T. Henriques-Coelho. 2015. "Exploring the Monocrotaline Animal Model for the Study of Pulmonary Arterial Hypertension: A Network Approach." *Pulmonary Pharmacology & Therapeutics* 35: 8–16.

Perros, F., D. Montani, P. Dorfmüller, et al. 2008. "Platelet-Derived Growth Factor Expression and Function in Idiopathic Pulmonary Arterial Hypertension." *American Journal of Respiratory and Critical Care Medicine* 178: 81–88.

10974652, 2025, 8, Downloaded from https://onlinelibrary.wiley.com/doi/10.1002/jcp.70085 by Chang Gung University Of, Wiley Online Library on [04/05/2026]. See the Terms and Conditions (https://onlinelibrary.wiley.com/terms-and-conditions) on Wiley Online Library for rules of use; OA articles are governed by the applicable Creative Commons License

Preston, I. R., G. Tang, J. U. Tilan, N. S. Hill, and Y. J. Suzuki. 2005. "Retinoids and Pulmonary Hypertension." *Circulation* 111: 782–790.

Pullamsetti, S. S., A. Mamazhakypov, N. Weissmann, W. Seeger, and R. Savai. 2020. "Hypoxia-Inducible Factor Signaling in Pulmonary Hypertension." *Journal of Clinical Investigation* 130: 5638–5651.

Ramiro-Diaz, J. M., C. H. Nitta, L. D. Maston, et al. 2013. "NFAT Is Required for Spontaneous Pulmonary Hypertension in Superoxide Dismutase 1 Knockout Mice." *American Journal of Physiology-Lung Cellular and Molecular Physiology* 304: L613–L625.

Relav, L., and C. A. Price. 2021. "Regulation of Dual Specificity Phosphatases by Fibroblast Growth Factor Signaling Pathways in Bovine Granulosa Cells." *Reproduction* 162: 367–374.

van Rhijn-Brouwer, F. C. C., H. Gremmels, J. O. Fledderus, and M. C. Verhaar. 2018. "Mesenchymal Stromal Cell Characteristics and Regenerative Potential in Cardiovascular Disease: Implications for Cellular Therapy." *Cell Transplantation* 27: 765–785.

Runo, J. R., and J. E. Loyd. 2003. "Primary Pulmonary Hypertension." *Lancet* 361: 1533–1544.

Sommer, N., H. A. Ghofrani, O. Pak, et al. 2021. "Current and Future Treatments of Pulmonary Arterial Hypertension." *British Journal of Pharmacology* 178: 6–30.

Su, V. Y. F., S. H. Chiou, C. S. Lin, M. H. Mo, and K. Y. Yang. 2019. "Induced Pluripotent Stem Cells Attenuate Endothelial Leakage in Acute Lung Injury via Tissue Inhibitor of Metalloproteinases-1 to Reduce Focal Adhesion Kinase Activity." *Stem Cells* 37: 1516–1527.

van Suylen, R. J., J. F. M. Smits, and M. J. A. P. Daemen. 1998. "Pulmonary Artery Remodeling Differs in Hypoxia- and Monocrotaline-Induced Pulmonary Hypertension." *American Journal of Respiratory and Critical Care Medicine* 157: 1423–1428.

Ta, S., A. N, and P. Pa. 2018. "Structure and Actions of Insulin-Like Growth Factor Binding Protein-2 (IGFBP-2)." *Medical Research and Innovations* 2.

Tachibana, A., M. R. Santoso, M. Mahmoudi, et al. 2017. "Paracrine Effects of the Pluripotent Stem Cell-Derived Cardiac Myocytes Salvage the Injured Myocardium." *Circulation Research* 121: e22–e36.

Takahashi, T., C. Kalka, H. Masuda, et al. 1999. "Ischemia- and Cytokine-Induced Mobilization of Bone Marrow-Derived Endothelial Progenitor Cells for Neovascularization." *Nature Medicine* 5: 434–438.

Tseng, V., K. Ni, A. Allawzi, et al. 2020. "Extracellular Superoxide Dismutase Regulates Early Vascular Hyaluronan Remodeling in Hypoxic Pulmonary Hypertension." *Scientific Reports* 10: 280.

Veit, F., O. Pak, B. Egemnazarov, et al. 2013. "Function of NADPH Oxidase 1 in Pulmonary Arterial Smooth Muscle Cells After Monocrotaline-Induced Pulmonary Vascular Remodeling." *Antioxidants & Redox Signaling* 19: 2213–2231.

Wong, C. M., G. Bansal, L. Pavlickova, L. Marcocci, and Y. J. Suzuki. 2013. "Reactive Oxygen Species and Antioxidants in Pulmonary Hypertension." *Antioxidants & Redox Signaling* 18: 1789–1796.

Wu, J., L. Yu, Y. Liu, et al. 2023. "Hypoxia Regulates Adipose Mesenchymal Stem Cells Proliferation, Migration, and Nucleus Pulposus-Like Differentiation by Regulating Endoplasmic Reticulum Stress via the HIF-1α Pathway." *Journal of Orthopaedic Surgery and Research* 18: 339.

Wu, K., H. Tang, R. Lin, et al. 2020. "Endothelial Platelet-Derived Growth Factor-Mediated Activation of Smooth Muscle Platelet-Derived Growth Factor Receptors in Pulmonary Arterial Hypertension." *Pulmonary Circulation* 10: 1–15.

Xu, D., H. Guo, X. Xu, et al. 2011. "Exacerbated Pulmonary Arterial Hypertension and Right Ventricular Hypertrophy in Animals With Loss of Function of Extracellular Superoxide Dismutase." *Hypertension* 58: 303–309.

Yi, D., B. Liu, T. Wang, et al. 2021. "Endothelial Autocrine Signaling Through CXCL12/CXCR4/FoxM1 Axis Contributes to Severe Pulmonary Arterial Hypertension." *International Journal of Molecular Sciences* 22: 3182.

Zhang, R., L. Wang, Q. H. Zhao, et al. 2020. "Alteration of Extracellular Superoxide Dismutase in Idiopathic Pulmonary Arterial Hypertension." *Frontiers in Medicine* 7: 509.

Supporting Information

Additional supporting information can be found online in the Supporting Information section.

Supplementary Figure 1: Oncogenic safety assessment of iPSC-CM treatment. **Supplementary Figure 2:** Comparative angiogenesis protein profiling of iPSC-conditioned medium versus MEF-conditioned medium.

10974652, 2025, 8, Downloaded from https://onlinelibrary.wiley.com/doi/10.1002/jcp.70085 by Chang Gung University Of, Wiley Online Library on [04/05/2026]. See the Terms and Conditions (https://onlinelibrary.wiley.com/terms-and-conditions) on Wiley Online Library for rules of use; OA articles are governed by the applicable Creative Commons License

International Immunopharmacology 164 (2025) 115360

Contents lists available at ScienceDirect

International Immunopharmacology

journal homepage: www.elsevier.com/locate/intimp

Lutein attenuates rheumatoid arthritis progression by suppressing MAPK/NF-κB signaling and MMP3 and MMP13 expression in fibroblast-like Synoviocytes

Chi-Jen Chang [a,b], Tsung-Ming Chang [c], Ying-Sui Sun [c], Ji-Fan Lin [d], Chiang-Wen Lee [e,f], Mei-Ling Fang [g,h], Ju-Fang Liu [d,i,j,*]

[a] School of Medicine, Fu Jen Catholic University, New Taipei City 24205, Taiwan
[b] Division of Pediatric Surgery, Shin Kong Wu Ho-Su Memorial Hospital, Taipei 111045, Taiwan
[c] School of Dental Technology, College of Oral Medicine, Taipei Medical University, Taipei 11031, Taiwan
[d] Translational Medicine Center, Shin Kong Wu Ho-Su Memorial Hospital, Taipei 111045, Taiwan
[e] Department of Nursing, Division of Basic Medical Sciences, and Chronic Diseases and Health Promotion Research Center, Chang Gung University of Science and Technology, Chiayi 61363, Taiwan
[f] Department of Respiratory Care, Chang Gung University of Science and Technology, Chiayi 61363, Taiwan
[g] Center for Environmental Toxin and Emerging-Contaminant Research, Cheng Shiu University, Kaohsiung 83347, Taiwan
[h] Super Micro Research and Technology Center, Cheng Shiu University, Kaohsiung 83347, Taiwan
[i] School of Oral Hygiene, College of Oral Medicine, Taipei Medical University, Taipei 11031, Taiwan
[j] Department of Medical Research, China Medical University, Hospital, China Medical University, Taichung 40402, Taiwan

ARTICLE INFO

Editor name: Dr. Yongchun Shen

Keywords:
Rheumatoid arthritis
Lutein
Matrix metalloproteinase (MMP)
MAPK
NF-κB
Fibroblast-like synoviocytes (FLS)

ABSTRACT

Rheumatoid arthritis (RA) is a chronic autoimmune disease affecting approximately 1 % of the global population, characterized by synovitis and joint destruction. Current therapies aim to control inflammation but often result in adverse effects or limited efficacy. Lutein is a natural carotenoid that possesses antioxidant and anti-inflammatory properties. However, the potential of lutein in mitigating the progression of RA remains unclear. In this study, we utilized dataset GSE55235, comprising transcriptomic profiles of synovial tissues from RA, OA, and healthy individuals, enabling precise discrimination of RA-specific gene signatures. Additionally, we analyzed dataset GSE1919, which contains whole-genome expression data comparing RA synovial tissues with OA and healthy donor tissues, facilitating the characterization of key pathogenic mechanisms underlying RA. Our gene expression analyses revealed significant upregulation of matrix metalloproteinases (MMPs), confirming their pivotal role in RA pathogenesis. RNA sequencing of lutein-treated fibroblast-like synoviocytes (FLS) identified differentially expressed genes, with gene set enrichment analysis indicating suppression of RA-related pathways and extracellular matrix degradation. Ingenuity Pathway Analysis demonstrated that lutein inhibits synovial invasion and cartilage destruction by downregulating MAPK and NF-κB signaling. In vitro experiments confirmed that lutein suppresses TNF-α-induced p38, ERK, and NF-κB activation, reducing MMP3 and MMP13 expression and inhibiting FLS migration. These findings were validated in a collagen-antibody-induced arthritis model, where lutein reduced synovial inflammation and joint damage. Collectively, this study highlights lutein's potential as a dietary supplement for RA management by alleviating oxidative stress, suppressing inflammatory responses, and preserving joint integrity. Further clinical studies are warranted to explore its therapeutic applications in RA treatment.

Abbreviations: RA, rheumatoid arthritis; TNF-α, tumor necrosis factor-alpha; IL-6, interleukin-6; FLS, fibroblast-like synoviocytes; ROS, reactive oxygen species; GEO, Gene Expression Omnibus; DEG, differentially expressed genes; GO, Gene Ontology; KEGG, Kyoto Encyclopedia of Genes and Genomes; GSEA, gene set enrichment analysis; CAIA, collagen antibody-induced arthritis; MMP, matrix metalloproteinases; ERK, extracellular signal-regulated kinase; JNK, c-Jun NH2-terminal kinase; MAPK, mitogen-activated protein kinase; PCR, polymerase chain reaction; NF-κB, nuclear factor kappa-light-chain-enhancer of activated B cells; DMARDs, disease-modifying antirheumatic drugs; NSAIDs, nonsteroidal anti-inflammatory drugs; MTX, methotrexate; ECM, extracellular matrix.

* Corresponding author at: School of Oral Hygiene, College of Oral Medicine, Taipei Medical University, No. 250, Wuxing Street, Taipei 11031, Taiwan.
E-mail address: jufangliu@tmu.edu.tw (J.-F. Liu).

https://doi.org/10.1016/j.intimp.2025.115360
Received 7 March 2025; Received in revised form 10 July 2025; Accepted 7 August 2025
Available online 14 August 2025
1567-5769/© 2025 Elsevier B.V. All rights are reserved, including those for text and data mining, AI training, and similar technologies.

1. Introduction

Rheumatoid arthritis (RA) is a chronic autoimmune disease characterized by persistent synovitis, joint damage, and the presence of cyclic citrullinated proteins [1]. Despite extensive research linking RA progression to genetic and environmental factors, its precise pathogenesis remains incompletely understood [2,3]. RA affects approximately 1 % of the global population, with a higher prevalence among older individuals and women [3,4]. Current treatment strategies focus on mitigating inflammation and preventing joint damage, utilizing disease-modifying antirheumatic drugs (DMARDs), nonsteroidal anti-inflammatory drugs (NSAIDs), glucocorticoids, and biologic response modifiers [5]. Methotrexate (MTX) is the first-line DMARD due to its efficacy and affordability; however, its structural similarity to folic acid disrupts folate metabolism, leading to adverse effects such as nausea and hepatic dysfunction [6–9]. For patients who are unresponsive to DMARDs or experience significant side effects, biologic agents and targeted therapies offer alternative options [10]. However, while effective, biological agents are costly and increase susceptibility to infections [5]. Furthermore, a substantial proportion of RA patients do not respond adequately to these advanced therapies [11], highlighting the need for novel therapeutic approaches.

Articular cartilage comprises chondrocytes and extracellular matrix (ECM) [12]. In RA, activated fibroblast-like synoviocytes (FLS) secrete matrix metalloproteinases (MMPs), which degrade ECM components, contributing to cartilage destruction [13]. MMPs mediate tissue degradation, regulate inflammatory cytokines and chemokines, activate inflammatory signaling pathways, and promote osteoclast differentiation [14,15]. These processes further enhance FLS migration, immune cell infiltration, and pannus formation, ultimately accelerating bone destruction [16–19]. Macrophage-derived tumor necrosis factor-alpha (TNF-α) plays a central role in RA pathogenesis by activating FLS, thereby perpetuating chronic synovitis [20]. Activated FLS sustains prolonged nuclear factor kappa-light-chain-enhancer of activated B cells (NF-κB) activation and continuously expresses inflammatory cytokines, driving an aggressive phenotype [21]. The TNF-α/NF-κB signaling pathway stimulates FLS to produce interleukin (IL)-6, IL-1β, TNF-α, and MMPs, exacerbating inflammation and joint tissue degradation [22]. TNF-α and IL-6 further contribute to RA pathology by promoting FLS proliferation within joint spaces, leading to synovial membrane thickening and ECM degradation [23,24]. Additionally, TNF-α and IL-1β activate FLS to secrete MMP1, MMP3, MMP9, and MMP13, enhancing FLS invasiveness and osteoclastogenesis, ultimately resulting in joint destruction [25]. Given this cascade of pathological events, identifying therapeutic agents capable of suppressing MMP production in activated FLS is crucial for RA treatment.

Lutein is found in many vegetables and is a type of carotenoid, which is a naturally derived plant pigment. Lutein has a variety of protective biological activities, including antioxidant, anti-apoptosis, and anti-inflammatory properties, and it can filter harmful blue light to protect the eyes [26]. Beyond its ocular benefits, lutein has demonstrated the potential to improve cognitive function and reduce cardiovascular disease risk [27,28]. Reactive oxygen species (ROS) are elevated in the synovial fluid of RA patients [29,30] and are closely associated with FLS-driven inflammation, hyperproliferation, and bone destruction [31,32]. Moreover, ROS enhances MMP activity, exacerbating ECM degradation [33,34]. Studies indicate that TNF-α-induced FLS proliferation and invasive behavior are linked to increased intracellular ROS levels [35]. These findings suggest that lutein may mitigate RA-associated bone destruction through its antioxidative properties, warranting further investigation into its therapeutic potential.

This study investigates the impact of lutein on RA pathogenesis by analyzing mRNA expressions in synovial tissues from RA patients using Gene Expression Omnibus (GEO) datasets to assess MMPs levels. RNA sequencing of lutein-treated FLS, followed by differential gene expression analysis and gene set enrichment analysis (GSEA), was performed to identify molecular pathways influenced by lutein. In vitro experiments demonstrated that lutein significantly suppressed TNF-α-stimulated phosphorylation of p38 and ERK, inhibited NF-κB transcriptional activation, reduced MMP3 and MMP13 expression, and impaired FLS migration. These findings were further validated in a collagen antibody-induced arthritis (CAIA) model. Collectively, this study highlights lutein's potential in alleviating RA symptoms and supports its exploration as a dietary supplement for RA management.

2. Materials and methods

2.1. Materials

We utilized horseradish peroxidase-conjugated secondary antibodies specific to mice and rabbit IgG for protein detection and analysis. Additionally, rabbit polyclonal primary antibodies were used to target various proteins, including MMP3, MMP13, GAPDH, JNK, phospho-JNK, ERK, phospho-ERK, p38, phospho-p38, p65, and phospho-p65. Fluorescence microscopy was conducted using goat anti-rabbit IgG (DyLight488). These antibodies were obtained from GeneTex (Irvine, CA, USA). Lutein (CAS# 127–40-2; PubChem CID: 5281243) was purchased from ChromaDex, Inc. (Irvine, CA, USA) and dissolved in DMSO or corn oil according to the experimental design. For in vitro studies, a final concentration of 10 μM lutein was selected based on previous studies demonstrating antioxidant and anti-inflammatory effects without cytotoxicity in various cell types, including neuronal and immune cells [36]. This dose was confirmed to be non-toxic and functionally effective in our MH7A cell assays. Other experimental reagents were sourced from Sigma-Aldrich (Burlington, MA, USA).

2.2. Gene database utilization and analysis

Publicly available gene datasets were obtained from the Gene Expression Omnibus (GEO) database (https://www.ncbi.nlm.nih.gov/geo/). The GSE55235 dataset comprised samples from 10 healthy individuals and 10 RA patients. The GSE1919 dataset, which contains synovial tissue samples from 5 healthy individuals and 5 RA patients, was also included for further validation. To identify shared differentially expressed genes (DEGs) across these datasets, InteractiVenn (https://www.interactivenn.net/) was utilized [37]. Gene set enrichment analysis was performed using ShinyGo v0.82 (http://bioinformatics.sdstate.edu/go/) to assess Gene Ontology (GO) categories and Kyoto Encyclopedia of Genes and Genomes (KEGG) pathways [38–40]. DEGs were identified using GEO2R, an online analytical tool within the GEO platform (https://www.ncbi.nlm.nih.gov/geo/geo2r/). This tool applies GEOquery and limma packages in R to process microarray data and identify genes with significant differential expression [41]. Genes were considered differentially expressed based on an adjusted p-value <0.05 and an absolute log fold change ($|\log_2 FC|$) > 1. This inclusive threshold was selected for exploratory analysis to capture a broader gene set for downstream validation. Functional relevance of identified genes was later confirmed through in vitro and in vivo experiments.

2.3. Cell cultures

MH7A cells were obtained from the Riken Cell Bank (Ibaraki, Japan). Cells were cultured in 10 cm dishes under an atmosphere containing 95 % air and 5 % CO_2. The growth medium consisted of RPMI 1640 (Life Technologies, NY, USA), supplemented with 10 % heat-inactivated fetal bovine serum (FBS), 2 mM L-glutamine, 100 U/mL penicillin, and 100 μg/mL streptomycin. The pH was maintained at 7.0 to optimize cell growth. Experimental results were derived from four independent replicates ($n = 4$) to ensure reproducibility.

2.4. RNA sequencing analysis

To assess the effects of lutein on rheumatoid arthritis, MH7A cells were cultured in media with or without lutein (10 μM) for 24 h. RNA was extracted using the Easy-BLUE Total RNA Extraction Kit (iNtRON Biotechnology, Korea) and sent to Biotools Co., Ltd. (Taiwan) for RNA sequencing. Sequencing was performed using the NovaSeq 6000 system (Illumina, USA) with a paired-end 150 bp approach. Sequence alignment was conducted using HISAT2, and expression data was normalized using Relative Log Expression (RLE) and Trimmed Mean of M-values (TMM). Differentially expressed genes were identified based on a p-value <0.05 and an absolute log fold change ($|\log_2 FC|$) > 1. Functional enrichment analysis was conducted using GSEA analysis. The RNA sequencing dataset for lutein-treated MH7A cells has been deposited in the NCBI Gene Expression Omnibus (GEO) under accession number GSE301891.

2.5. Quantitative real-time PCR

Following treatment, total RNA was extracted using the Easy-Blue Total RNA Extraction Kit. First-strand cDNA synthesis was performed using the qPCRBIO cDNA Synthesis Kit (PCR Biosystems, London, UK). Gene expression levels of MMP1, MMP3, MMP9, MMP13, and GAPDH were quantified using qPCR with the KAPA SYBR FAST qPCR Master Mix (2×) (Sigma-Aldrich) on a CFX Connect real-time PCR detection system (Bio-Rad, Hercules, CA, USA). Primers were purchased from Sigma-Aldrich, with GAPDH serving as the reference gene. Relative gene expression was analyzed using the $2^{-\Delta\Delta Ct}$ method.

2.6. Western blot analysis

Cell lysates were collected and centrifuged at 13,200 rpm for 15 min after treatment. Proteins were separated using SDS-PAGE (10–15 % gradient gel) and transferred onto 0.45-μm PVDF membranes (Merck, USA). Membranes were blocked with 5 % non-fat milk for 1 h at room temperature, then incubated overnight at 4 °C with primary antibodies (1:1000 dilution). After washing, secondary antibodies (1:10,000 dilution) were applied for 1 h at room temperature. Protein bands were visualized using an enhanced chemiluminescence system (RPN2235, Amersham Cytiva, USA) and detected using a chemiluminescence imaging system (UVP ChemiDOC-It 815, Analytik Jena US, USA).

2.7. Wound healing assay

MH7A cells (2.5×10^4) were cultured in Culture-Inserts (ibidi GmbH, Germany) for 24 h. Inserts were removed to create a wound, and cells were treated with TNF-α and lutein. Wound closure was monitored at 0 and 24 h using a microscope. Images were analyzed using ImageJ software version 1.52a. Experiments were performed in triplicate and repeated at least three times.

2.8. Immunofluorescence

Following treatment, MH7A cells were fixed with 4 % formaldehyde for 15 min, permeabilized with 0.1 % Triton X-100, and blocked with 3 % BSA in PBS. Cells were incubated overnight at 4 °C with primary antibodies (1:200 dilution) targeting p65. After washing, cells were incubated with DyLight488-labeled secondary antibodies and counterstained with DAPI. Fluorescence imaging was performed using a Nikon ECLIPSE Ti microscope.

2.9. Reporter gene assay

MH7A cells (2×10^5) were transfected with an NF-κB promoter reporter plasmid (Promega, Madison, WI, USA) and treated with TNF-α and lutein for 24 h. After incubation, cells were lysed, and luciferase activity was measured using the Luciferase Assay System (Promega) on a microplate luminometer (VICTOR X2, PerkinElmer, MA, USA). To assess pathway involvement, cells were also pretreated with MAPK kinase or NF-κB inhibitors before TNF-α stimulation.

2.10. CAIA induction and treatment

Seven-week-old male athymic nude (Nu/Nu) mice (18–20 g; BioLASCO Co., Ltd., Taipei, Taiwan) were acclimated for one week in a specific pathogen-free facility (12 h light/dark cycle, 22 ± 2 °C, 50 ± 10 % humidity, ad libitum food and water) and randomly assigned ($n = 6$ per group) to three experimental arms. Beginning on Day −7, Groups 1 (healthy control) and 2 (disease control) received 100 μL corn oil by oral gavage once daily, while Group 3 was gavaged with 40 mg/kg lutein dissolved in 100 μL corn oil. On Day 0, arthritis was induced in Groups 2 and 3 by a single intravenous injection of 1 mg of a five-clone anti–type II collagen monoclonal antibody cocktail (Chondrex, Redmond, WA, USA). To potentiate systemic inflammation, these mice received 50 μg lipopolysaccharide in 100 μL PBS via intraperitoneal injection on Day 3 [42]. On Day 22, all animals were euthanized under CO_2 asphyxiation followed by cervical dislocation; hind limbs were harvested, fixed in 10 % neutral buffered formalin, decalcified, and processed for histological and immunohistochemical evaluation of synovial hyperplasia and MMP expression. The CAIA induction rate exceeded 90 % based on macroscopic and histopathological criteria. All procedures conformed to Institutional Animal Care and Use Committee guidelines (Shin Kong Wu Ho-Su Memorial Hospital IACUC No. 112NSTCIACUC007) and were adapted from established CAIA protocols that recapitulate hallmark features of human rheumatoid arthritis [36,43–46]. The selected lutein dose (40 mg/kg/day) was based on previous studies demonstrating its efficacy and safety in murine models of inflammation, oxidative stress, and tissue injury [36,43–46].

2.11. Micro-computed tomography (Micro-CT)

High-resolution micro-CT scanning was performed on isolated trabecular bone samples using a MILabs scanner (Utrecht, Netherlands). Scanning parameters were set at 80 kVp for X-ray energy, with an anode current of 500 μA and an exposure time ranging from 300 to 350 milliseconds per projection over 360° rotation. These settings were selected to enhance bone contrast and minimize beam-hardening artifacts. The acquired data were reconstructed with a Hann filter, achieving a voxel resolution of 5 μm. Three-dimensional images were generated from the projection sets using Osiris imaging software (Geneva, Switzerland).

2.12. Safranin O–fast green staining

Formalin-fixed, paraffin-embedded tissue sections (7 μm thick) were subjected to standard deparaffinization and rehydration protocols. Sections were initially stained with Weigert's iron hematoxylin for 10 min to visualize nuclei, followed by a 10-min rinse in tap water. Subsequently, the sections were immersed in 0.05 % fast green for 5 min and briefly differentiated using 1 % acetic acid for 10–15 s. Cartilage matrix was stained with 0.1 % Safranin O solution for 5 min. After staining, sections were dehydrated through graded ethanol and cleared in xylene before mounting. Stained sections were examined under a light microscope (Nikon ECLIPSE Ti microscope).

2.13. Hematoxylin and eosin staining

Paraffin-embedded tissue sections (7 μm) were deparaffinized, rehydrated, and stained with hematoxylin and eosin. Stained sections were examined under a light microscope.

2.14. Immunohistochemistry

Tissue sections were processed for antigen retrieval and blocking before incubation with primary antibodies against MMP3 and MMP13. After washing, secondary antibodies were applied, and staining was developed using DAB. Slides were counterstained with hematoxylin and analyzed using ImageJ.

2.15. Statistics

Data were expressed as mean ± standard deviation (SD). Statistical analysis was performed using GraphPad Prism 8.0.2. Student's *t*-test was used for two-group comparisons, and one-way ANOVA was applied for multiple comparisons. A p-value <0.05 was considered statistically significant.

3. Results

3.1. Lutein modulates MMP expression and RA-related pathways in synovial cells

To establish a rationale for targeting MMPs in this study, we first analyzed gene expression profiles from two independent GEO datasets (GSE55235 and GSE1919). A total of 87 differentially expressed genes (DEGs) were consistently upregulated in RA synovial tissues compared to healthy controls (Fig. 1A). GO and KEGG enrichment analyses showed that these genes were predominantly involved in extracellular matrix composition and RA-associated pathways (Fig. 1B–C). Among the DEGs, key MMPs were markedly overexpressed in both datasets (Fig. 1D–E), underscoring their central role in joint destruction. Although the role of MMPs in RA is well established, this analysis provides data-driven validation for their selection as molecular targets in our experimental system. To assess the potential of lutein in modulating RA-related gene expression, we performed RNA sequencing of MH7A cells treated with lutein (10 μM, 24 h). Volcano plot and heatmap analyses revealed that lutein treatment significantly downregulated MMP1 and MMP3, as well as several pro-inflammatory mediators including IL6, IL1B, TRAF1, CTSS, and ACP5 (Fig. 1F–G), suggesting a broader anti-inflammatory and anti-osteolytic effect [47–50]. Gene Set Enrichment Analysis (GSEA) further demonstrated that lutein suppressed GO_Inflammatory_Response genes and upregulated GO_Cell_Matrix_Adhesion pathways (Fig. 1H–I), indicating reduced inflammatory signaling and enhanced ECM stability. These findings provided the foundation for subsequent mechanistic studies and in vivo validation.

3.2. Lutein reduces MMP3/13 expression and impairs MH7A cell migration

Building on RNA-seq insights, in vitro experiments were conducted to evaluate lutein's effects on fibroblast-like synoviocytes (FLS). For inflammation induction, cells were stimulated with human recombinant TNF-α (PeproTech, USA). A dose-response assay using 0, 5, and 10 ng/mL TNF-α was initially performed to determine the optimal concentration for MMP induction. Results showed that 5 and 10 ng/mL TNF-α significantly upregulated MMP3 and MMP13 expression (Fig. 2A-B), while higher concentrations caused excessive inflammatory stress and potential cytotoxicity. Based on these observations, 10 ng/mL TNF-α was selected for all subsequent experiments to ensure consistent stimulation without compromising cell viability. In addition, lutein (10 μM) treatment alone markedly downregulated their expression (Fig. 2C). Pre-treatment of MH7A cells with lutein (10 μM) prior to TNF-α (10 ng/mL) stimulation effectively inhibited TNF-α-induced MMP3 and MMP13 expression (Fig. 2D-E). Functional assays demonstrated that lutein (10 μM) significantly impaired TNF-α-induced wound healing and migration of FLS (Fig. 2F), supporting its potential to reduce synovial aggression in RA.

3.3. Lutein suppresses MMP expression and wound healing via inhibition of p38 and ERK activation

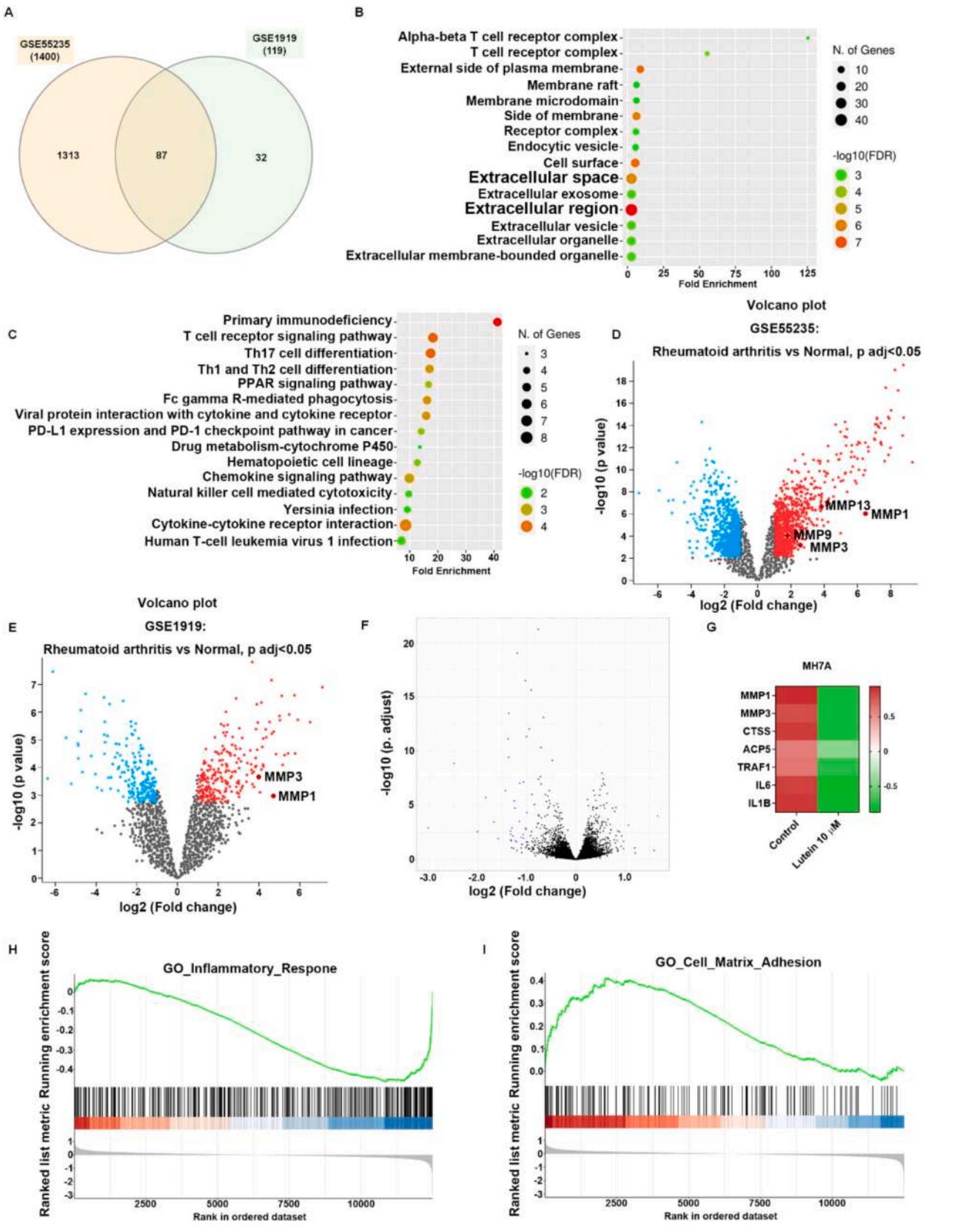
Ingenuity Pathway Analysis (IPA) of RNA-seq data revealed that multiple RA-related signaling pathways—including the Osteoarthritis Pathway, RHOGDI Signaling, RANK Signaling in Osteoclasts, IL-6 Signaling, and Chondrocyte Function in RA were inhibited (Fig. 3A), consistent with in vitro results. MAPK and NF-κB pathways, known contributors to RA progression, were notably suppressed by lutein (Fig. 3B) [51–53]. Further examination of MAPK signaling showed that TNF-α significantly enhanced p38 and ERK phosphorylation, while JNK activation remained unaffected (Fig. 3C). Specific MAPK inhibitors (SB203580 for p38 and PD98059 for ERK) significantly reduced TNF-α-induced MMP3 and MMP13 expression (Fig. 3D-E). Pre-treatment with lutein similarly inhibited p38 and ERK phosphorylation (Fig. 3F), suggesting that lutein attenuates MMP expression by targeting TNF-α-induced MAPK activation, offering a promising therapeutic avenue for RA.

3.4. Lutein suppresses MMP expression and wound healing via p38/ERK/NF-κB signaling

Since NF-κB plays a central role in RA, we investigated its involvement using RNA-seq and IPA analysis, consistent with previous literature [54,55]. TNF-α significantly induced NF-κB p65 phosphorylation (Fig. 4A). NF-κB inhibitors (TPCK and BAY11–7082) markedly reduced TNF-α-induced MMP3 and MMP13 expression (Fig. 4B-C). Furthermore, p38 and ERK inhibitors also diminished TNF-α-induced p65 phosphorylation (Fig. 4D-E). Immunofluorescence analysis showed that lutein, along with p38, ERK, and p65 inhibitors, significantly reduced TNF-α-induced p65 nuclear translocation (Fig. 4F). Luciferase reporter assays confirmed that TNF-α significantly increased NF-κB transcriptional activity, which was significantly suppressed by lutein and MAPK inhibitors (Fig. 4G-H). Additionally, pre-treatment with lutein effectively blocked TNF-α-induced NF-κB activation at multiple levels, including phosphorylation, nuclear translocation, and transcriptional activity (Fig. 4I-K). In Fig. 4K, although NF-κB activity in the TNF-α + lutein group appeared slightly lower than in the lutein-only group, statistical analysis showed no significant difference between these groups. These findings suggest that lutein suppresses MMP3 and MMP13 expression by inhibiting NF-κB activation through the p38/ERK signaling pathway, potentially reducing RA severity.

3.5. Lutein attenuates joint destruction and MMP expression in a CAIA mouse model

To validate our in vitro findings and assess the therapeutic efficacy of lutein in vivo, we employed a collagen antibody-induced arthritis (CAIA) mouse model. Animals were divided into three groups: healthy control, vehicle-treated CAIA, and lutein-treated CAIA (Fig. 5A). Micro-computed tomography (micro-CT) was used to evaluate bone architecture post-treatment. The results revealed that CAIA mice exhibited substantial trabecular bone loss and cortical surface erosion, while lutein treatment markedly preserved bone structure and integrity (Fig. 5B), indicating its potential to prevent inflammatory bone damage. To further assess joint protection, histological analysis was performed on hind limb sections. Safranin O staining showed significant cartilage degradation in the CAIA group, whereas lutein-treated mice retained greater cartilage integrity (Fig. 5C), suggesting that lutein may protect against cartilage matrix breakdown. In addition, hematoxylin and eosin (H&E) staining revealed that lutein significantly reduced synovial membrane thickening—a characteristic feature of rheumatoid arthritis (Fig. 5D). Given the close relationship between synovial proliferation and matrix metalloproteinase (MMP) activity, we next examined MMP3 and MMP13 expression via immunohistochemistry (IHC). Lutein-treated mice showed markedly lower levels of both MMPs in synovial tissues



(caption on next page)

Fig. 1. Lutein modulates MMP expression and RA-related pathways in MH7A cells. (A) Venn diagram of differentially expressed genes (DEGs) upregulated in rheumatoid arthritis (RA) tissues in Gene Expression Omnibus data set 55235 (GSE55235) and GSE1919. mRNA expression levels were normalized using *Z*-score calculations. (B—C) Gene ontology (GO) terms of cellular component (CC) and Kyoto encyclopedia of genes and genomes (KEGG) categories (colour marks false discovery rate (FDR). (D-E) Volcano plot illustrating DEGs in GSE55235 and GSE1919. Significantly upregulated DEGs are shown in red, downregulated DEGs in blue, and non-significant genes in gray. Thresholds for identifying differentially expressed genes were set at adjusted *p*-value <0.05 and $|\log_2 FC| > 1$ for exploratory analysis. (F) Volcano plot illustrating DEGs in MH7A cells treated with lutein (10 μM) for 24 h. Significantly upregulated DEGs are shown in red, downregulated DEGs in blue, and non-significant genes in black. (G) The heatmap displays the expression of extracellular matrix degradation and inflammation-related mRNA in MH7A cells. (H) Gene Set Enrichment Analysis (GSEA) of the GO_Inflammatory_Response gene set in MH7A cells after lutein treatment, showing reduced enrichment of inflammation-related genes. (I) GSEA analysis of the GO_Cell_Matrix_Adhesion gene set in MH7A cells treated with lutein, indicating enhanced cell-matrix adhesion. (For interpretation of the references to colour in this figure legend, the reader is referred to the web version of this article.)

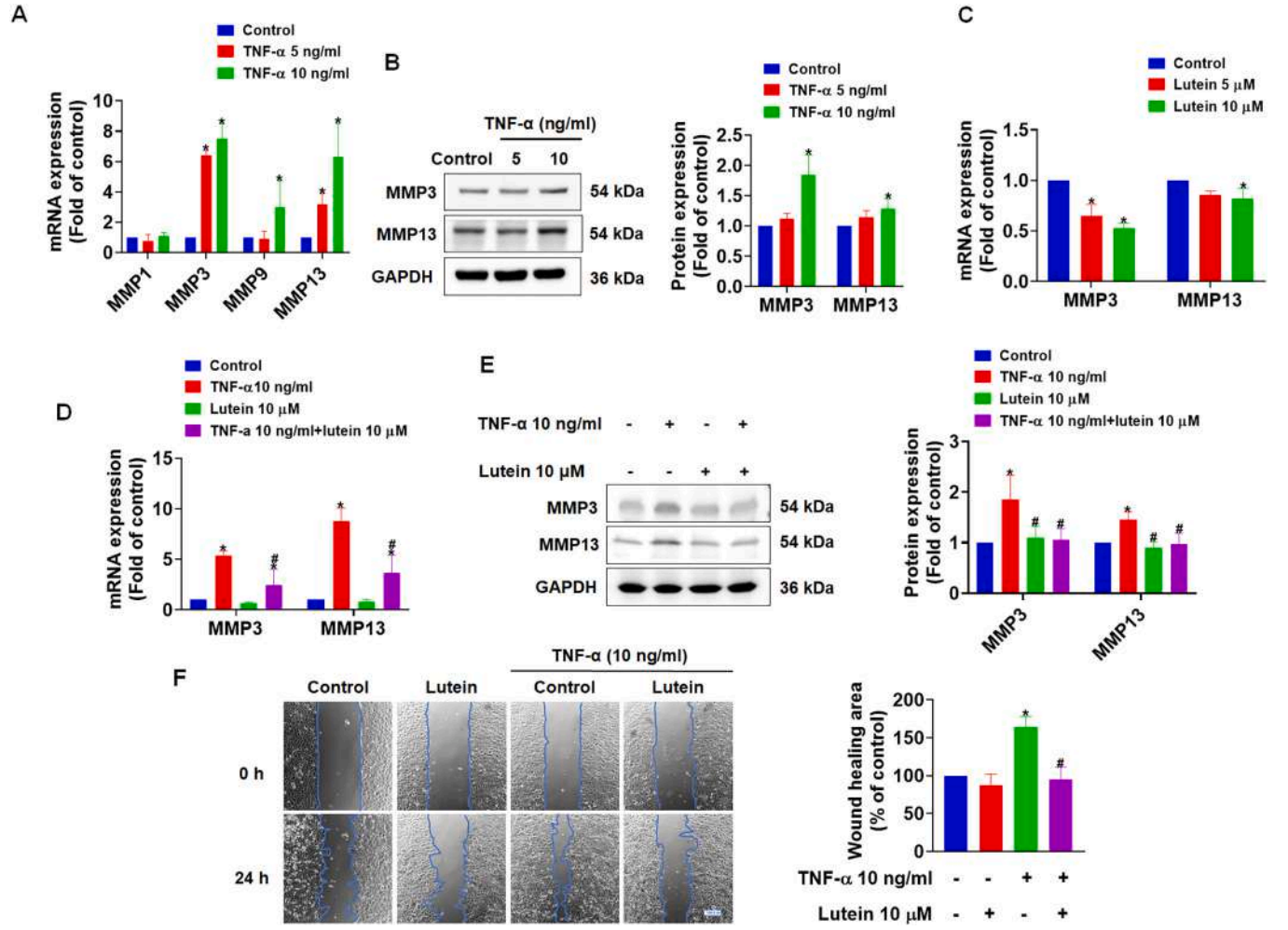


Fig. 2. Lutein suppresses TNF-α-induced MMP expression and attenuates fibroblast-like synoviocyte motility. (A) qPCR analysis of MMP1, MMP3, MMP9, and MMP13 mRNA levels in MH7A cells treated with increasing concentrations of TNF-α (0–10 ng/mL) for 24 h ($n = 4$). (B) Western blot analysis of MMP3 and MMP13 protein levels in MH7A cells treated with TNF-α (0–10 ng/mL) for 24 h (n = 4). (C) qPCR analysis of MMP3 and MMP13 mRNA levels in MH7A cells treated with lutein (0–10 μM) for 24 h (n = 4). (D) qPCR analysis of MMP3 and MMP13 mRNA levels in MH7A cells pre-treated with lutein (0 or 10 μM) for 1 h, followed by TNF-α (0 or 10 ng/mL) stimulation for 24 h (n = 4). (E) Western blot analysis of MMP3 and MMP13 protein levels in MH7A cells pre-treated with lutein (0 or 10 μM) for 1 h, followed by TNF-α stimulation for 24 h (n = 4). (F) Wound healing assay in MH7A cells pre-treated with lutein (0 or 10 μM) for 1 h, followed by TNF-α stimulation for 24 h. Wound closure was quantified at 24 h (n = 4). The scale bar indicates 100 nm. Data are presented as mean ± SD. * $p < 0.05$ vs. control; # $p < 0.05$ vs. TNF-α-only group.

compared to vehicle-treated CAIA mice, which was consistent with our in vitro results (Fig. 5E–F). Quantitative analysis using H-scores confirmed the downregulation of MMP expression following lutein treatment. Collectively, these results indicate that lutein effectively reduces synovial inflammation, cartilage degradation, and bone loss in the CAIA model, supporting its potential as a therapeutic agent for inflammatory arthritis.

4. Discussion

Current therapeutic strategies for rheumatoid arthritis (RA), including disease-modifying antirheumatic drugs (DMARDs), nonsteroidal anti-inflammatory drugs (NSAIDs), and biologic agents, have significantly improved symptom management. However, their limitations, including adverse side effects, high costs, and variable patient responses, underscore the need for novel therapeutic approaches [5–11]. Our study provides compelling evidence supporting the

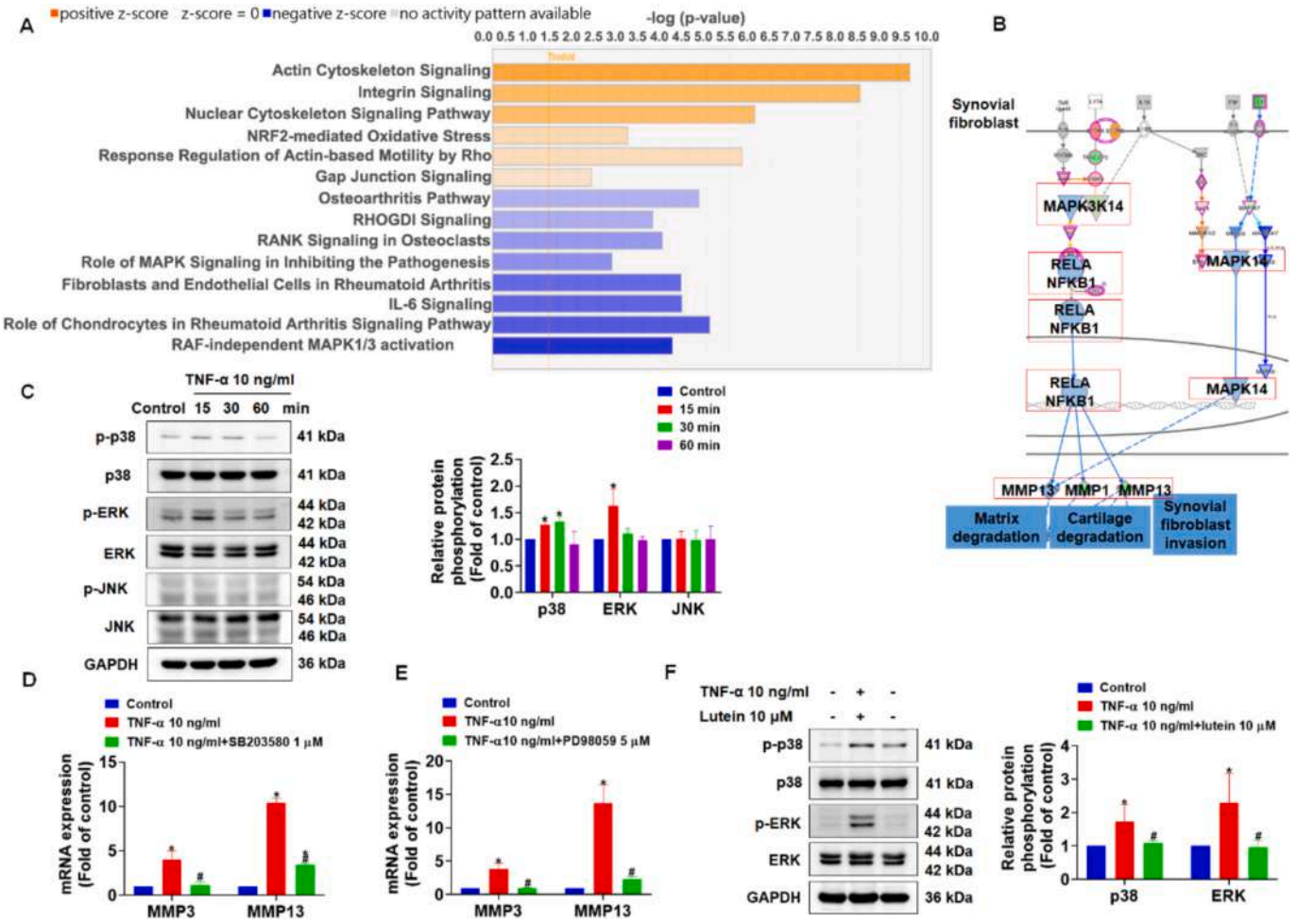


Fig. 3. Lutein inhibits TNF-α-induced p38/ERK activation and reduces MMP expression in MH7A cells. (A) Pathway enrichment analysis using Ingenuity Pathway Analysis (IPA), with Z-scores indicating activation status (blue: downregulated; orange: upregulated). (B) IPA-based mapping of RA-related intracellular signaling pathways. (C) Western blot analysis of MAPK phosphorylation in MH7A cells treated with TNF-α (10 ng/mL) for 0–60 min (n = 4). (D) qPCR analysis of MMP3 and MMP13 mRNA levels in MH7A cells pre-treated with the p38 inhibitor SB203580 (0 or 1 μM) for 1 h, followed by TNF-α stimulation for 24 h (n = 4). (E) qPCR analysis of MMP3 and MMP13 mRNA levels in MH7A cells pre-treated with the ERK inhibitor PD98059 (0 or 5 μM) for 1 h, followed by TNF-α stimulation for 24 h (n = 4). (F) Western blot analysis of p38 and ERK phosphorylation in MH7A cells pre-treated with lutein (0 or 10 μM) for 1 h, followed by TNF-α stimulation for 1 h (n = 4). Data are presented as mean ± SD. * $p < 0.05$ vs. control; # $p < 0.05$ vs. TNF-α-only group. (For interpretation of the references to colour in this figure legend, the reader is referred to the web version of this article.)

potential of lutein as a dietary supplement for RA management. Through a combination of in vitro and in vivo experiments, we demonstrate that lutein modulates key pathogenic mechanisms of RA, thereby attenuating inflammation and joint damage. The GSE database showed that MMPs are involved in regulating extracellular matrix composition and the progression of RA. RNA sequencing analysis of MH7A cells revealed that lutein downregulates critical molecular pathways associated with RA pathogenesis. GSEA indicated significant suppression of GO_Inflammatory_Response, suggesting that lutein reduces RA-related inflammatory activity. Furthermore, pathways associated with ECM maintenance, GO_Cell_Matrix_Adhesion, were positively enriched following lutein treatment, indicating a potential protective effect against joint degradation. These findings were further corroborated by in vitro assays demonstrating that lutein effectively inhibits TNF-α-induced activation of the p38/ERK/NF-κB signaling pathway, leading to reduced expression of MMP3 and MMP13, key mediators of ECM degradation. Consistent results in a CAIA mouse model validate the therapeutic potential of lutein in mitigating RA progression. The present study underscores the potential of lutein as a natural, cost-effective dietary supplement that targets multiple RA-related pathways. Unlike conventional therapies focusing on single targets, lutein demonstrates multi-faceted effects, including anti-inflammatory, antioxidant, and ECM-protective properties. Its ability to suppress MMP production, inhibit MAPK/NF-κB activation, and reduce FLS migration positions it as a promising adjunctive therapy for RA.

RA is a complex autoimmune disease driven by an intricate network of immune cells, cytokines, and signaling pathways. TNF-α, a major pro-inflammatory cytokine secreted by macrophages, fibroblast-like synoviocytes (FLS), and T cells, is pivotal in activating NF-κB, promoting inflammation, cell survival, and proliferation [56]. NF-κB activation in RA leads to the production of reactive oxygen species (ROS) and polarization of M1 macrophages, further exacerbating the disease [57]. FLS, the primary synovial cell type in joint tissues, exhibits an aggressive phenotype in RA, contributing to cartilage destruction, bone erosion, and sustained inflammation [56]. The interplay between FLS, T, and B cells perpetuates the inflammatory microenvironment, amplifying joint damage. A key driver of this process is the upregulation of MMPs, particularly MMP3 and MMP13, which directly mediate ECM breakdown [58]. Consistent with prior studies, our analysis of the GSE55235 dataset confirmed the elevated expression of MMPs in RA synovial tissues, reinforcing their role in disease pathology (Fig. 1A). Our findings suggest that lutein exerts its protective effects by targeting key

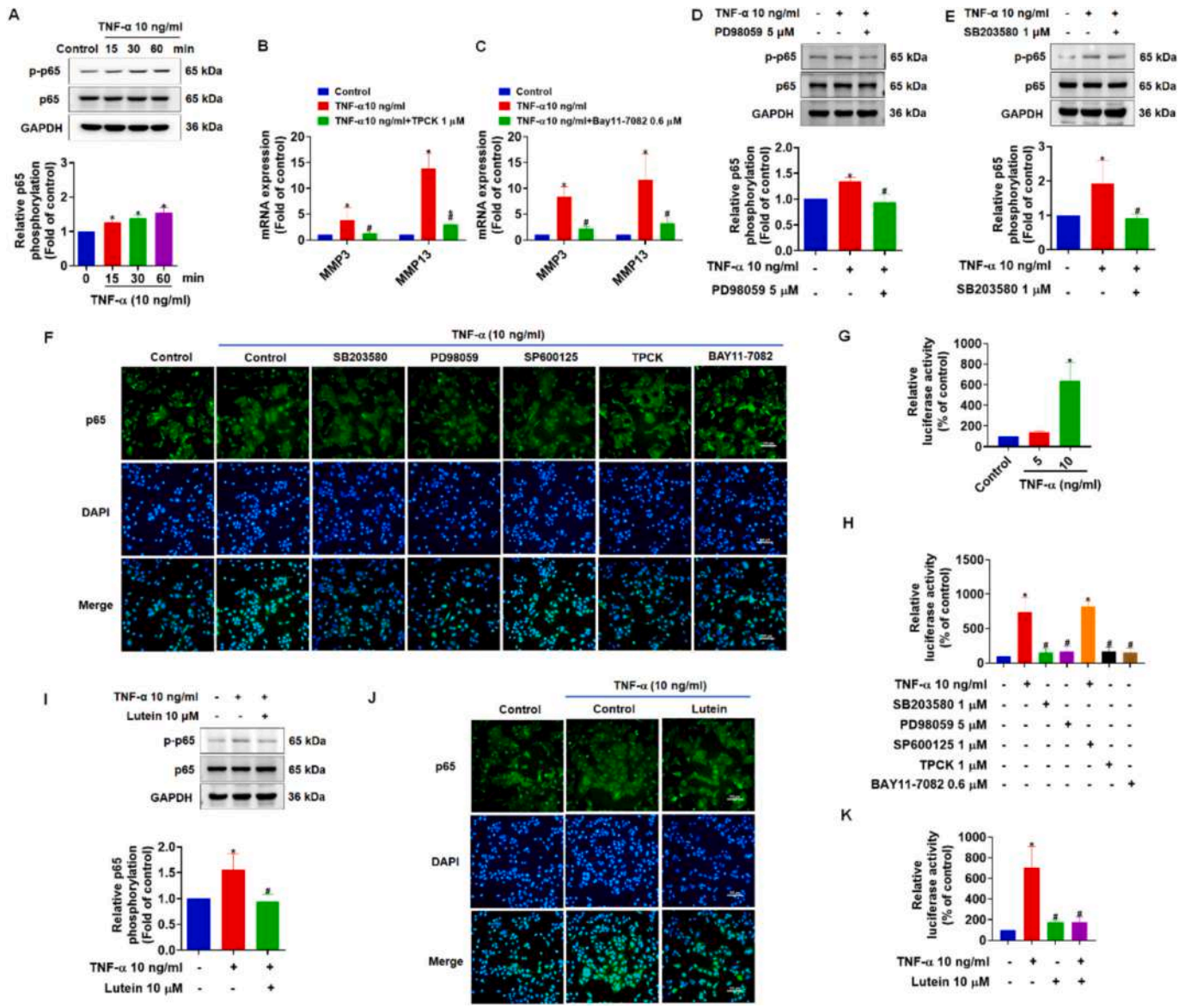


Fig. 4. Lutein inhibits TNF-α-induced NF-κB activation via p38 and ERK pathways in MH7A cells. (A) Western blot analysis of p65 phosphorylation in MH7A cells treated with TNF-α (10 ng/mL) for 0–60 min (n = 4). (B—C) qPCR analysis of MMP3 and MMP13 mRNA levels in MH7A cells pre-treated with p65 inhibitors TPCK (0 or 1 μM) or Bay11–7082 (0 or 0.6 μM) for 1 h, followed by TNF-α stimulation for 24 h (n = 4). (D-E) Western blot analysis of p65 phosphorylation in MH7A cells pre-treated with the ERK inhibitor PD98059 (0 or 5 μM) or the p38 inhibitor SB203580 (E, 0 or 1 μM) for 1 h, followed by TNF-α stimulation for 1 h (n = 4). (F) Immunofluorescence staining of p65 nuclear translocation in MH7A cells pre-treated with p38, ERK, and p65 inhibitors for 1 h, followed by TNF-α stimulation for 2 h. The scale bar indicates 100 μm. (G-H) Luciferase reporter assay for NF-κB transcriptional activity in MH7A cells treated with TNF-α (0–10 ng/mL) for 24 h or pre-treated with p38, ERK, and p65 inhibitors before TNF-α stimulation (n = 4). (I) Western blot analysis of p65 phosphorylation in MH7A cells pre-treated with lutein (0 or 10 μM) for 1 h, followed by TNF-α stimulation for 1 h (n = 4). (J) Immunofluorescence staining of p65 nuclear translocation in MH7A cells pre-treated with lutein for 1 h, followed by TNF-α stimulation for 2 h. The scale bar indicates 100 μm. (K) Luciferase reporter assay for NF-κB transcriptional activity in MH7A cells pre-treated with lutein for 1 h, followed by TNF-α stimulation for 24 h (n = 4). Data are presented as mean ± SD. * $p < 0.05$ vs. control; # $p < 0.05$ vs. TNF-α-only group.

inflammatory pathways that drive MMP upregulation and ECM degradation. Notably, suppressing MMPs, inflammation-related pathways, and ECM degradation following lutein treatment highlights its potential to modulate immune responses in RA.

In MH7A cells, inflammatory cytokines (TNF-α and IL-1β) induce MMP3, MMP9, and MMP13 expression through the MAPK/NF-κB signaling pathway, which is critical for FLS proliferation, migration, and invasion [59–64]. MH7A, an immortalized fibroblast-like synoviocyte (FLS) cell line derived from rheumatoid arthritis synovial tissue, was selected in this study due to its well-characterized responsiveness to pro-inflammatory stimuli such as TNF-α and its suitability for reproducible in vitro assays. While primary FLSs offer high physiological relevance, their limited availability, donor variability, and technical challenges in long-term culture hinder consistent experimental conditions, particularly in transcriptomic and pathway-focused analyses. Thus, the MH7A cell line provided a standardized platform for evaluating lutein's molecular effects. To address translational relevance, our in vivo CAIA mouse model further validated the anti-inflammatory and anti-degradative effects of lutein on joint tissues. Our RNA-seq and Ingenuity Pathway Analysis (IPA) confirmed that lutein downregulates MAPK and NF-κB pathways, leading to reduced FLS invasiveness, ECM degradation, and cartilage destruction (Fig. 3B). Given the central role of the MAPK/NF-κB axis in FLS activation and RA progression, we focused on this pathway to elucidate the anti-inflammatory effects of lutein. In this study, we used TNF-α stimulation to simulate the pro-inflammatory conditions commonly observed in RA. Rather than

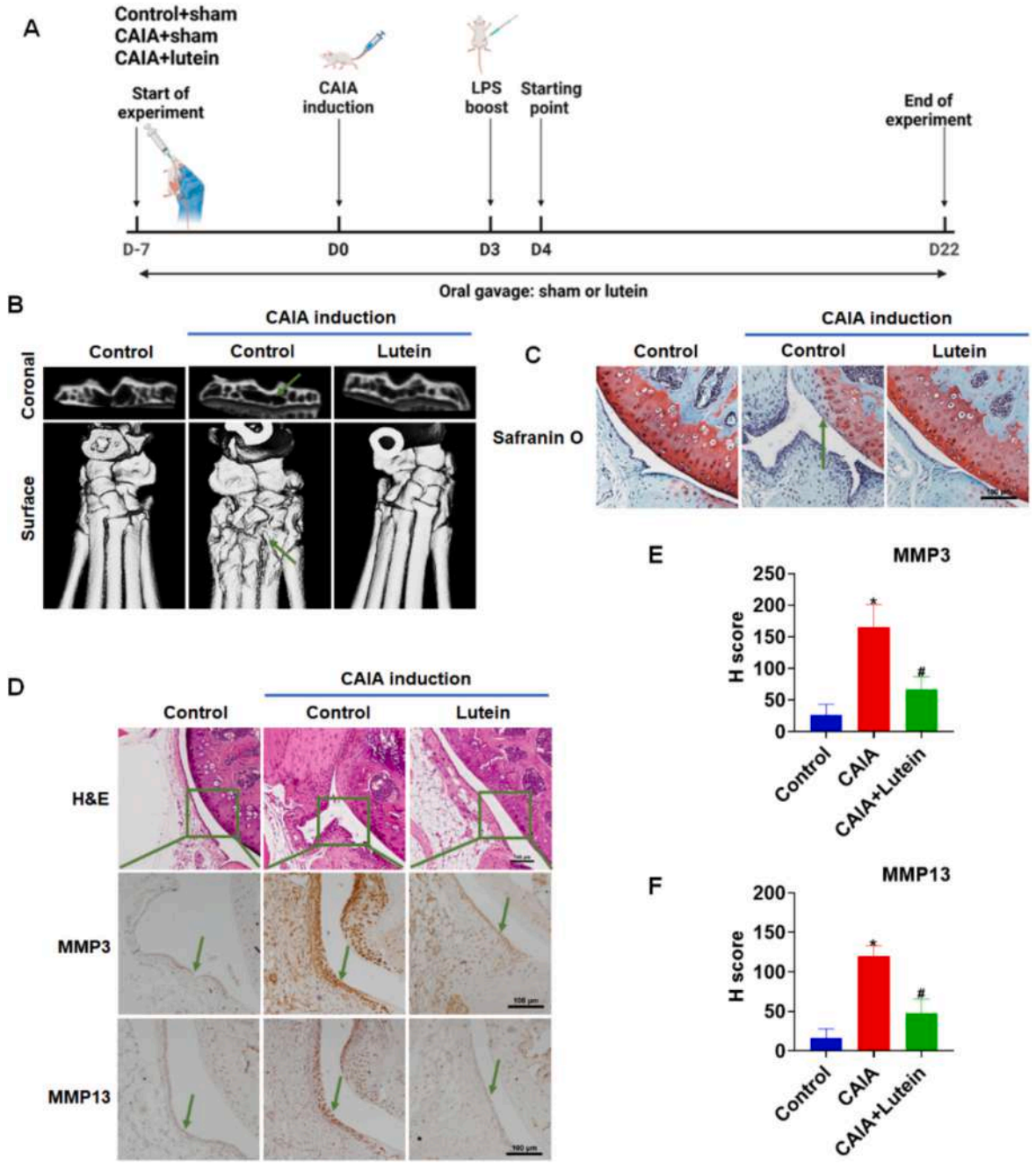


Fig. 5. Lutein reduces synovial thickening and MMP expression in the CAIA mouse model. (A) Schematic flow chart of CAIA model establishment and treatment protocol. Eighteen mice were randomly divided into three groups (n = 6/group): Control, CAIA + Vehicle, and CAIA + Lutein. CAIA was induced via collagen type II antibody cocktail and LPS injection. (B) Representative micro-computed tomography (micro-CT) images displaying coronal and 3D-rendered views of murine femoral bone structures. (C—D) Histological sections of mouse knee joints stained with Safranin O to assess cartilage integrity, alongside immunohistochemical (IHC) staining of synovial tissue to evaluate MMP3 and MMP13 protein expression in the joint microenvironment. The scale bar indicates 100 μm. (E-F) Quantitative assessment of IHC staining intensity using the H-score for MMP3 (E) and MMP13 (F) (n = 4). Data are presented as mean ± SD. * $p < 0.05$ vs. control; # $p < 0.05$ vs. CAIA vehicle-treated group.

directly targeting TNF-α, lutein appears to modulate the intracellular signaling cascades activated downstream of TNF-α stimulation. Our results suggest that lutein exerts anti-inflammatory effects by suppressing TNF-α-induced activation of p38 and ERK, which in turn inhibits NF-κB phosphorylation, nuclear translocation, and transcriptional activity. This cascade ultimately reduces MMP3 and MMP13 expression in MH7A cells. Therefore, lutein likely modulates RA-related inflammatory responses via interference with MAPK/NF-κB signaling, rather than by directly inhibiting TNF-α. Importantly, our in vivo experiments using the CAIA mouse model demonstrated that oral administration of lutein significantly mitigated RA-like joint pathology. Micro-CT imaging revealed that lutein preserved trabecular bone architecture and cortical bone surface integrity, indicating strong anti-erosive effects. Histological staining showed reduced cartilage degeneration and synovial membrane thickening, while immunohistochemistry confirmed the suppression of MMP3 and MMP13 expression in synovial tissues. These observations validate the translational relevance of our in vitro findings and support lutein's dual ability to reduce inflammation and protect structural components of the joint. Together, these results reinforce lutein's potential to serve as an adjunctive treatment strategy targeting

both molecular and morphological hallmarks of RA.

Epidemiological studies have reported that patients with rheumatoid arthritis exhibit significantly lower circulating levels of dietary antioxidants, including carotenoids such as lutein. De Pablo et al. (2007) found that reduced plasma levels of antioxidants were associated with increased cardiovascular risk in RA patients, highlighting the systemic inflammatory burden and potential protective role of carotenoids in RA pathogenesis [65]. Similarly, a prospective study by Hu et al. (2017) demonstrated that higher circulating carotenoid levels were inversely associated with the risk of developing RA among women, suggesting a preventive or modulatory role of these compounds in autoimmune inflammation [66]. Although the anti-inflammatory potential of lutein via suppression of MAPK and NF-κB signaling has been reported in other disease contexts, the current study is the first to demonstrate its therapeutic efficacy in both in vitro and in vivo models of RA. By integrating transcriptomic analysis, functional assays, and histopathological validation, we provide novel evidence that lutein mitigates synovial inflammation, matrix degradation, and joint destruction in RA. These findings, together with epidemiological observations of carotenoid deficiency in RA patients, further support the exploration of lutein as a potential adjunctive or preventive strategy in RA management.

The CAIA mouse model is widely used to investigate RA pathology, enabling histological assessment of synovial tissue changes. This model recapitulates key RA characteristics, including synovial hyperplasia, inflammatory infiltration, and elevated MMP expression [67,68]. Consistent with human RA pathology, CAIA models exhibit increased MMP production, which drives ECM degradation and cartilage destruction. Our histological evaluation revealed that lutein-treated CAIA mice exhibited significantly reduced synovial thickening, a hallmark of RA (Fig. 5D). Furthermore, immunohistochemistry (IHC) confirmed a marked reduction in MMP3 and MMP13 expression, consistent with our in vitro findings (Fig. 5D-F). These results provide compelling in vivo evidence of lutein's therapeutic efficacy in mitigating RA-associated joint destruction.

5. Conclusion

Our findings support the therapeutic potential of lutein in RA treatment. Lutein mitigates key pathogenic mechanisms driving joint destruction by selectively modulating inflammatory and ECM-degrading pathways. The consistency between in vitro and in vivo results highlights the robustness of these findings. Future clinical studies are warranted to further explore lutein's efficacy in RA patients, potentially paving the way for its integration into RA management strategies.

Patient consent for publication

Not applicable.

Use of artificial intelligence tools

Throughout the preparation of this work, the authors utilized Grammarly (https://www.grammarly.com/) to enhance the clarity and linguistic quality of the manuscript. Subsequently, the authors reviewed and edited the content, assuming complete responsibility for the final content of the manuscript.

CRediT authorship contribution statement

Chi-Jen Chang: Writing – original draft, Software, Formal analysis, Data curation, Methodology, Funding acquisition. **Tsung-Ming Chang:** Investigation, Conceptualization, Software, Resources, Project administration. **Ying-Sui Sun:** Funding acquisition, Software, Project administration, Methodology. **Ji-Fan Lin:** Formal analysis, Methodology. **Chiang-Wen Lee:** Investigation, Conceptualization. **Mei-Ling Fang:** Resources, Data curation. **Ju-Fang Liu:** Writing – review & editing, Funding acquisition, Conceptualization.

Ethics approval and consent to participate

Not applicable.

Funding

This work was supported by the Ministry of Science and Technology, Taiwan (NSTC113–2628-B-038-008-MY3, NSTC112–2221-E-038-006-MY3, and NSTC112–2811-E-038-004-MY3), and Shin Kong Wu Ho-Su Memorial Hospital (2021SKHADR010).

Declaration of competing interest

The authors declare that they have no known competing financial interests or personal relationships that could have appeared to influence the work reported in this paper.

Acknowledgement

Not applicable.

Data availability

Data will be made available on request.

References

[1] G.S. Firestein, I.B. McInnes, Immunopathogenesis of rheumatoid arthritis, Immunity 46 (2) (2017) 183–196.
[2] J.S. Smolen, D. Aletaha, I.B. McInnes, Rheumatoid arthritis, Lancet 388 (10055) (2016) 2023–2038.
[3] G.J. Tobon, P. Youinou, A. Saraux, The environment, geo-epidemiology, and autoimmune disease: rheumatoid arthritis, J. Autoimmun. 35 (1) (2010) 10–14.
[4] E. Myasoedova, C.S. Crowson, H.M. Kremers, T.M. Therneau, S.E. Gabriel, Is the incidence of rheumatoid arthritis rising?: results from Olmsted County, Minnesota, 1955-2007, Arthritis Rheum. 62 (6) (2010) 1576–1582.
[5] G.R. Burmester, J.E. Pope, Novel treatment strategies in rheumatoid arthritis, Lancet 389 (10086) (2017) 2338–2348.
[6] M. Abbasi, M.J. Mousavi, S. Jamalzehi, R. Alimohammadi, M.H. Bezvan, H. Mohammadi, S. Aslani, Strategies toward rheumatoid arthritis therapy; the old and the new, J. Cell. Physiol. 234 (7) (2019) 10018–10031.
[7] M.E. Weinblatt, Methotrexate in rheumatoid arthritis: a quarter century of development, Trans. Am. Clin. Climatol. Assoc. 124 (2013) 16–25.
[8] J.L. Nam, K. Takase-Minegishi, S. Ramiro, K. Chatzidionysiou, J.S. Smolen, D. van der Heijde, J.W. Bijlsma, G.R. Burmester, M. Dougados, M. Scholte-Voshaar, R. van Vollenhoven, R. Landewe, Efficacy of biological disease-modifying antirheumatic drugs: a systematic literature review informing the 2016 update of the EULAR recommendations for the management of rheumatoid arthritis, Ann. Rheum. Dis. 76 (6) (2017) 1113–1136.
[9] A.E. van Ede, R.F. Laan, M.J. Rood, T.W. Huizinga, M.A. van de Laar, C.J. van Denderen, T.A. Westgeest, T.C. Romme, D.J. de Rooij, M.J. Jacobs, T.M. de Boo, G. J. van der Wilt, J.L. Severens, M. Hartman, P.F. Krabbe, B.A. Dijkmans, F. C. Breedveld, L.B. van de Putte, Effect of folic or folinic acid supplementation on the toxicity and efficacy of methotrexate in rheumatoid arthritis: a forty-eight week, multicenter, randomized, double-blind, placebo-controlled study, Arthritis Rheum. 44 (7) (2001) 1515–1524.
[10] D. Aletaha, J.S. Smolen, Diagnosis and management of rheumatoid arthritis: a review, JAMA 320 (13) (2018) 1360–1372.
[11] E.G. Favalli, M.G. Raimondo, A. Becciolini, C. Crotti, M. Biggioggero, R. Caporali, The management of first-line biologic therapy failures in rheumatoid arthritis: current practice and future perspectives, Autoimmun. Rev. 16 (12) (2017) 1185–1195.
[12] C.G. Wilson, J.F. Nishimuta, M.E. Levenston, Chondrocytes and meniscal fibrochondrocytes differentially process aggrecan during de novo extracellular matrix assembly, Tissue Eng. Part A 15 (7) (2009) 1513–1522.
[13] H. Nagase, R. Visse, G. Murphy, Structure and function of matrix metalloproteinases and TIMPs, Cardiovasc. Res. 69 (3) (2006) 562–573.
[14] N. Mu, J. Gu, T. Huang, C. Zhang, Z. Shu, M. Li, Q. Hao, W. Li, W. Zhang, J. Zhao, Y. Zhang, L. Huang, S. Wang, X. Jin, X. Xue, W. Zhang, Y. Zhang, A novel NF-kappaB/YY1/microRNA-10a regulatory circuit in fibroblast-like synoviocytes regulates inflammation in rheumatoid arthritis, Sci. Rep. 6 (2016) 20059.
[15] D.S. Amarasekara, H. Yun, S. Kim, N. Lee, H. Kim, J. Rho, Regulation of osteoclast differentiation by cytokine networks, Immune Netw. 18 (1) (2018) e8.
[16] C.B. Little, A. Barai, D. Burkhardt, S.M. Smith, A.J. Fosang, Z. Werb, M. Shah, E. W. Thompson, Matrix metalloproteinase 13-deficient mice are resistant to

osteoarthritic cartilage erosion but not chondrocyte hypertrophy or osteophyte development, Arthritis Rheum. 60 (12) (2009) 3723–3733.
[17] M. Wolf, I. Maltseva, S.M. Clay, P. Pan, A. Gajjala, M.F. Chan, Effects of MMP12 on cell motility and inflammation during corneal epithelial repair, Exp. Eye Res. 160 (2017) 11–20.
[18] D. Elhaj Mahmoud, W. Kaabachi, N. Sassi, A. Mokhtar, L. Ben Ammar, S. Rekik, L. Tarhouni, M. Kallel-Sellami, E. Cheour, L. Laadhar, Expression of extracellular matrix components and cytokine receptors in human fibrocytes during rheumatoid arthritis, Connect. Tissue Res. 62 (6) (2021) 720–731.
[19] V.W. van Hinsbergh, M.A. Engelse, P.H. Quax, Pericellular proteases in angiogenesis and vasculogenesis, Arterioscler. Thromb. Vasc. Biol. 26 (4) (2006) 716–728.
[20] E.H. Noss, M.B. Brenner, The role and therapeutic implications of fibroblast-like synoviocytes in inflammation and cartilage erosion in rheumatoid arthritis, Immunol. Rev. 223 (2008) 252–270.
[21] H. Yang, C. Liu, X. Lin, X. Li, S. Zeng, Z. Gong, Q. Xu, D. Li, N. Li, Wogonin inhibits the migration and invasion of fibroblast-like synoviocytes by targeting PI3K/AKT/NF-kappaB pathway in rheumatoid arthritis, Arch. Biochem. Biophys. 755 (2024) 109965.
[22] Y. Huang, Y. Peng, H. Li, C. Li, Y. Wu, X. Wang, J. Chang, C. Miao, Wilforine inhibits rheumatoid arthritis pathology through the Wnt11/beta-catenin signaling pathway axis, Arthritis Res. Ther. 25 (1) (2023) 243.
[23] K. Kaneshiro, Y. Sakai, K. Suzuki, K. Uchida, K. Tateishi, Y. Terashima, Y. Kawasaki, N. Shibanuma, K. Yoshida, A. Hashiramoto, Interleukin-6 and tumour necrosis factor-alpha cooperatively promote cell cycle regulators and proliferate rheumatoid arthritis fibroblast-like synovial cells, Scand. J. Rheumatol. 48 (5) (2019) 353–361.
[24] Y.H. Wang, P. Gao, Y.Q. Wang, L.Z. Xu, K.W. Zeng, P.F. Tu, Small-molecule targeting PKM2 provides a molecular basis of lactylation-dependent fibroblast-like synoviocytes proliferation inhibition against rheumatoid arthritis, Eur. J. Pharmacol. 972 (2024) 176551.
[25] U. Muller-Ladner, J. Kriegsmann, B.N. Franklin, S. Matsumoto, T. Geiler, R.E. Gay, S. Gay, Synovial fibroblasts of patients with rheumatoid arthritis attach to and invade normal human cartilage when engrafted into SCID mice, Am. J. Pathol. 149 (5) (1996) 1607–1615.
[26] X. Li, R.R. Holt, C.L. Keen, L.S. Morse, A.M. Zivkovic, G. Yiu, R.M. Hackman, Potential roles of dietary zeaxanthin and lutein in macular health and function, Nutr. Rev. 81 (6) (2023) 670–683.
[27] E.J. Johnson, Role of lutein and zeaxanthin in visual and cognitive function throughout the lifespan, Nutr. Rev. 72 (9) (2014) 605–612.
[28] W. Ba, W. Xu, Z. Deng, B. Zhang, L. Zheng, H. Li, The antioxidant and anti-inflammatory effects of the Main carotenoids from tomatoes via Nrf2 and NF-kappaB signaling pathways, Nutrients 15 (21) (2023) 4652.
[29] N.T. Costa, T.M.V. Iriyoda, D.F. Alfieri, A.N.C. Simao, I. Dichi, Influence of disease-modifying antirheumatic drugs on oxidative and nitrosative stress in patients with rheumatoid arthritis, Inflammopharmacology 26 (5) (2018) 1151–1164.
[30] M.J. Smallwood, A. Nissim, A.R. Knight, M. Whiteman, R. Haigh, P.G. Winyard, Oxidative stress in autoimmune rheumatic diseases, Free Radic. Biol. Med. 125 (2018) 3–14.
[31] H.M. Khojah, S. Ahmed, M.S. Abdel-Rahman, A.B. Hamza, Reactive oxygen and nitrogen species in patients with rheumatoid arthritis as potential biomarkers for disease activity and the role of antioxidants, Free Radic. Biol. Med. 97 (2016) 285–291.
[32] T. Yamada, M.M. Steinz, E. Kenne, J.T. Lanner, Muscle weakness in rheumatoid arthritis: the role of ca(2+) and free radical signaling, EBioMedicine 23 (2017) 12–19.
[33] T. Okamoto, T. Akaike, T. Sawa, Y. Miyamoto, A. van der Vliet, H. Maeda, Activation of matrix metalloproteinases by peroxynitrite-induced protein S-glutathiolation via disulfide S-oxide formation, J. Biol. Chem. 276 (31) (2001) 29596–29602.
[34] S. Viappiani, A.C. Nicolescu, A. Holt, G. Sawicki, B.D. Crawford, H. Leon, T. van Mulligen, R. Schulz, Activation and modulation of 72kDa matrix metalloproteinase-2 by peroxynitrite and glutathione, Biochem. Pharmacol. 77 (5) (2009) 826–834.
[35] Y. Du, Q. Wang, N. Tian, M. Lu, X.L. Zhang, S.M. Dai, Knockdown of nrf2 exacerbates TNF-alpha-induced proliferation and invasion of rheumatoid arthritis fibroblast-like synoviocytes through activating JNK pathway, J. Immunol. Res. 2020 (2020) 6670464.
[36] Y.Q. Qiao, P.F. Jiang, Y.Z. Gao, Lutein prevents osteoarthritis through Nrf2 activation and downregulation of inflammation, Arch. Med. Sci. 14 (3) (2018) 617–624.
[37] H. Heberle, G.V. Meirelles, F.R. da Silva, G.P. Telles, R. Minghim, InteractiVenn: a web-based tool for the analysis of sets through Venn diagrams, BMC Bioinformatics 16 (1) (2015) 169.
[38] S.X. Ge, D. Jung, R. Yao, ShinyGO: a graphical gene-set enrichment tool for animals and plants, Bioinformatics 36 (8) (2020) 2628–2629.
[39] M. Kanehisa, M. Furumichi, Y. Sato, M. Ishiguro-Watanabe, M. Tanabe, KEGG: integrating viruses and cellular organisms, Nucleic Acids Res. 49 (D1) (2021) D545–D551.
[40] W. Luo, C. Brouwer, Pathview: an R/Bioconductor package for pathway-based data integration and visualization, Bioinformatics 29 (14) (2013) 1830–1831.
[41] T. Barrett, S.E. Wilhite, P. Ledoux, C. Evangelista, I.F. Kim, M. Tomashevsky, K. A. Marshall, K.H. Phillippy, P.M. Sherman, M. Holko, A. Yefanov, H. Lee, N. Zhang, C.L. Robertson, N. Serova, S. Davis, A. Soboleva, NCBI GEO: archive for functional genomics data sets–update, Nucleic Acids Res. 41 (Database issue) (2013) D991–D995.
[42] J.S. Park, D. Lee, S. Yang, H.Y. Jeong, H.S. Na, K.H. Cho, J. Choi, H. Koo, M.L. Cho, S.H. Park, Methotrexate-loaded nanoparticles ameliorate experimental model of autoimmune arthritis by regulating the balance of interleukin-17-producing T cells and regulatory T cells, J. Transl. Med. 20 (1) (2022) 85.
[43] Y. Chen, L. Wang, S. Huang, J. Ke, Q. Wang, Z. Zhou, W. Chang, Lutein attenuates angiotensin II- induced cardiac remodeling by inhibiting AP-1/IL-11 signaling, Redox Biol. 44 (2021) 102020.
[44] Y.J. Ahn, H. Kim, Lutein as a modulator of oxidative stress-mediated inflammatory diseases, Antioxidants (Basel) 10 (9) (2021) 1448.
[45] Y. Zhang, H. Ding, L. Xu, S. Zhao, S. Hu, A. Ma, Y. Ma, Lutein can alleviate oxidative stress, inflammation, and apoptosis induced by excessive alcohol to ameliorate reproductive damage in male rats, Nutrients 14 (12) (2022) 2385.
[46] R. Pap, E. Pandur, G. Janosa, K. Sipos, T. Nagy, A. Agocs, J. Deli, Lutein decreases inflammation and oxidative stress and prevents Iron accumulation and lipid peroxidation at glutamate-induced neurotoxicity, Antioxidants (Basel) 11 (11) (2022) 2269.
[47] K. Yokota, K. Sato, T. Miyazaki, Y. Aizaki, S. Tanaka, M. Sekikawa, N. Kozu, Y. Kadono, H. Oda, T. Mimura, Characterization and function of tumor necrosis factor and Interleukin-6-induced osteoclasts in rheumatoid arthritis, Arthritis Rheumatol. 73 (7) (2021) 1145–1154.
[48] T. Cheng, J. Wu, Y. Xu, C. Liu, H. Zhang, M. Wang, CD40/TRAF1 decreases synovial cell apoptosis in patients with rheumatoid arthritis through JNK/NF-kappaB pathway, J. Bone Miner. Metab. 40 (5) (2022) 819–828.
[49] D. Zisman, H. Sabtan, M.M. Rahat, E. Simanovich, A. Haddad, T. Gazitt, J. Feld, G. Slobodin, A. Kibari, M. Elias, M.A. Rahat, Tofacitinib regulates Endostatin via effects on CD147 and Cathepsin S, Int. J. Mol. Sci. 25 (13) (2024) 7267.
[50] T. Konno, H. Murachi, K. Otsuka, Y. Kimura, C. Sampei, Y. Arasaki, Y. Kohara, T. Hayata, Ctdnep1 phosphatase is required for negative regulation of RANKL-induced osteoclast differentiation in RAW264.7 cells, Biochem. Biophys. Res. Commun. 719 (2024) 150063.
[51] F. Liu, X.X. Feng, S.L. Zhu, H.Y. Huang, Y.D. Chen, Y.F. Pan, R.R. June, S.G. Zheng, J.L. Huang, Sonic hedgehog signaling pathway mediates proliferation and migration of fibroblast-like synoviocytes in rheumatoid arthritis via MAPK/ERK signaling pathway, Front. Immunol. 9 (2018) 2847.
[52] H. Du, X. Zhang, Y. Zeng, X. Huang, H. Chen, S. Wang, J. Wu, Q. Li, W. Zhu, H. Li, T. Liu, Q. Yu, Y. Wu, L. Jie, A novel phytochemical, DIM, inhibits proliferation, migration, invasion and TNF-alpha induced inflammatory cytokine production of synovial fibroblasts from rheumatoid arthritis patients by targeting MAPK and AKT/mTOR signal pathway, Front. Immunol. 10 (2019) 1620.
[53] T. Behl, T. Upadhyay, S. Singh, S. Chigurupati, A.M. Alsubayiel, V. Mani, C. Vargas-De-La-Cruz, D. Uivarosan, C. Bustea, C. Sava, M. Stoicescu, A.F. Radu, S.G. Bungau, Polyphenols targeting MAPK mediated oxidative stress and inflammation in rheumatoid arthritis, Molecules 26 (21) (2021) 6570.
[54] E.R. Puppala, S. Jain, P. Saha, M. Rachamalla, S. Np, S.S. Yalamarthi, M. Abubakar, A. Chaudhary, D. Chamundeswari, M. Usn, J.K. Gangasani, V.G.M. Naidu, Perillyl alcohol attenuates rheumatoid arthritis via regulating TLR4/NF-kappaB and Keap1/Nrf2 signaling pathways: a comprehensive study onin-vitro and in-vivo experimental models, Phytomedicine : international journal of phytotherapy and phytopharmacology 97 (2022) 153926.
[55] G.S. El-Tanbouly, R.S. Abdelrahman, Novel anti-arthritic mechanisms of trans-cinnamaldehyde against complete Freund's adjuvant-induced arthritis in mice: involvement of NF-small ka, CyrillicB/TNF-alpha and IL-6/IL-23/ IL-17 pathways in the immuno-inflammatory responses, Inflammopharmacology 30 (5) (2022) 1769–1780.
[56] H. Okamoto, T.P. Cujec, H. Yamanaka, N. Kamatani, Molecular aspects of rheumatoid arthritis: role of transcription factors, FEBS J. 275 (18) (2008) 4463–4470.
[57] Y. Li, Q. Liang, L. Zhou, Y. Cao, J. Yang, J. Li, J. Liu, J. Bi, Y. Liu, An ROS-responsive artesunate prodrug nanosystem co-delivers dexamethasone for rheumatoid arthritis treatment through the HIF-1alpha/NF-kappaB cascade regulation of ROS scavenging and macrophage repolarization, Acta Biomater. 152 (2022) 406–424.
[58] C. Shen, M. Xu, S. Xu, S. Zhang, W. Lin, H. Li, S. Zeng, Q. Qiu, L. Liang, Y. Xiao, H. Xu, Myricitrin inhibits fibroblast-like synoviocyte-mediated rheumatoid synovial inflammation and joint destruction by targeting AIM2, Front. Pharmacol. 13 (2022) 905376.
[59] Q. Geng, Q. Wei, S. Wang, H. Qi, Q. Zhu, X. Liu, X. Shi, S. Wen, Physcion 8-O-beta-glucopyranoside extracted from Polygonum cuspidatum exhibits anti-proliferative and anti-inflammatory effects on MH7A rheumatoid arthritis-derived fibroblast-like synoviocytes through the TGF-beta/MAPK pathway, Int. J. Mol. Med. 42 (2) (2018) 745–754.
[60] Y. Zhang, L. Wang, L. Bai, R. Jiang, J. Wu, Y. Li, Ebosin attenuates the inflammatory responses induced by TNF-alpha through inhibiting NF-kappaB and MAPK pathways in rat fibroblast-like synoviocytes, J. Immunol. Res. 2022 (2022) 9166370.
[61] X. Gao, X. Kang, H. Lu, E. Xue, R. Chen, J. Pan, J. Ma, Piceatannol suppresses inflammation and promotes apoptosis in rheumatoid arthritis-fibroblast-like synoviocytes by inhibiting the NF-kappaB and MAPK signaling pathways, Mol. Med. Rep. 25 (5) (2022) 180.
[62] Y. Shen, L. Teng, Y. Qu, J. Liu, X. Zhu, S. Chen, L. Yang, Y. Huang, Q. Song, Q. Fu, Anti-proliferation and anti-inflammation effects of corilagin in rheumatoid arthritis by downregulating NF-kappaB and MAPK signaling pathways, J. Ethnopharmacol. 284 (2022) 114791.
[63] Z. Wang, J. Li, J. Zhang, X. Xie, Sodium tanshinone IIA sulfonate inhibits proliferation, migration, invasion and inflammation in rheumatoid arthritis fibroblast-like synoviocytes, Int. Immunopharmacol. 73 (2019) 370–378.

[64] D. Pan, N. Li, Y. Liu, Q. Xu, Q. Liu, Y. You, Z. Wei, Y. Jiang, M. Liu, T. Guo, X. Cai, X. Liu, Q. Wang, M. Liu, X. Lei, M. Zhang, X. Zhao, C. Lin, Kaempferol inhibits the migration and invasion of rheumatoid arthritis fibroblast-like synoviocytes by blocking activation of the MAPK pathway, Int. Immunopharmacol. 55 (2018) 174–182.
[65] P. De Pablo, T. Dietrich, E.W. Karlson, Antioxidants and other novel cardiovascular risk factors in subjects with rheumatoid arthritis in a large population sample, Arthritis Rheum. 57 (6) (2007) 953–962.
[66] Y. Hu, J. Cui, J.A. Sparks, S. Malspeis, K.H. Costenbader, E.W. Karlson, B. Lu, Circulating carotenoids and subsequent risk of rheumatoid arthritis in women, Clin. Exp. Rheumatol. 35 (2) (2017) 309–312.
[67] L.N. Kirpotina, I.A. Schepetkin, D. Hammaker, A. Kuhs, A.I. Khlebnikov, M. T. Quinn, Therapeutic effects of Tryptanthrin and Tryptanthrin-6-oxime in models of rheumatoid arthritis, Front. Pharmacol. 11 (2020) 1145.
[68] Y. Takashima, S. Hayashi, K. Fukuda, T. Maeda, M. Tsubosaka, T. Kamenaga, K. Kikuchi, M. Fujita, Y. Kuroda, S. Hashimoto, N. Nakano, T. Matsumoto, R. Kuroda, Susceptibility of cyclin-dependent kinase inhibitor 1-deficient mice to rheumatoid arthritis arising from interleukin-1beta-induced inflammation, Sci. Rep. 11 (1) (2021) 12516.

Check for updates

Wiley
Journal of Food Biochemistry
Volume 2025, Article ID 9954087, 17 pages
https://doi.org/10.1155/jfbc/9954087

WILEY

Research Article

Protective Effect of Lutein in Cisplatin-Induced Intestinal Barrier Damage by Restoring ZO-1 Expression

Chi-Jen Chang,[1,2] Tsung-Ming Chang,[3] Ying-Sui Sun,[3] Ji-Fan Lin,[4] Chiang-Wen Lee,[5,6] Mei-Ling Fang,[7,8] and Ju-Fang Liu [4,9,10]

[1]*School of Medicine, Fu Jen Catholic University, Taipei 24205, Taiwan*
[2]*Division of Pediatric Surgery, Shin Kong Wu Ho-Su Memorial Hospital, Taipei 11101, Taiwan*
[3]*School of Dental Technology, College of Oral Medicine, Taipei Medical University, Taipei 11031, Taiwan*
[4]*Translational Medicine Center, Shin Kong Wu Ho-Su Memorial Hospital, Taipei 11101, Taiwan*
[5]*Department of Nursing, Division of Basic Medical Sciences, and Chronic Diseases and Health Promotion Research Center, Chang Gung University of Science and Technology, Chiayi 61363, Taiwan*
[6]*Department of Respiratory Care, Chang Gung University of Science and Technology, Chiayi 61363, Taiwan*
[7]*Center for Environmental Toxin and Emerging-Contaminant Research, Cheng Shiu University, Kaohsiung 83347, Taiwan*
[8]*Super Micro Research and Technology Center, Cheng Shiu University, Kaohsiung 83347, Taiwan*
[9]*School of Oral Hygiene, College of Oral Medicine, Taipei Medical University, Taipei 11031, Taiwan*
[10]*Department of Medical Research, China Medical University Hospital, China Medical University, Taichung 40402, Taiwan*

Correspondence should be addressed to Ju-Fang Liu; jufangliu@tmu.edu.tw

Received 26 January 2025; Revised 9 October 2025; Accepted 11 November 2025

Academic Editor: Irfan Ahmad

Copyright © 2025 Chi-Jen Chang et al. Journal of Food Biochemistry published by John Wiley & Sons Ltd. This is an open access article under the terms of the Creative Commons Attribution License, which permits use, distribution and reproduction in any medium, provided the original work is properly cited.

Cisplatin is a commonly used chemotherapy medication that damages the DNA of cancer cells; however, the nonselective toxic damage that it causes to both cancerous and normal cells leads to adverse side effects, such as inflammation of the intestinal mucosa. Intestinal inflammation reduces zonula occluden-1 (ZO-1) expression and impairs the integrity of tight junctions, resulting in intestinal barrier dysfunction. Lutein, a carotenoid with anti-inflammatory effects, has been proven beneficial in preventing eye diseases; however, whether lutein can ameliorate cisplatin-induced damage to intestinal epithelial cells remains unclear. This study thus investigated the protective effects of lutein against cisplatin-induced damage in normal IEC-6 rat small intestine epithelial cells. Cisplatin treatment reduced ZO-1 mRNA and protein levels without significantly affecting other junction proteins and aquaporins and suppressed wound healing capacity. Furthermore, cisplatin-induced intestinal barrier damage was linked to the activation of the p38 and ERK pathways, which promoted nuclear factor κ-light-chain-enhancer of activated B cells (NF-κB) nuclear translocation and increased its transcriptional activity. Importantly, pretreatment with lutein significantly reversed the suppressive effects of cisplatin on ZO-1 expression and improved wound healing by inhibiting the activation of p38 and ERK, as well as the transcriptional activity of NF-κB. These findings indicate that lutein protects against cisplatin-induced intestinal barrier damage. These insights support the potential use of lutein as a nutritional supplement to alleviate the gastrointestinal side effects of cisplatin chemotherapy.

Keywords: cisplatin; intestinal epithelial cells; intestinal mucosal barrier; lutein; NF-κB; ZO-1

1. Introduction

Cisplatin is a platinum-based chemotherapeutic agent widely used in the treatment of various solid tumors, but its clinical use is often limited by dose-dependent toxicities, especially gastrointestinal side effects such as intestinal mucositis. Among chemotherapeutic agents, cisplatin is remarkable due to its broad efficacy against a wide array of

cancers, including head and neck, esophageal, bladder, testicular, ovarian, uterine, cervical, breast, stomach, non–small cell lung, and small-cell lung cancers [1]. Cisplatin exerts its therapeutic effect by crosslinking purine bases within DNA, thereby disrupting DNA synthesis and cell division, especially in rapidly proliferating cells. Despite its effectiveness, the clinical application of cisplatin is hindered by its nonselective mechanism, i.e., damage to both cancerous and healthy cells, which results in serious side effects such as gastrointestinal mucositis, myelosuppression, and nephrotoxicity [2]. During chemotherapy, approximately 40% of patients undergoing standard-dose treatment and 100% of patients undergoing high-dose treatment experience damage to the intestinal mucosal barrier [3]. Intestinal mucositis occurs in 20%–40% of chemotherapy patients [4, 5]. Damage to gastrointestinal cells can also result in diarrhea, vomiting, and gastrointestinal mucositis [6, 7], impacting nutrient absorption and digestion and leading to nutritional deficiencies [8]. Intestinal barrier damage exacerbates the progression of mucositis by increasing permeability and promoting inflammatory responses, further compromising the integrity of the gastrointestinal tract during chemotherapy.

Intestinal epithelial cells construct a tight intercellular barrier to maintain water and solute balance. The barrier integrity is crucial for allowing the selective passage of vital ions, nutrients, and water. Intestinal epithelial cells are also an important barrier for preventing the infiltration of bacterial toxins and pathogens [9]. These functions are primarily facilitated by epithelial tight junction proteins and aquaporins (AQPs) [10], which play pivotal roles in minimizing the spaces between cells and significantly restricting the movement of hydrophilic molecules. Tight junctions consist of an intricate network of transmembrane and cytosolic proteins, such as occludins, claudins, and zonula occludens (ZOs) [11]. Interactions among these proteins connect with the cytoskeleton to create a complex structure. Loss of integrity of this barrier increases permeability, and this weakening allows for the invasion of pathogens and entry of immune cells, ultimately exacerbating inflammation [12, 13]. Among these junctional proteins, zonula occludens-1 (ZO-1) is a scaffolding protein that anchors transmembrane proteins to the actin cytoskeleton and is considered critical in maintaining junctional stability.

Several studies have reported that cisplatin treatment leads to a reduction in ZO-1 expression, contributing to epithelial barrier disruption. Notably, Liu et al. demonstrated that cisplatin significantly reduced the expression of tight junction proteins ZO-1 and occludin in mouse intestinal tissue, coinciding with increased permeability and mucosal damage [14–16]. However, the upstream signaling mechanisms leading to ZO-1 suppression are still not fully understood. Previous studies have shown that cisplatin-induced inflammation and epithelial injury often involve various pathways [17, 18]. Given the central role of ZO-1 in maintaining epithelial integrity, we hypothesized that these signaling cascades did contribute to its downregulation in response to cisplatin. Therefore, we further examined whether inhibition of these pathways by lutein preserved ZO-1 expression and protected intestinal epithelial barrier function.

Many previous studies aiming to reduce the side effects of cisplatin during chemotherapy have explored the use of natural compounds as nutritional supplements [19–21]. Among these, lutein, a natural carotenoid pigment, is well known for its anti-inflammatory, antioxidant, and membrane-stabilizing properties. Lutein has demonstrated therapeutic potential in rheumatoid arthritis, age-related macular degeneration, diabetic retinopathy, and liver injury through the regulation of oxidative stress and inflammatory responses [22–29]. Recent studies have begun to elucidate lutein's role in intestinal protection. Lutein was shown to attenuate intestinal barrier dysfunction in broilers challenged with LPS by upregulating tight junction proteins (ZO-1, occludin, and claudin-1) and downregulating the TLR4/MyD88/nuclear factor κ-light-chain-enhancer of activated B cells (NF-κB) inflammatory cascade, ultimately preserving epithelial integrity [30]. Similarly, in a murine model of alcohol-induced liver injury, lutein improved intestinal barrier function, reduced plasma endotoxins, and restored tight junction protein levels [31]. In a dietary intervention study, lutein improved gut permeability and tight junction expression in overweight adults, linking its systemic anti-inflammatory action to gut barrier health [32]. Moreover, lutein modulated gut microbiota and enhanced epithelial barrier resistance in mouse models of colitis [27]. Our previous study found that lutein could inhibit apoptosis caused by methotrexate-induced production of reactive oxygen species (ROS) in intestinal cells [33]. However, it remains unclear whether lutein can mitigate chemotherapy-induced intestinal barrier dysfunction and thus protect gastrointestinal epithelial cells. Therefore, a better understanding of the protective effects of lutein in cisplatin-induced intestinal barrier damage is crucial.

In light of the current lack of mechanistic understanding of how cisplatin disrupts intestinal barrier function, and considering the potential anti-inflammatory and antioxidant properties of lutein, this study aimed to investigate whether lutein could protect against cisplatin-induced intestinal epithelial barrier damage. We focused particularly on the role of ZO-1 expression and explored the involvement of MAPK and NF-κB signaling pathways in mediating this protective effect. Understanding this mechanism may provide novel insights into using dietary supplements to mitigate chemotherapy-induced mucosal injury.

2. Materials and Methods

2.1. Chemicals and Reagents. Anti-mouse and anti-rabbit IgG-conjugated horseradish peroxidase as well as rabbit polyclonal antibodies specific for ZO-1, occludin, E-cadherin, AQP3, AQP4, AQP8, β-actin, JNK, phospho-JNK, ERK, phospho-ERK, p38, phospho-p38, p65, and phospho-p65 plus goat anti-rabbit IgG, goat anti-rabbit IgG (DyLight488), and goat anti-mouse IgG were purchased from GeneTex (GeneTex, USA). All other reagents were purchased from Sigma-Aldrich (Merck, USA). Lutein was obtained from ChromaDex (CAS# 127-40-2; Los Angeles, CA, USA).

jfbc, 2025, 1, Downloaded from https://onlinelibrary.wiley.com/doi/10.1155/jfbc/9954087 by Chang Gung University Of, Wiley Online Library on [04/05/2026]. See the Terms and Conditions (https://onlinelibrary.wiley.com/terms-and-conditions) on Wiley Online Library for rules of use; OA articles are governed by the applicable Creative Commons License

2.2. Cell Cultures. Normal IEC-6 rat small intestine epithelial cells (BCRC Number: 60301) were obtained from Taiwan's Biological Resources Preservation and Research Center (BCRC). The cells were cultured in DMEM supplemented with 10% fetal bovine serum (FBS, Thermo Fisher, USA), 2 mM GlutaMAX-I (Thermo Fisher, USA), 100 units/mL penicillin, and 100 μg/mL streptomycin (Thermo Fisher, USA), with the pH adjusted to 7.0 using the recommended concentration of sodium bicarbonate, and maintained in a 5% CO_2 humidified incubator at 37°C, and the culture medium was replenished every 2 days.

2.3. Western Blot Analysis. Proteins were separated using 10%–15% SDS gel electrophoresis and then transferred onto 0.45-μm PVDF membranes (Merck, USA). The membranes were incubated with 5% nonfat milk at room temperature for 1 h and then probed with primary antibodies (1:1000) overnight at 4°C. After three washes with TBST to remove excess primary antibodies, the membranes were incubated with a secondary antibody (1:10,000) at room temperature for 1 h. The blots were then developed using enhanced chemiluminescence (RPN2235, Amersham™ Cytiva, USA) and visualized with a chemiluminescence detection system (UVP ChemiDOC-It 815, Analytik Jena US, USA) [34].

2.4. Quantitative Real-Time PCR. Cellular RNA from IEC-6 cells was extracted using the easy-BLUE total RNA extraction kit (iNtRON Biotechnology, KOR). First-strand cDNA was obtained using a qPCRBIO cDNA Synthesis Kit (Cat. #PB30.11-10, PCR Biosystems, UK). The mRNA expression of rat TJP1, OCLN, CDH1, AQP3, AQP4, AQP8, and β-actin was examined using qPCR. The specific primer sequences used were as follows: TJP1: forward: GACCGATTGCTGATGTTG CC; reverse: TGAAGGCGAATAATGCCCGA, amplification efficiency: 97.3%; OCLN: forward: ACGGGCATCTTTGGA GGAAG; reverse: TCTGGGGTCTGTGTACCCTC, amplification efficiency: 102.1%; CDH1: forward: CTGGGGTCATCA GTGTGGTC; reverse: CTTGACCCTGGTACGTGCTT, amplification efficiency: 95.7%; AQP3: forward: AGCAGATCT GAGTGGGCAGT; reverse: CTTGGGCTTAAGAGGGGA AC, amplification efficiency: 104.2%; AQP4: forward: TGG ACAGCTGTAAGTGTGGAC; reverse: ATGAGCATGGCC AGGAACTC, amplification efficiency: 96.0%; AQP8: forward: ACACCAATGTGTAGTATGGACCT; reverse: TGACCG ATAGACATCCGATGAAG, amplification efficiency: 102.0%; and β-actin: forward: AAGACCTCTATGCCAACAC; reverse: TGATCTTCATGGTGCTAGG, amplification efficiency: 103.8%. The KAPA SYBR FAST qPCR Master Mix (2×) kit from Sigma-Aldrich was used with a CFX Connect real-time PCR detection system (Bio-Rad, Hercules, USA), according to the manufacturer's instructions. All primers were purchased from Sigma-Aldrich. Gene expression levels were determined using the $2^{-\Delta\Delta Ct}$ method and normalized to β-actin as the internal control [34].

2.5. Immunofluorescence. After treatment, IEC-6 cells were fixed with 4% formaldehyde for 15 min at room temperature and then permeabilized with 0.1% Triton X-100 in PBS for 10 min. Nonspecific antibody-binding sites were blocked by incubating the cells with 3% BSA in PBS for 30 min. After washing, the cells were incubated with specific primary antibodies (1:200 dilution) for ZO-1 or p65 at 4°C overnight. Following another wash step, the cells were incubated with the goat anti-rabbit IgG (DyLight488) antibody for 1 h at room temperature and then incubated with a DAPI solution for 5 min. The cells were examined using a Nikon ECLIPSE Ti microscope (NIS Elements AR 5.02.01) [34]. Immunofluorescence staining results were analyzed manually by three independent and blinded evaluators. For each experimental group, four randomly selected microscopic fields were captured per biological replicate using a fluorescence microscope (Nikon Eclipse Ti). For ZO-1 expression, a cell was considered ZO-1–positive if ≥ 50% of its plasma membrane displayed a continuous and discernible fluorescence signal. The number of ZO-1–positive cells was divided by the total number of DAPI-stained nuclei in the same field. The resulting percentage was then normalized to the control group, which was defined as 100%. For p65 nuclear translocation, cells showing distinct p65 signal colocalized with DAPI staining (indicating nuclear localization) were counted as positive. The number of p65 nuclear-positive cells was divided by the total number of DAPI-stained nuclei and again normalized to the control group (100%).

2.6. Wound Healing Assay. IEC-6 cells (3×10^4) were seeded in a Culture-Insert (Cat. # No. 80209, ibidi GmbH, Germany) for 24 h. Afterward, the inserts were removed, and the cells were treated with cisplatin and lutein. The effect of lutein and cisplatin on wound healing was observed under a microscope at 0 and 24 h. To investigate the signaling pathways involved, cells were pretreated with MAPK kinase inhibitors or NF-κB inhibitors and then incubated with cisplatin for 24 h. The wound healing area was photographed and measured. All experiments were conducted in triplicate wells and repeated at least three times. The data were analyzed using ImageJ 1.52a [34].

2.7. Reporter Gene Assay. IEC-6 cells (1×10^5) were seeded in 24-well plates and transfected with an NF-κB promoter reporter plasmid (Promega, Madison, WI, USA). Subsequently, the cells were incubated with cisplatin and lutein for 24 h. The cells were then lysed using 100 μL of reporter lysis buffer (E153A, Promega, Madison, WI, USA) and collected after centrifugation at 13,200 rpm for 15 min. Cell suspensions (50 μL) were placed in the wells of an opaque white 96-well microplate, and 50 μL of luciferase substrate (Luciferase Assay System E151A, Promega, Madison, WI, USA) was added. To investigate the signaling pathways involved, IEC-6 cells were transfected with an NF-κB promoter reporter plasmid, pretreated with MAPK kinase or NF-κB inhibitors, and then incubated with cisplatin for an additional 24 h. Relative luciferase activity was measured using a microplate luminometer (VICTOR X2, PerkinElmer, MA, USA) [34].

2.8. Statistics. The data were presented as mean ± standard deviation (SD). Two groups of data were compared using Student's *t*-test. For comparisons involving more than two

jfbc, 2025, 1, Downloaded from https://onlinelibrary.wiley.com/doi/10.1155/jfbc/9954087 by Chang Gung University Of, Wiley Online Library on [04/05/2026]. See the Terms and Conditions (https://onlinelibrary.wiley.com/terms-and-conditions) on Wiley Online Library for rules of use; OA articles are governed by the applicable Creative Commons License

groups, one-way analysis of variance (ANOVA) was employed. All statistical analyses were conducted using GraphPad Prism 8.2 (GraphPad Software, San Diego, CA, USA). A p value of < 0.05 was considered significant.

3. Results

3.1. Cisplatin Caused Intestinal Epithelial Barrier Dysfunction. Intestinal mucositis is a common side effect of cisplatin chemotherapy treatment in cancer patients [35]. Cisplatin has been shown to damage the healthy intestinal barrier by decreasing tight junction and adherent junction proteins as well as altering the expression of AQPs in the intestines [14, 36–39]. We first investigated the effects of cisplatin on IEC-6 intestinal epithelial cells and found that cisplatin markedly suppressed the proliferation of intestinal epithelial cells (10 μM, 94.16 ± 2.12%; 25 μM, 74.86 ± 3.96%; 50 μM, 43.89 ± 2.64%) (Figure 1(a)). To examine the potential effects of cisplatin on the intestinal barrier, we treated rat intestinal epithelial cells with cisplatin. We found that cisplatin significantly reduced the expression of ZO-1 protein and mRNA (Figures 1(b), 1(h)) but did not affect the expression of other junction proteins or AQPs (Figures 1(c), 1(d), 1(e), 1(f), 1(g), 1(i), 1(j), 1(k), 1(l), 1(m)). Furthermore, a wound healing assay showed that cisplatin disrupted the healing of epithelial cells (Figure 1(n)). These results indicated that cisplatin causes intestinal epithelial barrier dysfunction and a decrease in ZO-1 expression.

3.2. Cisplatin Suppressed ZO-1 Expression in Intestinal Epithelial Cells by Activating p38 and ERK. The MAPK pathway is a critical signaling pathway that regulates intestinal barrier function [40]. In the current study, treatment with cisplatin significantly upregulated p38 and ERK kinase phosphorylation; however, there was no effect on JNK (Figures 2(a), 2(b), 2(c)). In addition, pretreatment with a p38 inhibitor (SB203580) and an ERK inhibitor (PD98059) restored ZO-1 expression (Figure 2(d)). Wound healing assays further implicated the involvement of p38 and ERK in cisplatin-induced damage to the epithelial cell barrier (Figure 2(e)). These results confirmed that cisplatin causes a decrease in epithelial cell repair mechanisms by triggering the phosphorylation of p38 and ERK.

3.3. Cisplatin Activated the p38 and ERK/NF-κB Cell Signaling Pathway in IEC-6 Cells. Cisplatin has been found to promote nephrotoxicity and kidney injury by activating the MAPK and NF-κB pathways [41–44]. Activation of the NF-κB pathway is further linked to decreased ZO-1 expression in intestinal epithelial cells [40, 45]. Thus, we investigated whether NF-κB was involved in the cisplatin-induced reduction of ZO-1 expression. Treating IEC-6 cells with cisplatin significantly increased the phosphorylation of p65 (Figure 3(a)), while the addition of NF-κB inhibitors mitigated the cisplatin-induced downregulation of ZO-1 and the impairment of wound healing (Figures 3(b), 3(c)).

We next explored whether cisplatin stimulated NF-κB transcriptional activity by activating p38 and ERK in IEC-6 cells. Indeed, pretreatment with p38 and ERK inhibitors suppressed cisplatin-induced p65 nuclear translocation (Figure 4(a)) and reduced cisplatin-induced NF-κB transcriptional activity (Figure 4(b)). Moreover, pretreatment of TPCK and BAY11-7082 significantly inhibited p65 nuclear translocation and NF-κB transcriptional activity (Figures 4(c), 4(d)). These results indicated that cisplatin inhibits the expression of ZO-1 and promotes barrier dysfunction in intestinal epithelial cells by activating the p38 and ERK/NF-κB signaling pathways.

3.4. Lutein Restored ZO-1 Expression and Wound Healing by Suppressing p38 and ERK/NF-κB Activation. Lutein has multiple cell-protective functions, including reducing inflammation by inhibiting the activation of MAPK and NF-κB pathways in human corneal epithelial cells [46]. To investigate the effects of lutein on the intestinal epithelial barrier, we analyzed the expression of tight junction proteins and AQPs after pretreating IEC-6 cells with lutein followed by cisplatin treatment. Pretreatment with lutein reversed cisplatin-induced reductions in ZO-1 protein and mRNA expression but did not affect the expression of other junction proteins and AQPs (Figures 5(a), 5(b), 5(c), 5(d), 5(e), 5(f), 5(g), 5(h), 5(i), 5(j), 5(k), 5(l)). Furthermore, the impaired wound healing of IEC-6 cells following cisplatin treatment was improved with lutein pretreatment (Figures 5(m), 5(n), 5(o)).

Finally, we investigated whether lutein regulated the expression of ZO-1 by inhibiting the increased activity of p38 and ERK/NF-κB signaling pathways following cisplatin treatment. Indeed, pretreatment of IEC-6 cells with lutein inhibited the cisplatin-induced phosphorylation of p38, ERK, and p65; note that there were no effects on JNK (Figures 6(a), 6(b), 6(c), 6(d)). Specifically, cisplatin-induced p65 nuclear translocation and NF-κB transcriptional activity were inhibited with lutein pretreatment (Figures 6(e), 6(f)). These results suggested that lutein protected intestinal epithelial cells by inhibiting the p38 and ERK/NF-κB pathways.

4. Discussion

Cisplatin is a commonly used anticancer medication for the treatment of lung, prostate, and head and neck cancers [1]. The primary mechanism of cisplatin's cytotoxicity involves the formation of DNA crosslinks, which interfere with DNA replication and transcription, leading to cell cycle arrest and apoptosis [47, 48]. Nevertheless, the cytotoxicity of cisplatin leads to numerous adverse effects, such as ototoxicity, nephrotoxicity, and gastrointestinal mucosal damage [15, 16, 49]. Approximately 40% of patients undergoing cisplatin therapy experience gastrointestinal mucositis, resulting in a diminished quality of life, adjustments in chemotherapy dosages, and in some cases, the discontinuation of chemotherapy [50, 51]. Intestinal mucositis during

jfbc, 2025, 1, Downloaded from https://onlinelibrary.wiley.com/doi/10.1155/jfbc/9954087 by Chang Gung University Of, Wiley Online Library on [04/05/2026]. See the Terms and Conditions (https://onlinelibrary.wiley.com/terms-and-conditions) on Wiley Online Library for rules of use; OA articles are governed by the applicable Creative Commons License

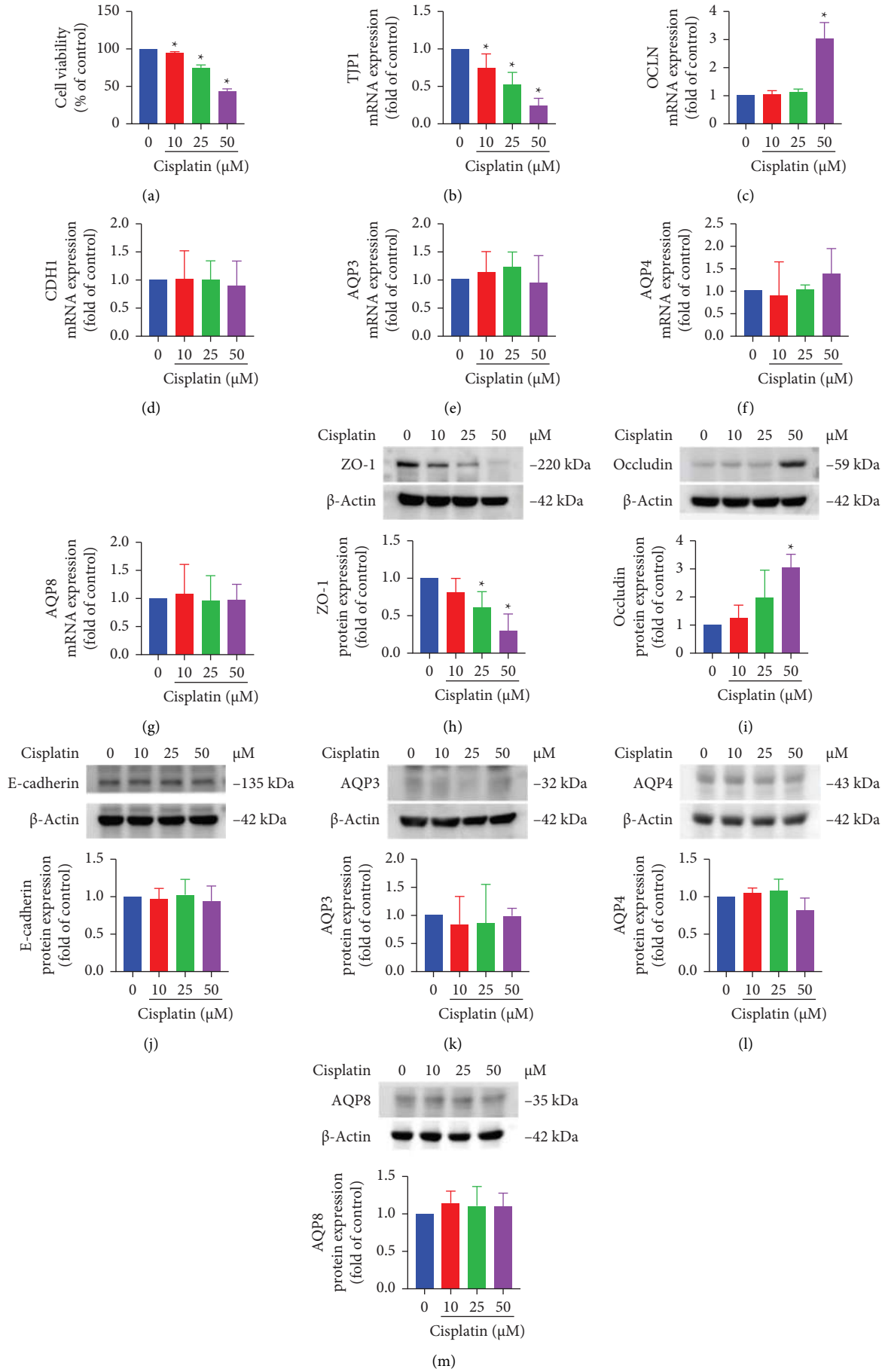


Figure 1: Continued.

jfbc, 2025, 1, Downloaded from https://onlinelibrary.wiley.com/doi/10.1155/jfbc/9954087 by Chang Gung University Of, Wiley Online Library on [04/05/2026]. See the Terms and Conditions (https://onlinelibrary.wiley.com/terms-and-conditions) on Wiley Online Library for rules of use; OA articles are governed by the applicable Creative Commons License

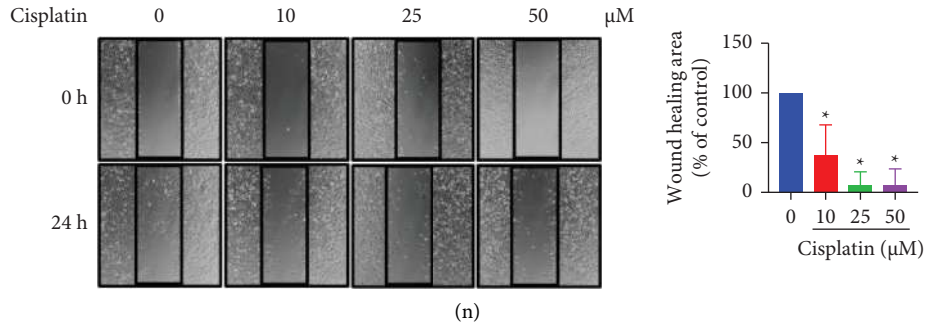


FIGURE 1: Cisplatin suppressed ZO-1 expression and wound healing capacity in IEC-6 cells. IEC-6 cells were treated with cisplatin (10–50 μM) for 24 h ($n = 4$). (a) Cell viability of IEC-6 cells was assessed by CCK-8 assay after treatment with varying concentrations of cisplatin (10, 25, and 50 μM) for 24 h. (b)–(g) Quantitative real-time PCR determined TJP1, OCLN, CDH1, AQP3, AQP4, and AQP8 mRNA expression. (h)–(m) Western blot analysis revealed ZO-1, occludin, E-cadherin, AQP3, AQP4, and AQP8 protein expression. (n) Wound healing assay demonstrated recovery capacity. Untreated cells were used as controls. Results are shown as means ± SD. $^{*}p < 0.05$ compared to untreated control.

chemotherapy has been linked to the downregulation of tight junction proteins [52–54]. The intestinal barrier comprises a single-cell layer consisting of intestinal epithelial cells, which are interconnected and upheld by tight junction proteins such as ZO-1, occludin, and claudin. In addition to serving as a physical barrier, the selective permeability of the intestinal barrier facilitates the absorption of specific nutrients [55, 56]. ZO-1 plays a crucial role in forming tight junctions and supporting the regulation of substance trafficking in the epithelium [57]. In normal cells, cisplatin-induced DNA damage triggers a cascade of cellular responses, including the activation of several signaling pathways such as p38 MAPK, ERK, and NF-κB [58, 59]. These pathways play crucial roles in mediating inflammatory responses and apoptosis [60, 61]. Specifically, the activation of NF-κB leads to the transcription of proinflammatory cytokines and chemokines, which contribute to the inflammatory milieu [62]. In the context of the intestinal mucosa, cisplatin-induced inflammation is characterized by the infiltration of immune cells, increased production of ROS, and the release of proinflammatory cytokines such as TNF-α, IL-1β, and IL-6 [63]. These inflammatory mediators disrupt the integrity of tight junctions by downregulating the expression of key proteins like ZO-1, leading to increased intestinal permeability and barrier dysfunction. Reduced ZO-1 expression due to cellular damage leads to tight junction defects, thereby increasing intestinal barrier permeability and allowing the infiltration of pathogens and endotoxins, ultimately inducing intestinal mucositis [64].

Our findings indicated that cisplatin exposure resulted in damage to IEC-6 rat intestinal epithelial cells, leading to inhibited cell proliferation, reduced ZO-1 expression, and impaired wound healing capacity. Note that cisplatin did not significantly reduce the expression of occludin, E-cadherin, and AQPs. The observed occludin upregulation following cisplatin exposure may represent a compensatory cellular response aimed at reinforcing tight junction integrity. For example, heat shock preconditioning induced HSF-1 activation, which bound to the occludin promoter, resulting in its transcriptional upregulation, interpreted as a protective mechanism to tighten the epithelial barrier under stress [65]. While there was an observed increase in occludin expression following cisplatin treatment, which suggested a cellular self-rescue mechanism, the impaired wound healing ability was not fully restored. In our study, cisplatin exposure selectively downregulated ZO-1, while the expression of other tight junction components such as occludin and E-cadherin, as well as AQPs, remained relatively unchanged. This specificity may be mechanistically attributed to the unique intracellular positioning and regulatory sensitivity of ZO-1. As a peripheral membrane scaffolding protein, ZO-1 directly interacts with the actin cytoskeleton and serves as a signaling hub integrating inflammatory and mechanical stress cues, particularly through MAPK and NF-κB pathways [66, 67]. In contrast, occludin and claudins are transmembrane components of the tight junction complex, whose regulation often depends on posttranslational modifications or trafficking events, which may not be acutely affected by inflammatory signaling [68]. Furthermore, claudin isoforms exhibit tissue- and context-specific expression and response patterns. As for AQPs, their expression is predominantly modulated by osmotic and hormonal stimuli, rather than oxidative stress or proinflammatory cascades triggered by cisplatin. Prior studies have shown that ZO-1, but not occludin or claudin-5, is significantly downregulated in endothelial cells exposed to LPS, suggesting selective sensitivity of ZO-1 to inflammatory stimuli. Additionally, ZO-1's amino- and carboxyl-terminal regions interact, respectively, with α-catenin and the actin cytoskeleton, reinforcing its role as a dynamic mediator between junction integrity and intracellular signaling [69]. This molecular architecture may underlie the pronounced vulnerability of ZO-1 to cisplatin-induced cellular stress.

The activation of the MAPK pathway and the transcription factor NF-κB were involved in various inflammatory processes, playing crucial roles in gastrointestinal mucosal damage and barrier defects [70, 71]. The phosphorylation of MAPK and NF-κB leads to the increased expression of various inflammatory cytokines and the reduced expression of ZO-1 [53]. cAMP-response

jfbc, 2025, 1, Downloaded from https://onlinelibrary.wiley.com/doi/10.1155/jfbc/9954087 by Chang Gung University Of, Wiley Online Library on [04/05/2026]. See the Terms and Conditions (https://onlinelibrary.wiley.com/terms-and-conditions) on Wiley Online Library for rules of use; OA articles are governed by the applicable Creative Commons License

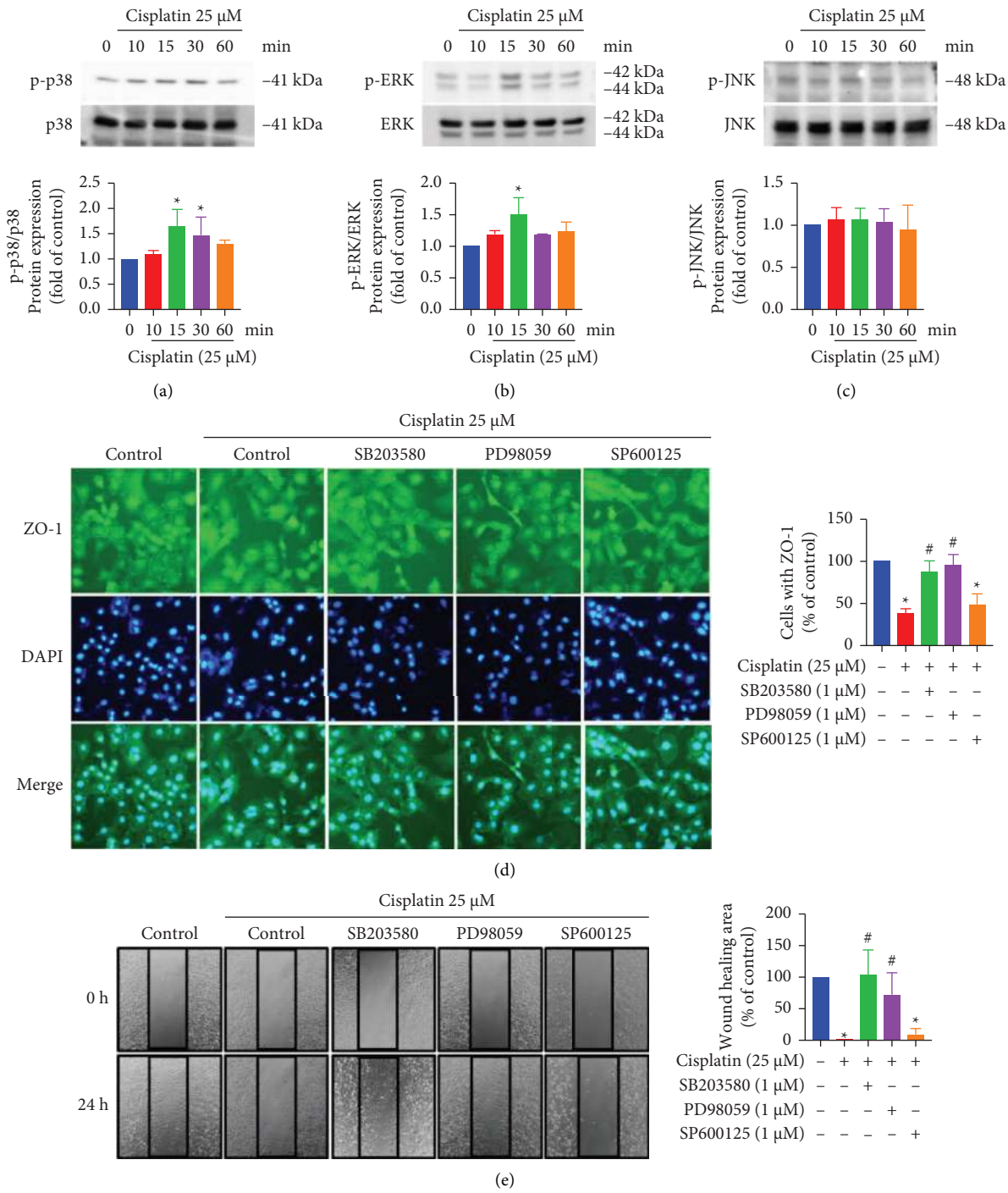


Figure 2: Cisplatin suppressed ZO-1 expression and wound healing capacity via p38 and ERK activation in IEC-6 cells. (a)–(c) Western blot analysis showed p38, ERK, and JNK phosphorylation in IEC-6 cells treated with cisplatin (25 μM) for 10–60 min ($n = 4$). (d) Immunofluorescence stain indicated ZO-1 expression in IEC-6 cells pretreated with p38 (SB203580: 1 μM), ERK (PD98059: 1 μM), or JNK (SP600125: 1 μM) inhibitors for 1 h and subsequently treated with cisplatin (25 μM) for 24 h ($n = 4$). (e) Wound healing assay revealed capacity of recovery after IEC-6 cells were pretreated with p38 (SB203580: 1 μM), ERK (PD98059: 1 μM), or JNK (SP600125: 1 μM) inhibitors for 1 h and subsequently treated with cisplatin (25 μM) for 24 h ($n = 4$). Untreated cells were used as controls. Results are shown as means ± SD. $^{*}p < 0.05$ compared to untreated control. $^{\#}p < 0.05$ compared to the cisplatin group.

jfbc, 2025, 1, Downloaded from https://onlinelibrary.wiley.com/doi/10.1155/jfbc/9954087 by Chang Gung University Of, Wiley Online Library on [04/05/2026]. See the Terms and Conditions (https://onlinelibrary.wiley.com/terms-and-conditions) on Wiley Online Library for rules of use; OA articles are governed by the applicable Creative Commons License

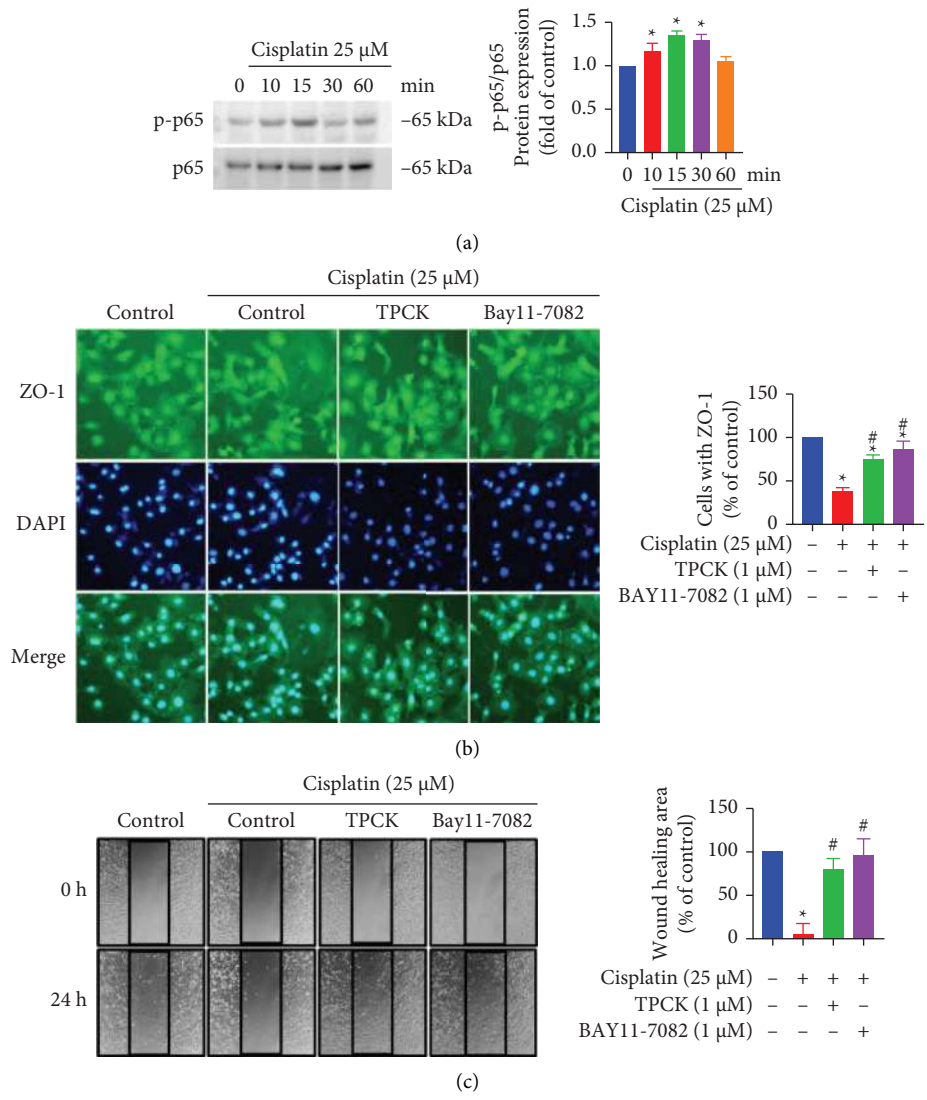


FIGURE 3: Cisplatin inhibited ZO-1 expression and wound healing capacity via activating the NF-κB pathway in IEC-6 cells. (a) Western blot analysis revealed p65 phosphorylation in IEC-6 cells treated with cisplatin (25 μM) for 10–60 min ($n = 4$). (b) Immunofluorescence stain indicated ZO-1 expression in IEC-6 cells pretreated with IKK (BAY11-7082: 1 μM) or IκBα (TPCK: 1 μM) inhibitors for 1 h and subsequently treated with cisplatin (25 μM) for 24 h ($n = 4$). (c) Wound healing assay showed capacity of recovery after IEC-6 cells were pretreated with IKK (BAY11-7082: 1 μM) or IκBα (TPCK: 1 μM) inhibitors for 1 h and subsequently treated with cisplatin (25 μM) for 24 h ($n = 4$). Untreated cells were used as controls. Results are shown as means ± SD. $^{*}p < 0.05$ compared to untreated control. $^{\#}p < 0.05$ compared to the cisplatin group.

element binding protein (CREB) and NF-κB serve as downstream transcription factors of the MAPK kinase [72] and bind to the same binding domain on the coactivating protein CREB-binding protein (CBP) to form transcriptional complexes. The activation of CREB facilitates the formation of a complex with CBP, thereby enhancing ZO-1 gene expression. Conversely, the activation of NF-κB leads to an increase in the NF-κB–CBP complex, which inhibits ZO-1 expression [73]. Concurrent reductions in CREB phosphorylation and increases in NF-κB phosphorylation result in decreases in the CREB–CBP complex and increases in the NF-κB–CBP complex, all of which contribute to reductions in ZO-1 expression [74]. In our study, cisplatin induced not only the activation of p38 and ERK kinases but also the phosphorylation of p65 in IEC-6 rat intestinal epithelial cells. Pretreatment with p38 and ERK inhibitors suppressed cisplatin-induced p65 nuclear translocation and transcriptional activity. These findings confirm the association between cell barrier defects induced by cisplatin and the p38 and ERK/NF-κB pathways.

Numerous agents have been shown to preserve intestinal barrier function under stress, providing a useful context for assessing the therapeutic relevance of lutein. For example, probiotics such as *Lactobacillus plantarum* and *Lactobacillus rhamnosus* have been demonstrated to strengthen epithelial integrity by upregulating tight junction proteins like occludin and ZO-1, enhancing cell proliferation, and decreasing intestinal permeability in epithelial injury models

jfbc, 2025, 1, Downloaded from https://onlinelibrary.wiley.com/doi/10.1155/jfbc/9954087 by Chang Gung University Of, Wiley Online Library on [04/05/2026]. See the Terms and Conditions (https://onlinelibrary.wiley.com/terms-and-conditions) on Wiley Online Library for rules of use; OA articles are governed by the applicable Creative Commons License

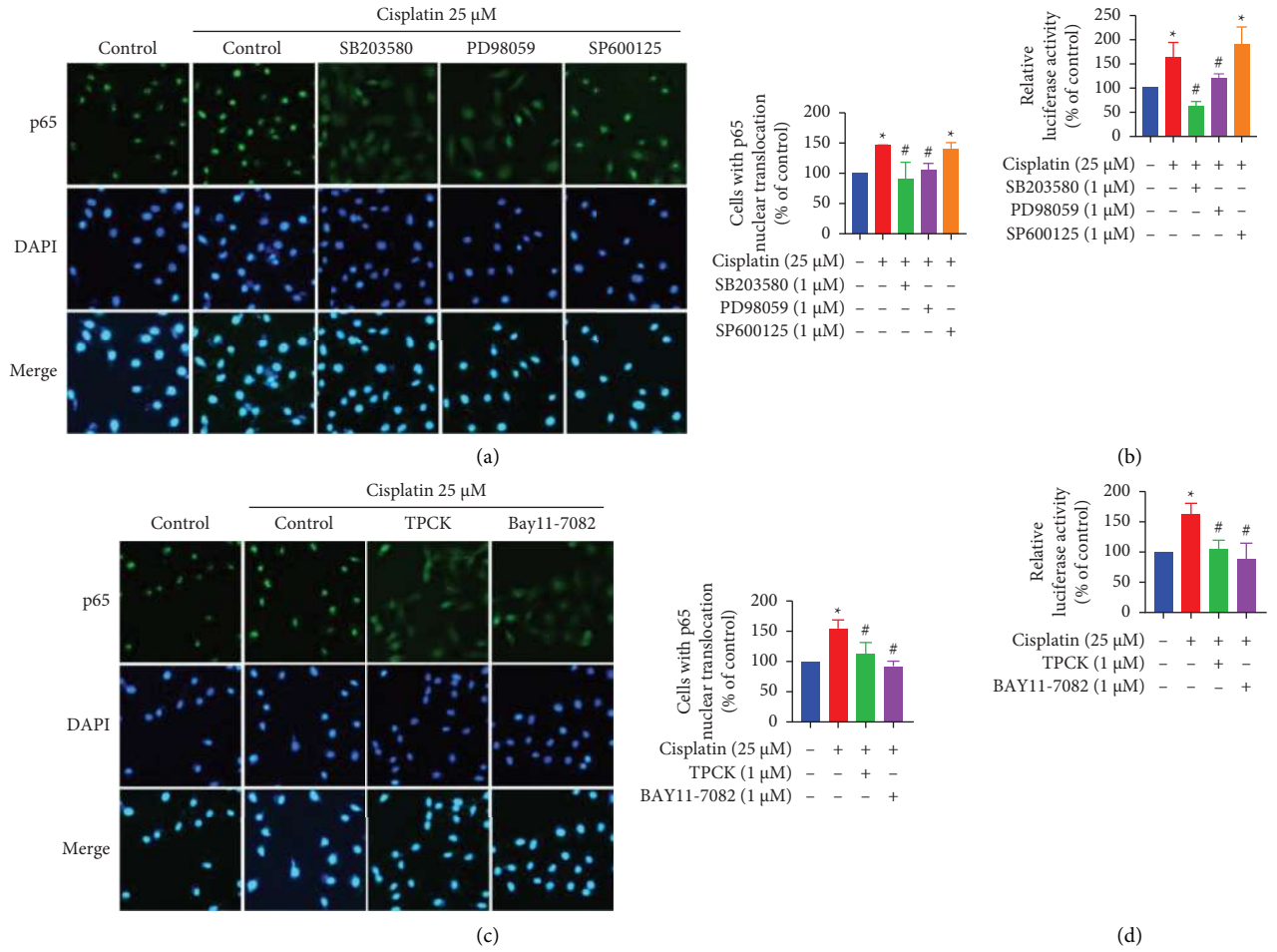


Figure 4: Cisplatin promoted NF-κB transcriptional activity via activating p38 and ERK in IEC-6 cells. (a) Immunofluorescence stain showed p65 nuclear translocation in IEC-6 cells pretreated with p38 (SB203580: 1 μM), ERK (PD98059: 1 μM), or JNK (SP600125: 1 μM) inhibitors for 1 h and subsequently treated with cisplatin (25 μM) for 1 h ($n = 4$). (b) Reporter gene assay demonstrated p65 transcriptional activity in IEC-6 cells pretreated with p38 (SB203580: 1 μM), ERK (PD98059: 1 μM), or JNK (SP600125: 1 μM) inhibitors for 1 h and subsequently treated with cisplatin (25 μM) for 24 h ($n = 4$). (c) Immunofluorescence stain revealed p65 nuclear translocation in IEC-6 cells pretreated with IKK (BAY11-7082: 1 μM) or IκBα (TPCK: 1 μM) inhibitors for 1 h and subsequently treated with cisplatin (25 μM) for 1 h ($n = 4$). (d) Reporter gene assay showed p65 transcriptional activity in IEC-6 cells pretreated with IKK (BAY11-7082: 1 μM) or IκBα (TPCK: 1 μM) inhibitors for 1 h and subsequently treated with cisplatin (25 μM) for 24 h ($n = 4$). Untreated cells were used as controls. Results are shown as means ± SD. $^{*}p < 0.05$ compared to untreated control. $^{\#}p < 0.05$ compared to the cisplatin group.

[75]. Similarly, glutamine, a primary fuel for enterocytes, has shown protective effects in chemotherapy-induced intestinal injury. It promotes epithelial repair by restoring proliferation markers such as PCNA and enhancing mucosal regeneration following cisplatin exposure [76]. In clinical settings, enteral glutamine supplementation has been associated with reduced mucosal toxicity and improved quality of life in patients undergoing chemotherapy [77]. While direct in vivo comparisons between lutein and other antioxidants remain limited, studies have reported that lutein protects intestinal barrier function by attenuating tight junction disruption and oxidative stress [27]. By contrast, in our study, lutein's mechanism of action extended beyond general antioxidant properties, involving targeted inhibition of the MAPK and NF-κB signaling cascades. This action led to restoration of ZO-1 expression and enhanced wound healing capacity. These results suggested that lutein may serve as a complementary or alternative therapeutic strategy, offering unique intracellular signaling modulation distinct from the trophic support of glutamine or microbial modulation by probiotics. Carotenoids with anti-inflammatory and antioxidant properties contribute to maintaining a healthy gut microbiota and intestinal barrier integrity in animals [78]. Lutein is a β-carotenoid antioxidant shown to possess anti-inflammatory effects as well as prevent and mitigate many eye diseases [79]. Lutein is generally recognized as safe (GRAS) by the U.S. Food and Drug Administration (FDA). Clinical studies have demonstrated that daily doses of up to 20 mg of lutein are safe for long-term consumption [80]. For example, a dose-ranging study on lutein supplementation in older adults showed that doses up to 10 mg/day were well tolerated without any adverse effects [81]. In animal studies, rats exhibited no signs of toxicity after receiving 639 mg/kg of

jfbc, 2025, 1, Downloaded from https://onlinelibrary.wiley.com/doi/10.1155/jfbc/9954087 by Chang Gung University Of, Wiley Online Library on [04/05/2026]. See the Terms and Conditions (https://onlinelibrary.wiley.com/terms-and-conditions) on Wiley Online Library for rules of use; OA articles are governed by the applicable Creative Commons License

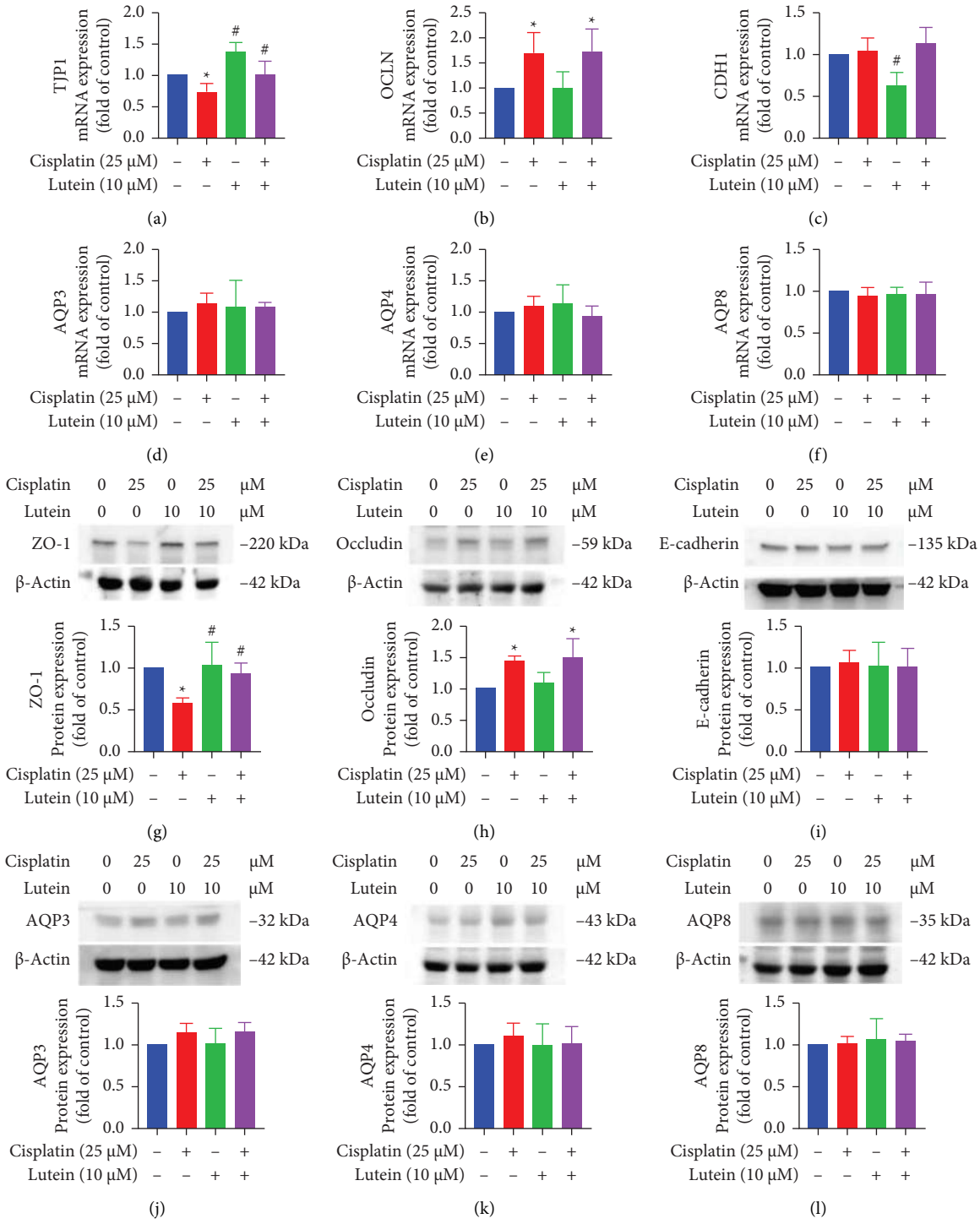


Figure 5: Continued.

jfbc, 2025, 1, Downloaded from https://onlinelibrary.wiley.com/doi/10.1155/jfbc/9954087 by Chang Gung University Of, Wiley Online Library on [04/05/2026]. See the Terms and Conditions (https://onlinelibrary.wiley.com/terms-and-conditions) on Wiley Online Library for rules of use; OA articles are governed by the applicable Creative Commons License

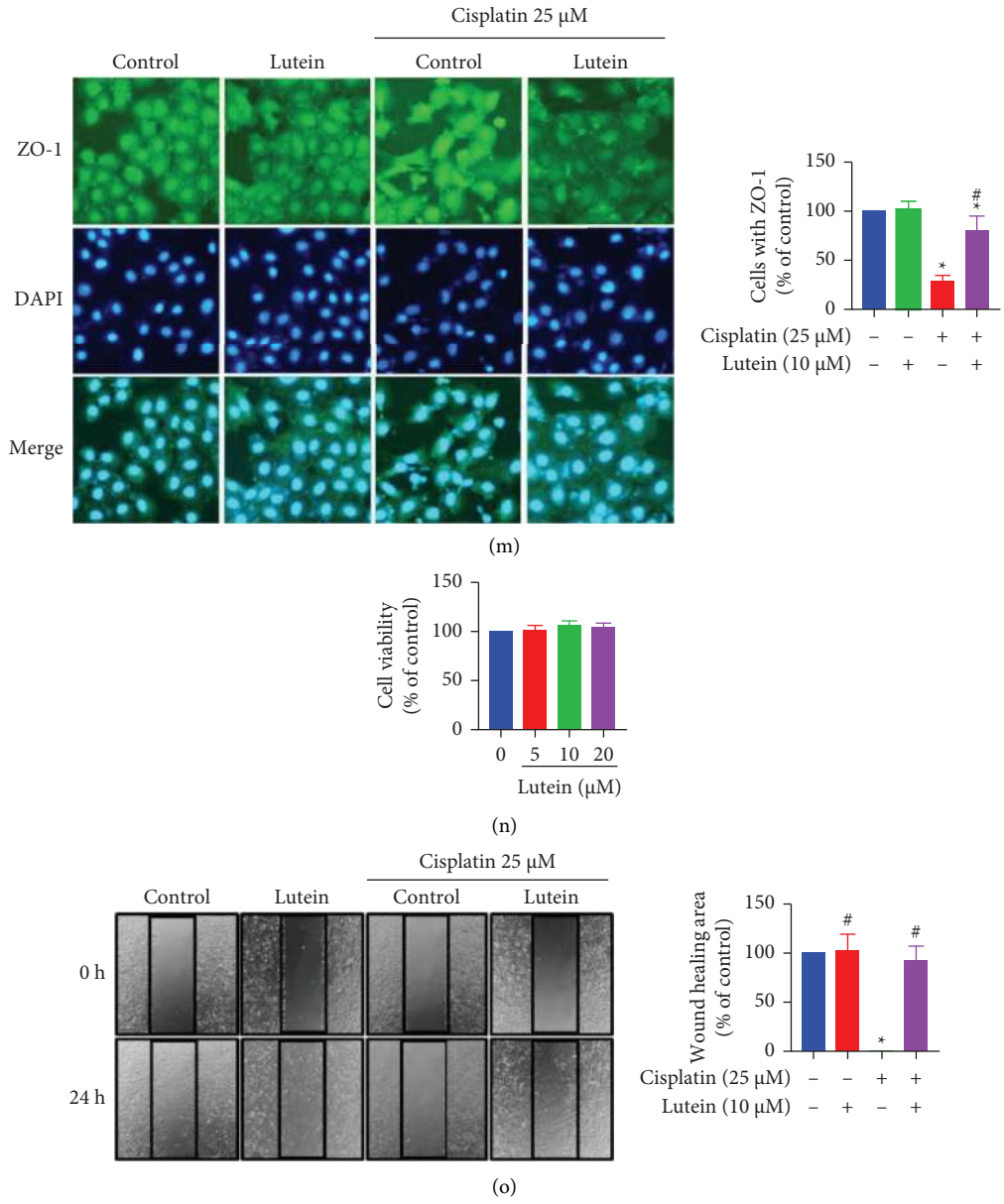


FIGURE 5: Lutein restored cisplatin-reduced ZO-1 expression in IEC-6 cells. IEC-6 cells were pretreated with lutein (10 μM) for 1 h and subsequently treated with cisplatin (25 μM) for 24 h ($n = 4$). (a)–(f) Quantitative real-time PCR determined TJP1, OCLN, CDH1, AQP3, AQP4, and AQP8 mRNA expression. (g)–(l) Western blot analysis showed ZO-1, occludin, E-cadherin, AQP3, AQP4, and AQP8 protein expression. (m) Immunofluorescence stain indicated ZO-1 expression. (n) CCK-8 assay showed cell viability treated with lutein for 24 h ($n = 4$). (o) Wound healing assay showed recovery capacity. Untreated cells were used as controls. Results are shown as means ± SD. $^{*}p < 0.05$ compared to untreated control. $^{\#}p < 0.05$ compared to the cisplatin group.

lutein daily [82]. Using the conversion factor between human and rat doses, a normal adult weighing 70 kg receiving 20 mg/day is equivalent to a rat daily dose of approximately 1.8 mg/kg (6.2 × 20 mg/70 kg). This dose is minimal compared to the doses used in the rat studies mentioned above. Additionally, lutein has been extensively studied for its benefits in eye health, with consistent reports of safety at similar dosage levels [80]. These findings support the safe use of lutein as a nutritional supplement. In this study, we found that lutein reversed the decreases in ZO-1 expression and demonstrated a beneficial impact on wound healing. Note that lutein did not significantly impact other junction proteins and AQPs. In addition, lutein inhibited the cisplatin-induced activation of p38, ERK, and p65, as well as NF-κB transcriptional activity. Lutein also reversed the decreased expression of ZO-1 and restored the impaired wound healing ability associated with cisplatin treatment. This inhibition could be attributed to lutein's antioxidant properties, which mitigate oxidative stress—a known activator of the MAPK/NF-κB pathway [83]. Lutein's ability to inhibit the activation of the MAPK/NF-κB pathway by cisplatin likely involved its antioxidant properties, thereby

jfbc, 2025, 1, Downloaded from https://onlinelibrary.wiley.com/doi/10.1155/jfbc/9954087 by Chang Gung University Of, Wiley Online Library on [04/05/2026]. See the Terms and Conditions (https://onlinelibrary.wiley.com/terms-and-conditions) on Wiley Online Library for rules of use; OA articles are governed by the applicable Creative Commons License

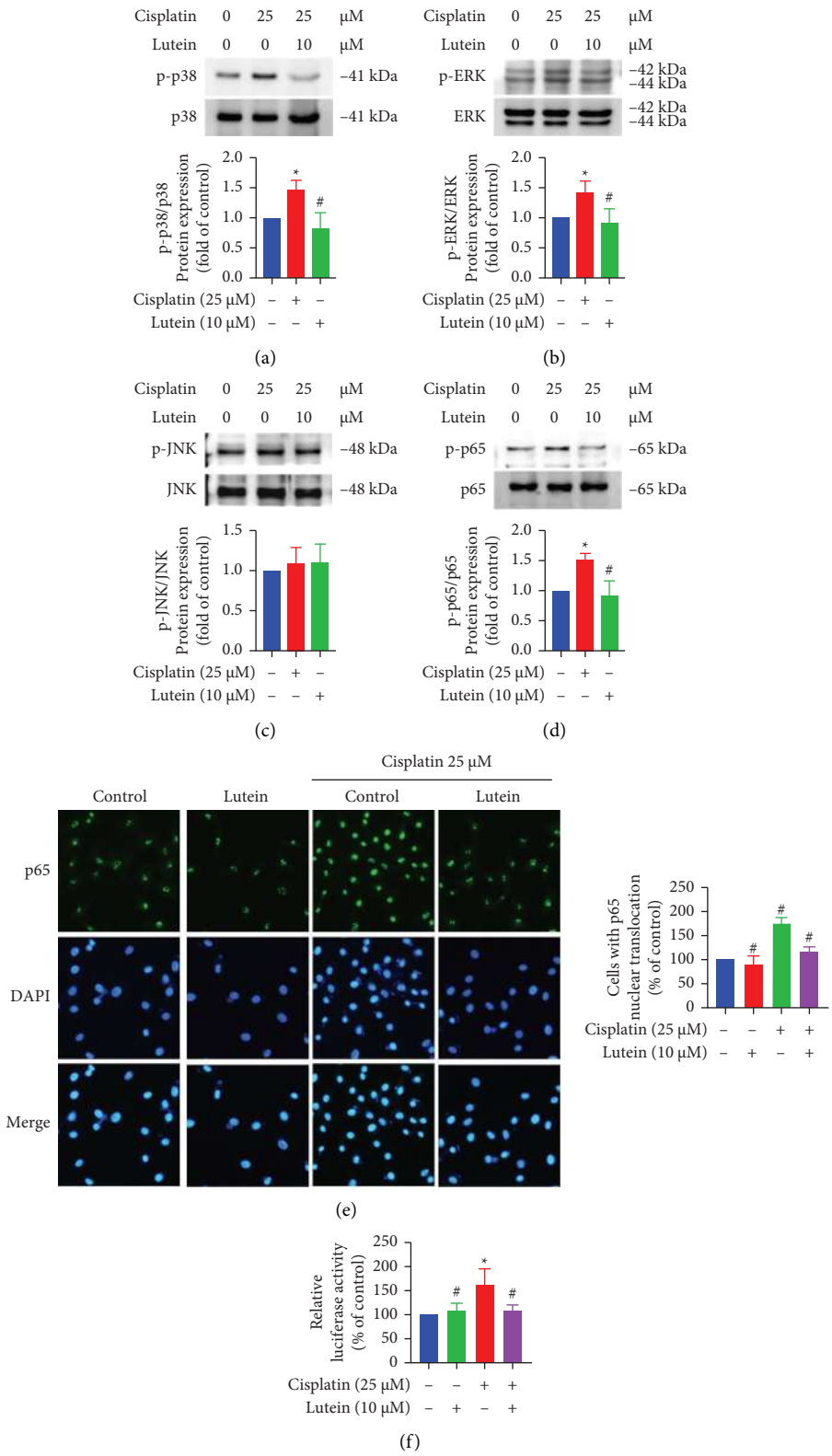


Figure 6: Lutein inhibited cisplatin-induced p38, ERK, and p65 activation as well as p65 transcriptional activity in IEC-6 cells. IEC-6 cells were pretreated with lutein (10 μM) for 1 h and subsequently treated with cisplatin (25 μM) for 15 min ($n = 4$). (a)–(d) Western blot analysis showed p38, ERK, JNK, and p65 phosphorylation. (e) Immunofluorescence stain revealed p65 nuclear translocation. (f) Reporter gene assay showed p65 transcriptional activity in IEC-6 cells pretreated with lutein (10 μM) for 1 h and subsequently treated with cisplatin (25 μM) for 24 h ($n = 4$). Untreated cells were used as controls. Results are shown as means ± SD. $^{*}p < 0.05$ compared to untreated control. $^{\#}p < 0.05$ compared to the cisplatin group.

jfbc, 2025, 1, Downloaded from https://onlinelibrary.wiley.com/doi/10.1155/jfbc/9954087 by Chang Gung University Of, Wiley Online Library on [04/05/2026]. See the Terms and Conditions (https://onlinelibrary.wiley.com/terms-and-conditions) on Wiley Online Library for rules of use; OA articles are governed by the applicable Creative Commons License

preventing downstream inflammatory effects and preserving ZO-1 expression [84]. While our data clearly demonstrate that lutein inhibits cisplatin-induced p65 phosphorylation and nuclear translocation, it remains unclear whether lutein directly interacts with NF-κB subunits (such as p65) or their coactivators. Most current evidence, including our findings, suggests that lutein likely modulates NF-κB activity indirectly by targeting upstream kinases such as p38 and ERK, possibly through its antioxidant properties that mitigate ROS-mediated MAPK activation. In support of this, no studies to date have demonstrated a direct binding interaction between lutein and NF-κB, suggesting that its regulatory role is modulatory rather than direct. Further investigations using molecular docking or binding assays (e.g., surface plasmon resonance) are warranted to clarify this potential direct interaction. These results are consistent with existing literature, which indicates that NF-κB activation disrupts ZO-1 expression and that pretreatment with lutein protects cells from barrier defects.

Despite the strengths of this study, several limitations should be acknowledged. First, all experiments were conducted using the IEC-6 cell line, which, although a well-characterized model for rat small intestinal crypt cells, does not fully recapitulate the complexity of the intestinal microenvironment. IEC-6 cells lack immune cell interactions, gut microbiota influences, and the architectural diversity present in vivo, such as villus–crypt dynamics and stromal support. Moreover, species differences between rodent and human epithelium may affect the extrapolation of signaling responses and drug sensitivities. As such, the absence of validation in human-derived intestinal epithelial models (e.g., Caco-2, HT-29, or organoids), as well as in vivo systems, limits the direct translational interpretation of our findings. Future investigations incorporating both human epithelial models and animal studies are warranted to confirm the clinical relevance and therapeutic potential of lutein in preventing chemotherapy-induced intestinal barrier disruption.

5. Conclusion

Our findings provide further evidence of the potential of lutein as a nutritional support in improving intestinal mucositis during chemotherapy. Lutein effectively restores the expression of ZO-1 and strengthens cellular barriers by modulating the activation of the MAPK pathway and NF-κB. Hence, lutein could serve as a promising supplement to alleviate gastrointestinal inflammation and a portion of the associated side effects during chemotherapy.

Data Availability Statement

The datasets generated for this study can be accessed upon request from the corresponding author.

Ethics Statement

Given that it did not contain human or animal trials, our study did not require ethical board approval.

Conflicts of Interest

The authors declare no conflicts of interest.

Author Contributions

Chi-Jen Chang: data curation, formal analysis, methodology, software, funding acquisition, and writing–original draft. Tsung-Ming Chang: conceptualization, project administration, investigation, resources, and software. Ying-Sui Sun: funding acquisition, methodology, project administration, and software. Ji-Fan Lin: formal analysis and methodology. Chiang-Wen Lee: investigation and funding acquisition. Mei-Ling Fang: data curation and resources. Ju-Fang Liu: conceptualization, funding acquisition, and writing–review and editing.

Funding

This work was supported by the Ministry of Science and Technology, Taiwan (NSTC113-2628-B-038-008-MY3, NSTC112-2221-E-038-006-MY3, NSTC112-2811-E-038-004-MY3), Chang Gung University of Science Foundation grants (ZRRPF6N0011), and Shin Kong Wu Ho-Su Memorial Hospital (2022SKHADR010).

Acknowledgments

We would like to thank acceptediting (https://acceptediting.tw/) for providing editorial and translation services for the preparation of this manuscript.

Supporting Information

Additional supporting information can be found online in the Supporting Information section. *(Supporting Information)*

The effectiveness of the signaling pathway inhibitors (SB203580 and PD98059) in suppressing their respective targets was validated by Western blot analysis (Supporting Figure 1).

References

[1] N. Martinho, T. C. B. Santos, H. F. Florindo, and L. C. Silva, "Cisplatin-Membrane Interactions and Their Influence on Platinum Complexes Activity and Toxicity," *Frontiers in Physiology* 9 (2019): 1898, https://doi.org/10.3389/fphys.2018.01898.

[2] B. N. Forgie, R. Prakash, and C. M. Telleria, "Revisiting the Anti-Cancer Toxicity of Clinically Approved Platinating Derivatives," *International Journal of Molecular Sciences* 23, no. 23 (2022): 15410, https://doi.org/10.3390/ijms232315410.

[3] A. El-Sheikh and Z. Khired, "Interactions of Analgesics With Cisplatin: Modulation of Anticancer Efficacy and Potential Organ Toxicity," *Medicina* 58, no. 1 (2021): 46, https://doi.org/10.3390/medicina58010046.

[4] C. H. Wu, J. L. Ko, J. M. Liao, et al., "D-methionine Alleviates Cisplatin-Induced Mucositis by Restoring the Gut Microbiota Structure and Improving Intestinal Inflammation," *Therapeutic Advances in Medical Oncology* 11 (2019):

jfbc, 2025, 1, Downloaded from https://onlinelibrary.wiley.com/doi/10.1155/jfbc/9954087 by Chang Gung University Of, Wiley Online Library on [04/05/2026]. See the Terms and Conditions (https://onlinelibrary.wiley.com/terms-and-conditions) on Wiley Online Library for rules of use; OA articles are governed by the applicable Creative Commons License

1758835918821021, https://doi.org/10.1177/1758835918821021.

[5] A. T. Sougiannis, B. N. VanderVeen, J. M. Davis, D. Fan, and E. A. Murphy, "Understanding Chemotherapy-Induced Intestinal Mucositis and Strategies to Improve Gut Resilience," *American Journal of Physiology-Gastrointestinal and Liver Physiology* 320, no. 5 (2021): G712–G719, https://doi.org/10.1152/ajpgi.00380.2020.

[6] Q. Q. Yu, H. Zhang, Y. Guo, B. Han, and P. Jiang, "The Intestinal Redox System and Its Significance in Chemotherapy-Induced Intestinal Mucositis," *Oxidative Medicine and Cellular Longevity* 2022, no. 1 (2022): 7255497, https://doi.org/10.1155/2022/7255497.

[7] K. V. Rolston, "The Burdens of Cancer Therapy: Clinical and Economic Outcomes of Chemotherapy-Induced Mucositis," *Cancer* 100, no. 6 (2004): 1324–1325, https://doi.org/10.1002/cncr.20101.

[8] M. Thomsen and L. Vitetta, "Adjunctive Treatments for the Prevention of Chemotherapy-and Radiotherapy-Induced Mucositis," *Integrative Cancer Therapies* 17, no. 4 (2018): 1027–1047, https://doi.org/10.1177/1534735418794885.

[9] L. W. Peterson and D. Artis, "Intestinal Epithelial Cells: Regulators of Barrier Function and Immune Homeostasis," *Nature Reviews Immunology* 14, no. 3 (2014): 141–153, https://doi.org/10.1038/nri3608.

[10] W. Zhang, B. Zhu, J. Xu, et al., "Bacteroides Fragilis Protects Against Antibiotic-Associated Diarrhea in Rats by Modulating Intestinal Defenses," *Frontiers in Immunology* 9 (2018): 1040, https://doi.org/10.3389/fimmu.2018.01040.

[11] B. Zhang, X. Wei, M. Ding, Z. Luo, X. Tan, and Z. Zheng, "Daidzein Protects Caco-2 Cells Against Lipopolysaccharide-Induced Intestinal Epithelial Barrier Injury by Suppressing PI3K/AKT and P38 Pathways," *Molecules* 27, no. 24 (2022): 8928, https://doi.org/10.3390/molecules27248928.

[12] L. Chen, L. Li, Y. Han, B. Lv, S. Zou, and Q. Yu, "Tong-Fu-Li-Fei Decoction Exerts a Protective Effect on Intestinal Barrier of Sepsis in Rats Through Upregulating ZO-1/occludin/claudin-1 Expression," *Journal of Pharmacological Sciences* 143, no. 2 (2020): 89–96, https://doi.org/10.1016/j.jphs.2020.02.009.

[13] L. Deng, H. Zeng, X. Hu, et al., "Se@Albumin Nanoparticles Ameliorate Intestinal Mucositis Caused by Cisplatin via Gut Microbiota-Targeted Regulation," *Nanoscale* 13, no. 25 (2021): 11250–11261, https://doi.org/10.1039/d0nr07981b.

[14] W. Liu, H. Zhang, Yy. Hou, et al., "Arginyl-Fructosyl-Glucose, a Major Maillard Reaction Product of Red Ginseng Mitigates Cisplatin-evoked Intestinal Toxicity in Vivo and in Vitro," *Food & Function* 13, no. 21 (2022): 11283–11297, https://doi.org/10.1039/d2fo00776b.

[15] J. J. Zhang, Jq. Wang, Xy. Xu, et al., "Red Ginseng Protects Against Cisplatin-Induced Intestinal Toxicity by Inhibiting Apoptosis and Autophagy via the PI3K/AKT and MAPK Signaling Pathways," *Food & Function* 11, no. 5 (2020): 4236–4248, https://doi.org/10.1039/d0fo00469c.

[16] B. I. Drogemoller, G. E. Wright, C. Lo, et al., "Pharmacogenomics of Cisplatin-Induced Ototoxicity: Successes, Shortcomings, and Future Avenues of Research," *Clinical Pharmacology & Therapeutics* 106, no. 2 (2019): 350–359, https://doi.org/10.1002/cpt.1483.

[17] L. Wen, Sh. Tao, F. Guo, et al., "Selective EZH2 Inhibitor zld1039 Alleviates Inflammation in Cisplatin-Induced Acute Kidney Injury Partially by Enhancing RKIP and Suppressing NF-κB p65 Pathway," *Acta Pharmacologica Sinica* 43, no. 8 (2022): 2067–2080, https://doi.org/10.1038/s41401-021-00837-8.

[18] Z. Yang, R. Ning, Q. Liu, R. Zang, S. Liu, and S. Sun, "Umbelliferone Attenuates Cisplatin-Induced Acute Kidney Injury by Inhibiting Oxidative Stress and Inflammation via NRF2," *Physiological Reports* 11, no. 23 (2023): e15879, https://doi.org/10.14814/phy2.15879.

[19] Y. T. Zou, J. Zhou, C. Y. Wu, et al., "Protective Effects of Poria Cocos and its Components Against Cisplatin-Induced Intestinal Injury," *Journal of Ethnopharmacology* 269 (2021): 113722, https://doi.org/10.1016/j.jep.2020.113722.

[20] S. Jin, et al., "Dioscin Alleviates Cisplatin-Induced Mucositis in Rats by Modulating Gut Microbiota, Enhancing Intestinal Barrier Function and Attenuating TLR4/NF-KappaB Signaling Cascade," *International Journal of Molecular Sciences* 23, no. 8 (2022).

[21] Q. Shen, X. M. Wei, J. N. Hu, et al., "Saponins From Platycodon Grandiflorum Reduces Cisplatin-Induced Intestinal Toxicity in Mice Through Endoplasmic Reticulum Stress-Activated Apoptosis," *The American Journal of Chinese Medicine* 50, no. 07 (2022): 1927–1944, https://doi.org/10.1142/s0192415x22500823.

[22] E. Kocyigit, et al., "A Narrative Review on Dietary Components & Patterns and Age-Related Macular Degeneration," *Nutrition Research Reviews* (2024): 1–79.

[23] D. Sharma, P. Chaubey, and V. Suvarna, "Role of Natural Products in Alleviation of Rheumatoid Arthritis-A Review," *Journal of Food Biochemistry* 45, no. 4 (2021): e13673, https://doi.org/10.1111/jfbc.13673.

[24] Y. Jin and R. Arroo, "The Protective Effects of Flavonoids and Carotenoids Against Diabetic complications-A Review of in Vivo Evidence," *Frontiers in Nutrition* 10 (2023): 1020950, https://doi.org/10.3389/fnut.2023.1020950.

[25] F. K. El-Baz, A. Salama, S. I. Ali, and R. Elgohary, "Lutein Isolated From Scenedesmus obliquus Microalga Boosts Immunity Against Cyclophosphamide-Induced Brain Injury in Rats," *Scientific Reports* 12, no. 1 (2022): 22601, https://doi.org/10.1038/s41598-022-25252-9.

[26] H. Zhang, T. Song, R. Kang, F. Ren, J. Liu, and J. Wang, "Plant Bioactive Compounds Alleviate Photoinduced Retinal Damage and Asthenopia: Mechanisms, Synergies, and Bioavailability," *Nutrition Research* 120 (2023): 115–134, https://doi.org/10.1016/j.nutres.2023.10.003.

[27] S. Zhao, Y. Zhang, H. Ding, et al., "Lutein Prevents Liver Injury and Intestinal Barrier Dysfunction in Rats Subjected to Chronic Alcohol Intake," *Nutrients* 15, no. 5 (2023): 1229, https://doi.org/10.3390/nu15051229.

[28] J. Yang, S. Qian, X. Na, and A. Zhao, "Association Between Dietary and Supplemental Antioxidants Intake and Lung Cancer Risk: Evidence From a Cancer Screening Trial," *Antioxidants* 12, no. 2 (2023): 338, https://doi.org/10.3390/antiox12020338.

[29] A. Kazemi, M. Golzarand, S. Shojaei-Zarghani, S. Babajafari, P. Mirmiran, and F. Azizi, "Is Variety More Important than Quantity of Fruits and Vegetables in Relation to Cardiovascular Disease Incidence and Mortality? Results From a Prospective Cohort Study," *International Journal of Food Sciences & Nutrition* 75, no. 3 (2024): 306–316, https://doi.org/10.1080/09637486.2024.2304134.

[30] M. Y. Wang, Y. Zhang, Y. X. Tong, et al., "Effects of Lutein on Jejunal Mucosal Barrier Function and Inflammatory Responses in Lipopolysaccharide-Challenged Yellow-Feather Broilers," *Poultry Science* 101, no. 12 (2022): 102191, https://doi.org/10.1016/j.psj.2022.102191.

jfbc, 2025, 1, Downloaded from https://onlinelibrary.wiley.com/doi/10.1155/jfbc/9954087 by Chang Gung University Of, Wiley Online Library on [04/05/2026]. See the Terms and Conditions (https://onlinelibrary.wiley.com/terms-and-conditions) on Wiley Online Library for rules of use; OA articles are governed by the applicable Creative Commons License

[31] Y. Dong, Q. Ni, Z. Zhang, et al., "Comparison of Four Characteristic Carotenoids (Lutein, Beta-Carotene, Lycopene, and Astaxanthin) in Alleviating DSS-Induced Colitis Through Gut Microbiota Regulation," *Food & Function* 16, no. 15 (2025): 6101–6114, https://doi.org/10.1039/d5fo00789e.

[32] M. C. Meurer, M. Mees, L. N. B. Mariano, et al., "Hydro-alcoholic Extract of *Tagetes erecta* L. Flowers, Rich in the Carotenoid Lutein, Attenuates Inflammatory Cytokine Secretion and Improves the Oxidative Stress in an Animal Model of Ulcerative Colitis," *Nutrition Research* 66 (2019): 95–106, https://doi.org/10.1016/j.nutres.2019.03.005.

[33] C. J. Chang, J. F. Lin, H. H. Chang, G. A. Lee, and C. F. Hung, "Lutein Protects Against Methotrexate-Induced and Reactive Oxygen species-mediated Apoptotic Cell Injury of IEC-6 Cells," *PLoS One* 8, no. 9 (2013): e72553, https://doi.org/10.1371/journal.pone.0072553.

[34] T. M. Chang, Y. C. Chiang, C. W. Lee, et al., "CXCL14 Promotes Metastasis of Non-Small Cell Lung Cancer Through ACKR2-depended Signaling Pathway," *International Journal of Biological Sciences* 19, no. 5 (2023): 1455–1470, https://doi.org/10.7150/ijbs.79438.

[35] T. Yamaguchi, A. Gaowa, E. J. Park, I. Tawara, and M. Shimaoka, "Recombinant Soluble Thrombomodulin Attenuates Cisplatin-Induced Intestinal Injury by Inhibiting Intestinal Epithelial Cell-Derived Cytokine Secretion," *Molecular Biology Reports* 50, no. 10 (2023): 8459–8467, https://doi.org/10.1007/s11033-023-08762-1.

[36] J. Trujillo, E. Molina-Jijón, O. N. Medina-Campos, et al., "Curcumin Prevents Cisplatin-Induced Decrease in the Tight and Adherens Junctions: Relation to Oxidative Stress," *Food & Function* 7, no. 1 (2016): 279–293, https://doi.org/10.1039/c5fo00624d.

[37] M. A. Afjal, P. Goswami, S. Ahmad, et al., "Tempol (4-hydroxy Tempo) Protects Mice From Cisplatin-Induced Acute Kidney Injury via Modulation of Expression of Aquaporins and Kidney Injury Molecule-1," *Drug and Chemical Toxicology* 45, no. 3 (2022): 1355–1363, https://doi.org/10.1080/01480545.2020.1831011.

[38] O. Oztopuz, "Melatonin Ameliorates Cisplatin-Induced Neurodegeneration in Medulla Oblongata Through the Expressions of Aqp-1,-4, Inflammation, and Apoptosis Pathway Genes," *Turkish Journal of Biology* 46, no. 2 (2022): 162–172, https://doi.org/10.55730/1300-0152.2583.

[39] L. Koral, M. A. Ovali, N. K. Tufekcioglu, E. Karakilic, Y. Adali, and M. Uzun, "The Role of AQP3 and AQP4 Channels in Cisplatin-Induced Cardiovascular Edema and the Protective Effect of Melatonin," *Molecular Biology Reports* 48, no. 11 (2021): 7457–7465, https://doi.org/10.1007/s11033-021-06763-6.

[40] S. Zhang, W. Xu, H. Wang, et al., "Inhibition of Creb-Mediated ZO-1 and Activation of Nf-Kb-Induced IL-6 by Colonic Epithelial MCT4 Destroys Intestinal Barrier Function," *Cell Proliferation* 52, no. 6 (2019): e12673, https://doi.org/10.1111/cpr.12673.

[41] I. H. Kim, M. J. Kwon, J. H. Jung, and T. J. Nam, "Protein Extracted From Porphyra Yezoensis Prevents Cisplatin-Induced Nephrotoxicity by Downregulating the MAPK and NF-κB Pathways," *International Journal of Molecular Medicine* 41, no. 1 (2018): 511–520, https://doi.org/10.3892/ijmm.2017.3214.

[42] S. Wang, S. Tang, X. Chen, et al., "Pulchinenoside B4 Exerts the Protective Effects Against Cisplatin-Induced Nephrotoxicity Through NF-κB and MAPK Mediated Apoptosis Signaling Pathways in Mice," *Chemico-Biological Interactions* 331 (2020): 109233, https://doi.org/10.1016/j.cbi.2020.109233.

[43] D. U. Kim, et al., "Ojeoksan Ameliorates Cisplatin-Induced Acute Kidney Injury in Mice by Downregulating MAPK and NF-kappaB Pathways," *International Journal of Molecular Sciences* 23, no. 20 (2022).

[44] X. Li, J. Shi, Y. Teng, and Z. Liu, "The Preventative Effect of Baihe Gujin Pill on Cisplatin-Induced Acute Kidney Injury by Activating the PI3K/AKT and Suppressing the NF-κB/MAPK Pathways," *Journal of Ethnopharmacology* 318, no. Pt B (2024): 117071, https://doi.org/10.1016/j.jep.2023.117071.

[45] S. Ibrahim, X. Zhu, X. Luo, Y. Feng, and J. Wang, "PIK3R3 Regulates ZO-1 Expression Through the NF-kB Pathway in Inflammatory Bowel Disease," *International Immunopharmacology* 85 (2020): 106610, https://doi.org/10.1016/j.intimp.2020.106610.

[46] S. C. Chao, C. W. Nien, C. Iacob, D. N. Hu, S. C. Huang, and H. Y. Lin, "Effects of Lutein on Hyperosmoticity-Induced Upregulation of IL-6 in Cultured Corneal Epithelial Cells and Its Relevant Signal Pathways," *Journal of Ophthalmology* 2016 (2016): 1–7, https://doi.org/10.1155/2016/8341439.

[47] Y. Jung and S. J. Lippard, "Direct Cellular Responses to Platinum-Induced DNA Damage," *Chemistry Review* 107, no. 5 (2007): 1387–1407, https://doi.org/10.1021/cr068207j.

[48] S. V. Hato, A. Khong, I. J. M. de Vries, and W. J. Lesterhuis, "Molecular Pathways: The Immunogenic Effects of Platinum-Based Chemotherapeutics," *Clinical Cancer Research* 20, no. 11 (2014): 2831–2837, https://doi.org/10.1158/1078-0432.ccr-13-3141.

[49] S. J. Holditch, C. N. Brown, A. M. Lombardi, K. N. Nguyen, and C. L. Edelstein, "Recent Advances in Models, Mechanisms, Biomarkers, and Interventions in Cisplatin-Induced Acute Kidney Injury," *International Journal of Molecular Sciences* 20, no. 12 (2019): 3011, https://doi.org/10.3390/ijms20123011.

[50] L. S. Elting, C. Cooksley, M. Chambers, S. B. Cantor, E. Manzullo, and E. B. Rubenstein, "The Burdens of Cancer Therapy. Clinical and Economic Outcomes of Chemotherapy-Induced Mucositis," *Cancer* 98, no. 7 (2003): 1531–1539, https://doi.org/10.1002/cncr.11671.

[51] K. R. Jordan, B. R. Loman, M. T. Bailey, and L. M. Pyter, "Gut Microbiota-Immune-Brain Interactions in Chemotherapy-Associated Behavioral Comorbidities," *Cancer* 124, no. 20 (2018): 3990–3999, https://doi.org/10.1002/cncr.31584.

[52] D. M. Alsholi, G. S. Yacoub, A. U. Rehman, et al., "Lactobacillus rhamnosus Attenuates Cisplatin-Induced Intestinal Mucositis in Mice via Modulating the Gut Microbiota and Improving Intestinal Inflammation," *Pathogens* 12, no. 11 (2023): 1340, https://doi.org/10.3390/pathogens12111340.

[53] L. Xiao, W. Dou, Y. Wang, H. Deng, H. Xu, and Y. Pan, "Treatment With S-adenosylmethionine Ameliorates Irinotecan-Induced Intestinal Barrier Dysfunction and Intestinal Microbial Disorder in Mice," *Biochemical Pharmacology Pharmacol* 216 (2023): 115752, https://doi.org/10.1016/j.bcp.2023.115752.

[54] S. R. Shen, W. J. Chen, H. F. Chu, S. H. Wu, Y. R. Wang, and T. L. Shen, "Amelioration of 5-fluorouracil-Induced Intestinal Mucositis by Streptococcus Thermophilus ST4 in a Mouse Model," *PLoS One* 16, no. 7 (2021): e0253540, https://doi.org/10.1371/journal.pone.0253540.

[55] K. R. Groschwitz and S. P. Hogan, "Intestinal Barrier Function: Molecular Regulation and Disease Pathogenesis," *Journal of Allergy and Clinical Immunology* 124, no. 1 (2009): 3–20, https://doi.org/10.1016/j.jaci.2009.05.038.

jfbc, 2025, 1, Downloaded from https://onlinelibrary.wiley.com/doi/10.1155/jfbc/9954087 by Chang Gung University Of, Wiley Online Library on [04/05/2026]. See the Terms and Conditions (https://onlinelibrary.wiley.com/terms-and-conditions) on Wiley Online Library for rules of use; OA articles are governed by the applicable Creative Commons License

[56] J. M. Bowen, R. J. Gibson, A. G. Cummins, and D. M. K. Keefe, "Intestinal Mucositis: the Role of the Bcl-2 Family, p53 and Caspases in Chemotherapy-Induced Damage," *Supportive Care in Cancer* 14, no. 7 (2006): 713–731, https://doi.org/10.1007/s00520-005-0004-7.

[57] L. Wang, R. Zhang, J. Chen, Q. Wu, and Z. Kuang, "Baicalin Protects Against TNF-Alpha-Induced Injury by Down-Regulating miR-191a That Targets the Tight Junction Protein ZO-1 in IEC-6 Cells," *Biological & Pharmaceutical Bulletin* 40, no. 4 (2017): 435–443, https://doi.org/10.1248/bpb.b16-00789.

[58] Y. Li, H. Yang, H. Nong, et al., "3-hydroxy-3-methylglutaryl-coenzyme A (HMG-CoA) Reductase (HMGCR) Protects Hair Cells From Cisplatin-Induced Ototoxicity in Vitro: Possible Relation to the Activities of p38 MAPK Signaling Pathway," *Archives of Toxicology* 97, no. 11 (2023): 2955–2967, https://doi.org/10.1007/s00204-023-03588-z.

[59] J. Yuan, X. Liang, W. Zhou, et al., "TRPA1 Promotes Cisplatin-Induced Nephrotoxicity Through Inflammation Mediated by the MAPK/NF-κB Signaling Pathway," *Annals of Translational Medicine* 9, no. 20 (2021): 1578, https://doi.org/10.21037/atm-21-5125.

[60] Q. Ren, F. Guo, S. Tao, R. Huang, L. Ma, and P. Fu, "Flavonoid Fisetin Alleviates Kidney Inflammation and Apoptosis via Inhibiting Src-Mediated NF-κB p65 and MAPK Signaling Pathways in Septic AKI Mice," *Biomedicine & Pharmacotherapy* 122 (2020): 109772, https://doi.org/10.1016/j.biopha.2019.109772.

[61] D. Xu, T. Kong, Z. Shao, et al., "Orexin-A Alleviates Astrocytic Apoptosis and Inflammation via Inhibiting OX1R-mediated NF-κB and MAPK Signaling Pathways in Cerebral Ischemia/Reperfusion Injury," *Biochimica et Biophysica Acta (BBA)-Molecular Basis of Disease* 1867, no. 11 (2021): 166230, https://doi.org/10.1016/j.bbadis.2021.166230.

[62] H. Yu, L. Lin, Z. Zhang, H. Zhang, and H. Hu, "Targeting NF-κB Pathway for the Therapy of Diseases: Mechanism and Clinical Study," *Signal Transduction and Targeted Therapy* 5, no. 1 (2020): 209, https://doi.org/10.1038/s41392-020-00312-6.

[63] X. Ma, C. Dang, H. Kang, et al., "Saikosaponin-D Reduces Cisplatin-Induced Nephrotoxicity by Repressing ROS-Mediated Activation of MAPK and NF-κB Signalling Pathways," *International Immunopharmacology* 28, no. 1 (2015): 399–408, https://doi.org/10.1016/j.intimp.2015.06.020.

[64] L. Liu, M. Xu, Z. Zhang, et al., "TRPA1 Protects Mice From Pathogenic Citrobacter rodentium Infection via Maintaining the Colonic Epithelial Barrier Function," *The FASEB Journal* 37, no. 2 (2023): e22739, https://doi.org/10.1096/fj.202200483rrr.

[65] K. Dokladny, M. N. Zuhl, and P. L. Moseley, "Intestinal Epithelial Barrier Function and Tight Junction Proteins With Heat and Exercise," *Journal of Applied Physiology* 120, no. 6 (2016): 692–701, https://doi.org/10.1152/japplphysiol.00536.2015.

[66] P. Zou, F. Yang, Y. Ding, et al., "Lipopolysaccharide Downregulates the Expression of ZO-1 Protein Through the Akt Pathway," *BMC Infectious Diseases* 22, no. 1 (2022): 774, https://doi.org/10.1186/s12879-022-07752-1.

[67] S. Yu, J. He, and K. Xie, "Zonula Occludens Proteins Signaling in Inflammation and Tumorigenesis," *International Journal of Biological Sciences* 19, no. 12 (2023): 3804–3815, https://doi.org/10.7150/ijbs.85765.

[68] M. K. Findley and M. Koval, "Regulation and Roles for Claudin-Family Tight Junction Proteins," *IUBMB Life* 61, no. 4 (2009): 431–437, https://doi.org/10.1002/iub.175.

[69] M. Itoh, A. Nagafuchi, S. Moroi, and S. Tsukita, "Involvement of ZO-1 in Cadherin-based Cell Adhesion Through Its Direct Binding to Alpha Catenin and Actin Filaments," *The Journal of Cell Biology* 138, no. 1 (1997): 181–192, https://doi.org/10.1083/jcb.138.1.181.

[70] L. Ye, Y. Wang, F. Xiao, et al., "F. Prausnitzii-Derived Extracellular Vesicles Attenuate Experimental Colitis by Regulating Intestinal Homeostasis in Mice," *Microbial Cell Factories* 22, no. 1 (2023): 235, https://doi.org/10.1186/s12934-023-02243-7.

[71] C. Liu, et al., "Staphylococcal Enterotoxin A Induces Intestinal Barrier Dysfunction and Activates NLRP3 Inflammasome via NF-kappaB/MAPK Signaling Pathways in Mice," *Toxins* 14, no. 1 (2022).

[72] M. Mellett, P. Atzei, R. Jackson, L. A. O'Neill, and P. N. Moynagh, "Mal Mediates TLR-Induced Activation of CREB and Expression of IL-10," *The Journal of Immunology* 186, no. 8 (2011): 4925–4935, https://doi.org/10.4049/jimmunol.1002739.

[73] Y. Zhong, B. Zhang, S. Y. Eum, and M. Toborek, "HIV-1 Tat Triggers Nuclear Localization of ZO-1 via Rho Signaling and Camp Response Element-Binding Protein Activation," *Journal of Neuroscience* 32, no. 1 (2012): 143–150, https://doi.org/10.1523/jneurosci.4266-11.2012.

[74] G. C. Parry and N. Mackman, "Role of Cyclic AMP Response Element-Binding Protein in Cyclic AMP Inhibition of NF-kappaB-mediated Transcription," *The Journal of Immunology* 159, no. 11 (1997): 5450–5456, https://doi.org/10.4049/jimmunol.159.11.5450.

[75] R. K. Rao and G. Samak, "Protection and Restitution of Gut Barrier by Probiotics: Nutritional and Clinical Implications," *Current Nutrition & Food Science* 9, no. 2 (2013): 99–107, https://doi.org/10.2174/1573401311309020004.

[76] Y. Tazuke, K. Maeda, M. Wasa, N. Satoko, and M. Fukuzawa, "Protective Mechanism of Glutamine on the Expression of Proliferating Cell Nuclear Antigen After Cisplatin-Induced Intestinal Mucosal Injury," *Pediatric Surgery International* 27, no. 2 (2011): 151–158, https://doi.org/10.1007/s00383-010-2798-8.

[77] H. Muranaka, R. Akinsola, S. Billet, et al., "Glutamine Supplementation as an Anticancer Strategy: A Potential Therapeutic Alternative to the Convention," *Cancers (Basel)* 16, no. 5 (2024): 1057, https://doi.org/10.3390/cancers16051057.

[78] T. Silva Meneguelli, M. Duarte Villas Mishima, H. H. M. Hermsdorff, H. S. D. Martino, J. Bressan, and E. Tako, "Effect of Carotenoids on Gut Health and Inflammatory Status: A Systematic Review of in Vivo Animal Studies," *Critical Reviews in Food Science and Nutrition* 64, no. 30 (2023): 11206–11221, https://doi.org/10.1080/10408398.2023.2234025.

[79] G. Faustine, A. R. Prijanti, and H. Wibowo, "Effect of Lutein on Ocular Goblet Cell, IFN-gamma, and IL-17 Concentration in Dry Eye-Induced Mice Model," *Cureus* 15, no. 7 (2023): e42009, https://doi.org/10.7759/cureus.42009.

[80] L. H. Li, J. C. Y. Lee, H. H. Leung, W. C. Lam, Z. Fu, and A. C. Y. Lo, "Lutein Supplementation for Eye Diseases," *Nutrients* 12, no. 6 (2020): 1721, https://doi.org/10.3390/nu12061721.

[81] J. M. Rosenthal, J. Kim, F. de Monastario, et al., "Dose-Ranging Study of Lutein Supplementation in Persons Aged 60 Years or Older," *Investigative Ophthalmology & Visual Science* 47, no. 12 (2006): 5227–5233, https://doi.org/10.1167/iovs.05-1513.

[82] C. L. Kruger, M. Murphy, Z. DeFreitas, F. Pfannkuch, and J. Heimbach, "An Innovative Approach to the Determination of Safety for a Dietary Ingredient Derived From a New Source:

jfbc, 2025, 1, Downloaded from https://onlinelibrary.wiley.com/doi/10.1155/jfbc/9954087 by Chang Gung University Of, Wiley Online Library on [04/05/2026]. See the Terms and Conditions (https://onlinelibrary.wiley.com/terms-and-conditions) on Wiley Online Library for rules of use; OA articles are governed by the applicable Creative Commons License

Case Study Using a Crystalline Lutein Product," *Food and Chemical Toxicology* 40, no. 11 (2002): 1535–1549, https://doi.org/10.1016/s0278-6915(02)00131-x.

[83] A. A. El-Kholy, M. A. Elkablawy, and D. S. El-Agamy, "Lutein Mitigates Cyclophosphamide Induced Lung and Liver Injury via NF-κB/MAPK Dependent Mechanism," *Biomedicine & Pharmacotherapy* 92 (2017): 519–527, https://doi.org/10.1016/j.biopha.2017.05.103.

[84] Y. J. Ahn and H. Kim, "Lutein as a Modulator of Oxidative Stress-Mediated Inflammatory Diseases," *Antioxidants* 10, no. 9 (2021): 1448, https://doi.org/10.3390/antiox10091448.

jfbc, 2025, 1, Downloaded from https://onlinelibrary.wiley.com/doi/10.1155/jfbc/9954087 by Chang Gung University Of, Wiley Online Library on [04/05/2026]. See the Terms and Conditions (https://onlinelibrary.wiley.com/terms-and-conditions) on Wiley Online Library for rules of use; OA articles are governed by the applicable Creative Commons License

BIOCELL

Tech Science Press

Doi:10.32604/biocell.2025.066223

ARTICLE

Targeting c-Src/PKCα/MAPK/NF-κB: Salvianolic Acid A as a Protective Agent against Silica Nanoparticle-Induced Lung Inflammation

Yan-Jyun Lin[1,#], I-Ta Lee[2,#], Wen-Bin Wu[3,4], Chien-Chung Yang[5,6], Chiang-Wen Lee[7,8,9], Fuu-Jen Tsai[10,11,12], Hui-Ching Tseng[13], Wei-Ning Lin[4], Li-Der Hsiao[4] and Chuen-Mao Yang[4,*]

[1]Institute of Translational Medicine and New Drug Development, College of Medicine, China Medical University, Taichung, 40402, Taiwan
[2]School of Dentistry, College of Oral Medicine, Taipei Medical University, Taipei, 11031, Taiwan
[3]School of Medicine, Fu Jen Catholic University, New Taipei City, 24205, Taiwan
[4]Graduate Institute of Biomedical and Pharmaceutical Science, Fu Jen Catholic University, New Taipei City, 24205, Taiwan
[5]Department of Traditional Chinese Medicine, Chang Gung Memorial Hospital at Taoyuan, Taoyuan, 33378, Taiwan
[6]School of Traditional Chinese Medicine, College of Medicine, Chang Gung University, Taoyuan, 33302, Tawan
[7]Department of Nursing, Division of Basic Medical Sciences, and Chronic Diseases and Health Promotion Research Center, Chang Gung University of Science and Technology, Chiayi, 61363, Taiwan
[8]Department of Respiratory Care, Chang Gung University of Science and Technology, Chiayi, 61363, Taiwan
[9]Department of Orthopaedic Surgery, Chang Gung Memorial Hospital, Chiayi, 61363, Taiwan
[10]School of Chinese Medicine, College of Chinese Medicine, China Medical University, Taichung, 40402, Taiwan
[11]Department of Medical Research, China Medical University Hospital, China Medical University, Taichung, 40402, Taiwan
[12]Division of Medical Genetics, China Medical University Children's Hospital, Taichung, 40447, Taiwan
[13]Research Center for Chinese Herbal Medicine, Graduate Institute of Health Industry Technology, Chang Gung University of Science and Technology, Taoyuan, 33303, Taiwan

*Corresponding Author: Chuen-Mao Yang. Email: chuenmao@mail.cmu.edu.tw

[#]These authors contributed equally to this work

Received: 01 April 2025; Accepted: 17 June 2025; Published: 25 July 2025

ABSTRACT: Background: Silica nanoparticles (SiNPs), commonly utilized in industrial and biomedical fields, are known to provoke pulmonary inflammation by elevating cyclooxygenase-2 (COX-2) levels in human pulmonary alveolar epithelial cells (HPAEpiCs). Salvianolic acid A (SAA), a water-soluble polyphenol extracted from *Salvia miltiorrhiza* (Danshen), possesses well-documented antioxidant and anti-inflammatory activities. Nevertheless, its potential to counteract SiNP-induced inflammatory responses in the lung has not been thoroughly explored. **Objective:** This study aimed to evaluate the protective role and mechanistic actions of SAA against SiNP-triggered inflammation in both cellular and animal models. **Methods:** HPAEpiCs were pre-incubated with SAA prior to SiNP exposure to investigate changes in COX-2 expression and prostaglandin E_2 (PGE_2) secretion. A murine model of SiNP-induced lung inflammation was used for *in vivo* validation. Key inflammatory signaling proteins, including c-Src, PKCα, p42/p44 MAPK, and NF-κB p65, were analyzed for phosphorylation status. NF-κB promoter activity was also assessed. Pharmacological inhibitors and siRNA-mediated silencing were employed to verify the signaling cascade responsible for COX-2 regulation. **Results:** SAA treatment markedly suppressed SiNP-induced upregulation of COX-2 and PGE_2 in both HPAEpiCs and mouse lung tissues. SAA also reduced the activation (phosphorylation) of c-Src, PKCα, p42/p44 MAPK, and NF-κB p65, alongside diminishing NF-κB transcriptional activity. Functional studies using inhibitors and gene silencing further supported the involvement of these pathways in mediating the observed anti-inflammatory effect. **Conclusion:** By concurrently targeting several upstream pro-inflammatory signaling pathways, SAA demonstrates robust potential in alleviating SiNP-induced lung inflammation. These results highlight SAA as a promising candidate for therapeutic intervention in environmentally triggered respiratory conditions.

Copyright © 2025 The Authors. Published by Tech Science Press.
This work is licensed under a Creative Commons Attribution 4.0 International License, which permits unrestricted use, distribution, and reproduction in any medium, provided the original work is properly cited.

KEYWORDS: Silica nanoparticles; salvianolic acid A; pulmonary inflammation; COX-2 expression; NF-κB signaling pathway

1 Introduction

Silica nanoparticles (SiNPs) have garnered significant attention due to their unique properties, making them highly valuable in various fields such as medicine, industry, and commercial applications. These applications include their use as drug delivery carriers, imaging agents, and components in biosensors, owing to their biocompatibility, high surface area, and ease of surface modification [1]. However, the widespread utilization of SiNPs inevitably leads to human exposure through multiple routes, including intravenous injection, inhalation, oral intake, and transdermal absorption [1]. With the increasing prevalence of SiNPs in industrial and medical practices, there is an urgent need to assess their potential risks to human health and establish regulatory guidelines.

Despite their beneficial applications, numerous studies have raised concerns about the adverse health effects associated with SiNPs exposure, particularly on the respiratory system [2]. The lungs, being one of the primary routes of nanoparticle exposure, are highly susceptible to SiNP-induced toxicity. SiNPs exposure is known to induce lung inflammation, injury, fibrosis, and granulomatous inflammation, as demonstrated *in vivo* through intratracheal and intranasal instillation in model organisms [3–5]. Additionally, occupational and environmental studies have reported respiratory complications in workers exposed to silica-containing dusts, including silicosis, chronic obstructive pulmonary disease (COPD), and lung cancer, which share similar pathological features, such as fibrosis and persistent inflammation, with nanoparticle-induced lung damage [6,7]. These findings highlight the need for a comprehensive understanding of the mechanisms underlying SiNP-induced respiratory toxicity to develop effective therapeutic strategies.

The inflammatory response induced by SiNPs is closely associated with the upregulation of cyclooxygenase-2 (COX-2) and prostaglandin E_2 (PGE_2) across various cell types, as our previous research has demonstrated [8,9]. COX-2 is an inducible enzyme that converts arachidonic acid (AA) into prostanoids, including prostaglandins (PGs), thromboxanes (TXs), and related molecules, which serve as key mediators in the processes of inflammation and pain [10]. Dysregulation of COX-2 signaling has been implicated in various pathological conditions, including COPD, asthma, and acute respiratory distress syndrome (ARDS) [10–12]. Although conventional anti-inflammatory drugs, such as non-steroidal anti-inflammatory drugs (NSAIDs) and COX-2 selective inhibitors, have been widely used to alleviate inflammation by targeting COX-2, they often carry significant side effects, including gastrointestinal damage, cardiovascular risk, and impaired renal function, which limit their long-term use [10,13,14]. Moreover, these drugs primarily act by blocking COX-2 enzymatic activity, without addressing the upstream signaling pathways and oxidative stress that contribute to chronic inflammation and tissue damage, potentially limiting their effectiveness in complex inflammatory conditions.

Salvianolic acid A (SAA) represents one of the principal water-soluble phenolic compounds isolated from *Salvia miltiorrhiza*, a traditional Chinese medicinal plant extensively employed for its pharmacological benefits [15]. Unlike conventional NSAIDs, SAA exerts its anti-inflammatory effects through a multi-target approach, providing a broader therapeutic spectrum [16]. It not only inhibits COX-2 expression but also modulates multiple upstream signaling pathways. Specifically, Liu et al. demonstrated that SAA suppresses c-Src signaling to protect cerebrovascular endothelial cells from ischemic injury [17]. Moreover, studies on related inflammatory models have shown that COX-2 expression can be regulated via PKCα, p42/p44 MAPK, and NF-κB cascades [18,19], suggesting that these pathways may also be involved in the anti-inflammatory mechanism of SAA. Additionally, SAA activates the Nrf2/HO-1 antioxidant pathway,

reducing oxidative stress and preventing cellular damage, a feature particularly beneficial for managing chronic inflammatory and fibrotic diseases [20–22]. Clinical studies have also suggested that SAA can reduce inflammation without the significant gastrointestinal, cardiovascular, and renal side effects commonly associated with NSAIDs, making it a promising candidate for long-term therapeutic use [16,23,24].

Moreover, SAA's ability to inhibit multiple pro-inflammatory mediators, including interleukins (e.g., IL-6), tumor necrosis factor-alpha (TNF-α), and matrix metalloproteinases (MMPs), positions it as a more comprehensive therapeutic agent for respiratory diseases [16,23,24]. Recent studies have demonstrated that SAA effectively attenuates lung injury in animal models of acute lung inflammation and fibrosis by modulating these pathways, supporting its potential clinical application in nanoparticle-induced lung disorders [25,26]. This multi-target therapeutic profile, combined with a favorable safety profile, underscores the potential of SAA to address the limitations of conventional anti-inflammatory therapies, providing a more integrated approach to managing complex inflammatory diseases.

Here, we aimed to investigate the effects of SAA on SiNPs-induced COX-2 expression in both *in vivo* and *in vitro* settings. Specifically, we sought to elucidate the underlying mechanisms by which SAA targets the signaling components in human pulmonary alveolar epithelial cells (HPAEpiCs). By understanding these mechanisms, we hope to provide insights into the potential therapeutic applications of SAA in treating SiNPs-induced pulmonary inflammation and injury. Our research focuses on the suppression of key signaling pathways, including c-Src, PKCα, p42/p44 MAPK, and NF-κB, which are known to be involved in the regulation of COX-2 expression and inflammatory responses in lung tissue. Additionally, this work contributes to the growing body of evidence supporting the use of bioactive compounds in mitigating nanoparticle-induced health risks, paving the way for safer industrial and medical practices involving nanotechnology.

2 Materials and Methods

2.1 Reagents and Antibodies

Dulbecco's Modified Eagle's Medium/Nutrient Mixture F-12 (DMEM/F-12) (#11330032), fetal bovine serum (FBS) (#A5256701), TRIzol™ Reagent (#15596018), and M-MLV Reverse Transcriptase Kit (#28025013) were purchased from Invitrogen, Carlsbad, CA, USA. The BioTrace™ NT Nitrocellulose Transfer Membrane (#66485) was obtained from Pall Corporation, Port Washington, NY, USA. GenMute™ siRNA Transfection Reagent (#SL100568-HepG2) was purchased from SignaGen Laboratories, Frederick, MD, USA. Src Kinase Inhibitor II (Srci II) (#sc-222325) was purchased from Santa Cruz Biotechnology, Dallas, TX, USA. Ro318220 (#HY-13866A), Gö6976 (#HY-10183), U0126 (#HY-12031A), and helenalin (#HY-119970) were purchased from MedChemExpress, Monmouth Junction, NJ, USA. Anti-β-actin antibody (#4967), anti-COX2 antibody (#12282), anti-GAPDH antibody (#2118), anti-phospho-c-Src (Tyr416) antibody (#2101), anti-phospho-p44/42 MAPK (Thr202/Tyr204) antibody (#9101), anti-phospho-NF-κB p65 (Ser536) antibody (#3033), anti-Src antibody (#2109), anti-PKCα antibody (#59754), anti-p44/42 MAPK antibody (#9102), and anti-NF-κB p65 antibody (#8242) were purchased from Cell Signaling Technology, Danvers, MA, USA. The anti-phospho-PKCα (Ser657) antibody (#ab180848) was purchased from Abcam, Cambridge, UK. Peroxidase-AffiniPure™ Goat Anti-Rabbit IgG (H + L) (#111-035-003) and Peroxidase-AffiniPure™ Goat Anti-Mouse IgG (H + L) (#115-035-003) were sourced from Jackson ImmunoResearch Laboratories, West Grove, PA, USA. Pierce™ BCA Protein Assay Reagent A (#23228) and Pierce™ BCA Protein Assay Reagent B (#23224) were obtained from Thermo Fisher Scientific, Waltham, MA, USA. Silica nanoparticles (SiNPs, nanopowder; particle size 10–20 nm) (#637238) and Salvianolic Acid A (SAA) (#SML4045) were purchased from Sigma-Aldrich, St. Louis, MO, USA.

2.2 Animals Experimental Design

All procedures involving animals were carried out in full compliance with the ARRIVE guidelines [27] and received prior approval from the Institutional Animal Care and Use Committee of Chang Gung University (Approval No. CGU 16-046). The study also adhered to the National Institutes of Health (NIH) Guide for the Care and Use of Laboratory Animals (NIH Publication No. 85-23, revised 1996). Male ICR (Institute of Cancer Research) mice, 6 to 8 weeks old and weighing around 25 g, were purchased from the National Laboratory Animal Center in Taipei, Taiwan. Only male mice were used to minimize the influence of hormonal variations on experimental outcomes. The mice were housed in a specific pathogen-free (SPF) facility with a controlled temperature of 25 ± 2°C and a 12 h light/dark cycle, with free access to autoclaved food and water. Cages were cleaned and sterilized regularly to maintain a clean and controlled environment, reducing the risk of infection and stress. Fifteen mice (n = 5 per group) were randomly divided into three experimental groups: a sham group (50 μL of sterile saline), a SiNPs group (10 mg/kg SiNPs), and an SAA + SiNPs group (50 mg/kg SAA administered by intraperitoneal injection 1 h before the SiNPs challenge, followed by 10 mg/kg SiNPs). SiNPs were administered via intratracheal instillation to ensure direct delivery to the lungs, as previously described [3]. Each mouse received a total dose of 10 mg/kg of SiNPs, which corresponds to 0.25 mg for a 25 g mouse. The SiNPs suspension was prepared in sterile saline and ultrasonicated for 15 min before administration to ensure uniform dispersion and prevent nanoparticle aggregation. Mice were anesthetized and positioned on a near-vertical board, with their tongues gently withdrawn using lined forceps to expose the trachea. The SiNPs suspension was then carefully instilled into the trachea, allowing the particles to be aspirated into the lungs over a 24 h period. The sham group received an equivalent volume (50 μL) of sterile saline using the same method. The SiNPs used in this study were high-purity, uncoated particles with a diameter of approximately 50 nm (purity > 99%). At the end of the experimental period, mice were sacrificed using a high dose of pentothal (100 mg/kg, i.p.) to ensure humane euthanasia. Lung tissues were collected for further analysis, with the right superior and post caval lobes used for protein extraction and the right middle and inferior lobes used for mRNA expression analysis of COX-2. Bronchoalveolar lavage (BAL) fluid was obtained via a tracheal cannula by instilling 1 mL of ice-cold PBS. To ensure objectivity, data collection and analysis for both *in vivo* and *in vitro* experiments were conducted in a blinded fashion, with investigators unaware of group assignments.

2.3 Immunohistochemical Staining

At 24 h after SiNPs administration, left lung tissues were collected, fixed in 4% paraformaldehyde at 4°C for 24 h, and processed for paraffin embedding. Sections were deparaffinized, rehydrated, and treated with 5 mg/mL BSA in PBS to block non-specific binding. COX-2 expression was detected by incubation with anti-COX-2 primary antibody (1:300, 16 h at 4°C), followed by HRP-conjugated goat anti-rabbit IgG (1:500, 1 h at room temperature). The signal was visualized using 3, 3-diaminobenzidine (DAB) (0.5 mg/mL; Sigma-Aldrich, D5637, St. Louis, MO, USA) and 0.01% hydrogen peroxide in 0.1 M Tris-HCl buffer for 5 min in the dark.

2.4 Cell Culture

HPAEpiCs (ScienCell Research Laboratories, 3200, San Diego, CA, USA) were confirmed to be mycoplasma-free and cultured as previously described [28]. Cells were maintained in DMEM/F-12 medium supplemented with 10% FBS and Antibiotic-Antimycotic Solution (Invitrogen, 15240062, Carlsbad, CA, USA), containing 100 U/mL penicillin G, 100 μg/mL gentamicin, and 250 ng/mL amphotericin B. Cells were seeded at appropriate densities in 12-well plates (1 mL/well), 6-well plates (2 mL/well), or 10 cm

dishes (10 mL/dish). Upon reaching confluence, they were serum-starved overnight in serum-free DMEM/F-12 to induce quiescence. All experiments were conducted using cells at passages 5–7. According to the manufacturer, HPAEpiCs are human lung-derived alveolar epithelial cells characterized by cytokeratin-18/19 positivity, and are known to retain epithelial properties under standard culture conditions.

2.5 Western Blot Analysis

Growth-arrested HPAEpiCs were treated with various concentrations of SiNPs at 37°C for the indicated time periods. For experiments involving pharmacological inhibitors, the compounds were added 1 h prior to SiNPs exposure, while SAA was applied 2 h in advance. Cell harvesting and protein extraction were performed according to standard protocols [29]. After treatment, cells were rinsed thoroughly, collected, and denatured by heating at 95°C for 15 min. Lysates were centrifuged at 45000× *g* for 15 min at 4°C to obtain whole-cell extracts. Protein samples were separated using 10% SDS-PAGE and transferred onto nitrocellulose membranes (66485, Pall Corporation). Membranes were blocked and incubated overnight at 4°C with primary antibodies diluted at 1:1000, as listed in Section 2.1. After washing, membranes were incubated with horseradish peroxidase (HRP) conjugated goat anti-rabbit IgG (1:2000, 111035003, Jackson ImmunoResearch Laboratories) or goat anti-mouse IgG (1:2000, 115035003, Jackson ImmunoResearch Laboratories), depending on the source of the primary antibody. Protein bands were visualized using enhanced chemiluminescence (ECL) substrate (Thermo Fisher Scientific, 34577, Waltham, MA, USA) and captured using the Azure Biosystems 260 imaging system (Dublin, CA, USA). Band intensities were quantified using UN SCAN IT gel analysis software (Silk Scientific, Orem, UT, USA).

2.6 Real-Time PCR Analysis

Total RNA was extracted from SiNP-treated HPAEpiCs using TRIzol reagent. RNA quality was assessed spectrophotometrically. As described previously [30], 5 μg of RNA was reverse transcribed into cDNA and analyzed by real-time PCR using the StepOnePlus™ system (Applied Biosystems™/Thermo Fisher Scientific, Waltham, MA, USA). COX-2 and GAPDH expression levels were quantified using gene-specific primers and the $2^{(Ct\ COX\text{-}2 - Ct\ GAPDH)}$ method (Ct = threshold cycle). The primer sequences were:

COX-2:

Sense: 5′-CAAACTGAAATTTGACCCAGAACTAC-3′

Anti-sense: 5′-ACTGTTGATAGTTGTATTTCTGGTCATGA-3′

GAPDH:

Sense: 5′-GCCAGCCGAGCCACAT-3′

Anti-sense: 5′-CTTTACCAGAGTTAAAAGCAGCCC-3′

2.7 Measurement of PGE_2 Release

HPAEpiCs rendered quiescent by serum starvation were pretreated with specific pharmacological inhibitors and subsequently exposed to SiNPs or vehicle control at 37°C for the indicated durations. Following treatment, supernatants were collected, and PGE_2 levels were measured using a PGE_2 ELISA kit (Enzo Life Sciences, ADI901001, Farmingdale, NY, USA) according to the manufacturer's protocol.

2.8 Transient Transfection with siRNAs

HPAEpiCs were seeded in 6-well plates and cultured until they reached approximately 80% confluence. SMARTpool siRNAs targeting scramble control, c-Src (SASI_Hs01_00112905, NM_198291.3), PKCα (SASI_Hs01_00018817, NM_002737), p42 (SASI_Hs01_00058601, NM_004364), and p65

(SASI_Hs01_00171091, NM_021975) were obtained from Sigma-Aldrich (St. Louis, MO, USA). HPAEpiCs were transfected with 100 nM siRNA using GenMute™ reagent (SL100568-HepG2, SignaGen Laboratories) according to the manufacturer's protocol. After sequential incubation in complete and serum-free DMEM/F-12 medium to ensure quiescence, cells were treated with SiNPs for the indicated durations.

2.9 Cell Viability

To assess cell viability, confluent HPAEpiCs were growth-arrested in serum-free DMEM/F-12 overnight, then treated with SAA. Viability was evaluated using the Cell Counting Kit-8 (CCK-8; Dojindo Molecular Technologies, CK04, Kumamoto, Japan), and absorbance was measured at 450 nm with a Synergy H1 microplate reader (BioTek Instruments, VT, USA).

2.10 Analysis of Luciferase Reporter Gene Activity

NF-κB transcriptional activity was assessed using the NF-κB Reporter Assay Kit (BPS Bioscience, 60614, San Diego, CA, USA) following the manufacturer's protocol. Firefly and Renilla luciferase signals were quantified with the Dual-Luciferase® Reporter Assay System (Promega, E1910, Madison, WI, USA), and luminescence was recorded using a Synergy H1 microplate reader (BioTek Instruments, VT, USA). Firefly signals were normalized to Renilla signals.

2.11 Statistical Analysis of Data

All results are presented as mean ± standard deviation (SD) from a minimum of three independent experiments. Statistical evaluation was conducted using GraphPad Prism version 6.0 (GraphPad Software, San Diego, CA, USA). Group differences were analyzed by one-way ANOVA followed by Tukey's post hoc test. A p-value < 0.05 was considered statistically significant.

3 Results

3.1 SAA Mitigates SiNP-Induced Pulmonary Inflammation and COX-2 Upregulation in Mice

Our previous study established that SiNPs induce alveolar inflammation [8]. In this study, we further explored the impact of SiNPs on COX-2 expression and the mitigating effects of SAA, focusing on both molecular and cellular responses. As shown in Fig. 1A, immunohistochemical staining revealed a significant increase in COX-2 protein expression in lung sections from SiNPs-treated mice. This upregulation of COX-2 was markedly reduced in mice pre-administered with SAA, compared to untreated mice, demonstrating the compound's ability to modulate inflammatory protein expression at the tissue level. To validate these observations, we employed Western blot and real-time PCR analyses, which confirmed elevated levels of COX-2 protein and mRNA in lung tissues from SiNPs-exposed mice (Fig. 1B,C). These molecular analyses further reinforced the robust inflammatory response elicited by SiNPs and the therapeutic efficacy of SAA in reversing these effects. Remarkably, SAA treatment led to a significant downregulation of both COX-2 protein and mRNA expression in these mice, highlighting SAA's potential to counteract SiNPs-induced inflammatory responses at the molecular level. Furthermore, leukocyte recruitment to pulmonary alveolar epithelial cells is a hallmark of lung inflammation, contributing to the pathological processes of various lung diseases [14]. Our data indicated that SiNPs-stimulated mice exhibited a substantial increase in leukocytes within the bronchoalveolar lavage fluid (BALF), as shown in Fig. 1D. This observation underscores the systemic impact of SiNP exposure on immune cell infiltration, exacerbating pulmonary inflammation. Notably, SAA pretreatment significantly reduced the number of leukocytes, suggesting its efficacy in mitigating SiNPs-induced pulmonary inflammation by modulating immune cell activity in addition to suppressing

COX-2 expression. These combined data strongly suggest that the accumulation of SiNPs triggers pulmonary inflammatory responses, characterized by increased COX-2 expression and leukocyte infiltration, which can be effectively attenuated by SAA. Given these findings, we extended our investigation to elucidate the signaling pathways involved in SiNPs-induced COX-2 expression and how SAA modulates these pathways. Specifically, we aimed to understand the molecular targets of SAA within the inflammatory signaling cascades, providing deeper insights into its role as a potential therapeutic agent. Understanding these mechanisms could provide deeper insights into the therapeutic potential of SAA in treating SiNPs-related pulmonary inflammation and guide future research into nanoparticle-induced respiratory diseases.

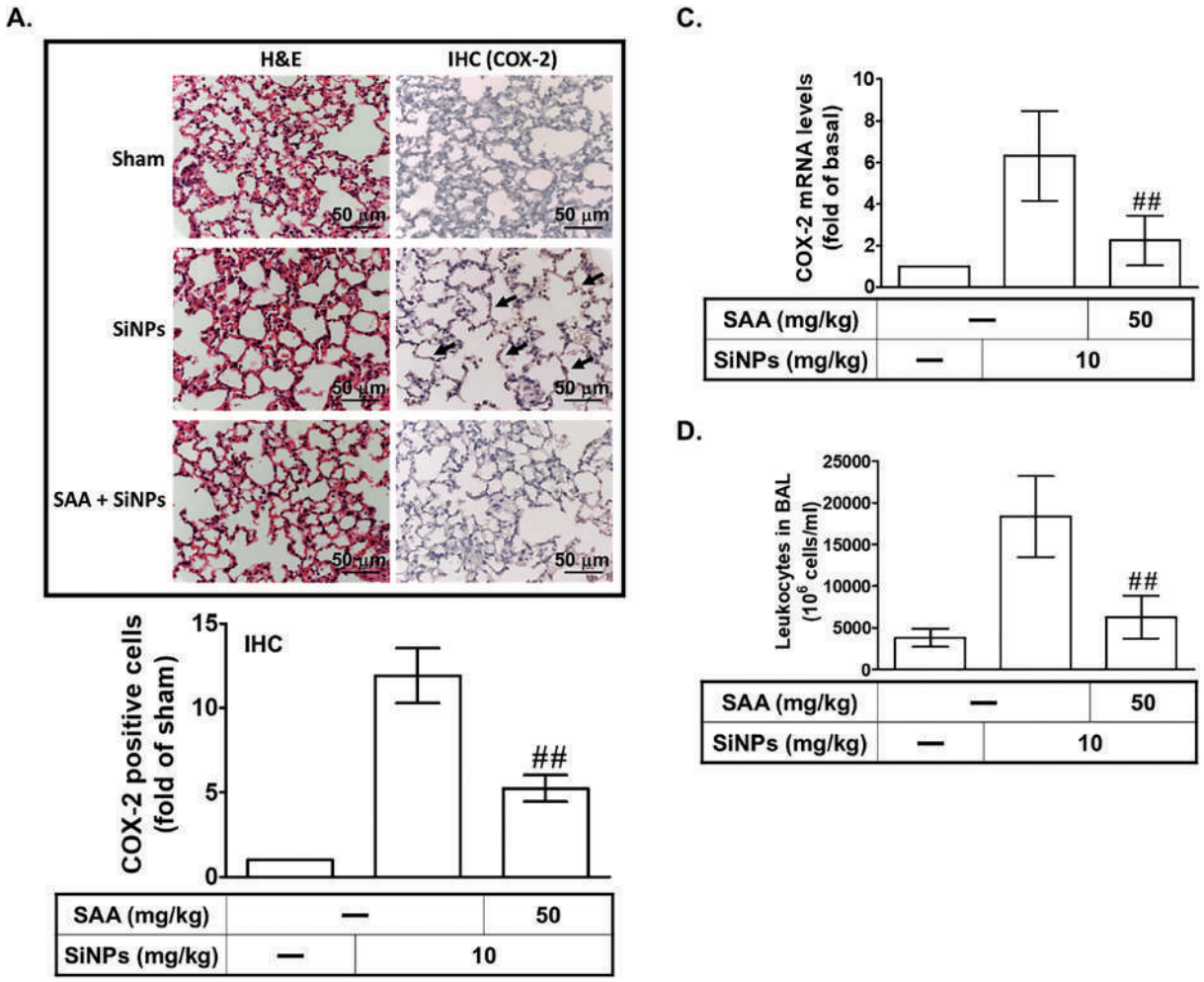


Figure 1: (Continued)

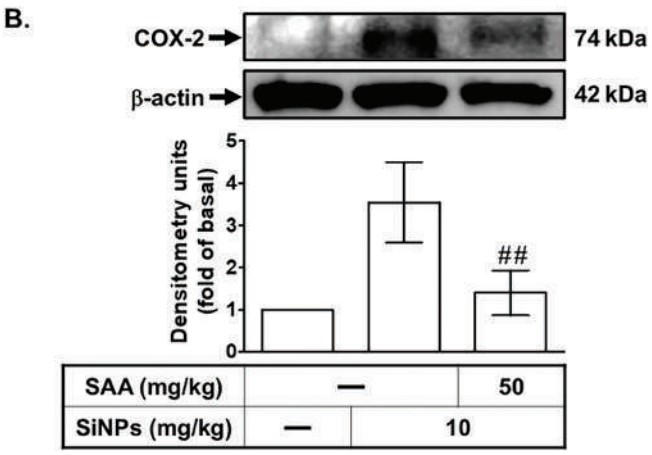


Figure 1: SAA alleviates SiNP-induced pulmonary inflammation and COX-2 expression *in vivo*. (**A**) Mice received an intraperitoneal injection of SAA (50 mg/kg) or vehicle 1 h prior to intratracheal instillation of SiNPs (10 mg/kg). After 24 h, lung tissues were collected for histological and immunohistochemical (IHC) analyses. H&E staining was used to assess inflammation and structural damage, while IHC staining for COX-2 visualized inflammatory protein expression. Representative images are shown for the sham group (50 μL sterile saline), SiNPs group (10 mg/kg SiNPs), and SAA + SiNPs group (50 mg/kg SAA plus 10 mg/kg SiNPs). Arrows indicate COX-2 expression in alveolar cells. (**B**,**C**) Lung homogenates were analyzed for COX-2 protein and mRNA levels using Western blot and real-time PCR, respectively. (**D**) Total leukocyte counts in bronchoalveolar lavage fluid (BALF) were determined for each group. Data are presented as mean ± SD from five independent experiments. ##$p < 0.01$ compared to the SiNPs group

3.2 SAA Inhibits SiNPs-Induced COX-2 Expression and PGE_2 Production in HPAEpiCs

To assess the effect of SAA on cell viability, HPAEpiCs were treated with SAA at various concentrations. As shown in Fig. 2A, cells treated with 0, 1, 10, 50, or 100 μM SAA for 24 h demonstrated that 1 and 10 μM SAA did not significantly affect cell viability, while higher concentrations (50 and 100 μM) caused marked cytotoxicity, significantly reducing cell viability. These findings indicate that 1 and 10 μM SAA are non-cytotoxic, while higher concentrations are detrimental to cell survival, underscoring the importance of selecting appropriate SAA concentrations for subsequent experiments. To examine the time-dependent effects of SAA on cell viability, HPAEpiCs were treated with 10 μM SAA for 0, 8, 12, 24, or 48 h. As shown in Fig. 2B, no significant reduction in cell viability was observed at any of the tested time points, confirming that 10 μM SAA is well-tolerated over extended exposure periods. To further investigate the effect of SAA on SiNPs-induced COX-2 expression, HPAEpiCs were pretreated with 1, 5, or 10 μM SAA for 2 h before SiNPs stimulation. As shown in Fig. 2C, SAA significantly reduced COX-2 protein levels in a concentration-dependent manner, indicating that SAA effectively modulates inflammatory pathways triggered by nanoparticle exposure. To assess the effect of SAA on COX-2 mRNA expression, HPAEpiCs were pretreated with 10 μM SAA for 2 h before SiNPs stimulation. As shown in Fig. 2D, SAA significantly reduced COX-2 mRNA levels, reinforcing its capability to suppress inflammation at the transcriptional level. Finally, to evaluate the effect of SAA on the secretion of downstream inflammatory mediators, PGE_2 levels were measured. As shown in Fig. 2E, SAA significantly reduced PGE_2 secretion, confirming its ability to inhibit the production of pro-inflammatory mediators. Together, these findings highlight the potential of SAA as a therapeutic agent in mitigating SiNPs-induced inflammation in pulmonary cells. By effectively downregulating COX-2 expression, reducing PGE_2 secretion, and maintaining cell viability at optimized concentrations, SAA could play a critical role in treating lung inflammation caused by nanoparticle exposure.

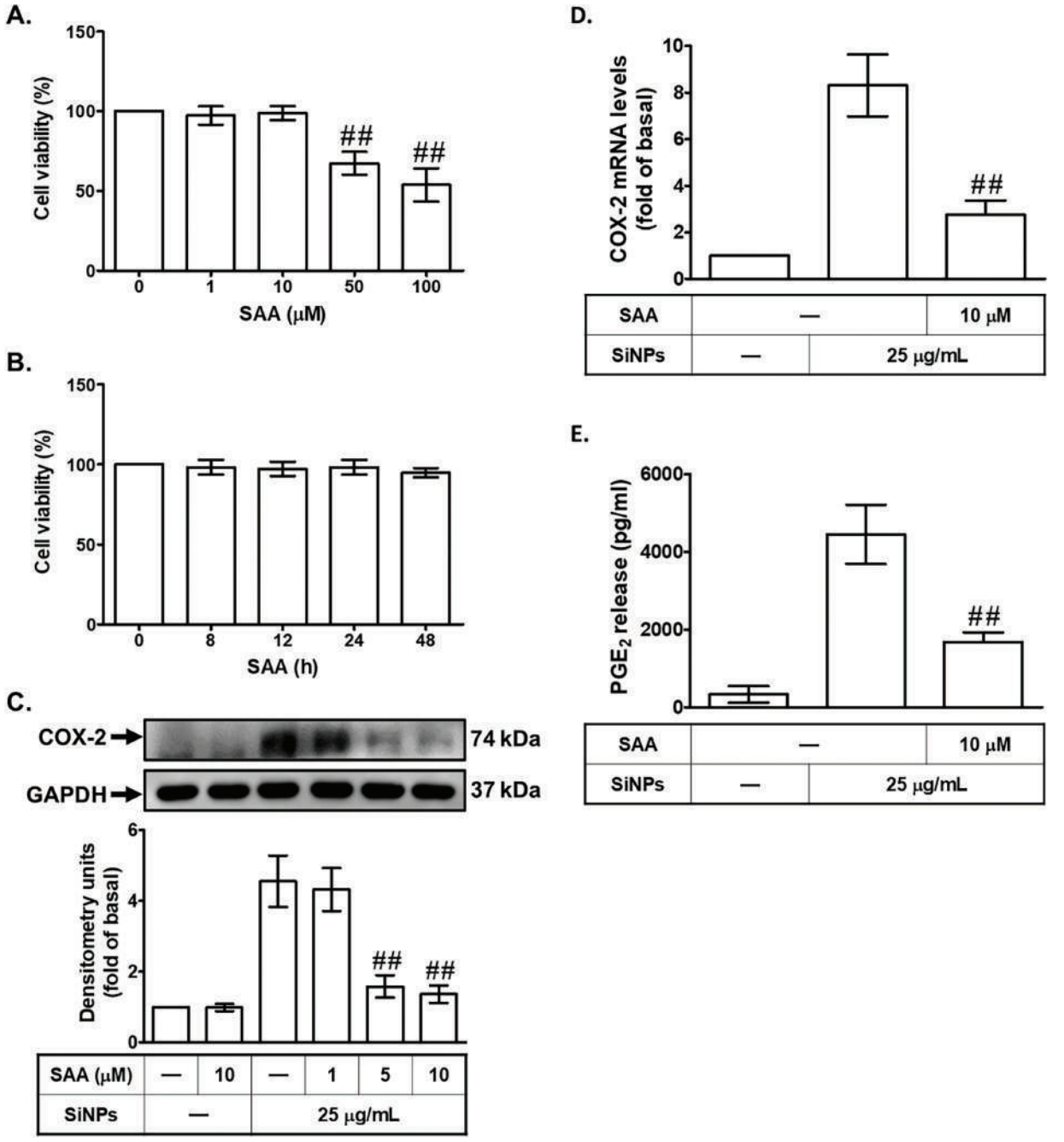


Figure 2: SAA inhibits SiNP-induced COX-2 expression and PGE_2 production in HPAEpiCs. (**A**) Cells were treated with increasing concentrations of SAA (0, 1, 10, 50, 100 μM) for 24 h to assess cytotoxicity. (**B**) Cells were treated with 10 μM SAA for varying durations (0, 8, 12, 24, 48 h) to evaluate time-dependent effects on cell viability. (**C**) HPAEpiCs were pretreated with SAA (1, 5, or 10 μM) for 2 h prior to SiNP stimulation, and COX-2 protein expression was analyzed by Western blot. (**D**) COX-2 mRNA levels were measured by real-time PCR after pretreatment with 10 μM SAA for 2 h followed by SiNP exposure. (**E**) PGE_2 levels in the culture supernatant were assessed under the same conditions as (**D**). Data are presented as mean ± SD from at least three independent experiments. ##$p < 0.01$ compared with the control group (**A**); ##$p < 0.01$ compared with cells exposed to SiNPs alone (**C**–**E**)

3.3 SAA Attenuates SiNPs-Induced COX-2 Expression by Suppressing c-Src Activation

Previous research has indicated that COX-2 expression can be mediated through Src kinase activity, a critical component of several inflammatory signaling pathways [31]. To explore the role of c-Src in SiNPs-induced COX-2 expression, we pretreated HPAEpiCs with Src inhibitor II (Srci II) before SiNPs exposure. Preincubation with Srci II significantly reduced SiNPs-induced COX-2 protein and mRNA expression (Fig. 3A,B), demonstrating the importance of c-Src in mediating the inflammatory response triggered by nanoparticles. This suggests that c-Src activation is crucial for the upregulation of COX-2 in response to SiNPs, highlighting its role as a key regulatory node in this process. To further investigate the role of c-Src, we transfected HPAEpiCs with c-Src siRNA, an approach that enables specific suppression of the c-Src gene. As shown in Fig. 3C, cells transfected with c-Src siRNA exhibited a decrease in COX-2 protein levels compared to cells transfected with scrambled siRNA, reinforcing the importance of c-Src in regulating COX-2 expression. This finding emphasizes that c-Src signaling is an upstream regulator of COX-2 expression in SiNP-exposed cells. Additionally, we examined the necessity of c-Src phosphorylation for COX-2 expression by exposing HPAEpiCs to SiNPs for various time periods. The results indicated that transfection with c-Src siRNA significantly reduced c-Src phosphorylation induced by SiNPs (Fig. 3D). Consistent with these findings, pretreatment with SAA also substantially decreased c-Src phosphorylation in HPAEpiCs exposed to SiNPs (Fig. 3E). This demonstrates that SAA can inhibit the activation of c-Src, which is a key mediator of COX-2 expression in response to SiNPs. Furthermore, we observed that Srci II reduced SiNPs-induced PGE_2 generation in HPAEpiCs (Fig. 3F), indicating that c-Src activity is also necessary for PGE_2 production. This reinforces the close relationship between c-Src activation and downstream inflammatory mediators. These results collectively suggest that SAA exerts its anti-inflammatory effects by suppressing the phosphorylation of c-Src, thereby downregulating SiNPs-stimulated COX-2 expression and subsequent PGE_2 production. By targeting c-Src activation, SAA effectively interferes with a critical pathway that drives inflammation in response to nanoparticle exposure. The implications of these findings are significant, as they highlight the potential of SAA to interfere with critical signaling pathways involved in inflammation, offering a promising therapeutic approach for conditions associated with nanoparticle-induced pulmonary inflammation. These insights open new avenues for further research to explore the broader applicability of SAA in managing inflammatory diseases caused by environmental and occupational nanoparticle exposure.

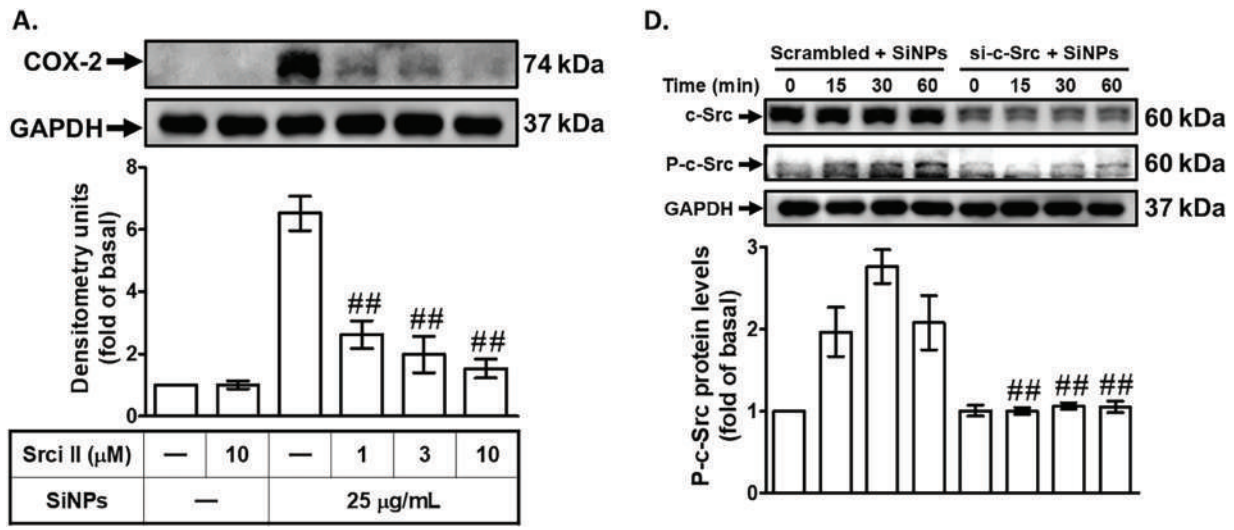


Figure 3: (Continued)

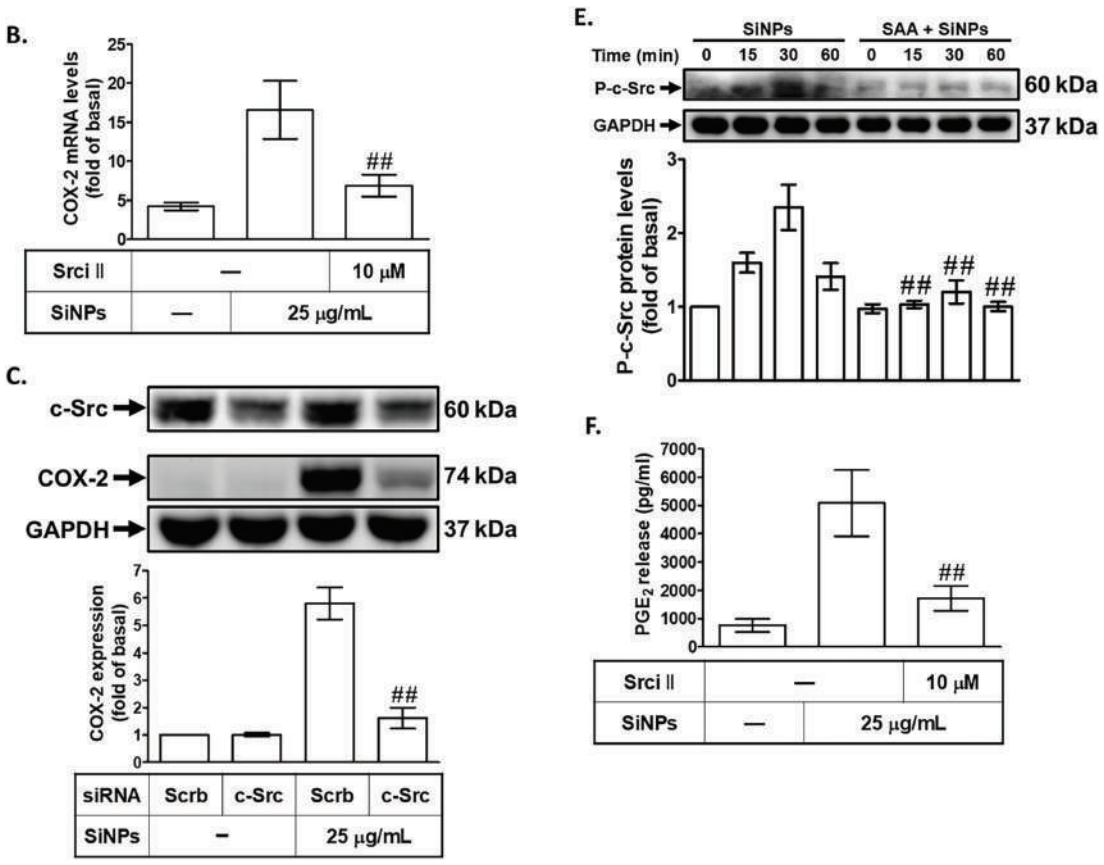


Figure 3: SAA reduces SiNP-induced COX-2 expression by inhibiting c-Src activation. (**A**,**B**) HPAEpiCs were pre-treated with Srci II at various concentrations or at 10 μM for 1 h, followed by exposure to 25 μg/mL SiNPs. COX-2 protein (**A**) and mRNA (**B**) levels were analyzed by Western blot and real-time PCR, respectively. (**C**) Knockdown of c-Src by siRNA reduced both total c-Src and COX-2 protein expression in response to SiNPs. (**D**) Transfection with c-Src siRNA suppressed both total and phosphorylated c-Src protein levels following SiNP treatment at 0, 15, 30, and 60 min. (**E**) Pretreatment with SAA (10 μM) attenuated the phosphorylation of c-Src over the same time course. (**F**) Srci II pretreatment reduced PGE_2 secretion in the supernatant after SiNP exposure. Data are presented as mean ± SD from at least three independent experiments. ##$p < 0.01$ compared with cells exposed to SiNPs alone (**A**,**B**,**E**,**F**); ##$p < 0.01$ compared to cells treated with SiNPs + scrambled siRNA (**C**,**D**)

3.4 SAA Attenuates SiNPs-Induced COX-2 Expression by Inhibiting PKC Phosphorylation

The role of PKC activation in SiNPs-induced COX-2 expression was investigated by pretreating HPAEpiCs with either a non-selective PKC inhibitor (Ro318220) or a PKCα inhibitor (Gö6976) before exposure to SiNPs. PKC, a family of serine/threonine kinases, plays a pivotal role in regulating cellular signaling pathways involved in inflammation and other pathological processes [32]. As shown in Fig. 4A,B, both Ro318220 and Gö6976 significantly reduced SiNPs-induced COX-2 protein and mRNA expression, providing compelling evidence that PKCα activation is critical for the upregulation of COX-2 in response to SiNPs. This finding underscores the importance of PKCα as a central mediator in the inflammatory cascade triggered by nanoparticle exposure. Additionally, transfection of HPAEpiCs with PKCα siRNA effectively knocked down PKCα protein expression and attenuated SiNPs-induced COX-2 protein levels (Fig. 4C). This result further highlights the specific involvement of PKCα in mediating COX-2 expression following

SiNPs exposure and validates its role as a potential therapeutic target. Further analysis revealed that SiNPs-induced PKCα phosphorylation occurred in a time-dependent manner, which was significantly suppressed by PKCα siRNA transfection, as shown in Fig. 4D. However, PKCα siRNA did not significantly reduce SiNPs-induced c-Src phosphorylation, indicating that PKCα acts downstream of c-Src in this signaling pathway. As shown in Fig. 4E, transfection with c-Src siRNA significantly reduced SiNPs-induced PKCα phosphorylation, demonstrating that c-Src activation is required for PKCα phosphorylation in this context. This finding supports the notion that c-Src is an upstream regulator of PKCα in the signaling cascade leading to COX-2 expression. Moreover, Fig. 4F demonstrates that SAA pretreatment significantly inhibited PKCα phosphorylation in SiNPs-stimulated HPAEpiCs, suggesting that SAA interferes with this critical signaling event, potentially by targeting upstream c-Src activation. Additionally, as shown in Fig. 4G, pretreatment with Ro318220 or Gö6976 significantly reduced PGE_2 generation in SiNPs-stimulated HPAEpiCs, further confirming the essential role of PKCα activation in the inflammatory response. These findings collectively suggest that SAA exerts its anti-inflammatory effects by inhibiting both c-Src and PKCα activation, thereby downregulating SiNPs-induced COX-2 expression and subsequent PGE_2 production. This highlights the interconnected nature of c-Src and PKCα signaling in the inflammatory response to nanoparticle exposure and underscores the therapeutic potential of SAA in targeting this signaling axis. Future studies should further explore the broader applicability of SAA in other models of inflammation and investigate its efficacy and safety in clinical settings to establish its potential as a viable treatment option for nanoparticle-induced pulmonary inflammation.

3.5 SAA Inhibits SiNPs-Induced COX-2 Expression by Suppressing p42/p44 MAPK Phosphorylation

To investigate the role of p42/p44 MAPK in SiNPs-induced COX-2 expression, we treated HPAEpiCs with a potent and selective MEK1/2 inhibitor, U0126, prior to SiNPs exposure. MEK1/2 is a well-established upstream kinase that directly activates p42/p44 MAPK through phosphorylation, making it an ideal target to probe the involvement of p42/p44 MAPK in inflammatory signaling [33]. Preincubation with U0126 significantly reduced SiNPs-induced COX-2 protein and mRNA expression in HPAEpiCs (Fig. 5A,B), demonstrating that p42/p44 MAPK activation is critical for the upregulation of COX-2 in response to SiNPs. This finding highlights the pivotal role of the p42/p44 MAPK pathway in mediating the inflammatory effects of nanoparticles. To further validate the involvement of p42/p44 MAPK in this process, we employed siRNA transfection targeting p42. This approach allows for specific gene silencing and provides direct evidence of the functional role of p42. As shown in Fig. 5C, transfection with p42 siRNA effectively decreased COX-2 protein levels in SiNPs-treated HPAEpiCs, confirming that p42/p44 MAPK is a key signaling component in the induction of COX-2 expression by SiNPs. This reduction underscores the direct contribution of p42/p44 MAPK to the inflammatory cascade initiated by SiNP exposure. Fig. 5D demonstrates that SiNPs-induced phosphorylation of p42/p44 MAPK in HPAEpiCs was significantly suppressed by p42 siRNA, confirming that p42/p44 MAPK is directly involved in this signaling pathway. However, transfection with p42 siRNA did not reduce SiNPs-induced phosphorylation of c-Src or PKCα, indicating that p42/p44 MAPK acts downstream of these kinases and does not provide feedback regulation to upstream signals. Additionally, as shown in Fig. 5E, transfection with PKCα siRNA significantly reduced p42/p44 MAPK phosphorylation in SiNPs-stimulated HPAEpiCs, indicating that PKCα acts as an upstream regulator of p42/p44 MAPK in this signaling pathway. This finding highlights the critical role of PKCα in mediating the activation of downstream MAPK pathways, which are essential for the upregulation of COX-2 in response to SiNPs exposure. Moreover, pretreatment with SAA effectively inhibited the SiNPs-induced phosphorylation of p42/p44 MAPK, demonstrating SAA's ability to interfere with this critical signaling event (Fig. 5F). This inhibition aligns with SAA's previously documented anti-inflammatory properties and further supports its

role in modulating key components of inflammatory pathways. Finally, as shown in Fig. 5G, pretreatment with the MEK1/2 inhibitor U0126 significantly reduced PGE_2 production in SiNPs-stimulated HPAEpiCs, confirming the essential role of p42/p44 MAPK activation in the inflammatory response. This finding underscores the importance of this signaling axis in regulating downstream inflammatory mediators and highlights the potential of MAPK inhibitors to counteract nanoparticle-induced inflammation. Together, these findings suggest that SAA inhibits COX-2 expression by suppressing the activation of p42/p44 MAPK, which is dependent on PKCα activity in HPAEpiCs. By targeting this signaling axis, SAA effectively reduces both COX-2 expression and PGE_2 production, thereby mitigating the inflammatory response induced by SiNPs. The implications of these results are significant, as they highlight the therapeutic potential of SAA in treating inflammation caused by nanoparticle exposure. Understanding the molecular mechanisms by which SAA modulates PKCα and p42/p44 MAPK signaling pathways provides valuable insights into its role in inflammation and offers a basis for developing targeted interventions to combat pulmonary diseases associated with environmental and occupational hazards. Future studies should further explore the long-term efficacy and safety of SAA in preclinical and clinical models, evaluating its potential to prevent or treat chronic inflammatory conditions arising from nanoparticle exposure.

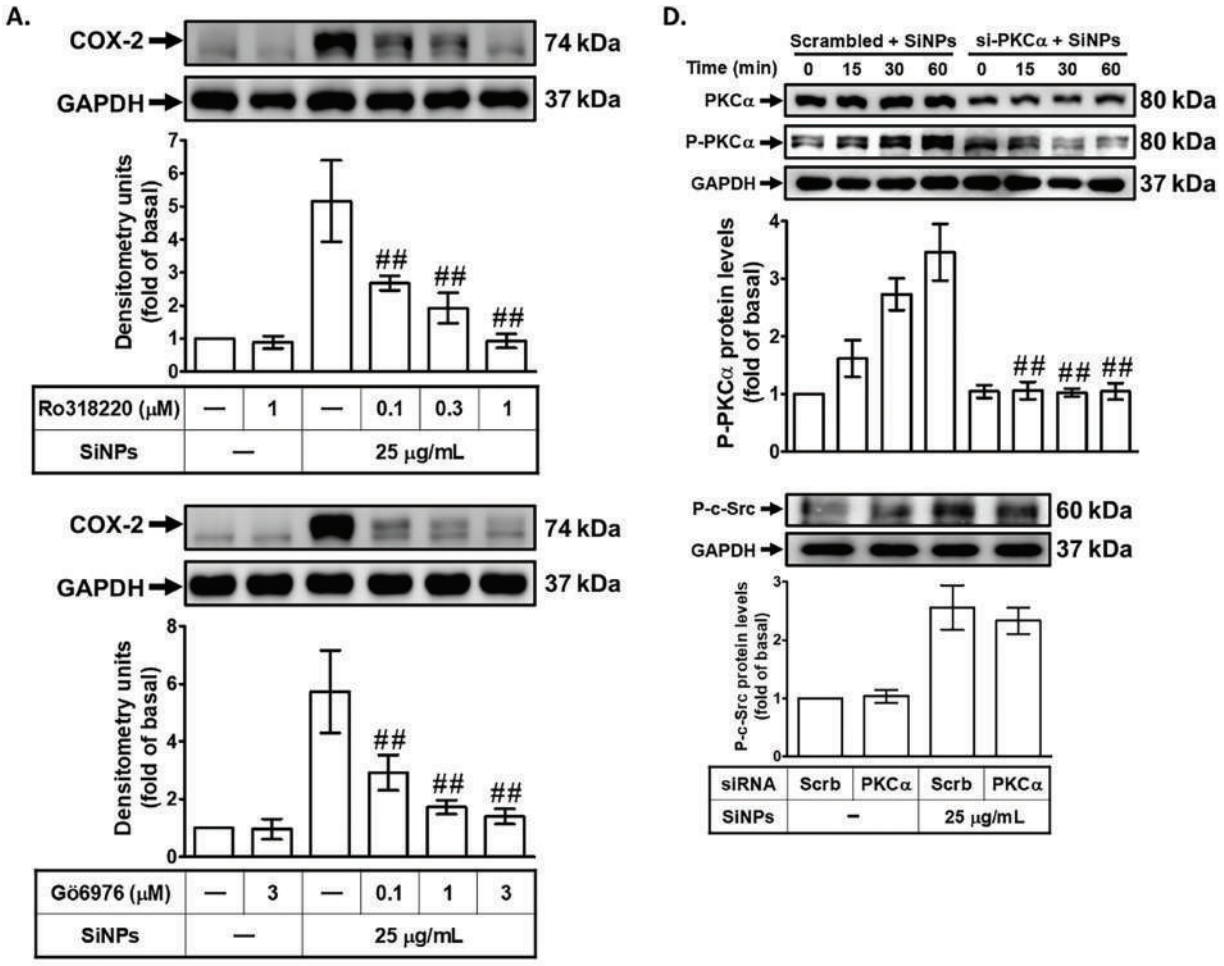


Figure 4: (Continued)

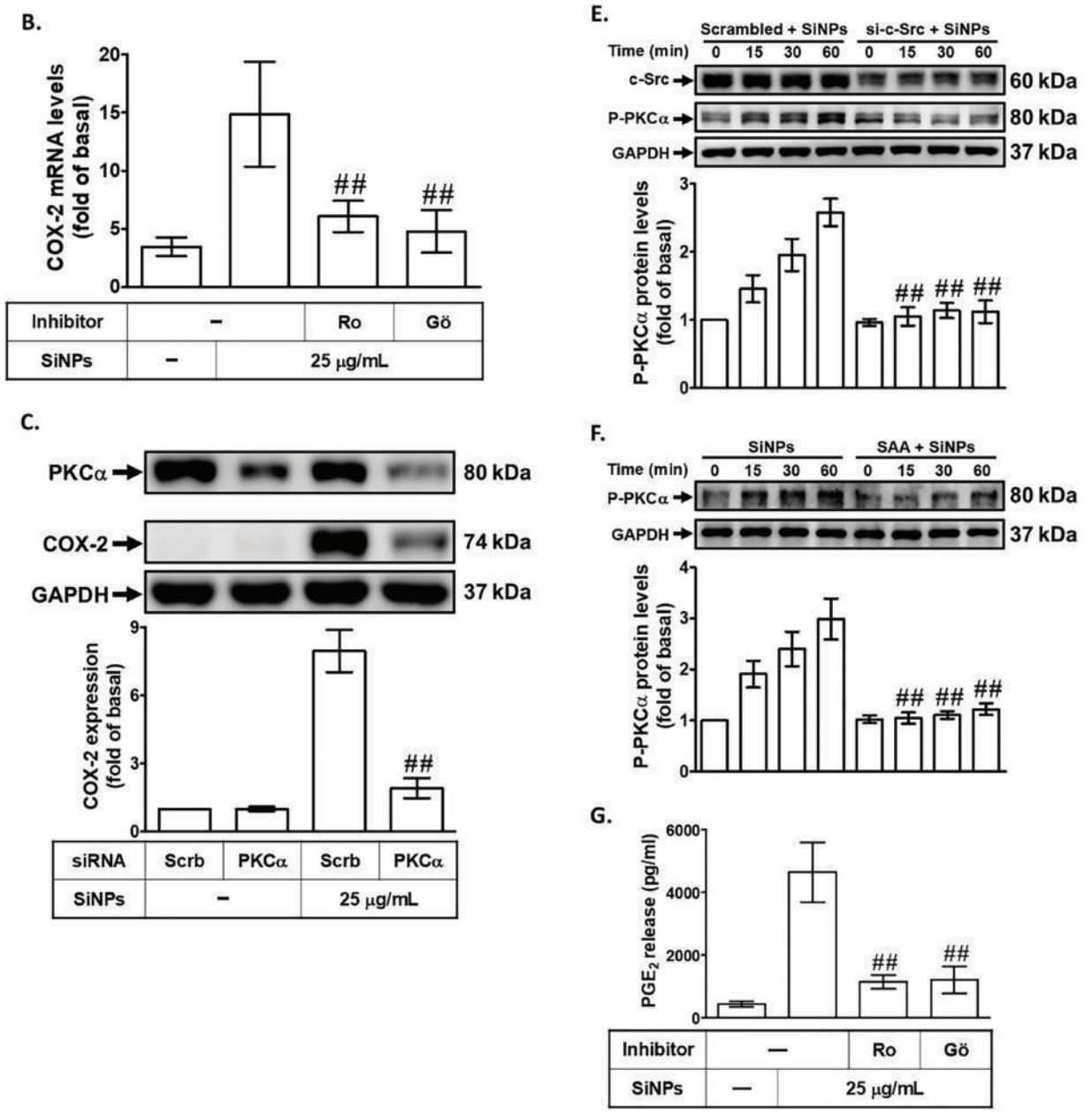


Figure 4: SAA reduces SiNP-induced COX-2 expression by suppressing PKCα phosphorylation. (**A**,**B**) Cells were pretreated with Ro318220 or Gö6976 at the indicated concentrations for 1 h, then stimulated with 25 μg/mL SiNPs. COX-2 protein (**A**) and mRNA (**B**) levels were measured using Western blot and real-time PCR, respectively. (**C**) Knockdown of PKCα by siRNA led to a reduction in both PKCα and COX-2 protein expression in response to SiNPs. (**D**) Silencing PKCα suppressed its own protein expression and phosphorylation, but did not affect c-Src phosphorylation. (**E**) In contrast, c-Src siRNA reduced PKCα phosphorylation, indicating that c-Src acts upstream of PKCα activation. (**F**) Pretreatment with SAA (10 μM, 2 h) attenuated the phosphorylation of PKCα induced by SiNPs. (**G**) Pretreatment with Ro318220 (1 μM) or Gö6976 (3 μM) significantly decreased PGE_2 secretion in the culture supernatant following SiNP exposure. Data are presented as mean ± SD from at least three independent experiments. ##$p < 0.01$ compared with cells exposed to SiNPs alone (**A**,**B**,**F**,**G**); ##$p < 0.01$ compared to cells treated with SiNPs + scrambled siRNA (**C**–**E**)

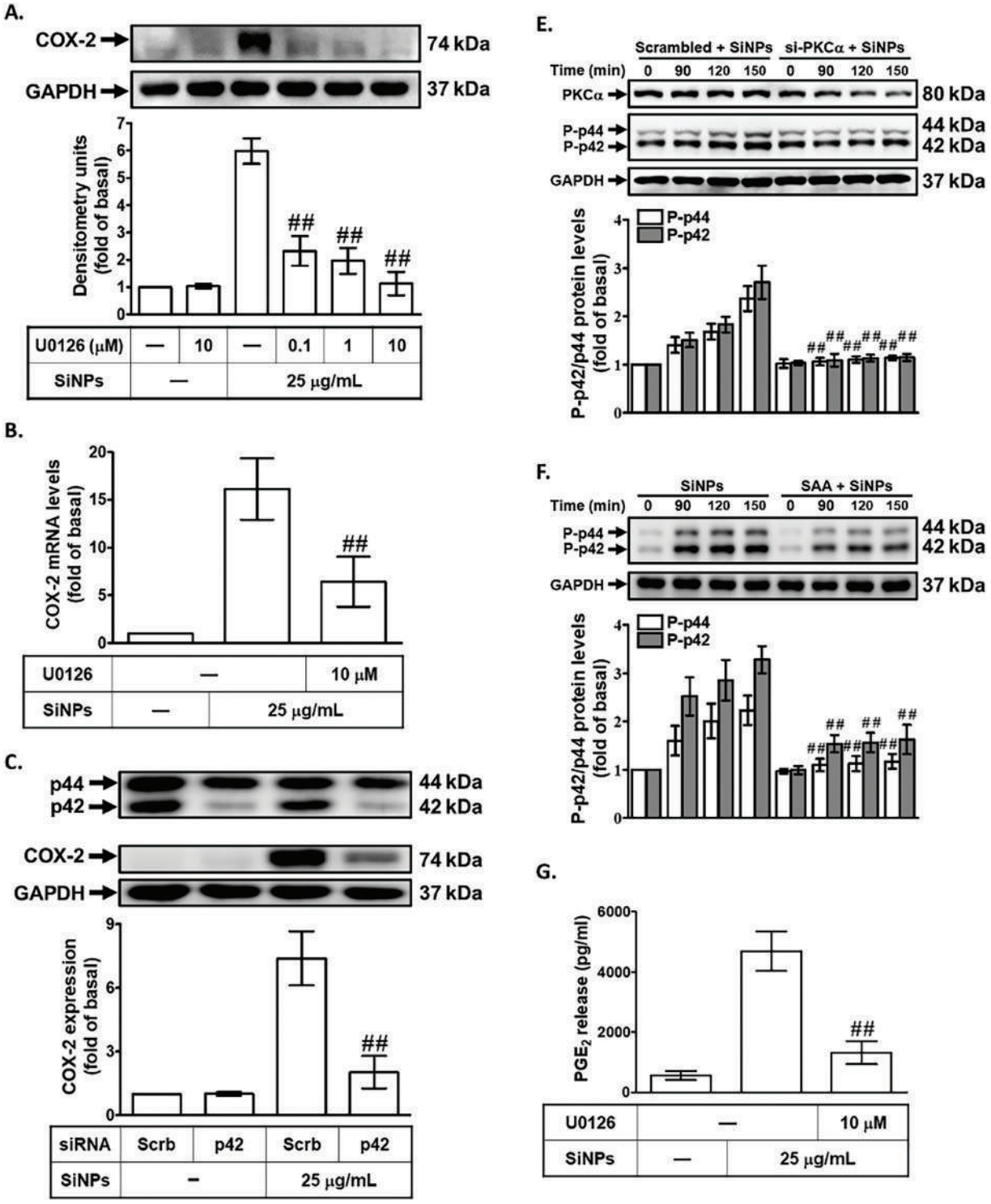


Figure 5: (Continued)

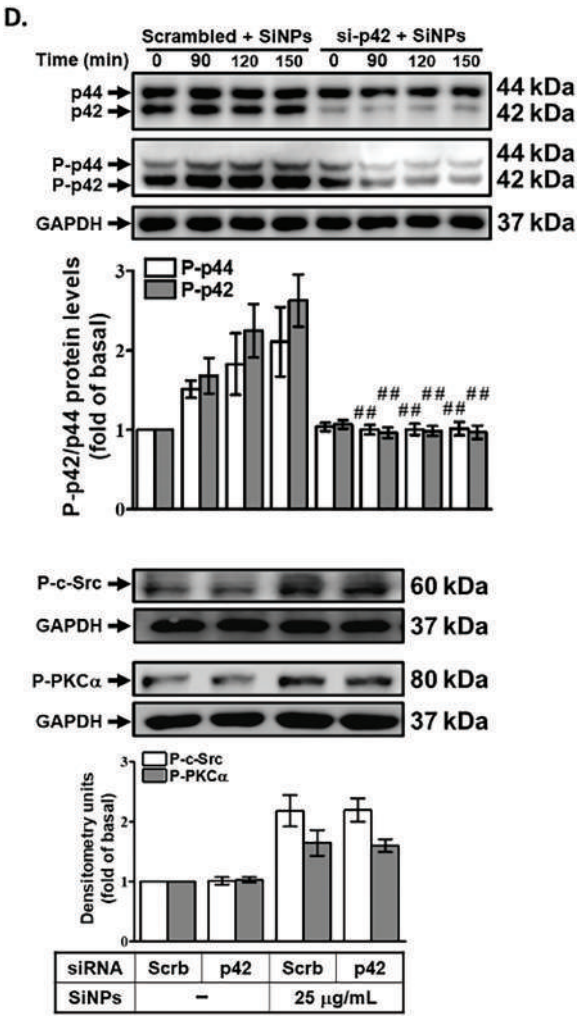


Figure 5: SAA suppresses SiNP-induced COX-2 expression by inhibiting p42/p44 MAPK activation. (**A**,**B**) HPAEpiCs were pretreated with U0126 (various doses or 10 μM) before SiNPs exposure. COX-2 protein (**A**) and mRNA (**B**) expression were assessed by Western blot and real-time PCR, respectively. (**C**) Knockdown of p42 by siRNA reduced SiNP-induced COX-2 expression and p42/p44 MAPK protein levels. (**D**) p42 siRNA did not alter PKCα or c-Src phosphorylation but suppressed phospho-p42/p44 MAPK expression in SiNP-treated cells. (**E**) Silencing PKCα attenuated p42/p44 MAPK phosphorylation in response to SiNPs. (**F**) Pretreatment with SAA (10 μM, 2 h) inhibited SiNP-induced phosphorylation of p42/p44 MAPK. (**G**) U0126 pretreatment reduced PGE_2 secretion following SiNP exposure. Data are presented as mean ± SD from at least three independent experiments. ##$p < 0.01$ compared with cells exposed to SiNPs alone (**A**,**B**,**F**,**G**); ##$p < 0.01$ compared to cells treated with SiNPs + scrambled siRNA (**C**–**E**)

3.6 SAA Attenuates COX-2 Expression by Downregulating NF-κB Activation and Translocation in SiNPs-Treated HPAEpiCs

To investigate the effect of SAA on COX-2 protein and mRNA expression in SiNPs-treated HPAEpiCs, we focused on the transcriptional regulation of COX-2, particularly the role of NF-κB. NF-κB is a key transcription factor that binds to the COX-2 promoter and plays a crucial role in inflammatory responses, orchestrating the expression of numerous pro-inflammatory mediators [18]. Dysregulated NF-κB activation has been implicated in the progression of various inflammatory and pathological conditions, making it a critical target for therapeutic intervention [34]. To determine whether NF-κB activation is required for

SiNPs-induced COX-2 expression in HPAEpiCs, we pretreated the cells with helenalin, a selective NF-κB inhibitor known to inhibit NF-κB DNA-binding activity [35]. This pretreatment significantly reduced SiNPs-induced COX-2 protein (Fig. 6A) and mRNA expression (Fig. 6B), providing strong evidence for the involvement of NF-κB in this inflammatory response. Further validating the role of NF-κB, we used p65 (an NF-κB subunit) siRNA to downregulate p65 protein expression. As shown in Fig. 6C, transfection with p65 siRNA also reduced SiNPs-induced COX-2 expression, confirming the pivotal role of p65 in regulating COX-2 levels. To further investigate the time-dependent activation of NF-κB in response to SiNPs, we measured NF-κB promoter activity in HPAEpiCs at various time points following SiNPs exposure. As shown in Fig. 6D, SiNPs treatment significantly increased NF-κB promoter activity in a time-dependent manner, reaching its peak at 60 min. This indicates that NF-κB is rapidly activated in response to SiNPs stimulation, aligning with its established role as a key transcriptional regulator of inflammatory responses. To assess the potential of SAA to inhibit this activation, HPAEpiCs were pretreated with SAA, U0126, or helenalin before SiNPs stimulation. As shown in Fig. 6E, each of these treatments significantly reduced SiNPs-induced NF-κB promoter activity, confirming that SAA can effectively inhibit NF-κB activation. This finding further supports the role of SAA in downregulating COX-2 expression by suppressing NF-κB activation and translocation, a critical step in the inflammatory cascade. Western blot analysis revealed that SiNPs stimulation led to increased phosphorylation of NF-κB p65 between 90 and 150 min after treatment, indicating a robust and sustained activation of this pathway (Fig. 6F,G). This phosphorylation was significantly reduced by transfection with either NF-κB p65 siRNA or p42 siRNA, highlighting the critical role of these upstream signaling molecules in NF-κB activation. Additionally, SAA preincubation effectively suppressed NF-κB p65 phosphorylation (Fig. 6H), suggesting that SAA inhibits COX-2 expression by targeting the PKCα/p42/p44 MAPK/NF-κB signaling axis. This finding supports the role of SAA as a potent modulator of inflammatory signaling, capable of disrupting key molecular events that drive inflammation. Moreover, helenalin pretreatment significantly reduced SiNPs-induced PGE_2 production (Fig. 6I), emphasizing the broader anti-inflammatory effects of NF-κB inhibition. Taken together, these results suggest that SAA's ability to downregulate NF-κB phosphorylation is crucial for its inhibitory effect on COX-2 expression. By targeting multiple components of this signaling pathway, SAA effectively mitigates the inflammatory response induced by SiNPs, highlighting its potential as a therapeutic agent for nanoparticle-induced inflammation.

4 Discussion

Several studies have noted the harm of nanoparticles to living organisms [36]. Babaei et al. reported that workers with chronic exposure to nanoparticles have some skin conditions accompanied by higher expression of inflammatory cytokines [7]. Nanoparticles can enter the body through different channels and cause damage to various organs, with the lungs being one of the primary targets. There is an increasing amount of research on how nanoparticles can cause or worsen lung inflammation [6]. Different concentrations of SiNPs have been reported to induce a pulmonary inflammatory response by increasing pulmonary cells and the levels of pro-inflammatory mediators in mice [37]. Wang et al. showed that intratracheal instillation of SiNPs causes severe lung injury accompanied by significant lung tissue edema and infiltration of inflammatory cells in mice [3]. Our study found that exposure to SiNPs resulted in tissue edema and increased levels of COX-2 protein and gene expression in mice. Although the time and dose of stimulation varied, our results were consistent with previous studies.

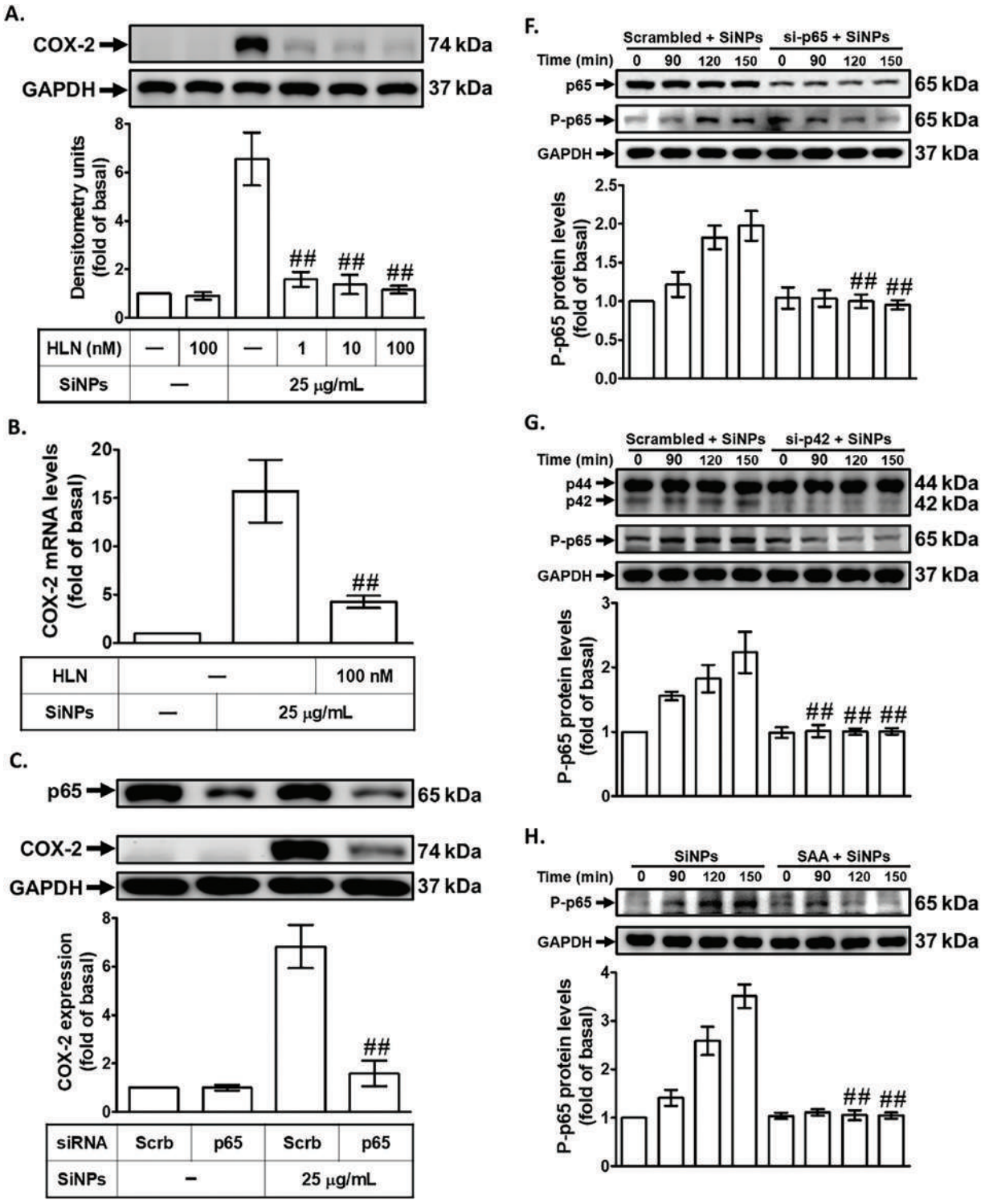


Figure 6: (Continued)

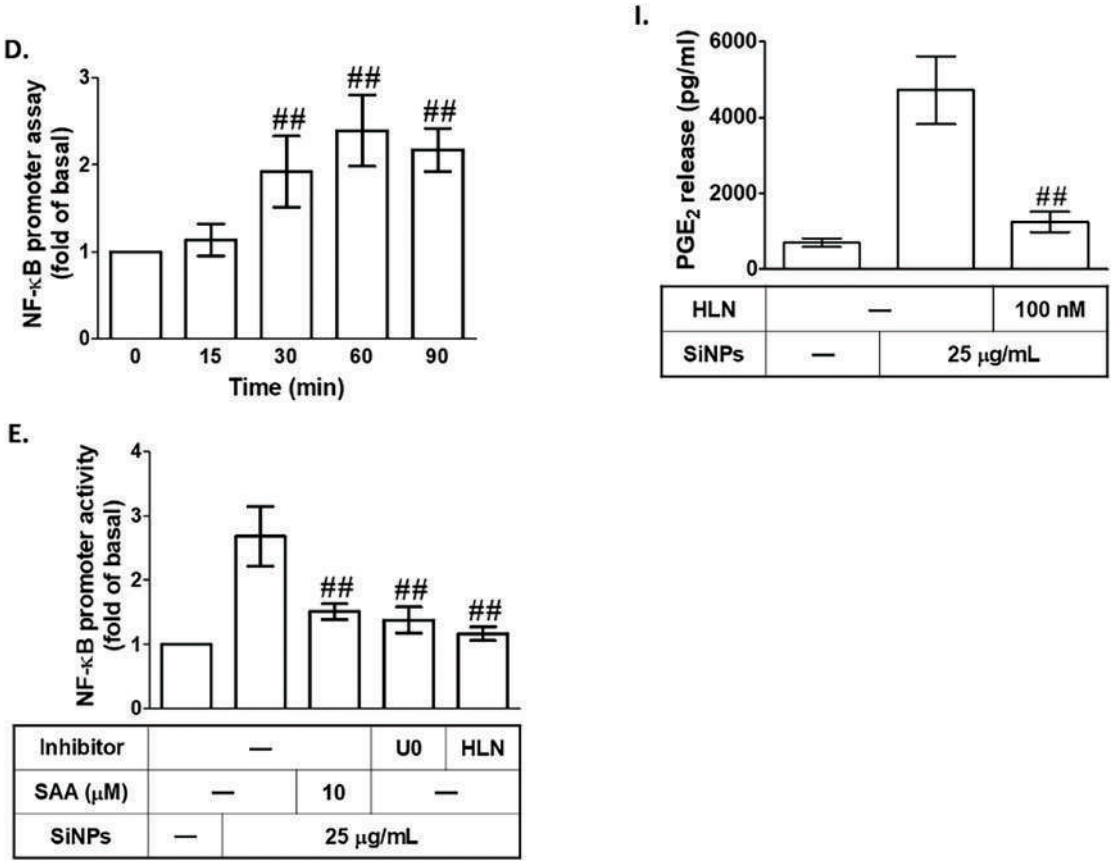


Figure 6: SAA attenuates COX-2 expression by downregulating NF-κB activation in SiNPs-treated HPAEpiCs. (**A**,**B**). HPAEpiCs were pretreated with varying doses of helenalin (HLN) prior to SiNPs exposure. COX-2 protein (**A**) and mRNA (**B**) levels were analyzed using Western blot and real-time PCR, respectively. (**C**) Knockdown of p65 by siRNA reduced SiNP-induced COX-2 and p65 protein expression. (**D**) SiNPs rapidly increased NF-κB promoter activity over time. (**E**) Pretreatment with SAA, U0126, or HLN attenuated SiNP-induced NF-κB activation. (**F**,**G**) Transfection with p65 or p42 siRNA suppressed SiNP-induced phosphorylation of p65. (**H**) SAA pretreatment reduced p65 phosphorylation after SiNP challenge. (**I**) HLN treatment reduced PGE_2 production in SiNP-stimulated cells. Data are presented as mean ± SD from at least three independent experiments. ##$p < 0.01$ compared with cells exposed to SiNPs alone (**A**,**B**,**E**,**H**,**I**); ##$p < 0.01$ compared to cells treated with SiNPs + scrambled siRNA (**C**,**F**,**G**); ##$p < 0.01$ compared with the control group (**D**)

As previously discussed, accumulating evidence supports the significant anti-inflammatory activity of SAA, as confirmed by multiple independent investigations. Salvianolic acids are capable of reducing intracellular oxidative stress, which shields cells from free radical damage, and also modulate intracellular kinase-associated signaling pathways, contributing to their anti-inflammatory effect [15]. The first question in this study sought to ascertain whether SAA could provide prevention or protection from SiNPs-caused inflammation. It has been reported that SAA inhibited the development of inflammation by reducing the levels of iNOS, COX-2, TNF-α, and IL-6 in LPS-stimulated macrophages [38]. In a study conducted by Feng et al., it was observed that SAA has anti-inflammatory and anti-arthritic effects by decreasing the expression of inflammatory factors such as MMP-1, MMP-13, COX-2, and iNOS in IL-1β-stimulated cells [16]. Similarly, results of Wu et al. suggested that SAA also downregulated the expression of inflammatory mediators,

specifically NO, TNF-α, IL-6, COX-2, PGE_2, and MMPs, in mouse chondrocytes that were triggered by IL-1β [39]. Thus, we have investigated the influence of SAA on the production of COX-2 under SiNPs treatment. This study confirmed that SAA markedly attenuated SiNP-induced upregulation of COX-2 under both *in vitro* and *in vivo* conditions.

Recent studies have shown that blocking the Src kinase can prevent lung inflammation by interfering with inflammatory signaling pathways. Src family kinase inhibitors have been found to impair neutrophil function and reduce inflammation [31]. In addition, inhibiting the Src kinase may hinder Src family kinase phosphorylation and affect other signaling pathways, ultimately improving lung injury and inflammation [40,41]. Consistent with previous findings, our study suggests that c-Src plays a key role in mediating SiNP-induced COX-2 expression, as evidenced by the reduced expression following pretreatment with a selective inhibitor (Srci II) and c-Src-targeted siRNA transfection. Interestingly, our research indicates that SAA can suppress the activation of c-Src triggered by SiNPs, potentially serving as a link between SAA and the decrease in COX-2 expression observed in response to SiNPs. Sperl et al. [42] proposed that the modulatory action of SAA is associated with its interference in SH2 domain-mediated interactions among Src family kinases such as Src and Lck. Additionally, the potential therapeutic properties of SAA have been observed in several diseases, including preventing cerebrovascular endothelial injury by acute ischemic stroke [17], and LPS-induced acute lung injury (ALI) and NETosis [25], through its ability to suppress c-Src phosphorylation. Thus, the protective role of SAA in response to SiNP exposure may be attributed, at least in part, to its ability to inhibit c-Src-mediated signaling.

Regarding the mechanism of SAA inhibiting SiNPs-induced inflammation, our results revealed that PKCα phosphorylation could be triggered by SiNPs in a time-dependent manner, which was decreased under SAA or c-Src siRNA treatment. This indicates that PKCα is involved in the signaling pathway of SAA against SiNPs-induced COX-2 expression as a downstream component of c-Src. The role of PKCα in the induction of COX-2 protein was further confirmed by Ro318220, Gö6976, or transfection with PKCα siRNA, all of which attenuated COX-2 expression. The relationship between c-Src and PKCα is intricate and involves multiple mechanisms. However, our findings support the research conducted by Mizrachy-Schwartz et al., which suggests that c-Src is upstream and leads to the phosphorylation of PKCα to regulate AMPK [43]. Tan et al. reported that PKCα is co-immunoprecipitated with c-Src and PKCα expression and activity can be decreased by inhibiting c-Src [44]. Activation of PKC regulates various cellular functions, with its most notable effects in airway epithelial cells being the production of pro-inflammatory cytokines [32]. Although information about the interaction between SAA and PKCα is limited in the previous research, our results provide some tentative initial evidence that SAA may possess anti-inflammatory effects that are associated with the c-Src-dependent activation of PKCα.

To further explore the anti-inflammatory effects of SAA, we examined its impact on the MAPK signaling pathway. The MAPK family consists of three key subgroups: p42/p44 MAPK, c-Jun N-terminal kinases (JNKs), and p38 MAPKs, all of which are involved in regulating essential physiological and pathological processes such as cell proliferation, differentiation, apoptosis, and inflammation [45]. In our previous study, we demonstrated that activation of p38 MAPKs and JNK1/2 plays a crucial role in mediating COX-2 expression induced by SiNPs in HPAEpiCs [8]. The present work further substantiates the involvement of MAPKs in the SiNP-induced upregulation of COX-2 in these cells. Treatment with the MEK1/2-specific inhibitor U0126 resulted in a notable reduction of both COX-2 mRNA and protein levels following SiNP stimulation. Similarly, silencing of p42 MAPK via siRNA significantly decreased COX-2 expression and MAPK phosphorylation in response to SiNPs, reinforcing the importance of MAPK activation in this inflammatory process. Previous studies have also reported the role of MAPKs in the anti-inflammatory action of SAA [46,47]. In line with these findings, we observed that SAA treatment suppressed SiNP-induced

phosphorylation of p42/p44 MAPK in HPAEpiCs, indicating that ERK1/2 is involved in mediating SAA's protective effects. Moreover, transfection with PKCα-targeted siRNA markedly inhibited the phosphorylation of p42/p44 MAPK induced by SiNPs, suggesting that PKCα acts upstream of MAPK in this signaling cascade. Based on these results, it is likely that SAA suppresses COX-2 expression and exerts its anti-inflammatory function by interfering with c-Src-dependent PKCα signaling, which governs the activation of p42/p44 MAPK in SiNP-exposed HPAEpiCs.

NF-κB serves as a key transcription factor involved in regulating pro-inflammatory gene expression and is commonly activated at sites of inflammation across a wide range of pathological conditions [19]. Its activation leads to the transcriptional upregulation of multiple cytokines and chemokines associated with inflammatory responses. Within the 5′-flanking region of the human COX-2 gene, NF-κB binding motifs have been identified among several potential regulatory elements [48,49]. In our study, we observed that the elevated expression of COX-2 and the enhanced production of PGE_2 induced by SiNPs were markedly suppressed by either helenalin, a selective NF-κB inhibitor, or by siRNA targeting the p65 subunit of NF-κB. These findings highlight the involvement of NF-κB in SiNP-induced COX-2 expression in HPAEpiCs. Furthermore, we demonstrated that SAA treatment significantly attenuated SiNP-induced p65 phosphorylation, similar to the effect observed with p65 siRNA, suggesting that SAA interferes with NF-κB activation. SiNPs also led to a rapid increase in NF-κB promoter activity, which was significantly diminished by pretreatment with SAA, U0126, or helenalin, further supporting the role of NF-κB in mediating the inflammatory response. Although previous research has linked MAPK activation to NF-κB regulation, our results specifically indicate that p42/p44 MAPK is critically involved in activating NF-κB in response to SiNPs. We showed that silencing p42 MAPK or inhibiting MEK1/2 substantially reduced p65 phosphorylation and activation, thereby reinforcing the connection between MAPK signaling and NF-κB activation in this context. Taken together, these data suggest that SAA mitigates SiNP-induced inflammatory responses in HPAEpiCs by modulating NF-κB activation through a signaling cascade involving c-Src, PKCα, and p42/p44 MAPK. These findings provide strong support for the potential use of SAA as a therapeutic agent targeting NF-κB signaling in nanoparticle-induced pulmonary inflammation.

In summary, we found that SAA provided prevention or protection from SiNPs-caused inflammation, which not only reduced the inflammatory response in the lungs of mice but also attenuated COX-2 expression and PGE_2 production in SiNPs-induced HPAEpiCs. According to our results, the mechanism by which SAA attenuates SiNPs-induced COX-2 expression may be mediated through the c-Src/PKCα/p42/p44 MAPK/NF-κB pathway (Fig. 7). The experimental findings of this study shed new light on SAA and its potential intervention for the management of nanoparticle-induced inflammatory lung disease. This study opens avenues for further research to explore the broader implications of SAA in treating various inflammatory conditions and its potential integration into therapeutic protocols for diseases caused by environmental and occupational exposure to nanoparticles. Nevertheless, several limitations should be acknowledged. First, the current study used only a single dose and time point for *in vivo* SiNPs exposure, which may not fully reflect the complexity of real-world, chronic or low-dose environmental exposures. Second, the use of male mice only limits the generalizability of the findings across sexes, as hormonal influences may modulate inflammatory responses. Third, although key signaling pathways were dissected, the contribution of other pathways and potential crosstalk mechanisms remains to be explored. Finally, while our results support the therapeutic potential of SAA, further pharmacokinetic and toxicological evaluations are necessary before clinical translation.

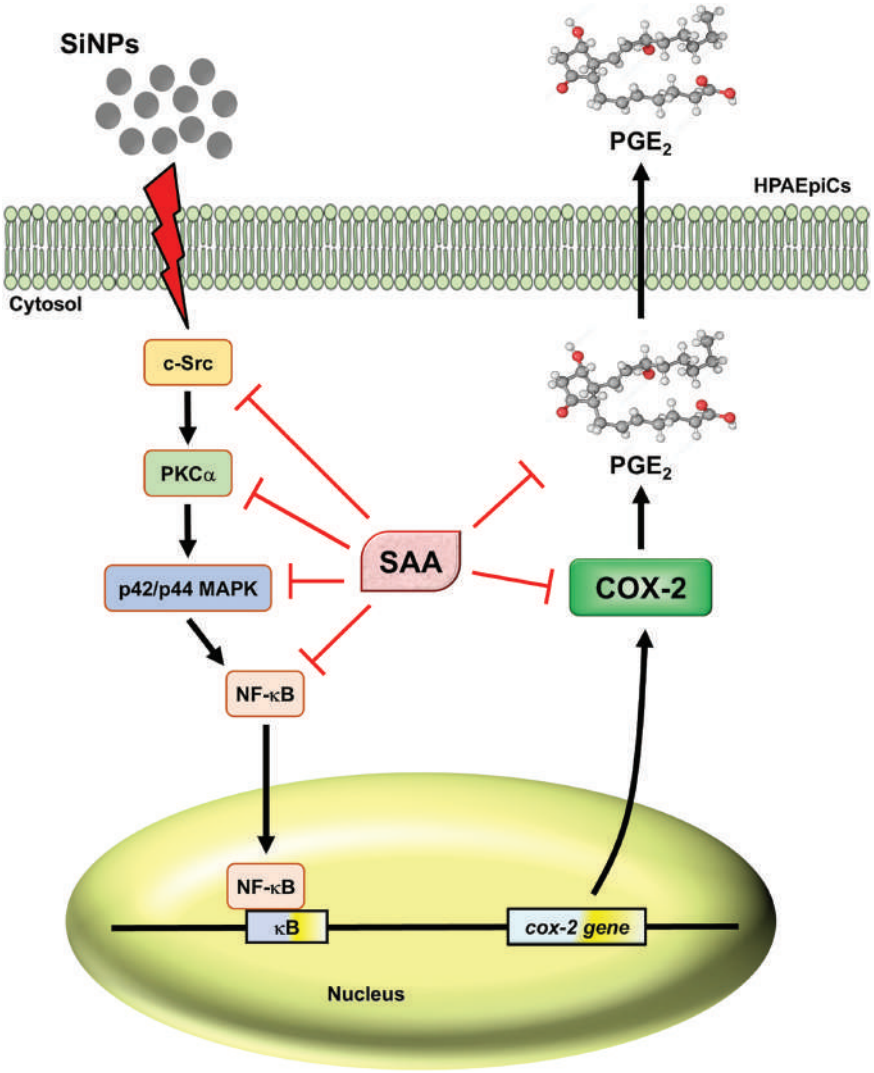


Figure 7: Proposed mechanism of SAA-mediated inhibition of SiNPs-induced inflammatory signaling in HPAEpiCs. This figure presents a proposed signaling mechanism by which SAA reduces SiNP-induced COX-2 expression and PGE_2 secretion in HPAEpiCs. Upon stimulation with SiNPs, c-Src undergoes rapid phosphorylation, initiating the activation of PKCα and subsequent phosphorylation of p42/p44 MAPK. These signaling events culminate in the phosphorylation of NF-κB p65, a key regulator of COX-2 gene transcription and PGE_2 production. Pretreatment with SAA disrupts this cascade at multiple levels. Specifically, SAA inhibits c-Src phosphorylation, thereby attenuating the downstream activation of PKCα and p42/p44 MAPK. This suppression further prevents NF-κB p65 activation, leading to reduced expression of COX-2 and diminished secretion of PGE_2. The diagram highlights the multi-level regulatory effect of SAA, providing mechanistic insight into its potent anti-inflammatory action against SiNP-induced pulmonary inflammation

Acknowledgement: The authors are deeply appreciative of Rou-Ling Cho for her invaluable technical assistance.

Funding Statement: This research was supported by the National Science and Technology Council, Taiwan [Grant number: NSTC111-2320-B-030-013], as well as the Chang Gung University of Science Foundation, Taiwan [Grant number: ZRRPF6N0011].

Author Contributions: The authors confirm contribution to the paper as follows: study conception and design: Yan-Jyun Lin, Chuen-Mao Yang, I-Ta Lee, Wen-Bin Wu; data collection: Yan-Jyun Lin, Hui-Ching Tseng, Wei-Ning Lin; analysis and interpretation of results: Yan-Jyun Lin, Chien-Chung Yang, Chiang-Wen Lee, Wen-Bin Wu, Hui-Ching Tseng, Li-Der Hsiao, Wei-Ning Lin; draft manuscript preparation: Yan-Jyun Lin, I-Ta Lee, Chuen-Mao Yang; project administration and funding acquisition: Wen-Bin Wu, Chiang-Wen Lee, Chuen-Mao Yang, Fuu-Jen Tsai; software and visualization: Yan-Jyun Lin, Li-Der Hsiao. All authors reviewed the results and approved the final version of the manuscript.

Availability of Data and Materials: The raw data supporting the conclusions of this article will be made available by the authors, without undue reservation.

Ethics Approval: All animal experiments were conducted in accordance with the ARRIVE guidelines and were approved by the Animal Care Committee of Chang Gung University (Approval Document No. CGU 16-046), in compliance with the NIH Guide for the Care and Use of Laboratory Animals (NIH Publication No. 85-23, revised 1996).

Conflicts of Interest: The authors declare no conflicts of interest to report regarding the present study.

References

1. Ding R, Li Y, Yu Y, Sun Z, Duan J. Prospects and hazards of silica nanoparticles: biological impacts and implicated mechanisms. Biotechnol Adv. 2023;69:108277. doi:10.1016/j.biotechadv.2023.108277.
2. Huang Y, Li P, Zhao R, Zhao L, Liu J, Peng S, et al. Silica nanoparticles: biomedical applications and toxicity. Biomed Pharmacother. 2022;151:113053. doi:10.1016/j.biopha.2022.113053.
3. Wang M, Li J, Dong S, Cai X, Simaiti A, Yang X, et al. Silica nanoparticles induce lung inflammation in mice via ROS/PARP/TRPM2 signaling-mediated lysosome impairment and autophagy dysfunction. Part Fibre Toxicol. 2020;17(1):23. doi:10.1186/s12989-020-00353-3.
4. Zhang L, Tian J, Li N, Wang Y, Jin Y, Bian H, et al. Exosomal miRNA reprogramming in pyroptotic macrophage drives silica-induced fibroblast-to-myofibroblast transition and pulmonary fibrosis. J Hazard Mater. 2025;483:136629. doi:10.1016/j.jhazmat.2024.136629.
5. Lv S, Li Y, Li X, Zhu L, Zhu Y, Guo C et al. Silica nanoparticles triggered epithelial ferroptosis via miR-21-5p/GCLM signaling to contribute to fibrogenesis in the lungs. Chem Biol Interact. 2024;399:111121. doi:10.1016/j.cbi.2024.111121.
6. Zhou X, Jin W, Ma J. Lung inflammation perturbation by engineered nanoparticles. Front Bioeng Biotechnol. 2023;11:1199230. doi:10.3389/fbioe.2023.1199230.
7. Babaei V, Ashtarinezhad A, Torshabi M, Teimourian S, Shahmirzaie M, Abolghasemi J, et al. High inflammatory cytokines gene expression can be detected in workers with prolonged exposure to silver and silica nanoparticles in industries. Sci Rep. 2024;14(1):5667. doi:10.1038/s41598-024-56027-z.
8. Lin YJ, Yang CC, Lee IT, Wu WB, Lin CC, Hsiao LD, et al. Reactive oxygen species-dependent activation of EGFR/Akt/p38 mitogen-activated protein kinase and JNK1/2/FoxO1 and AP-1 pathways in human pulmonary alveolar epithelial cells leads to up-regulation of COX-2/PGE_2 induced by silica nanoparticles. Biomedicines. 2023;11(10):2628. doi:10.3390/biomedicines11102628.
9. Wu WB, Lee IT, Lin YJ, Wang SY, Hsiao LD, Yang CM. Silica nanoparticles shed light on intriguing cellular pathways in human tracheal smooth muscle cells: revealing COX-2/PGE_2 production through the EGFR/Pyk2 signaling axis. Biomedicines. 2024;12(1):107. doi:10.3390/biomedicines12010107.
10. Tejwani V, Villabona-Rueda AF, Khare P, Zhang C, Le A, Putcha N, et al. Airway and systemic prostaglandin E2 association with COPD symptoms and macrophage phenotype. Chronic Obstr Pulm Dis. 2023;10(2):159–69. doi:10.15326/jcopdf.2022.0375.
11. Park GY, Christman JW. Involvement of cyclooxygenase-2 and prostaglandins in the molecular pathogenesis of inflammatory lung diseases. Am J Physiol Lung Cell Mol Physiol. 2006;290(5):L797–805. doi:10.1152/ajplung.00513.2005.

12. Wang SD, Chen PT, Hsieh MH, Wang JY, Chiang CJ, Lin LJ. Xin-Yi-Qing-Fei-Tang and its critical components reduce asthma symptoms by suppressing GM-CSF and COX-2 expression in RBL-2H3 cells. J Ethnopharmacol. 2024;330(2):118105. doi:10.1016/j.jep.2024.118105.
13. Cuzzocrea S, Mazzon E, Sautebin L, Dugo L, Serraino I, De Sarro A, et al. Protective effects of Celecoxib on lung injury and red blood cells modification induced by carrageenan in the rat. Biochem Pharmacol. 2002;63(4):785–95. doi:10.1016/s0006-2952(01)00908-x.
14. Ikdahl E, Kerola A, Sollerud E, Semb AG. Cardiovascular implications of non-steroidal anti-inflammatory drugs: a comprehensive review, with emphasis on patients with rheumatoid arthritis. Eur Cardiol. 2024;19:e27. doi:10.15420/ecr.2024.24.
15. Li CX, Xu Q, Jiang ST, Liu D, Tang C, Yang WL. Anticancer effects of salvianolic acid A through multiple signaling pathways (review). Mol Med Rep. 2025;32(1):176. doi:10.3892/mmr.2025.13541.
16. Feng S, Cong H, Ji L. Salvianolic acid a exhibits anti-inflammatory and antiarthritic effects via inhibiting NF-κB and p38/MAPK pathways. Drug Des Devel Ther. 2020;14:1771–8. doi:10.2147/DDDT.S235857.
17. Liu CD, Liu NN, Zhang S, Ma GD, Yang HG, Kong LL, et al. Salvianolic acid A prevented cerebrovascular endothelial injury caused by acute ischemic stroke through inhibiting the Src signaling pathway. Acta Pharmacol Sin. 2021;42(3):370–81. doi:10.1038/s41401-020-00568-2.
18. Yang CC, Hsiao LD, Su MH, Yang CM. Sphingosine 1-phosphate induces cyclooxygenase-2/prostaglandin E_2 expression via PKCα-dependent mitogen-activated protein kinases and NF-κB cascade in human cardiac fibroblasts. Front Pharmacol. 2020;11:569802. doi:10.3389/fphar.2020.569802.
19. Kim J, Lim CM, Kim N, Kim HG, Hong JT, Yang Y et al. Mutated IL-32θ (A94V) inhibits COX2, GM-CSF and CYP1A1 through AhR/ARNT and MAPKs/NF-κB/AP-1 in keratinocytes exposed to PM_{10}. Sci Rep. 2025;15(1):1994. doi:10.1038/s41598-024-83159-z.
20. Li S, Wang R, Song F, Chen P, Gu Y, Chen C et al. Salvianolic acid A suppresses CCl4-induced liver fibrosis through regulating the Nrf2/HO-1, NF-κB/IκBα, p38 MAPK, and JAK1/STAT3 signaling pathways. Drug Chem Toxicol. 2023;46(2):304–13. doi:10.1080/01480545.2022.2028822.
21. Martins-Gomes C, Nunes FM, Silva AM. *Thymus* spp. aqueous extracts and their constituent salvianolic acid a induce Nrf2-dependent cellular antioxidant protection against oxidative stress in caco-2 cells. Antioxidants. 2024;13(11):1287. doi:10.3390/antiox13111287.
22. Zhou F, Yao L, Lu X, Li Y, Han X, Wang P. Therapeutic targeting of GSK3β-regulated Nrf2 and NFκB signaling pathways by salvianolic acid a ameliorates peritoneal fibrosis. Front Med. 2022;9:804899. doi:10.3389/fmed.2022.804899.
23. Zhang HF, Wang YL, Gao C, Gu YT, Huang J, Wang JH, et al. Salvianolic acid A attenuates kidney injury and inflammation by inhibiting NF-κB and p38 MAPK signaling pathways in 5/6 nephrectomized rats. Acta Pharmacol Sin. 2018;39(12):1855–64. doi:10.1038/s41401-018-0026-6.
24. Ling Y, Jin L, Ma Q, Huang Y, Yang Q, Chen M, et al. Salvianolic acid A alleviated inflammatory response mediated by microglia through inhibiting the activation of TLR2/4 in acute cerebral ischemia-reperfusion. Phytomedicine. 2021;87:153569. doi:10.1016/j.phymed.2021.153569.
25. Liu Q, Zhu CL, Li HR, Xie J, Guo Y, Li P, et al. Salvianolic acid a protects against lipopolysaccharide-induced acute lung injury by inhibiting neutrophil NETosis. Oxid Med Cell Longev. 2022;2022:7411824. doi:10.1155/2022/7411824.
26. Wang P, Sun Y, Zhang R, Guo Y, Zhang Y, Guo S, et al. Salvianolic acid a attenuates lipopolysaccharide-induced acute lung injury by activating AMPK/SIRT1/Nrf2 signaling pathway. J Biochem Mol Toxicol. 2025;39(5):e70282. doi:10.1002/jbt.70282.
27. Percie du Sert N, Hurst V, Ahluwalia A, Alam S, Avey MT, Baker M et al. The ARRIVE guidelines 2.0: updated guidelines for reporting animal research. J Cereb Blood Flow Metab. 2020;40(9):1769–77. doi:10.1177/0271678x20943823.
28. Yang CM, Lin CC, Yang CC, Cho RL, Hsiao LD. Mevastatin-induced AP-1-dependent HO-1 expression suppresses vascular cell adhesion molecule-1 expression and monocyte adhesion on human pulmonary alveolar epithelial cells challenged with TNF-α. Biomolecules. 2020;10(3):381. doi:10.3390/biom10030381.

29. Lee IT, Yang CC, Lin YJ, Wu WB, Lin WN, Lee CW, et al. Mevastatin-induced HO-1 expression in cardiac fibroblasts: a strategy to combat cardiovascular inflammation and fibrosis. Environ Toxicol. 2025;40(2):264–80. doi:10.1002/tox.24429.
30. Yang CC, Hsiao LD, Wang CY, Lin WN, Shih YF, Chen YW, et al. HO-1 upregulation by kaempferol via ROS-dependent Nrf2-ARE cascade attenuates lipopolysaccharide-mediated intercellular cell adhesion molecule-1 expression in human pulmonary alveolar epithelial cells. Antioxidants. 2022;11(4):782. doi:10.3390/antiox11040782.
31. Yang CC, Lee IT, Lin YJ, Wu WB, Hsiao LD, Yang CM. Thrombin-induced COX-2 expression and PGE_2 synthesis in human tracheal smooth muscle cells: role of PKCδ/Pyk2-dependent AP-1 pathway modulation. Int J Mol Sci. 2023;24(20):15130. doi:10.3390/ijms242015130.
32. Xiao Q, Wang D, Li D, Huang J, Ma F, Zhang H, et al. Protein kinase C: a potential therapeutic target for endothelial dysfunction in diabetes. J Diabetes Complications. 2023;37(9):108565. doi:10.1016/j.jdiacomp.2023.108565.
33. Ronkina N, Gaestel M. MAPK-activated protein kinases: servant or partner? Annu Rev Biochem. 2022;91(1):505–40. doi:10.1146/annurev-biochem-081720-114505.
34. Kaszycki J, Kim M. Epigenetic regulation of transcription factors involved in NLRP3 inflammasome and NF-kB signaling pathways. Front Immunol. 2025;16:1529756. doi:10.3389/fimmu.2025.1529756.
35. Lyss G, Knorre A, Schmidt TJ, Pahl HL, Merfort I. The anti-inflammatory sesquiterpene lactone helenalin inhibits the transcription factor NF-kappaB by directly targeting p65. J Biol Chem. 1998;273(50):33508–16. doi:10.1074/jbc.273.50.33508.
36. Portugal J, Bedia C, Amato F, Juárez-Facio AT, Stamatiou R, Lazou A, et al. Toxicity of airborne nanoparticles: facts and challenges. Environ Int. 2024;190:108889. doi:10.1016/j.envint.2024.108889.
37. Park EJ, Kang MS, Jin SW, Lee TG, Lee GH, Kim DW, et al. Multiple pathways of alveolar macrophage death contribute to pulmonary inflammation induced by silica nanoparticles. Nanotoxicology. 2021;15(8):1087–101. doi:10.1080/17435390.2021.1969461.
38. Huang J, Qin Y, Liu B, Li GY, Ouyang L, Wang JH. *In silico* analysis and experimental validation of molecular mechanisms of salvianolic acid A-inhibited LPS-stimulated inflammation, in $RAW_{264.7}$ macrophages. Cell Prolif. 2013;46(5):595–605. doi:10.1111/cpr.12056.
39. Wu Y, Wang Z, Lin Z, Fu X, Zhan J, Yu K. Salvianolic acid a has anti-osteoarthritis effect *in vitro* and *in vivo*. Front Pharmacol. 2020;11:682. doi:10.3389/fphar.2020.00682.
40. El-Hashim AZ, Khajah MA, Renno WM, Babyson RS, Uddin M, Benter IF, et al. Src-dependent EGFR transactivation regulates lung inflammation via downstream signaling involving ERK1/2, PI3Kδ/Akt and NFκB induction in a murine asthma model. Sci Rep. 2017;7(1):9919. doi:10.1038/s41598-017-09349-0.
41. Severgnini M, Takahashi S, Tu P, Perides G, Homer RJ, Jhung JW, et al. Inhibition of the Src and Jak kinases protects against lipopolysaccharide-induced acute lung injury. Am J Respir Crit Care Med. 2005;171(8):858–67. doi:10.1164/rccm.200407-981OC.
42. Sperl B, Seifert MHJ, Berg T. Natural product inhibitors of protein-protein interactions mediated by Src-family SH2 domains. Bioorg Med Chem Lett. 2009;19(12):3305–9. doi:10.1016/j.bmcl.2009.04.083.
43. Mizrachy-Schwartz S, Cohen N, Klein S, Kravchenko-Balasha N, Levitzki A. Up-regulation of AMP-activated protein kinase in cancer cell lines is mediated through c-Src activation. J Biol Chem. 2011;286(17):15268–77. doi:10.1074/jbc.M110.211813.
44. Tan M, Li P, Sun M, Yin G, Yu D. Upregulation and activation of PKC alpha by ErbB2 through Src promotes breast cancer cell invasion that can be blocked by combined treatment with PKC alpha and Src inhibitors. Oncogene. 2006;25(23):3286–95. doi:10.1038/sj.onc.1209361.
45. Moens U, Kostenko S, Sveinbjørnsson B. The role of mitogen-activated protein kinase-activated protein kinases (MAPKAPKs) in inflammation. Genes. 2013;4(2):101–33. doi:10.3390/genes4020101.
46. Chuang CY, Ho YC, Lin CW, Yang WE, Yu YL, Tsai MC, et al. Salvianolic acid A suppresses MMP-2 expression and restrains cancer cell invasion through ERK signaling in human nasopharyngeal carcinoma. J Ethnopharmacol. 2020;252(3):112601. doi:10.1016/j.jep.2020.112601.
47. Diao HY, Zhu W, Liu J, Yin S, Wang JH, Li CL. Salvianolic acid a improves rat kidney injury by regulating MAPKs and TGF-β1/smads signaling pathways. Molecules. 2023;28(8):3630. doi:10.3390/molecules28083630.

48. Tanabe T, Tohnai N. Cyclooxygenase isozymes and their gene structures and expression. Prostaglandins Other Lipid Mediat. 2002;68–69:95–114. doi:10.1016/s0090-6980(02)00024-2.
49. Kang YJ, Mbonye UR, DeLong CJ, Wada M, Smith WL. Regulation of intracellular cyclooxygenase levels by gene transcription and protein degradation. Prog Lipid Res. 2007;46(2):108–25. doi:10.1016/j.plipres.2007.01.001.

Check for updates

Environmental Toxicology

WILEY

ENVIRONMENTAL TOXICOLOGY

RESEARCH ARTICLE

Mevastatin-Induced HO-1 Expression in Cardiac Fibroblasts: A Strategy to Combat Cardiovascular Inflammation and Fibrosis

I-Ta Lee[1] | Chien-Chung Yang[2,3] | Yan-Jyun Lin[4] | Wen-Bin Wu[5,6] | Wei-Ning Lin[6] | Chiang-Wen Lee[7,8,9] | Hui-Ching Tseng[10] | Fuu-Jen Tsai[11,12,13] | Li-Der Hsiao[6] | Chuen-Mao Yang[6]

[1]School of Dentistry, College of Oral Medicine, Taipei Medical University, Taipei, Taiwan | [2]Department of Traditional Chinese Medicine, Chang Gung Memorial Hospital at Taoyuan, Taoyuan, Taiwan | [3]School of Traditional Chinese Medicine, College of Medicine, Chang Gung University, Taoyuan, Taiwan | [4]Institute of Translational Medicine and new Drug Development, College of Medicine, China Medical University, Taichung, Taiwan | [5]School of Medicine, Fu Jen Catholic University, New Taipei City, Taiwan | [6]Graduate Institute of Biomedical and Pharmaceutical Science, Fu Jen Catholic University, New Taipei City, Taiwan | [7]Department of Nursing, Division of Basic Medical Sciences, and Chronic Diseases and Health Promotion Research Center, Chang Gung University of Science and Technology, Chiayi, Taiwan | [8]Department of Respiratory Care, Chang Gung University of Science and Technology, Chiayi, Taiwan | [9]Department of Orthopaedic Surgery, Chang Gung Memorial Hospital, Chiayi, Taiwan | [10]Research Center for Chinese Herbal Medicine, Graduate Institute of Health Industry Technology, Chang Gung University of Science and Technology, Taoyuan, Taiwan | [11]School of Chinese Medicine, College of Chinese Medicine, China Medical University, Taichung, Taiwan | [12]Department of Medical Research, China Medical University Hospital, China Medical University, Taichung, Taiwan | [13]Division of Medical Genetics, China Medical University Children's Hospital, Taichung, Taiwan

Correspondence: Chuen-Mao Yang (chuenmao@mail.cmu.edu.tw)

Received: 23 May 2024 | **Revised:** 1 August 2024 | **Accepted:** 29 September 2024

Funding: This work was supported by the Ministry of Science and Technology, Taiwan [Grant number: NSTC111-2320-B-030-013]; Chang Gung Medical Research Foundation, Taiwan [Grant number: CMRPG5M0161]; Chang Gung University of Science Foundation, Taiwan [Grant number: ZRRPF6N0011].

Keywords: anti-inflammation | antioxidant | carbon monoxide | heme oxygenase-1 | mevastatin | reactive oxygen species

ABSTRACT

Mevastatin (MVS) is known for its anti-inflammatory effects, potentially achieved by upregulating heme oxygenase-1 (HO-1), an enzyme involved in cytoprotection against oxidative injury. Nonetheless, the specific processes by which MVS stimulates HO-1 expression in human cardiac fibroblasts (HCFs) are not yet fully understood. In this study, we found that MVS treatment increased HO-1 mRNA and protein levels in HCFs. This induction was inhibited by pretreatment with specific inhibitors of p38 MAPK, JNK1/2, and FoxO1, and by siRNAs targeting NOX2, $p47^{phox}$, p38, JNK1, FoxO1, Keap1, and Nrf2. MVS also triggered ROS generation and activated JNK1/2 and p38 MAPK, both attenuated by NADPH oxidase or ROS inhibitors. Additionally, MVS promoted the phosphorylation of FoxO1 and Nrf2, which was suppressed by p38 MAPK or JNK1/2 inhibitor. Furthermore, MVS inhibited TNF-α-induced NF-κB activation and vascular cell adhesion molecule-1 (VCAM-1) expression via the HO-1/CO pathway in HCFs. In summary, the induction of HO-1 expression in HCFs by MVS is mediated through two primary signaling pathways: NADPH oxidase/ROS/p38 MAPK, and JNK1/2/FoxO1 and Nrf2. This research illuminates the underlying processes through which MVS exerts its anti-inflammatory effects by modulating HO-1 in cardiac fibroblasts.

I-Ta Lee and Chien-Chung Yang contributed equally to this work.

© 2024 Wiley Periodicals LLC.

1 | Introduction

Fibroblasts are crucial in the evolution of cardiac diseases, including cardiac inflammation, which is induced by chemical signals and mechanical stress [1]. Inflammatory agents like lipopolysaccharide (LPS) [2], angiotensin II (Ang II) [3], tumor necrosis factor (TNF)-α [4], interleukin (IL)-1β [4], and IL-1α [5] play a significant role in stimulating the activation and multiplication of fibroblasts. Recent research has established a strong connection between elevated TNF-α levels and the development of fibrotic cardiomyopathy, emphasizing the crucial interaction between mast cells and fibroblasts in cardiac fibrosis progression [6]. Turner et al.'s work highlights that TNF-α elevation is associated with higher IL-1β and IL-6 concentrations in cardiac fibroblasts [7]. These findings collectively point to the pivotal role of TNF-α in the pathogenesis of cardiovascular diseases. Fibrotic cardiomyopathy, characterized by excessive extracellular matrix deposition, involves complex pathophysiological mechanisms, notably the transformation of cardiac fibroblasts into myofibroblasts in response to cytokines, growth factors, and mechanical stress [1]. Central to this process is the role of transforming growth factor-β (TGF-β), which drives fibroblast proliferation, collagen synthesis, and inhibits matrix degradation through the Smad signaling pathway [8]. Ang II further exacerbates fibrosis by enhancing TGF-β production and stimulating matrix component synthesis [3]. Inflammatory cytokines, including TNF-α, IL-1β, and IL-6, amplify this pathological remodeling by recruiting inflammatory cells and promoting fibrogenic factor production [1]. Additionally, oxidative stress and the activation of NF-κB and MAPK signaling pathways are crucial in fibroblast activation and the fibrotic response. The interplay between mast cells and fibroblasts, contributing to collagen synthesis and proliferation, underscores the complexity of cellular interactions in cardiac fibrosis [6].

Heme oxygenase (HO)-1, an essential enzyme, plays a pivotal role in heme degradation, producing carbon monoxide, free iron, and biliverdin-IXα [9]. In mammals, biliverdin-IXα is converted to bilirubin-IXα, known for its radical scavenging abilities and recently identified anti-inflammatory properties [10]. The released free iron is rapidly absorbed by ferritin, the iron storage protein, providing additional antioxidant and anti-apoptotic benefits [9, 10]. Carbon monoxide, another byproduct, is crucial for various biological functions, including anti-apoptotic and anti-inflammatory effects [11]. Due to its significant role, HO-1 is increasingly viewed as a potential therapeutic target for various human diseases, especially those involving cardiovascular inflammation [12]. It has demonstrated protective effects against inflammatory responses and can be activated by diverse stimuli, including oxidative stress [10, 12]. Particularly noteworthy is its capacity to inhibit cardiomyocyte senescence, thereby enhancing heart function in conditions like myocardial infarction and in aging mice [13]. Recent studies highlight the NF-E2-related factor (Nrf2)/HO-1 signaling pathway as a key player in maintaining cardiovascular stability. This pathway is crucial in reducing oxidative stress, thereby preventing cardiac remodeling and heart failure linked to oxidative stress [14, 15].

Statins, a widely used class of drugs, are primarily known for their ability to reduce cholesterol levels by blocking HMG-CoA reductase, an enzyme crucial for cholesterol synthesis in the liver. Beyond their role in managing cholesterol, statins also possess a range of additional effects, such as improving bone metabolism, modulating the immune system, providing antioxidant benefits, and reducing inflammation [16]. The earliest statins identified were mevastatin (MVS), extracted from *Penicillium citrinum*, and lovastatin, sourced from *Aspergillus terreus* [16]. Notably, MVS has been shown to enhance HO-1 expression and deliver anti-inflammatory benefits via multiple signaling pathways, including p38 MAPK, Erk1/2, and protein kinase G [17]. Our study concentrates on exploring MVS's role in safeguarding cellular health and deciphering the processes through which MVS stimulates HO-1 expression in human cardiac fibroblasts (HCFs).

While MVS is widely used to treat hyperlipidemia, its impact on cardiovascular inflammatory conditions has not been extensively explored. In particular, the detailed mechanisms by which MVS stimulates HO-1 expression in HCFs are not fully understood. Our research provides initial evidence that MVS can effectively block TNF-α-induced NF-κB activation and the expression of vascular cell adhesion molecule-1 (VCAM-1) in HCFs, doing so via the HO-1/CO pathway. Furthermore, our study reveals that the induction of HO-1 by MVS in HCFs is driven by the activation of the NADPH oxidase/ROS/p38 MAPK and JNK1/2/FoxO1 and Nrf2 signaling pathways. These important findings could lay the groundwork for the development of new MVS-based treatments for cardiovascular diseases in the future.

2 | Materials and Methods

2.1 | Materials

We acquired various reagents and kits for our study from several suppliers. Invitrogen (Carlsbad, CA) supplied Dulbecco's modified Eagle's medium (DMEM)/F-12 medium, fetal bovine serum (FBS), TRIzol reagent, 2′,7′-dichlorofluorescin diacetate (H_2DCF-DA), dihydroethidium (DHE), and the M-MLV Reverse Transcriptase kit. The BioTrace NT nitrocellulose transfer membrane was obtained from Pall Corporation (Port Washington, NY), and the enhanced chemiluminescence reagent came from EMD Millipore Corporation (Burlington, MA). We procured the GenMute siRNA transfection reagent from SignaGen Lab (Gaithersburg, MD) and the anti-HO-1 (ADI-SPA-895) antibody from Enzo Life Sciences (Farmingdale, NY). EnCor (Gainesville, FL) provided the anti-GAPDH (#MCA-1D4) antibody. From Cell Signaling Technology (Danvers, MA), we received several antibodies: anti-p65 (#8242S), anti-phospho-p65 (Ser^{536}, #3031L), anti-phospho-p38 MAPK (Thr^{180}/Tyr^{182}, #9211L), anti-p38 MAPK (#8690), anti-phospho-SAPK/JNK (Thr^{183}/Tyr^{185}, #4668S), anti-phospho-FoxO1 (Ser^{256}, #9461S), and anti-FoxO1 (#2880S). Santa Cruz (Santa Cruz, CA) supplied us with anti-β-actin (C4) (sc-47778) and anti-JNK1/2 (sc-137020) antibodies. From Abcam (Cambridge, UK), we purchased Anti-VCAM-1 [EPR5038(2)] (ab174279), anti-NOX2 (ab129068), anti-Nrf2

15227278, 2025, 2, Downloaded from https://onlinelibrary.wiley.com/doi/10.1002/tox.24429 by Chang Gung University Of, Wiley Online Library on [04/05/2026]. See the Terms and Conditions (https://onlinelibrary.wiley.com/terms-and-conditions) on Wiley Online Library for rules of use; OA articles are governed by the applicable Creative Commons License

(ab137550), anti-phospho-Nrf2 (ab76026), and anti-Keap1 (ab227828) antibodies. Assay Biotech (Fremont, CA) provided anti-phospho-p47^{phox} (Ser^{370}, A1171) and anti-p47^{phox} (R12-3284) antibodies. Additionally, we sourced various chemicals and inhibitors from Biomol (Plymouth Meeting, PA), including apocynin (APO), *N*-acetyl-cysteine (NAC), edaravone (Eda), diphenyleneiodonium (DPI), mevastatin (MVS), p38 MAPK inhibitor VIII (p38i VIII), SP600125, actinomycin D (Act. D), cycloheximide (CHI), TNF-α, tricarbonyldichlororuthenium(II) dimer (CORM-2), hemoglobin (Hb), helenalin (HLN), and AS1842856. For enzymes and other chemicals, we turned to Sigma (St. Louis, MO).

2.2 | Cell Culture

HCFs obtained from ScienCell Research Laboratories (San Diego, CA, USA) were utilized in this study. The culture conditions and procedures followed previously published references [18].

2.3 | Western Blot

In our experiments, cells underwent incubation with MVS at a temperature of 37°C under various conditions. This was followed by conducting Western blot analysis as per the protocols developed in our laboratory [18]. During this process, the membranes were treated with a range of primary antibodies, including anti-VCAM-1, anti-HO-1, anti-phospho-Nrf2, anti-phospho-p65, anti-phospho-p38 MAPK, anti-phospho-JNK1/2, anti-phospho-FoxO1, and anti-phospho-p47^{phox}, and were incubated for a period of 24 h. Post this incubation, we further exposed the membranes to anti-mouse or anti-rabbit horseradish peroxidase antibodies for 1 h. The immunoreactive bands were detected using enhanced chemiluminescence (ECL) reagents. For capturing the immunoblot images, we used a UVP BioSpectrum 500 imaging system based in Upland, CA. The densitometry analysis of these images was carried out using the UN-SCAN-IT gel software located in Orem, UT.

2.4 | Transient Transfection With siRNAs

We procured scrambled siRNAs, along with p38α (HSS102352, HSS102353, HSS175313; NM_001315.3) siRNAs, from Invitrogen Life Technologies in Carlsbad, CA. Additionally, siRNAs targeting p47^{phox} (SASI_Hs02_00302212), NOX2 (SASI_Hs01_00086110), JNK1 (SASI_Hs02_00319556), Nrf2 (SASI_Hs02_00302212), FoxO1 (SASI_Hs01_0076732; NM_002015), and Keap1 (SASI_Hs01_00080908) were acquired from Sigma, located in St. Louis, MO. The transient transfection of these siRNAs, at a concentration of 100 nM, was performed using the GenMute Reagent, strictly adhering to the protocol provided by SignaGen Laboratories in Frederick, MD.

2.5 | Real-Time PCR

Using the TRIzol reagent, total RNA was extracted. Following this, the extracted mRNA was reverse-transcribed into cDNA. We then carried out real-time PCR analysis, utilizing SYBR Green PCR reagents obtained from Applied Biosystems (Branchburg, NJ, USA). All these experimental steps were conducted in accordance with the protocols previously established and published by our laboratory [19]. For real-time PCR analysis of HO-1, VCAM-1, and GAPDH, the following primers can be used:

HO-1:

Forward: 5′-CTCAAACCTCCAAAAGCC-3′

Reverse: 5′-TCAAAAACCACCCCAACCC-3′

VCAM-1:

Forward: 5′-GGCTCGTACACCATCCGC-3′

Reverse: 5′-CGGTTTTCGATTCACACTCGT-3′

GAPDH:

Forward: 5′-GTCTCCTCTGACTTCAACAGCG-3′

Reverse: 5′-ACCACCCTGTTGCTGTAGCCAA-3′

2.6 | Adhesion Assay

THP-1, a human monocytic leukemia cell line, was obtained from the Bioresource Collection and Research Center (BCRC 60430; Food Industry Research and Development Institute, Hsinchu, Taiwan). THP-1 cells underwent treatment with 10 μM BCECF-AM from Invitrogen, CA, at a temperature of 37°C for 1 h in RPMI-1640 medium supplied by Gibco BRL, Grand Island, NY. Following this, the cells were subjected to a wash through centrifugation. Subsequently, confluent HCFs were treated with THP-1 cells at a density of 2×10^6 cells/ml and incubated at 37°C for 1 h. The nonadherent THP-1 cells were then removed, and the culture plates received a gentle wash with PBS. We assessed the number of adherent THP-1 cells by counting them in four separate fields of each well, using a fluorescent microscope (Zeiss, Axiovert 200 M) at a magnification of 200×. In each well, four high-power fields were randomly selected for counting.

2.7 | Determination of NADPH Oxidase Activity

After incubation under various experimental conditions, the HCFs were meticulously detached using a mild scraping technique and subsequently centrifuged at 400×g for 10 min at a temperature of 4°C. The assessment of NADPH oxidase activity in these cells was carried out using the methodologies detailed in our previously published works [19].

2.8 | Measurement of Intracellular ROS Accumulation

The intracellular H_2O_2 levels were measured by determining the fluorescence intensity of H_2DCF-DA using a Zeiss Axiovert 200 M fluorescence microscope. This was done at an excitation wavelength of 495 nm and an emission wavelength of 529 nm. Simultaneously, $O_2^{\bullet-}$ levels were quantified by analyzing the fluorescence of DHE under the same

15227278, 2025, 2, Downloaded from https://onlinelibrary.wiley.com/doi/10.1002/tox.24429 by Chang Gung University Of, Wiley Online Library on [04/05/2026]. See the Terms and Conditions (https://onlinelibrary.wiley.com/terms-and-conditions) on Wiley Online Library for rules of use; OA articles are governed by the applicable Creative Commons License

microscope, using an excitation wavelength of 518 nm and an emission wavelength of 605 nm. In the experimental process, HCFs were first rinsed with warm Hank's Balanced Salt Solution (HBSS) and then incubated in either HBSS or cell medium mixed with 10 μM H_2DCF-DA or DHE at 37°C for 45 min. Following this, the HBSS or medium containing the

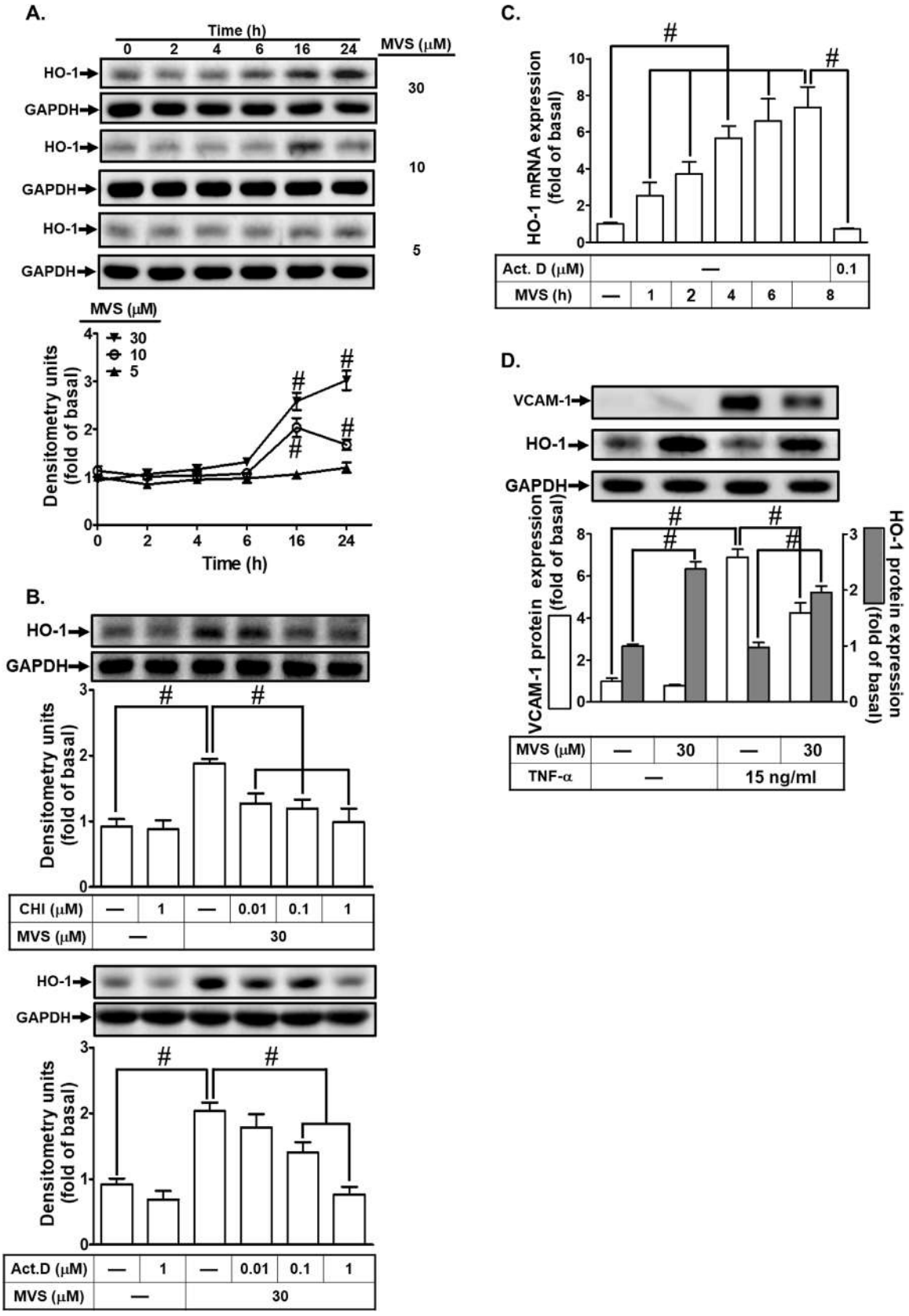


FIGURE 1 | Legend on next page

15227278, 2025, 2, Downloaded from https://onlinelibrary.wiley.com/doi/10.1002/tox.24429 by Chang Gung University Of, Wiley Online Library on [04/05/2026]. See the Terms and Conditions (https://onlinelibrary.wiley.com/terms-and-conditions) on Wiley Online Library for rules of use; OA articles are governed by the applicable Creative Commons License

fluorescent dyes was replaced with fresh medium. We varied the concentrations of MVS added to the cells during the incubation. Post-treatment, the cells were washed twice with PBS and detached using trypsin/EDTA. Finally, a FACScan flow cytometer (BD Biosciences, San Jose, CA) was used to analyze the fluorescence intensity of the cells, employing an excitation wavelength of 518 nm and an emission wavelength of 605 nm for DHE, and an excitation wavelength of 495 nm and an emission wavelength of 529 nm for DCF [19].

2.9 | Analysis of Luciferase Reporter Gene Activity

In our study, we assessed the transcriptional activity of Nrf2 in HCFs using the ARE Reporter kit from BPS Bioscience in San Diego, CA. The luciferase activity was quantified in accordance with the manufacturer's instructions [19].

2.10 | Chromatin Immunoprecipitation Assay

Our examination of the interactions between nuclear proteins and the human HO-1 promoter involved conducting chromatin immunoprecipitation (ChIP) analysis, adhering to the methods we previously described [20]. This ChIP analysis entailed purifying DNA fragments that had been immunoprecipitated using an anti-Nrf2 antibody. After purification, the DNA was solubilized in H_2O and then put through PCR amplification. The resulting PCR products were visualized and assessed using 1% agarose gels, which were stained with ethidium bromide. We employed primers targeting the distal E2 (−9.0 kb) ARE region of the HO-1 promoter, utilizing the sequences forward 5′-CCCTGCTGAGTAATCCTTTCCCGA-3′ and reverse 5′-ATGTCCCGACTCCAGACTCCA-3′. These primers were specifically chosen to amplify a region known to interact with Nrf2, ensuring our focus on relevant Nrf2 binding sites within the HO-1 promoter.

2.11 | Statistical Analysis

For data analysis in our experiment, we utilized GraphPad Prism software from GraphPad in San Diego, CA, USA. We expressed all quantitative data as the mean ± standard error of the mean (S.E.M.). For statistical assessment, we employed one-way ANOVA with subsequent Tukey's post hoc test for multiple comparisons. We established statistical significance at a p-value of less than 0.05.

3 | Results

3.1 | MVS Triggers HO-1 Expression and Counteracts TNF-α-Induced VCAM-1

Recent investigations have revealed that MVS has the capability to induce the expression of HO-1 in human pulmonary alveolar epithelial cells [21]. In our own study, we observed a time-dependent increase in HO-1 protein expression in HCFs when exposed to MVS, with the highest levels reached between 16 and 24 h (Figure 1A). To probe the underlying mechanisms of MVS-induced HO-1 expression, we employed inhibitors of transcription (Act. D) and translation (CHI) to pretreat HCFs before MVS stimulation. As shown in Figure 1B, either Act. D or CHI completely abolished the MVS-mediated induction of HO-1, indicating that de novo protein synthesis is essential for MVS to trigger HO-1 expression in HCFs. Furthermore, our results demonstrated that MVS promoted a time-dependent increase in HO-1 mRNA levels, and this effect was significantly attenuated when cells were pretreated with Act. D (Figure 1C), suggesting that MVS enhances the transcription of the HO-1 gene. Expanding on our prior research, where we showed that MVS-induced HO-1 could suppress the TNF-α-induced VCAM-1 expression in pulmonary alveolar epithelial cells [21], we investigated whether a similar response occurs in HCFs. As expected, MVS effectively inhibited TNF-α-induced VCAM-1 expression in HCFs (Figure 1D). Interestingly, along with the inhibition of VCAM-1, MVS also upregulated HO-1 expression in response to TNF-α stimulation. These findings imply that MVS may exert its anti-inflammatory effects in HCFs by upregulating HO-1 expression, which subsequently counteracts TNF-α-induced inflammatory responses. In conclusion, our study highlights the capacity of MVS to trigger a time-dependent increase in HO-1 expression in HCFs. The induction of HO-1 by MVS requires de novo protein synthesis and involves enhanced gene transcription. Moreover, MVS effectively inhibits TNF-α-induced VCAM-1 expression in HCFs, and this effect is associated with the upregulation of HO-1 expression. These findings provide valuable insights into the potential therapeutic applications of MVS in mitigating inflammatory responses in cardiac tissue.

3.2 | CORM-2 Exerts Inhibitory Effects on TNF-α-Induced VCAM-1 Expression

In this research, we focused on the enzyme HO-1, crucial for breaking down heme into carbon monoxide, free iron, and biliverdin-IXα [12]. Furthermore, in mammals, biliverdin-IXα is converted into bilirubin-IXα. According to recent studies

FIGURE 1 | MVS induces HO-1 expression and inhibits TNF-α-induced VCAM-1 in HCFs. (A) Cells were incubated with MVS for the indicated time points and then the protein expression of HO-1 was determined. (B) Cells were pretreated with cycloheximide (CHI) or actinomycin D (Act. D) for 1 h and then treated with MVS for 16 h. The protein expression of HO-1 was determined. (C) Cells were treated with MVS for the indicated time points or pretreated with Act. D for 1 h and then incubated with MVS for 8 h. The mRNA levels of HO-1 were determined. (D) Cells were treated with TNF-α in the absence or presence of MVS and then the protein levels of VCAM-1 and HO-1 were observed. Data are presented as mean ± S.E.M. of three independent experiments. $^{\#}p < 0.01$ indicates a significant difference from the baseline control condition at time 0 (A). $^{\#}p < 0.01$ for significant difference between the groups (B–D).

15227278, 2025, 2, Downloaded from https://onlinelibrary.wiley.com/doi/10.1002/tox.24429 by Chang Gung University Of, Wiley Online Library on [04/05/2026]. See the Terms and Conditions (https://onlinelibrary.wiley.com/terms-and-conditions) on Wiley Online Library for rules of use; OA articles are governed by the applicable Creative Commons License

[22, 23], these metabolites might have cytoprotective roles, displaying anti-inflammatory and anti-proliferative effects. Our aim was to explore whether carbon monoxide and bilirubin-IXα could suppress VCAM-1 expression induced by TNF-α in HCFs. Our results, as shown in Figure 2A–C, indicate that CORM-2 (a carbon monoxide donor) significantly reduced both the protein expression and mRNA levels of TNF-α-induced VCAM-1. In contrast, bilirubin did not demonstrate a similar

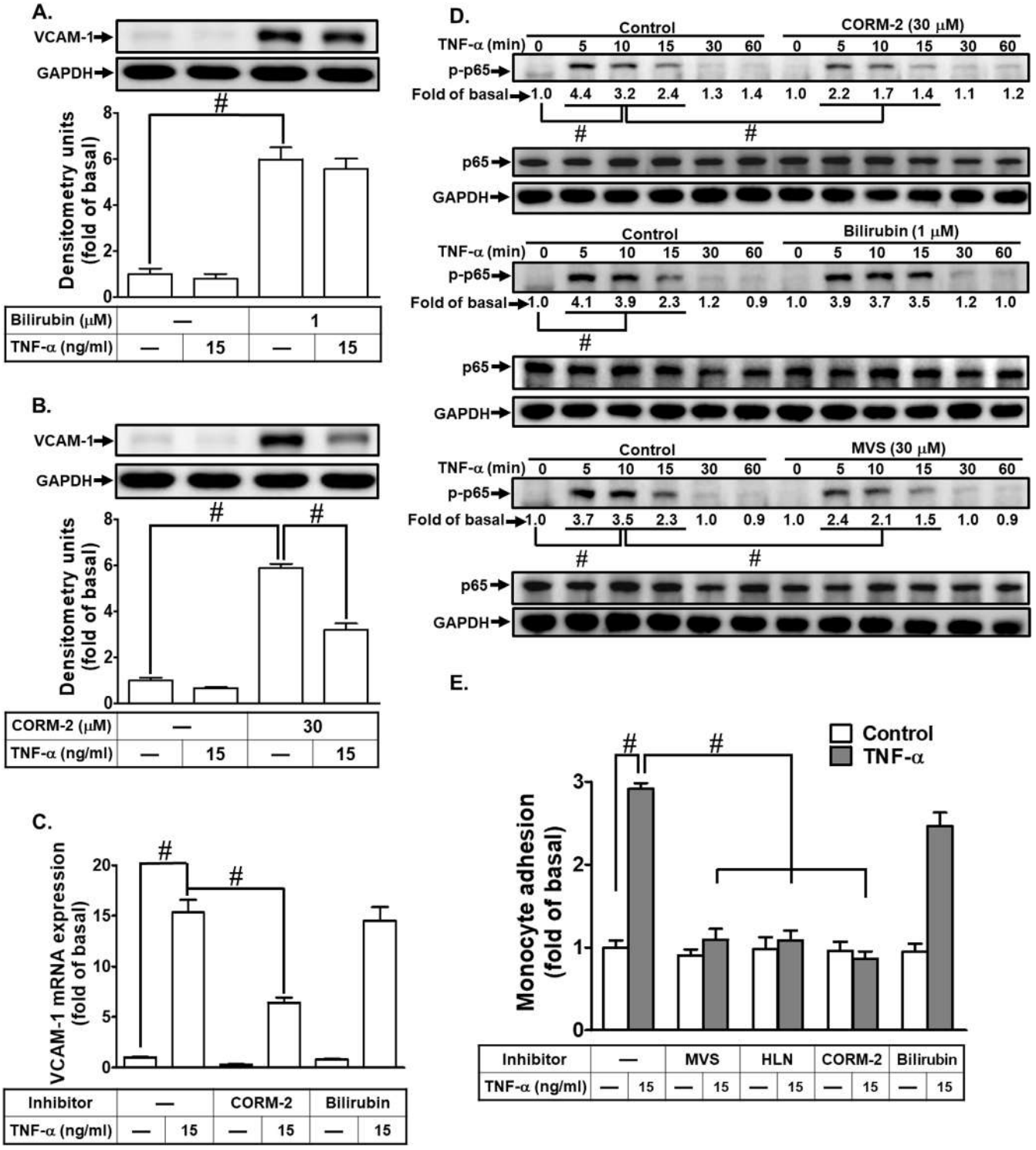


FIGURE 2 | CORM-2 inhibits TNF-α-induced VCAM-1 expression. HCFs were pretreated with (A) bilirubin or (B) CORM-2 for 1 h and then treated with TNF-α for 16 h. The protein expression of VCAM-1 was determined. (C) HCFs were pretreated with bilirubin or CORM-2 for 1 h and then treated with TNF-α. The mRNA expression of VCAM-1 was determined. (D) HCFs were preincubated with MVS, bilirubin, or CORM-2 and then incubated with TNF-α for the indicated time intervals. The protein expression of phospho-p65 was determined. (E) Cells were pretreated with MVS, helenalin (HLN), CORM-2, or bilirubin and then incubated with TNF-α. The THP-1 cells adherence was determined. Data are presented as mean ± S.E.M. of three independent experiments. $^{\#}p < 0.01$ for significant difference between the groups.

15227278, 2025, 2, Downloaded from https://onlinelibrary.wiley.com/doi/10.1002/tox.24429 by Chang Gung University Of, Wiley Online Library on [04/05/2026]. See the Terms and Conditions (https://onlinelibrary.wiley.com/terms-and-conditions) on Wiley Online Library for rules of use; OA articles are governed by the applicable Creative Commons License

inhibitory impact. Previous studies [24, 25] have shown that NF-κB is involved in the induction of VCAM-1 in various cell types. We also assessed the effects of MVS, CORM-2, and bilirubin on the activation of NF-κB p65 in HCFs stimulated by TNF-α, as depicted in Figure 2D. The findings reveal that MVS and CORM-2 diminished the TNF-α-enhanced activation of NF-κB p65, whereas bilirubin did not show comparable effects. Additionally, we examined the efficacy of MVS, CORM-2, and HLN (a NF-κB inhibitor) in inhibiting TNF-α-induced monocyte adherence, as illustrated in Figure 2E. The data demonstrate that MVS, CORM-2, and HLN successfully reduced TNF-α-induced monocyte adherence, while bilirubin did not exhibit this property. In summary, our study establishes that MVS can effectively attenuate TNF-α-induced inflammation in HCFs via the HO-1/carbon monoxide signaling pathway. However, in this context, bilirubin does not seem to play a significant role in reducing TNF-α-induced VCAM-1 expression, NF-κB p65 activation, or monocyte adherence.

3.3 | MVS Triggers the Upregulation of HO-1 by Engaging NADPH Oxidase and Promoting ROS Production

Extensive research has demonstrated the critical role of ROS in initiating HO-1 expression in a variety of cell types [26, 27]. Additionally, NADPH oxidase is recognized as a major enzyme responsible for ROS production in several pathological scenarios. Our study delved into the role of NADPH oxidase in the ROS production associated with HO-1 expression following MVS exposure. According to Figure 3A,B, MVS notably escalates ROS generation (including superoxide and H_2O_2) and amplifies NADPH oxidase activity in HCFs. NADPH oxidase is composed of two transmembrane proteins, $p22^{phox}$ and $gp91^{phox}$ (also referred to as NOX2, forming cytochrome b_{558}), and four cytosolic proteins ($p47^{phox}$, $p67^{phox}$, $p40^{phox}$, and GTPases Rac1 or Rac2). These components assemble at membrane sites when cells are activated [28]. Our observations suggest that suppressing NOX2 or $p47^{phox}$ with siRNA considerably reduces the HO-1 expression induced by MVS in HCFs, as shown in Figure 3C. To further confirm that the ROS production is a result of NADPH oxidase activation, we used specific inhibitors, APO and DPI. As depicted in Figure 4A,B, pretreating cells with APO or DPI significantly lowers MVS-induced ROS production in HCFs. The activation of NADPH oxidase can be triggered by various stimuli, relying on the phosphorylation of the cytosolic component $p47^{phox}$ [28]. Our study also reveals that APO or DPI treatment substantially reduces the MVS-stimulated activation of $p47^{phox}$, as evident in Figure 4C. Collectively, these results robustly affirm that MVS induces HO-1 expression in HCFs primarily through ROS generation mediated by NADPH oxidase activation.

3.4 | MVS Triggers the Upregulation of HO-1 Through the Activation of the ROS/p38 MAPK Signaling Pathway

Prior research has shown that p38 MAPK plays a crucial role in stimulating HO-1 in adipocytes [29]. In our study, we explored the influence of p38 MAPK on HO-1 expression following exposure to MVS in HCFs. As illustrated in Figure 5A,B, treatment with a p38 MAPK inhibitor (p38i VIII) significantly curtailed the upregulation of HO-1 protein and mRNA levels induced by MVS in HCFs. To further corroborate the role of p38 MAPK in this process, we employed p38 siRNA. The results, shown in Figure 5C, indicate that transfecting cells with p38 siRNA effectively reduced the HO-1 protein levels induced by MVS. It is well-documented that ROS generation can activate the p38 MAPK signaling pathway [30]. Consistent with this, our observations revealed that MVS led to a time-dependent increase in the phosphorylation of p38 MAPK. This activation was significantly decreased when cells were pretreated with the p38i VIII or ROS inhibitors (NAC and Eda), as seen in Figure 5D. These findings collectively suggest that the induction of HO-1 expression by MVS in HCFs occurs via the ROS/p38 MAPK signaling pathway.

3.5 | The Induction of HO-1 Expression by MVS Occurs Through Activation of the ROS/JNK1/2 Signaling Pathway

Past studies have established the role of JNK1/2 in promoting HO-1 expression in RAW264.7 macrophages [31]. Our current research focused on the relationship between JNK1/2 and HO-1 expression in HCFs in the context of MVS exposure. Our findings revealed that pretreating HCFs with a JNK1/2 specific inhibitor (SP600125) prior to MVS exposure significantly reduced the induction of HO-1 protein and mRNA levels, as evidenced in Figure 6A,B. To further ascertain the role of JNK1/2 in this process, we utilized JNK1 siRNA to diminish JNK1 expression. According to Figure 6C, transfection with JNK1 siRNA notably suppressed the MVS-induced HO-1 protein levels in HCFs. It is well-documented in literature [32] that ROS generation can lead to the activation of the JNK1/2 signaling pathway. Consistent with this, our study observed that MVS treatment resulted in a time-dependent phosphorylation of JNK1/2 in HCFs. This phosphorylation was effectively counteracted by pretreatment with the JNK1/2 inhibitor (SP600125) or ROS inhibitors (NAC and Eda), as shown in Figure 6D. These combined results imply that MVS promotes HO-1 expression in HCFs through the ROS/JNK1/2 signaling pathway. Essentially, MVS triggers ROS production, which then activates the JNK1/2 pathway, culminating in the upregulation of HO-1 expression in HCFs.

3.6 | MVS Triggers the Expression of HO-1 by Activating FoxO1

The role of FoxO1 in HO-1 induction in primary human cardiomyocytes has been previously established [33]. In our current research, we focused on understanding how FoxO1 influences HO-1 expression in HCFs when exposed to MVS. The data, as shown in Figure 7A,B, reveal that using the FoxO1 inhibitor (AS1842856) prior to MVS exposure effectively reduced HO-1 protein expression and mRNA levels in HCFs. To further substantiate the involvement of FoxO1 in this process, we employed FoxO1 siRNA. The results in Figure 7C demonstrate that transfecting HCFs with FoxO1 siRNA curtailed the MVS-induced HO-1 protein levels. Previous research [33] has shown that both JNK1/2 and p38 MAPK can activate FoxO1 signaling in primary human cardiomyocytes. Consistent with this, our study

15227278, 2025, 2, Downloaded from https://onlinelibrary.wiley.com/doi/10.1002/tox.24429 by Chang Gung University Of, Wiley Online Library on [04/05/2026]. See the Terms and Conditions (https://onlinelibrary.wiley.com/terms-and-conditions) on Wiley Online Library for rules of use; OA articles are governed by the applicable Creative Commons License

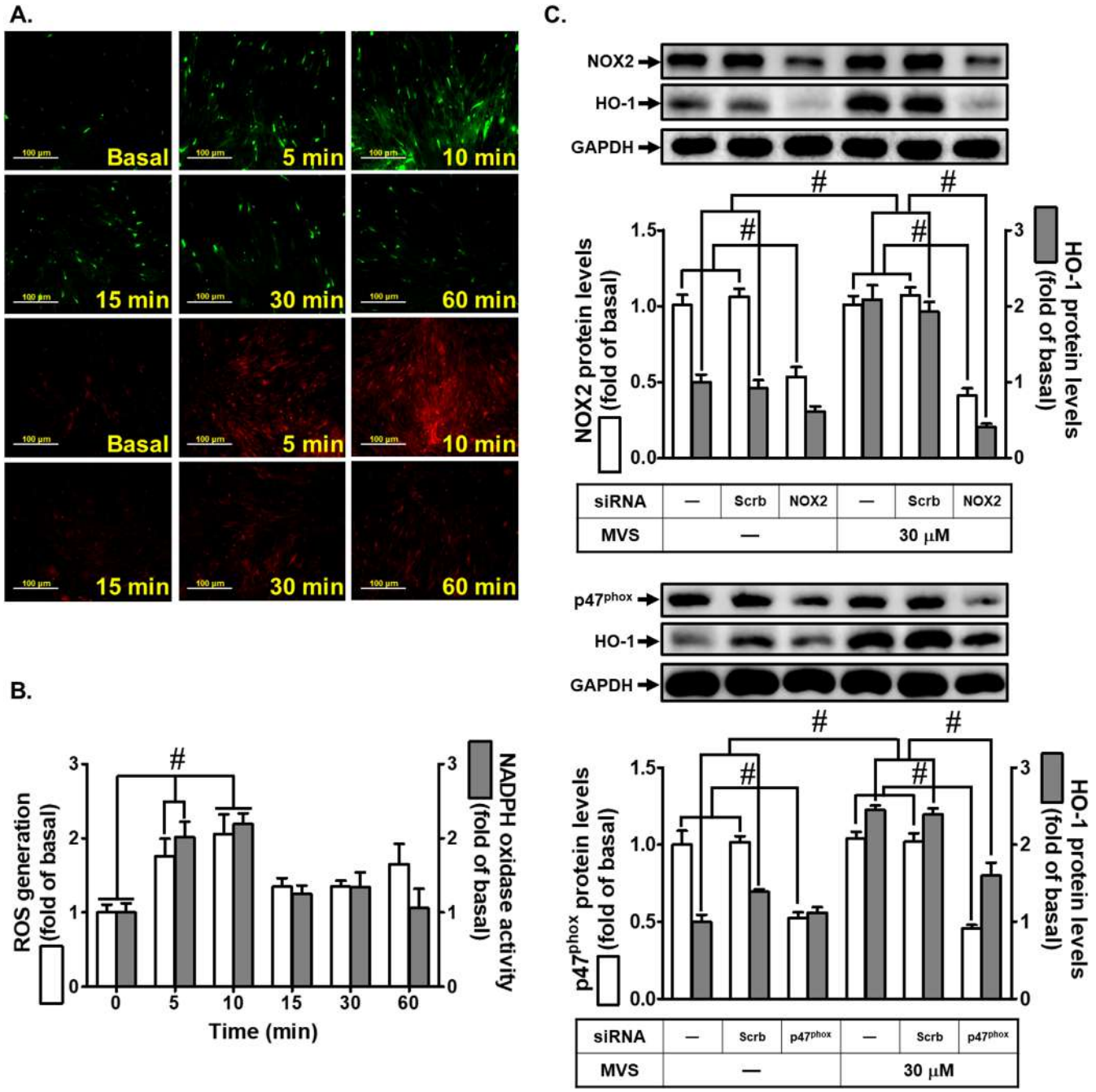


FIGURE 3 | MVS induces HO-1 expression via NADPH oxidase and ROS. (A) DCF (green) or DHE (red) fluorescence image after stimulation with MVS (30 μM). Images shown are representative of three independent experiments with similar results. (B) Cells were treated with MVS (30 μM) for the indicated time points. The NADPH oxidase activity and ROS generation were measured. (C) Cells were transfected with siRNA of scrambled (scrb), NOX2, or p47^{phox} and then treated with MVS (30 μM). The protein levels of HO-1, p47^{phox}, and NOX2 were determined. Data are presented as mean ± S.E.M. of three independent experiments. $^{\#}p < 0.01$ for significant difference between the groups.

observed that MVS treatment led to time-dependent FoxO1 phosphorylation in HCFs. This phosphorylation was significantly reduced by pretreatment with inhibitors specific to FoxO1 (AS1842856), JNK1/2 (SP600125), or p38 MAPK (p38i VIII), as indicated in Figure 7D. These combined observations suggest that MVS may promote HO-1 expression in HCFs via a pathway that involves either p38 MAPK or JNK1/2-dependent activation of FoxO1 signaling.

3.7 | MVS Induces HO-1 Expression Through the Involvement of Nrf2

The Keap1/Nrf2/ARE signaling system, known for its redox sensitivity, plays a vital role in cellular homeostasis under various stress conditions like inflammation, carcinogenesis, and apoptosis [34]. Nrf2, in particular, has been implicated in driving HO-1 expression in diverse cell types [35, 36]. In this

15227278, 2025, 2, Downloaded from https://onlinelibrary.wiley.com/doi/10.1002/tox.24429 by Chang Gung University Of, Wiley Online Library on [04/05/2026]. See the Terms and Conditions (https://onlinelibrary.wiley.com/terms-and-conditions) on Wiley Online Library for rules of use; OA articles are governed by the applicable Creative Commons License

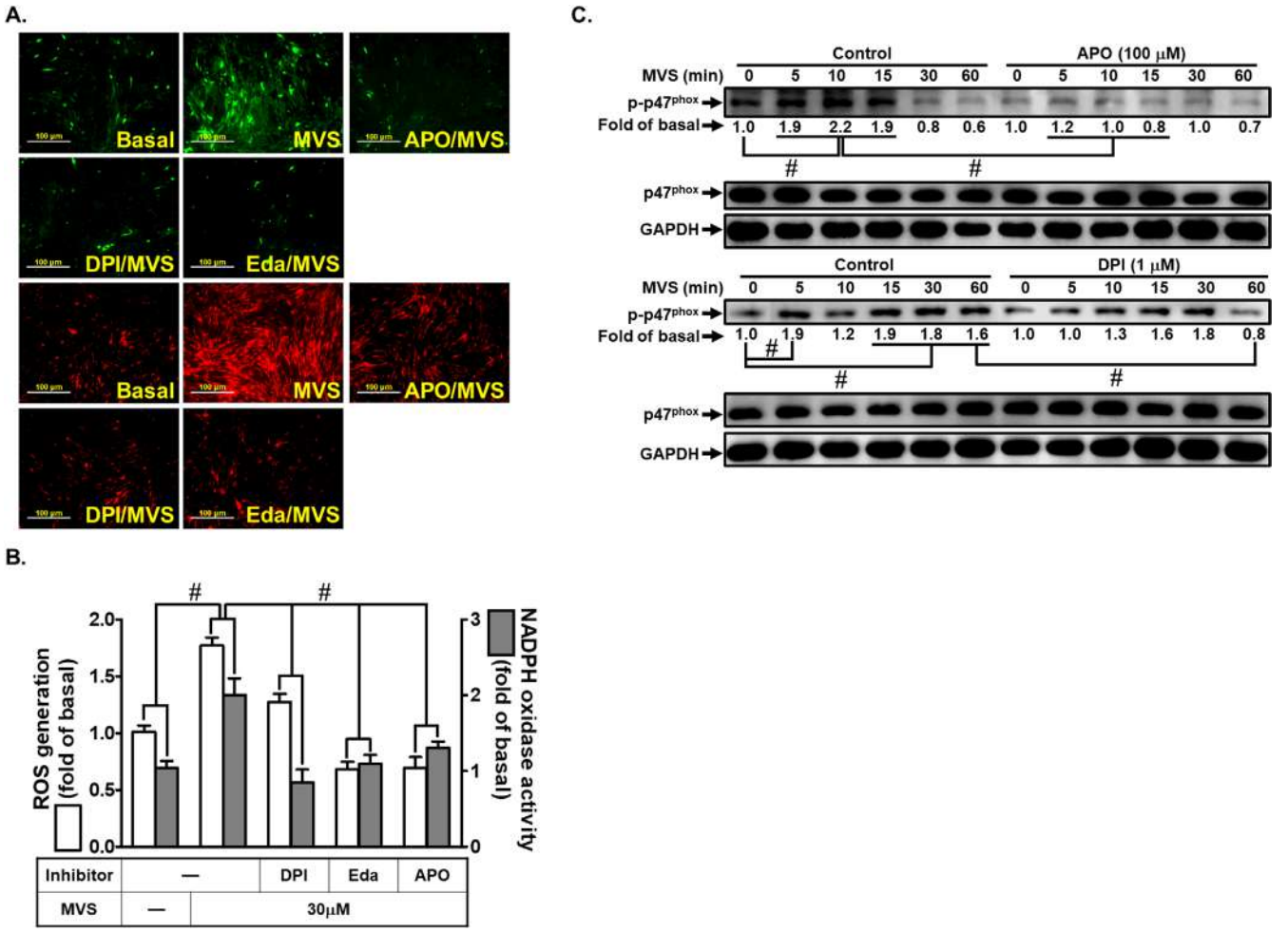


FIGURE 4 | MVS induces NADPH oxidase-derived ROS production. (A) DCF (green) or DHE (red) fluorescence image after stimulation with MVS (30 μM) in the presence or absence of apocynin (APO, 100 μM), diphenyleneiodonium (DPI, 1 μM), or edaravone (Eda, 3 μM). Images shown are representative of three independent experiments with similar results. (B) Cells were pretreated with APO, DPI, or Eda for 2 h and then treated with MVS (30 μM). The NADPH oxidase activity and ROS generation were measured. (C) Cells were treated with MVS in the presence or absence of APO or DPI for the indicated time points. The protein expression of phospho-p47^{phox} was determined. Data are presented as mean ± S.E.M. of three independent experiments. $^{\#}p < 0.01$ for significant difference between the groups.

research, we explored the roles of Keap1 and Nrf2 in modulating HO-1 expression in HCFs in response to MVS. Our findings, as illustrated in Figure 8A–C, show that silencing Keap1 or Nrf2 with siRNA notably decreased MVS-induced HO-1 protein and mRNA levels in HCFs. Additionally, we noted that MVS induced a time-dependent phosphorylation of Nrf2, which was hindered by transfection with Nrf2 siRNA or pretreatment with p38i VIII or SP600125, as shown in Figure 8D. The Nrf2-ARE pathway is a crucial defense mechanism against oxidative stress [34–36]. Our study revealed that MVS significantly escalated the activity of ARE-luciferase in a time-dependent manner, an effect reduced by pretreatment with p38i VIII or SP600125, as depicted in Figure 8E. Furthermore, through a ChIP assay, we evaluated Nrf2's DNA binding activity. Our results indicate that MVS facilitated the binding of Nrf2 to ARE sequences in the HO-1 promoter regions in HCFs, as presented in Figure 8F. In summary, our study corroborates that MVS stimulates HO-1 expression via the Nrf2-ARE signaling pathway in HCFs, highlighting the mechanism behind MVS-induced cellular responses, particularly in terms of its influence on the Nrf2-mediated antioxidant defense system.

4 | Discussion

Cardiac fibrosis is a key characteristic in the progression of almost all heart diseases, with HCFs being the primary cell type responsible for this condition. These cells are crucial in maintaining the structure of cardiac myocytes, secreting growth factors, and responding to myocardial injuries. HCFs produce the extracellular matrix in the heart during both developmental and pathological processes, playing a vital role in scar tissue formation following myocardial infarction or cardiac fibrosis. Research has demonstrated that the Nrf2/HO-1 axis can mitigate cardiac hypertrophy and fibrosis following transverse aortic constriction [37]. In a different context, HMG-CoA reductase inhibitors like MVS, known for their cholesterol-lowering properties, have been observed to stimulate HO-1 expression, presenting a novel therapeutic avenue. However, the detailed mechanisms by which MVS triggers HO-1 expression in HCFs were previously unclear. Our study found that MVS effectively counteracts TNF-α-induced inflammatory responses in HCFs via the HO-1/carbon monoxide pathway.

15227278, 2025, 2, Downloaded from https://onlinelibrary.wiley.com/doi/10.1002/tox.24429 by Chang Gung University Of, Wiley Online Library on [04/05/2026]. See the Terms and Conditions (https://onlinelibrary.wiley.com/terms-and-conditions) on Wiley Online Library for rules of use; OA articles are governed by the applicable Creative Commons License

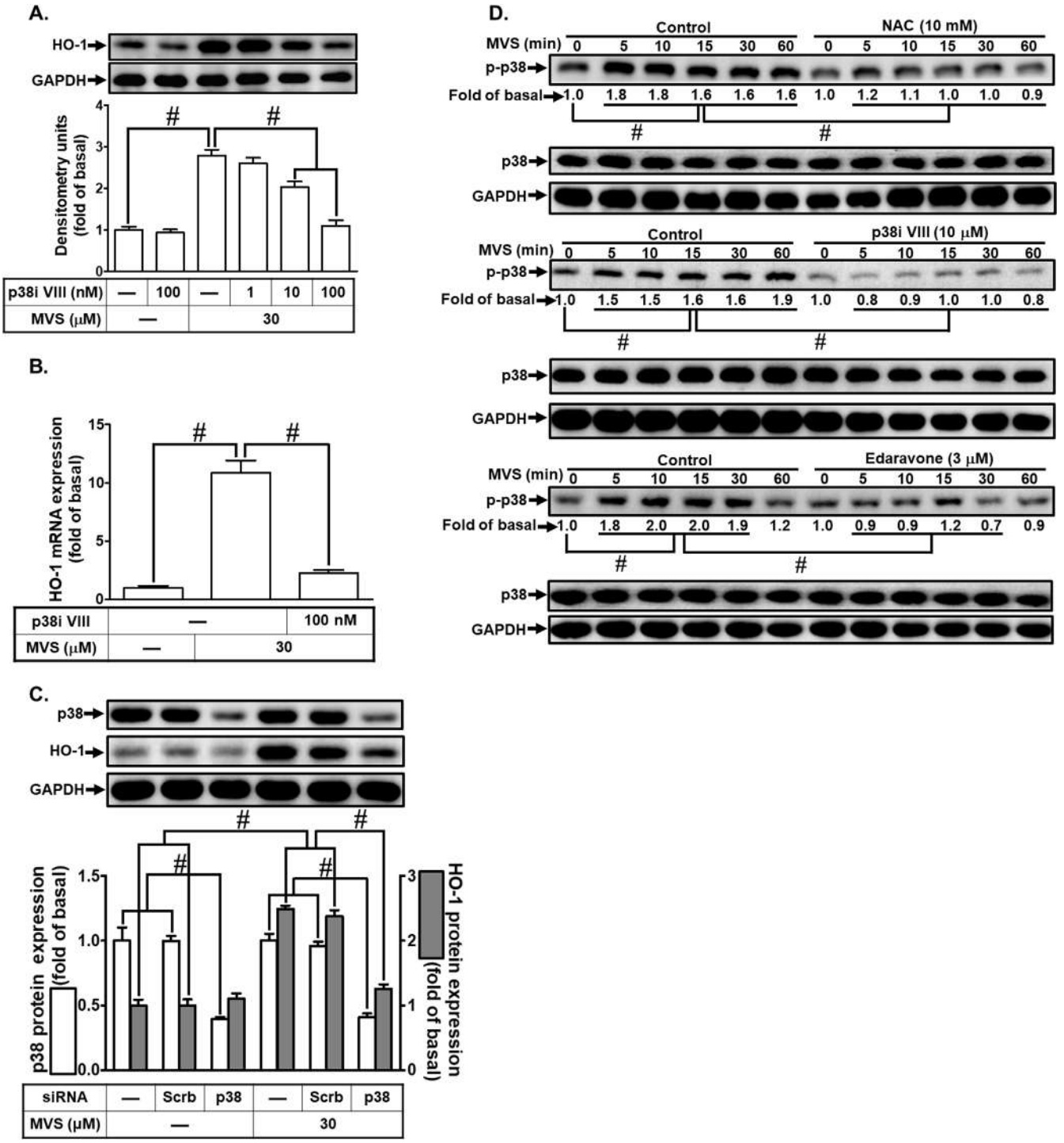


FIGURE 5 | MVS induces HO-1 expression via ROS/p38 MAPK. Cells were pretreated with p38 MAPK inhibitor VIII (p38i VIII) for 1 h and then treated with MVS. The (A) protein expression and (B) mRNA levels of HO-1 were determined. (C) Cells were transfected with siRNA of scrambled (scrb) or p38 and then treated with MVS (30 μM). The protein levels of HO-1 and p38 were determined. (D) Cells were treated with MVS in the presence or absence of NAC, p38i VIII, or Eda for the indicated time points. The protein expression of phospho-p38 was determined. Data are presented as mean ± S.E.M. of three independent experiments. $^{\#}p < 0.01$ for significant difference between the groups.

Additionally, we identified that MVS-induced HO-1 expression in these cells is regulated through the activation of multiple signaling pathways, including NADPH oxidase/ROS/p38 MAPK, JNK1/2/FoxO1, and Nrf2. This research illuminates the mechanisms underlying MVS's protective effects against cardiac fibrosis, underscoring its potential as a therapeutic strategy for heart disease.

MVS, like other statins such as atorvastatin and simvastatin, has been shown to upregulate HO-1 expression via the

15227278, 2025, 2, Downloaded from https://onlinelibrary.wiley.com/doi/10.1002/tox.24429 by Chang Gung University Of, Wiley Online Library on [04/05/2026]. See the Terms and Conditions (https://onlinelibrary.wiley.com/terms-and-conditions) on Wiley Online Library for rules of use; OA articles are governed by the applicable Creative Commons License

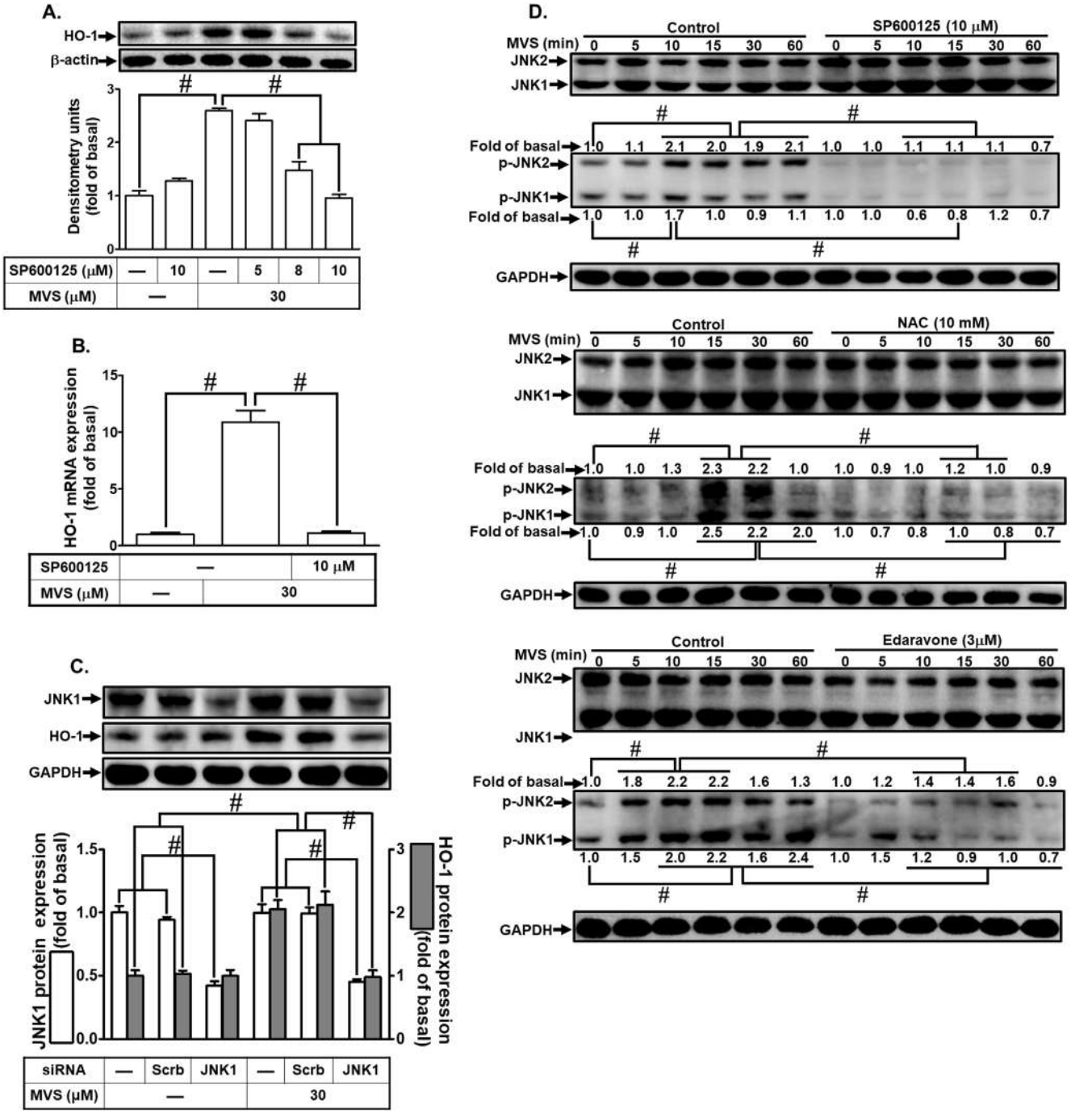


FIGURE 6 | MVS induces HO-1 expression via ROS/JNK1/2. Cells were pretreated with SP600125 for 1 h and then treated with MVS. The (A) protein expression and (B) mRNA levels of HO-1 were determined. (C) Cells were transfected with siRNA of scrambled (scrb) or JNK1 and then treated with MVS (30 μM). The protein levels of HO-1 and JNK1 were determined. (D) Cells were treated with MVS in the presence or absence of NAC, SP600125, or Eda for the indicated time points. The protein expression of phospho-JNK1/2 was determined. Data are presented as mean ± S.E.M. of three independent experiments. $^{\#}p < 0.01$ for significant difference between the groups.

activation of the p38 MAPK and JNK1/2 signaling pathways. However, the extent of HO-1 induction and its downstream effects can vary depending on the specific statin and the cellular context. For example, atorvastatin has demonstrated robust effects on endothelial cells, while simvastatin has shown particular efficacy in hepatocytes. In our study, MVS significantly induced HO-1 expression in HCFs, effectively neutralizing TNF-α-induced inflammatory responses. This suggests that MVS may uniquely modulate inflammatory pathways in cardiac cells, potentially positioning it as a superior candidate for treating inflammation-associated cardiovascular conditions. The findings of this study suggest that MVS holds promise as a therapeutic agent for cardiovascular diseases, particularly those associated with inflammation and fibrosis. By upregulating HO-1 and modulating key inflammatory pathways, MVS could reduce the progression of cardiac fibrosis and

15227278, 2025, 2, Downloaded from https://onlinelibrary.wiley.com/doi/10.1002/tox.24429 by Chang Gung University Of, Wiley Online Library on [04/05/2026]. See the Terms and Conditions (https://onlinelibrary.wiley.com/terms-and-conditions) on Wiley Online Library for rules of use; OA articles are governed by the applicable Creative Commons License

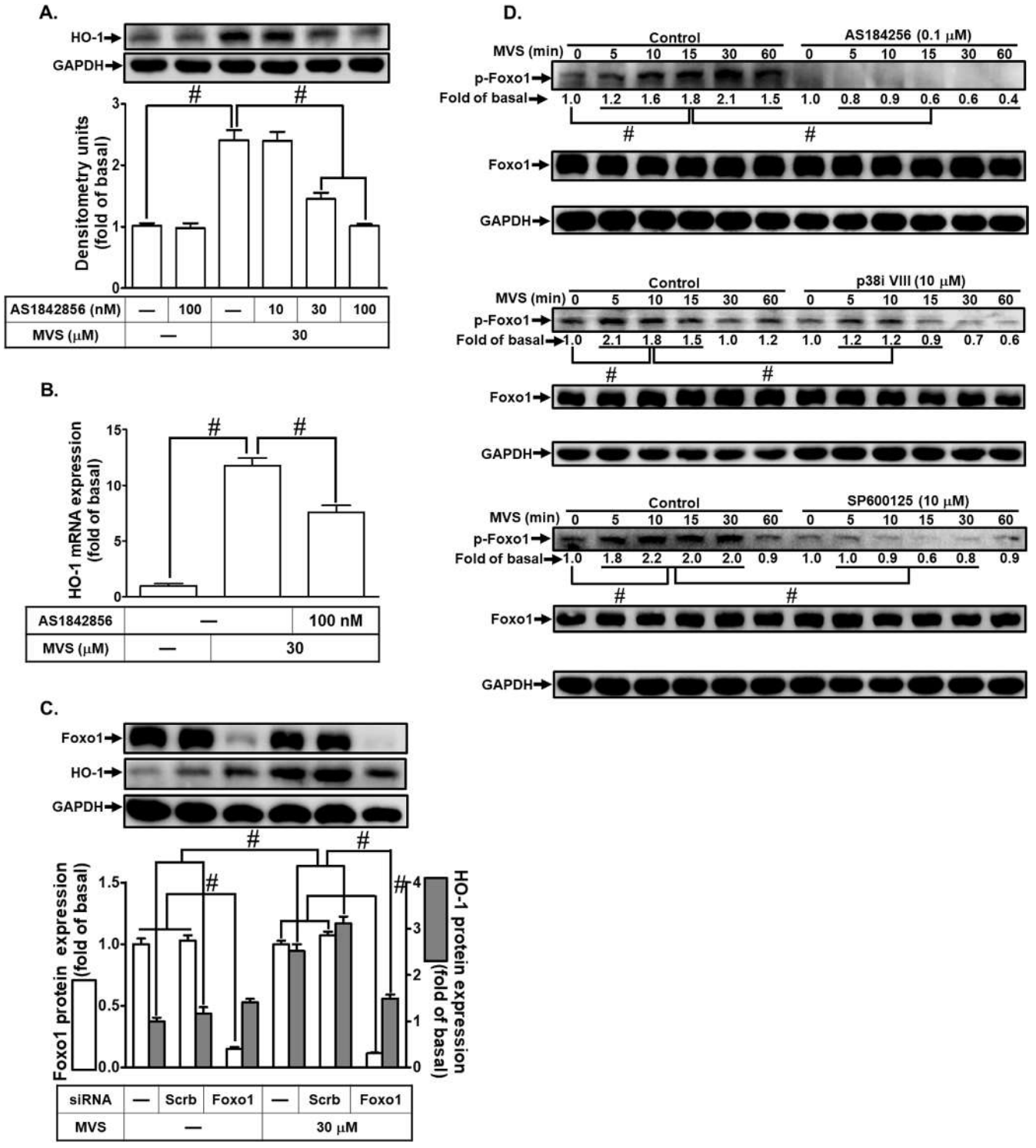


FIGURE 7 | MVS induces HO-1 expression via FoxO1. Cells were pretreated with AS1842856 for 1 h and then treated with MVS. The (A) protein expression and (B) mRNA levels of HO-1 were determined. (C) Cells were transfected with siRNA of scrambled (scrb) or FoxO1 and then treated with MVS (30 μM). The protein levels of HO-1 and FoxO1 were determined. (D) Cells were treated with MVS in the presence or absence of AS1842856, p38i VIII, or SP600125 for the indicated time points. The protein expression of phospho-FoxO1 was determined. Data are presented as mean ± S.E.M. of three independent experiments. $^{\#}p < 0.01$ for significant difference between the groups.

improve cardiac function. Exploring MVS as part of combination therapy with other cardiovascular drugs could further enhance its therapeutic effects. The translational potential of these findings warrants further investigation through well-designed clinical trials to evaluate the safety, efficacy, and optimal dosing of MVS in patients with cardiovascular diseases. Such trials could provide critical insights into the practical application of MVS in clinical settings, paving the way for new treatment strategies aimed at mitigating inflammation and fibrosis in the heart. While our study has identified key

15227278, 2025, 2, Downloaded from https://onlinelibrary.wiley.com/doi/10.1002/cox.24429 by Chang Gung University Of, Wiley Online Library on [04/05/2026]. See the Terms and Conditions (https://onlinelibrary.wiley.com/terms-and-conditions) on Wiley Online Library for rules of use; OA articles are governed by the applicable Creative Commons License

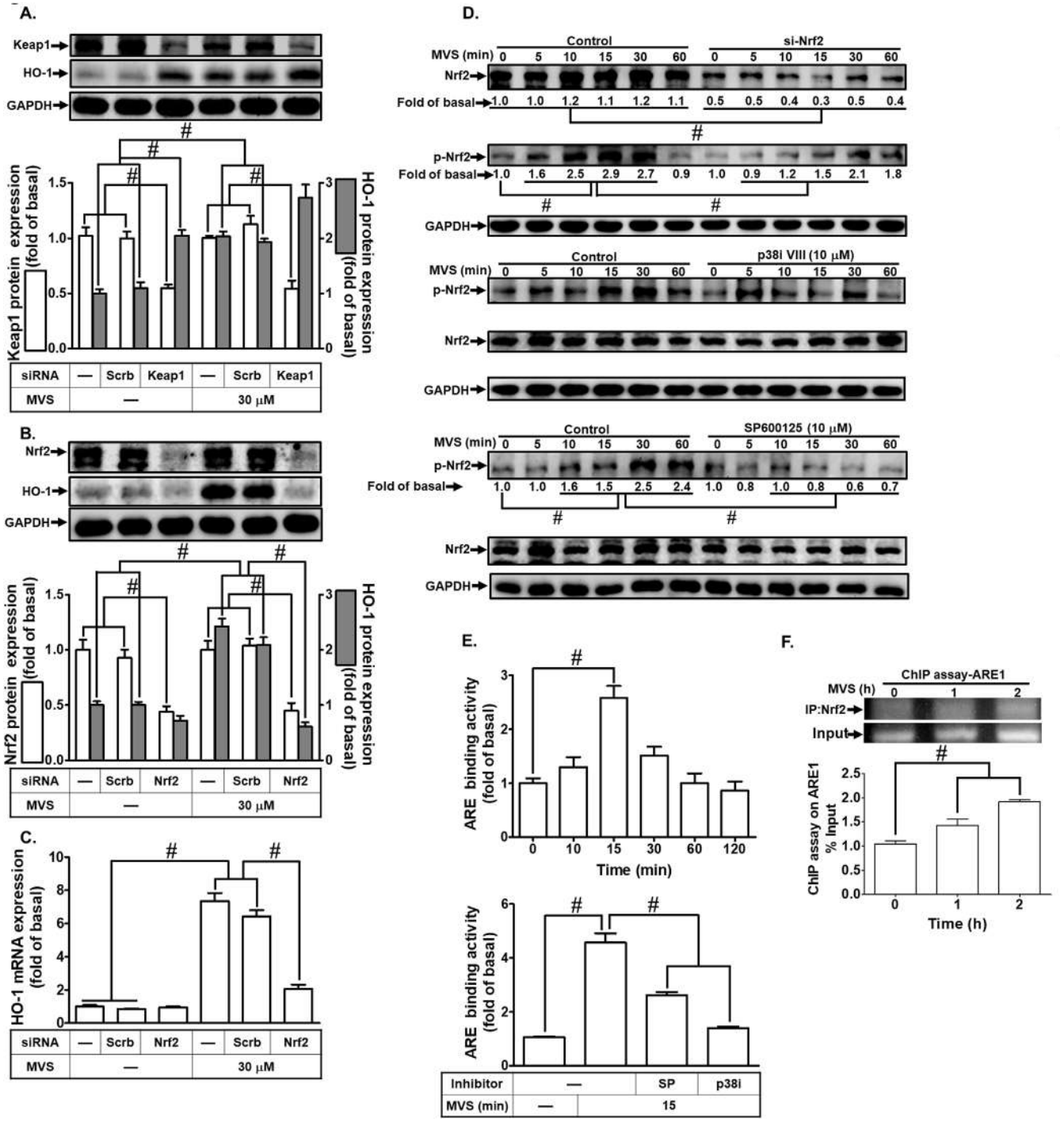


FIGURE 8 | Involvement of Nrf2 in MVS-induced HO-1 expression. (A, B) HCFs were transfected with siRNA of scrambled (scrb), Keap1, or Nrf2 and then treated with MVS for 16 h. The protein levels of Nrf2, HO-1, and Keap1 were determined. (C) HCFs were transfected with siRNA of scrambled (scrb) or Nrf2 and then treated with MVS. The mRNA levels of HO-1 were determined. (D) Cells were transfected with Nrf2 siRNA or pretreated with SP600125 or p38i VIII and then treated with MVS for the indicated time points. The protein expression of phospho-Nrf2 was determined. (E) Cells were treated with MVS for the indicated time points or pretreated with SP600125 or p38i VIII for 1 h and then treated with MVS for 15 min. The ARE-luciferase activity was determined. (F) The DNA binding activity of Nrf2 was determined by a ChIP assay using anti-Nrf2 antibody. The immunoprecipitated DNA or inputs were subject to determine by gel electrophoresis and a pair of primers flanking the ARE1 biding site within the HO-1 promoter. Data are presented as mean ± S.E.M. of three independent experiments. $^{\#}p < 0.01$ for significant difference between the groups.

signaling pathways such as NADPH oxidase/ROS/p38 MAPK and JNK1/2/FoxO1/Nrf2 in HO-1 induction, further research is necessary to delineate the precise molecular interactions within these pathways across different cell types and disease models. Understanding these interactions could reveal additional therapeutic targets and help optimize MVS's efficacy.

15227278, 2025, 2, Downloaded from https://onlinelibrary.wiley.com/doi/10.1002/tox.24429 by Chang Gung University Of, Wiley Online Library on [04/05/2026]. See the Terms and Conditions (https://onlinelibrary.wiley.com/terms-and-conditions) on Wiley Online Library for rules of use; OA articles are governed by the applicable Creative Commons License

Moreover, exploring the synergistic effects of MVS when used in combination with other therapeutic agents could enhance its protective effects against cardiac fibrosis and other cardiovascular diseases. Investigating the role of MVS in various models, including in vivo studies and clinical trials, will be essential to fully realize its therapeutic potential and to translate these findings into clinical applications.

HO-1, also known as heat shock protein 32, is a vital enzyme in the heme degradation pathway, breaking down hemoglobin into biliverdin, free iron, and carbon monoxide [12]. Biliverdin is subsequently converted into bilirubin by biliverdin reductase, both of which are recognized for their antioxidant properties [9, 12]. The carbon monoxide produced by HO-1 acts as a second messenger, influencing various physiological and pathological processes such as cell proliferation, inflammation, apoptosis, and tissue injury [33]. As a cytoprotective enzyme, HO-1 is crucial for maintaining cellular equilibrium. It is the inducible variant among the three HO isoenzymes (HO-1, HO-2, and HO-3). Under normal conditions, HO-1 levels are generally low in most tissues but can be upregulated in response to various pathophysiological stimuli like hypoxia, ultraviolet radiation, inflammatory agents, heme, and ischemia. This upregulation serves as a defense mechanism against oxidative and inflammatory damage, regulated primarily by redox-sensitive transcription factors including Nrf2, AP-1, hypoxia-inducible factor, and Bach1 [38]. Additionally, genetic polymorphisms in the HO-1 gene's promoter region have been linked to its expression and associated with diseases like coronary atherosclerosis, rheumatoid arthritis, and viral infections [38]. MVS, primarily used for cholesterol reduction and managing hyperlipidemia, belongs to the class of HMG-CoA reductase inhibitors, commonly known as statins [16]. It is effective in treating high cholesterol and conditions related to atherosclerosis, where plaque builds up in the arteries [16, 39]. Research has shown that MVS can reduce the production of proinflammatory cytokines and chemokines, thereby diminishing inflammation [21, 40]. Additionally, MVS has been noted for its ability to prevent the adhesion and infiltration of inflammatory cells into blood vessel walls and tissues [40]. MVS is also known to promote HO-1 expression and exert anti-inflammatory effects through various signaling pathways, including p38 MAPK, Erk1/2, and protein kinase G [17]. Our research found that MVS displayed anti-inflammatory properties in HCFs by enhancing HO-1 expression, which effectively neutralized the inflammatory responses triggered by TNF-α. Our findings also revealed that both MVS and CORM-2 significantly reduced TNF-α-induced NF-κB p65 activation, whereas bilirubin did not exhibit similar effects. These results provide valuable insights into MVS's potential therapeutic applications in reducing inflammation in cardiac tissues. The induction of the HO-1/carbon monoxide pathway by MVS presents a promising therapeutic approach for mitigating inflammatory processes in various cardiac diseases.

Further clinical research is crucial to comprehensively understand MVS's therapeutic potential and mechanisms in treating inflammation-associated cardiac conditions. Low levels of ROS have been recognized for their protective functions, as they are known to stimulate the upregulation of antioxidant enzymes like HO-1 through various cell signaling pathways [41]. Specifically, ROS production via $p47^{phox}$/NOX2 or NOX4 components has been observed to inhibit inflammatory signaling and alleviate inflammation, especially in the context of aging [42]. The critical balance between NOX/ROS generation and antioxidant activity plays a pivotal role in disease progression, serving as a secondary messenger that regulates cellular activities and safeguards cells from damage [43]. In our study, we examined the interplay between $p47^{phox}$/NOX-dependent ROS production and HO-1 expression in HCFs. Aligning with earlier findings, our research showed that knocking down NOX2 or $p47^{phox}$ with siRNA significantly reduced the MVS-induced expression of HO-1 in these cells. Additionally, we found that pretreatment with APO or DPI markedly decreased both MVS-induced ROS generation and $p47^{phox}$ activation. These results collectively reinforce the conclusion that MVS promotes HO-1 expression in HCFs predominantly through the generation of ROS derived from NADPH oxidase activity.

The MAPK pathways are known to react to various external and internal stimuli, including peptide growth factors, cytokines, hormones, as well as stressors like oxidative stress and endoplasmic reticulum stress [44]. These pathways are crucial in controlling many cellular functions, including proliferation, differentiation, survival, and apoptosis [44]. Disruptions in the regulation of these MAPK signaling pathways have been linked to the development and progression of numerous human diseases [45]. In our research, we observed that inhibiting JNK1/2 and p38 MAPK markedly reduced the induction of HO-1 expression in HCFs in response to MVS. Interestingly, inhibition of ERK1/2 did not produce a similar effect (data not shown). Prior studies have solidly confirmed that ROS production activates the p38 MAPK and JNK1/2 signaling pathways [30, 32]. Our results showed that using ROS inhibitors significantly diminished the activation of p38 MAPK and JNK1/2 caused by MVS. This finding underscores the critical role of ROS signaling in modulating the activation of these MAPK pathways in response to MVS.

FoxOs are multifaceted transcription factors regulated through their expression, nuclear translocation, DNA binding, and interactions with other proteins [46]. They are crucial in maintaining cellular homeostasis and adapting to environmental shifts [46]. A previous study [33] highlighted FoxO1's role in triggering HO-1 expression in primary human cardiomyocytes. Additionally, it has been shown that the JNK1/2 and p38MAPK pathways can activate the FoxO1 signaling in these cells [33]. The Keap1/Nrf2/ARE signaling system, known for its redox sensitivity, plays a vital role in upholding cellular balance under various stress conditions, including inflammation, carcinogenesis, and apoptosis [34]. Nrf2 is recognized for its role in promoting HO-1 expression across different cell types [35, 36], acting as an innate defense against oxidative stress [34–36]. In our research, we found substantial evidence for the involvement of both FoxO1 and Nrf2 in the HO-1 expression induction in HCFs in response to MVS. Using targeted inhibitors and siRNAs against FoxO1 and Nrf2, we observed a significant decrease in MVS-induced HO-1 expression. This underscores the pivotal roles of these transcription factors in the cellular response to MVS-induced stress in HCFs.

Our findings elucidate the complex relationship between FoxO1 and Nrf2 in regulating the HO-1 induction pathway, underscoring their importance as potential therapeutic targets in managing cellular responses under stress conditions. While these insights highlight the therapeutic potential of MVS in pathological conditions characterized by elevated TNF-α levels, it is equally crucial

15227278, 2025, 2, Downloaded from https://onlinelibrary.wiley.com/doi/10.1002/jcx.24429 by Chang Gung University Of, Wiley Online Library on [04/05/2026]. See the Terms and Conditions (https://onlinelibrary.wiley.com/terms-and-conditions) on Wiley Online Library for rules of use; OA articles are governed by the applicable Creative Commons License

to consider its baseline activity and safety profile under normal physiological conditions. Under normal physiological conditions, the expression of HO-1 is tightly regulated, serving as a cytoprotective mechanism against cellular stressors [47]. Preliminary evidence suggests that MVS, even in the absence of elevated TNF-α levels, can modestly upregulate HO-1 expression, potentially offering a preemptive defense mechanism without disrupting cellular homeostasis [48]. This subtle upregulation underscores the drug's capacity for fine-tuning cellular responses, aligning with its well-documented safety profile in vivo. Comprehensive in vivo studies have extensively documented MVS's safety, highlighting its minimal side effects and low toxicity across a range of doses. Notably, investigations into the long-term administration of MVS have not reported adverse effects related to its modulation of HO-1 levels, suggesting a favorable safety profile that supports its consideration as a therapeutic agent. Furthermore, the safety characterization of MVS in vivo has revealed its efficacy in not only reducing cholesterol levels but also in exerting anti-inflammatory effects without detrimental impacts on physiological processes or cellular equilibrium [49]. These findings are particularly relevant given the potential for MVS to induce HO-1 in a controlled manner, thereby offering protective benefits in both pathological and normal TNF-α conditions. However, it is acknowledged that detailed mechanistic insights into the effects of MVS on HO-1 expression under normal conditions remain to be fully elucidated. Future research endeavors will aim to bridge this gap, employing rigorous in vivo models to assess the nuanced interplay between MVS administration, HO-1 expression, and overall cardiac health. Such investigations will be critical in affirming MVS's therapeutic potential and ensuring its safe application in the management of cardiovascular diseases, ultimately paving the way for novel treatment strategies that harness the protective capacities of HO-1 in cardiac fibrosis and beyond.

To summarize, our research has established that MVS effectively diminishes TNF-α-induced inflammatory responses in HCFs by engaging the HO-1/carbon monoxide pathway. Additionally, it implicates several key signaling pathways in this process, including NADPH oxidase/ROS/p38 MAPK, JNK1/2/FoxO1, and Nrf2, as illustrated in Figure 9. These insights underscore the potential of MVS as a therapeutic agent in the management of inflammation-associated cardiac disorders. Looking forward, it

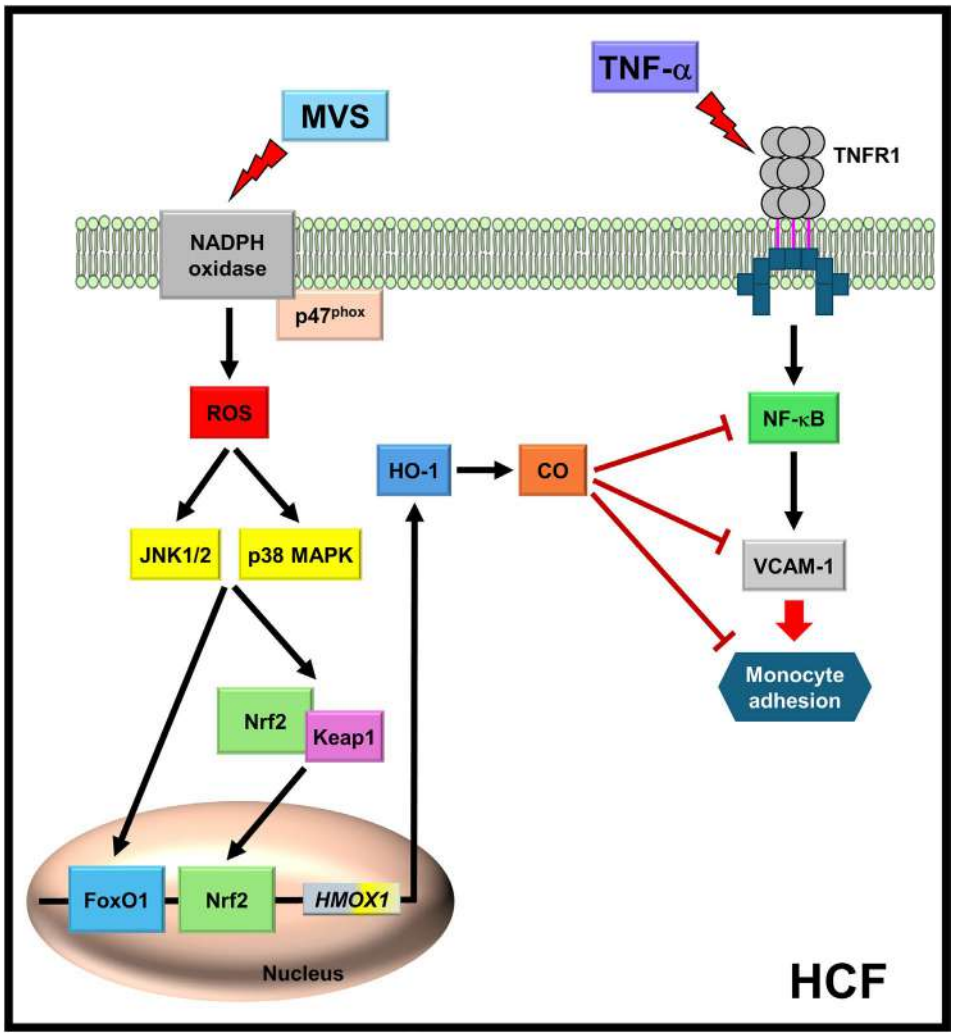


FIGURE 9 | Proposed scheme for anti-inflammatory effects of MVS in TNF-α-exposed HCFs. In HCFs, TNF-α triggers the upregulation of VCAM-1 through the NF-κB signaling pathway, promoting monocyte adhesion that contributes to inflammation development. Interestingly, MVS-induced HO-1 inhibits the expression of VCAM-1, thereby preventing these pathological events. Additionally, the induction of HO-1 by MVS is mediated through the activation of the NADPH oxidase/ROS/p38 MAPK and JNK1/2/FoxO1 and Nrf2 signaling pathway.

15227278, 2025, 2, Downloaded from https://onlinelibrary.wiley.com/doi/10.1002/tox.24429 by Chang Gung University Of, Wiley Online Library on [04/05/2026]. See the Terms and Conditions (https://onlinelibrary.wiley.com/terms-and-conditions) on Wiley Online Library for rules of use; OA articles are governed by the applicable Creative Commons License

is imperative to delve deeper into the detailed molecular mechanisms by which MVS interacts with the NADPH oxidase/ROS/p38 MAPK and JNK1/2/FoxO1 pathways. Understanding these interactions is crucial for comprehending how MVS regulates HO-1 expression and its overall impact on cardiac health. Moreover, conducting extensive in vivo studies and clinical trials is essential to confirm MVS's effectiveness in treating cardiac fibrosis and other related cardiovascular diseases. This would not only validate the drug's therapeutic potential but also help in optimizing its clinical applications. Additionally, exploring the synergistic potential of MVS when combined with other therapeutic agents or treatments that target different facets of cardiac fibrosis could pave the way for more comprehensive and effective treatment strategies for heart disease. For instance, investigating how MVS works in conjunction with lifestyle changes, dietary modifications, or other pharmacological interventions could provide insights into multifaceted treatment approaches. Continued research in this field promises to open new avenues for developing innovative therapies to combat cardiac fibrosis, thereby enhancing the quality of life and prognosis for patients suffering from various cardiac conditions. The exploration of these pathways not only contributes to our understanding of cardiac pathophysiology but also aids in the identification of novel therapeutic targets for heart diseases.

Author Contributions

Conceptualization: I-Ta Lee, Chien-Chung Yang, Yan-Jyun Lin, Wen-Bin Wu, Wei-Ning Lin, Chiang-Wen Lee, Li-Der Hsiao, and Chuen-Mao Yang. Methodology: I-Ta Lee, Chien-Chung Yang, Yan-Jyun Lin, Wen-Bin Wu, Wei-Ning Lin, and Chuen-Mao Yang. Software: I-Ta Lee, Chien-Chung Yang, Yan-Jyun Lin, Wen-Bin Wu, Wei-Ning Lin, Li-Der Hsiao, and Chuen-Mao Yang. Validation: I-Ta Lee, Chien-Chung Yang, Yan-Jyun Lin, Wen-Bin Wu, Wei-Ning Lin, Li-Der Hsiao, and Chuen-Mao Yang. Formal analysis: Yan-Jyun Lin and Li-Der Hsiao. Investigation: Chien-Chung Yang, Yan-Jyun Lin, Wen-Bin Wu, and Li-Der Hsiao. Resources: Chien-Chung Yang and Chuen-Mao Yang. Data curation: Yan-Jyun Lin and Li-Der Hsiao. Writing – original draft preparation: I-Ta Lee and Wen-Bin Wu. Writing – review and editing: I-Ta Lee, Chien-Chung Yang, Wen-Bin Wu, Chiang-Wen Lee, and Chuen-Mao Yang. Visualization: Chuen-Mao Yang. Supervision: Chuen-Mao Yang. Project administration: Chuen-Mao Yang. Funding acquisition: Chien-Chung Yang and Chuen-Mao Yang. All authors have read and agreed to the published version of the manuscript.

Acknowledgments

We appreciated Ya-Fan Shih for her technical assistance.

Ethics Statement

The authors have nothing to report.

Consent

The authors have nothing to report.

Conflicts of Interest

The authors declare no conflicts of interest.

Data Availability Statement

The data that support the findings of this study are available from the corresponding author upon reasonable request.

References

1. A. Deb and E. Ubil, "Cardiac Fibroblast in Development and Wound Healing," *Journal of Molecular and Cellular Cardiology* 70 (2014): 47–55.

2. S. M. Wang, G. Q. Liu, H. B. Xian, J. L. Si, S. X. Qi, and Y. P. Yu, "LncRNA NEAT1 Alleviates Sepsis-Induced Myocardial Injury by Regulating the TLR2/NF-κB Signaling Pathway," *European Review for Medical and Pharmacological Sciences* 23 (2019): 4898–4907.

3. R. Zhang, Y. Y. Zhang, X. R. Huang, et al., "C-Reactive Protein Promotes Cardiac Fibrosis and Inflammation in Angiotensin II-Induced Hypertensive Cardiac Disease," *Hypertension* 55 (2010): 953–960.

4. S. D. Prabhu and N. G. Frangogiannis, "The Biological Basis for Cardiac Repair After Myocardial Infarction: From Inflammation to Fibrosis," *Circulation Research* 119 (2016): 91–112.

5. N. A. Turner, A. Das, P. Warburton, D. J. O'Regan, S. G. Ball, and K. E. Porter, "Interleukin-1α Stimulates Proinflammatory Cytokine Expression in Human Cardiac Myofibroblasts," *American Journal of Physiology. Heart and Circulatory Physiology* 297 (2009): H1117–H1127.

6. Z. Zhang, W. Cui, G. Li, et al., "Baicalein Protects Against 6-OHDA-Induced Neurotoxicity Through Activation of Keap1/Nrf2/HO-1 and Involving PKCα and PI3K/AKT Signaling Pathways," *Journal of Agricultural and Food Chemistry* 60 (2012): 8171–8182.

7. N. A. Turner, R. S. Mughal, P. Warburton, D. J. O'Regan, S. G. Ball, and K. E. Porter, "Mechanism of TNFα-Induced IL-1α, IL-1β and IL-6 Expression in Human Cardiac Fibroblasts: Effects of Statins and Thiazolidinediones," *Cardiovascular Research* 76 (2007): 81–90.

8. X. Shi, C. D. Young, H. Zhou, and X. Wang, "Transforming Growth Factor-β Signaling in Fibrotic Diseases and Cancer-Associated Fibroblasts," *Biomolecules* 10 (2020): 1666.

9. X. Zhang, Y. Yu, H. Lei, et al., "The Nrf-2/HO-1 Signaling Axis: A Ray of Hope in Cardiovascular Diseases," *Cardiology Research and Practice* 2020 (2020): 5695723.

10. M. M. Facchinetti, "Heme-oxygenase-1," *Antioxidants & Redox Signaling* 32 (2020): 1239–1242.

11. S. W. Ryter and L. E. Otterbein, "Carbon Monoxide in Biology and Medicine," *BioEssays* 26 (2004): 270–280.

12. M. L. Wu, Y. C. Ho, and S. F. Yet, "A Central Role of Heme Oxygenase-1 in Cardiovascular Protection," *Antioxidants & Redox Signaling* 15 (2011): 1835–1846.

13. H. Shan, T. Li, L. Zhang, et al., "Heme Oxygenase-1 Prevents Heart Against Myocardial Infarction by Attenuating Ischemic Injury-Induced Cardiomyocytes Senescence," *eBioMedicine* 39 (2019): 59–68.

14. S. Zhou, W. Sun, Z. Zhang, and Y. Zheng, "The Role of Nrf2-Mediated Pathway in Cardiac Remodeling and Heart Failure," *Oxidative Medicine and Cellular Longevity* 2014 (2014): 260429.

15. G. E. Mann, "Nrf2-Mediated Redox Signalling in Vascular Health and Disease," *Free Radical Biology & Medicine* 75, no. Suppl 1 (2014): S1.

16. S. O. Almeida and M. Budoff, "Effect of Statins on Atherosclerotic Plaque," *Trends in Cardiovascular Medicine* 29 (2019): 451–455.

17. J. C. Chen, K. C. Huang, and W. W. Lin, "HMG-CoA Reductase Inhibitors Upregulate Heme Oxygenase-1 Expression in Murine RAW264.7 Macrophages via ERK, p38 MAPK and Protein Kinase G Pathways," *Cellular Signalling* 18 (2006): 32–39.

18. C. C. Yang, L. D. Hsiao, H. H. Lin, et al., "Induction of HO-1 by 5,8-Dihydroxy-4′,7-Dimethoxyflavone via Activation of ROS/p38 MAPK/Nrf2 Attenuates Thrombin-Induced Connective Tissue Growth Factor Expression in Human Cardiac Fibroblasts," *Oxidative Medicine and Cellular Longevity* 2020 (2020): 108018.

19. T. T. T. Vo, H. W. Huang, Y. Wee, et al., "Surfactin Reduces Particulate Matter-Induced VCAM-1-Dependent Monocyte Adhesion in

15227278, 2025, 2, Downloaded from https://onlinelibrary.wiley.com/doi/10.1002/cox.24429 by Chang Gung University Of, Wiley Online Library on [04/05/2026]. See the Terms and Conditions (https://onlinelibrary.wiley.com/terms-and-conditions) on Wiley Online Library for rules of use; OA articles are governed by the applicable Creative Commons License

Human Gingival Fibroblasts by Increasing Nrf2-Dependent HO-1 Expression," *Journal of Periodontal Research* 57 (2022): 115–130.

20. C. W. Lee, I. T. Lee, C. C. Lin, H. C. Lee, W. N. Lin, and C. M. Yang, "Activation and Induction of Cytosolic Phospholipase A2 by IL-1β in Human Tracheal Smooth Muscle Cells: Role of MAPKs/p300 and NF-κB," *Journal of Cellular Biochemistry* 109 (2010): 1045–1056.

21. C. C. Lin, W. N. Lin, R. L. Cho, et al., "Induction of HO-1 by Mevastatin Mediated via a Nox/ROS-Dependent c-Src/PDGFRα/PI3K/Akt/Nrf2/ARE Cascade Suppresses TNF-α-Induced Lung Inflammation," *Journal of Clinical Medicine* 9 (2020): 226.

22. D. J. Slebos, S. W. Ryter, and A. M. Choi, "Heme Oxygenase-1 and Carbon Monoxide in Pulmonary Medicine," *Respiratory Research* 4, no. 1 (2003): 7.

23. K. A. Nath, "Heme Oxygenase-1: A Provenance for Cytoprotective Pathways in the Kidney and Other Tissues," *Kidney International* 70 (2006): 432–443.

24. H. Ye, Q. Zhou, S. Zheng, et al., "Tumor-Associated Macrophages Promote Progression and the Warburg Effect via CCL18/NF-κB/VCAM-1 Pathway in Pancreatic Ductal Adenocarcinoma," *Cell Death & Disease* 9, no. 5 (2018): 453.

25. N. Hadad, L. Tuval, V. Elgazar-Carmom, R. Levy, and R. Levy, "Endothelial ICAM-1 Protein Induction Is Regulated by Cytosolic Phospholipase A2α via Both NF-κB and CREB Transcription Factors," *Journal of Immunology* 186, no. 3 (2011): 1816–1827.

26. Z. Zhao, J. Zhao, J. Xue, X. Zhao, and P. Liu, "Autophagy Inhibition Promotes Epithelial-Mesenchymal Transition Through ROS/HO-1 Pathway in Ovarian Cancer Cells," *American Journal of Cancer Research* 6, no. 10 (2016): 2162–2177.

27. Y. Hu, X. Feng, J. Chen, Y. Wu, and L. Shen, "Hydrogen-Rich Saline Alleviates Early Brain Injury Through Inhibition of Necroptosis and Neuroinflammation via the ROS/HO-1 Signaling Pathway After Traumatic Brain Injury," *Experimental and Therapeutic Medicine* 23, no. 2 (2022): 126.

28. J. El-Benna, P. M. Dang, M. A. Gougerot-Pocidalo, J. C. Marie, and F. Braut-Boucher, "p47phox, the Phagocyte NADPH Oxidase/NOX2 Organizer: Structure, Phosphorylation and Implication in Diseases," *Experimental & Molecular Medicine* 41, no. 4 (2009): 217–225.

29. Z. Wang, S. O. Ka, Y. Lee, B. H. Park, and E. J. Bae, "Butein Induction of HO-1 by p38 MAPK/Nrf2 Pathway in Adipocytes Attenuates High-Fat Diet Induced Adipose Hypertrophy in Mice," *European Journal of Pharmacology* 799 (2017): 201–210.

30. J. Liu, Y. Wei, W. Jia, et al., "Chenodeoxycholic Acid Suppresses AML Progression Through Promoting Lipid Peroxidation via ROS/p38 MAPK/DGAT1 Pathway and Inhibiting M2 Macrophage Polarization," *Redox Biology* 56 (2022): 102452.

31. W. K. Jeon, H. Y. Hong, and B. C. Kim, "Genipin Up-Regulates Heme Oxygenase-1 via PI3-Kinase-JNK1/2-Nrf2 Signaling Pathway to Enhance the Anti-Inflammatory Capacity in RAW264.7 Macrophages," *Archives of Biochemistry and Biophysics* 512 (2011): 119–125.

32. Z. Zhang, M. Guo, S. Zhao, J. Shao, and S. Zheng, "ROS-JNK1/2-Dependent Activation of Autophagy Is Required for the Induction of Anti-Inflammatory Effect of Dihydroartemisinin in Liver Fibrosis," *Free Radical Biology & Medicine* 101 (2016): 272–283.

33. P. T. Chien, C. C. Lin, L. D. Hsiao, and C. M. Yang, "Induction of HO-1 by Carbon Monoxide Releasing Molecule-2 Attenuates Thrombin-Induced COX-2 Expression and Hypertrophy in Primary Human Cardiomyocytes," *Toxicology and Applied Pharmacology* 289, no. 2 (2015): 349–359.

34. X. Ding, T. Jian, Y. Wu, et al., "Ellagic Acid Ameliorates Oxidative Stress and Insulin Resistance in High Glucose-Treated HepG2 Cells via miR-223/keap1-Nrf2 Pathway," *Biomedicine & Pharmacotherapy* 110 (2019): 85–94.

35. K. Shen, Y. Jia, X. Wang, et al., "Exosomes From Adipose-Derived Stem Cells Alleviate the Inflammation and Oxidative Stress via Regulating Nrf2/HO-1 Axis in Macrophages," *Free Radical Biology & Medicine* 165 (2021): 54–66.

36. X. Ding, H. Zhao, and C. Qiao, "Icariin Protects Podocytes From NLRP3 Activation by Sesn2-Induced Mitophagy Through the Keap1-Nrf2/HO-1 Axis in Diabetic Nephropathy," *Phytomedicine* 99 (2022): 154005.

37. A. M. Syed, S. Kundu, C. Ram, et al., "Up-Regulation of Nrf2/HO-1 and Inhibition of TGF-β1/Smad2/3 Signaling Axis by Daphnetin Alleviates Transverse Aortic Constriction-Induced Cardiac Remodeling in Mice," *Free Radical Biology & Medicine* 186 (2022): 17–30.

38. Q. Yang and W. Wang, "The Nuclear Translocation of Heme Oxygenase-1 in Human Diseases," *Frontiers in Cell and Development Biology* 10 (2022): 890186.

39. C. R. Sirtori, E. Tremoli, and R. Paoletti, "New Strategies in the Development of Anti-Atherosclerotic Drugs," *Artery* 8 (1980): 507–518.

40. T. Helbing, R. Rothweiler, J. Heinke, et al., "BMPER Is Upregulated by Statins and Modulates Endothelial Inflammation by Intercellular Adhesion Molecule-1," *Arteriosclerosis, Thrombosis, and Vascular Biology* 30 (2010): 554–560.

41. A. Loboda, M. Damulewicz, E. Pyza, A. Jozkowicz, and J. Dulak, "Role of Nrf2/HO-1 System in Development, Oxidative Stress Response and Diseases: An Evolutionarily Conserved Mechanism," *Cellular and Molecular Life Sciences* 73 (2016): 3221–3247.

42. J. R. Chen, O. P. Lazarenko, M. L. Blackburn, K. E. Mercer, T. M. Badger, and M. J. Ronis, "p47phox-Nox2-Dependent ROS Signaling Inhibits Early Bone Development in Mice but Protects Against Skeletal Aging," *Journal of Biological Chemistry* 290 (2015): 14692–14704.

43. J. Zhang, X. Wang, V. Vikash, et al., "ROS and ROS-Mediated Cellular Signaling," *Oxidative Medicine and Cellular Longevity* 2016 (2016): 4350965.

44. E. K. Kim and E. J. Choi, "Pathological Roles of MAPK Signaling Pathways in Human Diseases," *Biochimica et Biophysica Acta* 1802 (2010): 396–405.

45. E. K. Kim and E. J. Choi, "Compromised MAPK Signaling in Human Diseases: An Update," *Archives of Toxicology* 89 (2015): 867–882.

46. M. Katoh and M. Katoh, "Human FOX Gene Family (Review)," *International Journal of Oncology* 25 (2004): 1495–1500.

47. M. D. Maines, "The Heme Oxygenase System: A Regulator of Second Messenger Gases," *Annual Review of Pharmacology and Toxicology* 37 (1997): 517–554.

48. C. M. Yang, C. C. Lin, C. C. Yang, R. L. Cho, and L. D. Hsiao, "Mevastatin-Induced AP-1-Dependent HO-1 Expression Suppresses Vascular Cell Adhesion Molecule-1 Expression and Monocyte Adhesion on Human Pulmonary Alveolar Epithelial Cells Challenged With TNF-α," *Biomolecules* 10 (2020): 381.

49. M. K. Jain and P. M. Ridker, "Anti-Inflammatory Effects of Statins: Clinical Evidence and Basic Mechanisms," *Nature Reviews. Drug Discovery* 4 (2005): 977–987.

15227278, 2025, 2, Downloaded from https://onlinelibrary.wiley.com/doi/10.1002/tox.24429 by Chang Gung University Of, Wiley Online Library on [04/05/2026]. See the Terms and Conditions (https://onlinelibrary.wiley.com/terms-and-conditions) on Wiley Online Library for rules of use; OA articles are governed by the applicable Creative Commons License

frontiers | Frontiers in Medicine

TYPE Clinical Trial
PUBLISHED 29 January 2025
DOI 10.3389/fmed.2024.1503678

Check for updates

OPEN ACCESS

EDITED BY
Marcos Ferreira Minicucci,
São Paulo State University, Brazil

REVIEWED BY
Sampath Kumar Amaravadi,
University of Chichester, United Kingdom
Zefei Jiang,
Chengdu University of Traditional Chinese Medicine, China

*CORRESPONDENCE
Hui-Ling Lin
huiling@mail.cgu.edu.tw
Jui-Fang Liu
jfliu01@mail.cgust.edu.tw

†These authors have contributed equally to this work

‡These authors share first authorship

RECEIVED 29 September 2024
ACCEPTED 23 December 2024
PUBLISHED 29 January 2025

CITATION
Wang S-J, Fang T-P, Rowley DD, Liu N-W, Chen J-O, Liu J-F and Lin H-L (2025) Inspiratory muscle training facilitates liberation from mechanical ventilation in subacute critically ill patients—a randomized controlled trial.
Front. Med. 11:1503678.
doi: 10.3389/fmed.2024.1503678

COPYRIGHT
© 2025 Wang, Fang, Rowley, Liu, Chen, Liu and Lin. This is an open-access article distributed under the terms of the Creative Commons Attribution License (CC BY). The use, distribution or reproduction in other forums is permitted, provided the original author(s) and the copyright owner(s) are credited and that the original publication in this journal is cited, in accordance with accepted academic practice. No use, distribution or reproduction is permitted which does not comply with these terms.

Inspiratory muscle training facilitates liberation from mechanical ventilation in subacute critically ill patients—a randomized controlled trial

Shu-Jane Wang[1†‡], Tien-Pei Fang[2,3†‡], Daniel D. Rowley[4], Nan-Wei Liu[5], Jui-O Chen[6], Jui-Fang Liu[3,7*†] and Hui-Ling Lin[2,3,8*†]

[1]Department of Respiratory Therapy, Zuoying Armed Forces General Hospital, Kaohsiung, Taiwan, [2]Department of Respiratory Therapy, Chiayi Chang Gung Memorial Hospital, Chiayi, Taiwan, [3]Department of Respiratory Care, Chang Gung University of Science and Technology, Chiayi, Taiwan, [4]Respiratory Therapy Services, University of Virginia Medical Center, Charlottesville, VA, United States, [5]Department of English, National Chengchi University, Taipei, Taiwan, [6]Department of Nursing, Tajen University, Pingtung, Taiwan, [7]Chronic Diseases and Health Promotion Research Center, Chang Gung University of Science and Technology, Chiayi, Taiwan, [8]Department of Respiratory Therapy, Chang Gung University, Taoyuan, Taiwan

Background: Patients undergoing mechanical ventilation often develop rapid diaphragmatic atrophy, respiratory muscle weakness, and dysfunction, which are associated with prolonged duration of ventilation. This study aimed to evaluate whether Inspiratory Muscle Training (IMT) facilitates weaning from mechanical ventilation and enhances muscle strength in critically ill, subacute adult patients, while examining the relationship between IMT and relevant clinical laboratory values.

Methods: In this randomized clinical trial, patients admitted to the intensive care unit requiring mechanical ventilation for more than 2 days, with stable hemodynamics and resolved acute conditions, were enrolled. Participants were randomly assigned to the IMT or no-IMT group. The IMT group received training twice daily, 5 days a week, for three consecutive weeks. The primary outcome was ventilator duration. The primary outcome measure was the number of days until liberation from mechanical ventilation. The secondary outcomes of interest were respiratory muscle strength and biomarker levels.

Results: Thirty-three subjects (17 in the IMT group, 16 in the no-IMT group) were included in the final analysis. The IMT group had significantly shorter ventilator days (12.6 $\pm$ 5.2 vs. 18.1 $\pm$ 8.8, $p = 0.04$). IMT intervention significantly reduced rapid shallow breathing index and improved respiratory muscle strength, with greater maximum inspiratory pressure ($p < 0.01$), maximum expiratory pressure ($p = 0.03$), and peak expiratory flow ($p = 0.01$). A moderate positive correlation was observed between IMT and increased creatinine levels (rs = 0.54, $p = 0.01$), whereas the no-IMT group showed a reduction.

Conclusion: IMT significantly shortened ventilator duration and improved respiratory muscle strength. A moderate correlation between increased creatinine levels and respiratory muscle strength was observed, suggesting that creatinine may be a potential biomarker for muscle recovery during IMT.

Clinical trial registration: This study was registered at ClinicalTrials.gov (NCT06611683).

KEYWORDS

inspiratory muscle training, subacute critical ill, mechanical ventilation support, rapid shallow breathing index, respiratory muscle strength, creatinine

1 Introduction

Acute respiratory failure is the primary reason that mechanical ventilation is aimed at maintaining sufficient ventilation to support life. Patients on mechanical ventilation often experience rapid diaphragm atrophy on the second day, resulting in diaphragm myofiber changes, respiratory muscle weakness, dysfunction, and impaired physical function (1–3). These changes can cause severe complications such as frailty and infections, leading to an increased duration of mechanical ventilation, extended intensive care unit (ICU) stay, and higher 1-year mortality (4).

Clinical studies have explored enhancing diaphragm and respiratory muscle strength and endurance through inspiratory muscle, expiratory muscle, and combined respiratory muscle training (5, 6). Training methods include flow-resistive, pressure threshold, and resistance training using electronic devices (7, 8). These strategies enhance respiratory muscle strength and endurance, promoting muscle fiber overload through increased training intensity, duration, and frequency (9, 10). Clinical practice guidelines and systematic reviews have highlighted the significant effects of inspiratory muscle training (IMT) on improving respiratory muscle strength, particularly in enhancing diaphragm weakness in patients undergoing invasive mechanical ventilation (5, 11). IMT has also been shown to increase maximal inspiratory and expiratory pressure, shorten mechanical ventilation duration, and reduce ICU length of stay (12, 13). Moreover, the total weaning time from mechanical ventilation was shorter in both low-to-moderate intensity and high-intensity threshold IMT groups (14). These findings underscore the importance of respiratory muscle training in clinical practice as an effective strategy for reducing the duration of mechanical ventilation and its associated complications (13). However, the majority of IMT studies have been conducted on patients who failed to wean from mechanical ventilation or required mechanical ventilator use for more than 7 days (12, 15). Since inspiratory muscle weakness and diaphragm atrophy can occur soon after patients undergo mechanical ventilation, we hypothesize that patients would benefit from inspiratory muscle training during the subacute stage, once the cause of intubation has been resolved and their vital signs have stabilized.

Additionally, muscle training has been shown to alter biochemical parameters and clinical laboratory test results in healthy individuals. Fragala et al. reported that increased participation in aerobic and strength exercises was associated with higher creatinine levels, percent oxygen saturation, and iron (16). Furthermore, serum creatinine levels are linked to lean body mass and handgrip strength in healthy individuals (17). Hemoglobin is responsible for transporting oxygen to tissues and its serum level is associated with exercise capacity. Albumin is essential for transporting substances in the blood, such as proteins, hormones, and electrolytes which is crucial for maintaining the osmotic balance. Albumin levels have been found to be associated with strenuous exercise. Creatinine is associated with not only renal function, but also muscle mass. The association between these clinical laboratory values and muscle training in critically ill patients has not yet been explored.

The purpose of this study was to determine if IMT significantly facilitates liberation from mechanical ventilation and improves respiratory muscle strength among subacute critically ill adult patients when compared to no IMT among subacute critically ill adult patients. The secondary aim was to investigate the relationship among IMT, respiratory parameters, and clinical laboratory test results.

2 Methods

2.1 Study design

This single-center randomized controlled clinical trial was conducted in medical and surgical intensive care units (ICUs) at the Zuoying Armed Forces General Hospital in Kaohsiung City, Taiwan. The Institutional Review Board of the Kaohsiung Armed Forces General Hospital approved the study protocol (approval number: KAFGHIRB107-027). All the measurements complied with the ethical standards of the Declaration of Helsinki. The study registered at ClinicalTrials.gov identifier: NCT06611683, on September 25, 2024. This work was reported in line with the Consolidated Standards of Reporting Trials (CONSORT) Guidelines.

Subjects admitted to the adult ICU were screened daily by a study investigator (S-J, W) who reviewed the bed occupancy in each ICU to identify potential study participants. Electronic medical records were reviewed for inclusion and exclusion criteria. Eligible participants were adult human subjects aged ≥18 years who required invasive mechanical ventilation for >2 days in an ICU. Subjects were excluded from the study if they met any of the following criteria: hemodynamic instability (heart rate > 120 beats/min, unstable blood pressure, vasopressor infusion), inadequate oxygenation (PEEP >8 cmH2O, FiO2 > 50%), body temperature > 38.5°C, sepsis, use of sedative infusion, steroid administration, and home ventilator use before ICU admission. The study investigator approached all eligible participants and invited them to participate in the study. All subjects provided informed consent signed by their proxy before enrollment in the study.

2.2 Randomization

We used a simple parallel randomization scheme to allocate subjects to one of the two equal (1:1) groups. A computer-generated random numbers generator (Researcher Randomizer website) randomly allocated the study subjects into the IMT or no-IMT groups. Group allocation was performed before the commencement of the study. Each randomly generated number was printed, shuffled, placed, and sealed in a sequentially numbered opaque envelope by a person not-affiliated with the study. To ensure concealment, the allocation was hidden until the envelope was opened. Study group allocation was concealed from the study investigators, subjects, and all healthcare providers until written informed consent was obtained. At this point, the study investigator was given a sequentially numbered and sealed envelope to open and reveal the group assignments. A double-blind

study was not feasible due to the distinct IMT device appearance. Blinding was only applied to the individuals responsible for statistical analysis and outcome preparation.

2.3 Inspiratory muscle training

Training was performed by registered respiratory therapists in ICUs. Airway secretions were removed by tracheal suction, and the artificial airway cuff was inflated to prevent potential air leakage before IMT was initiated. Subjects were positioned supine in the bed with the head-of-bed elevated to 60-degrees. They were then removed from the ventilator, and an IMT device was connected to the artificial airway. The threshold IMT device (Galmed Corp., Taiwan) used a starting resistance set to 30% maximum inspiratory pressure (MIP). If the subject tolerated IMT in the previous session, the resistance was increased by 5–10%, up to a maximum of 50% of the MIP. The subjects were instructed to perform fast and forceful inspirations against added inspiratory resistance while being coached by a study investigator to ensure full inspiration and expiration during each breath cycle. Each session consisted of three breaths per set, followed by a one-minute break during which the ventilator was reconnected. Ten sets (totaling 30 breaths) were completed per IMT session, conducted twice daily over five consecutive days, followed by a two-day rest period. This regimen was continued for three consecutive weeks or until the subject no longer required ventilator support. The inhalation port of the IMT device was occluded in subjects who were unable to follow IMT instructions. This action stimulates a strong neural output from the brainstem, enhancing diaphragm myofiber contraction, leading to deeper breathing. Vital signs and subject tolerance of IMT were monitored closely during therapy sessions by performance of regular assessments and solicitation of subject feedback. IMT was discontinued if the subject experienced a respiratory rate > 40 breaths/min, heart rate increase >20 beats/min, systolic blood pressure increase >20 mmHg, SpO2 < 90%, multifocal premature ventricular contraction, cold sweating, agitation, subjective discomfort, or change in consciousness. IMT was terminated if the subject experienced life-threatening arrhythmia twice during the IMT session.

2.4 Outcome measures

Baseline demographic and clinical characteristics, including age, sex, acute physiology and chronic health evaluation score, Glasgow Comma score, primary diagnosis, intensive care unit, artificial airway type, ventilator settings, mechanical ventilation duration, and ICU length of stay were collected from each participant's electronic medical records. The primary outcome measure was the number of days until liberation from mechanical ventilation among subjects who received IMT (IMT group) compared to subjects who did not receive IMT (no-IMT group).

The secondary outcomes of interest were respiratory muscle strength and biomarker level. Measures of respiratory muscle strength included the maximum inspiratory pressure (MIP), maximum expiratory pressure (MEP), peak inspiratory flow, and peak expiratory flow. Respiratory measurements were performed by a designated respiratory therapist. MIP was measured by having each subject exert maximum inspiratory force against a pressure gauge (Galmed Corp, Taiwan) for three consecutive breaths. The highest value obtained from three consecutive maximum inspiratory efforts was recorded. Similarly, peak inspiratory flow was measured using a respiratory mechanics monitor (VENTCheck, Novametrix Medical Systems Inc., Pennsylvania, U.S.) during three forceful inspirations, with the highest of the three peak inspiratory flow measurements being recorded. During forceful expirations, the MEP and peak expiratory flow were measured using the same method. The tidal volume was measured with a respirometer (Haloscale Wright Respirometer, Ferraris Development & Engineering Co., London) during 1 min of quiet breathing, and the respiratory rate was recorded simultaneously. Additionally, the rapid shallow breathing index (RSBI), which is the threshold for determining the likelihood of successful liberation from invasive mechanical ventilation, was recorded. The RSBI was calculated by dividing the respiratory rate by the tidal volume (L). MIP was measured before IMT intervention for threshold resistance adjustment and daily for the no-IMT group during study enrollment or until the subject was successfully liberated from mechanical ventilation within 48 consecutive hours. Additionally, blood samples were obtained to measure and examine biomarkers, including hemoglobin, albumin, and creatinine levels, to determine their relationship with IMT intervention and outcomes.

2.5 Statistical analysis

A priori power analysis was performed to determine the study sample size before commencement of the study. A review of the literature showed that tracheotomized subjects who received IMT during mechanical ventilation in the ICU experienced seven fewer days on the ventilator than patients who did not receive IMT (18). With alpha set at 0.05, and beta set at 0.2, we estimated that 30 subjects per group would be necessary to power our study to 80%.

Nonparametric statistical analyses were performed because of the small sample size. Continuous variables with non-normal distribution are reported as median (interquartile range), and the Mann–Whitney U test was used for group comparisons. For categorical variables, data were reported as frequency counts and percentages. The frequency count of participants in each category with normal approximation was compared using the chi-square of independence test or Fisher's exact test if the expected frequency count of a category was less than 5, as appropriate. The relationship between muscle strength and biomarkers was investigated using Spearman's rho test. All *p*-values were two-tailed, and values less than 0.05 were considered statistically significant. Data were analyzed using SPSS 26 for Windows (IBM, Armonk, New, USA).

3 Results

From July 2019 to December 2020, 307 patients who required invasive mechanical ventilation in our medical and surgical ICUs were screened for eligibility. The trial was completed as planned upon reaching a predetermined sample size. Of the 307 screened subjects were excluded from the study enrollment. The most common reason for exclusion was unstable hemodynamics (n = 87 of 247). Sixty

subjects who met the study inclusion criteria were equally randomized and allocated to either the IMT group ($n = 30$) or the no-IMT group ($n = 30$). Thirteen of the 30 subjects (43%) in the IMT group and 14 of the 30 subjects (47%) in the no-IMT group experienced early study termination ($p = 0.79$). The most common reason for early study termination in both groups was unstable hemodynamics ($p = 0.57$). Seventeen subjects in the IMT group and 16 subjects in the no-IMT group were included in the final data analysis (Figure 1).

The baseline demographic and clinical characteristics of the patients are summarized in Table 1. There were no significant differences between the two groups in terms of age, sex, diagnosis, or baseline clinical variables. The median age was 74 years, and

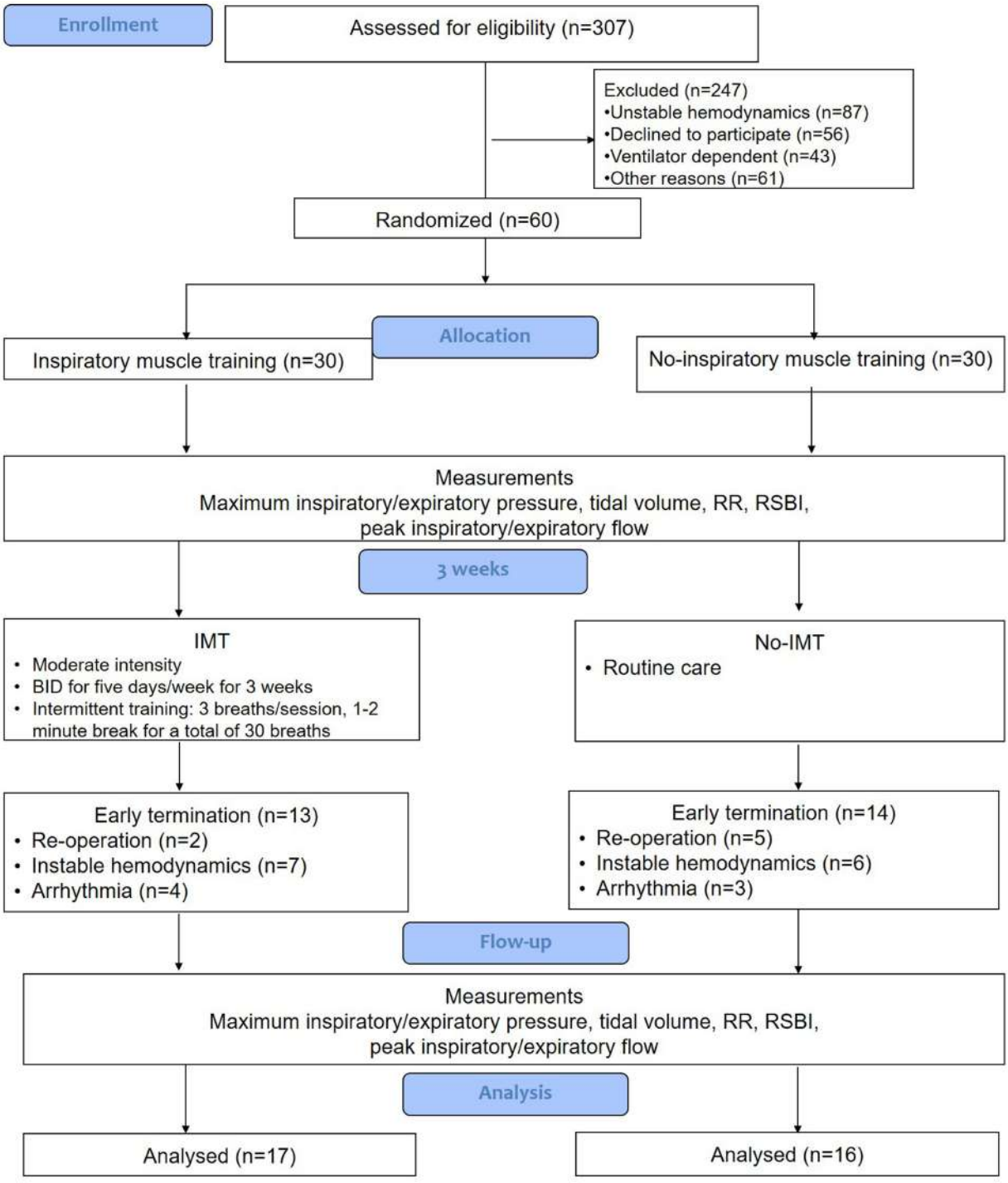


FIGURE 1
Design and flow of subjects through the trial.

10.3389/fmed.2024.1503678

males represented 52% ($n = 17$ of 33) of the study population ($p = 0.73$). The majority (67%) of subjects had a primary diagnosis of a respiratory system disorder ($n = 14$ of 33) or neurological or neurosurgical disorders ($n = 8$ of 33). The majority (84.5%) of subjects received an artificial airway with an endotracheal tube. While 61 % of the subjects were ventilated with Pressure Control mode at the time of study enrollment, when compared to the synchronized intermittent mandatory ventilation + pressure support and pressure support ventilation modes, the difference was not significant ($p = 0.32$).

Table 2 compares the primary outcomes between the two groups, which were similar at baseline when the subjects were enrolled in the study. Subjects in the IMT group experienced 4.5 fewer days of mechanical ventilation (13 [8–16] days) than those in the no-IMT group (17.5 [9.7–24] days; $p = 0.038$); however, the ICU duration was similar between groups (IMT group 20 [13–30] vs. no-IMT group (20 [17–25]), $p = 0.92$) Subjects who received IMT experienced 4.5 fewer days on mechanical ventilation than those who did not receive IMT ($p = 0.04$). The ICU duration was similar between the two groups. The number of subjects passing

TABLE 1 Subject demographic and clinical characteristics.

Parameters	IMT ($n = 17$)	No-IMT ($n = 16$)	p- value
Age (yr)	74 (69–78)	74 (71–80)	0.30[a]
APACHE II Score	23.5 (19–27)	21 (16–26)	0.24[b]
Glosgow Coma Score	8 (6–9)	9 (7–11)	0.36[b]
Sex: Male, *n* (%)	8 (47.1)	9 (56.3)	0.59[b]
Intensive care unit			
Medical, *n* (%)	13 (76.5)	10 (62.5)	0.38[b]
Surgical, *n* (%)	4 (23.5)	6 (37.5)	
Diagnosis			0.41[b]
Respiratory system disorders, *n* (%)	8 (47.1)	6 (37.6)	
Neurological and Neurosurgical Disorders, *n* (%)	2 (11.8)	6 (37.6)	
Trauma and critical care, *n* (%)	5 (29.5)	2 (12.6)	
Cardiac disorder, *n* (%)	2 (11.8)	2 (12.6)	
Artificial airway type			0.58[b]
Endotracheal tube, *n* (%)	15 (88.2)	13 (81.2)	
Tracheostomy tube, *n* (%)	2 (11.8)	3 (18.8)	
Ventilator setting			0.32[b]
PCV, *n* (%)	10 (58.8)	10 (62.5)	
SIMV+PSV, *n* (%)	3 (17.6)	5 (31.5)	
PSV, *n* (%)	4 (23.5)	1 (6.3)	
PEEP (cmH_2O)	5	5	> 0.99[a]
FiO_2 (%)	33 (30–37)	35 (35–40)	0.45[a]

Data are expressed as medians (interquartile ranges). $p < 0.05$ is considered significant. [a]statistical analysis by Mann–Whitney U test; [b]statistical analysis by chi-square test.
IMT, inspiratory muscle training; APACHE, Acute Physiology and Chronic Health Evaluation; PCV, pressure control ventilation; SIMV+ PSV, synchronized intermittent mandatory ventilation + pressure support ventilation; PSV, pressure support ventilation; PEEP, positive end-expiratory pressure; FiO2, fraction of inspired oxygen.

TABLE 2 Comparisons of outcomes between two groups.

Parameters	IMT ($n = 17$)	No-IMT ($n = 16$)	p- value
Mechanical ventilation duration (day)	13 (8–16)	17.5 (9.7–24)	0.038[a]
ICU length of stay (day)	20 (17–25)	20 (13–30)	0.92[a]
RSBI <105 (*n*, %)			
Baseline	2 (11.7%)	4 (25%)	0.58[b]
At the time of MV liberation	11 (64.7%)	5 (31.2%)	0.01[b]

Data are expressed as medians (interquartile ranges). $p < 0.05$ is considered significant. [a]statistical analysis by Mann–Whitney U test; [b]statistical analysis by chi-square test.
RSBI: rapid shallow breathing index; MV: mechanical ventilation.

TABLE 3 Comparisons of respiratory strength and biomarkers between groups.

	Baseline			At time of MV liberation		
	IMT (n = 17)	No-IMT (n = 16)	p-value	IMT (n = 17)	No-IMT (n = 16)	p-value
RSBI (breath/min/L)	153 (119–181)	125 (102–191)	0.43	88 (65–114)	132 (98–177)	0.042
MIP (cmH_2O)	26 (18–36)	20 (12.7–24)	0.15	30 (27–36)	22 (13–26)	<0.01
MEP (cmH_2O)	18 (14.3–29)	20 (16–26)	0.73	28 (21–37)	25 (14–28)	0.03
PIFR (L/min)	24 (18–30)	27 (18–31)	0.55	30 (27–40)	27 (19–31)	0.07
PEFR (L/min)	27 (25–33)	30 (26–31)	0.46	34 (31–37)	29 (21–34)	0.01
Hemoglobin (mg/dL)	10.1 (8.8–11.5)	9.8 (8.8–10.5)	0.45	10.4 (9.3–11)	10.2 (9.7–106)	0.95
Albumin (mg/dL)	3.1 (2.8–3.2)	3.0 (2.8–3.2)	0.83	3.1 (2.6–3.5)	2.9 (2.9–3.2)	0.89
Creatinine (mg/dL)	1.1 (0.8–2.4)	1.2 (0.9–2.5)	0.53	1.2 (0.6–2.4)	0.8 (0.58–1.9)	0.38

Data are expressed as median (interquartile range); [a] statistical analysis was performed by Mann–Whitney U test.
IMT, inspiratory muscle training; MIP, Maximum inspiratory pressure; MEP, Maximum expiratory pressure; PIFR, peak inspiratory flow rate; PEFR, peak expiratory flow rate; RSBI, rapid shallow breathing index.

TABLE 4 Respiratory and biomarker changes from baseline to three-week point.

	IMT (n = 17)	No-IMT (n = 16)	MD (95% CI)	p-value
RSBI %	−35.72 ((−66.94)–0.71)	−9.37 ((−23.2)–31.0)	14.4 (8.8–67.9)	0.01
MIP %	29.41 (7.14–50.0)	9.17 (2.78–21.25)	−25.6 ((−54.2)–3.0)	0.08
MEP %	16.67 (9.09–58.33)	2.08 ((−18.09)–25.55)	−44.6 ((−83.5)–(−5.7))	0.03
PIFR %	36.84 (5.88–78.79)	2.5 ((−21.92)–14.06)	−39.8 ((−68.3)–(−11.3))	0.01
PEFR %	21.21 (9.09–40.0)	−4.95 ((−41.8)–5.11)	−37.1 ((−69.6)–(−4.5))	0.03
Hemoglobin (mg/dL)	0.0 ((−0.9)-0.9)	0.05 ((−0.8)-1.45)	0.54 ((−0.79)–1.88)	0.42
Albumin (mg/dL)	0.0 (0–0.3)	0.9(0.1–(−0.4))	0.15 ((−0.51)–0.09)	0.15
Creatinine (mg/dL)	0.31 (0.93)	−0.72 (0.92)	−1.03 (−1.68–(−0.37))	<0.01

%: change % of the value from the baseline. Data are expressed as medians (interquartile range). $p < 0.05$ were considered significant. Statistical analysis performed by Mann–Whitney U test.
IMT, inspiratory muscle training; MIP, Maximum inspiratory pressure; MEP, Maximum expiratory pressure; PIFR, peak inspiratory flow rate; PEFR, peak expiratory flow rate; RSBI, rapid shallow breathing index (breaths/min/L); MD, mean difference.

the critical point (RSBI <105 breaths/min/L) was significantly greater in the IMT group (n = 11) than in the no-IMT group (n = 5) at the time of mechanical ventilation liberation (p = 0.01).

Table 3 compares the muscle strength and biomarkers between groups. The IMT group experienced a significant decrease in RSBI and evidence of significantly improved respiratory muscle strength at the time of MV liberation when compared with baseline measurements. The RSBI results showed a significant reduction in the IMT group (88 breaths/min/L) compared with the no-IMT group (132 breaths/min/L, p = 0.04). Additionally, more subjects in the IMT group (n = 11) passed the RSBI critical value of <105 breaths/min/L when compared to the no-IMT group (n = 5) (Table 2). The secondary outcome of this study was respiratory muscle strength. Subjects who received IMT showed significant increases in MIP ($p < 0.01$), MEP (p = 0.03), and peak expiratory flow rate ($p < 0.01$).

Table 4 demonstrates the changes in measurements between baseline and at the time of MV liberation for the two groups. All changes in respiratory parameters significantly improved, including the RSBI, MIP, MEP, peak inspiratory flow rate, and peak expiratory flow rate. Notably, a significant change in creatinine level was detected between the groups ($p < 0.01$). The variation in creatinine level was demonstrated by a positive moderate correlation with IMT (r_s = 0.54, p = 0.01).

4 Discussion

Loss of respiratory muscle strength occurs in most critically ill patients and is directly associated with prolonged mechanical

ventilation, ICU stay, and hospitalization duration. Our study identified clinical benefits experienced by subacute critically ill adult subjects who received IMT during mechanical ventilation. Our findings indicate that initiating IMT early, once the patient is clinically stable, significantly shortens the duration of mechanical ventilation. This early intervention also enhances respiratory muscle strength and promotes spontaneous breathing, as demonstrated by reduced RSBI and improved respiratory mechanics during the subacute phase. Our data also revealed a moderate correlation between IMT and creatinine levels, potentially indicating increased muscle mass.

4.1 Enhanced breathing patterns and facilitation of ventilator weaning in subacute stage

The optimal goal of IMT in critically ill patients is to improve respiratory muscle strength, thereby enhancing respiratory efficiency and facilitating liberation from mechanical ventilation support. Previous studies have used MIP and MEP as the primary outcomes to evaluate the effectiveness of IMT in patients receiving mechanical ventilation (19, 20). Improvement in MIP or MEP measurements reflects enhanced strength of the respiratory muscles during forceful inspiration or expiration, respectively. MIP and MEP serve as critical indicators of effective coughing ability, a vital function for airway secretion clearance, during ventilator weaning (21, 22). Successful ventilator weaning necessitates adequate ventilation capacity, encompassing both strength and endurance.

The primary goal of patient care at the subacute stage of critical illness is liberation from mechanical ventilation. Generally, the RSBI is a clinical predictor used to inform about patient readiness and the likelihood of remaining liberated from mechanical ventilation. A higher RSBI suggests that the patient is breathing rapidly or has a small tidal volume. Although the specificity of the RSBI has been debated, a cutoff value of greater than 105 has been established to predict a higher likelihood of ventilator removal failure (11, 23). Previous studies have shown that a high RSBI indicates an inadequate ventilation pattern, leading to respiratory muscle weakness or an increased ventilation load (23). We coupled routine care with IMT at the subacute critically ill stage as soon as the patients exhibited hemodynamic stability and a supplemental oxygen concentration requirement of less than 50%. Our results demonstrated that IMT improved respiratory muscle strength, endurance, and breathing patterns. Consequently, the duration of mechanical ventilation was significantly reduced by 6 days when IMT was added to routine care.

While the cost of medical care is on the rise, a systematic study estimated that a single ventilated ICU day costs €1,654 in France, with mechanical ventilation accounting for approximately 50% of the daily cost (24). Our study demonstrated a 4.5-day reduction in duration of mechanical ventilation, potentially resulting in cost savings of at least €3,600. Moreover, early extubation helps prevent additional costs associated with mechanical ventilation, such as ventilator-associated pneumonia, ventilator-induced lung injury, and complications resulting from upper airway trauma and artificial airway securing device pressure related skin ulcer injury.

4.2 Intermittent moderate-intensity training protocol and duration of training

The training duration and methods employed in previous studies have exhibited discrepancies. Inspiratory muscle training is used in some intensive care units; however, its effectiveness remains uncertain (6). Given that patients were just past the acute phase of critical illness, we designed the IMT with low-to-moderate intensity threshold resistance to prevent intolerance and overuse of the inspiratory muscles. A systematic review of low-to-medium vs. high intensity revealed that the high-intensity threshold IMT groups in critically ill patients concluded that both intensities achieved statistically significant MIP improvement (14). Additionally, low-to-moderate-intensity IMT reduced the duration of mechanical ventilation. In contrast to our study, a systematic review found that RSBI results favored high-intensity IMT over low-intensity IMT.

Previous studies have also shown a wide variation in the duration of IMT interventions, ranging from 3 days to 6 weeks, for patients with diverse medical conditions (11). Bissett et al. conducted a study incorporating 2 weeks of moderate-intensity IMT in patients receiving mechanical ventilation, which demonstrated significant improvements in inspiratory strength and quality of life (19). Their subsequent analysis found that patients who benefited the most from IMT were those with moderate inspiratory muscle weakness (MIP >28 cmH2O) within 48 h of ventilatory weaning (18). Similarly, in this three-week moderate-intensity IMT study, our subjects in the IMT group, with a median MIP of 26 cmH2O, showed significant improvement in respiratory muscle strength and respiratory pattern parameters. Our study demonstrated a significantly shorter duration of mechanical ventilation which likely resulted from the addition of IMT intervention to regular standard of care.

4.3 Correlation between creatinine level to IMT

Our results demonstrated significant differences in post-IMT creatinine level changes between subjects who received IMT when compared to subjects who did not receive IMT. We identified a moderate correlation between creatinine level and improvement in respiratory muscle strength. To our knowledge, this study is the first to observe a relationship between creatinine levels and IMT outcomes in adult mechanically ventilated subjects. Muscle weakness is a major concern for critically ill patients who require mechanical ventilation because they are often sedated and underfed during the acute stage of care. Serum creatinine level reflects both creatinine production and elimination, making it a standard clinical biomarker that critical care clinicians use to monitor renal function trends. Creatinine production primarily arises from phosphocreatine metabolism in the skeletal muscle and is correlated with muscle mass (25). Serum creatinine could indicate muscle mass and it is affected by altered nutritional status and skeletal muscle wasting. Low serum creatinine levels are indicative of low muscle mass, malnutrition, fluid overload, and advanced liver

diseases (24). A reduction in muscle mass can be determined by a decrease in serum creatinine level. Our study revealed a significant reduction in creatinine level among subjects who did not receive IMT (−0.72 mg/dL) whereas creatine level increased slightly among subjects that received IMT (0.31 mg/dL). The increased creatinine level in the IMT group may indicate maintained inspiratory and diaphragm muscle mass, as opposed to the possibility of muscle wasting in the no-IMT group. Previous studies have found that diaphragmatic atrophy occurs more frequently in patients with septic shock than in those on mechanical ventilation (26, 27). The IMT intervention has been shown to increase diaphragm thickness and improve peripheral muscle strength, peripheral muscle thickness, diaphragm muscle thickness, and diaphragm muscle mobility (28). The increased creatinine level observed in our study may be attributed to diaphragmatic training, which is the largest inspiratory muscle. In contrast, patient hydration status may greatly effect creatinine levels. Future clinical studies are necessary for deeper exploration and external validation of our findings.

4.4 Limitations

This study had limitations that must be considered. This single-center RCT was conducted in medical and surgical ICUs, which limits the generalizability of our findings. Recruitment and retention of subjects in the study also presented challenges, reflected by a dropout rate of 43%, when they were in the subacute stage of the illness. Surrogates are often reluctant to consent for subject participation in the study owing to safety concerns. Additionally, patient medical conditions can change rapidly in the subacute stage, which partly explains the high dropout rate observed in both groups and the small sample size included in our final data analysis. To address this issue, we suggest strategies to improve participant retention in future clinical studies. Regularly communicate with study subjects and surrogates to address any study related concerns. Due to the difficult in recruiting subacute critically ill patients, our sample size was small. Larger multicenter clinical trials are warranted in the future. A double-blinded study design was not feasible due to the nature of the IMT device, and as a result, performance bias may have been introduced into our study during IMT training sessions as participants were encouraged to push closer to their limits. However, a blinded approach was implemented during statistical analysis to minimize bias in the interpretation of the results.

5 Conclusion

Reducing respiratory muscle strength in critically ill patients often leads to prolonged mechanical ventilation and an extended hospital stay. Our randomized clinical trial demonstrated that IMT facilitates earlier liberation from mechanical ventilation and improves respiratory muscle strength. These findings underscore the potential benefit that IMT may offer as an adjunct to regular standard of care for subacute critically ill adult patients requiring mechanical ventilation. Further research in large clinical trials is needed to explore the relationship between serum creatine levels and respiratory muscle strength. Establishing precise serum creatine and respiratory muscle strength and retention cut-off values that demonstrate clinical benefits could enhance clinical practice and improve patient outcomes.

Data availability statement

The original contributions presented in this study are included in the article, and further inquiries can be directed to the corresponding authors.

Ethics statement

The studies involving humans were approved by the Institutional Review Board of Zuoying Armed Forces General Hospital. The studies were conducted in accordance with the local legislation and institutional requirements. The participants provided their written informed consent to participate in this study.

Author contributions

S-JW: Conceptualization, Funding acquisition, Investigation, Project administration, Writing – original draft. T-PF: Formal analysis, Funding acquisition, Writing – original draft. DR: Writing – original draft, Writing – review & editing. N-WL: Data curation, Visualization, Writing – original draft. J-OC: Project administration, Writing – original draft. J-FL: Conceptualization, Software, Supervision, Writing – original draft, Writing – review & editing. H-LL: Data curation, Formal analysis, Visualization, Writing – original draft, Writing – review & editing.

Funding

The author(s) declare that financial support was received for the research, authorship, and/or publication of this article. This research was funded by the Zuoying Armed Forces General Hospital, grant number ZBH 108–33, and the APC was funded by Chiayi Chang Gung Memorial Hospital.

Conflict of interest

The authors declare that the research was conducted without any commercial or financial relationships that could be construed as potential conflicts of interest.

Generative AI statement

The author(s) declare that no Gen AI was used in the creation of this manuscript.

Publisher's note

All claims expressed in this article are solely those of the authors and do not necessarily represent those of their affiliated organizations, or those of the publisher, the editors and the reviewers. Any product that may be evaluated in this article, or claim that may be made by its manufacturer, is not guaranteed or endorsed by the publisher.

References

1. Adler D, Dupuis-Lozeron E, Richard JC, Janssens JP, Brochard L. Does inspiratory muscle dysfunction predict readmission after intensive care unit discharge? *Am J Respir Crit Care Med*. (2014) 190:347–50. doi: 10.1164/rccm.201404-0655LE

2. Kim WY, Suh HJ, Hong SB, Koh Y, Lim CM. Diaphragm dysfunction assessed by ultrasonography: influence on weaning from mechanical ventilation. *Crit Care Med*. (2011) 39:2627–30. doi: 10.1097/CCM.0b013e3182266408

3. Dres M, Dubé BP, Mayaux J, Delemazure J, Reuter D, Brochard L, et al. Coexistence and impact of limb muscle and diaphragm weakness at time of liberation from mechanical ventilation in medical intensive care unit patients. *Am J Respir Crit Care Med*. (2017) 195:57–66. doi: 10.1164/rccm.201602-0367OC

4. Busl KM, Ouyang B, Boland TA, Pollandt S, Temes RE. Prolonged mechanical ventilation is associated with pulmonary complications, increased length of stay, and unfavorable discharge destination among patients with subdural hematoma. *J Neurosurg Anesthesiol*. (2015) 27:31–6. doi: 10.1097/ANA.0000000000000085

5. Bissett B, Leditschke IA, Green M, Marzano V, Collins S, Van Haren F. Inspiratory muscle training for intensive care patients: a multidisciplinary practical guide for clinicians. *Aust Crit Care*. (2019) 32:249–55. doi: 10.1016/j.aucc.2018.06.001

6. Bonnevie T, Villiot-Danger JC, Gravier FE, Dupuis J, Prieur G, Médrinal C. Inspiratory muscle training is used in some intensive care units, but many training methods have uncertain efficacy: a survey of French physiotherapists. *J Physiother*. (2015) 61:204–9. doi: 10.1016/j.jphys.2015.08.003

7. Ramli MI, Hamzaid NA, Engkasan JP, Usman J. Respiratory muscle training: a bibliometric analysis of 60 years' multidisciplinary journey. *Biomed Eng Online*. (2023) 22:50. doi: 10.1186/s12938-023-01103-0

8. Ballew SH, Zhou L, Surapaneni A, Grams ME, Windham BG, Selvin E, et al. A novel creatinine muscle index based on creatinine filtration: associations with frailty and mortality. *J Am Soc Nephrol*. (2023) 34:495–504. doi: 10.1681/ASN.0000000000000037

9. Kim CY, Lee JS, Kim HD, Lee DJ. Short-term effects of respiratory muscle training combined with the abdominal drawing-in maneuver on the decreased pulmonary function of individuals with chronic spinal cord injury: a pilot randomized controlled trial. *J Spinal Cord Med*. (2017) 40:17–25. doi: 10.1080/10790268.2016.1198576

10. Bissett B, Gosselink R, van Haren FMP. Respiratory muscle rehabilitation in patients with prolonged mechanical ventilation: a targeted approach In: J-L Vincent, editor. Annual update in intensive care and emergency medicine 2020. Cham: Springer International Publishing (2020). 595–609.

11. Vorona S, Sabatini U, Al-Maqbali S, Bertoni M, Dres M, Bissett B, et al. Inspiratory muscle rehabilitation in critically ill adults. A systematic review and meta-analysis. *Ann Am Thorac Soc*. (2018) 15:735–44. doi: 10.1513/AnnalsATS.201712-961OC

12. Elkins M, Dentice R. Inspiratory muscle training facilitates weaning from mechanical ventilation among patients in the intensive care unit: a systematic review. *J Physiother*. (2015) 61:125–34. doi: 10.1016/j.jphys.2015.05.016

13. Magalhães PAF, Camillo CA, Langer D, Andrade LB, Duarte M, Gosselink R. Weaning failure and respiratory muscle function: what has been done and what can be improved? *Respir Med*. (2018) 134:54–61. doi: 10.1016/j.rmed.2017.11.023

14. Patsaki I, Kouvarakos A, Vasileiadis I, Koumantakis GA, Ischaki E, Grammatopoulou E, et al. Low-medium and high-intensity inspiratory muscle training in critically ill patients: a systematic review and meta-analysis. *Medicina (Kaunas)*. (2024) 60:869. doi: 10.3390/medicina60060869

15. Martin AD, Smith BK, Davenport PD, Harman E, Gonzalez-Rothi RJ, Baz M, et al. Inspiratory muscle strength training improves weaning outcome in failure to wean patients: a randomized trial. *Crit Care*. (2011) 15:R84. doi: 10.1186/cc10081

16. Fragala MS, Bi C, Chaump M, Kaufman HW, Kroll MH. Associations of aerobic and strength exercise with clinical laboratory test values. *PLoS One*. (2017) 12:e0180840. doi: 10.1371/journal.pone.0180840

17. Bartholomae E, Knurick J, Johnston CS. Serum creatinine as an indicator of lean body mass in vegetarians and omnivores. *Front Nutr*. (2022) 9:996541. doi: 10.3389/fnut.2022.996541

18. Tonella RM, Ratti L, Delazari LEB, Junior CF, Da Silva PL, Herran A, et al. Inspiratory muscle training in the intensive care unit: a new perspective. *J Clin Med Res*. (2017) 9:929–34. doi: 10.14740/jocmr3169w

19. Bissett BMP, Wang JM, Neeman TP, Leditschke IM, Boots RP, Paratz JP. Which ICU patients benefit most from inspiratory muscle training? Retrospective analysis of a randomized trial. *Physiother Theory Pract*. (2020) 36:1316–21. doi: 10.1080/09593985.2019.1571144

20. Bissett BM, Leditschke IA, Neeman T, Boots R, Paratz J. Inspiratory muscle training to enhance recovery from mechanical ventilation: a randomised trial. *Thorax*. (2016) 71:812–9. doi: 10.1136/thoraxjnl-2016-208279

21. Postma K, Vlemmix LY, Haisma JA, De Groot S, Sluis TA, Stam HJ, et al. Longitudinal association between respiratory muscle strength and cough capacity in persons with spinal cord injury: an explorative analysis of data from a randomized controlled trial. *J Rehabil Med*. (2015) 47:722. doi: 10.2340/16501977-1986

22. MacIntyre NR. Respiratory mechanics in the patient who is weaning from the ventilator. *Respir Care*. (2005) 50:275.

23. Roberts KJ, Goodfellow LT, Battey-Muse CM, Hoerr CA, Carreon ML, Sorg ME, et al. AARC clinical practice guideline: spontaneous breathing trials for liberation from adult mechanical ventilation. *Respir Care*. (2024) 69:891–901. doi: 10.4187/respcare.11735

24. Kaier K, Heister T, Motschall E, Hehn P, Bluhmki T, Wolkewitz M. Impact of mechanical ventilation on the daily costs of ICU care: a systematic review and meta-regression. *Epidemiol Infect*. (2019) 147:e314. doi: 10.1017/S0950268819001900

25. Barreto EF, Poyant JO, Coville HH, Dierkhising RA, Kennedy CC, Gajic O, et al. Validation of the sarcopenia index to assess muscle mass in the critically ill: a novel application of kidney function markers. *Clin Nnut*. (2019) 38:1362–7. doi: 10.1016/j.clnu.2018.05.031

26. Vivier E, Roussey A, Doroszewski F, Rosselli S, Pommier C, Carteaux G, et al. Atrophy of diaphragm and pectoral muscles in critically ill patients. *Anesthesiology*. (2019) 131:569–79. doi: 10.1097/ALN.0000000000002737

27. Dot I, Pérez-Terán P, Francés A, Díaz Y, Vilà-Vilardell C, Salazar-Degracia A, et al. Association between histological diaphragm atrophy and ultrasound diaphragm expiratory thickness in ventilated patients. *J Intensive Care*. (2022) 10:40. doi: 10.1186/s40560-022-00632-5

28. Sari F, Oskay D, Tufan A. The effect of respiratory muscle training on respiratory muscle strength, diaphragm thickness/mobility, and exercise capacity in patients with systemic lupus erythematosus and associated shrinking lung syndrome. *Lupus*. (2024) 33:289–92. doi: 10.1177/09612033241226755

29. De Rosa S, Greco M, Rauseo M, Annetta MG. The good, the bad, and the serum creatinine: exploring the effect of muscle mass and nutrition. *Blood Purif*. (2023) 52:775–85. doi: 10.1159/000533173

Stem Cell Research & Therapy

RESEARCH

Open Access

MiR221/222 in the conditioned medium of adipose-derived stem cells attenuates particulate matter and high-fat diet-induced cardiac apoptosis

Ya-Chun Chen[1], Chi-Ming Pu[2,3], Shu-Rung Lin[4,5], Shu-Wha Lin[6], I-Shing Yu[7], Ho-Jun Shih[1], Chiang-Wen Lee[8], Ming-Hsueh Lee[9,10], Yen-Ting Kuo[11*] and Yuh-Lien Chen[1*]

Abstract

Background Air pollution and obesity are crucial risk factors for cardiovascular disease (CVD), with epidemiological evidence indicating that air pollution exacerbates obesity-induced cardiac damage. Treatment with adipose-derived stem cells (ADSCs) attenuates cardiac damage by releasing paracrine factors. However, the effects of ADSCs on air pollution- and obesity-induced cardiomyocyte apoptosis and the related mechanisms are still unclear.

Methods Palmitic acid (PA) and a high-fat diet (HFD) were used to cause obesity, and particulate matter (PM) was used to simulate air pollution in the study. We studied the impact of conditioned medium from adipose-derived stem cells (ADSC-CM) on the apoptosis of PA + PM-treated H9c2 cells and HFD + PM-treated mouse cardiomyocytes and the underlying mechanisms involved.

Results The levels of apoptosis-related proteins (PUMA and cleaved caspase-3) were significantly increased in PA + PM-treated H9c2 cells and HFD + PM-treated mouse cardiomyocytes, whereas the antiapoptotic protein Bcl-2 expression was reduced. However, ADSC-CM treatment effectively reduced the PUMA and cleaved caspase-3 expression but increased the Bcl-2 expression. ADSC-CM significantly reduced PA + PM- and HFD + PM-induced cardiomyocyte apoptosis, as detected by the TUNEL assay. RT-qPCR revealed that PA + PM and HFD + PM significantly reduced *miR221/222* levels, whereas ADSC-CM treatment increased *miR221/222* levels. Furthermore, knockout (KO) and transgenic (TG) mice were used to demonstrate that *miR221/222* in ADSC-CM ameliorated cardiac apoptosis that was induced by HFD + PM treatment. Furthermore, PA + PM treatment increased the reactive oxygen species (ROS) production, which triggered mitochondrial fission and contributed to apoptosis. However, ADSC-CM effectively reduced ROS levels and regulated mitochondrial fission, alleviating cellular apoptosis.

Conclusions Our findings demonstrated that ADSC-CM attenuated PA + PM-induced cardiomyocyte apoptosis by modulating *miR221/222* levels and suppressing ROS production.

Keywords Particulate matter (PM), Palmitic acid (PA), High-fat diet (HFD), Conditioned medium from cultured adipose-derived stem cell (ADSC-CM), *miR221/222*, Reactive oxygen species (ROS), Mitochondrial fission

*Correspondence:
Yen-Ting Kuo
50505peter@gmail.com
Yuh-Lien Chen
ylchenv@ntu.edu.tw
Full list of author information is available at the end of the article

© The Author(s) 2025. **Open Access** This article is licensed under a Creative Commons Attribution 4.0 International License, which permits use, sharing, adaptation, distribution and reproduction in any medium or format, as long as you give appropriate credit to the original author(s) and the source, provide a link to the Creative Commons licence, and indicate if changes were made. The images or other third party material in this article are included in the article's Creative Commons licence, unless indicated otherwise in a credit line to the material. If material is not included in the article's Creative Commons licence and your intended use is not permitted by statutory regulation or exceeds the permitted use, you will need to obtain permission directly from the copyright holder. To view a copy of this licence, visit http://creativecommons.org/licenses/by/4.0/.

Background

Cardiovascular disease (CVD) is the primary cause of mortality globally [1, 2]. Lifestyle choices and environmental factors are crucial for the incidence of CVD. Among them, ordinary lifestyle choices, such as a high-fat diet (HFD), are essential for CVD because they can initiate or aggravate pathophysiological processes, leading to dyslipidemia and obesity in the population [3, 4]. Obesity is closely associated with persistent inflammation and oxidative stress, leading to potential health problems [5, 6]. In addition, air pollution is a serious environmental threat to health worldwide [7]. Many epidemiological and clinical reports have shown that short- and long-term exposure to air pollution, especially particulate matter (PM), significantly enhances the risk of CVDs, including cardiac arrhythmia, hypertension, atherosclerosis, ischemia, and heart failure [8–12]. PM can penetrate the alveolar-capillary barrier, enter the blood, damage the heart, and impair the cardiovascular system [13]. It is generally believed that air pollution causes CVD through oxidative stress. Given that obese patients have poorer oxidative defenses, they were particularly vulnerable to the impact effects of air pollution on cardiovascular health. Additionally, recent research suggests that obese individuals breathe more air per day than normal-weight individuals do and may therefore be more susceptible to the effects of air pollutants [14, 15]. The incidence of CVD resulting from long-term exposure to fine-suspended PM2.5 was closely related to an increased body mass index (BMI), according to a prospective cohort study, suggesting that obese people are more susceptible to the effects of PM2.5 [16, 17]. The mechanisms of the damage to cardiomyocytes caused by PM2.5 exposure and a high-fat diet are unclear, and there is no effective treatment.

Stem cells are undifferentiated cells that possess key characteristics such as differentiation and self-renewal [18]. Adipose-derived stem cells (ADSCs), which belong to mesenchymal stem cells, are derived from human adipose tissue and can differentiate into adipogenic, osteogenic, myogenic, and chondrogenic lineages, as shown by an in vitro study [19]. Because adipose tissue is readily available and preparing ADSCs is relatively easy, ADSCs may be a promising source for cell-based therapies [20]. ADSCs can also repair damaged organs and tissues by secreting large amounts of microRNAs, cytokines, and other bioactive substances. ADSC therapy has been proven to be effective and safe in a variety of animal models [21]. In addition, our previous reports revealed that ADSCs could protect the flap and heart and alleviate the damage caused by ischemia/reperfusion injury [22–24]. However, whether ADSCs can improve cardiomyocyte damage induced by an HFD and PM and the related mechanisms remain to be elucidated. MicroRNA (miRNA) is a small noncoding RNA molecule consisting of 19–25 nucleotides, with highly conserved and tissue-specific expression. They affect gene expression by complete or partial complementary binding to the mRNA of the target gene [25, 26]. MiRNAs affect a variety of biological responses, such as cell apoptosis, proliferation, differentiation, embryogenesis, and tumorigenesis [27]. MiRNAs regulate the activities of cardiomyocytes, endothelial cells, fibroblasts, and smooth muscle cells, which are the constituent cells within the cardiovascular system [28]. MiRNAs are crucial in regulating cardiomyocyte growth and contractility, maintaining the heart rhythm, modulating plaque formation, influencing lipid metabolism, and promoting angiogenesis [27, 29, 30]. Previous studies have reported that *miR221/222* are associated with the progression of cardiovascular pathologies, such as inflammation, apoptosis, angiogenesis, hypertrophy, remodeling, and cardiac fibrosis [31, 32]. Bioinformatics analysis revealed that PUMA is a candidate target of *miR221/222*, and a previous study also revealed that PUMA could regulate apoptosis [33, 34]. Our earlier report demonstrated that enrichment of *miR221/222* in ADSC-CM could alleviate I/R injury [23]. However, the significance of *miR221/222* in the heart during exposure to an HFD and PM remains unclear.

Reactive oxygen species (ROS) are generated as cellular metabolic byproducts and highly reactive oxygen-containing molecules. Several studies have demonstrated that ROS-mediated apoptosis is a critical contributor to the development of CVD [35–37]. Research has also indicated that prolonged exposure to elevated ROS levels may trigger cardiomyocyte dysfunction, leading to cardiac remodeling, apoptosis, necrosis, and fibrosis [38]. Mitochondria are essential organelles in eukaryotic cells and are responsible for ATP synthesis. The mitochondrial electron transport chain is the primary source of ROS during normal metabolic processes. However, excessive intracellular ROS levels can lead to mitochondrial oxidative damage and dysfunction, leading to heart failure, diabetes, neurodegenerative diseases, and cancer [39–41]. Mitochondria in living cells are highly plastic and dynamic organelles that are constantly remodeled through fission and fusion, which affects the number, function, distribution location, and morphology of mitochondria in response to stress. Maintaining the balance between mitochondrial fission and fusion is crucial for the integrity and function of the mitochondrial network. A previous study showed that defects in mitochondrial fusion or fission might affect embryonic development in mice and lead to embryonic lethality [42]. Furthermore, mitochondrial fission has been shown to occur during heart failure [43–46]. Therefore, considering the above

factors, the study was designed to explore the impact effects of obesity and air pollution on apoptotic events and to evaluate whether *miR221/222* in ADSC-CM are essential for regulating cardiomyocyte apoptosis by targeting PUMA. In this study, in vitro palmitic acid (PA) treatment and in vivo HFD feeding were used to induce obesity, and PM was used as the air pollution model both in vivo and in vitro. The study revealed that ADSC-CM exerted the cardioprotective function on the reduction in PA + PM-induced cardiomyocyte apoptosis through regulating *miR221/222* and inhibiting ROS production. These findings may provide strategies for preventing and treating HFD + PM-caused cardiac damage in clinical practice.

Materials and methods

Cell preparation

The H9c2 cell line, which was derived from embryonic rat cardiac myoblasts, was obtained from the American Type Culture Collection (VA, USA). H9c2 cells were incubated in Dulbecco's modified Eagle's medium (DMEM; Gibco, NY, USA) supplemented with 10% (v/v) fetal bovine serum (FBS; Biological Industries, CT, USA), 1% (v/v) L-glutamine (Biological Industries), and 1% penicillin–streptomycin-amphotericin (PSA; Biological Industries). The cells were cultured in a humidified incubator at 37°C and 5% CO_2.

Human adipose-derived stem cells (ADSCs) were bought from Lonza (Basel, Switzerland) and incubated in DMEM supplemented with 20% (v/v) FBS and 1% PSA. All experiments used cells between passages 3 and 8.

PM preparation

This study used standard reference material 2786 (SRM 2786; <4 μm) as the PM. SRM2786 was collected in 2005 from Prague, Czech Republic, and purchased from the Nation Institute of Standards and Technology (MD, USA). To prepare the SRM 2786 stock solution, the pellet was suspended in a cell culture medium at 20 mg/mL concentration and then sonicated three times in cold water for 15 min each. The solution was then preserved at −20 °C. Before the experiment, the PM suspension was vortexed thoroughly for 1 min to ensure uniform dispersion.

Preparation of ADSC-conditioned medium (ADSC-CM)

ADSCs were seeded in 10 cm culture dishes at 5×10^5 cells per dish. The culture was continued for 24 h, and the medium was collected and stored at −20 °C for further studies. ADSC-CM was prepared by mixing the collected culture medium with DMEM in equal proportions (50% of the total volume of the culture medium) immediately before use.

MTT method

Cell viability was detected using an MTT method. H9c2 cells were plated at a 5×10^3 cells/well density in 96-well plates and incubated overnight. They were then treated with PA (0, 50, 100, or 200 μM) or PM (0, 10, 20, or 40 μg/mL) for 24 h. Subsequently, 0.5 mg/mL MTT solution was added to each well and incubated for 4 h. Dissolve the purple formazan crystals in 150 μL DMSO and measure the absorbance at 570 nm by a microplate reader.

Western blot analysis

The levels of specific proteins expression were investigated by Western blot. Cells were treated with PA (50 μM), PM (20 μg/mL), or ADSC-CM, and radioimmunoprecipitation assay (RIPA) buffer was used to obtain cell lysates. Equal amounts of protein were separated by 10%, 12%, or 15% SDS-PAGE and transferred to polyvinylidene difluoride (PVDF) membranes. These membranes were treated with 5% blocking buffer at room temperature (RT) for 1 h and then treated overnight with primary antibodies including against β-actin (1:5000; A5441, Sigma, MO, USA), GAPDH (1:5000; 60004–1-Ig, Proteintech, IL, USA), PUMA (1:1000; ab9643, Abcam, Cambridge, MA, USA), Bcl-2 (1:1000; 3498S, Cell Signaling Technology, MA, USA), cleaved caspase-3 (cCASP3) (1:1000; #9661, Cell Signaling Technology), SOD1 (1:1000; GTX100554, GeneTex, CA, USA), SOD2 (1:1000; GTX630559, GeneTex), SOD3 (1:1000; GTX81678, GeneTex), p-DRP1 (1:1000; 4494S, Cell Signaling Technology), and FIS1 (1:1000; 10956–1-AP, Proteintech) at 4 °C. These PVDF membranes were washed with Tris-buffered saline with Tween 20 for six times and then treated with a secondary antibody (anti-mouse or anti-rabbit) at RT for 1 h. Bands in immunoblots were examined using the Western Lightning™ chemiluminescence reagent and the Biospectrum 600 imaging system (UVP, CA, USA).

TdT-mediated dUTP nick end-labeling (TUNEL) assay

According to the instructions, the TUNEL method evaluated apoptosis with a kit (Roche, CA, USA). H9c2 cells were seeded on coverslips (1×10^5) and incubated overnight, followed by treatment with PA (50 μM), PM (20 μg/mL), or ADSC-CM for 24 h. These cells were fixed with 4% paraformaldehyde for 30 min at RT and then incubated with 0.1% Triton X-100 for 5 min at RT. Thereafter, they were labeled with the TUNEL reagent at 37 °C for 1 h, and nuclei were counterstained with DAPI (1 μg/mL) solution for 5 min. After a series of washes, the slides were covered with coverslips. The experimental results

were observed and photographed by a fluorescence microscope using appropriate filters.

Annexin V-FITC/propidium iodide (PI) staining

Apoptosis was examined with an annexin V–FITC/PI detection kit (#640914; BioLegend, Amsterdam, The Netherlands) according to the instructions. H9c2 cells were plated at 2×10^5 cells/well in 6-well plates, cultured overnight, and continued to be treated with PA (50 μM), PM (20 μg/mL), or ADSC-CM for 24 h. Next, the cells were trypsinized, centrifuged, and washed with cold PBS. These cells were subsequently treated with 5 μL of annexin V–FITC and 5 μL of PI at RT for 15 min in the dark. After the above reaction, add 400 μL Annexin V Binding Buffer and immediately detect the results by flow cytometry.

Real-time quantitative PCR

Samples were collected after the defined treatments. Total RNA was extracted with the TRIzol reagent (Thermo, MA, USA), and the cDNA template was obtained with a TaqMan microRNA reverse transcription kit (Invitrogen, CA, USA) following the manufacturer's protocol. The *miR221/222* expression levels were analyzed by qPCR using TaqMan Universal PCR Master Mix (Applied Biosystems, CA, USA). The TaqMan microRNA assay kits for *miR221* (000524), *miR222* (002276), and *RNU6B* (001973) were purchased from Applied Biosystems. *MiR221/222* were quantified using the $2^{-\Delta\Delta Ct}$ method, and their levels were expressed as relative amounts after normalization to the *RNU6B* housekeeping gene.

Transient transfection

H9c2 cells were cultured in a 6-well plate at a density of 2×10^5 cells per well and incubated for 24 h. Then, specific *miR221/222* mimics or inhibitors (Dharmacon, CO, USA) were transfected using Lipofectamine 3000 (Invitrogen) under the manufacturer's instructions. The levels of apoptosis of *miR221/222*-overexpressing or *miR221/222*-knockdown cells were evaluated.

Animal experiments

Male C57BL/6 (B6) mice, miR221/222 knockout (KO) mice, and miR221/222 transgenic (TG) mice (8–12 weeks old, weighing 20 g) were used. B6 mice were purchased from the Laboratory Animal Center of National Taiwan University. This mouse strain was provided by the Jackson Laboratory (Stock No. 000664, Bar Harbor, Maine, USA). MiR-221/222 KO mice were generated by deleting the X-linked miR-221/222 gene and backcrossed on a B6 background for 10 generations. All experimental procedures were conducted under the guidelines of the Institutional Animal Care and Use Committee (IACUC; No. 20210334), National Taiwan University College of Medicine and College of Laboratory Animal Center. All animals were maintained under specific pathogen-free (SPF) conditions with individually ventilated cages, a 12-h light/dark cycle, and free access to food and water. B6 and KO mice were randomly divided into four groups (6–10 in each group): (1) the control group (Con); (2) the high-fat diet + particulate matter (HFD + PM) group; (3) the high-fat diet + particulate matter + ADSC-CM (HFD + PM + CM) group; and (4) the ADSC-CM (CM) group. TG mice were randomly divided into two groups (6 in each group): (1) the Con group and (2) the HFD + PM group. A total of 76 mice were used in this study. The number of mice in each group was greater than or equal to 6, allowing for biostatistics. A single mouse was considered the experimental unit for this study. The mice were fed a regular diet or an HFD (DIO rodent purified diet containing 60% energy from fat-blue; 58Y1) for 4 weeks. In the HFD + PM and HFD + PM + CM groups, intratracheal injections of PM (10 mg/kg) were administered at the 3rd and 4th weeks. Briefly, mouse was anesthetized using 2% isoflurane, and the trachea was carefully exposed. The PM was applied to the anterior wall using an insulin syringe held at a 45° angle to minimize posterior wall damage. After the injection, the trachea and wound were sutured. The mouse was returned to cages after regaining consciousness. The mice in the HFD + PM + CM and CM groups were injected with CM through the tail vein at the 3rd and 4th weeks. After 4 weeks, mice were anesthetized with 2% isoflurane until they were utterly unconscious and then subjected to cervical dislocation to ensure that euthanasia was performed humanely and quickly. Randomising the order of examination reduced bias. Moreover, objective measures were employed, including qPCR for miRNA levels, Western blot for protein expression, and TUNEL-positive cell counting for apoptosis evaluation, to minimize potential bias. The work is reported in line with the ARRIVE guidelines 2.0.

Cardiac function assessment

Cardiac functional and structural examinations were conducted using a high-resolution small animal ultrasound system (Prospect; S-Sharp, Taiwan) with a 40-MHz single-element sensor. M-mode imaging of the left ventricular short-axis view and mitral valve Doppler echocardiography were performed; three consecutive cycles and the average of three measurements were averaged. The fractional shortening (FS), ejection fraction (EF), left ventricular posterior wall thickness in diastole (LVPWd), left ventricular posterior wall thickness in systole (LVPWs), left ventricular isovolumetric contraction

time (IVCT), left ventricular isovolumetric relaxation time (IVRT), mitral E/A ratio, and stroke volume (SV) were calculated using standard formulas.

Histopathological staining

Mouse hearts were collected and fixed with 4% paraformaldehyde. Cardiac tissues were embedded in paraffin and subsequently cut at 5 μm thickness. The sections were conducted to hematoxylin and eosin staining, TUNEL staining, or PUMA immunohistochemical staining.

MitoSOX Red staining

MitoSOX Red (Invitrogen) was used to detect ROS in mitochondria. In this experiment, H9c2 cells were plated in 4-well chamber slides (5×10^4 cells/well), cultured overnight, and then incubated with PA (50 μM), PM (20 μg/mL), or ADSC-CM. After 24 h, the media was removed, and these cells were incubated with a 5 μM MitoSOX reagent at 37 °C for 10 min in the dark. Nuclei were stained with Hoechst. After washing the samples with PBS, fluorescence detection was performed using a fluorescence microscope (Leica, Germany) with an excitation wavelength (510 nm) and an emission wavelength (580 nm). For flow cytometry experiments, H9c2 cells were incubated overnight at 2×10^5 cells/well in 6-well plates following the same protocol. They were trypsinized and examined on an LSRFortessa flow cytometer (BD Biosciences, CA, USA).

JC-1 staining

The fluorescent probe 5,5′,6,6′-tetrachloro-1,1′,3,3′-tetraethylbenzimidazolocarbocyanine iodide (JC-1; BD Biosciences) was used to examine the mitochondrial membrane potential (Δψm). H9c2 cells were plated overnight in 4-well chamber slides (5×10^4 cells/well). Cells were incubated with PA, PM, or ADSC-CM for 24 h, the medium was removed, and then the cells were treated with 1 μg/mL JC-1 solution for 30 min at 37 °C in the dark. The images were photographed by fluorescent microscopy. The monomeric form of JC-1 emits green, whereas the aggregated form becomes red. For flow cytometry experiments, H9c2 cells were incubated overnight at a density of 2×10^5 cells per well in 6-well plates following the same protocol. The cells were trypsinized and examined by an LSRFortessa flow cytometer.

ATP measurement

According to the guidelines, the ATP levels were analyzed using an ATP assay kit (Thermo). After the indicated treatments, H9c2 cells were trypsinized and centrifuged at 900 × g for 10 min. The pellets were then suspended in RIPA buffer and incubated for 20 min at 4 °C. The solution was subsequently centrifuged at 17,000 × g for 20 min at 4 °C. The supernatants were collected. Finally, 10 μL of the supernatant was mixed with 90 μL of ATP assay buffer to determine ATP levels, and luminescence was examined by a microplate reader. The ATP concentrations were normalized and assessed via a standard curve, and changes were compared with those in the control group.

Assessment of mitochondrial length

Fluorescence staining for mitochondrial identification was performed by using MitoTracker Red (Thermo). After H9c2 cells were subjected to specific treatments, they were incubated with a 400 nM MitoTracker Red solution for 45 min at 37 °C in the dark. Subsequently, images were obtained by total internal reflection fluorescence microscopy (TIRFM; Zeiss) combined with DIC optics. The mitochondrial length was quantified through the ImageJ software.

Statistical analysis

The data are expressed as the means ± SEM and were examined using a one-way analysis of variance (ANOVA) with Fisher's post hoc test. P values < 0.05 indicated significant differences for all analyses.

Results

Combined treatment with PA and PM significantly increases cell apoptosis, whereas ADSC-CM reduces this effect

PA remarkably decreased cell viability in a concentration-dependent manner (50, 100, and 200 μM) by the MTT assay (Fig. 1A). PM also significantly reduced cell viability at different doses (10, 20, and 40 μg/mL; Fig. 1B). Furthermore, the combined treatment with 50 μM PA and 20 μg/mL PM significantly increased the expression levels of the apoptosis-related proteins PUMA and cCASP3, while the antiapoptotic protein Bcl-2 expression was decreased (Fig. 1C; Figure S1 for the full-length blot). To further determine whether combined stimulation with 50 μM PA and 20 μg/mL PM has an additive effect on H9c2 cell apoptosis, we measured cell viability and protein levels of PUMA, Bcl-2, and cCASP3. As shown in Fig. 1D, compared with PA or PM alone, H9c2 cells co-treated with PA and PM for 24 h considerably reduced the cell viability. Furthermore, PA + PM increased the levels of PUMA and cCASP3 and reduced the expression of Bcl-2 (Fig. 1E; full-length blots are provided in Figure S2).

To detect the impact effect of ADSC-CM on PA + PM-treated H9c2 cells, these cells were further treated with ADSC-CM under the cotreatment of PA and PM for 24 h. As shown in Fig. 1F, ADSC-CM significantly restored cell viability. The TUNEL assay indicated that PA + PM

resulted in a remarkable increase in apoptotic cells; however, ADSC-CM reduced PA + PM-induced apoptosis (Fig. 1G; quantitative analysis of TUNEL-positive cells is shown in Fig. 1H). As shown in Fig. 1I, increases in early (annexin V^+ and PI^-) and late (annexin $V^+$and PI^-) cell apoptosis were observed in PA + PM-treated H9c2 cells. In contrast, ADSC-CM reduced both early and late apoptosis. In Fig. 1J (full-length blots in Fig. S3), PA + PM increased the expression levels of PUMA and cCASP3 and reduced the Bcl-2 expression. In contrast, ADSC-CM decreased the PUMA and cCASP3 levels and increased the Bcl-2 expression levels. These above results showed that PA and PM induced H9c2 cell apoptosis, whereas ADSC-CM protected H9c2 cells from PA- and PM-induced apoptosis.

ADSC-CM protects cardiomyocytes from PA + PM-induced apoptosis via *miR221/222*

The above results confirmed that ADSC-CM could reduce PA- and PM-induced cardiomyocyte apoptosis, but the specific mechanism remains unclear. An earlier study revealed that ADSC-CM is enriched in *miR221/222*, potentially protecting cardiomyocytes from hypoxia/reperfusion-induced injury [23]. To confirm that ADSC-CM contained high amounts of *miR221/222*, CM was collected from H9c2 cells or ADSCs, and DMEM was used as a control. Compared with DMEM and H9c2-CM, ADSC-CM contained more *miR221/222*, as shown by the qPCR assay (Fig. 2A). PA + PM significantly reduced *miR221/222* levels, whereas ADSC-CM reduced this effect (Fig. 2B). Bioinformatics analysis of *miR221/222* was performed to predict their gene targets, particularly PUMA as a potential target, and the study aimed to understand the roles of *miR221/222* in PA + PM-induced apoptosis. In Fig. 2C, the amounts of *miR221/222* in H9c2 cells transfected with *miR221/222* mimics were remarkably higher than those in the negative control (NC) miRNA group under both PA and PM conditions. Under combined treatment with PA and PM, cells transfected with the *miR221/222* mimics presented significantly decreased PUMA and cCASP3 levels and increased Bcl-2 expression (Fig. 2D; full-length blots are shown in Fig. S4). To further elucidate the roles of *miR221/222* in PA + PM-induced apoptosis, H9c2 cells were transfected with the *miR221/222* inhibitor or negative control inhibitor. To effectively inhibit *miR221/222* expression, we used PA + PM stimulation to reduce *miR221/222* expression and inhibited endogenous *miR221/222* expression by transfection, as shown in Fig. 2E. PA + PM considerably decreased the levels of *miR221/222* expression compared with control treatment. The combination of the *miR221/222* inhibitor and PA + PM treatment (PA + PM + miR221/222 inhibitor) significantly decreased the *miR221/222* levels; however, ADSC-CM treatment increased the *miR221/222* levels. Subsequently, this study used Western blot to analyze the changes in the levels of apoptosis-related protein expression under the same conditions. As shown in Fig. 2F (full-length blots in Fig. S5), the PA + PM or PA + PM + *miR221/222* inhibitor considerably increased the PUMA and cCASP3 expression levels and reduced the Bcl-2 expression. In contrast, ADSC-CM decreased the PUMA and cCASP3 expression levels and increased the Bcl2 expression. Herein, we demonstrated that *miR221/222* in CM effectively increased *miR221/222* levels, whereas PA + PM treatment and the transfection with the *miR221/222* inhibitors decreased *miR221/222* levels. These results showed that PUMA was negatively regulated by *miR221/222* in PA + PM-treated H9c2 cells. *MiR221/222* inhibits apoptosis by targeting PUMA to further regulate downstream apoptotic pathways.

Since ADSC-CM contains large amounts of secreted growth factors, cytokines, and miRNAs, to determine whether *miR221/222* or other factors in ADSC-CM affect apoptosis, we treated ADSCs with *miR221/222* inhibitors or negative control miRNA inhibitors and collected

(See figure on next page.)

Fig. 1 Effects of ADSC-CM on PA + PM-induced H9c2 cell apoptosis. **A** H9c2 cells were treated with PA at various concentration (0, 50, 100, and 200 μM) for 24 h. An MTT method measured cell viability. **B** H9c2 cells were incubated with various doses (0, 10, 20, and 40 μg/mL) of PM for 24 h. An MTT method measured cell viability. **C** H9c2 cells were co-treated with the defined concentratin of PA and PM for 24 h. The expression levels of PUMA, Bcl-2, and cCASP3 were checked by Western blot. **D** H9c2 cells were incubated with PA (50 μM), PM (20 μg/mL), or PA (50 μM) + PM (20 μg/mL) for 24 h. An MTT method measured cell viability. **E** H9c2 cells were treated with PA (50 μM), PM (20 μg/mL), or PA (50 μM) + PM (20 μg/mL) for 24 h. **F** H9c2 cells were treated with 50 μM PA, 20 μg/mL PM, and ADSC-CM for 24 h. An MTT method measured cell viability. **G** H9c2 cells were treated with 50 μM PA, 20 μg/mL PM, and ADSC-CM for 24 h and then examined for apoptosis via a TUNEL method (TUNEL-positive cells: green; nuclei: blue). Scale bar = 100 μm. **H** The bar graph depicts the quantitative analysis results of counting the number of TUNEL-positive cells. **I** H9c2 cells were incubated with 50 μM PA, 20 μg/mL PM, and ADSC-CM for 24 h. Cell death was investigated by detecting annexin V-FITC and propidium iodide (PI) staining and analyzing by flow cytometry. **J** H9c2 cells were incubated with 50 μM PA, 20 μg/mL PM, and ADSC-CM for 24 h. Western blot examined the PUMA, Bcl-2, and cCASP3 expression levels. Experiments were conducted at least five times, and the quantitative data were presented as mean ± SEM. *$P < 0.05$ is defined as statistically significant. PA: palmitic acid; PM: particulate matter; CM: ADSC-CM; cCASP3: cleaved caspase-3

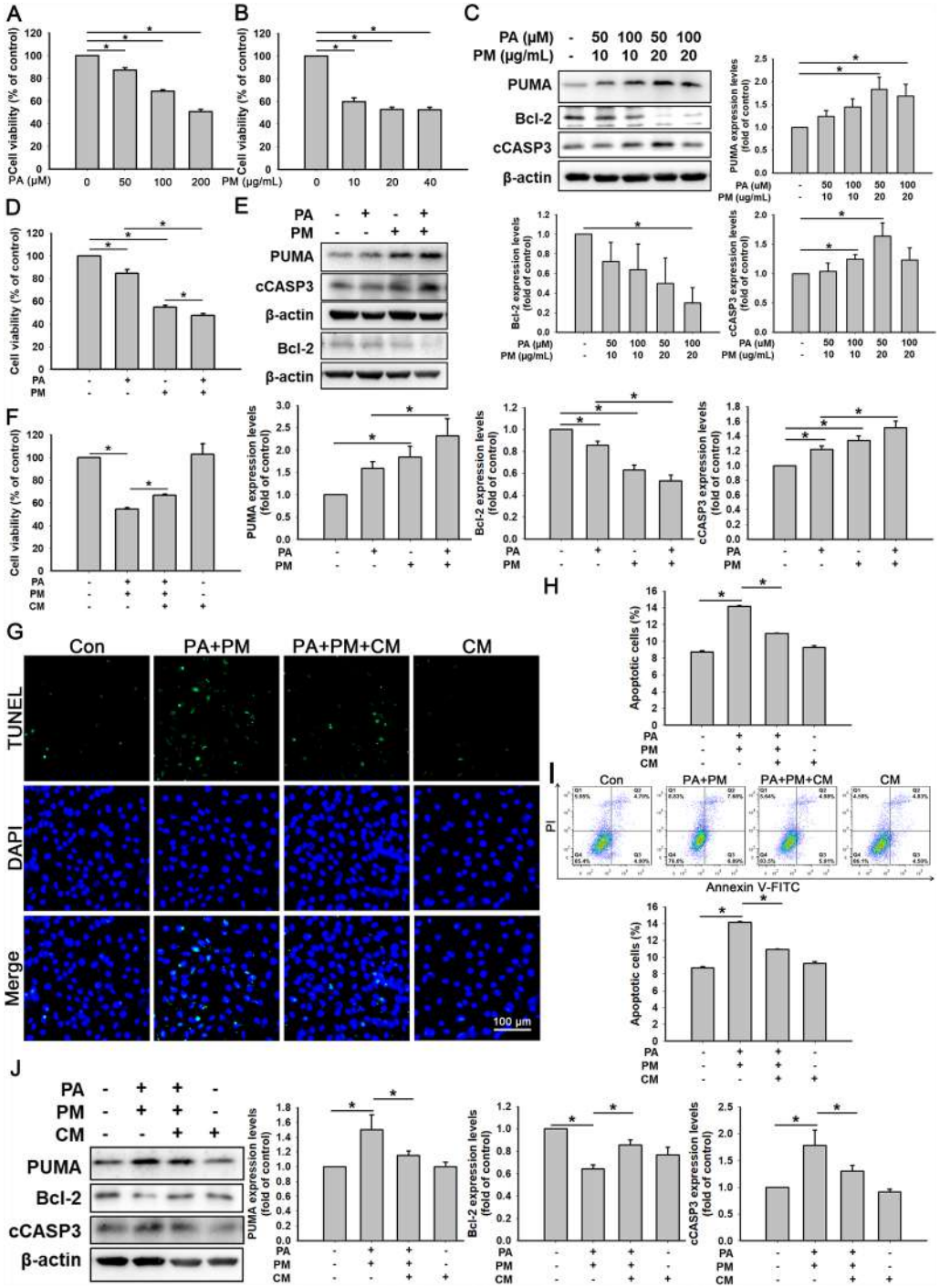


Fig. 1 (See legend on previous page.)

miRKD-CM and NCKD-CM, respectively. In combination with PA and PM treatment, the levels of *miR221/222* in H9c2 cells incubated with miRKD-CM were considerably lower than those in cells treated with NCKD-CM, as provided in Fig. 2G. The TUNEL method indicated that apoptotic cells increased markedly after miRKD-CM treatment (Fig. 2H and I). Compared with NCKD-CM treatment, miRKD-CM treatment also considerably increased PUMA and cCASP3 levels and decreased Bcl-2 expression levels (Fig. 2J; full-length blots are presented in Fig. S6). These data suggest that ADSC-CM administration reduces PA + PM-induced apoptosis,

mainly because ADSC-CM contains large amounts of *miR221/222*. These results also revealed that *miR221/222* were potent regulators of cardiomyocyte apoptosis.

ADSC-CM protects B6 and KO mice from HFD + PM-induced apoptosis via *miR221/222*

The study used C57BL/6 (B6) and *miR221/222* knockout (KO) mouse strains to investigate the effects of *miR221/222* on HFD- and PM-induced cardiomyocyte apoptosis in vivo. Initially, the absence of *miR221/222* expression in KO mice was demonstrated using qPCR (Fig. 3A). B6 and KO mice were divided into control, HFD + PM, HFD + PM + ADSC-CM, and ADSC-CM groups. As shown in Fig. 3B, in B6 mice, the levels of *miR221/222* were considerably lower in the HFD + PM group than those in the control group. Compared with the HFD + PM group, the expression levels of *miR221/222* in the HFD + PM + ADSC-CM group were remarkably increased. In KO mice, we also found that the levels of *miR221/222* increased under ADSC-CM treatment in both the HFD + PM + ADSC-CM and ADSC-CM groups. These findings confirmed that ADSC-CM contained *miR221/222*, which could effectively persist in KO mice. We also studied the impact of the HFD on the body weight of mice. Figure 3C shows that after 4 weeks of feeding, the body weights of the animals in the HFD + PM group were significantly greater than those in the control group, whereas those in the ADSC-CM group were lower. Additionally, we used echocardiographic analysis to evaluate cardiac function (Fig. 3D). An M-mode ultrasound cardiac examination revealed that in the HFD + PM group, the EF and FS were lower and the LVPWd and LVPWs were greater than those in the Con group. In contrast, the EF and FS were greater in the HFD + PM + ADSC-CM group than those in the HFD + PM group. The LVPWd and LVPWs were lower in the HFD + PM + ADSC-CM group than those in the HFD + PM group (Fig. 3E–H). Doppler echocardiography was used to examine diastolic function (Fig. 3I). Compared with those in the Con group, the IVCT and IVRT increased and the mitral valve E/A ratio and SV decreased in the HFD + PM group. In contrast, IVCT and IVRT were decreased, and mitral E/A ratio and SV were increased in the HFD + PM + ADSC-CM group compared to those in the HFD + PM group (Fig. 3J–M). The experimental results suggest that combined HFD and PM treatment impairs cardiac function in mice; however, ADSC-CM treatment improves this function. Next, hematoxylin and eosin staining examined the morphology of the cardiac tissues histologically (Fig. 3N). We observed no differences among the Con, HFD + PM, HFD + PM + CM, and CM groups of B6 or KO mice. We used TUNEL analysis to determine whether ADSC-CM affects HFD + PM-induced cell apoptosis. In the HFD + PM group, more apoptotic cells were observed; however, ADSC-CM significantly reduced the number of HFD + PM-induced apoptotic cells in the B6 and KO mice (Fig. 3O). In addition, a comparison between the B6 and KO mice revealed higher numbers of TUNEL-positive cells in the Con and HFD + PM groups of the KO mice than in those of the B6 mice. To confirm the relationship between *miR221/222* and PUMA expression, we used immunohistochemistry. As shown in Fig. 3P, in the B6 and KO mice, PUMA expression was stronger in the HFD + PM groups than in the HFD + PM + ADSC-CM groups. Comparison between the respective HFD + PM groups showed that the PUMA expression in the KO mice was greater than that in the B6 mice. PUMA and cCASP3 expression levels were increased, and the Bcl-2 expression levels were reduced in the HFD + PM groups. In contrast, ADSC-CM reduced these effects (Fig. 3Q; full-length blots are presented in Figure S7). These results suggest that HFD- and PM-induced myocardial injury may be more severe in the absence of *miR221/222*. HFD + PM can cause cardiomyocyte apoptosis by downregulating *miR221/222*.

(See figure on next page.)

Fig. 2 Effects of ADSC-CM on PA + PM-induced H9c2 cell apoptosis through *miR221/222*. **A** *MiR221/222* levels were determined in DMEM, H9c2-CM, and ADSC-CM by qPCR. **B** H9c2 cells were incubated with 50 μM PA, 20 μg/mL PM, and ADSC-CM for 24 h. The expression levels of *miR221/222* were evaluated by qPCR. **C**, **D** H9c2 cells were transfected with the corresponding negative control (NC) or *miR221/222* mimics for 24 h and then incubated with 50 μM PA and 20 μg/mL PM for 24 h. *MiR221/222* expression levels were examined by qPCR (**C**), and PUMA, Bcl-2, and cCASP3 protein expression levels were investigated by Western blot (**D**). **E**, **F** H9c2 cells were transfected with a scramble sequence or *miR221/222* inhibitors for 24 h and then treated with 50 μM PA, 20 μg/mL PM, and ADSC-CM for 24 h. The *miR221/222* expression levels were assessed by qPCR (**E**). PUMA, Bcl-2, and cCASP3 expression levels were investigated by Western blot (**F**). **G** ADSCs were transfected with the corresponding negative control (NC) or *miR221/222* inhibitors for 24 h. These cells were then incubated in a standard culture medium for another 24 h, and NCKD-CM and miRKD-CM were collected, respectively. The levels of *miR221/222* were measured by qPCR. **H** Apoptosis was assessed via a TUNEL method (TUNEL-positive cells: green; nuclei: blue). Scale bar = 100 μm. **I** Quantification data of TUNEL-positive cells is shown in the bar graphs. **J** Western blot measures the PUMA, Bcl-2, and cCASP3 expression levels. Experiments were conducted at least five times, and the quantitative data were presented as mean ± SEM. *$P < 0.05$ is defined as statistically significant. NC mimic: negative control mimic; miR mimic: *miR221/222* mimic; NC inhibitor: negative control inhibitor; miR inhibitor: *miR221/222* inhibitor; NCKD-CM: CM obtained after the knockdown of the negative control in ADSCs; miRKD-CM: CM obtained after the knockdown of *miR221/222* in ADSCs

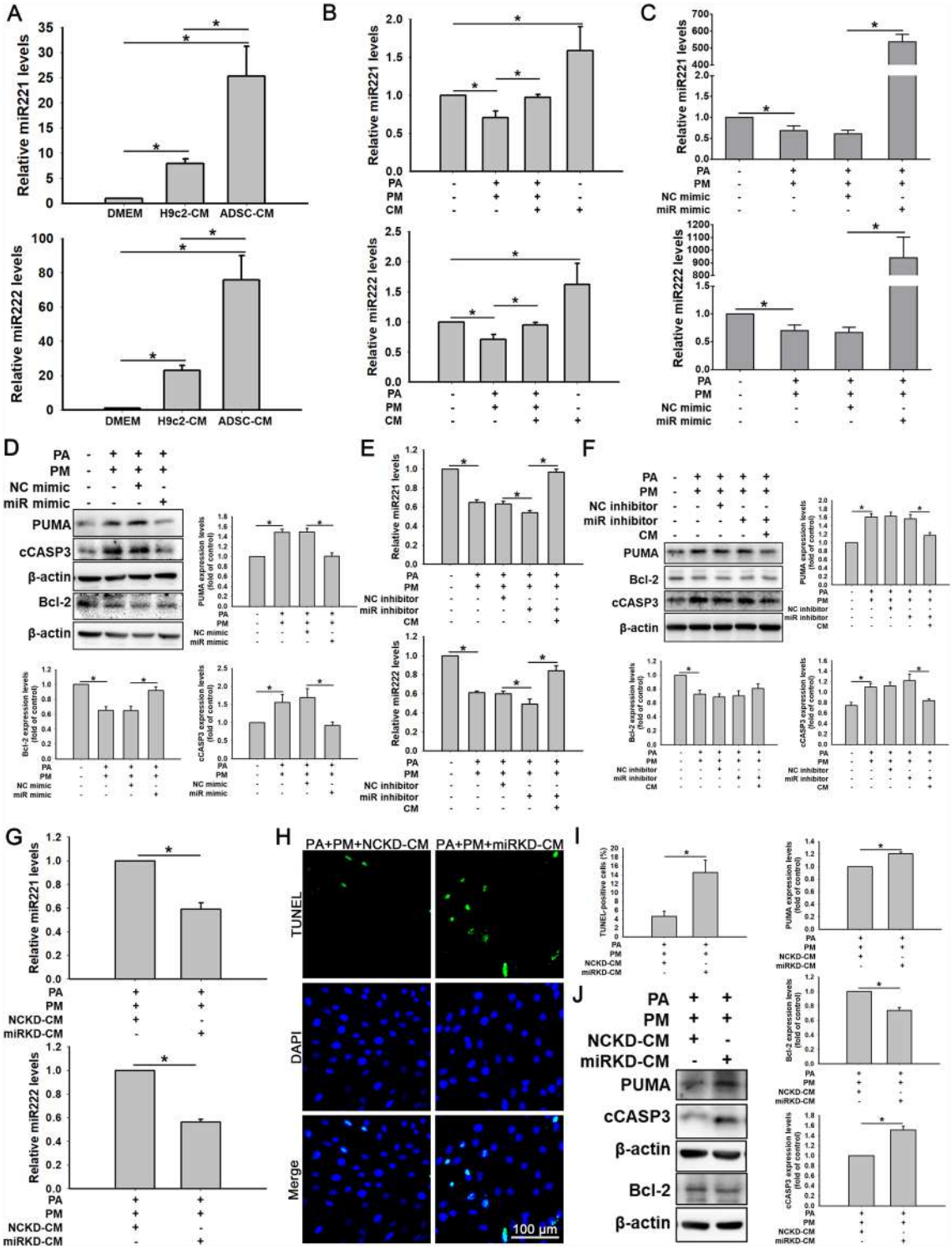


Fig. 2 (See legend on previous page.)

MiR221/222 TG mice presented fewer apoptotic cells under HFD and PM conditions

The functional involvement of *miR221/222* expression in the effects of ADSC-CM on HFD- and PM-induced cardiomyocyte apoptosis was further evaluated in the *miR221/222* TG mice. The TG mice were divided into

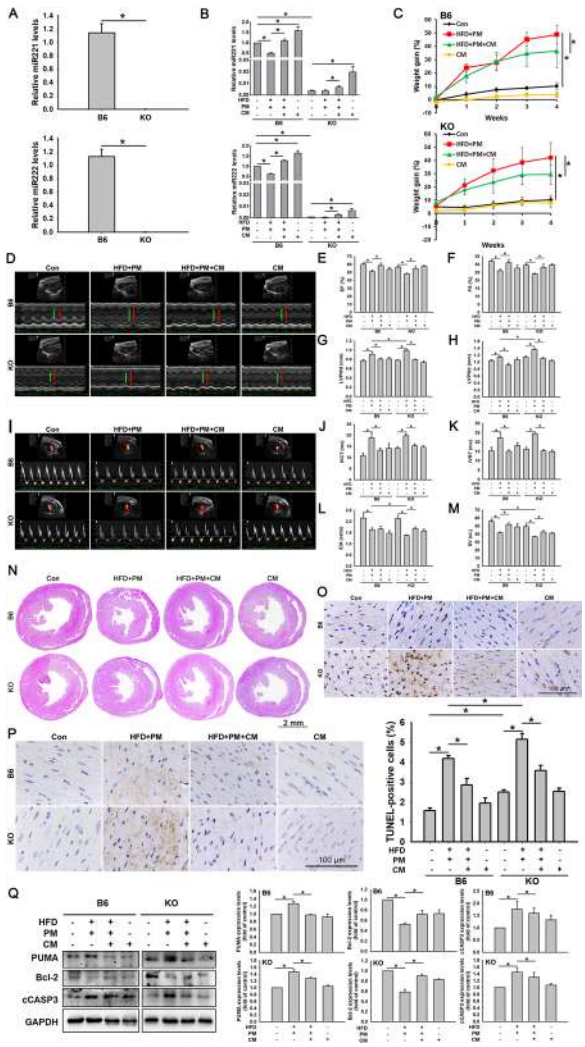


Fig. 3 Effects of ADSC-CM on high-fat diet (HFD) + PM-induced apoptosis in B6 and KO mice via *miR221/222*. **A** Determination of *miR221/222* levels in heart tissues from B6 and KO mice by qPCR. **B** Mice were fed a HFD for 4 weeks and were injected with or without PM and CM at the third and fourth weeks. The levels of *miR221/222* in heart tissues were determined by qPCR. **C** Mice were weighed before the start of the experiment and weekly thereafter. **D** Representative photographs of transthoracic echocardiographic morphology in M mode. **E**–**H** Measurements of the ejection fraction (EF), fractional shortening (FS), diastolic left ventricular posterior wall thickness (LVPWd), and systolic left ventricular posterior wall thickness (LVPWs). **I** Representative images of mitral valve waveforms from transthoracic echocardiography. **J**–**M** Measurements of the left ventricular isovolumetric contraction time (IVCT), left ventricular isovolumetric relaxation time (IVRT), mitral valve E/A ratio, and stroke volume (SV). **N** Representative images of HE-stained cardiac tissue (scale bar = 2 mm). **O** Apoptosis was assessed in cardiac tissue using a TUNEL assay. The positive reaction product is brown. The nuclei were counterstained with hematoxylin solution. **P** The location of PUMA expression in cardiac tissue was investigated by immunohistochemical staining. The positive reaction product is brown. The nuclei were counterstained with hematoxylin solution. **Q** PUMA, Bcl-2, and cCASP3 expression levels were examined by Western blot. Experiments were conducted at least six times, and the quantitative data were presented as mean ± SEM. **P* < 0.05 is defined as statistically significant. B6: C57B/L6 mice; KO: *miR221/222* knockout mice; HFD: high-fat diet

two experimental groups, receiving or not receiving combined HFD and PM treatment. B6 mice served as the control group and were divided into the HFD + PM and HFD + PM + ADSC-CM groups. The qPCR results revealed that in the TG mice, the levels of *miR221/222* were greater without HFD and PM treatment, whereas HFD and PM treatment reduced their expression. Importantly, *miR221/222* levels in TG mice were remarkably higher than those in B6 mice that received the same HFD and PM treatment (Fig. 4A). We then monitored changes in the body weight, as shown in Fig. 4B. After 4 weeks of experimental feeding, the body weights of the B6 and TG mice treated with the HFD and PM increased significantly. Subsequently, the ventricular function was assessed with echocardiography (Fig. 4C). By comparing the differences between the HFD + PM groups of the B6 and TG mice in M mode, we found that the EF and FS values of the TG mice tended to increase compared with those of the B6 mice. However, the LVPWd and LVPWs tended to decrease (Fig. 4D–G). Mitral valve Doppler ultrasound cardiac examination revealed that

(See figure on next page.)

Fig. 4 Effects of *miR221/222* on apoptosis of high-fat diet (HFD) + PM-treated TG mice. **A** Mice were fed an HFD for 4 weeks and injected with or without PM and CM at the third and fourth weeks. The levels of *miR221/222* were determined by qPCR. **B** Mice were weighed before the start of the experiment and weekly thereafter. **C** Representative M-mode images of transthoracic echocardiography. **D**–**G** Measurements of the EF, FS, LVPWd, and LVPWs. **H** Representative images of mitral valve waveforms from transthoracic echocardiography. **I**–**L** Measurements of the IVCT, IVRT, mitral E/A ratio, and SV. **M** Representative images of HE-stained cardiac tissues (scale bar = 2 mm). **N** Apoptosis was examined in cardiac tissues using a TUNEL assay. The positive reaction product is brown. The nucleus was counterstained with hematoxylin solution. Scale bar = 100 μm. **O** Immunohistochemistry was used to detect the location of PUMA expression in cardiac tissue. The positive reaction product is brown. The nuclei were counterstained with hematoxylin solution. **P** Western blot examined the PUMA, Bcl-2, and cCASP3 expression levels. These experiments were conducted at least six times, and the quantitative data were presented as mean ± SEM. **P* < 0.05 is defined as statistically significant. TG: *miR221/222* transgenic mice

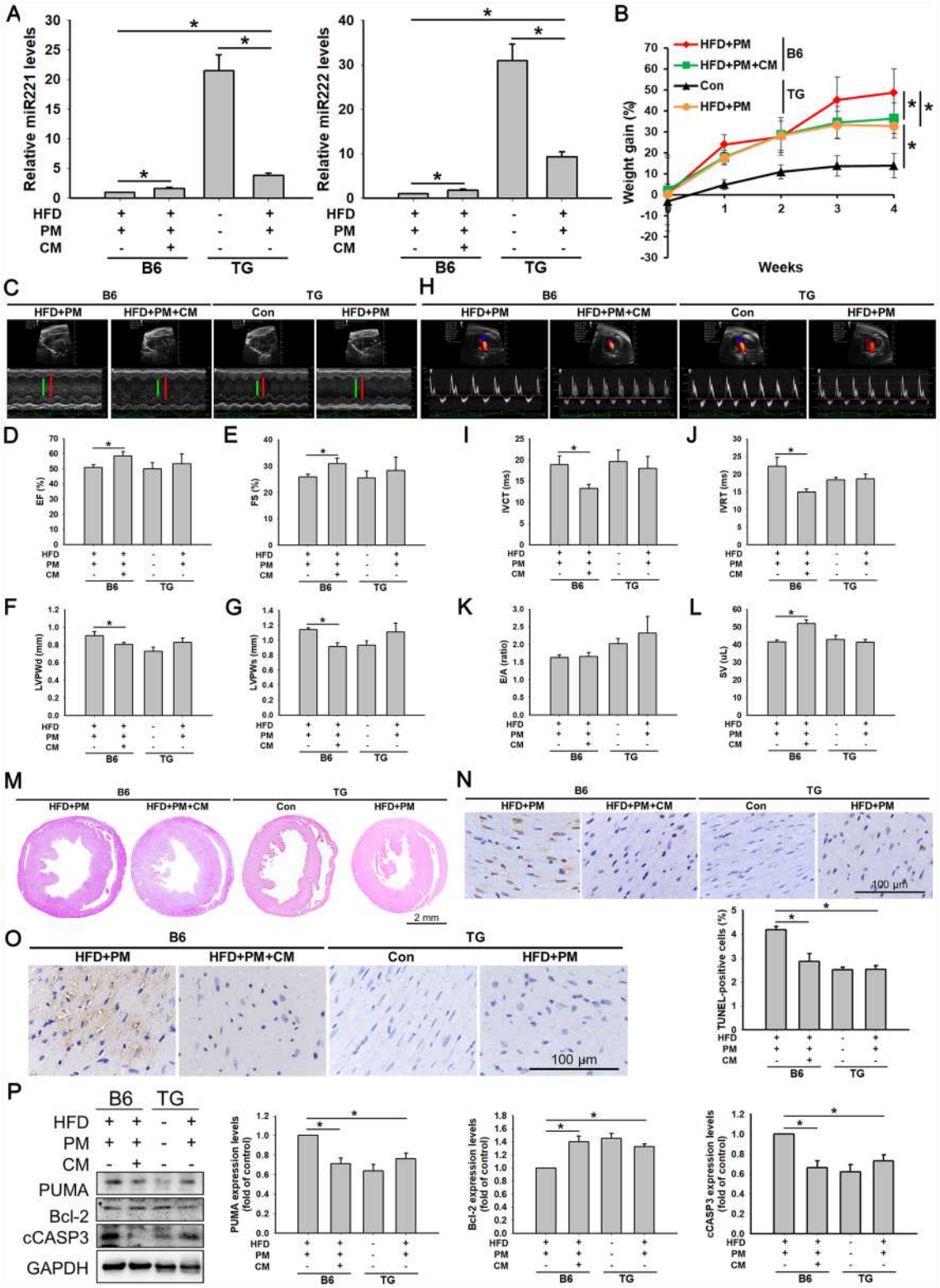


Fig. 4 (See legend on previous page.)

compared with those of the B6 mice, the IVCT and IVRT values of the TG mice were lower, whereas the E/A value was greater. There was no apparent difference in the SV indices between the HFD + PM groups of the B6 and TG mice (Fig. 4H–L). These results demonstrated that elevated levels of *miR221/222* mitigated the deleterious effects of HFD and PM on cardiac diastolic and systolic function in mice.

Heart sections were subsequently histologically examined using hematoxylin and eosin staining. As shown in Fig. 4M, no apparent differences were observed between the B6 and TG mouse groups. However, evaluation of apoptosis in cardiac tissue using a TUNEL staining assay revealed that in the respective HFD + PM groups, the percentage of apoptotic cells in the TG mice was markedly lower than that in the B6 mice (Fig. 4N). Furthermore, we evaluated the expression of PUMA using immunohistochemistry to determine its relationship with *miR221/222* levels. Upon HFD and PM treatment, PUMA expression in the TG mice was remarkably lower than that in the B6 mice, as shown in Fig. 4O. The levels of PUMA and cCASP3 were consistently reduced. In contrast, the expression level of Bcl-2 was more significant in the HFD + PM group of the TG mice than in that of the B6 mice (Fig. 4P; full-length blots are presented in Figure S8). These results show that *miR221/222* can inhibit PUMA expression and alleviate the harmful impact of HFD and PM on cardiomyocyte apoptosis. Furthermore, *miR221/222* in ADSC-CM are intrinsically involved in reducing HFD- and PM-induced cardiomyopathy.

ADSC-CM attenuated PA- and PM-induced mitochondrial ROS (mROS) production in H9c2 cells

Overproduction of ROS and excessive oxidative stress are closely related to the pathogenesis of CVD. The previous study showed that concomitant HFD intake and PM2.5 exposure exacerbated cardiac fibrosis through ROS production in C57BL6/J mice [47]. In this study, MitoSOX Red staining revealed that PA + PM increased the mROS production, as shown through fluorescent microscopy and flow cytometry (Fig. 5A and B). Mitoquinone (MitoQ), a mitochondrion-targeted antioxidant, reduced PA- and PM-induced ROS production in H9c2 cells. A TUNEL method was conducted to determine whether lowering ROS production could ameliorate PA- and PM-induced H9c2 cell death. In the PA and PM combined treatment group, MitoQ significantly reduced H9c2 cell apoptosis (Fig. 5C). The bar graph in Fig. 5D shows the results of the quantitative analysis of the number of TUNEL-positive cells. MitoQ treatment also decreased the PUMA and cCASP3 levels and increased the Bcl-2 expression levels (Fig. 5E; full-length blots are presented in Figure S9). These results indicate that a reduction in ROS production can reduce PA- and PM-induced cell death.

Compared with that in the PA + PM treatment group, ROS production was decreased by ADSC-CM treatment (Fig. 5F and G). ADSC-CM reduced PA- and PM-induced apoptosis by inhibiting ROS production. These results confirmed that ADSC-CM contained high levels of *miR221/222*, which can hinder PA- and PM-induced cardiomyocyte apoptosis. To gain further insights into the relationship between *miR221/222* and ROS levels in cardiomyocyte apoptosis, cells were transfected with *miR221/222* mimics to determine whether they inhibit PA + PM-induced ROS production. As shown in Fig. 5H and I, the overexpression of *miR221/222* did not inhibit PA- and PM-induced ROS production. Conditioned media from cultures of H9c2 cells did not reduce PA and PM-induced mROS production in H9c2 cells. In contrast, ADSC-CM or miRKD-CM treatment reduced it (Fig. 5J and K). The findings indicate that the reduction of PA + PM-induced ROS production by ADSC-CM may be independent of *miR221/222*. On the other hand, PA + PM may promote cardiomyocyte apoptosis through two pathways, namely, by increasing ROS production and reducing *miR221/222* expression. Therefore, we believe that ADSC-CM increases the expression level of

(See figure on next page.)

Fig. 5 Effects of ADSC-CM on ROS production in PA- and PM-treated H9c2 cells. **A**–**E** H9c2 cells were incubated with 50 μM PA, 20 μg/mL PM, and 100 nM MitoQ for 24 h. MitoSOX Red staining measures mitochondrial ROS levels using fluorescent microscopy (**A**) and flow cytometry (**B**). Apoptosis was detected using a TUNEL method (TUNEL-positive cells: green; nuclei: blue) (**C**). The statistical graph depicts the quantification of TUNEL-positive cell count (**D**). The PUMA, Bcl-2, and cCASP3 expression levels were investigated by Western blot (**E**). **F**, **G** H9c2 cells were treated with 50 μM PA, 20 μg/mL PM, and CM for 24 h. They were then treated with MitoSOX Red and detected by fluorescent microscopy (**F**) and flow cytometry (**G**). **H**, **I** H9c2 cells were incubated with the corresponding negative control (NC) or *miR221/222* mimics for 24 h and then incubated with 50 μM PA and 20 μg/mL PM for 24 h. They were treated with MitoSOX Red and checked via fluorescence microscopy (**H**) or flow cytometry (**I**). **J**, **K** ADSCs were transfected with *miR221/222* inhibitors and then miRKD-CMs were collected. H9c2 cells were co-treated with 50 μM PA, 20 μg/mL PM, and DMEM or CM from H9c2, ADSCs, and miRKD (H9c2-CM, ADSC-CM, and miRKD-CM) for 24 h. The cells were then treated with MitoSOX Red and detected by fluorescent microscopy (**J**) and flow cytometry (**K**). **L** The SOD1, SOD2, and SOD3 expression levels were analyzed using Western Blot. The experiments were conducted at least five times, and the quantitative data were presented as mean ± SEM. **P* < 0.05 is defined as statistically significant. Scale bar = 100 μm

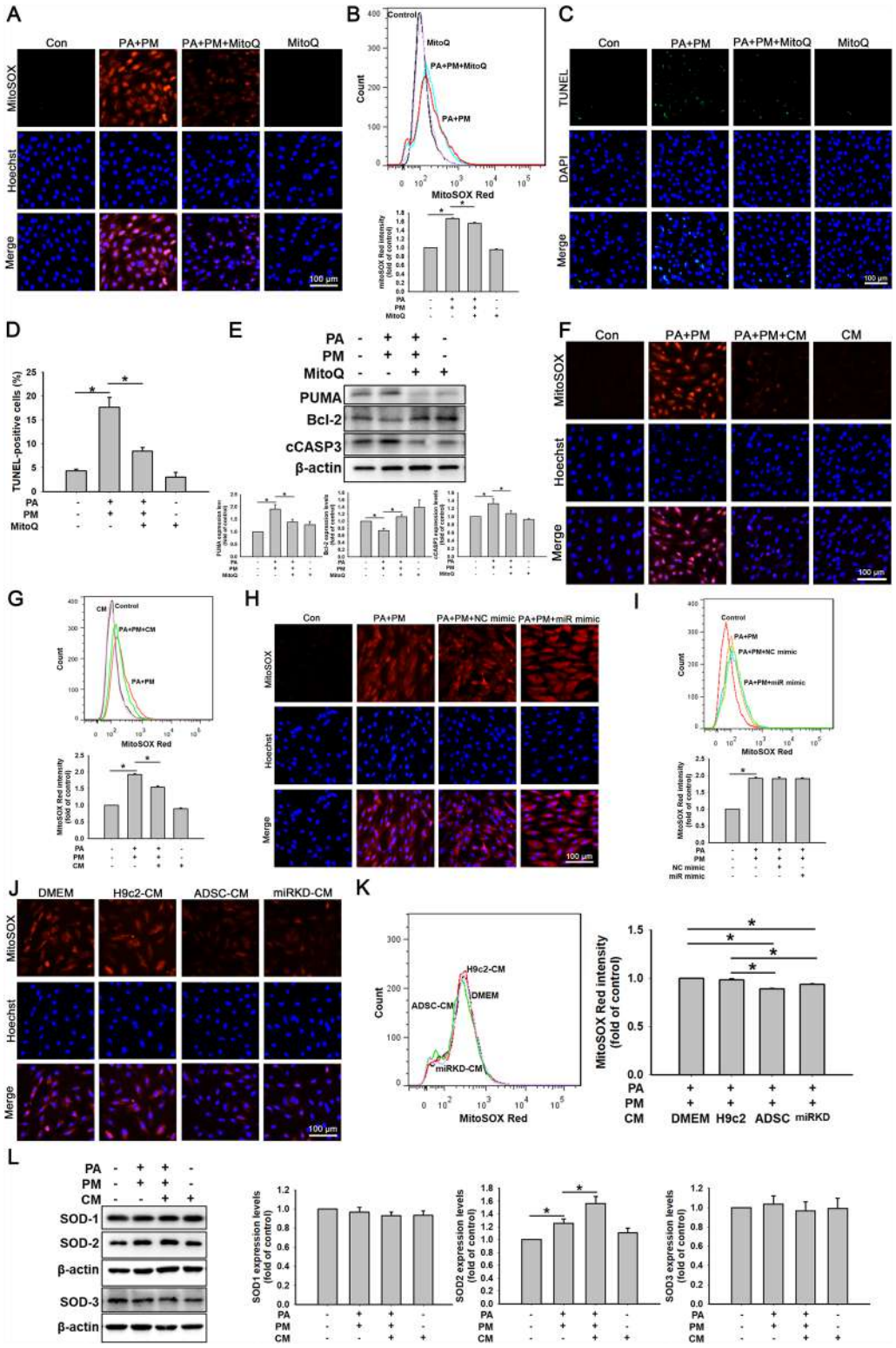


Fig. 5 (See legend on previous page.)

miR221/222 and inhibits the production of ROS, thereby decreasing PA + PM-induced cardiomyocyte apoptosis. Furthermore, intracellular ROS levels are regulated by the balance between ROS production and the levels of antioxidant enzymes, such as SOD1, SOD2, and SOD3 expression. Therefore, we also studied SOD1, SOD2, and SOD3 expression levels in PA + PM-treated H9c2 cells. Figure 5L (full-length blots are shown in Figure S10) shows that the level of the antioxidant enzyme SOD2 was increased in H9c2 cells treated with PA + PM. Furthermore, ADSC-CM treatment significantly increased the expression of SOD2 under PA + PM conditions. In summary, ADSC-CM can reduce ROS production by increasing the expression of the mitochondrial enzyme SOD2, further reducing PA + PM-induced cell death.

ADSC-CM reduced PA- and PM-induced mitochondrial fission in H9c2 cells

To study the effect of ADSC-CM on mitochondrial function in H9c2 cells cotreated with PA and PM, the ΔΨm was examined via JC-1 staining. Control cells fluoresced red, had minimal green fluorescence, and displayed a normal ΔΨm (Fig. 6A). Cells treated with PA and PM for 24 h emitted green fluorescence, with slight red fluorescence, and presented a relatively low ΔΨm. However, ADSC-CM treatment significantly reduced these effects, and flow cytometry confirmed these results (Fig. 6B). Furthermore, compared with the Con group, the PA + PM group presented significantly lower ATP concentrations, whereas ADSC-CM increased ATP production (Fig. 6C).

To elucidate whether PA- and PM-induced apoptosis is related to mitochondrial fission, H9c2 cells were stained with MitoTracker. As shown in Fig. 6D, PA + PM treatment reduced the mitochondrial length compared to the control group. Conversely, ADSC-CM increased the mitochondrial length in H9c2 cells under PA + PM conditions. PA and PM increased the levels of the mitochondrial fission-associated proteins p-DRP1 and FIS1 expression. However, ADSC-CM reduced these effects (Fig. 6E; full-length blots are presented in Figure S11). Mdivi-1, a mitochondrial fission inhibitor, reduced PA- and PM-induced apoptosis and mitochondrial fission (Fig. 6F–H; full-length blots are presented in Figure S12). These results indicate that combined treatment with PA and PM induced apoptosis by increasing mitochondrial fission in H9c2 cells, whereas ADSC-CM attenuated this effect. To further confirm the correlation between ROS production and mitochondrial fission, PA- and PM-treated cardiomyocytes were incubated with MitoQ and subjected to fluorescent microscopy and flow cytometry via JC-1 staining (Fig. 6I and J). MitoQ treatment increased the low ΔΨm that was induced by PA and PM. MitoQ treatment also increased the ATP production and mitochondrial length in PA- and PM-treated H9c2 cells (Fig. 6K and L). As shown in Fig. 6M (full-length blots are provided in Figure S13), H9c2 cells treated with MitoQ under PA + PM conditions presented significantly reduced levels of p-DRP1 and FIS1. To further investigate the role of ROS in regulating mitochondrial fission, we used H_2O_2 (100 μM, 24 h) to elevate mROS levels. H_2O_2 treatment significantly reduced ΔΨm (Fig. 6N and O), reduced ATP levels (Fig. 6P), shortened mitochondrial length (Fig. 6Q), and upregulated p-DRP1 and FIS1 protein expression (Fig. 6R; full-length blots are presented in Figure S14), indicating that ROS promotes mitochondrial fission. In addition, we also detected whether Mdivi-1 could attenuate ROS production. As shown in Fig. 6S and T, Mdivi-1 treatment did not significantly alter PA + PM-induced mROS levels, indicating that ROS generation is not the downstream of mitochondrial fission in this model. On the basis of these results, loss- and gain-of-function analyses confirmed that ROS production activated mitochondrial fission and led to apoptosis in H9c2 cells. The relationships among ROS, mitochondrial fission, and *miR221/222* in H9c2 cells treated with PA and

(See figure on next page.)

Fig. 6 Effects of ADSC-CM on PA- and PM-induced mitochondrial fission in H9c2 cells and the relationship between mitochondrial fission and ROS production. **A**, **B** H9c2 cells were treated with 50 μM PA, 20 μg/mL PM, and CM for 24 h. ΔΨm was assessed by JC-1 staining via fluorescence microscopy (**A**; scale bar = 100 μm) and flow cytometry (**B**). **C** ATP assay evaluated mitochondrial function. **D** Mitochondrial morphology was examined using MitoTracker. Scale bars = 20 μm (upper), 10 μm (lower). **E** Western blot analyzed p-DRP1 and FIS1 expression. **F**, **G** TUNEL assay (F; green: TUNEL-positive; blue: nuclei) and quantification (**G**) assessed Mdivi-1 (10 μM) pretreatment effects on apoptosis. **H** Western blot examined p-DRP1, PUMA, and cCASP3 expression. **I**–**K** Effects of MitoQ on ΔΨm and ATP levels were assessed by JC-1 staining (**I**; scale bar = 100 μm), flow cytometry (**J**), and ATP assay (**K**). **L**, **M** MitoTracker staining and Western blot assessed the effects of MitoQ (100 nM) on mitochondrial morphology. Scale bars = 20 μm (upper), 10 μm (lower) (**L**) and protein expression (**M**) in H9c2 cells treated with PA and PM. **N**–**R** H9c2 cells were treated with H_2O_2 (100 μM) and CM for 24 h. The changes of ΔΨm (**N**, **O**), ATP levels (**P**), mitochondrial morphology (**Q**), and protein expression (**R**) were analyzed. **S**, **T** mROS levels were assessed by MitoSOX Red staining (**S**; scale bar = 100 μm) and flow cytometry (**T**) after Mdivi-1 and PA + PM treatment. **U**–**W** Cells transfected with negative control (NC) or *miR221/222* mimics for 24 h and then treated with PA and PM for 24 h. ΔΨm was examined by JC-1 (**U**; scale bar = 100 μm) and flow cytometry (**V**); ATP levels were measured (**W**). **X** Western blot assessed expression of p-DRP1, FIS1, and SOD2. The experiments were conducted at least five times, and the quantitative data were presented as mean ± SEM. **P* < 0.05 is defined as statistically significant

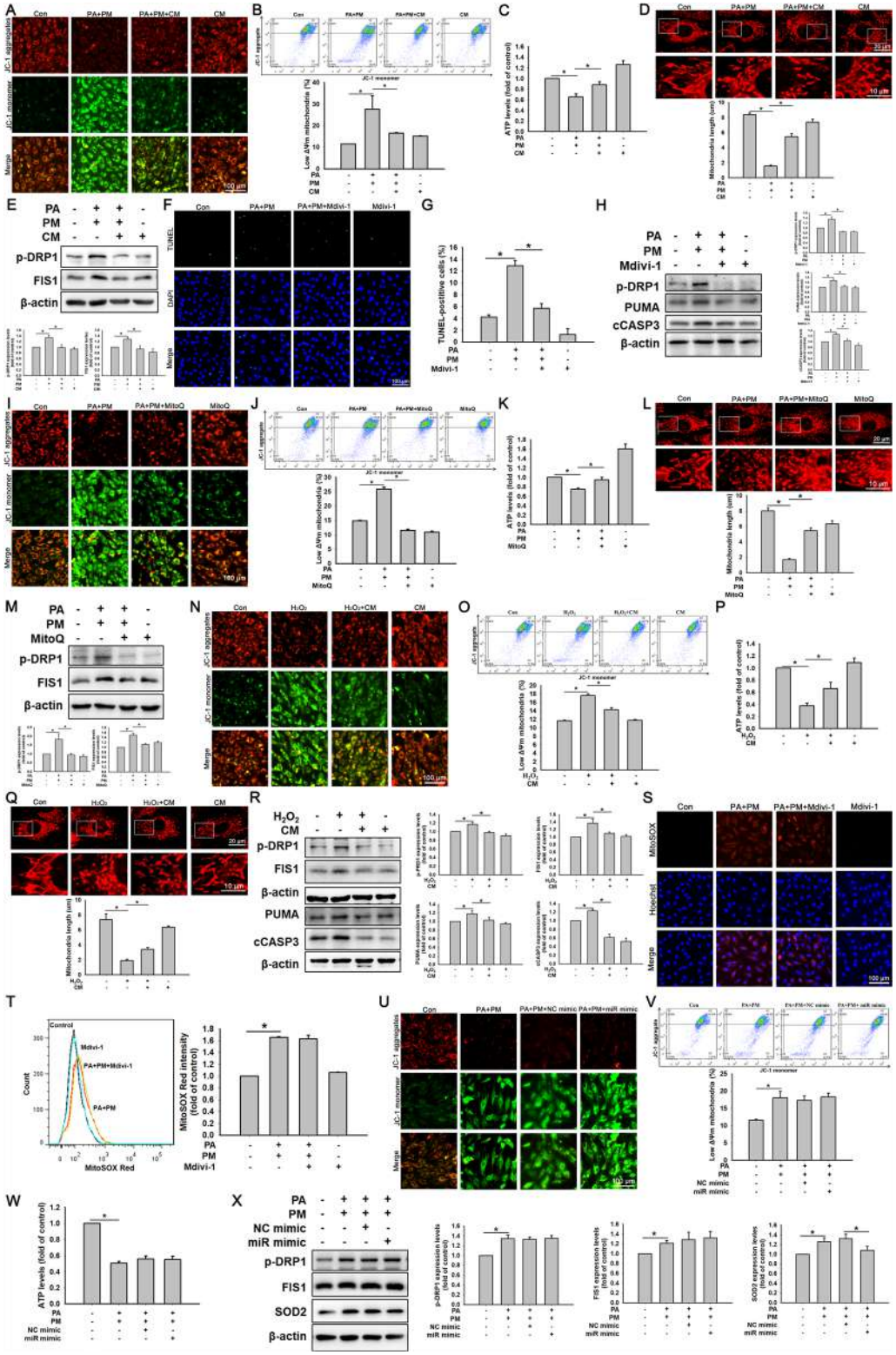


Fig. 6 (See legend on previous page.)

PM were further explored. H9c2 cells were transfected with *miR221/222* mimics and treated with PA and PM, followed by JC-1 staining and ATP assays. As shown in Fig. 6U–W, the *miR221/222* mimics failed to reverse the changes in the ΔΨm and ATP levels in PA + PM-treated H9c2 cells. Additionally, Western blot analysis showed the treatment with the *miR221/222* mimics did not reduce the levels of p-DRP1 and FIS1 but significantly reduced the expression of SOD2 (Fig. 6X; full-length blots are presented in Figure S15). These results strongly suggest that ADSC-CM inhibits the production of ROS, thereby reducing PA + PM-induced cardiomyocyte apoptosis. This pathway has no positive correlation with *miR221/222* levels.

Discussion

Currently, obesity has become a global epidemic, and increasing evidence shows that HFD-induced obesity is a high-risk factor for impaired cardiac function. Additionally, epidemiological reports have shown that an increased risk of CVD is closely associated with long-term exposure to PM2.5 [48, 49]. Based on current environmental data, individuals living in areas with high ambient PM2.5 levels in developing countries may inhale up to 16 mg/kg PM2.5 annually, significantly when average concentrations exceed 200 μg/m^3 [50–52]. Mice were intratracheally instilled with PM at 10 mg/kg once a week for two weeks, resulting in a cumulative exposure of 20 mg/kg. We employed the mouse model reflects a subacute high-dose scenario, approximately equivalent to 1–2 months of realistic exposure in a highly polluted urban environment. It has been reported that air pollution can exacerbate cardiovascular diseases caused by obesity [17]. This study revealed that an HFD and PM could reduce *miR221/222* levels, causing cardiac dysfunction and increasing the expression of apoptosis-related proteins. However, ADSC-CM treatment effectively alleviated HFD- and PM-induced cardiac dysfunction and cell apoptosis. ADSC-CM protected the heart from HFD- and PM-induced cardiomyocyte apoptosis via two pathways. One pathway is related to large amounts of *miR221/222* in ADSC-CM, which can reduce cardiac cell apoptosis by targeting PUMA and further reducing the activity of downstream apoptotic pathways. Another major pathway is related to the ability of ADSC-CM to reduce the production of ROS and thus reduce cardiomyocyte apoptosis.

ADSCs have been widely used in various clinical fields in recent years, including the treatment of chronic wounds [53], multiple sclerosis [54], Crohn's disease [55], chronic discogenic low back pain [56], stress urinary incontinence [57], and myocardial ischemia [23]. ADSCs are easy to obtain by liposuction and are relatively free of ethical issues compared with other sources of stem cells. Furthermore, ADSCs have low senescence levels, are nonimmunogenic, and have multipotent differentiation potential, which makes them superior to stem cells from other sources [58]. Our previous study revealed that ADSC-CM could reduce cardiac apoptosis during I/R injury through *miR221/222* [23]. Our present study demonstrated that cardiomyocytes could take up and internalize ADSC-CM, which resulted in the inhibition of apoptosis by downregulating PUMA expression in PA + PM-treated H9c2 cells and HFD + PM-treated mice. Based on these results, ADSC-CM can be used to improve cardiomyocyte dysfunction therapeutically.

Abnormal levels of miRNA expression have been described in many reports associated with pathological events such as ischemia/reperfusion and heart failure [59]. *MiR221/222* are encoded in tandem on chromosome X with identical seed sequences. Our previous studies revealed that *miR221/222*-containing conditioned media [23] and exosomes [60] from adipose stem cells could protect against ischemia/reperfusion-induced cardiac injury. We also reported in earlier publications that *miR221/222* regulated TNF-α-induced ICAM-1 expression in endothelial cells [61] and lung epithelial cells [62]. Additionally, some studies have shown that *miR221/222* regulate the cell cycle by targeting p27 and p57 [63, 64]. Previous research has also demonstrated that targeting PUMA with *miR221/222* promotes glioblastoma cell survival [65]. Herein, we confirmed the high levels of *miR221/222* in ADSC-CM by qPCR and performed various studies on the cardioprotective mechanisms of *miR221/222* using cell culture and animal models. The data indicated that ADSC-CM contained more *miR221/222* than H9c2-CM did, which is consistent with our earlier experimental results. In addition, bioinformatics analysis revealed that the 3′ UTR of the PUMA mRNA contained a highly conserved predicted binding site for *miR221/222*. In this study, our data clearly revealed that PA + PM or HFD + PM conditions reduced the levels of *miR221/222*. Treatment of cells with ADSC-CM, which is enriched with *miR221/222*, or transfection with *miR221/222* mimics resulted in significant downregulation of PUMA expression. However, transfection with *miR221/222* inhibitors failed to reduce PUMA expression, suggesting that *miR221/222* in ADSC-CM may ameliorate PA + PM- or HFD + PM-induced cardiac injury by downregulating PUMA. We also used *miR221/222* KO and *miR221/222* TG mice to demonstrate that *miR221/222* could attenuate HFD + PM-induced cardiomyocyte apoptosis. We showed that *miR221/222* affected cell survival by targeting PUMA. The administration of large amounts of *miR221/222* to cardiomyocytes can protect the heart

from damage caused by exposure to stimuli in the external environment.

Dysregulated ROS generation and oxidative stress are associated with CVDs, including cardiac hypertrophy, atherosclerosis, heart failure, ischemia/reperfusion injury, and diabetic cardiomyopathy [66–70]. Previous studies have shown that PA induces ROS accumulation, leading to cardiac cell apoptosis and inflammation [71, 72]. In addition, PM reduces cell viability, promotes cell apoptosis, and increases the intracellular ROS levels in H9c2 cells [73]. PM is involved in the pathogenesis of CVDs such as arrhythmia and hypertension by increasing the generation of ROS [74, 75]. This study revealed that PA and PM significantly induced excessive ROS production and increased H9c2 cell apoptosis. However, pretreatment with MitoQ (a ROS inhibitor) attenuated PA + PM-induced ROS generation and cell apoptosis. Notably, ADSC-CM effectively reduced PA + PM-induced ROS production. In addition, we found that ADSC-CM treatment increased the expression of SOD2, a well-known antioxidant enzyme. Increased SOD2 expression may be beneficial for reducing ROS production. During diabetic cardiomyopathy, SOD2 can protect cardiac morphology and ultimately normalize cardiomyocyte contractility [76]. Therefore, we believe that ADSC-CM inhibits ROS production by increasing SOD2 expression. However, cell transfection with the *miR221/222* inhibitor failed to reduce ROS generation. Studies have shown that *miR222-3p* directly binds to the 3′ UTR of SOD2. Furthermore, treating human cardiomyocytes with *miR222* mimics or inhibitors reduced or increased SOD2 expression, respectively [77]. These findings are consistent with our experimental results showing that *miR221/222* could not reduce PA + PM-induced ROS production. These results indicate that ADSC-CM attenuated PA + PM-induced apoptosis via the following two pathways: (1) abundant *miR221/222* in ADSC-CM reduced PUMA expression and (2) ADSC-CM reduced ROS production.

Accumulating evidence suggests that changes in mitochondrial morphology affect cell apoptosis and that a decreased ΔΨm is associated with mitochondrial dysfunction. A previous study revealed that when HL-1 cardiomyocytes were exposed to ischemia, mitochondria underwent fission and produced many fragments [78]. Regulating the mitochondrial membrane modification process through dynamic family proteins could reduce excessive mitochondrial fusion and fission in H9c2 cells after ischemia/reperfusion-like injury, improving the survival rate of cells, reducing ROS levels, and inhibiting cell apoptosis [79, 80]. In the present study, PA and PM reduced the ΔΨm and ATP production and increased the p-DRP1 and FIS1 expression levels, which are associated with mitochondrial fission. These findings are consistent with the previous report, which showed that PA exposure induces mitochondrial fission, characterized by the activation and phosphorylation of DRP1, a central regulator of mitochondrial dynamics [81]. Furthermore, exposure of offspring rats to PM2.5 was reported to increase the levels of DRP1 and FIS1, leading to cardiac developmental toxicity [82]. In contrast, the administration of ADSC-CM under PA and PM conditions reversed the ΔΨm change, increased ATP production, and inhibited the levels of p-DRP1 and FIS1. Furthermore, the inhibition of mitochondrial fission with the DRP1 inhibitor Mdivi-1 attenuated PA + PM-induced apoptosis. ROS are products of oxidative phosphorylation in mitochondria and play vital roles in cell signaling and developmental processes at low concentrations. However, when ROS are overproduced in defective mitochondria, they may act as cytotoxic factors, leading to excessive inflammation and apoptosis [83, 84]. A previous study revealed that ROS overproduction occurred during acute I/R injury, leading to mitochondrial fission [85]. In this study, we used MitoQ to clarify whether PA + PM-induced mitochondrial fission was due to excess ROS. The present findings showed that PA and PM could increase the production of ROS, thereby triggering mitochondrial fission and inducing the apoptosis of H9c2 cells. ADSC-CM treatment increased H9c2 cell survival, reduced ROS levels and mitochondrial fission, and prevented apoptosis.

Conclusions

Obesity increases the risk of cardiovascular disease, and environmental pollution exacerbates this risk. Overall, we found that PA and PM stimulation simultaneously suppressed *miR221/222* levels and increased ROS production, thereby inducing cardiomyocyte apoptosis. ADSC-CM reduced PA + PM-induced cardiomyocyte apoptosis by regulating *miR221/222* levels and inhibiting ROS production. Animal experiments confirmed that *miR221/222* in ADSC-CM could improve cardiac function and prevent damage (Fig. 7). ADSC-CM can serve as a therapeutic agent to alleviate PA + PM-induced apoptosis via two signaling pathways. However, the composition of ADSC-CM is complex, and its mechanism of reducing ROS generation is still unclear. Although this study focused on *miR221/222*, future studies should employ proteomic and transcriptomic analyses to characterize other bioactive components in ADSC-CM and determine their individual and synergistic effects. Therefore, the specific mechanism still needs further study. Furthermore, clinical translation must address several key challenges. The long-term efficacy and safety of ADSC-CM need to be further verified. By overcoming these mechanistic and translational challenges, ADSC-CMs could

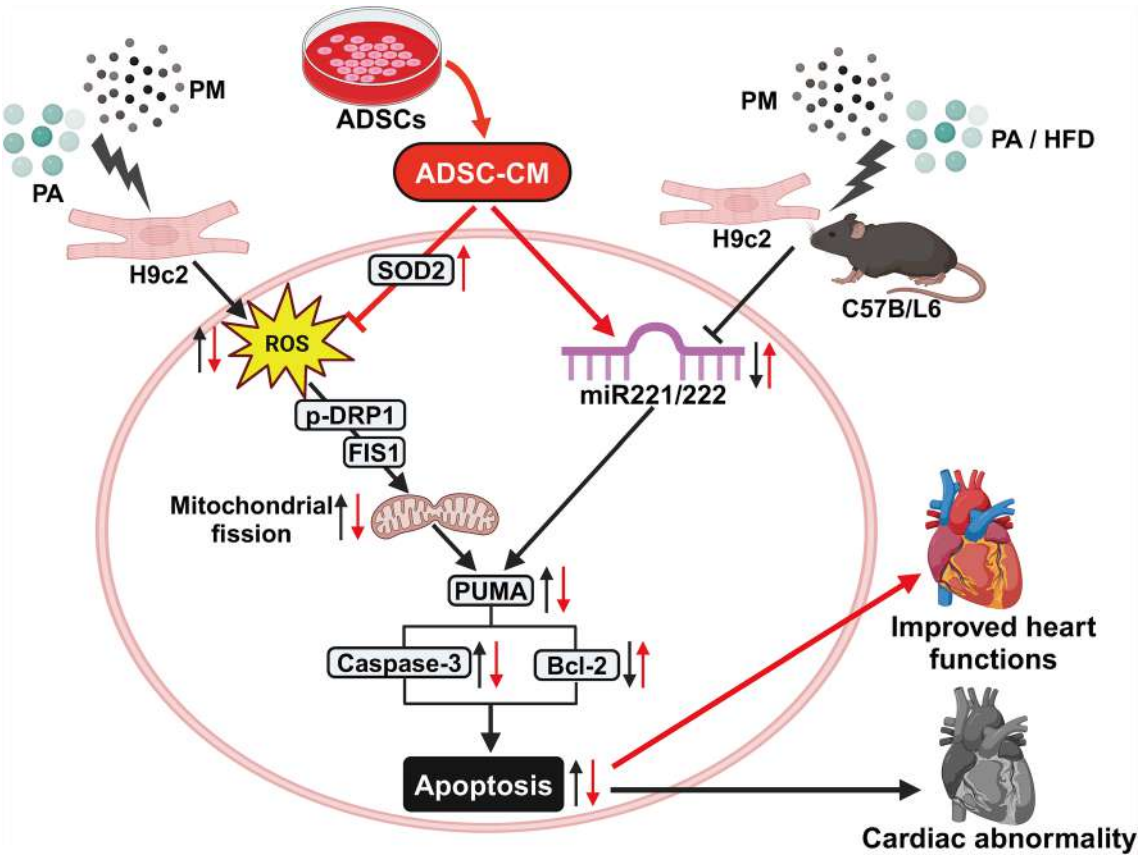


Fig. 7 A graphical abstract summarizing the study findings. This schematic illustration summarizes the effects of obesity and air pollution on cardiomyocyte apoptosis and the potential protective role of ADSC-CM. In vitro, PA treatment and PM exposure simulated obesity and air pollution, respectively. In vivo, an HFD and PM were combined to replicate these conditions. This study revealed that ADSC-CM could reduce PA/HFD + PM-induced cardiomyocyte apoptosis in vitro and in vivo studies

become promising therapeutic agents to alleviate obesity- and pollution-induced cardiac dysfunction.

Abbreviations

ADSCs	Adipose-derived stem cells
ADSC-CM	Adipose-derived stem cell-conditioned medium
B6	C57B/L6 mice
cCASP3	Cleaved caspase-3
CVD	Cardiovascular disease
DMEM	Dulbecco's modified Eagle's medium
EF	Ejection fraction
FS	Fractional shortening
HFD	High-fat diet
IVCT	Left ventricular isovolumetric contraction time
IVRT	Left ventricular isovolumetric relaxation time
KO	*miR221/222* Knockout mice
LVPWd	Diastolic left ventricular posterior wall thickness
LVPWs	Systolic left ventricular posterior wall thickness
miR inhibitor	*miR221/222* Inhibitor
miR mimic	*miR221/222* Mimic
miRKD-CM	CM obtained after knockdown of *miR221/222* in ADSCs
NC inhibitor	Negative control inhibitor
NC mimic	Nnegative control mimic
NCKD-CM	CM obtained after knockdown negative control in ADSCs
PA	Palmitic acid
PM	Particulate matter
ROS	Reactive oxygen species
SV	Stroke volume
TG	*miR221/222* Transgenic mice

Supplementary Information

The online version contains supplementary material available at https://doi.org/10.1186/s13287-025-04381-8.

Additional file 1.

Acknowledgements
The authors declare that they have not use AI-generated work in this manuscript.

Author contributions
Ya-Chun Chen: Conceptualization, Data curation, Formal analysis, Investigation, Validation, Writing—Original Draft, Writing—Review & Editing. Chi-Ming Pu: Conceptualization, Formal analysis, Writing—Review & Editing. Shu-Rung Lin: Resources. Shu-Wha Lin: Resources. I-Shing Yu: Resources. Ho-Jun Shih: Data curation. Chiang-Wen Lee: Resources, Ming-Hsueh Lee: Resources, Yen-Ting Kuo: Conceptualization. Yuh-Lien Chen: Conceptualization, Formal analysis, Funding acquisition, Writing—Review & Editing.

Funding
This work was supported by research grants from the National Science and Technology Council [MOST 108-2320-B-002-065-MY3; NSTC 111- 2320-B-002-022-MY3 to Y.L.C.], Chang Gung University of Science Foundation [grant ZRRPF6N0011 to C.W.L.], and Chang Gung Medical Research Program Foundation [grants CORPF6P0041, CORPF6P0042, CORPF6P0043 to C.W.L.]

Availability of data and materials
All additional files are included in the manuscript.

Declarations

Ethics approval and consent to participate
The studies involving experimental animals were performed according to the guidelines of the Institutional Animal Care and Use Committee, National Taiwan University College of Medicine, and College of Laboratory Animal Center (Project title: To study the effects of particulate matter 2.5 and high fat on cardiac injury: the role of mitochondrial dynamics and mitophagy; Approval number: 20210334; Date of approval: Aug 1, 2022). ADSCs were purchased from LONZA (Basel, Switzerland), and the cells were used with permission for research applications.

Consent for publication
Not applicable.

Competing interests
The authors have no conflicts of interest.

Author details
[1]Department of Anatomy and Cell Biology, College of Medicine, National Taiwan University, No. 1, Sec 1, Ren-Ai Road, Taipei 10051, Taiwan, ROC. [2]Division of Plastic Surgery, Department of Surgery, Cathay General Hospital, Taipei, Taiwan, ROC. [3]School of Medicine, College of Life Science and Medicine, National Tsing Hua University, Hsinchu City, Taiwan, ROC. [4]Department of Bioscience Technology, College of Science, Chung Yuan Christian University, Taoyuan, Taiwan, ROC. [5]Center for Nanotechnology, Chung Yuan Christian University, Taoyuan, Taiwan, ROC. [6]Department of Clinical Laboratory Sciences and Medical Biotechnology, College of Medicine, National Taiwan University, Taipei, Taiwan, ROC. [7]Laboratory Animal Center, College of Medicine, National Taiwan University, Taipei, Taiwan, ROC. [8]Department of Respiratory Care and Chronic Diseases and Health Promotion Research Center, Chang Gung University of Science and Technology, Chiayi, Taiwan, ROC. [9]Division of Neurosurgery, Department of Surgery, Chang Gung Memorial Hospital, Chiayi, Taiwan, ROC. [10]Department of Respiratory Care, Chang Gung University of Science and Technology, Chiayi, Taiwan, ROC. [11]Department of Emergency Medicine, Chang Gung Memorial Hospital, No. 8, Sec. West, Jiapu Rd., Puzi City, Chiayi 61363, Taiwan, ROC.

Received: 5 February 2025 Accepted: 7 May 2025
Published online: 03 June 2025

References

1. Li T, Providencia R, Mu N, Yin Y, Chen M, Wang Y, et al. Association of metformin monotherapy or combined therapy with cardiovascular risks in patients with type 2 diabetes mellitus. Cardiovasc Diabetol. 2021;20:30.
2. Li T, Mu N, Yin Y, Yu L, Ma H. Targeting AMP-activated protein kinase in aging-related cardiovascular diseases. Aging Dis. 2020;11:967–77.
3. Sacks FM, Lichtenstein AH, Wu JHY, Appel LJ, Creager MA, Kris-Etherton PM, et al. Dietary fats and cardiovascular disease: a presidential advisory from the american heart association. Circulation. 2017;136:e1–23.
4. Wali JA, Jarzebska N, Raubenheimer D, Simpson SJ, Rodionov RN, O'Sullivan JF. Cardio-metabolic effects of high-fat diets and their underlying mechanisms-a narrative review. Nutrients. 2020;12:1505.
5. Savini I, Catani MV, Evangelista D, Gasperi V, Avigliano L. Obesity-associated oxidative stress: strategies finalized to improve redox state. Int J Mol Sci. 2013;14:10497–538.
6. Matsuda M, Shimomura I. Roles of adiponectin and oxidative stress in obesity-associated metabolic and cardiovascular diseases. Rev Endocr Metab Disord. 2014;15:1–10.
7. Landrigan PJ, Fuller R, Acosta NJR, Adeyi O, Arnold R, Basu NN, et al. The lancet commission on pollution and health. Lancet. 2018;391:462–512.
8. Balluz L, Wen XJ, Town M, Shire JD, Qualter J, Mokdad A. Ischemic heart disease and ambient air pollution of particulate matter 2.5 in 51 counties in the U.S. Public Health Rep. 2007;122:626–33.
9. Shah AS, Langrish JP, Nair H, McAllister DA, Hunter AL, Donaldson K, et al. Global association of air pollution and heart failure: a systematic review and meta-analysis. Lancet. 2013;382:1039–48.
10. Cosselman KE, Navas-Acien A, Kaufman JD. Environmental factors in cardiovascular disease. Nat Rev Cardiol. 2015;12:627–42.
11. Basith S, Manavalan B, Shin TH, Park CB, Lee W-S, Kim J, Lee G. The impact of fine particulate matter 2.5 on the cardiovascular system: a review of the invisible killer. Nanomaterials. 2022;12(15):2656. https://doi.org/10.3390/nano12152656.
12. Krittanawong C, Qadeer YK, Hayes RB, Wang Z, Thurston GD, Virani S, Lavie CJ. PM2.5 and cardiovascular diseases: state-of-the-art review. Int J Cardiol Cardiovasc Risk Prev. 2023;19:200217. https://doi.org/10.1016/j.ijcrp.2023.200217.
13. Wang C, Yifan T, Zongliang Y, Rongzhu L. PM2.5 and cardiovascular diseases in the elderly: an overview. Int J Environ Res Public Health. 2015;12(7):8187–97. https://doi.org/10.3390/ijerph120708187.
14. Brochu P, Bouchard M, Haddad S. Physiological daily inhalation rates for health risk assessment in overweight/obese children, adults, and elderly. Risk Anal. 2014;34:567–82.
15. Li LY, Hu DY, Zhang WL, Cui LY, Jia X, Yang D, et al. Effect of short-term exposure to particulate air pollution on heart rate variability in normal-weight and obese adults. Environ Health. 2021;20:29.
16. Miller KA, Siscovick DS, Sheppard L, Shepherd K, Sullivan JH, Anderson GL, et al. Long-term exposure to air pollution and incidence of cardiovascular events in women. N Engl J Med. 2007;356:447–58.
17. Weichenthal S, Hoppin JA, Reeves F. Obesity and the cardiovascular health effects of fine particulate air pollution. Obesity. 2014;22:1580–9.
18. Tapp H, Hanley EN Jr, Patt JC, Gruber HE. Adipose-derived stem cells: characterization and current application in orthopaedic tissue repair. Exp Biol Med (Maywood). 2009;234:1–9.
19. Zhang J, Liu Y, Chen Y, Yuan L, Liu H, Wang J, et al. Adipose-derived stem cells: current applications and future directions in the regeneration of multiple tissues. Stem Cells Int. 2020;2020:8810813.
20. Kern S, Eichler H, Stoeve J, Kluter H, Bieback K. Comparative analysis of mesenchymal stem cells from bone marrow, umbilical cord blood, or adipose tissue. Stem Cells. 2006;24:1294–301.
21. Shukla L, Yuan Y, Shayan R, Greening DW, Karnezis T. Fat Therapeutics: the clinical capacity of adipose-derived stem cells and exosomes for human disease and tissue regeneration. Front Pharmacol. 2020;11:158.
22. Pu CM, Liu CW, Liang CJ, Yen YH, Chen SH, Jiang-Shieh YF, et al. Adipose-derived stem cells protect skin flaps against ischemia/reperfusion injury via IL-6 expression. J Invest Dermatol. 2017;137:1353–62.
23. Lee TL, Lai TC, Lin SR, Lin SW, Chen YC, Pu CM, et al. Conditioned medium from adipose-derived stem cells attenuates ischemia/reperfusion-induced cardiac injury through the microRNA-221/222/PUMA/ETS-1 pathway. Theranostics. 2021;11:3131–49.
24. Lee T-L, Shen W-C, Chen Y-C, Lai T-C, Lin S-R, Lin S-W. Mir221-and Mir222-enriched adsc-exosomes mitigate PM exposure-exacerbated cardiac ischemia-reperfusion injury through the modulation of the BNIP3-MAP1LC3B-BBC3/PUMA pathway. Autophagy. 2024;21(2):374–93. https://doi.org/10.1080/15548627.2024.2395799.
25. Wu X, Yan F, Wang L, Sun G, Liu J, Qu M, et al. MicroRNA: another pharmacological avenue for colorectal cancer? Front Cell Dev Biol. 2020;8:812.
26. Guo Q, Li D, Luo X, Yuan Y, Li T, Liu H, et al. The regulatory network and potential role of LINC00973-miRNA-mRNA ceRNA in the progression of non-small-cell lung cancer. Front Immunol. 2021;12:684807.
27. Hata A. Functions of microRNAs in cardiovascular biology and disease. Annu Rev Physiol. 2013;75:69–93.
28. Wojciechowska A, Braniewska A, Kozar-Kaminska K. MicroRNA in cardiovascular biology and disease. Adv Clin Exp Med. 2017;26:865–74.
29. Condorelli G, Latronico MV, Cavarretta E. microRNAs in cardiovascular diseases: current knowledge and the road ahead. J Am Coll Cardiol. 2014;63:2177–87.

30. Quiat D, Olson EN. MicroRNAs in cardiovascular disease: from pathogenesis to prevention and treatment. J Clin Invest. 2013;123:11–8.
31. Chistiakov DA, Sobenin IA, Orekhov AN, Bobryshev YV. Human miR-221/222 in physiological and atherosclerotic vascular remodeling. Biomed Res Int. 2015;2015:354517.
32. Corsten MF, Heggermont W, Papageorgiou AP, Deckx S, Tijsma A, Verhesen W, et al. The microRNA-221/-222 cluster balances the antiviral and inflammatory response in viral myocarditis. Eur Heart J. 2015;36:2909–19.
33. Mandl A, Pham LH, Toth K, Zambetti G, Erhardt P. Puma deletion delays cardiac dysfunction in murine heart failure models through attenuation of apoptosis. Circulation. 2011;124:31-U104.
34. Jiang F, Huang Q, Nian J, Yang S. miR-221/222/PUMA axis promotes oral squamous cell carcinoma apoptosis. Open J Stomatol. 2023;13:367–83.
35. Hutcheson R, Rocic P. The metabolic syndrome, oxidative stress, environment, and cardiovascular disease: the great exploration. Exp Diabetes Res. 2012;2012:271028.
36. Mei Y, Thompson MD, Cohen RA, Tong X. Autophagy and oxidative stress in cardiovascular diseases. Biochim Biophys Acta. 2015;1852:243–51.
37. Yang X, Li Y, Li Y, Ren X, Zhang X, Hu D, et al. Oxidative stress-mediated atherosclerosis: mechanisms and therapies. Front Physiol. 2017;8:600.
38. D'Oria R, Schipani R, Leonardini A, Natalicchio A, Perrini S, Cignarelli A, et al. The role of oxidative stress in cardiac disease: from physiological response to injury factor. Oxid Med Cell Longev. 2020;2020:5732956.
39. Sawyer DB, Colucci WS. Mitochondrial oxidative stress in heart failure—"oxygen wastage" revisited. Circ Res. 2000;86:119–20.
40. Chen G, Kroemer G, Kepp O. Mitophagy: an emerging role in aging and age-associated diseases. Front Cell Dev Biol. 2020;8:200.
41. Luo YD, Ma JJ, Lu WQ. The significance of mitochondrial dysfunction in cancer. Int J Mol Sci. 2020;21:5598.
42. Wakabayashi J, Zhang ZY, Wakabayashi N, Tamura Y, Fukaya M, Kensler TW, et al. The dynamin-related GTPase drp1 is required for embryonic and brain development in mice. J Cell Biol. 2009;186:805–16.
43. Martens S, McMahon HT. Mechanisms of membrane fusion: disparate players and common principles. Nat Rev Mol Cell Biol. 2008;9:543–56.
44. Chen YR, Zweier JL. Cardiac mitochondria and reactive oxygen species generation. Circ Res. 2014;114:524–37.
45. Knowlton AA, Chen L, Malik ZA. Heart failure and mitochondrial dysfunction: the role of mitochondrial fission/fusion abnormalities and new therapeutic strategies. J Cardiovasc Pharmacol. 2014;63:196–206.
46. Quiles JM, Gustafsson ÅB. The role of mitochondrial fission in cardiovascular health and disease. Nat Rev Cardiol. 2022;19:723–36.
47. Jiang J, Li Y, Liang S, Sun B, Shi Y, Xu Q, et al. Combined exposure of fine particulate matter and high-fat diet aggravate the cardiac fibrosis in C57BL/6J mice. J Hazard Mater. 2020;391:122203.
48. Chen CC, Wang YR, Liu JS, Chang HY, Guo YL, Chen PC. Burden of cardiovascular disease attributable to long-term exposure to ambient PM2.5 concentration and the cost-benefit analysis for the optimal control level. Sci Total Environ. 2023;892:164767.
49. Nethery RC, Josey K, Gandhi P, Kim JH, Visaria A, Bates B, et al. Air pollution and cardiovascular and thromboembolic events in older adults with high-risk conditions. Am J Epidemiol. 2023;192:1358–70.
50. World Health Organization. WHO global air quality guidelines: particulate matter (PM2.5 and PM10), ozone, nitrogen dioxide, sulfur dioxide and carbon monoxide. Geneva: World Health Organization; 2021. Available from: https://www.who.int/publications/i/item/9789240034228
51. Zhang JJ, Wei Y, Fang Z. Ozone pollution: a major health hazard worldwide. Front Immunol. 2019;10:2518.
52. IQAir. 2023 World Air Quality Report. Goldach, Switzerland: IQAir; 2024. Available from: https://www.iqair.com/world-air-quality-report
53. Zhang Y, Xing Y, Jia L, Ji Y, Zhao B, Wen Y, et al. An in vitro comparative study of multisource derived human mesenchymal stem cells for bone tissue engineering. Stem Cells Dev. 2018;27:1634–45.
54. Fernandez O, Izquierdo G, Fernandez V, Leyva L, Reyes V, Guerrero M, et al. Adipose-derived mesenchymal stem cells (AdMSC) for the treatment of secondary-progressive multiple sclerosis: a triple blinded, placebo controlled, randomized phase I/II safety and feasibility study. PLoS ONE. 2018;13:e0195891.
55. Panes J, Garcia-Olmo D, Van Assche G, Colombel JF, Reinisch W, Baumgart DC, et al. Long-term efficacy and safety of stem cell therapy (Cx601) for complex perianal fistulas in patients with crohn's disease. Gastroenterology. 2018;154(1334–42):e4.
56. Kumar H, Ha DH, Lee EJ, Park JH, Shim JH, Ahn TK, et al. Safety and tolerability of intradiscal implantation of combined autologous adipose-derived mesenchymal stem cells and hyaluronic acid in patients with chronic discogenic low back pain: 1-year follow-up of a phase I study. Stem Cell Res Ther. 2017;8:262.
57. Arjmand B, Safavi M, Heidari R, Aghayan H, Dehghani S, et al. Concomitant transurethral and transvaginal-periurethral injection of autologous adipose derived stem cells for treatment of female stress urinary incontinence: a phase one clinical trial. Acta Med Iran. 2017;55:368–74.
58. Kim EH, Heo CY. Current applications of adipose-derived stem cells and their future perspectives. World J Stem Cells. 2014;6:65–8.
59. Sessa F, Salerno M, Esposito M, Cocimano G, Pomara C. miRNA dysregulation in cardiovascular diseases: current opinion and future perspectives. Int J Mol Sci. 2023;24:5196.
60. Lai TC, Lee TL, Chang YC, Chen YC, Lin SR, Lin SW, et al. MicroRNA-221/222 mediates ADSC-exosome-induced cardioprotection against ischemia/reperfusion by targeting PUMA and ETS-1. Front Cell Dev Biol. 2020;8:569150.
61. Liu CW, Sung HC, Lin SR, Wu CW, Lee CW, Lee IT, et al. Resveratrol attenuates ICAM-1 expression and monocyte adhesiveness to TNF-alpha-treated endothelial cells: evidence for an anti-inflammatory cascade mediated by the miR-221/222/AMPK/p38/NF-kappaB pathway. Sci Rep. 2017;7:44689.
62. Sung HC, Liu CW, Hsiao CY, Lin SR, Yu IS, Lin SW, et al. The effects of wild bitter gourd fruit extracts on ICAM-1 expression in pulmonary epithelial cells of C57BL/6J mice and microRNA-221/222 knockout mice: Involvement of the miR-221/-222/PI3K/AKT/NF-kappaB pathway. Phytomedicine. 2018;42:90–9.
63. le Sage C, Nagel R, Egan DA, Schrier M, Mesman E, Mangiola A, et al. Regulation of the p27(Kip1) tumor suppressor by miR-221 and miR-222 promotes cancer cell proliferation. EMBO J. 2007;26:3699–708.
64. Fornari F, Gramantieri L, Ferracin M, Veronese A, Sabbioni S, Calin GA, et al. MiR-221 controls CDKN1C/p57 and CDKN1B/p27 expression in human hepatocellular carcinoma. Oncogene. 2008;27:5651–61.
65. Zhang CZ, Zhang JX, Zhang AL, Shi ZD, Han L, Jia ZF, et al. MiR-221 and miR-222 target PUMA to induce cell survival in glioblastoma. Mol Cancer. 2010;9:229.
66. Maulik SK, Kumar S. Oxidative stress and cardiac hypertrophy: a review. Toxicol Mech Methods. 2012;22:359–66.
67. Batty M, Bennett MR, Yu E. The role of oxidative stress in atherosclerosis. Cells. 2022;11:3843.
68. Tsutsui H, Kinugawa S, Matsushima S. Oxidative stress and heart failure. Am J Physiol Heart Circ Physiol. 2011;301:H2181–90.
69. Misra MK, Sarwat M, Bhakuni P, Tuteja R, Tuteja N. Oxidative stress and ischemic myocardial syndromes. Med Sci Monit. 2009;15:Ra209–19.
70. Liu Q, Wang SD, Cai L. Diabetic cardiomyopathy and its mechanisms: Role of oxidative stress and damage. J Diabetes Investig. 2014;5:623–34.
71. Wei CD, Li Y, Zheng HY, Tong YQ, Dai W. Palmitate induces H9c2 cell apoptosis by increasing reactive oxygen species generation and activation of the ERK1/2 signaling pathway. Mol Med Rep. 2013;7:855–61.
72. Wu KM, Hsu YM, Ying MC, Tsai FJ, Tsai CH, Chung JG, et al. High-density lipoprotein ameliorates palmitic acid-induced lipotoxicity and oxidative dysfunction in H9c2 cardiomyoblast cells via ROS suppression. Nutr Metab (Lond). 2019;16:36.
73. Cao J, Qin G, Shi R, Bai F, Yang G, Zhang M, et al. Overproduction of reactive oxygen species and activation of MAPKs are involved in apoptosis induced by PM25 in rat cardiac H9c2 cells. J Appl Toxicol. 2016;36:609–17.
74. Sun QH, Yue PB, Ying ZK, Cardounel AJ, Brook RD, Devlin R, et al. Air pollution exposure potentiates hypertension through reactive oxygen species-mediated activation of Rho/ROCK. Arterioscler Thromb Vasc Biol. 2008;28:1760–6.
75. Kim JB, Kim C, Choi E, Park S, Park H, Pak HN, et al. Particulate air pollution induces arrhythmia via oxidative stress and calcium calmodulin kinase II activation. Toxicol Appl Pharmacol. 2012;259:66–73.
76. Shen X, Zheng SR, Metreveli NS, Epstein PN. Protection of cardiac mitochondria by overexpression of MnSOD reduces diabetic cardiomyopathy. Diabetes. 2006;55:798–805.
77. Dubois-Deruy E, Cuvelliez M, Fiedler J, Charrier H, Mulder P, Hebbar E, et al. MicroRNAs regulating superoxide dismutase 2 are new circulating biomarkers of heart failure. Sci Rep. 2017;7:14747.

78. Brady NR, Hamacher-Brady A, Gottlieb RA. Proapoptotic BCL-2 family members and mitochondrial dysfunction during ischemia/reperfusion injury, a study employing cardiac HL-1 cells and GFP biosensors. Biochim Biophys Acta. 2006;1757:667–78.
79. Zhao L, Zhuang J, Wang Y, Zhou D, Zhao D, Zhu S, et al. Propofol ameliorates H9c2 cells apoptosis induced by oxygen glucose deprivation and reperfusion injury via inhibiting high levels of mitochondrial fusion and fission. Front Pharmacol. 2019;10:61.
80. Cheng QQ, Wan YW, Yang WM, Tian MH, Wang YC, He HY, et al. Gastrodin protects H9c2 cardiomyocytes against oxidative injury by ameliorating imbalanced mitochondrial dynamics and mitochondrial dysfunction. Acta Pharmacol Sin. 2020;41:1314–27.
81. Hu Q, Zhang H, Gutierrez Cortes N, Wu D, Wang P, Zhang J, et al. Increased Drp1 acetylation by lipid overload induces cardiomyocyte death and heart dysfunction. Circ Res. 2020;126:456–70.
82. Wang H, Peng X, Cao F, Wang Y, Shi H, Lin S, et al. Cardiotoxicity and mechanism of particulate matter 2.5 (PM2.5) exposure in offspring rats during pregnancy. Med Sci Monit. 2017;23:3890–6.
83. Zhang J, Wang X, Vikash V, Ye Q, Wu D, Liu Y, et al. ROS and ROS-mediated cellular signaling. Oxid Med Cell Longev. 2016;2016:4350965.
84. Liu J, Han X, Zhang T, Tian K, Li Z, Luo F. Reactive oxygen species (ROS) scavenging biomaterials for anti-inflammatory diseases: from mechanism to therapy. J Hematol Oncol. 2023;16:116.
85. Plotnikov EY, Vasileva AK, Arkhangelskaya AA, Pevzner IB, Skulachev VP, Zorov DB. Interrelations of mitochondrial fragmentation and cell death under ischemia/reoxygenation and UV-irradiation: protective effects of SkQ1, lithium ions and insulin. FEBS Lett. 2008;582:3117–24.

Publisher's Note

Springer Nature remains neutral with regard to jurisdictional claims in published maps and institutional affiliations.

Biomedicine & Pharmacotherapy 192 (2025) 118622

Contents lists available at ScienceDirect

Biomedicine & Pharmacotherapy

journal homepage: www.elsevier.com/locate/biopha

TAS4464, a neddylation inhibitor, mitigates *Staphylococcus aureus*-induced periprosthetic joint infection by modulating immunosuppressive cell functions

Kuo-Ti Peng [a,b], Jiun-Liang Chen [a], Yu-Chien Hsieh [a], Chun-Yuan Hsiao [a], Chia-Ching Yang [a], Ju-Fang Liu [c], Chiang-Wen Lee [a,d,e], Yao-Chang Chiang [d], Pey-Jium Chang [f,g,*]

[a] *Department of Orthopedic Surgery, Chang Gung Memorial Hospital, Chiayi, Taiwan*
[b] *College of Medicine, Chang Gung University, Taoyuan, Taiwan*
[c] *School of Oral Hygiene, College of Oral Medicine, Taipei Medical University, Taipei, Taiwan*
[d] *Department of Nursing, Division of Basic Medical Sciences, Chronic Diseases and Health Promotion Research Center, Chang Gung University of Science and Technology, Chiayi, Taiwan*
[e] *Department of Safety Health and Environmental Engineering, Ming Chi University of Technology, New Taipei City, Taiwan*
[f] *Graduate Institute of Clinical Medical Sciences, College of Medicine, Chang Gung University, Taoyuan, Taiwan*
[g] *Department of Nephrology, Chang Gung Memorial Hospital, Chiayi, Taiwan*

ARTICLE INFO

Keywords:
Staphylococcus aureus
Periprosthetic joint infection
Biofilm
Neddylation
Myeloid-derived suppressor cells
M2 macrophages

ABSTRACT

Staphylococcus aureus (*S. aureus*) is a leading cause of biofilm-associated periprosthetic joint infections (PJIs), in part due to its ability to induce an immunosuppressive environment. Biofilm formation promotes the expansion of myeloid-derived suppressor cells (MDSCs) and M2 macrophages, which impair host immune responses and facilitate infection persistence. Targeting these immunosuppressive cells offers a promising therapeutic strategy for treating *S. aureus* biofilm-associated PJIs. Neddylation, a post-translational modification involving the conjugation of the ubiquitin-like protein NEDD8 to target proteins, regulates various cellular processes and may influence immune cell function during infection. Here, we investigated the role of neddylation in *S. aureus* biofilm-induced immunosuppression. We found that TAS4464, a selective neddylation inhibitor, markedly suppressed the expansion of MDSCs and M2 macrophages in bone marrow cells (BMCs) stimulated by *S. aureus* biofilm. TAS4464 also reduced the expression of inflammation-associated cytokines in these cells. Mechanistically, *S. aureus* biofilm upregulated key components of the neddylation pathway and markers of MDSCs and M2 macrophages in a dose-dependent manner; however, this upregulation is effectively counteracted by TAS4464. Furthermore, in a mouse model of PJI, TAS4464 treatment significantly reduced bone destruction and inflammation, which correlates with the inhibition of the neddylation pathway and a decrease in circulating MDSCs and M2 macrophages. These findings suggest that TAS4464 mitigates *S. aureus* biofilm-associated PJIs by disrupting the immunosuppressive microenvironment and highlight neddylation as a potential therapeutic target.

1. Introduction

Periprosthetic joint infection (PJI) is a serious complication following joint replacement surgery, such as total hip or knee arthroplasty [1–3]. Despite advancements in treatment strategies, including debridement with prosthesis retention, one- or two-stage reimplantation, and antibiotic therapy [4,5], failure rates remain high, ranging from 10 % to 30 % during follow-up [6–9]. Particularly, managing PJIs caused by methicillin-resistant *Staphylococcus aureus* (MRSA) remains a significant challenge for orthopedic surgeons [3,10]. In addition to acquiring antimicrobial resistance through genetic mutations, *S. aureus* promotes the formation of biofilm, a structured bacterial community encased in a protective extracellular polymeric matrix [11,12]. These biofilms can develop on medical device surfaces, shielding bacteria from antibiotics and immune system attacks [13,14]. To evade immune defenses, *S. aureus* biofilm infections have been shown to promote the expansion and activity of myeloid-derived suppressor cells (MDSCs) and M2-macrophages [15–17], thereby creating an immunosuppressive

* Correspondence to: Graduate Institute of Clinical Medical Sciences, College of Medicine, Chang Gung University, Guishan, Taoyuan 33302, Taiwan.
E-mail address: peyjiumc@mail.cgu.edu.tw (P.-J. Chang).

https://doi.org/10.1016/j.biopha.2025.118622
Received 4 August 2025; Received in revised form 22 September 2025; Accepted 1 October 2025
Available online 3 October 2025
0753-3322/© 2025 The Author(s). Published by Elsevier Masson SAS. This is an open access article under the CC BY-NC license (http://creativecommons.org/licenses/by-nc/4.0/).

microenvironment at PJI sites. Given the high failure rates of current treatments, targeting these immunosuppressive cells may offer a promising strategy for improving PJI management.

Neddylation is a post-translational modification process in which the ubiquitin-like protein NEDD8 (neural precursor cell-expressed developmentally downregulated protein 8) is covalently attached to target proteins [18,19]. Similar to ubiquitination, neddylation is catalyzed by a sequential enzymatic cascade involving E1 (NEDD8-activating enzyme; NAE), E2 (NEDD8-conjugating enzyme), and E3 (NEDD8 ligase). This modification is primarily known for its role in regulating cullin subunits of cullin-RING ubiquitin ligases (CRLs), the largest class of E3 ubiquitin ligases. The conjugation of NEDD8 to the cullin subunit is essential for CRL activation, thereby influencing protein ubiquitination and degradation [19,20]. In addition to cullins, several non-cullin targets of neddylation have been identified in recent years [21,22]. Given its involvement in various biological processes, aberrant neddylation has been strongly associated with multiple human diseases, including cancer [22]. Overactive neddylation has been observed in diverse cancer tissues, where dysregulated neddylation can contribute to cancer progression by disrupting cell cycle control, apoptosis and DNA repair mechanisms [19]. Despite its significance, the role of the neddylation pathway in the progression of PJIs remains unclear.

Several neddylation inhibitors targeting E1 (NAE inhibitors), E2 (UBF2M and UBE2F inhibitors) and E3 (RBX1/RBX2/SAG inhibitors) have been discovered and developed [23–26]. However, most neddylation inhibitors with potential clinical advancement primarily focus on the E1 NEDD8-activating enzyme (NAE), a heterodimer composed of APPBP1 (amyloid precursor protein-binding protein 1) and UBA3 (ubiquitin-like modifier activating enzyme 3) [23–26]. Among these NAE inhibitors, MLN4924 and TAS4464 are well-characterized as specific neddylation inhibitors [23,24]. TAS4464 has shown strong anti-tumor activity in multiple preclinical models, including hematologic and solid malignancies [24,27]. Given that TAS4464 is more potent and specific than MLN4924 in inhibiting NAE [24], it holds promise for enhancing therapeutic efficacy while minimizing off-target effects.

In this study, we explored the relationship between the neddylation pathway and the regulation of specific immunosuppressive cell types involved in *S. aureus* biofilm infection models both *in vitro and in vivo*. Our findings suggest that inhibiting the neddylation pathway with TAS4464 effectively reduced *S. aureus* biofilm-induced expansion of MDSCs and M2 macrophages in cultured mouse bone marrow cells and a mouse PJI model. Importantly, TAS4464 treatment in the mouse PJI model significantly reduces osteolytic lesions and decreases the expression of several inflammation-related cytokines as well as protein markers linked to the activation of MDSCs and M2 macrophages.

2. Materials and methods

2.1. Bacterial strain, culture media, and reagents

The MRSA stain of *Staphylococcus aureus* (ATCC43300) was obtained from the Bioresource Collection and Research Center (BCRC, Taiwan). TAS4464 was purchased from MedChemExpress (#HY-128586; MCE, USA). TAS4464 was dissolved in DMSO (#D2650; Sigma) before the experiments were performed. RPMI 1640 medium was obtained from GIBCO (#11875095; Grand Island, NY, USA), and brain heart infusion (BHI) broth used for culturing *S. aureus* was obtained from Bacto (#237500; Detroit, MI, USA).

2.2. Cultivation of Staphylococcus aureus and biofilm preparation

S. aureus biofilms were prepared by culturing the bacteria in BHI media for four days, as previously described [17]. The resulting biofilm communities were harvested by centrifugation at 3900 ×g for 15 min and subsequently sterilized by autoclaving. The biofilms were then resuspended in RPMI 1640 medium, and the protein concentration was measured using a BCA protein assay kit (#23225; Thermo Fisher Scientific). The biofilm suspension was adjusted to a final concentration of 0.3 mg/ml in RPMI 1640 medium. For the *in vivo* animal study, *S. aureus* pellets were collected by centrifugation, washed three times with normal saline, and resuspended in the same solution. Bacterial concentrations were estimated by measuring the absorbance at 600 nm (A_{600}) using a spectrophotometer, and colony forming units (CFU) were counted on agar plate to validate the optical measurements.

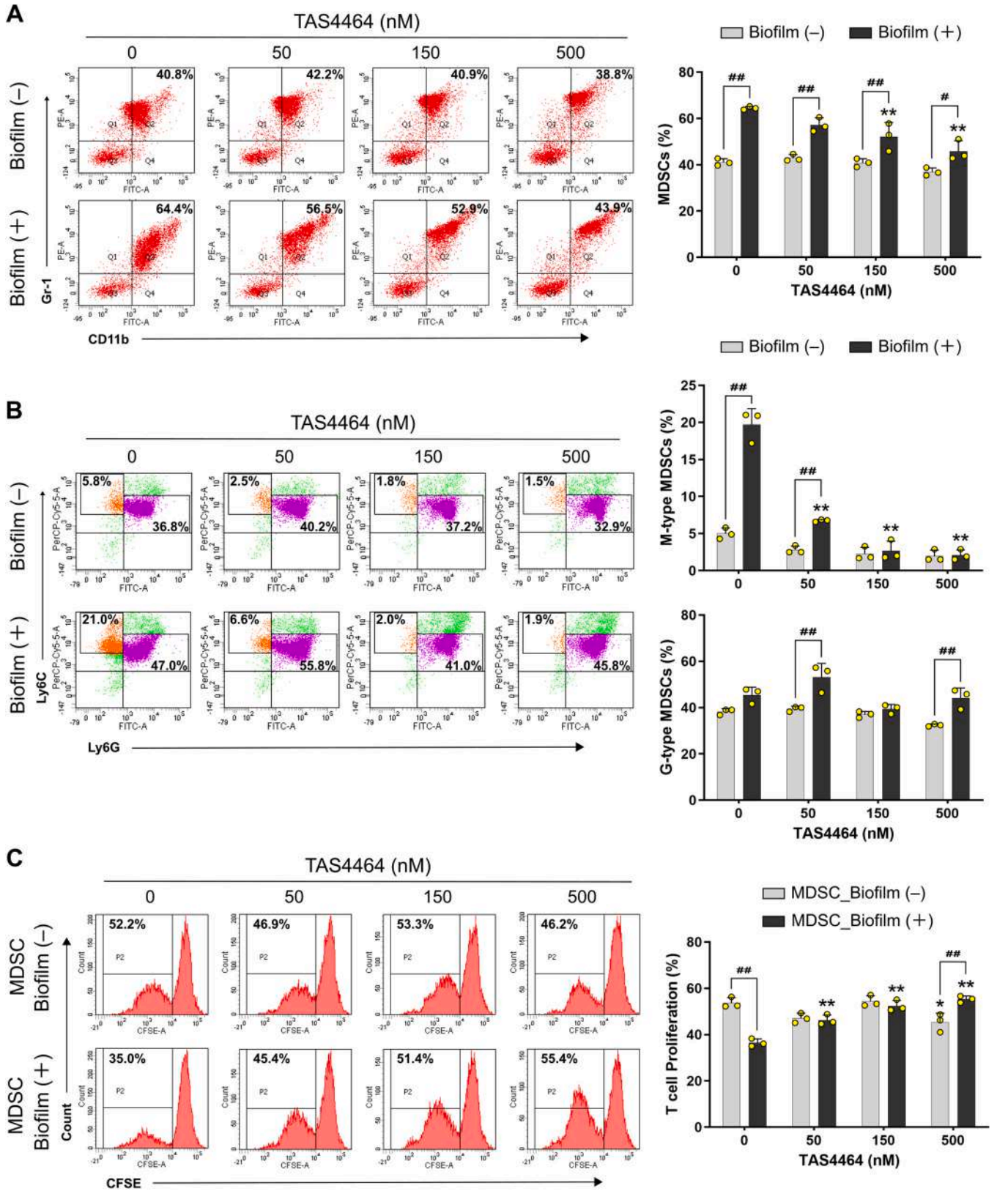
2.3. Animal experiments

Male C57BL/6 J mice (8–12 weeks old, 22–25 g), were obtained from the National Laboratory Animal Center in Taiwan. They were acclimated in a controlled environment (25°C, 50 ± 10 % humidity) under a 12-hour light/dark cycle (lights on 07:00–19:00). All animal experiments were approved by the Institutional Animal Care and Use Committee of Chang Gung Memorial Hospital (IACUC permit number: 2023092503), and conducted in accordance with the Animal Protection Law of the Ministry of Agriculture, Executive Yuan (Taiwan), and the National Research Council (USA) guidelines for the care and use of laboratory animals.

A mouse model of PJI induced by with *S. aureus* infection was established as previously descried [17]. Briefly, male C57BL/6 J mice were anesthetised using a 1:1 mixture of Zoletil 50 and Rompun 2 % (1 ml/kg). The skin around the right knee was disinfected with povidone-iodine, followed by a small incision. A 26-gauge needle was used to create a burr hole in the femoral intercondylar notch, reaching into the intramedullary canal. A 0.5 cm segment of orthopedic-grade Kirschner (K) wire (0.6 mm diameter) was implanted into the intramedullary canal. Subsequently, 2×10^3 CFU of *S. aureus* was inoculated. The burr hole was sealed with bone wax, and the incision was closed using coated Vicryl* 4–0 sutures. For analgesia, mice received intramuscular injections of Ketorolac (0.5–1 mg/kg) immediately after surgery and again 24 h later. The mice were randomly divided into six groups (n = 4 per group): (1) Sham group (sterile implant only); (2) TAS4464 only group (40 mg/kg in 20 % DMSO); (3) *S. aureus*-infected group treated with 20 % DMSO (vehicle control); (4–6) *S. aureus*-infected groups treated with TAS4464 at 10, 20, or 40 mg/kg in 20 %DMSO. TAS4464 was administered intraperitoneally three times per week, starting three days after infection. Two weeks after infection, X-ray imaging (MobileArt evolution, SHIMADZU) was performed. The mice were then euthanized, and their femurs were fixed in 10 % formalin. After fixation, micro-CT (nanoScan® SPECT/CT, Mediso) was used to assess bone healing.

2.4. In vitro co-culture of mouse bone marrow cells with S. aureus biofilm and TAS4464

Mouse bone marrow cells (BMCs) were isolated from femurs were seeded in a 6-well plates. The cells were co-cultured with *S. aureus* biofilm (0.3 mg/ml) and varying concentrations of TAS4464, which were loaded into transwell inserts with a 0.4 μm pore size. All cultures were maintained in RPMI 1640 medium supplemented with 10 % fetal bovine serum (FBS). After 48 h of co-culture, cells were harvested and stained with specific antibodies for flow cytometry analysis (BD FACSCanto II). The following antibodies were used for surface marker staining: CD11b-FITC (#553310; BD Biosciences), Gr-1-PE (#553128; BD Biosciences), Ly6G-APC (#560599; BD Bioscience), Ly6C-PerCP-Cy5.5 (#45–5932; eBioscience), F4/80-PE (#12–4801; eBioscience), CD80-APC (#104713; Biolegend), and CD206-PerCP-Cy5.5 (#141715; Biolegend). Cells were incubated with antibodies for 30 min at room



(caption on next page)

Fig. 1. TAS4464 inhibits the expansion and immunosuppressive activity of MDSCs in cultured mouse bone marrow cells (BMCs) stimulated by *S. aureus* biofilm. (A) The effects of TAS4464 (50, 150 and 500 nM) on MDSC expansion were assessed in BMC cultures with or without *S. aureus* biofilm stimulation (0.3 mg/ml). After 48 h of treatment, the proportions of MDSCs ($CD11b^+Gr\text{-}1^+$) were analyzed by flow cytometry (left panel). Quantitative data (right panel) represent the mean ± SD from three independent experiments. $^{**}P < 0.01$ versus corresponding groups without TAS4464 treatment; $^{\#}P < 0.05$, $^{\#\#}P < 0.01$ versus corresponding groups without biofilm stimulation. (B) The effects of TAS4464 on the proportions of monocytic MDSCs (M-MDSCs, $CD11b^+Ly6C^{high}Ly6G^-$) and granulocytic MDSCs (G-MDSCs, $CD11b^+Ly6C^{low}Ly6G^+$) were evaluated under the conditions. After 48 h of treatment, the proportions of M-MDSCs and G-MDSCs were determined by flow cytometry (left panel), and the results are presented as mean ± SD from three independent experiments (right panel). $^{**}P < 0.01$ versus corresponding groups without TAS4464 treatment; $^{\#\#}P < 0.01$ versus corresponding groups without biofilm stimulation. (C) The effects of TAS4464 on the suppressive function of MDSCs was assessed using cells sorted from BMCs cultured with or without *S. aurus* biofilm. Purified MDSCs were co-cultured with CFSE-labelled T cells at a 1:2 ratio, and T-cell proliferation were analyzed. Quantitative results (right panel) are shown as mean ± SD from three independent experiments. $^{*}P < 0.05$, $^{**}P < 0.01$ versus corresponding groups without TAS4464 treatment; $^{\#\#}P < 0.01$ versus corresponding groups without biofilm stimulation.

temperature in the dark. A total of 10, 000 events per sample were acquired, and data were analyzed using FACSDiva software (BD Biosciences).

2.5. Isolation of MDSCs from mouse bone marrow cells

Mouse BMCs were co-cultured with *S. aureus* biofilm and varying concentrations of TAS4464 for 48 h. Following incubation, $CD11b^+Gr1^+$ double-positive cells (MDSCs) were labelled using FITC-conjugated anti-CD11b and PE-conjugated anti-Gr1 antibodies. The labelled cells were then sorted using a FACSAria Fusion cell sorter (BD Biosciences, Franklin Lakes, NJ, USA). Flow cytometry was performed to confirm the purity of the isolated cell population.

2.6. T cell proliferation assays

T cell proliferation assays were performed as described previously [17]. Briefly, spleen T cells were isolated by gently pressing mouse spleens through a strainer using the plunger end of a syringe to obtain a single-cell suspension. The cells were then washed with PBS and treated with ACK lysing buffer (#A10492–01; Thermo Fisher Scientific). The resulting cell suspension were loaded onto a nylon wool column pre-equilibrated with 2 ml of warm RPMI medium, washed with additional RPMI, sealed, and incubated at 37°C in 5 % CO2 for 45 min. T cells were subsequently eluted using 10 ml of warm RPMI medium. Purified MDSCs from BMCs were then co-cultured with CFSE-labelled spleen T cells that had been stimulated with Dynabeads Mouse T-Activator CD3/CD28 (#11452D, Gibco) for 48 h. The ratio of MDSCs to T cells (2×10^5 cells/well) was 1:2 in a 96-well round bottom plate containing RPMI 1640 with 10 % FBS. After 72 h of co-culture, the proliferation of CFSE-labelled T cells was examined by flow cytometry.

2.7. Preparation of blood samples for flow cytometry analysis

Blood samples were collected for flow cytometry analysis to assess dynamic changes in peripheral immune cell populations in mice. Red blood cells were lysed using ACK lysing buffer, and the remaining leukocytes were resuspended in PBS containing 2 % FBS. The cells were then stained with CD11b-FITC, Gr-1-PE, F4/80-PE and CD206-PerCP-Cy5.5 for 30 min at room temperature, protected from light. Flow cytometric analysis was performed using a BD FACSCanto II system.

2.8. Analysis of cytokines in culture medium and plasma

Cytokine levels in cell culture supernatants or in blood plasma were measured using the BD Cytometric Bead Array Mouse Inflammation kit (#552364; BD Biosciences) according to the manufacturer's instructions. Briefly, 50 μL of cell culture supernatant or blood plasma was incubated with capture beads and the PE-conjugated mouse inflammation detection reagent. After incubation, the samples were washed with wash buffer. Flow cytometry data were acquired using a BD FACSCanto II flow cytometer and analyzed with FACSDiva software.

2.9. Western blot analysis

Western blot analysis was performed as described previously [28]. Briefly, cell samples were lysed on ice for 15 min using the RIPA Lysis Buffer System (#sc-24948, Santa Cruz), followed by centrifugation at 13,000 rpm for 20 min at 4°C. Protein concentrations were determined using the Pierce BCA Protein Assay (#23225; Thermo Fisher Scientific). Nuclear protein fractions were prepared using the Fraction-PREP Cell Fractionation kit (#ab288085; Abcam). Equal amounts of proteins were separated by SDS-PAGE and transferred onto PVDF membranes (#ISEQ00010, Millipore). Membranes were then incubated with specific primary antibodies, including those against NEDD8 (#2745; Cell Signaling), APPBP1 (#sc-390002; Santa Cruz), UBA3 (#sc-377272; Santa Cruz), Arg-1 (#16001–1-AP; Proteintech), iNOS (#06–573; Millipore), SOD2 (#ab68155; Abcam), phospho-STAT3 (#9145; Cell Signalling), STAT3 (#ab68153; Abcam), NFκB p65 (#ab32536; Abcam), Histone H3 (#4499; Cell Signaling), and β-Actin (#sc-47778; Santa Cruz). Following overnight incubation at 4°C, membranes were washed and incubated with HRP-conjugated secondary antibodies for 1 h at room temperature. Protein bands were visualized using the SuperSignal West Femto Maximum Sensitivity Substrate (#34096, Thermo Fisher Scientific) and imaged using the G:Box Chemi XX9 (SYNGENE). Band intensities were quantified using Image J software (Version 1.49 v; National Institutes of Health, Bethesda, MD, USA).

2.10. Hematoxylin and eosin (H&E) staining and immunohistochemistry staining

The femurs of sacrificed mice were fixed in 10 % formalin for at least 48 h. Prior to embedding, femur samples were demineralized using 10 % ethylenediaminetetraacetic acid to remove calcium. Following demineralization, the samples were dehydrated, embedded in paraffin, and sectioned at a thickness of 4 μm. The sections were deparaffinized with xylene, dehydrated in a graded ethanol series (100 %, 95 %, 80 %, and 75 %), and rinsed with sterilized water. For hematoxylin and eosin (H&E) staining, slides were re-dehydrated using 80 %, 95 %, and three changes of 100 % ethanol, then cleared with xylene and mounted with s a sealing solution. The inflammation score index was measured according to the method described by Rigoni et al. [29].

For immunohistochemistry (IHC), slides underwent dewaxingg, dehydration, rehydration, antigen retrieval, and blocking. Sections were incubated overnight with the following primary antibodies: anti-NEDD8 (1:200, #2745; Cell signaling), anti-NF-κB p65 (1:100, #ab32536; Abcam), anti-TNF-α (1:200, #ab6671, Abcam), and anti-IL-6 (1:100, #bs-0782R; Bioss), followed by incubation with anti-rabbit secondary antibodies. Images were acquired using the Pannoramic SCAN (3DHISTECH). Protein expression levels of NEDD8, NFκB p65, TNF-α, and IL-6 were quantified using H-score method, calculated as follows: H-Score = Σ(pi × i) = (percentage of weak intensity × 1) + (percentage of moderate intensity × 2) + (percentage of strong intensity × 3).

2.11. Data analyses and statistics

All data were evaluated and graphed with Microsoft Excel software

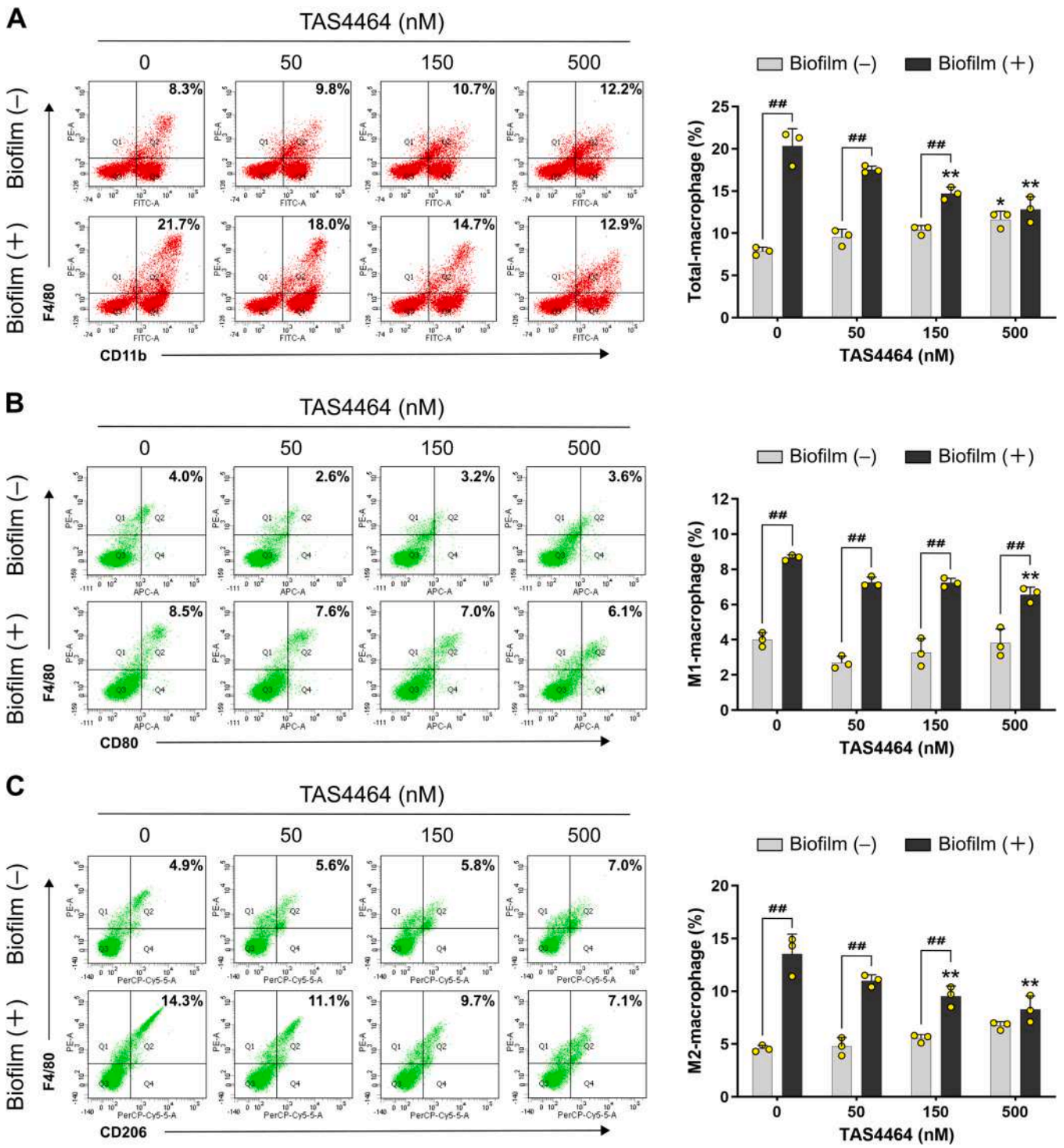


Fig. 2. TAS4464 reduces the overall macrophage population, with a pronounced effect on M2-macrophages, in biofilm-induced BMCs. Mouse BMCs were either left untreated or treated with S. aureus biofilm (0.3 mg/ml) in the presence of increasing concentrations of TAS4464 (50, 150 and 500 nM) for 48 h. The proportions of (A) total macrophages ($CD11b^+F4/80^+$), (B) M1-macrophages ($CD11b^+F4/80^+CD80^+$), and (C) M2-macrophages ($CD11b^+F4/80^+CD206^+$) were analyzed by flow cytometry. The right panels present the mean ± SD from three independent experiments. $^*P < 0.05$, $^{**}P < 0.01$ compared to the corresponding group without TAS4464 treatment; $^{\#\#}P < 0.01$ compared to the corresponding group without biofilm stimulation.

(Microsoft, Redmond, WA, USA). Results were expressed as the mean ± standard deviation (SD). Statistical analysis was performed using one-way or two-way analysis of variance (ANOVA) followed by Tukey's post-hoc test, conducted with GraphPad Prism (GraphPad Software, San Diego, CA, USA). A *P*-value less than 0.05 was considered statistically significant.

3. Results

3.1. TAS4464 inhibits MDSC expansion and function in S. aureus biofilm-induced mouse bone marrow cells

Previously, we demonstrated that *S. aureus* biofilm enhances the expansion and immunosuppressive activity of MDSCs in cultured mouse

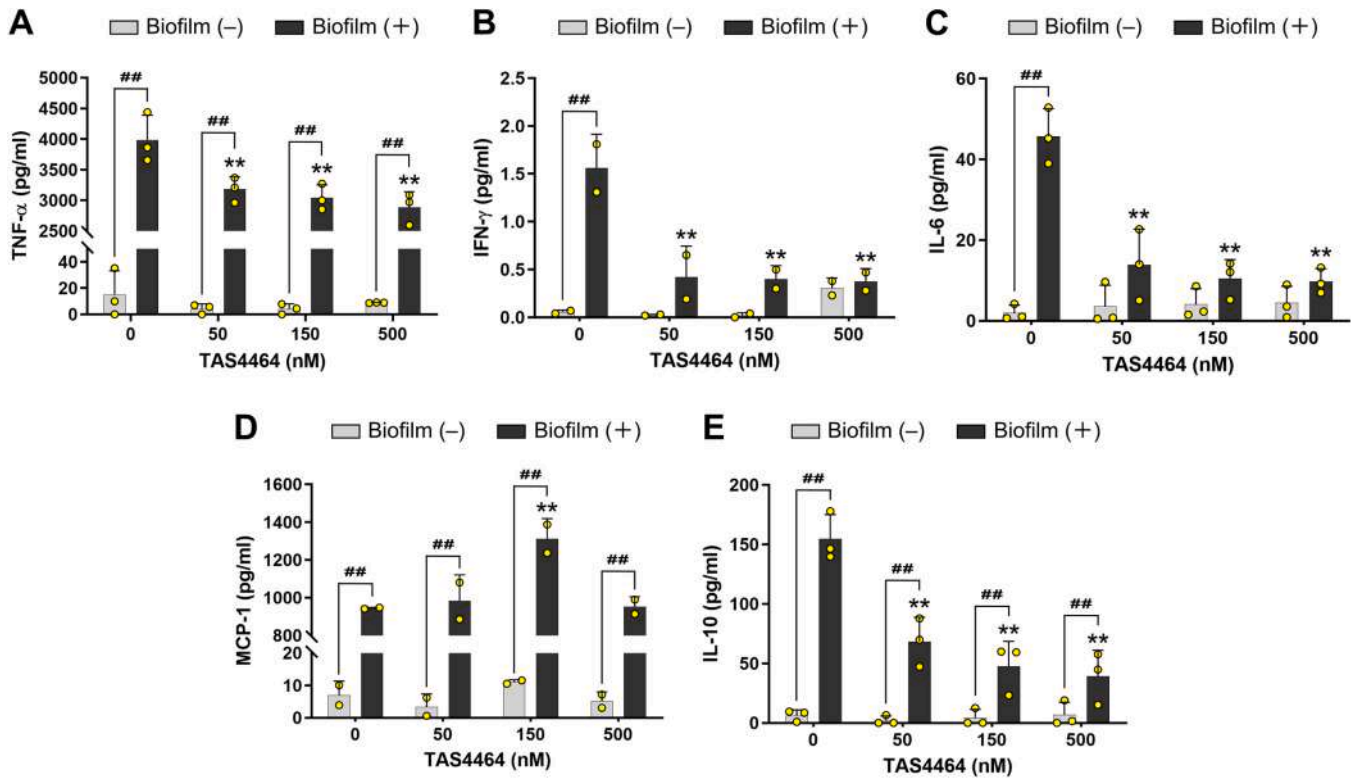


Fig. 3. Effects of TAS4464 on the secretion of pro-inflammatory and anti-inflammatory cytokines in cultured BMCs with or without biofilm stimulation. Mouse BMCs were treated biofilm and TAS4464 for 48 h, and then cytokine levels were measured using a CBA kit followed by flow cytometry. The secretion of pro-inflammatory cytokines, including TNF-α (A), IFN-γ (B), IL-6 (C) and MCP-1 (D), as well as the anti-inflammatory cytokine IL-10 (E) were assessed in each treatment group. Data are presented as the mean ± SD from three independent experiments. $^{**}P < 0.01$ versus the corresponding group without TAS4464 treatment; $^{\#\#}P < 0.01$ versus the corresponding group without biofilm stimulation.

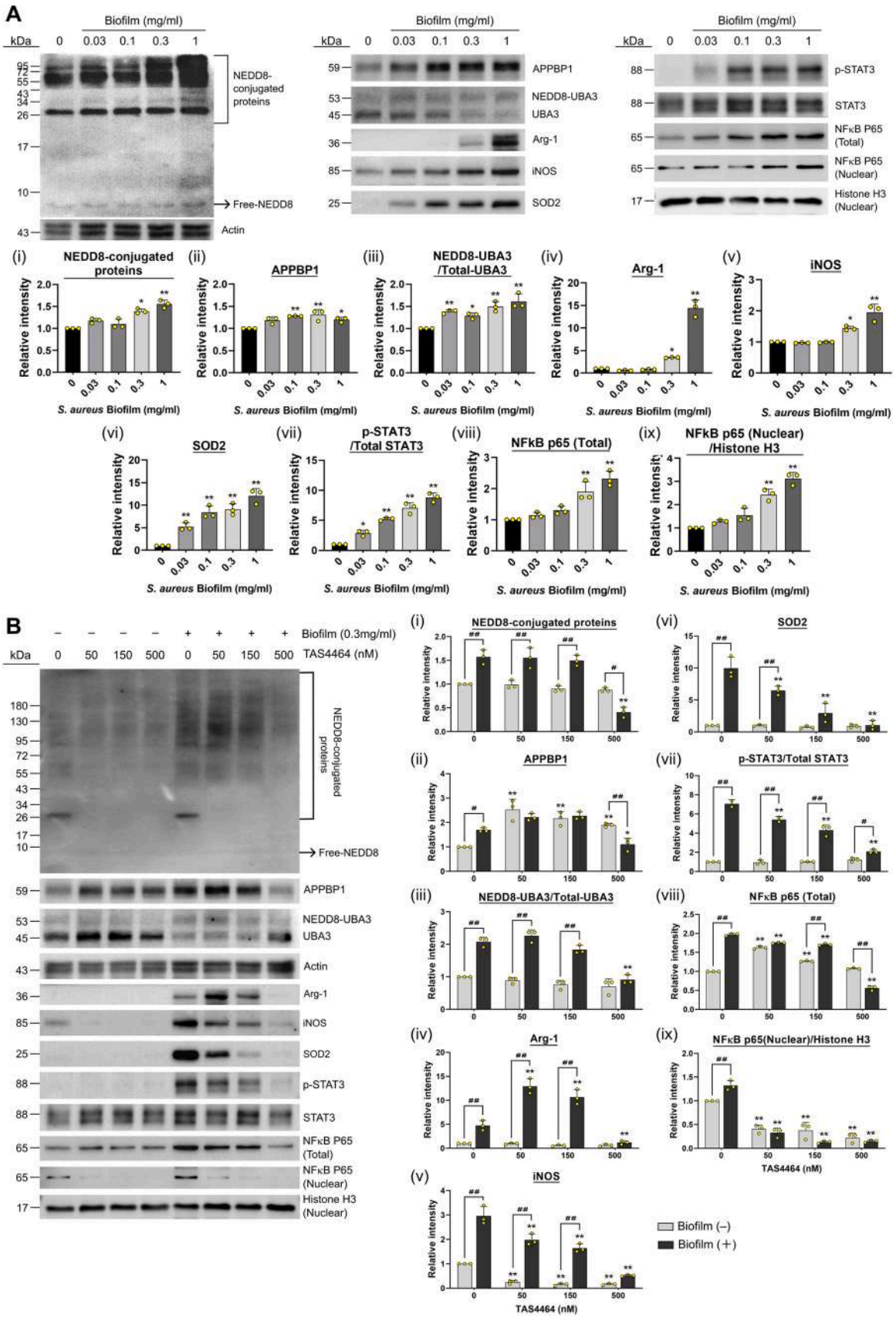
bone marrow cells (BMCs) [17]. Herein, we investigated whether neddylation inhibition affects MDSC expansion and function in biofilm-induced BMCs. To assess the impact of neddylation inhibition, mouse BMCs were treated with varying concentrations of TAS4464 (50, 150 and 500 nM), with or without biofilm exposure (0.3 mg/ml). Notably, TAS4464 at the concentrations (50–500 nM) displayed only weak cytotoxic effects on mouse BMCs (Figure S1). As expected, *S. aureus* biofilm exposure for 48 h increased MDSC ($CD11b^+Gr\text{-}1^+$) proportions by 1.5-fold, from 41 % in untreated cells to 64 % in biofilm-exposed cells (Fig. 1A). Notably, TAS4464 treatment significantly reduced MDSC expansion in biofilm-stimulated BMCs in a dose-dependent manner, decreasing from 64 % to 56 %, 53 % and 44 % at 50 nM, 150 nM, and 500 nM, respectively. However, TAS4464 had minimal effects on MDSC expansion in BMCs not exposed to *S. aureus* biofilm stimulation under the same conditions (Fig. 1A).

MDSCs can be classified into two main subtypes: monocytic-MDSCs (M-MDSCs; $CD11b^+Ly6C^{high}Ly6G^-$) and granulocytic-MDSCs (G-MDSCs; $CD11b^+Ly6C^{low}Ly6G^+$) [30–32]. We then analyzed the changes in these MDSC subtypes under experimental conditions. Upon exposure of mouse BMCs to *S. aureus* biofilm, the proportion of M-MDSCs significantly increased by up to 3.5-fold, rising from 6 % to 21 % (Fig. 1B). In contrast, the proportion of G-MDSCs exhibited only a slightly increase, from 37 % to 47 % (Fig. 1B). Notably, we found that TAS4464, at concentrations of 50 nM, 150 nM and 500 nM, significantly reduced the proportion of M-MDSCs in biofilm-treated BMCs, lowering it from 21 % to 7 %, 2 %, and 2 %, respectively (Fig. 1B). However, TAS4464 did not show a noticeable effect on the proportion of G-MDSCs in biofilm-treated BMCs. These findings indicate that TAS4464 effectively inhibits the expansion of MDSCs, particularly M-MSDCs, in biofilm-treated BMCs.

To investigate whether TAS4464 influences the immunosuppressive function of biofilm-stimulated MDSCs, MDSCs were first isolated from mouse BMCs that were either untreated or exposed to *S. aureus* biofilm, along with different concentrations of TAS4464 (Fig. 1C). Subsequently, the isolated MDSCs were co-cultured for 72 h with CFSE-labeled responder T cells, which had been activated using anti-CD3/CD28 antibody-conjugated magnetic beads. Consistent with our previous studies, MDSCs from biofilm-treated BMCs demonstrated stronger immunosuppressive activity than those from non-biofilm-treated BMCs, as indicated by a reduction in T cell proliferation from 52 % to 35 % (Fig. 1C). Importantly, the enhanced immunosuppression activity of biofilm-activated MDSCs was progressively diminished with increasing concentrations of TAS4464 (50, 150 and 500 nM), thereby leading to the T cell proliferation rate from 35 % to 45 %, 51.6 % and 55 %, respectively (Fig. 1C). Taken together, these findings suggest that TAS4464 may effectively prevent the expansion and activity of MDSCs in cultured BMCs stimulated by *S. aureus* biofilm.

3.2. TAS4464 suppresses macrophage generation, particularly M2 marcophages, in cultured BMCs stimulated by S. aureus biofilm

Previous studies have shown that exposure to *S. aureus* biofilm prompts M-MDSCs to differentiate into M2 macrophages [17], which differ from classically activated M1 macrophages. M1 macrophages are considered to enhance inflammatory responses and support host defence against bacterial infections, whereas M2 macrophages suppress inflammation, facilitating bacterial survival [16,33–35]. Therefore, we evaluated changes in total macrophage populations, as well as M1 and M2 macrophages, in mouse BMCs following *S. aureus* biofilm stimulation and TAS4464 treatment. As shown in Fig. 2A, stimulation with *S. aureus* biofilm significantly increased the total macrophage population ($CD11b^+F4/80^+$) from 8 % to 22 %. TAS4464 treatment at 150 nM and



(caption on next page)

Fig. 4. TAS4464 suppresses the upregulation expression of neddylation pathway components and MDSC-associated proteins induced by *S. aureus* biofilm in cultured BMCs. (A) *S. aureus* biofilm induces the expression of neddylation pathway components and MDSC-associated proteins in cultured BMCs. Mouse BMCs were treated with increasing concentrations of *S. aureus* biofilm (0.03, 0.1, 0.3 and 1 mg/ml). Cell lysates were analyzed by Western blot (top panels) for neddylation pathway components (NEDD8-conjugated proteins, APPBP1, and UBA3) and MDSC-associated markers (Arg-1, iNOS, SOD2, phospho-STAT3, total NF-κB, and nuclear NF-κB). Quantitative analyses are shown in bottom panels for: (i) NEDD8-conjugated proteins, (ii) APPBP1, (iii) UBA3, (iv) Arg-1, (v) iNOS, (vi) SOD2, (vii) phospho-STAT3, (viii) total NF-κB, and (ix) nuclear NF-κB. Data are presented as mean ± SD from three independent experiments. $^{*}P < 0.05$, $^{**}P < 0.01$ versus the groups without biofilm treatment. (B) TAS4464 reduces the expression of biofilm-induced neddylation pathway components and MDSC-associated proteins. Representative Western blot results are shown (left panels), with corresponding quantification (right panels). Data are presented as mean ± SD from three independent experiments. $^{**}P < 0.01$ versus groups without TAS4464 treatment; $^{\#}P < 0.05$, $^{\#\#}P < 0.01$ versus groups without biofilm stimulation.

500 nM effectively reduced this increase, bringing macrophage levels down to 15 % and 13 %, respectively. Further analysis of M1 macrophages ($CD11b^{+}F4/80^{+}CD80^{+}$) and M2 macrophages ($CD11b^{+}F4/80^{+}CD206^{+}$) showed that both populations were significantly elevated by *S. aureus* biofilm (Figs. 2B and 2C). Although treatment with higher concentrations of TAS4464 reduced both M1 and M2 macrophage populations in biofilm-stimulated BMCs, we noticed that M2 macrophages appeared more sensitive to TAS4464 inhibition than M1 macrophages (Figs. 2B and 2C). These results indicate that TAS4464 may inhibit the generation of total macrophages, particularly M2-macrophages, in *S. aureus* biofilm-stimulated BMCs.

3.3. TAS4464 partially reduces the levels of specific inflammation-related cytokines in cultured BMCs induced by S. aureus biofilm

The levels of pro-inflammatory cytokines such as TNF-α, IFN-γ, IL-6 and MCP-1, as well as an anti-inflammatory cytokine IL-10, which are closely associated with PJIs [36,37], were measured in cultured BMCs treated with *S. aureus* biofilm and TAS4464. After 48 h of treatment with biofilm and different concentrations of TAS4464, cytokine levels in the culture media were quantified using a cytometric bead assay (CBA) system. As illustrated in Fig. 3, stimulation of cultured BMCs with biofilm significantly increased the levels of all tested cytokines, including TNF-α, IFN-γ, IL-6, MCP-1, and IL-10 (Fig. 3A–E). Notably, TAS4464 dose-dependently reduced the levels of all tested cytokines, except MCP-1 (Fig. 3A–E). However, in non-biofilm samples, TAS4464 had no significant effect on cytokine levels.

3.4. S. aureus biofilm enhances the neddylation pathway in cultured BMCs

Based on the findings above, aberrant neddylation may occur in biofilm-stimulated BMCs, potentially contributing to the enhanced expansion of immunosuppressive cells (MDSCs and M2 macrophages) and the upregulation of inflammation-related cytokines. To determine the underlying molecular mechanism, we co-cultured mouse BMCs with *S. aureus* biofilm and analyzed the expression levels of key components of the neddylation pathway, metabolic enzymes, and signaling mediators by Western blot analysis. The examined neddylation pathway components included NEDD8, APPBP1 (amyloid precursor protein-binding protein 1) and UBA3 (ubiquitin-like modifier activating enzyme 3). Metabolic enzymes analyzed were Arg-1 (arginase-1), iNOS (inducible nitric oxide synthase), and SOD2 (superoxide dismutase 2), while signaling mediators and transcription factors included pSTAT3 (phosphorylated signal transducer and activator of transcription 3) and NF-κB (nuclear factor kappa-light-chain-enhancer of activated B cells). Among these target proteins, APPBP1 and UBA3 are the subunits of the E1 NEDD8-activating enzyme [26], and the other examined proteins are commonly overexpressed in MDSCs or M2 macrophages [30,32,38–40].

After 48 h of treatment with varying concentrations of *S. aureus* biofilm (0, 0.03, 0.1, 0.3, 1 mg/ml), we observed a dose-dependent increase in total NEDD8-modified proteins, APPBP1 and NEDD8-conjugated UBA3 (Fig. 4A, i–iii). These results indicate that *S. aureus* biofilm significantly induces the neddylation pathway in cultured BMCs. In addition, *S. aureus* biofilm markedly upregulated the expression of markers associated with MDSCs or M2 macrophages, including Arg-1, iNOS, SOD2, pSTAT3, total NF-κB, and nuclear NF-κB (Fig. 4A, iv–ix). These findings suggest a potential link between an overactive neddylation pathway and *S. aureus* biofilm-induced immunosuppression in BMCs.

To further confirm the importance of neddylation in *S. aureus* biofilm-induced immunosuppression, we evaluated the effect of TAS4464 on the expression of target proteins. As expected, TAS4464 downregulated total protein neddylation in biofilm-stimulated BMCs in a dose-dependent manner (Fig. 4B, i). Furthermore, TAS4464 reduced the proportion of NEDD8-conjugatged UBA3 in a dose-dependent manner (Fig. 4B, iii). Noteworthily, TAS4464 treatment at 50 and 150 nM concentrations paradoxically enhanced APPBP1 expression in non-biofilm-treated and biofilm-treated BMCs (Fig. 4B, ii), suggesting that a compensatory gene expression response upon NEDD8-activating enzyme inhibition.

Additionally, we assessed the expression of protein markers associated with MDSCs and M2 macrophages, including Arg-1, iNOS, SOD2, pSTAT3, total NF-κB, nuclear NF-κB. TAS4464 treatment generally led to a dose-dependent decrease in these factors (Fig. 4B, iv–ix). Notably, Arg-1 expression exhibited a biphasic response, with an initial increase at 50 nM before gradually decrease at higher concentrations (Fig. 4B, iv). These results highlight the critical role of the neddylation pathway in *S. aureus* biofilm-induced activation of MDSCs and M2 macrophages, and suggest that targeting this pathway could modulate the function of MDSCs and M2 macrophages in BMCs.

3.5. TAS4464 treatment promotes the recovery of osteolytic lesions in a PJI mouse model

To evaluate the therapeutic potential of TAS4464 for treating PJIs, an *in vivo* analysis was conducted using a previously established mouse PJIs model caused by *S. aureus* infection [17]. The experiments included six groups: a sham control group, a TAS4464-only control group, and four PJI groups that were either left untreated or treated with TAS4464 at concentrations of 10, 20 or 40 mg/kg. Herein, the X-ray imaging (Fig. 5A) and micro-CT analysis (Fig. 5B) displayed severe osteolytic bone destruction and pathologic fractures in the PJI group that did not receive TAS4464, whereas the sham-operated and TAS4464-only control groups showed significantly less damage. After intraperitoneal injection of TAS4464 (10, 20, or 40 mg/kg) in PJI groups, osteolytic destruction were significantly reduced compared to the untreated PJI group. Furthermore, hematoxylin and eosin (H&E) staining revealed that TAS4464 treatment effectively reduced inflammation, as evidenced by less tissue swelling, fewer bone fractures, and reduced lymphocyte infiltration (Fig. 5C). The inflammatory index scores for these treated groups were assessed and shown in Fig. 5D. Due to the importance of an immunosuppressive microenvironment for the progression of PJIs to chronic osteomyelitis, we further investigated whether TAS4464 affected the proportion of circulating MDSCs and M2 macrophages in PJI groups. Compared to the sham-operated group, *S. aureus* infection significantly increased the proportions of MDSCs and M2-marcrophages by approximately 1.5 fold (Figs. 5E and 5F). Importantly, TAS4464 treatment significantly reduced these elevated proportions in a dose-dependent manner (Figs. 5E and 5F).

Additionally, various plasma cytokines related to inflammation, including TNF-α, IFN-γ, IL-6, MCP-1, IL-10 and IL-1β, were measured. As

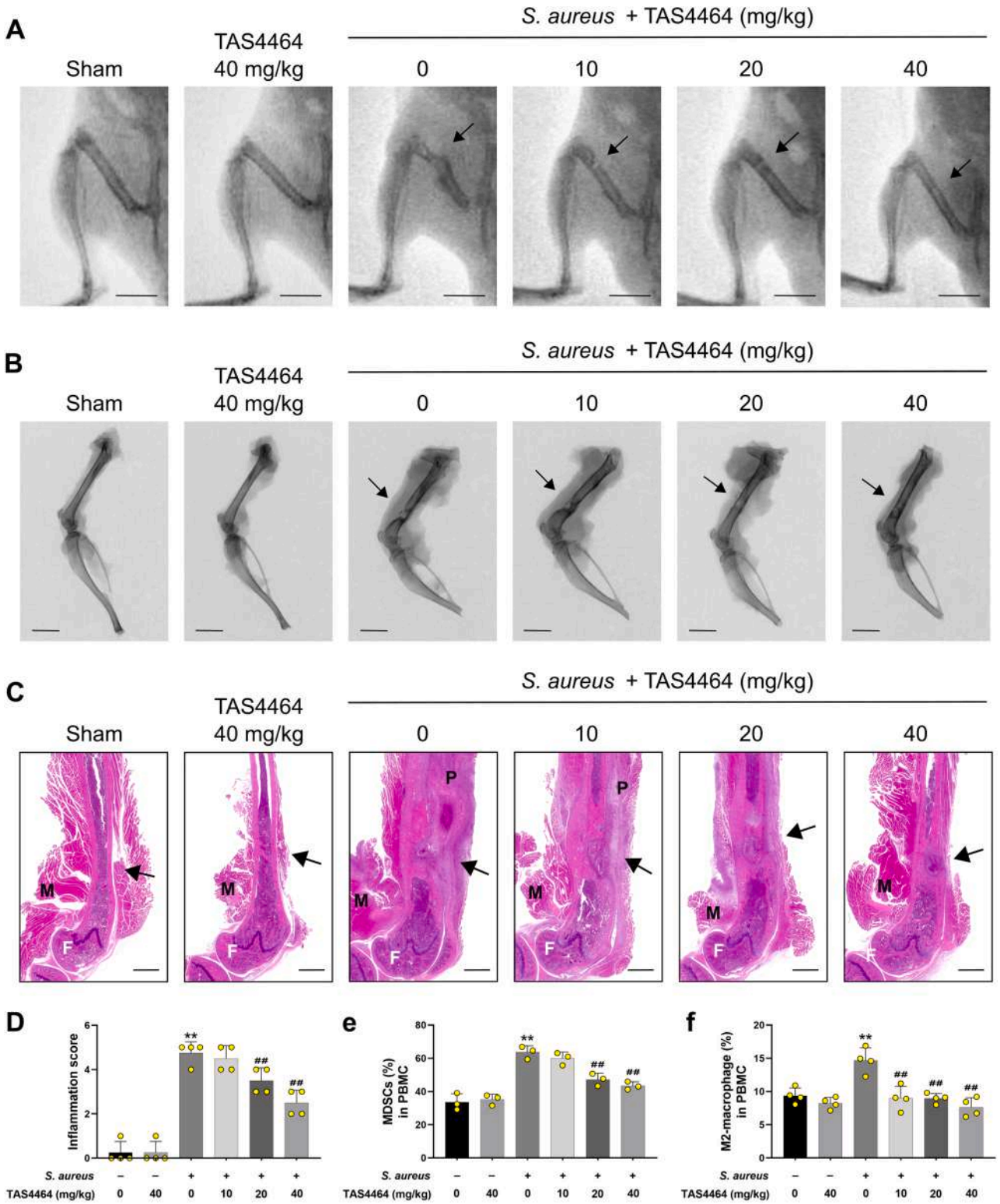


Fig. 5. TAS4464 significantly reduces bone destruction and inflammation in a mouse PJI model infected with *S. aureus*, while decreasing circulating MDSC and M2-macrophage populations. (A) Radiographic images of femurs from mice infected with *S. aureus* and treated with different doses of TAS4464. Black arrows indicate the sites of *S aureus* infection and areas of bone destruction. Scale bars, 5 mm. (B) Micro-Computed Tomography (micro-CT) images of femurs from infected mice treated with different TAS4464 doses. Black arrows highlight infection sites and bone damage. Scale bars, 5 mm. (C) H&E staining of femurs from infected mice following treatment with different doses of TAS4464. F: femur; M: muscle; P: pustule. Scale bars, 1 mm. (D) Inflammatory index score assessment of femurs across treatment groups. (E) Quantification of circulating MDSCs in blood samples from various treatment groups (F) Quantification of circulating M2-macrophages in blood samples from different treatment groups. Quantitative data are presented as mean ± SD (n ≥ 3). $^{**}P < 0.01$ versus untreated group; $^{\#\#}P < 0.01$ versus biofilm-treated group without TAS4464 administration.

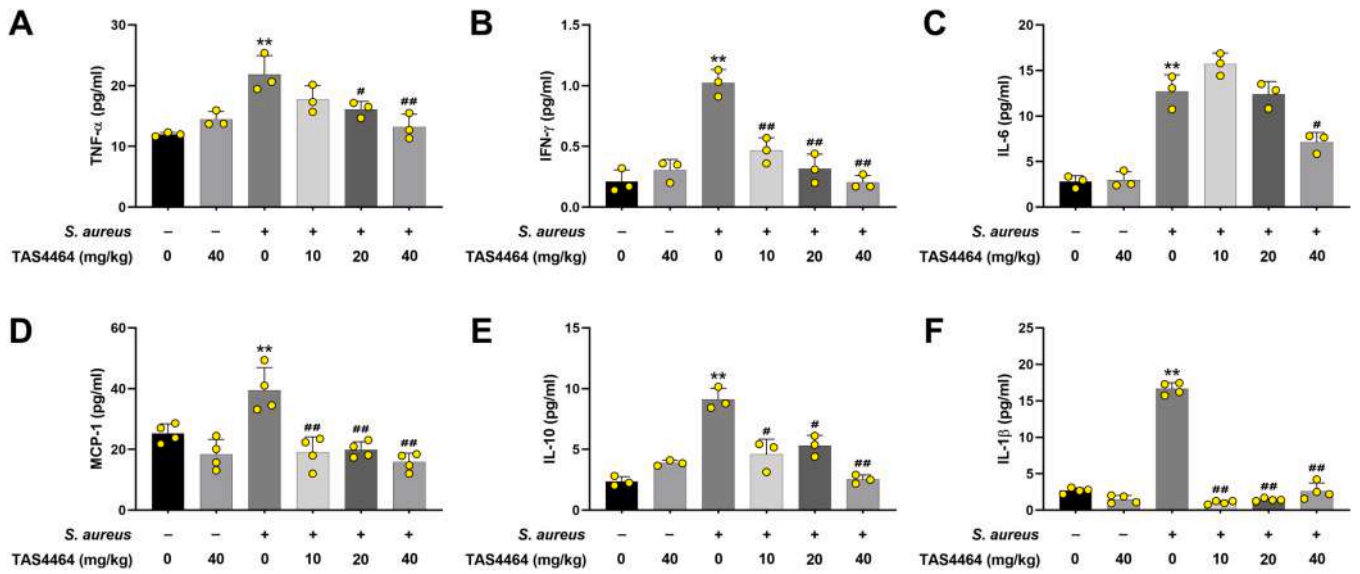


Fig. 6. TAS4464 reduces elevated secretion of both pro-inflammatory and anti-inflammatory cytokines in a mouse PJI model infected with *S. aureus*. Cytokine levels, including TNF-α (A), IFN-γ (B), IL-6 (C), MCP-1 (D), IL-10 (E) and IL-1β (F), were measured in blood samples from each treatment group using a CBA assay. Data are presented as mean ± SD (n ≥ 3). $^{**}P < 0.01$ versus untreated group; $^{\#}P < 0.05$, $^{\#\#}P < 0.01$ versus biofilm-treated group without TAS4464 administration.

expected, *S. aureus* infection markedly increased the plasma levels of these cytokines (Fig. 6A–F). However, treatment with higher concentrations of TAS4464 (20 and 40 mg/kg) significantly reduced these elevated levels (Fig. 6A–F). These results suggest that TAS4464 has potential as a therapeutic agent for *S. aureus* biofilm-infected PJIs.

To gain deeper insight into the molecular inhibitory mechanism of TAS4464 in PJI mice, we analyzed the expression levels of NEDD8, NF-κB, TNF-α and IL-6 at infected sites using immunohistochemistry (IHC). IHC analysis showed that the expression of NEDD8, NF-κB, TNF-α and IL-6 were significantly upregulated at the sites infected with *S. aureus* (Fig. 7 and Figure S2). In contrast, TAS4464 treatment effectively downregulated the expression levels of these markers (Fig. 7A–E). These results suggest that excessive neddylation and NF-κB signaling paly key roles in *S. aureus*-induced PJI, and that suppressing elevated neddylation with TAS4464 mitigates *S. aureus*-induced responses in the mouse model.

4. Discussion

The biofilm produced by *S. aureus* plays a pivotal role in PJI pathogenesis by shielding the bacteria from antibiotic treatment and promoting the expansion of immunosuppressive cells, such as MDSCs and M2 macrophages, which help the pathogen evade host immune responses [15,17]. In this study, we show that treatment with the neddylation inhibitor TAS4464 significantly attenuates *S. aureus* biofilm-induced expansion of MDSCs and M2 macrophages in cultured mouse BMCs (Figs. 1 and 2) and in a mouse PJI model (Fig. 5). Importantly, TAS4464 treatment is also associated with a marked decrease in osteolytic lesions caused by *S. aureus* infection in the mouse PJI model (Fig. 5). These results highlight TAS4464 as a promising therapeutic candidate for mitigating the immunosuppressive effects linked to *S. aureus* infection. To our knowledge, this is the first report to establish a link between neddylation activation and *S. aureus* biofilm-induced immunosuppression.

The immune system is highly dynamic, constantly balancing pro- and anti-inflammatory signals to prevent excessive tissue damage while maintaining homeostasis [41,42]. Similar to other chronic diseases, *S. aureus* biofilm-associated infections exhibit a coexistence of both pro-inflammatory and anti-inflammatory responses. During such infections, inflammatory signaling remains persistently activated due to incomplete pathogen clearance. Elevated levels of pro-inflammatory cytokines, including TNF-α, IFN-γ, IL-6, and IL-1β, are detectable under *S. aureus* biofilm-treated conditions (Figs. 3 and 6). Concurrently, the biofilm promotes anti-inflammatory microenvironment that facilitates immune evasion, such as through the expansion of MDSCs. Notably, we found that *S. aureus* biofilm strongly induces the neddylation pathway in BMCs, both *in vitro* and in a mouse PJI model (Figs. 4 and 7). Western blot analysis revealed upregulation of key neddylation components (e.g., NEDD8-conjugated proteins, APPBP1 and NEDD8-conjugated UBA3) in cultured mouse BMCs, along with increased expression of the master inflammatory regulator NF-κB (Fig. 4). In addition, proteins associated with MDSC expansion and function were also elevated in response to biofilm exposure, including Arg-1, iNOS, SOD2 and pSTAT3 (Fig. 4). Intriguingly, inhibition of the neddylation pathway using TAS4464 significantly reduced both pro- and anti-inflammatory responses in BMCs *in vitro* and in a mouse PJI model. While the precise regulatory mechanisms remain to be fully elucidated, our findings strongly suggest that *S. aureus* biofilm-induced neddylation plays a crucial role in driving both pro- and anti-inflammatory signaling in these contexts (Summary in Fig. 8).

Macrophages can be broadly categorized into M1 and M2 subsets based on their activation states and functions. M1 macrophages play a crucial role in defending against bacterial infections, whereas M2 macrophages suppress inflammation to limit tissue damage but can also promote bacterial survival by inhibiting T-cell proliferation [43–45]. Like MDSCs, M2 macrophages also express high levels of anti-inflammatory markers such as Arg-1 and IL-10 [40,46]. Previous studies have shown that M1 macrophages predominate during the acute/early phase (hours to 1–3 days) of *S. aureus* infection in animal models, but gradually shift toward M2 macrophages during the chronic biofilm phase (days to weeks) [47–50]. In this chronic biofilm phase, both M1 and M2 macrophages may coexist. While M1 macrophages contribute to bacterial clearance, *S. aureus* can exploit M2 polarization to evade immunity, resulting in a prolonged or dysregulated balance. In our study, exposure to *S. aureus* biofilm led to a significant increase in total macrophage populations in cultured BMCs (Fig. 2A), indicating the immune-modulatory effects of bacterial biofilms. However, treatment with TAS4464 substantially reduced the total macrophage population in biofilm-stimulated BMCs. Notably, although TAS4464 decreases both M1 and M2 macrophage proportions, M2 macrophages were more sensitive to its inhibitory effects (Figs. 2B and 2C). While M1 macrophages are essential for infection control, their overactivation can cause

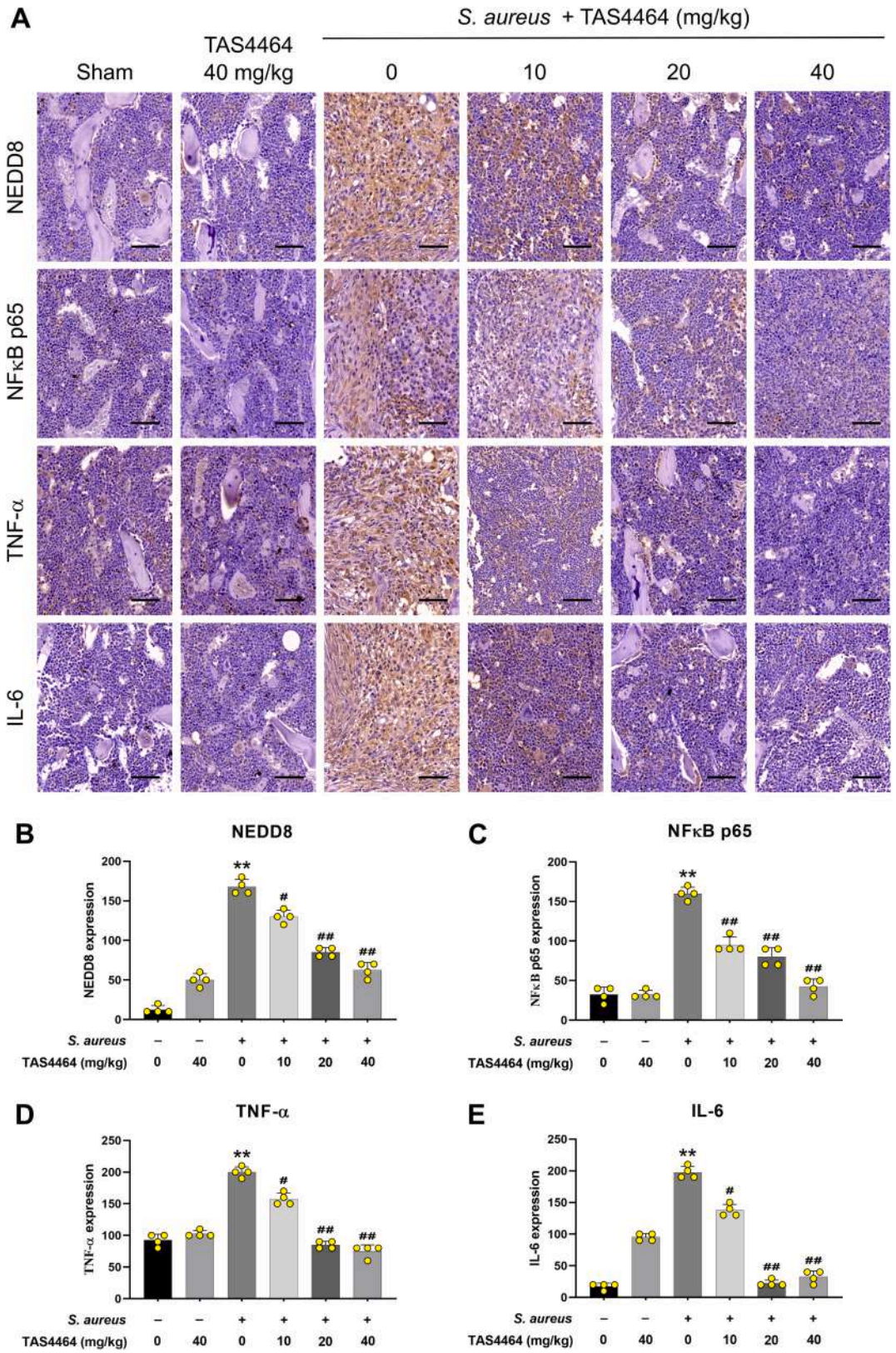


Fig. 7. Immunohistochemical (IHC) analysis of the neddylation pathway and inflammatory markers in a mouse PJI model infected with *S. aureus* following TAS4464 administration. (A) Representative IHC staining for NEDD8, NF-κB, TNF-α and IL-6 in infected femoral tissues from different treatment groups. Scale bars: 50 μm. (B–E) Quantitative analysis of integrated optical density (IOD) for NEDD8, NEDD8, NF-κB, TNF-α and IL-6 staining in infected femoral tissues across different treatment groups. Data are presented as mean ± SD (n = 4). $^{**}P < 0.01$ versus untreated group; $^{\#}P < 0.05$, $^{\#\#}P < 0.01$ versus biofilm-treated group without TAS4464 administration.

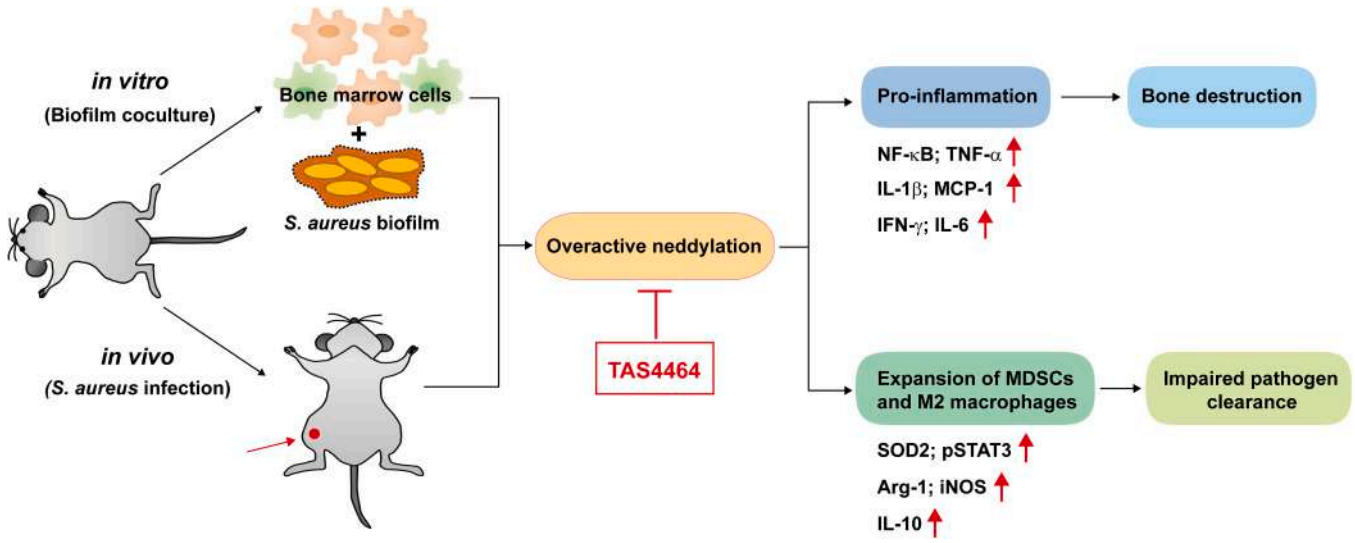


Fig. 8. Proposed model of overactive neddylation driving pro-inflammatory and immunosuppressive responses during *S. aureus* biofilm infection.

tissue damage; thus, TAS4464's partial suppression of M1 macrophages may help limit this risk. In contrast, reducing M2 macrophages, which contribute to immunosuppressive and impaired T-cell function, may enhance the host's ability to clear *S. aureus* biofilms. These findings highlight TAS4464 as a promising therapeutic agents for counteracting the immunosuppressive environment that supports bacterial persistence.

Although TAS4464 can efficiently and consistently reduce *S. aureus* biofilm-induced phenotypes in cultured BMCs and in a mouse PJI model, several important questions remain to be addressed. These include (i) the molecular mechanisms underlying the induction of the neddylation pathway by *S. aureus* biofilm, (ii) the potential for TAS4464 to impact various biological processes induced by *S. aureus* biofilm, and (iii) differential outcomes of TAS4464 observed in the *in vitro* and *in vivo* studies. Fore example, although the effects of TAS4464 on *S. aureus* biofilm-stimulated BMCs were generally consistent with those observed in a mouse PJI model, we observed a notable difference in MCP-1 levels. Specifically, TAS4464 treatment significantly reduced MCP-1 levels in the mouse PJI model (Fig. 6D), but not in *S. aureus* biofilm-stimulated BMCs (Fig. 3D). MCP1 (monocyte chemoattractant protein-1) is well-known as a potent chemotactic factor for the recruitment and infiltration of inflammatory cells such as monocytes and macrophages, and plays a key role in bone remodeling and the regulation of bone turnover [51,52]. This discrepancy may reflect the greater complexity of the immune system *in vivo*, suggesting that TAS4464's effects may differ depending on the experimental model. Additionally, it is important to consider that TAS4464 may exert concentration-dependent and even opposing effects under the same conditions. For instance, we observed a biphasic response in Arg-1 expression in biofilm-stimulated BMCs: treatment with a low concentration of TAS4464 (50 nM) upregulated Arg-1 expression, whereas higher concentrations (150 and 500 nM) led to a gradual downregulation (Fig. 4B, iv).

5. Conclusion

Overall, the evidence presented in this study shows that TAS4464 has strong therapeutic potential by repressing the expansion and differentiation of MDSCs and M2 macrophages, restoring T-cell function, and inhibiting key inflammatory pathways. These findings highlight its promise as a treatment for biofilm-associated infections, particularly in chronic inflammatory conditions such as PJIs. Further investigation into the molecular mechanisms underlying TAS4464's regulatory effects may facilitate the development of more targeted anti-biofilm therapies that enhance host immunity and reduce bacterial persistence.

CRediT authorship contribution statement

Chiang-Wen Lee: Software, Resources, Methodology. **Ju-Fang Liu:** Validation, Resources, Formal analysis. **Chia-Ching Yang:** Validation, Methodology, Investigation. **Chun-Yuan Hsiao:** Software, Resources, Formal analysis. **Yao-Chang Chiang:** Software, Methodology, Formal analysis. **Pey-Jium Chang:** Writing – review & editing, Writing – original draft, Supervision, Formal analysis, Conceptualization. **Hsieh Yu-Chieh:** Project administration, Methodology. **Jiun-Liang Chen:** Methodology, Formal analysis, Conceptualization. **Kuo-Ti Peng:** Writing – original draft, Validation, Funding acquisition, Formal analysis, Conceptualization.

Ethics approval and consent to participate

All animal experiments were performed using protocols approved by the Institutional Animal Care and Use Committee of the Chang Gung Memorial Hospital (IACUC permit number: 2023092503).

Funding

This work was supported by Chang Gung Memorial Hospital at Chiayi, Taiwan (grant numbers CMRPG6N0291–0292, CMRPG6L0441–0443, and CORPG6P0011–12), and by the National Science and Technology Council in Taiwan (grant numbers NMRPG6P0021 and NMRPG6Q0051) [NSTC 113–2314-B-182A-100 and NSTC 114–2314-B-182A-073].

Supporting Information

Supplementary Figure S1 and Supplementary Figure S2

Declaration of Competing Interest

The authors declare that they have no known competing financial interests or personal relationships that could have appeared to influence the work reported in the paper.

Acknowledgments

We thank Laboratory Animal Center, Department of Medical

Research, Chang Gung Memorial Hospital at Chiayi for animal experiments, and Precious Instrumentation Core Laboratory, Department of Medical Research, Chang Gung Memorial Hospital at Chiayi.

Appendix A. Supporting information

Supplementary data associated with this article can be found in the online version at doi:10.1016/j.biopha.2025.118622.

Data Availability

No data was used for the research described in the article.

References

[1] L. Kong, J. Cao, Y. Zhang, W. Ding, Y. Shen, Risk factors for periprosthetic joint infection following primary total hip or knee arthroplasty: a meta-analysis, Int. Wound J. 14 (3) (2017) 529–536.

[2] K.J. Bozic, E. Lau, S. Kurtz, K. Ong, H. Rubash, T.P. Vail, D.J. Berry, Patient-related risk factors for periprosthetic joint infection and postoperative mortality following total hip arthroplasty in Medicare patients, J. Bone Jt. Surg. Am. 94 (9) (2012) 794–800.

[3] E.J. Weinstein, A.J. Stephens-Shields, C.W. Newcomb, R. Silibovsky, C.L. Nelson, J. A. O'Donnell, L.J. Glaser, E. Hsieh, J.S. Hanberg, J.P. Tate, K.M. Akgun, J. T. King Jr., V. Lo Re, 3rd, incidence, microbiological studies, and factors associated with prosthetic joint infection after total knee arthroplasty, JAMA Netw. Open 6 (10) (2023) e2340457.

[4] N. Rao, B.H. Ziran, B.A. Lipsky, Treating osteomyelitis: antibiotics and surgery, Plast. Reconstr. Surg. 127 (1) (2011).

[5] L. Fagotti, J. Tatka, M.J.C. Salles, M.C. Queiroz, Risk factors and treatment options for failure of a Two-Stage exchange, Curr. Rev. Musculoskelet. Med 11 (3) (2018) 420–427.

[6] F. Vilchez, J.C. Martinez-Pastor, S. Garcia-Ramiro, G. Bori, F. Macule, J. Sierra, L. Font, J. Mensa, A. Soriano, Outcome and predictors of treatment failure in early post-surgical prosthetic joint infections due to *staphylococcus aureus* treated with debridement, Clin. Microbiol Infect. 17 (3) (2011) 439–444.

[7] C.E. Kandel, R. Jenkinson, N. Daneman, D. Backstein, B.E. Hansen, M.P. Muller, K. C. Katz, J. Widdifield, E. Bogoch, S. Ward, A. Sajja, F.G. Jeldes, A. McGeer, Predictors of treatment failure for hip and knee prosthetic joint infections in the setting of 1- and 2-Stage exchange arthroplasty: a multicenter retrospective cohort, Open Forum Infect. Dis. 6 (11) (2019).

[8] A. Bhanushali, L. Tran, J. Nairne-Nagy, S. Bereza, S.A. Callary, G.J. Atkins, B. Ramasamy, L.B. Solomon, Patient-Related predictors of treatment failure after Two-Stage total hip arthroplasty revision for periprosthetic joint infection: a systematic review and Meta-Analysis, J. Arthroplast. 39 (9) (2024) 2395–2402.

[9] R. Chao, S.D. Rothenberger, A.J. Frear, B.R. Hamlin, B.A. Klatt, N.B. Shah, K. L. Urish, Benefits and adverse events associated with extended antibiotic use for one year following periprosthetic joint infection in total knee arthroplasty: a prospective cohort analysis, J. Arthroplast. (2024).

[10] M.R. Hays, B.J. Kildow, C.W. Hartman, E.R. Lyden, B.D. Springer, T.K. Fehring, K. L. Garvin, Increased incidence of Methicillin-Resistant *staphylococcus aureus* in knee and hip prosthetic joint infection, J. Arthroplast. 38 (6S) (2023) S326–S330.

[11] K.M. Craft, J.M. Nguyen, L.J. Berg, S.D. Townsend, Methicillin-resistant *staphylococcus aureus* (MRSA): antibiotic-resistance and the biofilm phenotype, Medchemcomm 10 (8) (2019) 1231–1241.

[12] A. Kaushik, H. Kest, M. Sood, B.W. Steussy, C. Thieman, S. Gupta, Biofilm producing Methicillin-Resistant *staphylococcus aureus* (MRSA) infections in humans: clinical implications and management, Pathogens 13 (1) (2024).

[13] B.F. Ricciardi, G. Muthukrishnan, E. Masters, M. Ninomiya, C.C. Lee, E.M. Schwarz, *staphylococcus aureus* evasion of host immunity in the setting of prosthetic joint infection: biofilm and beyond, Curr. Rev. Musculoskelet. Med 11 (3) (2018) 389–400.

[14] Z. Van Roy, P. Arumugam, B.P. Bertrand, D.D. Shinde, V.C. Thomas, T. Kielian, Tissue niche influences immune and metabolic profiles to *staphylococcus aureus* biofilm infection, Nat. Commun. 15 (1) (2024) 8965.

[15] C.E. Heim, D. Vidlak, T.D. Scherr, J.A. Kozel, M. Holzapfel, D.E. Muirhead, T. Kielian, Myeloid-derived suppressor cells contribute to *staphylococcus aureus* orthopedic biofilm infection, J. Immunol. 192 (8) (2014) 3778–3792.

[16] L.R. Thurlow, M.L. Hanke, T. Fritz, A. Angle, A. Aldrich, S.H. Williams, I. L. Engebretsen, K.W. Bayles, A.R. Horswill, T. Kielian, *staphylococcus aureus* biofilms prevent macrophage phagocytosis and attenuate inflammation in vivo, J. Immunol. 186 (11) (2011) 6585–6596.

[17] K.T. Peng, C.C. Hsieh, T.Y. Huang, P.C. Chen, H.N. Shih, M.S. Lee, P.J. Chang, *staphylococcus aureus* biofilm elicits the expansion, activation and polarization of myeloid-derived suppressor cells *in vivo* and *in vitro*, PLoS One 12 (8) (2017) e0183271.

[18] J. Ying, M. Zhang, X. Qiu, Y. Lu, Targeting the neddylation pathway in cells as a potential therapeutic approach for diseases, Cancer Chemother. Pharm. 81 (5) (2018) 797–808.

[19] L. Zhou, Y. Jiang, Q. Luo, L. Li, L. Jia, Neddylation: a novel modulator of the tumor microenvironment, Mol. Cancer 18 (1) (2019) 77.

[20] Y. Zhao, M.A. Morgan, Y. Sun, Targeting neddylation pathways to inactivate cullin-RING ligases for anticancer therapy, Antioxid. Redox Signal 21 (17) (2014) 2383–2400.

[21] R.I. Enchev, B.A. Schulman, M. Peter, Protein neddylation: beyond cullin-RING ligases, Nat. Rev. Mol. Cell Biol. 16 (1) (2015) 30–44.

[22] S. Zhang, Q. Yu, Z. Li, Y. Zhao, Y. Sun, Protein neddylation and its role in health and diseases, Signal Transduct. Target Ther. 9 (1) (2024) 85.

[23] T. Tanaka, T. Nakatani, T. Kamitani, Inhibition of NEDD8-conjugation pathway by novel molecules: potential approaches to anticancer therapy, Mol. Oncol. 6 (3) (2012) 267–275.

[24] C. Yoshimura, H. Muraoka, H. Ochiiwa, S. Tsuji, A. Hashimoto, H. Kazuno, F. Nakagawa, Y. Komiya, S. Suzuki, T. Takenaka, M. Kumazaki, N. Fujita, T. Mizutani, S. Ohkubo, TAS4464, a highly potent and selective inhibitor of NEDD8-Activating enzyme, suppresses neddylation and shows antitumor activity in diverse cancer models, Mol. Cancer Ther. 18 (7) (2019) 1205–1216.

[25] H. Muraoka, C. Yoshimura, R. Kawabata, S. Tsuji, A. Hashimoto, H. Ochiiwa, F. Nakagawa, Y. Fujioka, K. Matsuo, S. Ohkubo, Activity of TAS4464, a novel NEDD8 activating enzyme E1 inhibitor, against multiple myeloma via inactivation of nuclear factor kappab pathways, Cancer Sci. 110 (12) (2019) 3802–3810.

[26] X. Qin, X. Han, Y. Sun, Discovery of small molecule inhibitors of neddylation catalyzing enzymes for anticancer therapy, Biomed. Pharm. 179 (2024) 117356.

[27] H. Ochiiwa, G. Ailiken, M. Yokoyama, K. Yamagata, H. Nagano, C. Yoshimura, H. Muraoka, K. Ishida, T. Haruma, A. Nakayama, N. Hashimoto, K. Murata, M. Nishimura, Y. Kawashima, O. Ohara, S. Ohkubo, T. Tanaka, TAS4464, a NEDD8-activating enzyme inhibitor, activates both intrinsic and extrinsic apoptotic pathways via c-Myc-mediated regulation in acute myeloid leukemia, Oncogene 40 (7) (2021) 1217–1230.

[28] K.T. Peng, M.H. Tsai, C.W. Lee, Y.C. Chiang, P.C. Chen, C.C. Chen, C.H. Chang, H. N. Shih, P.J. Chang, Dysregulated expression of antioxidant enzymes in polyethylene particle-induced periprosthetic inflammation and osteolysis, PLoS One 13 (8) (2018) e0202501.

[29] R. Rigoni, E. Fontana, S. Guglielmetti, B. Fosso, A.M. D'Erchia, V. Maina, V. Taverniti, M.C. Castiello, S. Mantero, G. Pacchiana, S. Musio, R. Pedotti, C. Selmi, J.R. Mora, G. Pesole, P. Vezzoni, P.L. Poliani, F. Grassi, A. Villa, B. Cassani, Intestinal microbiota sustains inflammation and autoimmunity induced by hypomorphic RAG defects, J. Exp. Med 213 (3) (2016) 355–375.

[30] D.I. Gabrilovich, S. Nagaraj, Myeloid-derived suppressor cells as regulators of the immune system, Nat. Rev. Immunol. 9 (3) (2009) 162–174.

[31] M. Ost, A. Singh, A. Peschel, R. Mehling, N. Rieber, D. Hartl, Myeloid-Derived suppressor cells in bacterial infections, Front Cell Infect. Microbiol. 6 (2016) 37.

[32] F. Veglia, E. Sanseviero, D.I. Gabrilovich, Myeloid-derived suppressor cells in the era of increasing myeloid cell diversity, Nat. Rev. Immunol. 21 (8) (2021) 485–498.

[33] M. Benoit, B. Desnues, J.L. Mege, Macrophage polarization in bacterial infections, J. Immunol. 181 (6) (2008) 3733–3739.

[34] J.D. Thiriot, Y.B. Martinez-Martinez, J.J. Endsley, A.G. Torres, Hacking the host: exploitation of macrophage polarization by intracellular bacterial pathogens, Pathog. Dis. 78 (1) (2020).

[35] F. Siwczak, Z. Cseresnyes, M.I.A. Hassan, K.O. Aina, S. Carlstedt, A. Sigmund, M. Groger, B.G.J. Surewaard, O. Werz, M.T. Figge, L. Tuchscherr, B. Loffler, A. S. Mosig, Human macrophage polarization determines bacterial persistence of *staphylococcus aureus* in a liver-on-chip-based infection model, Biomaterials 287 (2022) 121632.

[36] F. Bottner, A. Wegner, W. Winkelmann, K. Becker, M. Erren, C. Gotze, Interleukin-6, procalcitonin and TNF-alpha: markers of peri-prosthetic infection following total joint replacement, J. Bone Jt. Surg. Br. 89 (1) (2007) 94–99.

[37] A. Elgeidi, A.E. Elganainy, N. Abou Elkhier, S. Rakha, Interleukin-6 and other inflammatory markers in diagnosis of periprosthetic joint infection, Int Orthop. 38 (12) (2014) 2591–2595.

[38] T. Condamine, D.I. Gabrilovich, Molecular mechanisms regulating myeloid-derived suppressor cell differentiation and function, Trends Immunol. 32 (1) (2011) 19–25.

[39] P. Trikha, W.E. Carson, 3rd, signaling pathways involved in MDSC regulation, Biochim Biophys. Acta 1846 (1) (2014) 55–65.

[40] K.S. Cho, S.A. Kang, S.D. Kim, S.J. Mun, H.S. Yu, H.J. Roh, Dendritic cells and M2 macrophage play an important role in suppression of Th2-mediated inflammation by adipose stem cells-derived extracellular vesicles, Stem Cell Res. 39 (2019) 101500.

[41] D.B. Sacdalan, J.A. Lucero, The association between inflammation and immunosuppression: implications for ICI biomarker development, Oncol. Targets Ther. 14 (2021) 2053–2064.

[42] A.A. Al-Qahtani, F.S. Alhamlan, A.A. Al-Qahtani, Pro-inflammatory and anti-inflammatory interleukins in infectious diseases: a comprehensive review, Trop. Med. Infect. Dis. 9 (1) (2024).

[43] S. Huber, R. Hoffmann, F. Muskens, D. Voehringer, Alternatively activated macrophages inhibit T-cell proliferation by Stat6-dependent expression of PD-L2, Blood 116 (17) (2010) 3311–3320.

[44] A. Mantovani, S. Sozzani, M. Locati, P. Allavena, A. Sica, Macrophage polarization: tumor-associated macrophages as a paradigm for polarized M2 mononuclear phagocytes, Trends Immunol. 23 (11) (2002) 549–555.

[45] U. Saqib, S. Sarkar, K. Suk, O. Mohammad, M.S. Baig, R. Savai, Phytochemicals as modulators of M1-M2 macrophages in inflammation, Oncotarget 9 (25) (2018) 17937–17950.

[46] S. Chen, A. Saeed, Q. Liu, Q. Jiang, H. Xu, G.G. Xiao, L. Rao, Y. Duo, Macrophages in immunoregulation and therapeutics, Signal Transduct. Target Ther. 8 (1) (2023) 207.

[47] G.R. Pidwill, J.F. Gibson, J. Cole, S.A. Renshaw, S.J. Foster, The role of macrophages in *staphylococcus aureus* infection, Front Immunol. 11 (2020) 620339.
[48] M. Li, J. Yu, G. Guo, H. Shen, Interactions between macrophages and biofilm during *staphylococcus aureus*-associated implant infection: difficulties and solutions, J. Innate Immun. 15 (1) (2023) 499–515.
[49] L.R. Thurlow, G.S. Joshi, A.R. Richardson, Peroxisome proliferator-activated receptor gamma is essential for the resolution of *staphylococcus aureus* skin infections, Cell Host Microbe 24 (2) (2018) 261–270.
[50] M.L. Hanke, A. Angle, T. Kielian, MyD88-dependent signaling influences fibrosis and alternative macrophage activation during *staphylococcus aureus* biofilm infection, PLoS One 7 (8) (2012) e42476.
[51] B.S. Mulholland, M.R. Forwood, N.A. Morrison, Monocyte chemoattractant Protein-1 (MCP-1/CCL2) drives activation of bone remodelling and skeletal metastasis, Curr. Osteoporos. Rep. 17 (6) (2019) 538–547.
[52] S. Singh, D. Anshita, V. Ravichandiran, MCP-1: function, regulation, and involvement in disease, Int. Immunopharmacol. 101 (Pt B) (2021) 107598.

Journal of Dental Sciences 20 (2025) 1716–1722

Available online at www.sciencedirect.com

ScienceDirect

journal homepage: www.e-jds.com

Original Article

Impacts of surface characteristics on biological responses and biofilm formation of 3D-printed denture base resins: An in vitro study

Chien-Fu Tseng [a,b,c†], Chia-Chih Sung [b,c†], Ya-Ting Yang [d†], Fen-Ni Chen [e], Yuichi Mine [g], Yao-Chang Chiang [h,i], Zih-Chan Lin [h], Mei-Ling Fang [j,k], Hsin-Ming Chen [a,l,m], Sang-Heng Kok [a,m], Tzu-Yu Peng [f*]

[a] *Graduate Institute of Clinical Dentistry, School of Dentistry, College of Medicine, National Taiwan University, Taipei, Taiwan*
[b] *Department of Dentistry, Taoyuan General Hospital, Ministry of Health and Welfare, Taoyuan, Taiwan*
[c] *Research Center for Tooth Bank and Dental Stem Cell Technology, College of Oral Medicine, Taipei Medical University, Taipei, Taiwan*
[d] *Department of Dentistry, Taipei Medical University Shuang Ho Hospital, New Taipei City, Taiwan*
[e] *School of Dental Technology, College of Oral Medicine, Taipei Medical University, Taipei, Taiwan*
[f] *School of Dentistry, College of Oral Medicine, Taipei Medical University, Taipei, Taiwan*
[g] *Department of Medical Systems Engineering, Hiroshima University Graduate School of Biomedical and Health Sciences, Hiroshima City, Japan*
[h] *Chronic Diseases and Health Promotion Research Center, Center for Drug Research and Development, Chang Gung University of Science and Technology, Chiayi, Taiwan*
[i] *Department of Nursing, Division of Basic Medical Sciences, Chang Gung University of Science and Technology, Chiayi, Taiwan*
[j] *Center for Environmental Toxin and Emerging-Contaminant Research, Cheng Shiu University, Kaohsiung, Taiwan*
[k] *Department of Civil Engineering and Geomatics, Cheng Shiu University, Kaohsiung, Taiwan*
[l] *Graduate Institute of Oral Biology, School of Dentistry, College of Medicine, National Taiwan University, Taipei, Taiwan*
[m] *Department of Dentistry, National Taiwan University Hospital, College of Medicine, National Taiwan University, Taipei, Taiwan*

Received 21 March 2025
Available online 4 April 2025

* Corresponding author. School of Dentistry, College of Oral Medicine, Taipei Medical University, 250 Wu-Hsing Street, Taipei 11031, Taiwan.
E-mail address: typeng@tmu.edu.tw (T.-Y. Peng).
† These three authors contributed equally to this study.

https://doi.org/10.1016/j.jds.2025.03.027
1991-7902/© 2025 Association for Dental Sciences of the Republic of China. Publishing services by Elsevier B.V. This is an open access article under the CC BY-NC-ND license (http://creativecommons.org/licenses/by-nc-nd/4.0/).

KEYWORDS
3D printing;
Denture base resin;
Cell viability;
Biofilm formation;
Surface characteristics

Abstract *Background/purpose:* With advancements in digital technology, fully digital workflow for complete denture fabrication using 3D-printed denture base resin (DBR) has gained increasing clinical acceptance in recent years. However, the surface characteristics, biocompatibility, and biofilm formation of 3D-printed DBR materials remain insufficiently understood. Therefore, in this study, we investigated and analyzed these aspects.
Materials and methods: Disk-shaped DBR specimens (Ø 2.5 mm, 3 mm thick) were fabricated using packed (PA), milled (ML), and 3D-printed (3D) processes. All specimens were ground with silicon carbide sandpaper (#600) and ultrasonically cleaned. Surface microtopography and submicron roughness were analyzed using scanning electron microscopy and atomic force microscopy, while a goniometer was used to measure contact angles to calculate the surface energy. Human gingival fibroblasts and *Aggregatibacter actinomycetemcomitans* were cultured on the specimens to assess the cytotoxicity and biofilm formation. Statistical analyses were performed with a significance level set to 0.05.
Results: Microscopic imaging revealed that the 3D group exhibited a more uniformly distributed texture, while it also had the lowest surface roughness (0.85 μm). Additionally, the PA group had the most hydrophobic surface (82.47°) and the highest surface free energy (46.08 mN/m). Notably, no group showed cytotoxic effects after 72 h of testing. In addition, the 3D group demonstrated the lowest biofilm formation after both 24 h and 72 h of microbial culture.
Conclusion: 3D-printed DBRs exhibited the lowest surface roughness, maintaining non-cytotoxic and superior resistance to microbial adhesion, suggesting their potential for complete denture fabrication, easy maintenance of oral hygiene, and long-term clinical performance.
© 2025 Association for Dental Sciences of the Republic of China. Publishing services by Elsevier B.V. This is an open access article under the CC BY-NC-ND license (http://creativecommons.org/licenses/by-nc-nd/4.0/).

Introduction

For edentulous patients whose treatment options are limited due to systemic conditions, oral health status, or financial constraints, complete dentures remain the treatment of choice.[1] Denture base resin (DBR), as the primary material for complete dentures, must exhibit excellent mechanical strength, biocompatibility, and stability to ensure long-term durability and patient comfort.[2,3] Currently, polymethyl methacrylate (PMMA) remains the most commonly used DBR in clinical practice due to its ease of processing, esthetic properties, cost-effectiveness, and adequate mechanical performance.[4] Conventional fabrication methods for DBRs primarily include cold-curing and heat-curing polymerization. Cold-cured DBRs are polymerized through chemical self-curing, offering convenient handling;[5] however, they tend to have higher residual monomer contents.[6] In contrast, heat-cured DBRs undergo polymerization under elevated temperature and pressure, effectively reducing porosity and enhancing flexural strength and wear resistance.[7] Nonetheless, the heat-curing process still suffers from polymerization shrinkage, which compromises the fit of the denture.[8] Additionally, the conventional fabrication workflow is complex and requires highly skilled technicians. Therefore, improving the properties of DBRs while simplifying the manufacturing process has become a crucial area of development in digital dental technology.[9–11]

The full digitalization of denture fabrication workflows has emerged as a significant trend in recent years, leading to notable improvements in both efficiency and precision.[10–12] Among these advancements, milling and three-dimensional (3D) printing are the most representative digital manufacturing techniques. The milling process utilizes pre-polymerized PMMA blocks for high-precision cutting, which not only enhances the fitting accuracy of dentures and minimizes the deformation issues associated with conventional heat-curing processes but reduces the release of residual monomers.[13,14] However, milling results in considerable material waste and involves high equipment costs.[15,16] In comparison, 3D printing reduces material waste through layer-by-layer photopolymerization and enables the fabrication of DBRs with complex geometries and customized designs.[16–18] While digital manufacturing techniques have significantly advanced DBR applications, most research has focused on comparing the mechanical properties, dimensional accuracy, and color stability of conventionally packed, milled, or 3D-printed DBRs; yet comprehensive evaluations of their biocompatibility and biofilm formation remain limited.

To our knowledge, only a few 3D-printed DBR materials or brands have received medical device licenses from the Taiwanese government or international regulatory agencies, highlighting the need for further investigation. Therefore, in this study, we analyzed the surface characteristics, biocompatibility, and biofilm formation of DBRs fabricated using three different processes: conventional cold-polymerized packing (SR Triplex Cold), milling (IvoBase CAD Pink V), and 3D printing (FREEPRINT denture). The findings will provide scientific evidence for evaluating the

clinical safety and feasibility of 3D-printed DBRs and contribute to the advancement of fully digital denture fabrication technologies.

Materials and methods

Fabrication of test specimens

Disk-shaped samples (ø10.0 mm, 3.0 mm thick) were fabricated using conventional packing (PA), five-axis milling (ML), and 3D printing (3D) processes. The materials used and fabrication methods in this study are listed in Table 1. All samples were ground with silicon carbide paper, cleaned with distilled water in an ultrasonic cleaner, and air-dried.

Surface characterization

Surface microtopography was observed using a thermal field emission scanning electron microscope (FE-SEM; JSM-7800F Prime, JEOL, Tokyo, Japan), with images recorded at 2500 × and 5000 × magnification. An atomic force microscope (AFM; Bruker Dimension Icon VT-1000, Santa Barbara, CA, USA) was used to measure submicron surface roughness over a 5 × 5-μm area ($n = 10$). Contact angles of distilled water (CA_W) and diiodomethane (CA_D) were measured on 10 specimens per group using a goniometer (Phoenix Mini, Surface Electro Optics, Seoul, South Korea), with three 10 μL drops of each liquid measured per specimen. The surface energy (SE) was further calculated using the method of Owens, Wendt, Rabel and Kaelble via Surfaceware software (vers. 9, Surface Electro Optics) based on contact angle data.

Cell cultures and cell cytotoxicity

The human gingival fibroblast (HGF-1) cell line (ATCC #CRL-2014) was cultured in Dulbecco's modified Eagle medium (DMEM), following a method described by Peng et al.[19] Autoclaved specimens (121 °C, 1.2 kg/cm^2, 30 min) from each processing were immersed in DMEM at 37 °C for 72 h to prepare extracts for the cytotoxicity assay. HGF-1 cells were seeded in a 96-well plate (at 10^6 cells/well). After cell attachment, the culture medium was replaced with DMEM containing specimen extracts. After 24 h of incubation, cell viability was assessed using the PrestoBlue reagent according to the manufacturer's instructions.

Microbial cultures and biofilm formation assay

An *Aggregatibacter actinomycetemcomitans* microbial strain (BCRC #80375) was cultured in brain heart infusion broth, following a method described by Peng et al.[20] The optical density at 600 nm (OD600) was adjusted to 1.0 using fresh broth to obtain a standard inoculum of 3×10^8 colony-forming units (CFU)/mL. *Aggregatibacter actinomycetemcomitans* (10^6 CFU/mL) was inoculated into all wells of a 24-well plate containing DBR samples (PA, ML, or 3D) and incubated at 37 °C for 24 h and 72 h. After incubation, the medium was removed, and wells were washed twice with phosphate-buffered saline (PBS) and air-dried for 1 h. Crystal violet (150 μL of 0.1 % w/v) was added to each well and incubated at room temperature for 10—15 min. The absorbance at 490 nm (OD490) was measured on an enzyme-linked immunosorbent assay (ELISA) microplate reader (Molecular Devices, San Jose, CA, USA).

Statistical analysis

Data are expressed as the mean ± standard deviation (SD). Normality was confirmed using the Shapiro—Wilk test, allowing for parametric analysis. Ra values and hydrophilicity comparisons were conducted using a one-way analysis of variance (ANOVA), followed by Tukey's post-hoc honest significant difference (HSD) test for multiple group comparisons (PA, ML, and 3D). Biological evaluation assays (cytotoxicity and biofilm formation) were performed with three replicates per group and analyzed using a one-way ANOVA with Tukey's HSD post-hoc test. Statistical analyses were conducted using SPSS (vers. 19, IBM, Amork, NY, USA) and Prism (vers. 10, GraphPad Software, San Diego, CA, USA), with significance set to $P < 0.05$.

Table 1 Materials used in this study.

Identification (Manufacturer)	Composition[a]	Fabrication process	Machine (Manufacturer)	Abbreviation
SR triplex cold (ivoclar Vivadent AG, Schaan, Liechtenstein)	Powder: PMMA, catalyst, pigments Liquid: MMA, dimethacrylate, catalyst, stabilizer	Conventional packing (self-curing)	—	PA
IvoBase CAD Pink V (ivoclar Vivadent AG, Schaan, Liechtenstein)	PMMA, co-polymer for impact toughness modification, pigments	Universal five-axis production unit	inLab MC X5 (Dentsply Sirona, long island City, NY, USA)	ML
FREEPRINT denture (Detax, Ettlingen, Germany)	—	DLP light-curing 3D printer	3Demax (DMG medical devices, Hamburg, Germany)	3D

PMMA, polymethylmethacrylate; MMA, methylmethacrylate; DLP, digital light processing.
[a] Composition information was provided by the manufacturer, while the 3D printing manufacturer did not provide the detailed composition.

Results

Surface microtopography and topography

Based on microscopic images shown in Fig. 1, all specimens exhibited distinct linear grinding marks. The PA group showed the most pronounced texture, the ML group featured parallel deep grooves, and the 3D group presented a uniformly distributed microstructure. The surface roughness and topography of the DBRs are summarized in Table 2 and Fig. 1. The Ra value of the PA group was significantly higher than those of the ML and 3D groups ($P < 0.05$), and Rq values followed a similar trend, indicating that the PA group exhibited greater surface microtopographical variations and more-pronounced height fluctuations. Rz, which represents the maximum height roughness, was greatest in the PA group, followed by the ML and 3D groups, with a significant difference between the PA and 3D groups ($P < 0.05$).

Surface wettability

The surface wettability results are presented in Table 2. CA_W, which reflects the surface wettability to polar liquids, was significantly lower in the PA group than in the ML and 3D groups ($P < 0.05$), indicating higher hydrophilicity. CA_D, representing wettability to non-polar liquids, ranged 25.92°–28.88°, with no significant differences among the three groups ($P > 0.13$). Although the PA group exhibited a lower CA_W value, no significant differences in SE were observed among the three groups ($P > 0.24$).

Cytotoxicity

The cytotoxicity assessment results (Fig. 2) showed no significant differences in cell viabilities among the processing groups compared to the blank group (NT) at any time points ($P > 0.95$). This indicated that different DBR fabrication processes did not induce immediate or intermediate cytotoxicity in HGF-1 cells. Cell viability remained stable, confirming the excellent cytocompatibility of DBR materials and the absence of significant cytotoxic substance release.

Biofilm formation

Fig. 3 illustrates *A. actinomycetemcomitans* biofilm formation on DBRs fabricated using the three processes. The PA group exhibited significantly greater biofilm formation at 72 h than at 24 h ($P < 0.05$), indicating a clear accumulation trend over time. In contrast, the ML and 3D groups showed minimal variations between 24 h and 72 h ($P > 0.06$), suggesting more-stable bacterial adhesion. Notably, the 3D group demonstrated the lowest biofilm formation at both time points compared to the PA and ML groups, suggesting that the surface characteristics of the 3D-printed DBRs may inhibit *A. actinomycetemcomitans* adhesion.

Discussion

Compared to conventional packing (self-curing) and five-axis milling, digital light processing (DLP) 3D printing significantly reduces the surface roughness of DBRs. This improvement stems from its high-precision layer-by-layer stacking, the self-leveling effect of liquid resin, reduced mechanical stresses, and controlled post-processing.[21,22] DLP technology employs a digital light source to simultaneously cure the entire resin layers, achieving a minimum layer thickness of 50 μm, which enhances surface smoothness.[23] The liquid resin fills minor irregularities before photopolymerization, minimizing defects.[21–23] In contrast, conventional packing is prone to polymerization shrinkage, air bubbles, and mold limitations, while milling introduces tool marks, increasing roughness.[5,6,15,16] Additionally, DLP

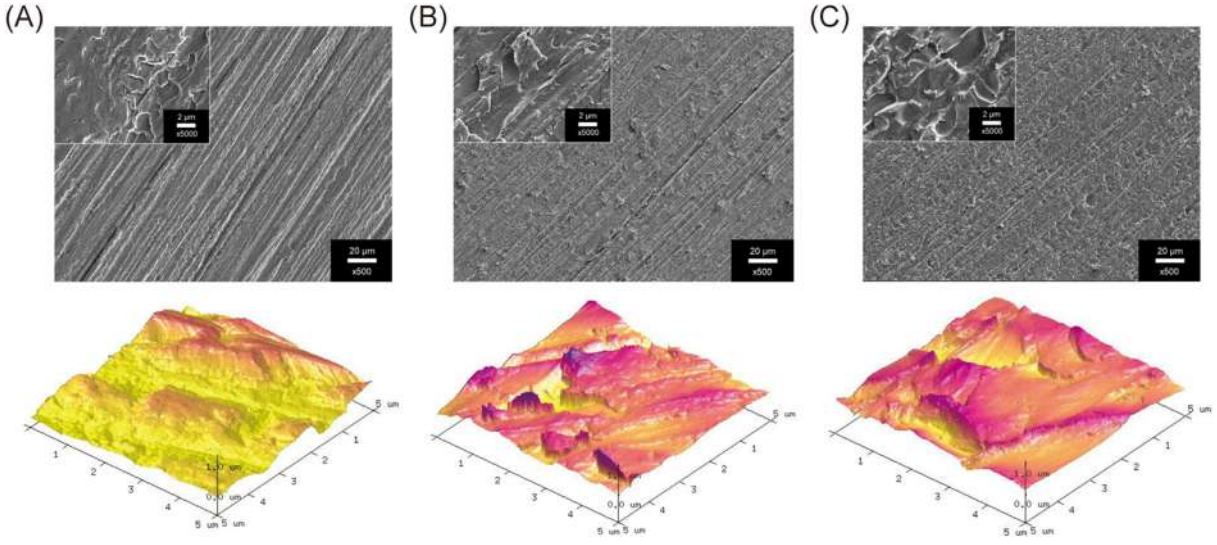


Figure 1 Surface microtopography and topography of denture base resins (DBRs) fabricated using (A) conventional packing, (B) a universal five-axis production unit, and (C) a digital light processing (DLP) light-curing 3D printer.

eliminates tool-induced microcracks and scratches. Post-processing, including isopropanol cleaning and secondary curing, further reduces roughness. The uniform cross-linked molecular structure formed during DLP printing minimizes microscopic defects, ensuring superior surface quality compared to thermosetting or self-polymerizing resins.[23–25]

To the best of our knowledge, most 3D-printable DBRs are primarily designed for provisional (temporary) or immediate dentures. However, the FREEPRINT denture (Detax) used in this study is the material that has received approval from the US Food and Drug Administration and European Union Medical Devices Regulation, allowing its use in definitive dentures. Given its long-term clinical application, it is crucial to further evaluate its biocompatibility, as potential cytotoxicity may arise from the release of unpolymerized monomers, residual polymerization initiators, or other degradation byproducts.[6,13,14] In this study, none of the tested DBR materials induced significant cytotoxic reactions (Fig. 2), indicating that their chemical composition and fabrication processes support stable cell growth without adverse effects on HGF-1 cells. The observed stable cell viability and favorable biocompatibility further reinforced the clinical safety of these materials, supporting their feasibility for use in definitive denture fabrication.[26]

Surface roughness plays a crucial role in determining the wettability and bacterial adhesion characteristics of materials.[1,27] The PA group exhibited higher Ra and Rz values (Table 2), indicating a greater degree of surface microtopography, which may promote moisture retention and the exposure of polar functional groups such as hydroxyl (—OH) and carboxyl (—COOH), thereby increasing hydrophilicity (lower CA_W).[28,29] Hydrophilic surfaces tend to more readily adsorb water and biomolecules, such as proteins, providing initial conditions favorable for bacterial adhesion.[30,31] The pronounced surface polarity of the PA group may facilitate early bacterial colonization and accelerate biofilm development. Studies showed that moderately hydrophilic surfaces create a conducive wetting environment for bacterial adhesion and proliferation,[32] which explains the significant increase in biofilm formation in the PA group within 72 h. In contrast, the ML and 3D groups exhibited significantly higher CA_W values than the PA group, indicating greater hydrophobicity. Notably, the 3D group displayed the lowest Ra, Rq, and Rz values (Table 2), resulting in the smoothest surface, which may have further influenced the bacterial adhesion behavior. Generally, smoother surfaces reduce microscopic pores and depressions, making it more difficult for bacteria to establish stable attachment and aggregation, thereby limiting biofilm accumulation.[32] The specific micro-layered structure generated by 3D printing may also affect the water contact angle and bacterial adhesion mechanisms, which may have led to lower biofilm formation at both 24 h and 72 h compared to the PA and ML groups.[33] This suggests that 3D-printed DBRs may inhibit the adhesion of periodontal pathogens.

Table 2 Surface roughness and wettability of the denture base resins (DBRs).

Group	Surface roughness			Surface wettability		
	Ra (μm)	Rq (μm)	Rz (μm)	CA_W (°)	CA_D (°)	SE (mN/m)
PA	0.90 ± 0.16^a	1.14 ± 0.28^a	6.40 ± 1.75^a	82.47 ± 1.44^a	25.92 ± 0.68^a	46.09 ± 0.43^a
ML	0.84 ± 0.11^b	1.02 ± 0.13^b	$6.01 \pm 1.40^{a,b}$	86.43 ± 1.16^b	26.69 ± 2.42^a	45.34 ± 0.95^a
3D	0.83 ± 0.14^b	1.03 ± 0.14^b	5.73 ± 0.88^b	85.05 ± 1.98^b	28.88 ± 3.99^a	44.64 ± 1.75^a

DBRs were fabricated using conventional packing (PA), a universal five-axis production unit (ML), and a DLP light-curing 3D printer (3D). Ra, arithmetic mean deviation; Rq, root mean square deviation; Rz, maximum height of profile; CA_W, contact angle of distilled water; CA_D, contact angle of diiodomethane; SE, surface energy.
[a] and [b]: Different superscript letters in the same column indicate a significant difference in the mean of the parameter between the two groups.

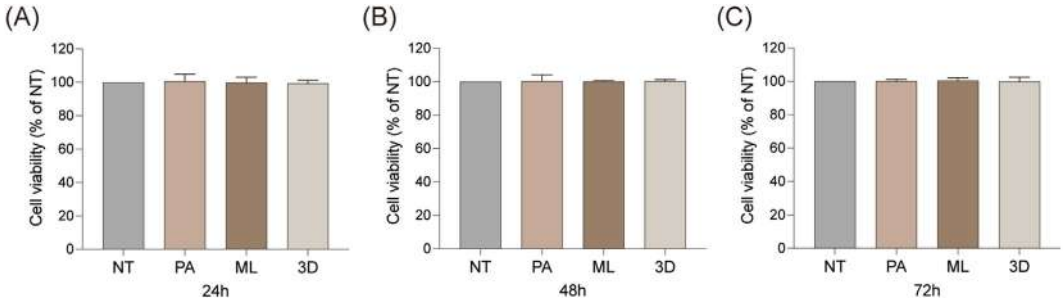


Figure 2 Assessment of human gingival fibroblast (HGF-1) cytotoxicity on denture base resin (DBR) surfaces after (A) 24 h, (B) 48 h, and (C) 72 h, as determined using the PrestoBlue cell viability reagent. NT, blank group without a DBR specimen; DBRs were fabricated using conventional packing (PA), a universal five-axis production unit (ML), and a digital light processing (DLP) light-curing 3D printer (3D).

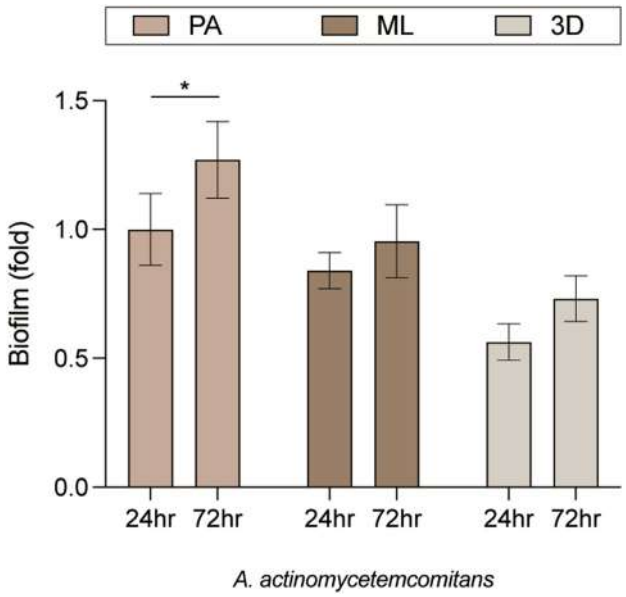


Figure 3 Biofilm formation ability of *A. actinomycetemcomitans* on denture base resin (DBR) surfaces fabricated using conventional packing (PA), a universal five-axis production unit (ML), and a digital light processing (DLP) light-curing 3D printer (3D). * Significantly differs from PA at 24 h and 72 h ($P < 0.05$).

It is noteworthy that biofilm formation on DBR surfaces is closely associated with surface roughness values.[34] Previous studies demonstrated that when the Ra of resin exceeds the clinically acceptable threshold of 0.2 μm, bacterial adhesion and biofilm formation significantly increase.[35] Therefore, controlling the surface roughness of DBR materials below this threshold is essential for minimizing bacterial attachment and preventing biofilm-associated infections. However, in this study, all DBR samples were subjected only to sandpaper polishing without additional polishing treatments, resulting in surface roughness values exceeding the threshold. Consequently, biofilm formation was observed on all material surfaces, consistent with previous research findings. This highlights an important clinical recommendation that DBR should undergo appropriate polishing procedures to reduce surface roughness and prevent microbial adhesion in clinical applications.

There are several limitations in this study, including optical properties, water absorption, and dimensional stability of 3D-printed DBRs which were not investigated. Additionally, the biocompatibility and biofilm formation assays utilized only a single cell line and microbial strain, which might not comprehensively reflect the complex oral microbiome and clinical environment. Future research should further explore these factors to obtain more-complete evaluations. Despite these limitations, the findings of this study indicate that DBRs fabricated using different manufacturing processes (PA, ML, and 3D) exhibited good biocompatibility, and that surface wettability and roughness significantly influence biofilm formation. Due to its higher hydrophobicity and lower surface roughness, 3D-printed DBRs may reduce moisture retention and bacterial adhesion, leading to more-stable biofilm formation and lower bacterial counts over time compared to other manufacturing methods. This suggests that its surface characteristics may help mitigate biofilm development, thereby reducing the risk of infection and biofilm-associated complications. Overall, 3D printing technology provides a simple and efficient method for DBR fabrication, and the findings of this study can serve as a valuable reference for clinical applications and material selection.

Declaration of competing interest

The authors have no conflicts of interest relevant to this article.

Acknowledgments

This work was supported by research grants from the National Science and Technology Council of Taiwan (112-2314-B-038-118-MY2), Division of Research Planning and Development, Department of Research and Development, Taoyuan General Hospital, Ministry of Health and Welfare (PTH114058), and the College of Oral Medicine, Taipei Medical University (TMUCOM202402).

References

1. Gad MA, Abdelhamid AM, ElSamahy M, et al. Effect of aging on dimensional accuracy and color stability of CAD-CAM milled and 3D-printed denture base resins: a comparative *in vitro* study. *BMC Oral Health* 2024;24:1124.
2. Paulino MR, Alves LR, Gurgel BCV, et al. Simplified versus traditional techniques for complete denture fabrication: a systematic review. *J Prosthet Dent* 2015;113:12—6.
3. Alqutaibi AY, Baik A, Almuzaini SA, et al. Polymeric denture base materials: a review. *Polymers* 2023;15:3258.
4. Alp G, Johnston WM, Yilmaz B. Optical properties and surface roughness of prepolymerized poly(methyl methacrylate) denture base materials. *J Prosthet Dent* 2019;121:347—52.
5. Zafar MS. Prosthodontic applications of polymethyl methacrylate (PMMA): an update. *Polymers* 2020;12:2299.
6. Taylor PB, Frank SL. Low temperature polymerization of acrylic resins. *J Dent Res* 1950;29:486—92.
7. Ferracane JL. Hygroscopic and hydrolytic effects in dental polymer networks. *Dent Mater* 2006;22:211—22.
8. Lee S, Hong SJ, Paek J, et al. Comparing accuracy of denture bases fabricated by injection molding, CAD/CAM milling, and rapid prototyping method. *J Adv Prosthodont* 2019;11:55—64.
9. Temizci T, Bozoğulları HN. Effect of thermal cycling on the flexural strength of 3-D printed, CAD/CAM milled and heat-polymerized denture base materials. *BMC Oral Health* 2024;24:357.
10. Yu HJ, Kang YJ, Park Y, et al. A comparison of the mechanical properties of 3D-printed, milled, and conventional denture base resin materials. *Dent Mater J* 2024;43:813—21.
11. Arora O, Ahmed N, Nallaswamy D, et al. Denture base materials: an i*n vitro* evaluation of the mechanical and color properties. *J Dent* 2024;145:104993.
12. Abualsaud R, Gad MM. Flexural strength of CAD/CAM denture base materials: systematic review and meta-analysis of in-vitro studies. *J Int Soc Prev Community Dent* 2022;12:160—70.
13. Batisse C, Nicolas E. Comparison of CAD/CAM and conventional denture base resins: a systematic review. *Appl Sci* 2021;11:5990.

14. Takhtdar M, Azizimoghadam N, Kalantari MH, et al. Effect of denture cleansers on color stability and surface roughness of denture bases fabricated from three different techniques: conventional heat-polymerizing, CAD/CAM additive, and CAD/CAM subtractive manufacturing. *Clin Exp Dent Res* 2023;9:840—50.
15. Dimitrova M, Corsalini M, Kazakova R, et al. Comparison between conventional PMMA and 3D printed resins for denture bases: a narrative review. *J Compos Sci* 2022;6:87.
16. Sidhom M, Zaghloul H, Mosleh IE, et al. Effect of different CAD/CAM milling and 3D printing digital fabrication techniques on the accuracy of PMMA working models and vertical marginal fit of PMMA provisional dental prosthesis: an in vitro study. *Polymers* 2022;14:1285.
17. Jeong YG, Lee WS, Lee KB. Accuracy evaluation of dental models manufactured by CAD/CAM milling method and 3D printing method. *J Adv Prosthodont* 2018;10:245—51.
18. Etemad-Shahidi Y, Qallandar OB, Evenden J, et al. Accuracy of 3-dimensionally printed full-arch dental models: a systematic review. *J Clin Med* 2020;9:3357.
19. Peng TY, Ma TL, Lee IT, et al. Enhancing dental cement bond strength with autofocus-laser-cutter-generated grooves on polyetheretherketone surfaces. *Polymers* 2023;15:3670.
20. Peng TY, Lin DJ, Mine Y, et al. Biofilm formation on the surface of (poly)ether-ether-ketone and in vitro antimicrobial efficacy of photodynamic therapy on peri-implant mucositis. *Polymers* 2021;13:940.
21. Kaushik A, Garg RK. Effect of printing parameters on the surface roughness and dimensional accuracy of digital light processing fabricated parts. *J Mater Eng Perform* 2024;33:11863—75.
22. Kang JW, Jeon J, Lee JY, et al. Surface-wetting characteristics of DLP-based 3D printing outcomes under various printing conditions for microfluidic device fabrication. *Micromachines* 2024;15:61.
23. Zhang ZC, Li PL, Chu FT, et al. Influence of the three-dimensional printing technique and printing layer thickness on model accuracy. *J Orofac Orthop* 2019;80:194—204.
24. Chaudhary R, Fabbri P, Leoni E, et al. Additive manufacturing by digital light processing: a review. *Prog Addit Manuf* 2023;8:331—51.
25. Hussain MI, Xia M, Ren X, et al. Digital light processing 3D printing of ceramic materials: a review on basic concept, challenges, and applications. *Int J Adv Manuf Technol* 2024;130:2241—67.
26. Rosa V, Silikas N, Yu B, et al. Guidance on the assessment of biocompatibility of biomaterials: fundamentals and testing considerations. *Dent Mater* 2024;40:1773—85.
27. Kreve S, dos Reis AC. Effect of surface properties of ceramic materials on bacterial adhesion: a systematic review. *J Esthetic Restor Dent* 2022;34:461—72.
28. Yue X, Suopajärvi T, Sun S, et al. High-purity lignin fractions and nanospheres rich in phenolic hydroxyl and carboxyl groups isolated with alkaline deep eutectic solvent from wheat straw. *Bioresour Technol* 2022;360:127570.
29. Gorbounov M, Halloran P, Masoudi Soltani S. Hydrophobic and hydrophilic functional groups and their impact on physical adsorption of CO_2 in presence of H_2O: a critical review. *J CO_2 Util* 2024;86:102908.
30. Barberi J, Spriano S. Titanium and protein adsorption: an overview of mechanisms and effects of surface features. *Materials* 2021;14:1590.
31. Talapko J, Juzbašić M, Meštrović T, et al. Aggregatibacter actinomycetemcomitans: from the oral cavity to the heart valves. *Microorganisms* 2024;12:1451.
32. Oopath SV, Baji A, Abtahi M, et al. Nature-inspired biomimetic surfaces for controlling bacterial attachment and biofilm development. *Adv Mater Interfac* 2023;10:2201425.
33. Fiore AD, Meneghello R, Brun P, et al. Comparison of the flexural and surface properties of milled, 3D-printed, and heat polymerized PMMA resins for denture bases: an in vitro study. *J Prosthodont Res* 2022;66:502—8.
34. Burgueño-Barris G, Camps-Font O, Figueiredo R, et al. The influence of implantoplasty on surface roughness, biofilm formation, and biocompatibility of titanium implants: a systematic review. *Int J Oral Maxillofac Implants* 2021;36:e111—9.
35. Freitas R, Duarte S, Feitosa S, et al. Physical, mechanical, and anti-biofilm formation properties of CAD-CAM milled or 3D printed denture base resins: *In vitro* analysis. *J Prosthodont* 2023;32:38—44.